REPORT NO. FAA-RD-78-146

GROUND-BASED MEASUREMENTS OF THE WAKE VORTEX CHARACTERISTICS OF A B-747 AIRCRAFT IN VARIOUS CONFIGURATIONS

U.S. Department of Transportation
Research and Special Programs Administration
Transportation Systems Center
Cambridge MA 02142

DECEMBER 1978

FINAL REPORT

Prepared for

U.S. DEPARTMENT OF TRANSPORTATION
FEDERAL AVIATION ADMINISTRATION
Systems Research and Development Service
Washington DC 20591

NOTICE

This document is disseminated under the sponsorship of the Department of Transportation in the interest of information exchange. The United States Government assumes no liability for its contents or use thereof.

NOTICE

The United States Government does not endorse products or manufacturers. Trade or manufacturers' names appear herein solely because they are considered essential to the object of this report.

Technical Report Documentation Page

1. Report No.	2. Government Accession No.	3. Recipient's Catalog No.
FAA-RD-78-146		

4. Title and Subtitle
GROUND-BASED MEASUREMENTS OF THE WAKE VORTEX CHARACTERISTICS OF A B-747 AIRCRAFT IN VARIOUS CONFIGURATIONS

5. Report Date
December 1978

6. Performing Organization Code

7. Author(s) D.C. Burnham*, J.N. Hallock*, I.H. Tombach†, M.R. Brashears**, and M.R. Barber††

8. Performing Organization Report No.
DOT-TSC-FAA-78-28

9. Performing Organization Name and Address
*U.S. Department of Transportation
Research and Special Programs Administration
Transportation Systems Center
Cambridge MA 02142

10. Work Unit No. (TRAIS)
FA-905/R9111

11. Contract or Grant No.

13. Type of Report and Period Covered
Final Report
Dec. 1975 - July 1978

12. Sponsoring Agency Name and Address
U.S. Department of Transportation
Federal Aviation Administration
Systems Research and Development Service
Washington DC 20591

14. Sponsoring Agency Code

15. Supplementary Notes

†AeroVironment, Inc.
145 Vista Avenue
Pasadena CA 91107

**Lockheed Missiles & Space Company
Huntsville Research & Eng. Ctr.
4800 Bradford Drive
Huntsville AL 35807

††NASA
Dryden Flight Research Center
Edwards CA 93523

16. Abstract

A Boeing 747 aircraft flew 54 passes at low altitude over ground-based sensors. Vortex velocities were measured by a laser Doppler velocimeter, an array of monostatic acoustic sounders, and an array of propeller anemometers. Flow visualization of the wake was achieved using smoke and balloon tracers and was recorded photographically. Data were obtained on vortex velocity fields, vortex decay, and the effects of spoilers and differential flap settings on the dissipation and structure of the vortices.

17. Key Words
Aircraft Wake Vortices
Vortices
Vortex Transport and Decay
B-747

18. Distribution Statement
DOCUMENT IS AVAILABLE TO THE PUBLIC THROUGH THE NATIONAL TECHNICAL INFORMATION SERVICE, SPRINGFIELD, VIRGINIA 22161

19. Security Classif. (of this report)	20. Security Classif. (of this page)	21. No. of Pages	22. Price
Unclassified	Unclassified	582	

Form DOT F 1700.7 (8-72) Reproduction of completed page authorized

PREFACE

The behavior of aircraft wake vortices has been studied in numerous ways: Wind tunnels and water channels have been used to simulate flight in the atmosphere, with various detecting techniques (cameras, hot-wire anemometers, laser velocimeters, etc.) used to quantify vortex properties. The smoke-marked vortices of light general-aviation aircraft have been photographed. Extensive airport tests involving vortex-tracking equipment have been, and are being, conducted to learn how vortices move and decay under various meteorological conditions; and, aircraft have been deliberately flown into the wakes of other aircraft to study the ensuing response as a function of aircraft spacings. Each of the methods for studying wakes has yielded important information about the nature and life cycle of vortices. A controlled flight test combining the essentials of each of the methods was deemed an important step to the unification of the plethora of sometimes conflicting data.

The genesis of the test program described in this report occurred at a DOT/NASA Steering Group meeting on 6-7 August 1975. It was decided that a joint flight-test program between DOT and NASA could answer a number of pressing questions. NASA offered the use of the Space Shuttle Carrier B-747, and sought data on the rollup of multiple vortices and on the nature of vortices in ground effect when vortex-alleviation techniques (i.e., spoiler deployment and differential flap settings) are used. DOT offered to provide various vortex detection and tracking equipment primarily to study the decay of vortices near the ground, especially the instability mode known as core bursting or vortex breakdown.

The flight test took place on 2-3 December 1975. The test site was the Rosamond Dry Lake on Edwards Air Force Base, California. The DOT Transportation Systems Center (TSC) provided a monostatic acoustic system for vortex tracking and strength determination and assisted in the test coordination. Under contract to TSC, AeroVironment, Inc., provided photographic coverage, three

baselines of anemometers for vortex tracking, meteorological measurements, and most of the flight-test coordination. The Lockheed Missiles of Space Company, Inc., under contract to TSC, used a mobile laser Doppler velocimeter to collect detailed velocity signatures for additional vortex-tracking and strength measurements. NASA Marshall Space Flight Center made available a filter bank processor allowing the Lockheed laser system to collect data at a higher speed than usual. NASA Flight Research Center (now the Dryden Flight Research Center) provided the primary test vehicle--the B-747--with provision for smoke marking of the vortices.

TABLE OF CONTENTS

CONTENTS (CONT'D)

CONTENTS (CONT'D)

ILLUSTRATIONS

ILLUSTRATIONS (CONT'D)

ILLUSTRATIONS (CONT'D)

ILLUSTRATIONS (CONT'D)

ILLUSTRATIONS (CONT'D)

ILLUSTRATIONS (CONT'D)

ILLUSTRATIONS (CONT'D)

ILLUSTRATIONS (CONT'D)

ILLUSTRATIONS (CONT'D)

ILLUSTRATIONS (CONT'D)

ILLUSTRATIONS (CONT'D)

ILLUSTRATIONS (CONT'D)

ILLUSTRATIONS (CONT'D)

ILLUSTRATIONS (CONT'D)

ILLUSTRATIONS (CONT'D)

ILLUSTRATIONS (CONT'D)

ILLUSTRATIONS (CONT'D)

ILLUSTRATIONS (CONT'D)

ILLUSTRATIONS (CONT'D)

ILLUSTRATIONS (CONT'D)

ILLUSTRATIONS (CONT'D)

ILLUSTRATIONS (CONT'D)

TABLES

METRIC CONVERSION FACTORS

Approximate Conversions to Metric Measures

Symbol	When You Know	Multiply by	To Find	Symbol
		LENGTH		
in	inches	2.5	centimeters	cm
ft	feet	30	centimeters	cm
yd	yards	0.9	meters	m
mi	miles	1.6	kilometers	km
		AREA		
in^2	square inches	6.5	square centimeters	cm^2
ft^2	square feet	0.09	square meters	m^2
yd^2	square yards	0.8	square meters	m^2
mi^2	square miles	2.6	square kilometers	km^2
	acres	0.4	hectares	ha
		MASS (weight)		
oz	ounces	28	grams	g
lb	pounds	0.45	kilograms	kg
	short tons (2000 lb)	0.9	tonnes	t
		VOLUME		
tsp	teaspoons	5	milliliters	ml
Tbsp	tablespoons	15	milliliters	ml
fl oz	fluid ounces	30	milliliters	ml
c	cups	0.24	liters	l
pt	pints	0.47	liters	l
qt	quarts	0.95	liters	l
gal	gallons	3.8	liters	l
ft^3	cubic feet	0.03	cubic meters	m^3
yd^3	cubic yards	0.76	cubic meters	m^3
		TEMPERATURE (exact)		
°F	Fahrenheit temperature	5/9 (after subtracting 32)	Celsius temperature	°C

Approximate Conversions from Metric Measures

Symbol	When You Know	Multiply by	To Find	Symbol
		LENGTH		
mm	millimeters	0.04	inches	in
cm	centimeters	0.4	inches	in
m	meters	3.3	feet	ft
m	meters	1.1	yards	yd
km	kilometers	0.6	miles	mi
		AREA		
cm^2	square centimeters	0.16	square inches	in^2
m^2	square meters	1.2	square yards	yd^2
km^2	square kilometers	0.4	square miles	mi^2
ha	hectares (10,000 m^2)	2.5	acres	
		MASS (weight)		
g	grams	0.035	ounces	oz
kg	kilograms	2.2	pounds	lb
t	tonnes (1000 kg)	1.1	short tons	
		VOLUME		
ml	milliliters	0.03	fluid ounces	fl oz
l	liters	2.1	pints	pt
l	liters	1.06	quarts	qt
l	liters	0.26	gallons	gal
m^3	cubic meters	35	cubic feet	ft^3
m^3	cubic meters	1.3	cubic yards	yd^3
		TEMPERATURE (exact)		
°C	Celsius temperature	9/5 (then add 32)	Fahrenheit temperature	°F

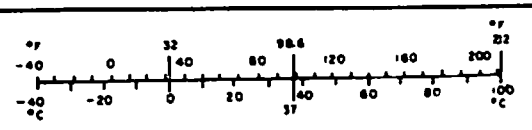

1. TEST OBJECTIVES

Four major objectives were set for the flight test: (a) to study vortex-alleviation techniques in ground effect, (b) to study vortex bursting, (c) to investigate full-scale experimental techniques, and (d) to characterize the B-747 wake.

NASA has been developing techniques to reduce the severity of a wake encounter. Through extensive wind-tunnel and water-channel testing, two potential operationally vortex-alleviation schemes have been identified for the B-747 during landing: (1) the use of a differential flap setting (the inboard flaps are deployed at 30 degrees and the outboard flaps at 1 degree) and (2) the extension of spoilers with the flaps at the normal 30-degree settings. Both schemes have been demonstrated with apparent success at altitude using intentional probings of the vortices with a high-performance aircraft. However, to be operationally useful the techniques must also be effective near the ground. The objective for the flight test was to obtain detailed measurements of alleviated and nonalleviated vortices, so that NASA could evaluate the effectiveness of the alleviation techniques for flight near the ground--the evaluation, by mutual agreement, is not addressed in this report.

In the terminal environment, the decay of vortices plays an important role in the setting of aircraft-separation standards. Before an aircraft can safely follow another aircraft to a landing, the vortices from the first aircraft must either move away from the approach corridor or their strength must decay to a level which cannot affect a following aircraft. A primary mode of decay, and the mode about which the least is known, is core bursting or vortex breakdown; that is, a sudden abrupt widening of the vortex core occurs. Core bursting has been studied in the laboratory and with small aircraft. It has been suggested that there may be an aircraft Reynolds number, or scale effect, playing a dominant role in the mechanism and in the mode of decay.

Many experimental techniques have been used to study aircraft wake vortices. In the test program, two or more methods were employed to measure the same two phenomena--vortex motion and decay. A comparison of the techniques is thus possible. The effect of the aircraft flight path is examined from the flight-test data. For instance, when the aircraft passed over the apparatus in landing configuration, sometimes it was flying straight and level (as was usually done in past tests); and sometimes it was simulating flight along a glide slope in descent.

The fourth and most important objective, however, has been to characterize the B-747 wake. Measurements were made of the wake aloft and in ground plane interaction. The rollup of the multiple vortices was recorded, and the motion and decay of the familiar vortex pair were studied. Wakes from normal landing and takeoff configurations were recorded, and the effect of superposition of the alleviation schemes on these configurations was explored.

All the useful reduced data are included in the appendixes to permit extended analyses.

2. TEST DESCRIPTION

On 2-3 December 1975, a Boeing 747 aircraft (B-747) operated by the NASA [Dryden] Flight Research Center flew 54 passes at low level over an array of ground-based sensors on the lake bed of Rosamond Dry Lake on Edwards Air Force Base, California. The vortices of the B-747 were marked by Corvis-oil smoke generators at 8 spanwise locations on the wings to enable detailed visual analysis of the behavior of the flow field in various aircraft operational configurations. Figures 1 and 2 are photographs of the tests.

Measurements and observations of vortex behavior were made simultaneously by the DOT Transportation Systems Center, the NASA [Dryden] Flight Research Center, the Lockheed Missiles & Space Company, and AeroVironment, Inc. AeroVironment coordinated the activities of the participating organizations. Test operations took place along unused runway 07-25 on Rosamond Dry Lake (Figure 3). The instrumentation array was erected across this runway (Figure 4).

The test flights were performed during early daylight hours (0700 to 1100 hours) under a range of meteorological conditions, which resulted from the natural evolution of the meteorology; i.e., from calm and stable at sunrise, to windier and more unstable conditions in the late morning, the termination of each day's tests. A variety of aircraft configurations and heights above the ground were explored although most tests were run in the normal landing configuration in level flight at a height of 60 m above ground level.

2.1 TEST AIRCRAFT

The aircraft used for these tests was a Boeing 747-123 (B-747). The aircraft's usual purpose is carrying the Space Shuttle. It was made available for these tests during a slack time in its schedule.

FIGURE 1. BOEING-747 TEST AIRCRAFT APPROACHING THE INSTRUMENTED ARRAYS. All eight smoke generators have just been turned on.

FIGURE 2. BOEING-747 TEST AIRCRAFT IN LANDING CONFIGURATION JUST AFTER PASSING OVER THE INSTRUMENTED ARRAYS. Only two smoke generators are being used.

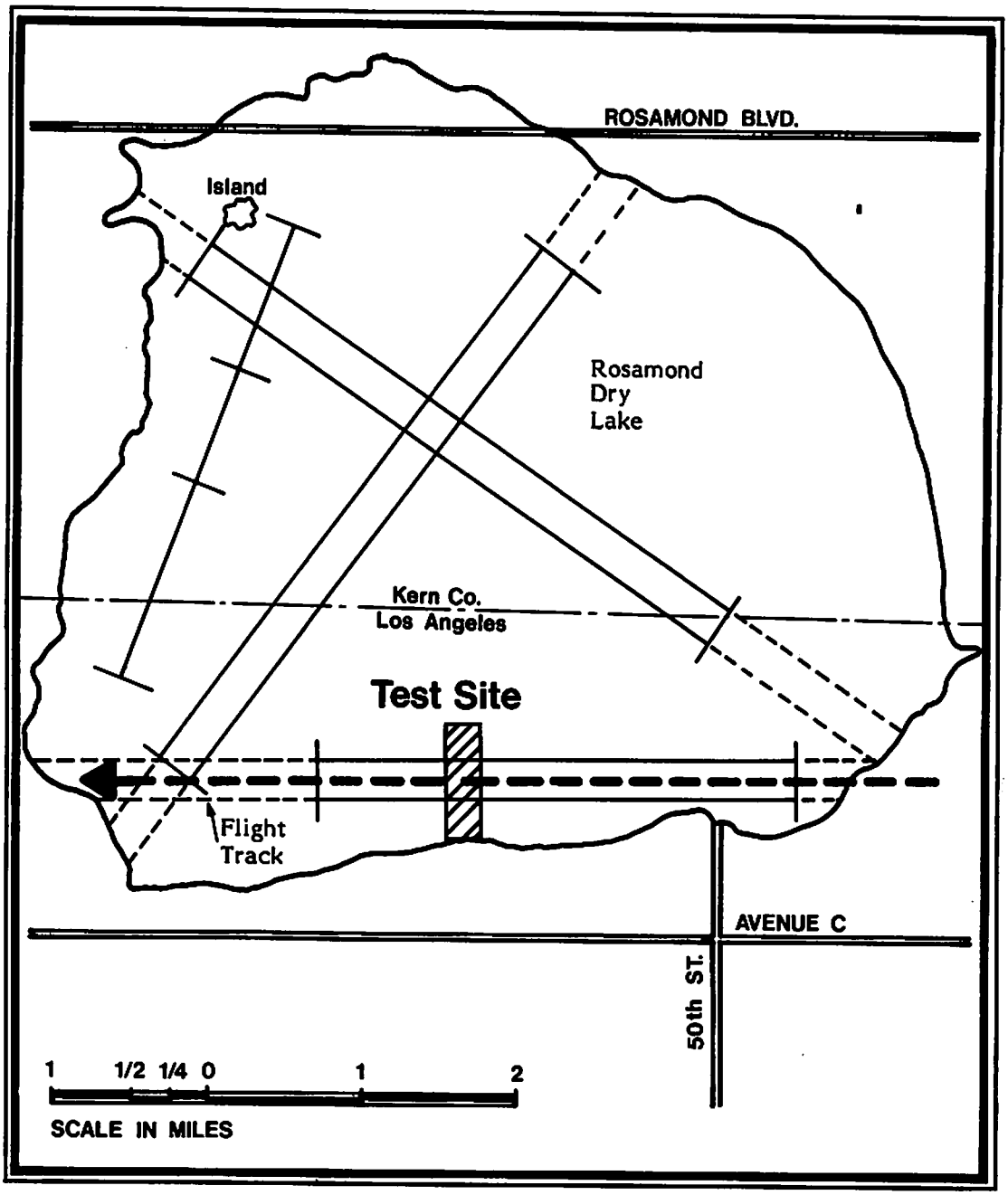

FIGURE 3. LOCATION OF TEST SITE AND FLIGHT TRACK ON ROSAMOND DRY LAKE.

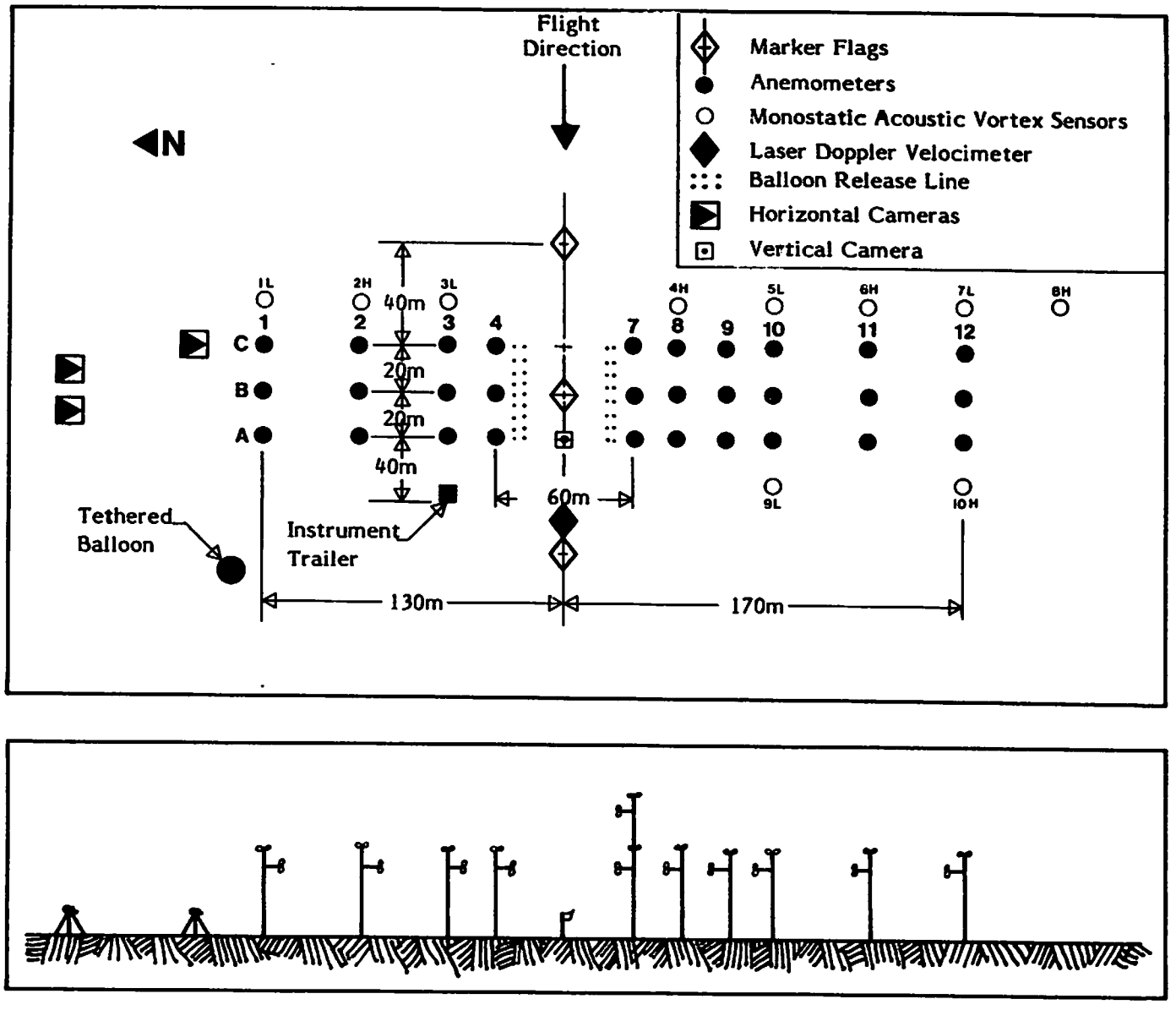

FIGURE 4. GROUND-BASED INSTRUMENTATION LAYOUT

Figure 5 presents a three-view drawing of the aircraft, and Table 1 presents the pertinent physical characteristics. Throughout this report, reference will be made to modified flaps and spoiler configurations of the test aircraft. Figure 6 presents the details of the flaps and spoilers.

The vortices were marked by Corvis-oil smoke generators at 8 spanwise locations (each wingtip, outboard ends of outboard flaps, outboard ends of inboard flaps, and inboard ends of inboard flaps). Generator locations are numbered 1 through 8 from left to right wingtips. Each generator had enough fuel and oil for about 10 minutes operation. Not all smoke generators were used on each run so that a full day's testing was possible without refilling them. The generators used to mark the vortices during a given run varied with the flap configuration and run objective. They were generally selected so as best to mark the cores of the vortices generated from the wingtips and, as appropriate, the ends of the outboard and inboard flaps.

2.2 VORTEX GENERATION

The test was flown in 7 sorties, each of which consisted of 8 runs (except for the sortie, No.3, which had to be truncated because of aircraff hydraulic problems). The intervals between the sorties were used for meteorological measurements and equipment adjustments. Data were collected for a total of 54 runs. Table 2 presents the parameters for each run on the 2 test days.

Aircraft configuration varied from run to run, with emphasis placed on as close to a normal landing configuration as operating conditions allowed. The clean configuration was also studied, and special flap and spoiler configurations were investigated for vortex-alleviation effectiveness. The Boeing 747 flew at 30 to 250 m above the ground level of 700 m mean sea level. Runs were made in straight and level flight as well as in descending and climbing flight. Descents were at about 250 m/min. A lift coefficient of about 1.4 was used for all flaps-down runs.

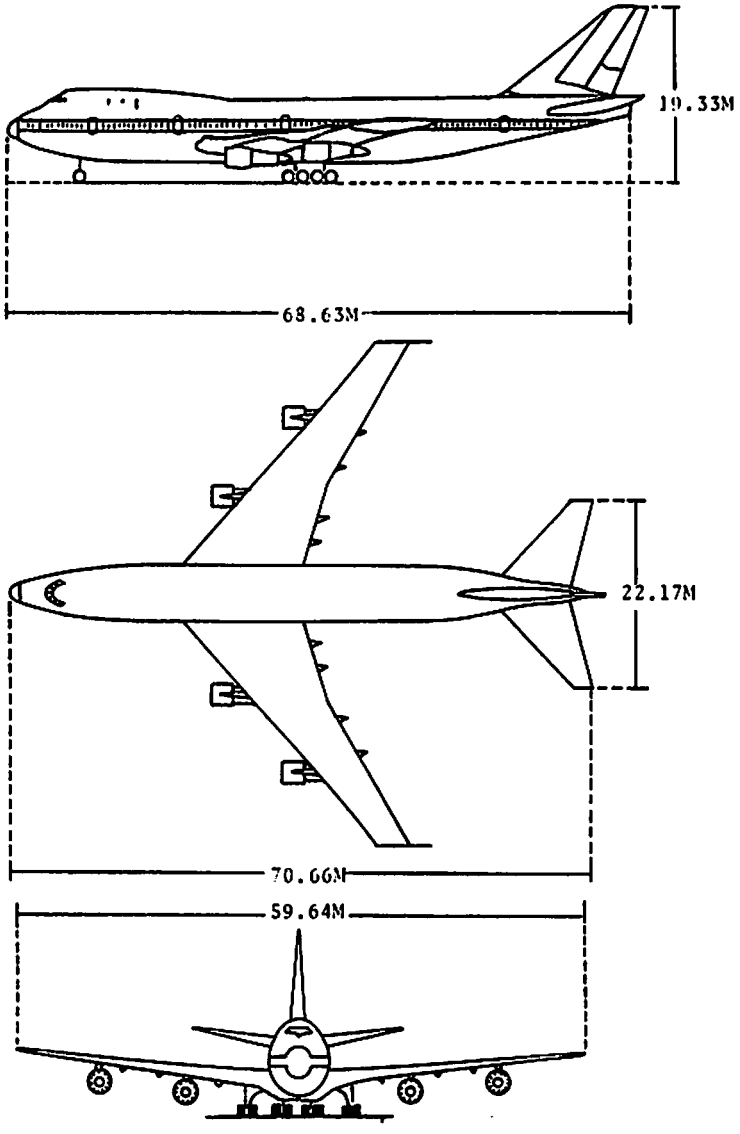

FIGURE 5. B-747 PROFILES

TABLE 1. BOEING-747 PHYSICAL CHARACTERISTICS

Length, m (ft)	70.51(231.33)
Height, m (ft)	19.33(63.42)
Wing:	
Area, m^2 (ft^2)	511(5,500)
Span, m (ft)	69.64(195.67)
Aspect ratio	6.96
Sweep at quarter chord	37.5
Mean aerodynamic chord, m (ft)	8.33(27.32)
Incidence angle, deg	2
Dihedral angle, deg	7
Taper ratio	0.356
Control surfaces:	
Rudder area, m^2 (ft^2)	22.9 (247)
Rudder deflection, deg	15
Elevator area, m^2 (ft^2)	32.5 (350)
Elevator deflection, deg	-23 to 17
Aileron area (total), m^2 (ft^2)	20.9 (222)
Aileron deflection, deg -	
Inboard	20
Outboard	-25 to 15
Spoiler area (total), m^2 (ft^2)	30.8 (331)
Spoiler deflection, deg -	
Panels 6 to 8	20
Panels 1 to 4, 9 to 12	45
Trailing edge flap area (total), m^2 (ft^2)	76.7 (847)
Trailing edge flap defection, deg	30
Leading edge flap area (total), m^2 (ft^2)	48.1 (518)
Weight, kg (lb):	
Empty	158,220(348,816)
Maximum takeoff	322,050(710,000)

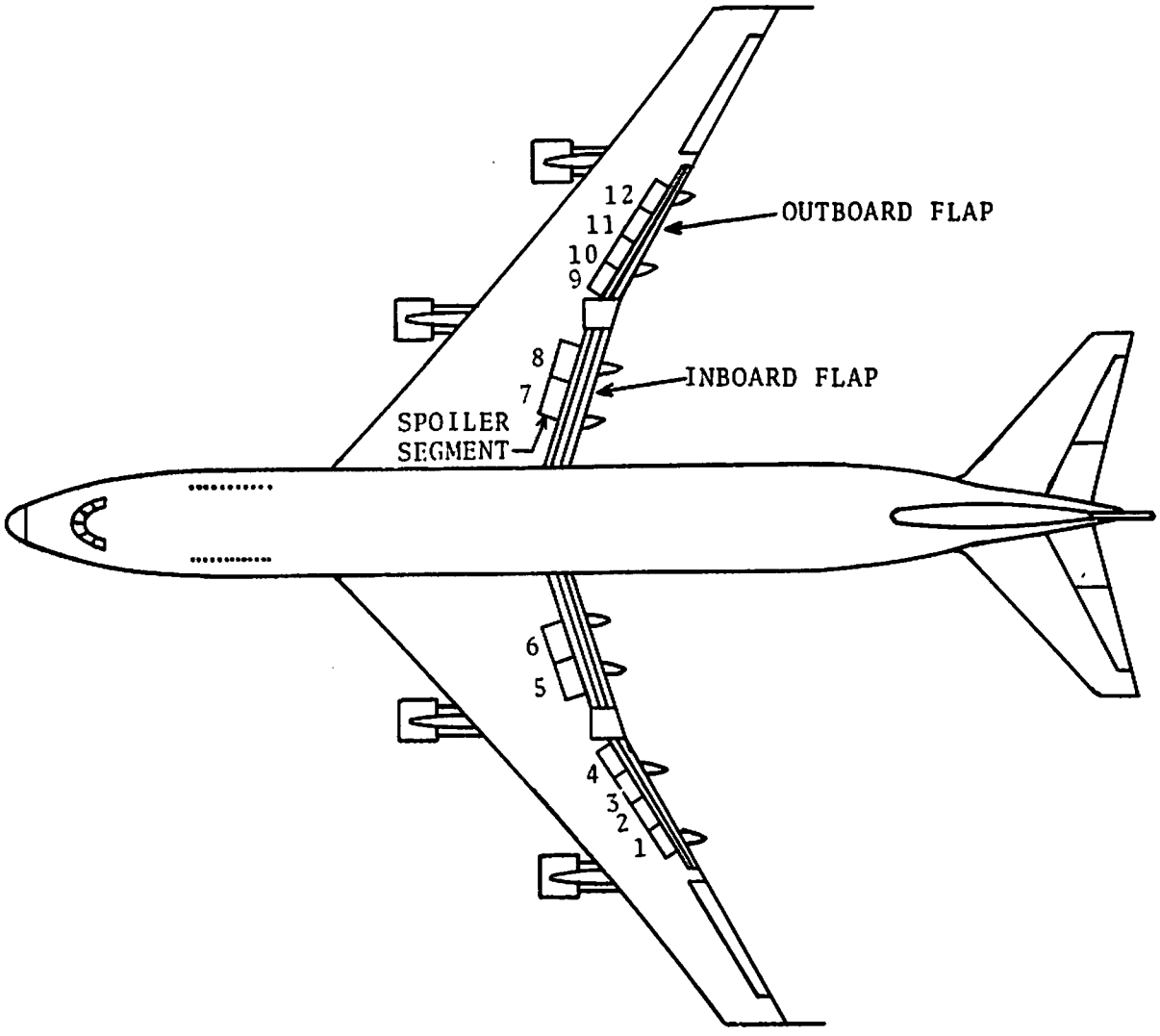

FIGURE 6. B-747 SPOILERS AND FLAPS

TABLE 2. BOEING-747 TEST-CONDITION SUMMARY

WS - Wind speed at 7 m above the surface
WD - Direction from which the wind blows
$\varepsilon^{1/3}$ - Atmospheric turbulence dissipation rate at the flight altitude
γ - Atmospheric stability, dT/dz, at the flight altitude
Ldg - Aircraft descending over array
TO - Aircraft climbing over array
* - Nominal altitude assigned to aircraft; measured value not obtained

Time (PST)	Run	Test Configuration							Meteorology			
		Altitude (m)	TAS (m/s)	Weight (10^3kg)	Flap (deg)	Gear	Spoiler	Thrust (EPR)	WS (m/s)	WD (deg)	$\varepsilon^{1/3}$ ($cm^{2/3}s^{-1}$)	γ (C/100m)
12/2/75												
0707	1	66	79	255	30/30	Dn	No	1.25	0	190	0.7	12
0713	2	62	79	251	30/30	Dn	No	1.21	1	190	0.7	11
0718	3	68	78	250	30/30	Dn	No	1.25	1	180	0.8	10
0725	4	65	78	249	30/30	Dn	No	1.22	1	180	0.8	9
0730	5	122*	78	248	30/30	Dn	No	1.22	1	210	0.8	9
0735	6	122*	78	247	30/30	Dn	No	1.23	1	240	0.9	8
0740	7	244*	77	245	30/30	Dn	No	1.23	1	270	1.4	1
0745	8	244*	77	244	30/30	Dn	No	1.20	1	310	1.4	1
0818	9	61*	77	235	30/30	Dn	Yes	1.26	1	140	2.8	1
0823	10	122*	77	234	30/30	Dn	Yes	1.26	1	210	0.7	2
0824	11	91*	77	233	30/30	Dn	Yes	1.25	1	280	1.4	5
0835	12	244*	77	231	30/30	Dn	Yes	1.25	1	0	1.0	3
0841	13	64	77	230	30/30	Dn	Yes	1.24	1	0	2.5	1
0847	14	65	75	228	30/30	Dn	No	1.20	1	10	2.5	0
0852	15	61*	75	227	30/30	Dn	No	1.20	1	10	2.6	0
0858	16	61*	75	226	30/30	Dn	No	1.18	1	10	2.7	0

TABLE 2. BOEING-747 TEST-CONDITION SUMMARY (CONTINUED)

Time (PST)	Run	Test Configurations							Meteorology			
		Altitude (m)	TAS (m/s)	Weight (10^3 kg)	Flap (deg)	Gear	Spoiler	Thrust (EPR)	WS (m/s)	WD (deg)	$\varepsilon^{1/3}$ ($cm^{2/3}s^{-1}$)	γ (C/100m)
0932	17	30*	76	222	30/1	Dn	No	1.19	1	20	2.5	1
0938	18	37	76	217	30/1	Dn	No	1.18	1	60	3.0	1
0942	19	38	76	216	30/1	Up	No	1.18	1	100	3.0	1
0947	20	67	75	215	30/1	Dn	No	1.18	1	130	3.0	0
0951	21	64	75	213	30/1	Up	No	1.16	0	--	3.0	-1
0956	22	91*	75	212	30/1	Dn	No	1.23	0	--	4.0	-1
12/3/75												
0654	23	122*	79	260	30/30	Dn	No	1.24	1	190	0.6	8
0658	24	122*	119	258	0/0	Up	No	1.03	1	190	0.6	8
0703	25	122*	79	257	30/30	Dn	No	1.24	1	180	0.6	7
0707	26	122*	116	256	0/0	Up	No	1.06	1	180	0.6	7
0712	27	67 Ldg	79	255	30/30	Dn	No	1.20	1	180	0.6	6
0716	28	66	79	255	30/30	Dn	No	1.20	1	180	0.6	6
0721	29	72 Ldg	79	253	30/30	Dn	No	1.14	1	180	0.6	6
0725	30	66	78	251	30/30	Dn	No	1.24	1	180	0.7	6
0750	31	106*TO	84	243	10/10	Up	No	1.38	0	--	0.9	5
0801	32	65	84	242	10/10	Up	No	1.11	0	--	0.5	6
0806	33	57 TO	84	241	10/10	Up	No	1.36	1	310	0.5	6
0811	34	59	77	240	10/10	Up	No	1.15	1	320	0.5	6
0816	35	63	77	239	30/30	Dn	No	1.20	1	340	0.5	6
0821	36	68	77	238	30/30	Up	No	1.20	1	0	0.5	5
0826	37	67	76	237	30/30	Dn	No	1.21	1	10	0.5	5
0831	38	61*	76	236	30/30	Up	No	1.22	1	20	0.5	5

TABLE 2. BOEING-747 TEST-CONDITION SUMMARY (CONTINUED)

Time (PST)	Run	Test Configuration							Meteorology			
		Altitude (m)	TAS (m/s)	Weight (10^3 kg)	Flap (deg)	Gear	Spoiler	Thrust (EPR)	WS (m/s)	WD (deg)	$\epsilon^{1/3}$ ($cm^{2/3}s^{-1}$)	γ (C/100m)
12/3/75												
0902	39	47 TO	82	230	10/10	Up	Yes	1.36	0	--	1.1	1
0907	40	46	82	228	10/10	Up	No	1.36	1	110	1.3	1
0913	41	48	81	227	10/10	Up	Yes	1.36	1	120	1.5	1
0919	42	54	81	226	10/10	Up	No	1.40	1	130	1.7	1
0924	43	61*	75	225	30/30	Dn	No	1.24	1	110	1.9	1
0929	44	63 Ldg	75	224	30/30	Dn	No	1.12	1	90	2.1	-1
0935	45	50	75	223	30/30	Dn	No	1.16	1	80	2.3	-1
0940	46	37	74	222	30/30	Dn	No	1.24	1	60	2.5	-1
1012	47	91*	73	215	30/30	Dn	No	1.15	1	160	3.2	0
1016	48	91*	73	214	30/30	Dn	Yes	1.20	1	160	3.2	0
1022	49	37	72	212	30/30	Dn	Yes	1.20	1	150	3.2	-1
1026	50	91*Ldg	72	211	30/30	Dn	No	1.11	1	150	2.0	0
1031	51	122*	108	210	0/0	Dn	No	1.11	1	140	1.0	2
1035	52	122	108	208	0/0	Up	No	1.03	1	130	0.8	2
1039	53	122	72	208	30/30	Dn	No	1.22	1	120	0.7	2
1043	54	122	108	207	0/0	Up	No	1.05	1	120	0.5	2

Of the 54 runs, 35 (or about 65 percent) were made with both the inboard flaps lowered 30 degrees and the outboard flaps lowered 30 degrees (denoted 30/30); 8 (approximately 15 percent) with 10/10 flaps; and 5 (approximately 9 percent) with flaps retracted. The remaining 6 runs had the inboard flaps lowered 30 degrees and the outboard flaps lowered 1 degree, to test the effects of this configuration on vortex alleviation. For each flap setting, runs were conducted with the landing gear down or retracted, and on some runs, spoilers were deployed in addition to the flaps.

In Table 2, the flap angles are given for the inboard flaps first, then for the outboard flaps. Whenever spoiler extension is indicated, this denotes that the number 1, 2, 11 and 12 spoilers were deflected upward 41 degrees.

2.3 VORTEX MEASUREMENTS

Five types of intrumentation were used to record vortex behavior and to monitor the atmospheric conditions prevailing at the test site. Vortex-induced velocities were measured by a laser Doppler velocimeter (LDV), an array of monostatic acoustic sounders, and an array of propeller anemometers. Qualitative details of the visual behavior of the smoke-marked vortices were recorded photographically by an assortment of motion and still cameras on the ground and overhead in a helicopter. The atmospheric winds, turbulence, and stability were monitored by various sensors on the ground, suspended from a tethered balloon, and carried in a light aircraft.

Comprehensive discussions of the various experimental techniques are contained in Sections 3 through 7. The basic principles of each technique and the measurements made by each are reviewed here.

The LDV, operated by the Lockheed Missiles & Space Company, first emits a beam of radiation. Then, it senses the Doppler shift in the wavelength of signal scattered back by small particles in the air along the laser beam, thereby measuring the speed of these

particles (and hence, the air) toward or away from the laser. The signals from the LDV receiver were recorded on magnetic tape at two sampling rates for subsequent computer analysis.

On the first test day (December 2), the LDV was directly under the flight path and scanned arcs in a plane perpendicular to the flight path, with a complete arc every second. Scans were at fixed range until the vortex passed through the scan arc, at which time the sensor range was lowered and remained fixed again until the vortex descended through the new range. On the second test day (December 3,) the LDV was moved 60 m north of the flight path, and scanned simultaneously over elevation and range, with elevation scanning at a frequency of 0.2 Hz and range scanning at a rate of 2 to 2.5 Hz. On the last sortie, the laser was swung in azimuth whenever cross winds caused a vortex to pass over it, and thus, it looked at axial flow briefly before scanning to the north side as the vortex moved away from it. The effective range of the LDV for these tests was greater than 300 m.

An attempt was made to use the LDV to obtain atmospheric wind profiles. The winds on the test days were generally quite low, however, and were generally within only the first velocity gate of the spectral analyzer. Consequently, useful information on the variation of winds with height could not be obtained in this way.

The monostatic acoustic vortex sensor system (MAVSS) was operated by the Transportation Systems Center. It consisted of 10 vertically pointing monostatic acoustic sounders. Each sounder transmitted a pulse of sound every 400 ms, and then, detected the Doppler shift in the frequency of the sound scattered by small-scale temperature structure in the air. Thus, the vertical speed of air was determined directly over the antenna. The signals from the returned echoes were recorded in analog form on magnetic tape, and were subsequently analyzed for the Doppler shift. The return signals were divided into 15 range gates, each of which is approximately 4-m high; thus, the total range was 60 m. As a vortex passed over a MAVSS antenna, transported by a cross wind or by its own induction, a profile of the vertical velocities in the vortices was

obtained. The MAVSS configuration differed slightly on the second day from that of the first day as antennas 9 and 10 (see Fig. 4) were both moved about 40 m west to reduce interference with the main sensor line.

The anemometer array, operated by AeroVironment Inc., consisted of 30 standards, each of which supported at least two R.M. Young propeller anemometers. Except for standards 7A, 7B, and 7C (see Fig. 4), the anemometers were mounted in pairs at 4 m above the ground. The axis of one was oriented toward the flight path centerline to measure the horizontal wind component transverse to the flight path. The axis of the second was oriented vertically to measure the vertical component. Thus, these sensors recorded the tangential velocities induced by the vortices. The standards in row 7 also had an additional anemometer at the 4-m level with its axis oriented along the flight path to detect axial flow in the vortices. A second identical set of three anemometers was placed at the 7-m level on each of the same standards. In addition, a 3-component hot-wire anemometer system was located at the 7-m level on standard 7B to record vortex velocities with a higher frequency response than possible with the propeller anemometers. The propeller anemometers have a response threshold of 0.2 m/s and a 1/e response distance of about 1 m.

Data from this anemometer array were recorded at 0.5-sec intervals on digital magnetic tape with backup recording of all channels on light-beam oscillographs. The same recording system also recorded the data from the turbulence and temperature measurement system below the tethered balloon. The clock in this recording system was the master clock for the experiments; the clocks for the cameras were synchronized with it. Synchronization of the records of the AeroVironment, DOT-TSC, and Lockheed recording systems was obtained by recording a time mark at the moment that the aircraft crossed over the flag at the east end of the array.

Photographic equipment was operated at various locations at the test site by both AeroVironment and NASA to record vortex motion and decay. A 35-mm still camera directly beneath the flight

path, operated at a high framing rate, recorded the rollup of the vortices. Two cameras (one 35-mm still and one 16-mm motion) to the north side of the flight path photographed vortex descent and visual indications of vortex decay and instability. A 35-mm camera in a helicopter hovering 400 to 500 m overhead provided records of the lateral motion of the vortices. General observation of vortex behavior was made with a 16-mm motion-picture camera to the east of the test array.

As a visual indication of axial flow in the vortex cores, during a few runs, AeroVironment released several small buoyant balloons from the ground after the B-747 had passed. These balloons rose to the wake height and, if close enough to the vortex core, were centrifuged into the lower pressure area in the core. The axial motion of these balloons was recorded photographically by cameras, including one motion-picture camera operated specifically for this purpose.

Marker flags at various locations in the array provided definite location references for the various ground-based and airborne cameras, and were used for calling out timing marks to indicate aircraft passage.

2.4 METEOROLOGICAL MEASUREMENTS

A variety of meteorological measurements were made during the tests. A light aircraft (Cessna 182, operated by AeroVironment) was instrumented with a temperature sensor and a Universal Indicated Turbulence System. This aircraft flew alongside the B-747 to record ambient temperature during each run, and performed vertical soundings from the surface to 300 m above the ground at the beginning and end of each sortie.

A second turbulence and temperature system (developed by AeroVironment) was suspended beneath a tethered balloon just northeast of the array. The sensors for this system were generally suspended at flight altitude (with a maximum height of 60 m) during the runs, and were used to obtain detailed soundings from 7 to 60 m above

the ground at the beginning and end of each sortie.

Winds were measured continuously by the anemometer array, and vertical profiles of wind were recorded between sorties by photographic tracking of pilot balloons (by AeroVironment) and, as mentioned earlier, by the LDV system.

3. METEOROLOGICAL MEASUREMENTS

The meteorology which apparently most affects vortex behavior is defined by vertical profiles of temperature and turbulence and by a three-dimensional description of the wind vector field. The flight tests were performed under a wide range of meteorological conditions, which resulted from the natural evolution of the meteorology from calm and stable conditions at sunrise to windier and more unstable conditions at the termination of each day of tests. The information previously presented in Table 2 characterizes these conditions for the flight test.

3.1 MEASUREMENT TECHNIQUES

The wind data in Table 2 were obtained from the 7-m anemometer during each run, prior to the time at which the vortices had descended sufficiently to affect the anemometer readings.

The turbulence and lapse rate data were obtained by both the meteorological aircraft and the tethered balloon system. The primary source of the turbulence information was the Universal Indicated Turbulence System (UITS) aboard the meteorological aircraft. The UITS measured horizontal turbulent wind-speed variations, and processed the information to compute the turbulence dissipation rate, $\varepsilon^{1/3}$, under the assumption of homogeneity and isotropy of the turbulence field. Since the meteorological aircraft flew alongside the B-747, the turbulence field which affected the vortices generated during each run was defined. Further, to define the vertical profile of $\varepsilon^{1/3}$, and as a backup measurement, soundings from the surface to 300 m were made before and after each sortie.

A totally separate turbulence system, which consisted of 2 vertically oriented propellers suspended above each other, 10 m apart, under the tethered balloon, is shown in Fig. 7. The root-mean-square (rms) difference in the vertical speeds measured by the two propellers is the basis for computing the velocity-structure

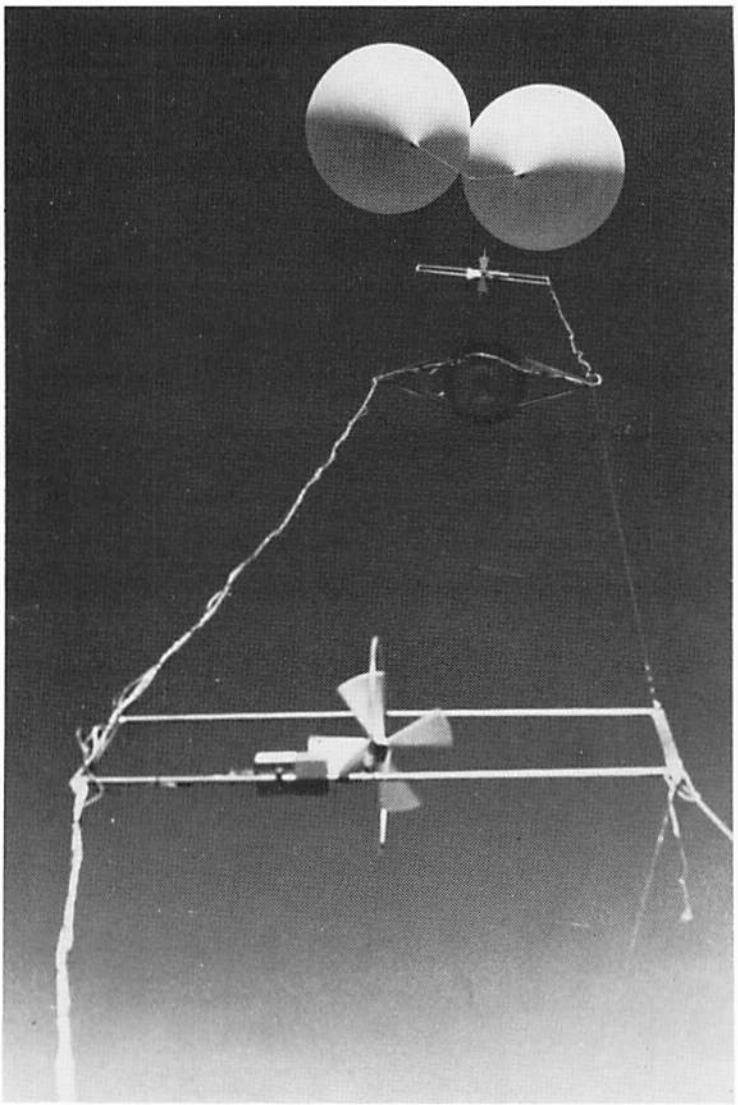

FIGURE 7. VIEW UPWARD AT TURBULENCE AND TEMPERATURE SENSORS SUSPENDED BENEATH TWO TETHERED BALLOONS

function of the atmosphere, which relates directly to the dissipation rate, $\epsilon^{1/3}$, if isotropy is assumed. The sensors under the balloon were suspended at the flight altitude of the B-747 (if under 60 m; otherwise they were placed at 60 m above the ground) during the test runs. In addition, they were used for soundings; i.e., 1-minute samples at 8, 15, 30, and 60 m between sorties.

Both the aircraft and the balloon systems also included temperature sensors, which provided vertical temperature profiles (in terms of the lapse rate $\gamma = \frac{\partial T}{\partial z}$) during the soundings. The redundancy in measurements allowed cross checks of the data, and increased the amount of reliable data obtained.

The winds aloft were profiled before and after each sortie by the LDV and by the photographic tracking of the ascent of pilot ballons (pibals). The LDV measurements were not successful at providing wind-aloft data because the LDV wind-speed gates were set up for the higher speed vortex flows, and were not optimum for the low wind speeds encountered. The pibals provided wind data from the surface to 300 m.

3.2 DISCUSSION OF RESULTS

Table 2 summarized the important meteorological features which influenced the vortices during each run. Figures 8 and 9 display the temperature and turbulence structure of the atmosphere during the two test days.

By way of interpretation, the temperature profiles at the beginning of a test day (at dawn) indicated a very stable atmosphere near the surface; one resistant to vertical disturbances. The lowest temperatures were encountered at the ground level, which had cooled by radiation during the night. Consequently, the near-ground air temperature usually increased with altitude to some inversion height, above which the temperature decreased adiabatically with height. After sunrise, the ground and the air immediately above warmed gradually until, by mid-morning, the temperature profile was neutrally stable (decreased adiabatically with height)

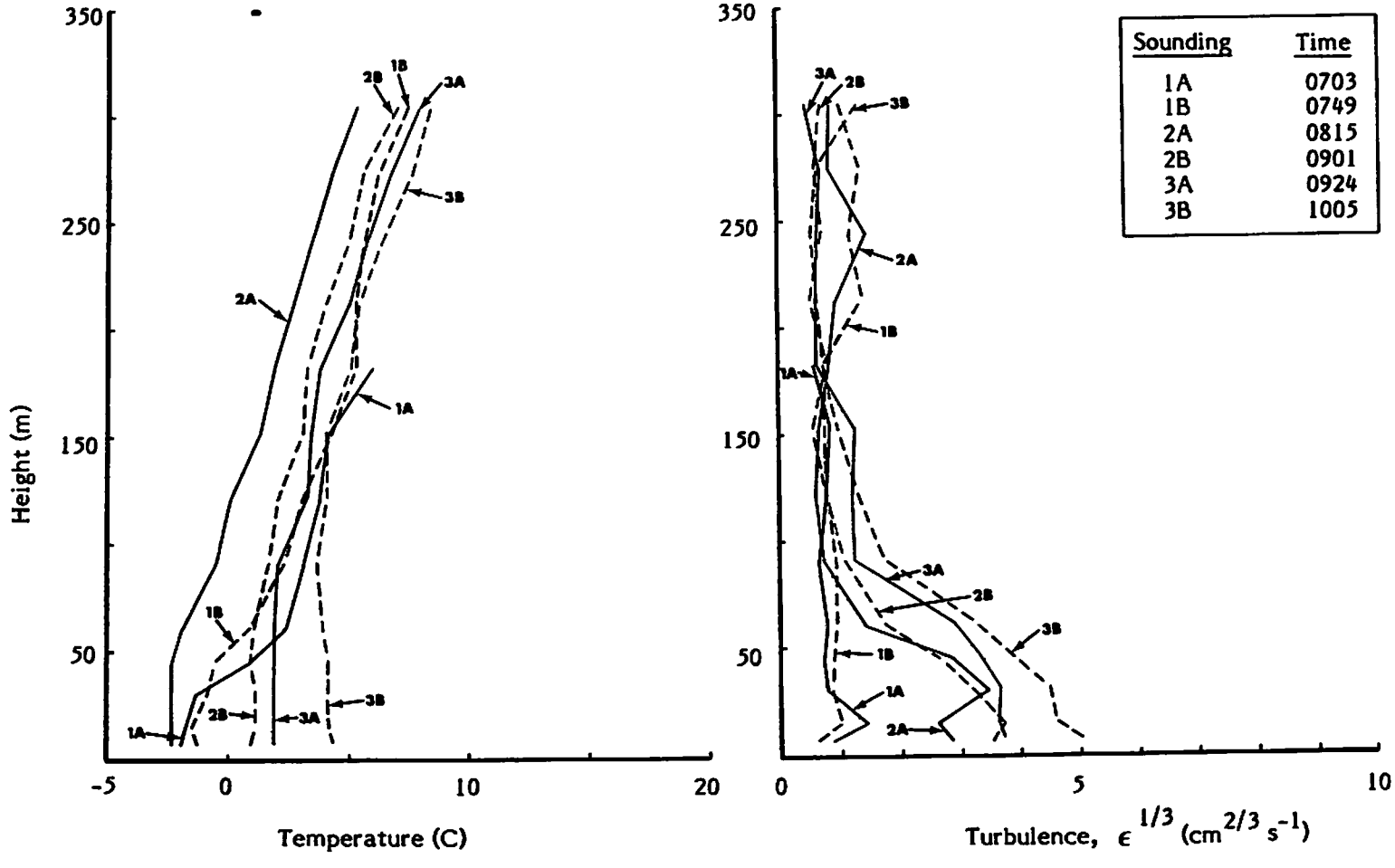

FIGURE 8. TEMPERATURE AND TURBULENCE VERSUS ALTITUDE FROM AIRCRAFT SOUNDINGS ON 2 DECEMBER 1975

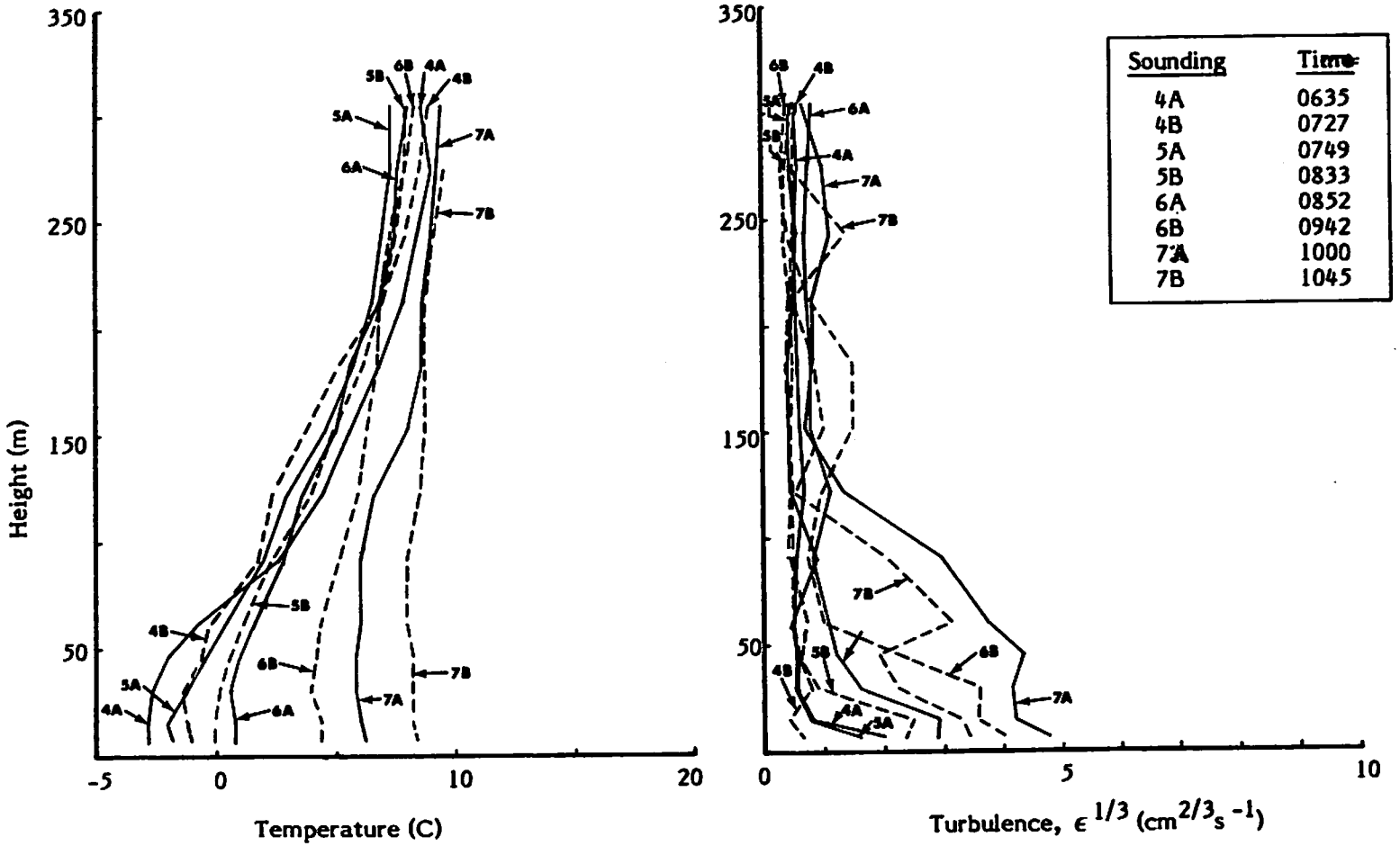

FIGURE 9. TEMPERATURE AND TURBULENCE VERSUS ALTITUDE FROM AIRCRAFT SOUNDINGS ON 3 DECEMBER 1975

to become unstable when the warmer-than-adiabatic air near the ground rose vertically, and caused a turbulent overturning motion in the atmosphere.

The turbulence levels at the low flight altitudes generally increased as the atmosphere became less stable as the morning progressed. An anomalous situation occurred in the lowest 30 m in the very stable early morning period, however. The drainage flow from nearby mountains caused stable layers to slide over one another, and the resulting shears generated turbulence in spite of the very stable density distribution. This situation has been discussed by Tombach et al. (Ref. 1).

The desert winds were generally light in the early morning and were mainly caused by drainage flow from the south. The result was airflow crosswise to the flight path. The wind direction became variable as the morning progressed, without a measurable increase in wind speed. As an example, Fig. 10 shows the wind profile at 1000 Pacific Standard Time on 2 December. There is no appreciable wind throughout the 125-m record height. A shear layer, such as the one near 80 m, was frequently observed.

The lapse rate γ and turbulence $\varepsilon^{1/3}$ listed in Table 2 were those for the region of the atmosphere just below the generating aircraft. Usually, the variation in γ and $\varepsilon^{1/3}$ with height was not very rapid, and thus, this γ and ε adequately defined the average atmospheric condition encountered by the decending vortices. There was a notable exception, however, around 60 m above ground level during Runs 10 through 18. A strong gradient in turbulence was present at that level, with turbulence below that level much greater than above it. Note large difference in turbulence between Runs 13 and 14 in Table 2 as the turbulent layer grew and engulfed the flight level). Soundings 2A and 2B in Fig. 8 show the development of this turbulent layer. Fig. 10 shows the shear layer at 80 m in a sounding mode just after Run 18. Since the gradients were rather abrupt, a small error in the altitude of the meteorological aircraft vis-a-vis the B-747 could alter the listed turbulence level by a considerable amount.

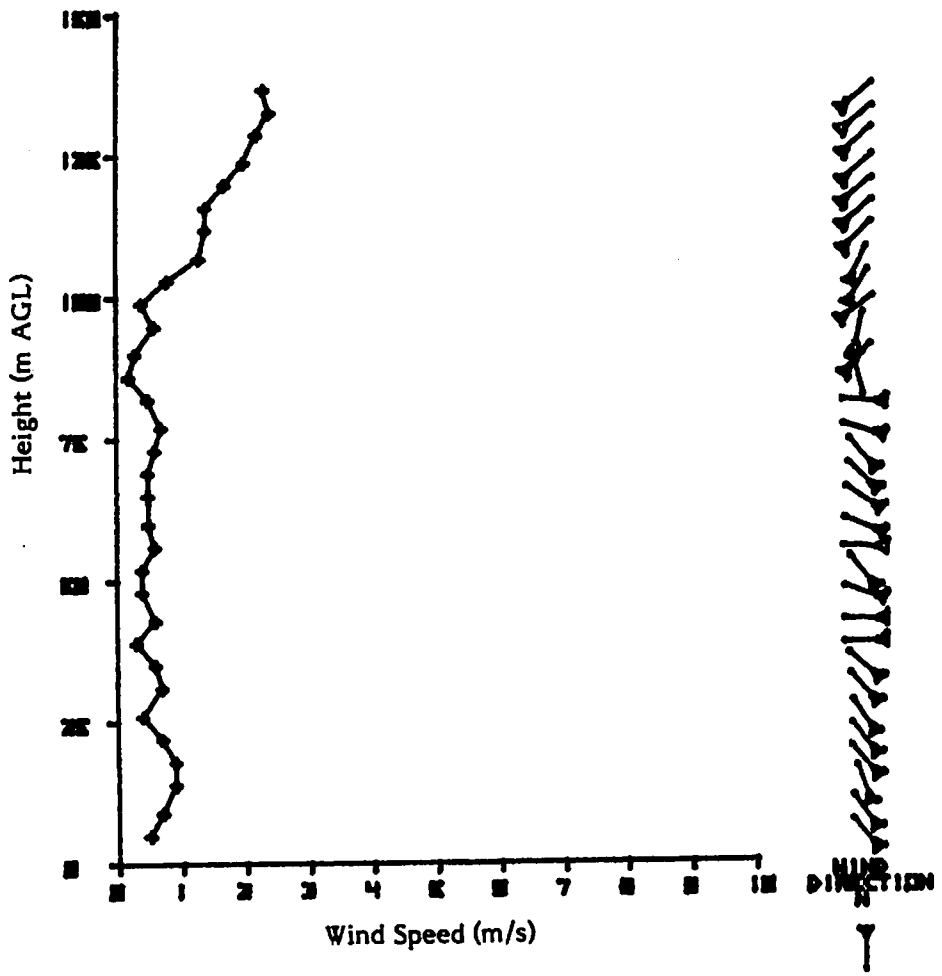

FIGURE 10. PILOT BALLOON MEASUREMENT OF NEAR-SURFACE WIND PROFILE AT 1000 ON 2 DECEMBER 1975

4. PHOTOGRAPHIC MEASUREMENTS

Photography of the smoke-marked vortices was used to define vortex behavior, including specifically:

Vortex rollup immediately behind the aircraft,
Trajectories of vortex descent and lateral motion,
Development of vortex instabilities, and
Axial flow, as marked by smoke and buoyant balloons.

4.1 MEASUREMENT TECHNIQUES

To visualize vortex rollup, a motor-driven 35-mm still camera with an extreme wide-angle lens was mounted directly beneath the flight path, looking upward. It photographed the aircraft passage and subsequently marked the vortex behavior at 1/2-second intervals for the first 18 seconds after aircraft passage.

Two camera locations were used to record vortex transport and breakdown. Motor-driven 35-mm still cameras to the side of the flight path and directly overhead (in a helicopter) took pictures of the vortices at 5-second intervals as long as the smoke persistence allowed. Digital clocks installed on the cameras allowed synchronization of the photographs. In addition, a 16-mm motion-picture camera was collocated with the 35-mm camera to the side of the flight path, to record the dynamic aspects of transport and decay.

To visualize the axial flow in the vortices, small buoyant balloons were released from the ground as the B-747 passed overhead, as shown in Fig. 11. Because of their buoyancy, these balloons ascended, and some of them were centrifuged into the low-pressure vortex cores (see Fig. 12). There, they followed the mean velocity of the portion of the core comparable in size with their diameter. The motion of these balloons was photographed by the normal vortex-tracking cameras, as well as in greater detail by a 16-mm motion-picture camera used specifically for the purpose.

FIGURE 11. BUOYANT BALLOONS BEING RELEASED TO MARK THE AXIAL FLOW IN THE DESCENDING VORTEX JUST AT THE TOP OF THE PHOTOGRAPH. The vortex is not visible in this reproduction.

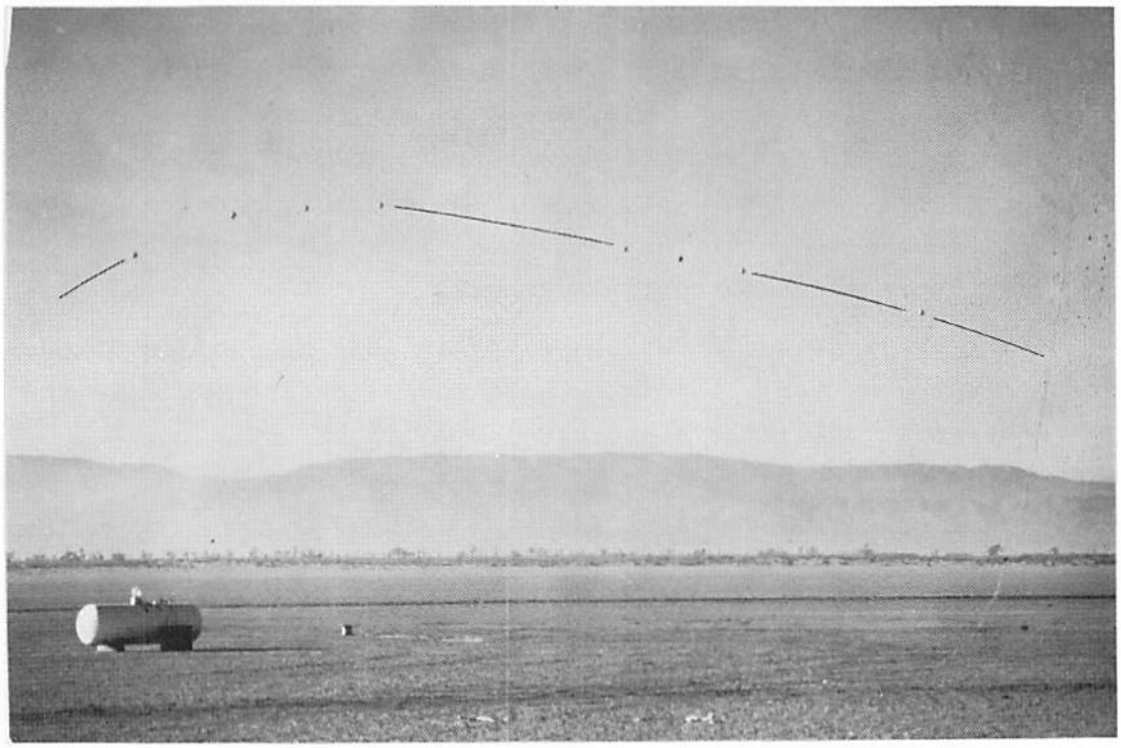

FIGURE 12. BUOYANT BALLONS MARKING THE CORE OF ONE VORTEX. The solid lines show the vortex centerline implied by the balloons.

4.2 VORTEX ROLLUP

The initial development of the trailing vortices was of interest for understanding the effects of flaps, spoilers, and landing gear, and of normal and unusual combinations of them, on the ultimate behavior and decay of the organized vortex wake. Photographs of the vortices for the first few spans behind the aircraft, taken in rapid sequence by an upward-pointing camera on the ground, illustrate this initial behavior.

As an example of the results obtained, Fig. 13 shows several montages of photographs of the vortex rollup process for the first 7 to 9 seconds. The photographs were taken at 1/2-second intervals by a camera pointing directly upward. A cable above the camera, strung crosswise to the flight path, provides a reference for direction and position, and is visable on each frame. The frames have been mounted in spatial sequence in Fig. 13 to illustrate the apparent evolution of the wake behind the aircraft. Actually, all frames have been taken of the same point in space, and thus, show the behavior of the same vortex segments.

The first sequence shows the B-747 in landing configuration, and descending as for a landing; while the second sequence is the same configuration, in straight-and-level flight. The third sequence shows a clean configuration wake, and the fourth is a landing configuration moments later.

Previous studies (Refs. 2 and 3) have shown the importance of the spanwise positions of smoke injection, injection directly into the vortex core is necessary for meaningful interpretation of the size and dissipation of the visualized vortices. Because the apparent origin of vortices moves inboard as the flaps are lowered, the tip smoke generators (1 and 8) were used for the clean configuration, while those at the inboard ends of the outboard flaps (2 and 7) were used with flaps down. Even so, the smoke injection was not always perfectly into the core; note the spiraling of smoke around the top (port) vortex at 1 to 2 seconds on Run 29 (Fig. 13).

Run 29 Aircraft landing, 30/30 flaps, gear down, smokers 2 and 7

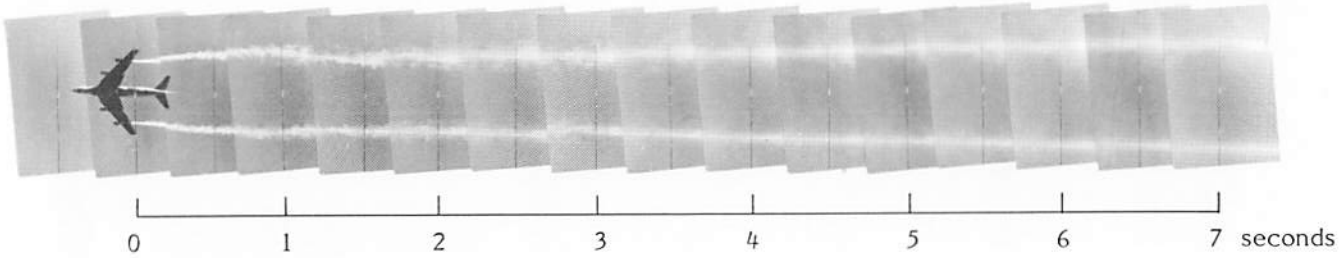

Run 47 Level flight, 30/30 flaps, gear down, smokers 2 and 7

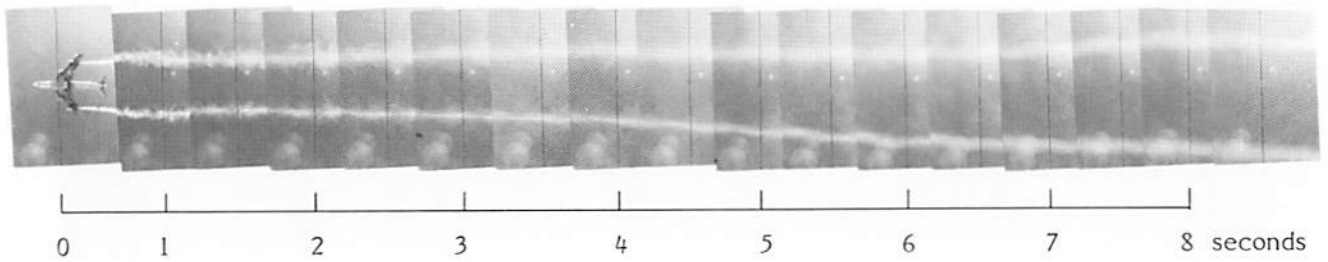

FIGURE 13. SEQUENCES OF PHOTOGRAPHS OF ROLLUP OF VORTICES. Although mounted in sequence to show the spatial evolution, the photos actually all show the same vortex segment at 1/2-sec intervals. The horizontal and vertical scales are identical for Run 29, all others use the same time scale, which results in a distortion of the horizontal-length scale. The apparent vortex spreading to the right is an optical effect resulting from the vortices descending closer to the camera.

Run 52 Level flight, 0/0 flaps, gear up, smokers 1, 4, 5 and 8

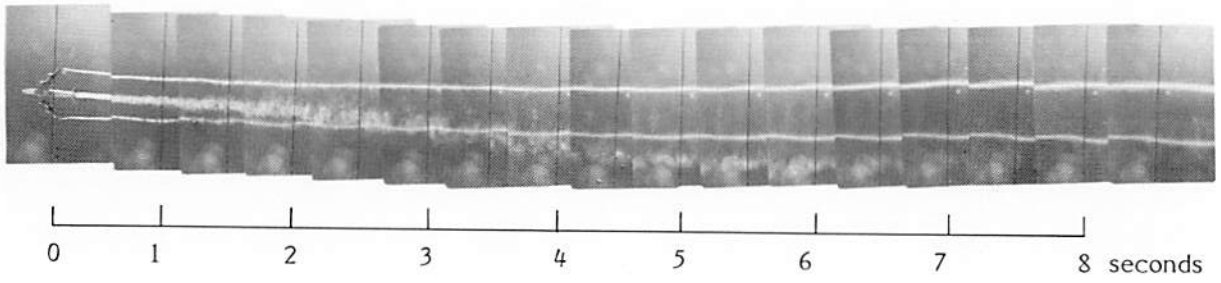

Run 53 Level flight, 30/30 flaps, gear down, smokers 2 and 7

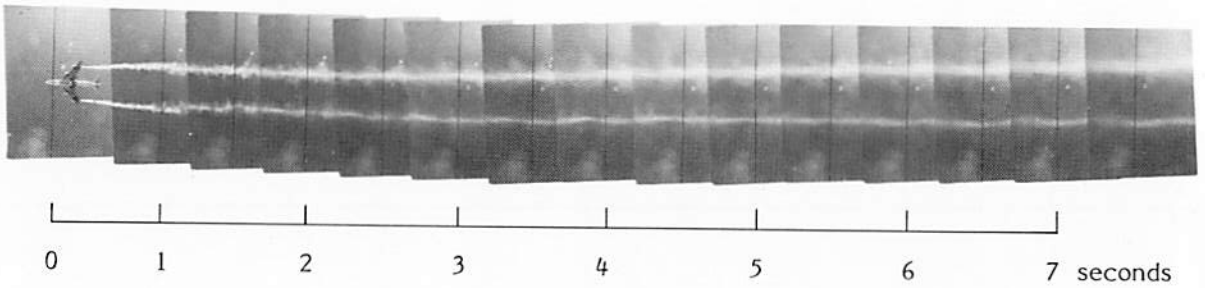

FIGURE 13. (CONCLUDED)

The landing-configuration vortices appear to be larger and, possibly (taking into account the difficulty of smoke injection into the core), more diffuse than the clean-configuration vortices which remain rather tightly formed. Runs 52 and 53 offer a good comparison in identical atmospheric conditions. Note, though, the diffuse shell surrounding the clean vortices after about 5 seconds of age (Fig. 13). There seems to be no major effect of aircraft glidepath on the vortices; only configuration seems to matter. For Run 52, the center smokers (4 and 5) are also on. Their smoke does not mingle with the vortices, but rather descends downward under the vortex induction, and then, drifts outward laterally beneath them.

Further discussion of this approach to study of vortex rollup was given by Tombach et al. (Ref. 3). They used multi-colored smoke marking to study the wake of a Lockheed Lodestar aircraft. There, multiple vortices emanating from points of large spanwise change in lift distribution were observed. Such multiple vortices were found here whenever the flaps of the B-747 were lowered.. For example, Fig. 14 shows a mosaic of the first 5 photographs for 3 runs where most of the smokers operated. The spacing between photos was set by superposing the first 2 photos which include the aircraft. The same spacing was used for all the following pictures. Scaling the photographs to the wingspan and using the air speed gives a photo time spacing of 1.07, 0.76, and 0.69 seconds, respectively, for Runs 11, 23, and 32. A comparison of Runs 11 and 23 shows that the deployment of spoilers for 30/30 flaps strongly affects the vortex at the outer flap edge. However, it does not have any immediate effect on the vortex from the wing tip.

The photographs for Runs 23 and 32 can be interpreted on the basis of a 2-vortex model. The tip and outer-flap vortices appear to spiral around each other with apparently little interaction with vortices from inboard lift discontinuities. A simple calculation for 2 line vortices of strength Γ_1 and Γ_2 , both of the same sign, with separation d shows that they will rotate around each other with angular frequency ω:

RUN 11 30/30 FLAPS, SPOILERS

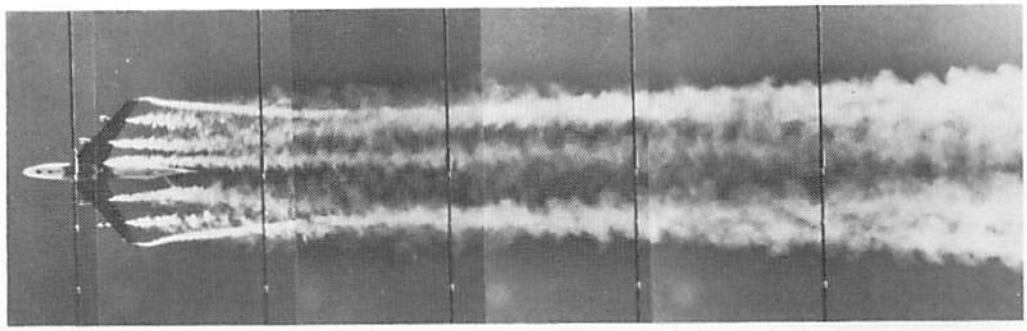

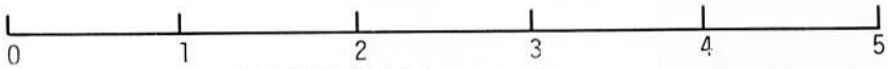

ELAPSED TIME (seconds)

RUN 23 30/30 FLAPS

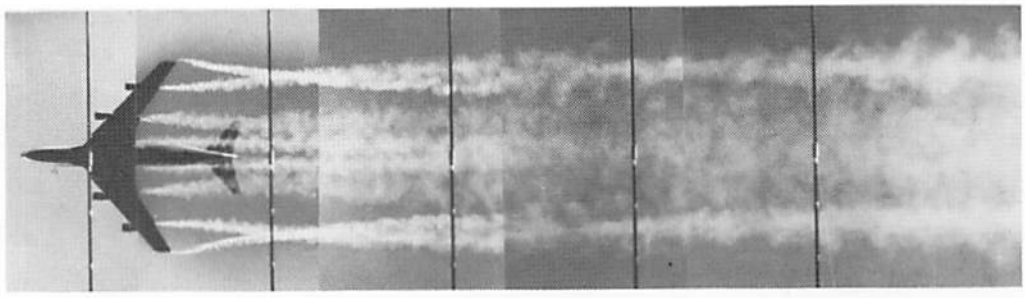

ELAPSED TIME (seconds)

RUN 32 10/10 FLAPS

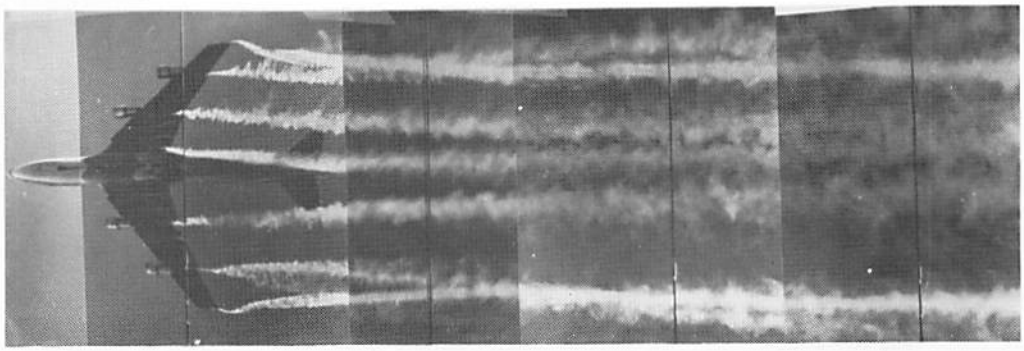

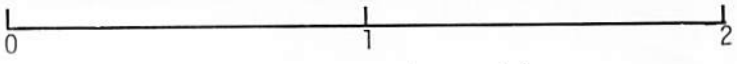

ELAPSED TIME (seconds)

FIGURE 14. COMPARISON OF VORTEX ROLLUP FOR THREE AIRCRAFT CONFIGURATIONS

$$\omega = (\Gamma_1 + \Gamma_2)/2\pi d^2. \quad (1)$$

The angular frequency depends strongly on the vortex spacing. The center of the motion is between the two vortices at a distance:

$$x = \frac{d\,\Gamma_2}{\Gamma_1 + \Gamma_2} \quad (2)$$

from vortex 1. Table 3 lists measurements scaled from the photographs for Runs 23 and 32. Run 23 appears to complete a three-quarters revolution before the vortices merge. The $\pi/2$ and $3\pi/2$ positions are defined by the two vortex pairs having the same separation. It appears that the flap and tip vortices are not level at the trailing edge of the wing tip (taken as time zero). The flap vortex is lower because of the downward projection of the flap and also the sweepback of the wing. If one assumes constant angular frequency and extrapolates the rotation angle back to time zero from the $\pi/2$ and $3\pi/2$ positions, one obtains an initial rotation angle δ of $\pi/6$ which is not unreasonable. The time for one-half revolution is 1.58 seconds. Equation (1) can be used to obtain $\Gamma_1 + \Gamma_2$ if the vortex spacing d can be estimated. If one uses the value d = 5.8 m observed at π rotation, one obtains $\Gamma_1 + \Gamma_2$ = 420 m^2/sec, which is about 80 percent of the elliptic loading value. In contrast, if one takes the initial separation of the two vortices from one wing, d = 8.5 m, the circulation is more than twice as large, which is physically unreasonable. The spacing of the vortices at the crossing points ($\pi/2$, $3\pi/2$) and after merger is consistent with a constant centroid of vorticity at about 49-m spacing, some 4 meters greater than the far downstream vortex spacing of about 45 m.

The ratio of the flap-vortex strength to the tip-vortex strength can be calculated from the vortex separations at π rotation to be 1.3 to 1.6, depending on the centroid spacing used. The fact that these two vortices are comparable in strength for 30/30 flaps is consistent with the observation that neither appears to dominate the merging process. The case of 10/10 flaps for Run 32 is

TABLE 3. PHOTOGRAPHIC ANALYSIS

Time (Seconds)	Rotation (radians)	Tip-Vortex Separation† (meters)	Flap-Vortex Separation† (meters)
Run 23			
0	≈0(δ)	59.4	42.4
0.54	π/2	49.5	49.5
1.18	π	42.4	54.0
2.11	3π/2	49.8	49.8
3.38	merged*	-	-
Run 32			
0	≈0(δ)	59.3	44.4
0.70	π/2	49.9	49.9
1.4	π	51.7	62.6
2.0	merged*	-	-

†Corrections for vortex descent were not made.

*Vortex-pair separation was 48.8 m for Run 23 and 51.1 to 52.3 m for Run 32.

considerably different in that the wing-tip vortex clearly dominates the vortex merger. The aircraft was flown at a much lower altitude and has slightly laterally offset from the center. These factors exagerate image distortion and contribute to parallel problems, which lead to data which are somewhat harder to interpret than that for Run 23. The pictures do not line up as well from shot to shot, and the time until the vortices line up ($\pi/2$) after rotating, is not the same for both vortices. The average time of 0.70 second was used in Table 3. If one estimates $\delta=\pi/20$ and takes the π-rotated vortex separation as d=5.45 m, the vortex-strength sum is $\Gamma_1+\Gamma_2$ = 450 m^2/sec, a reasonable value. It is not possible to estimate the ratio of the two vortex strengths except to say that the tip vortex is much stronger, and is essentially located at the centroid.

4.3 DETERMINATION OF VORTEX POSITION

To define the precise position of each vortex element over the array required photogrammetric analysis of the photographs taken by cameras in the helicopter and to the side of the flight path. Because the helicopter position could not be controlled and the ground-based cameras had to be pointed slanting upward to observe the vortices, the vortices were obliquely photographed when they were positioned over the rectangular sensor array shown previously in Fig. 4. Due to the elevation of the vortices and the tilt of the cameras, the actual positions and altitudes of the vortices were thus not as visualized in the photographs. There was, however, sufficient information contained in the two simultaneous photographic views to determine the exact position and altitude of the vortices by methods of photogrammetry (since the positions of all the array elements were known from a ground survey conducted prior to the test program, and known reference points were photographed by all cameras). The detailed methodology used to define the paths of vortex motion is described in Appendix A.

Sufficient photographic data were available to define at least a portion of the vortex trajectory for 23 of the runs. The

fields of view of the side cameras precluded measurements of vortices higher than 70 m above the surface. This prevented analysis of about 1/3 of the runs (although the later positions of descent of some vortices generated above this height were tracked in 4 cases.)

Illustrated examples of relatively complete vortex trajectories are shown in Fig. 15. The first 2 cases in Fig. 15 show trajectories for 2 runs with 30/30 flaps and landing gear lowered, both generated at about 60 m above ground. Their behavior in both cases is very similar, with vortices at early times separated by about 40 m (about 2/3 wingspan) and descending downward while drifting with the cross wind. The vortex induction in ground effect is sufficient to cause the port vortex to move up wind as the vortices separate at a height of about 20 to 30 m above ground. There is a tendency for the vortices to rise as they travel in ground effect, which is consistent with the behavior noted in the water-tank tests (Ref. 3).

The last 2 cases in Fig. 15 show 2 slightly different trajectories. The last (Run 29) is in the same configuration as the previous examples, except that the aircraft was descending through the 60-m altitude, as though on approach to landing. Because of an apparently stronger cross wind, the starboard vortex enters ground effect and attempts to travel up wind at a speed which appears to just match that of the prevailing wind (apparently about 2 m/s), resulting an an almost stationary, rising vortex. Otherwise, the behavior looks no different than for Runs 14 and 16.

The third trajectory (Run 22) was generated with 30/1 flaps, gear-down configuration, which was tested for its effectiveness in alleviating the vortices. As far as they could be tracked photographically, the trajectories of these vortices were not noticeably different from the other cases considered here. The smoke visualization was not adequate to allow following the vortices into ground effect or to their final decay.

The second case (Run 16) shows two trajectories at two locations separated by 60 m along the flight axis, and shows the

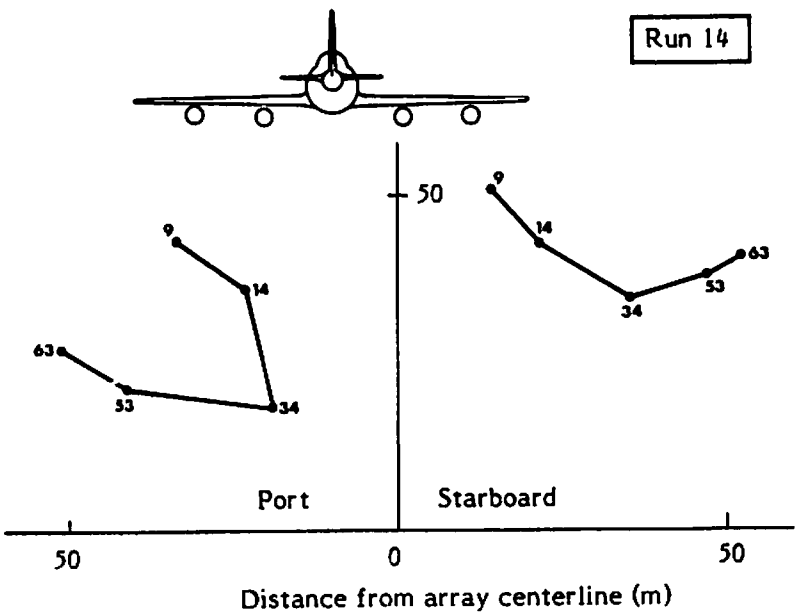

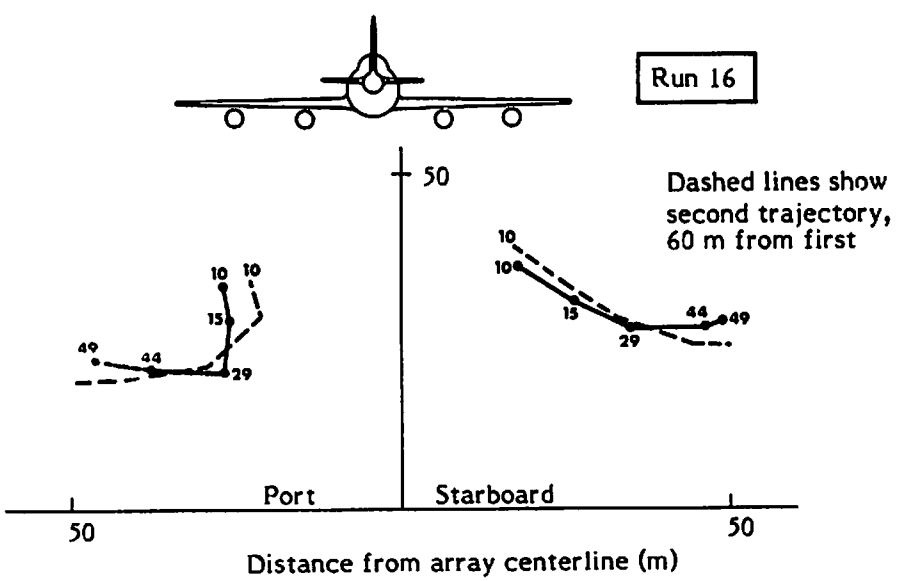

FIGURE 15. PHOTOGRAMMETRICALLY DETERMINED VORTEX TRAJECTORIES OVER THE INSTRUMENT ARRAY FOR SELECTED RUNS. The approximate aircraft position passing over the array is shown. Small numerals denote time, in seconds, since aircraft passage.

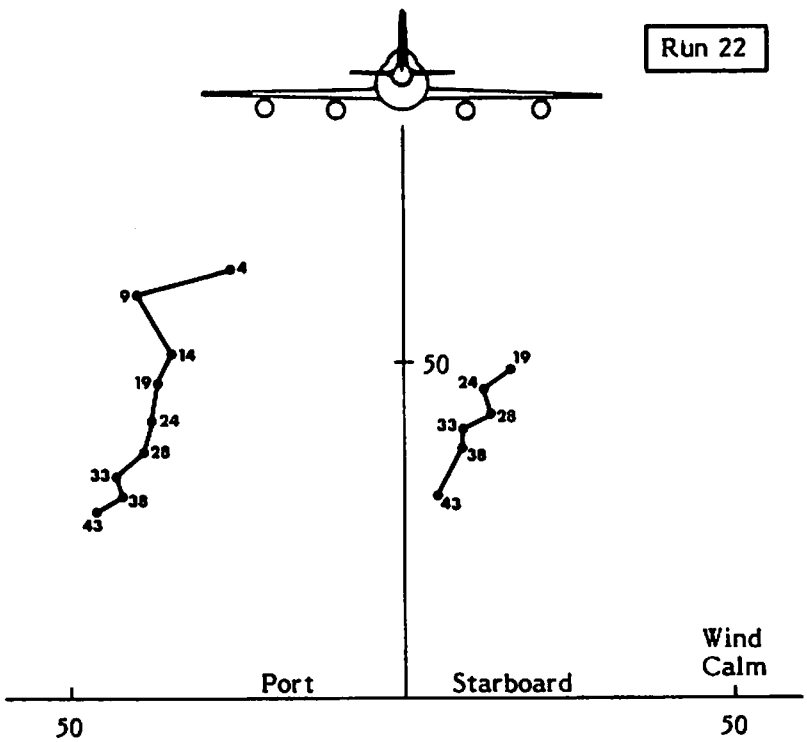

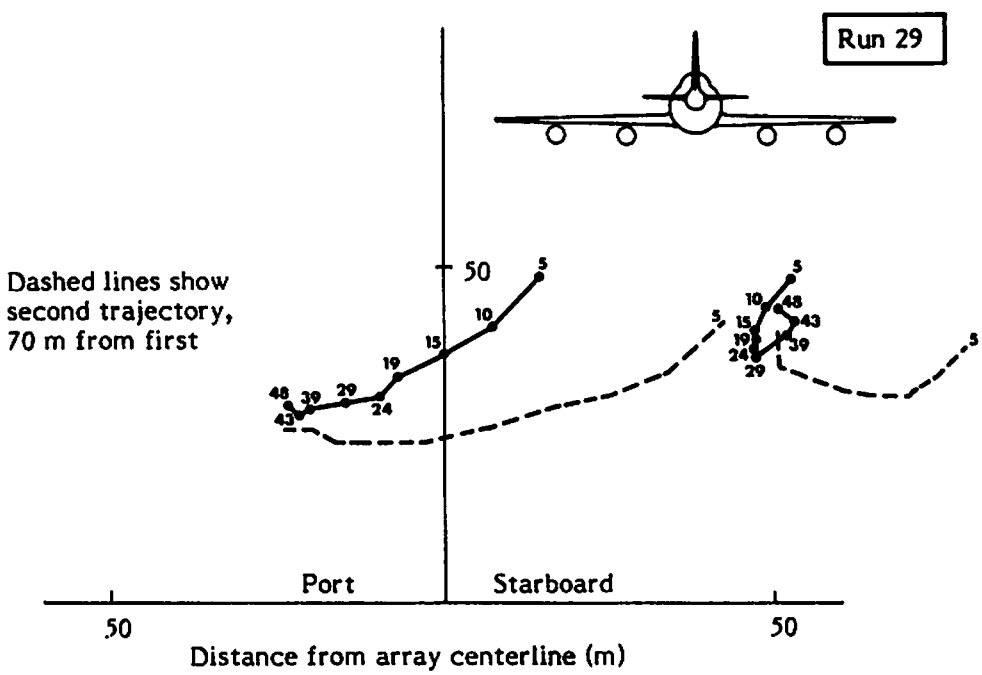

FIGURE 15. (CONCLUDED)

longitudinal variability of the vortex position. Another example of two simultaneous trajectories is shown for Run 29. The accuracy of the photogrammetric technique is typically of the order of 1 m, but the smoke-marked vortex center cannot be located as precisely on the photographs. Thus, the maximum error of this technique is probably about 5 m under most circumstances, and somewhat worse when the smoke marking is especially poor. The two trajectories for Run 16 agree within these tolerances, suggesting little longitudinal vortex deformation. The two cases shown for Run 29 differ greatly, on the other hand; the initial closeness of the two dotted lines is particularly unusual (and unexplained).

Runs 14 and 16 both show that the up wind vortex ultimately descends lower than the down wind vortex. The vertical separation increases with time, leading to the phenomenon of wake banking, which has been observed previously by several investigators, and has been analyzed by Brashears et al (Ref. 4) and Tombach et al. (Ref. 1). The behavior of Runs 14 and 16 agrees with their interpretations if "weak shear" is assumed for the former analysis.

The case of Run 29 appears to show the behavior postulated by Ref. 4 for strong shear, with the up-wind vortex rising relative to the down wind though the tilting was not great. The wind was no stronger on this run than on any of the other three studied, but there was a shear layer at about 25 m above the surface, with a complete reversal of wind direction occurring across that level. Whether this shear played a role in the tilting is not known.

The direction of wake drift in Fig. 15 does not always agree with the wind direction listed in Table 2. The winds in Table 2 are surface winds; there was variability in wind direction with height. The winds were generally quite light (typically under 1 m/s) and of variable direction from moment to moment. The average wind direction before a run, or the pibal soundings between sorties, did not necessarily represent the behavior of the wind at the precise moment the wake trajectory was studied.

4.4 VORTEX DECAY

All of the still photographs and motion pictures were studied to define the ultimate fate of the vortices. Several types of results would have been possible, based on similar studies performed in the past:

The marking smoke could fade from view; subsequent vortex behavior would be unknown though some form of vortex dissipation may have occurred;

An abrupt radial bursting of the smoke cylinder could occur, denoting a vortex breakdown such as discussed in detail by Tombach et al (Ref. 3);

A sinuous instability in the motion of the vortex pair could occur, leading to contact of one vortex with the other, and resulting in a linking of the line vortices into vortex rings. This mechanism has been discussed in detail by Crow (Ref. 5), and by Crow and Bate (Ref. 6); or

The contact of a vortex with the ground would occur, which would be indicated either by appearance of a dust devil when a vortex linked with its imaginary image beneath the ground (theory for which is given by Tombach, Crow, and Bate (Ref. 7)), or by a bursting of the vortex.

Occasionally, the end behavior of the vortex might be indeterminate because the photography ceased before the vortex decayed.

For this particular test program, in those cases where the demise of a vortex was observed (which was obtained for less than half of the runs), a time was assigned to the moment when the organized motion of the line vortex appeared to cease either through core bursting or pair linking. Table 4 summarizes the times at which these events occurred, identifies any unusual aspects of the wake behavior, and lists the corresponding aircraft operational and meteorological characteristics. This table shows those runs for which usable data could be derived from the photographs; a complete summary of all run conditions and meteorological

TABLE 4. SUMMARY OF VISUALLY OBSERVED BEHAVIOR OF BOEING-747 VORTICES

Time (PST)	Run	Test Configuration					Meteorology		Behavior		
		Altitude (m)	TAS (m/s)	Flap (deg)	Gear	Spoiler	$\varepsilon^{1/3}$ ($cm^{2/3}s^{-1}$)	γ (C/100m)	Descent	Breakdown and Time	
										Port	Starboard
2/2/75											
0725	4	65	78	30/30	Dn	No	0.6	9	W	Bu 42	B 42
0730	5	122*	78	30/30	Dn	No	1.0	9	W	Bu 63	--
0735	6	122*	78	30/30	Dn	No	1.5	8	WD	Bu 57	Bu 57
0847	14	65	75	30/30	Dn	No	2.1	0	WD	Bu 74***	> 70***
0859	16	61*	75	30/30	Dn	No	2.7	0	WD	>110***	Bu 89***
0942	19	38	76	30/1	Up	No	3.7	1		Bu 38	Bu 19
0947	20	67	75	30/1	Dn	No	3.1	0	W	> 60	Bu 58
0951	21	64	75	30/1	Up	No	2.7	-1		Bu 29	Bu 29
0956	22	91*	75	30/1	Dn	No	0.8	-1	W	> 60	> 60
12/3/75											
0654	23	122*	79	30/30	Dn	No	0.6	8		Bu 47	--
0658	24	122*	119	0/0	Up	No	0.5	8	W	Bu 76	Bu 53
0703	25	122*	79	30/30	Dn	No	0.4	7	W	Bu 50	Bu 60
0707	26	122*	116	0/0	Up	No	0.6	7		Bu 66	Bu 80
0712	27	67(Ldg)	79	30/30	Dn	No	1.1	6	WD	Bu 60	Bu 50
0716	28	66	79	30/30	Dn	No	0.9	6		Bu 51	> 50
0721	29	72(Ldg)	79	30/30	Dn	No	0.9	6		Bu 60	Bu 50
0725	30	66	78	30/30	Dn	No	1.0	6		Bu 64	Bu 56
0801	32	65	84	10/10	Up	No	0.6	6	W	> 55	> 55
0811	34	59	77	10/10	Up	No	1.5	6	Rap	> 70	Bu** 52
0816	35	63	77	30/30	Dn	No	1.9	6		> 45	Bu 42
0821	36	68	77	30/30	Up	No	1.5	5		Bu 52	Bu 56
0831	38	61*	76	30/30	Up	No	0.7	5		Bu 52	Bu 57
0919	42	54	81	10/10	Up	No	1.0	1		> 30	> 30
1012	47	91*	73	30/30	Dn	No	1.5	0		> 60	> 60
1016	48	91*	73	30/30	Dn	Yes	1.4	0		> 70	> 75
1022	49	37	72	30/30	Dn	Yes	3.9	-1		Bu 10	Bu 10
1031	51	122	108	0/0	Dn	No	1.8	2	W	Bu 20	Bu 80
1035	52	122	108	0/0	Up	No	1.3	2		> 48	> 48
1039	53	122	72	30/30	Dn	No	1.3	2		> 56	> 56

* Nominal altitude

**Small core left behind.

***See discussion in text

conditions appeared previously in Table 2. A key to the abbreviations used in Table 4 is given below:

Term	Definition
Descent	
W	Wavy -- The vortex column is distorted along its length so that its shape appears wavy. The apparent wavelength is usually on the order of tens to hundreds of meters and the amplitude is a small fraction of the wavelength. Often small wavelength waves are seen traveling along the distorted core edge.
D	Detraining -- The vortex core appears to throw off patches of smoke when descending, and leaves them behind in a wake.
Breakdown	
Bu	Burst -- Sudden breakdown of smoke-marked vortex structure.
General	
Rap	Rapidly

Occasionally, the photo record ended before the vortex had decayed for any of several operational flow-visualization reasons. Such cases are marked in Table 4 with lower limits for decay time, with such limits being the ends of the visible photographic records. The actual persistence time for these cases is unknown.

The method of defining the meteorology was discussed previously in Section 3. The discussion in Section 3.2 regarding turbulent gradients observed during Runs 10-18 is particularly relevant for the interpretation of the data for these runs in Table 4.

Surprisingly, the type of behavior related to the sinuous instability was not observed photographically during the runs listed in Table 4 although it was observed a few times (Runs 5, 8, 51, 52, 53, and 54) at locations out of view of the cameras. A correlated, parallel test program in similar meteorological conditions with a Lockheed Lodestar aircraft (Ref. 3) also showed only a few cases of linking, and then only with the underground image vortex. This behavior contrasts sharply with results obtained in earlier tests (Refs. 1 and 8) with smaller aircraft operating out of ground effect, and with smaller aircraft in ground effect (Ref. 7). On the other hand, the linking of contrails from large aircraft at high altitudes is a commonly observed phenomenon. Thus, it appears that some combination of large scale and proximity to the ground may result in the observed absence of linking, while either smaller scale or greater flight altitude will permit linking.

Reference 7 showed theoretically that a parameter of the form $\zeta = h/b_v$, with h the flight altitude and b_v the vortex spacing governs the linking behavior near the ground (for $1<\zeta<4$). The effect of decreasing wake-generation height is the damping of sinuous instability. Such damping due to the ground proximity would not be expected for the core-bursting type of instability because of its smaller scale. Thus, the preponderant instability mode near the ground should be one of vortex breakdown, in agreement with the results of these tests.

Reference 3 extensively analyzed the vortex-breakdown phenomenon observed during this experiment. Using a heuristic approach, it was surmised that the time of vortex breakdown (T_b) can be related to the ambient turbulence and the aircraft configuration through a functional relationship

$$T_b = G\frac{b^2}{\Gamma_o}\left(\frac{\Gamma_o^3}{(k+\varepsilon)\ b^4}^{\alpha}\right), \qquad (3)$$

where: G is a constant,
b is the wingspan,
Γ_o is the original vortex circulation,
k is a configuration constant,
ε is the turbulence-dissipation rate, and
α is a constant, most likely an integer multitude of 1/3.

No explicit effect of vortex height above the ground was noted in the analysis.

Analysis of experimental data, such as that in Table 4, for four aircraft; i.e., the Boeing 747, a Lockheed L-18 Lodestar, an Aero Commander 560F, and a Cessna 170 led Tombach et al (Ref. 3) to the conclusion that α=1/3 fitted the data best. Also, that good choices for k and G were k=0.05 cm^2s^{-3} for an aircraft in clean configuration, k=4 cm^2s^{-3} for an aircraft with flaps and gear down, and G $\approx$ 1/3 regardless of configuration.

These constants gave a general time-to-breakdown relation, usable for aircraft ranging from a Cessna 170 to the Boeing 747:

$$T_b \approx \frac{1}{3}\left(\frac{b^2}{k+\varepsilon}\right)^{1/3} \qquad (4)$$

This relationship is generally correct within a factor of 2 for all the aircraft considered; the standard error of estimate is typically less than 10 seconds. (For the B-747, a choice of G = 0.31 and k = 5.66 cm^2s^{-3} gives a best correlation coefficient of 0.82 with a standard error of estimate of 8.5 seconds; the

general form above predicts slightly longer times, by about 10 seconds in very weak turbulence.)

4.5 AXIAL FLOW

Axial flow in the vortex core is often assigned a contributory role in various vortex-decay mechanisms. As noted in Section 4.1, buoyant balloons released from the ground were used to visualize this axial flow.

The axial flow in the B-747 vortices was found to be either jet-like (away from the aircraft) or so weak as to not be noticeable. Jet-like flow in the cores was found when the B-747 was in takeoff configuration (10/10 flaps, either spoiler and gear position, aircraft climbing) or in landing configuration (30/30 flaps, gear down, no spoilers, aircraft descending). Little axial flow was observed when the aircraft was "dirty" (30/30 flaps, gear down, no spoilers) and in straight-and-level flight.

The balloon observations of axial flow direction were corroborated by visual observation of the ends of the smoke-marked portions of the vortices, where axial flow would cause a "spike" of smoke or a hollow core.

In the related experiment described in Ref. 3, Lockheed Lodestar vortices were similarly marked by small buoyant balloons. In contrast to the B-747 vortices, the Lodestar tests invariably showed axial flow toward the aircraft. Reference 3 analyzed this behavior in terms of the induced and profile-drag coefficients of the aircraft. They noted that a jet-like flow will occur for a sufficiently large value of the ratio C_{Di}/C_{Do} while a wake-like flow will occur if the same ratio is sufficiently small.

When viewed from this perspective, the experimental observations suggest that the Lodestar is generally relatively "dirty," and thus, has wake-like core flows, while the B-747 is generally "clean" with jet-like flows initially. The one B-747 case which shows no axial flow occurs when a relatively dirty configuration has enough thrust added to maintain level flight. It is likely

that the turbulence added by the thrust is sufficient to cause rapid decay of any initial jet-like wake, and thus, no axial flow was observed in the core by the time the balloons were captured.

Local axial flow also occurred whenever a vortex-pair linking occurred in the Lockheed Lodestar wake (linking of B-747 wakes was not noted when the balloons were used). In such cases, the axial flow was away from the instability manifestation, in both directions along the vortex, indicating the presence of higher pressures at the burst or link point. The instability-induced axial flow was stronger than the normal axial flow in the vortex, and thus, the local flow was totally dominated by the links or bursts.

Axial flow need not be confined only to the core centerline, and shells of axial motion have been observed in tests of aircraft flying past smoke sources. The flow-visualization techniques of these experiments could not illuminate non-centerline core flows.

5. ANEMOMETER MEASUREMENTS

Arrays of anemometers on the ground were used previously to detect the presence of vortices near the ground, especially at the approach end of a runway (Ref. 9 and 10). Tombach et al. (Ref.3) applied the same techniques to the study of the decay mechanisms of vortices for both Lockheed Lodestar and Boeing 747 aircraft. This section briefly reviews the approach and results.

5.1 MEASUREMENT TECHNIQUES

A description of the array of anemometers was given in Section 2.3. Twenty-seven of the 30 anemometer locations contained 2 propeller anemometers mounted 4 m above the ground, with 1 propeller axis oriented vertically and the other oriented toward the flight path, as shown in Fig. 16. The other 3 standards had 3-component anemometers at both the 4- and 7-m levels, and one also had a 3-component hot-wire anemometer at the 7-m level.

The anemometer-measurement concept is shown in Fig. 17. The combination of horizontal and vertical axis anemometers allows sensing of the presence of a vortex as long as it is creating any flow at the anemometer.

All anemometer readings were recorded on magnetic tape at 1/2-sec intervals, and also on continuous light-sensitive oscillographic recording charts.

5.2 DISCUSSION OF RESULTS

Although the anemometer data can be analyzed for a variety of purposes, the primary objective of the anemometer measurements is in the context of vortex-breakdown studies (Ref. 3). To date, the only analysis of these records has been from that perspective. Plots of anemometer data from selected runs are given in Appendix B.

Figure 18 shows a representative record of horizontal wind speeds around the time a vortex breakdown is observed in the

FIGURE 16. TWO-COMPONENT PROPELLER ANEMOMETER

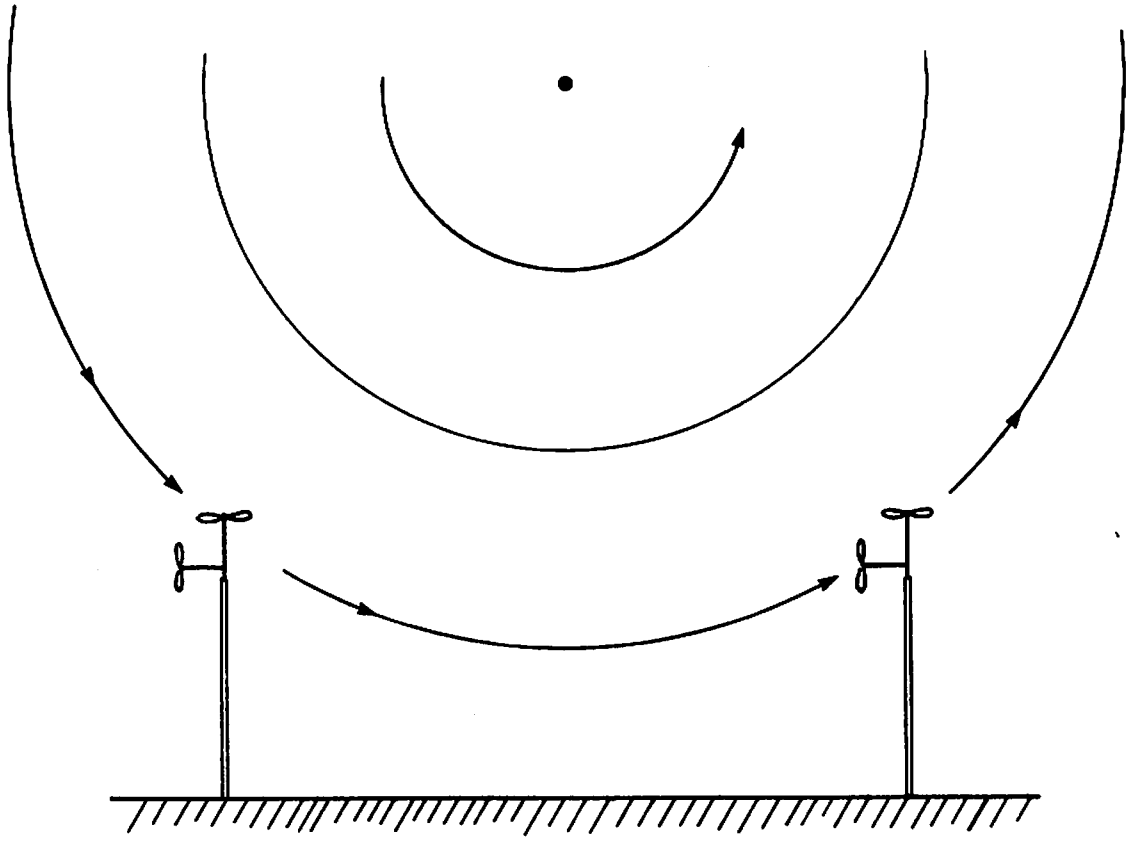

FIGURE 17. USE OF PROPELLER ANEMOMETERS TO MEASURE VORTEX FLOW FIELD

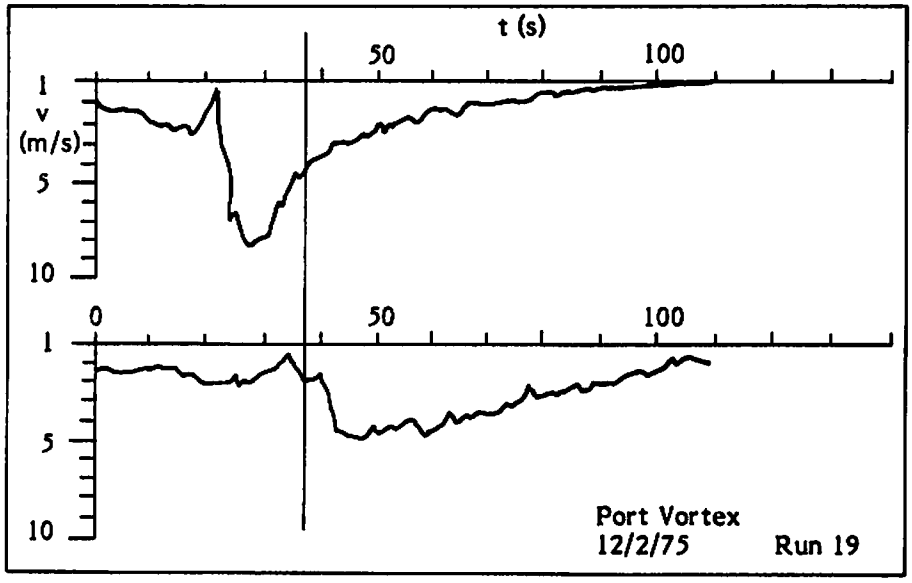

FIGURE 18. ANEMOMETER RECORD OF VORTEX BREAKDOWN. The top graph shows the horizontal speed history at an anemometer before a burst; the lower trace shows the record at the adjacent anemometer after the burst. The time of breakdown is shown by the vertical line.

motion-picture records. The time of breakdown thus defined is shown by the heavy vertical line at 38 sec of vortex age. Each trace in Fig. 18 represents the horizontal wind speed, transverse to the flight path, recorded by an anemometer as a function of time as the vortex travels horizontally above it in ground effect. The top trace shows the vortex structure before a burst is seen to occur above the array. The lower trace shows the vortex structure at the next anemometer reached by the vortex after the breakdown.

The effect of the vortex burst is to flatten the velocity profile by reducing the peak velocity under the center of the vortex (to about 50 percent of its prior value), but without major effect on the speeds away from the center of the vortex. A definite vortex flow remains, however, indicating that core bursting does not totally eliminate the vortex. The persistence of the outer-flow speeds suggests that such bursting may not alleviate the vortex hazard to aircraft with wing spans larger than the core size.

This pattern of behavior was consistently observed in both Boeing 747 and Lockheed Lodestar tests, with the typical peak velocity after breakdown being about 30 percent of its prior value. A few of the cases studied showed total alleviation of all vortex velocities by a vortex breakdown, with no residual vortex structure remaining. The flow visualization showed no visible difference between the partial and total vortex-decay breakdowns, except that the presence of a residual visible core corresponded (obviously) to a case of partial alleviation. Aircraft configuration was not an obvious factor in selecting one form over the other.

The smoke marking often showed a small filament of smoke remaining after a vortex breakdown had occurred, which confirmed the continued presence of organized vortical motion seen in the anemometer records. The small balloons released into the cores also showed vortex motion to be present after a visible vortex breakdown. In several cases, the balloons were still spinning in the vortex core at a vortex age of around 150 sec, in excess of

the observed core breakdown times in the smoke-marked vortices. The vortex strengths, however, were greatly reduced. In one case, the balloons in the core were overtaken by a moving breakdown, and then, remained firmly trapped in the now invisible vortex core after the breakdown had passed.

Earlier work (e.g., Ref. 11) has also suggested that a vortex breakdown does not necessarily imply a destruction of organized vortex motion, but rather represents a rearrangement of vortex structure. The present work supports this concept, and indicates that the visually observed behavior of the smoke does not always provide a complete picture of the vortex lifetime.

6. LASER DOPPLER VELOCIMETER MEASUREMENTS

The wake vortex and some atmospheric wind measurements were carried out by means of a scanning LDV system contained in a mobile van. Preliminary processing of the data was carried out with a mini-computer aboard the van. Reduction and analysis of the vortex and wind signatures were carried out by off-line processing at Lockheed-Huntsville, NASA Marshall Space Flight Center, and DOT TSC. This section describes the LDV instrumentation, the data-processing methods, and the results for the Rosamond tests.

6.1 LASER DOPPLER VELOCIMETER SYSTEM

A photograph of the van-mounted LDV system is given in Fig. 19. The wake measurements were accomplished as follows: (1) the wake generated by the aircraft was scanned by the CO_2 laser, (2) the radiation backscattered from the aerosol in the wake was collected, (3) the radiation was photomixed with a portion of the transmitted beam on a photodetector, and (4) the intensity and Doppler shift frequency of the signal were displayed.

The difference in frequency between the transmitted and backscattered signal generated at the photodetector, the Doppler shift frequency, is a measure of the aerosol's line-of sight velocity within the laser focal volume.

$$|\bar{V}| = \frac{\lambda \, \Delta f}{2 \cos\gamma}, \qquad (5)$$

where $|\bar{V}|$ is the magnitude of the velocity component in the region being sensed, λ is the laser-radiation wavelength (10.6 μm), Δf is the Doppler shift, and γ is the angle subtended by the velocity vector and the optic system line of sight. From equation (5), it is noted that the Doppler shift is a direct and absolute measure of aerosol-velocity component and a frequency shift of 188 kHz corresponds to a 1 m/s speed.

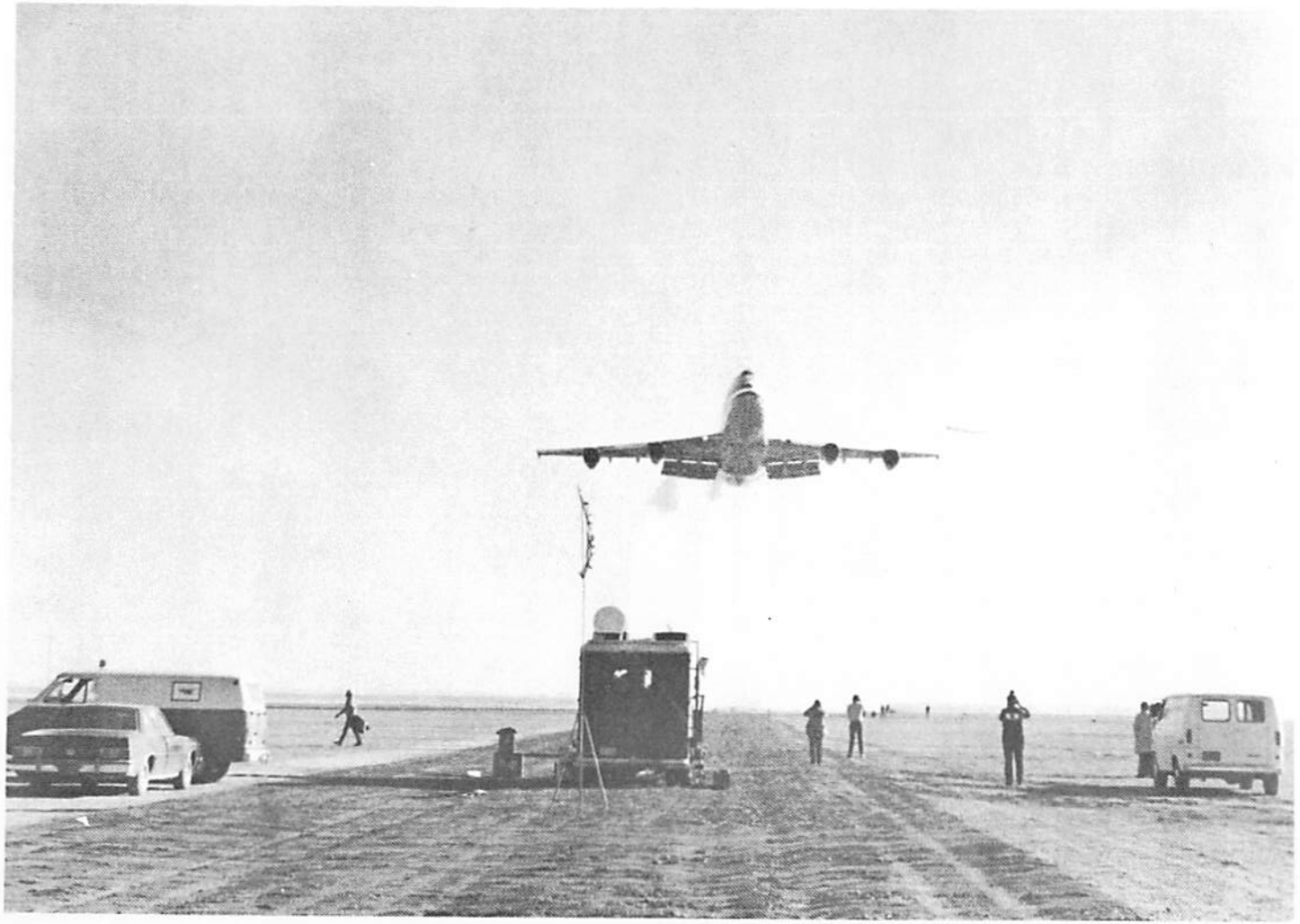

FIGURE 19. LDV SYSTEM MONITORING WAKE VORTICES GENERATED BY A B-747 AIRCRAFT AT ROSAMOND DRY LAKE

A sketch of the optical and electronic equipment for measuring the intensity and frequency spectrums of the coherent backscatter from the focal volume is shown in Fig. 20, and is described in detail in Refs. 12 and 13. Photographs of the optical and electronic equipment for measuring the aerosol backscatter are shown in Figs. 21 to 23.

The pertinent operating characteristics of the LDV are summarized as follows:

a. Performance
   1) Threshold of Magnitude of Velocity Component: 0.5 m/s (adjustable),
   2) Range of Magnitude of Velocity Component: 0.5 to 28 m/s (adjustable).

b. Sample Rate
   1) Low Data Rate: 70 Hz (adjustable),
   2) High Data Rate: 500 Hz (using the NASA filter-bank processor).

c. Spatial Resolution
   1) Range Accuracy: $\pm$ 0.4 m at 30 m, $\pm$ 44 m at 300 m,
   2) Elevation Angle Accuracy: $\pm$ 0.25 deg.

d. Scan Modes
   1) Range or Line Scan,
   2) Elevation,
   3) Altitude,
   4) Azimuth,
   5) Horizontal Wind
   6) Vertical Wind,
   7) Wind Direction,
   8) Line-of-Sight Velocity Component.

The characteristic output signal from the LDV system is an intensity versus frequency spectrum illustrated in Fig. 24. The output parameters V_{pk} and V_{ms} are indicative of the magnitude of the velocity component in the LDV focal volume corresponding to the fastest particle (or particles) above the amplitude threshold and the particle (or particles) having the highest backscatter, respectively. The bandwidth, N, is a measure of the range of particle velocities in the focal volume. Intensity and frequency

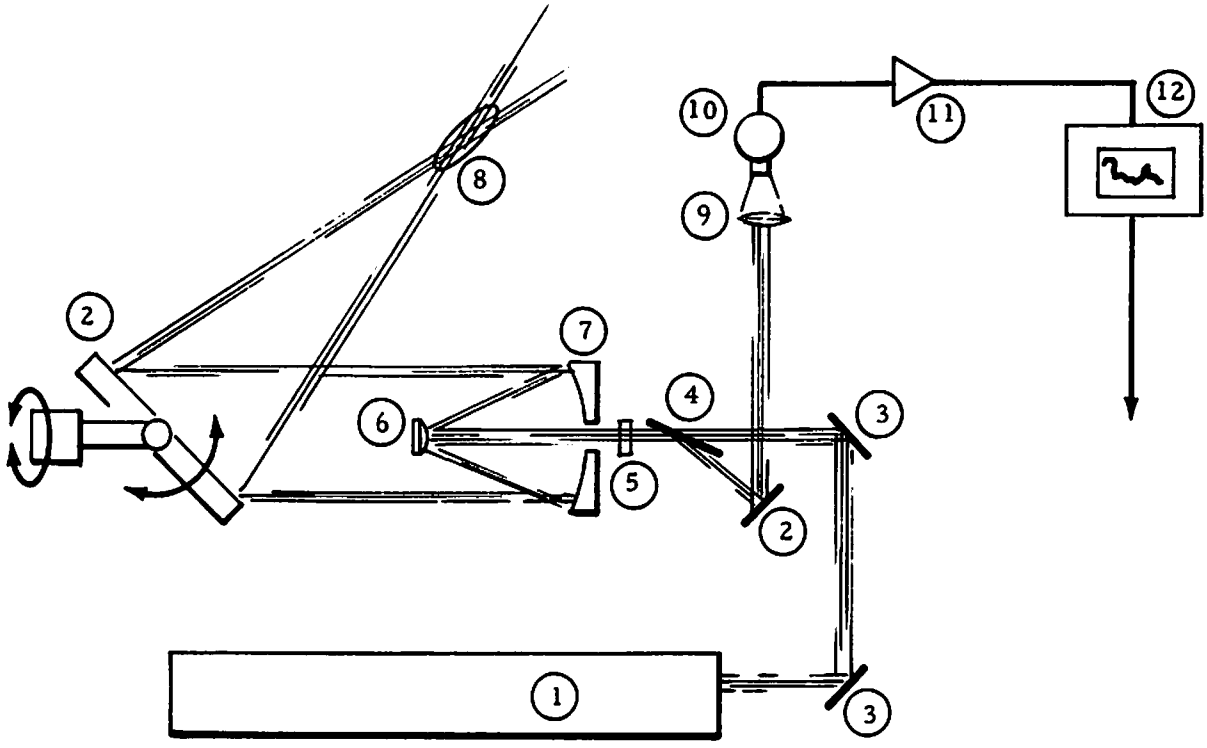

1. CO_2 Laser
2. Mirror
3. Mirror
4. Brewster Window
5. Quarter Wave Plate
6. Secondary Mirror
7. Primary Mirror
8. Focal Volume
9. Lens
10. Photodetector
11. Preamplifier
12. Spectrum Analyzer

FIGURE 20. COMPONENT CONFIGURATION OF THE LASER DOPPLER VELOCIMETER

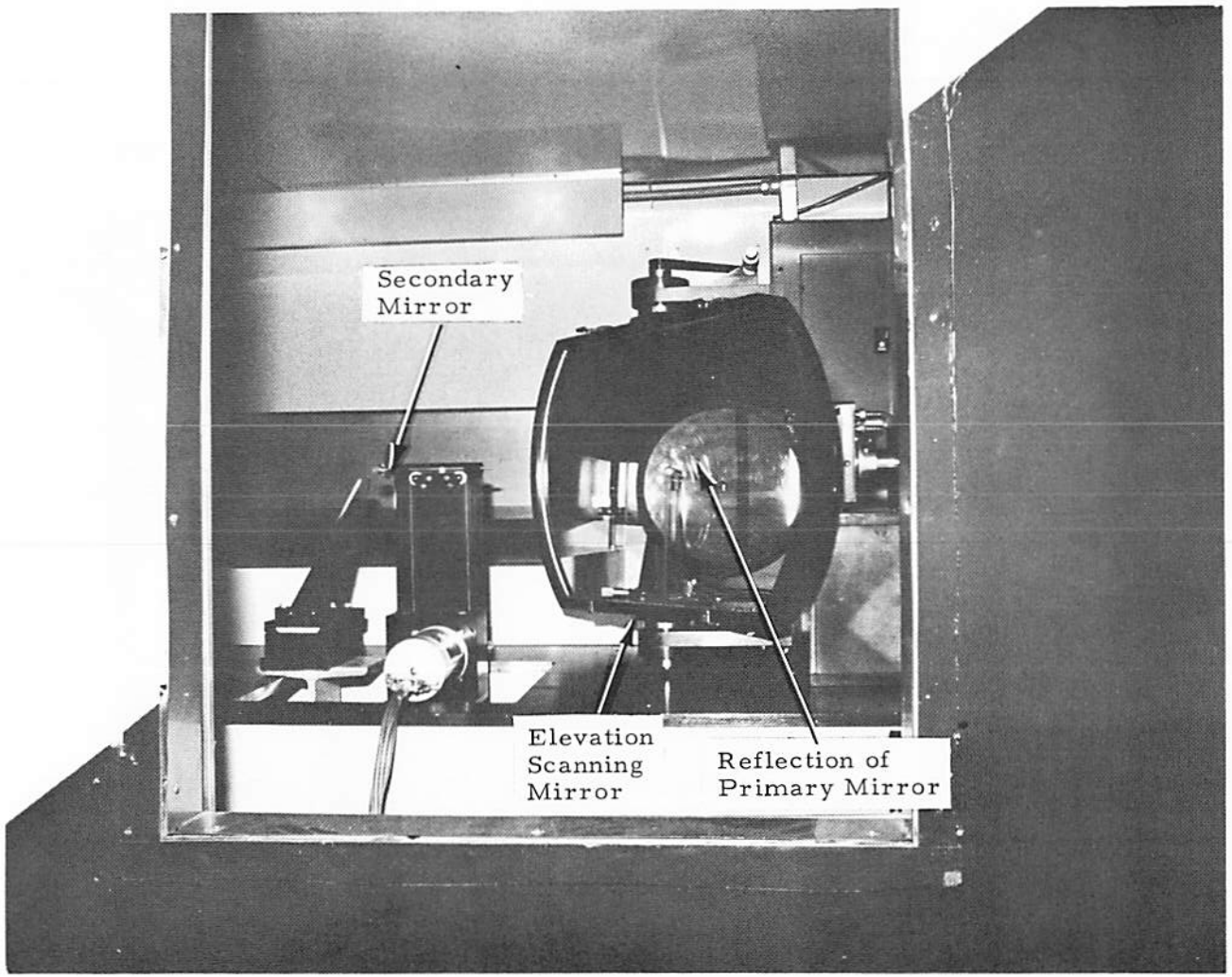

FIGURE 21. VIEW THROUGH SIDE WINDOW OF LASER DOPPLER VELOCIMETER DEPICITING SCANNING OPTICS. Note reflection of telescope primary mirror in elevation scanning mirror.

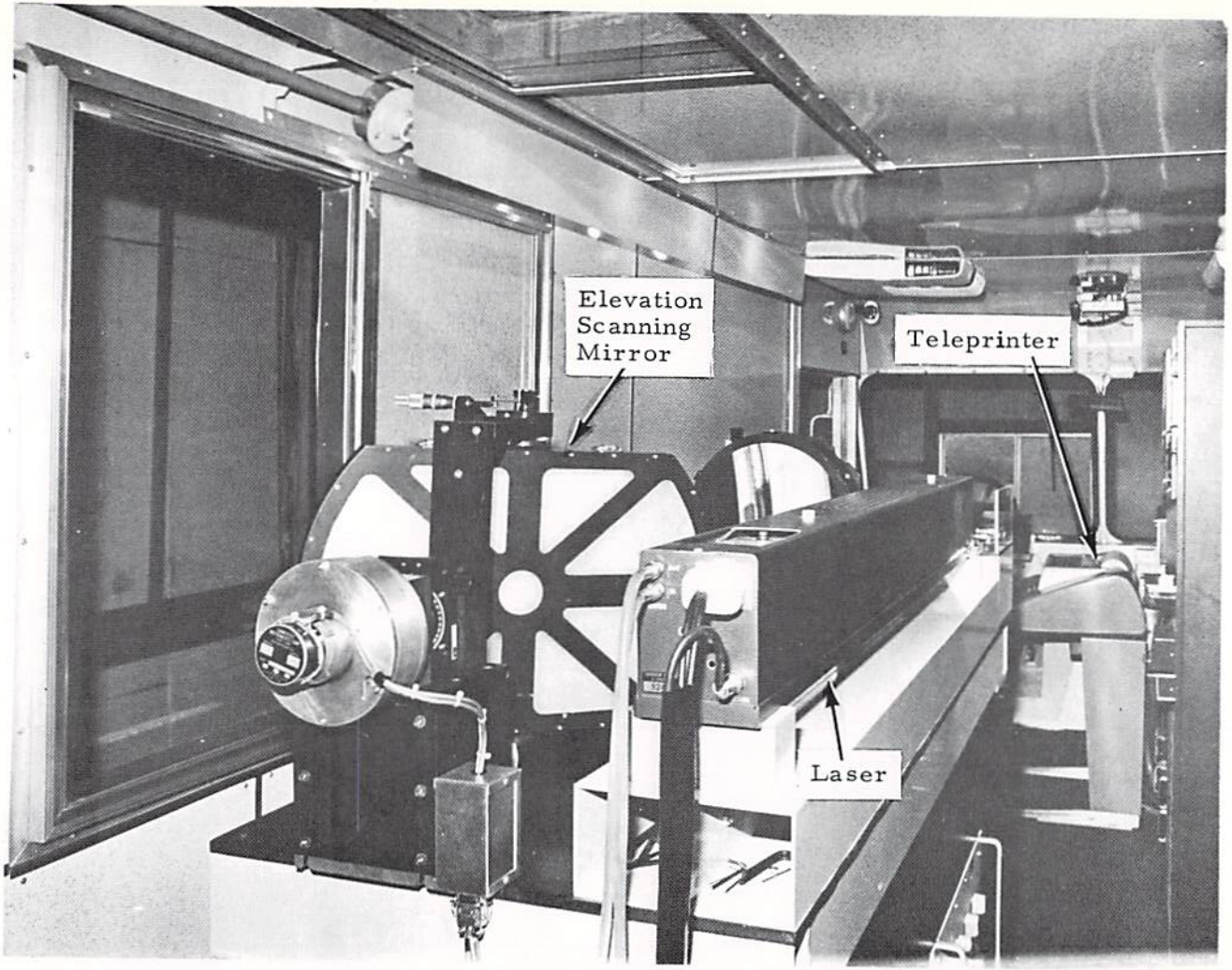

FIGURE 22. INTERIOR VIEW OF LASER DOPPLER VELOCIMETER VAN LOOKING FORWARD. Depicted in foreground is elevation-scanning mirror on left and laser on right. Teleprinter is in right rear.

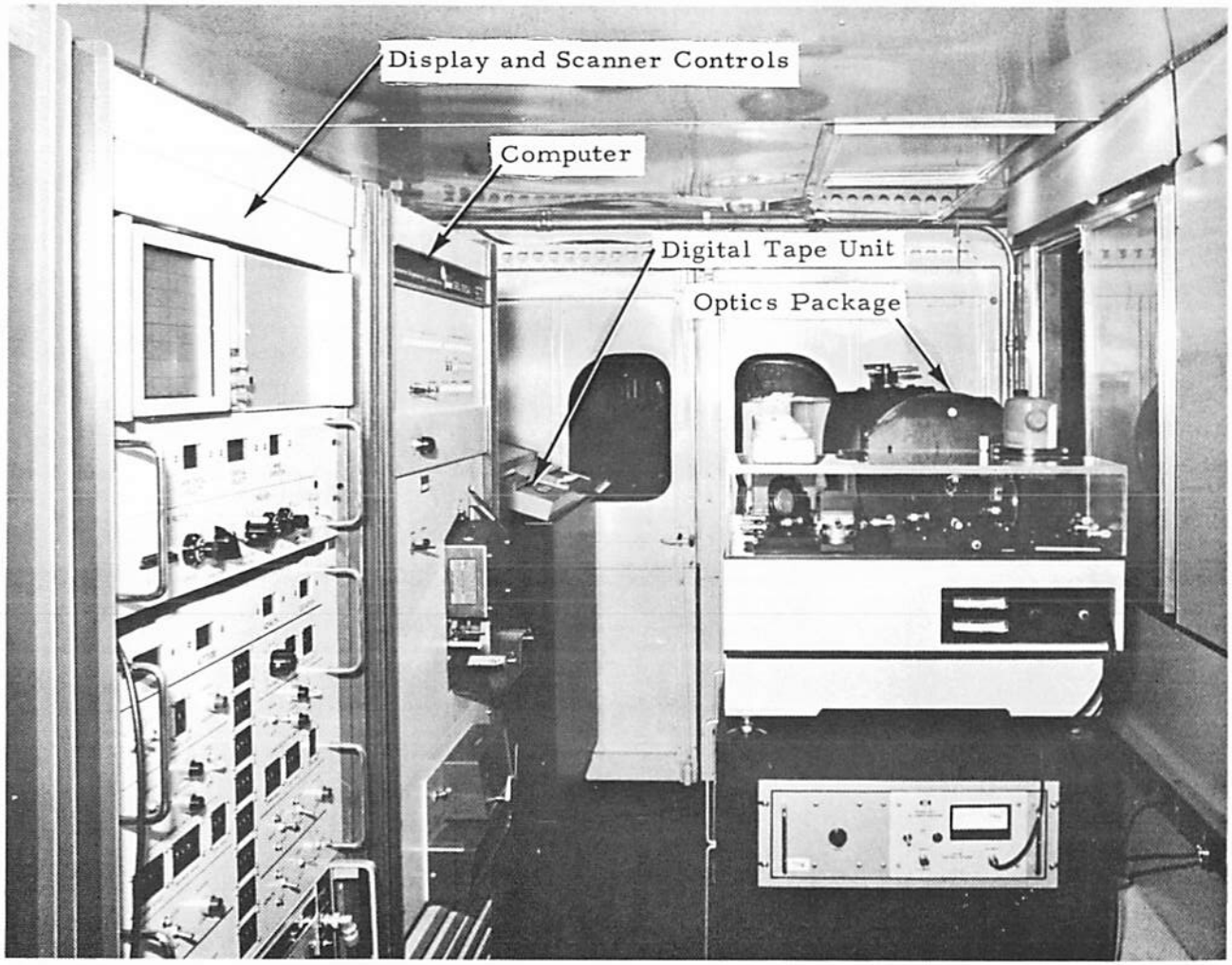

FIGURE 23. INTERIOR VIEW OF LASER DOPPLER VELOCIMETER VAN. Display and scanner controls in first rack, computer in second rack, digital-tape unit aft, and optics package on right.

V_{pk} = Magnitude of velocity component of highest channel above amplitude threshold

V_{ms} = Magnitude of velocity component of the channel having the peak signal

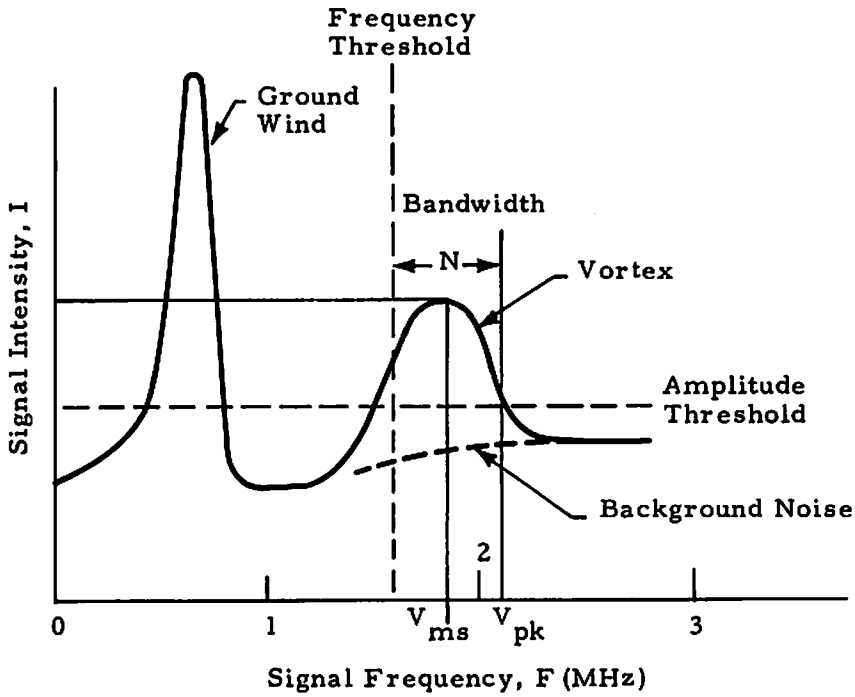

FIGURE 24. DEFINITION OF LASER DOPPLER VELOCIMETER OUTPUT SIGNATURE

thresholds are applied to the signal, as shown, to eliminate noise and to improve the resolution of the system. For example, in the vortex-tracking mode, the frequency threshold of the LDV is set relatively high to filter out the low-frequency signal associated with the ambient wind.

The velocity resolution of the LDV is determined by the signal-to-noise ratio characteristics of the system as well as the atmospheric aerosol particle-size distribution. Because of the smoke injected into the vortices during the Rosamond tests, no difficulty was encountered detecting the highest velocity regions (as high as 28 m/s) associated with the wake vortex phenomenon. The very low ambient winds, on the order of 1 to 2 m/s, were also detected by the LDV at Rosamond when they were above the system's threshold set at 0.5 m/s.

The spatial resolution of the LDV is determined by the size of the laser beam-sensing volume where the beam is focused. The extent of the laser Doppler system-sensing volume as a function of range is $2\Delta r = 9.84 \times 10^{-4}\ (m^{-1})\ R^2$ and is obtained from calibration measurements (Ref. 13):

Range to Focus, R(m)	Sensing-Volume Length (Half-Power Value) 2 Δr (m)
50	2.5
100	9.8
200	39.4

For example, if the LDV system is tracking wake vortices at a range of 60 m, a needle-shaped volume of the vortex 3.54 m long and 4 mm in diameter is sampled. During the Rosamond tests, the typical vortex range was 60 m, so that the spatial resolution due to the spreading of the focal volume was 3.54 m.

The range response of the LDV, derived in Ref. 14, has the theoretical form

$$I(R) = [R^2\ (1 + K^2\ (R^{-1} - f^{-1})^2)]^{-1}, \qquad (6)$$

where f is the focal distance of the LDV telescope, R is the range to a scatterer, and K is a constant (measured to be 2032 m for this LDV). The total scattered signal is given by the range integral of I(R) multiplied by the scattering cross section as a function of range. Near the focal point (R ≈ f), equation (6) can be approximated by

$$I(R) = [f^2(1 + [(R-f)/\Delta R]^2)]^{-1}, \qquad (7)$$

where the 3-dB distance is $\Delta R = f^2/K$. Unfortunately, equation (7) does not fall off very rapidly with distance from the focal spot. The response is down only 10 dB at a distance of 3 ΔR, and 20 dB at 10 ΔR. This broad response can lead to measurements of vortex velocities even when the focal volume is far from the vortex, particularly when the scattering cross section is enhanced by smoke injected into the vortex. The interpretation of the LDV spectrum, shown in Fig. 24, is based on this effect. The signal return from the vortex region generates larger Doppler shifts than those from the ambient wind. In fact, the largest Doppler shift (V_{pk}) measures the vortex velocity at the point where the laser beam is tangent to the vortex tangential velocity. Since the laser beam and the vortex velocity remain tangent for a distance along the beam, the Doppler spectrum tends to have a peak near V_{pk}. Thus, the vortex tangential velocity is readily measured as V_{pk}, even when the laser is focused far from the vortex. The analysis of some finger-scan data showed that the range resolution for measuring the vortex velocity from low-speed data was 6 to 8 times ΔR.

In addition to the finite focal volume, the sampling rate of the LDV plays an important role in determining the overall resolution of the system. During the Rosamond tests, measurements were recorded at two data rates, 70 and 500 Hz.

There was an intrinsic difference in the signal-to-noise ratio between the high- and low-speed data. The high-speed spectral data came from a surface acoustic wave (SAW) spectrum analyzer which effectively integrated all the power in each

spectral bin. The low-speed data came from a scanning filter spectrum analyzer which accepted only a small portion of the power, and therefore, had a signal-to-noise ratio of about 13 dB less than the high-speed data. This difference in sensitivity was even greater for many runs because the intensity threshold for saving low-speed data was inadvertently set too high above the noise. Thus, the high-speed data were notably superior to the low-speed data, both in resolution (discussed below) and in sensitivity. Unfortunately, the playback process for high-speed data was so expensive and complicated that only selected runs could be analyzed.

6.1.1 Arc-Scan Mode of Operation

In the arc-scan mode, the LDV interrogates the vortex wake at a fixed range along an arc normal to the aircraft flight path. As shown in Fig. 25, the sensing volume is moved between two elevation limits (the typical cone angle is 2α = 30 deg) at a fixed rate (the typical scan rate is 0.5 Hz), while the vortex drifts past the scanned arc. Thus, the arc-scan measurements indicate the spanwise downwash distribution in the wake of the aircraft, provided that the vortex range is sufficiently close to the selected scan range. The vortex range, however, cannot be readily determined.

During one arc scan, the vortex is sampled at discrete points approximately evenly spaced along the arc shown in Fig. 25. The slow response of the angle servo rounds off the angle scan at the ends of the arc, thereby decreasing the spacing of the data samples in those regions. The separation between successive sample points, ΔS, based on the sampling rate f, range R, and cone angle 2α, is given approximately by

$$\frac{\Delta S}{R} = \frac{2\pi}{360^{\circ}} \quad \frac{2\alpha/\text{sec}}{f} \quad , \tag{8}$$

where 2α is the elevation-angle scan rate at the frequency of 0.5 Hz used in the tests. For a typical arc-scan wake vortex measurement at Rosamond, f = 500 and 70 Hz, R = 60 m, and 2α = 30 deg,

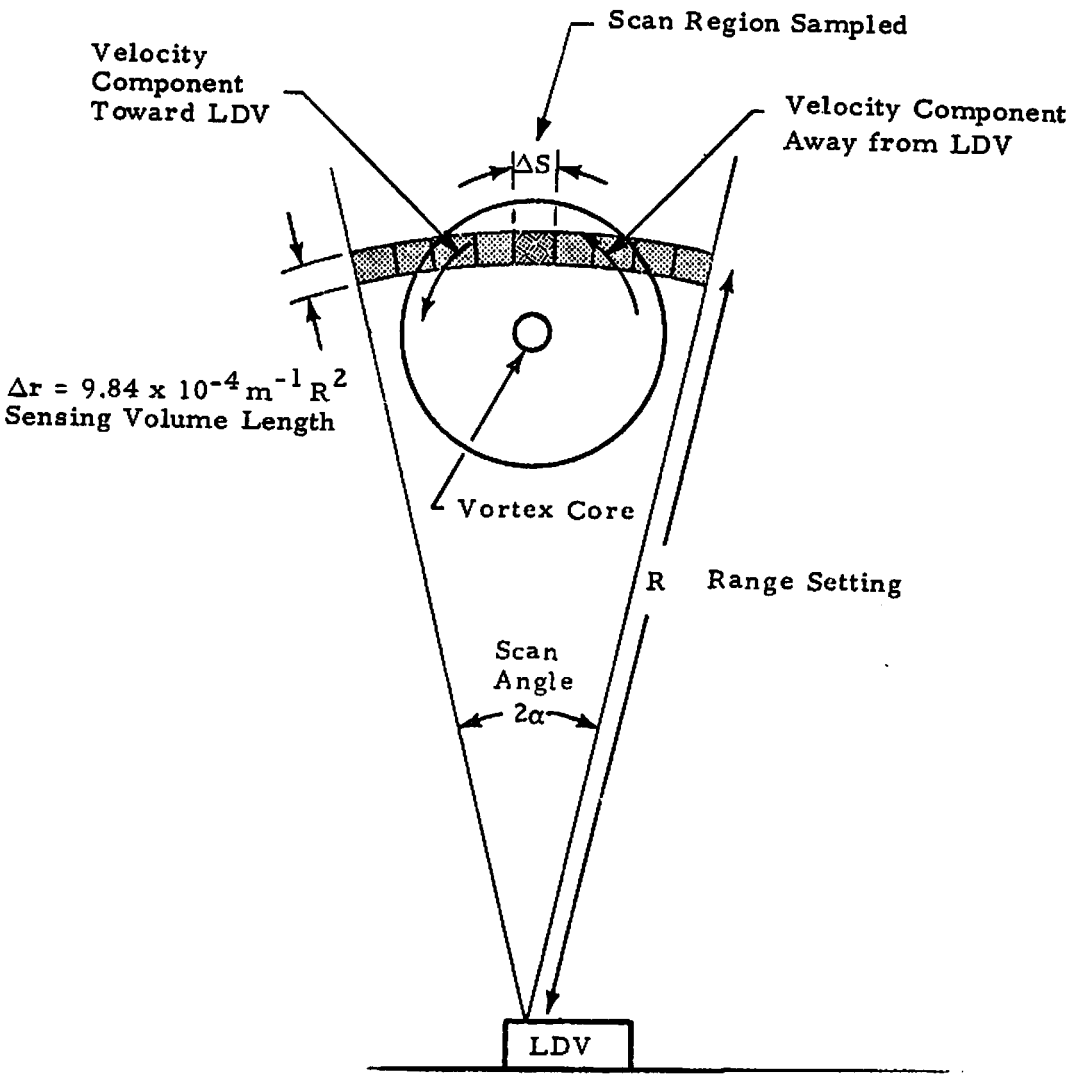

FIGURE 25. GEOMETRY FOR ARC SCANNING FOR ROSAMOND WAKE VORTEX TESTS

so that the wake vortex flow field is sampled every 0.06 and 0.4 m at the high and low data rates, respectively. Since the range of vortex-core diameters measured for a B-747 aircraft is 0.3 to 2 m based on tower flybys (Ref. 15), the sampling rate of the LDV system is sufficient to obtain several cuts through the vortex core along the arc (or essentially, in the spanwise direction), particularly at the high data rate.

The arc-scan mode was employed on the first test day. The LDV was located directly under the flight path (Fig. 4) and scanned arcs in a plane perpendicular to the flight path with a complete scan every 2 sec. Scans were at a fixed range until the vortex passed through the scan arc, at which time the sensor range was lowered and remained fixed again until the vortex descended through the new range. The objective of the overhead arc-scan measurements was the measurement of the initial downwash field and the wake vortex rollup process.

Figure 26 shows the low-speed data velocity measurements from one arc scan (66 to 108 deg elevation angle) of Run 5. Because the sign of the velocity is not determined, the vortex center at sample 22 appears as a dip between two peaks, rather than as a reversal of velocity sign. The other vortex center is beyond the end of the scan. In Fig. 26, the scattered signal was too weak between the vortices and outside of them to produce a valid velocity measurement. The vortex-core region is seen clearly because of the scattering aerosols injected by the smoke generators.

6.1.2 Finger-Scan Mode of Operation

During the second day of the Rosamond flight tests, the LDV wake vortex measurements employed the finger-scan mode. The LDV van was located 60 m north of the flight path (Fig. 4). In the finger-scan mode, both the range and elevation of the laser-beam focus were varied simultaneously and linearly with time, producing a multiple-lobe-scan pattern, shown in Fig. 27. The settings and sampling rates for the finger-scan mode are given in Appendix C.

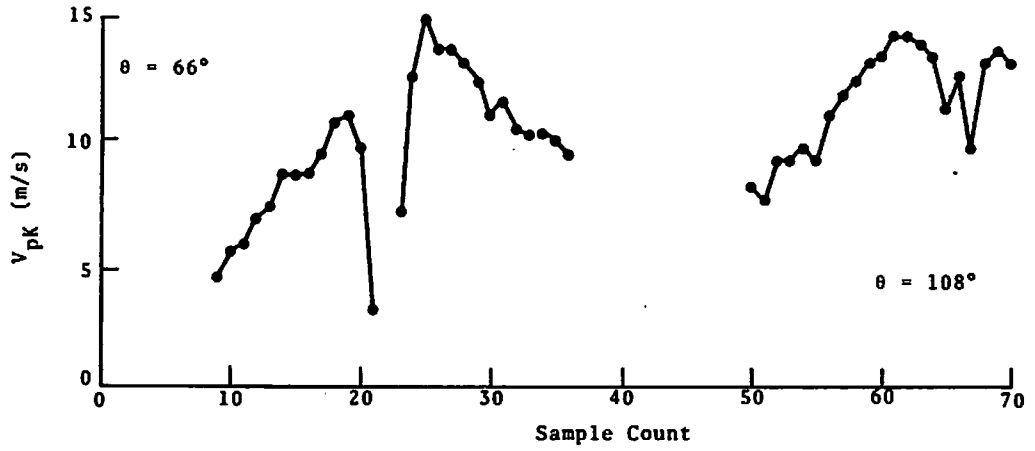

FIGURE 26. VELOCITY DATA FOR ONE ARC SCAN OF RUN 5 AT 10 SECONDS ELAPSED TIME

The distance between sample points for the finger-scan mode is higher than for the previous arc-scan mode. From Appendix C, it is noted that the typical range-scan excursion for the finger-scan mode is 105 m, and the normal range and angle rates are 3.5 and 0.2 Hz, respectively. It follows that the beam-scan velocity is 735 m/s. Because the LDV measurements have been sampled every 2.0 and 14.3 m/s at the low and high data rates, the wake vortex flow field is measured at every 1.5- and 10.5-m increment in range respectively. In 2.5 sec, the finger-scan mode can interrogate its complete scan area. This rapid scan is desirable for vortex tracking, but it has limitations for measuring vortex-velocity profiles.

Figure 28 shows the range scan and the vortex velocity for one complete angle scan (45 to 17 deg in elevation angle) for Run 27, where the finger-scan mode is employed. As in the arc-scan mode, the vortex center (sample 103) is indicated by a dip between 2 peaks in the line-of-sight velocity. In this case, however, the velocity profile is not continuous since the focal range is not always close enough to the vortex to measure the tangential velocity. The plot shows a complete lack of data when the range is too low (a consequence of the narrow-range resolution at short ranges), and a dip in V_{pk} for ranges that are too large. The solid line on the velocity plot has been drawn to connect the points where the range is near the vortex. The gaps in the data can be misinterpreted as the vortex core, especially for the alleviated runs where the velocity magnitude is constant across the vortex. (The X's on the range plot show the vortex range selected for each range scan according to a processing algorithm to be discussed subsequently.)

6.2 OPERATION OF LASER DOPPLER VELOCIMETER

The LDV system was set up and calibrated at the Rosamond test site prior to conducting the actual wake surveys. During the set up process, the optical bench was leveled with external van jacks, using a bubble level for reference (estimated accuracy of

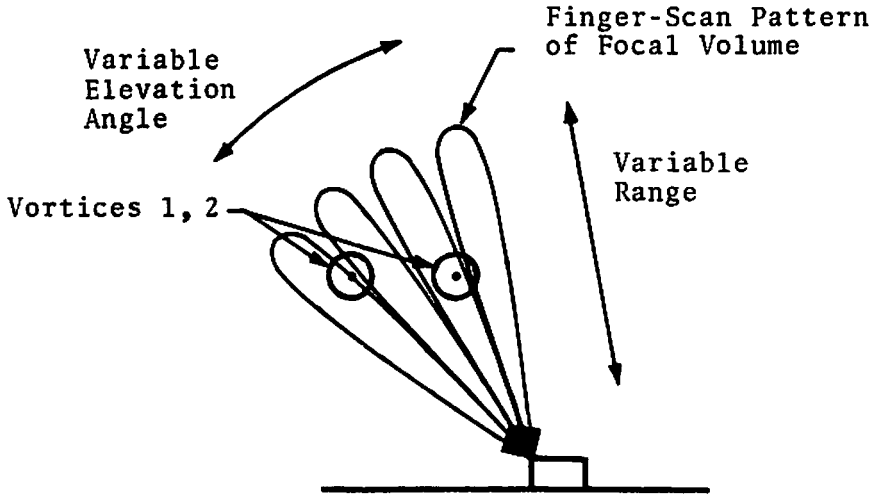

FIGURE 27. FINGER-SCAN MODE

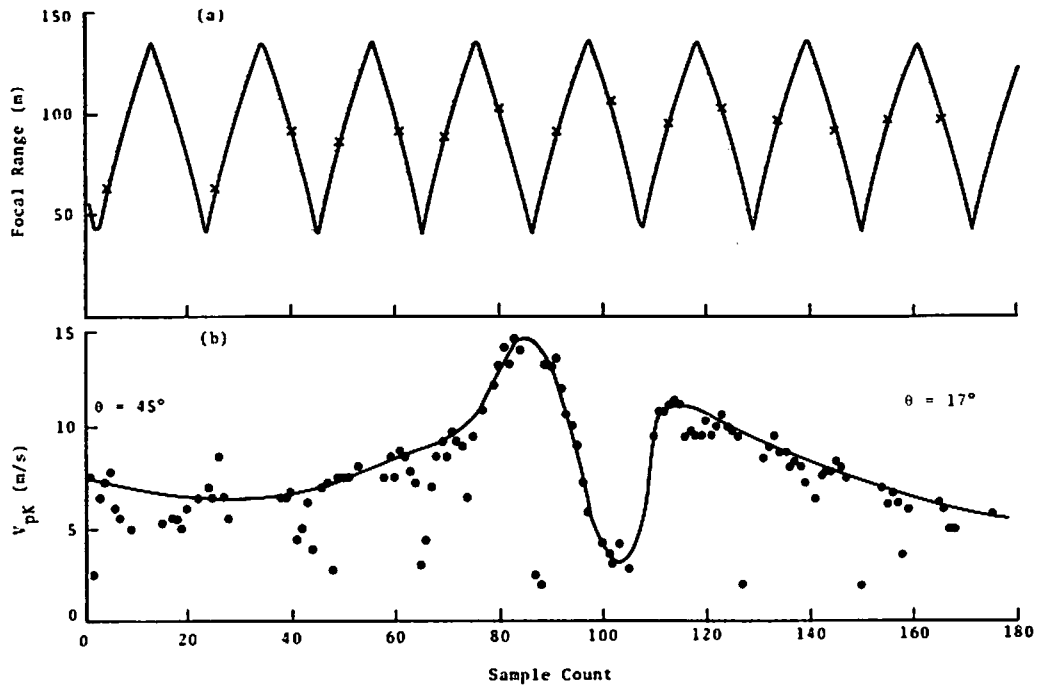

FIGURE 28. RANGE (a) AND VELOCITY (b) FOR ONE ANGLE SCAN OF RUN 27 AT ABOUT 10 SECONDS OF ELAPSED TIME

± 0.5 deg). For the second day of the tests, the scanner was offset 45 deg using a tri-square for reference (estimated accuracy of ± 0.5 deg). Prior to the actual wake surveys, the elevation- and azimuth-angle readouts from the LDV were calibrated to account for the offset. The calibration involved pointing the optical system at the sun and comparing the observed elevation- and azimuth-angle readouts with those given in the ephemeris. The results indicated that a -3 deg and ± 139 deg correction should be applied to the raw elevation and azimuth readouts from the LDV, respectively.

During the Rosamond tests, the range-resolution and signal-to-noise-ratio characteristics of the LDV were not recalibrated. The range and signal-to-noise-ratio calibrations taken a few months earlier, and documented in Ref. 16, were assumed to be representative of the system's overall performance.

6.3 DATA PROCESSING

The output from the LDV system consisted of the Doppler spectrum of the backscattered signal as a function of the location of the focal volume in space. The output was processed to yield the aircraft downwash field and the wake vortex characteristics. The first reduction and analysis (Ref. 16) of the LDV measurements were carried out as follows: (1) the low-speed signal was digitized and stored on magnetic tape by the on-board minicomputer, and subsequently, processed off-line on a Univac 1108 computer, and (2) the high-speed data were both digitized and processed off-line on a Univac 1108 computer, and the vortex tracks computed on a PDP 11 computer. A flow chart of the data-processing sequence used for this initial Rosamond wake-decay study is shown in Fig. 29. The software system for processing the low- and high-speed LDV data is described in more detail in Refs. 13 and 17, respectively. Because of processing difficulties in the first study of the data, the digital spectral data were reprocessed to yield better vortex tracks and velocity profiles, and the results are contained herein.

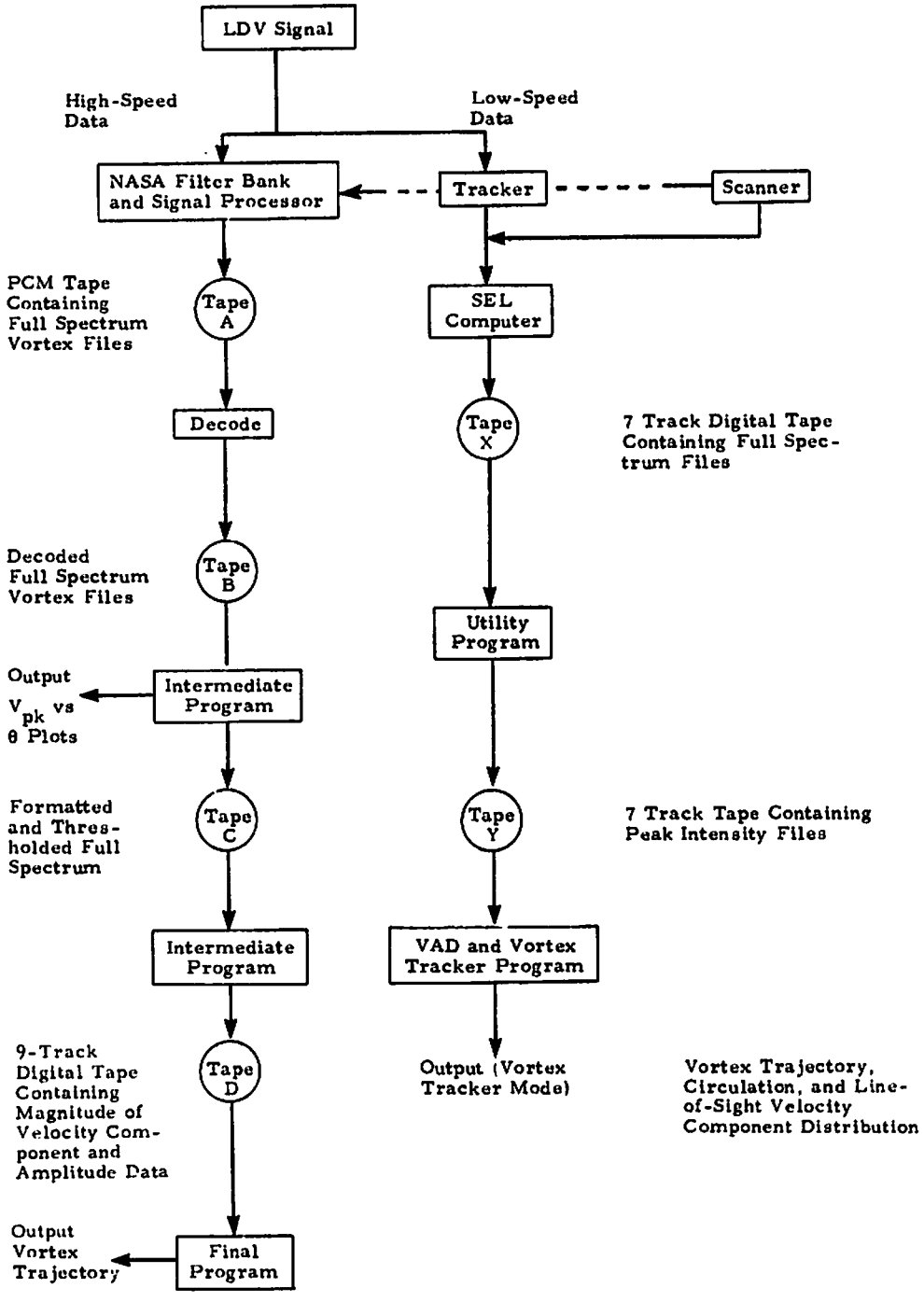

FIGURE 29. DATA-PROCESSING SEQUENCE CARRIED OUT FOR THE ROSAMOND WAKE-DECAY MEASUREMENTS

Both the low- and high-speed data suffered from anomalies in the recorded elevation angle. The low-speed data recorded the commanded angle rather than the actual angle. The actual angle lagged behind the commanded angle by about 0.3 sec, and is rounded off at the ends of the scan. The second study of the data (discussed herein) corrected the data for the time delay but not for the rounding. In the high-speed data, the angle exhibited abrupt steps of about 0.7 deg, which spoiled the high-resolution vortex-velocity plots. This problem was traced to an error in the transverse coordinate, which was corrected by requiring continuous motion of the focal spot. The range magnitude was also incorrect by approximately a factor of 3 in the high-speed data. The correctly recorded ranges on the low-speed data were used to analyze the high-speed arc-scan data.

Because most of the results from the initial study of the data (Ref. 16) have been corrupted by these anomalies, only a small portion of those results are included here. Accordingly, the discussion of data processing concentrates on the second study, which has not been documented elsewhere.

6.3.1 Low-Speed Data

In the second study, the low-speed data were first scanned by means of line-printer plots of the Doppler spectra. Each spectrum was plotted on a line with different characters denoting different levels of spectral intensity. These plots showed that, for some runs, excellent vortex-velocity profiles could be obtained.

For the arc-scan data, it is possible to identify the angle of the vortex core by looking for a region of high velocities with a dip in the moddle. Figure 30 shows the vortex-velocity profile resulting from the data of Fig. 26. The velocity has been reversed at the vortex core, and the elevation angle has been converted to vortex radius by assuming the vortex is at the focal distance. If one knows the vortex-velocity profile, one can calculate [equation (13)] the circulation profile shown in Fig. 31.

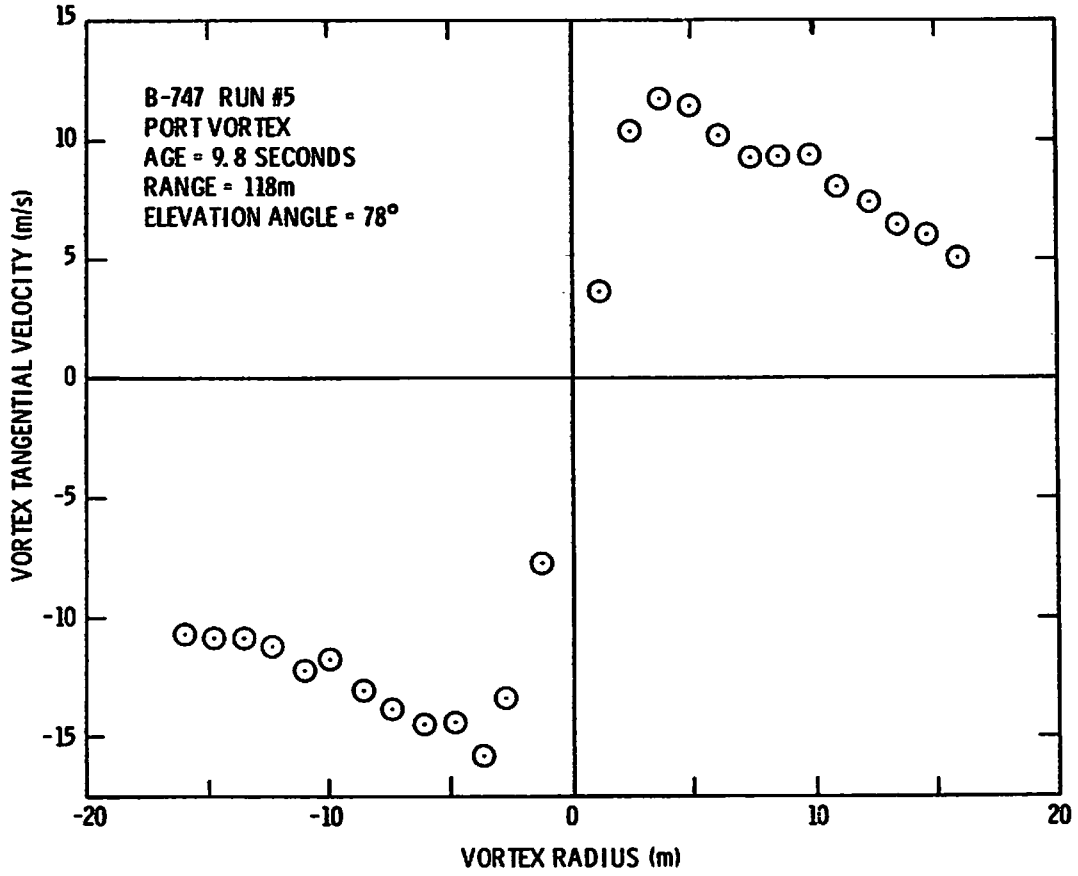

FIGURE 30. VORTEX VELOCITY PROFILE FROM ARC-SCAN DATA

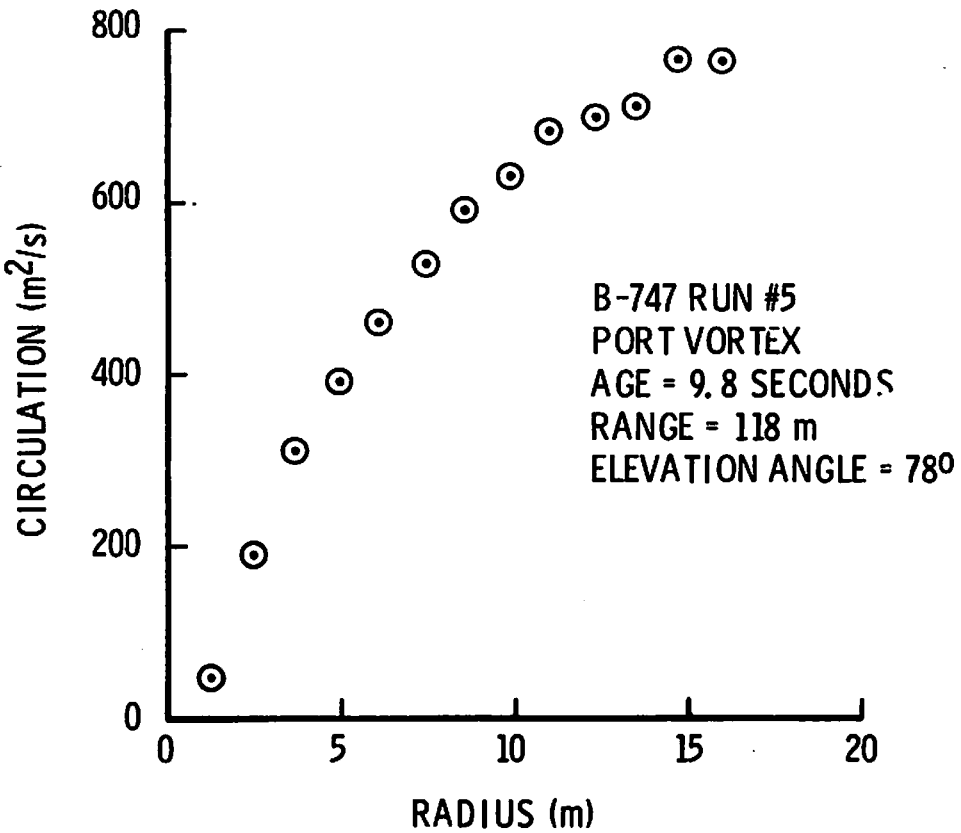

FIGURE 31. VORTEX-CIRCULATION PROFILE

One should note that any error in vortex range introduces proportional errors in circulation. In addition, one can calculate the average circulation [equation (16)] for various radii. Figure 32 shows the decay in Γ' for the first 40 sec of Run 5.

The techniques for processing finger-scan data were more complicated since they had to deal with simultaneous variation of both range and angle. Each range scan was first examined to find the range of highest intensity, interpolating between sample points where appropriate. These ranges were marked as X's in Fig. 28. The various range scans were examined for the highest velocity, which indicated the edge of the vortex core. The vortex range was taken as the average range for nearby range scans. The vortex range was used to calculate a window of ranges over which the velocity measurement was valid (6 to 8 times ΔR in equation (7)). These velocities were then used to find the vortex core as an angle about which the velocity profile was symmetric. The last step was unreliable because of missing data; consequently, the vortex angles were picked by eye from the line-printer spectral plots. Figure 33 shows a velocity profile obtained by this approach (from the data in Fig. 28). Figure 34 shows vortex tracks for Run 27. For comparison, the photographic tracks for this run are also shown. The LDV height data are more consistent than the lateral position data because the dominant source of error is poor range resolution. For the relatively low elevation angles observed here, the range resolution has influenced the lateral position more than the height.

6.3.2 High-Speed Data

The second study of LDV high-speed data started with NASA data tapes containing the spectral amplitude for all 104 frequency bins. Figure 35 shows two spectra, one with vortex data and one without. Zero frequency corresponds to the large spike at bin 25. The background level varies strongly with frequency; the cause is unknown. To apply a uniform threshold to the vortex data, the background was averaged at a time when no vortex was present, and

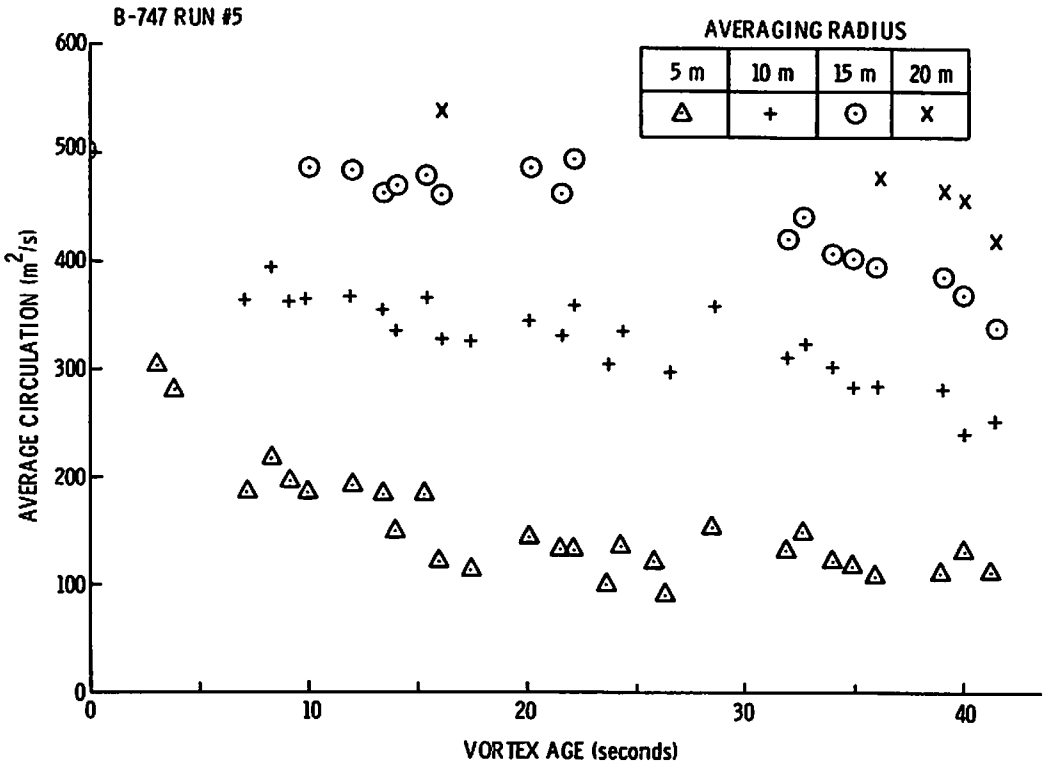

FIGURE 32. VORTEX AVERAGE CIRCULATION VERSUS AGE

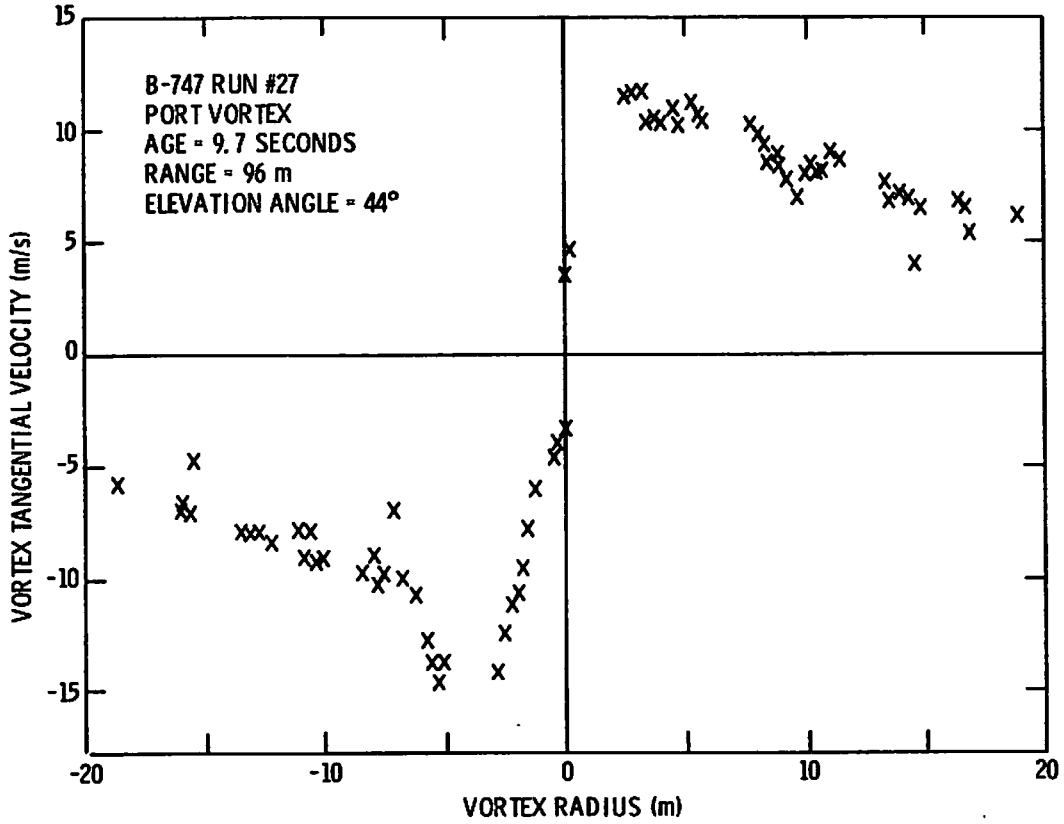

FIGURE 33. VORTEX-VELOCITY PROFILE FROM FINGER-SCAN DATA

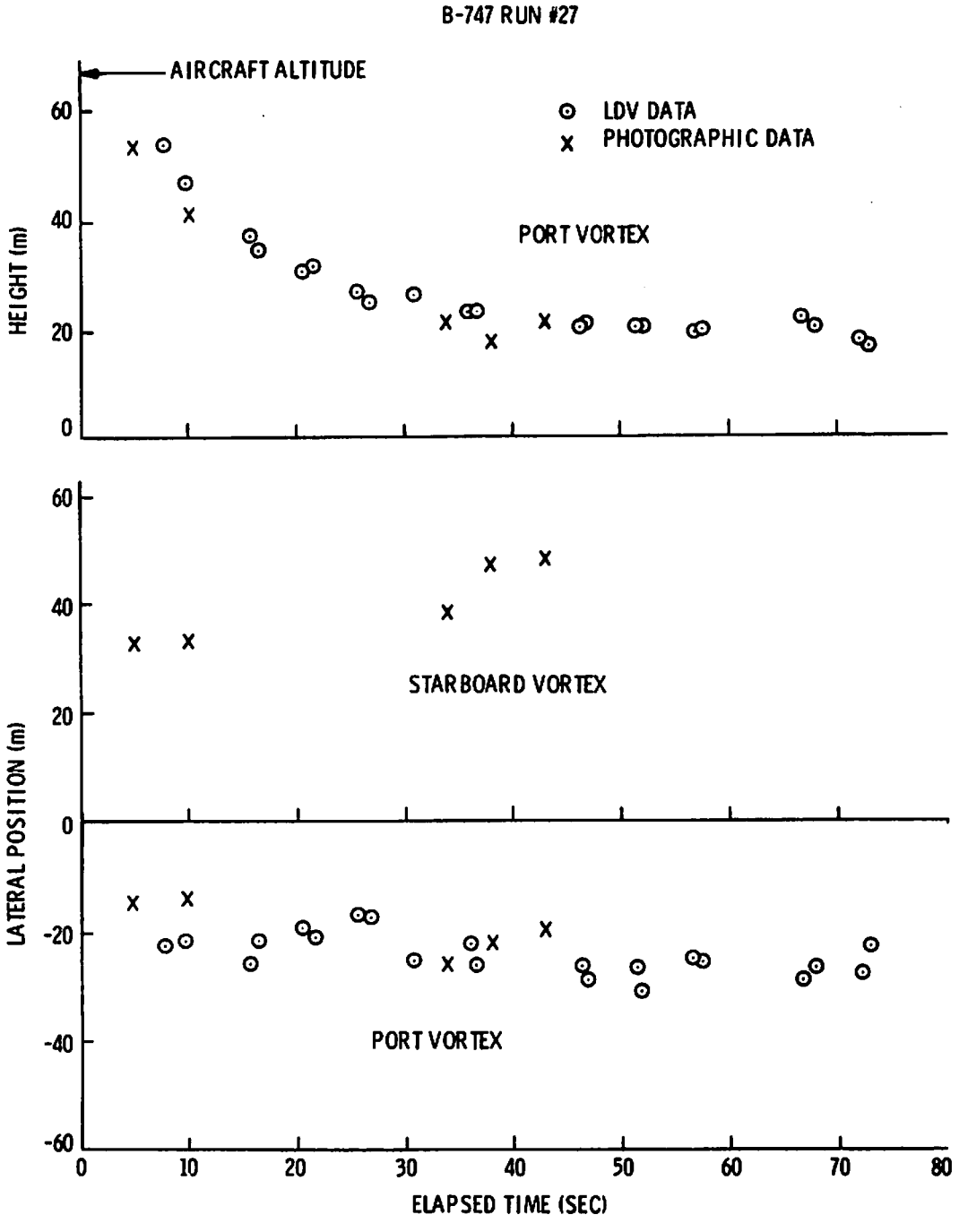

FIGURE 34. VORTEX TRACKS FROM LOW-SPEED DATA

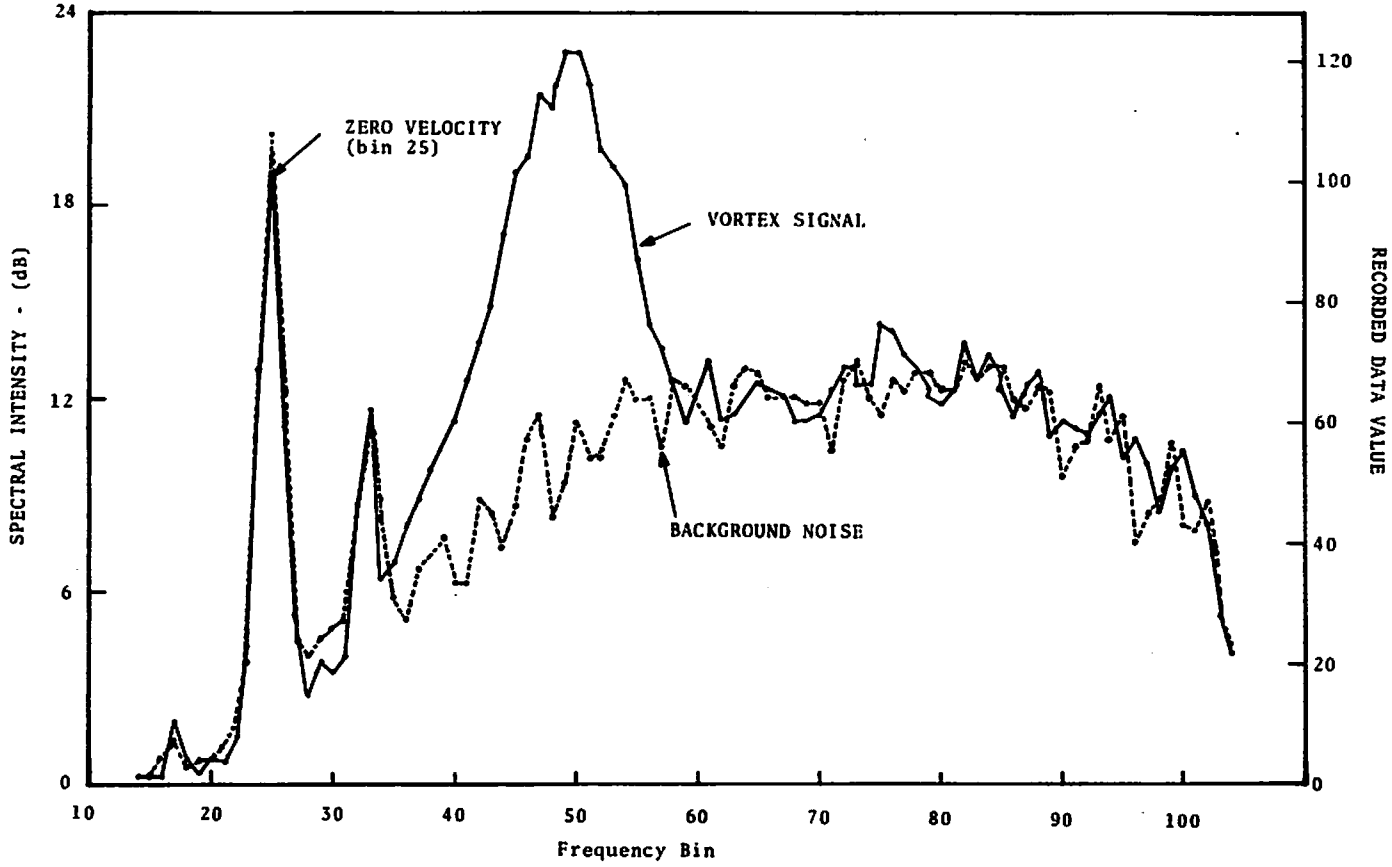

FIGURE 35. LDV SPECTRA FROM HIGH-SPEED DATA

then set to a value (25) which was just sufficient to gate out all noise points. This procedure provided a more continuous vortex-velocity profile (using the highest velocity bin with acceptable data) than simply applying a threshold to the raw data. The high-speed data were stored in a compressed form which approximated the logarithmic response (32 equals 6 dB) plotted in Fig. 35. The subtraction technique, outlined above, was therefore a proper procedure if the background variation in Fig. 35 were due to white noise passing through a system with a frequency-dependent gain.

The purpose of the second analysis of the high-speed data is to study the decay of the vortex-velocity profile. For this purpose, the most useful runs are those employing the arc-span mode at high altitudes. The decreased range resolution of the LDV at long ranges assures that good vortex-velocity profiles can be obtained even when the vortex is far from the LDV focal distance. Run 8, a landing configuration run at 240-m altitude, yields excellent velocity profiles out to 89 seconds in time. Figure 36 shows selected arc scans from this run. (The full-velocity history is shown in Appendix D.) The velocity V_{pk} is plotted against arc distance using the estimated range of the vortex to convert elevation angle to arc distance. The zero distance in Fig. 36 corresponds to 90-deg elevation. The elapsed times of the ends of the scan are marked as T = time (sec).

Run 12, also in landing configuration at 240-m altitude but with spoilers deployed, was then examined. The vortices were observed to move out of the field of view within 30 sec, thus not allowing any observation of vortex decay. Run 11, in the same configuration but at 180-m altitude, was found to have useful velocity profiles out to 85 sec. Thus, Runs 8 and 11 allowed a direct comparison of the detailed decay of alleviated and non-alleviated vortices. Figure 37 shows selected arc scans from Run 11. The complete data of Runs 11 and 12 are also in Appendix D.

The fundamental problem in processing the high-speed arc-scan data is to estimate the range to the vortices so that the arc-angle measurements can be converted to spatial distances. The clue to

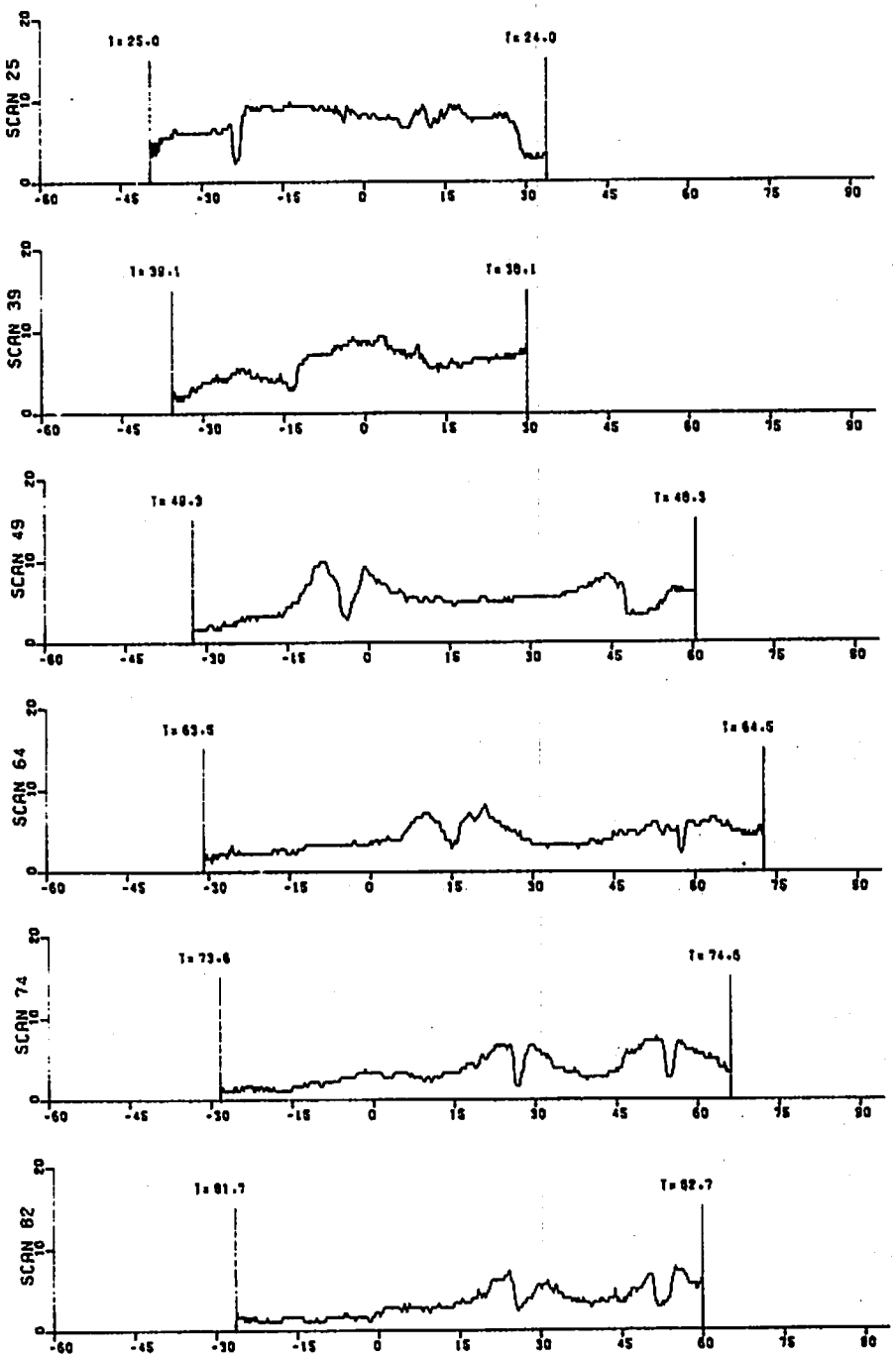

FIGURE 36. V_{pk} VERSUS VORTEX ARC DISTANCE FOR SELECTED SCANS OF RUN 8

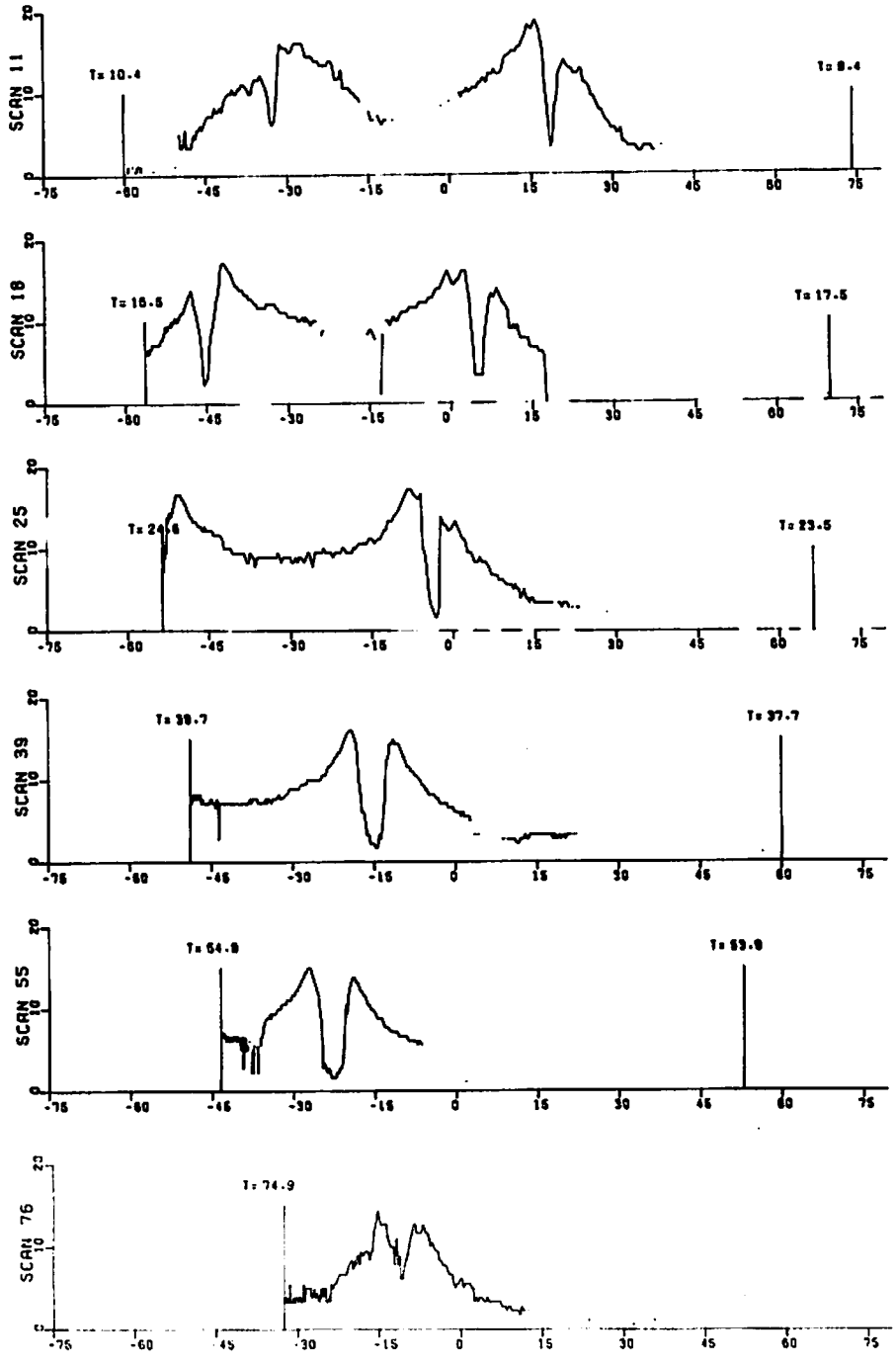

FIGURE 37. V_{pk} VERSUS VORTEX ARC DISTANCE FOR SELECTED SCANS OF RUN 11

the LDV range determination is the laser intensity scattered by the vortex. A number of different ways of evaluating the vortex scattered intensity have been investigated. The intensity algorithm finally adopted integrates the vortex Doppler spectrum above a speed of 4.5 m/s. This limit assures that only scattering near the vortex is included. The algorithm actually sums all data points above frequency bin 33 (see Fig. 35) which have an intensity above threshold after background subtraction. The intensity is uncompressed from its logarithmic form before the sum is carried out. A measure of the scattered intensity from the whole vortex is then obtained by averaging the integrated spectral intensity over the region of 10 m on either side of the vortex center.

The vortex centers have been identified visually as the middle of the velocity dip and the distance calculation used the LDV range. The resulting plot of vortex intensity versus arc-scan number is shown for Run 8 in Fig. 38. Each arc scan represents 1 sec to 1 percent accuracy. Also shown in this figure are the LDV focal range and an estimate of the vortex range (both solid lines). The dashed lines show the $\pm$ 3 dB response ranges for the LDV. The arrows in the intensity plot indicate the points where the LDV range is changed. If the range change were to bring the focal range closer to the vortex range, the intensity should increase. This pattern was observed in Run 8, and was used to estimate the vortex range. An initial descent rate of 2 m/s was based on the observed velocity of 8 m/s midway between the two vortices, which should be 4 times the descent velocity if the 2 vortices were distinct and axisymmetric.

Once the vortex range is known, the velocity data can be processed to give the time dependence of a variety of vortex parameters. One should be aware, however, that any parameters involving the vortex radius or separation can have a systematic error proportional to the error in vortex range. For Run 8 this error is probably less than 15 percent. Figure 39 shows the angular location of the two vortices for Run 8 and the separation between the two vortices when both can be seen. Vortex 1 is lost at scan

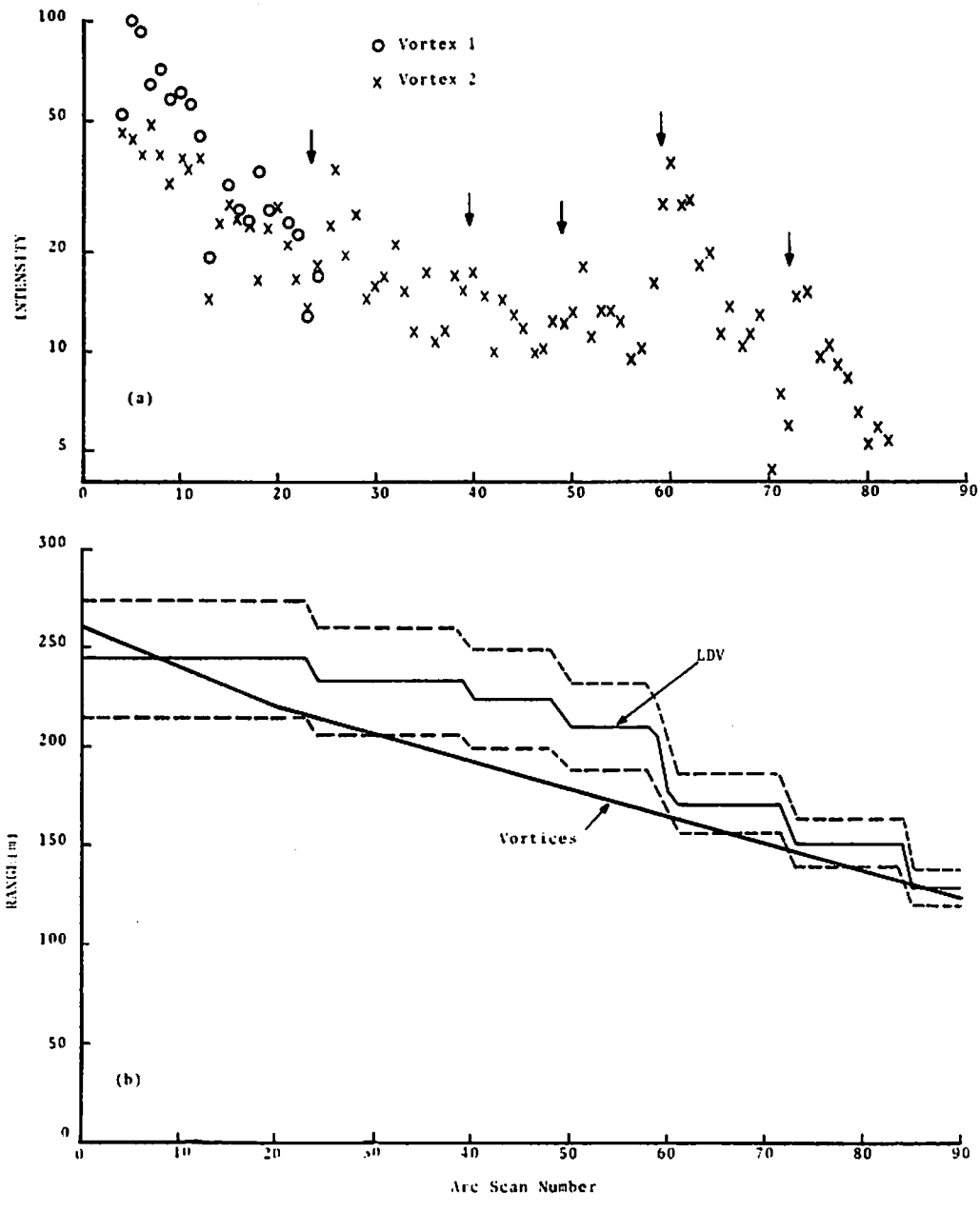

FIGURE 38. INTENSITY (a) AND RANGE (b) FOR RUN 8. The arrows in (a) indicate where the LDV range is changed.

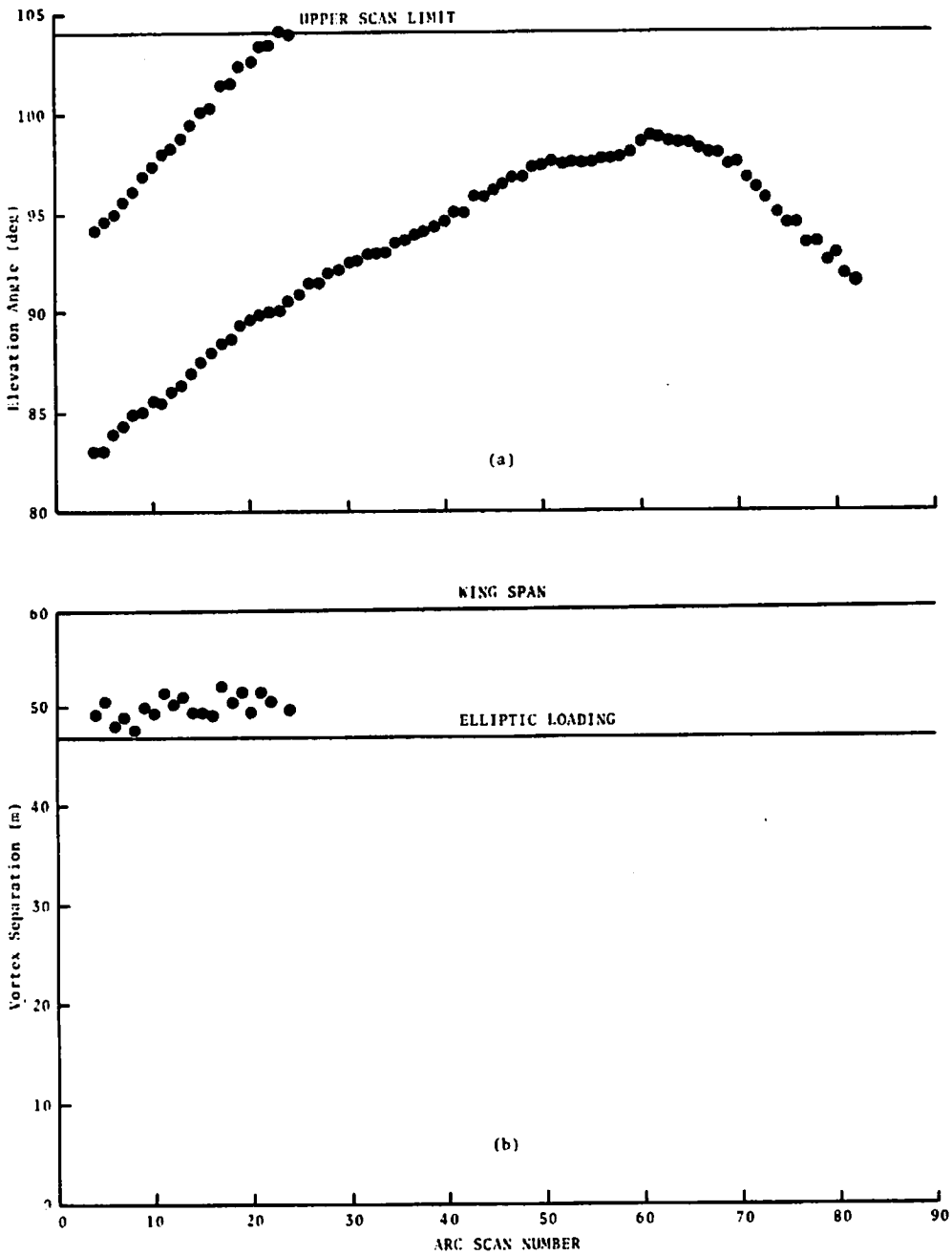

FIGURE 39. VORTEX ANGULAR LOCATION (a) AND SEPARATION (b) FOR RUN 8

24 when it passes beyond the maximum elevation angle which the scanner can reach. For this short time, the vortex separation remains roughly constant at slightly larger than the value for elliptic loading. The vortex-velocity profile can be integrated to give the average circulations [equation (16)] shown in Fig. 40 for three values of averaging radius. The values on each side of a vortex are averaged to eliminate most of the effects of the other vortex.

The wake-velocity profiles can be interpreted as the sum of the velocity profiles from two distince centers of vorticity (the vortex cores) and any other vorticity generated by buoyancy and decay mechanisms. The data for one vortex can be analyzed by subtracting the effect of the other vortex, and by assuming that any other effects simply add a constant velocity to the vortex. According to Fig. 39, the vortex separation b' is 50 m which can be used even when the other vortex is out of the field of view. The vortex circulation Γ_∞ can be estimated from v_c, the velocity between the vortices, as $\Gamma_\infty = \pi b' v_c$, which gives 628 m^2/s for v_c= 8 m/s. The velocity data have been processed as follows:

a) Subtract the effect of the other vortex.

b) Average the velocities with radii in 3-m intervals (0 to 3 m, 3 m to 6 m, etc.). Gaps in the velocity data of more than 5 points terminate the processing.

c) Find the velocity offset which gives the least sum of the square of the differences of the averages on each side of the vortex, and calculate the standard deviation of the differences.

d) Adjust the assumed vortex-center location to minimize the standard deviation, using quadratic interpolation to find the absolute minimum.

e) Reject data where the standard deviation is greater than 1.6 m/s.

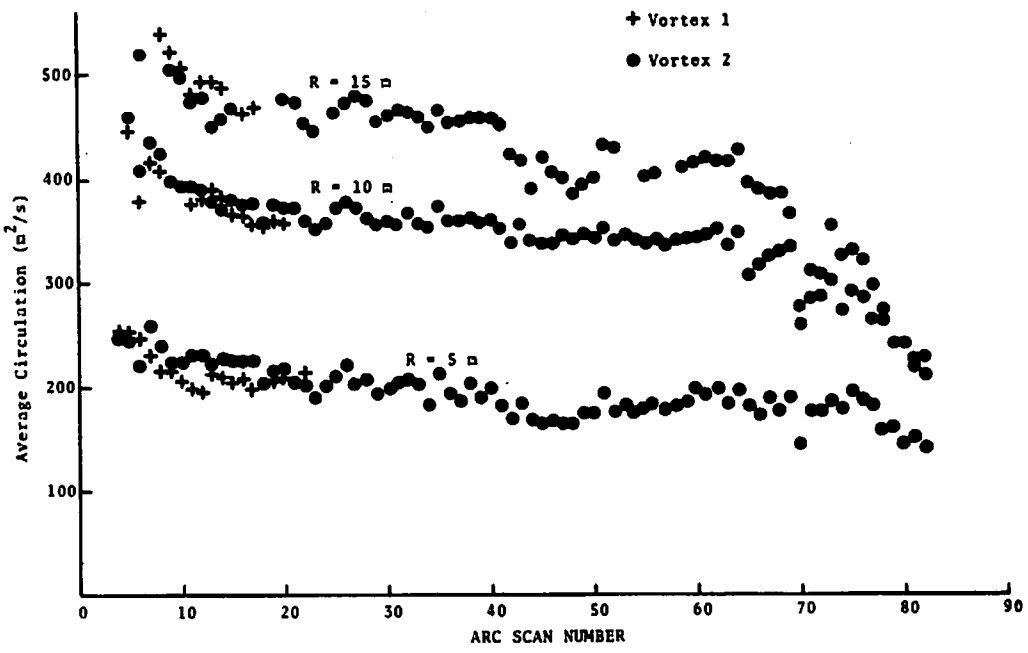

FIGURE 40. AVERAGE CIRCULATION VERSUS ARC-SCAN NUMBER FOR RUN 8 USING AVERAGING RADII OF 5, 10 AND 15 M

The results of this procedure are two-fold:

1) The velocity profile of the vortex, shown in Fig. 41a, and
2) The descent velocity of the vortex shown in Fig. 42a.

If the vortex is symmetrical, as shown in Fig. 41, the descent velocity is given by the asymmetry in the wake-velocity profile. It is simply the sum of the velocity induced by the other vortex and the offset velocity needed to symmetrize the vortex. In Fig. 42b, the time integral of the descent velocity is compared with the previously assumed vortex range, which is essentially the vortex altitude for the observed elevation angles near 90 deg (Fig. 39).

Some care was exercised in selecting the distance over which the vortex could be assumed to be symmetrical. After the vortex began to decay, the maximum radius used in the processing was reduced from 24 m to 12 m. The measured descent velocity was found to vary little with large changes in the assumed value of the circulation of the other vortex. The circulation was assumed to be zero after scan 70, when the other vortex had apparently disappeared.

The vortex-velocity profile of Fig. 41a is transformed in Fig. 41b to a plot of circulation ($\Gamma = 2\pi rv$) versus vortex radius. Figure 43 shows the plot versus the logarithm of the radius. The presence of a straight-line portion in this plot is consistent with a turbulent vortex according to the analysis of Hoffman and Joubert (Ref. 18). The circulation takes the form:

$$\Gamma(r) = \Gamma(r_c)\{(1 + \ln(r/r_c)\}, \qquad (9)$$

where r_c is the radius of maximum velocity (r_c = 2.51 m and $\Gamma(r_c)$ = 253 m^2/sec in Fig. 43). The velocity corresponding to the solid line in Fig. 43 is plotted as a solid line in Fig. 41a.

The processing of Run 11 has been more difficult than Run 8 because of some anomalies which appear in the data. Figure 44 shows the intensity, LDV ranges, and estimated vortex ranges for

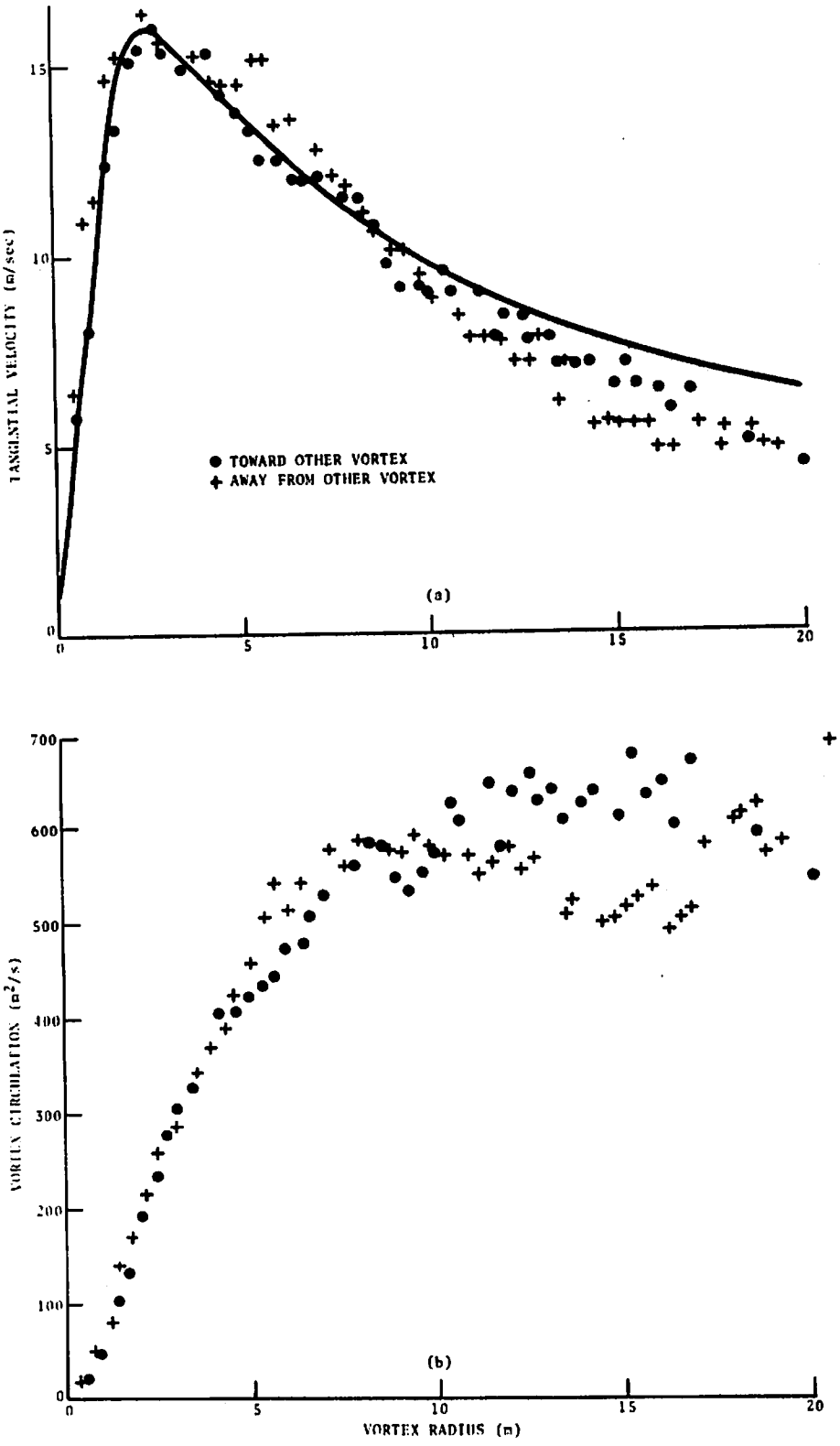

FIGURE 41. VORTEX TANGENTIAL VELOCITY (a) AND CIRCULATION (b) PROFILES FOR VORTEX 2 AT ARC SCAN 11 OF RUN 8

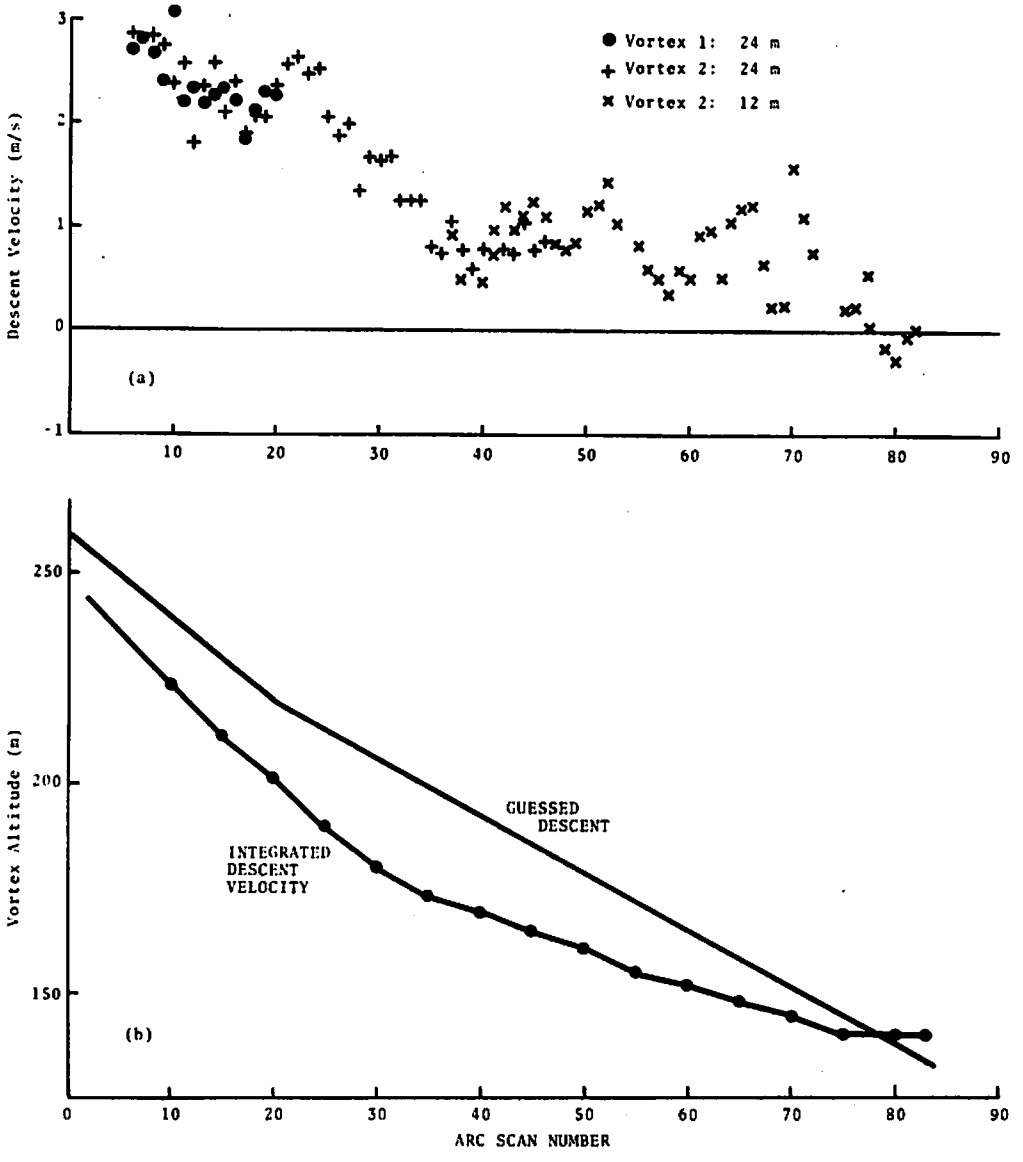

FIGURE 42. VORTEX-DESCENT VELOCITY (a) AND VORTEX ALTITUDE (b) VERSUS ARC-SCAN NUMBER FOR RUN 8

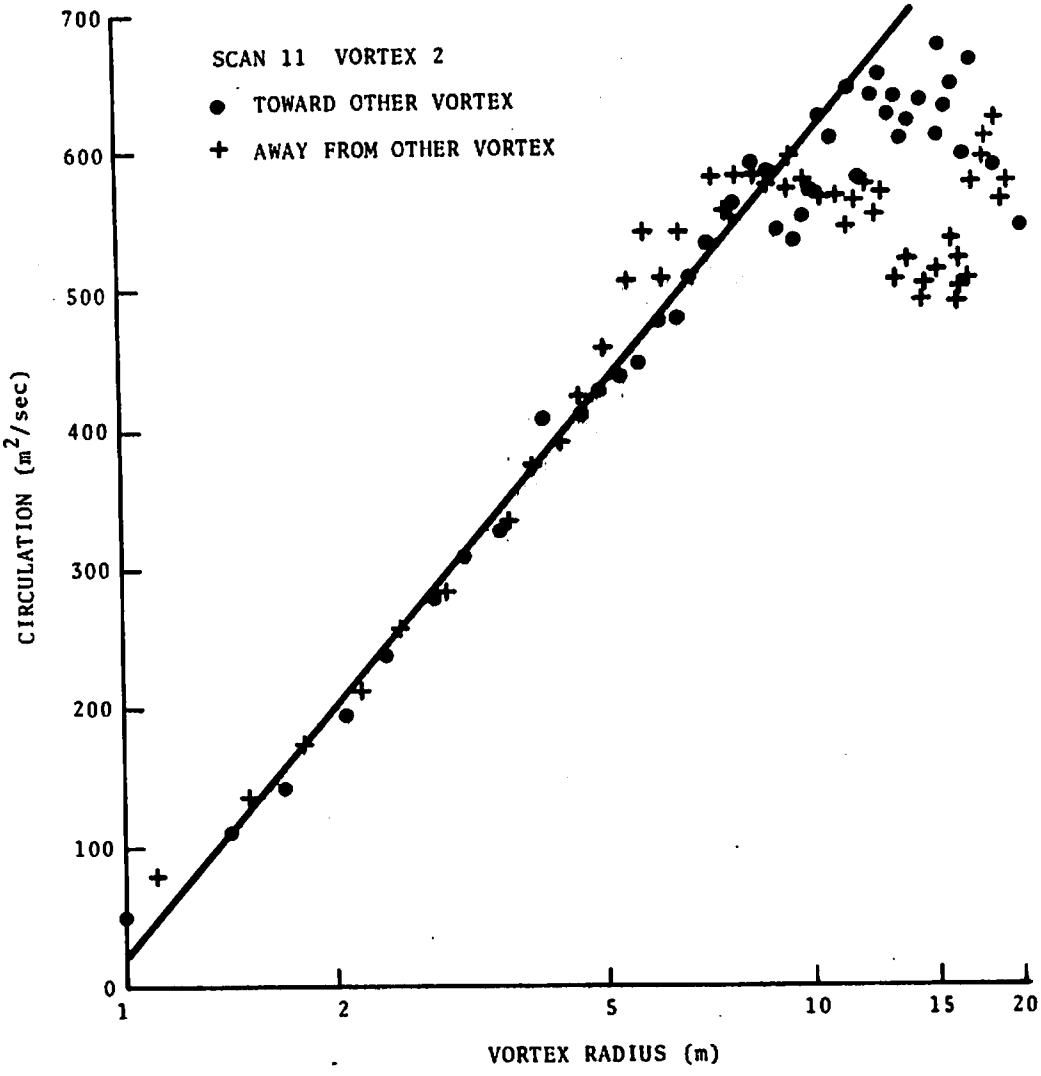

FIGURE 43. CIRCULATION VERSUS THE LOGARITHM OF VORTEX RADIUS FOR VORTEX 2 OF RUN 8 AT ARC SCAN 11

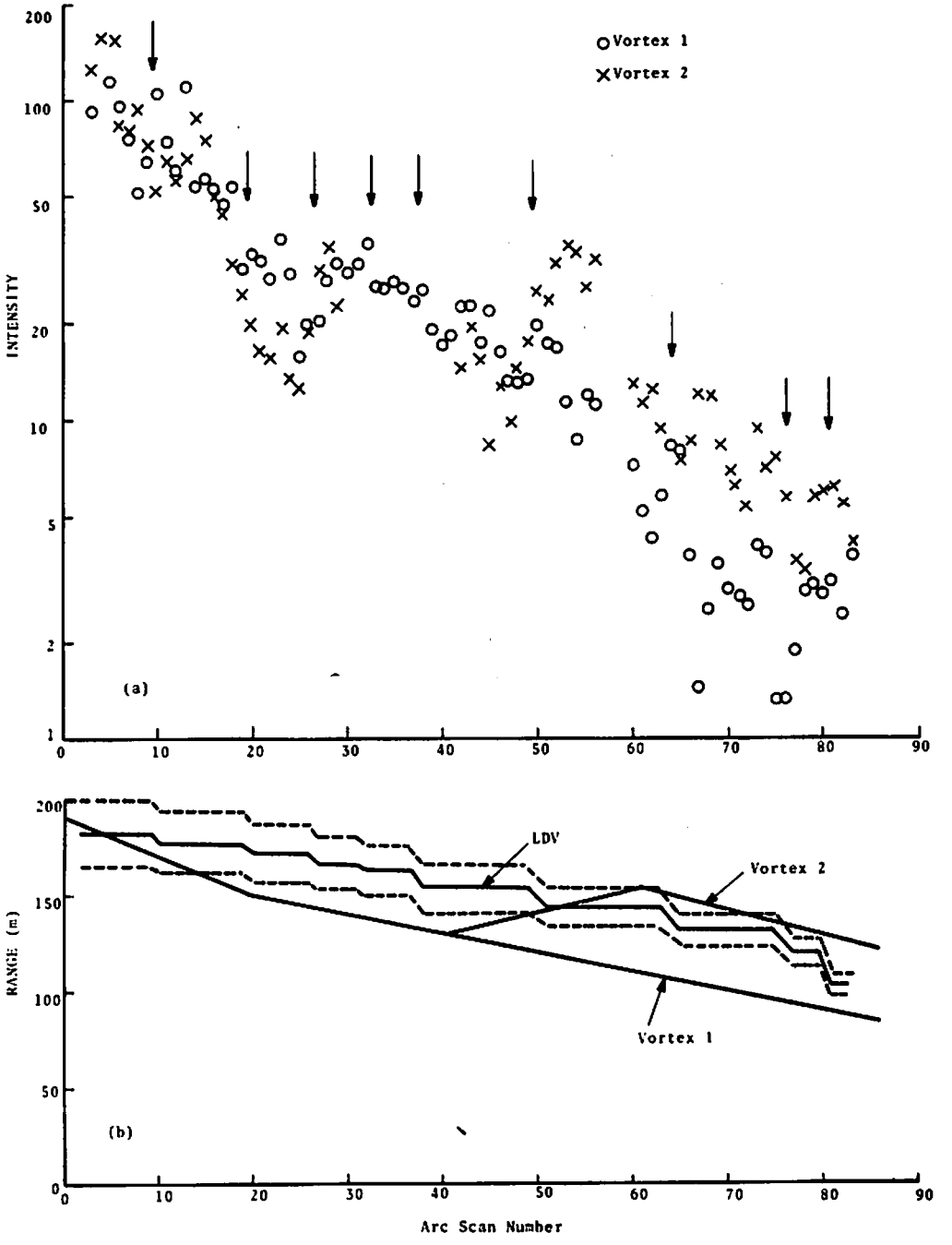

FIGURE 44. INTENSITY (a) AND RANGE (b) FOR RUN 11. The arrows in (a) indicate where the LDV range is changed.

Run 11. Figure 45 shows the elevation angles for the two vortices. One immediate complication is that vortex 2 drops to an elevation angle where the range and height cannot be taken as identical. If one assumes that the vortices are at the same altitude, the angular locations give a vortex separation which decreases by more than a factor of 2 (see Fig. 46). A more reasonable assumption is that the vortices tilt (vortex 2 being higher), giving an increased range to vortex 2 and a reduced angular separation. The estimated vortex ranges in Fig. 44 are based on keeping the vortex separation approximately constant (see Fig. 46b), and attributing the intensity peak for vortex 2 at scan 53 (Fig. 44a) to the vortex range crossing the LDV range. (The wake profiles in Fig. 37 have used the average range to the two vortices to compute the arc distance.) The range estimates in Fig. 44 lead to the tilt angle and vortex separations plotted in Fig. 46. The vortex separations for level vortices in Fig. 46b use the estimated range for vortex 1 to give the vortex altitude. The time history of the average circulations for Run 11 is shown in Fig. 47. The inset after 40 sec shows the results if the vortices are assumed to be at the same altitude as discussed above. The systematic range errors for Run 11 can be as large as 30 percent in view of possible misinterpretations of the data. Note that, the vortex range for Run 12 has been obtained by assuming an initial range of 250 m and the same descent as Run 11.

The velocity profiles for Run 11 have been processed in the same way as for Run 8. The derived descent velocity is plotted in Fig. 48. Figure 49 shows the velocity and circulation profiles for arc scan 25. The straight-line fit in Fig. 49b corresponds to a circulation proportional to the radius; i.e., a constant tangential velocity (7.3 m/s). For comparison with Run 8, the circulation is plotted against the logarithm of radius in Fig. 50; no straight-line region exists.

The processing of the velocity profiles becomes somewhat uncertain at the time when the vortices begin to tilt. The effect of the other vortex is subtracted by using the apparent vortex

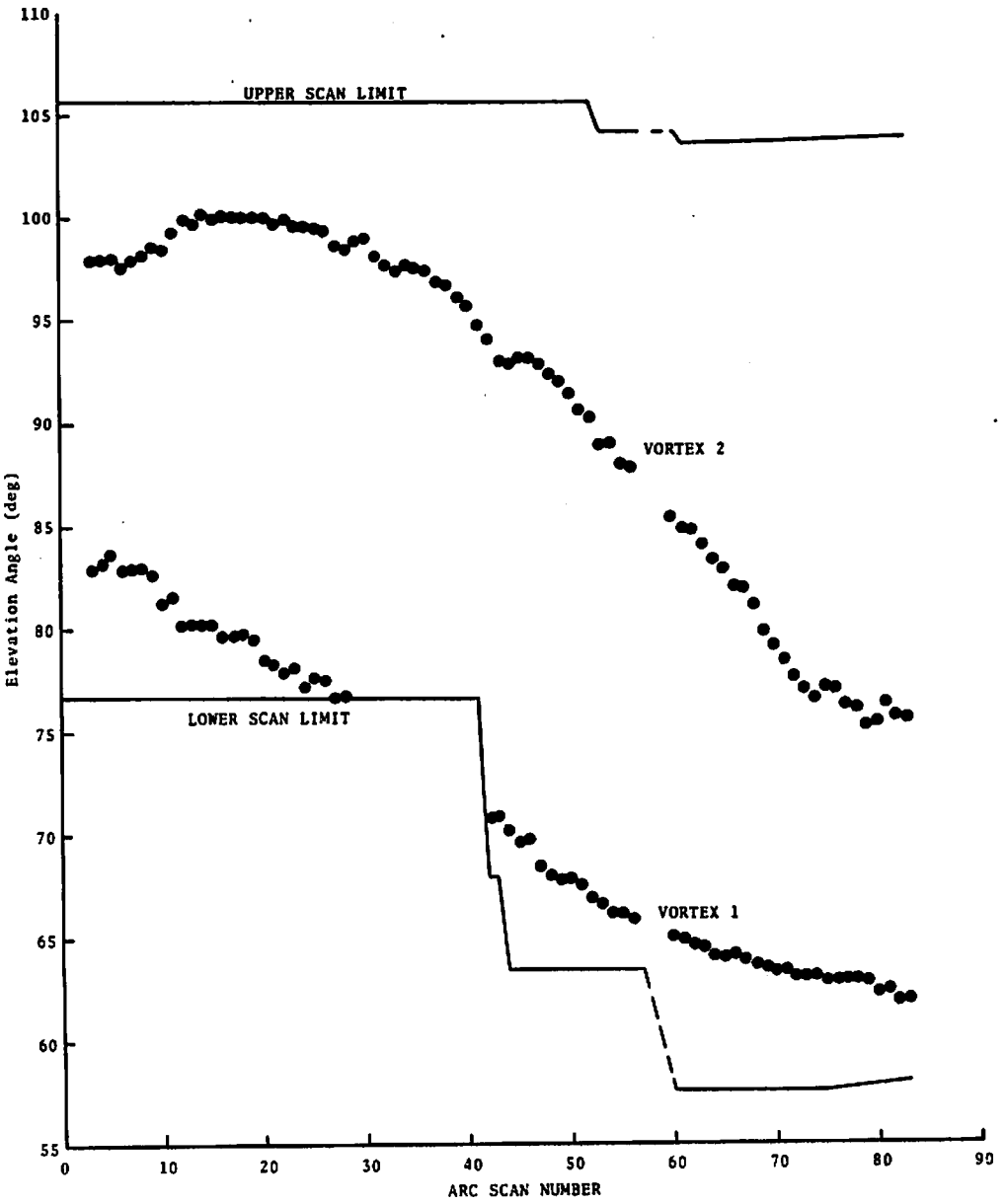

FIGURE 45. VORTEX ELEVATION ANGLE VERSUS ARC-SCAN NUMBER FOR RUN 11

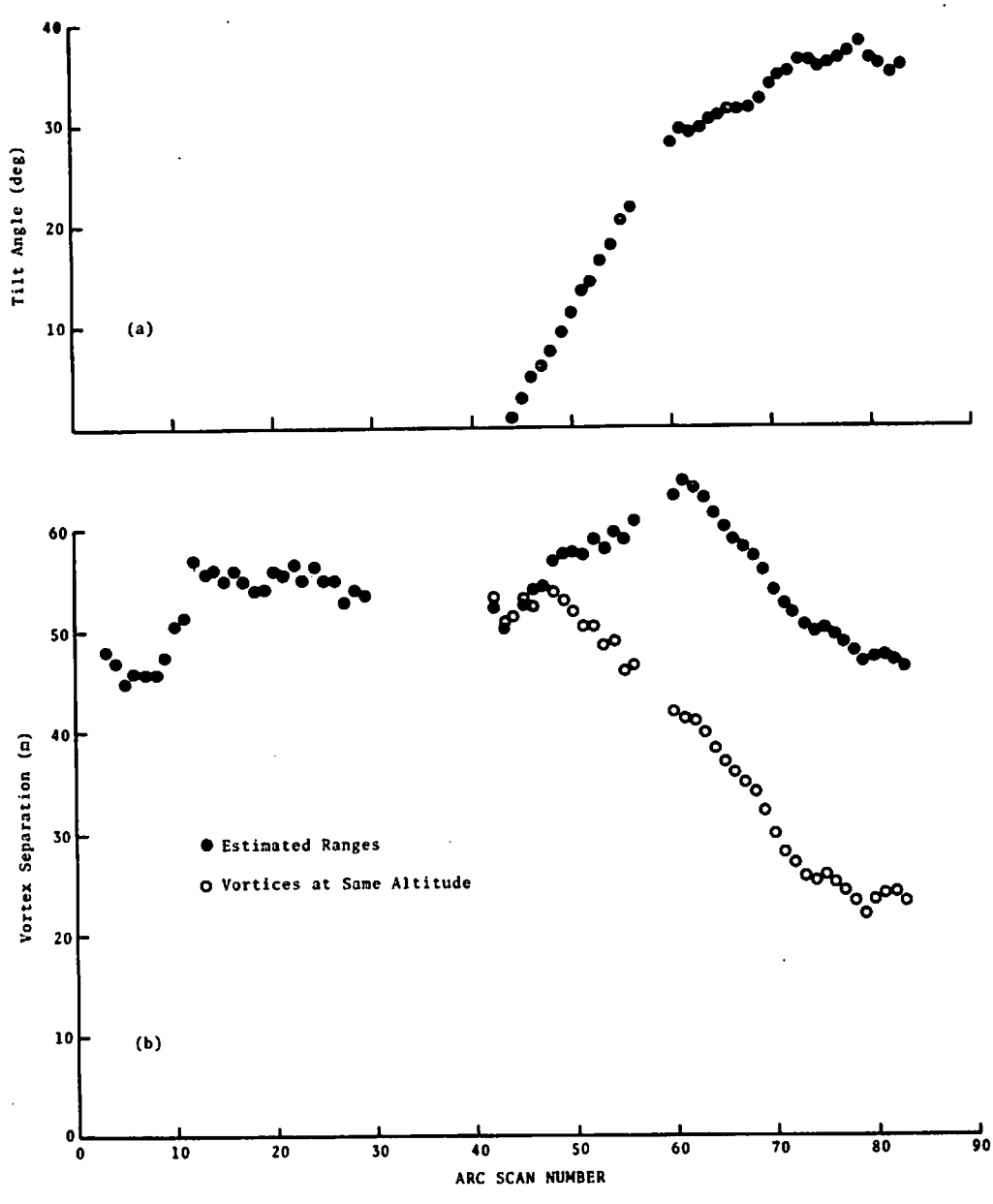

FIGURE 46. VORTEX TILT ANGLE (a) AND SEPARATION (b) FOR RUN 11

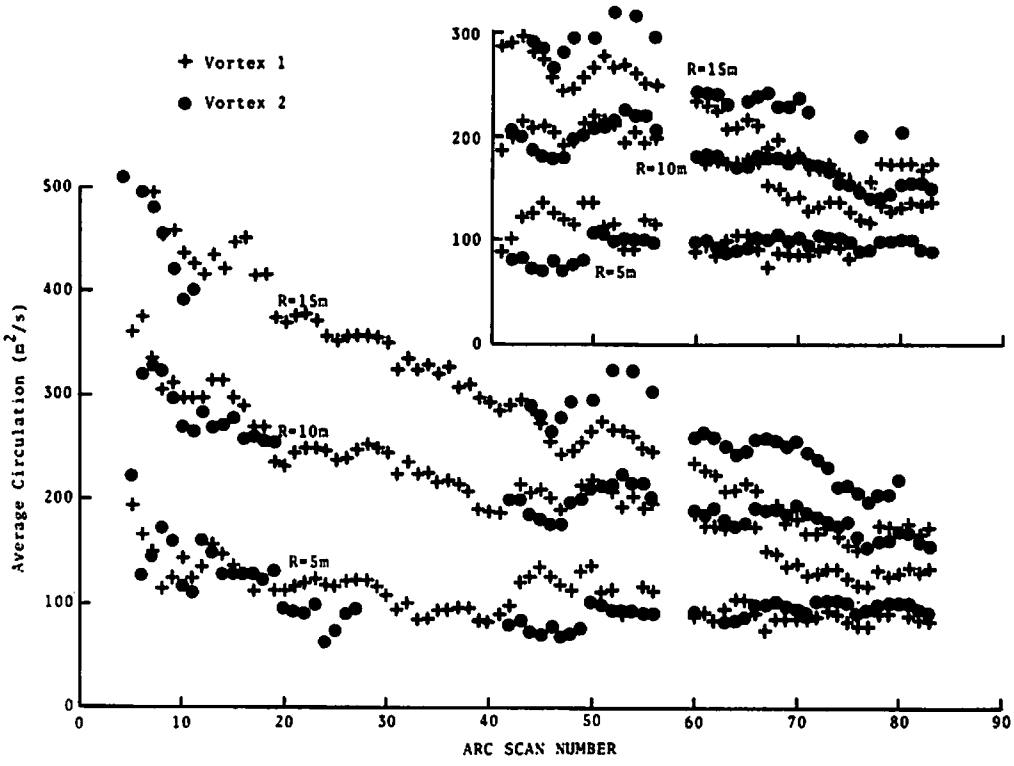

FIGURE 47. AVERAGE CIRCULATION VERSUS ARC-SCAN NUMBER FOR RUN 11 USING AVERAGING RADII OF 5, 10 AND 15 M. The insert shows the effect of assuming level vortices.

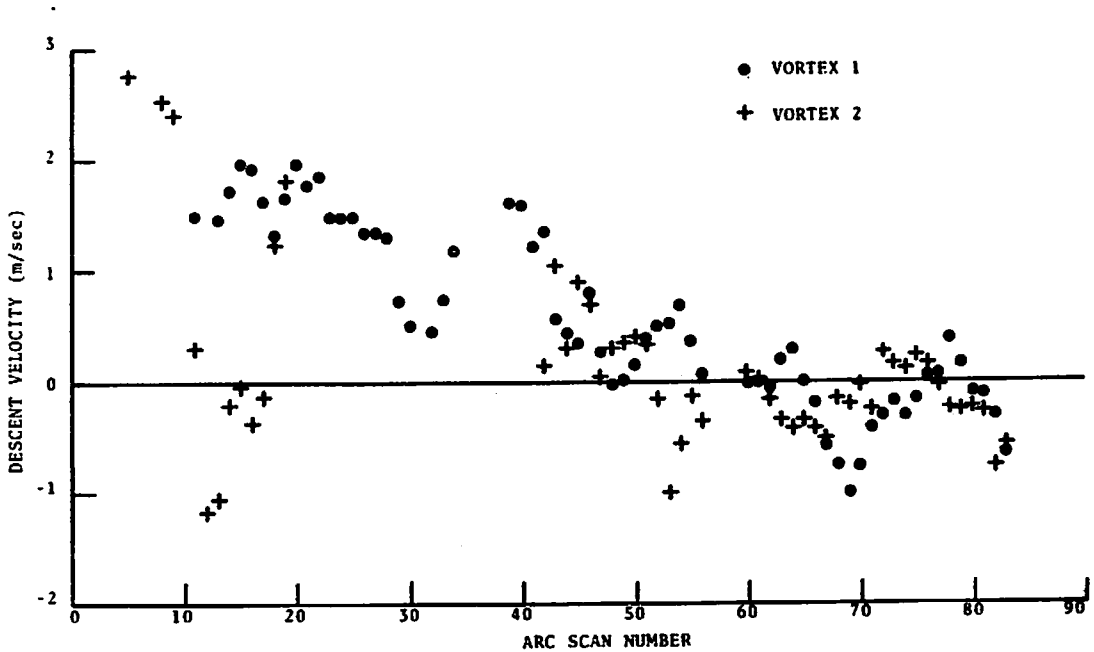

FIGURE 48. DESCENT VELOCITY VERSUS ARC-SCAN NUMBER FOR RUN 11

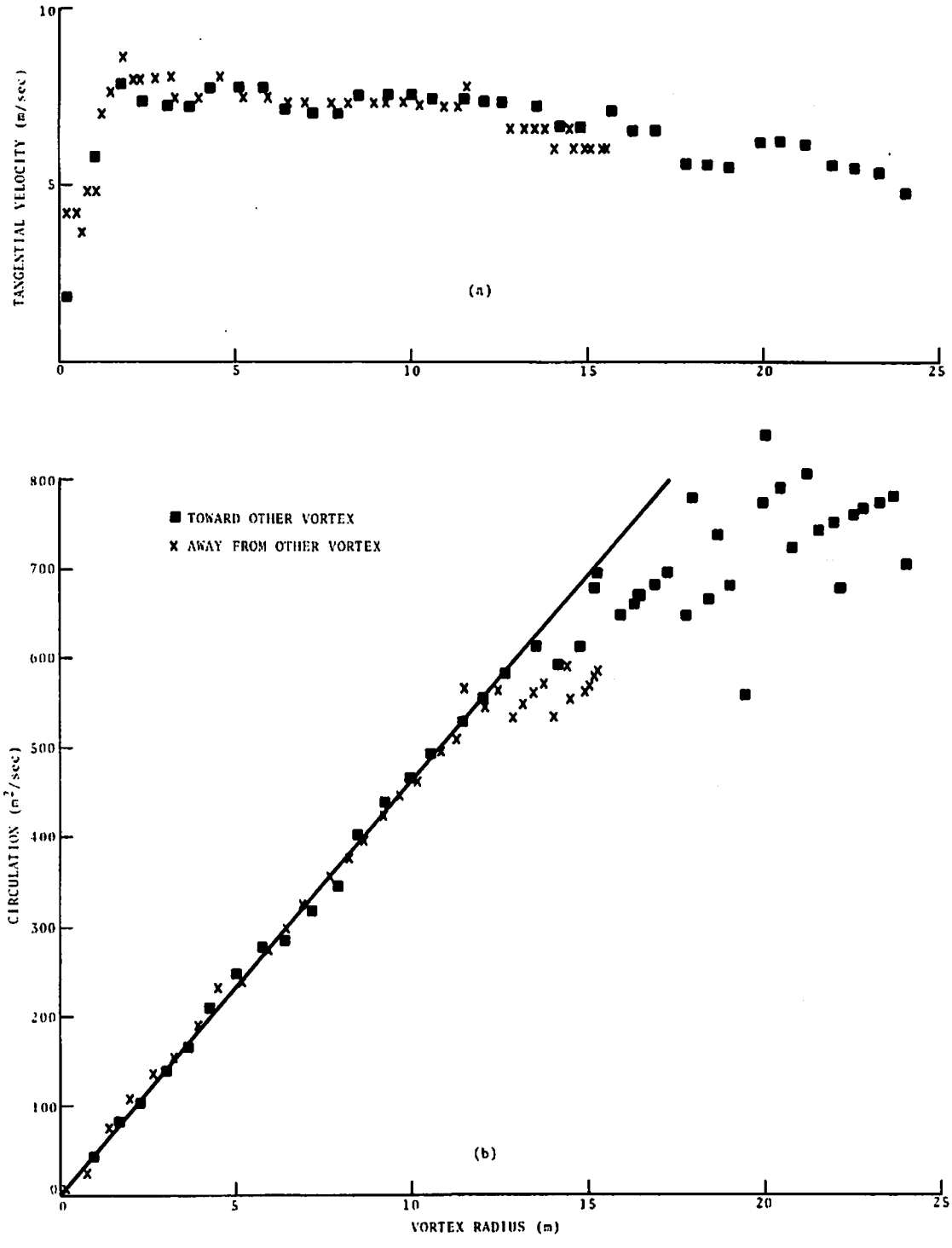

FIGURE 49. TANGENTIAL VELOCITY (a) AND CIRCULATION (b) FOR VORTEX 1 OF RUN 11 AT ARC-SCAN 25

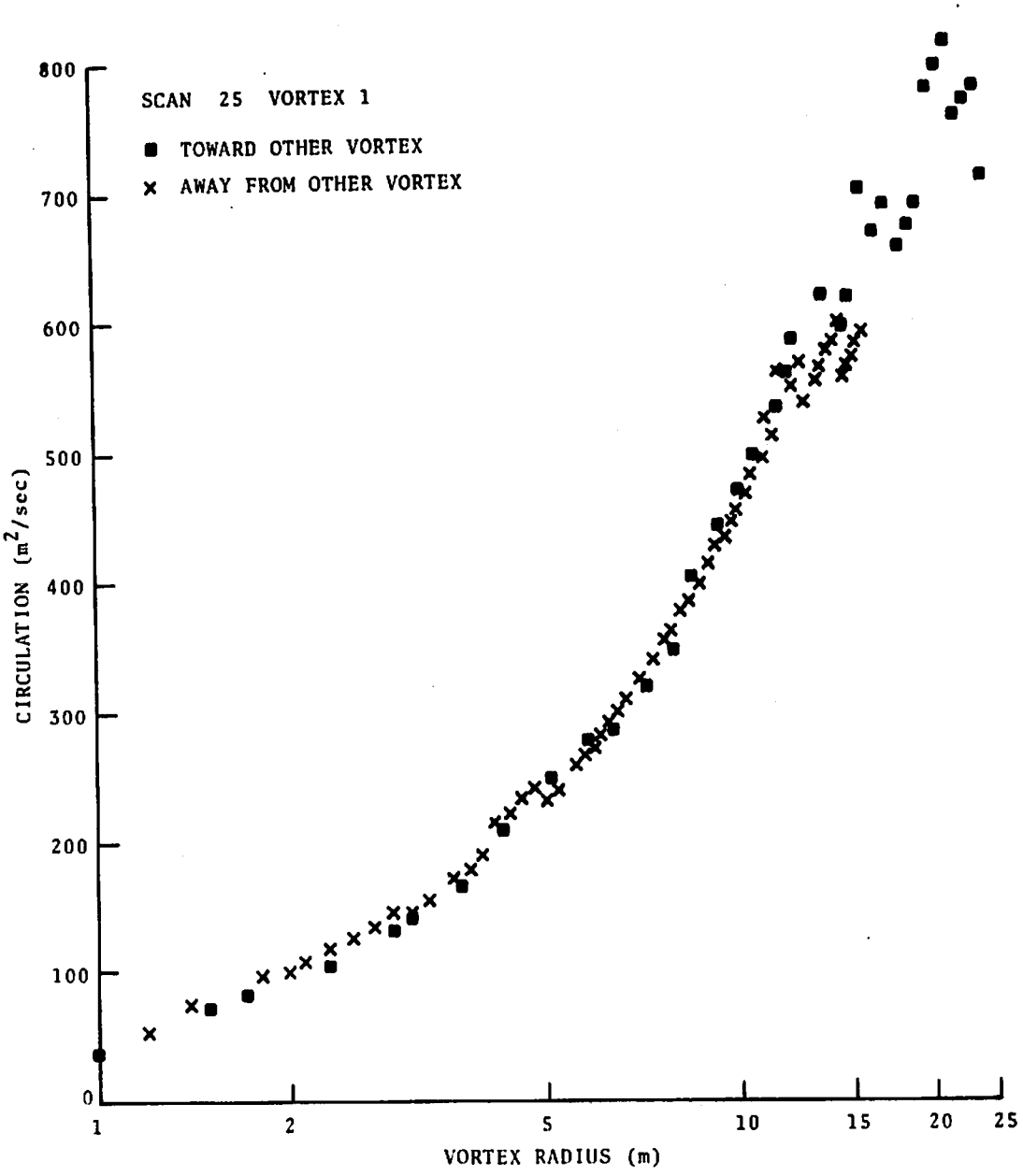

FIGURE 50. CIRCULATION VERSUS LOGARITHM OF RADIUS FOR VORTEX 1 OF RUN 11 AT ARC SCAN 25

spacing and a strength which approximates the velocity midway between the two vortices. The errors from this procedure are small near the vortex core where a different strength simply means a different velocity offset is used. Larger errors can occur at larger vortex radii; the major effect is an asymmetry between the two sides of the vortex. One should note that the plots obtained for velocity and circulation profiles do not include all the points measured. For Run 11, typically, every third point is plotted.

6.4 RESULTS OF LDV WAKE VORTEX MEASUREMENTS

The LDV measurements obtained during the Rosamond tests have been analyzed to determine the dominant characteristics of the B-747 wake. In the following discussion, the observed wake vortex characteristics are described including the vortex rollup, transport, and decay.

6.4.1 Vortex Rollup

To observe the vortex rollup, the downwash field behind the B-747 aircraft was measured with the LDV operated in a constant-range arc-scan mode.

6.4.1.1 Initial Spanwise Downwash Distribution - The magnitude of the peak line-of-sight velocity component, $|V_{pk}|$ in m/s, from the high-speed data is shown as a function of arc distance in Figs. 51 and 52 for Runs 8 and 11, respectively, for the first 10 arc scans. One should note that, because the wake remains near the vortex focal region for this period of time (1 sec per arc scan), the measured velocity is the maximum occurring along the laser beam. In the presence of multiple vortices at different ranges, the wake signatures become a superposition of the velocity peaks of all the vortices.

The wake profile for Run 8 in landing (30/30) configuration shows a rapid rollup (5 sec or less) to a defined pair of vortices with a spacing which remains constant (see Fig. 39) at about 82

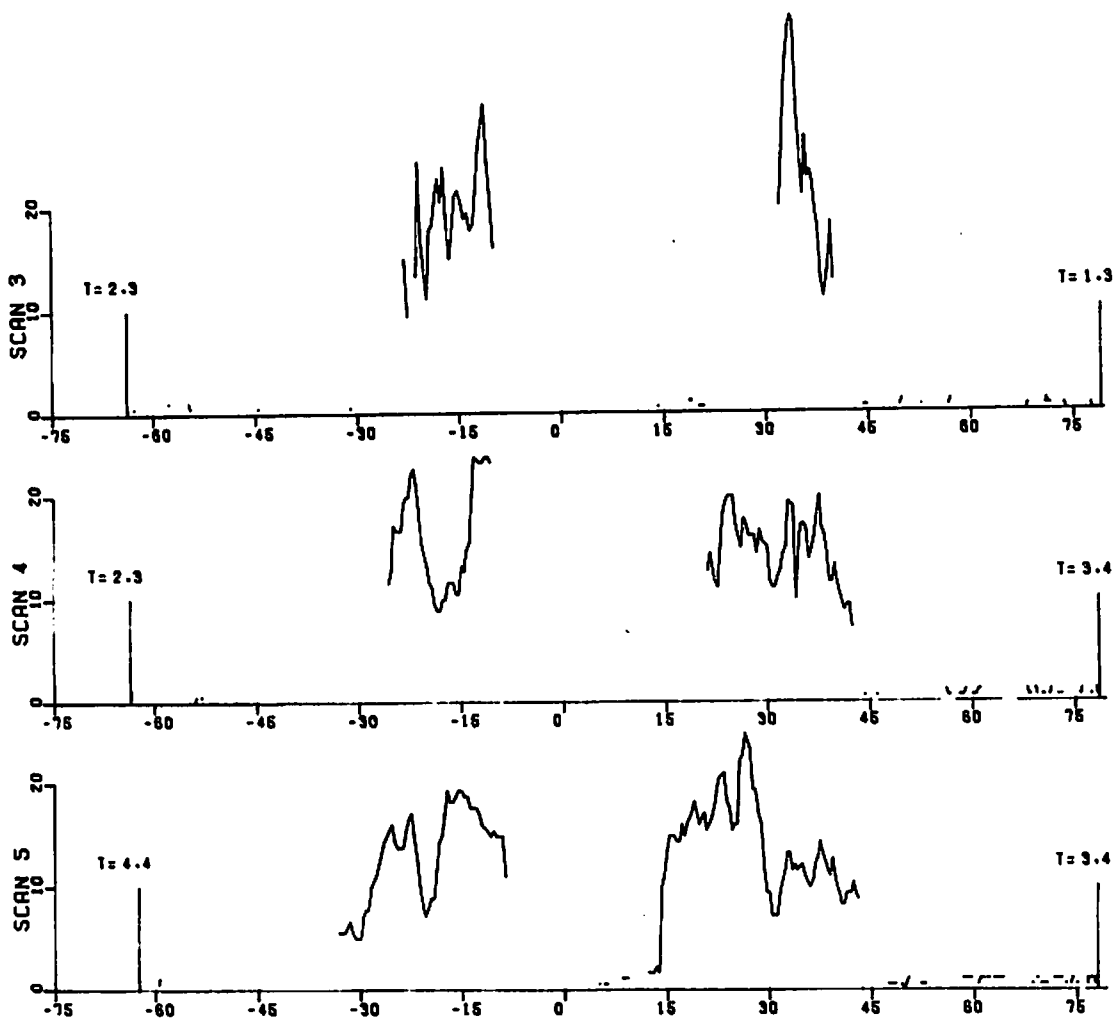

FIGURE 51. VELOCITY PROFILES FOR RUN 8 UP TO ARC SCAN 10

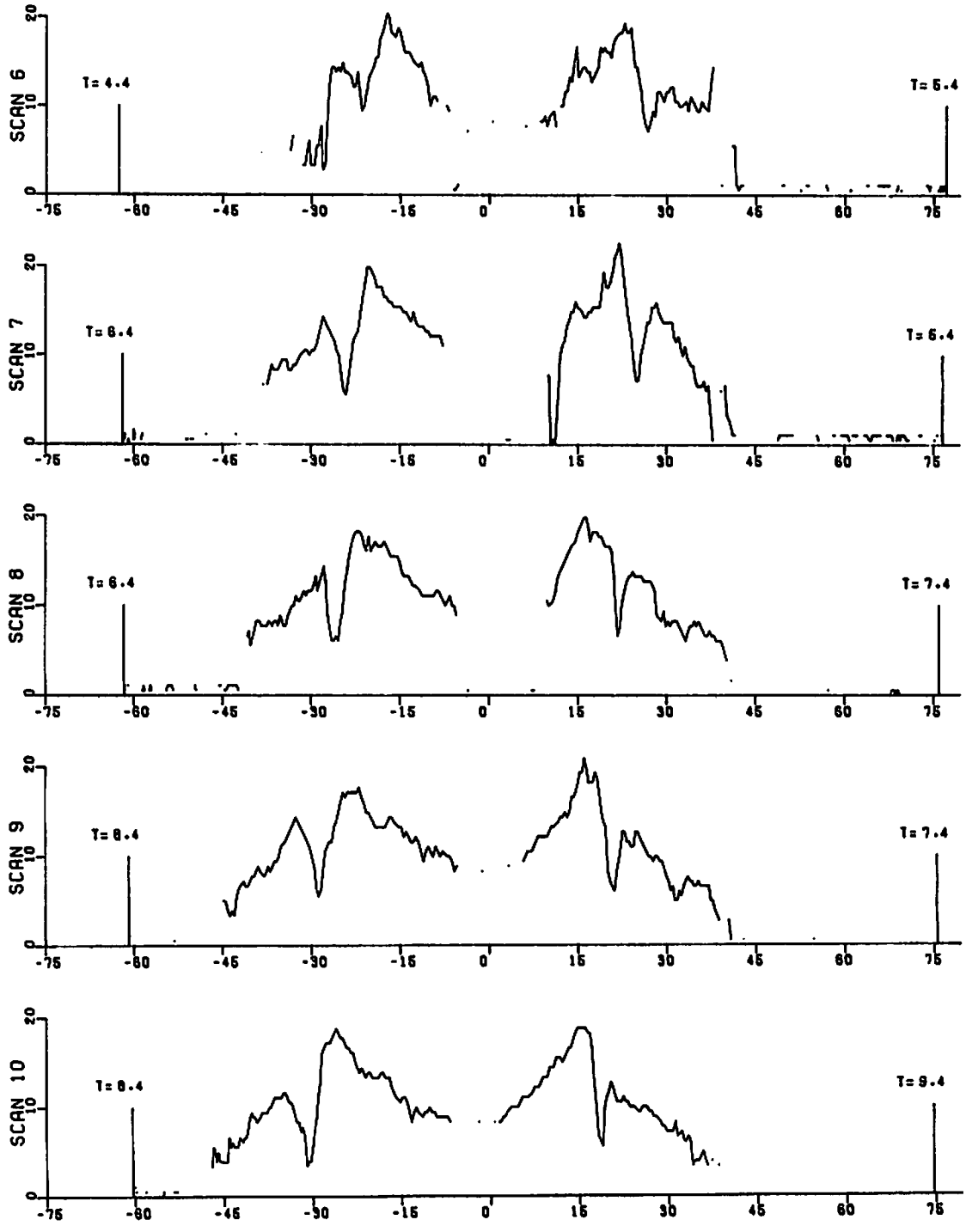

FIGURE 51. (CONCLUDED)

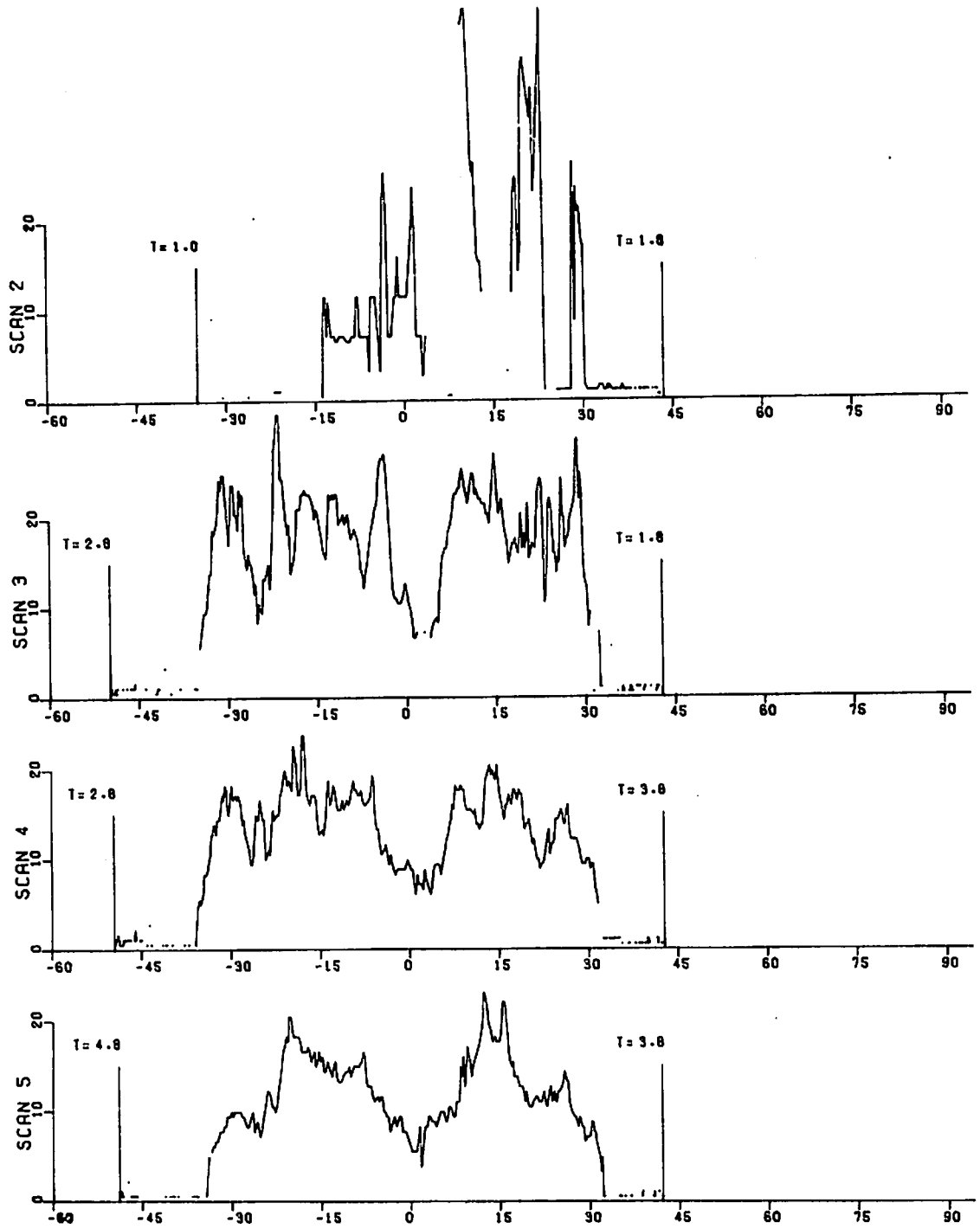

FIGURE 52. VELOCITY PROFILES FOR RUN 11
UP TO ARC SCAN 10

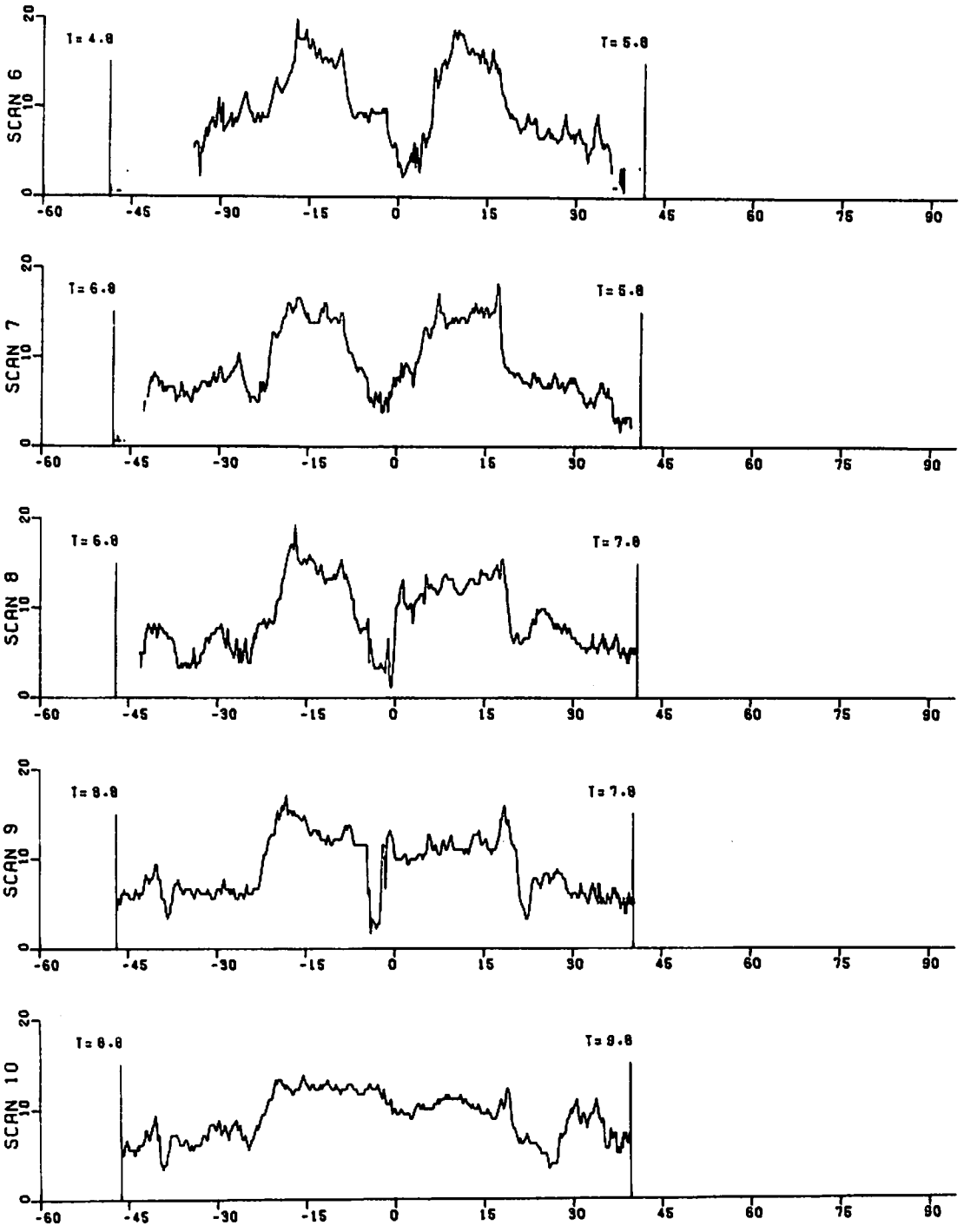

FIGURE 52. (CONCLUDED)

percent of the wingspan. Although the vortex-pair formation is rapid, the wake does not become steady until after 20 sec. Small scan-to-scan variations in the shape of the vortices are apparent before this time. The shape of the velocity profile is close to the logarithmic circulation form expected from a turbulent vortex at arc scan 11 (see Fig. 41). A particularly striking feature of the wake profiles for Run 8 is the absence of data away from the vortex core where the smoke from the 2 outer flap smokers (2,7) is concentrated. The diffusion of smoke does not fill in between the vortices until arc scan 25 (see Appendix D).

The deployment of the 2 outer spoilers for Run 11 dramatically modifies the wake rollup. Figure 52 shows a broad high-velocity region punctuated by moving spikes and dips. Part of the difference from Fig. 51 is due to the use of all the smokers which flood the entire wake with scattering aerosols. The spoilers appear to induce multiple vortices and to retard the wake rollup. The wake profile does not become stable until after 20 sec. (See Appendix D for the complete set of arc scans.)

The shape of the velocity profile with spoilers deployed is close to a constant velocity (linear increase of circulation with radius as in Fig. 49b). Figure 53 compares the velocity profiles for Runs 8 and 11 at arc scan 25 where the profiles have stabilized. The spoilers have flattened out the high-velocity region of the vortex leaving the core and periphery unchanged.

To get some idea of the consistency of the results, compare the data in Runs 11 and 12 (Appendix D) which are taken under the same conditions except for aircraft altitude. The results generally agree, but the detailed bumps on the velocity profiles appear to differ. These differences are somewhat similar to the scan-to-scan variations of data for the same vortex.

6.4.1.2 Vortex Pair Characteristics - The analysis of Runs 8 and 11 in terms of a pair of vortices was successful in producing a symmetrical velocity profile (Figs. 41 and 49) and a vortex-descent

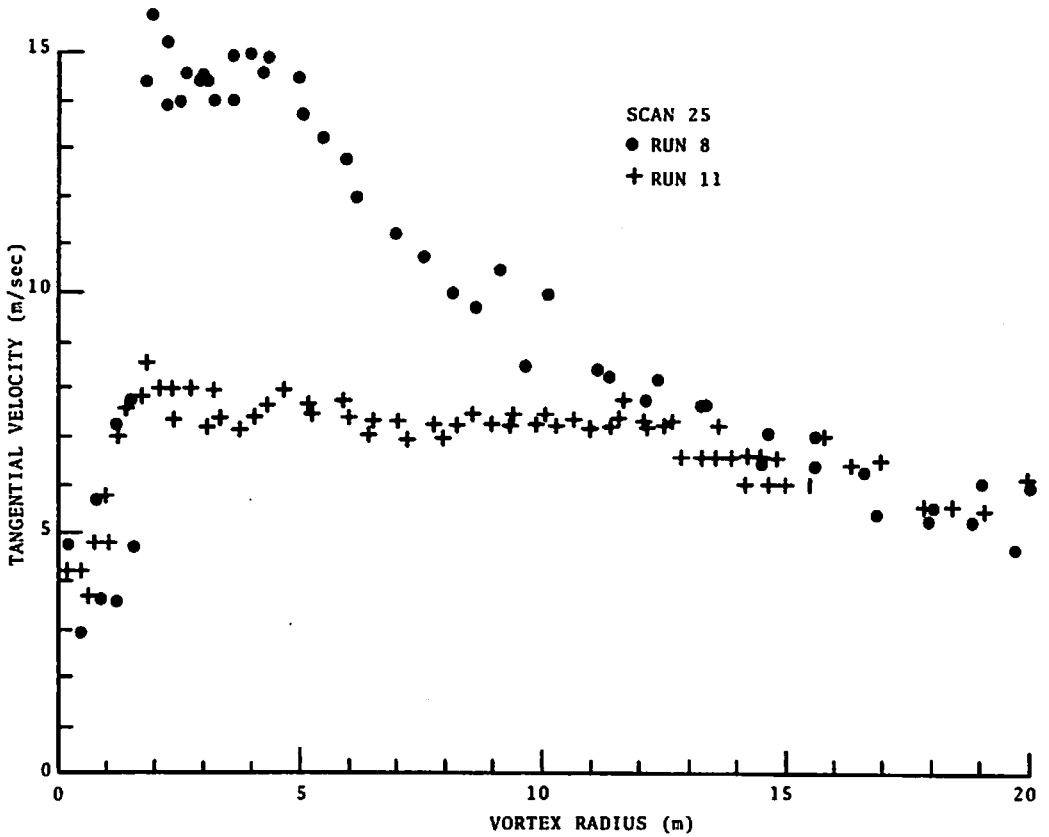

FIGURE 53. EFFECT OF SPOILER DEPLOYMENT ON THE WAKE VORTEX-VELOCITY PROFILE (RUN 8 WITHOUT SPOILERS, RUN 11 WITH SPOILERS)

profile (Figs. 42 and 48). The observed values of circulation were somewhat larger then expected for elliptic loading for the parameters of the run:

$$\Gamma_\infty = \frac{4}{\pi} \frac{L}{bV\rho} = 542 \text{ m}^2/\text{s} , \qquad (10)$$

where $L = 2.39 \times 10^6$ Newtons is the lift, $b = 59.6$ m is the wingspan, $V = 73.6$ m/s is the air speed, and $\rho = 1.28$ kg/m^3 is the air density.

The technique used for measuring the vortex-velocity profile has an inherent bias toward higher velocities. The highest velocity bin with intensity above threshold will be higher than the mean value of the vortex tangential velocity by an amount which depends on the intrinsic signal width and the signal-to-noise ratio. A reasonable value for this bias may be 2 frequency bins (200 kHz) which corresponds to a velocity of 1.1 m/s. The effect of this size error on the circulation at 20-m radius is a decrease of 138 m^2/sec, which brings the measured circulations more in line with the elliptic loading value. The effect on the values of average circulation can be integrated to give decreases of 17, 35, and 52 m^2/s, respectively, for averaging radii of 5, 10, and 15 m.

One feature of a vortex pair which influences the wake profiles is the existence of an elliptical oval around the vortex pair within which the fluid is trapped. The width of this oval is 2.09 times the vortex spacing (Ref. 19). Thus, one may expect to see the entrained smoke mark this distance which extends 27.3 m beyond the vortex core. Indeed, the velocity data are observed to reach this distance soon after the middle of the vortex pair is filled in at arc scan 25. The smoke extends to this distance for arc scans 30 through 33, after which it extends farther. At scan 38, a data hole appears just inside the vortex oval and persists until scan 44. The aerosols outside the vortex oval disappear at scan 50, and do not reappear until scan 65 when the other vortex apparently dies, thereby destroying the oval. The loss of aerosols outside the oval is not surprising since they may be left behind as the vortex pair descends. The flow around the

oval tends to leave them centered between the vortices, where they may not be seen from below.

6.4.2 Vortex Transport

The LDV data collected in the finger-scan mode can be used to obtain accurate vortex tracks, as shown in Fig. 34, which compares LDV and photographic tracks. The procedures involved in generating Fig. 34 have required some visual scanning of the data, and therefore, have not been completed for other runs. The automatic part of the processing indicates that the range values are more consistent when the vortex is near the middle of the range scan, as in Run 27, than when it is near the edge. The velocity profiles are also better since the effective sampling rate is twice per range-scan cycle for centered vortices and only once per cycle for peripheral vortices.

The automatic tracking programs used in the initial data analysis (Ref. 16) gave unreliable results due to utilizing command rather than actual elevation angle. The high-speed data tracks also exhibited anomalies whose origin was uncertain.

6.4.3 Vortex Decay

The vortex decay can be examined in a number of different ways:

1) Change in velocity profile;
2) Change in circulation profile;
3) Change in average circulations; and
4) Change in rotational velocity,

each of which has useful features.

6.4.3.1 Decay of Velocity Profile - Perhaps, the most fascinating pictures of vortex decay are the wake-velocity profiles of Runs 8 and 11 in Figs. 36 and 37 and in Appendix D. For Run 8, the velocity profile evolves smoothly until arc scan 38, when something happens at the outer edge of the vortex oval. At arc scan

42, a narrow disturbance develops between the 2 vortices. At about arc scan 61, a drastic disturbance begins between the 2 vortices. By arc scan 75, the vortex-velocity profile becomes symmetric as if the other vortex (unseen) has disappeared. At arc scan 83, the velocity dip marking the vortex core disappears. A possible interpretation of this event is that the core becomes very turbulent so that both positive and negative velocities become mixed. The vortex then appears to decay rapidly.

The decay in velocity profile for Run 11 is generally more gradual. One strange event starts at arc scan 42, where a narrow spiked vortex core appears in vortex 1. Run 11 also shows unusual variations in the width of the vortex cores. Perhaps, some of the observed anomalies in the vortex-velocity profiles are caused by variations in the concentration of aerosol scatterers.

6.4.3.2 Decay of Circulation Profile - The decay of the vortex-circulation profile is perhaps the most useful measure of how the vortex is decaying. For axial symmetry, the circulation at a radius is given by the area integral of the vorticity which is contained inside that radius. Since vorticity is conserved in inviscid processes and all decay processes can be treated as inviscid for the time scales of interest in wake vortices, changes in the circulation profile show how vorticity diffuses through the vortex. Figure 54 shows the circulation profiles at various times for Run 8. The solid line in each plot is the line fitted to the data in Fig. 43 at arc scan 11 (r_c = 2.51 m and $\Gamma(r_c)$ = 253 m^2/s). It gives a plausible fit to the data at some point for all plots except the last. For arc scan 5, a dashed line (r_c = 2.91 m and $\Gamma(r_c)$ = 305 m^2/s) is drawn as an alternative fit. The dashed-line fit in the last plot at arc scan 76 is for r_c = 3.04 m and $\Gamma(r_c)$ = 243 m^2/s. When the vortex core has finally decayed to a new logarithmic profile, it appears that $\Gamma(r_c)$ remains approximately constant while the core radius increases.

The apparent decay of the vortex core at arc scans 39 and 55 may be partly due to a centrifugal loss of aerosols at the high-

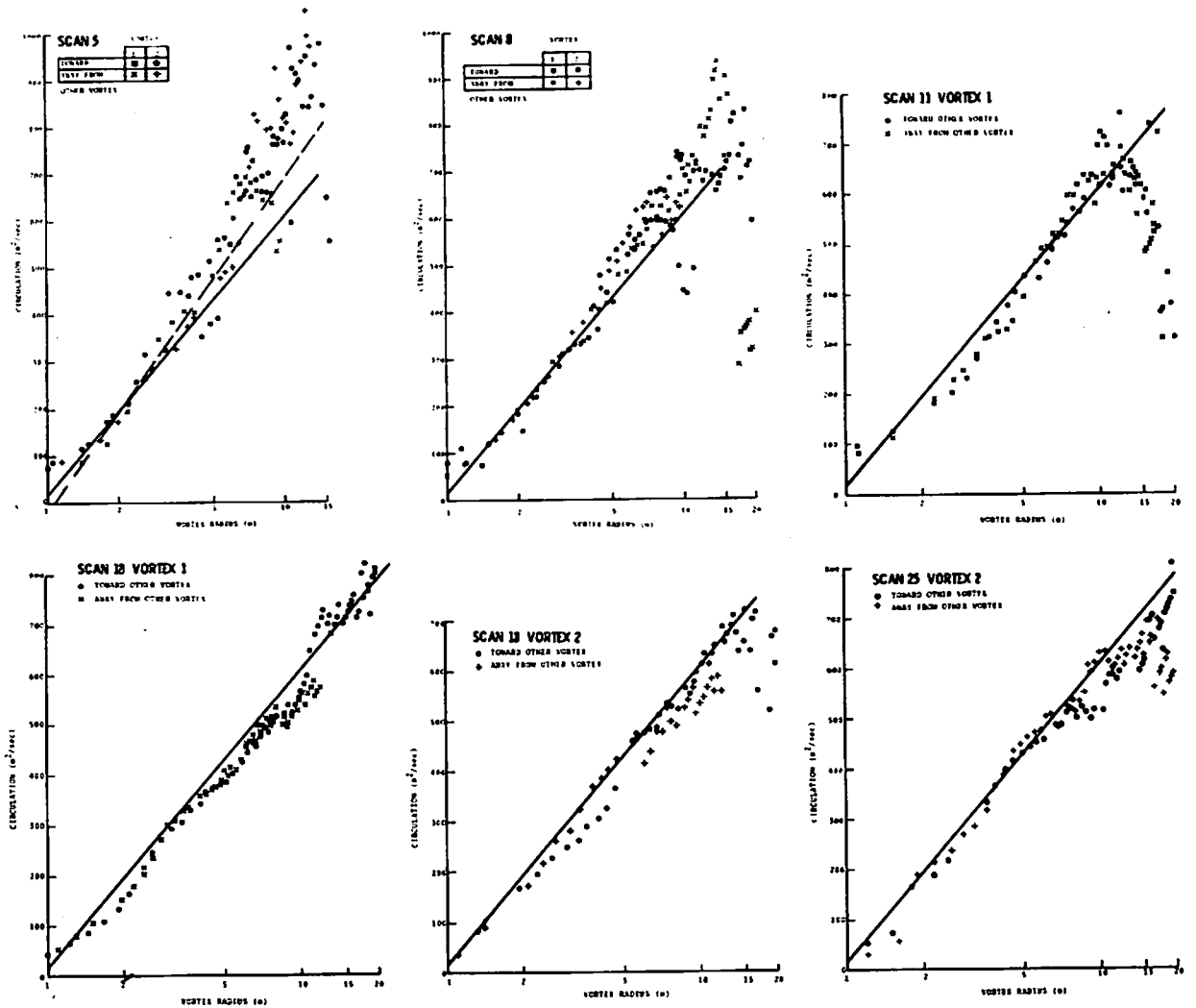

FIGURE 54. CIRCULATION PROFILES FOR RUN 8 AT ARC SCANS 5, 8, 11, 18, 25, 33, 55, AND 74. These plots used different ranges for the two vortices as shown in Fig. 44.

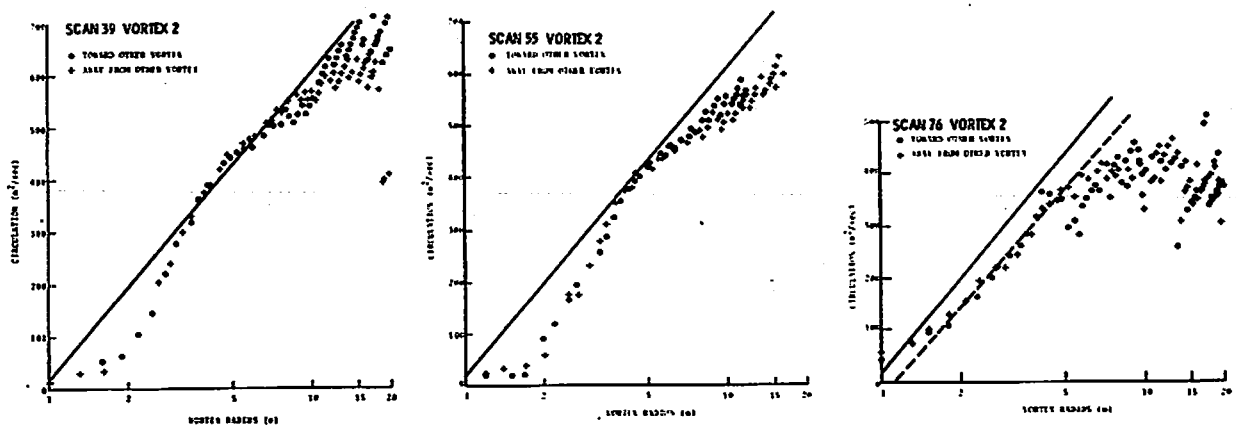

FIGURE 54. (CONCLUDED)

velocity regions of the vortex. After the catastrophic event occurring between arc scans 61 and 74, the vortex-core circulation actually increases between 1- and 3-m radius perhaps because the event has injected new aerosols into that region. It is unlikely that the vorticity can become more concentrated as the result of a decay event. An alternative explanation of this effect is the somewhat larger separation between the vortex and LDV ranges for scans 39 and 55 than for scan 76 (see Fig. 38). Another circulation-decay process is observed at large radii. The circulation at the edge of the vortex gradually decays below the logarithmic line. The vortex strength at scan 76 has dropped to about 400 m^2/s.

Figure 55 shows the circulation decay of Run 11 with spoilers deployed. In this case, the solid line is the straight line fitted to the data at scan 25 (Fig. 49). For this run, the vortex core decays negligibly over the time for which the data are processed. The vortex strength, however, decays gradually to about 180 m^2/s.

The observed vortex decay is surprisingly similar for the 2 runs. The dominant feature is a constancy of the vortex core, accompanied by a steady decrease in circulation for large radii. This observation suggests that, based on 2 runs, the most important vortex-decay mechanism works from the outside of the vortex toward the center.

6.4.3.3 Decay of Average Circulation - The average circulation for a radius b/2 can be related to the rolling moment induced on a wing of span b centered in the vortex. This quantity can be evaluated from the data without going through all the manipulations required to isolate the velocity field of a single vortex since the effects of both vortices on the wing should be included. The plots of average circulation in Figs. 40 and 47 show the same features discussed above. The vortices for these runs tend to decay faster. The decay event at scan 65 for Run 8 begins a more rapid decay of vortex strength. The high-speed data in Fig. 40 for Run 8 can be compared with the low-speed data for Run 5, which

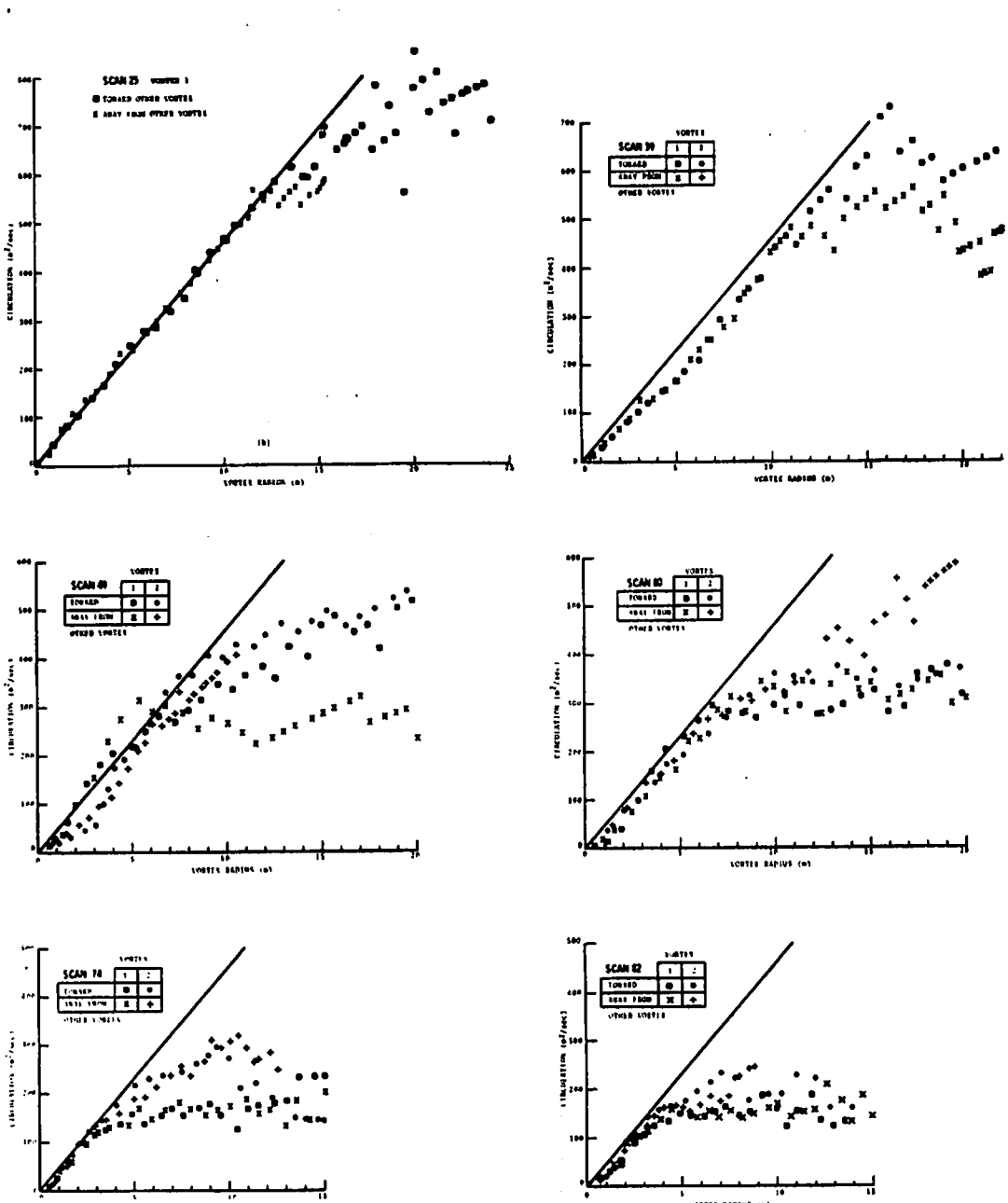

FIGURE 55. CIRCULATION PROFILES FOR RUN 11 AT ARC SCANS 25, 39, 49, 60, 74, AND 82

is in the same configuration but at half of the altitude. The initial values for the average circulation agree reasonable well, but the decay is more rapid for the smaller radii for Run 5. This faster decay may be due to the poorer signal-to-noise ratio for low-speed data rather than an actual physical difference. A lower signal-to-noise ratio tends to give an anomalously wide vortex-core dip which yields a lower average circulation for small averaging radii.

6.4.3.4 Decay of Rotational Velocity - The decay of rotational velocity can be studied without the complications of tracking by simply taking the largest velocity observed during an arc scan. Some restrictions must be applied to make sure spurious data are not included. For example, one must be sure that the vortex is in the scan volume, and that isolated noise points are rejected. Reference 16 presents a way of analyzing the data which unfortunately does not assure valid data. (The data shown herein have been verified by 2 different techniques). Figure 56 shows the decay of V_{pk} for Runs 8 and 11 taken in the arc-scan mode. The velocity plots in Appendix D have been scanned visually to measure the points. Figures 57 through 60 are generated by scanning line-printer spectral plots of the low-speed finger-scan data and selecting values near the vortex core. One can readily verify that the vortex is within the angle range scanned, but it is more difficult to verify that the vortex is not too far outside the range scanned to give valid velocities. The starborad vortices can be lost at short range, and the port vortices at long range. The measured values are lower bounds to the actual maximum vortex tangential velocity which may not be intercepted by the scan pattern for very small cores. The latter effect is responsible for the large scatter in the results for 0/0 and 10/10 flap settings (Figs. 57 and 60b).

Figure 57 compares the plots of maximum V_{ms} with those of maximum V_{pk} (see Fig. 24 for the definitions). For small vortex cores, as here for 0/0 flaps, there is a difference between them; V_{ms} often does not reach V_{pk}. For larger cores, as in the 30/30

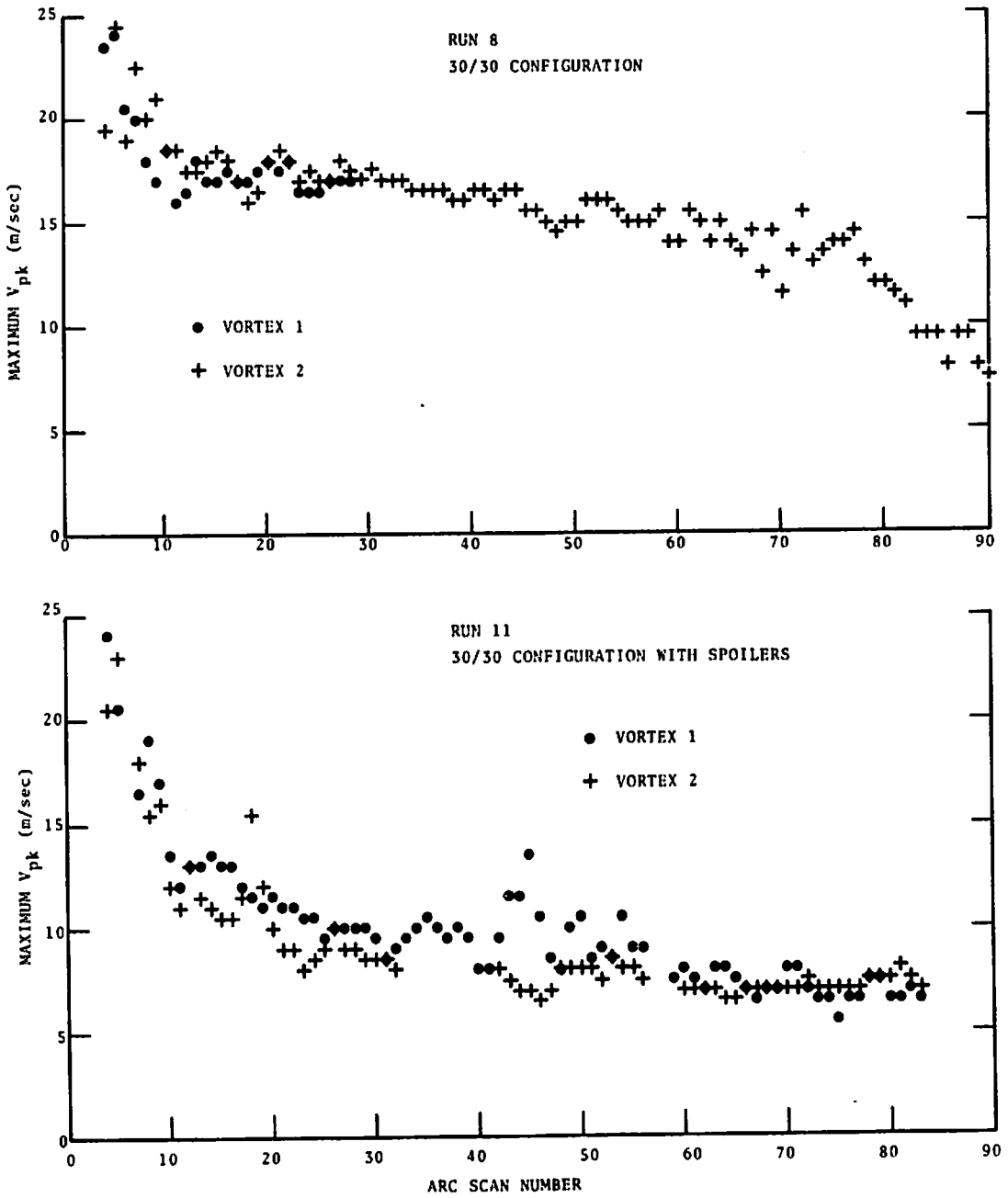

FIGURE 56. DECAY OF PEAK VORTEX VELOCITY FOR RUNS 8 AND 11

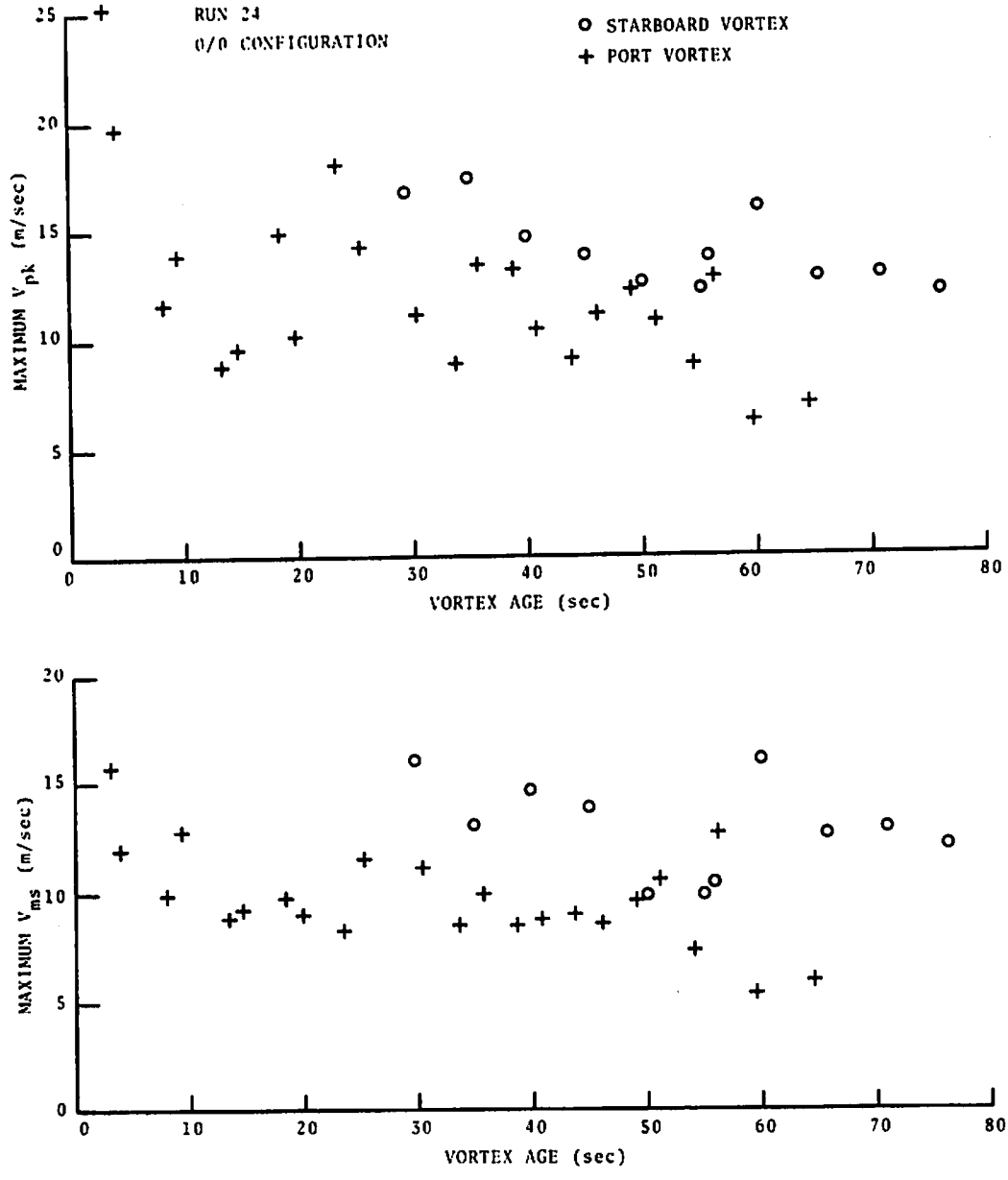

FIGURE 57. COMPARISON OF MAXIMUM V_{pk} AND V_{ms} FOR RUN 24.

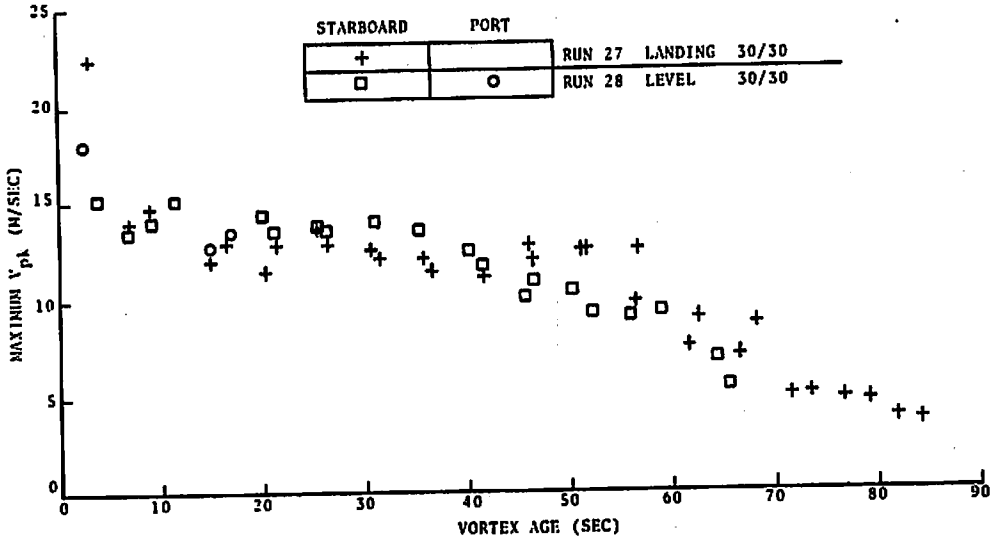

FIGURE 58. DECAY OF PEAK VORTEX VELOCITY FOR RUNS 27 AND 28

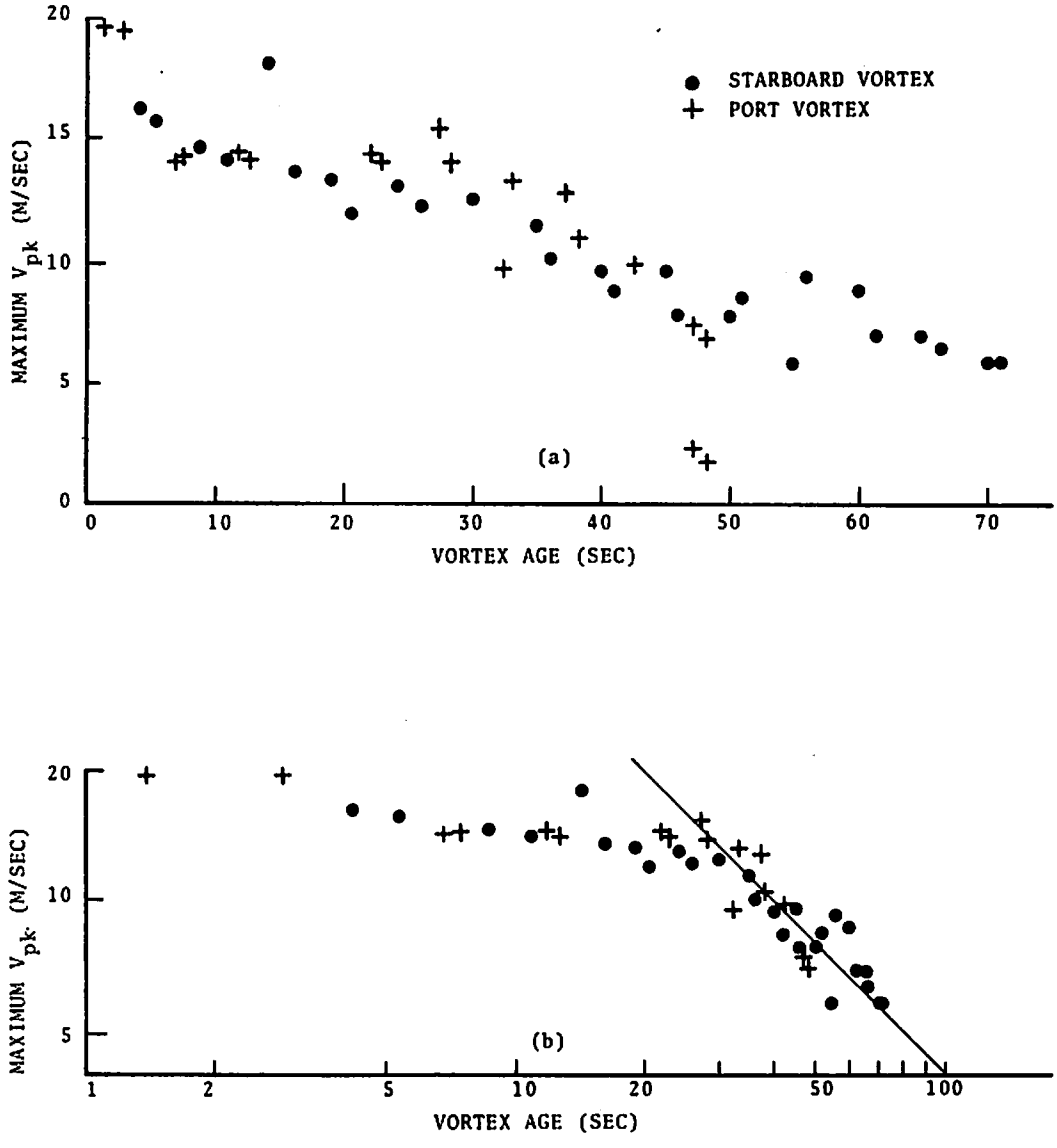

FIGURE 59. PEAK TANGENTIAL VELOCITY VERSUS VORTEX AGE FOR RUN 44. (a) Linear plot and (b) log-log plot.

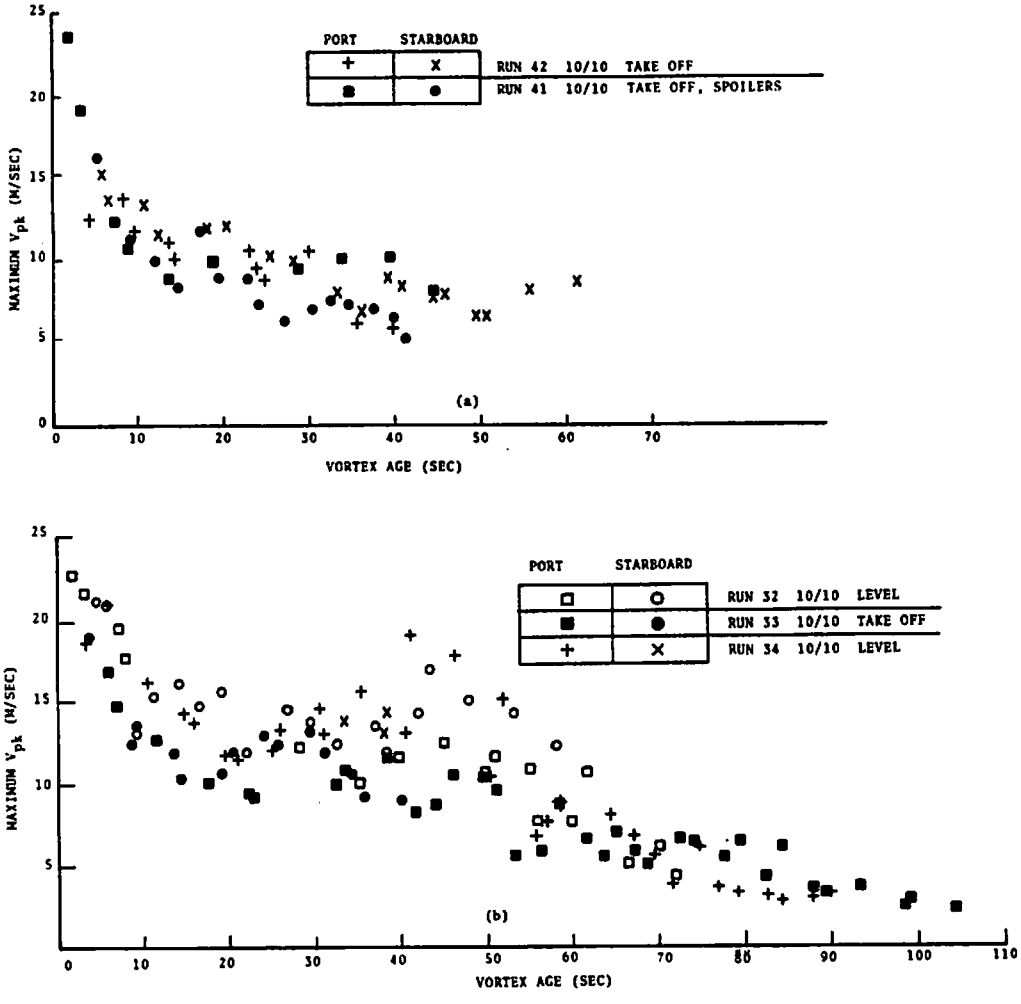

FIGURE 60. DECAY OF PEAK VORTEX VELOCITY FOR FIVE 10/10 FLAPS RUNS

runs of Fig. 58, the plots are very similar. Figure 59 shows the data for Run 40 plotted in 2 ways; the log-log plot indicates the presence of a region decaying roughly as inverse time, i.e., a slope of -1 as indicated by the line in Fig. 59b. Figure 60 shows some comparison runs for 10/10 flaps. The data in Fig. 60b indicate that the engine thrust for a simulated takeoff reduces the peak vortex velocities. Figure 60a shows the effect of adding spoilers to the 10/10 configuration with full takeoff power. The spoilers appear to reduce slightly the maximum vortex velocities.

Figure 61 shows the velocity decay for Run 22 which had 30/1 flaps (gear down) and used the arc-scan mode of data collection. The port vortex drifted away from the arc-scan region after about 25 sec. Later the starboard vortex, which remained stalled near the aircraft flight path, drifted into the scan region and was observed until an age of 2 min. Figure 62 shows velocity profiles for this run at times when the arc appeared to pass near the vortex core. This 30/1 vortex had slightly lower maximum vortex velocities than the 30/30 runs.

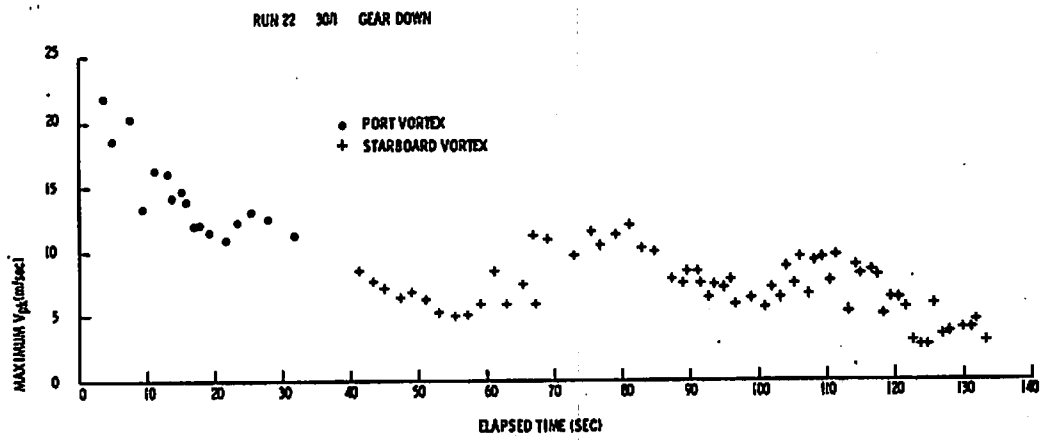

FIGURE 61. PEAK TANGENTIAL VELOCITY VERSUS ELAPSED TIME FOR RUN 22

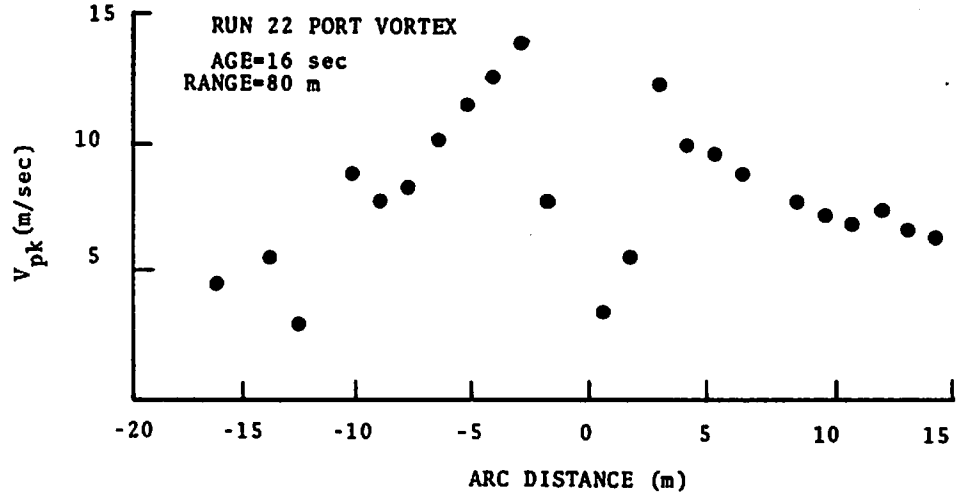

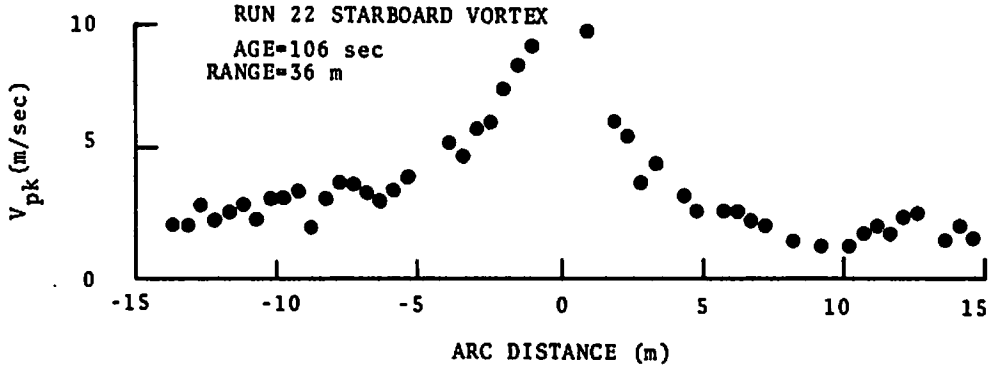

FIGURE 62. VELOCITY PROFILES FOR RUN 22

7. MONOSTATIC ACOUSTIC SENSOR MEASUREMENTS

The Monostatic Acoustic Vortex Sensing System (MAVSS) has been developed by the DOT Transportation Systems Center as a simple technique for studying the decay of wake vortices in the airport environment (Ref. 20). Its basic function is to measure a vertical profile of the vertical component of the wind. Since the vertical component of the ambient wind is small near the ground, the vortex winds are measured with little interference from the ambient wind. A single MAVSS antenna can measure the velocity profile of a wake vortex as it drifts over the antenna.

An array of antennas can sample the vortex at different times, and thereby measure vortex decay. This mode of data collection requires that the vortex pass over an antenna in a time short compared with its decay time. The Rosamond Lake installation (Fig. 4 and Table 5) is designed for this mode of operation. It consists of an array of 8 antennas placed to observe the wake vortices as they separate in ground effect at an expected transport speed of about 2 m/s. The array is longer toward the south because northerly ambient winds are predicted. An additional 2-antenna array displaced by 80 m (later 120 m) is intended to allow a measurement of the longitudinal variation in vortex decay.

A maximum range of 60 m was selected to cover the expected heights of vortices in ground effect. Unfortunately, the descent of vortices into ground effect with subsequent separation was observed only on the last sortie of each day. Thus, the planned experimental configuration was by no means optimum for the earlier sorties. Some new data-analysis techniques had to be developed to deal with the slowly moving vortices of the early sorties.

7.1 SENSOR OPERATION

The MAVSS antenna configuration is illustrated in Fig. 63. A short pulse of acoustic energy is transmitted into a narrow vertical beam. Acoustic signals scattered by temperature

TABLE 5. MAVSS ANTENNA LOCATIONS

Antenna No.	Longitudinal Position	Lateral Position
1	40	130
2	40	90
3	40	50
4	40	-50
5	40	-90
6	40	-130
7	40	-170
8	40	-210
9	-40 (-84.6)*	-90
10	-40 (-79.6)*	-170

All dimensions are in meters.

*Tests on 3, December 1975.

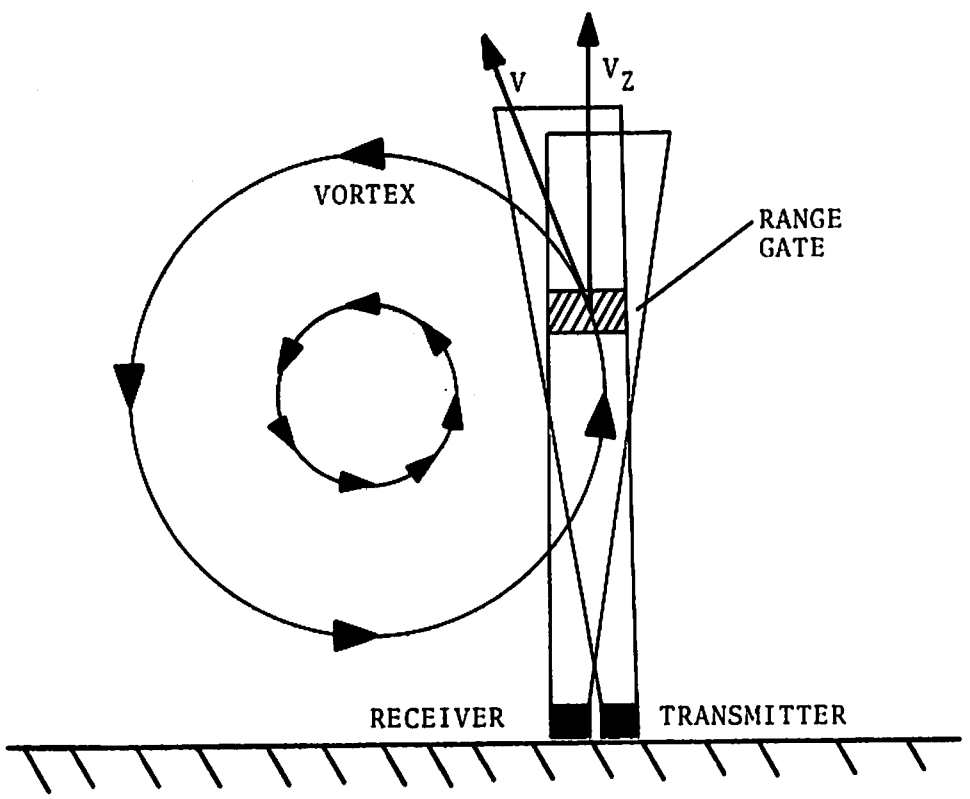

FIGURE 63. MONOSTATIC ACOUSTIC VORTEX SENSING SYSTEM CONFIGURATION

fluctuations in the air are received by an overlapping receiver beam. Separate transmitting and receiving antennas are employed to prevent antenna ringing from obscuring low-altitude returns. The altitude z of the region being probed is determined from the time delay t after the transmitted pulse.

$$z = c\,t/2, \tag{11}$$

where c is the speed of sound.

The data are analyzed by sampling the return signals at various times (i.e., range gates) during the 400-ms period between transmissions. Normally, 16 range gates with 22-ms spacing are processed. The horizontal extent of the region contributing to a range gate depends upon the antenna beamwidth (estimated at 7 deg full width). The vertical resolution of a range gate depends upon the transmitted pulsewidth (-6 dB width = 20 ms), the processor integration time (-3 dB width = 16 ms) and the range-gate scan time (11 to 13 ms depending upon the frequency band covered).

The average vertical component of the wind in a range gate is measured from the Doppler shifts in the return signals:

$$v_z = \frac{-c(\bar{f}-f_o)}{2\,f_o}, \tag{12}$$

where f_o is the transmitted frequency, and $\bar{f}$ is the mean frequency of the power spectral density. The mean square deviation of the frequency $(f-\bar{f})^2$ is also computed to give an indication of confidence in the mean value $\bar{f}$. The rms frequency deviation is normally 25 Hz for good data. In the presence of strong velocity gradients (e.g., at the vortex core) or poor signal-to-noise ratios, the frequency deviation becomes larger.

The Doppler spectra are analyzed with a real-time spectrum analyzer having a -3 dB width of 30 Hz and a sample spacing of 20 Hz. Two different transmitted frequencies f_o are used: 2950 and 3600 Hz. Normally, the data from 2 antennas are mixed together so that 2 spectrum analyzers operating simultaneously under computer control can process the data from 4 antennas. Under these conditions, a frequency range of $\pm$280 Hz is scanned. When

each spectrum analyzer processes data from only 1 antenna, a range of ±360 Hz can be scanned. Most of the data in this report employed the latter mode of operation which gives a velocity range of ±20 m/s at 2950 Hz and ±17 m/s at 3600 Hz according to equation (12).

Figure 64 shows some raw spectral data where a CRT display is illuminated whenever the spectral intensity is above a threshold. For each range gate, successive spectra are plotted as a function of elapsed time. One can see that the intensity increases near the vortex core (where the Doppler shifts change sign), and that the positive Doppler shifts (downward wind velocity) reach the edge of the ±280 Hz spectral window.

7.2 EXPERIMENTAL PROBLEMS

The MAVSS equipment operated properly for all runs except numbers 36 and 37 when a temporary generator problem ruined the data. Two problems observed on the first day were rectified on the second. First, it was noticed that side-lobe signals from antennas 9 and 10 produced some interference at the antennas on the main baseline. Antennas 9 and 10 were moved farther away on the second day to eliminate the interference. After the move, only a small amount of interference remained on the main array; some antennas 80 m apart showed small pulses at an apparent range of 40 m. Second, the MAVSS data for the first day were partially corrupted by noise from the helicopter overhead taking vortex-tracking photographs. On the second day, the helicopter flew a trajectory away from the MAVSS antennas, and much less noise was observed.

As far as the MAVSS data were concerned, the biggest surprise of the Rosamond Lake tests was the large scattering cross sections observed early in the morning. Apparently, the vortex induced mixing of the strong temperature inversion caused thermal fluctuation levels 25 times higher than normally observed. The abnormally high signals led to some signal clipping in the electronics.

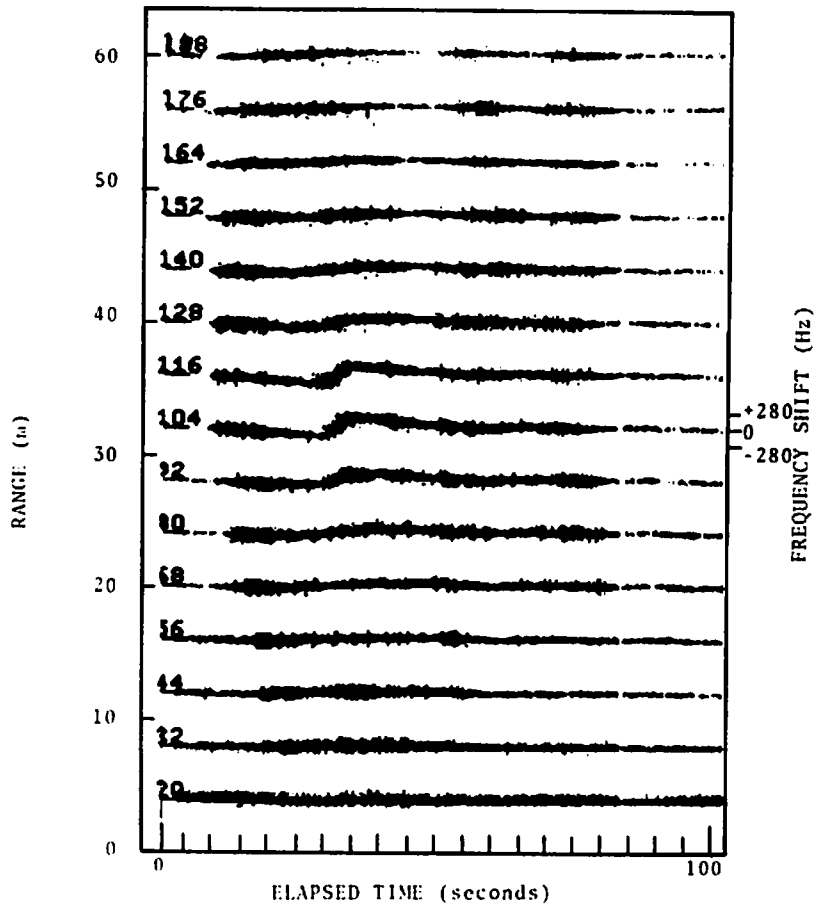

FIGURE 64. SPECTRAL INTENSITY VERSUS RANGE GATE AND ELAPSED TIME (RUN 1, ANTENNA 3)

7.3 DATA PROCESSING

The basic data supplied by a single antenna are shown in Figs. 65, 66, and 67. (Fig. 64 showed the raw spectral data for this run and antenna.) Figure 65 plots the vertical velocity in each range gate versus the time after aircraft passage. Figure 66 plots the mean square frequency deviation $(f-\bar{f})^2$ in the same format. Figure 67 plots the amplitude of the scattered signal. The numbers at the left-hand edge of a range gate are half of the time (in milliseconds) at which the range-gate analysis started. A number of timing corrections are required to convert this number into the range given by equation (11).

The vortex arrival in Fig. 65 is signaled by a reversal of the vertical velocity components in many range gates. The height of the vortex can be estimated as the range showing the largest velocities before and after the reversal. The first analysis of the MAVSS data consisted simply of visually scanning the velocity plots and picking out the vortex-arrival times and heights. These values are plotted as vortex tracks as shown in Fig. 68 (Appendix E.1 contains the remaining vortex tracks).

The spectral-spread data of Fig. 66 give an indication of the validity of the velocity measurement in Fig. 65. When the ambient-noise level is very high, for example, just after the aircraft passage, the spectral width is large for all range gates. A linear time-variable gain is used to compensate for the range dependence of the scattered signal. Consequently, the effects of ambient noise are more pronounced at higher ranges. Excessive spectral width will also occur for regions with abnormally small scattered signal, even with normal ambient noise. The vortex arrivals which have been contaminated by ambient noise (presumably from the helicopter) are identified by examining the spectral-width data. The other source of excessive spectral width is velocity variation within the MAVSS resolution cell. This effect is generally most pronounced at the vortex core. Occasionally, increased width appears to be associated with strong turbulence, either on the edge of the vortex oval or after the vortex core

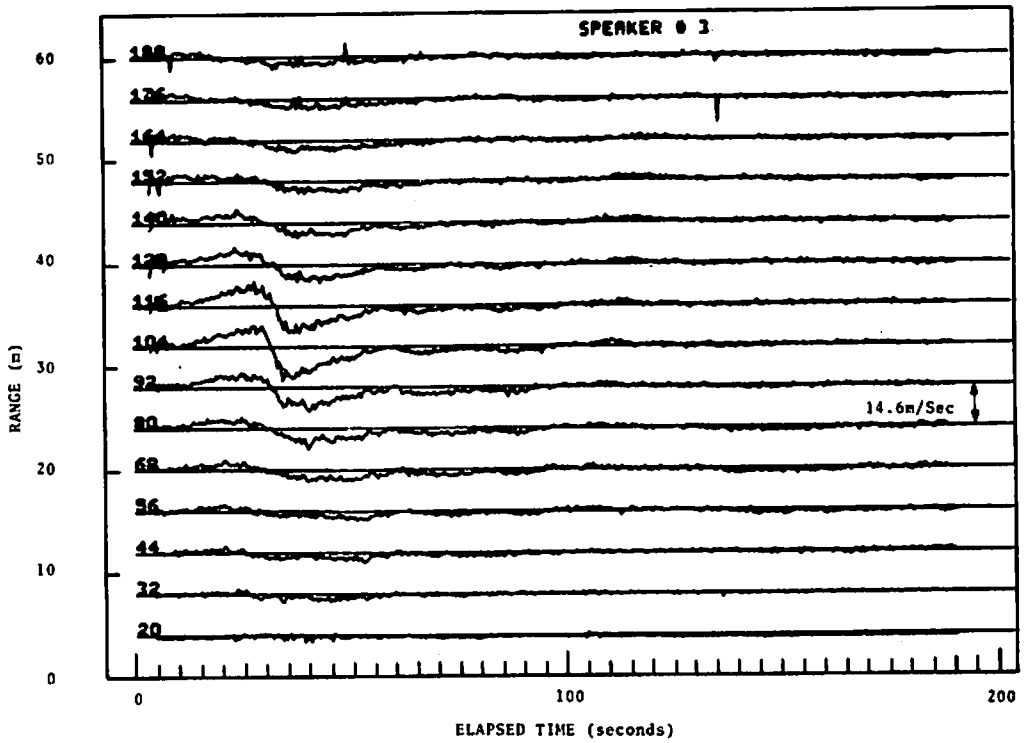

FIGURE 65. VELOCITY VERSUS RANGE GATE AND ELAPSED TIME (RUN 1, ANTENNA 3)

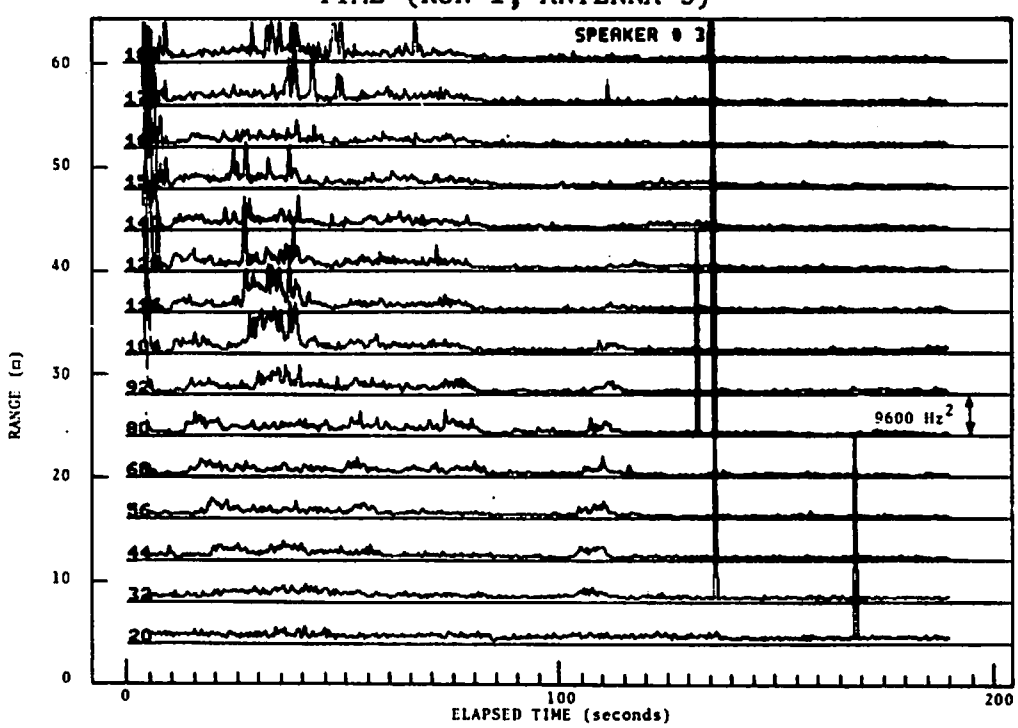

FIGURE 66. MEAN SQUARE FREQUENCY DEVIATION VERSUS RANGE GATE AND ELAPSED TIME (RUN 1, ANTENNA 3)

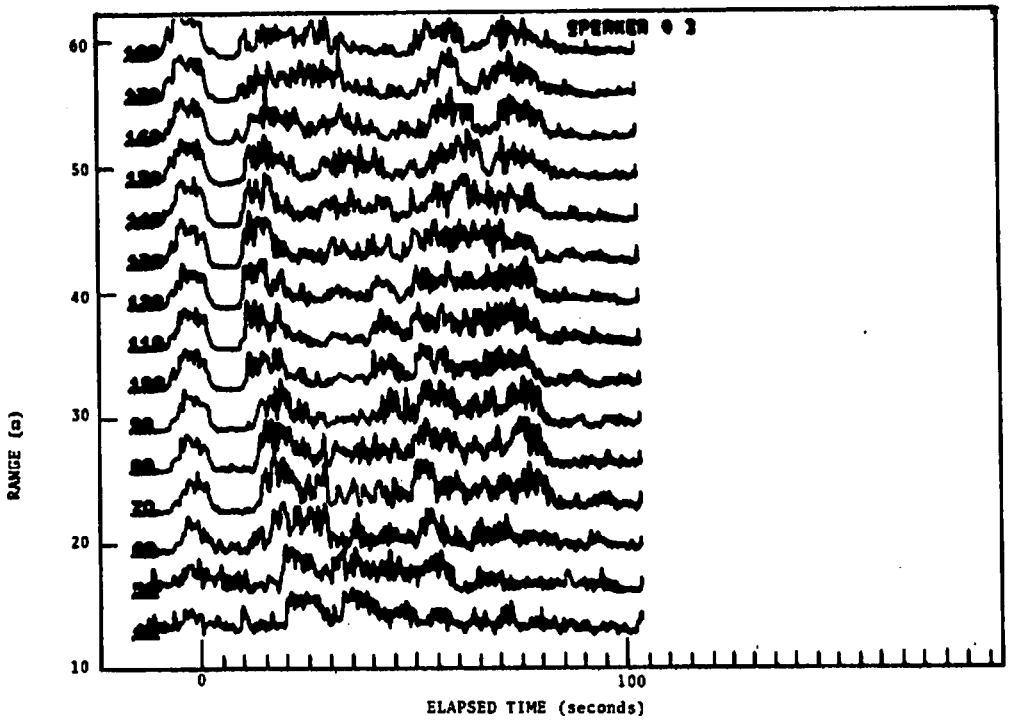

FIGURE 7.5. SCATTERED SIGNAL AMPLITUDE VS RANGE GATE AND ELPASED TIME: RUN 1, ANTENNA #3

FIGURE 67. SCATTERED SIGNAL AMPLITUDE VERSUS RANGE GATE AND ELAPSED TIME (RUN 1, ANTENNA 3)

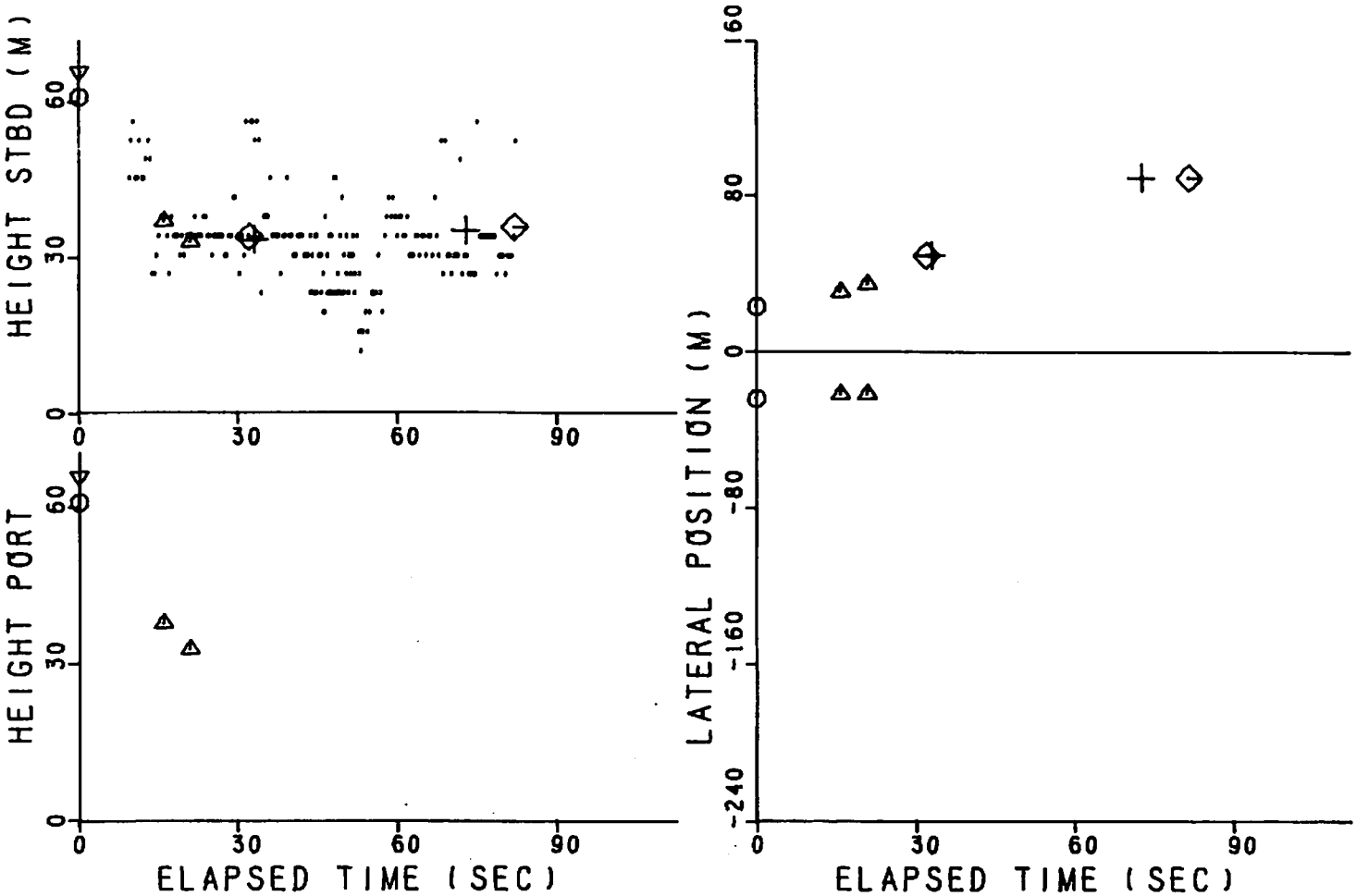

FIGURE 68. VORTEX-TRACKING DATA. (Circles = nominal initial positions; Squares = visual MAVSS arrival times and heights; X, + = computer MAVSS data; triangles = photographic data (apex down for data extrapolated from another longitudinal position); short vertical line segments = MAVSS height of maximum velocity).

has decayed. Sometimes, very large spikes occur in the frequency spread data; they are flags for a variety of processing errors, and are not actually frequency spreads.

Figure 67 plots the integrated signal amplitude as a function of range gate and elapsed time. The scattering amplitude (with linear time-variable gain) is proportional to the square root of the scattering cross section. It is thus a measure of the temperature-structure constant C_T (Ref. 21). Portions of the scattering amplitude plots are clipped because of saturation in the tape recorder or the electronics. The recorder-clipping level is constant with range while the electronic clipping occurs only at low ranges. The level of the aircraft noise at zero elapsed time in Fig. 67 shows the recorder-clipping level.

7.3.1 Standard Analysis for Moving Vortices

The standard method of extracting vortex information from the MAVSS data assumes that the vortex passes over the antenna at constant transport speed V_T and at roughly constant height h. In this case, the vertical velocity at range z=h directly measures the radial dependence of the vortex tengential velocity v(r), assuming negligible vortex decay during passage. The transport speed V_T is used to convert elapsed time T to radius r via the relationship $r = V_T(T-T_o)$, where T_o is the vortex-arrival time. Since a given value of r is observed twice during the vortex passage, the two values of v(r) are generally averaged together in some fashion. The vortex circulation $\Gamma(r)$ can then be evaluated from the equation

$$\Gamma(r) = 2\pi r\, v(r). \qquad (13)$$

Since r is proportional to the estimated value of V_T, the circulation is also proportional to V_T. Thus, this method of measuring vortex circulation is strongly dependent upon V_T being defined, accurately measured, and large enough to ignore decay. Several methods for estimating V_T have been used. Preliminary studies have assumed that the vortex starts at the runway center-

line and moves at constant speed to the antenna at a distance D from the centerline. The arrival time T_o then gives the transport speed $V_T = D/T_o$. For the final results, V_T is taken from the measured vortex trajectory (Fig. 68), making use of both MAVSS and photographic data.

The computerized data analysis begins with a search for the vortex-arrival times. The data are correlated with a function that looks like a vortex. It consists of a rectangular gate about 18 m high (5 range gates) in range z and a single cycle square wave of length 20 m in lateral distance x. As shown in Fig. 69, 4 overlapping velocity sums of 5 range gates are computed for each range scan. They are then correlated with the square wave in time which expands with time T_o to keep the spatial wavelength constant. The two vortex arrival times are taken as the values of T_o giving the most positive and most negative correlation. If the absolute value of the correlation is above a threshold, the vortex arrival is considered valid and is plotted as a vertical line in Fig. 69 with a slash on the sum giving the highest correlation. A search is conducted for the range gate giving the highest correlation with the square wave. This height is then plotted as a large cross on the height plot in Fig. 69, which will be described in the next section. To eliminate invalid velocity data, a threshold is set on the spectral spread ($(f-\bar{f})^2 = 4700\ Hz^2$) above which velocities are excluded from the sums in Fig. 69. Figure 69 shows data from only one antenna; the more normal case is shown in Fig. 70 where 4 antennas are scanned for vortex arrivals.

After the computer has identified all the vortex arrivals in Fig. 70, it generates the plots in Fig. 71 which show vortex tracks and the velocity and spectral spread profiles at the range gate of maximum correlation for each antenna. The indicated transport velocity, estimated from the arrival times at successive antennas, is used to plot the vortex data out to 30-m radius. These plots give a picture of the vortex decay as it passes over successive antennas. The data from the range gate plotted in Fig. 71 and 4 adjacent range gates are stored for subsequent

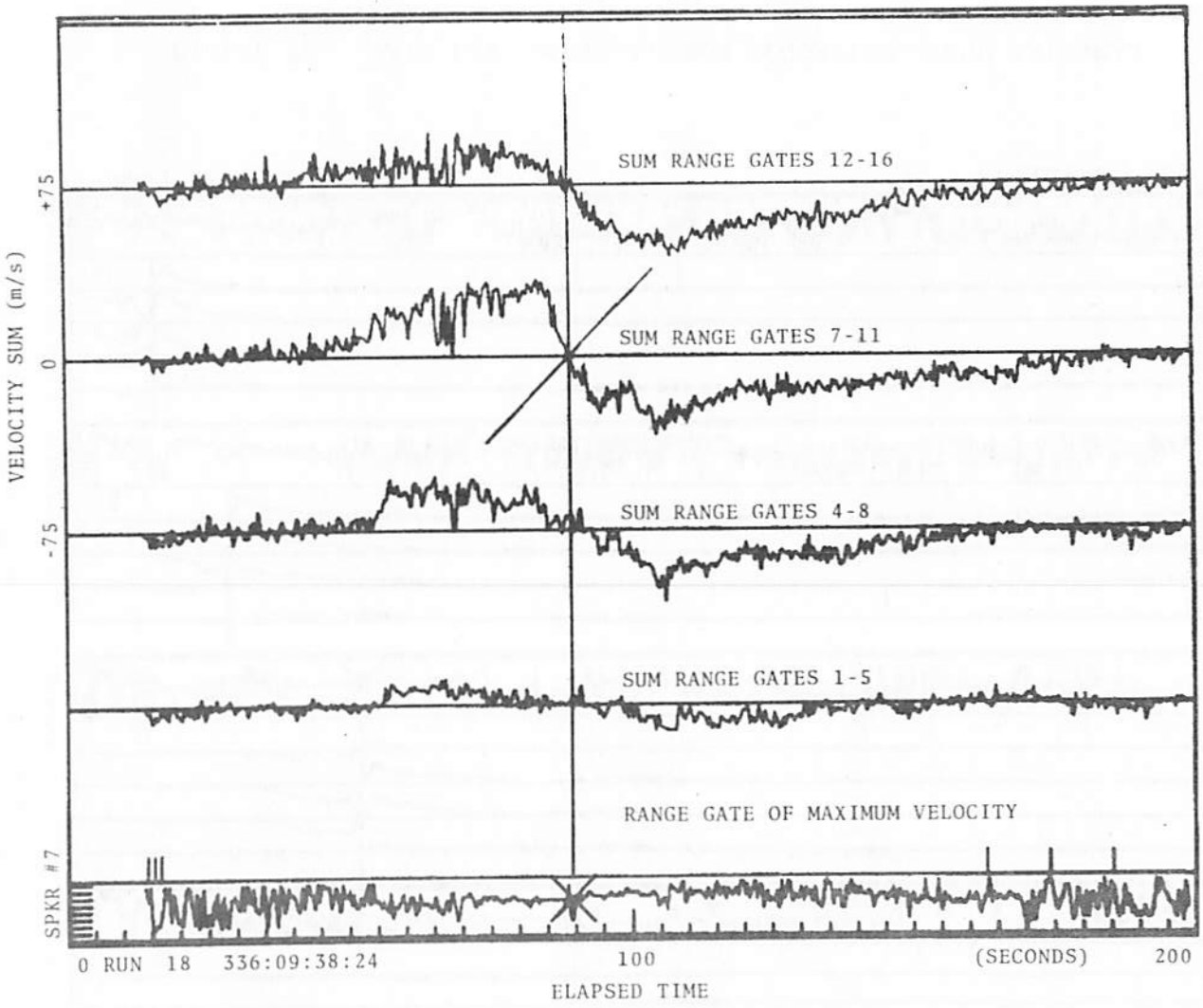

FIGURE 69. DATA FOR VORTEX-SEARCH ALFORITHM-ONE ANTENNAS

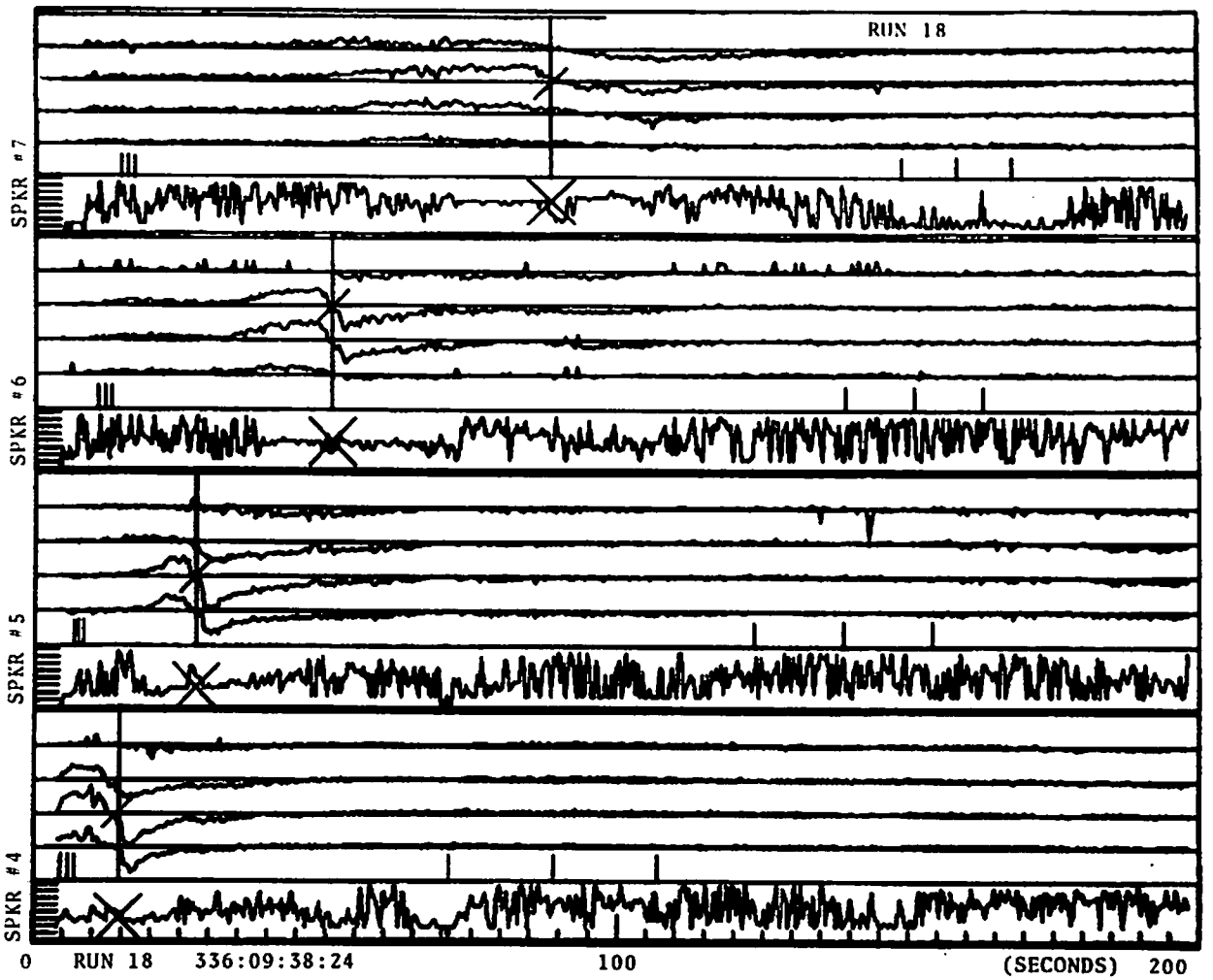

FIGURE 70. DATA FOR VORTEX-SEARCH ALGORITHM--FOUR ANTENNAS

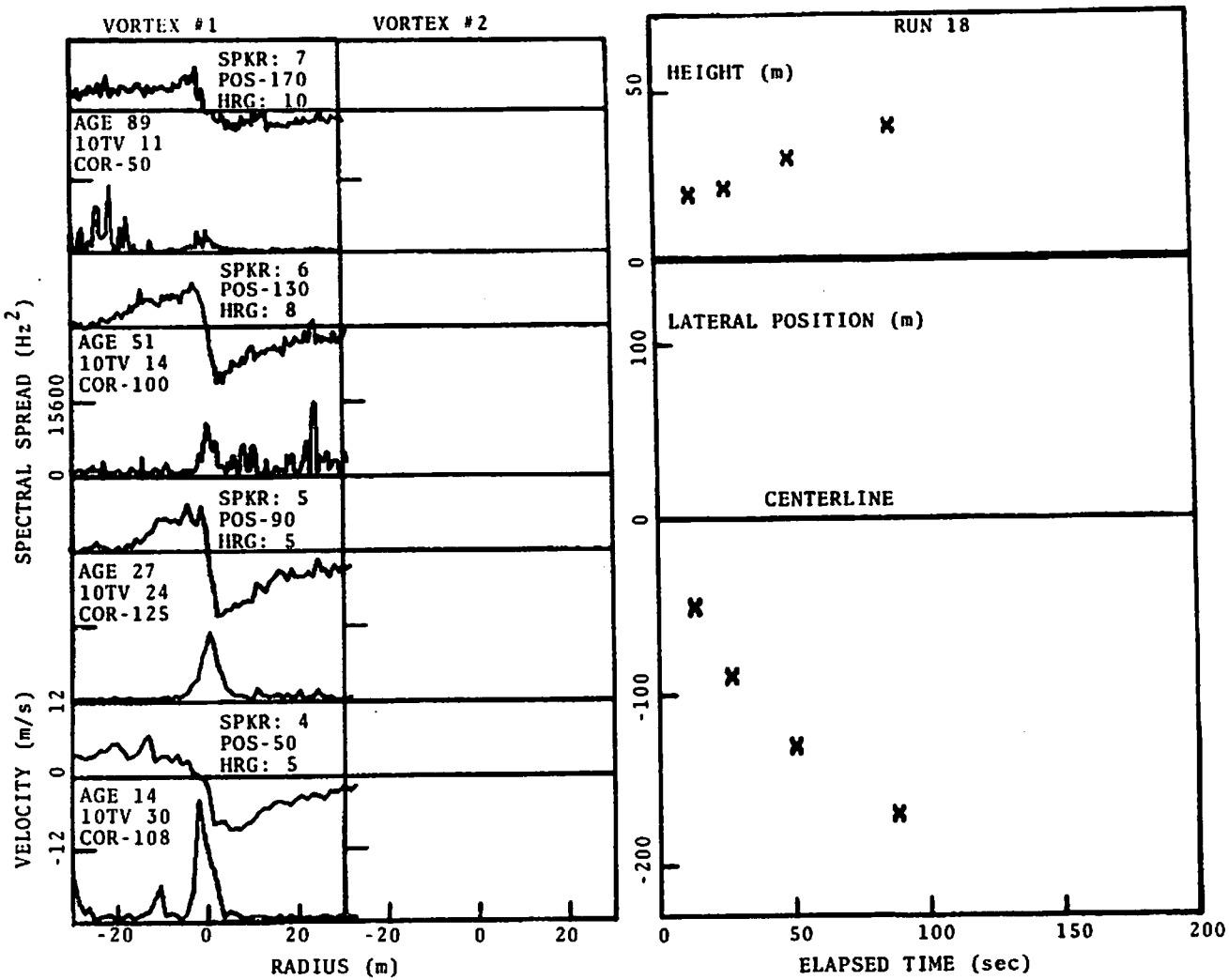

FIGURE 71. VELOCITY AND SPECTRAL WIDTH PROFILES AND VORTEX TRACKS FOR DETECTED VORTICES

analysis in terms of circulation. Figure 72 shows the data stored for 1 vortex: the vertical velocity and spectral width for 5 range gates. Appendix E.3 contains all the other velocity and spectral-spread profiles and the circulation profiles.

Several methods are used to relate vortex strength to the measured vertical-velocity field. The simplest procedures identify the vortex tangential velocity v(r) with the vertical velocity at the range gate of maximum correlation. This velocity profile is plotted as circles in Fig. 73. The corresponding circulation [equation (13)] and averages for positive and negative radii are also plotted in Fig. 73. A simple 2-parameter vortex model is used to fit the data. The vortex circulation is given by

$$\Gamma(r) = \Gamma_\infty \, r^2 / \, (r^2 + r_c^2), \qquad (14)$$

where the 2-parameters are the vortex total circulation ($\Gamma_\infty = \Gamma(\infty)$) and the vortex-core radius (r_c). This vortex model has the virtue that the maximum tangential velocity occurs at r_c, and that $\Gamma(r_c) = \Gamma_\infty/2$. The solid lines in Fig. 73 are fits of the velocity data to the form:

$$v(r) = (\Gamma_\infty/2\pi) \, r/(r^2 + r_c^2) + \bar{v} \, . \qquad (15)$$

The values of core radius resulting from these fits are actually convolutions of the actual core radius with the MAVSS spatial resolution. Thus, the maximum measured velocity has little relationship to the actual maximum vortex velocity unless the core is resolved. Using the measured spectral widths to assist in the deconvolution has been considered.

Another method of evaluating vortex strength is to calculate the average vortex circulation up to radius b:

$$\Gamma'(b) = \frac{1}{b}\int_0^b \Gamma(r)dr, \qquad (16)$$

which is proportional to the rolling moment on a wing of span 2b under some simple assumptions. This integral is plotted as (+) in Fig. 73. Because $\Gamma'(b)$ is an integral over the experimental data, it is much less affected by aberrations in the data than is the fitted circulation.

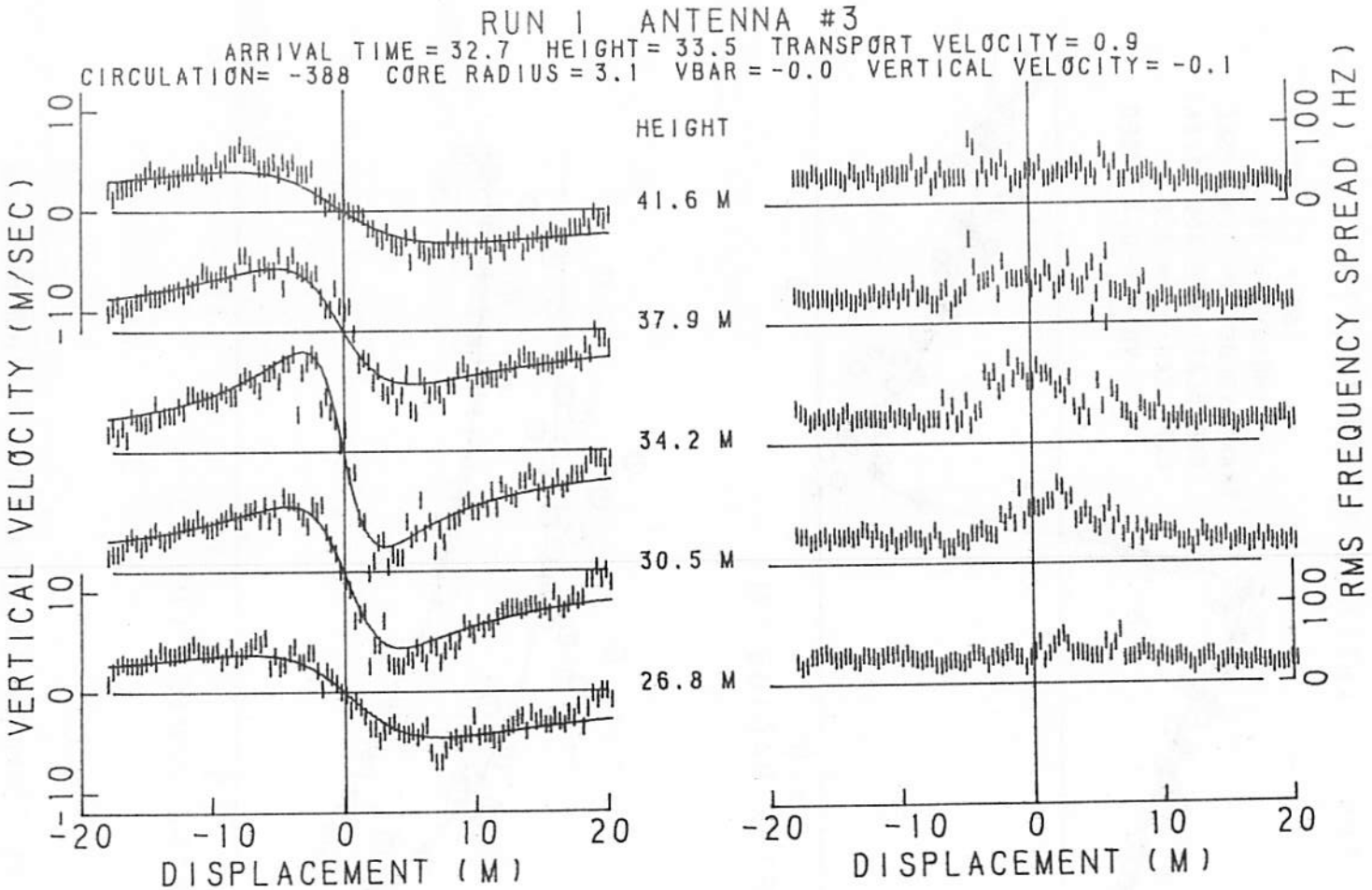

FIGURE 72. VORTEX-VELOCITY AND SPECTRAL WIDTH PROFILES FOR FIVE RANGE GATES

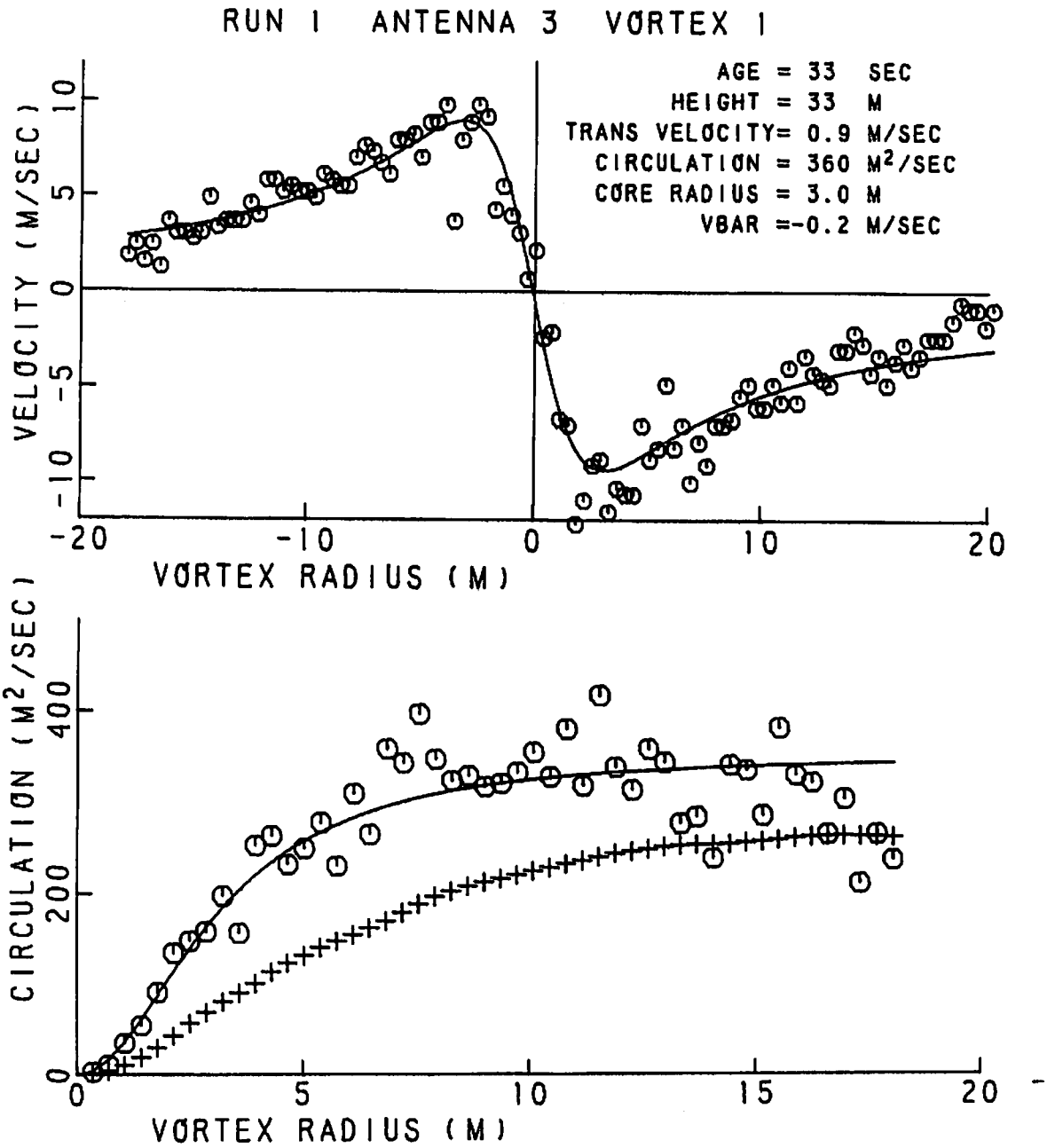

FIGURE 73. VORTEX-VELOCITY AND CIRCULATION PROFILES FOR ONE RANGE GATE

The assumption that the range gate of highest correlation measures the vortex tangential velocity introduces error when the vortex is not centered in a range gate or when the vortex has vertical motion. If one adds additional parameters of vortex location and vertical motion, one can fit the simple vortex model to all the vortex data in Fig. 72 (the fit is shown as solid lines). This procedure not only accounts for vortex-position errors but also makes use of all the available data rather than just a portion.

7.3.2 Analysis for Stalled Vortices

The occurrence of many slowly moving and stalled vortices during these tests provide an incentive for further development of some concepts which can provide vortex information from a single range scan independent of vortex transport. The basic concept, shown in Fig. 74, is to use the MAVSS data to compute a portion of the line integral around the vortex, which is one definition of vortex circulation. If the line-integral contour is outside the vorticity of the vortex, the line integral will yield Γ_∞.

Since the MAVSS measures the component of velocity along its beam, it is ideally suited for computing the line integral

$$G = \int_{z_1}^{z_2} \bar{V} \cdot d\bar{s} \qquad (17)$$

along its beam. G is computed simply by summing the velocities at all range gates multiplied by the length of a range gate. Neglecting the image vortex and assuming that the vortex circulation is constant over the radii of the integration, the line integral is simply related to the vortex circulation by

$$G = (1/2)\ \Gamma_\infty \left(\frac{\alpha_1 + \alpha_2}{\pi} \right) \qquad (18)$$

where the angles α_1 and α_2 are in radians. The line integral is proportional to the vortex angle subtended by the integration path. The effect of the image vortex is simply to subtract a term pro-

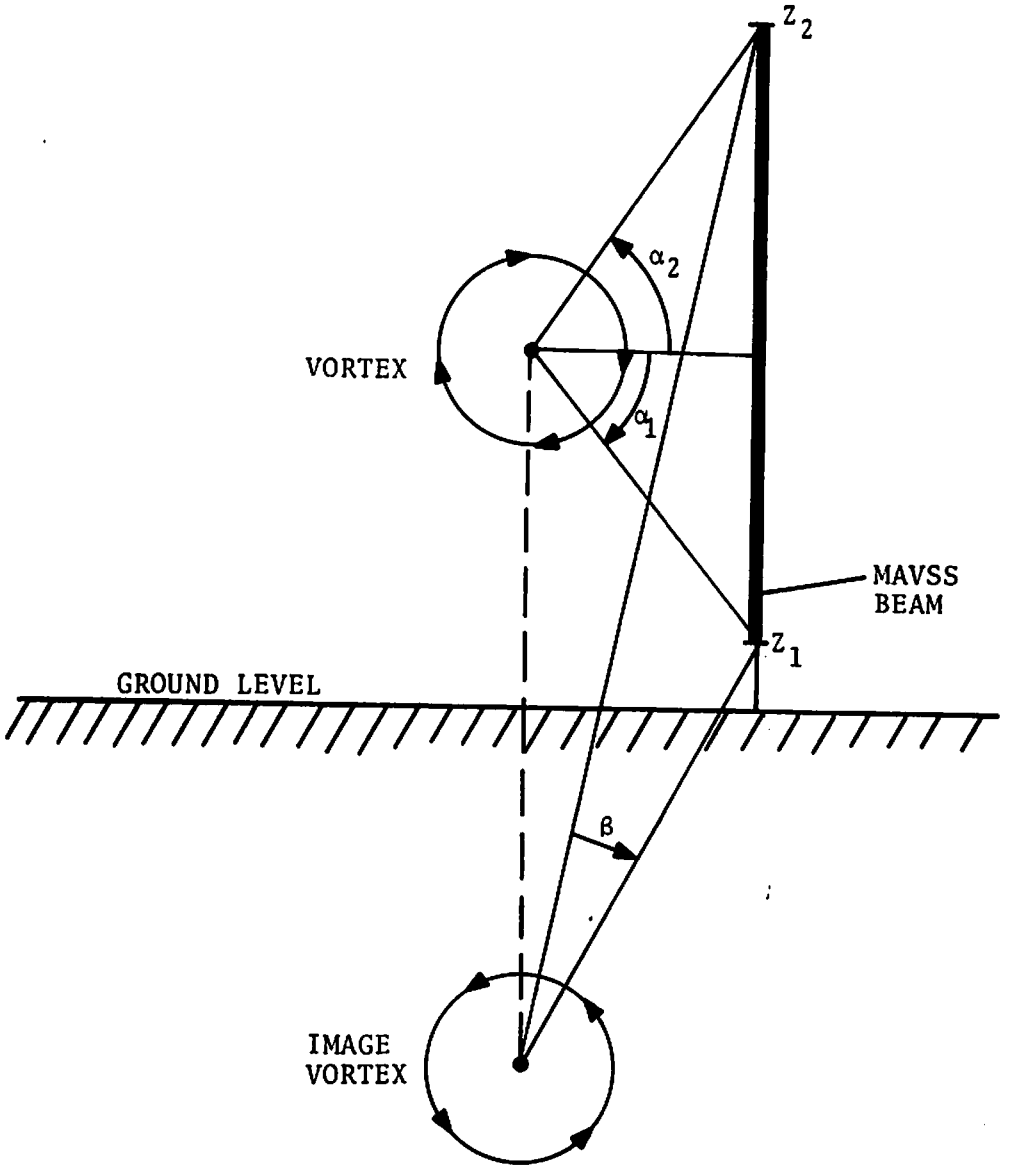

FIGURE 74. MONOSTATIC ACOUSTIC VORTEX SENSING SYSTEM LINE-INTEGRAL GEOMETRY

portional to the angle β subtended at the image vortex:

$$G = (1/2)\ \Gamma_\infty\ \frac{(\alpha_1 + \alpha_2 - \beta)}{\pi}. \qquad (19)$$

The maximum value of G will occur for vortex displacements large enough to avoid the circulation decrease at the vortex core, yet small enough to have small angular losses.

Figure 75 shows a plot of the vortex line integral versus elapsed time, again using a spectral-width threshold to eliminate noisy data. Since the purpose of the line integral is to estimate vortex circulation, what is plotted is 2G which has the limiting value Γ_∞. The range giving the maximum contribution to the line integral is indicated in the lower plot of Fig. 75 and shows the range gate giving the largest sum of the velocities in three adjacent range gates. This range can be shown to give a reasonable estimate of vortex height as long as the vortex displacement is less than the vortex height. This height measurement fails (see also Fig. 69 and 70) when the vortex is directly over the antenna since then the velocities are approximately zero.

Figure 76 shows all of the line integral data for a run. Plots of this type have been scanned for all runs, and the times showing reasonably consistent height data are selected for the plots shown in Fig. 68. The data selected are indicated by a double line on the time axis in Fig. 76. Appendix E.2 contains all the other line integral plots.

It may be desirable to correct the line integral data to give a valid measurement of the total circulation Γ_∞. Two approaches are feasible: (1) If one knows the vortex location, one can correct 2G by the angular terms in equation (19). (2) The line integral can be completed by using measurements of the horizontal wind at the ground, and by neglecting the high-altitude contribution to Γ_∞. Considerable effort has been expanded in trying to estimate the vortex lateral displacement from MAVSS data for a single antenna, but is has been found unreliable because of vortex distortion. However, the MAVSS data for several antennas can be

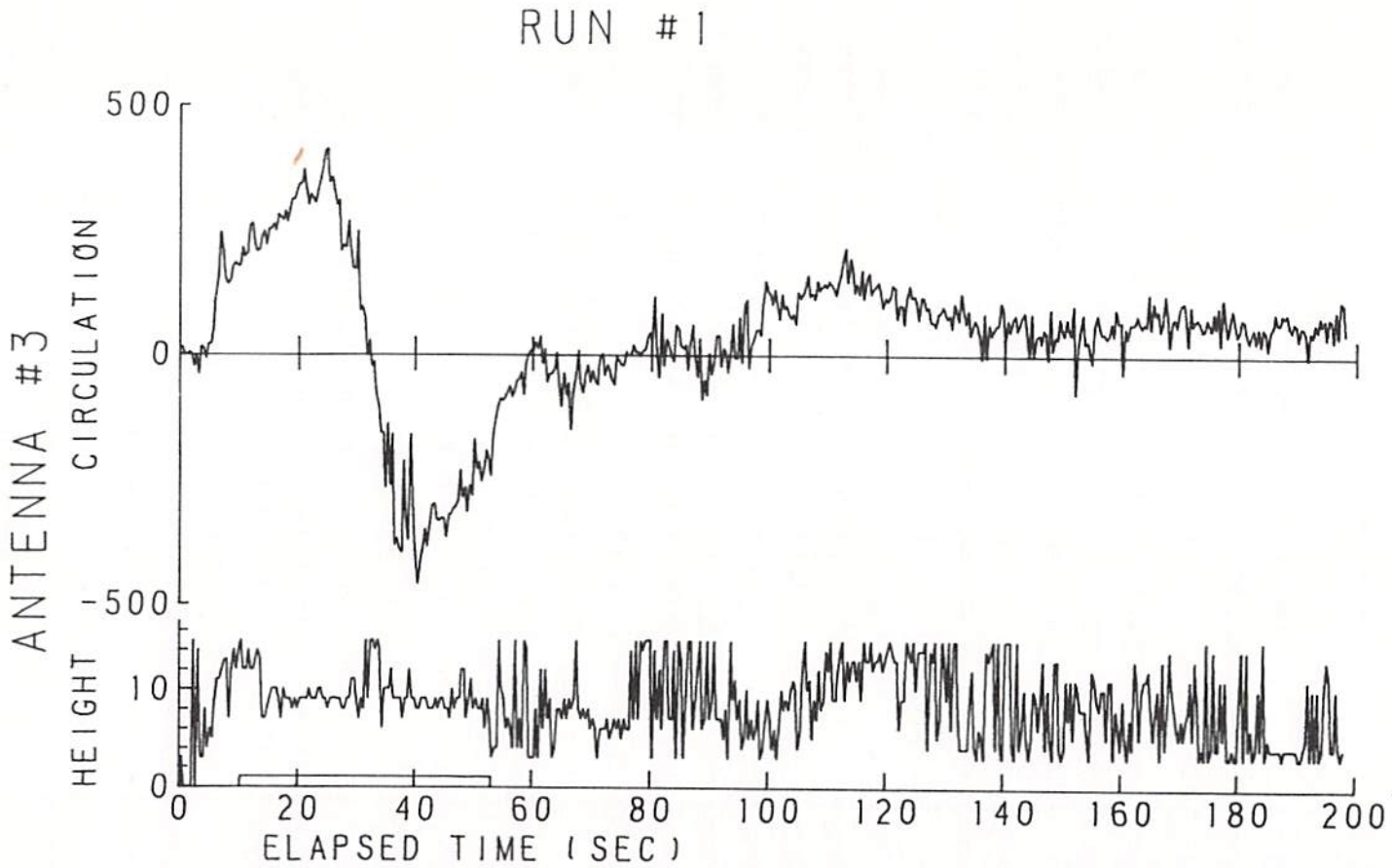

FIGURE 75. LINE-INTEGRAL AND HEIGHT DATA FOR ONE MAVSS ANTENNA

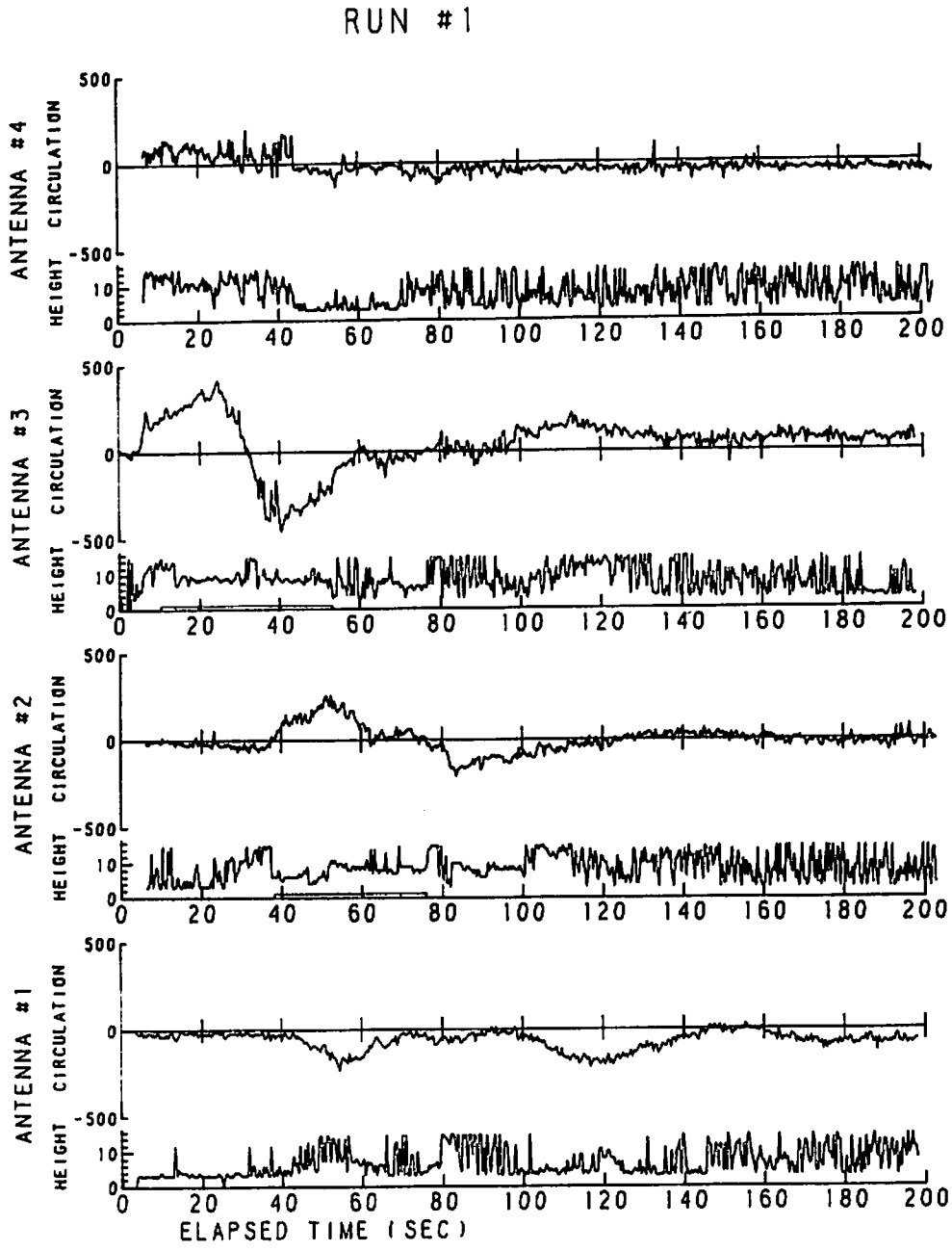

FIGURE 76. LINE-INTEGRAL AND HEIGHT DATA FOR ALL ANTENNAS

used to estimate a vortex track, and thereby, correct the line integrals. Figure 77 shows some estimated tracks based on the data of Fig. 68. Figure 78 shows the circulation-decay plots resulting from the corrected line integrals. Dips occur when a vortex passes over an antenna because of the finite core radius. This approach does not appear to yield particularly useful results.

7.4 RESULTS

The most reliable MAVSS vortex-strength parameter is the average circulation Γ'. Figures 79 through 90 plot for three radii (5, 10, and 15 m) all the runs which have defined vortex arrivals. The data from vortices which passed more than 1 antenna are connected by lines. These data are more accurate than single points because the transport velocity can be estimated with less error. The data points for normal (30/30) landing configurations are plotted in Figs. 79, 80, and 81. For comparison, the low-speed LDV values for Run 5 are shown as heavy solid lines. The high-speed LDV data from Run 8 are shown as heavy dashed lines. The LDV values appear to be consistently larger for 10 and 15 m.

The data points for the 30/1 configuration are plotted in Figs. 82, 83, and 84. These runs gave outstanding MAVSS data since the ambient wind was just sufficient to move the vortices past the whole MAVSS array before the vortices died. The 30/1 vortices appeared to last somewhat longer than the 30/30 vortices. The difference between gear up and gear down, which was noted at altitude in Ref. 22, did not appear here in ground effect. Figures 85, 86, and 87 show the 30/30 runs with spoilers deployed. The heavy solid lines indicate the high-speed LDV data from Run 11. The vortices appeared somewhat weaker than those generated without spoilers. The last set of figures, 88, 89, and 90, show the results for takeoff (10/10) configuration. For these limited data, the difference between level flight and climb out was not great.

The MAVSS data, particularly the scattering amplitude C_T plots, give some useful information about the interaction of the wake vortex oval (Ref. 19) with the ambient atmosphere. During

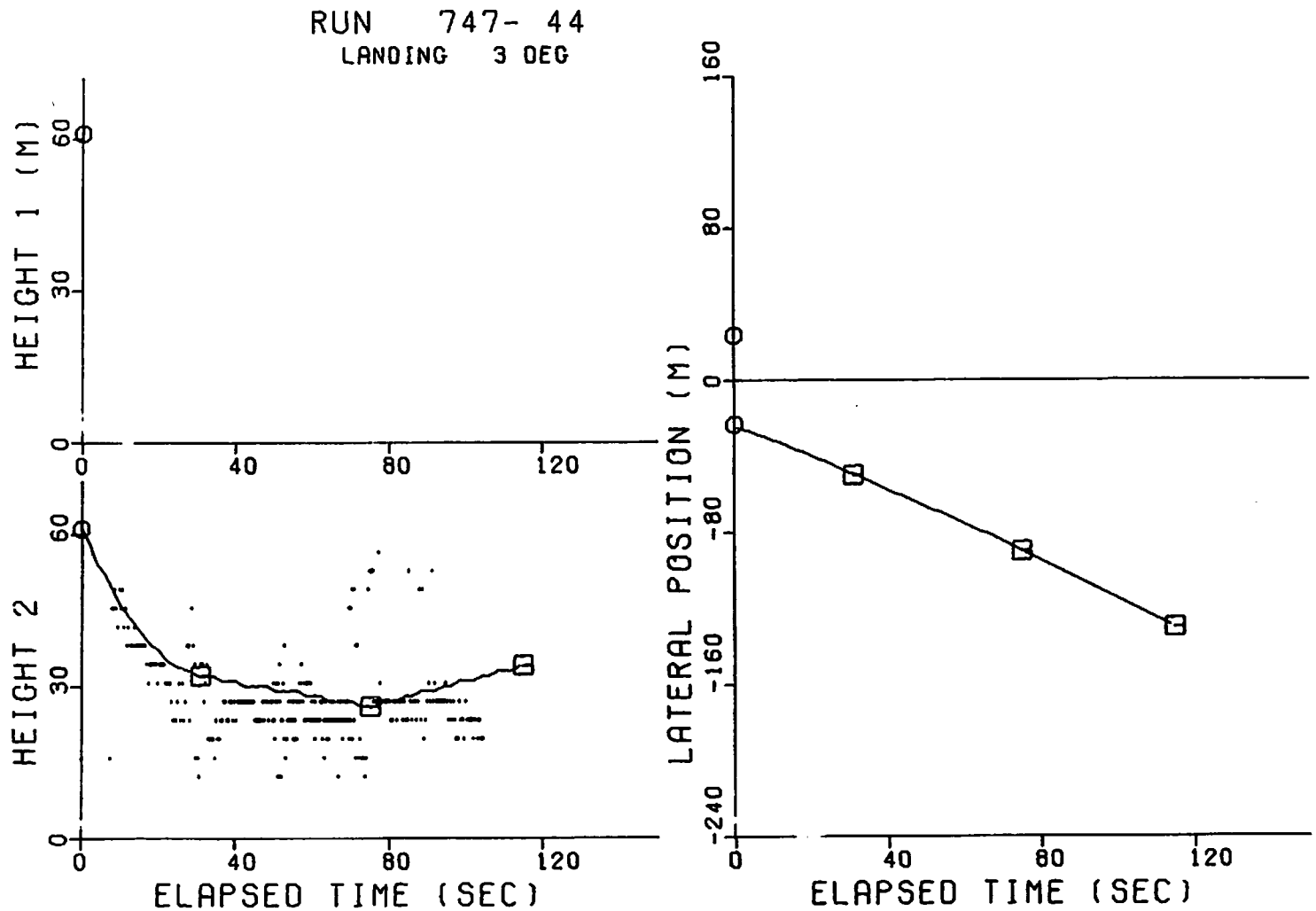

FIGURE 77. ESTIMATED VORTEX TRACKS

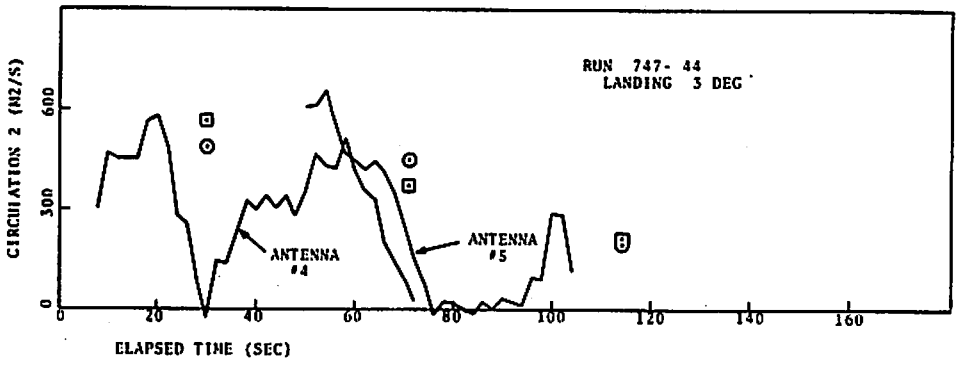

FIGURE 78. VORTEX CIRCULATION VERSUS TIME. Lines are corrected line integral data; points are from least square fits (squares for 5 range gates, circles for 1 range gate).

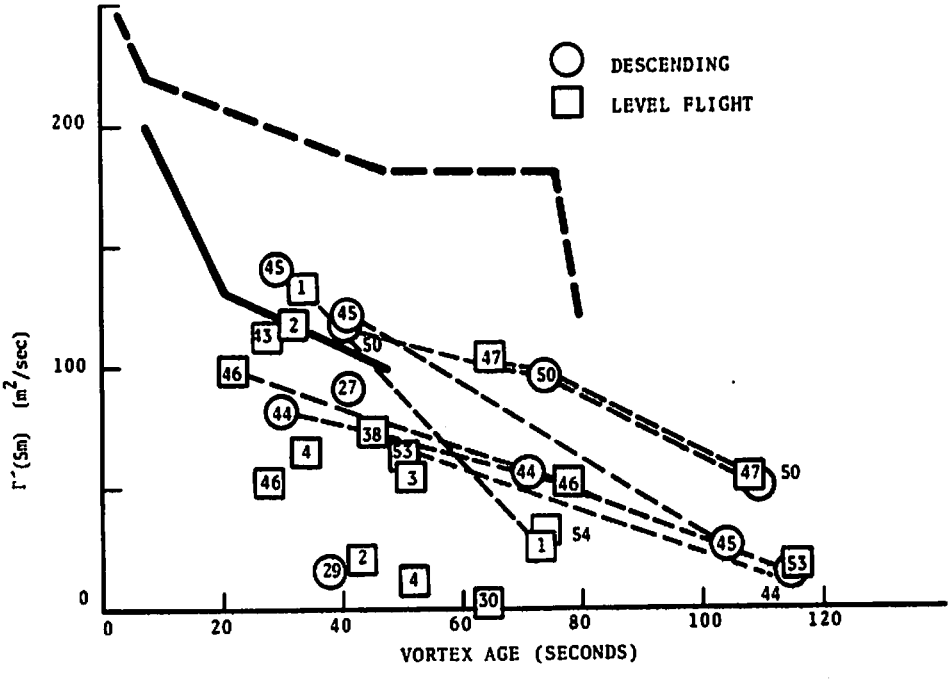

FIGURE 79. DECAY OF 5-METER AVERAGE CIRCULATION FOR 30/30 RUNS. The heavy solid line shows the low-speed LDV data for Run 5, and the heavy dashed line shows the high-speed LDV data for Run 8.

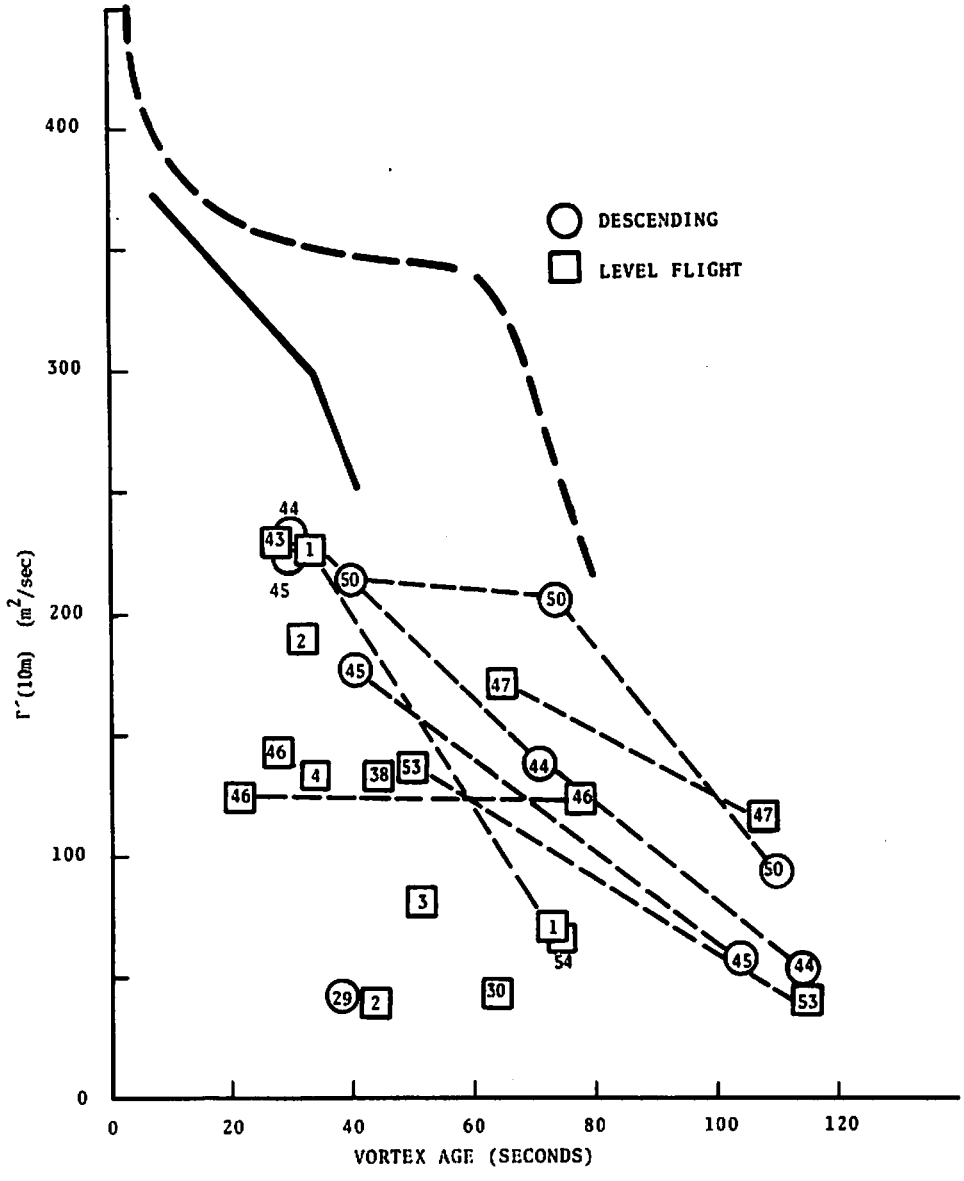

FIGURE 80. DECAY OF 10-METER AVERAGE CIRCULATION FOR 30/30 RUNS. The heavy solid line shows the low-speed LDV data for Run 5, and the heavy dashed line shows the high-speed LDV data for Run 8.

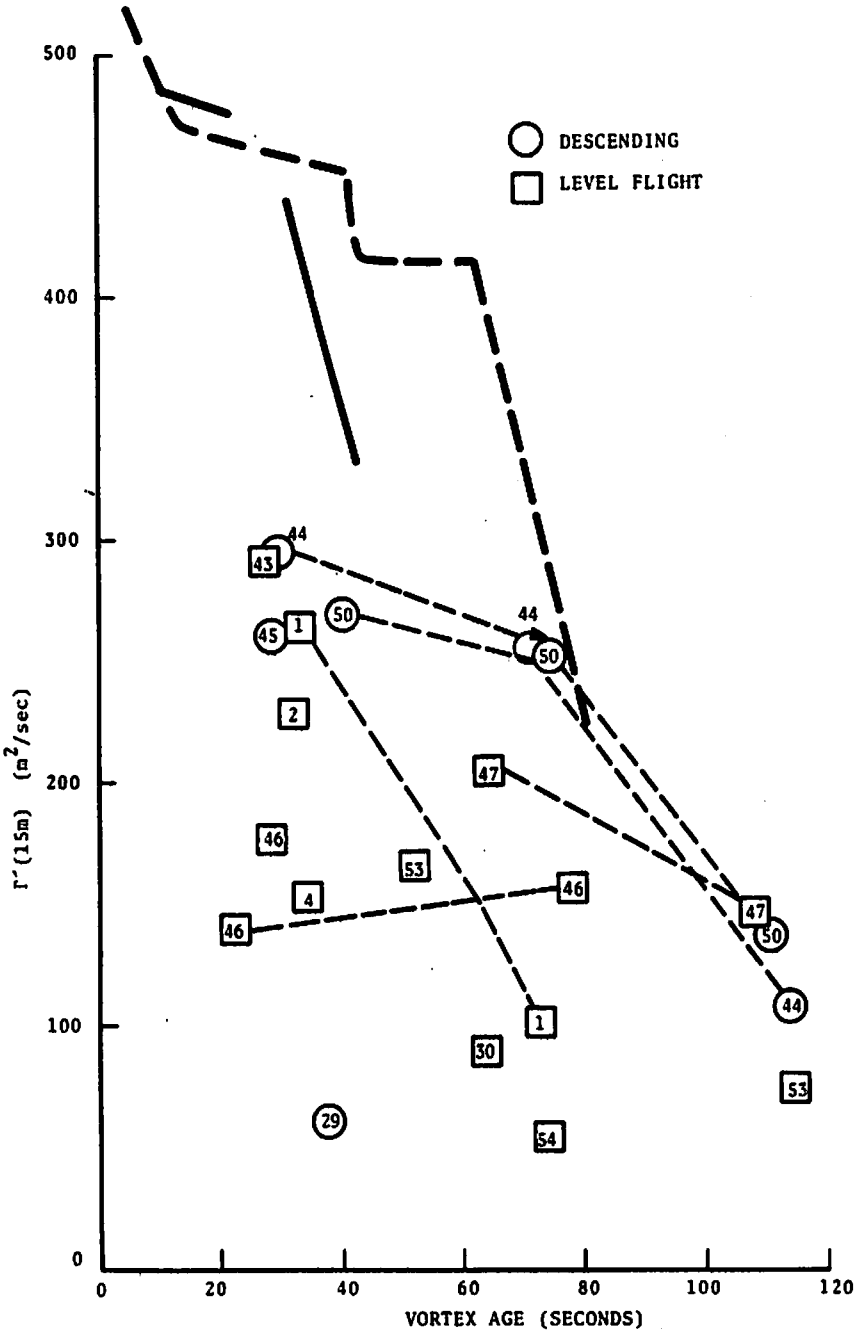

FIGURE 81. DECAY OF 15-METER AVERAGE CIRCULATION FOR 30/30 RUNS. The heavy solid line shows the low-speed LDV data for Run 5, and the heavy dashed line shows the high-speed LDV data for Run 8.

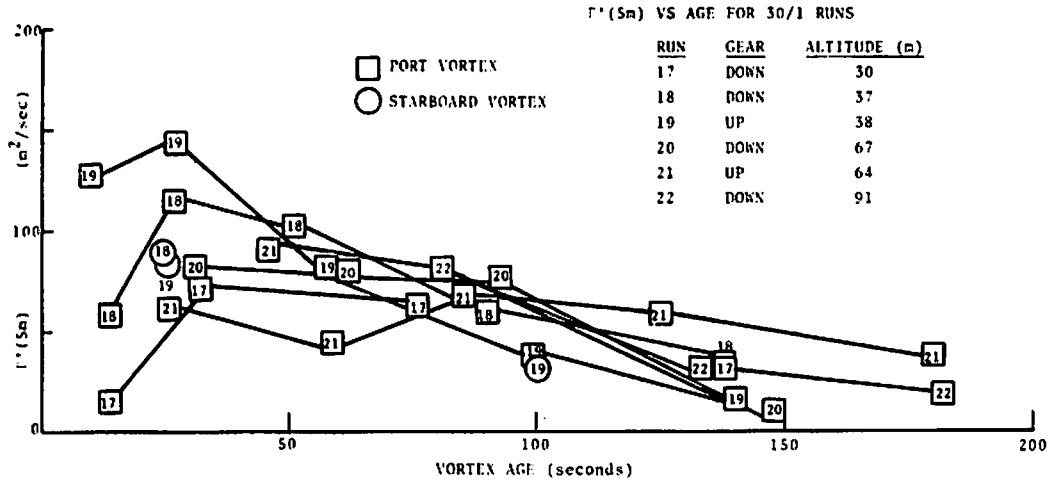

FIGURE 82. DECAY OF 5-METER AVERAGE CIRCULATION FOR 30/1 RUNS

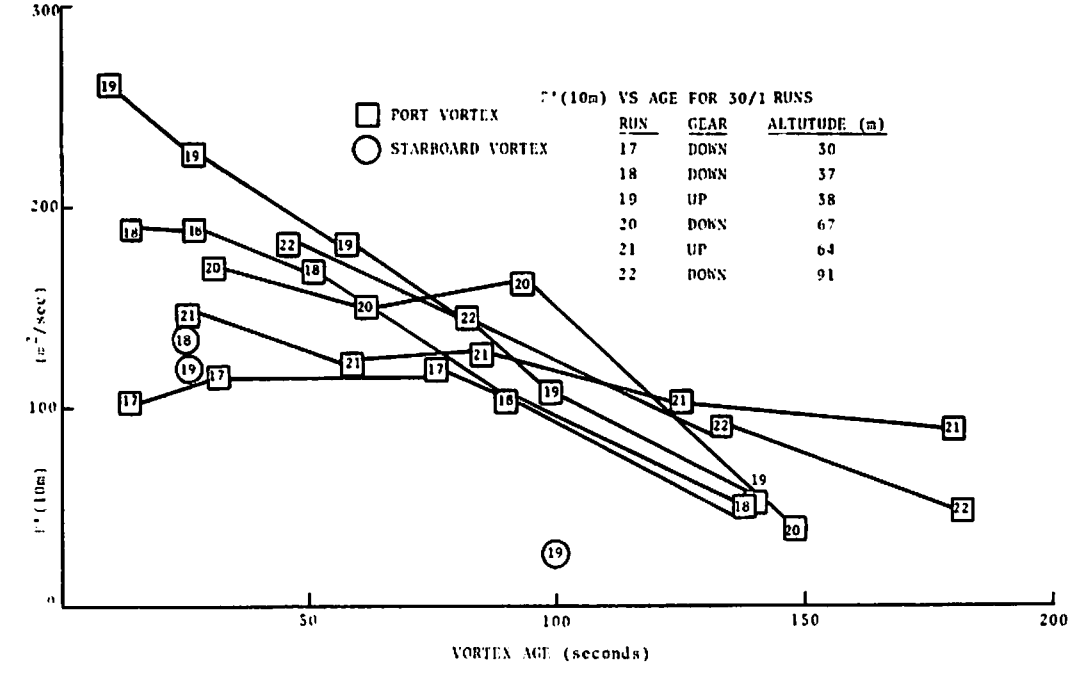

FIGURE 83. DECAY OF 10-METER AVERAGE CIRCULATION FOR 30/1 RUNS

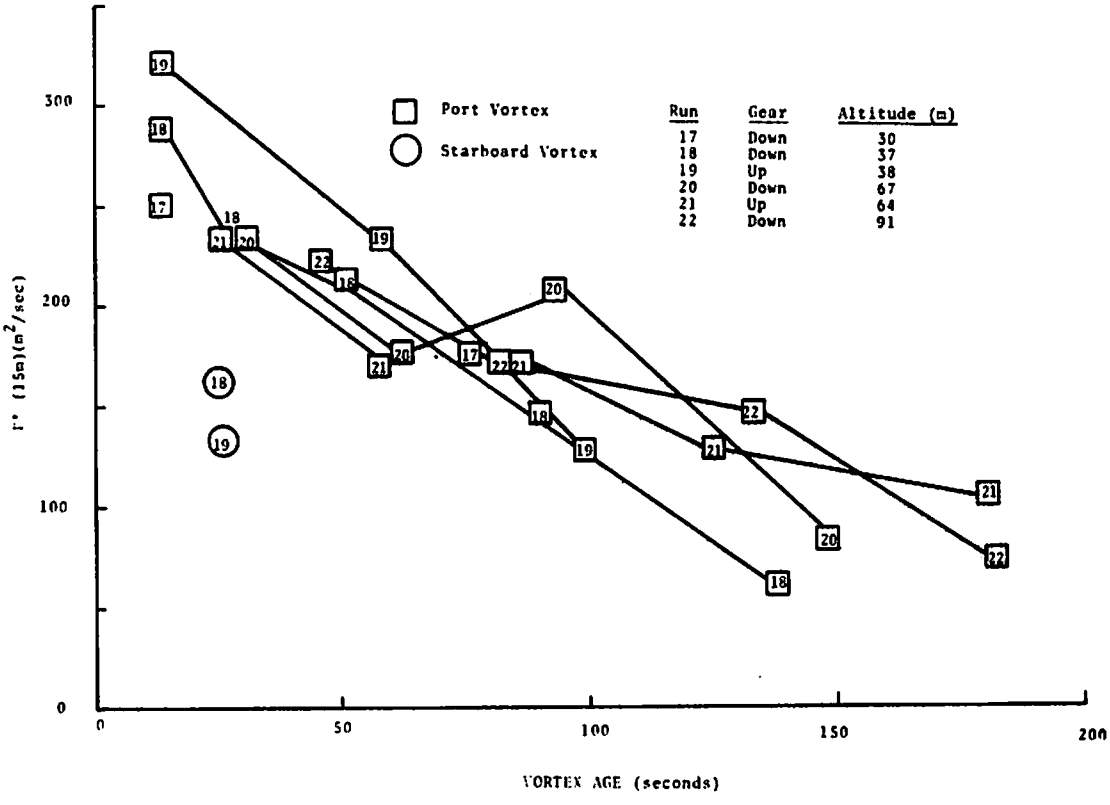

FIGURE 84. DACAY OF 15-METER AVERAGE CIRCULATION FOR 30/1 RUNS

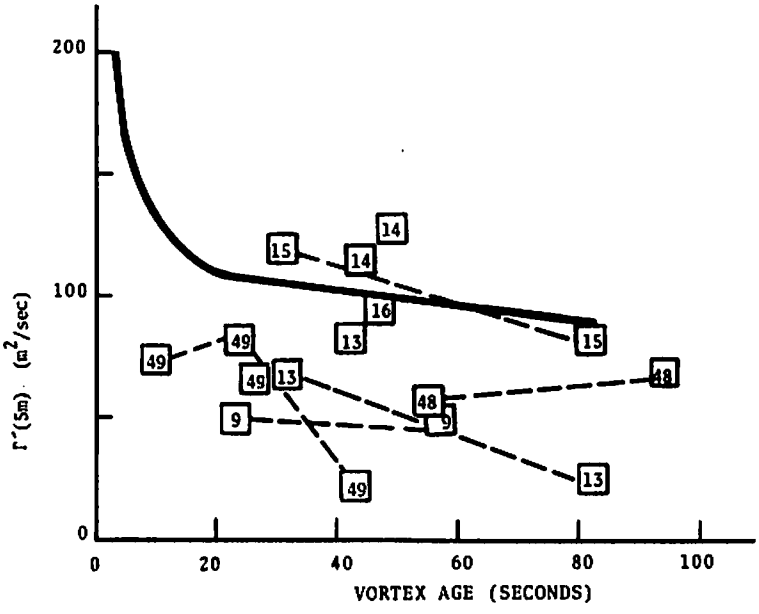

FIGURE 85. DECAY OF 5-METER AVERAGE CIRCULATION FOR 30/30 RUNS WITH SPOILERS. The heavy solid line shows the high-speed LDV data for Run 11.

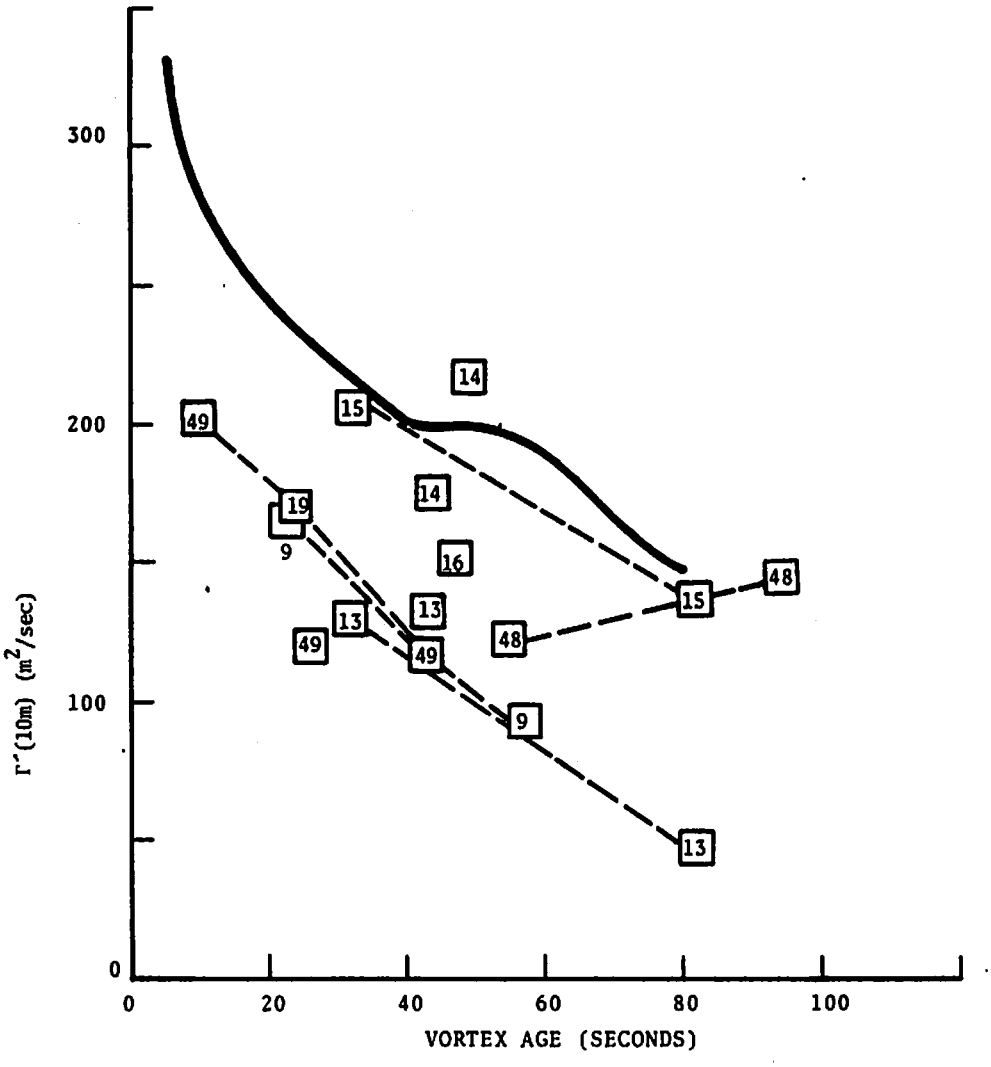

FIGURE 86. DECAY OF 10-METER AVERAGE CIRCULATION FOR 30/30 RUNS WITH SPOILERS. The heavy solid line shows the high-speed LDV data for Run 11.

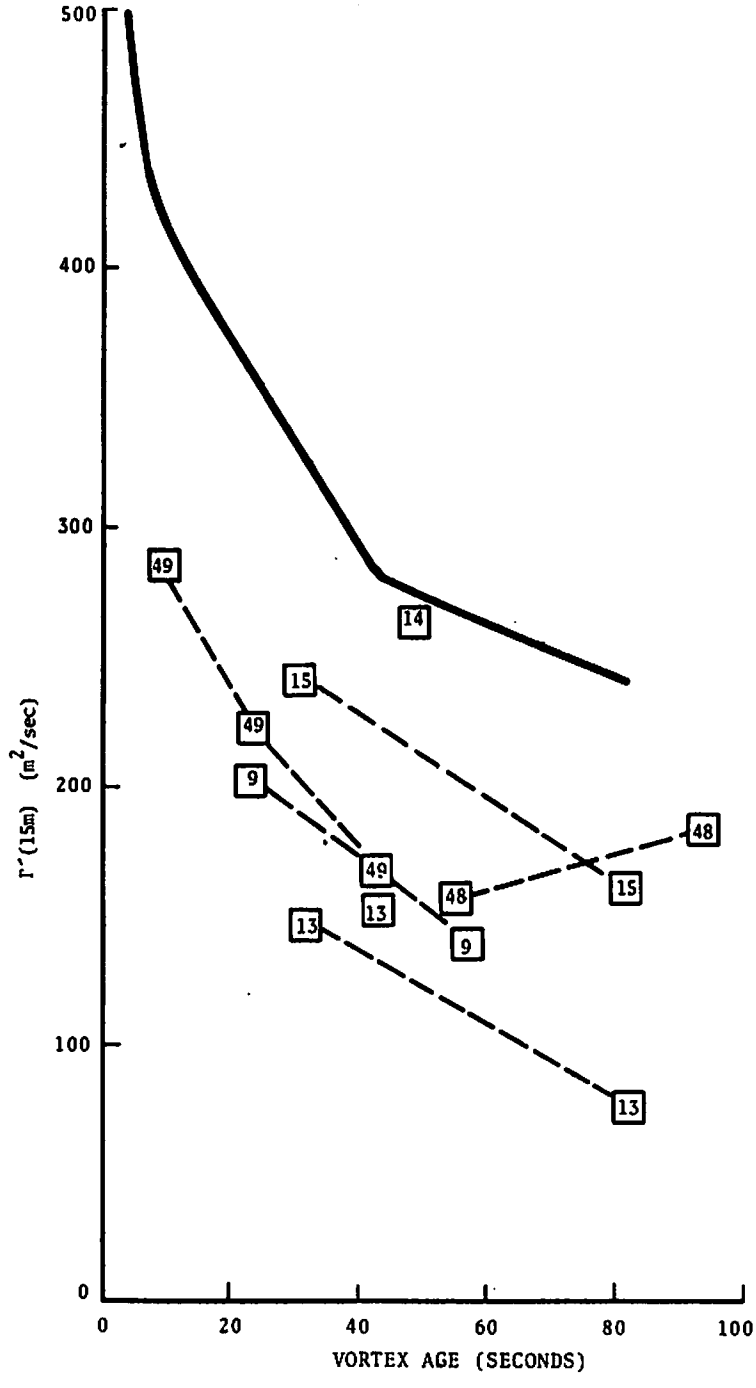

FIGURE 87. DECAY OF 15-METER AVERAGE CIRCULATION FOR 30/30 RUNS WITH SPOILERS. The heavy solid line shows the high-speed LDV data for Run 11.

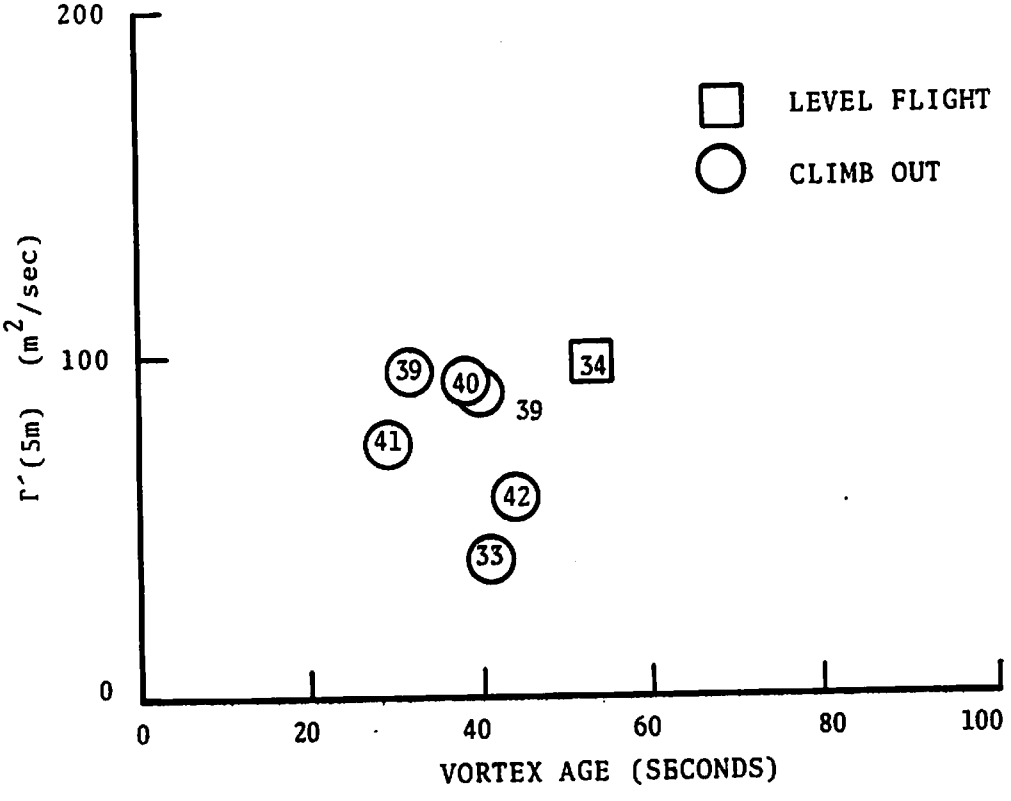

FIGURE 88. AVERAGE CIRCULATION AT 5 METERS FOR 10/10 RUNS

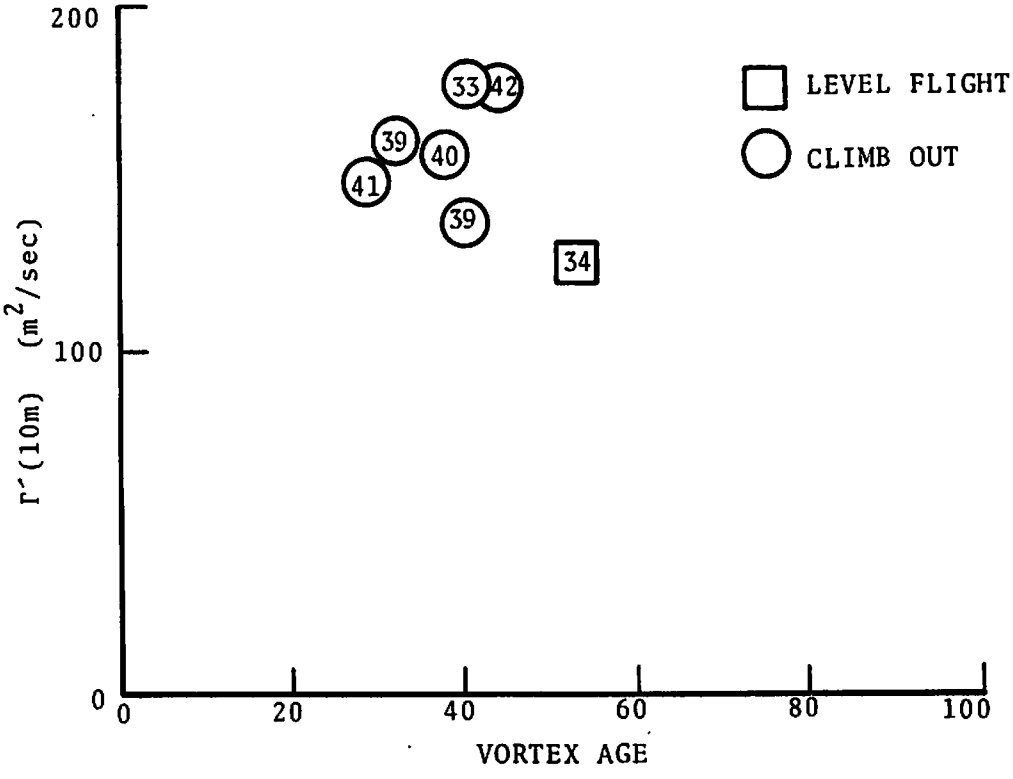

FIGURE 89. AVERAGE CIRCULATION AT 10 METERS FOR 10/10 RUNS

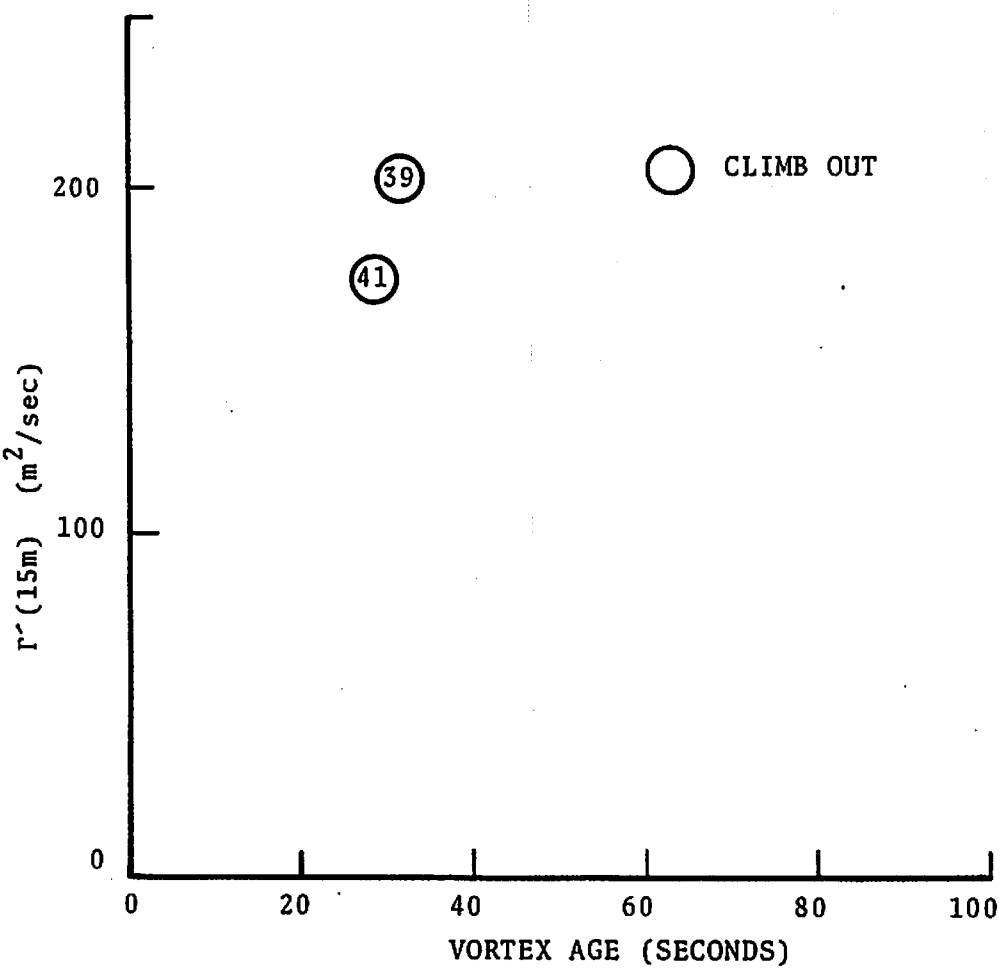

FIGURE 90. AVERAGE CIRCULATION AT 15 METERS FOR 10/10 RUNS

the early sorties when a strong inversion was present, the dominant mechanism for producing thermal fluctuations was the vortex-induced mixing of different layers of the atmosphere. Plots of C_T then give a picture of the motion and mixing of the vortex oval as it descended toward the ground. Figure 65 through 67 and 90 through 94 show the relevant data for Run 1. Figure 94 is a different way of plotting the scattered intensity. The scattered amplitude is integrated for 4 ms and a point is illuminated on a CRT display if the result is above a threshold. The motion of the wake across the three antennas (3,2,1) is evident in Fig. 94. A rapid increase of C_T in Fig. 67 and 92 occurs when the oval first passes over each MAVSS antenna. The temperature fluctuations are largest at the edge of the oval where the temperature gradient is largest. The scattering at the vortex core is less than at the edges until the vortex has decayed. The spectral-spread plots (Fig. 66 and 90) show an enhanced spectal width at the edges of the oval which is probably due to turbulence (although it may be due to signal clipping since the gain is too high for Run 1). The strong rising band starting at 105 sec on antenna 3 in Fig. 94 has no obvious explanation, but it appears consistently in other runs also.

The MAVSS data for 30/1 Runs 20 and 21 show an extra vortex of opposite polarity from the main vortex. From the smoke marking, it can be seen that this vortex comes from the inner side of the inner flap. These vortices descend quickly toward the ground, and then, move out rapidly ahead of the main vortex. They thus appear as smaller vortices arriving at the nearest MAVSS antennas (3 and 4) below and before the main vortex. Figure 95 shows the detections of these secondary vortices by the tracking program. They appear in antennas 4 and 5 in Run 20 and antennas 3 and 4 in Run 21. The velocity plots for these detections are shown in Figs. 96 and 97. The gear-up flap vortex (Run 21) is somewhat stronger than the one with gear down (Run 20) as can be seen in antenna 4. Visually, the gear-up vortex is a clean tube of smoke, while the gear-down vortex is simply a smudge, with no indication of a

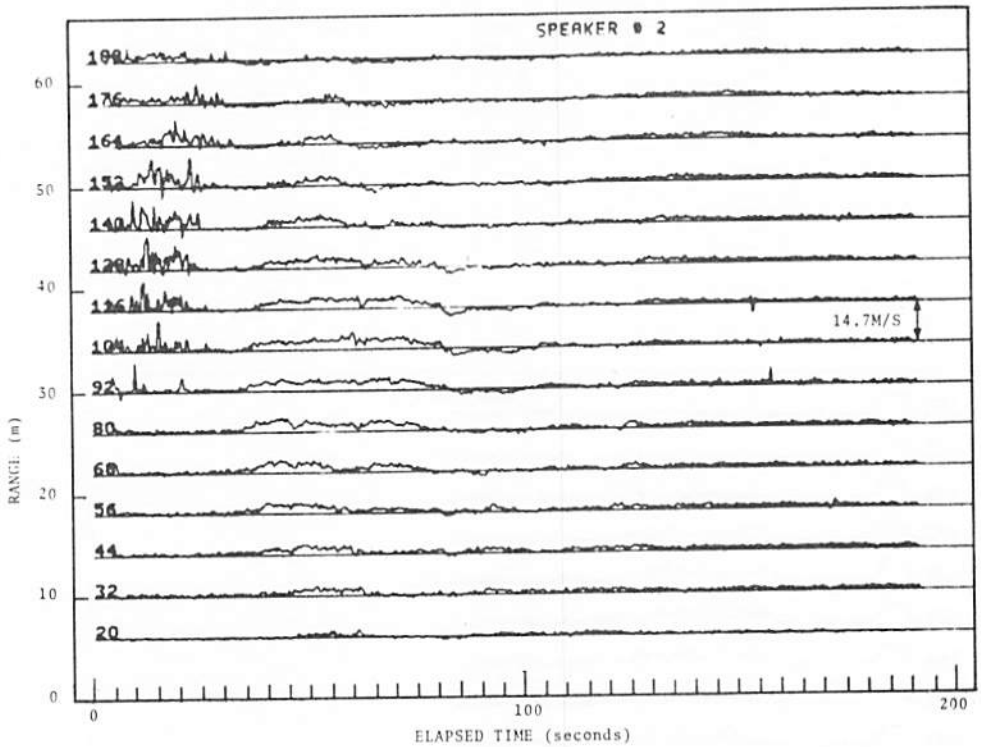

FIGURE 91. VERTICAL VELOCITY PROFILE (RUN 1, ANTENNA 2)

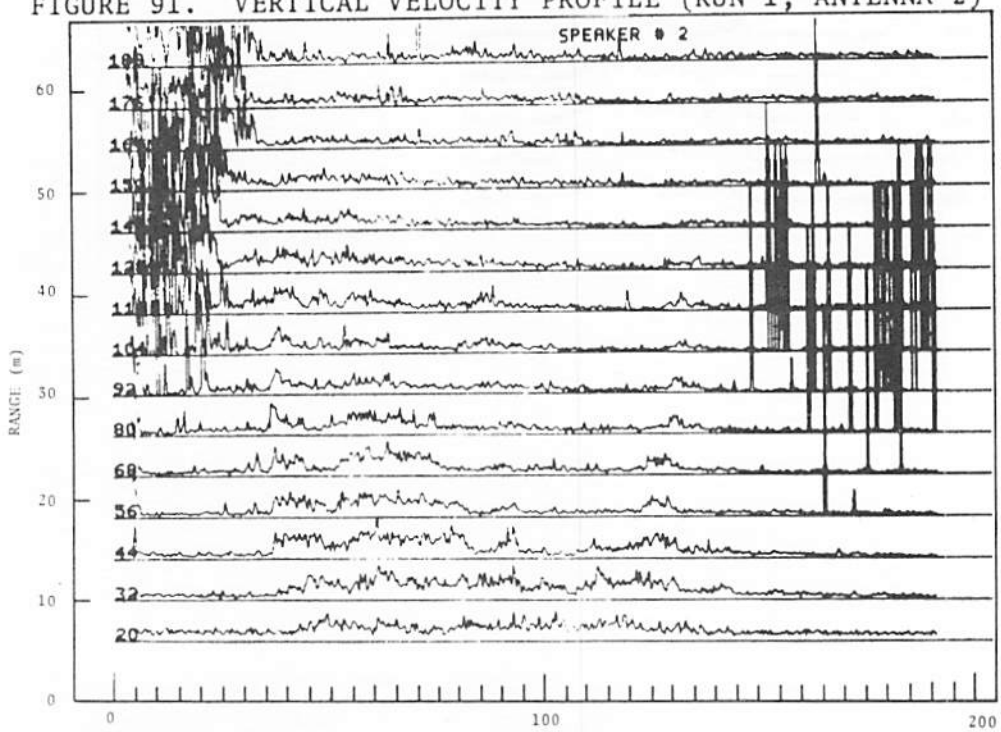

FIGURE 92. PROFILE OF MEAN SQUARE FREQUENCY DEVIATION (RUN 1, ANTENNA 2)

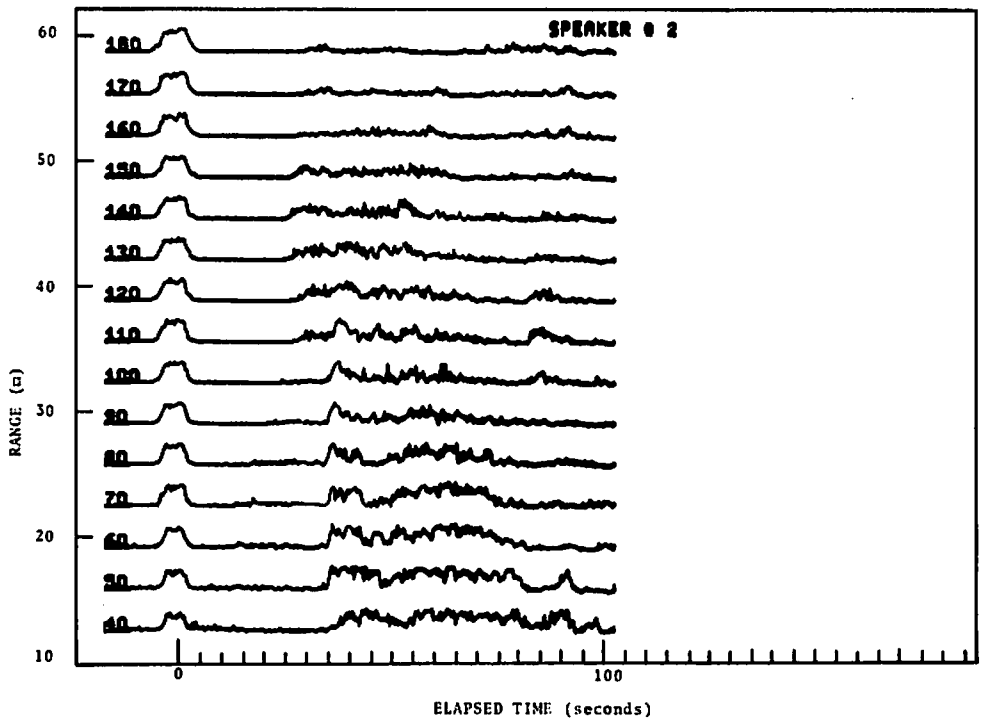

FIGURE 93. SCATTERED AMPLITUDE PROFILE (RUN 1, ANTENNA 2)

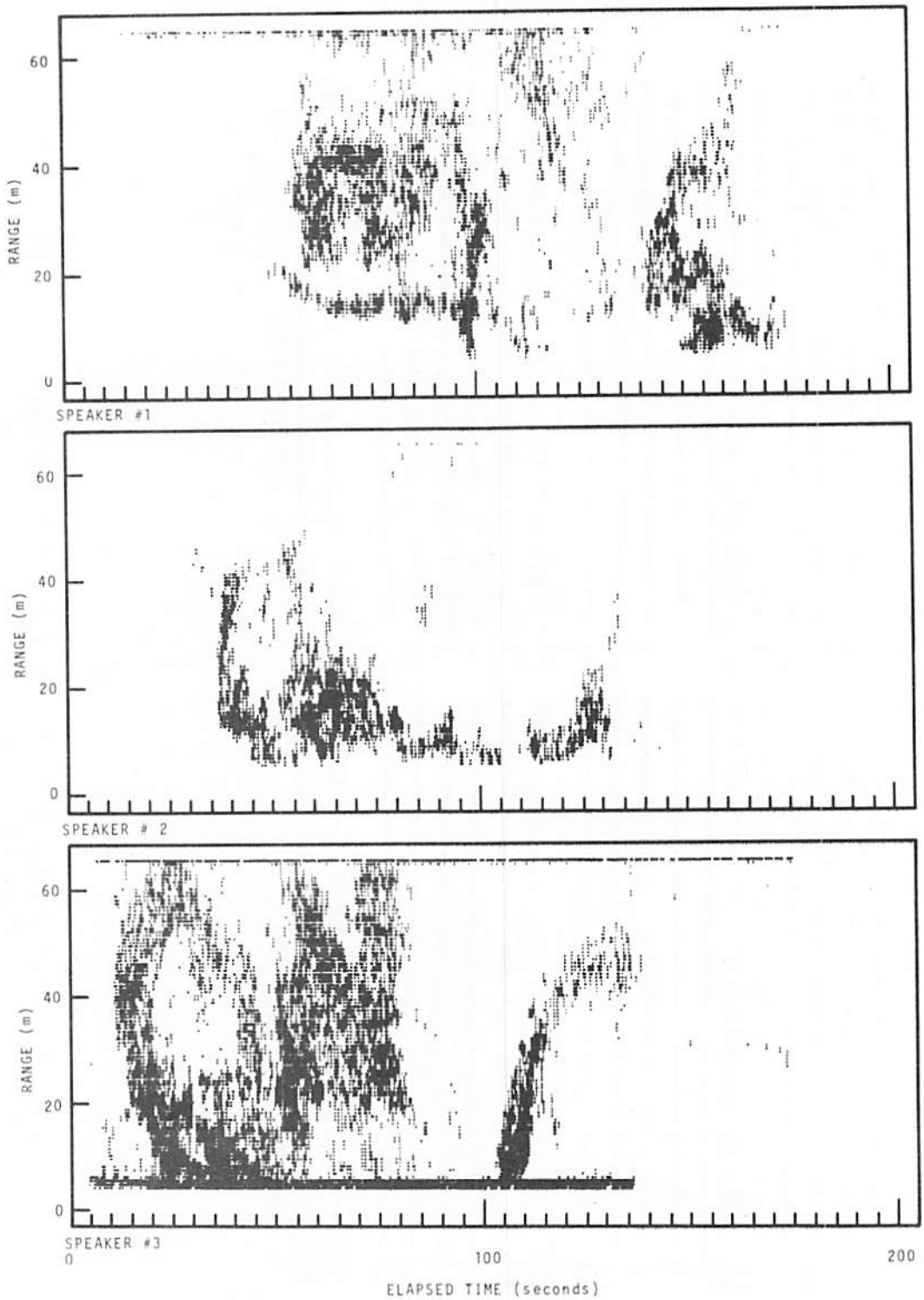

FIGURE 94. SCATTERED INTENSITY VERSUS RANGE AND ELAPSED TIME (RUN 1, ANTENNAS 1-3)

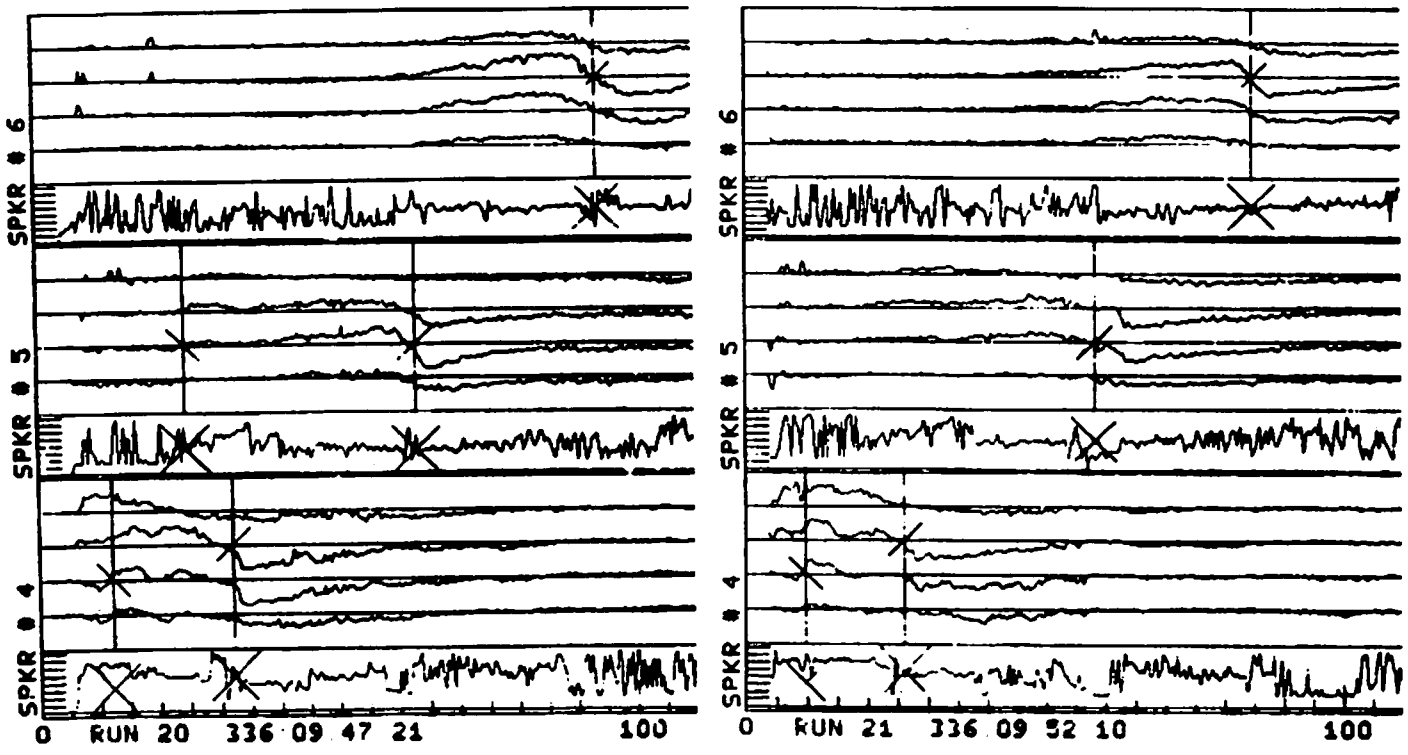

FIGURE 95. COMPARISON OF VELOCITY SUM PLOTS FOR RUNS 20 AND 21.
See Fig. 69 for annotations.

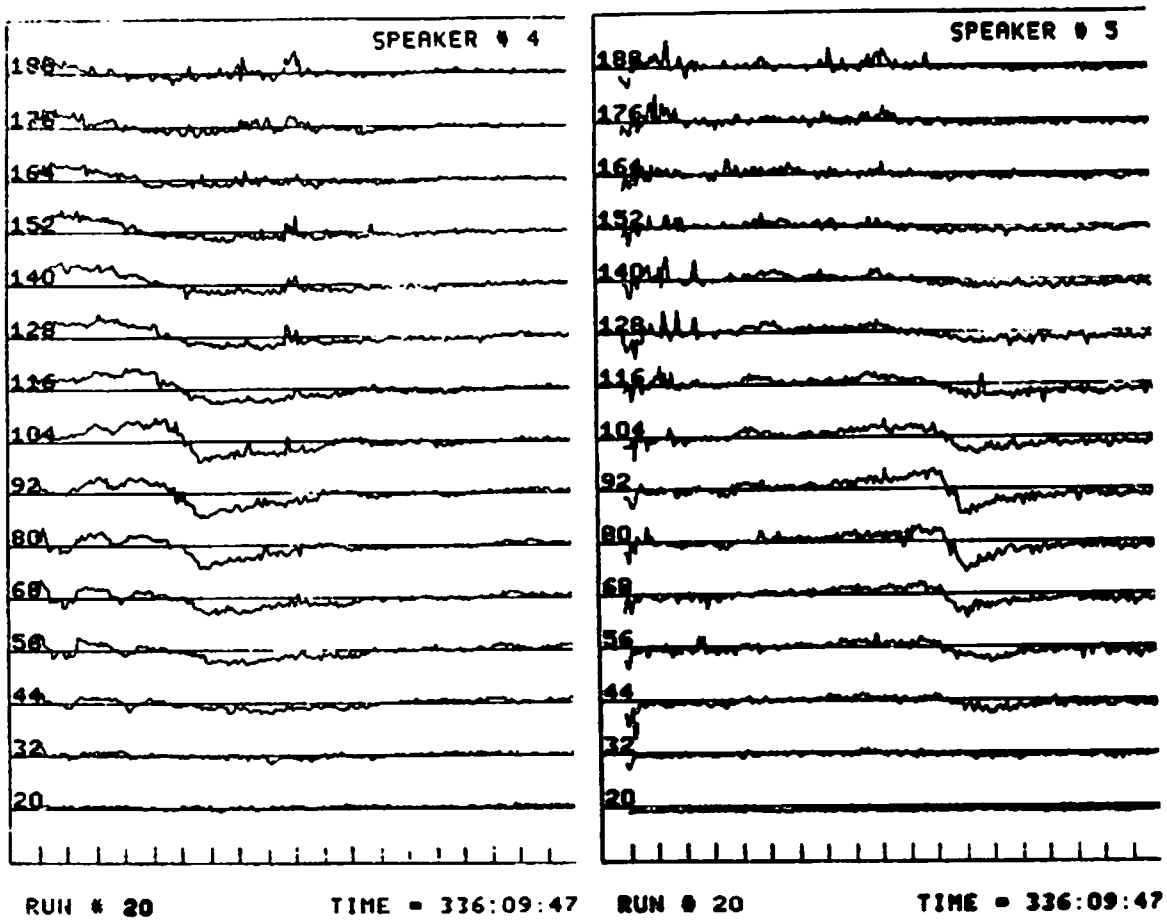

FIGURE 96. SUBSIDIARY VORTICES FOR RUN 20

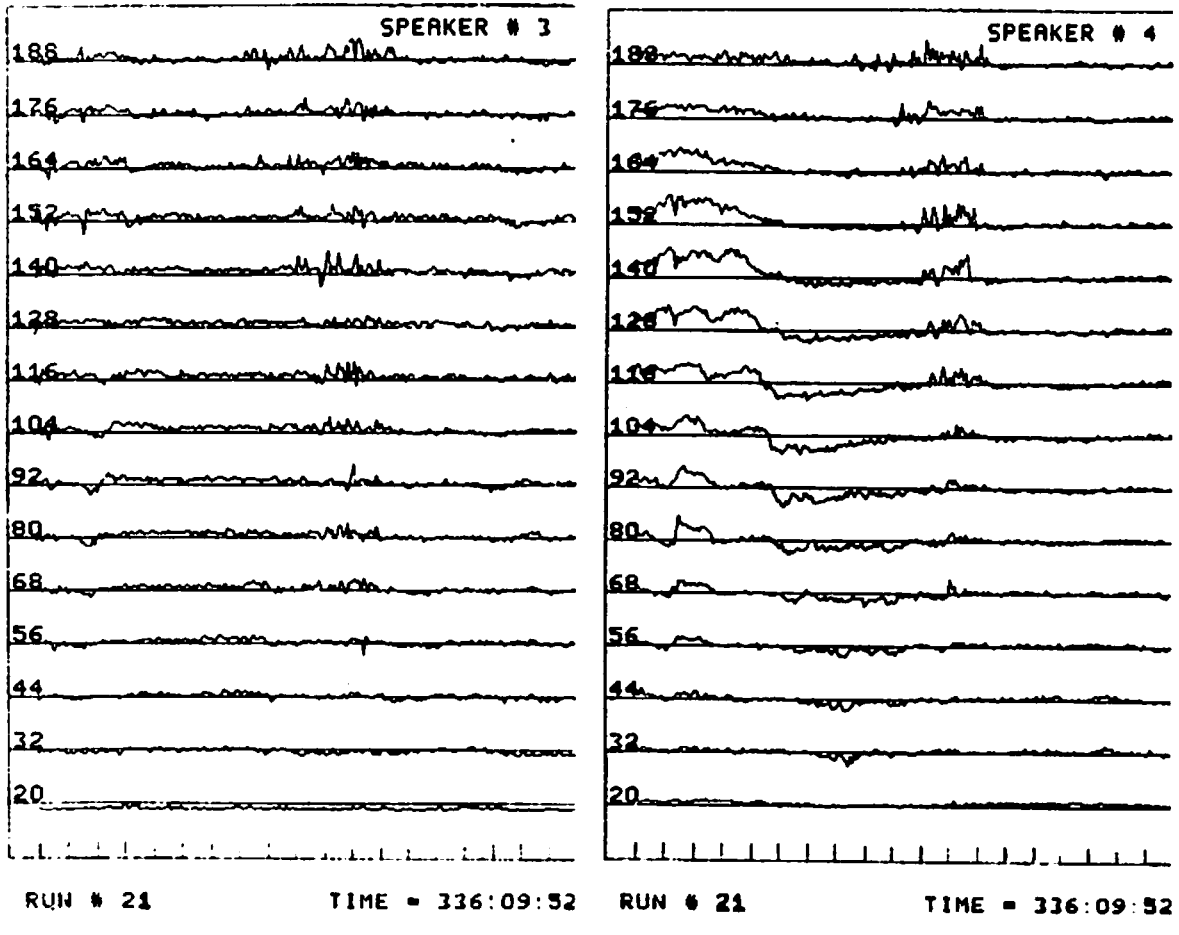

FIGURE 97. SUBSIDIARY VORTICES FOR RUN 21

vortex. The existance of this vortex with no visual indication is another example of the danger in relying on smoke patterns to describe vortex decay.

The velocity-sum data in Fig. 95 show the effects of delayed vortex rollup for the 30/1 configuration. The velocity oscillates in antenna 4 until 25 sec when the vortex passes. The vortex profile appears relatively smooth in antenna 4 after 25 sec and in subsequent antennas. The multiple vortices in the 30/1 configuration appear to coalese into a single vortex at about 25 sec.

8. COMPARISON OF EXPERIMENTAL TECHNIQUES

One of the major objectives set for the flight test was an investigation of experimental techniques. Numerous experimental techniques were used to study aircraft wake vortices. By design the test program used more than one method to measure the same phenomena to facilitate comparisons. Smoke-marked vortices permitted visual and photographic study of the rollup and merging of the vortices; a qualitative assessment of the effects on the vortices by the deployment of spoilers, the lowering of the gear, and the use of different flap and thrust settings; and an indication of the strength of the vortices. Balloons were released to mark the axial flow in the vortices and to indicate the existence of a vortex after the smoke detrained or after the vortices left the test area. The MAVSS tracked the vortices, yielded velocity profiles from which the decay of vortex strength was studied, and permitted an examination of the wake oval. The LDV tracked the vortices, measured velocity profiles during and after rollup, and yielded information on the decay of the vortices. Finally, anemometers were used to examine the vortex flow field before and after bursting.

The most striking characteristic of the various techniques is that they complement each other rather than duplicate the measurements. For example, it was not possible to obtain good LDV and MAVSS data on the same vortex. For highest quality data, the LDV required that the vortex remain fixed within the scan volume, and that the MAVSS required that the vortex be moving with a defined transport velocity. The best LDV data were taken on high-altitude runs where the wake remained in the scan volume until it decayed. The best MAVSS data were taken on the last sortie of each day when the aircraft altitudes were low and a cross wind had developed. Figure 98 shows a comparison of MAVSS and LDV velocity profiles for Run 22 where one vortex moves across most of the MAVSS antennas and the other remains stalled in the LDV beam.

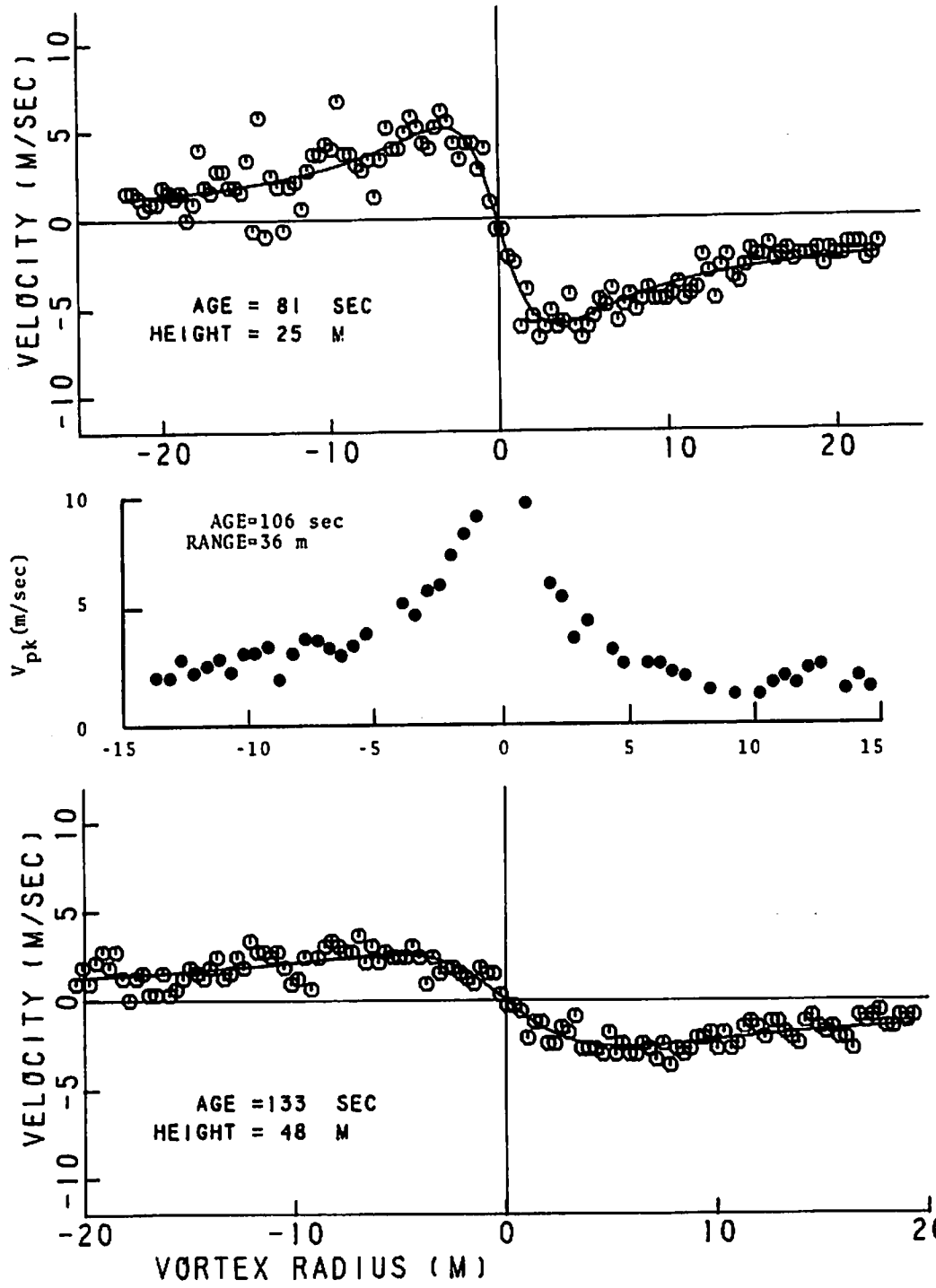

FIGURE 98. COMPARISON OF LASER DOPPLER VELOCIMETER AND MONOSTATIC ACOUSTIC VORTEX SENSING SYSTEM DATA FOR RUN 22. Top and bottom plots: MAVSS data (antennas 5 and 6) on port vortex. Center plot: LDV data on starboard vortex (the sign of the velocity is not determined).

Figures 79 through 81 and 85 through 87 compare the time decay of average circulation using LDV data for high-altitude runs and MAVSS data for low-altitude runs. The data are generally consistent in that the shape of the curves show similar trends. Note the scatter in the MAVSS data. Unfortunately, the number of LDV runs is insufficient to determine whether comparable scatter may occur there. The MAVSS scatter may be due to measurement problems, such as errors in transport velocity, or it may reflect the influence of the ground on vortex decay. Therein lies a fundamental problem in comparing the two techniques. Because they observe vortices under different conditions of altitude and transport, it is not easy to separate physical effects from instrumental ones.

One can compare the velocity and spatial resolution of the LDV and MAVSS data for the 30/30 flap runs which have been repeated often to standardize the data. The core radius for the MAVSS least-square fits is usually about 3.0 m for reasonably fresh vortices. This value compares favorably with the 2.5-m LDV core radius (which uses a different form to fit the data). The MAVSS spectra are somewhat broadened at the vortex core, thus indicating the presence of velocity gradients across the MAVSS beam. The maximum observed velocities are somewhat less (12 m/s versus 15 m/s) for the MAVSS data than for the LDV data. The spatial averaging over the MAVSS resolution volume tends to reduce the MAVSS peak velocity. Conversely, the LDV velocities have systematic errors toward high velocity because of the use of the extreme spectral frequency to get the vortex velocity. Only one MAVSS vortex detection is made on the aircraft configurations producing a tighter core than given by 30/30 flaps. For Run 34, the fitted core radius is less than 2 m (see Appendix E); the transport velocity, however, is not sufficiently established to be certain of this value.

The use of smoke marking to study the decay of wake vortices was shown to be risky by these tests. Distinct vortex cores were repeatedly found by other techniques (LDV, MAVSS, buoyant balloons) after the smoke marking had disappeared.

has been observed, as would be expected, since the vortex-core region is formed from the outer portion of the wing.

The deployment of spoilers near the outer-flap edge dramatically alters the final vortex form. The velocity profile is

flattened, and the strength is not appreciably changed (see Fig. 53). According to the smoke pictures (Fig. 14), the spoilers immediately spread out the flap vortex. The tip vortex remains unaffected until the vortex merger which appears to occur sooner than without spoiler deflection. After merger, the smoke marking rapidly expands to fill much of the vortex oval.

9.1.2 Modified Landing Configuration (30/1)

For these runs, the vortex generated on the inboard edge of the inner flap descended rapidly toward the ground, and then, rapidly moved out past the other vortices. The deployment of the landing gear destroyed the smoke marking of the vortex, reduced its tangential velocity, but did not change its motion (Runs 20 and 21). Because the wingtip smokers were not used for the 30/1 runs, no direct observations were made on the interactions between the tip and flap vortices. Oscillations, however, were observed in the MAVSS data (Fig. 95) with a period of about 8 sec — the oscillations could be at the half-rotation period or the full-rotation period depending upon the geometry and relative vortex strength. If one assumes $\Gamma_1 + \Gamma_2 = 500\ m^2/s$, the vortex spacing is 14 m or 10 m, respectively, for half of a rotation or a full rotation according to equation (1). The initial spacing between the flap and tip vortex is 19 m. A reduction in spacing from 19 m to 14 m appears to be in keeping with the photo observations (Section 4.2) for 30/30 flaps, and also corresponds to the more likely case of one period of velocity oscillaiton per half of a revolution. The oscillations last about 30 sec for these 65-m altitude runs. The flap and tip vortices thus appear to remain distinct for that length of time. The LDV velocity profile for Run 22 with 30/1 flaps (Fig. 61) is similar to that for the 30/30 runs but with somewhat lower velocities at the same elapsed time. The direct effect of 30/1 flaps on peak tangential velocity (Fig. 62) is much less than that of spoilers. The alleviation effect of the 30/1 flap configuration appears to be lost in ground effect; the proximity of the ground prevents the inner flap vortex from mixing with the tip and outer-flap vortices.

9.1.3 Takeoff Configuration (10/10)

The wingtip vortex dominates the rollup for 10/10 flap setting. The flap vortex is much weaker, and it eventually disintegrates instead of merging with the tip vortex (see Fig. 14). The vortex core is generally small as marked by the smoke, and has high tangential velocities (see Fig. 60b) and strong jet-like axial flows. When full takeoff thrust is applied, the flap vortex disintegrates more quickly, and eventually, the tip vortex also appears to be affected. The smoke marking shows more turbulence and the peak tangential velocities appear to be lower (Fig. 60b). The deployment of spoilers for 10/10 flap setting is done only for full thrust. The spoilers appear to have a minor additional effect in further reducing the peak tangential velocities. The MAVSS data (Appendix E) give some indication that the spoilers reduce the turbulence in the vortex core.

9.1.4 Holding Configuration (0/0)

For a clean wing, the vortex core is derived directly from the wing tip. The smoke marking shows a tight, small diameter core with large tangential velocities.

9.2 VORTEX TRANSPORT

The largest departure from normal vortex-transport properties was the limited vortex descent and limited ground-effect separation for the early morning sorties when a strong temperature inversion was present.

9.3 VORTEX DECAY

A list of vortex-decay mechanisms includes: Crow instability, core bursting, and viscous decay. The first two have been discussed in Section 4.4. The third, viscous decay, is usually modeled by an eddy viscosity (i.e., turbulent diffusion) which is constant over the vortex, and therefore, causes the highest velocity-gradient regions to decay first. The resulting decay thus should start in the core and spread out, according to this model.

Perhaps, the most striking observation of vicous decay in these tests comes from the 2 high-altitude runs (8 and 11), where the vortex is observed to "decay" from the outside toward the center (Fig. 54). The vortex core remains intact. In some ways, this result should not be unexpected. The vortex core tends to be laminar, and therefore, can be expected to have a small eddy viscosity, and thus, little decay. For landing configuration, the outer region of the vortex is turbulent, and fits the circulation profile (Fig. 43) proposed by Hoffman and Joubert (Ref. 18). This turbulence promotes the rapid diffusion of the organized vorticity, thus causing the vortex to "decay" from the outside toward the center. The organized vorticity in spreading outward faster at the outer regions of the vortex, but the total vorticity within the vortex may or may not be decreasing. Thus, for a given radius of the vortex, the strength within is "decreasing". This observation also explains how the vortex strength can begin to decay quickly as has been observed in MAVSS data collected at airports (Ref. 11). In contrast, the simple viscous-decay model cannot account for any strength decay until the vortex core is totally obliterated.

The descent of the vortex pair in a stable atmosphere may also contribute to vortex decay (Refs. 7 and 8). The vorticity generated by the descent is located on the edge of the vortex oval, and appears to be accompanied by enhanced turbulence according to the MAVSS data. This, or some other similar, effect may account for the observation that the runs on earlier sorties, where the vortices remain stalled in a strong temperature inversion, show shorter lifetimes than the later sorties, where the inversion is gone and the vortices are free to separate. The similar decay for the stalled and moving vortex for Run 22 (Fig. 98) indicates that this difference is probably related to the inversion rather than to transport effects.

10. CONCLUSIONS

The results of the Rosamond Lake tests served more to open new avenues of study than to solidify previous hypotheses, particularly in the question of vortex decay. Non-routine data-processing requirements were in large measure responsible for the delay in producing this report.

One of the surprising features of the tests was how little comparison of different experimental techniques could be done due to the pretest objectives set for each technique. Each sensing technique had its own role, and supplied information not readily available from another source.

Undoubtedly, the success of the tests is the superb velocity profiles obtained by the LDV in the arc-scan mode for the high-altitude runs. These profiles show vortex "decay" from the outside toward the core. Decay, here, means the spreading outward of the organized vorticity which takes place faster at the outer regions of the vortex than near the core. For a finite sampling size, such as a penetrating aircraft wing, this spreading leads to a weakening of vortex strength. This picture of vortex decay has already proved useful in interpreting MAVSS data collected at airports. The success of the arc-scan mode at Rosamond Lake has led to the use of a stepped arc-scan mode for LDV data collection at airports. This scan mode successively scans arcs at 8 ranges, thereby giving a fix on vortex position and strength every 8 sec.

One working hypothesis has come from the Rosamond Lake measurements and the observation of vortex decay from the edge toward the center. It appears that descent in a stratified atmosphere accelerates vortex decay.

Perhaps, the most valuable contribution these tests have made to the study of wake vortices has been to define the methodology for obtaining detailed measurements of wake vortex decay. The next section outlines suggestions for future work.

The various measurement techniques were found to complement each other. The LDV produced excellent data in the arc-scan mode for the high-altitude runs, but relatively difficult-to-interpret data in the finger-scan mode for the near ground runs. The MAVSS was useless for the high-altitude runs, but produced good data when the B-747 passed over the array at low altitudes. It was necessary, however, that the vortices be translating laterally for the MAVSS to yield dependable results. Anemometer arrays, on the other hand, gave velocity profiles which were more useful when the low-altitude vortices were slowly translating.

11. SUGGESTIONS FOR FUTURE TESTS

11.1 IMPROVEMENTS

In retrospect, a number of changes in the experimental set up may have resulted in improved data from these tests. Each system will be discussed below in turn.

11.1.1 Photographic Coverage

The lack of long-term photographic coverage of the high-altitude runs detracted from the usefulness of the excellent LDV data obtained for those runs. A sequence of 5-sec photographs lasting for 120 sec would be very useful in interpreting the strange decay effects of the velocity profiles measured in the LDV arc-scan mode. Good locations for the cameras would be under the flight path, at the LDV site, and displaced to both sides of the flight path. Angle grids should be installed above the cameras to allow simple measurements of vortex-elevation angles. The side cameras would allow the vortex descent to be measured directly as long as the smoke markings remained distinct.

11.1.2 Anemometers

A full evaluation of the use of anemometer arrays was not done in the Rosamond tests. It is known, however, from extensive vortex data-collection trials at airports (Refs. 9 and 10) that the arrays could yield useful data with some limitations. Future tests should include an anemometer standard beneath the aircraft on the centerline of the ground track and, perhaps, closer spacing between the standards.

11.1.3 Laser Doppler Velocimeter

Problems arose in processing the LDV data because of the way the data were recorded. They should be corrected in future tests. A more intrinsic problem was the difficulty experienced in playing back the high-speed data. A better recording and playback system

should be devised. Another intrinsic problem was the lack of adequate real-time computer displays to monitor the LDV signatures and to allow reliable changes in the scanner range and angle limits. Particularly useful for the arc-scan data would be a display comparing outputs for several ranges near the vortices. The range could then be changed to track the vortices. (This capability has since been incorporated into the LDV system.)

11.1.4 Monostatic Acoustic Vortex Sensing System

The major limitation of the MAVSS setup was the absence of antennas near the flight path. If the 2 antennas located on the separate baseline had, instead, been placed in the middle of the MAVSS array, the number of runs with useful data would have increased. The MAVSS system also should have been set for higher range (about 120 m) for the high-altitude runs. Such altitudes have been successfully probed.

11.2 FUTURE OBJECTIVES

The experience of these tests allows one to plan future tests with a better understanding of how one may accomplish certain objectives.

11.2.1 Decay of Vortices out of Ground Effect

The use of the LDV arc-scan data at 250-m aircraft altitude gives superb data on the decay of wake vortices. Smokers are necessary to mark the vortices for photographic tracking of descent, to indicate visually decay modes, and to give higher LDV signal-to noise ratios. Various configurations, both alleviated and non-alleviated, can be easily compared. Particular configurations should be repeated at least 3 or 4 times to allow verification of how consistently a particular decay pattern is observed.

11.2.2 Vortex-Velocity Changes During a Burst

The measurement of vortex decay at 250-m altitude with the LDV arc-scan mode and photographic coverage gives a direct full-

scale measurement of what happens during a vortex burst. Some of the anomalies observed in Run 8 may have been related to a burst.

11.2.3 Effect of Stratification on Decay and Descent

The descent of a vortex in a stratified atmosphere may actually enhance the vortex decay compared with that experienced in a neutral atmosphere by the mixing of vorticity at the wake boundary. The hypothesis can be tested by measuring vortex decay at different altitudes or at different times; it is difficult at best to separate turbulent from stability effects (Refs. 1,7, and 8). It may be desirable to fill the vortex with a large quantity of smoke so that the velocity effects taking place on the edge of the vortex oval can be observed.

11.2.4 Effect of Alleviated Configurations on Decay in Ground Effect

The most useful data on vortices in ground effect are obtained from a MAVSS array. It may be useful to install the array at an actual runway which has other traffic besides the test aircraft. Such data can then be more easily compared with the large amount of data collected at airports. It will be highly desirable to have a defined crosswind for such measurements. An anemometer array should be deployed in such an experiment, to facilitate comparison with airport data.

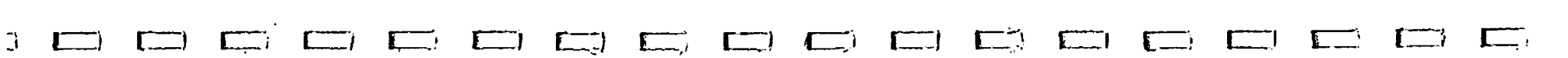

APPENDIX A
REDUCTION OF VORTEX PHOTOGRAPHS

A series of vortex photographs were taken from the air and on the ground during the B-747 vortex wake flight tests. The photographs were of B-747 wingtip vortices which were visualized when they entrained smoke produced by Sanders Corvis oil smoke generators mounted in various positions along the B-747 wings. Aerial photographs were taken from a helicopter which maintained an altitude of approximately 500 m above the terrain for all tests. The vortices were always less than 250 m above the terrain and usually less than 100 m. The vortices were obliquely photographed when they were positioned over a rectangular sensor array 300 by 40 m. This is shown in Fig. 99. The positions of all the array elements were known from a ground survey conducted prior to the present test program. In addition to the aerial photographs, vortex photographs were taken from the side with a camera positioned on the ground 180 m north of the array along the array centerline. The purpose of both sets of photographs was to determine the trajectories of the vortices relative to the array as a function of time. Due to the elevation of the vortices and the tilt of the cameras, the actual positions and altitudes of the vortices were not as visualized in the photographs. There was, however, sufficient information contained in the two simultaneous photographic views to determine the exact position and altitude of the vortices by methods of photogrammetry (Ref. 25).

A.1 AERIAL PHOTOGRAPHS

The first and most serious problem was to determine the exact position of the helicopter camera and the tilt of the camera for each photograph. The method used was the space-resection technique of Church discussed in detail by Merritt (Ref. 26). In the Church method, the interior orientation (the photographic coordinates and focal length of the camera) is assumed to be

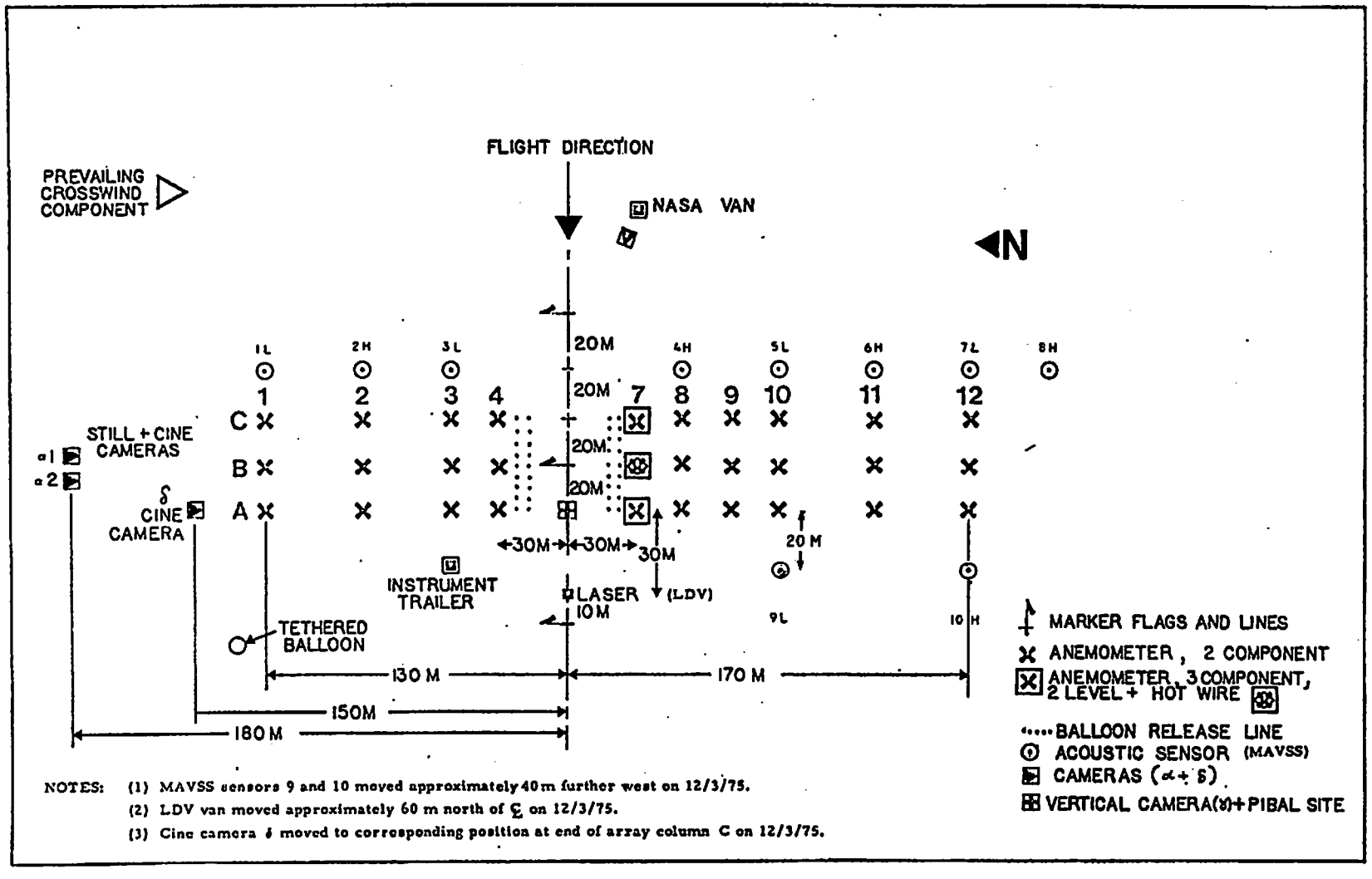

FIGURE 99. TEST-ARRAY LAYOUT

known. To determine the camera position and the tilt, three known ground control points are required (A, B, C). For this analysis, the three points chosen were elements of the rectangular sensor array. The position of the images of these three points (a, b, c) was determined by measuring them on each photograph relative to the photographic axes with the center of the photograph as origin. The ground-control points, the photographic images of the ground-control points, and the emerging nodal point L (which depends on the camera focal length) form two similar triangular pyramids, a photo pyramid and a ground pyramid, as shown in Fig. 100. When the object distance is large, as in this case, the height of the photo pyramid is closely approximated by the focal length. The height of the ground pyramid is unknown, but is determined by the following analysis. By knowing the position of control-point images and the focal length of the camera, the apex angles, α, β, γ (or their cosines), can be determined from the following:

$$L_a = (x_a^2 + y_a^2 + f^2)^{\frac{1}{2}}, \tag{A1}$$

and similarly for L_b and L_c. Also,

$$\cos \alpha = (x_b x_c + y_b y_c + f^2)/(L_b L_c), \tag{A2}$$

and similarly for cos β and cos γ.

The position of the nodal point $L(X_L, Y_L, Z_L)$ is known in terms of the ground coordinates, but lengths and cosines can be formed as in (A1) and (A2):

$$L_A = [(X_L-X_A)^2 + (Y_L-Y_A)^2 + (Z_L-Z_A)^2]^{\frac{1}{2}}, \tag{A3}$$

and similarly, for L_B and L_C. Also,

$$\cos \alpha = [(X_L-X_B)(X_L-X_C) + (Y_L-Y_B)(Y_L-Y_C) + (Z_L-Z_B)(Z_L-Z_C)]/(L_B L_C), \tag{A4}$$

and similarly, for cos β and cos γ.

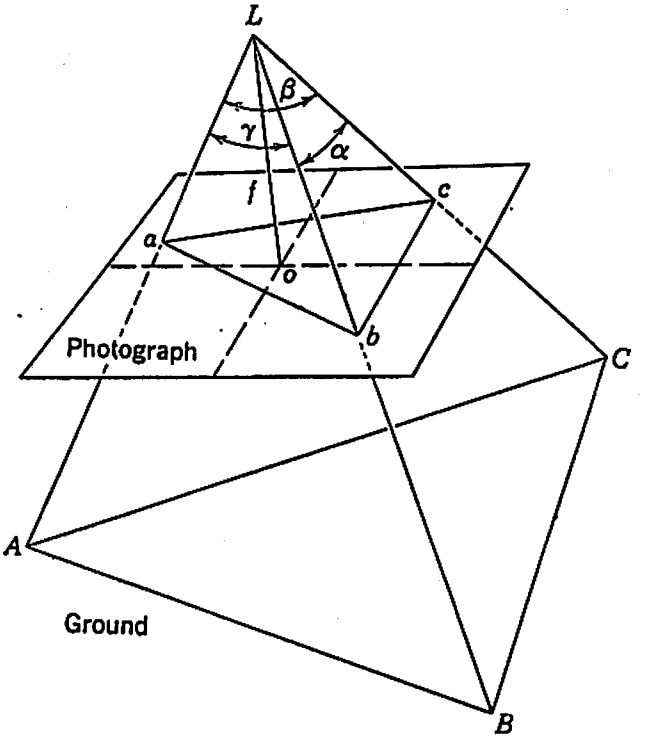

FIGURE 100. PHOTOGRAPH AND GROUND PYRAMIDS

Equations (A2) and (A4) can be combined to yield three equations for the three unknowns X_L, Y_L, Z_L (the ground coordinates of the nodal point L and the helicopter). The three equations are solved iteratively using a Newton-Raphson method by forming the differtials:

$$
\begin{aligned}
& L_B\, L_C \sin\alpha\, \Delta\alpha = \\
& \Delta X \left[X_B' \left(1 - \cos\alpha \frac{L_C}{L_B}\right) + X_C' \left(1 - \cos\alpha \frac{L_B}{L_C}\right)\right] \\
& +\Delta Y \left[Y_B' \left(1 - \cos\alpha \frac{L_C}{L_B}\right) + Y_C' \left(1 - \cos\alpha \frac{L_C}{L_B}\right)\right] \\
& +\Delta Z \left[Z_B' \left(1 - \cos\alpha \frac{L_C}{L_B}\right) + Z_C' \left(1 - \cos\alpha \frac{L_C}{L_B}\right)\right].
\end{aligned}
\tag{A5}
$$

where

$$X_B' = X_B - X_G,$$

and

X_B is the known ground coordinate

X_G is the trial guess for the coordinate of the helicopter X_L,

and similarly, for X_A', X_C', etc.,

$$\Delta\alpha = \alpha - \alpha',$$

where α' is calculated from (A4) using X_G, Y_G, Z_G, and α is calculated from (A2). Two additional equaticns can be formed for the angles β and γ resulting in equations of the form

$$
\begin{aligned}
& a_{11}\,\Delta X + a_{12}\,\Delta Y + a_{13}\,\Delta Z + b_1 = 0 \\
& a_{21}\,\Delta X + a_{22}\,\Delta Y + a_{23}\,\Delta Z + b_2 = 0 \\
& a_{31}\,\Delta X + a_{32}\,\Delta Y + a_{33}\,\Delta Z + b_3 = 0.
\end{aligned}
\tag{A6}
$$

Equations (A6) are solved simultaneously to determine ΔX, ΔY, ΔZ. These values are used in turn to correct X_G, Y_G, Z_G. The process is repeated until the residues $\Delta\alpha$, $\Delta\beta$, $\Delta\gamma$ become vanishingly small. When convergence is achieved, the values X_G, Y_G, Z_G

yield the coordinates of the helicopter X_L, Y_L, Z_L (the apex of the ground pyramid).

With the position of the camera determined, the next problem is to find the orientation of the camera, the direction of the principal line (the line of maximum inclination on a tilted photograph), and the azimuth of the principal plane (vertical plane containing the principal line) with respect to the ground survey. The principal line can be determined by "dropping" a plumb line from the nodal point L to the ground. The point where the plumb line pierces the photograph is called the nadir point, and the line from the photo center to the nadir point is the principal line.

The position of the nadir point and direction of the principal line can be determined by forming the vertical angles m_a, m_b, m_c, as shown in Fig. 101. From the ground pyramid:

$$\cos m_a = \frac{Z_L - Z_A}{L_A}, \text{ etc.} \tag{A7}$$

Also, from the photograph,

$$\cos m_a = \frac{x_a x_v + y_a y_v + f^2}{L_a L_v}, \tag{A8}$$

and similarly, for $\cos m_b$ and $\cos m_c$.

Solving equations (A7) and (A8) for L_v

$$\frac{x_a x_v + y_a y_v + f^2}{L_a \cos m_a} = \frac{x_b x_v + y_b y_v + f^2}{L_b \cos m_b} = \frac{x_c x_v + y_c y_y + f^2}{L_c \cos m_c}, \tag{A9}$$

which yields two equations of the form

$$\begin{aligned} c_{11} x_v + c_{12} y_v + d_1 &= 0 \\ c_{21} x_v + c_{22} y_v + d_2 &= 0, \end{aligned} \tag{A10}$$

where

$$c_{11} = x_a - x_b L_a \cos m_a / L_b \cos m_b, \text{ etc.},$$

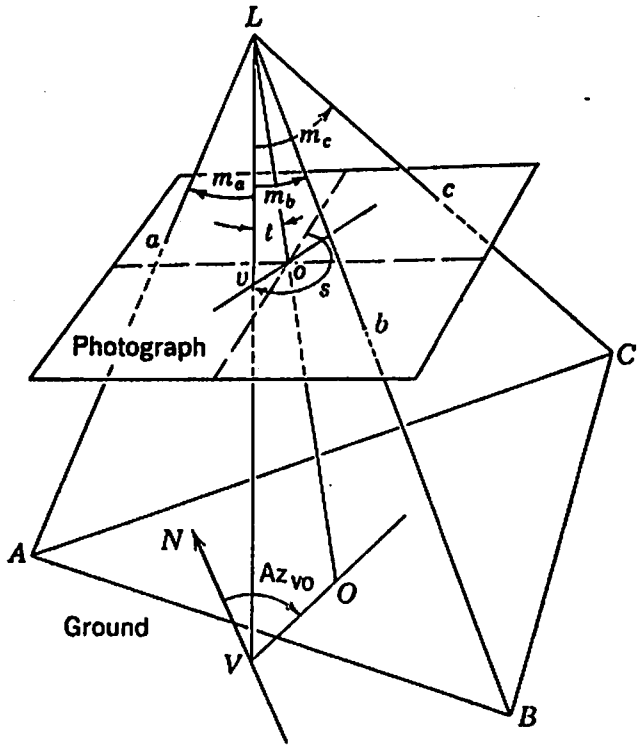

FIGURE 101. ELEMENTS OF ORIENTATION OF TILTED PHOTOGRAPH

and

$$d_1 = f^2 \ (1 - L_a \cos m_a / L_b \cos m_b), \text{ etc.}$$

Equations (A10) yield the coordinates of the nadir point v. The tilt t of the camera (angle from the vertical) is determined from

$$\tan t = (x_v^2 + y_v^2)^{\frac{1}{2}}/f. \qquad \text{(A11)}$$

The direction of the principal line is determined from the swing angle S which is the clockwise angle from the positive y axis defined in terms of angle Ψ measured counterclockwise positive from the x axis as:

$$S = \text{modulo } 360° \ (450° - \Psi), \qquad \text{(A12)}$$

where $\Psi = \tan^{-1}(y_v/x_v)$.

The azimuth of the principal plane can be determined if the coordinates of any ground point P are known (Ref. 27). The coordinates of the photographic image of the point P are measured relative to a coordinate system with v as the origin and the principal line as the positive y axis (Fig. 102). Then, the horizontal angle on the photograph between the new y axis and any line vp is given by:

$$\tan \rho = \frac{x_p}{y_p \cos t}. \qquad \text{(A13)}$$

The azimuth of the ground line VP is readily computed since P is known and V has the same X and Y coordinates as the nodal point L. The azimuth of the principal plane, therefore, is

$$Az_{VO} = Az_{VP} - \rho. \qquad \text{(A14)}$$

A.2 CORRECTING FOR TILT

To correct the photograph for the effect of tilt, it is most convenient to express all the photographic points in terms of an x′, y′ coordinate system (Figs. 102 and 103) with origin at the nadir point v and principal line vo as the positive y axis. In terms of the original geometric axis of the photograph (x,y), this can be accomplished by rotating the axes through an angle θ

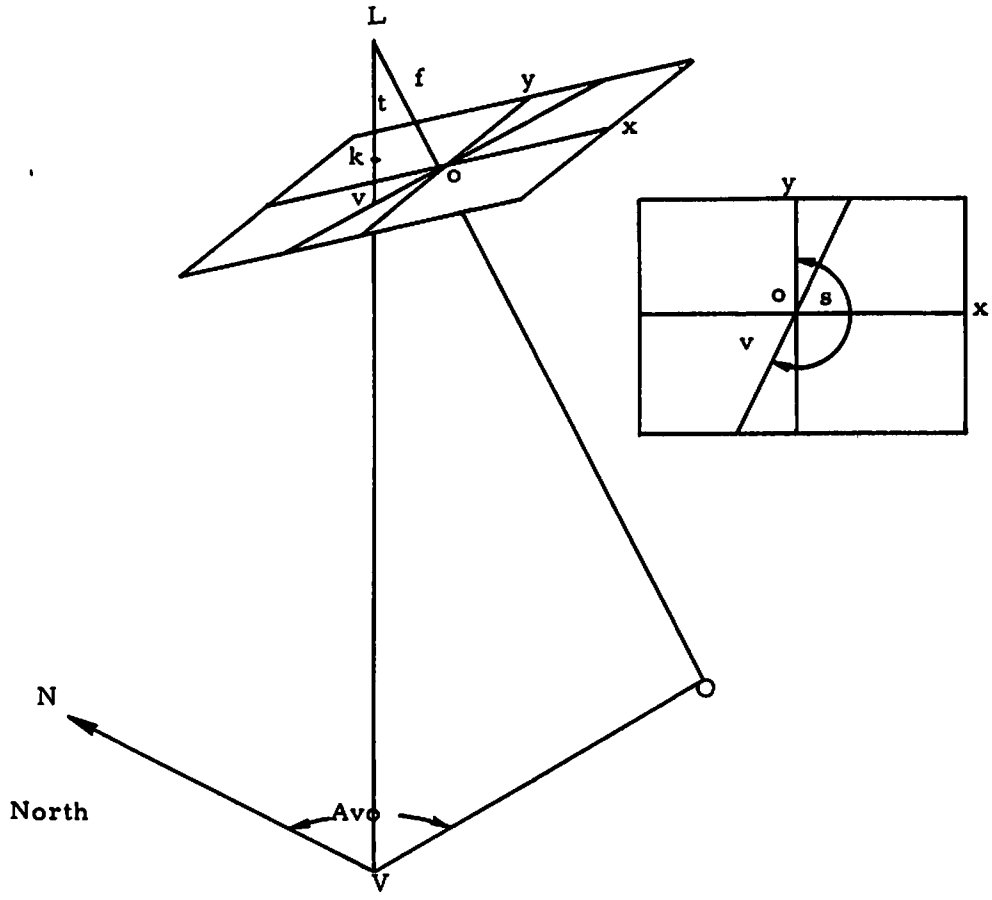

FIGURE 102. COORDINATES OF PHOTOGRAPHIC IMAGE OF POINT P

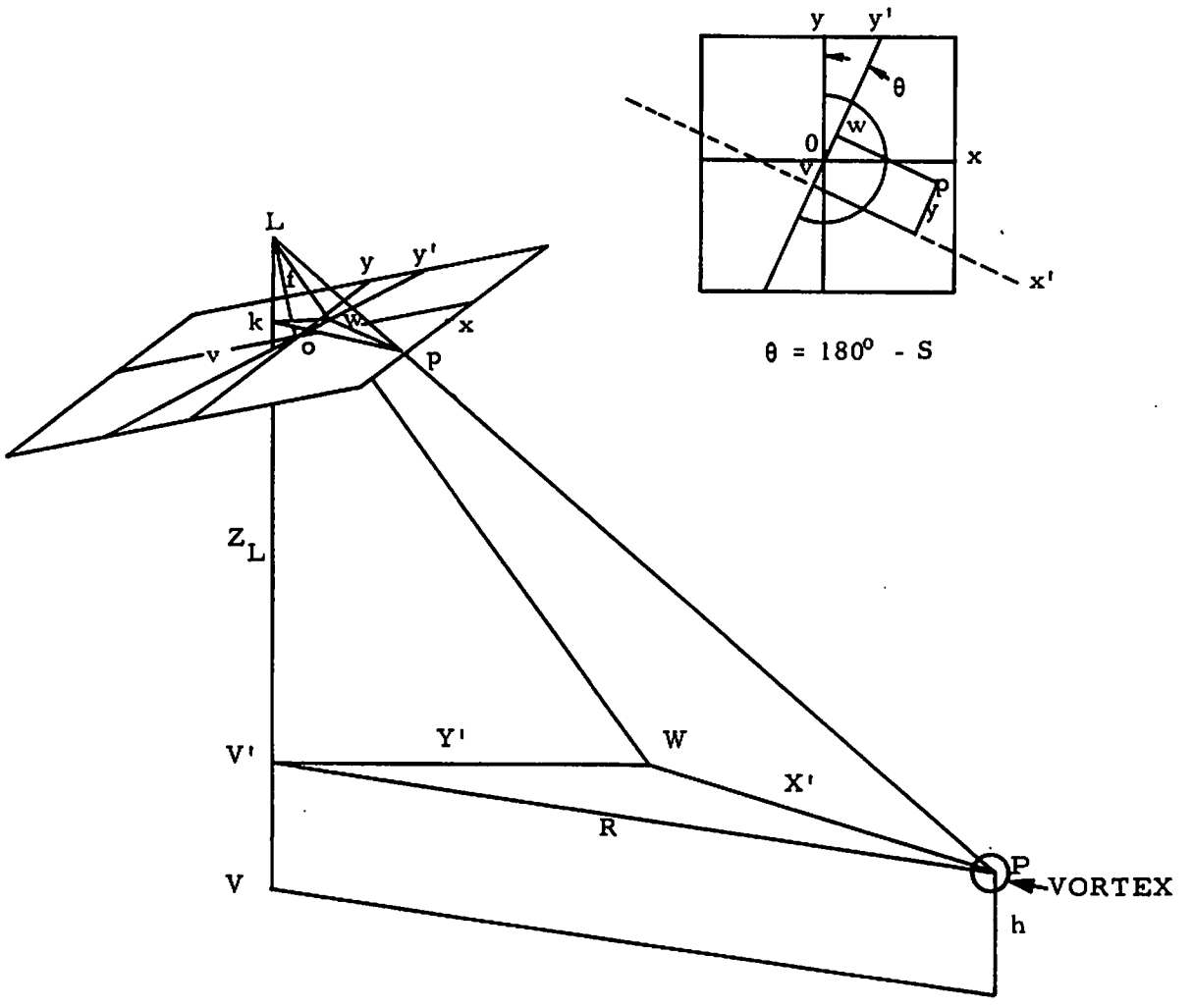

FIGURE 103. GEOMETRY FOR COORDINATE TRANSFORMATIONS

and translating the origin from the center to v:

$$\theta = 180° - S,$$

$$x' = x \cos\theta + y \sin\theta, \qquad \text{(A15)}$$

$$y' = -x \sin\theta + y \cos\theta + f \tan t.$$

Let ground coordinates corresponding to $x'y'$ be designated $X' Y'$ referred to the ground nadir point as origin and the principal plane as positive Y. From similar triangles (Fig. 103),

$$X' = \frac{Z_L - h}{\sec t - y' \sin t} x', \qquad \text{(A16)}$$

$$Y' = \frac{Z_L - h}{f \sec t - y' \sin t} y' \cos t, \qquad \text{(A17)}$$

where h is the unknown elevation of the vortex, f is the camera focal length, and t is the camera tilt. (The coordinates X', Y' can ultimately be expressed in terms of the ground survey by rotating back through an angle ρ which is equal to the azimuth of the principal plane AZ_{VO} and translating to the survey origin.)

A.3 GROUND PHOTOGRAPHS

The same analysis applies to the reduction of ground photographs in a much simplified manner. The position of the ground camera is fixed, and the angle is constrained to remain in a plane perpendicular to the path of the vortices. For side-view photographs, the vertical axis of the photograph is the principal line, and the nadir point is the intersection of the principal line and the horizon. The angle of tilt can be determined from the displacement of the horizon from the photo center and the focal length.

To calculate the position (X,Y) of a vortex relative to the array and the elevation of this vortex, simultaneous measurements from an aerial photograph and a ground photograph are required. The ground position (X', Y') of an element of the vortex is calculated using equations (A16) and (A17) with the coordinates x', y' measured from an aerial photograph and assuming h_1 for the

vortex elevation. The angle of elevation (ξ) of the vortex is determined from a ground photograph assuming that the vortex is projected into some vertical plane a distance X_c from the camera using

$$\tan \xi = h_c/X_c. \tag{A18}$$

The altitude h_c is calculated using the relation

$$h_c = \frac{X_c h_m \cos t}{f \sec t - h_m \sin t}, \tag{A19}$$

where h_m = elevation of the vortex above the horizon measured from the side photograph,

f = focal length of the side camera, and

t = tilt of the side camera.

The elevation (h_2) of the vortex is calculated using the angle ξ determined from the ground camera and the position X determined by rotating and translating X′ calculated from (A16) with the equation

$$h_2 = X \tan \xi. \tag{A20}$$

The two elevations (h_1 and h_2) are compared. A correction is applied to the assumed elevation (h_1) of the aerial photograph, and the process is repeated until the difference between the elevations calculated from both photographs becomes less than some predetermined limit. In this manner, the elevation and position of the vortex over the array are completely determined. The technique presented is valid for any degree of tilt and limited only by the accuracy of the photographic measurements, the accuracy of the ground survey, and the selected convergence intervals. The process is repeated for several elements selected along each vortex and for several photographs selected at various time intervals to determine a complete vortex trajectory.

APPENDIX B
ANEMOMETER DATA

Figures 104 to 128 are computer-generated plots showing time histories of the anemometer-measured cross winds at line B (see Fig. 4). Data from the first 38 runs are shown; the magnetic-tape recordings from Runs 39 to 54 were lost. However, the data were not lost since the back-up light-sensitive oscillographic recording charts for these runs were available. Figures 104 to 128 include only those runs where the B-747 passed over the anemometer array below an altitude of 75 m. When the aircraft passed over the array at higher altitudes, the anemometer response was barely, if at all, observable.

The ground track of the B-747 passed between anemometers B4 and B7 (Fig. 4). The long vertical line near the origin of the time axis represents the start-of-run signal.

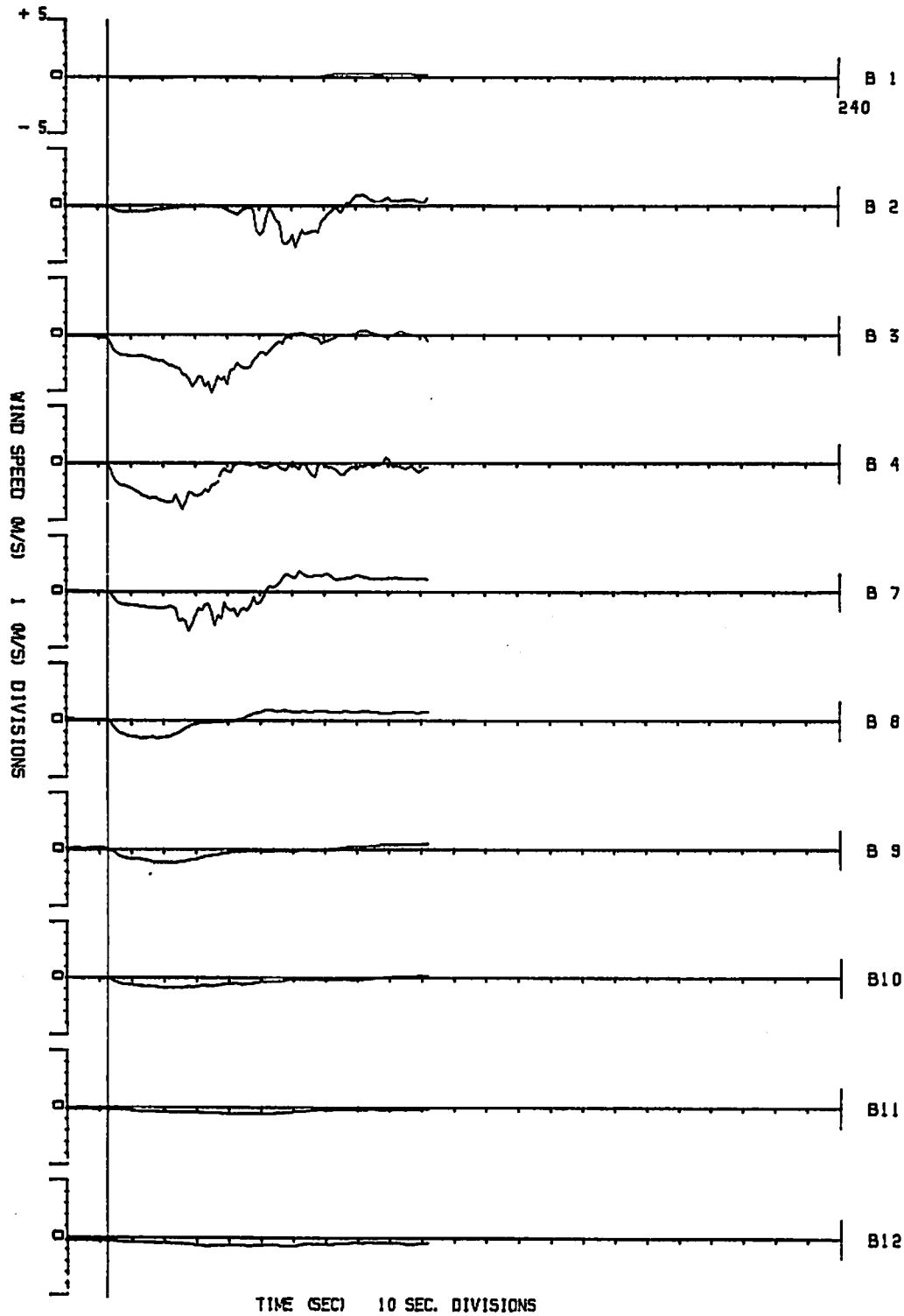

FIGURE 104. ANEMOMETER RECORDS FOR RUN 1

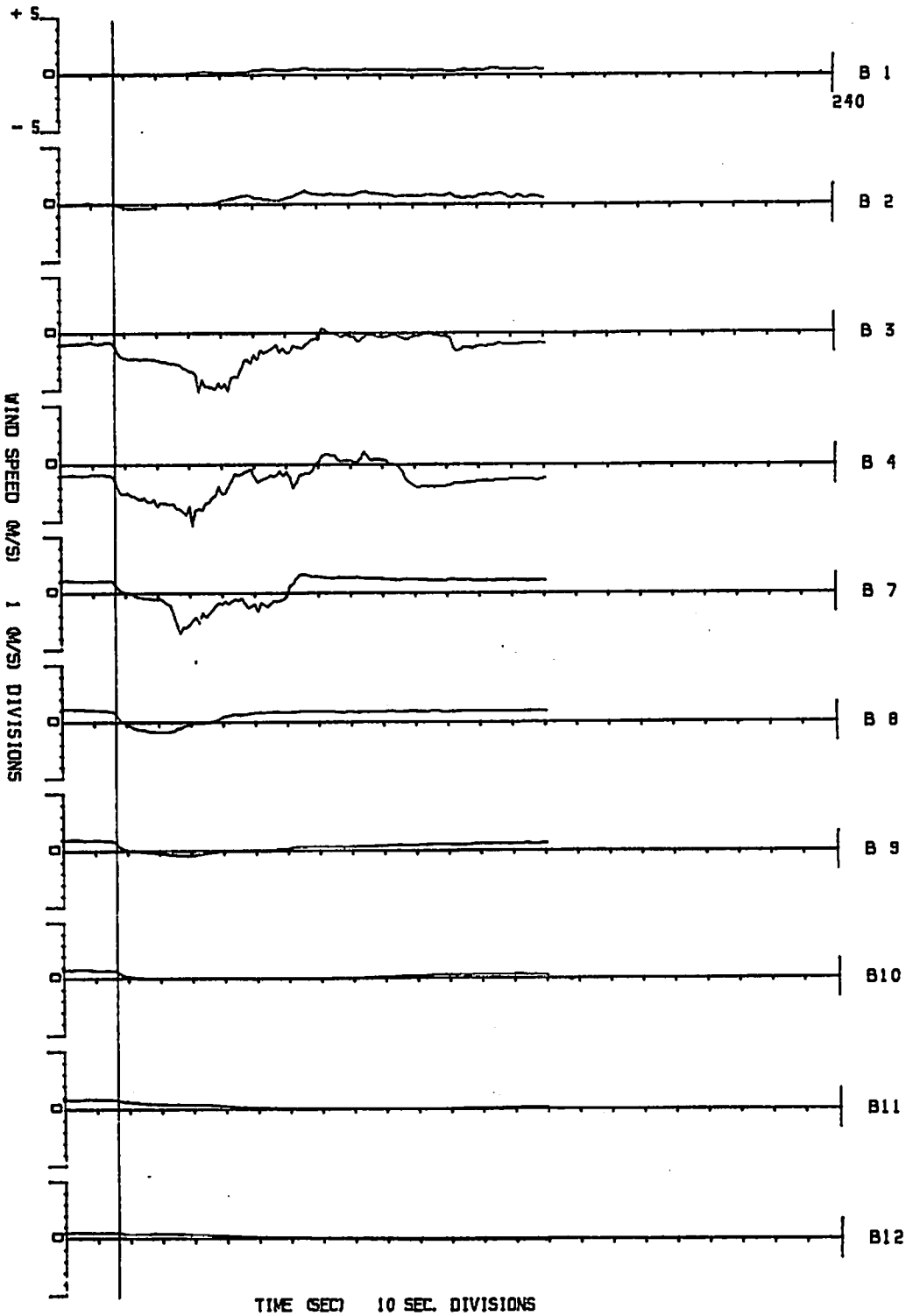

FIGURE 105. ANEMOMETER RECORDS FOR RUN 2

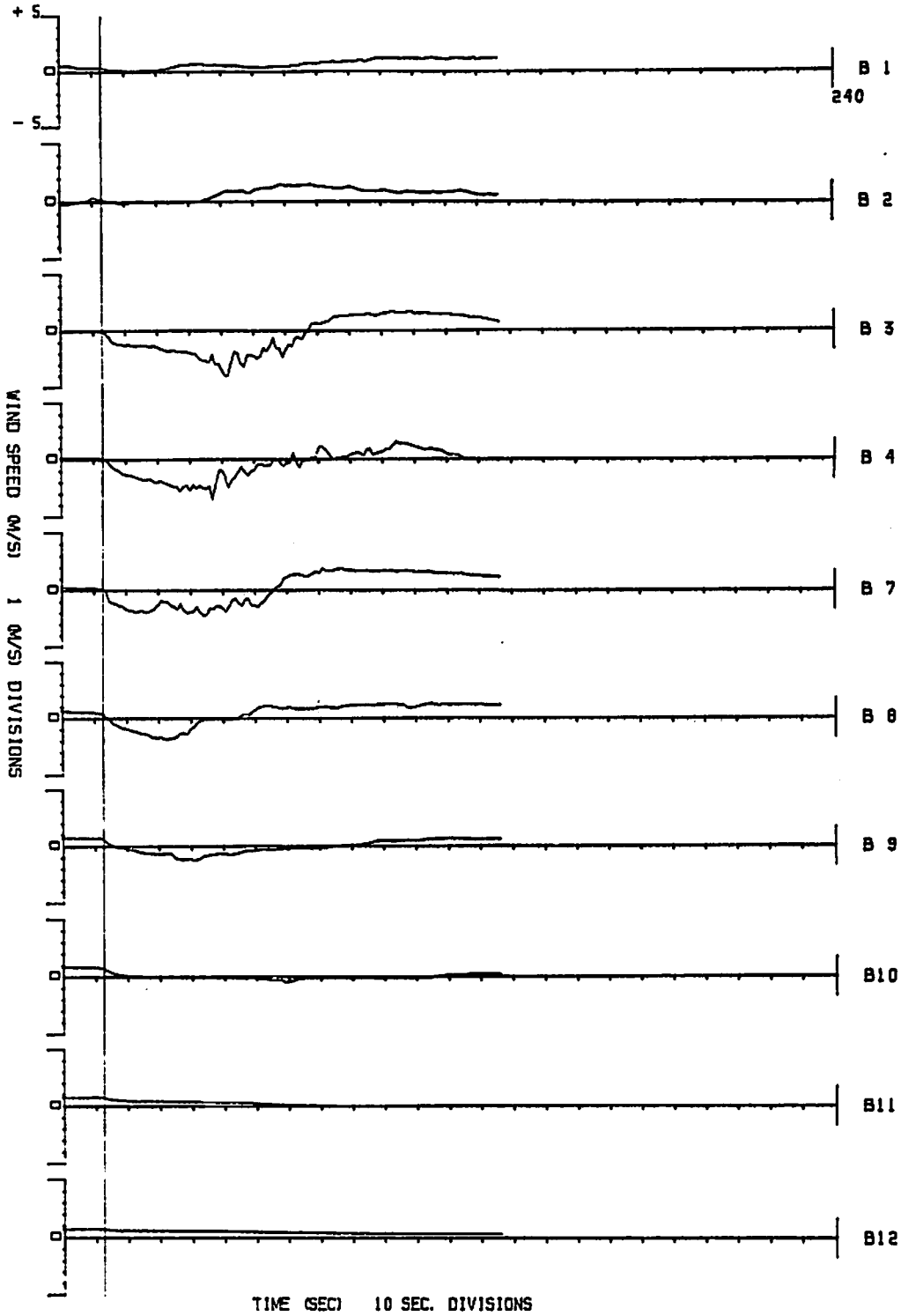

FIGURE 106. ANEMOMETER RECORDS FOR RUN 3

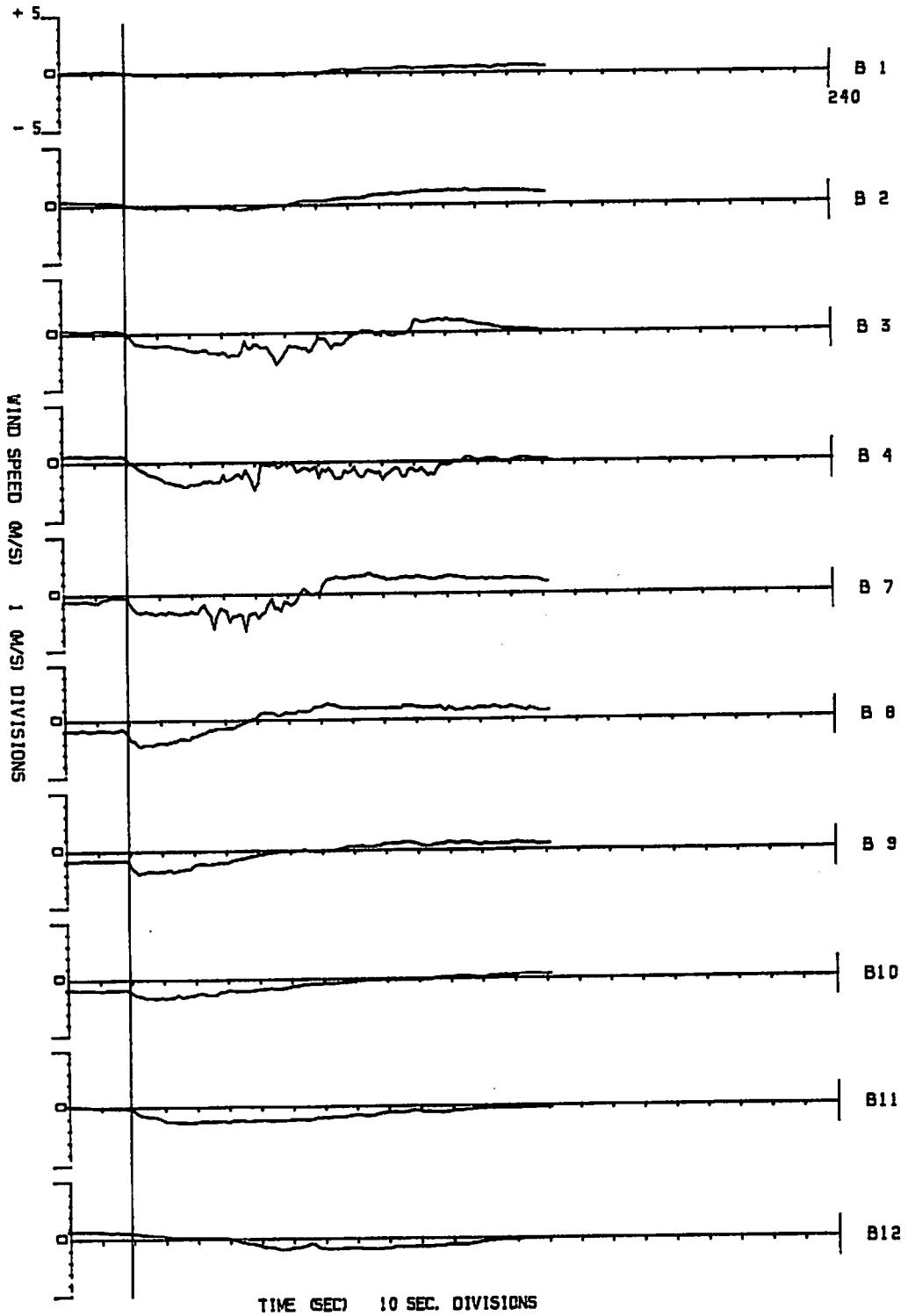

FIGURE 107. ANEMOMETER RECORDS FOR RUN 4

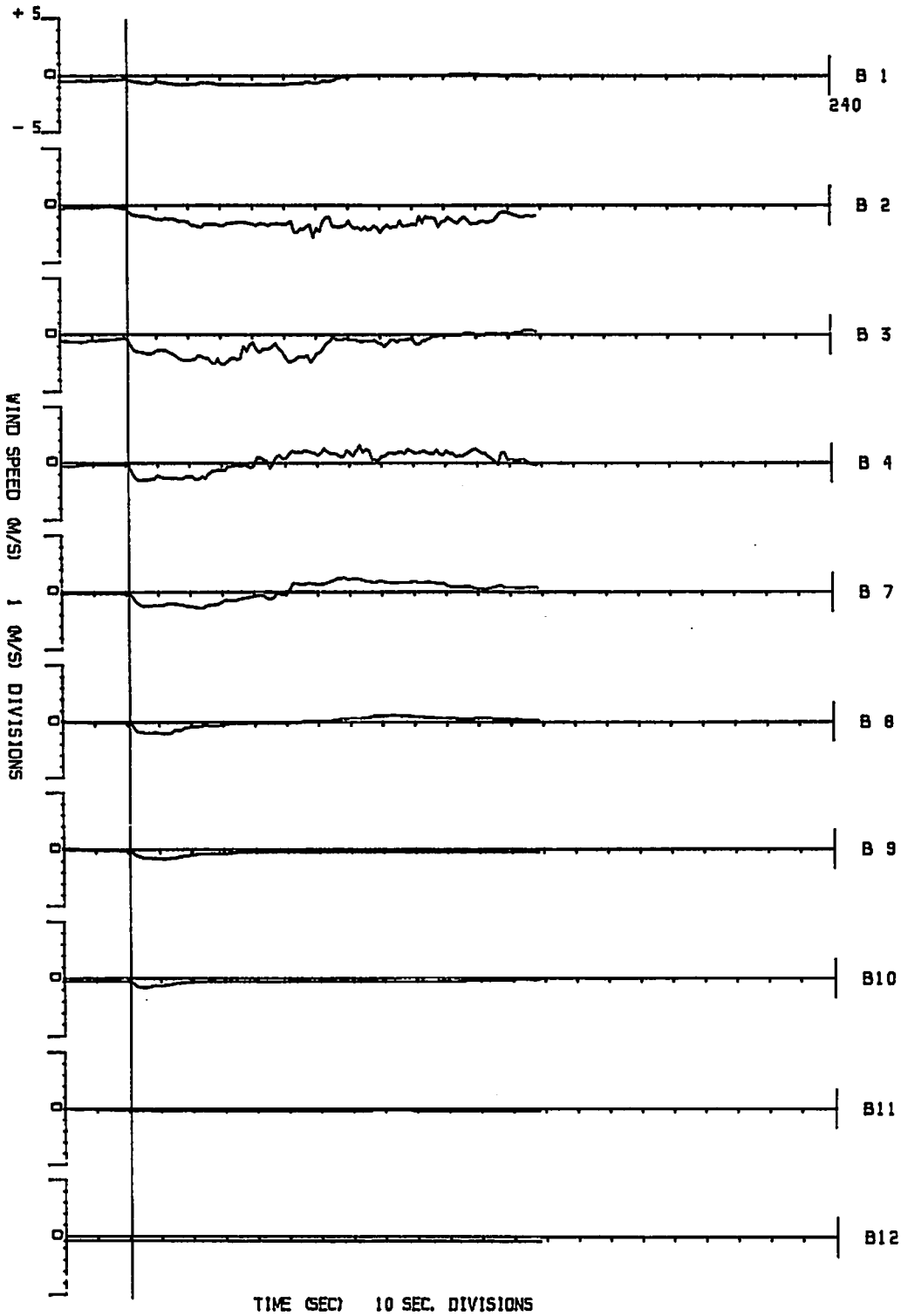

FIGURE 108. ANEMOMETER RECORDS FOR RUN 9

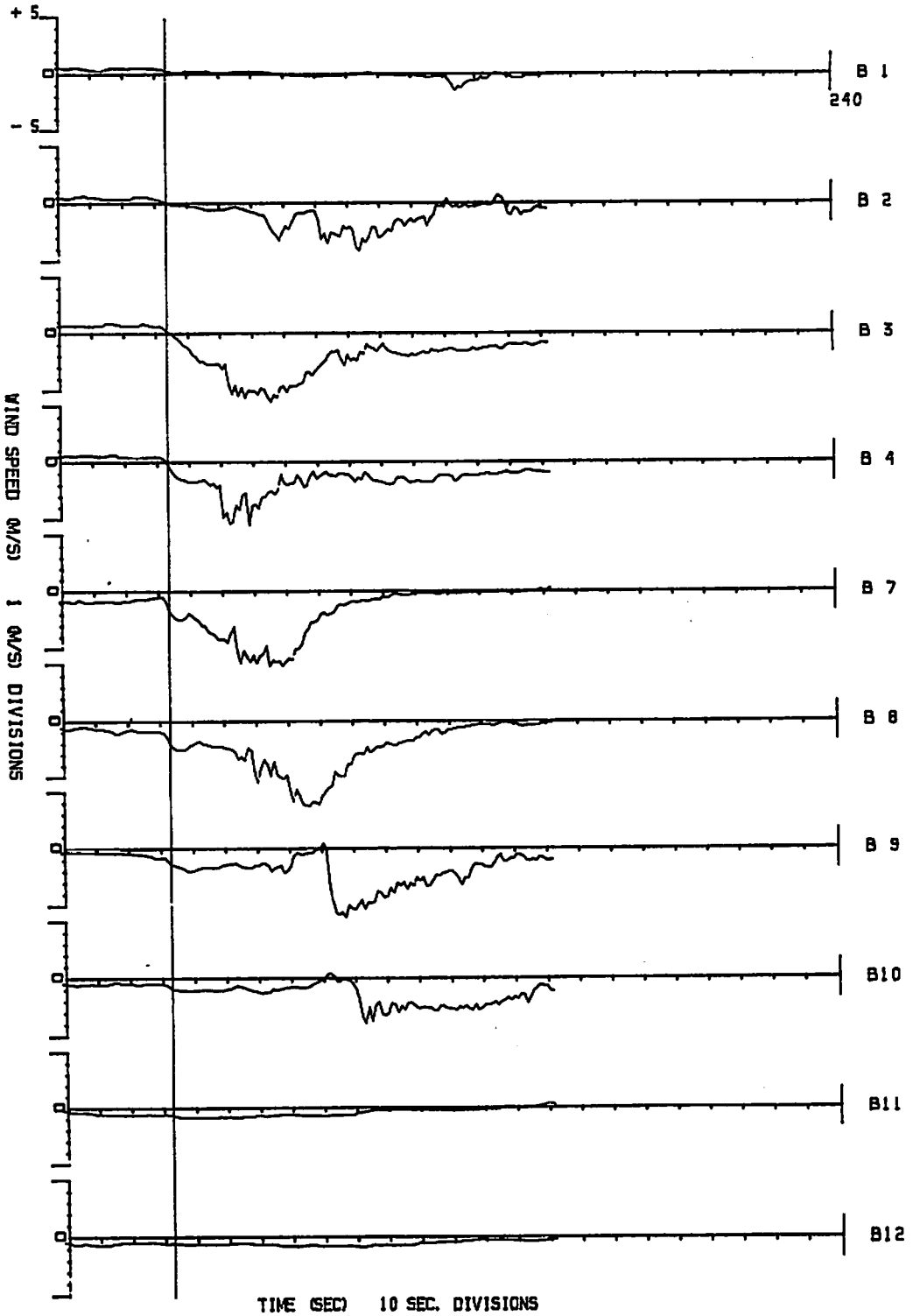

FIGURE 109. ANEMOMETER RECORDS FOR RUN 13

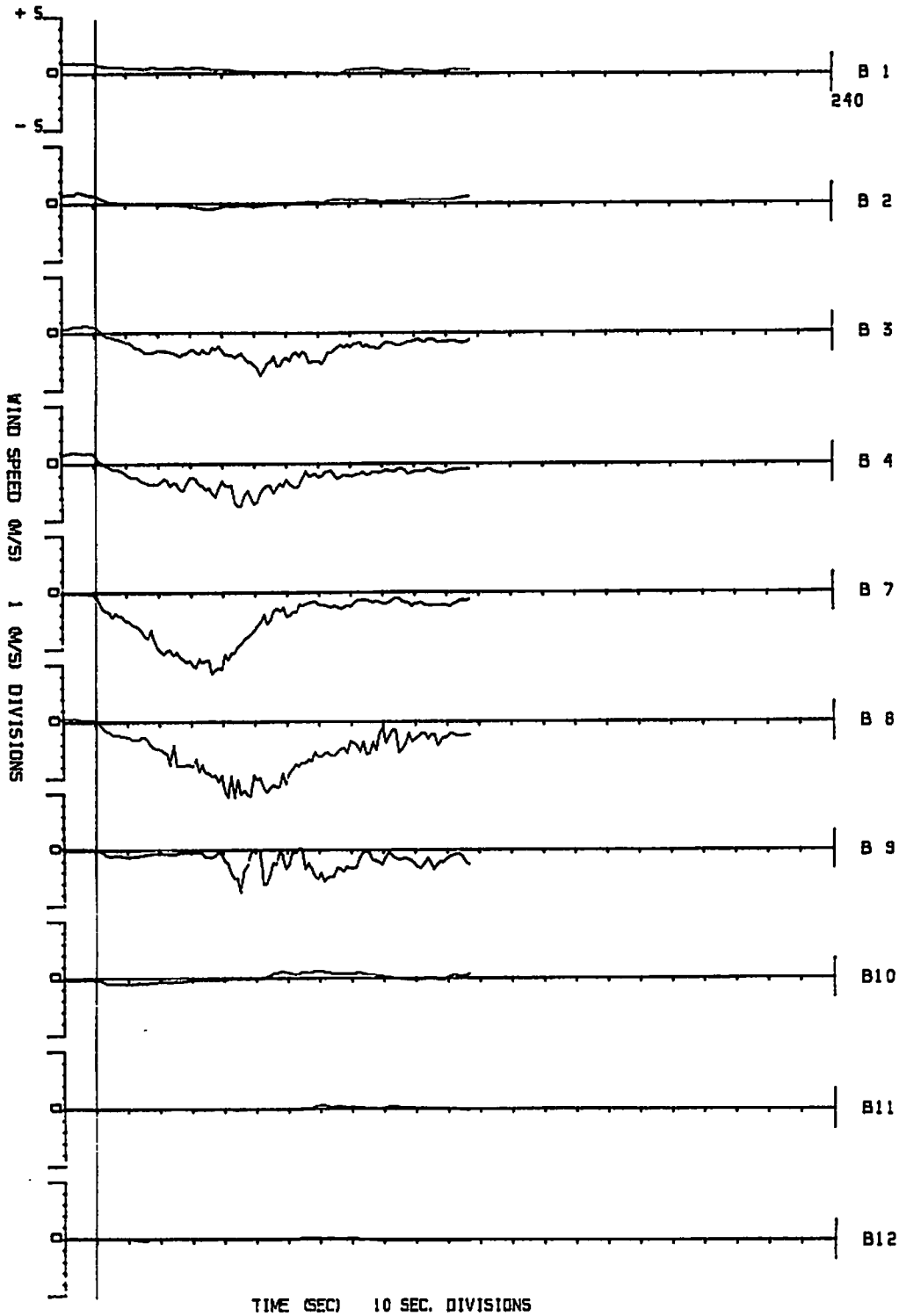

FIGURE 110. ANEMOMETER RECORDS FOR RUN 14

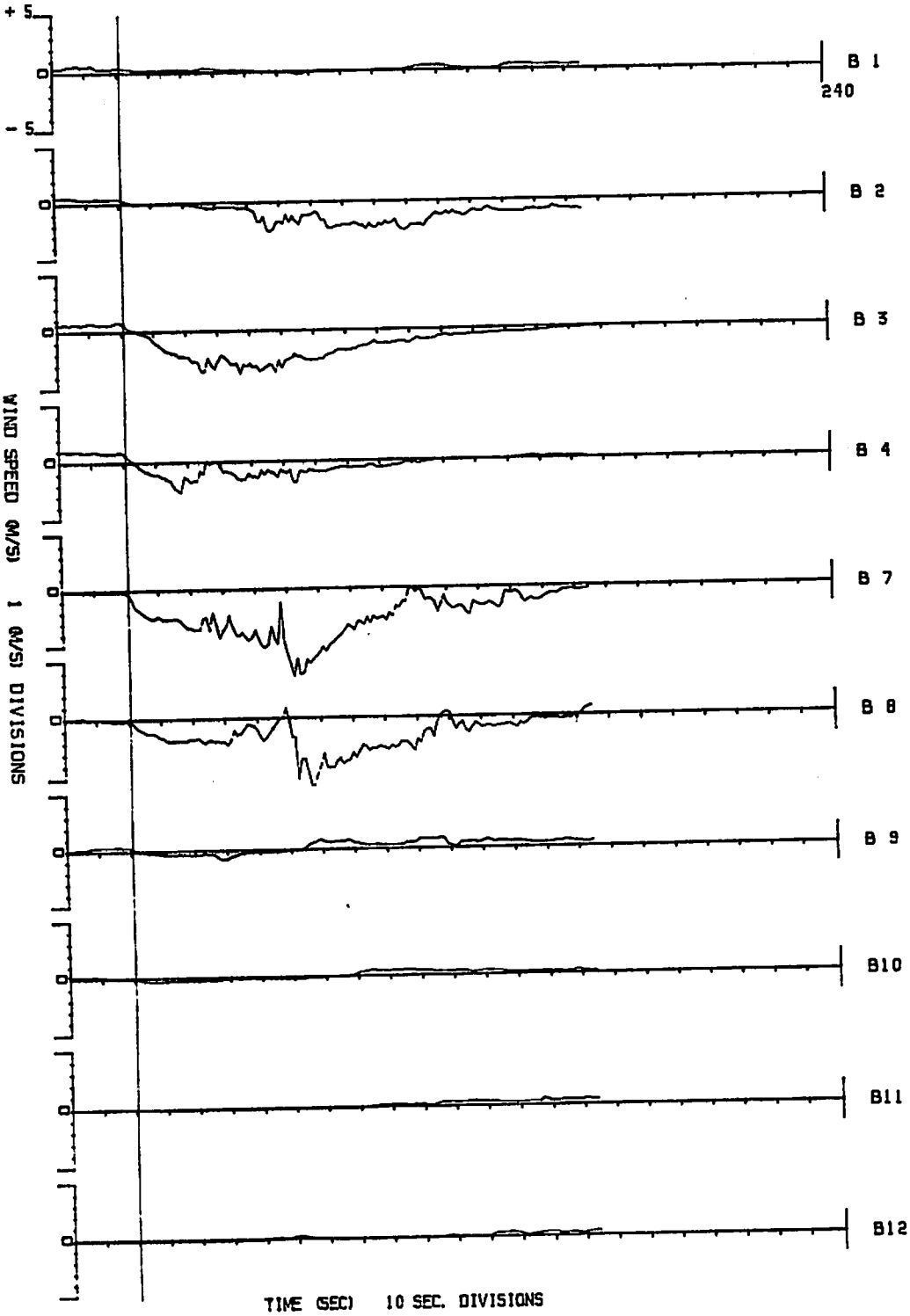

FIGURE 111. ANEMOMETER RECORDS FOR RUN 15

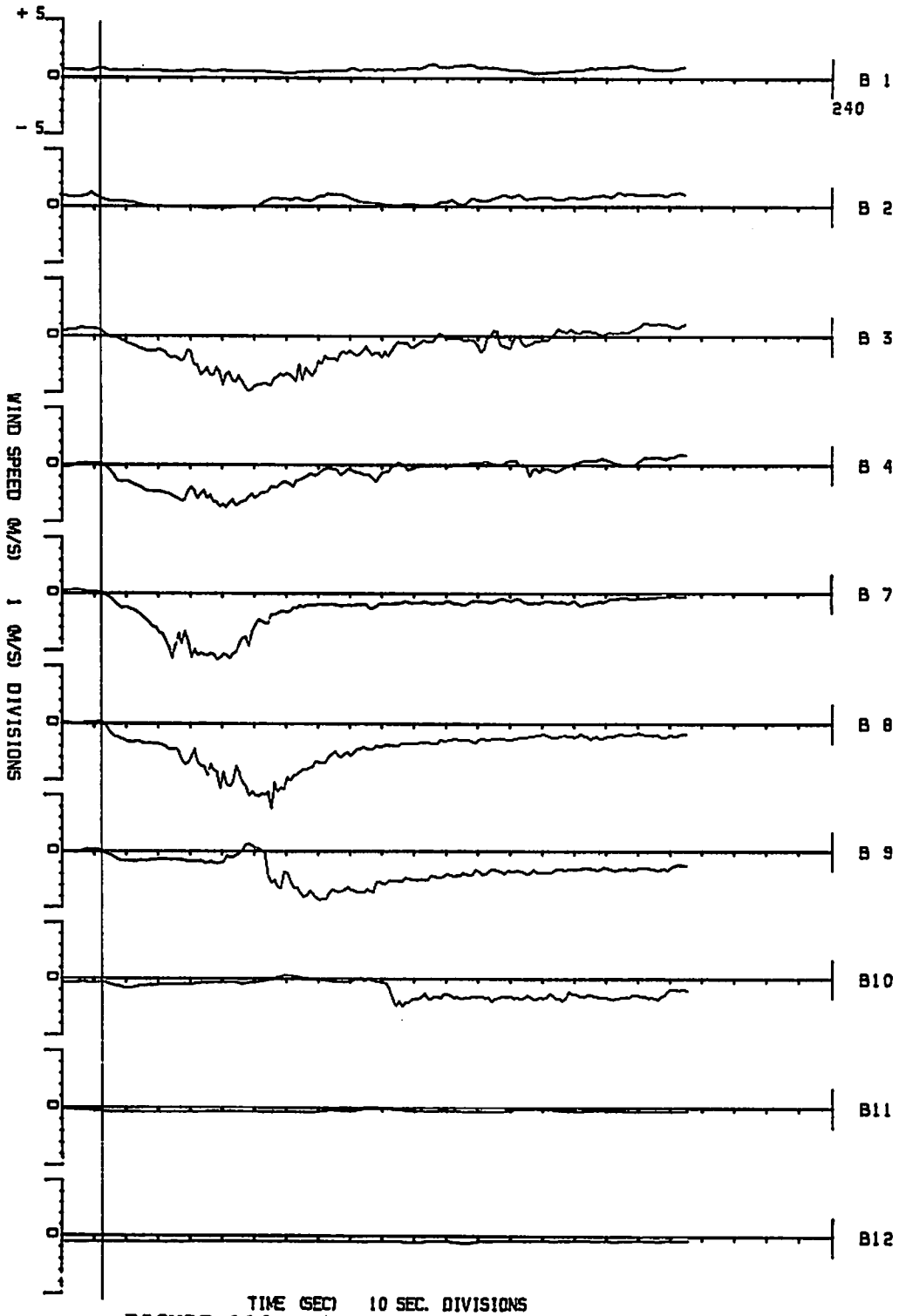

FIGURE 112. ANEMOMETER RECORDS FOR RUN 16

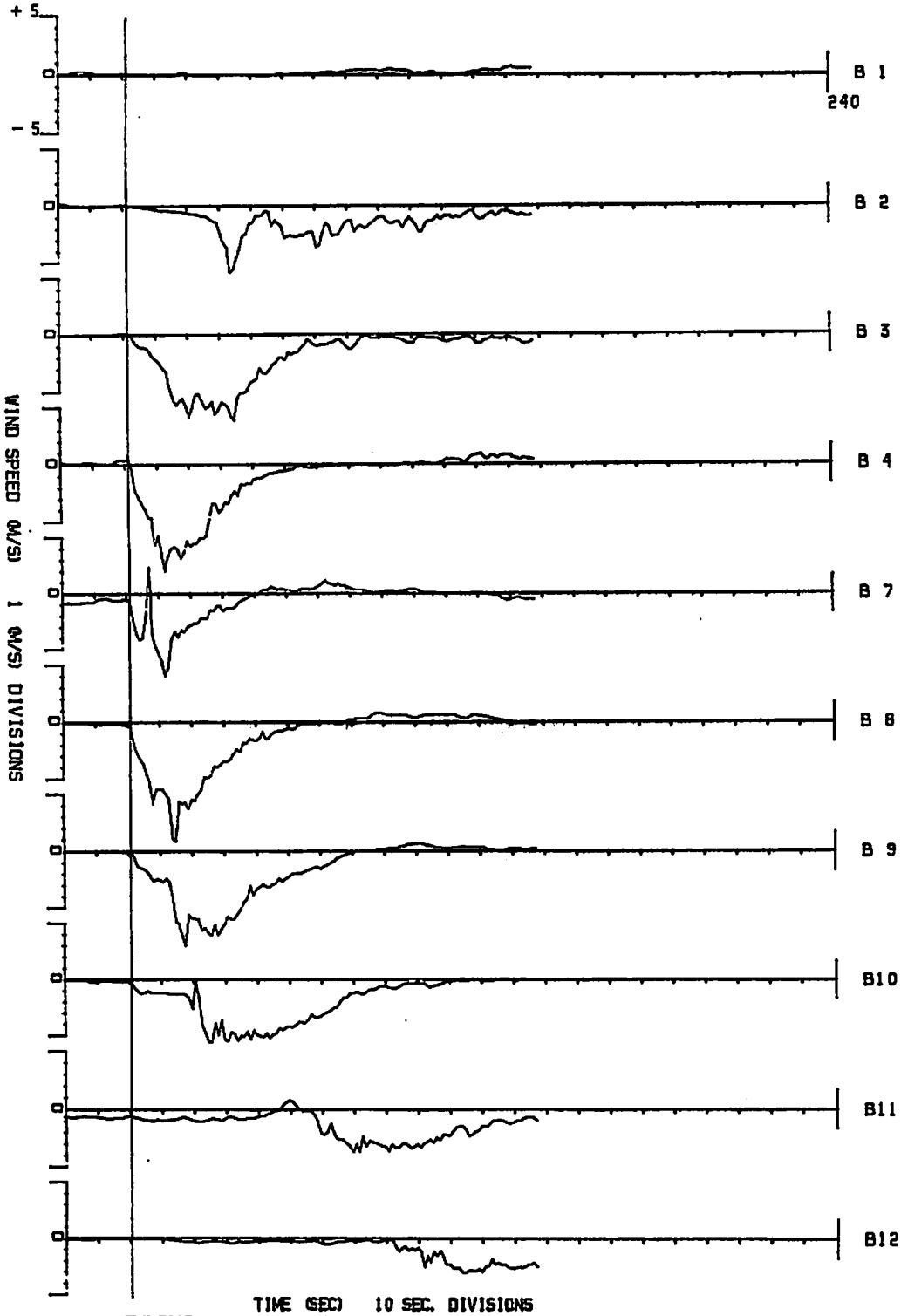

FIGURE 113. ANEMOMETER RECORDS FOR RUN 17

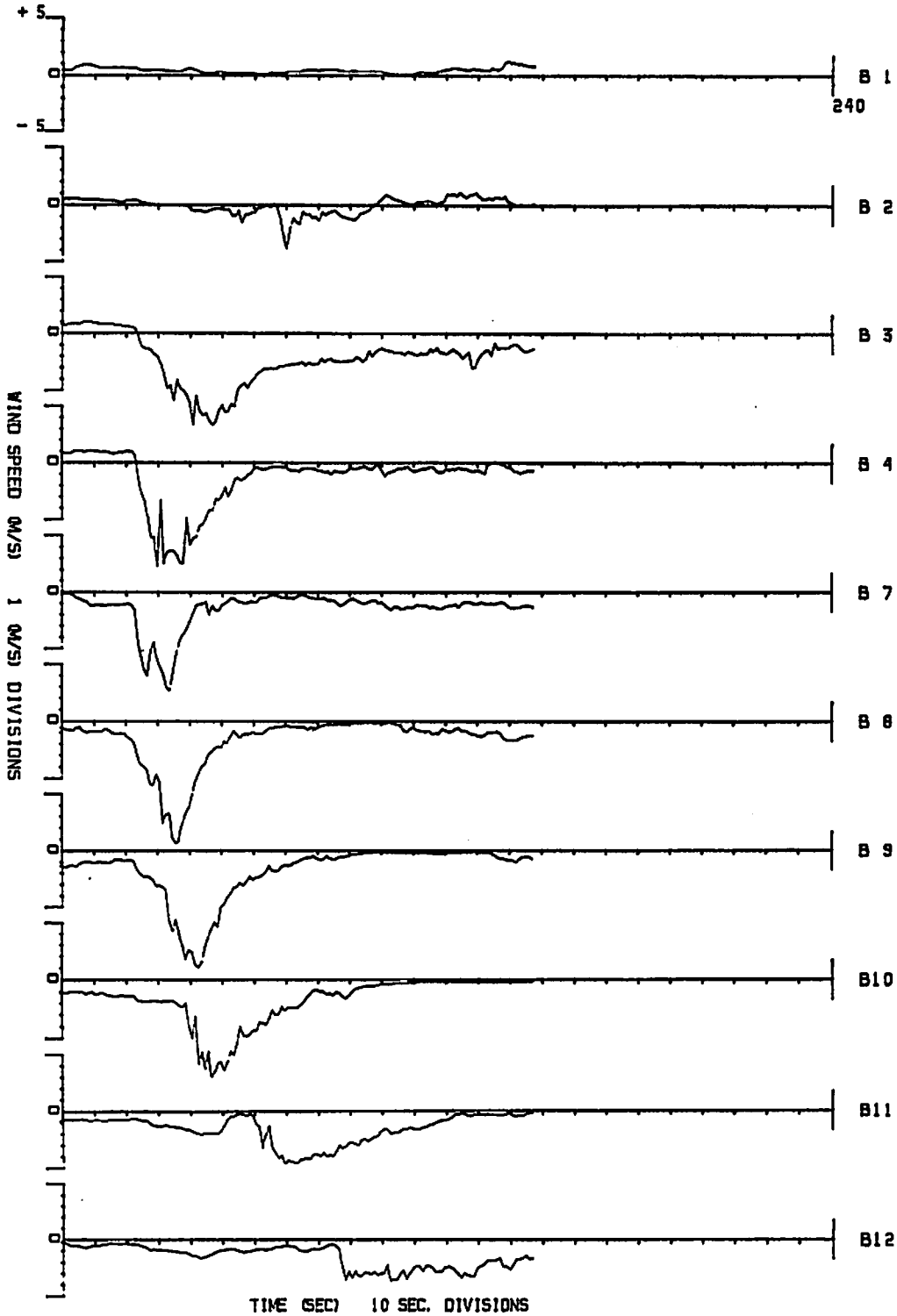

FIGURE 114. ANEMOMETER RECORDS FOR RUN 18

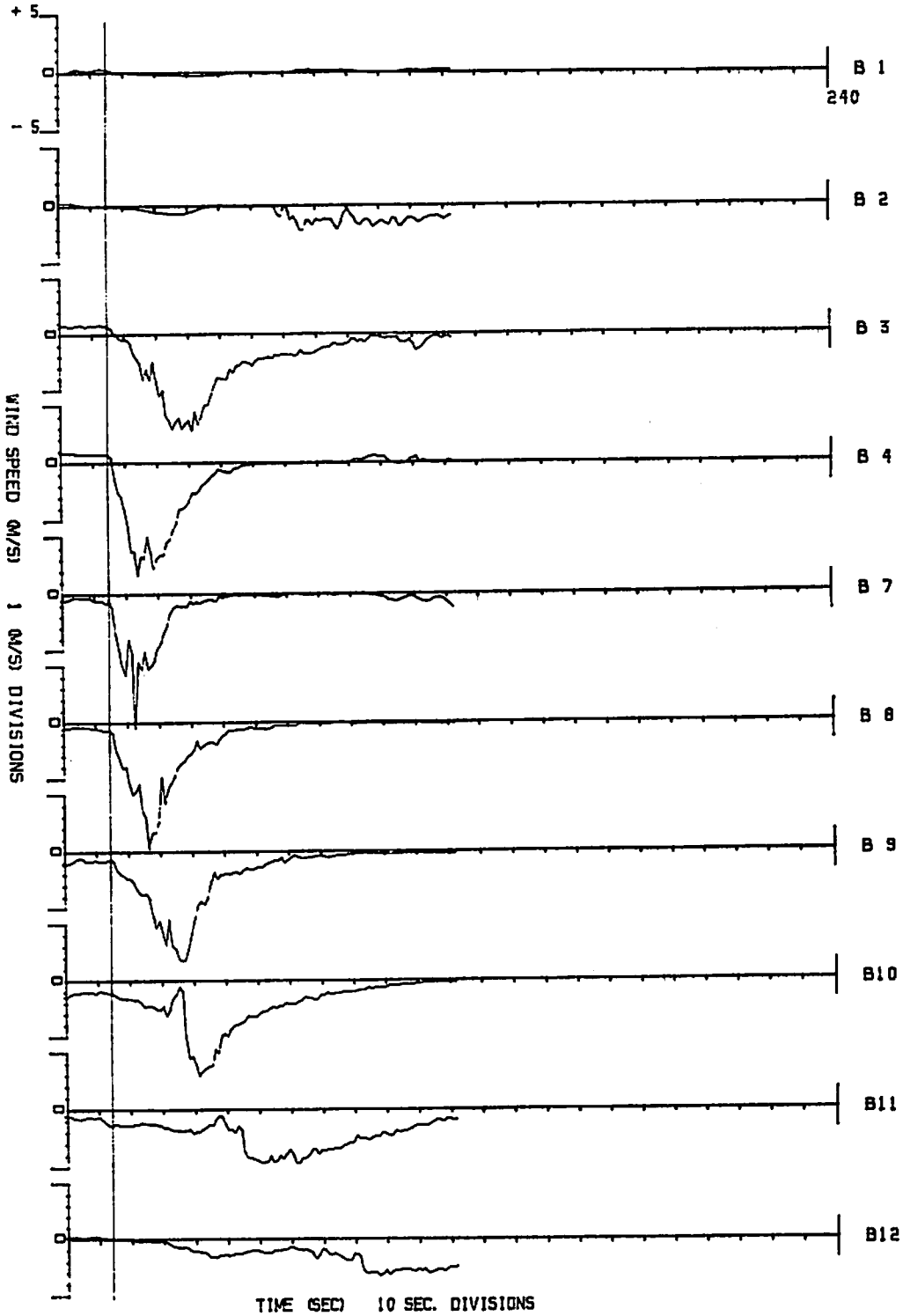

FIGURE 115. ANEMOMETER RECORDS FOR RUN 19

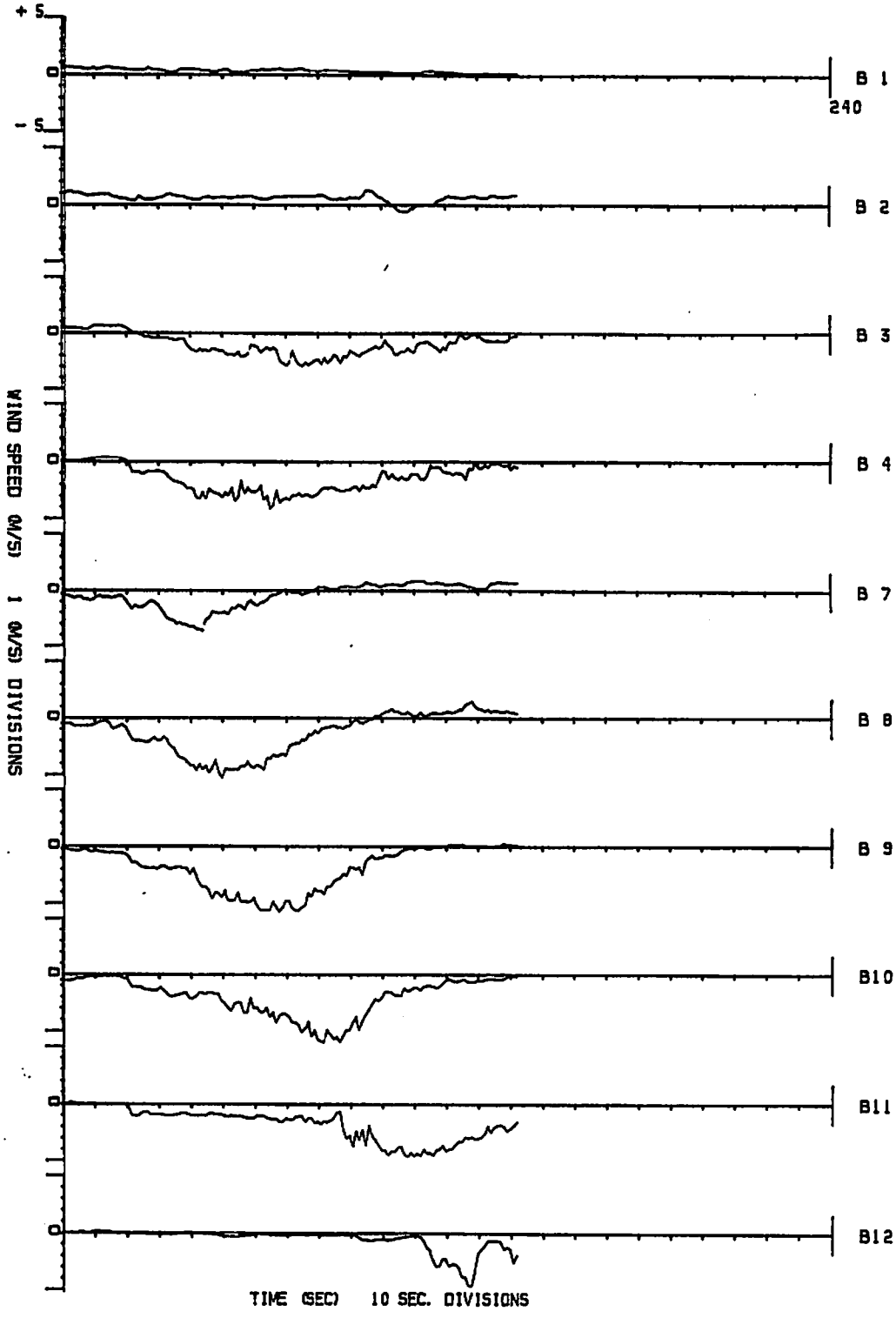

FIGURE 116. ANEMOMETER RECORDS FOR RUN 20

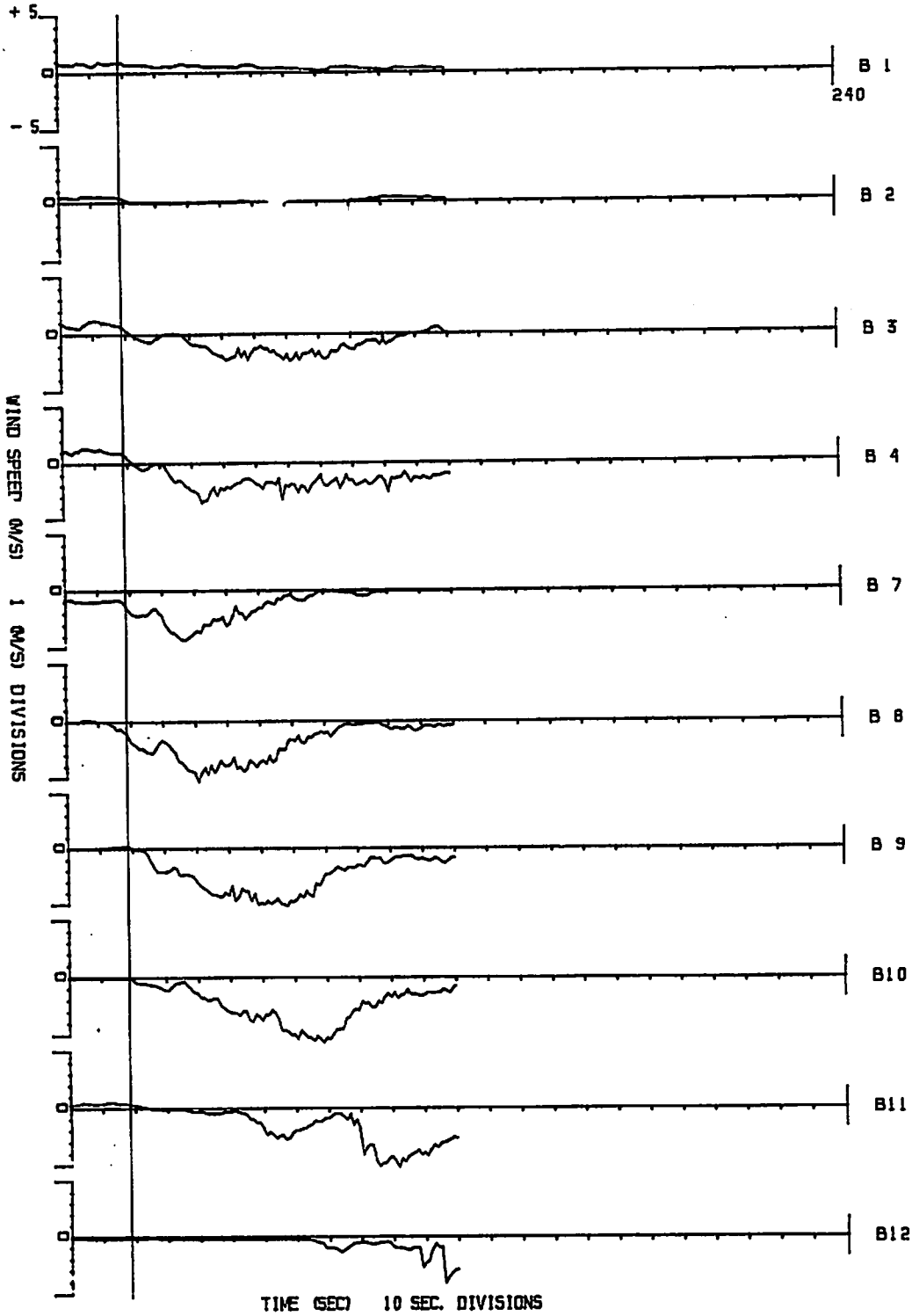

FIGURE 117. ANEMOMETER RECORDS FOR RUN 21

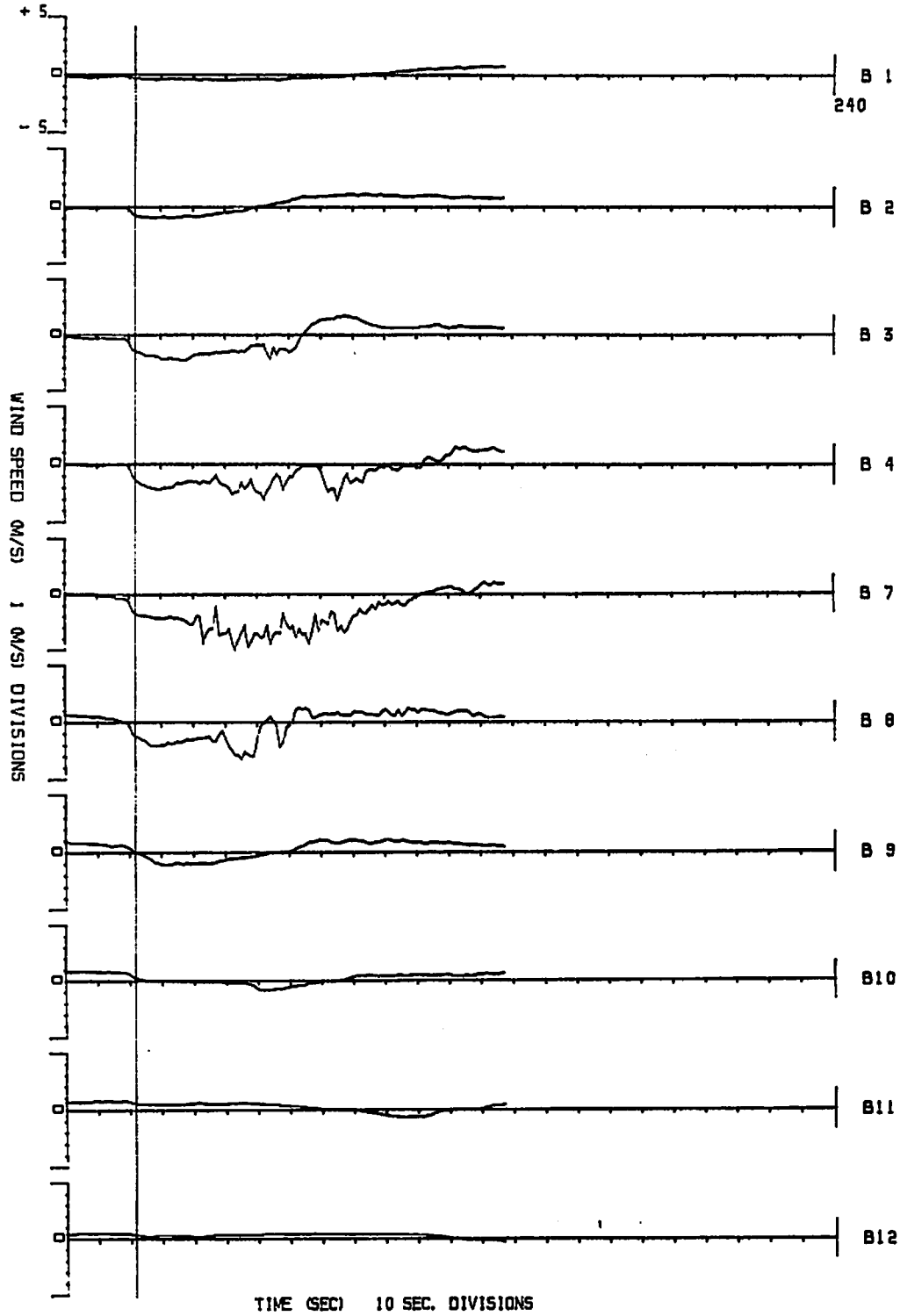

FIGURE 118. ANEMOMETER RECORDS FOR RUN 27

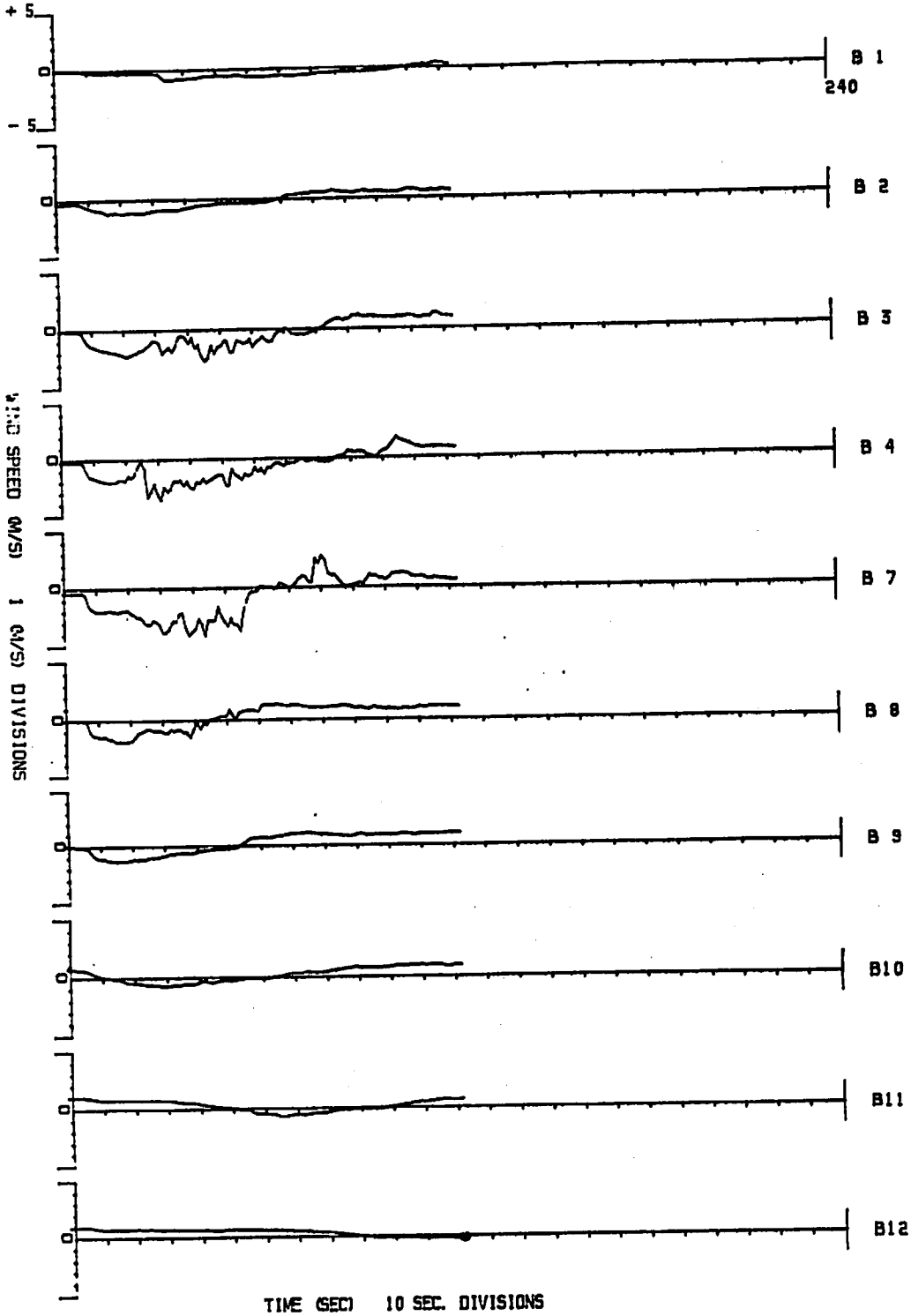

FIGURE 119. ANEMOMETER RECORDS FOR RUN 28

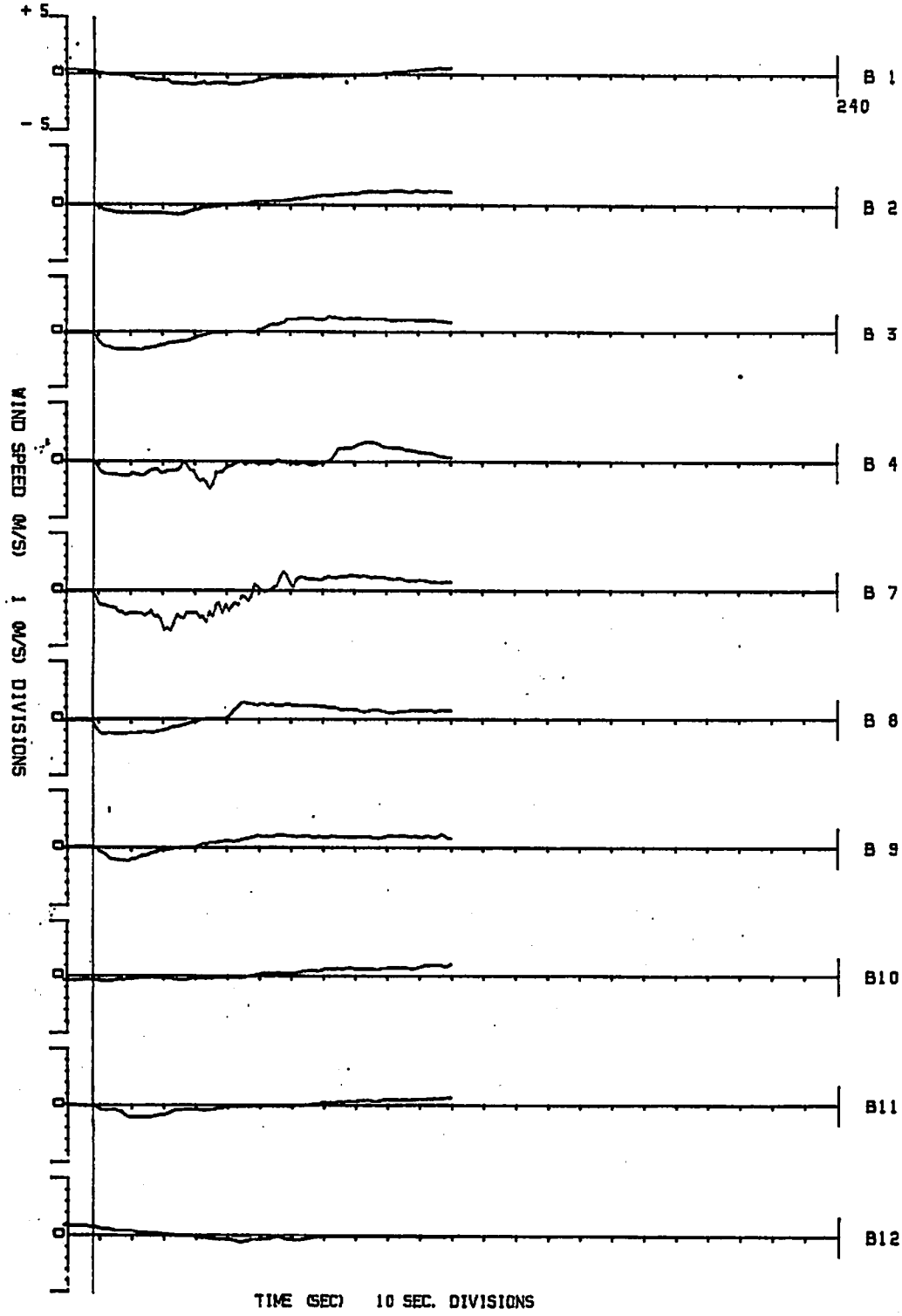

FIGURE 120. ANEMOMETER RECORDS FOR RUN 29

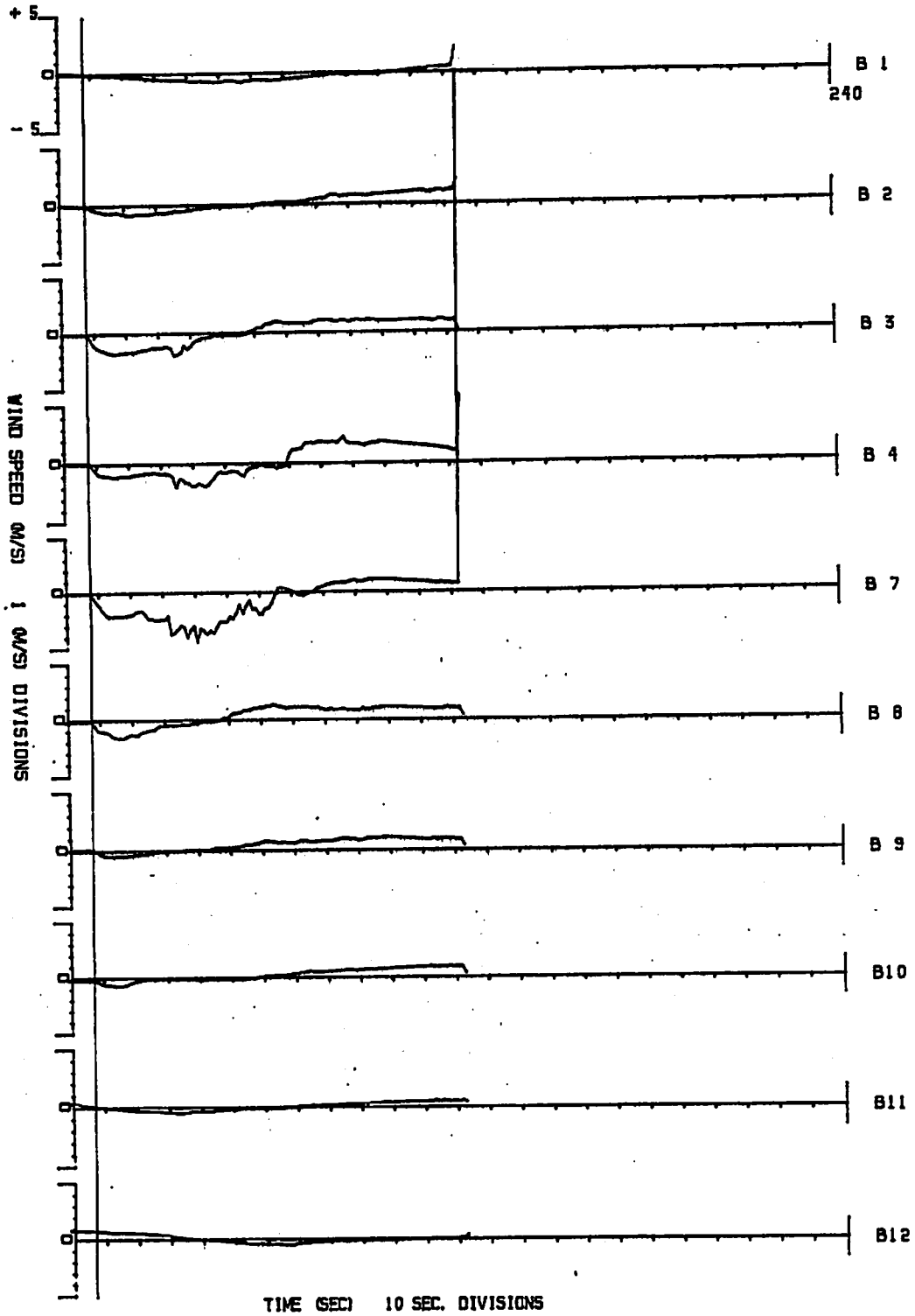

FIGURE 121. ANEMOMETER RECORDS FOR RUN 30

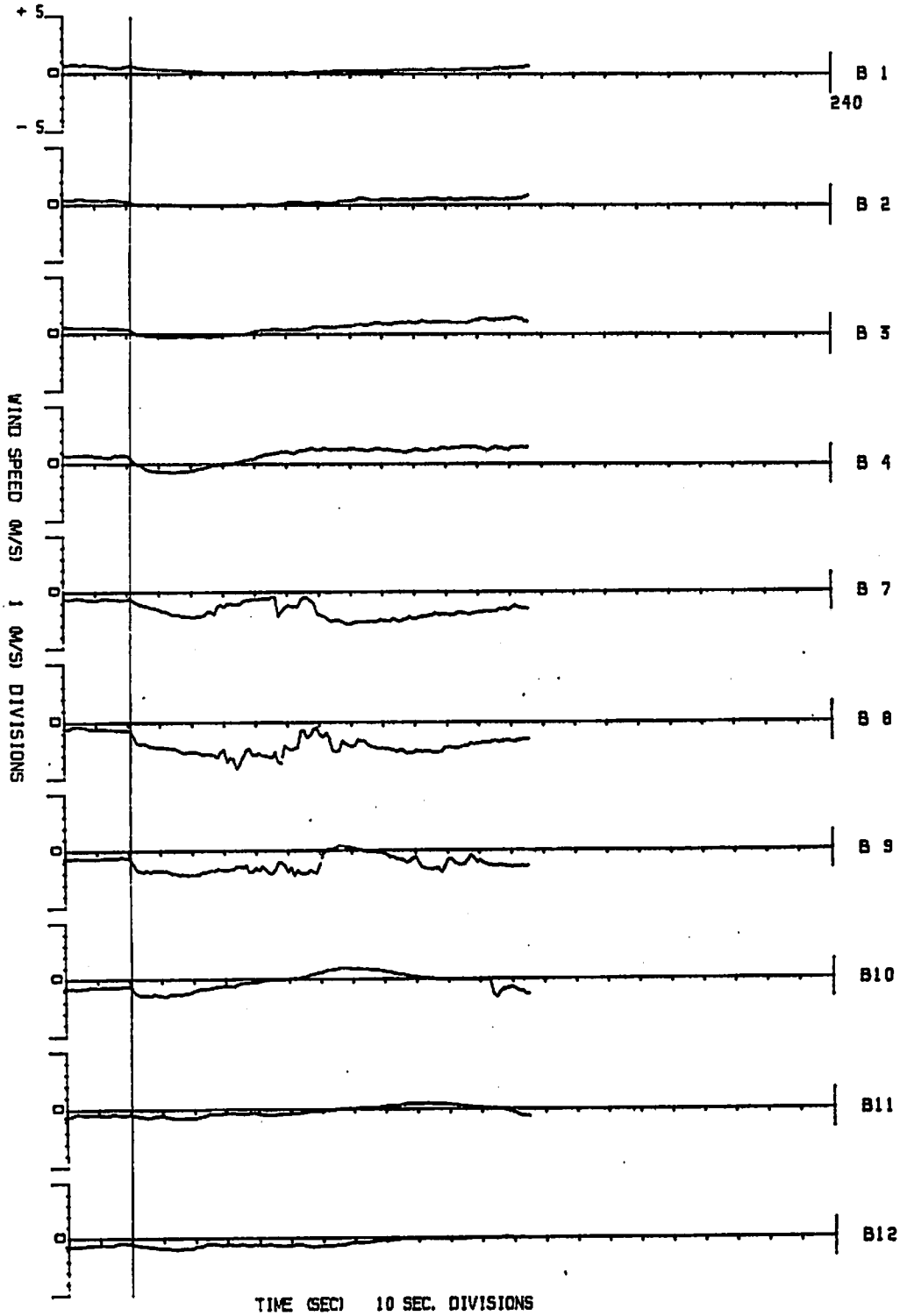

FIGURE 122. ANEMOMETER RECORDS FOR RUN 32

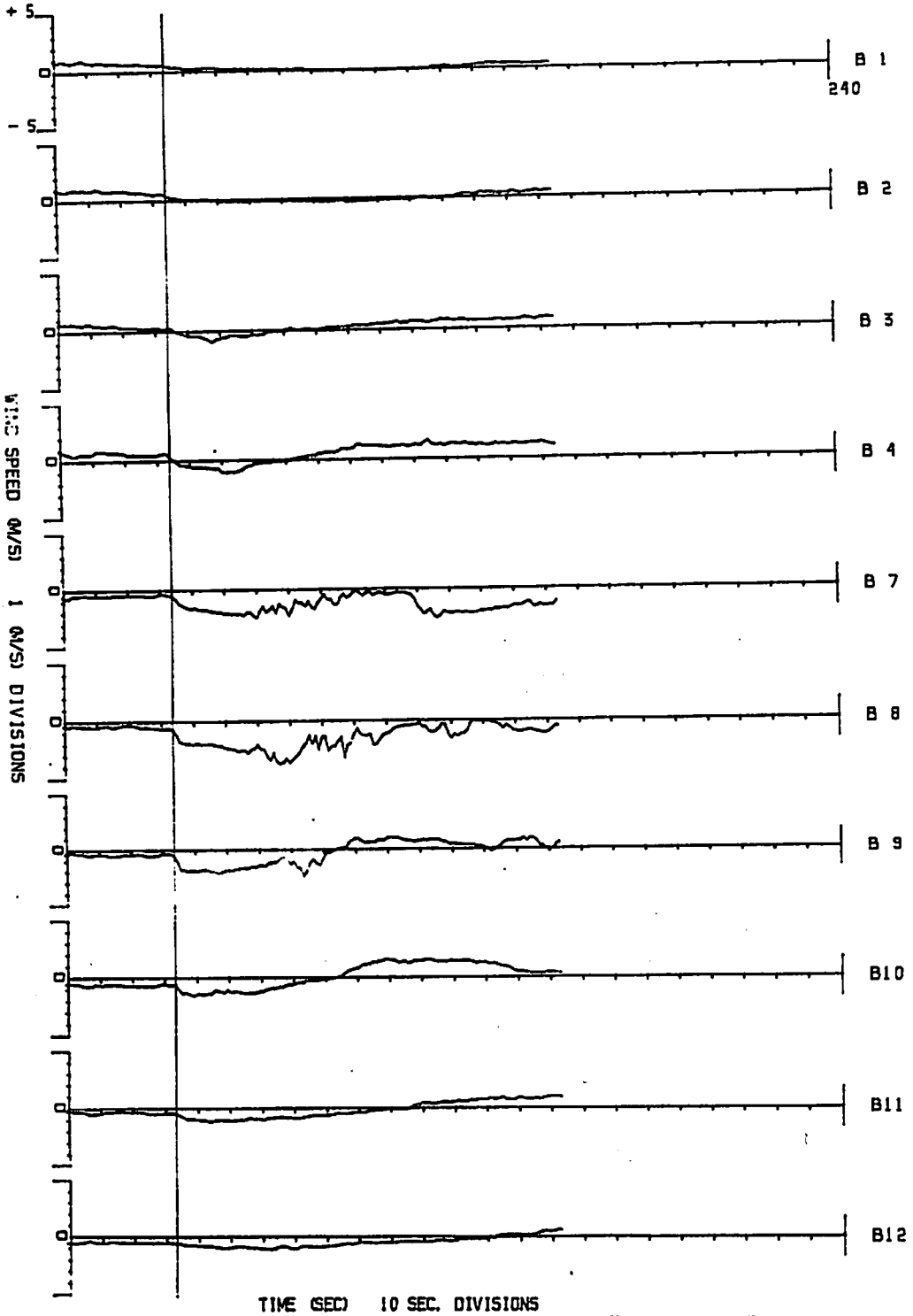

FIGURE 123. ANEMOMETER RECORDS FOR RUN 33

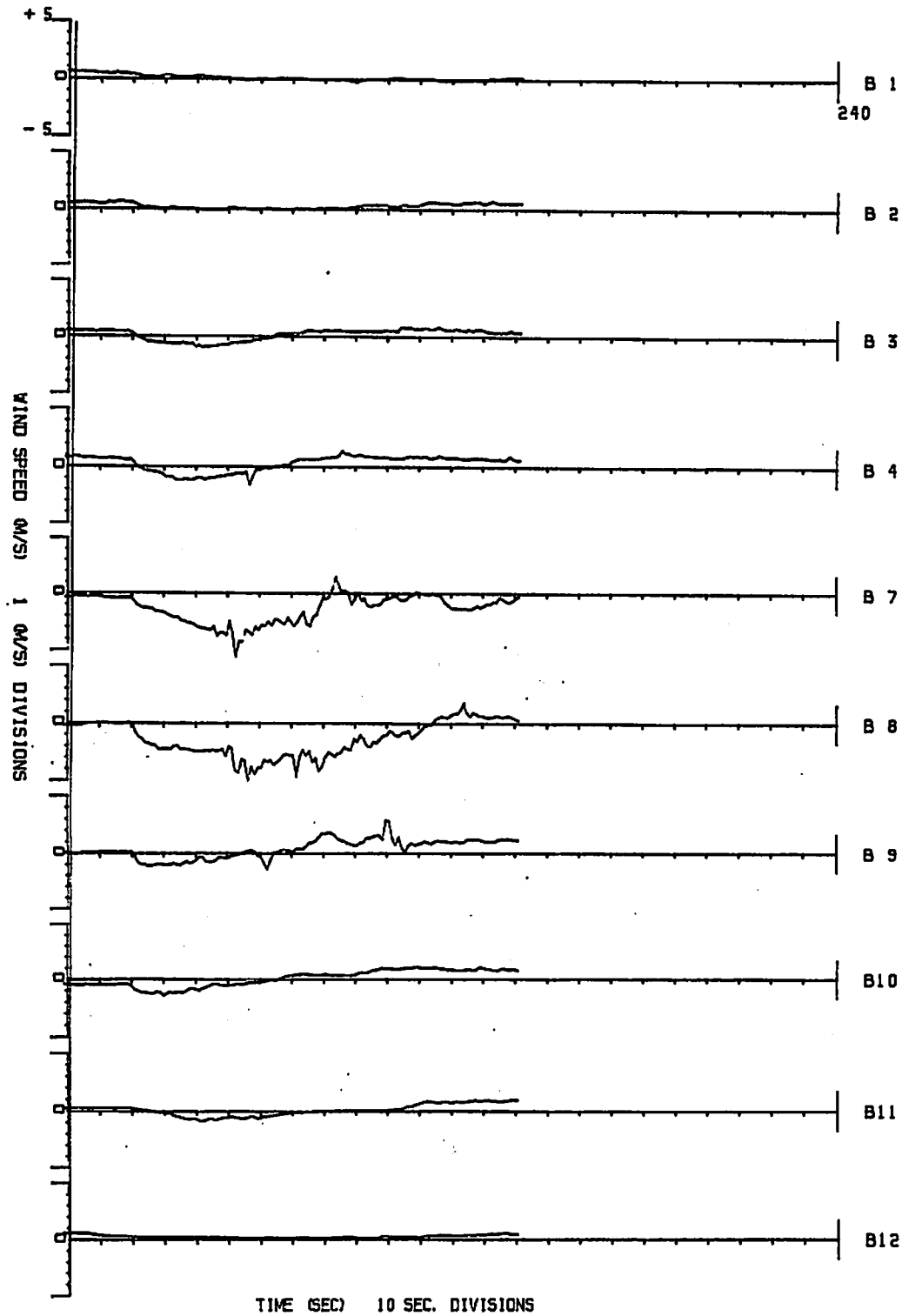

FIGURE 124. ANEMOMETER RECORDS FOR RUN 34

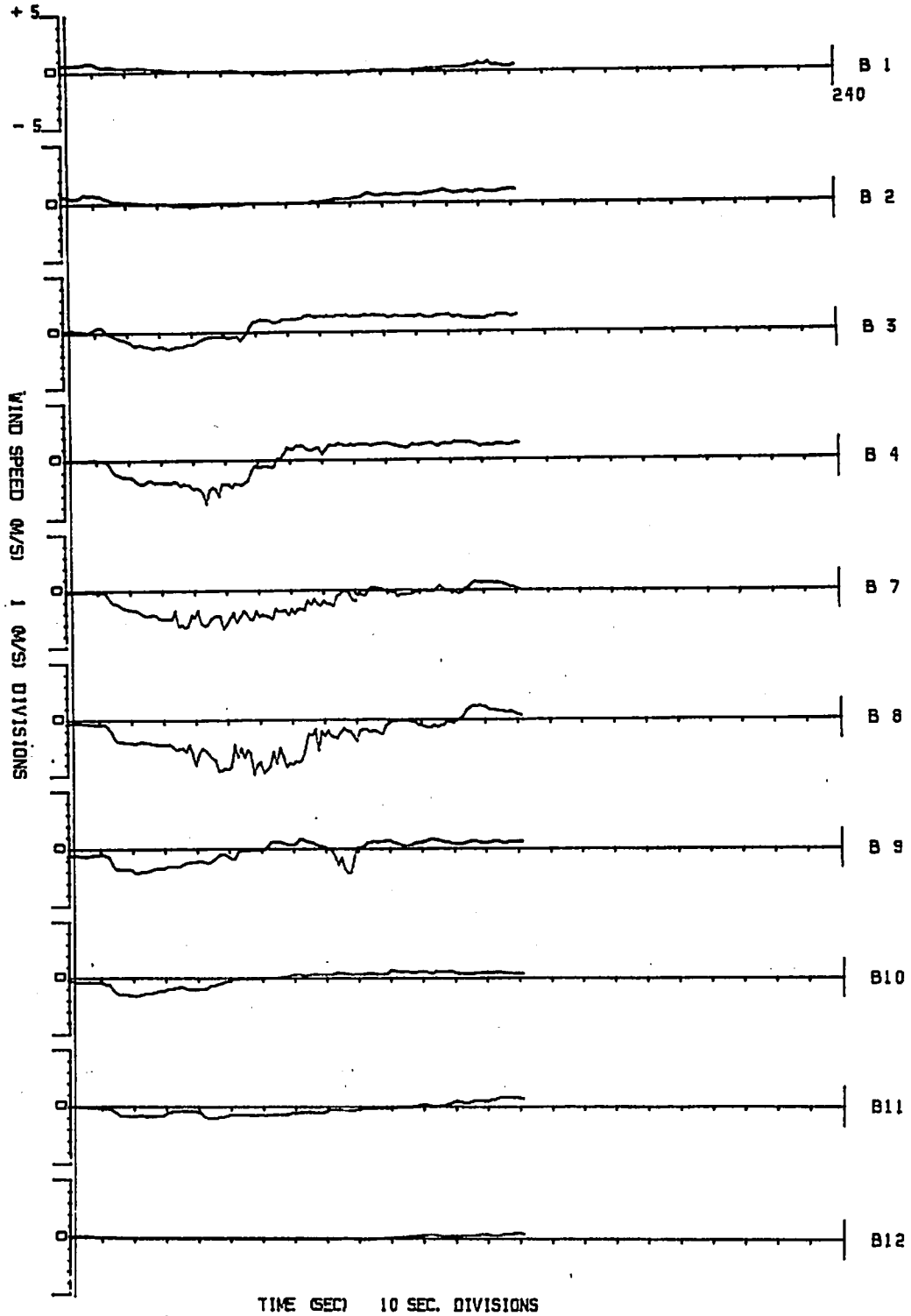

FIGURE 125. ANEMOMETER RECORDS FOR RUN 35

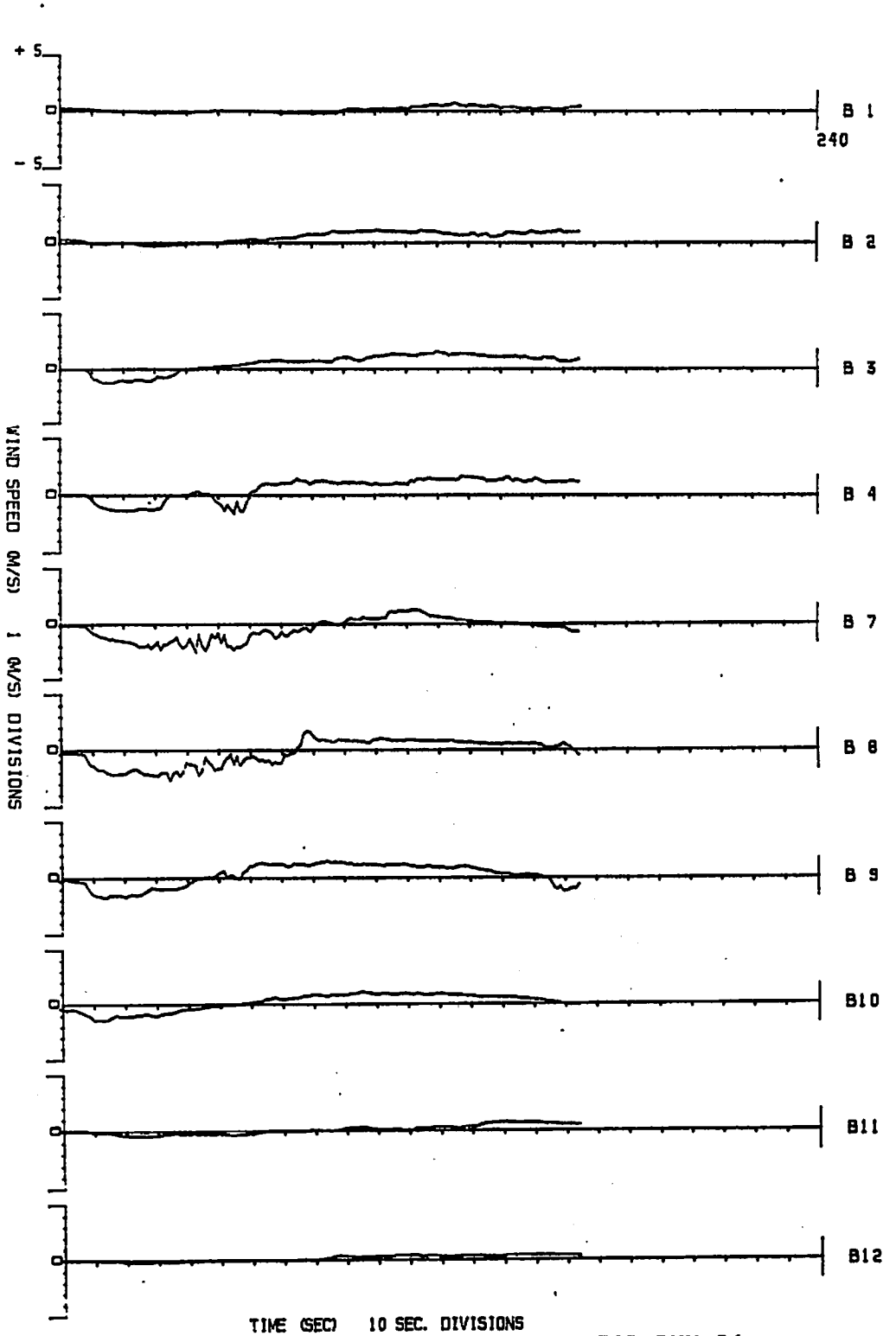

FIGURE 126. ANEMOMETER RECORDS FOR RUN 36

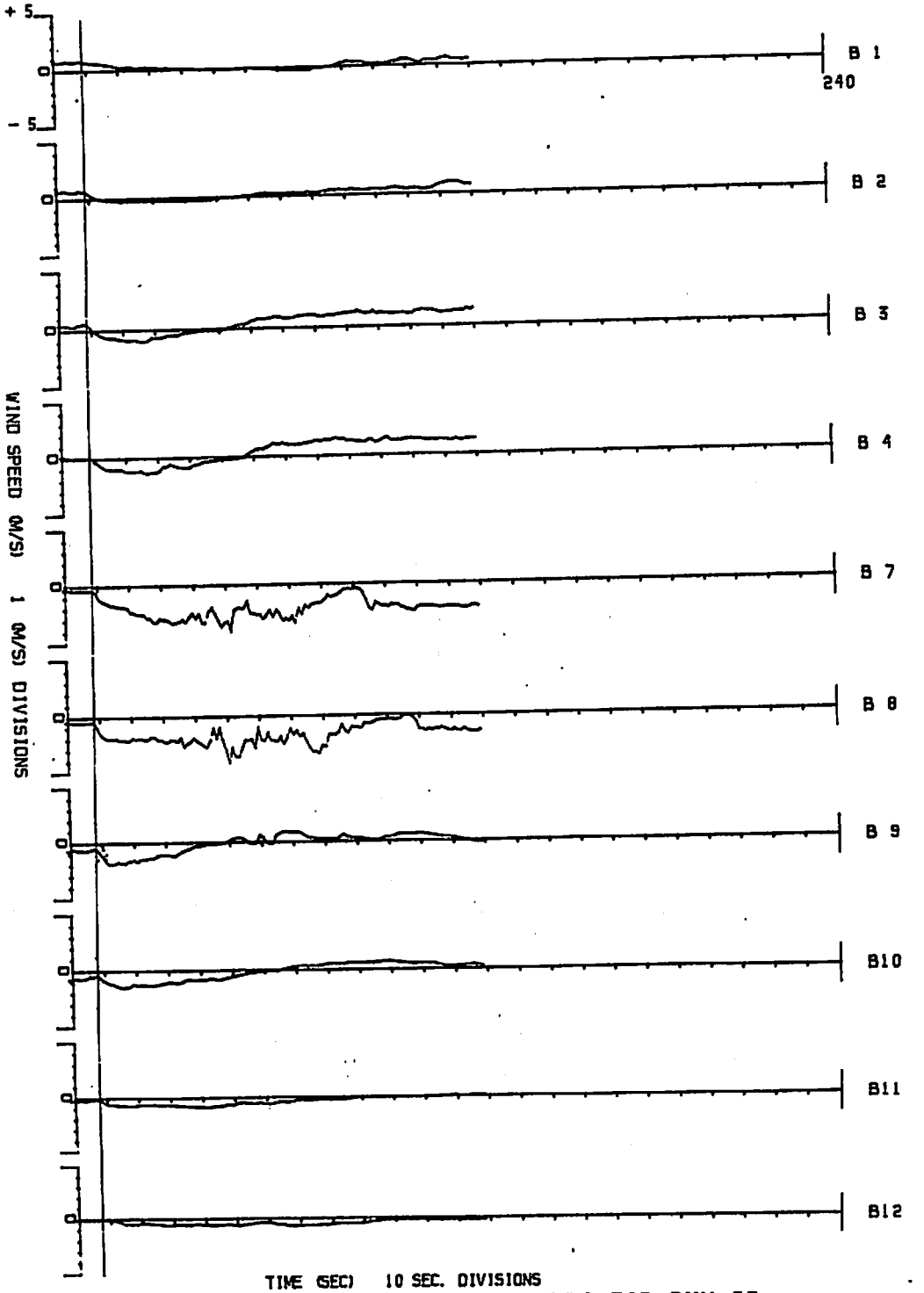

FIGURE 127. ANEMOMETER RECORDS FOR RUN 37

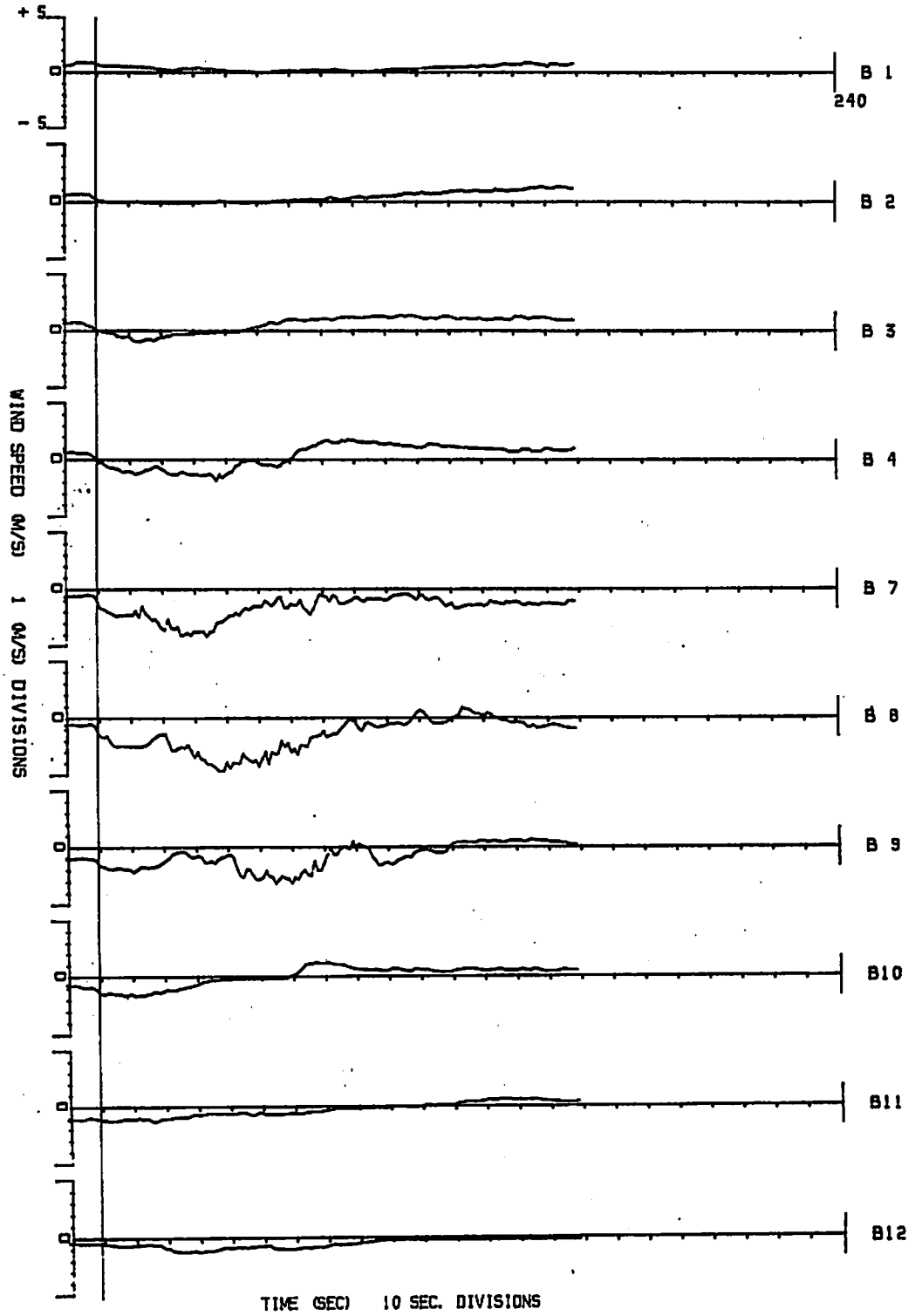

FIGURE 128. ANEMOMETER RECORDS FOR RUN 38

APPENDIX C
EXTERNAL LOGS FOR ROSAMOND TESTS

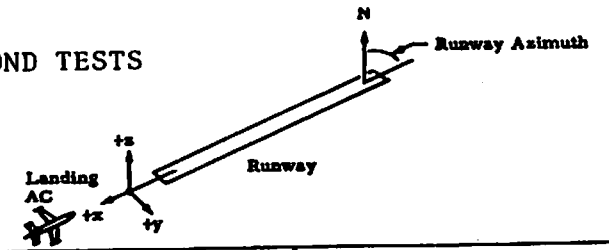

Location: Rosamond Dry Lake Van X Position: _____ Ref. Pt. _____ Runway Azimuth: _____

Date: 12/2/15 - Day 1 Van Y Position: Ref. Pt. Center of RW Mirror Azimuth for Switch _____

Sheet 1 of 2

Run ID		Spectrum Analyzer						Scanner						Computer		Time		Estimated Wind Azimuth (from)	azimuth 42° is normal to runway. Comments
				Freq. Span (MHz)				Range			Elevation								
No.	AC Type or VAD	B.W. (kHs)	Log Lin	Min.	f_c	Max.	Rate (msec)	Max.	Min.	Rate	Max.	Min.	Rate	Tape No.	No. Records	Start	Stop		
1	VAD	10	LN	0	2cm.	.5	1							DR01		6:45:00	6:49:30	est. from North	alt. at 31, 46, 61, 76, 91, 122, 244, 488 at 1 rev/alt.
2	VAD															6:50:00	6:59:00		same alt.
3	AC 1	30		1	0	2		57			63	3	.1kg			7:04:09	7:06:06		
4	AC 2	100		1		6							.5kg			7:09:37	7:11:25		
5	AC 3															7:15:08	7:17:17		
6	AC 4			0	1cm	5		60								7:20:49	7:22:53		
7	AC 5							118			63	20				7:25:56	7:27:40		Time mark on sight; ant has Alt. going 5-10° past 90°
8	AC 6	30						118			63	03				7:31:27	7:33:25		
9	AC 7										63	30				7:35:13	7:37:02		Run stop-comp. halt; Gen. fail; Precision run number 5 of 11 No: 6
10	AC 8							240			63	21				7:40:39	7:42:34		azimuth 180° + 42° (= 222°)
11	VAD	10		0		.5	1									7:50:00	7:58:00		Some alt. as run 1. Sync. clock 07:56:00 Our clock 07:55:05
12	AC 9	30		0	1/2cm	5		58			63	03	.5			8:12:09	8:15:17		222° azimuth
13	AC 10							120			63	15				8:18:28	8:19:56		
14	AC 11							183			63	25				8:23:37	8:25:39		
15	AC 12							240			62	35				8:29:21	8:31:21		
16	AC 13							57			62	03				8:35:37	8:36:56		
17	AC 14							57								8:40:34	8:41:50		Precisely in middle for 1st min (or longer) / Analog tape run out this run.
18	AC 15							57								8:45:06	8:46:19		
19	AC 16							68								8:51:07	8:52:45		Range 68 m; Az. at 42°; Amplitude threshold not changed.
20	VAD	10		0	1.3cm	.5										8:58:00	9:07:02	est. from north	same alt. as run 1.
21	AC 17	30		0	.6cm	5		35			62	03				9:32:12	9:33:32		Az. 42°. Corrected time code this run.
22	AC 17A															9:37:44	9:38:58		repeat of previous run (run 17)
23	AC 18															9:42:16	9:43:26		

EXTERNAL LOGS FOR ROSAMOND TESTS (CONTINUED)

Location: Rosamond Dry Lake
Date: 12/2/75 - Day 1
Sheet 2 of 2

Van X Position: Ref. Pt. _____
Van Y Position: Ref. Pt. Center of RW

Runway Azimuth: _____
Mirror Azimuth for Switch _____

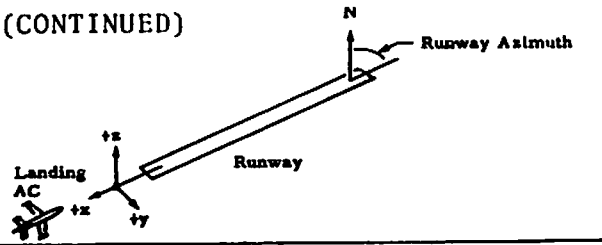

Run ID		Spectrum Analyzer						Scanner						Computer		Time		Estimated Wind Azimuth (from)	Comments
				Freq. Span (MHz)				Range			Elevation								
No.	AC Type or VAD	B.W. (kHz)	Log / Lin	Min.	f_c	Max.	Rate (msec)	Max.	Min.	Rate	Max.	Min.	Rate	Tape No.	No. Records	Start	Stop		
24	AC 19	30		0	.6cm	5		63			62	03				9:46:21	9:48:02		
25	AC 20							63								9:50:58	9:52:58		
26	AC 21							90								9:55:00	9:57:58		Good run. Vortices over van – high velocities
27	AC 22																		* 4 sec run
28	VAD	10		0	1¼cm	.5										10:03	10:12		same alt. as run 1.
																			* NOTE: 3rd SORTIE aborted due to hydraulic problem on 747.

EXTERNAL LOGS FOR ROSAMOND TESTS (CONTINUED)

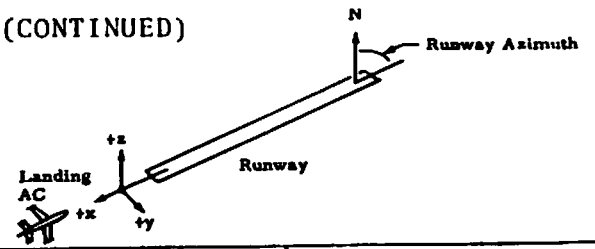

Location: Rosamond Dry Lake
Date: 12/3/75 - Day 8
Sheet 1 of 2

Van X Position: _____
Ref. Pt. _____

Van Y Position: 200' N of RW
Ref. Pt.

Runway Azimuth: _____

Mirror Azimuth for Switch _____

Run ID		Spectrum Analyzer						Scanner						Computer		Time		Estimated Wind Azimuth (from)	Comments
				Freq. Span (MHz)				Range			Elevation								
No.	AC Type or VAD	B.W. (kHz)	Log Lin	Min.	f_c	Max.	Rate (msec)	Max.	Min.	Rate	Max.	Min.	Rate	Tape No.	No. Records	Start	Stop		
1	VAD	10	lin	0	2cm	.5	1							DEV2		6:29	6:35	est. from south	alt. at 31, 46, 61, 76, 91, 122, 244, 488 at 1 rev./alt.
2	AC 23	30		0	1cm	5	1	140	35	3.5	63	10	.2			6:55:36	6:57:03		processor ram no. not updated for
3	AC 24															6:59:04	7:01:12		run 3 (AC run 24)
4	AC 25															7:03:32	7:05:38		
5	AC 26															7:07:47	7:10:01		
6	AC 27										45	17				7:12:33	7:14:41		
7	AC 28										40	17				7:16:50	7:18:58		
8	AC 29															7:21:23	7:23:32		
9	AC 30										45	17				7:25:17	7:27:18		
10	VAD	10		0	2cm	.5										7:31	7:39		alt. same as run 1.
11	AC 31	30		0	8cm	5		140	35	3.5	45	17	.2			7:56:09	7:58:20		pilot came in at 350 ft. instead of 200.
12	AC 32															8:00:47	8:03:11		elev. scanner sweep up prior to this run but recorded
13	AC 33										55	30				8:06:09	8:08:36	←	to work alt. before run started.
14	AC 34															8:11:18	8:13:29		Run AC 33: pilot came in at 210 ft. Also,
15	AC 35															8:15:49	8:17:59	←	Mel switch run no. in processor to 34
16	AC 36															8:18:09	8:22:48	←	during run.
17	AC 37															8:25:17	8:27:19		Run AC 35: Analog tape run set this run,
18	AC 38															8:30:30	8:32:38		Run AC 36: Lost CRT power during
																			run 36. Plug to mainframe pulled out,
																			restored at 8:22:30. Also, osc
																			time "mark" and AV "mark" not
																			synchronous for run 36.
19	VAD	10		0	15cm	.5										8:34	8:46		alt. same as run 1.

EXTERNAL LOGS FOR ROSAMOND TESTS (CONCLUDED)

Location: Rosamond Dry Lake
Date: 12/3/15 - day 2
Sheet 2 of 2

Van X Position: Ref. Pt. _____
Van Y Position: Ref. Pt. 200' N of RW

Runway Azimuth: _____
Mirror Azimuth for Switch _____

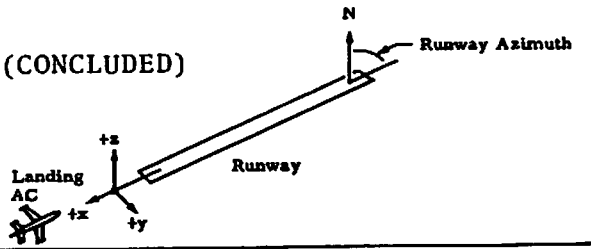

Run ID		Spectrum Analyzer						Scanner						Computer		Time		Estimated Wind Azimuth (from)	Comments
				Freq. Span (MHz)				Range			Elevation								
No.	AC Type or VAD	B.W. (kHz)	Log Lin	Min.	f_c	Max.	Rate (msec)	Max.	Min.	Rate	Max.	Min.	Rate	Tape No.	No. Records	Start	Stop		
20	AC 39	30	Lin	0	.6cm	5	1	140	35	3.5			.2			9:01:11	9:02:39	44 from N.W.	
21	AC 40										55	23				9:06:52	9:08:57		
22	AC 41															9:12:30	9:14:34		
23	AC 42															9:18:06	9:20:26		
24	AC 43							150	35							9:23:37	9:26:24		
25	AC 44							160	35							9:28:40	9:30:55		
26	AC 45															9:33:57	9:36:46		
27	AC 46							180	35							9:39:09	9:42:11		
28	VAD	10		0	2cm	.5										9:44	9:52		alt. same as run 1. (sheet 1)
29	AC 47	30		0	.8cm	5		140	35	3.5	63	23	.2			10:00:59	10:03:11		
30	AC 48							160	35							10:05:23	10:07:37		wind from south, both vertical towards VAN.
31	AC 49															10:20:26	10:23:10		wheeling run, 180 at, dusty, dust storm, visibility 5% by VAN.
32	AC 50							140	35							10:34:11	10:37:48		Rotated scan 180° @ 10:35:07
33	AC 51															10:29:31	10:32:13		Rotated scan 90° @ 10:30:46 (aft)
34	AC 52															10:33:37	10:36:24		Rotated scan forward 90° @ 10:35:00
35	AC 53															10:37:50	10:40:39		Rotated scan aft 90° @ 10:31:58; rotated 90° @ 10:39:55
36	AC 54															10:41:51	10:44:56		Rotated scan aft 90° @ 10:43:29
																			NOTE: AC Run 53: picked up vertical @ 10:39:16 after 1st rotation.
37	VAD	10		0	2cm	.5										10:49:20	10:51:35		alt. same as run 1. (sheet 1)
						NOTES:		TIME CHECK @ END OF SORTIE 9											
									CDR TIME			AV TIME							
									10:46:13			10:48:10							

Range checked after runs O.K.

APPENDIX D
LDV VELOCITY PROFILES

This appendix contains the velocity profiles obtained for Runs 8, 11, and 12 from the high-speed LDV data. The procedures for obtaining these plots are described in Section 6.2.2.

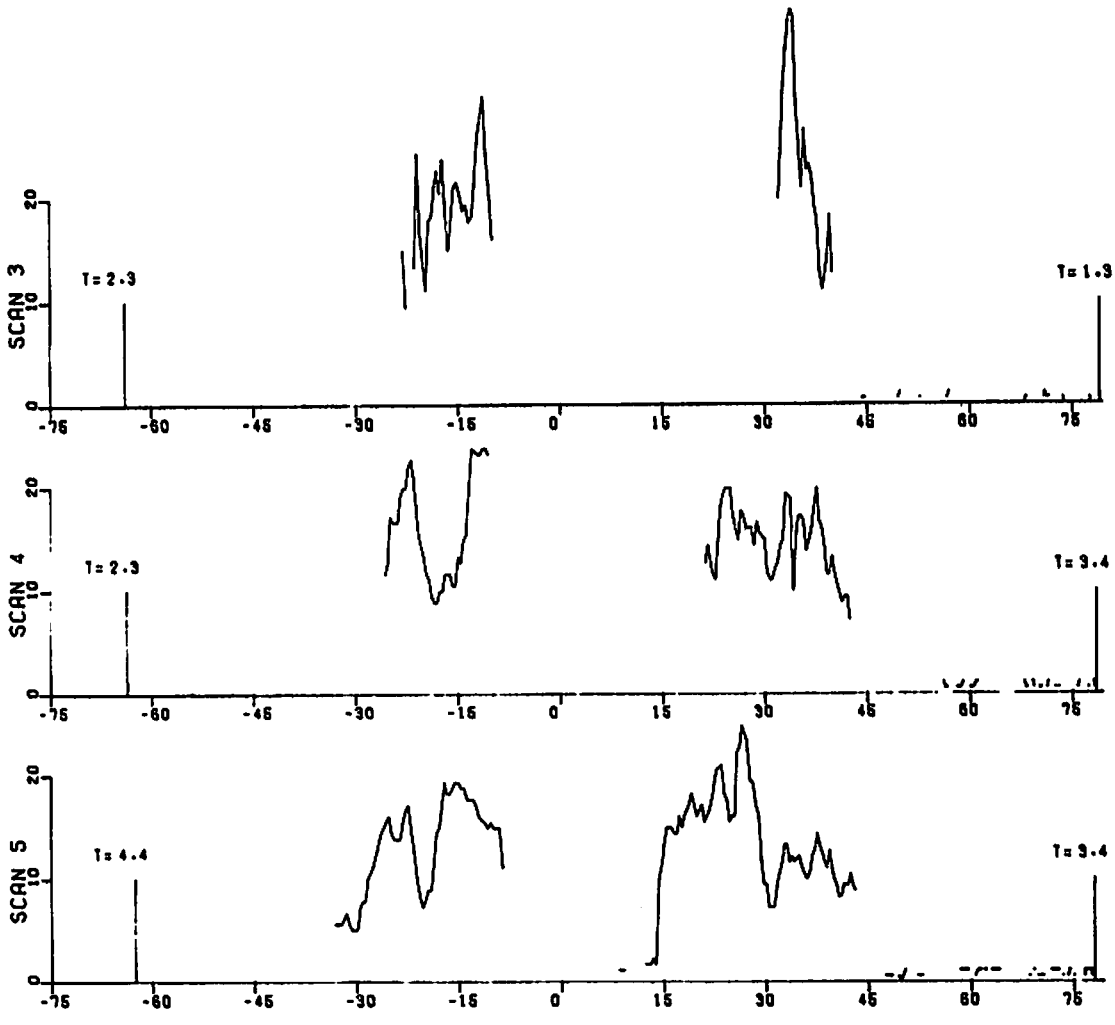

ARC DISTANCE (meters)

FIGURE 129. VELOCITY PROFILES FOR RUN 8

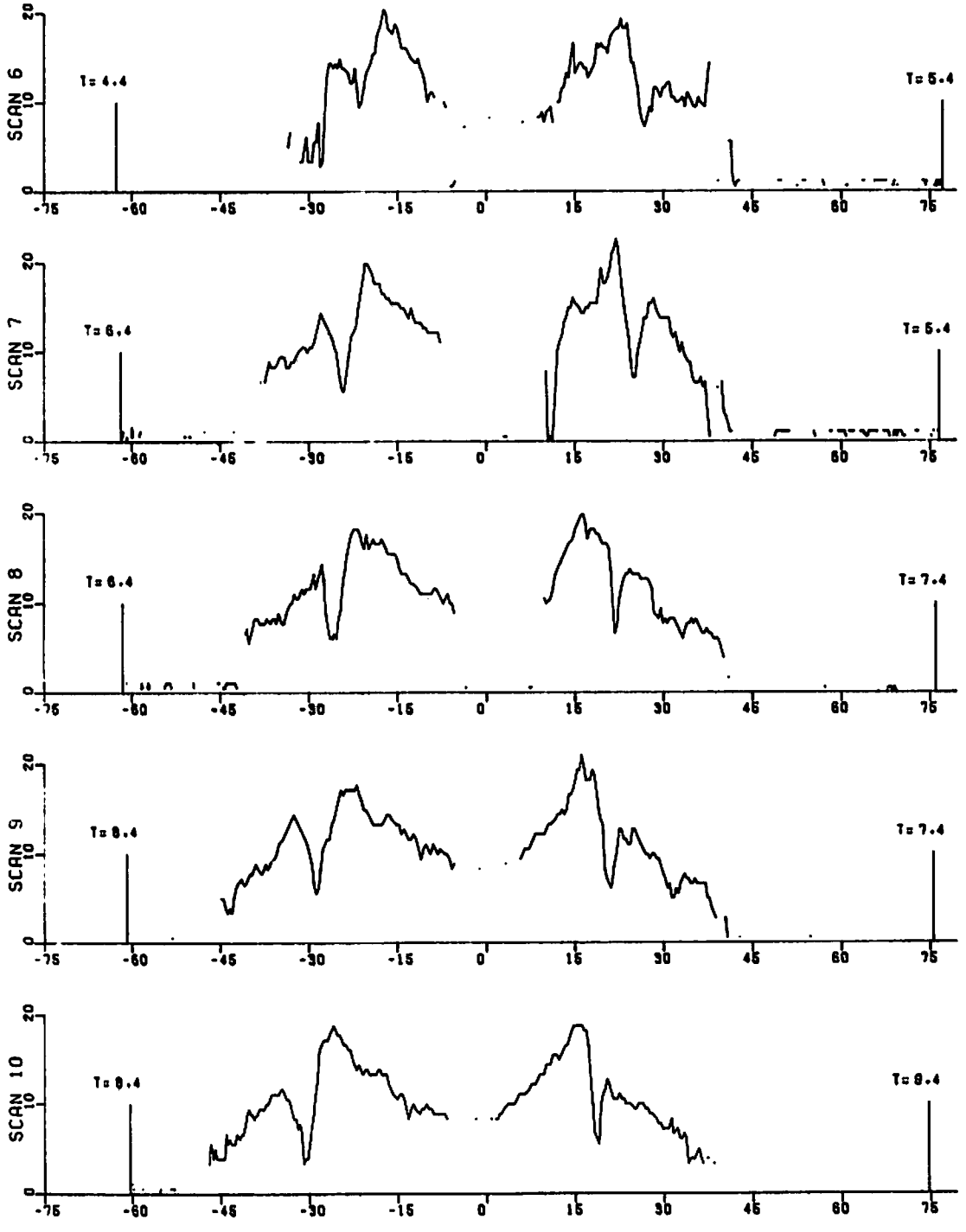

ARC DISTANCE (meters)

FIGURE 129. (CONTINUED)

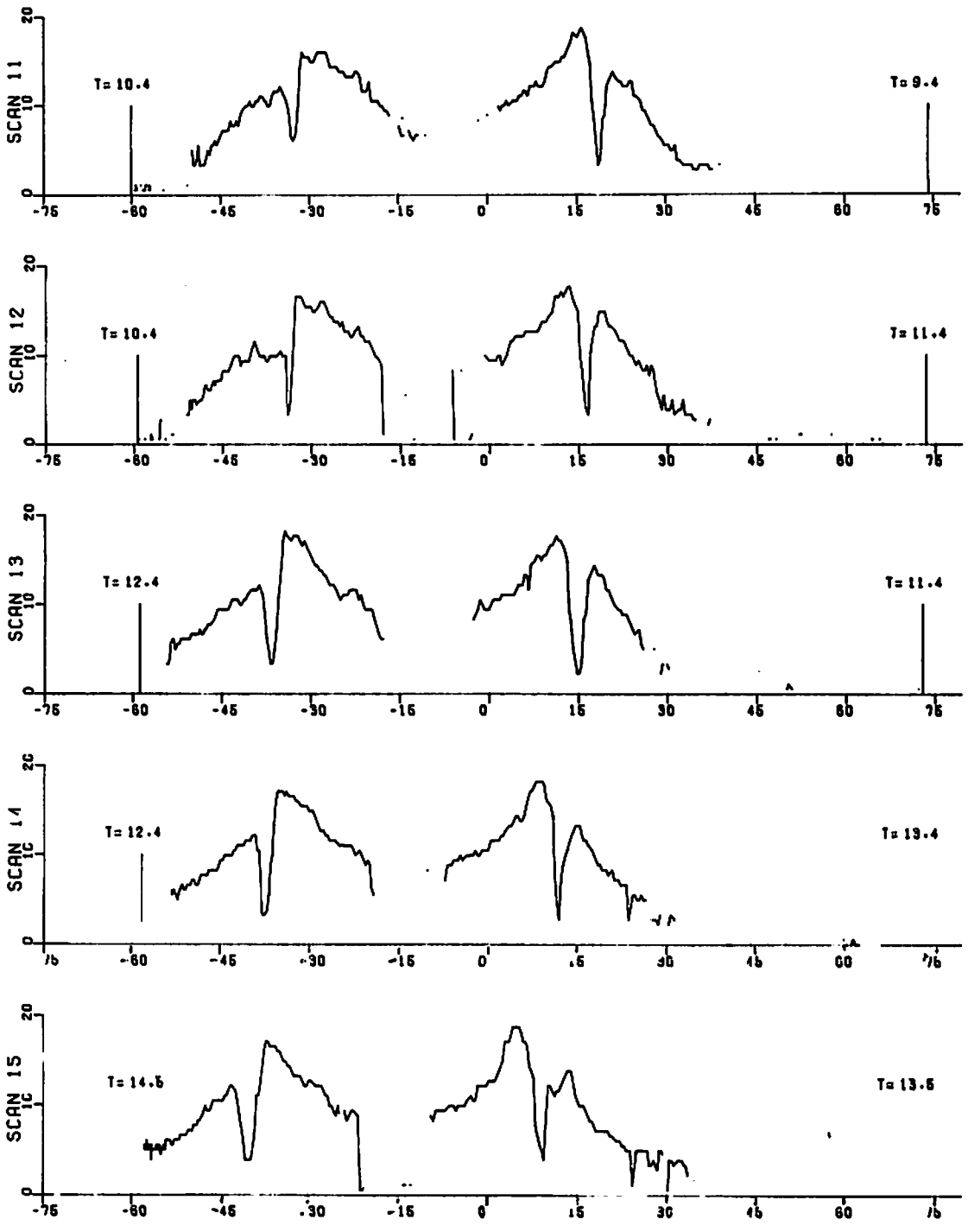

FIGURE 129. (CONTINUED)

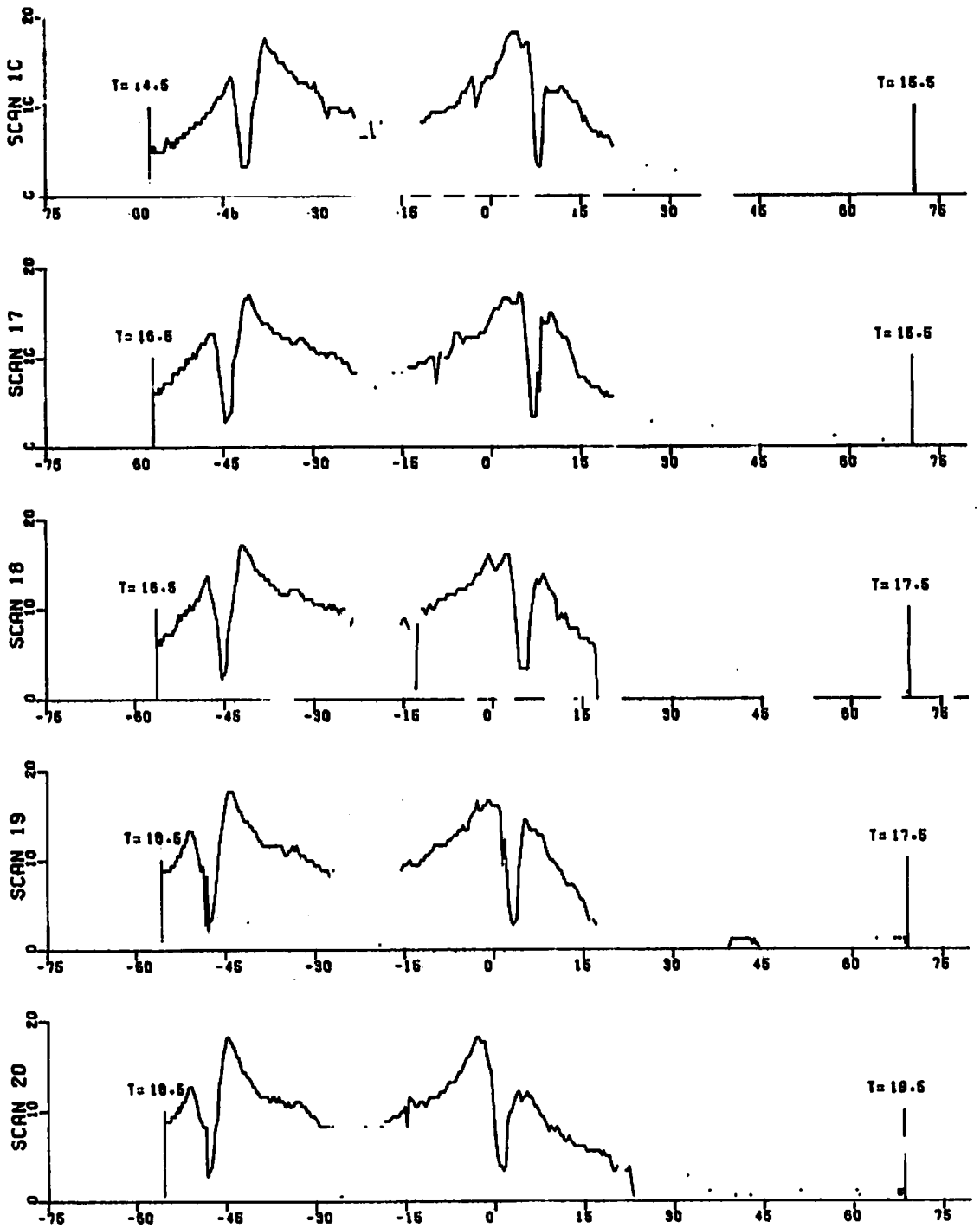

FIGURE 129. (CONTINUED)

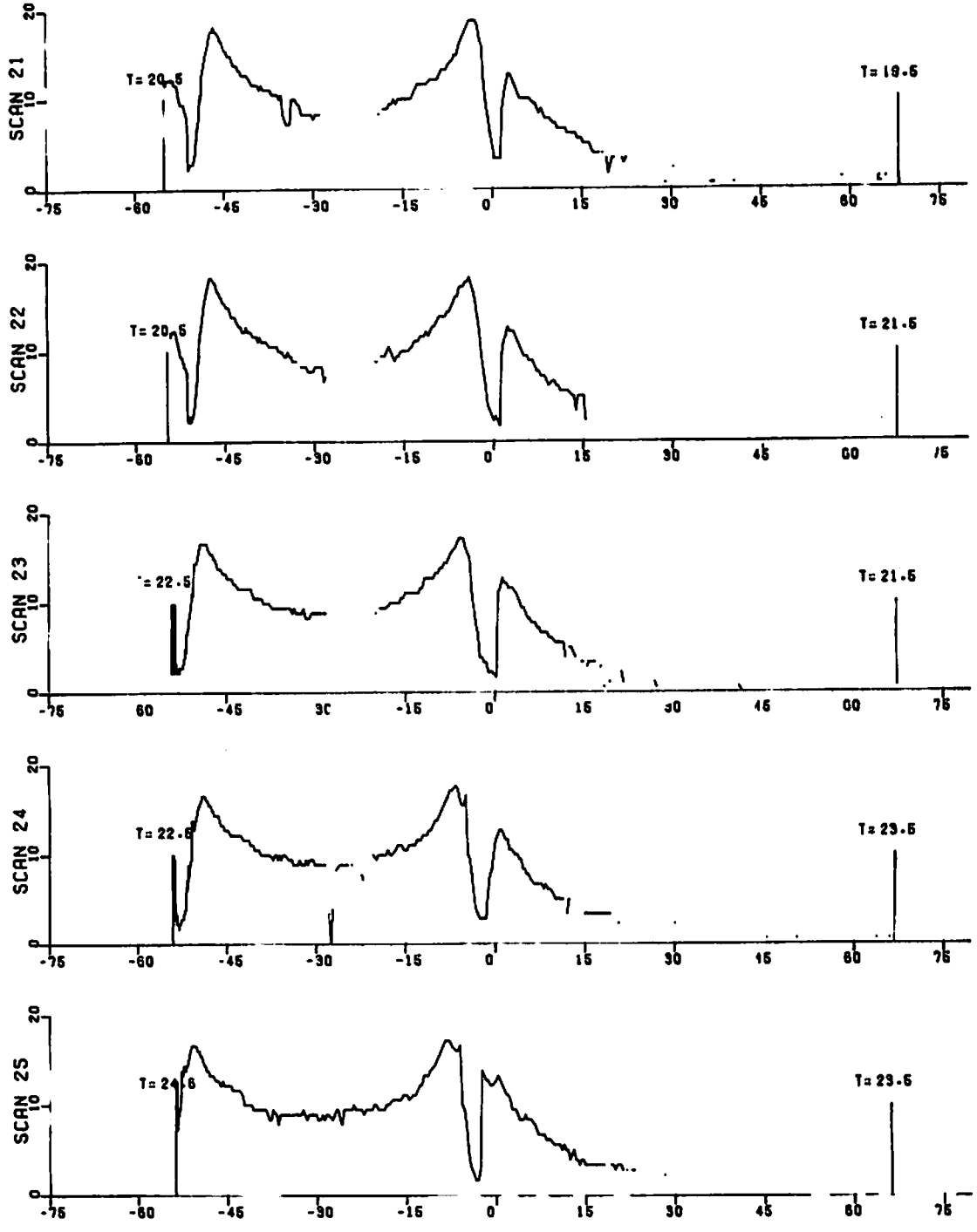

ARC DISTANCE (meters)

FIGURE 129. (CONTINUED)

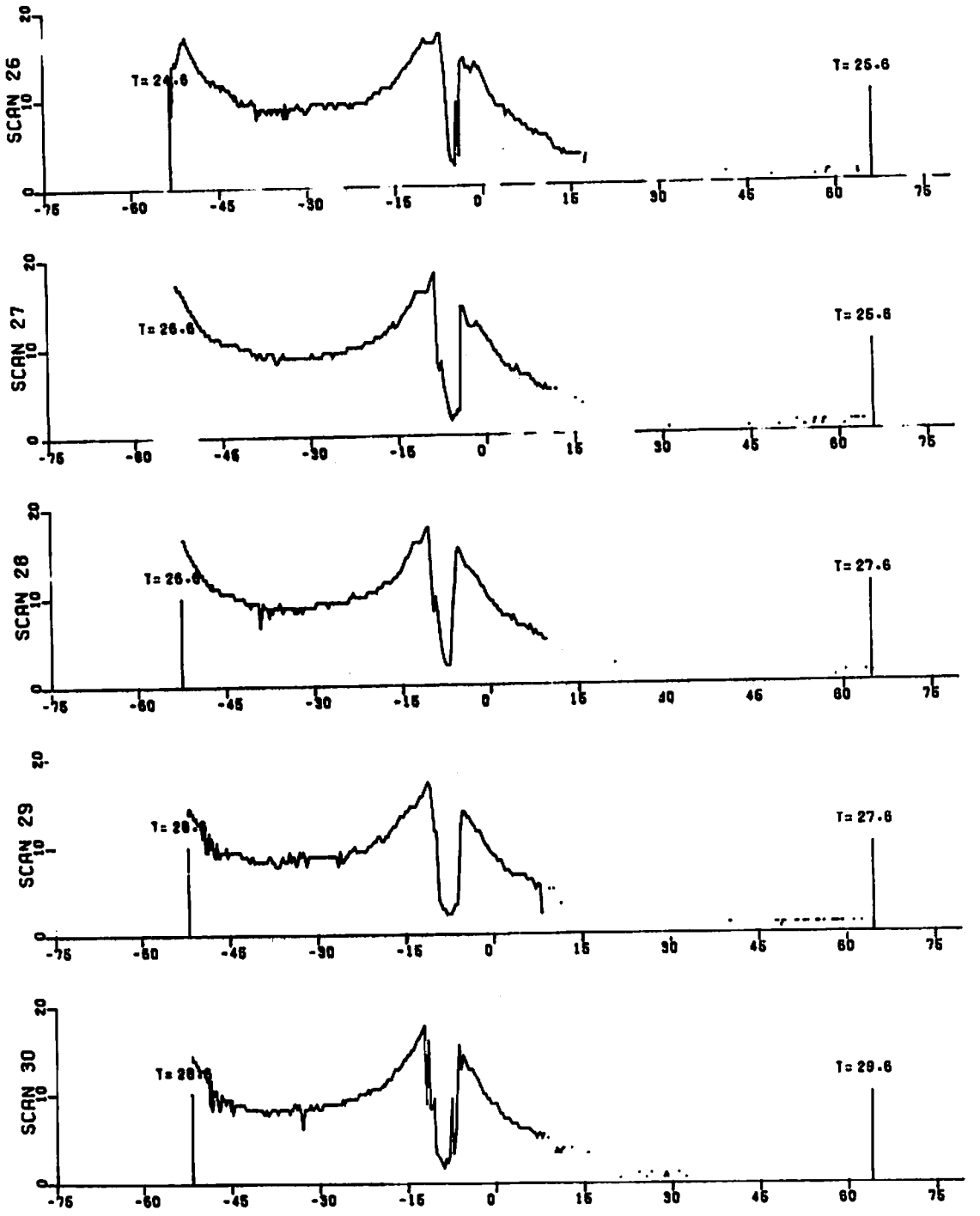

ARC DISTANCE (meters)

FIGURE 129. (CONTINUED)

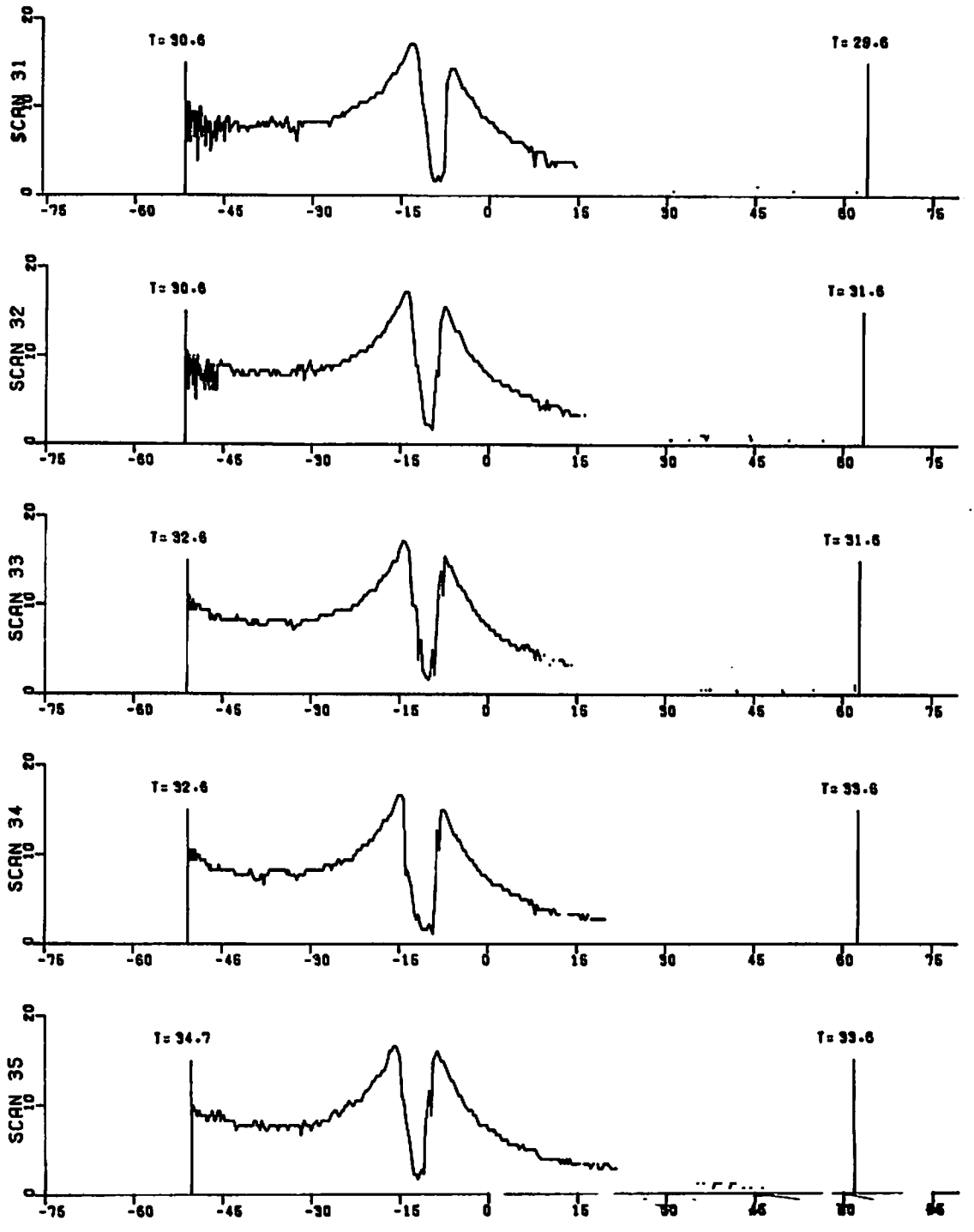

ARC DISTANCE (meters)

FIGURE 129. (CONTINUED)

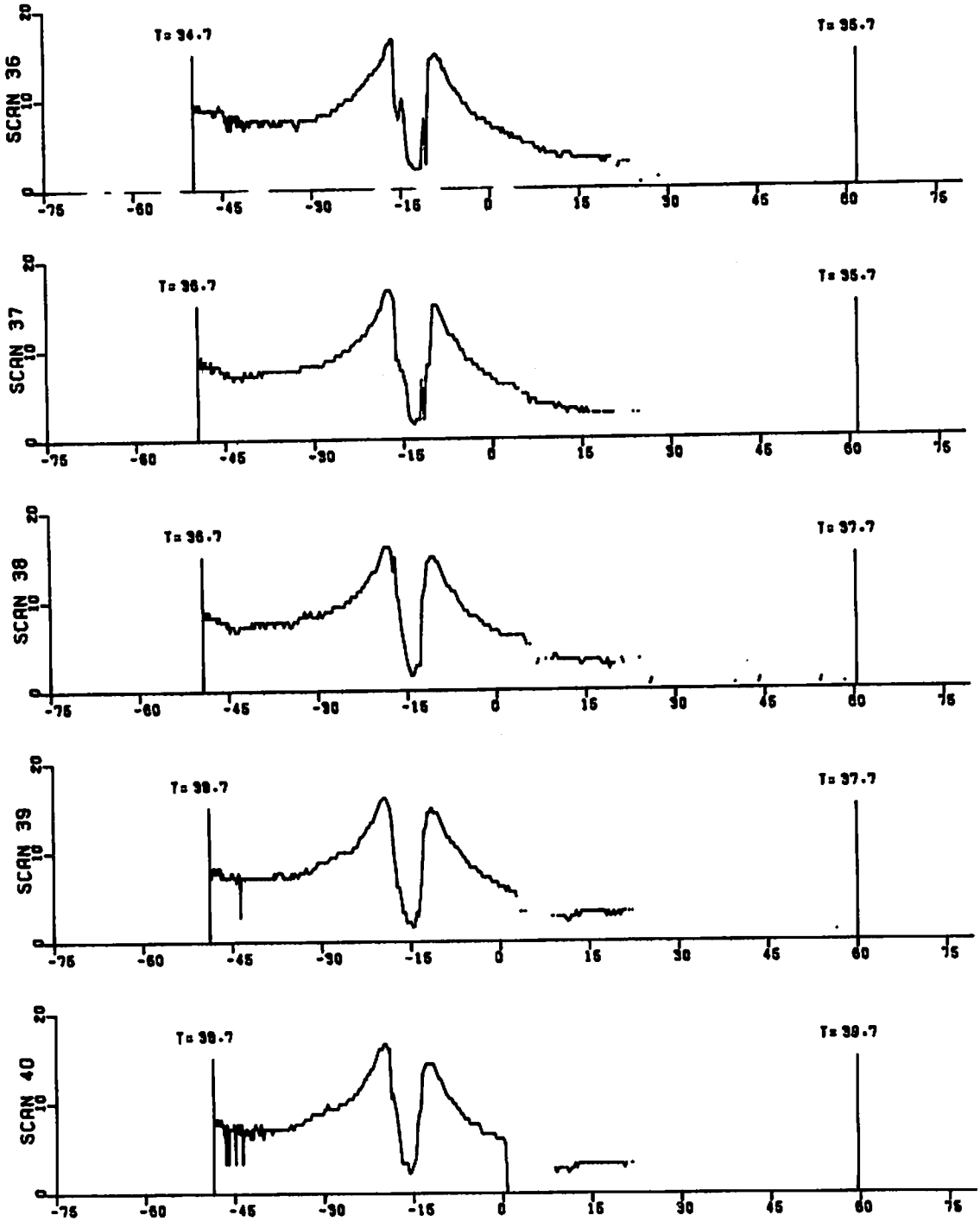

ARC DISTANCE (meters)

FIGURE 129. (CONTINUED)

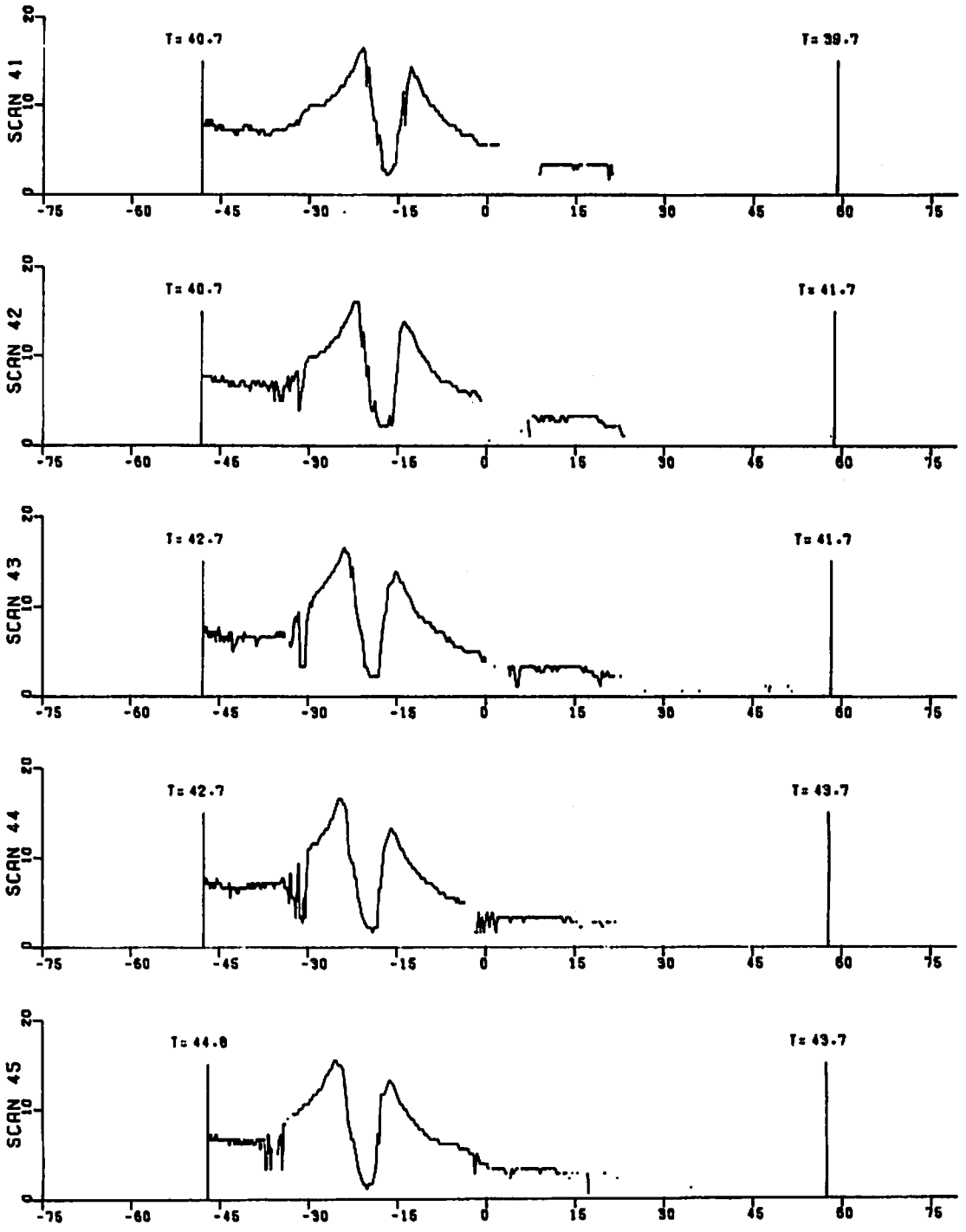

ARC DISTANCE (meters)

FIGURE 129. (CONTINUED)

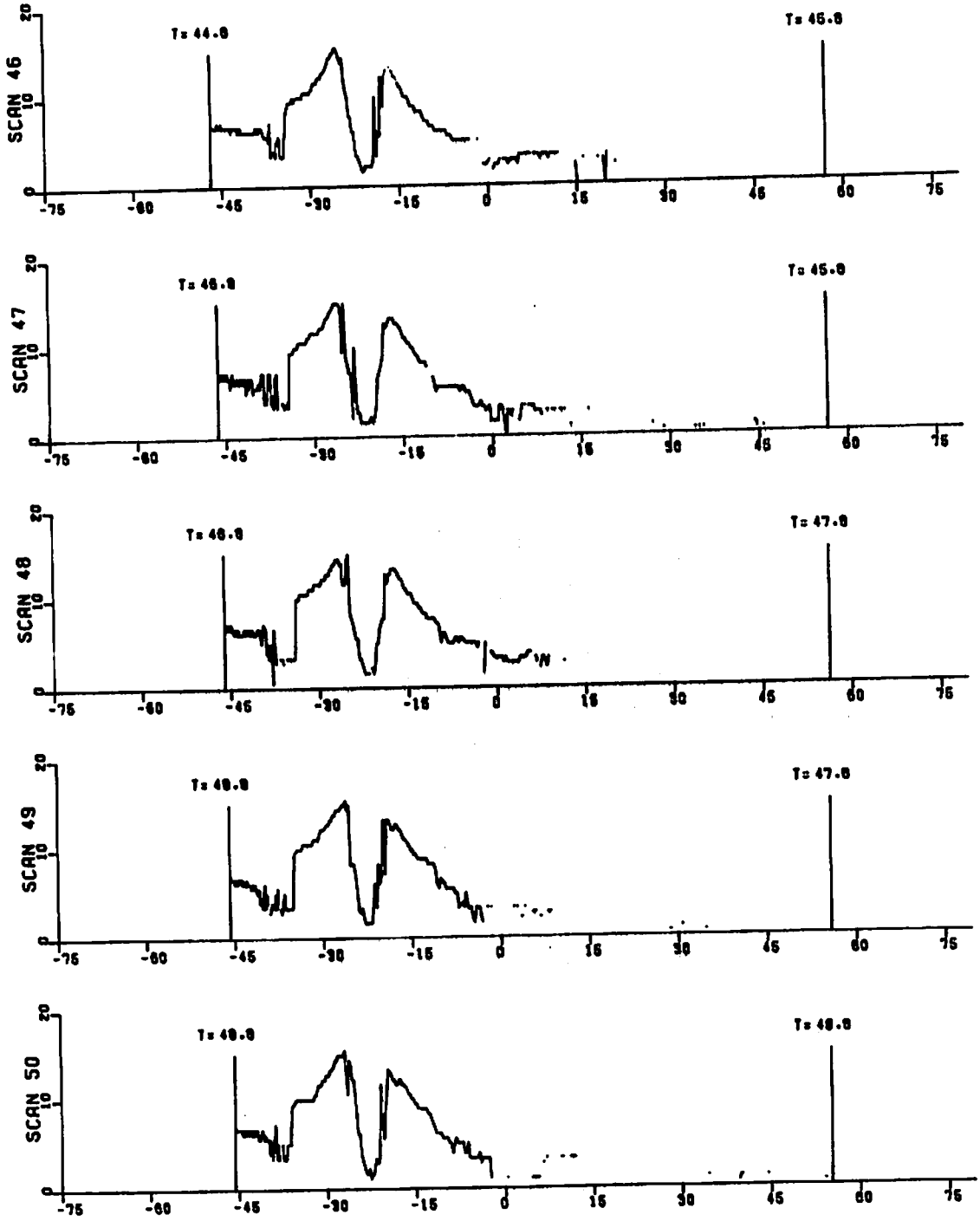

ARC DISTANCE (meters)

FIGURE 129. (CONTINUED)

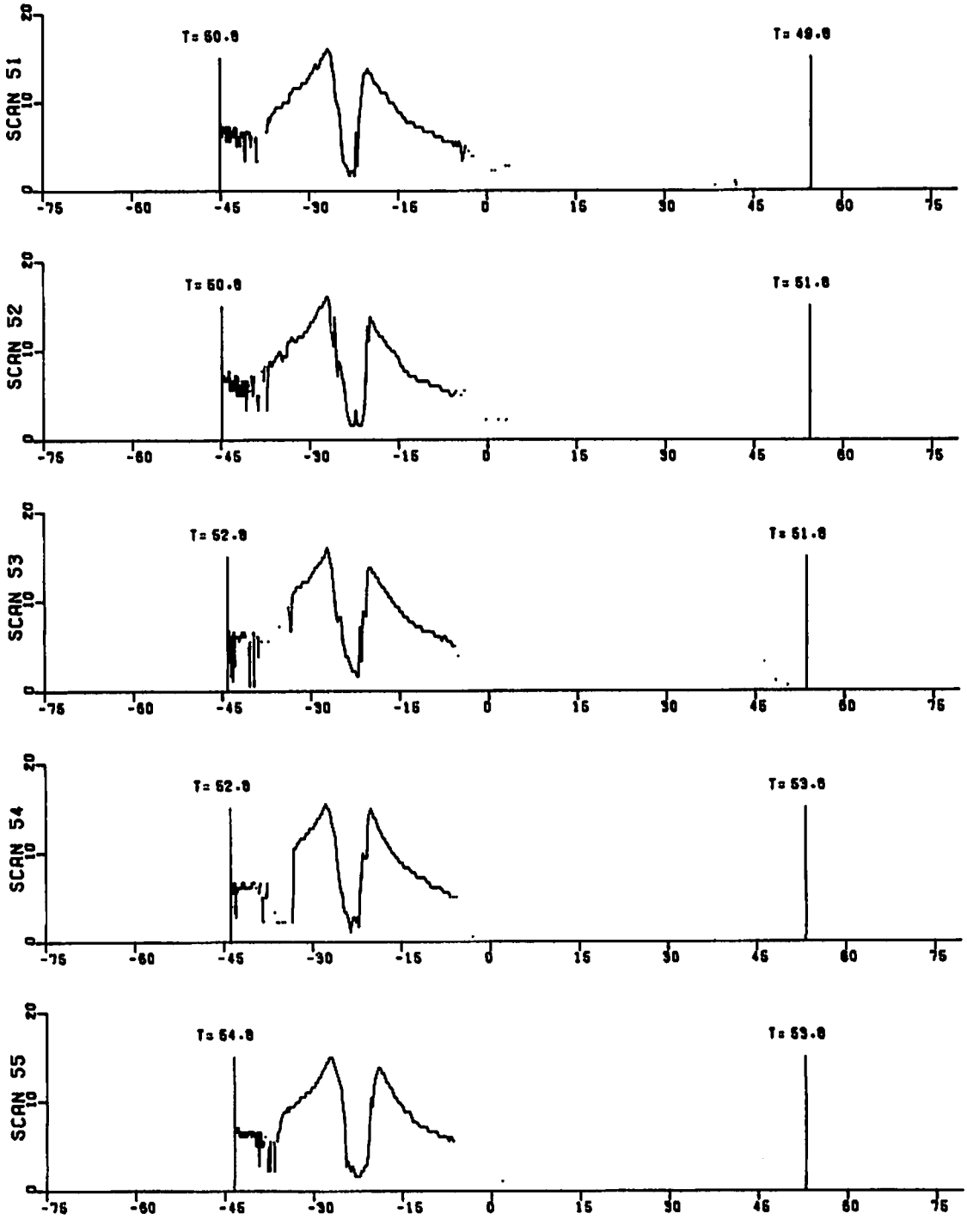

ARC DISTANCE (meters)

FIGURE 129. (CONTINUED)

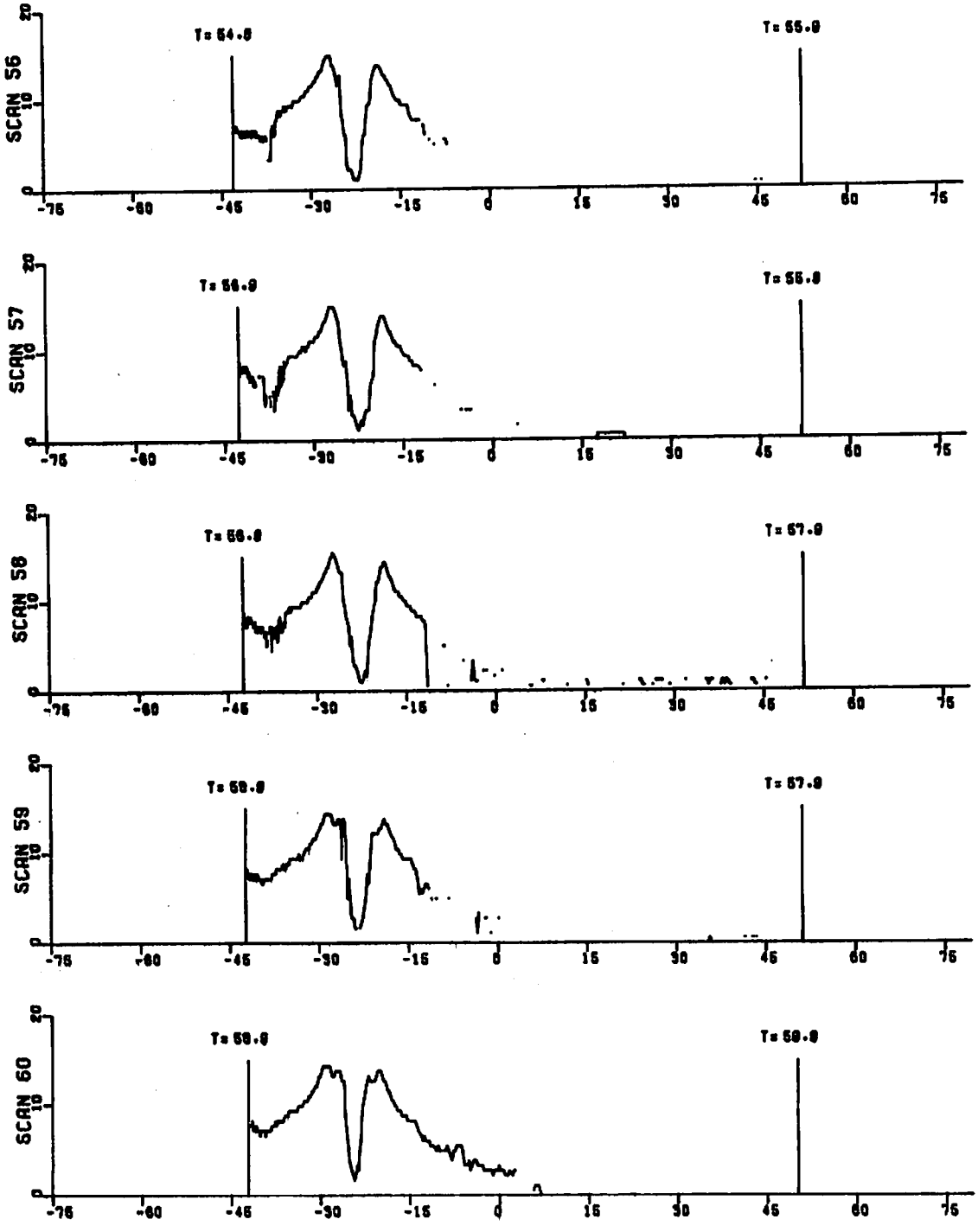

ARC DISTANCE (meters)

FIGURE 129. (CONTINUED)

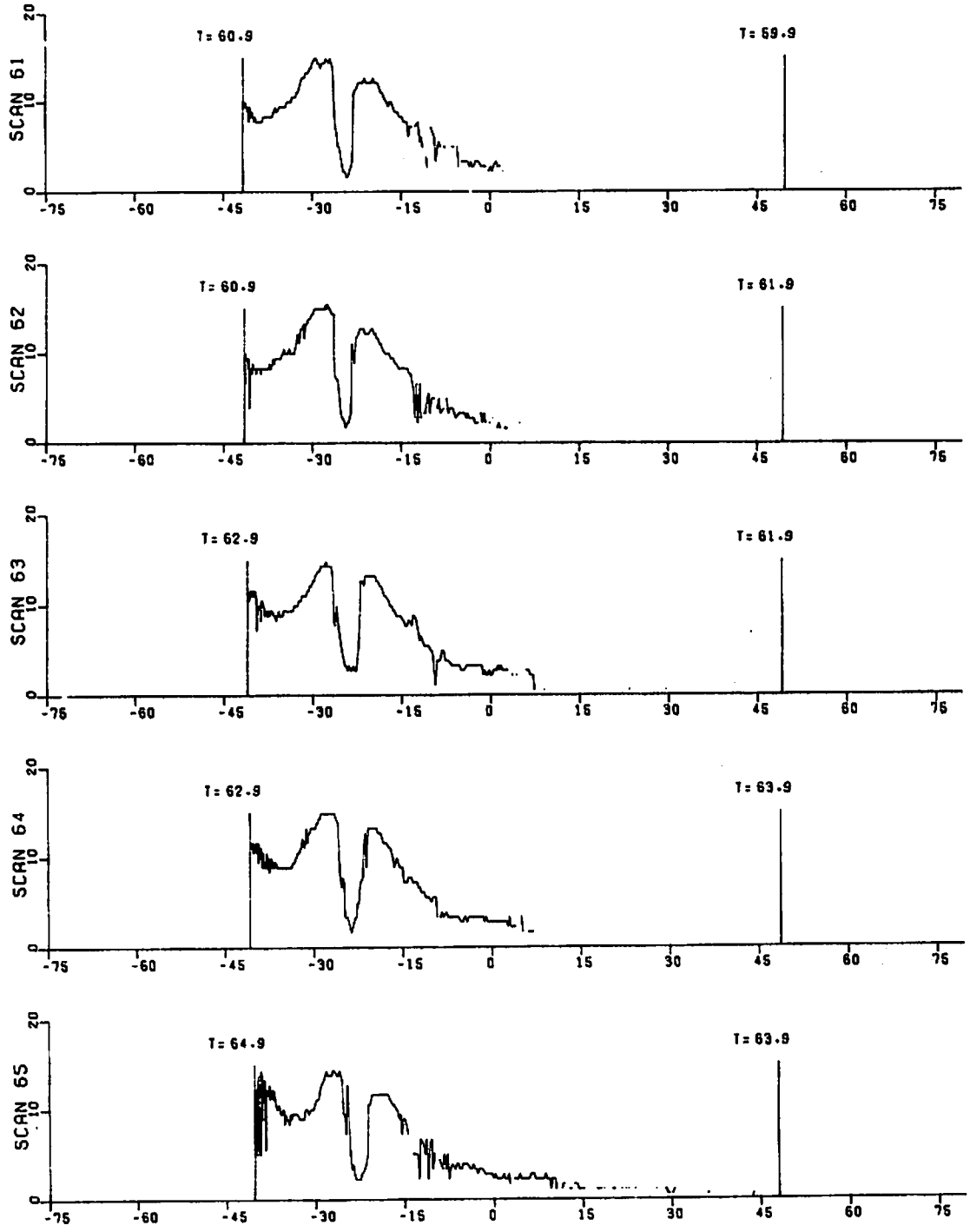

ARC DISTANCE (meters)

FIGURE 129. (CONTINUED)

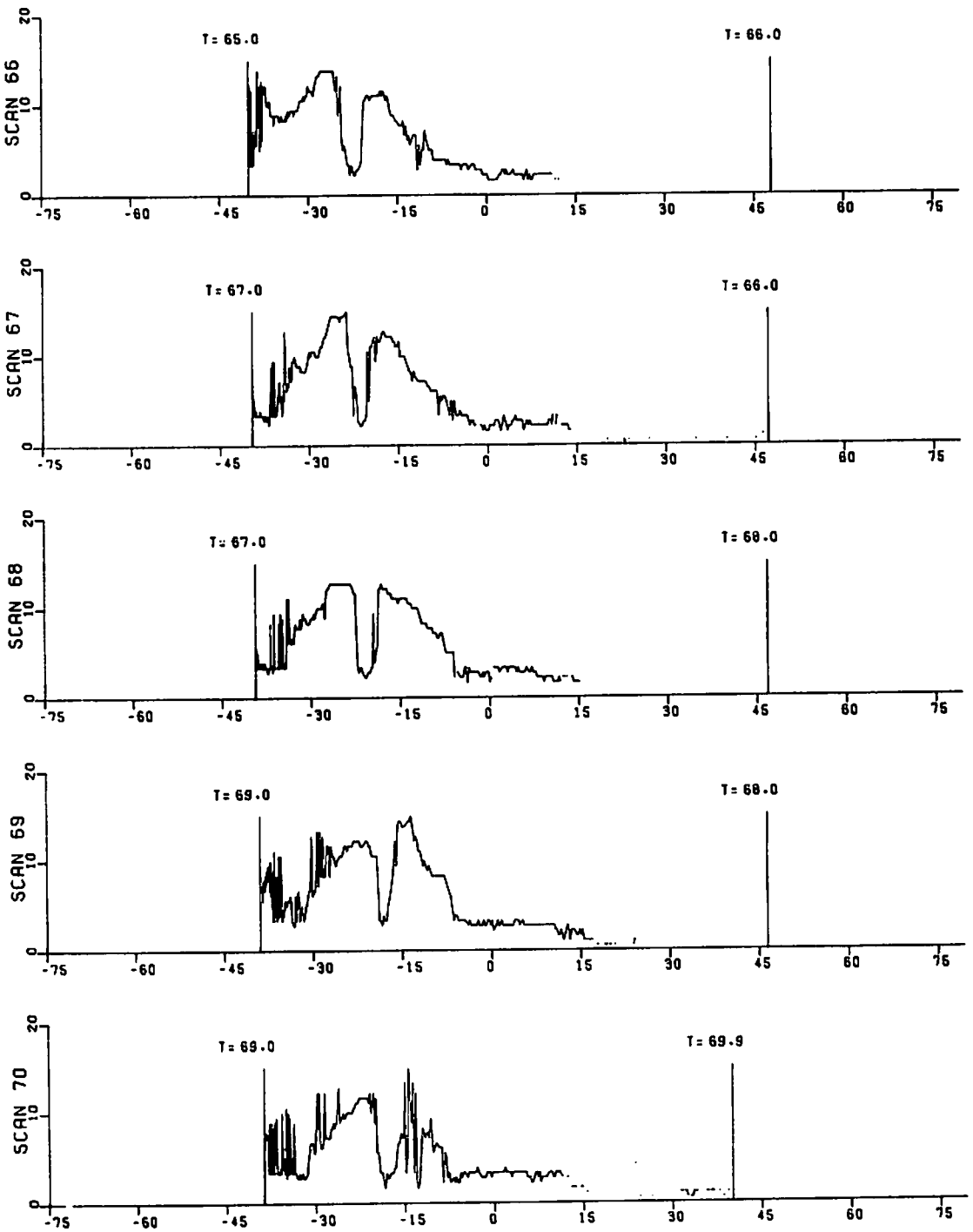

ARC DISTANCE (meters)

FIGURE 129. (CONTINUED)

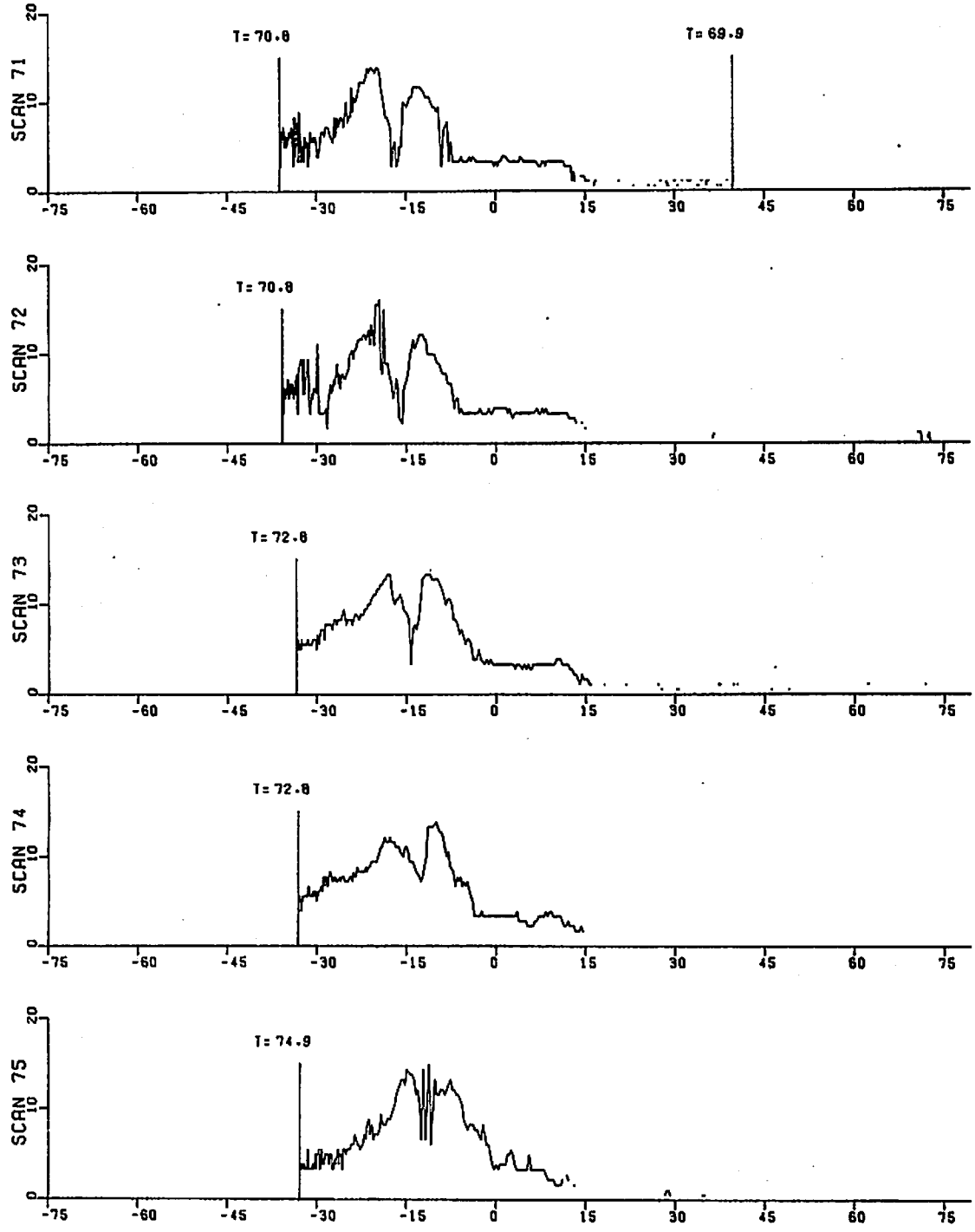

ARC DISTANCE (meters)

FIGURE 129. (CONTINUED)

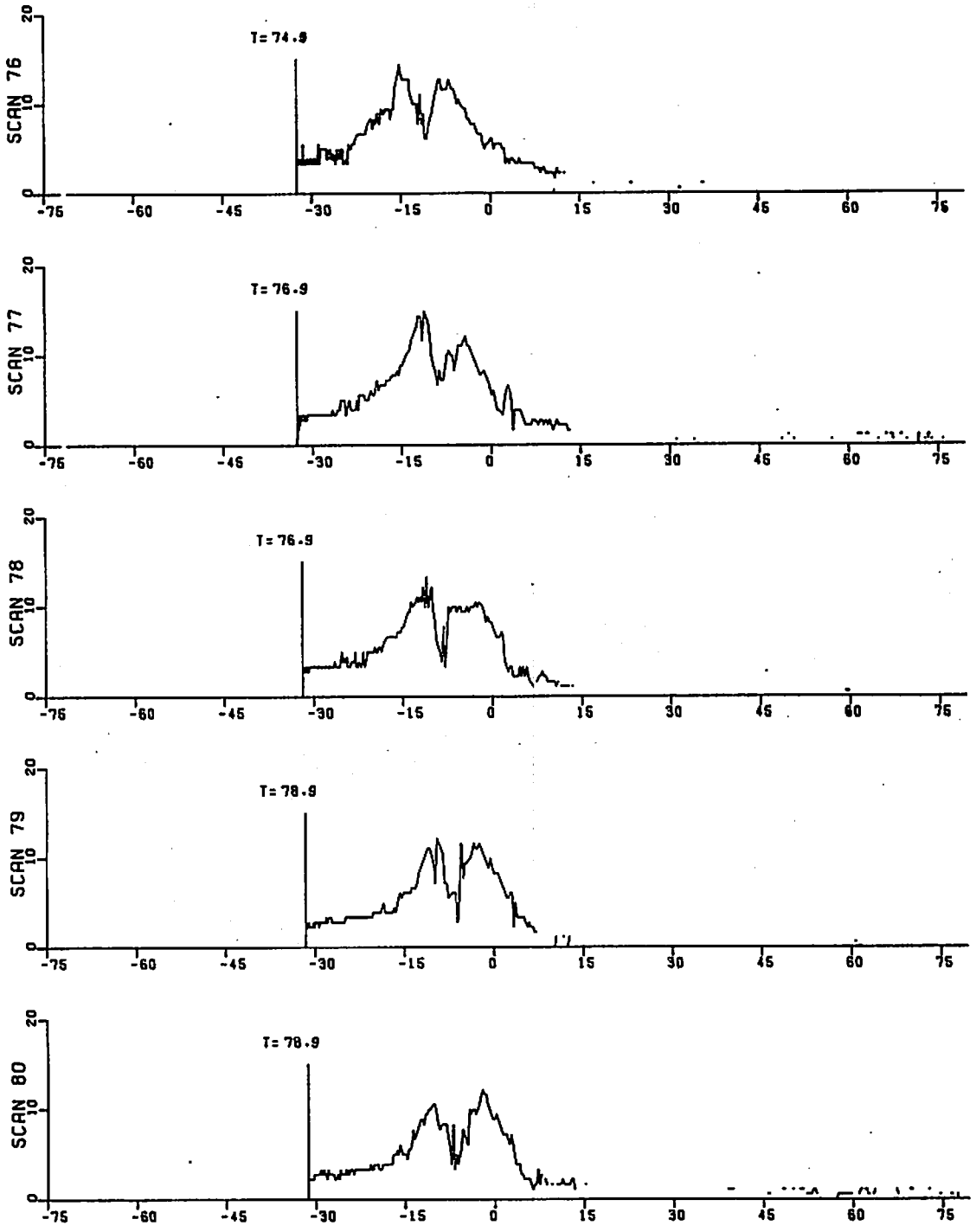

ARC DISTANCE (meters)

FIGURE 129. (CONTINUED)

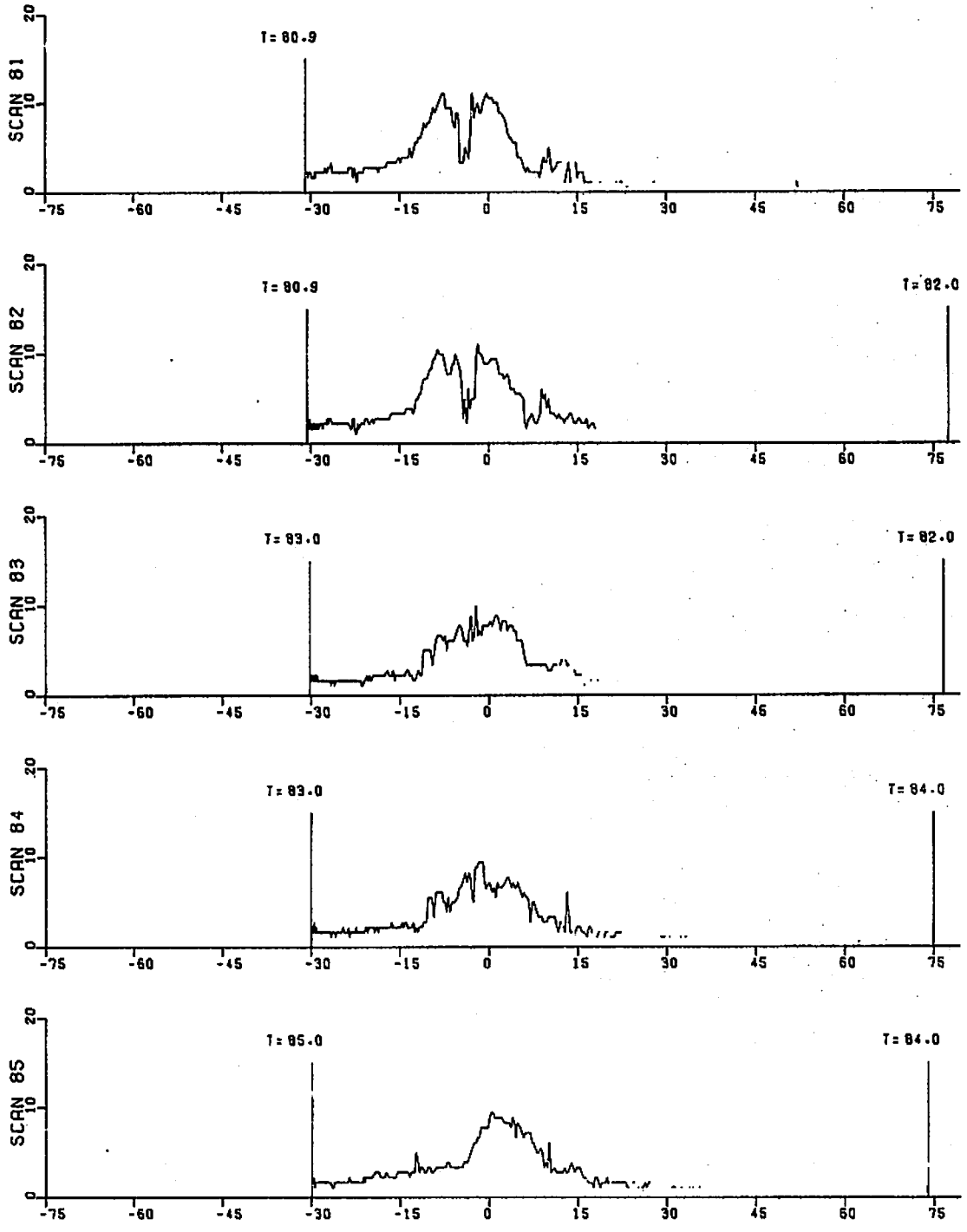

ARC DISTANCE (meters)

FIGURE 129. (CONTINUED)

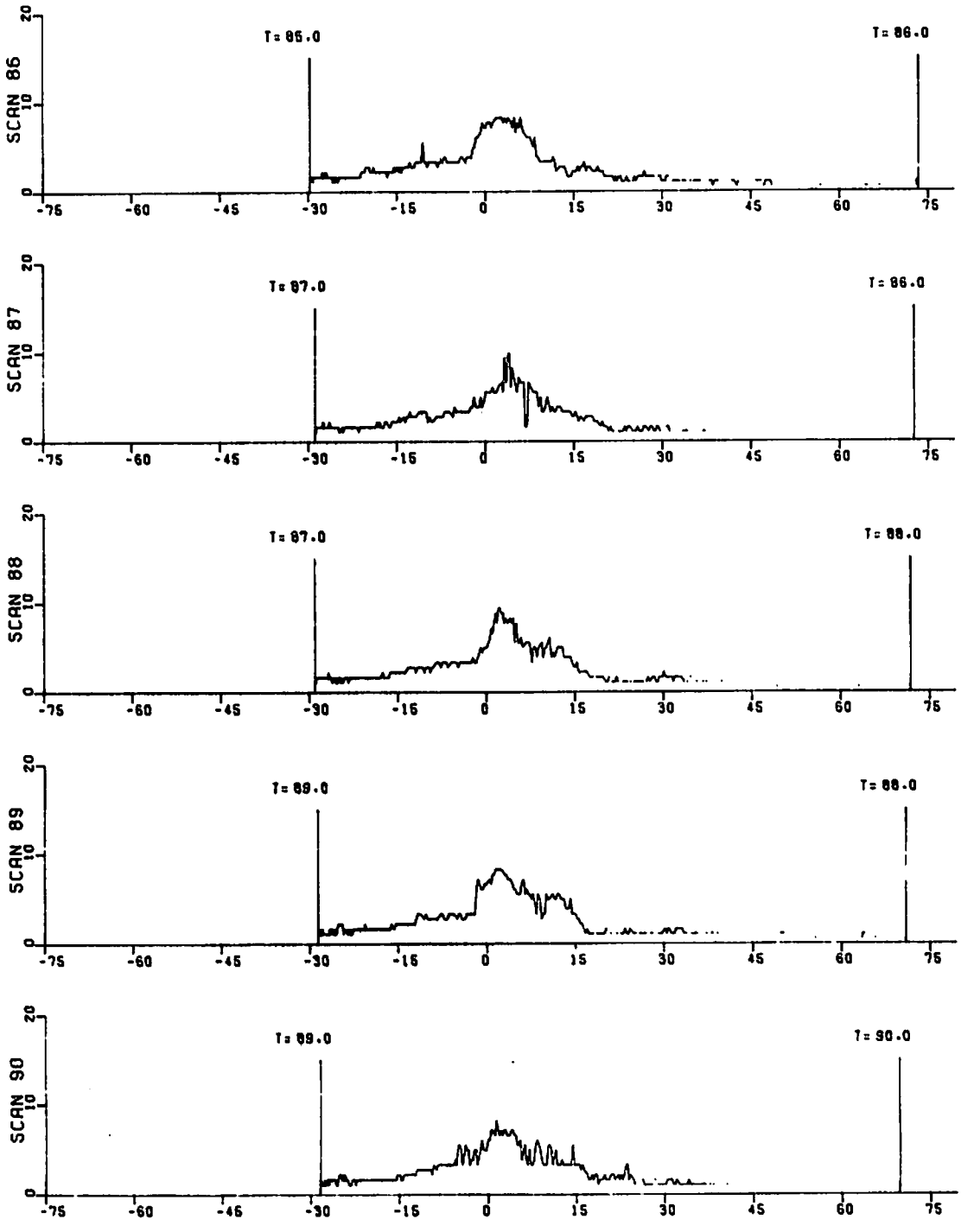

ARC DISTANCE (meters)

FIGURE 129. (CONCLUDED)

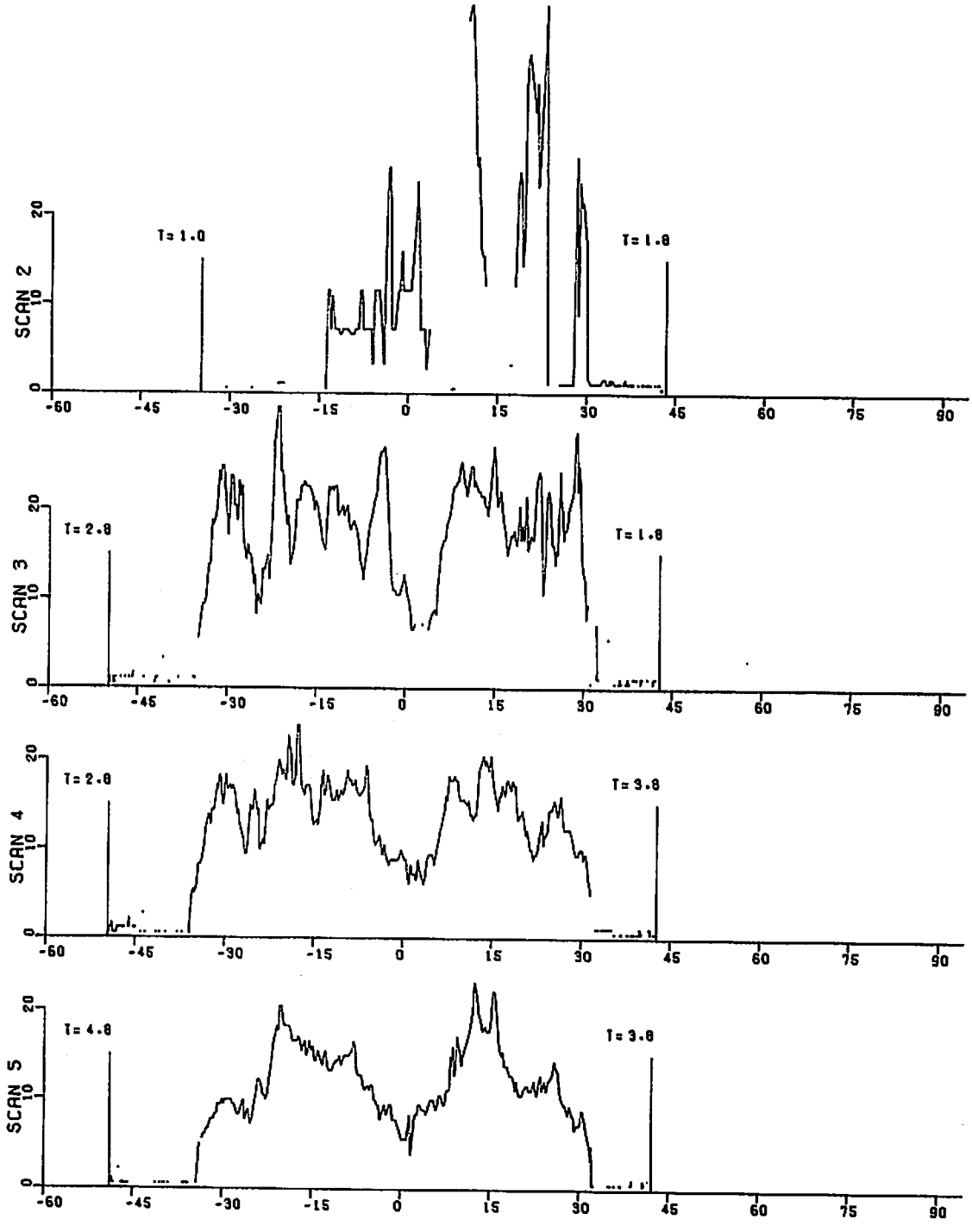

FIGURE 130. VELOCITY PROFILES FOR RUN 11

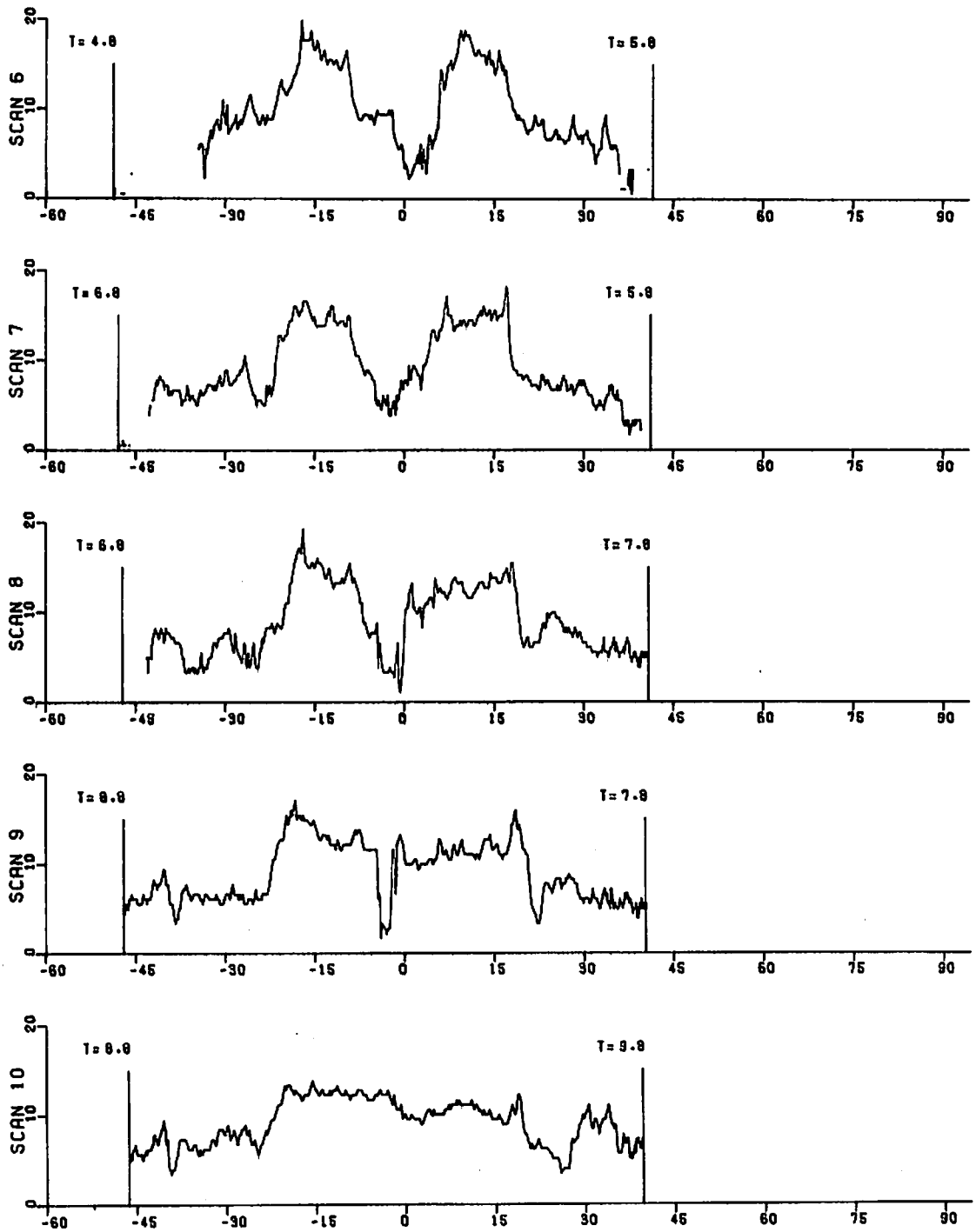

ARC DISTANCE (meters)

FIGURE 130. (CONTINUED)

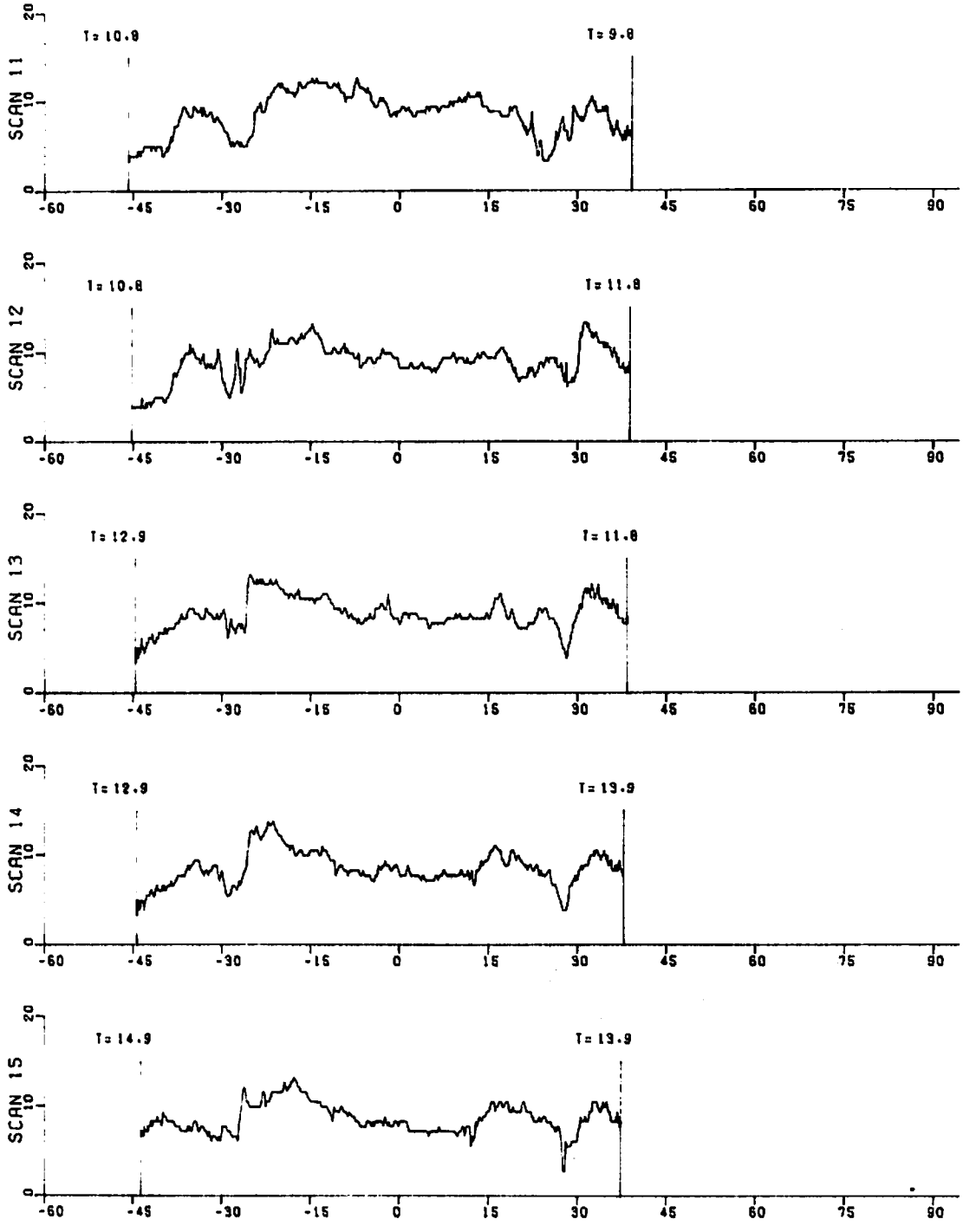

ARC DISTANCE (meters)

FIGURE 130. (CONTINUED)

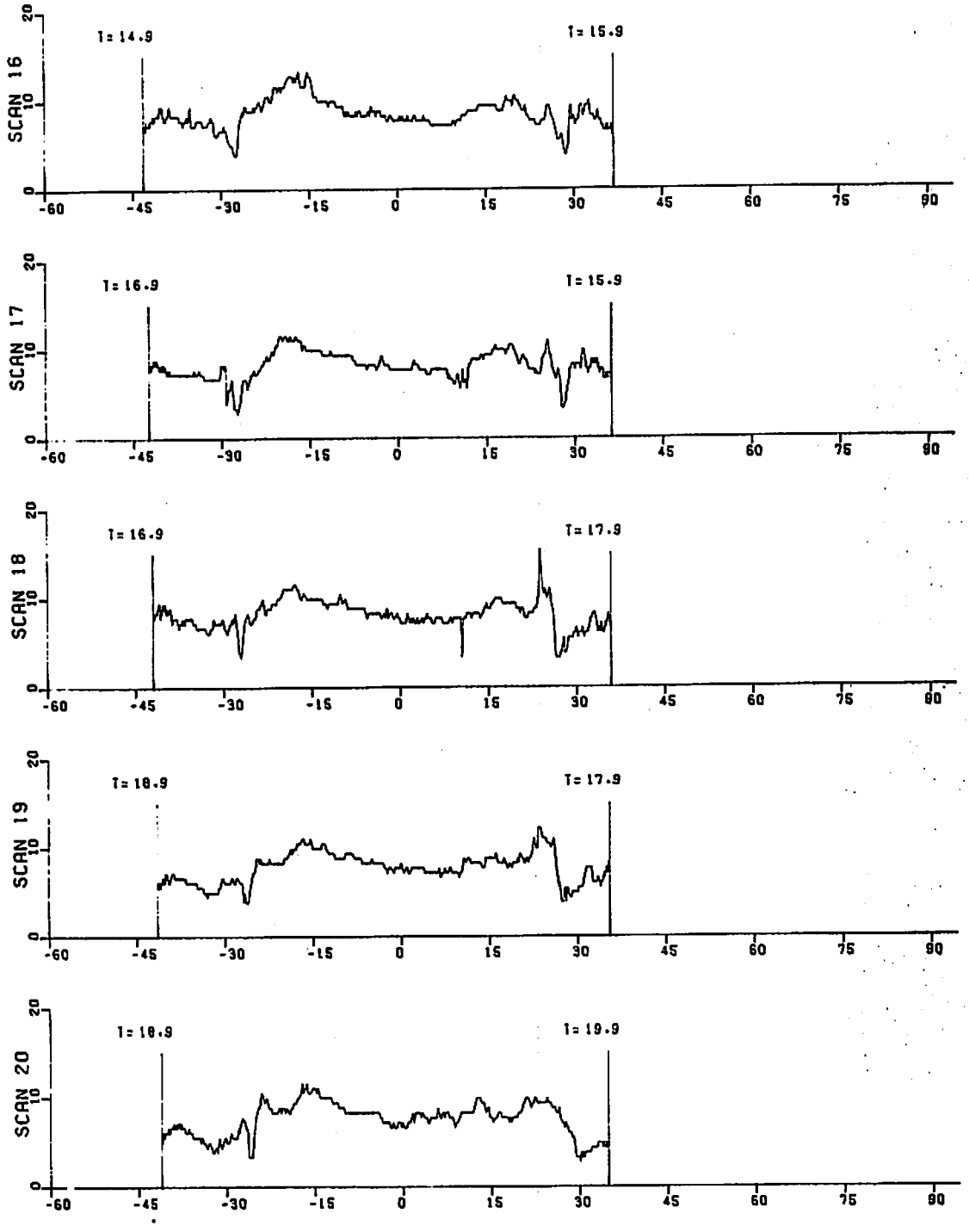

ARC DISTANCE (meters)

FIGURE 130. (CONTINUED)

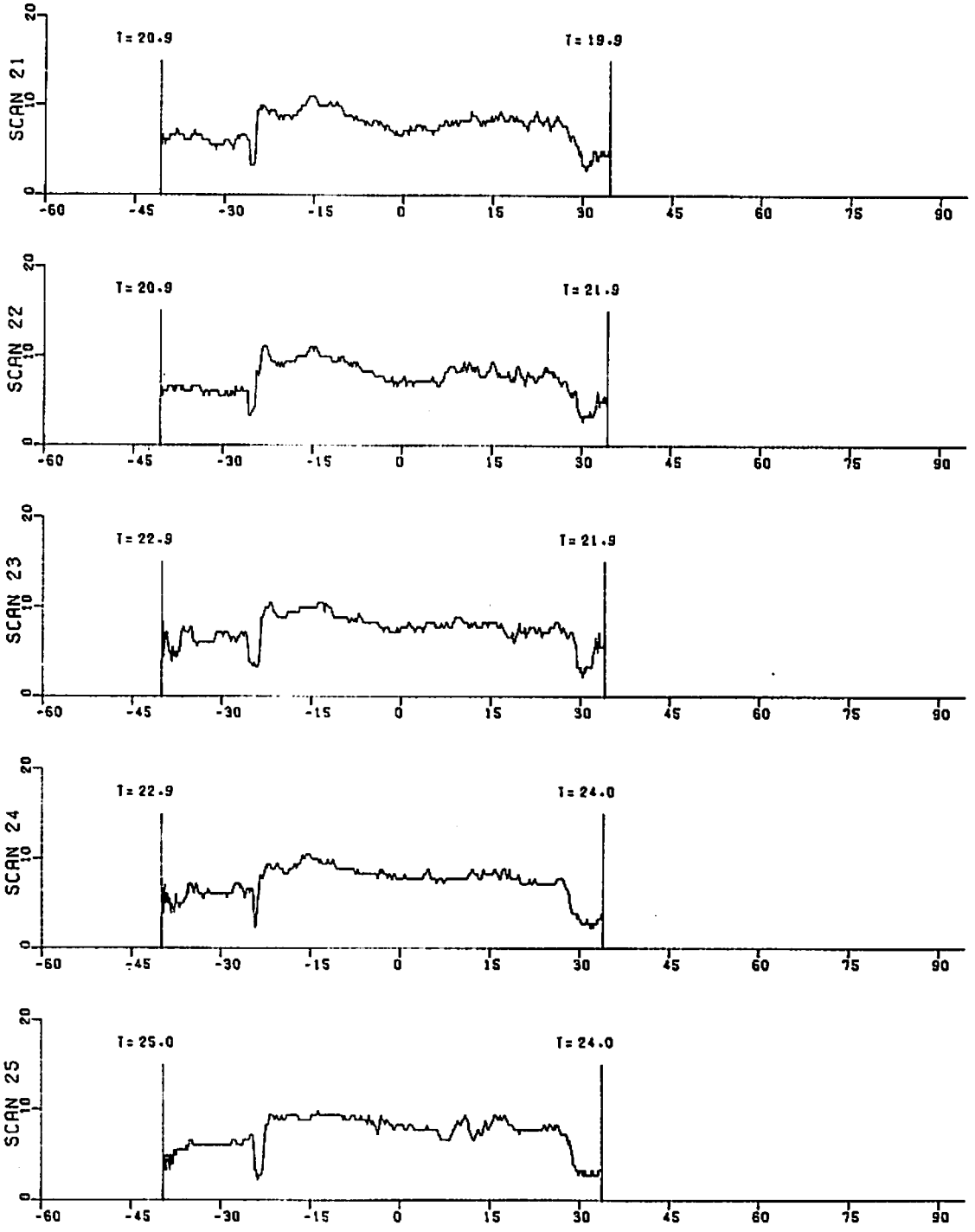

ARC DISTANCE (meters)

FIGURE 130. (CONTINUED)

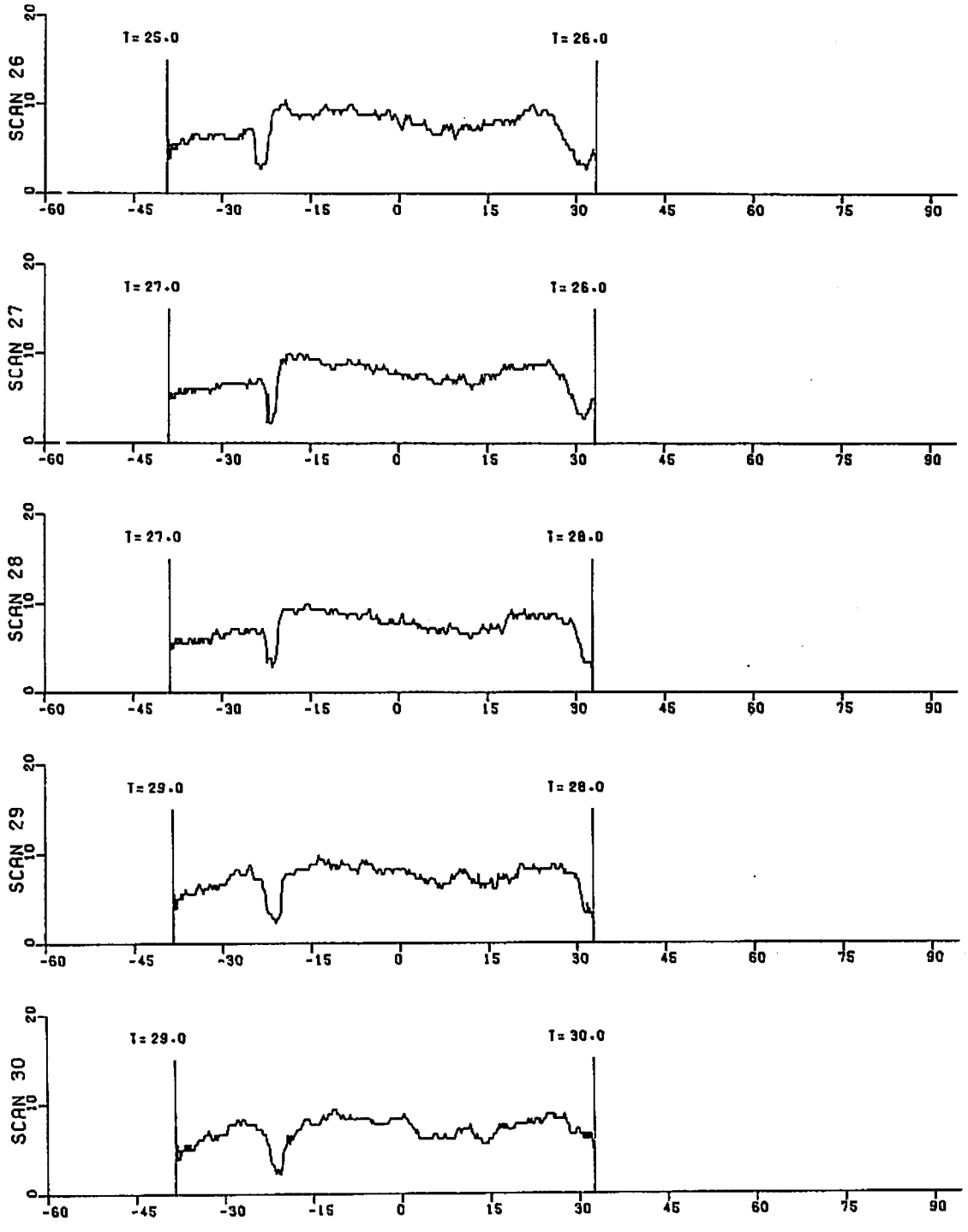

FIGURE 130. (CONTINUED)

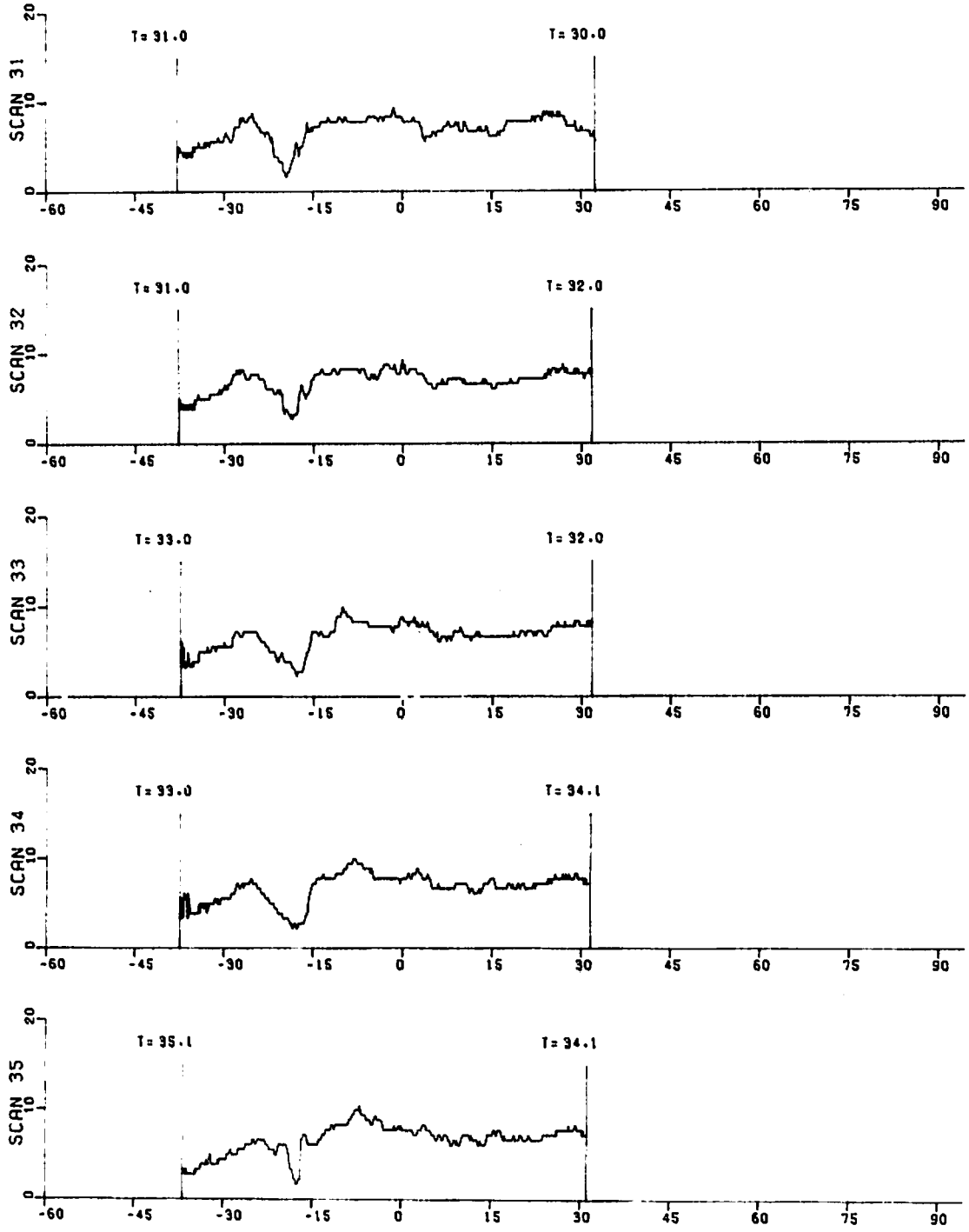

ARC DISTANCE (meters)

FIGURE 130. (CONTINUED)

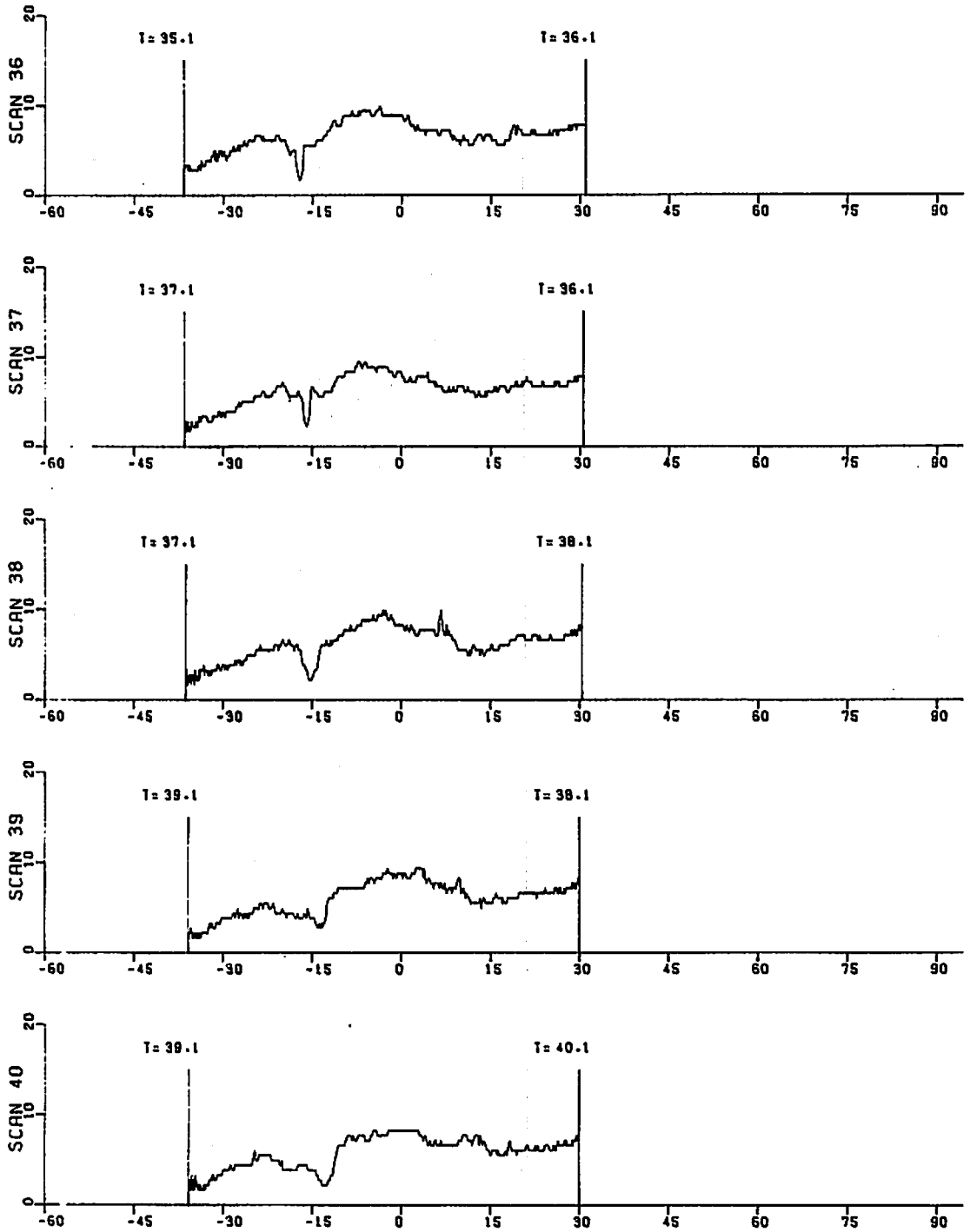

ARC DISTANCE (meters)

FIGURE 130. (CONTINUED)

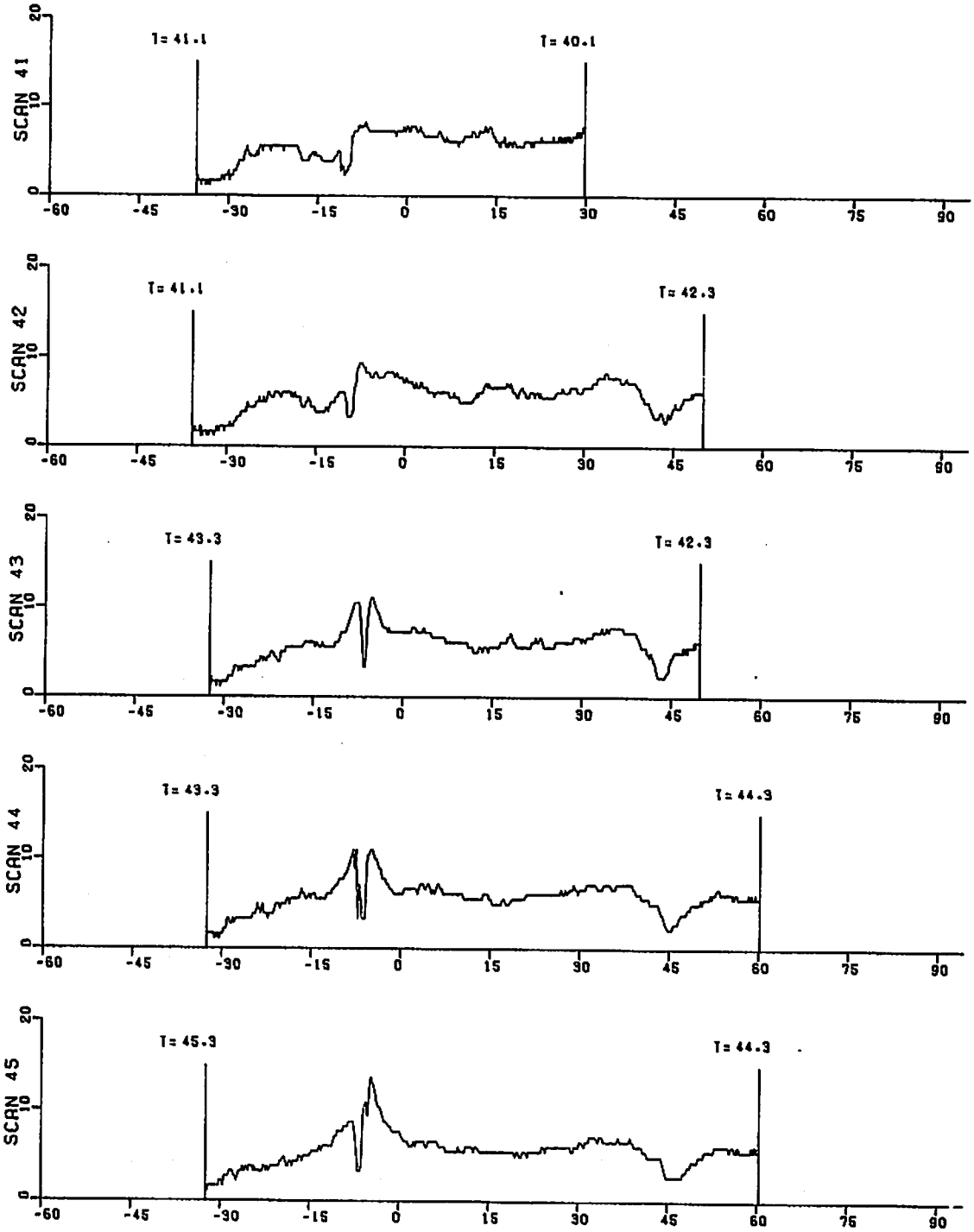

ARC DISTANCE (meters)

FIGURE 130. (CONTINUED)

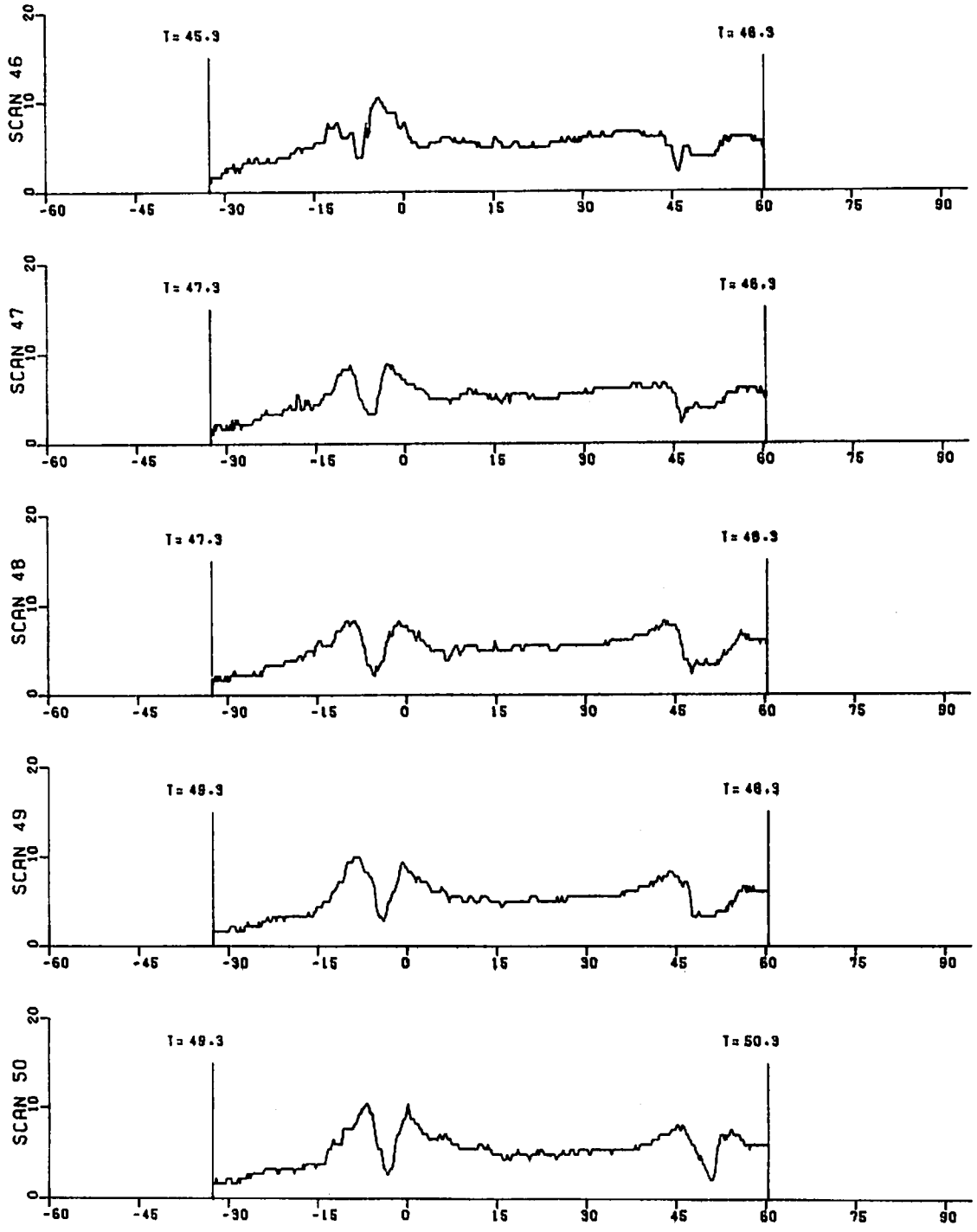

ARC DISTANCE (meters)

FIGURE 130. (CONTINUED)

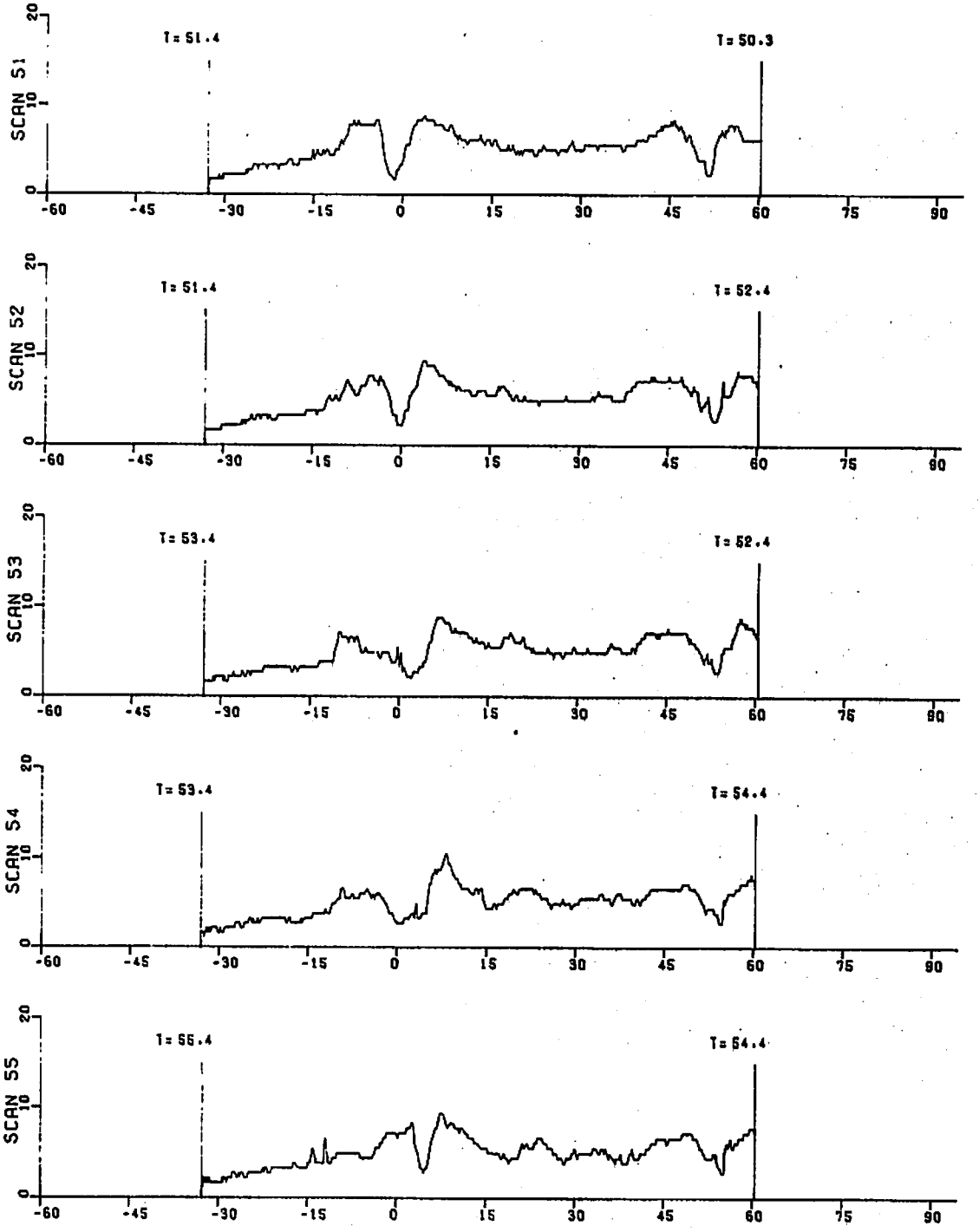

ARC DISTANCE (meters)

FIGURE 130. (CONTINUED)

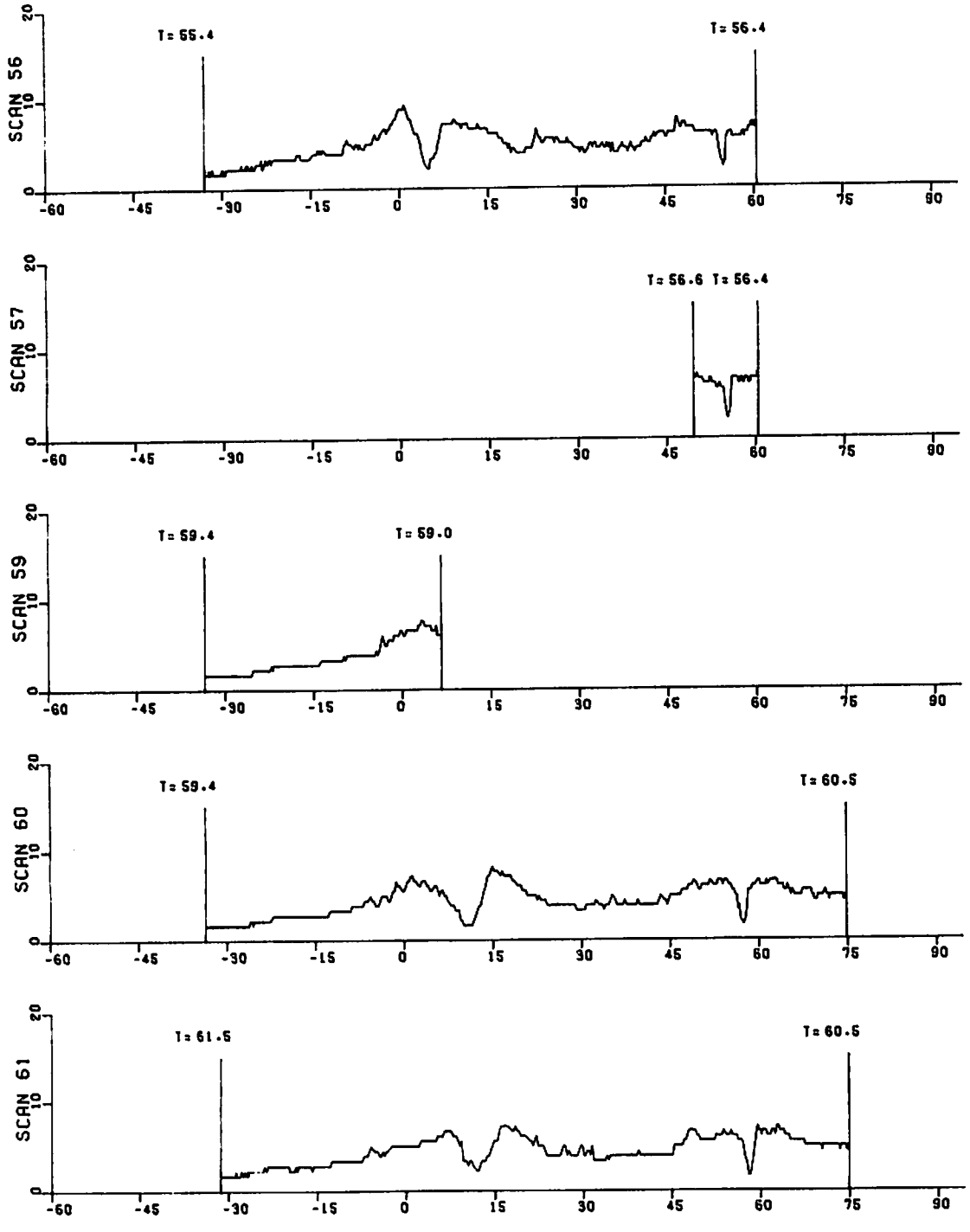

ARC DISTANCE (meters)

FIGURE 130. (CONTINUED)

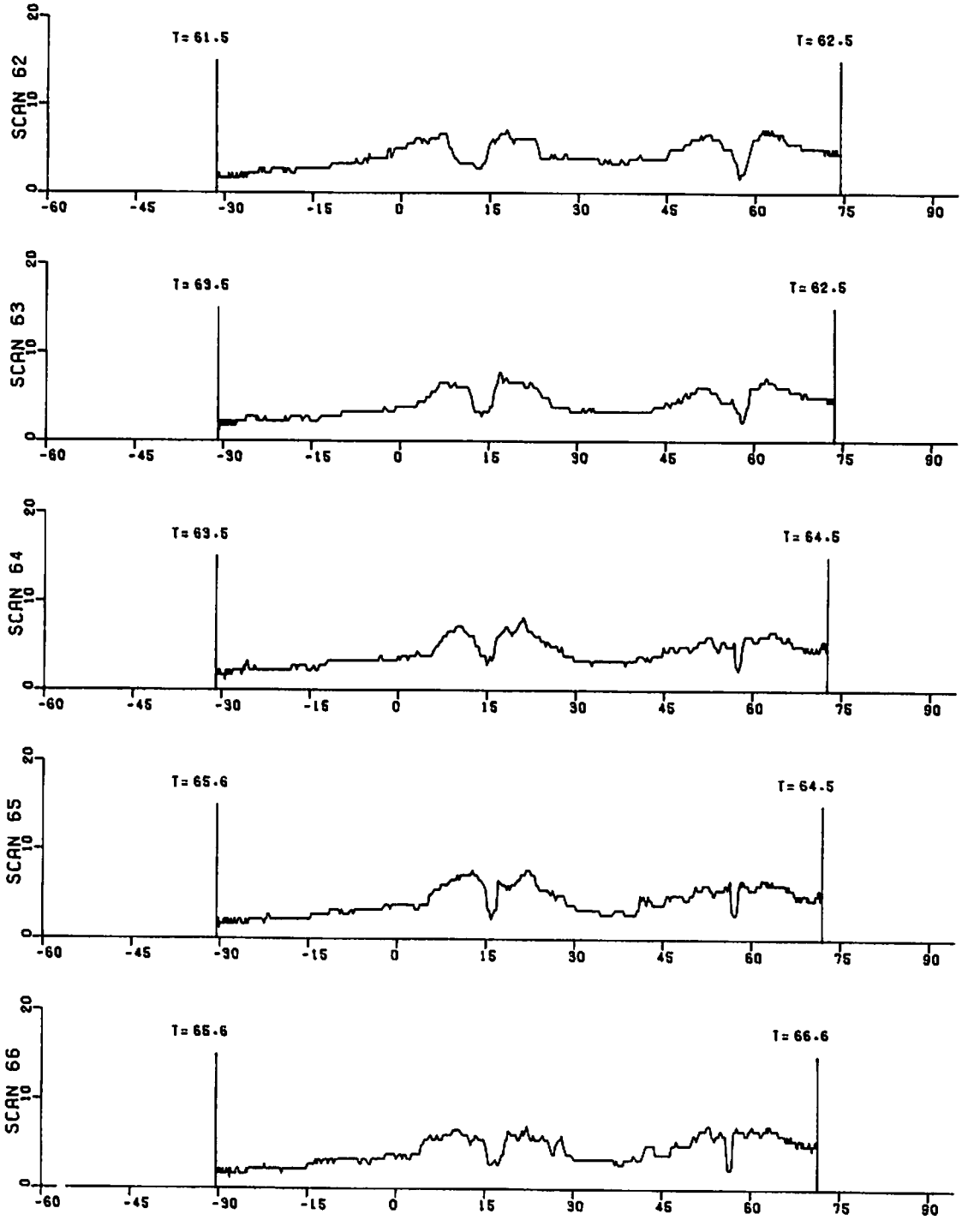

ARC DISTANCE (meters)

FIGURE 130. (CONTINUED)

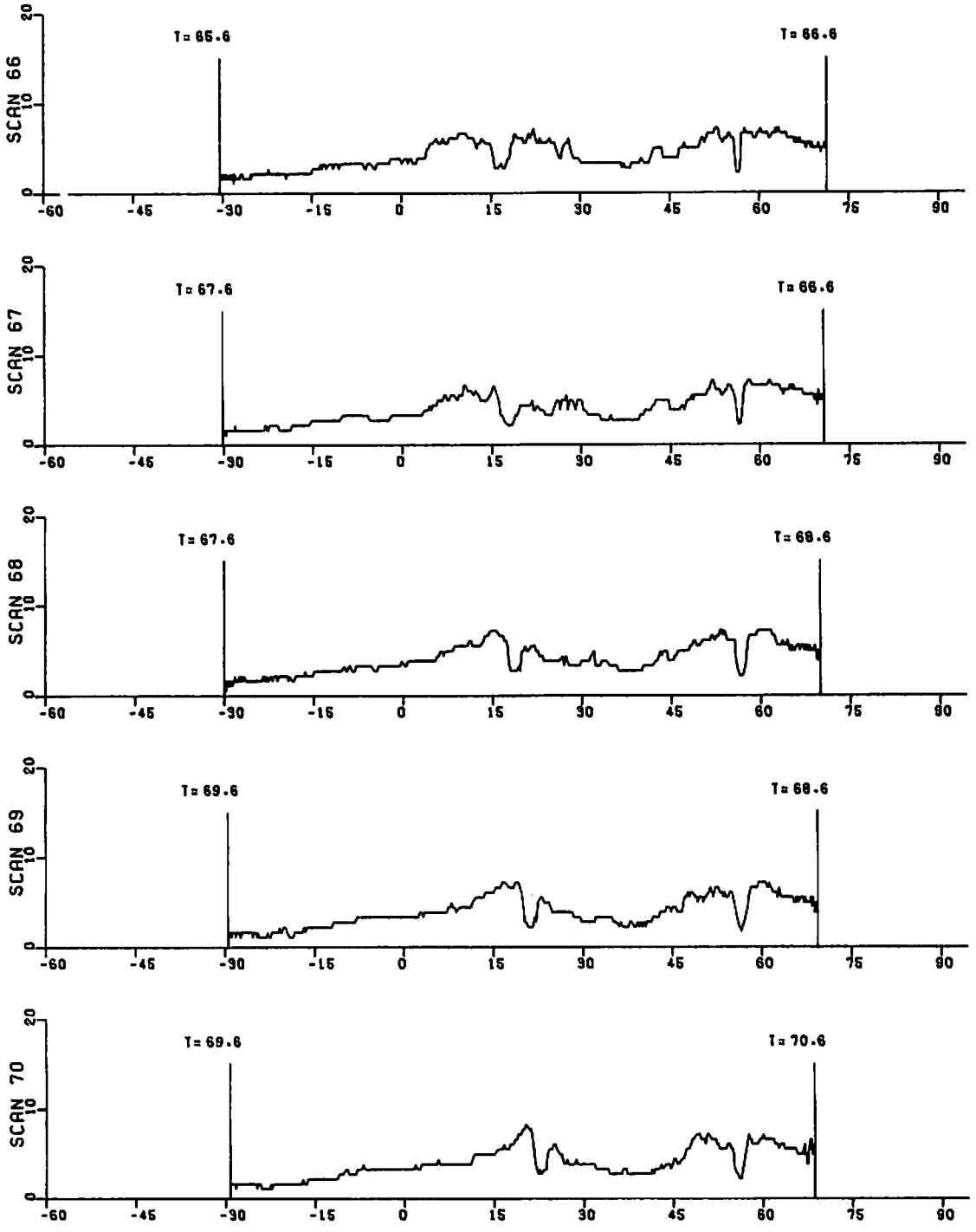

FIGURE 130. (CONTINUED)

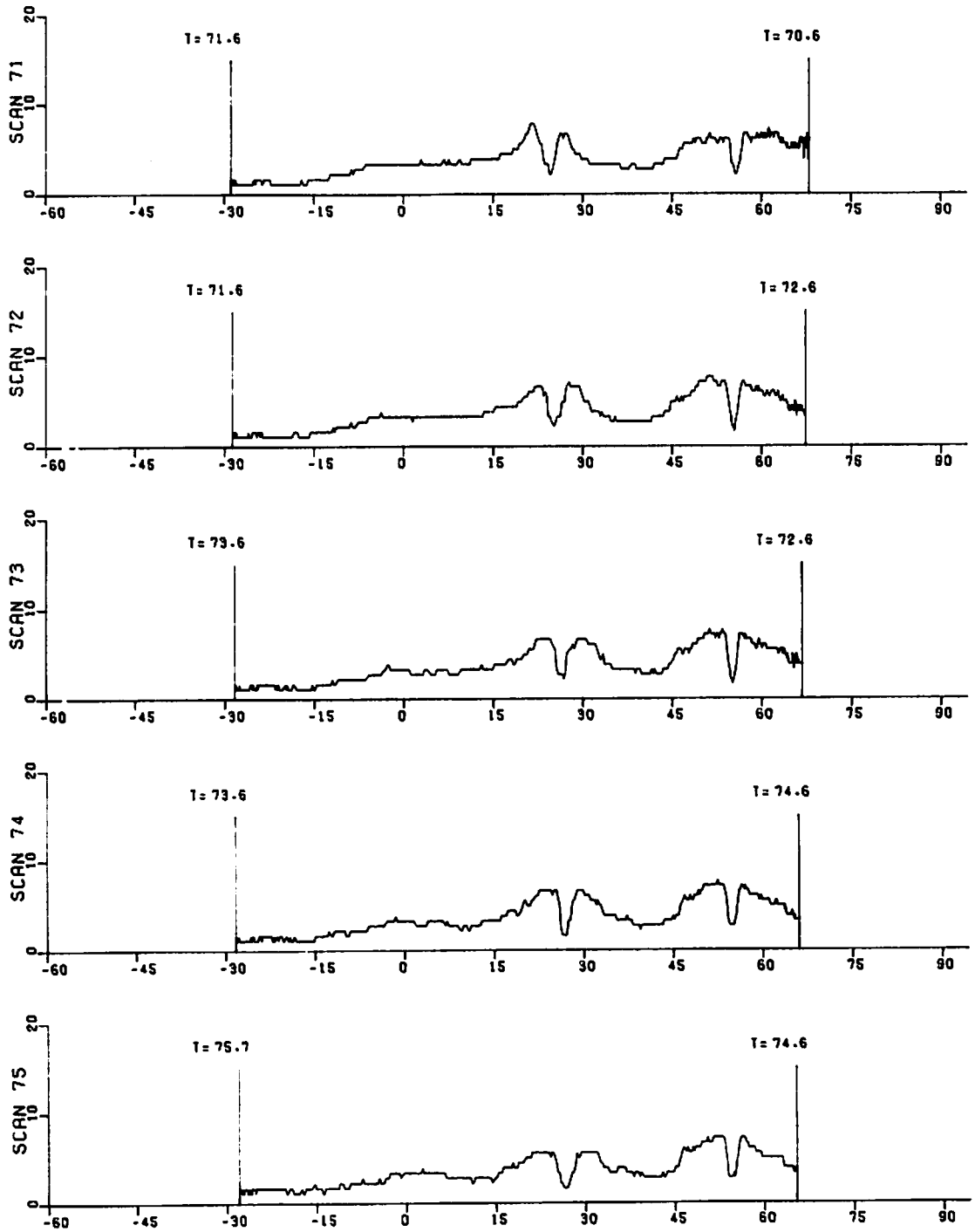

FIGURE 130. (CONTINUED)

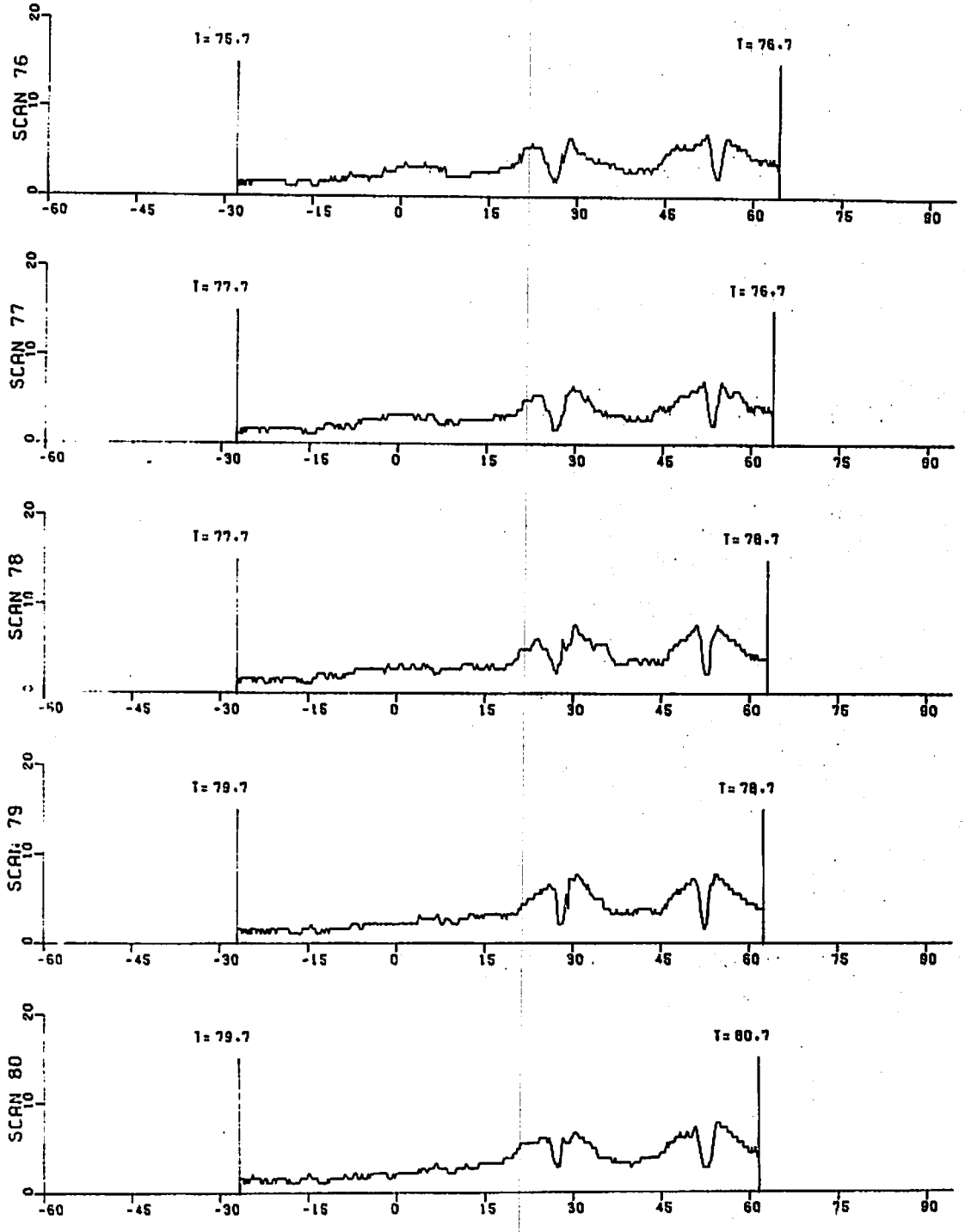

FIGURE 130. (CONTINUED)

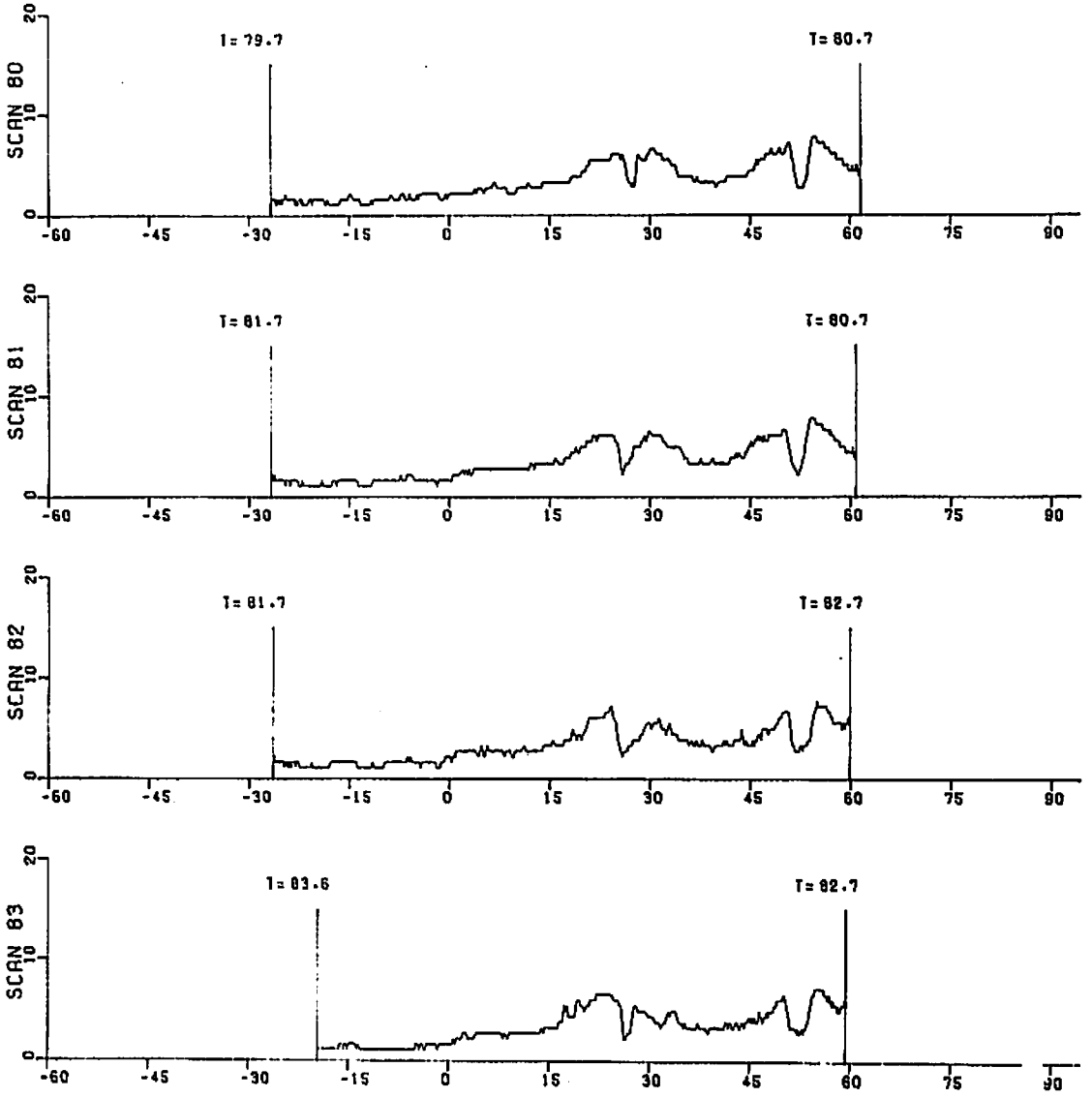

ARC DISTANCE (meters)

FIGURE 130. (CONCLUDED)

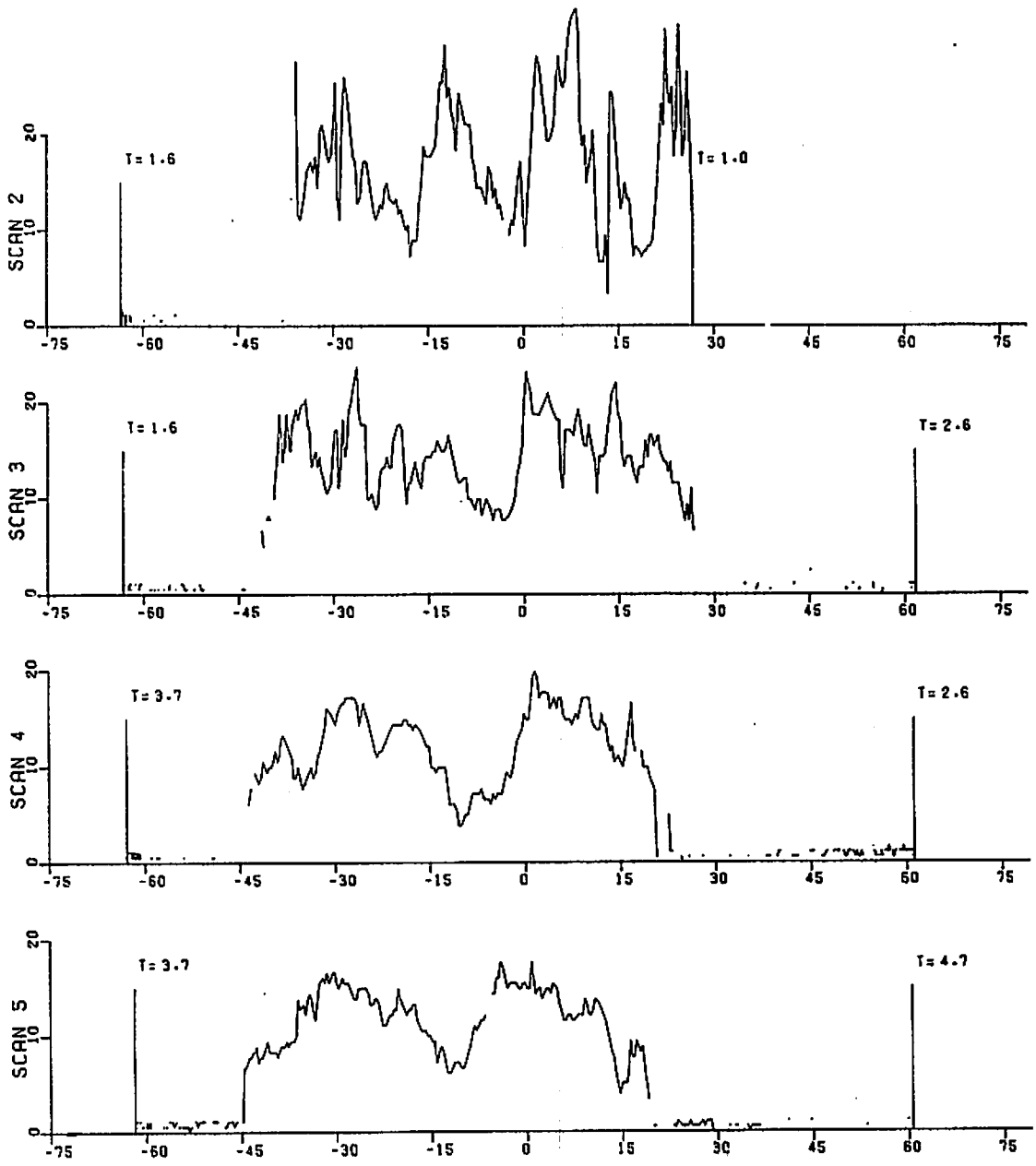

FIGURE 131. VELOCITY PROFILES FOR RUN 12

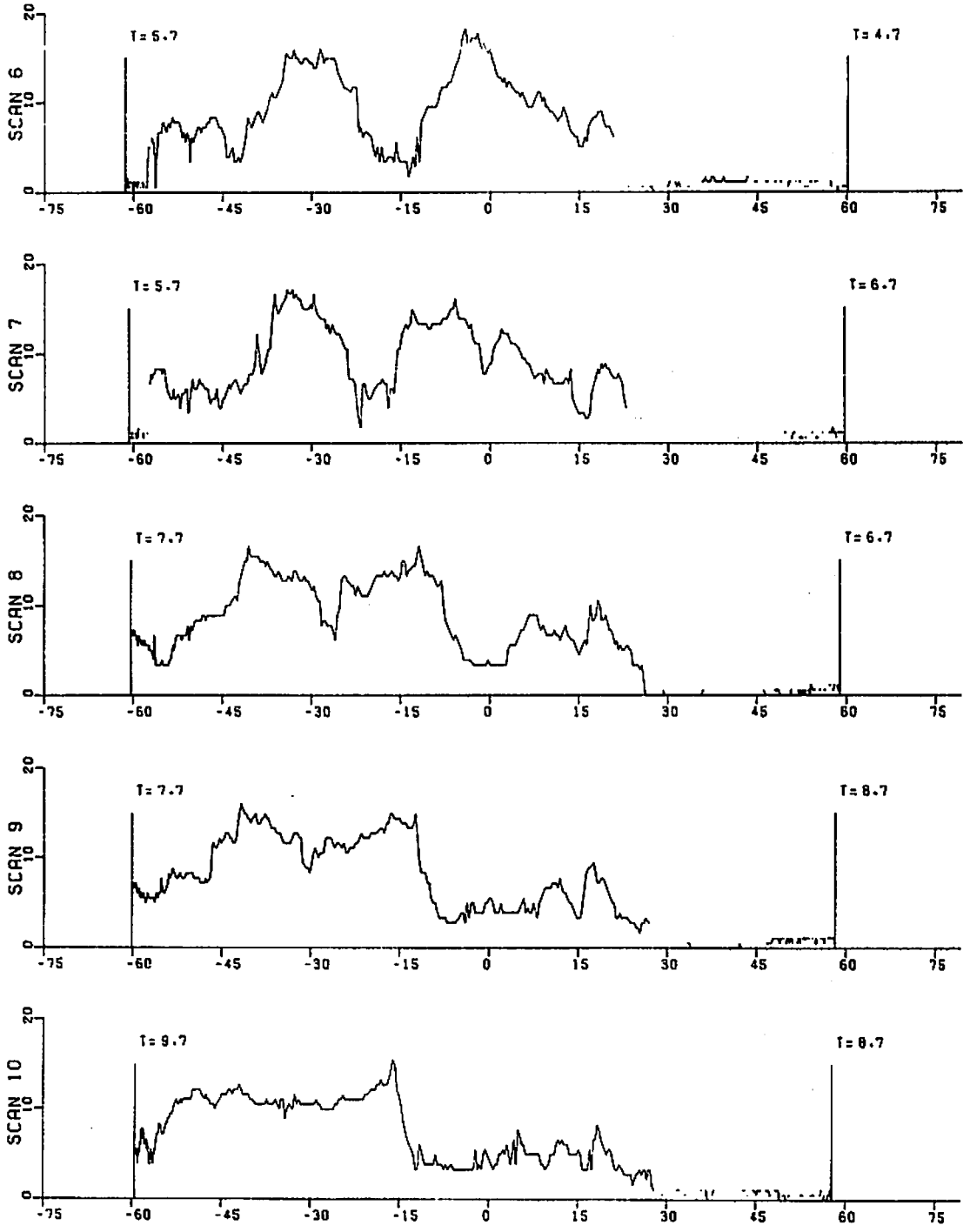

FIGURE 131. (CONTINUED)

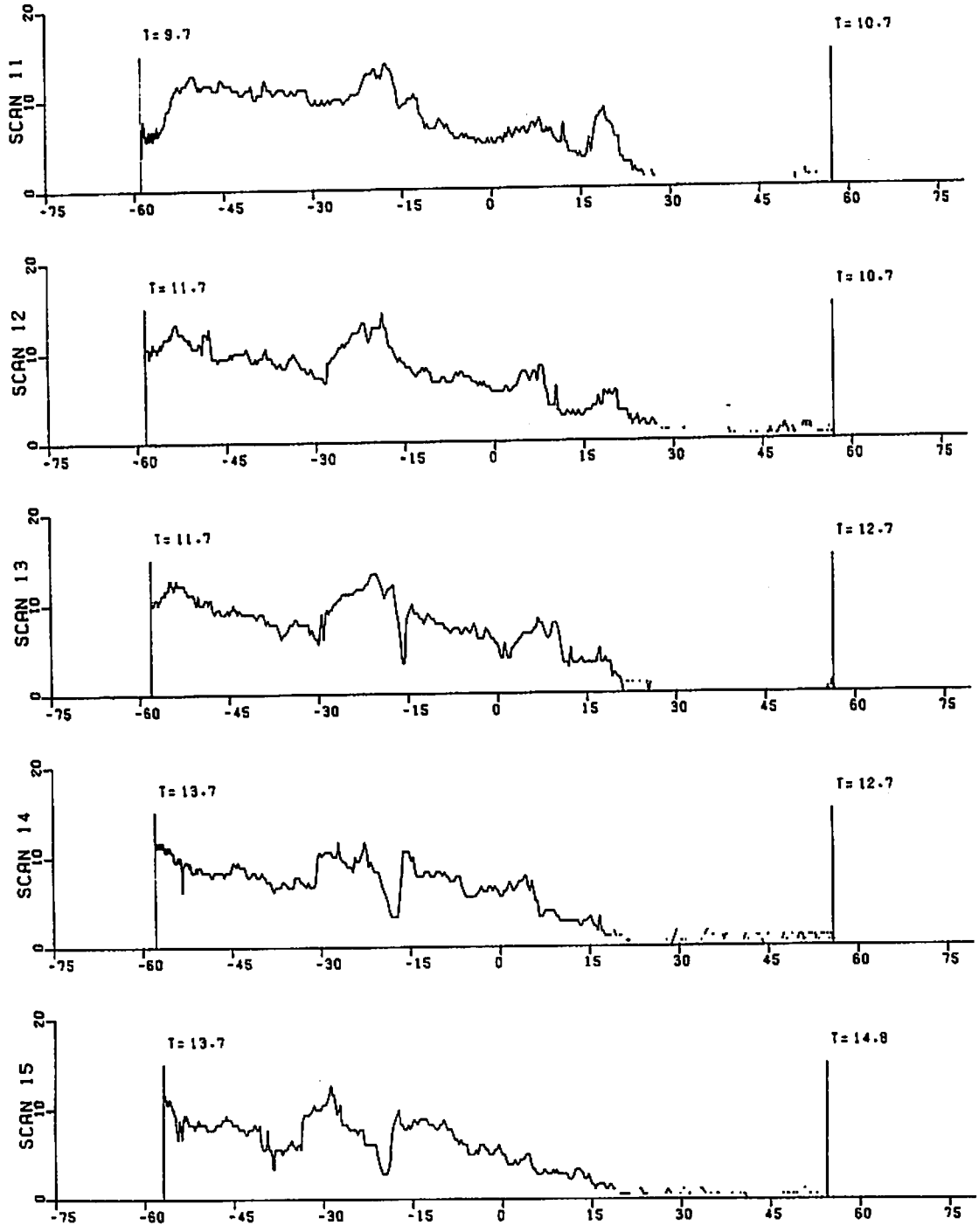

ARC DISTANCE (meters)

FIGURE 131. (CONTINUED)

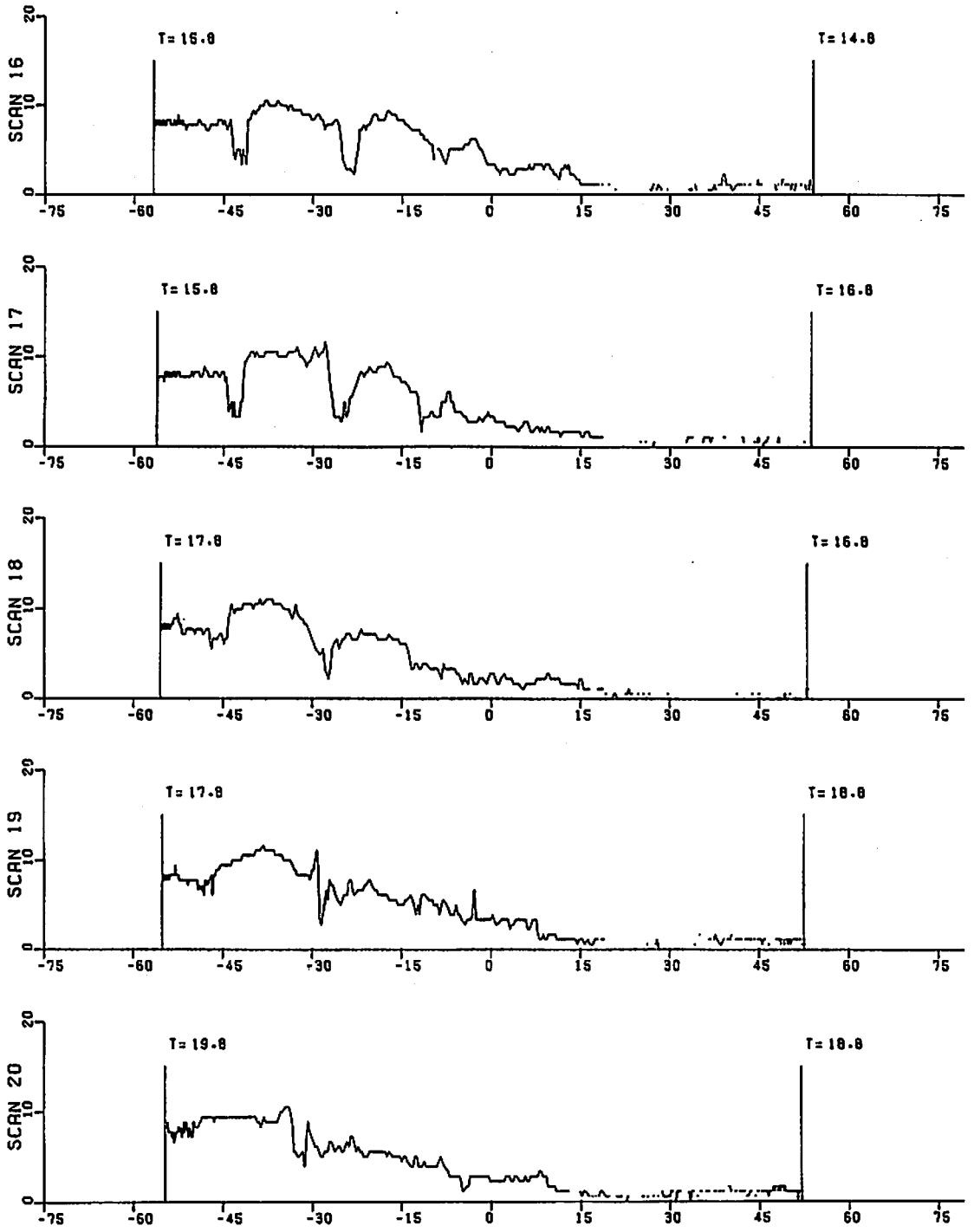

FIGURE 131. (CONTINUED)

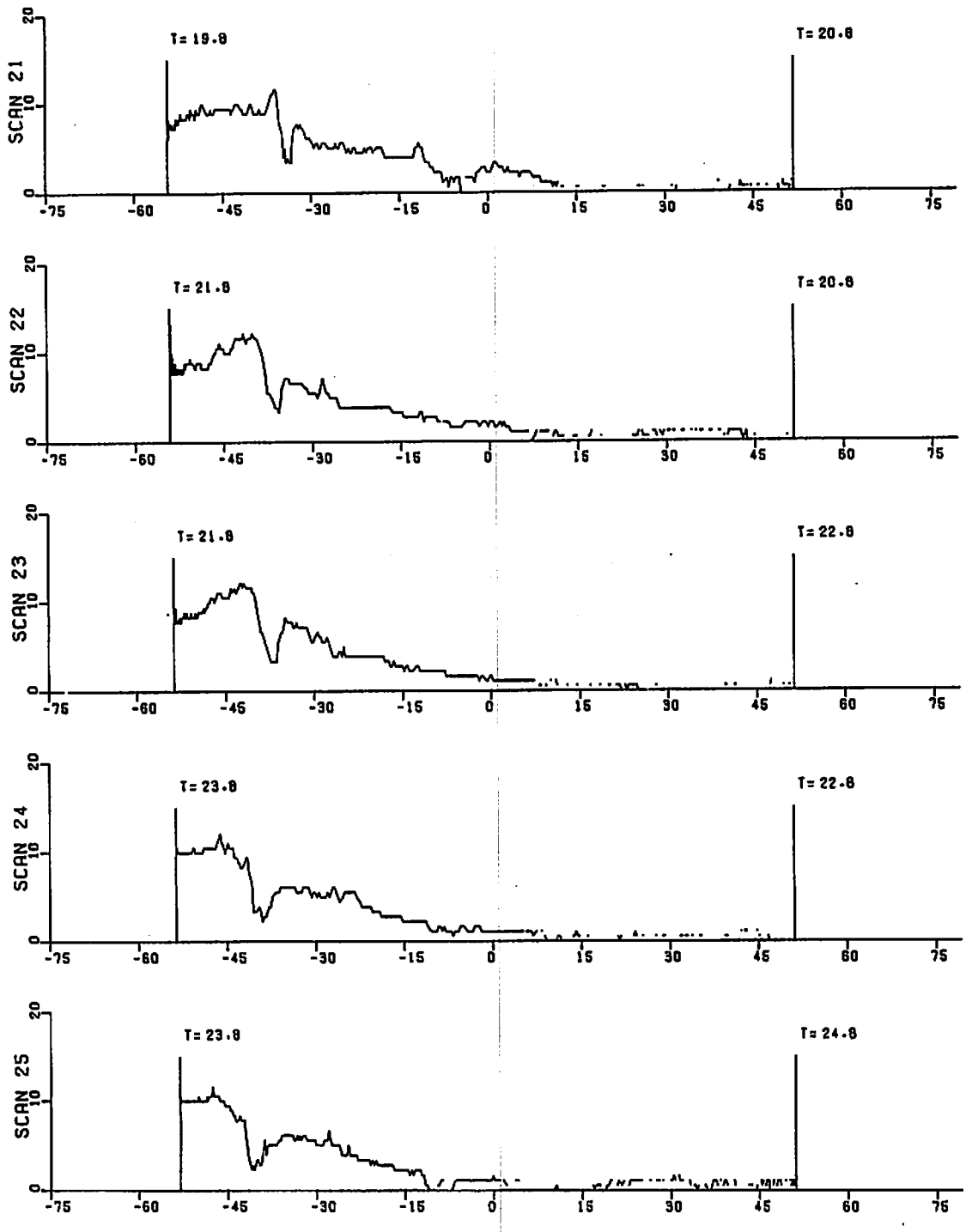

ARC DISTANCE (meters)

FIGURE 131. (CONTINUED)

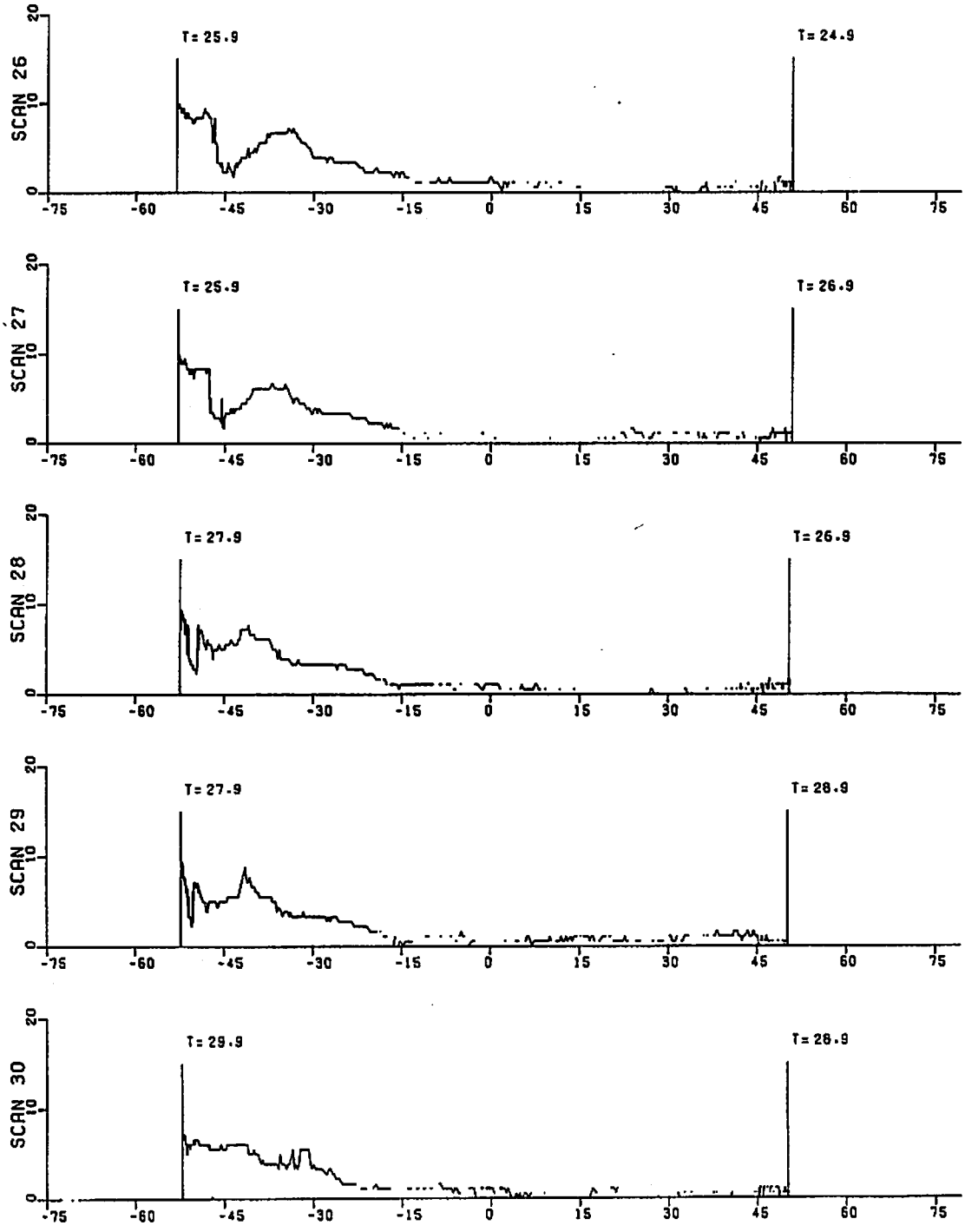

FIGURE 131. (CONCLUDED)

APPENDIX E
MONOSTATIC ACOUSTIC VORTEX SENSING SYSTEM DATA

This appendix presents three types of MAVSS plots: tracking information (as in Figure 68), line-integral information (as in Figure 76), and vortex-profile information (as in Figures 72 and 73). The nature of these plots is described in the text of Section 7. The tracking data are shown first for all runs with useful MAVSS data. The line-integral data are shown in the second section for all antennas where the influence of the wake has been noted. The two types of profile data are shown in the third section for almost all cases where a vortex passed over an antenna. Several cases were lost because the data could not be fitted by the least-squares fitting algorithm, usually because of asymmetric decay or noise. A couple of cases were lost because of data-entry errors.

E.1 VORTEX-TRACKING PLOTS

The following tracking plots (similar to Figure 68 in the body of the report) show the heights of the two vortices and their lateral positions at the location of the long MAVSS baseline. The data points plotted as circles are the nominal aircraft altitudes. The triangular points are the vortex locations based on photographs. The apex of the triangle points down if the position is extrapolated from adjacent longitudinal positions. The squares and diamonds are the arrivals of the vortices at MAVSS antennas based on a visual scan of the data. The crosses and X's are the same positions determined by computer rather than by eye. The multitude of short vertical-line segments are the height of the vortex based on the height of the velocity peak observed at an adjacent MAVSS antenna.

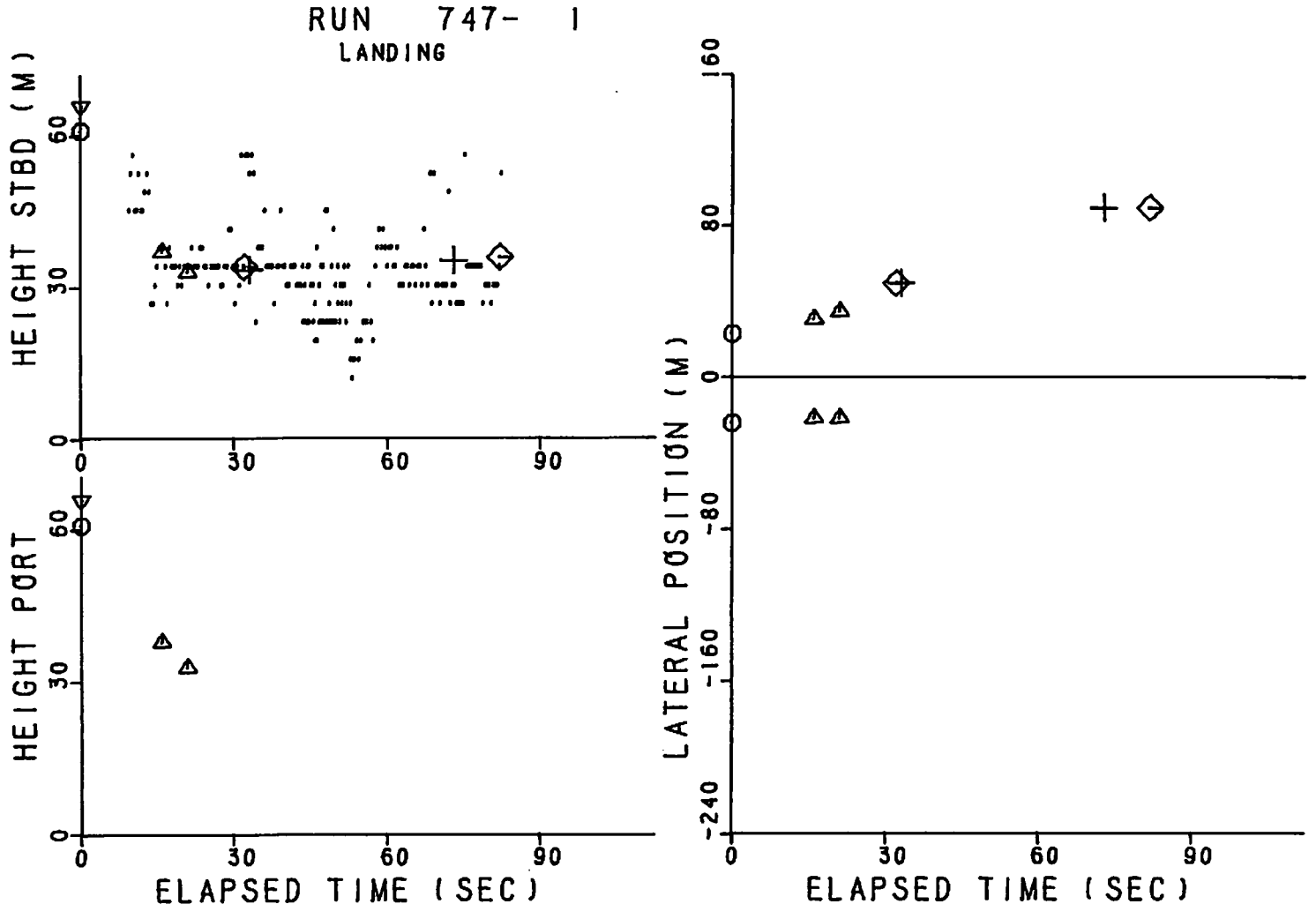

FIGURE 132. VORTEX-TRACKING DATA, RUN 1

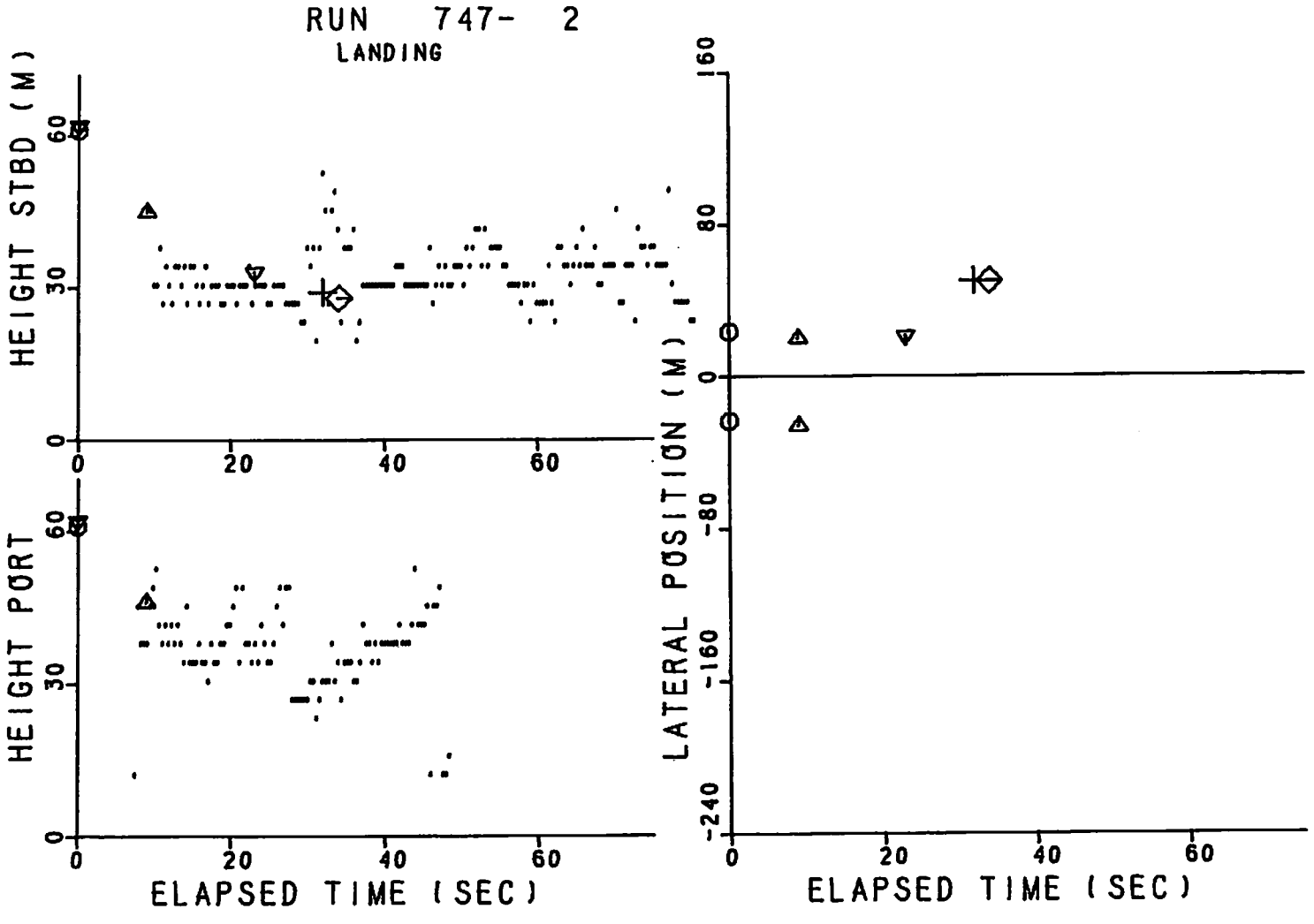

FIGURE 133. VORTEX-TRACKING DATA, RUN 2

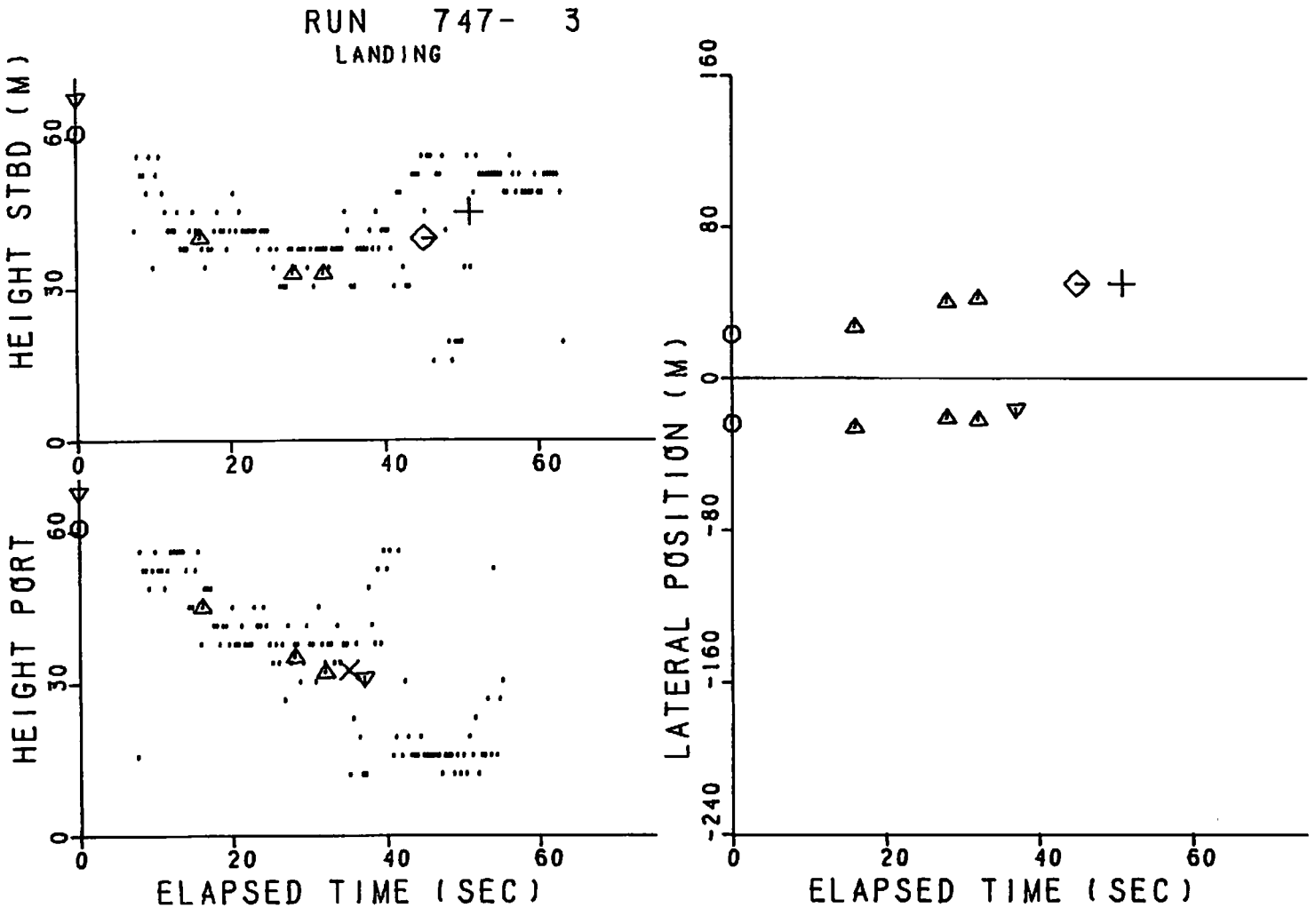

FIGURE 134. VORTEX-TRACKING DATA, RUN 3

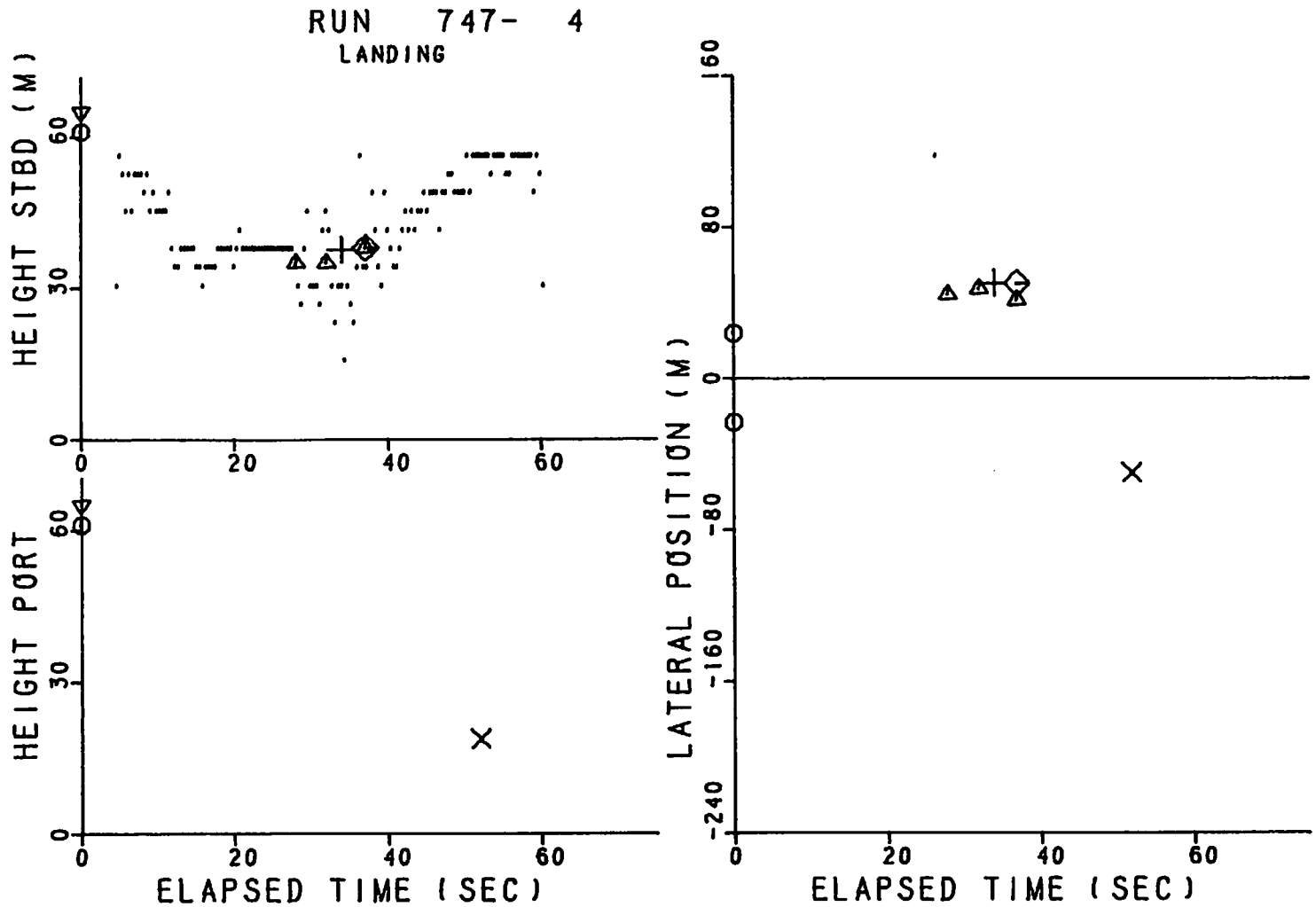

FIGURE 135. VORTEX-TRACKING DATA, RUN 4

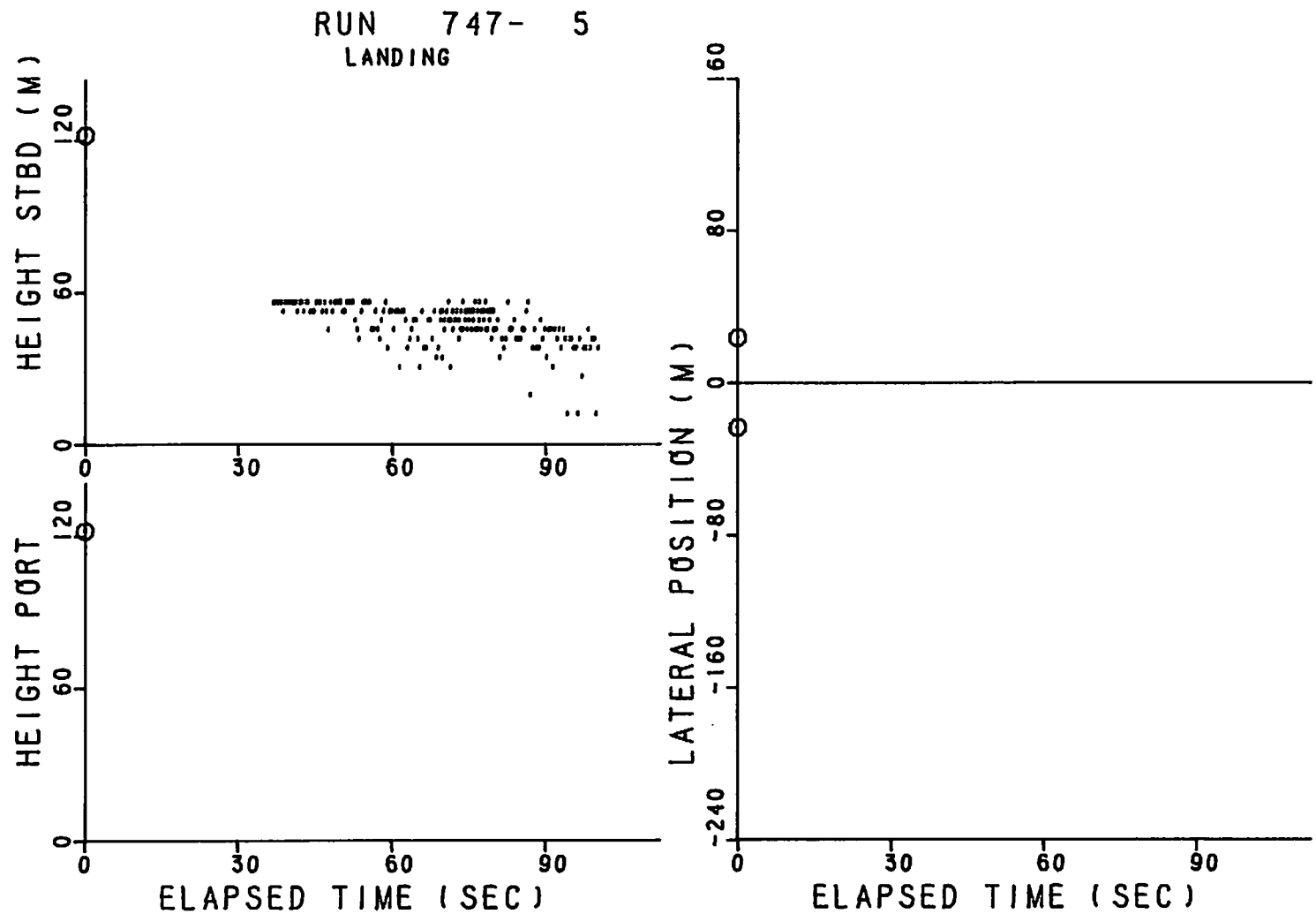

FIGURE 136. VORTEX-TRACKING DATA, RUN 5

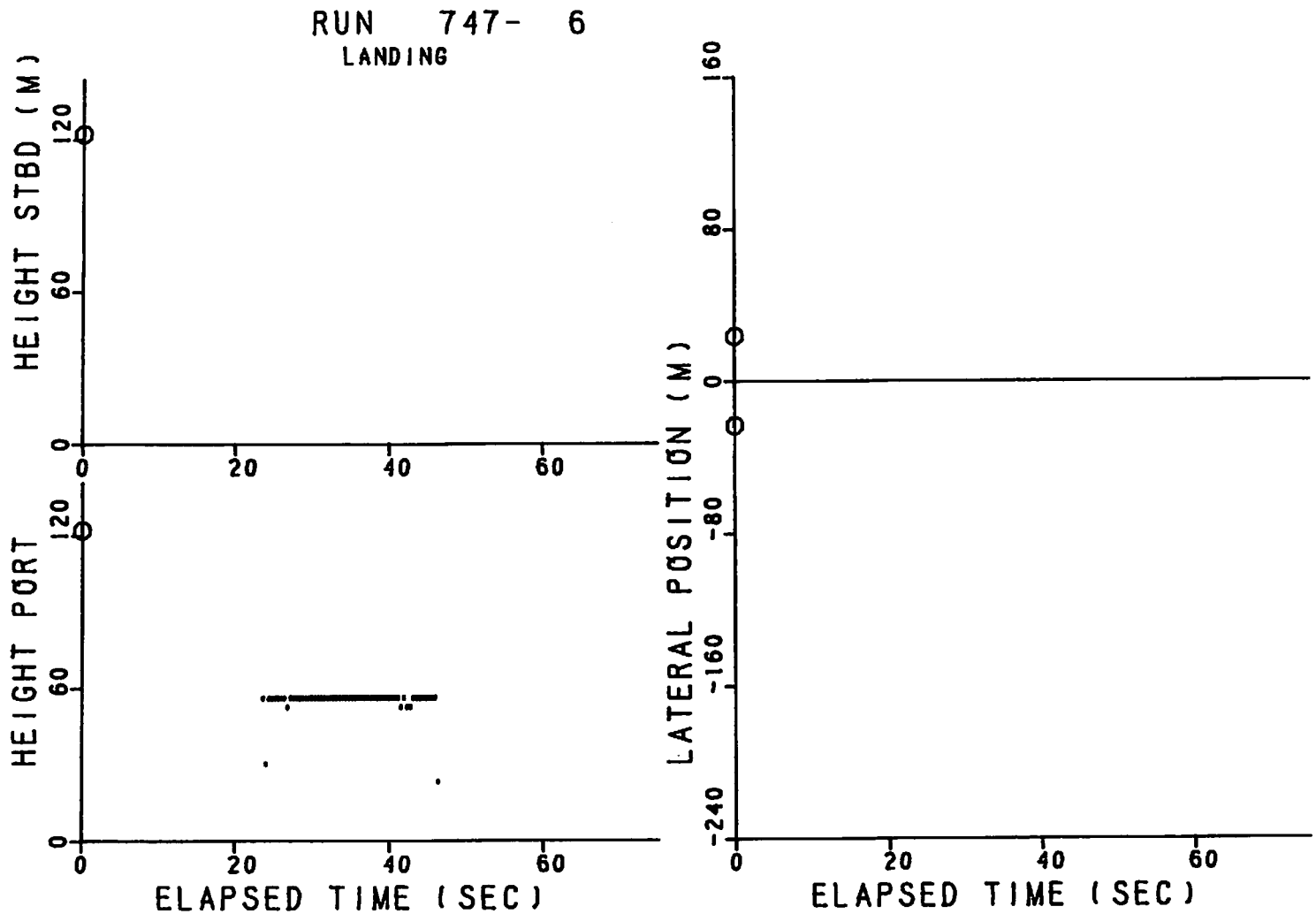

FIGURE 137. VORTEX-TRACKING DATA, RUN 6

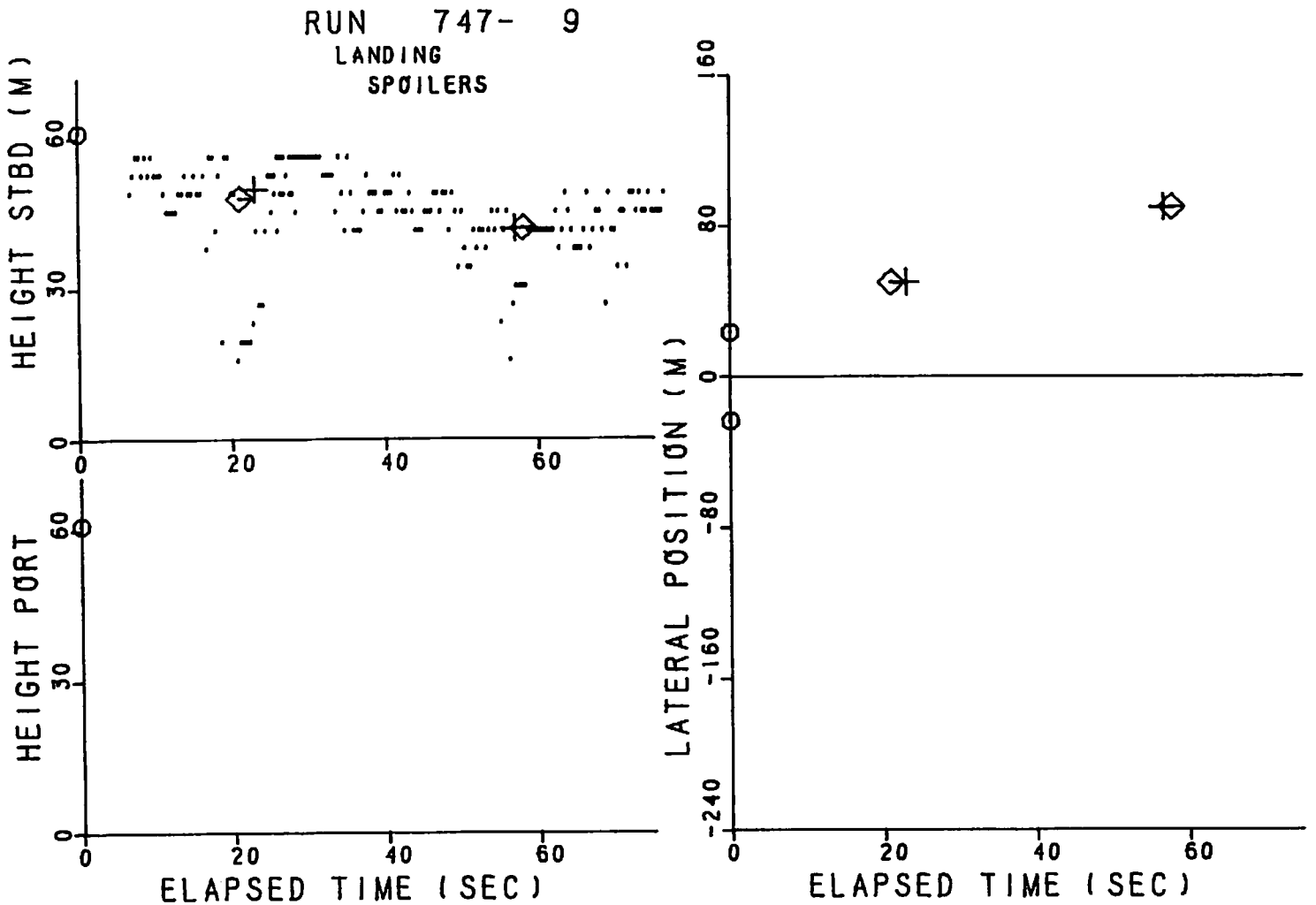

FIGURE 138. VORTEX-TRACKING DATA, RUN 9

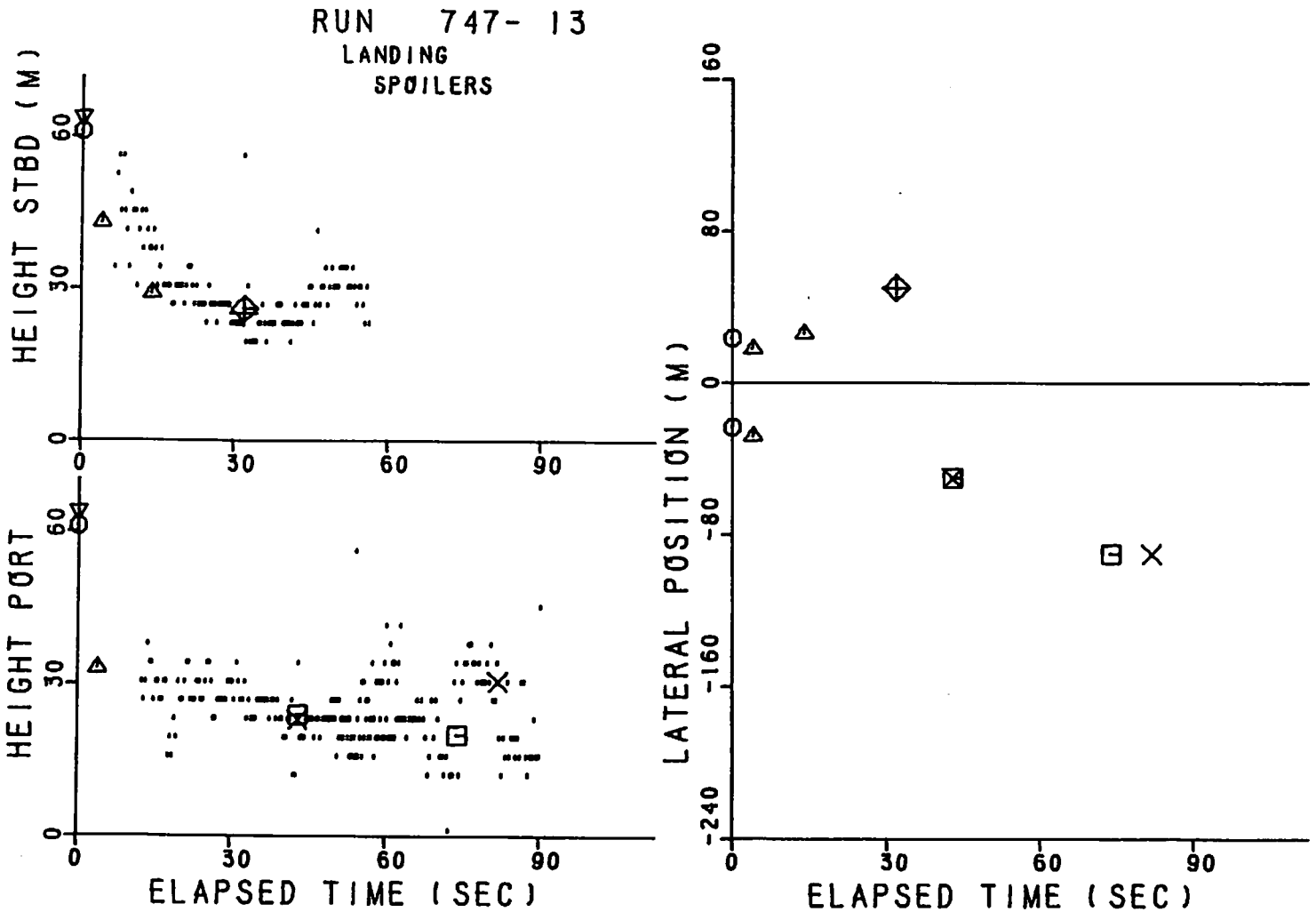

FIGURE 139. VORTEX-TRACKING DATA, RUN 13

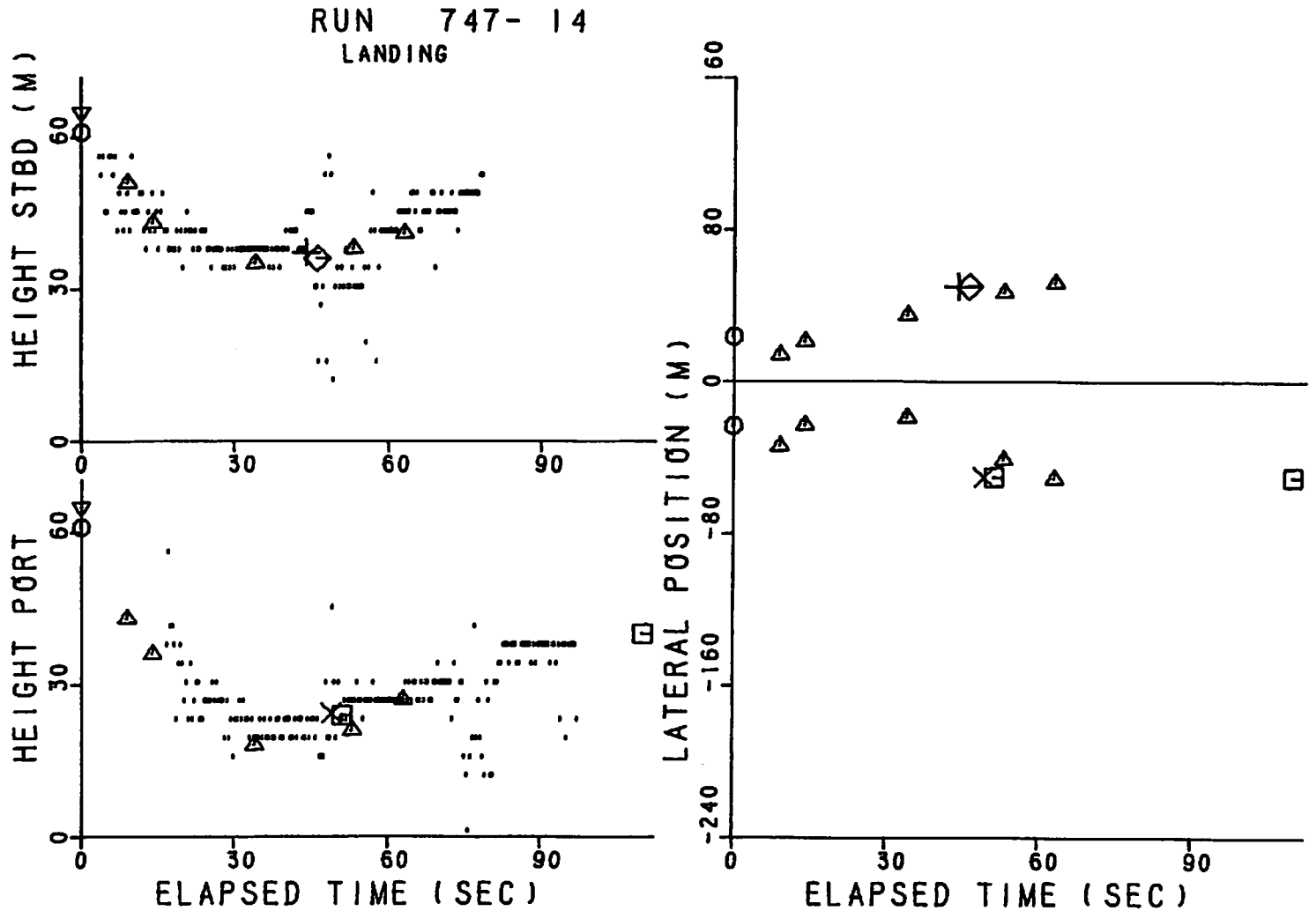

FIGURE 140. VORTEX-TRACKING DATA, RUN 14

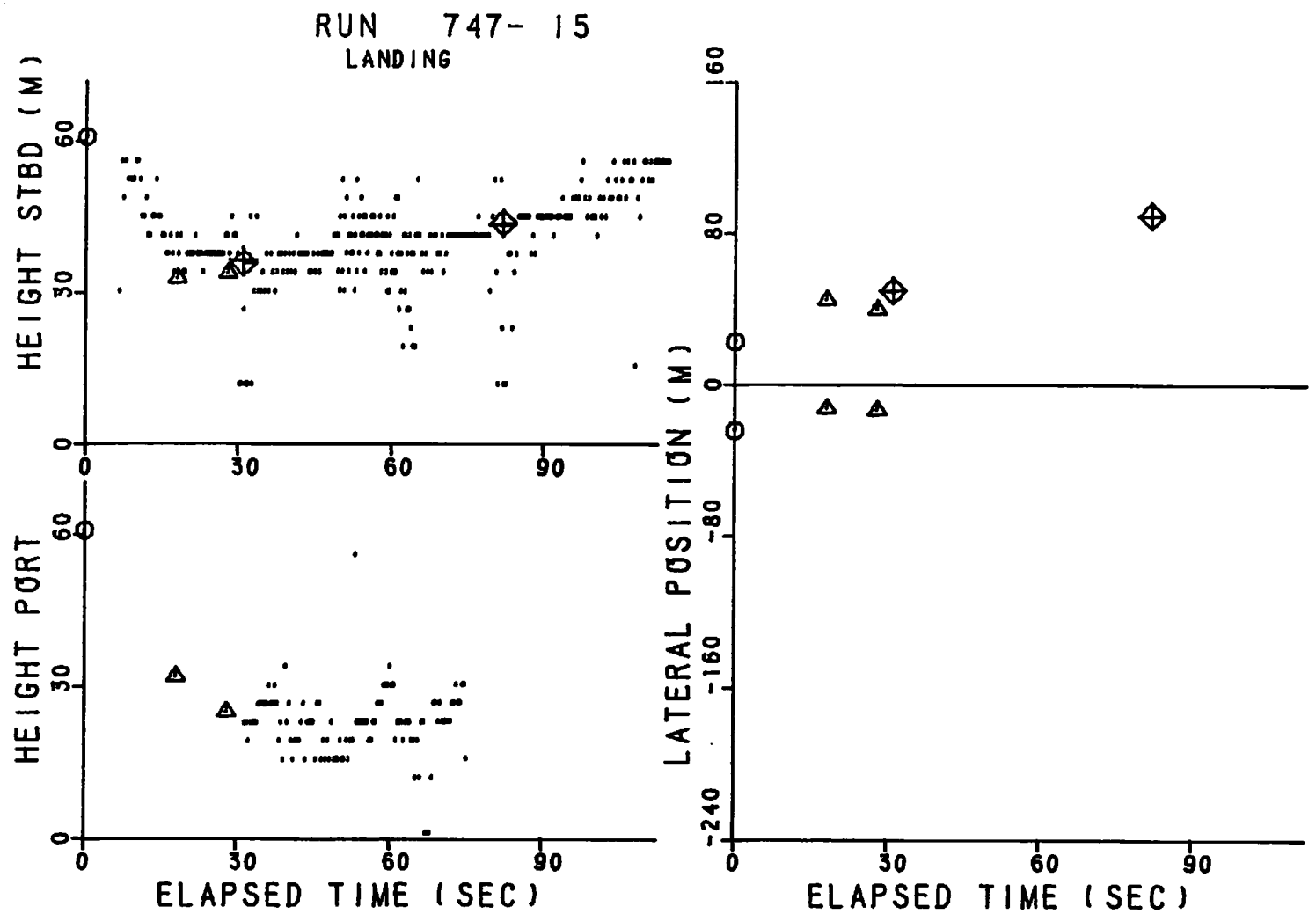

FIGURE 141. VORTEX-TRACKING DATA, RUN 15

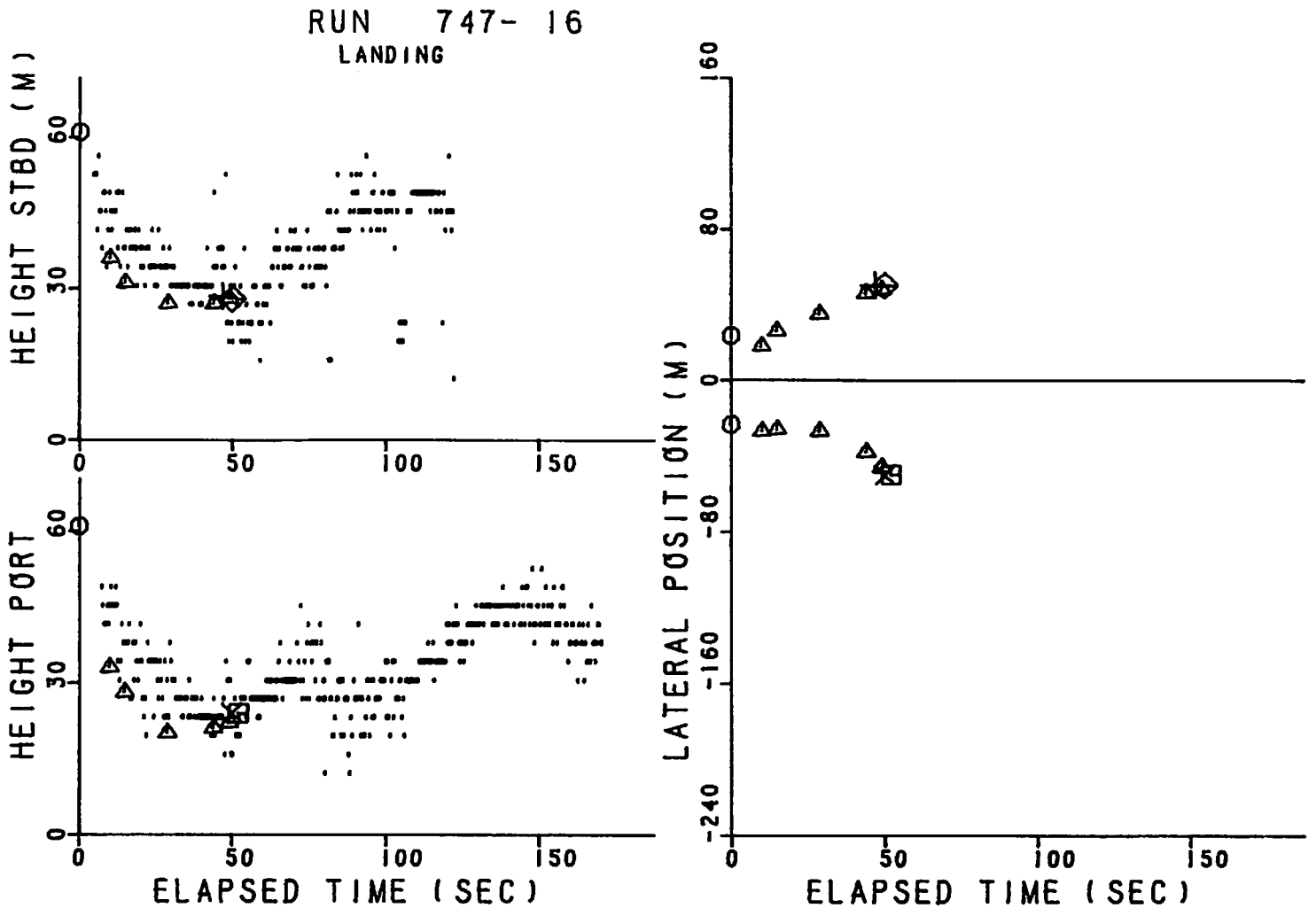

FIGURE 142. VORTEX-TRACKING DATA, RUN 16

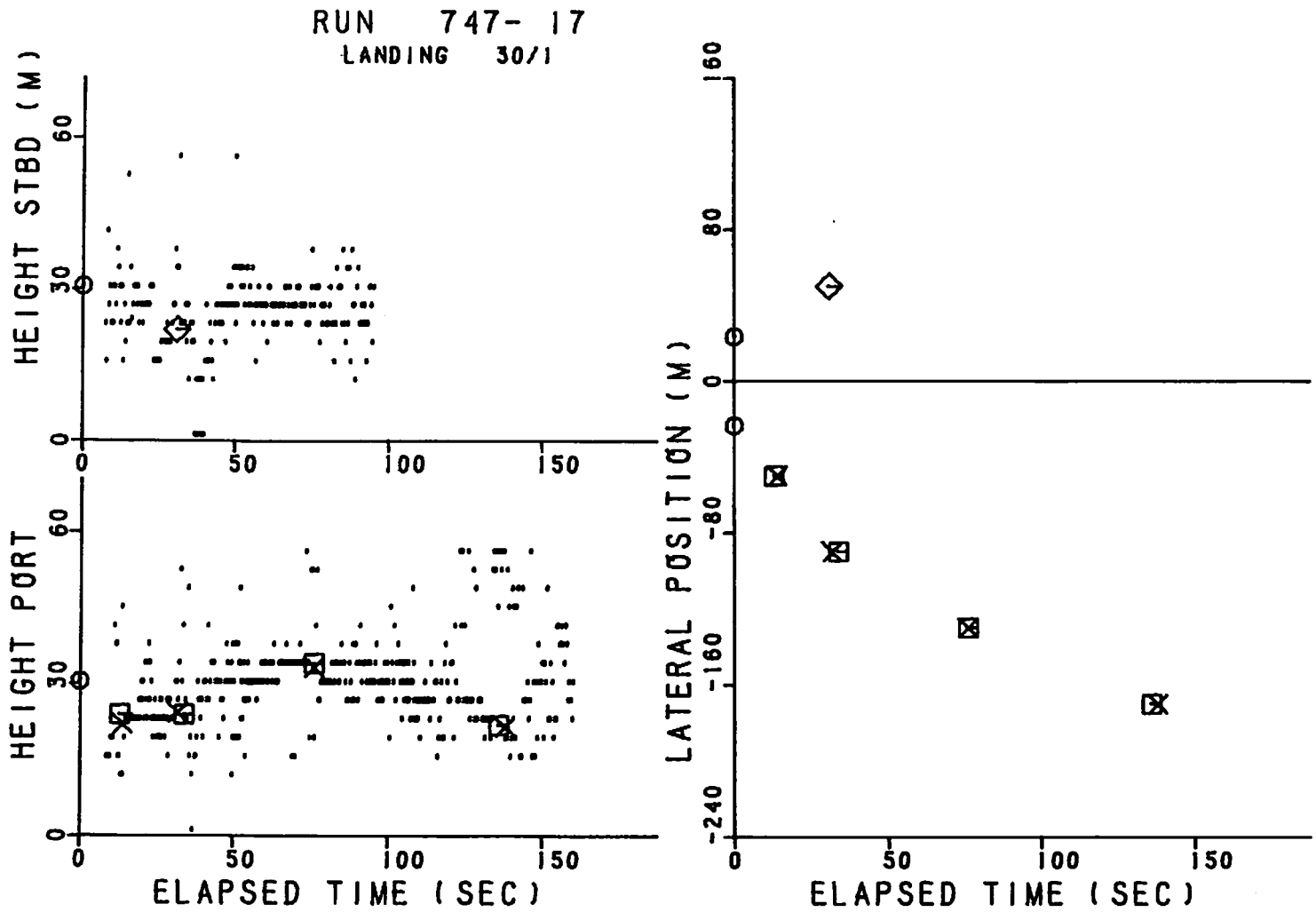

FIGURE 143. VORTEX-TRACKING DATA, RUN 17

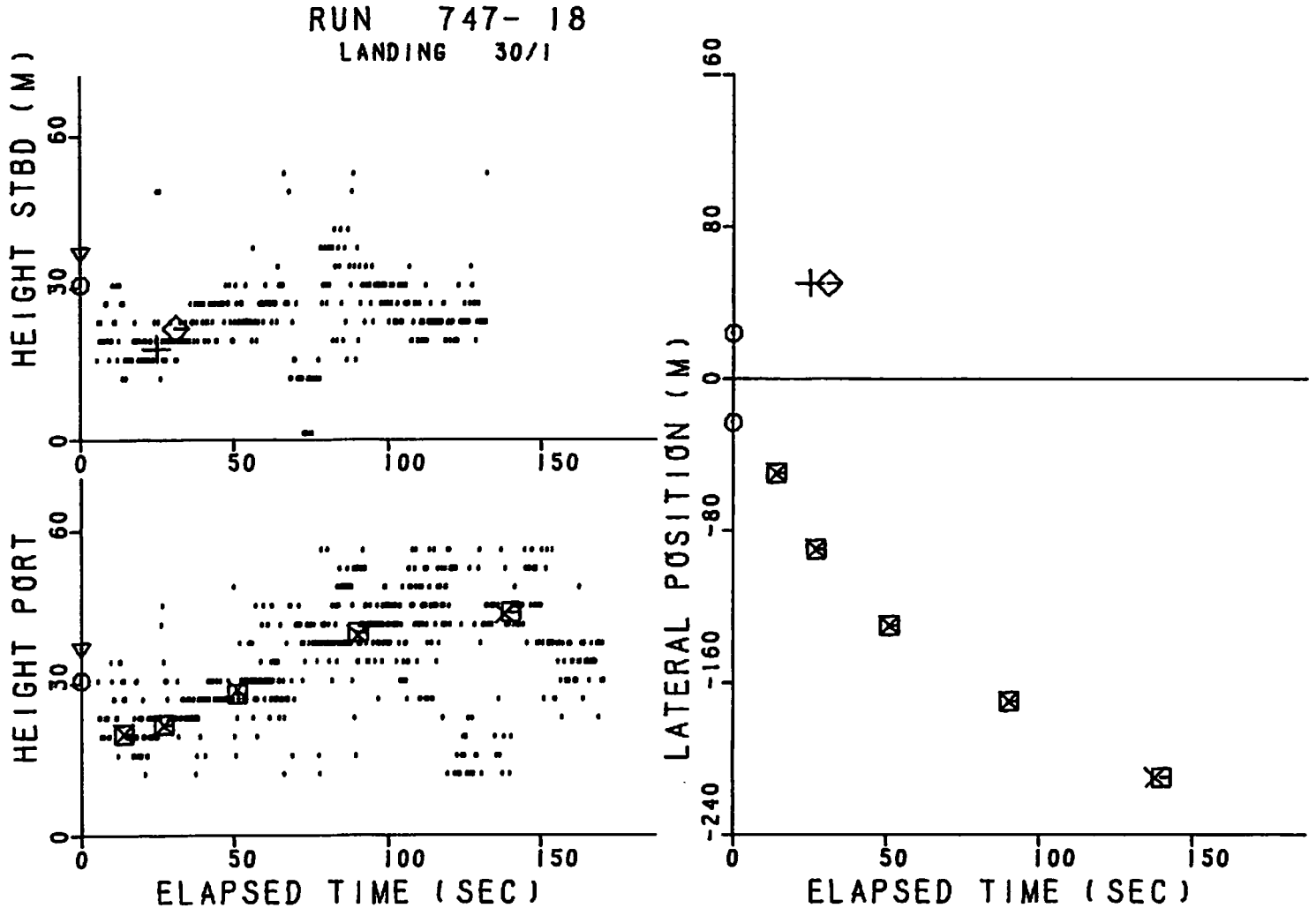

FIGURE 144. VORTEX-TRACKING DATA, RUN 18

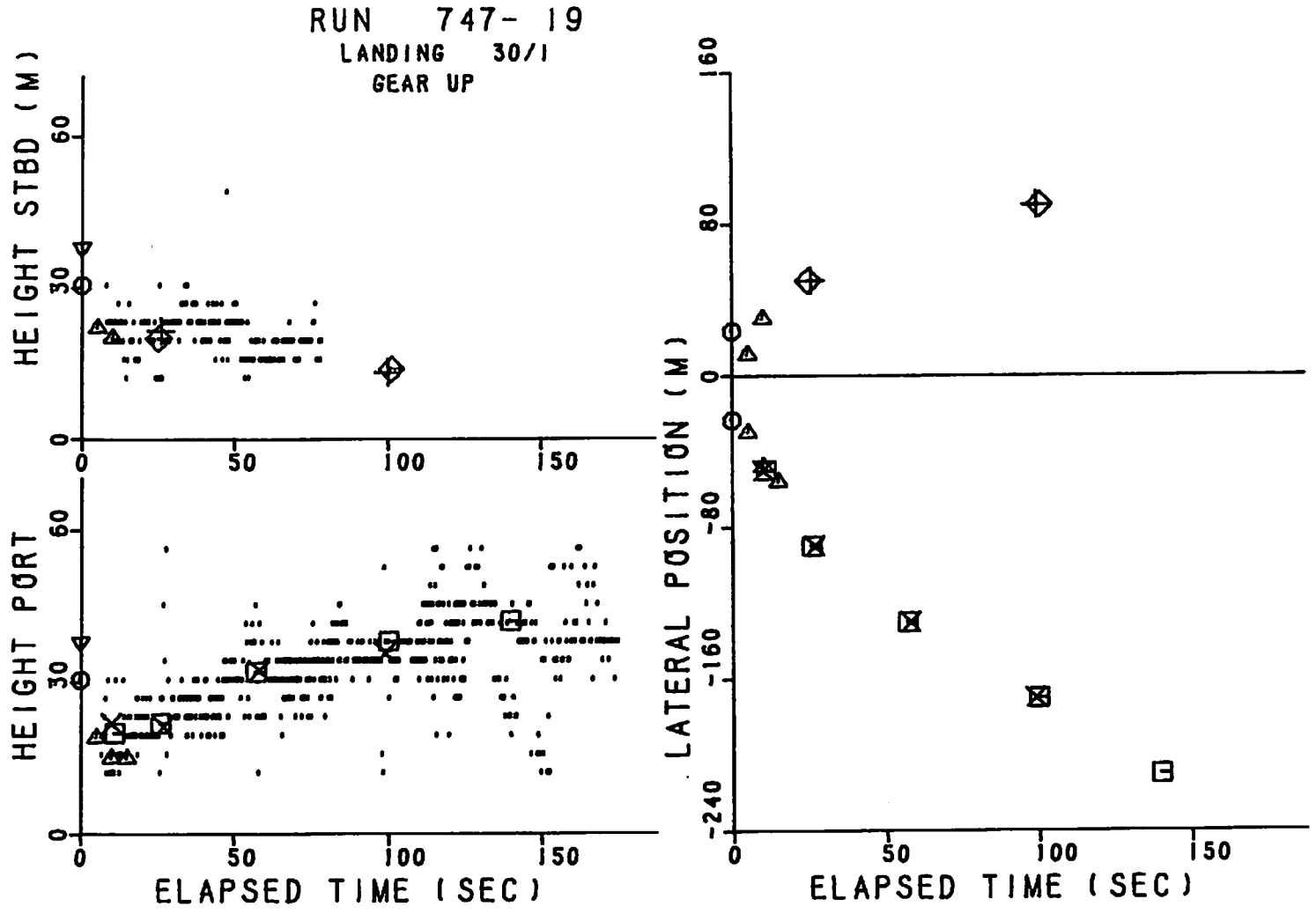

FIGURE 145. VORTEX-TRACKING DATA, RUN 19

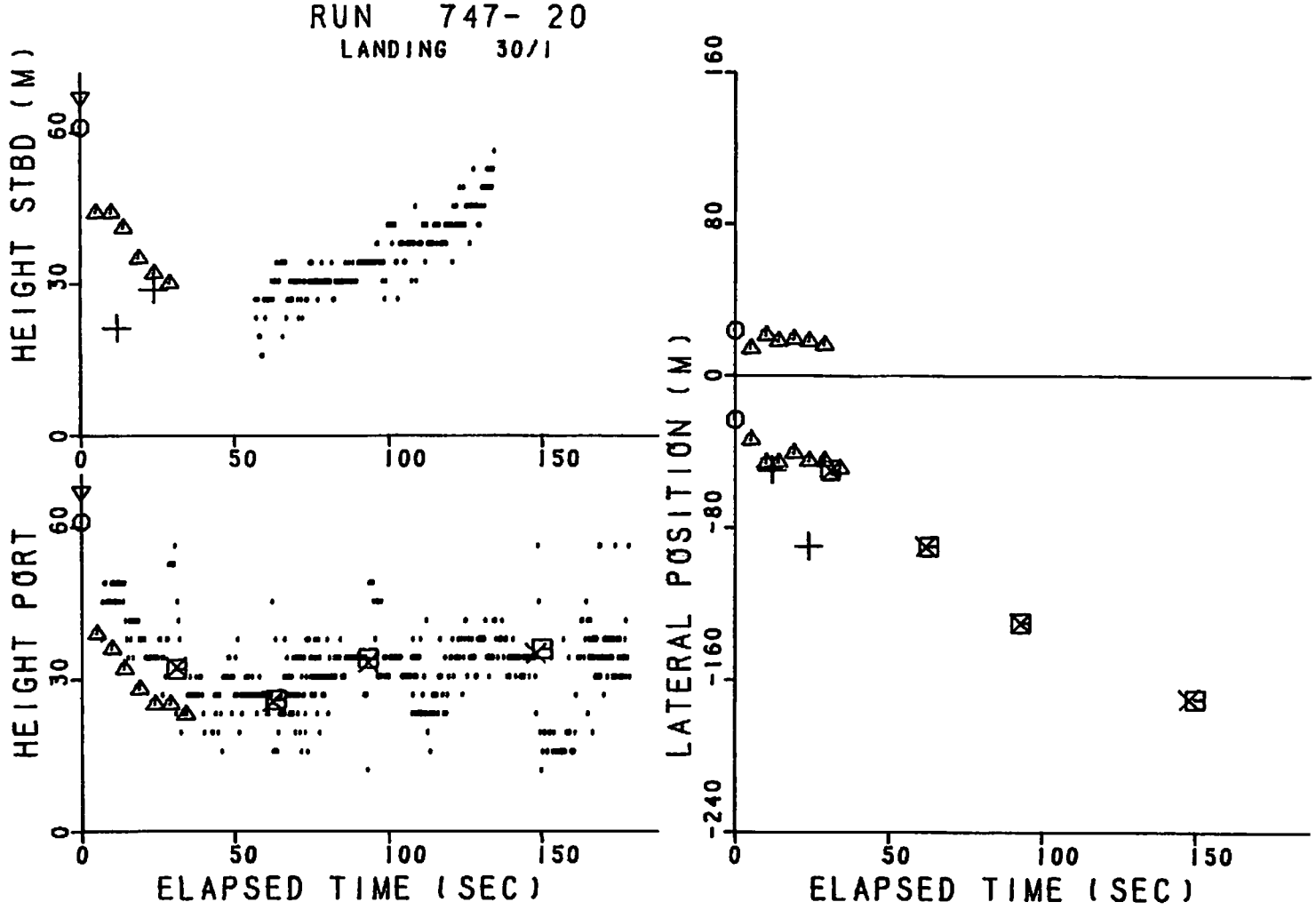

FIGURE 146. VORTEX-TRACKING DATA, RUN 20

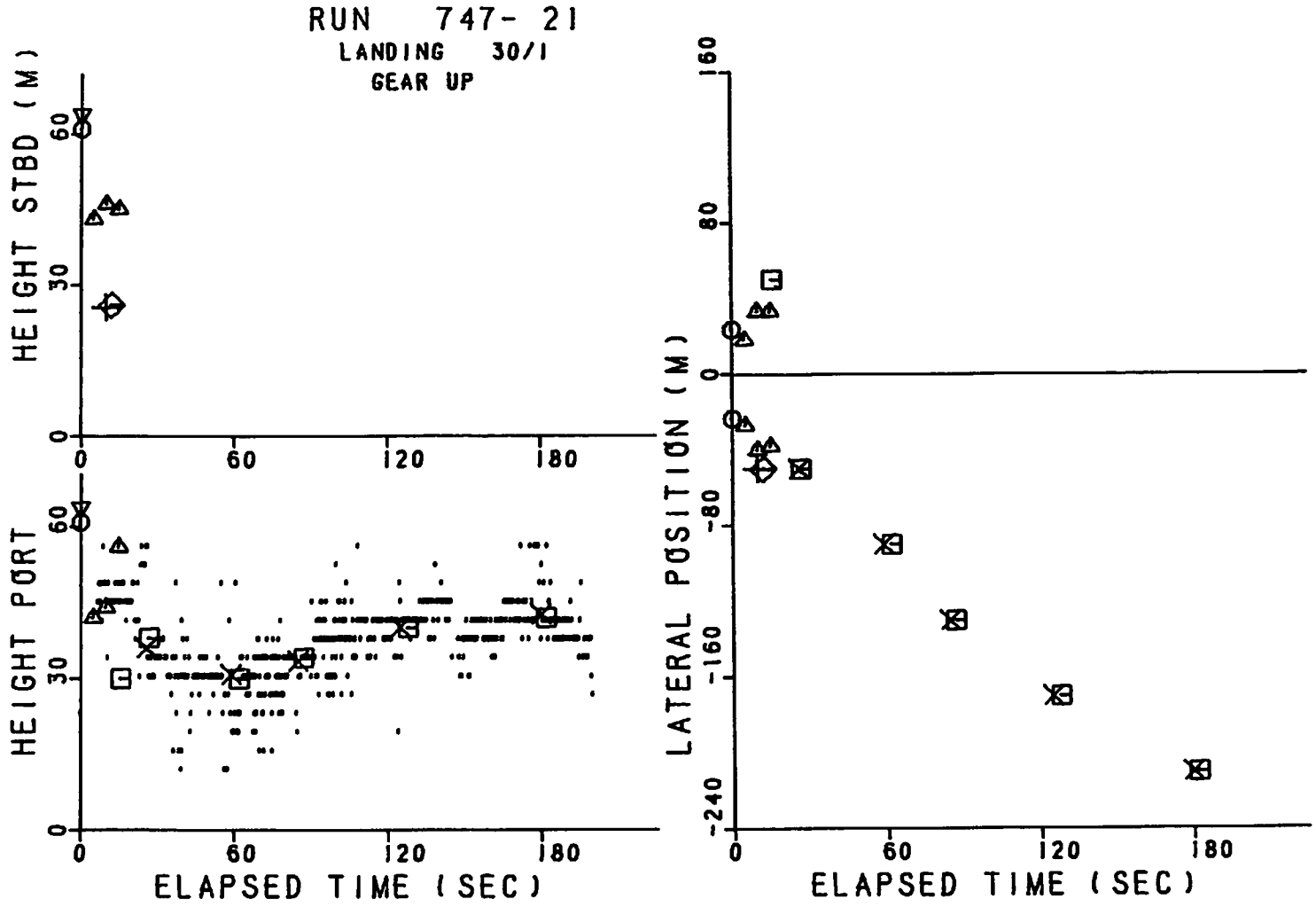

FIGURE 147. VORTEX-TRACKING DATA, RUN 21

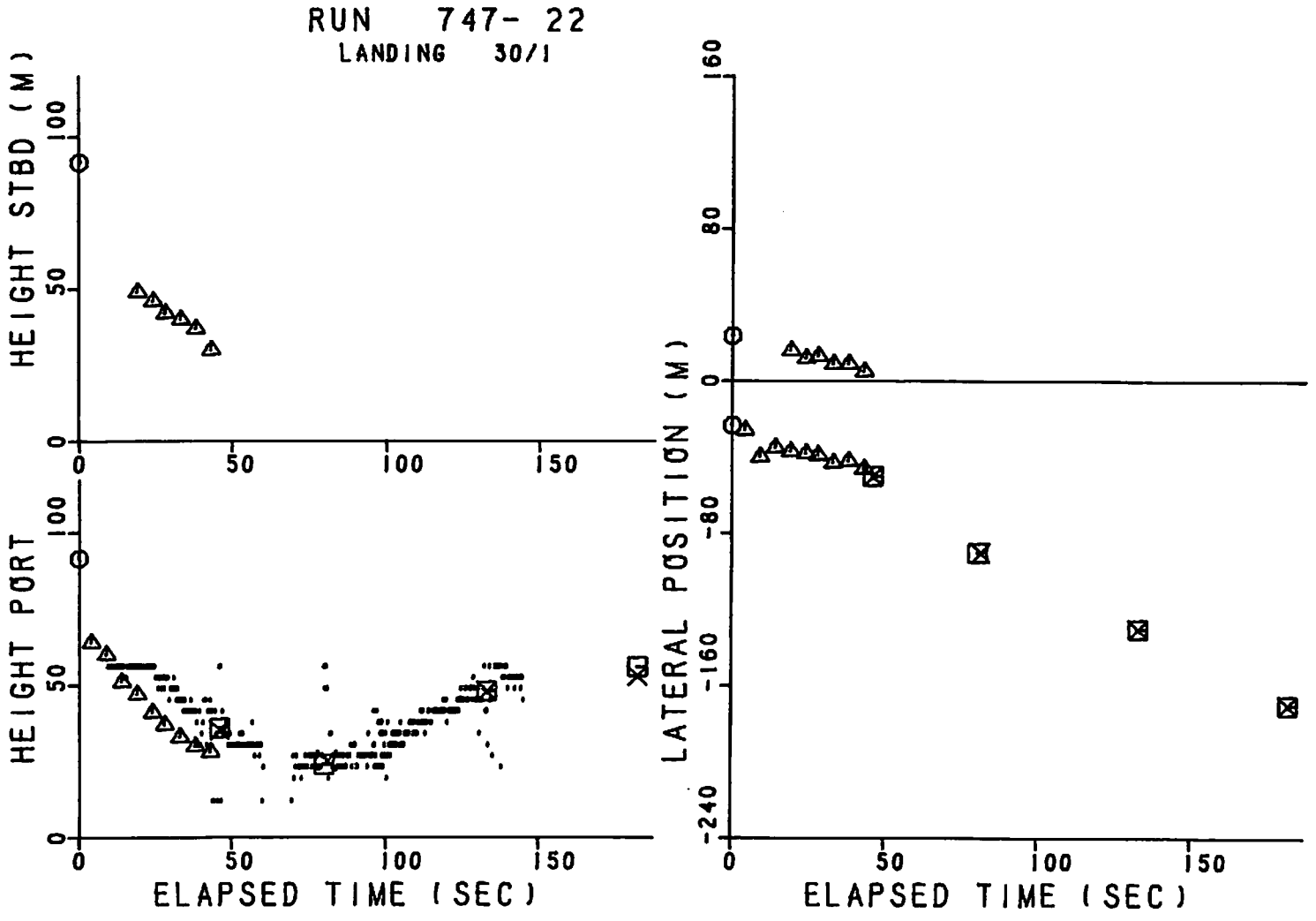

FIGURE 148. VORTEX-TRACKING DATA, RUN 22

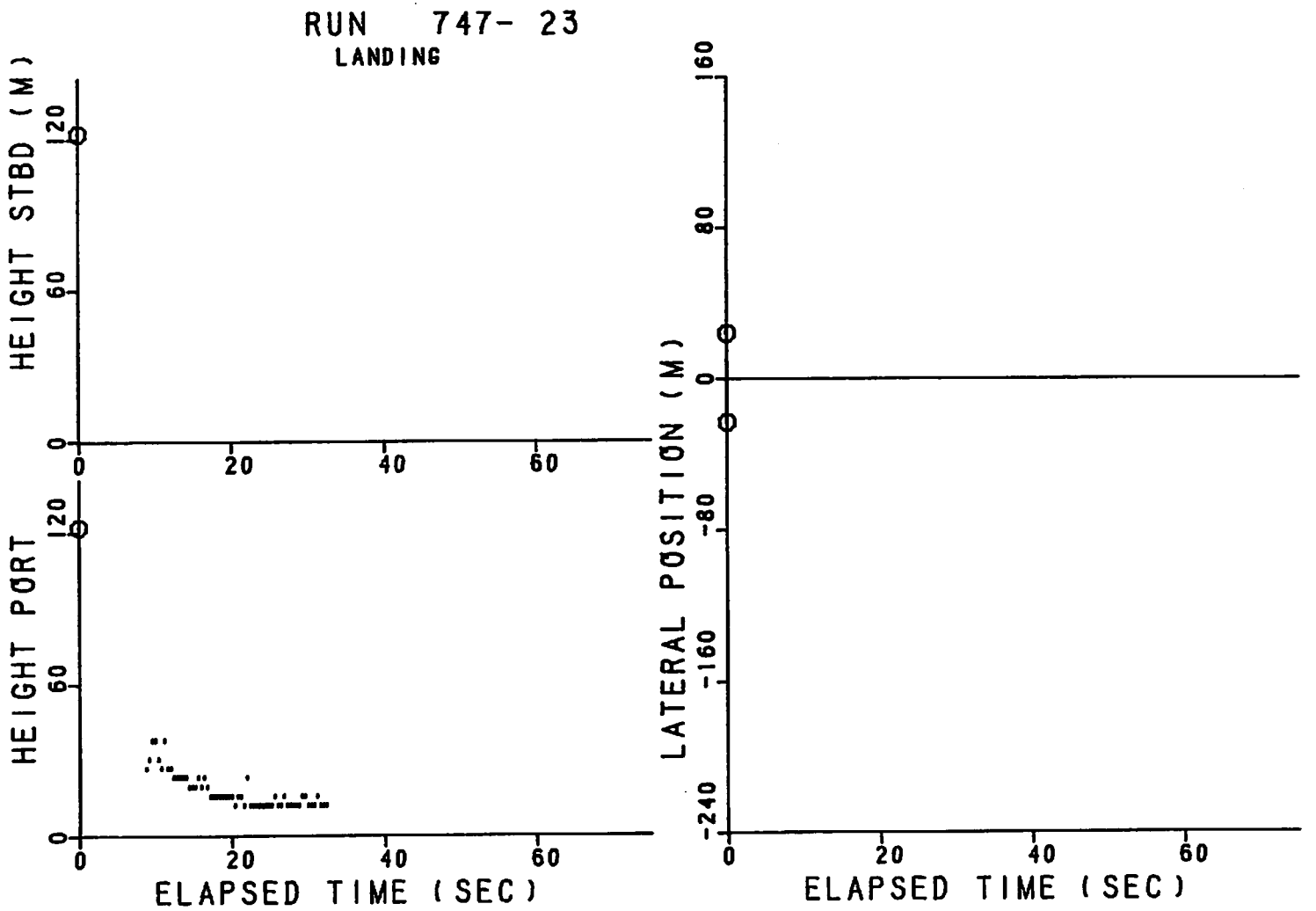

FIGURE 149. VORTEX-TRACKING DATA, RUN 23

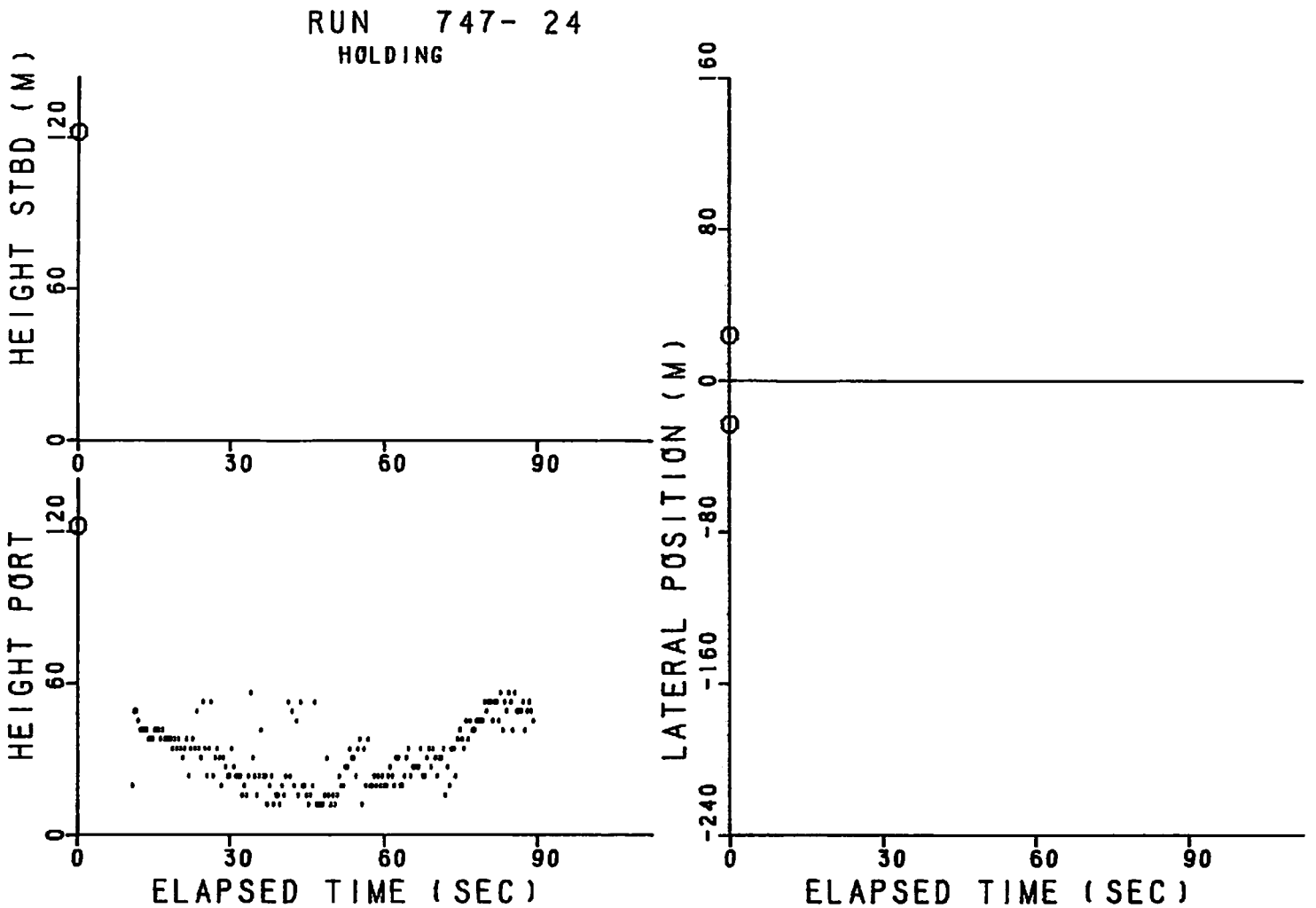

FIGURE 150. VORTEX-TRACKING DATA, RUN 24

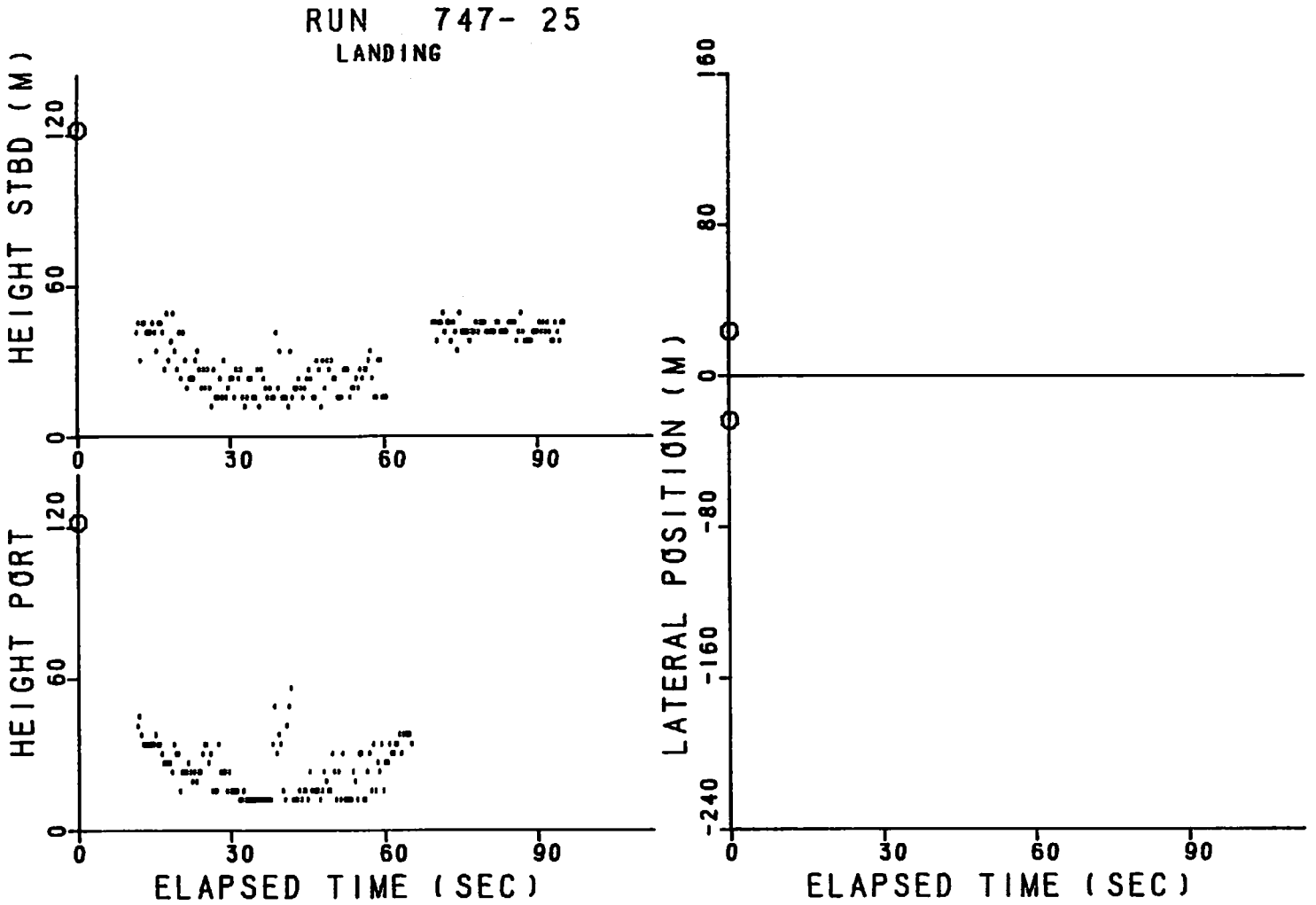

FIGURE 151. VORTEX-TRACKING DATA, RUN 25

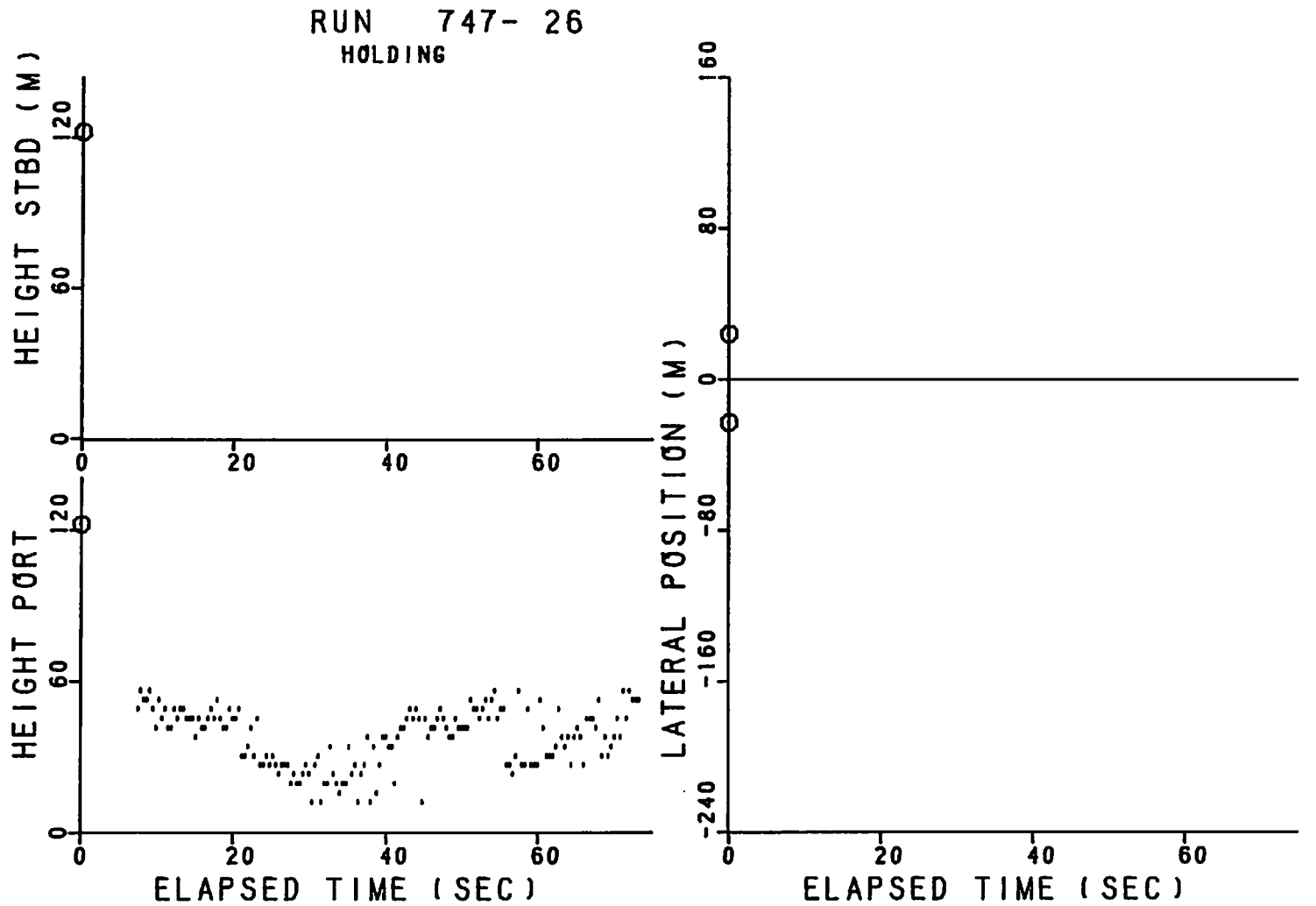

FIGURE 152. VORTEX-TRACKING DATA, RUN 26

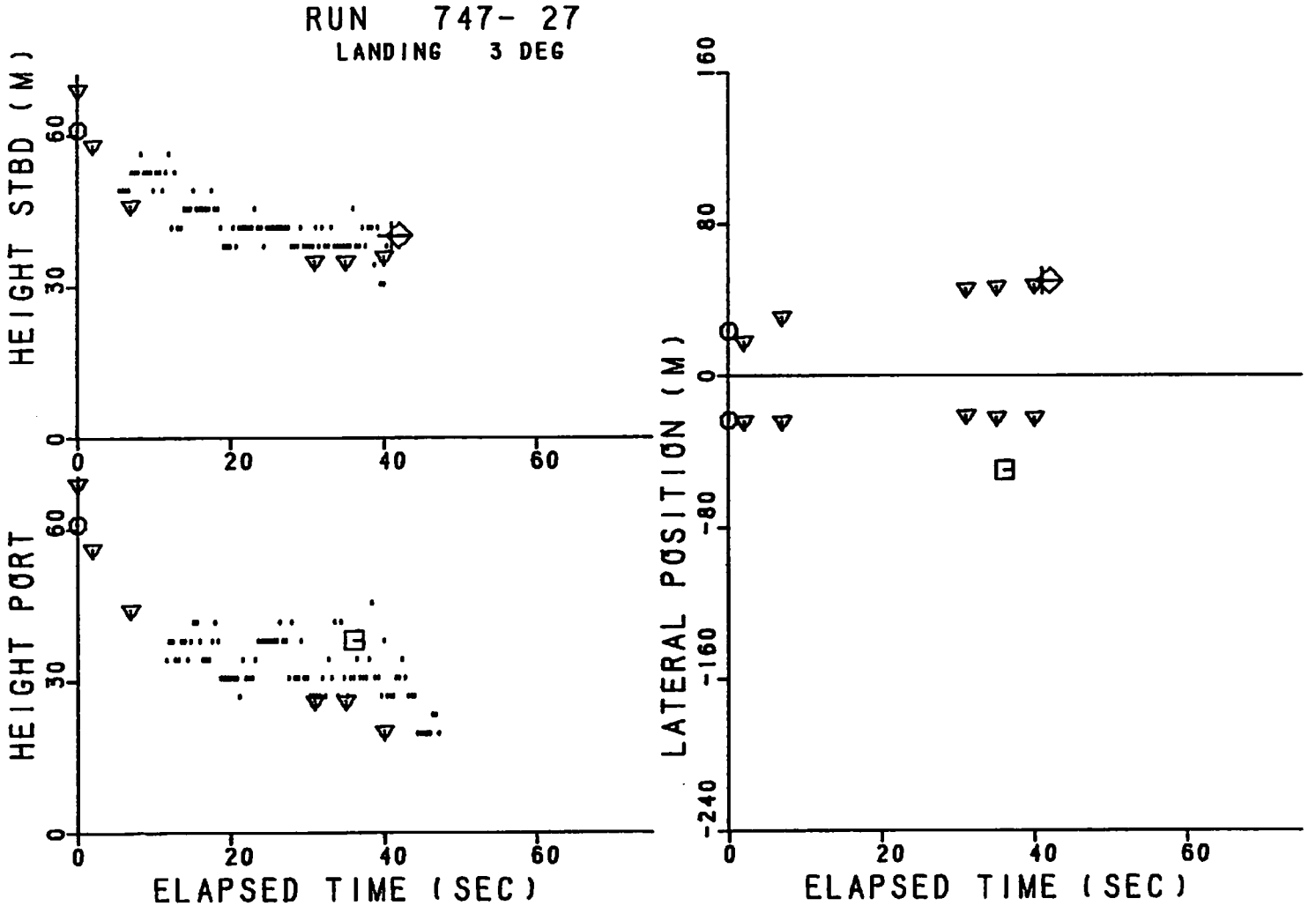

FIGURE 153. VORTEX-TRACKING DATA, RUN 27

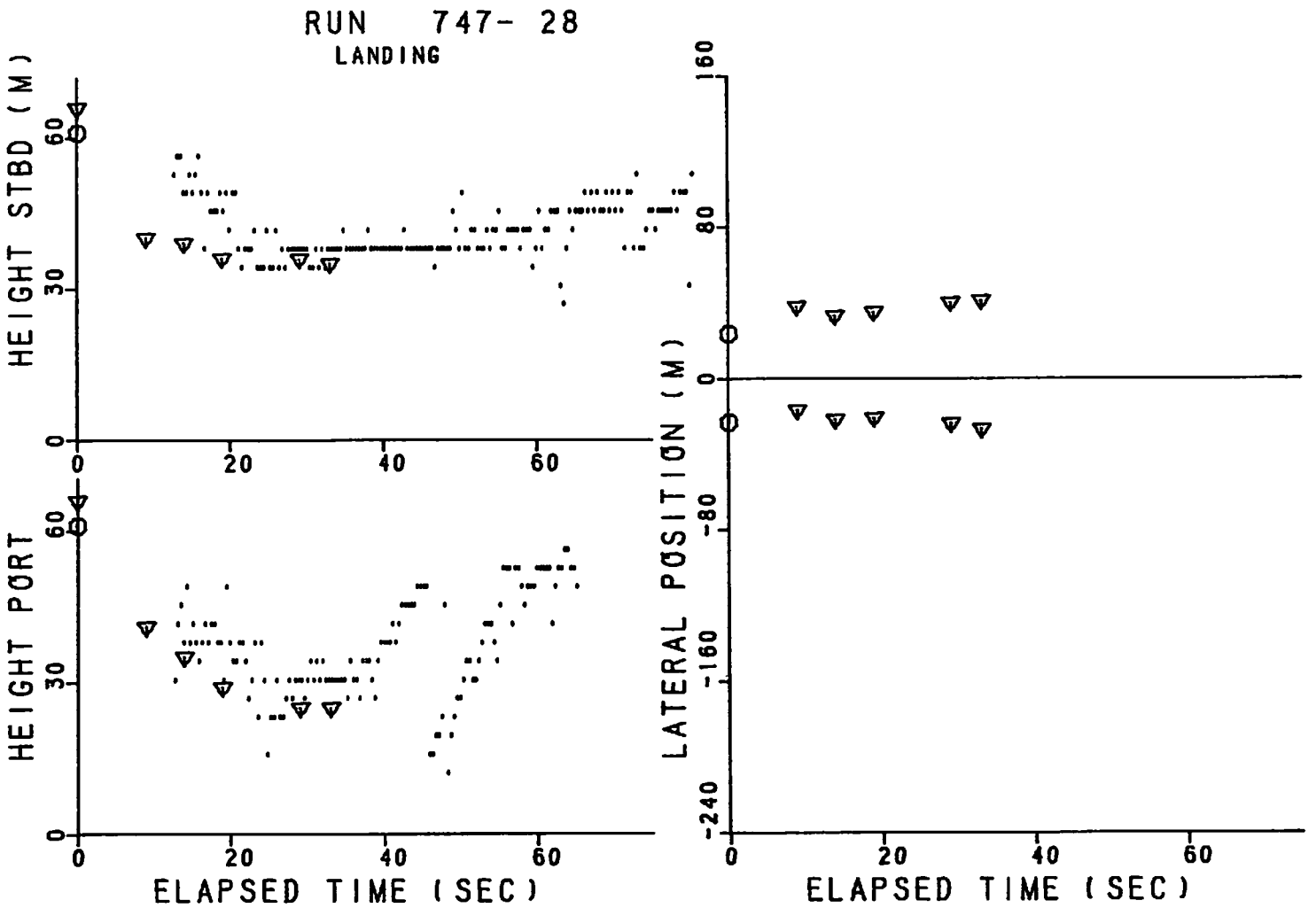

FIGURE 154. VORTEX-TRACKING DATA, RUN 28

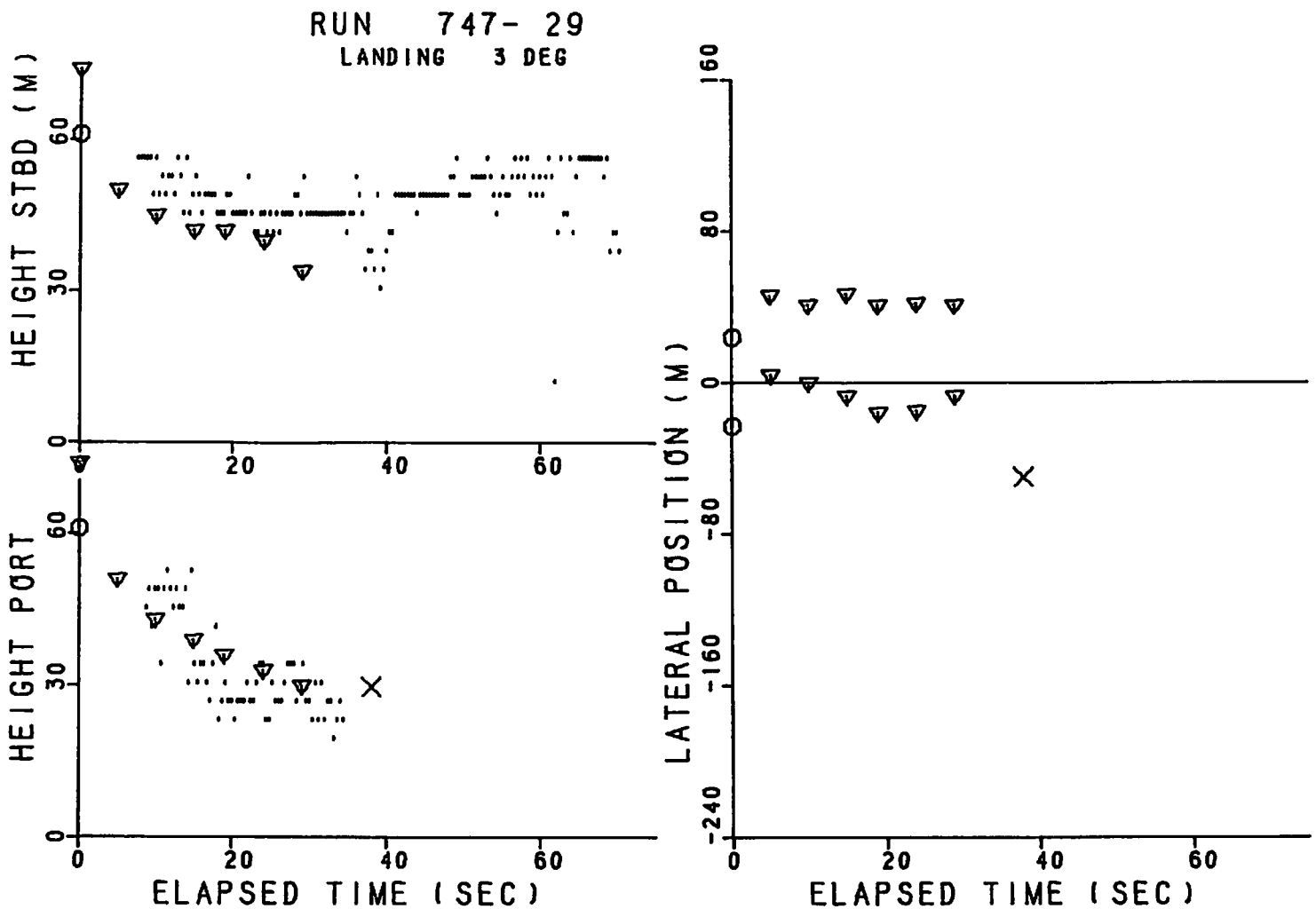

FIGURE 155. VORTEX-TRACKING DATA, RUN 29

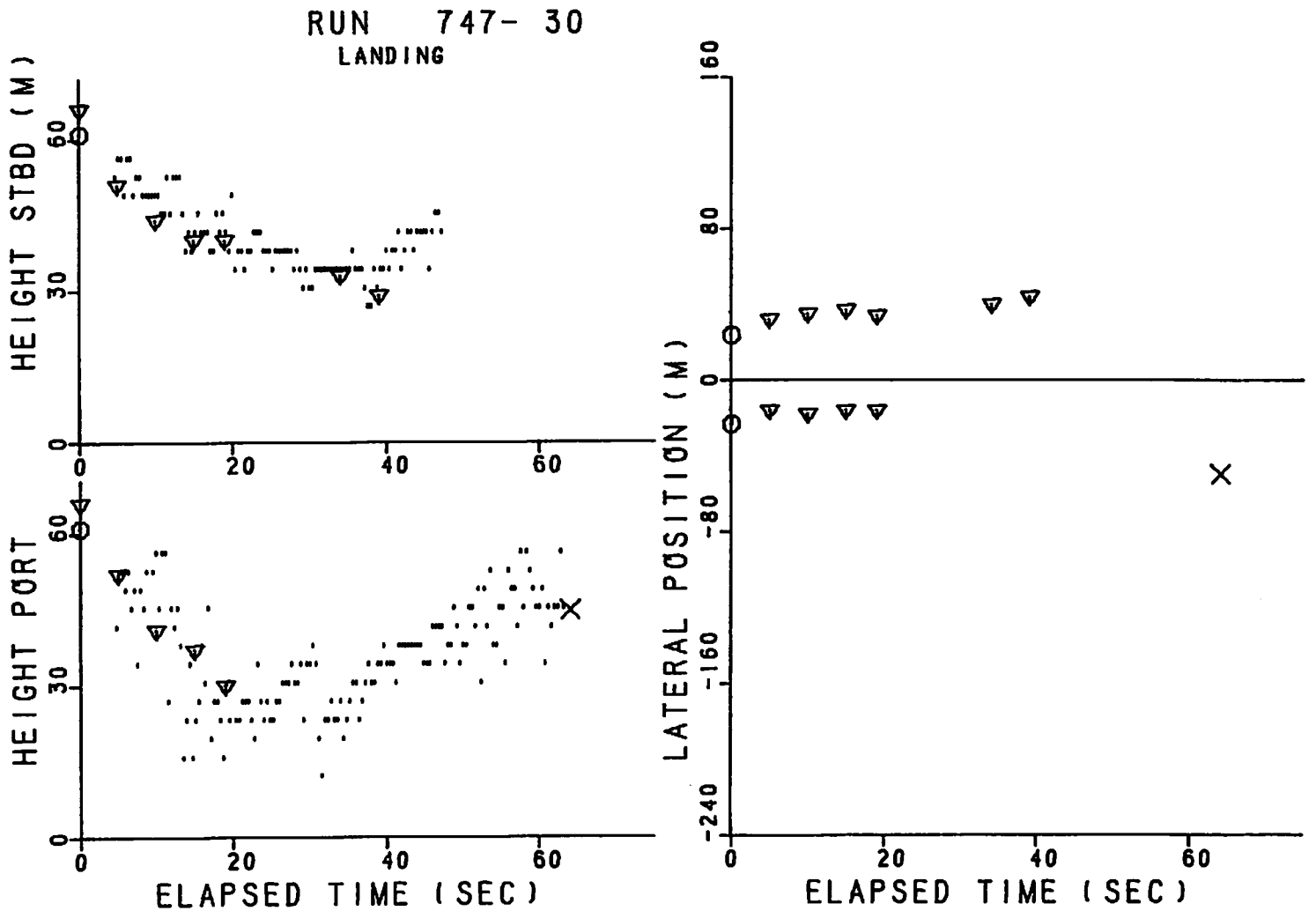

FIGURE 156. VORTEX-TRACKING DATA, RUN 30

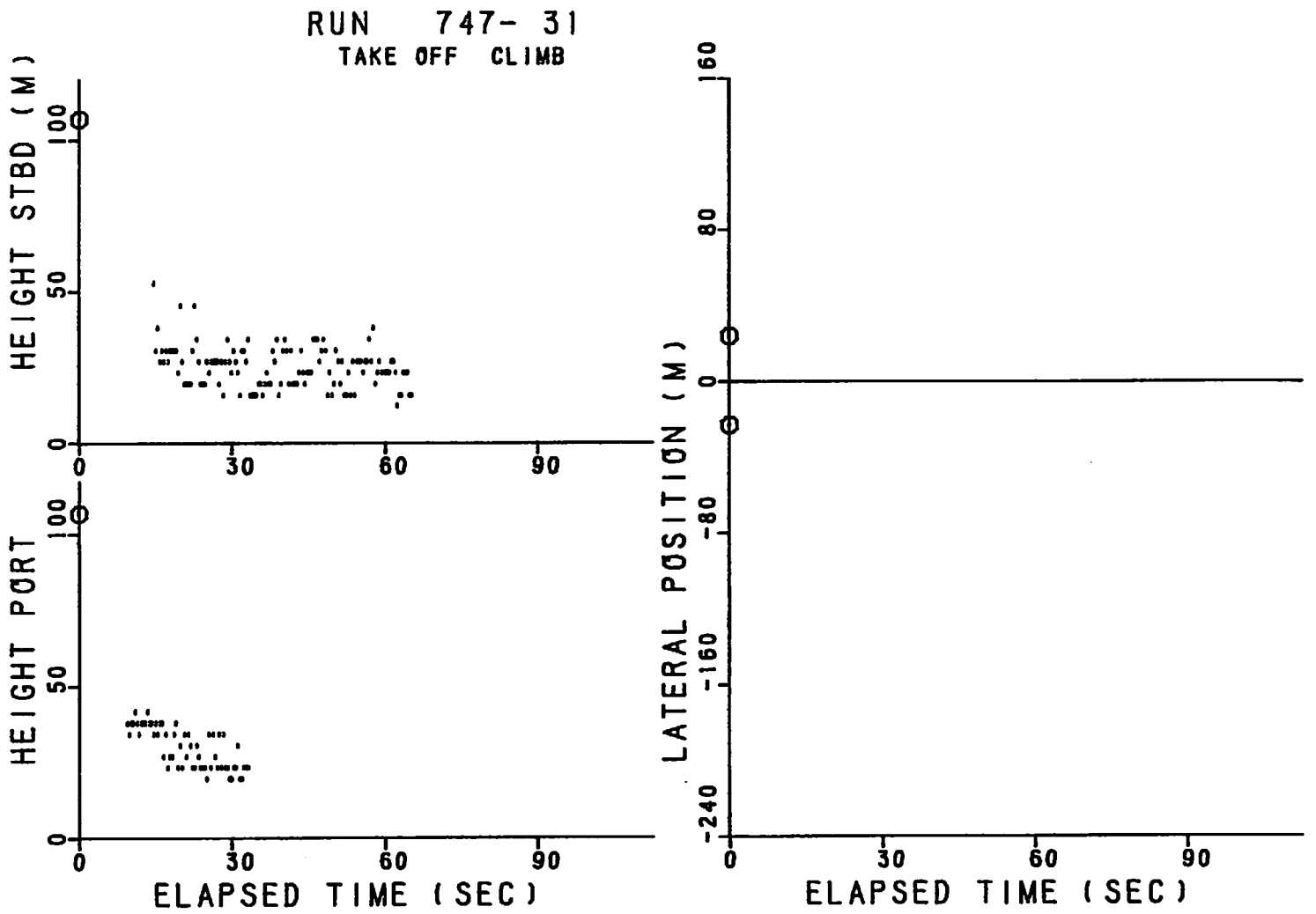

FIGURE 157. VORTEX-TRACKING DATA, RUN 31

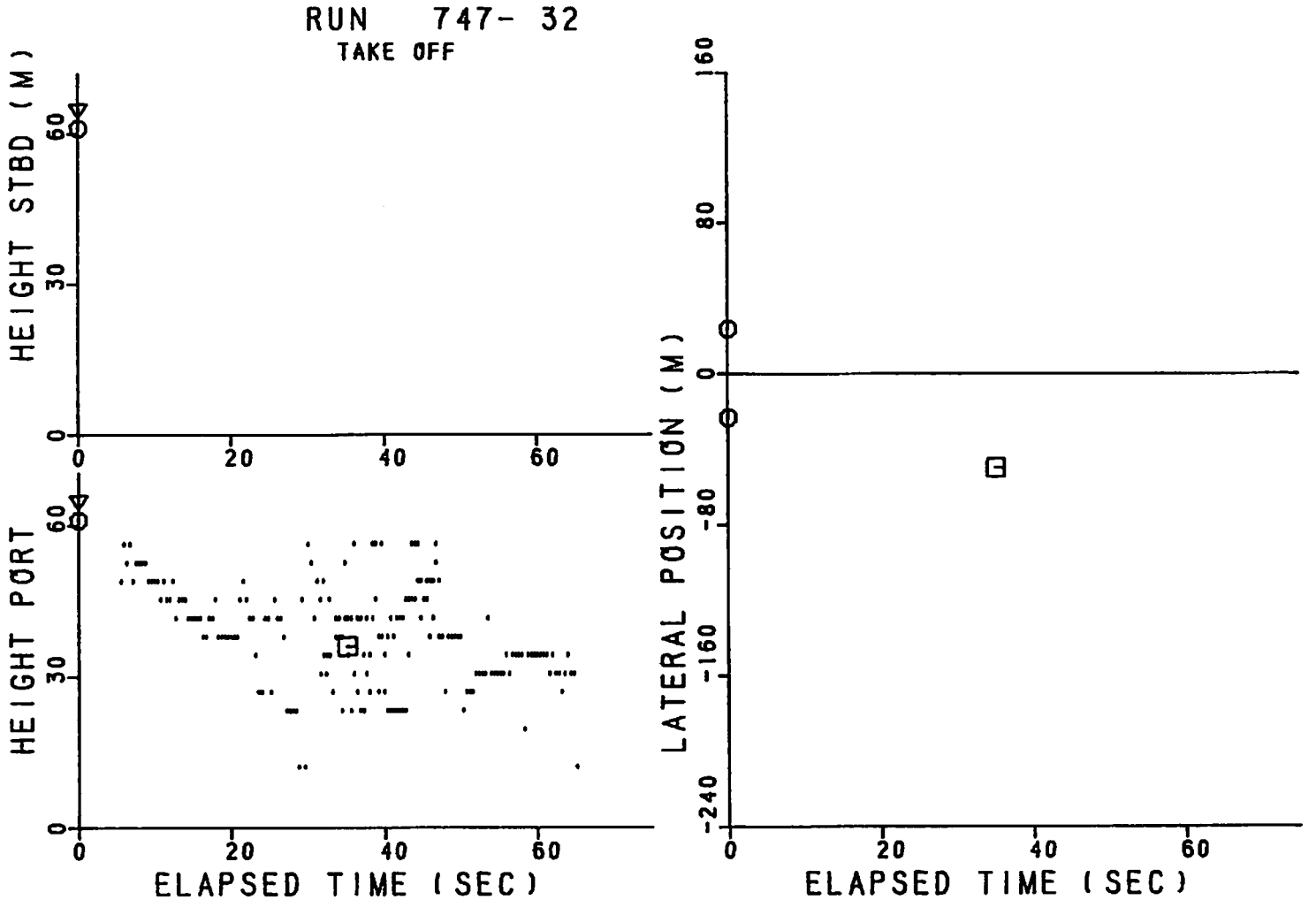

FIGURE 158. VORTEX-TRACKING DATA, RUN 32

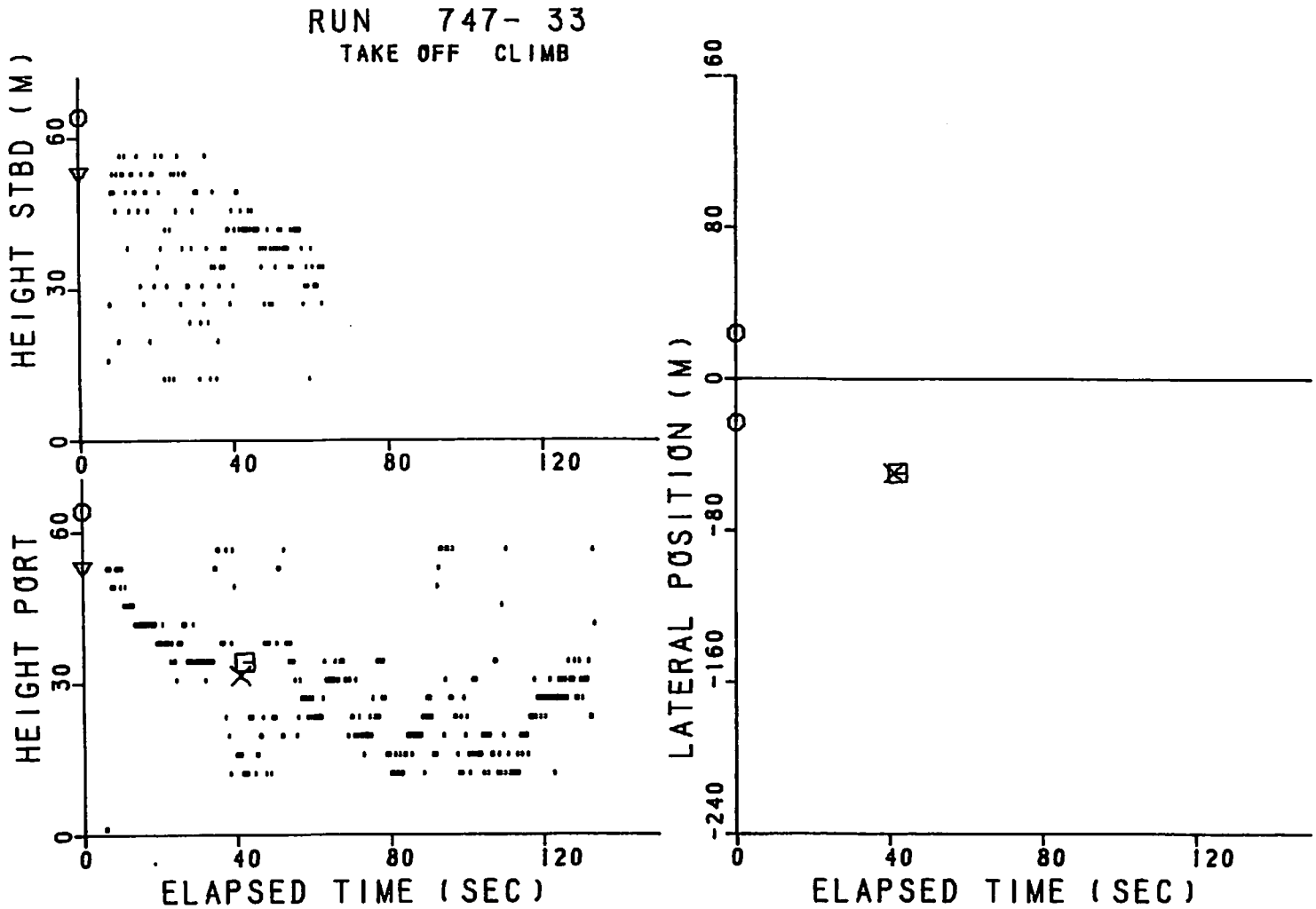

FIGURE 159. VORTEX-TRACKING DATA, RUN 33

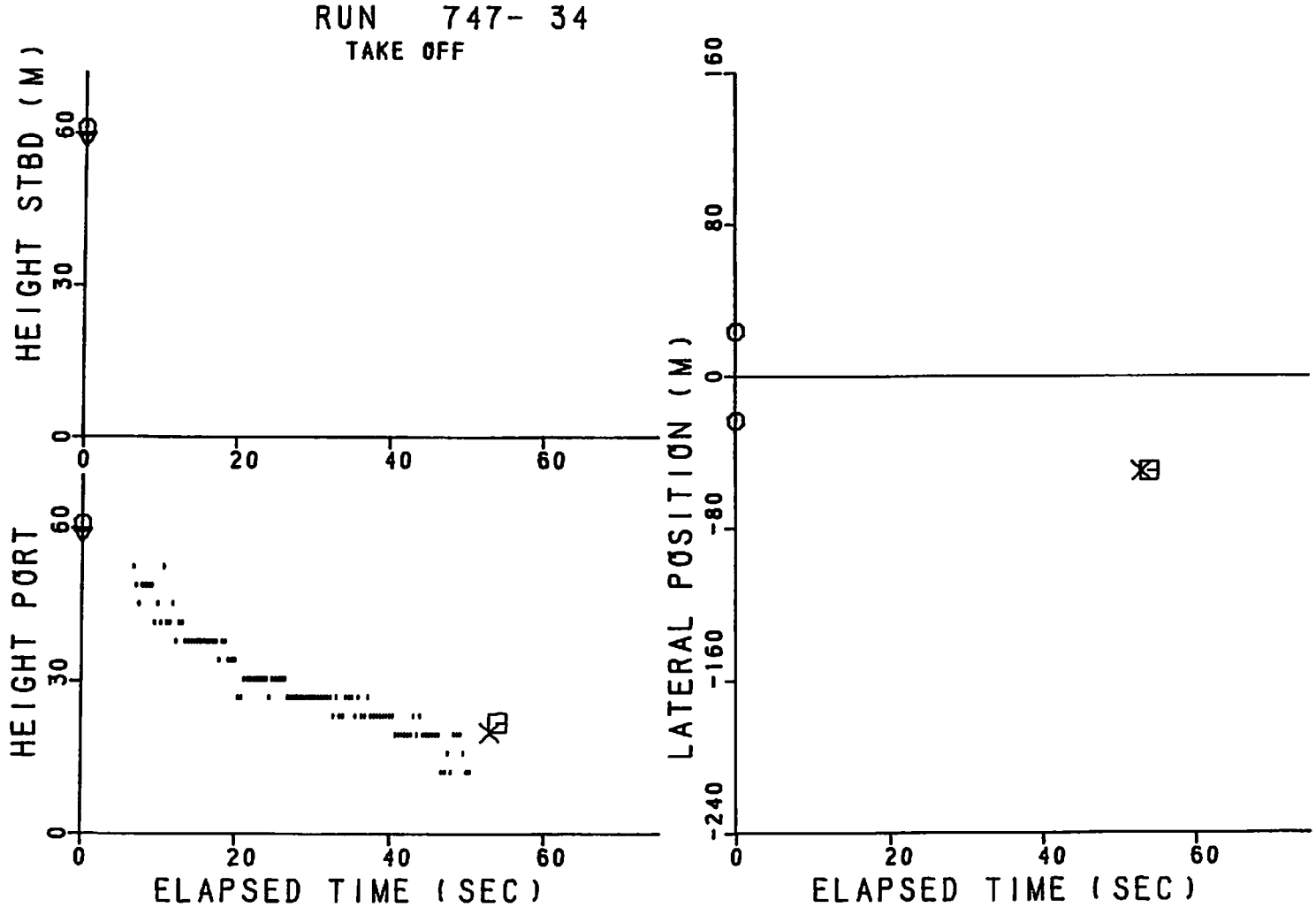

FIGURE 160. VORTEX-TRACKING DATA, RUN 34

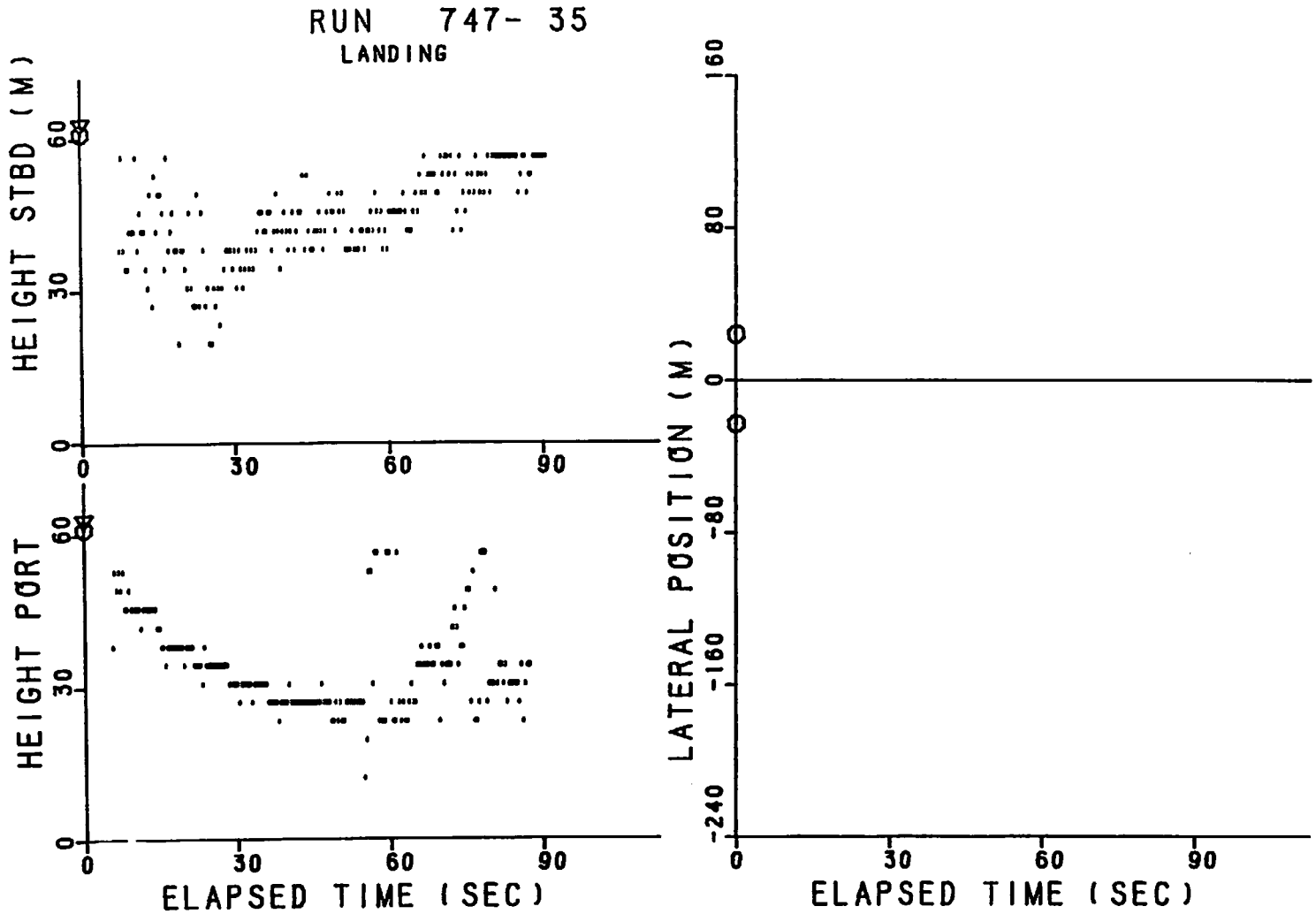

FIGURE 161. VORTEX-TRACKING DATA, RUN 35

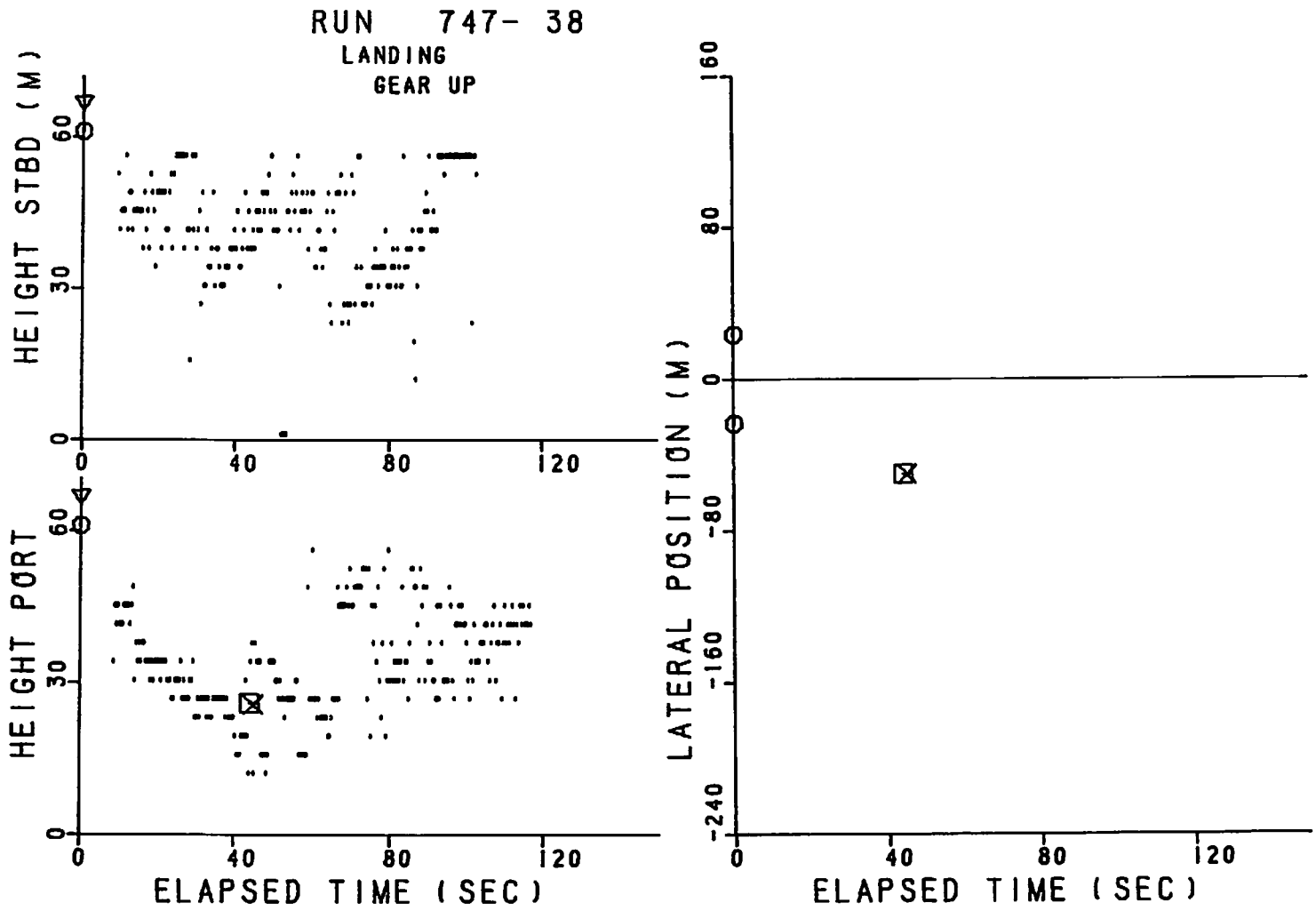

FIGURE 162. VORTEX-TRACKING DATA, RUN 38

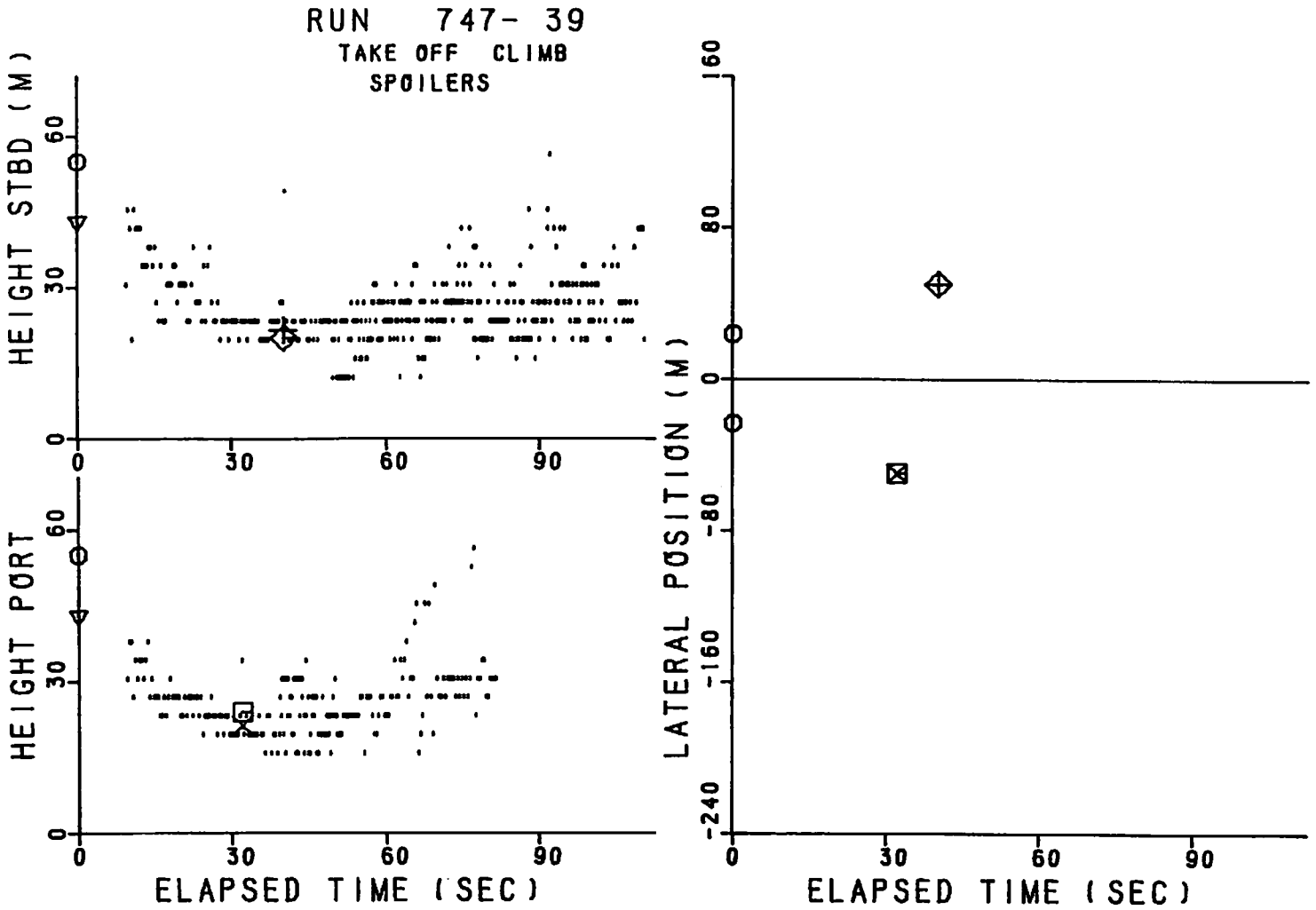

FIGURE 163. VORTEX-TRACKING DATA, RUN 39

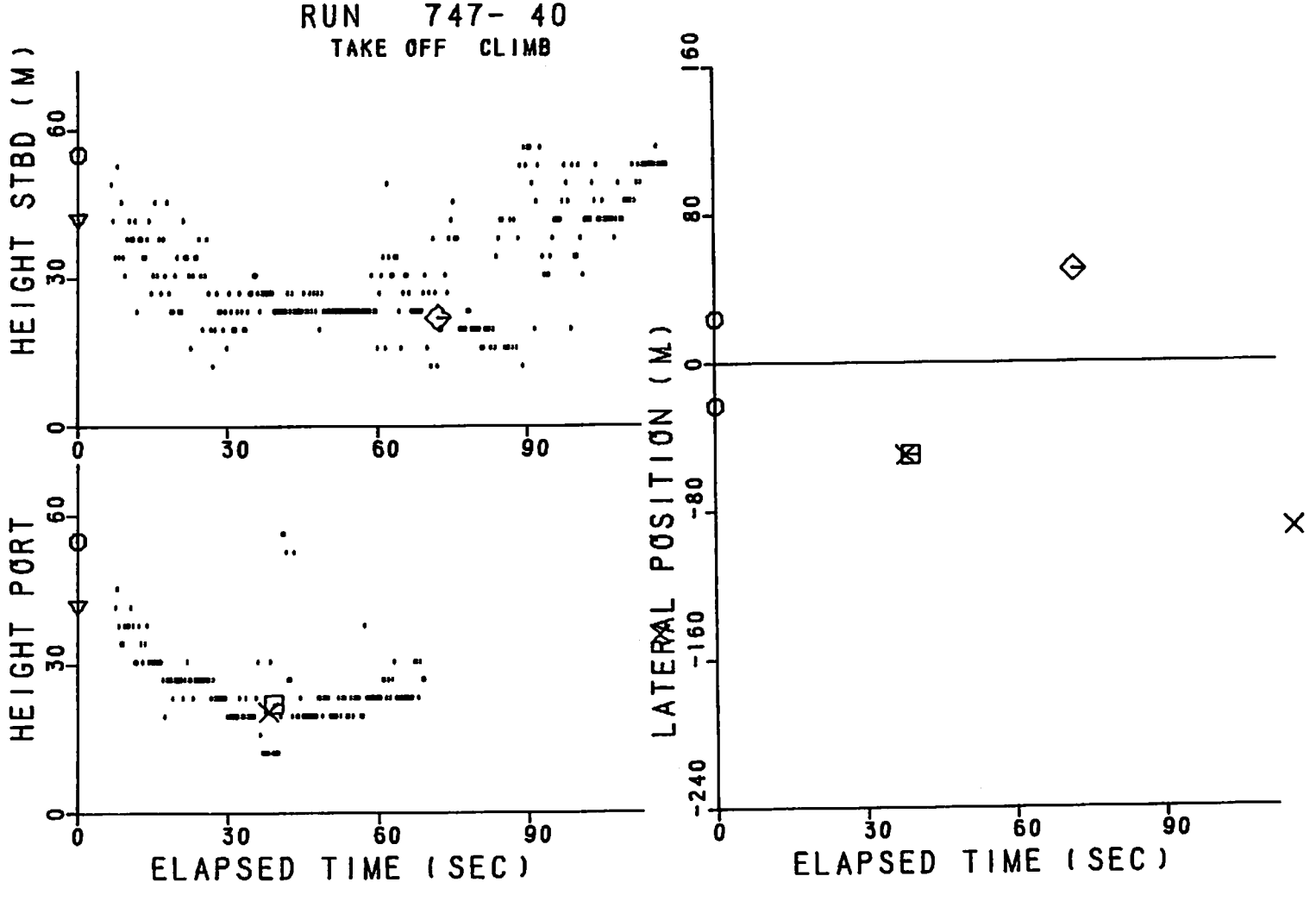

FIGURE 164. VORTEX-TRACKING DATA, RUN 40

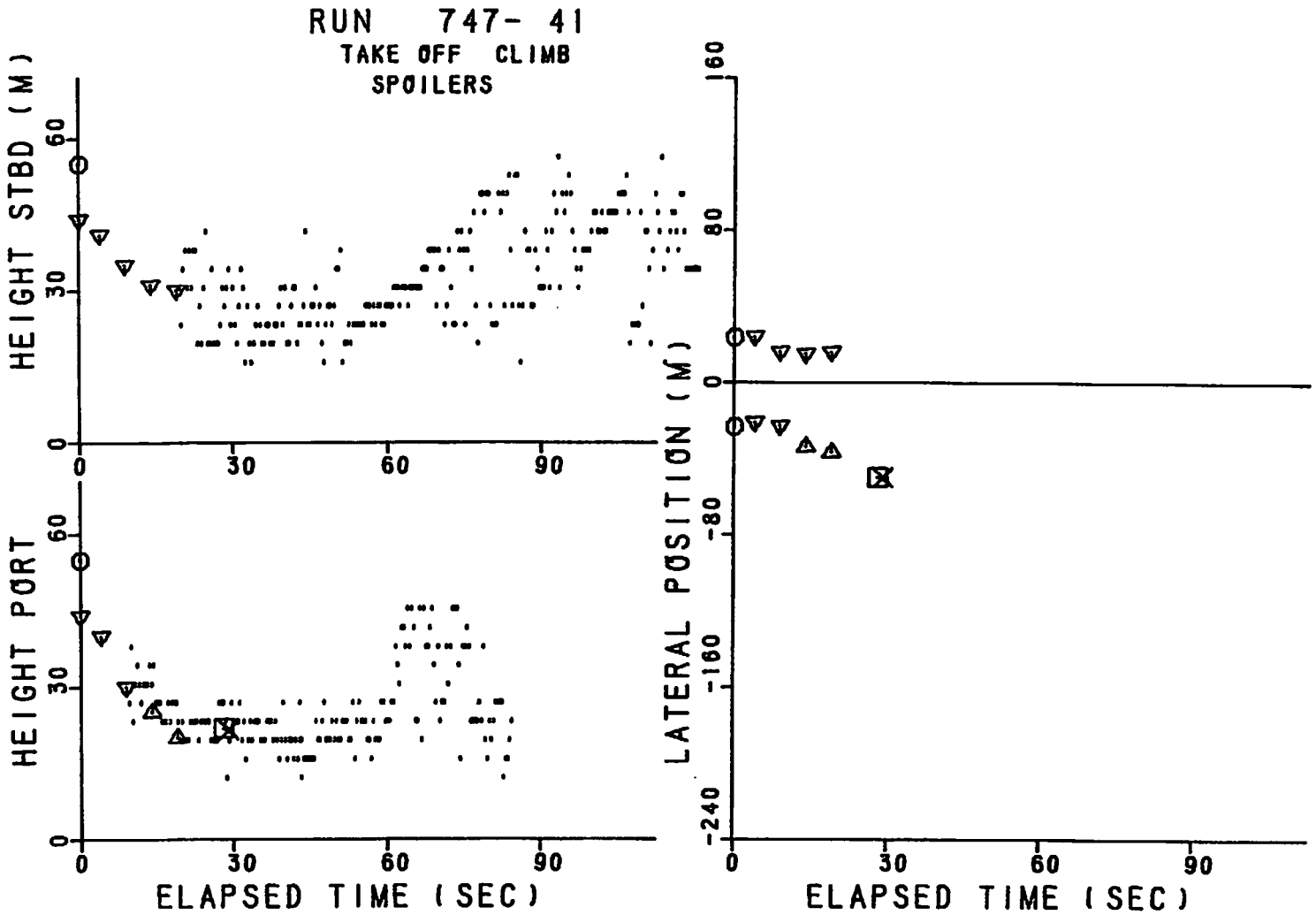

FIGURE 165. VORTEX-TRACKING DATA, RUN 41

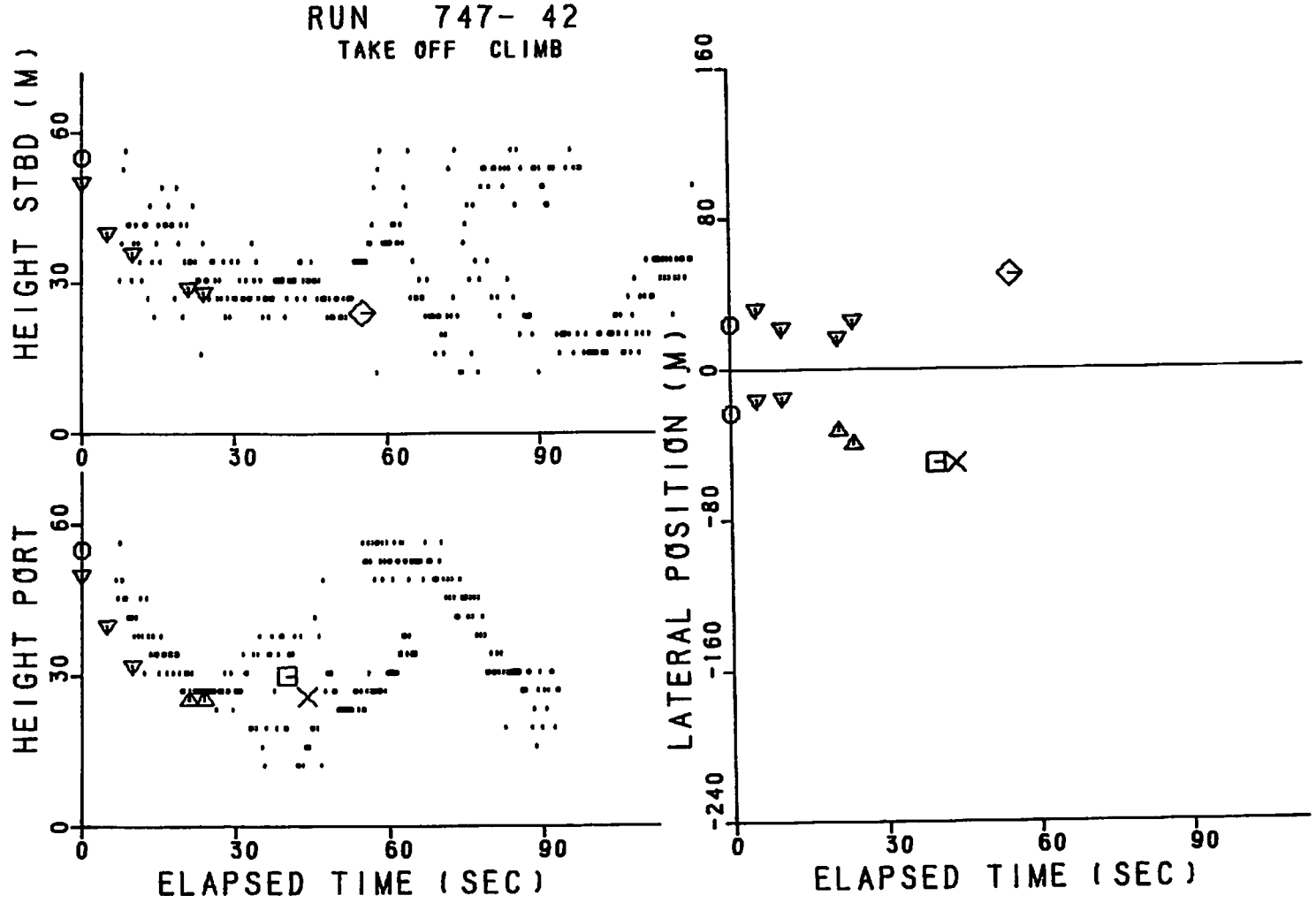

FIGURE 166. VORTEX-TRACKING DATA, RUN 42

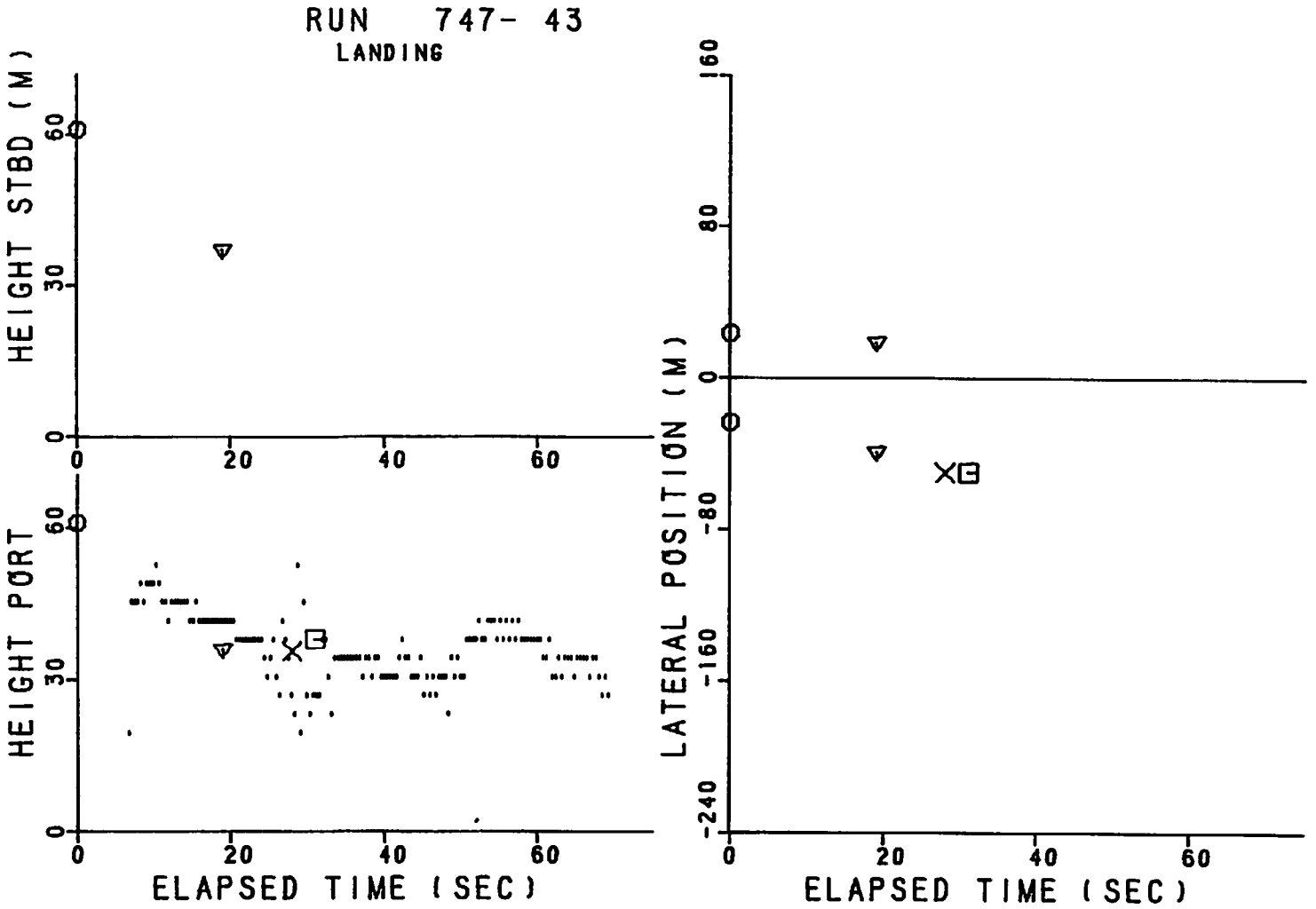

FIGURE 167. VORTEX-TRACKING DATA, RUN 43

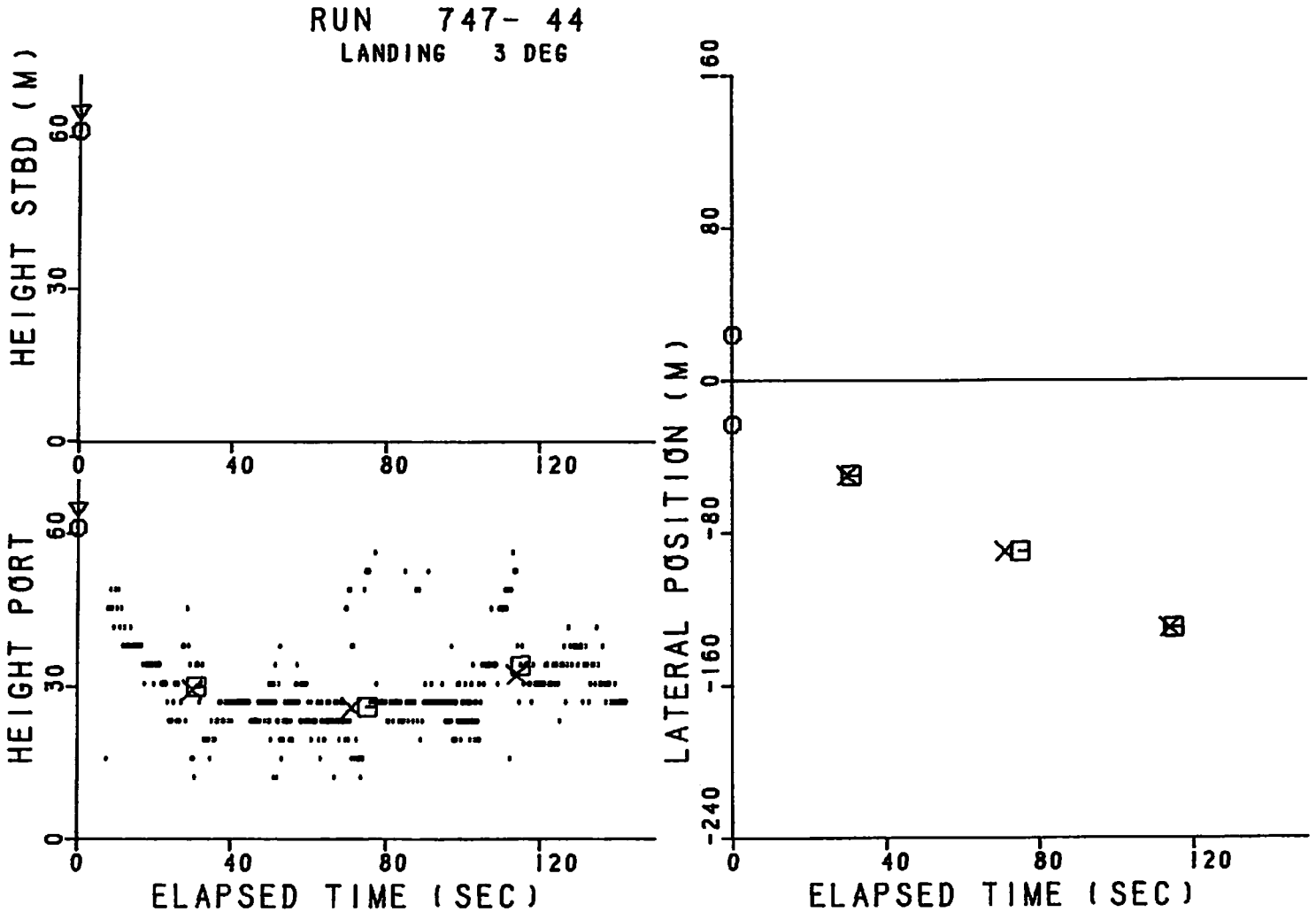

FIGURE 168. VORTEX-TRACKING DATA, RUN 44

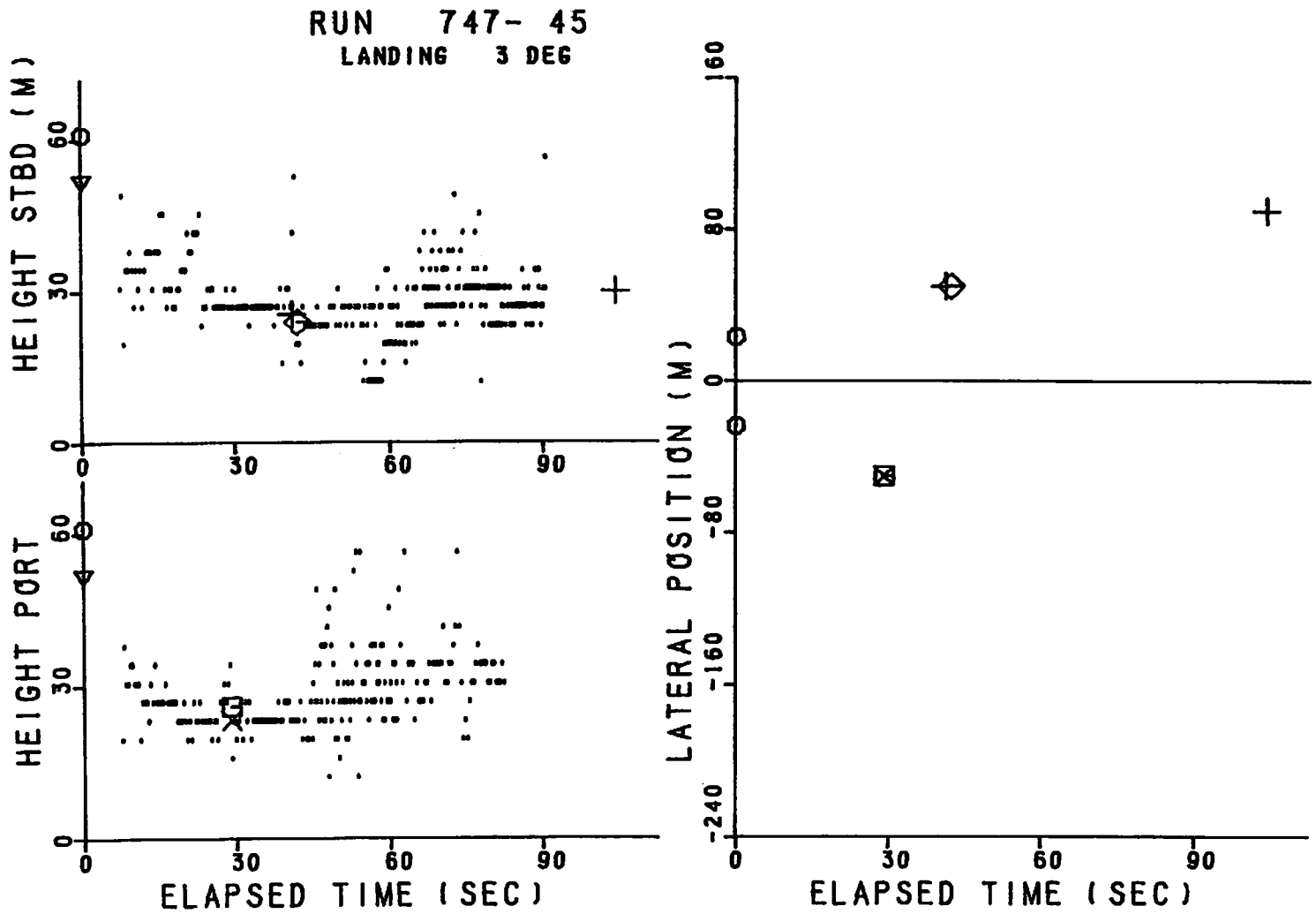

FIGURE 169. VORTEX-TRACKING DATA, RUN 45

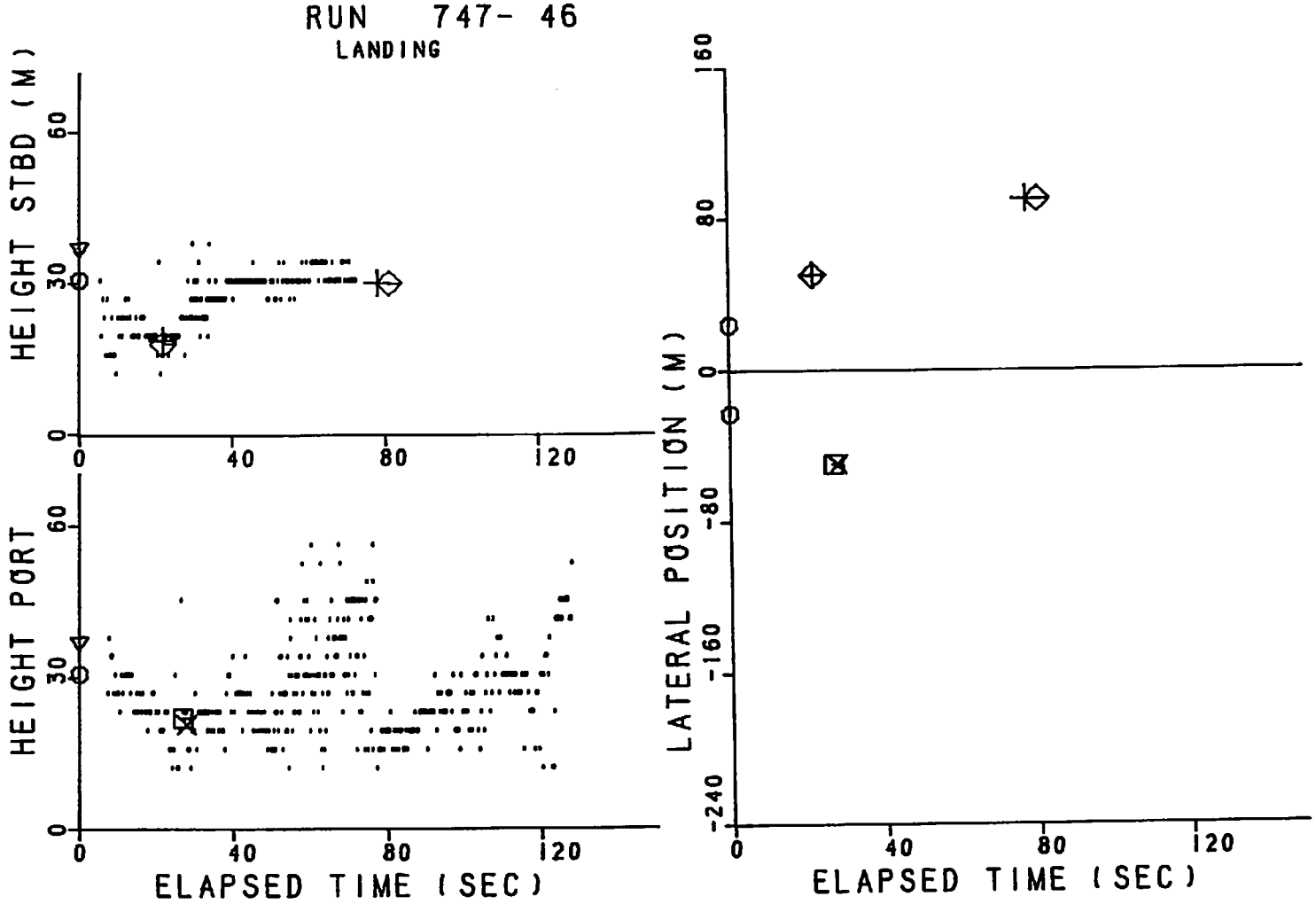

FIGURE 170. VORTEX-TRACKING DATA, RUN 46

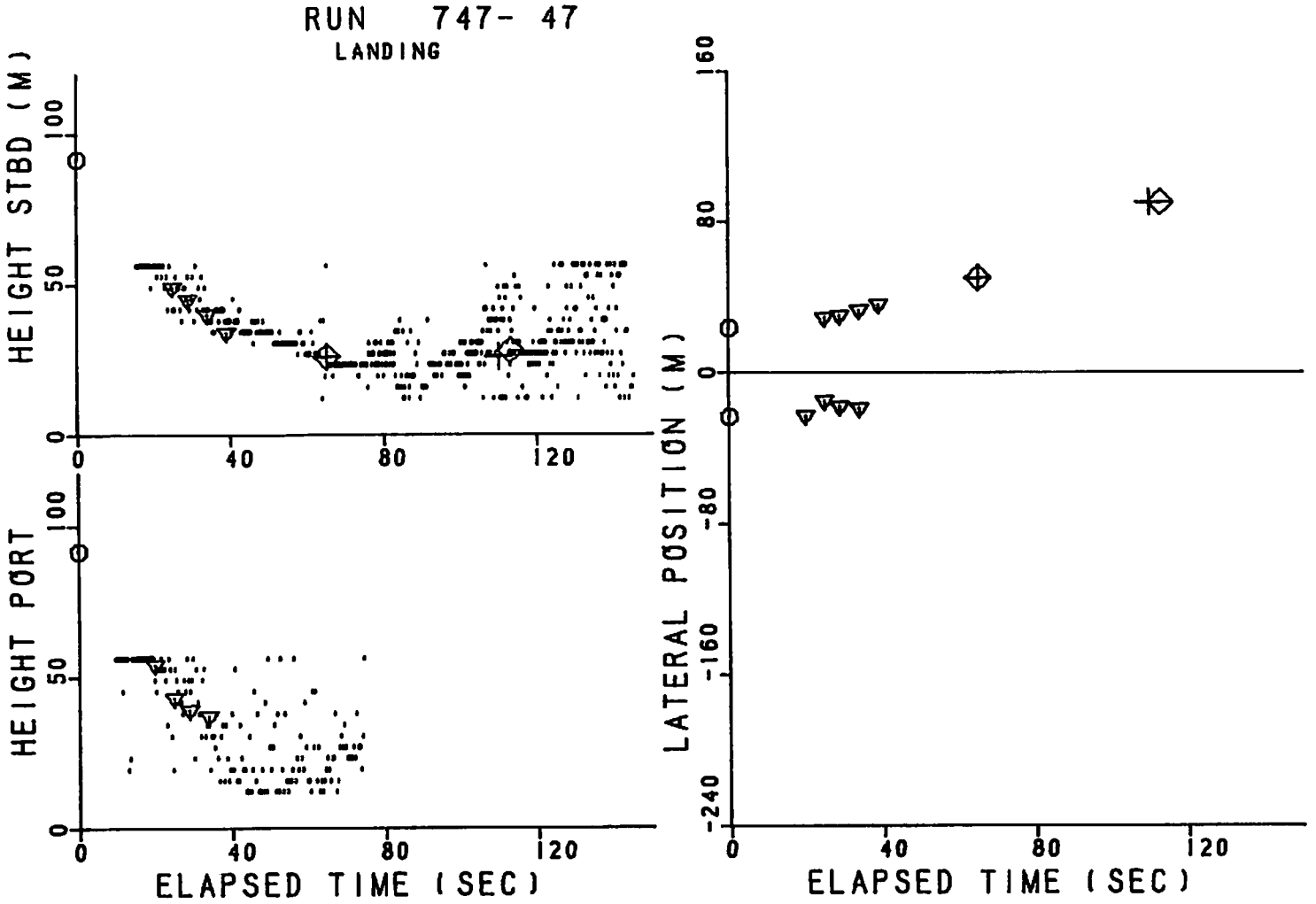

FIGURE 171. VORTEX-TRACKING DATA, RUN 47

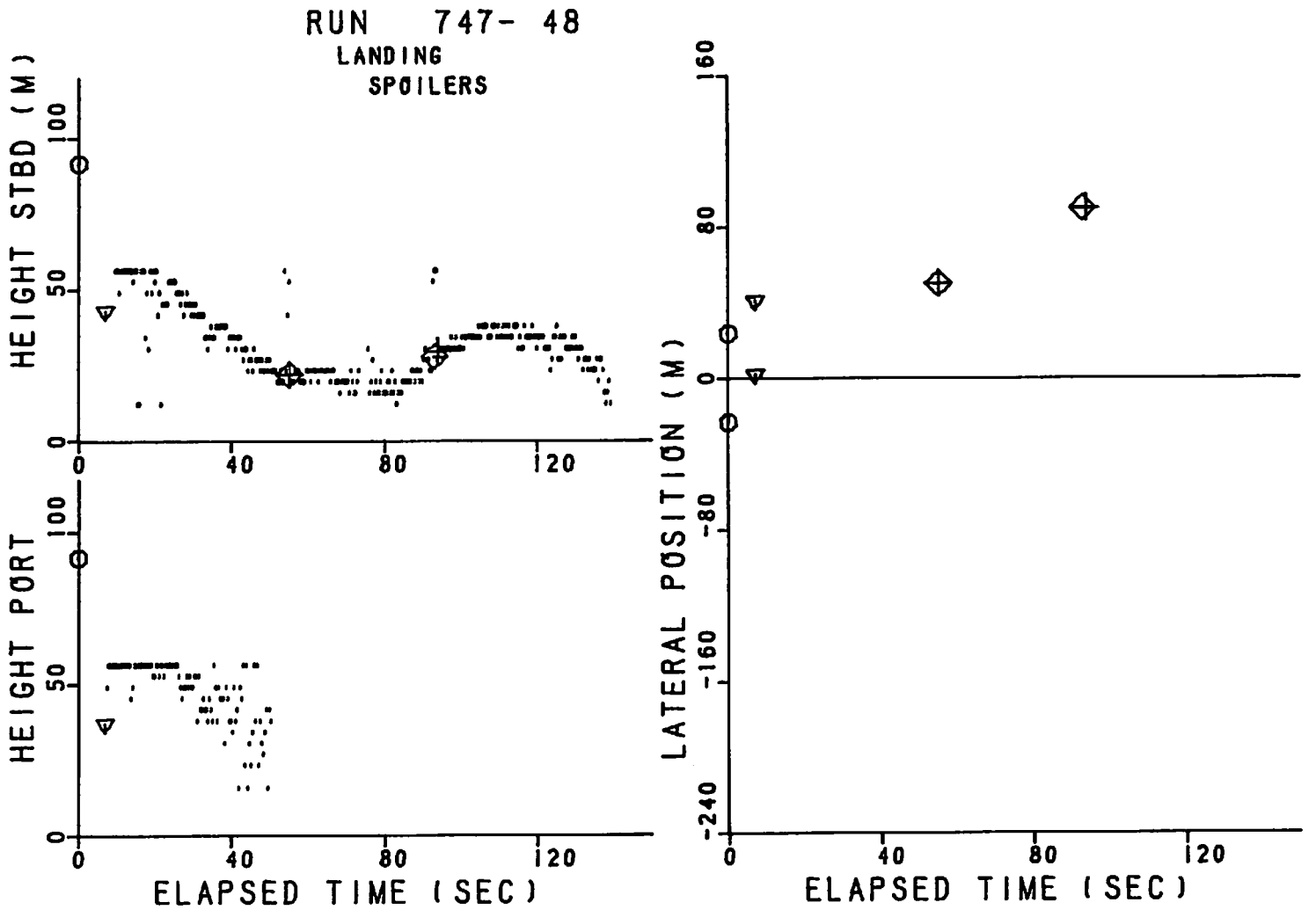

FIGURE 172. VORTEX-TRACKING DATA, RUN 48

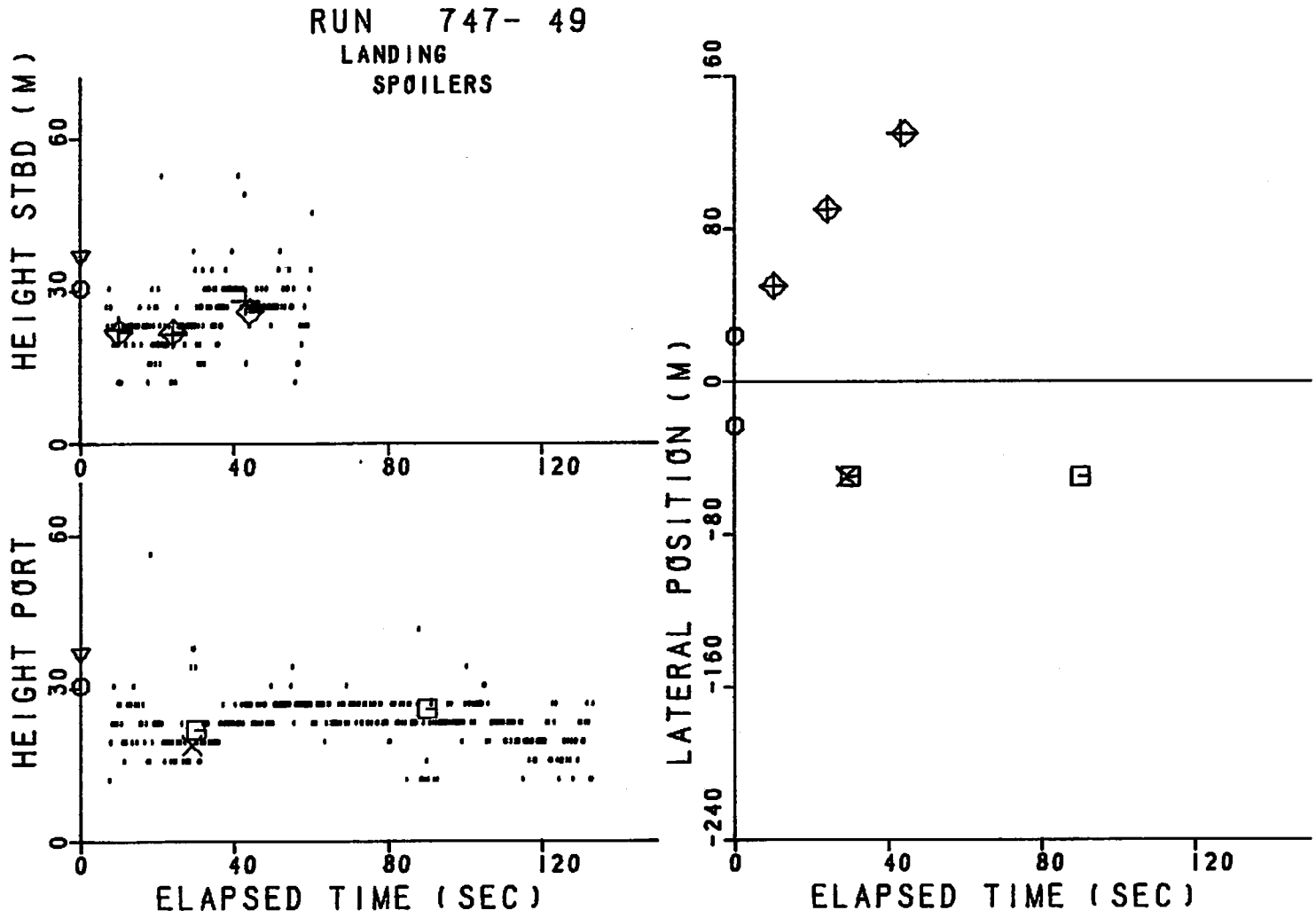

FIGURE 173. VORTEX-TRACKING DATA, RUN 49

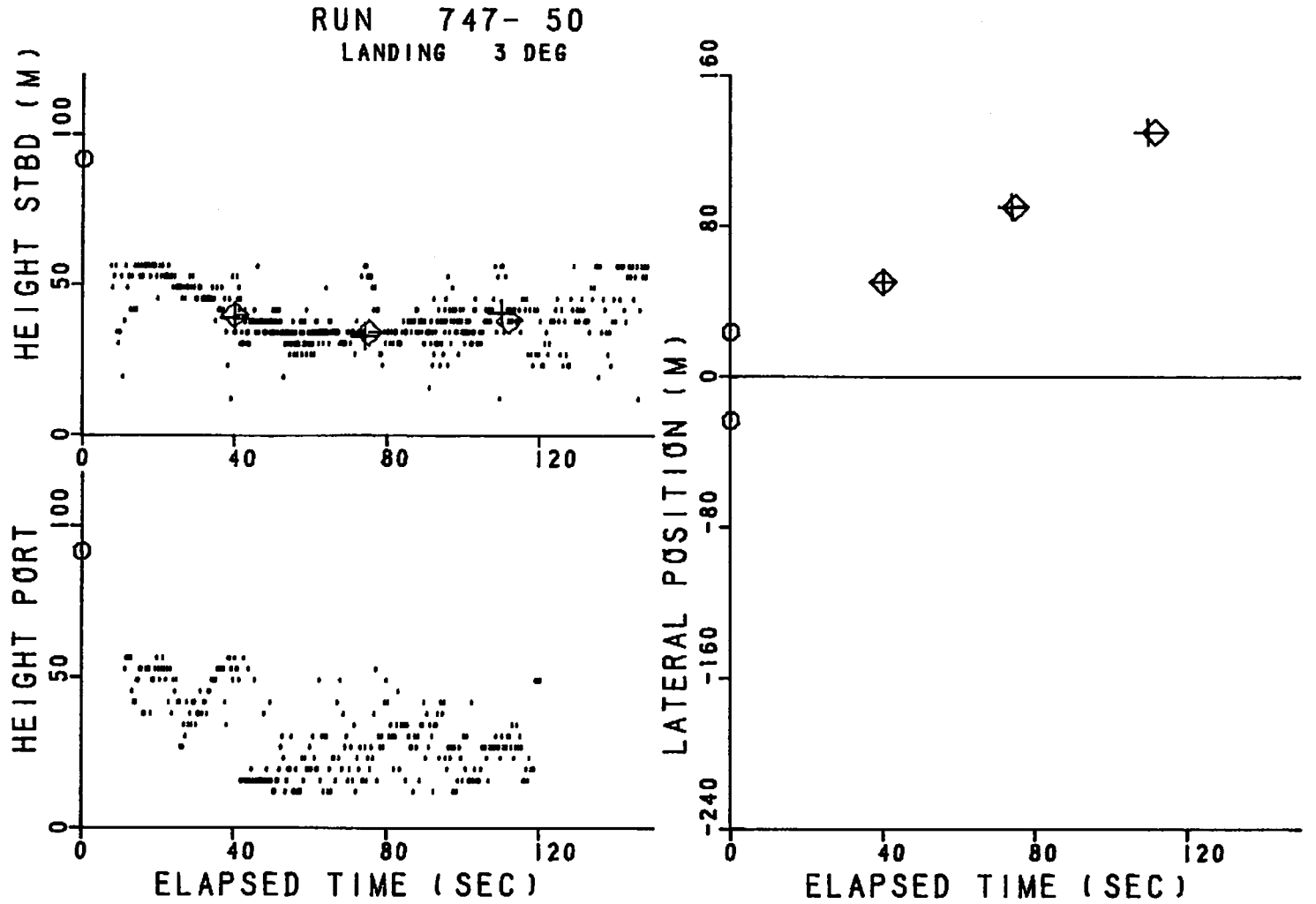

FIGURE 174. VORTEX-TRACKING DATA, RUN 50

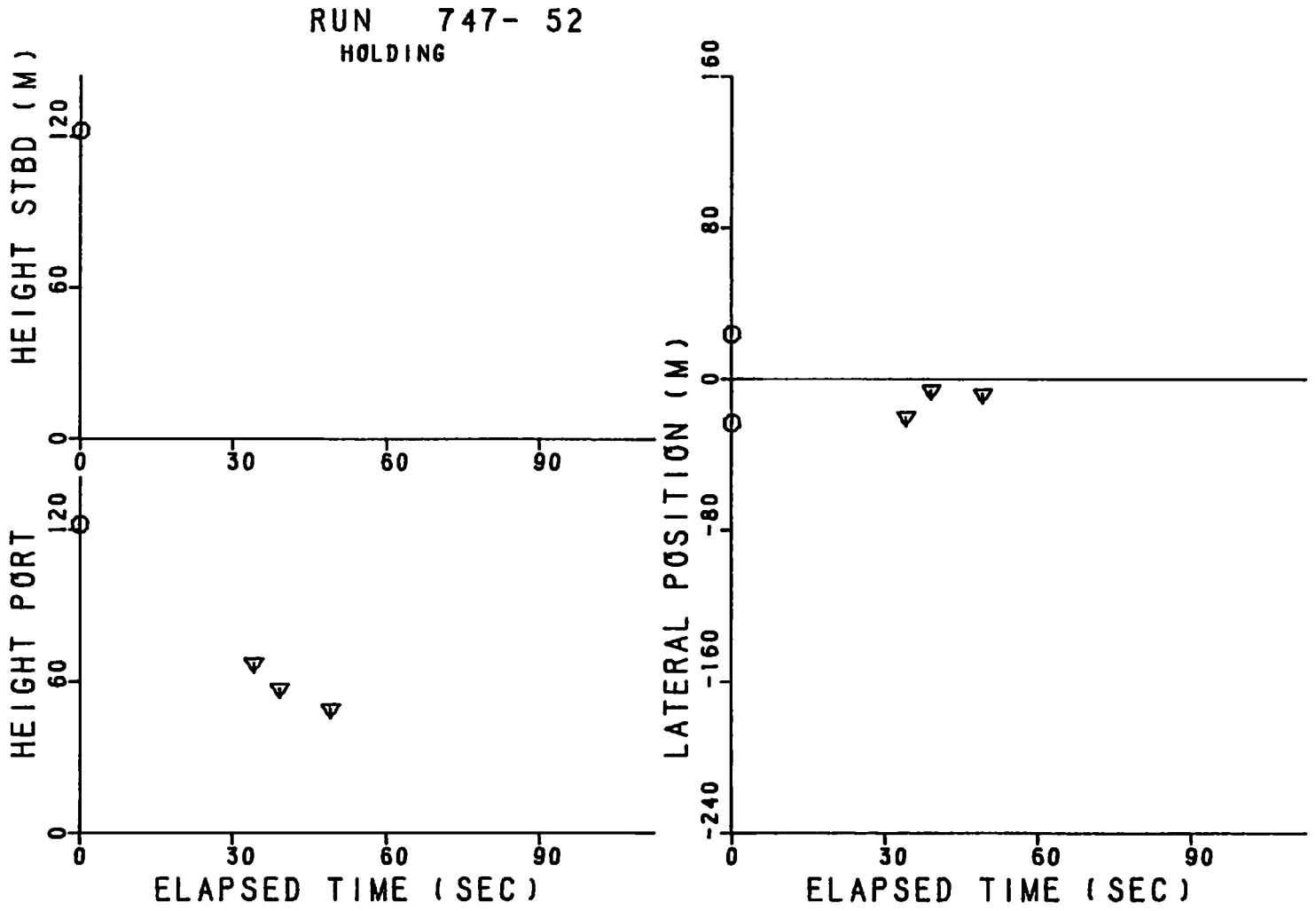

FIGURE 175. VORTEX-TRACKING DATA, RUN 52

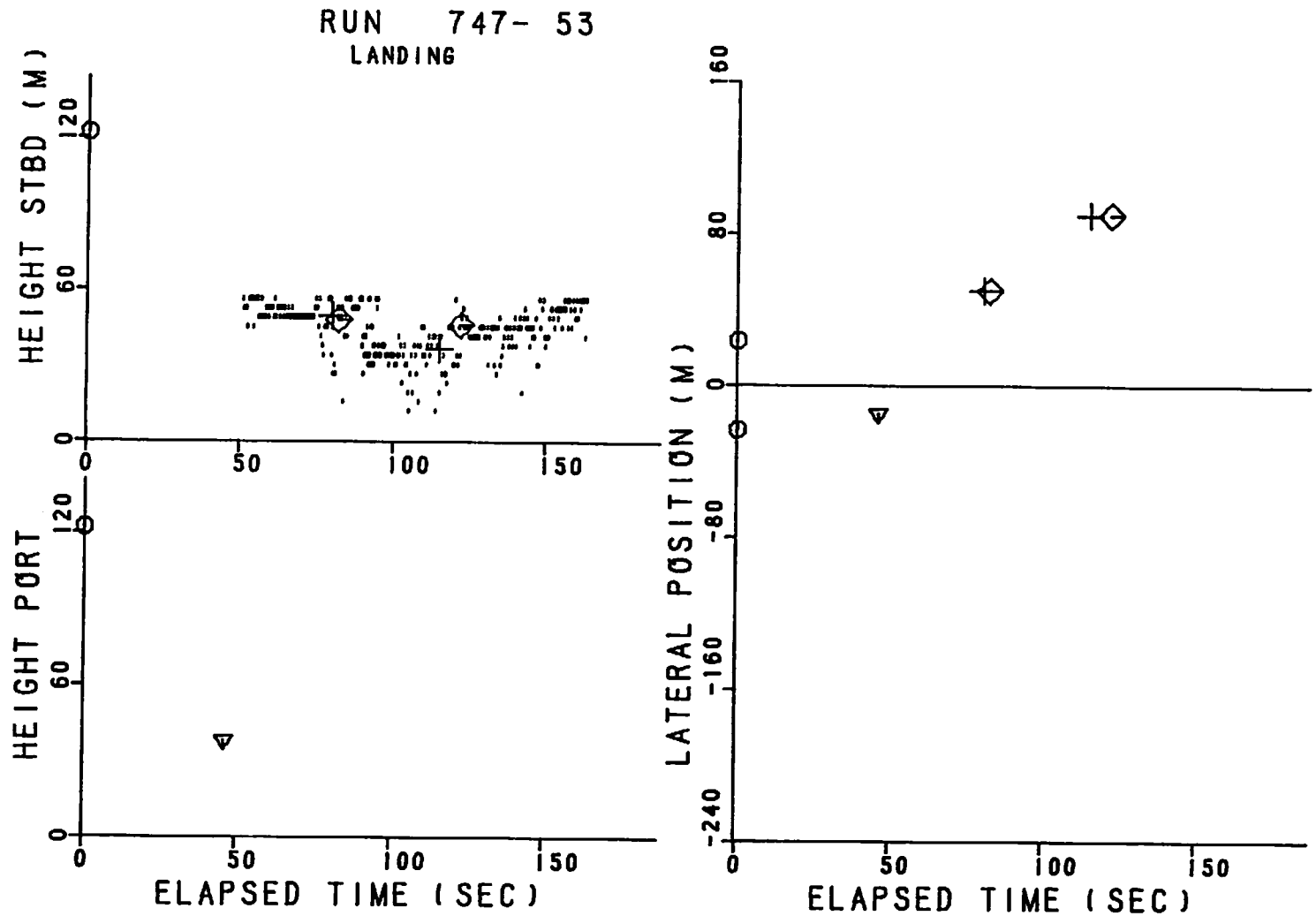

FIGURE 176. VORTEX-TRACKING DATA, RUN 53

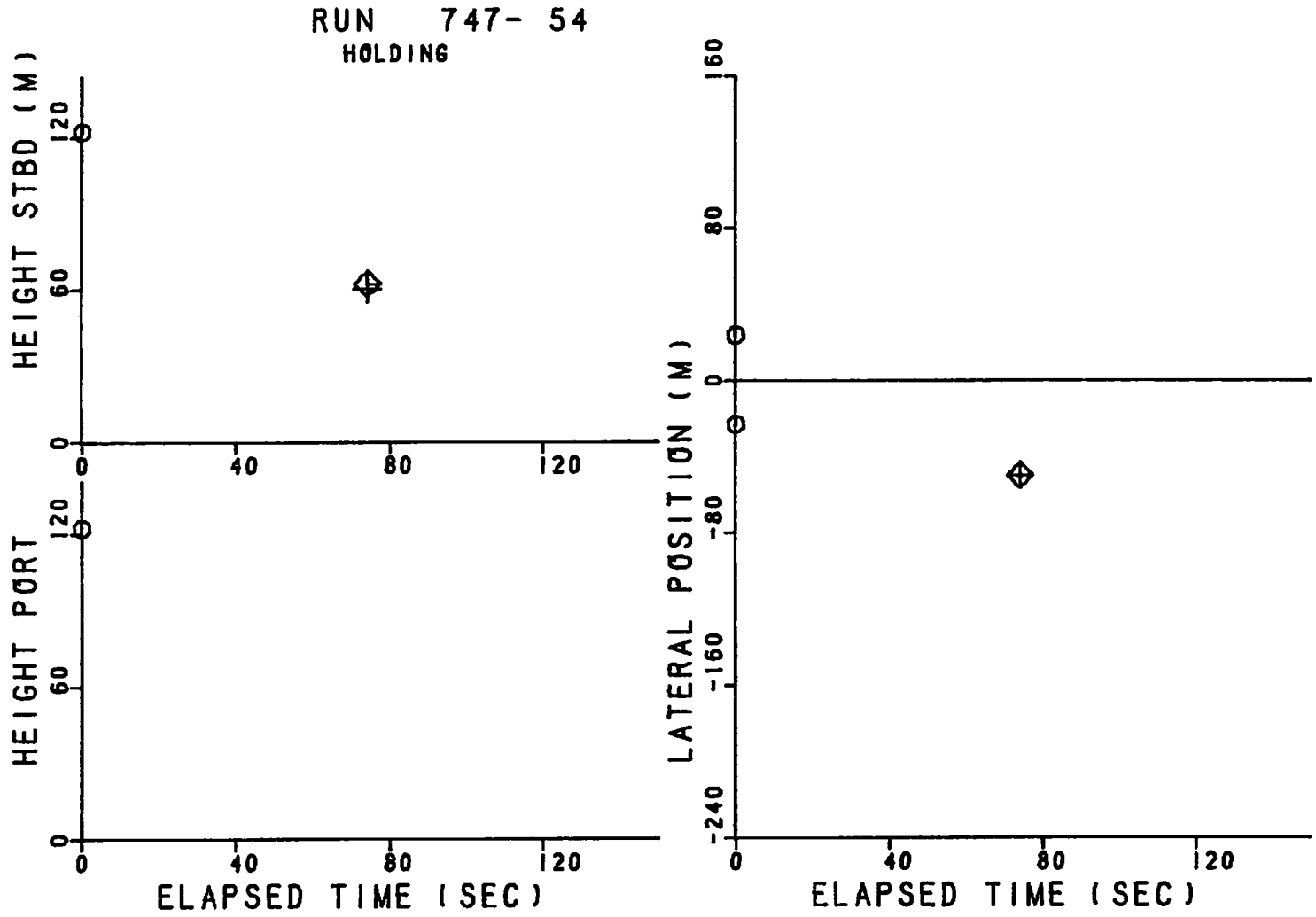

FIGURE 177. VORTEX-TRACKING DATA, RUN 54

E.2 VORTEX LINE-INTEGRAL PLOTS

The following plots show the line integral of the MAVSS vertical velocity measurements and the height making the largest contribution to the line integral (see Figs. 75 and 76). The line integral is multiplied by two before it is plotted, so that it gives an approximate measurement of the vortex strength when the vortex center is near the antenna beam. The height is plotted as the range-gate number (1 to 16). The times when the height data appeared to give a consistent indication of vortex height are marked with a double line on the time axis; these data were plotted in the preceding tracking plots. The antennas showing no useful vortex activity are omitted.

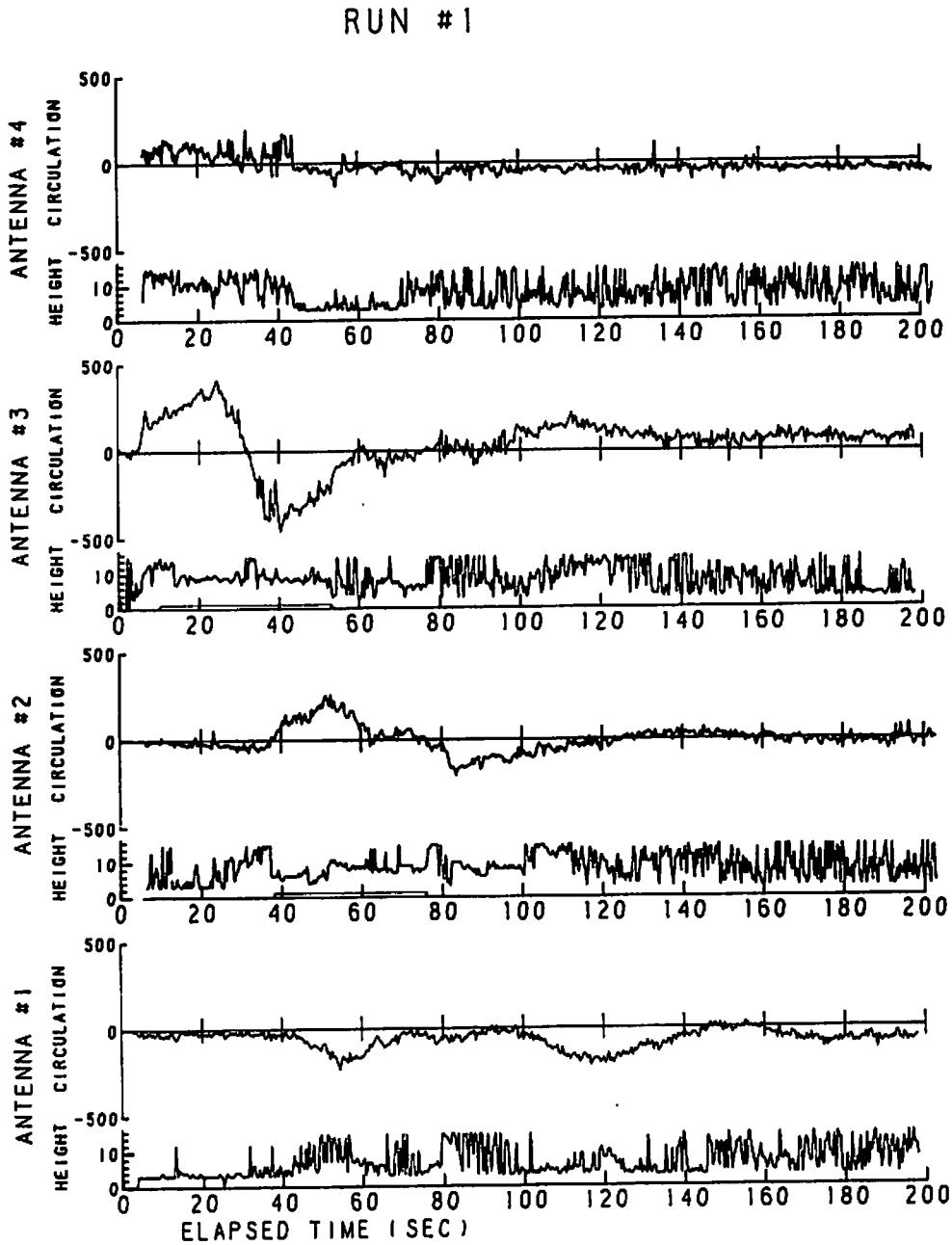

FIGURE 178. LINE-INTEGRAL AND HEIGHT DATA FOR RUN 1

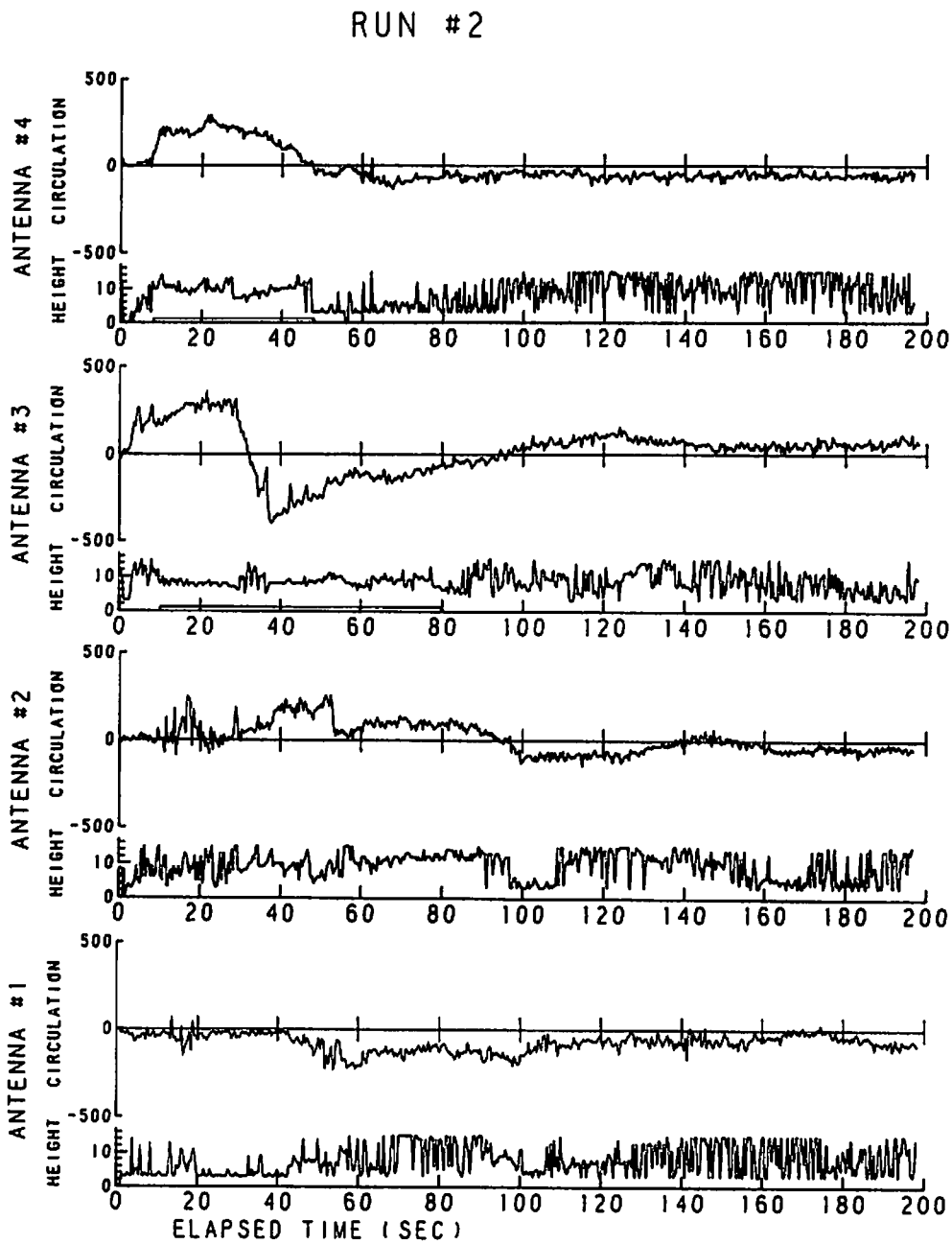

FIGURE 179. LINE-INTEGRAL AND HEIGHT DATA FOR RUN 2

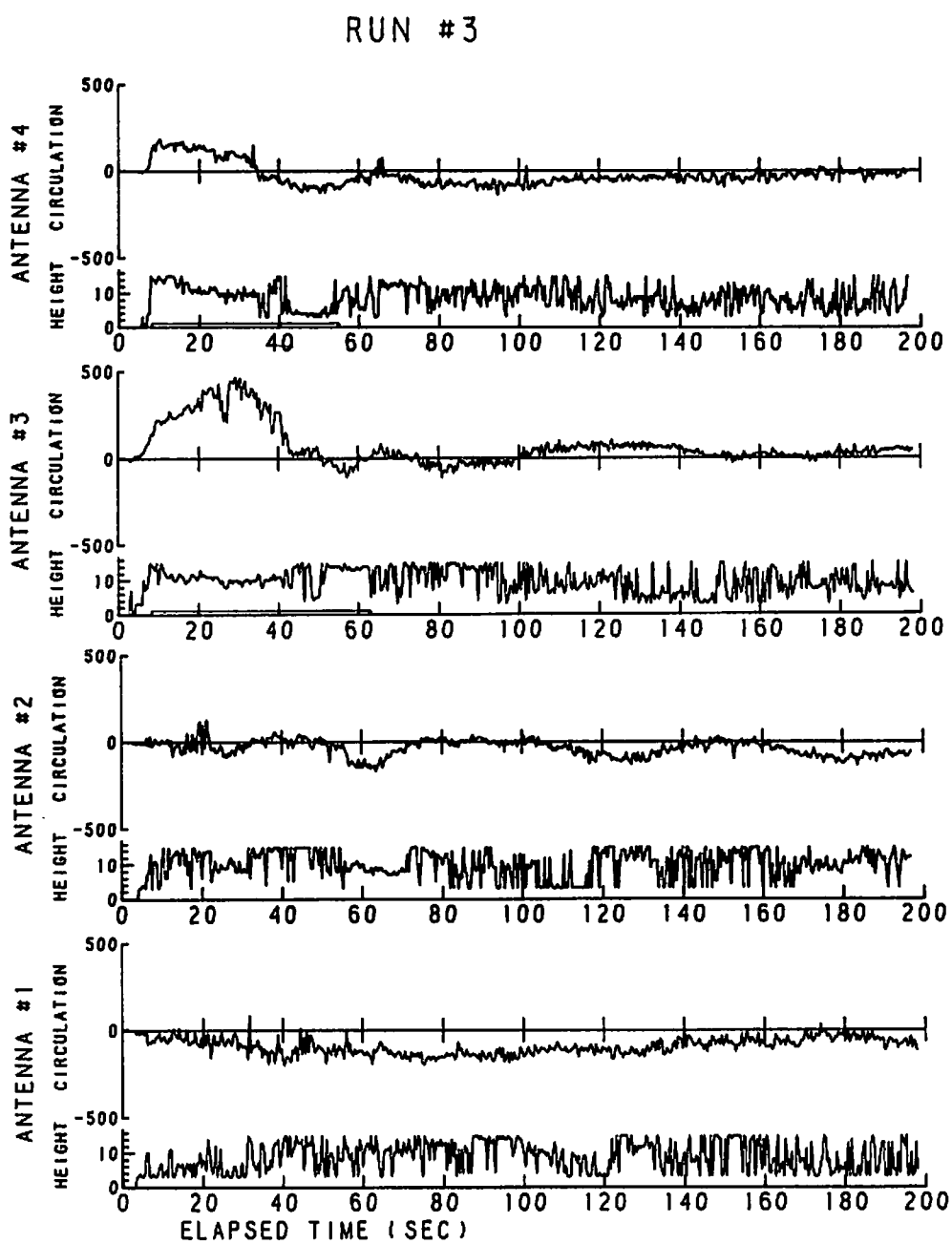

FIGURE 180. LINE-INTEGRAL AND HEIGHT DATA FOR RUN 3

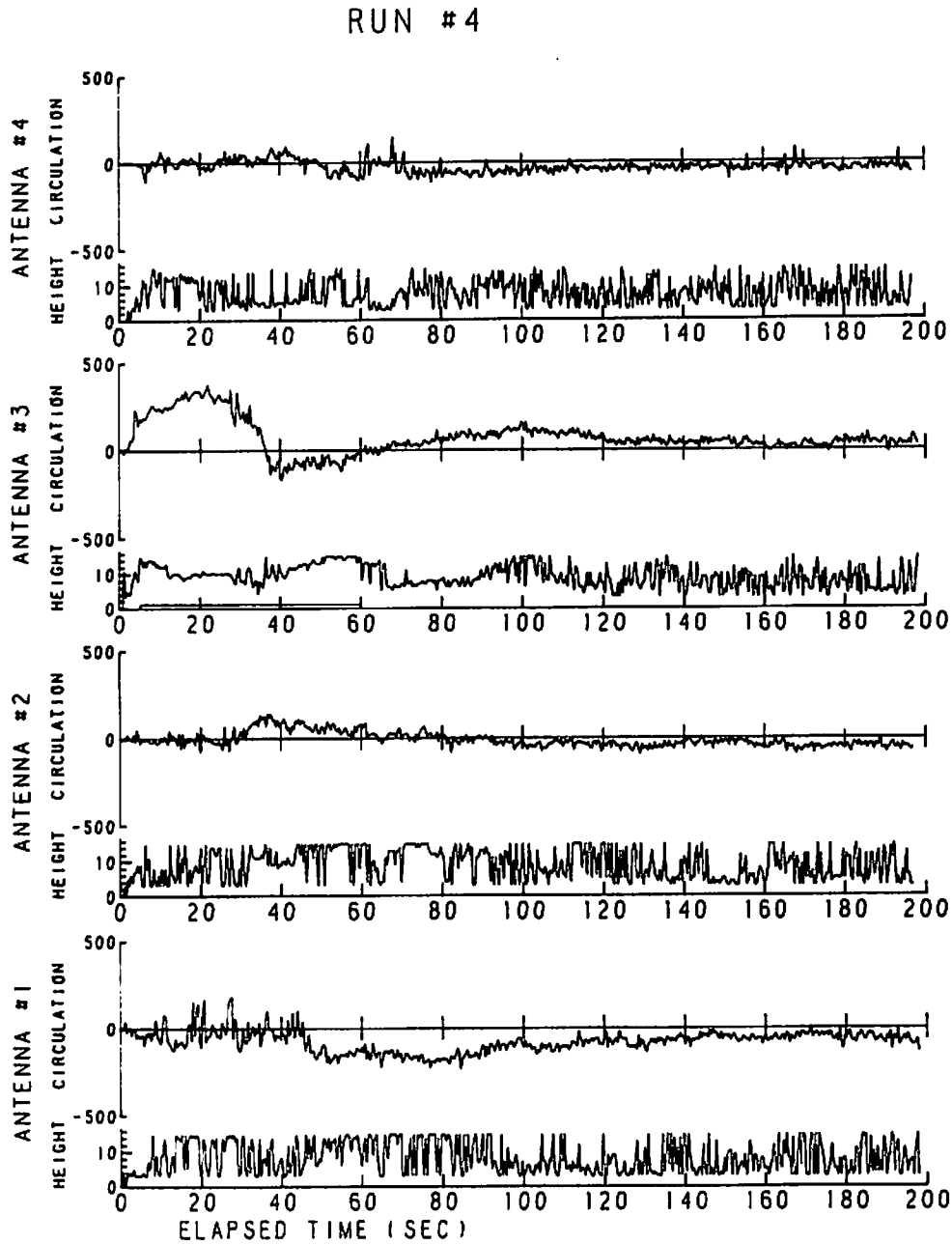

FIGURE 181. LINE-INTEGRAL AND HEIGHT DATA FOR RUN 4

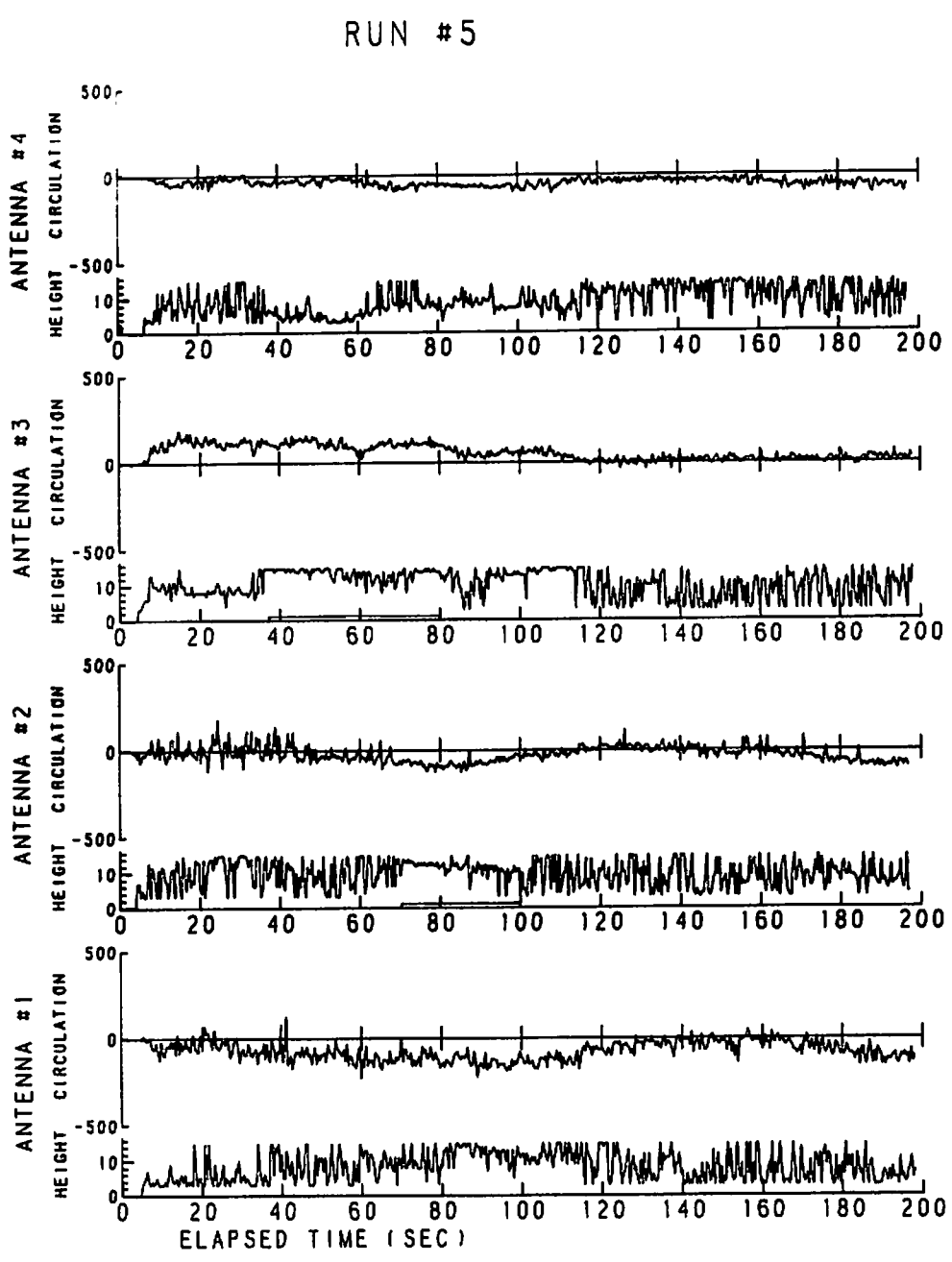

FIGURE 182. LINE-INTEGRAL AND HEIGHT DATA FOR RUN 5

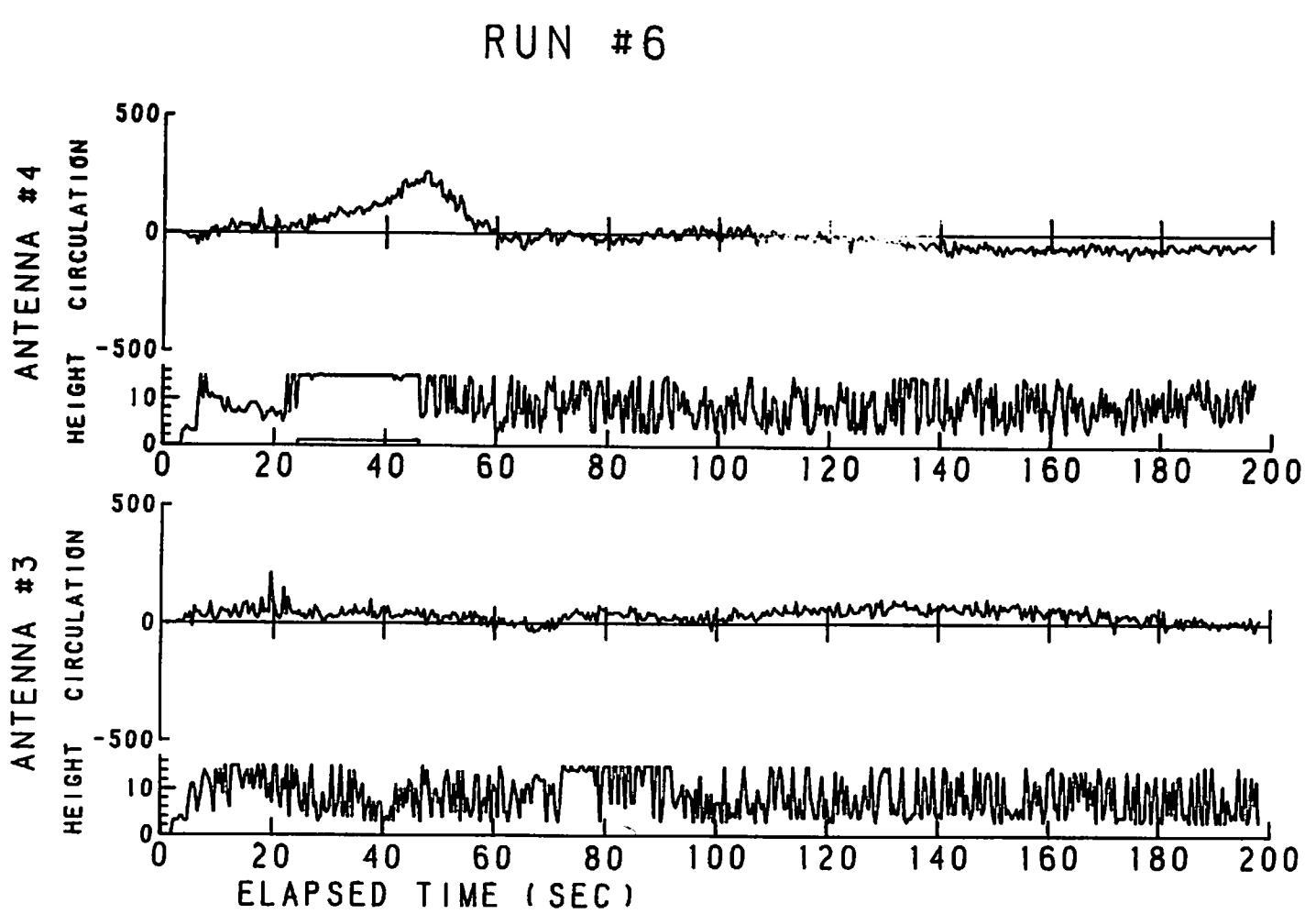

FIGURE 183. LINE-INTEGRAL AND HEIGHT DATA FOR RUN 6

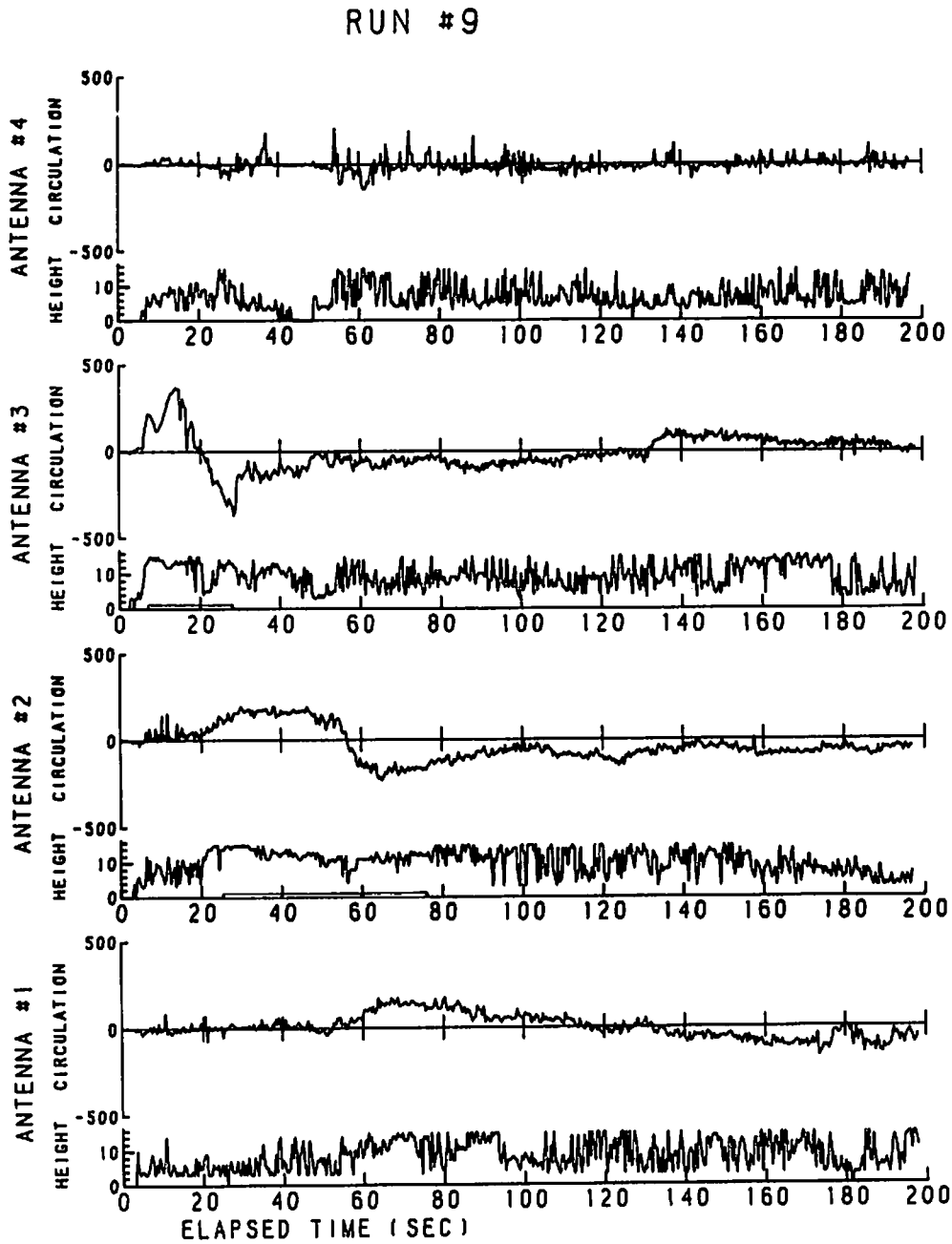

FIGURE 184. LINE-INTEGRAL AND HEIGHT DATA FOR RUN 9

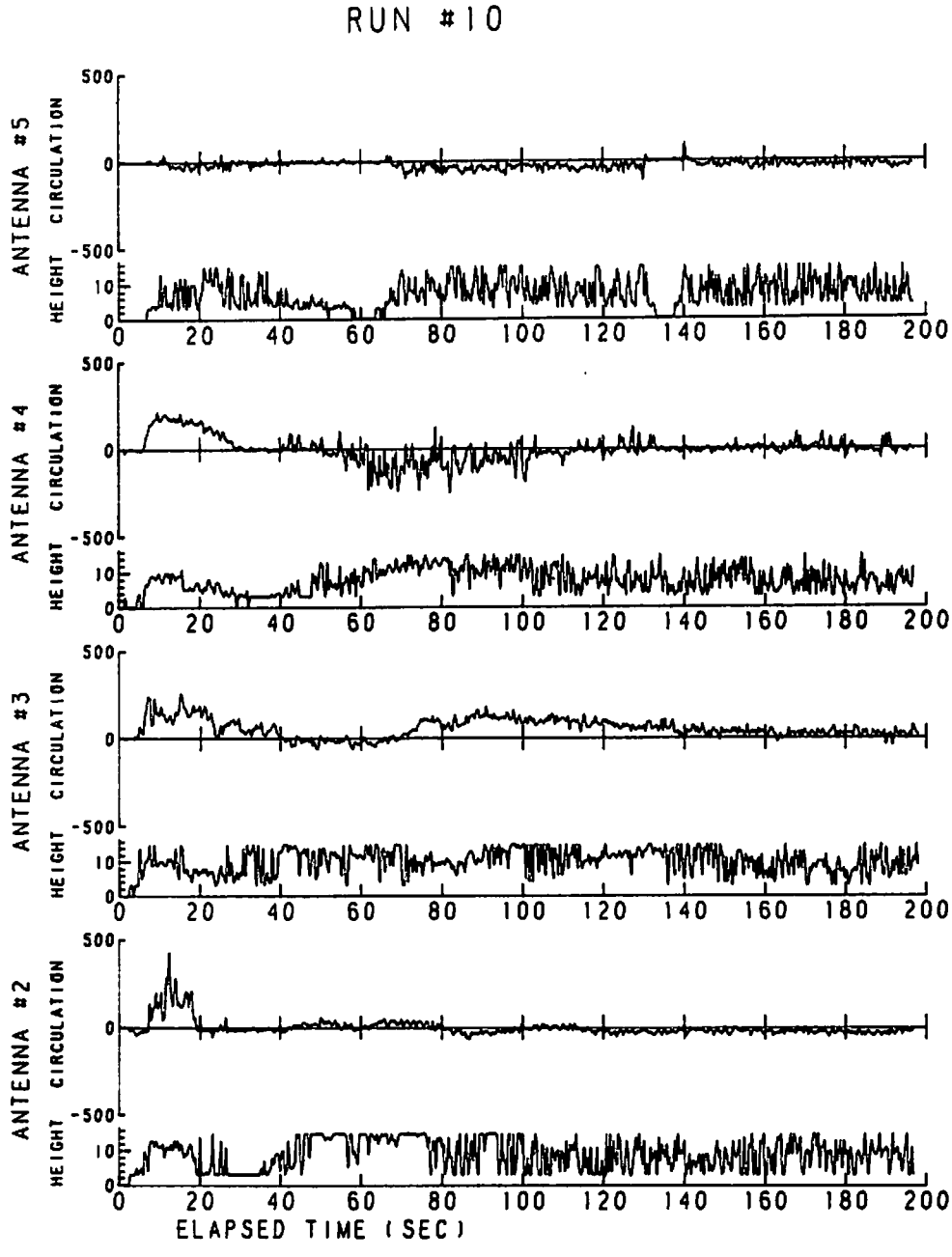

FIGURE 185. LINE-INTEGRAL AND HEIGHT DATA FOR RUN 10

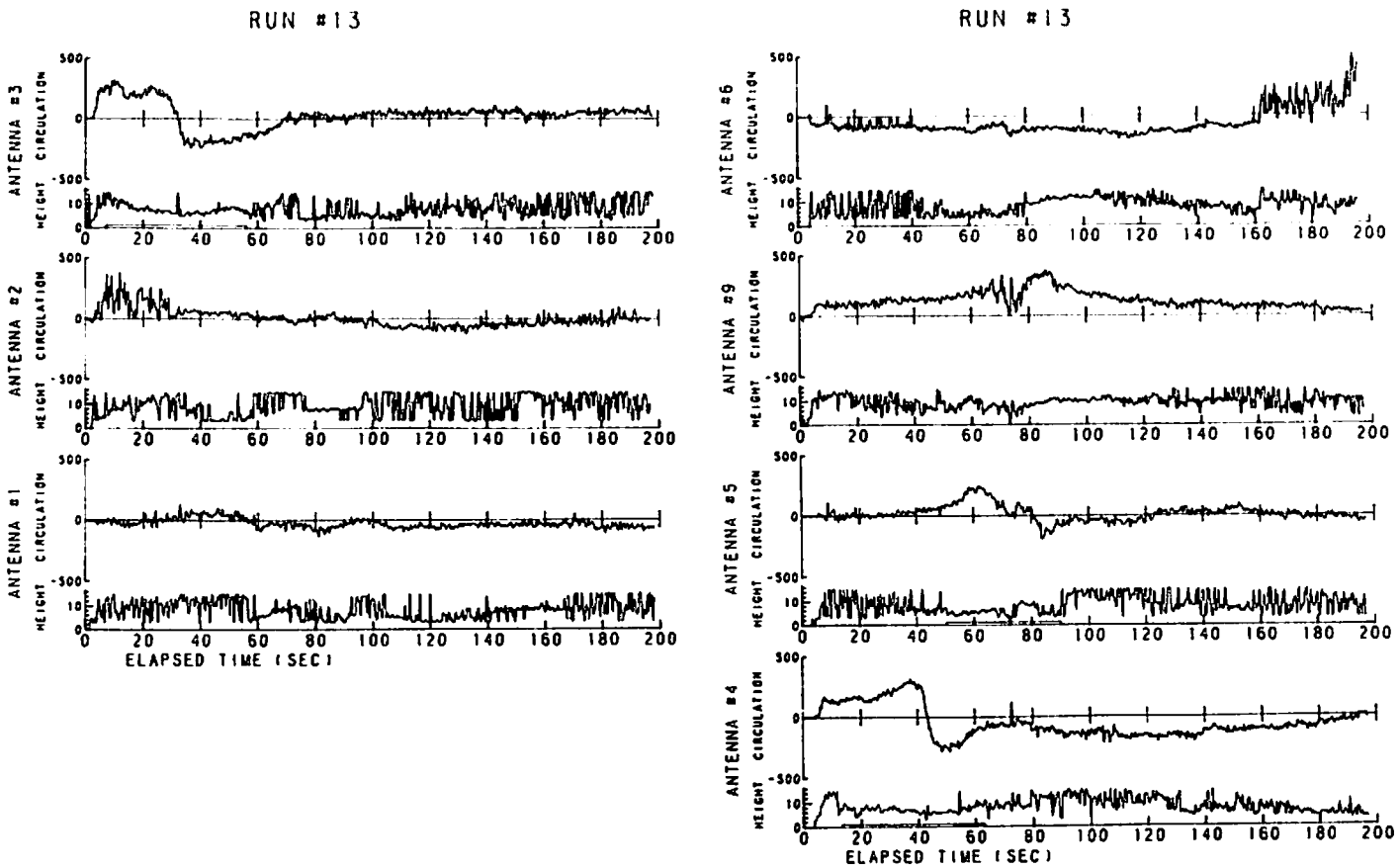

FIGURE 186. LINE-INTEGRAL AND HEIGHT DATA FOR RUN 13

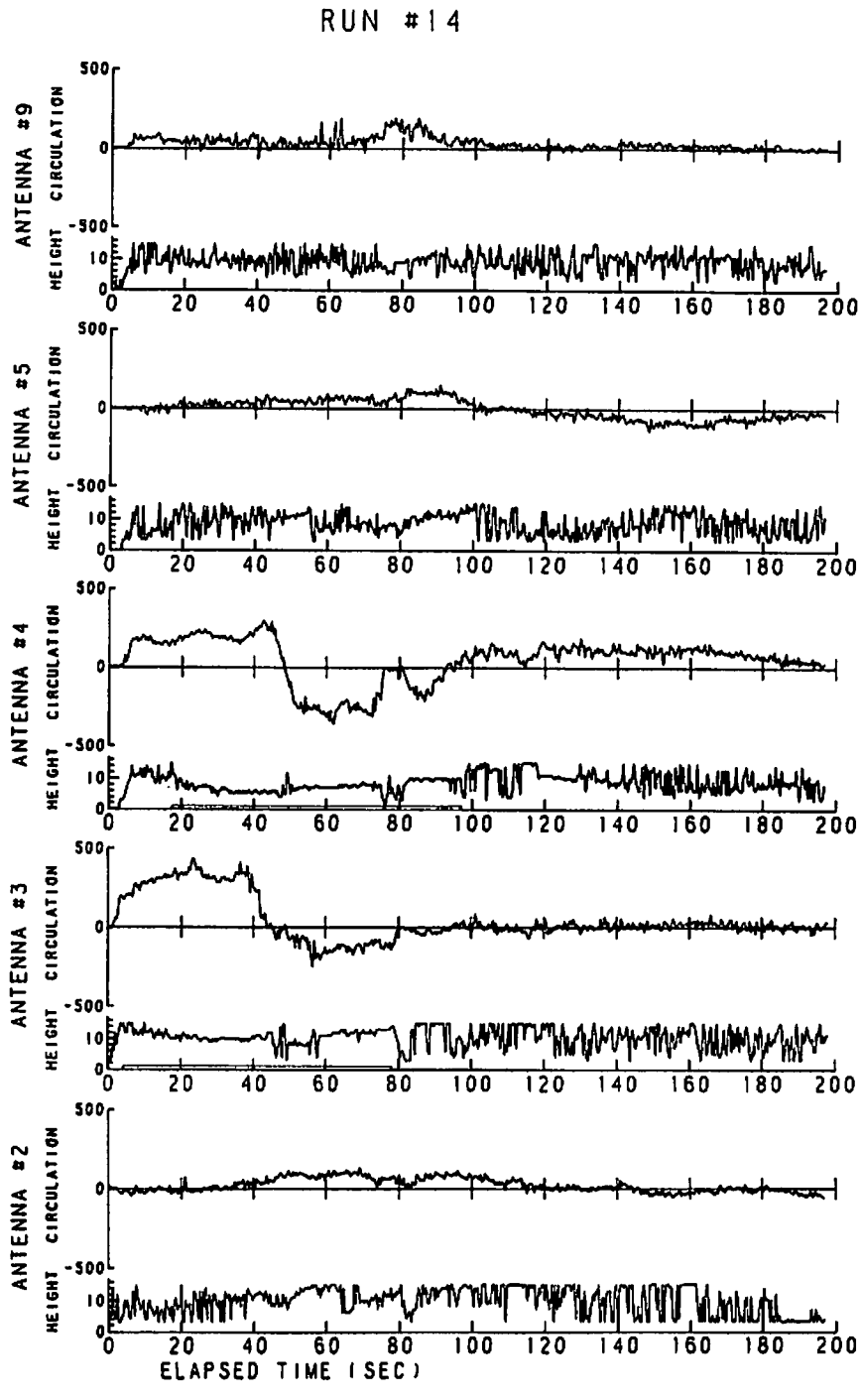

FIGURE 187. LINE-INTEGRAL AND HEIGHT DATA FOR RUN 14

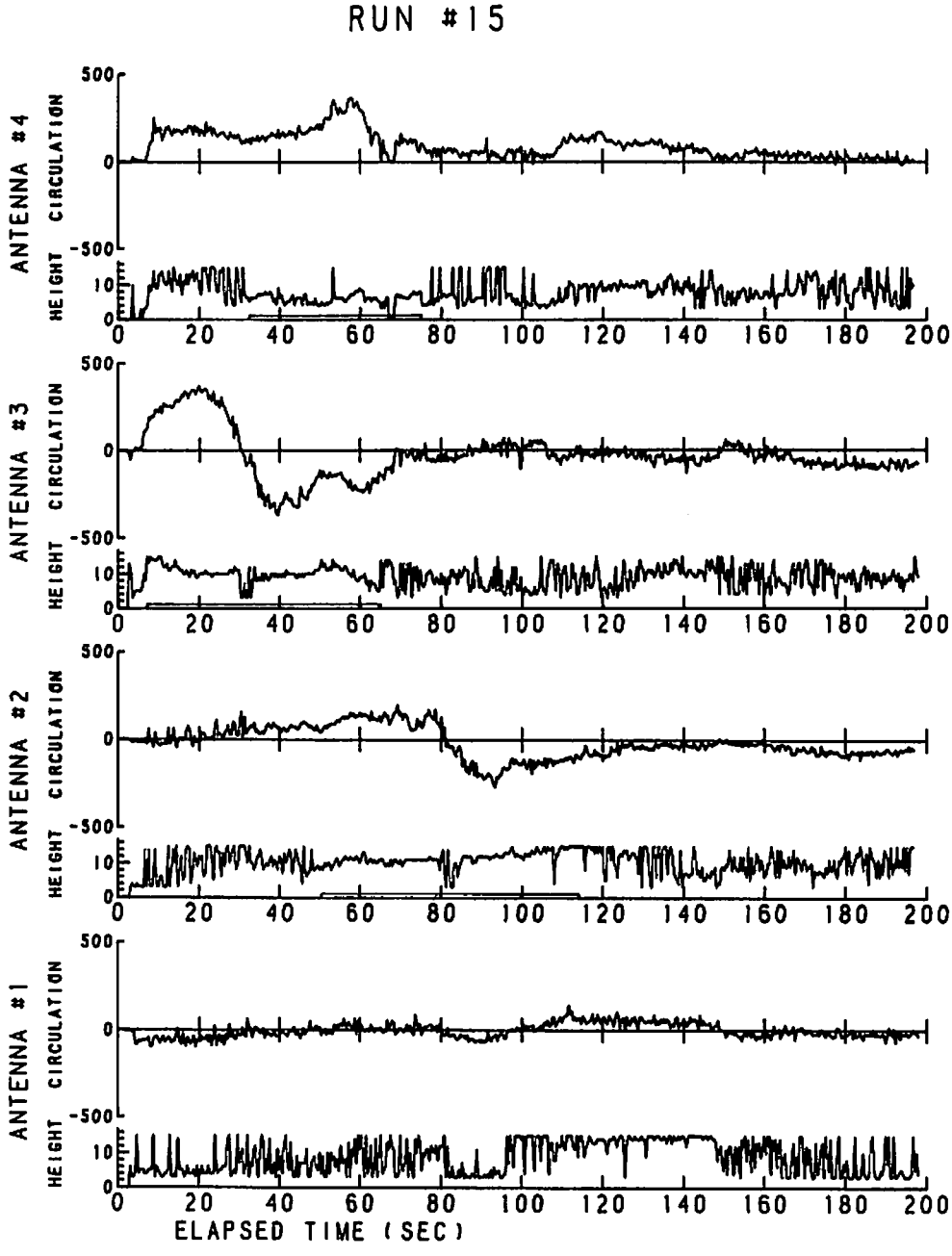

FIGURE 188. LINE-INTEGRAL AND HEIGHT DATA FOR RUN 15

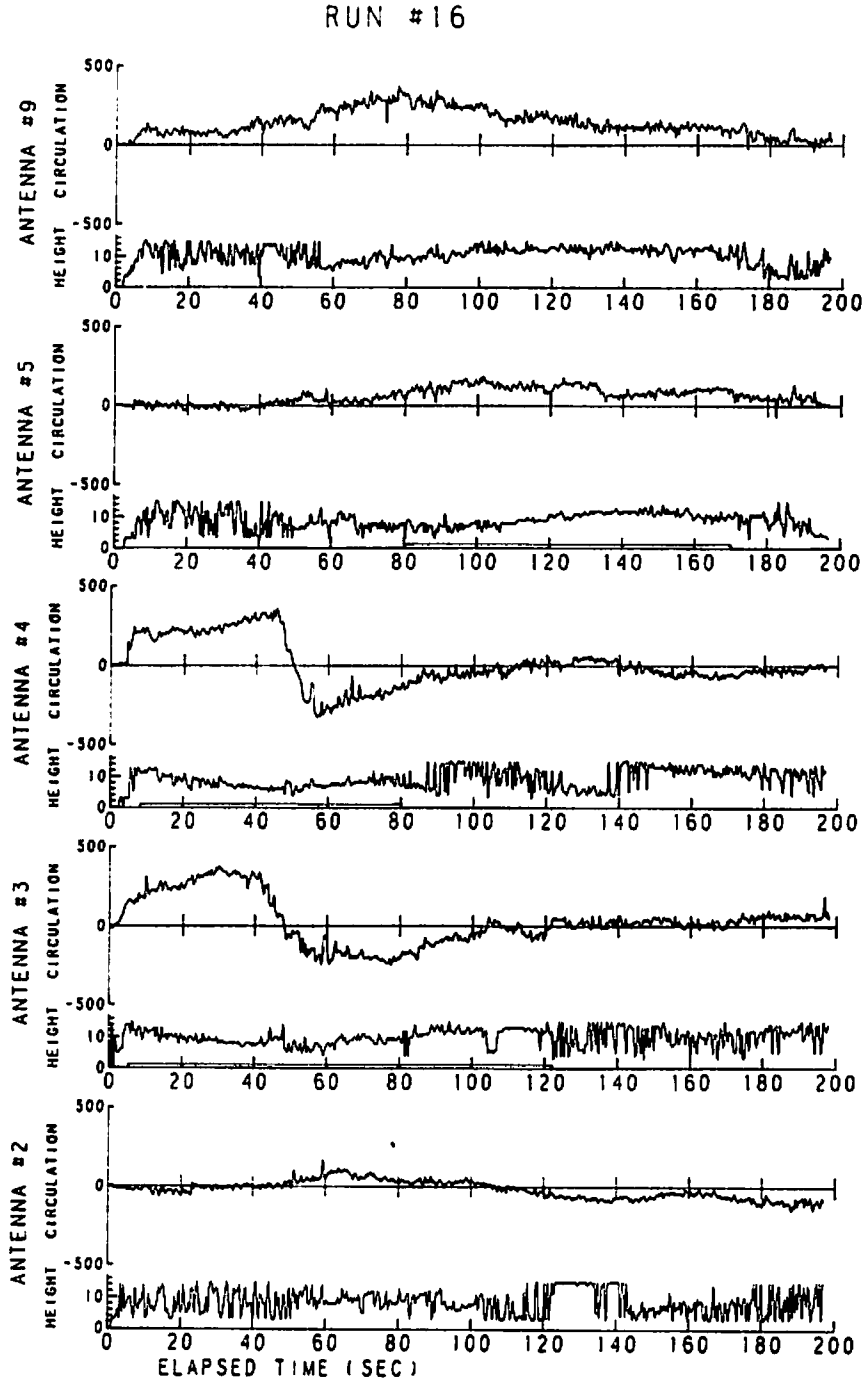

FIGURE 189. LINE-INTEGRAL AND HEIGHT DATA FOR RUN 16

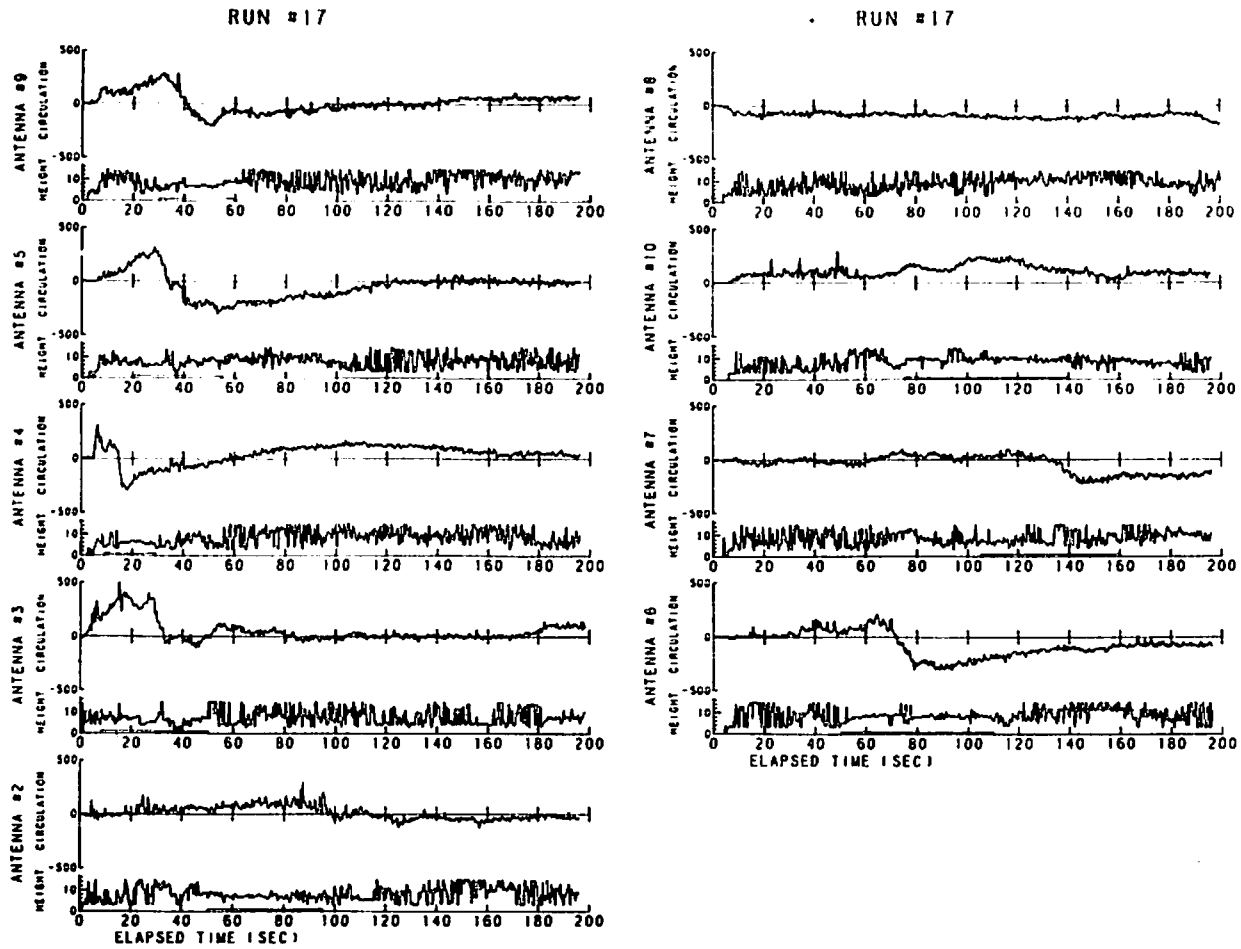

FIGURE 190. LINE-INTEGRAL AND HEIGHT DATA FOR RUN 17

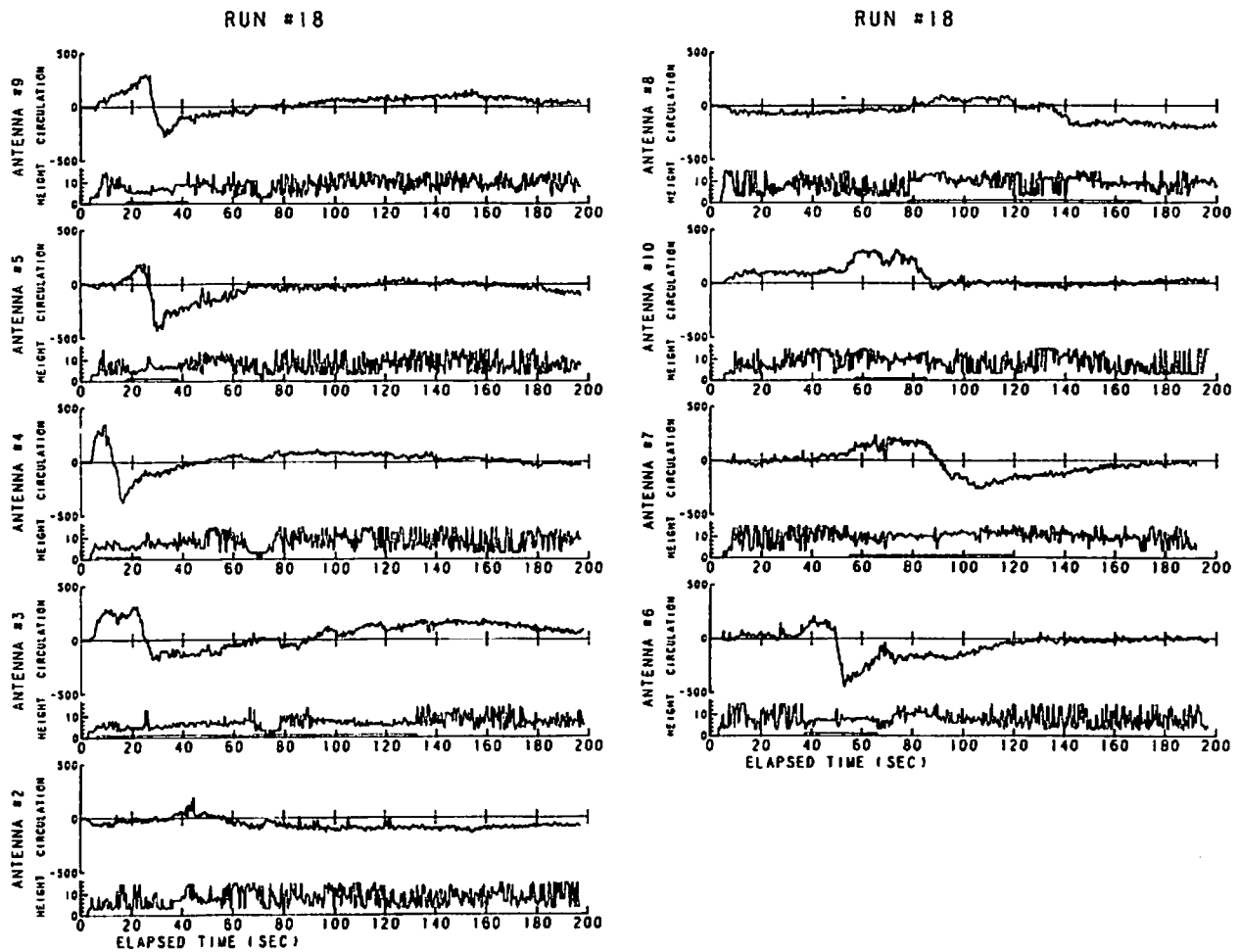

FIGURE 191. LINE-INTEGRAL AND HEIGHT DATA FOR RUN 18

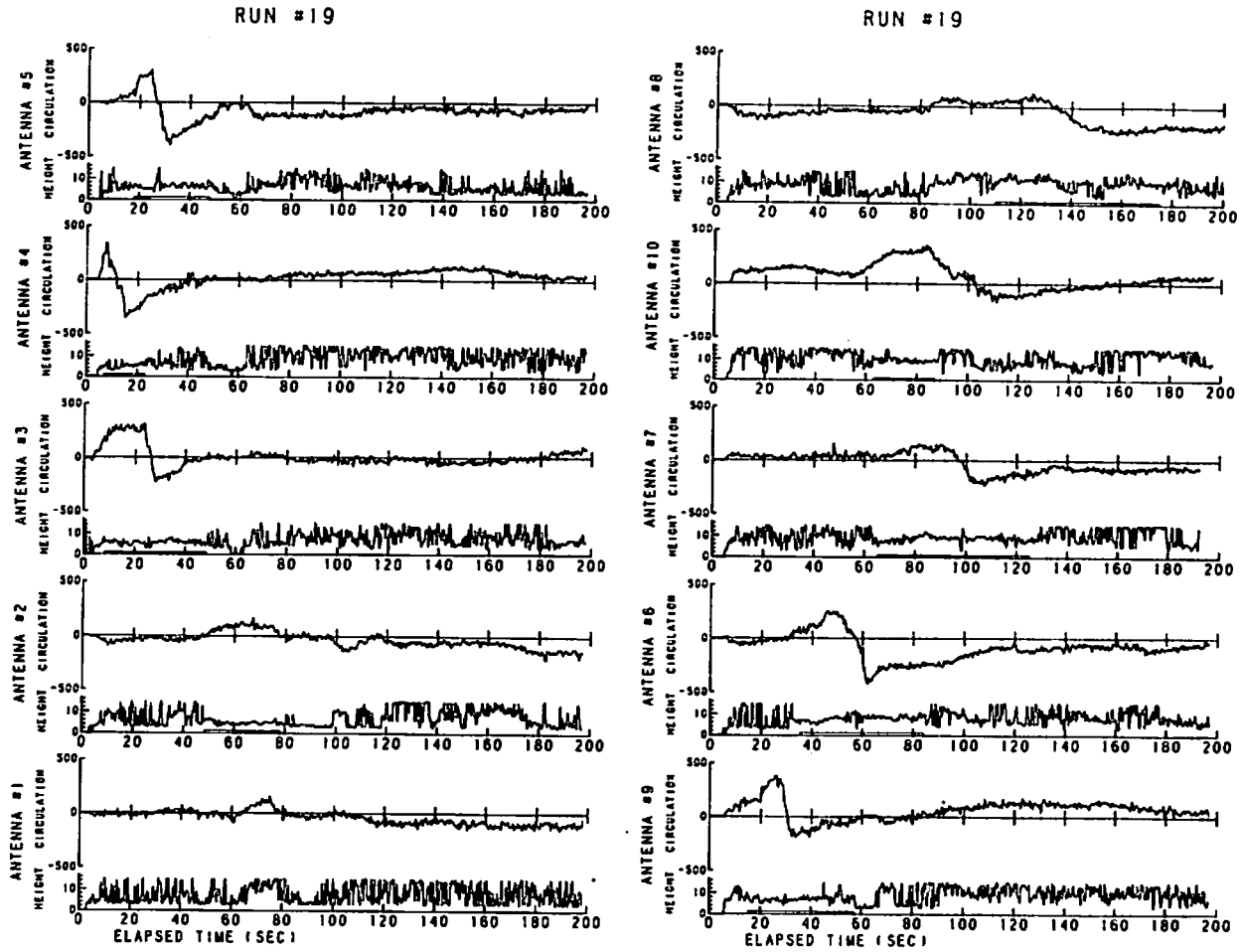

FIGURE 192. LINE-INTEGRAL AND HEIGHT DATA FOR RUN 19

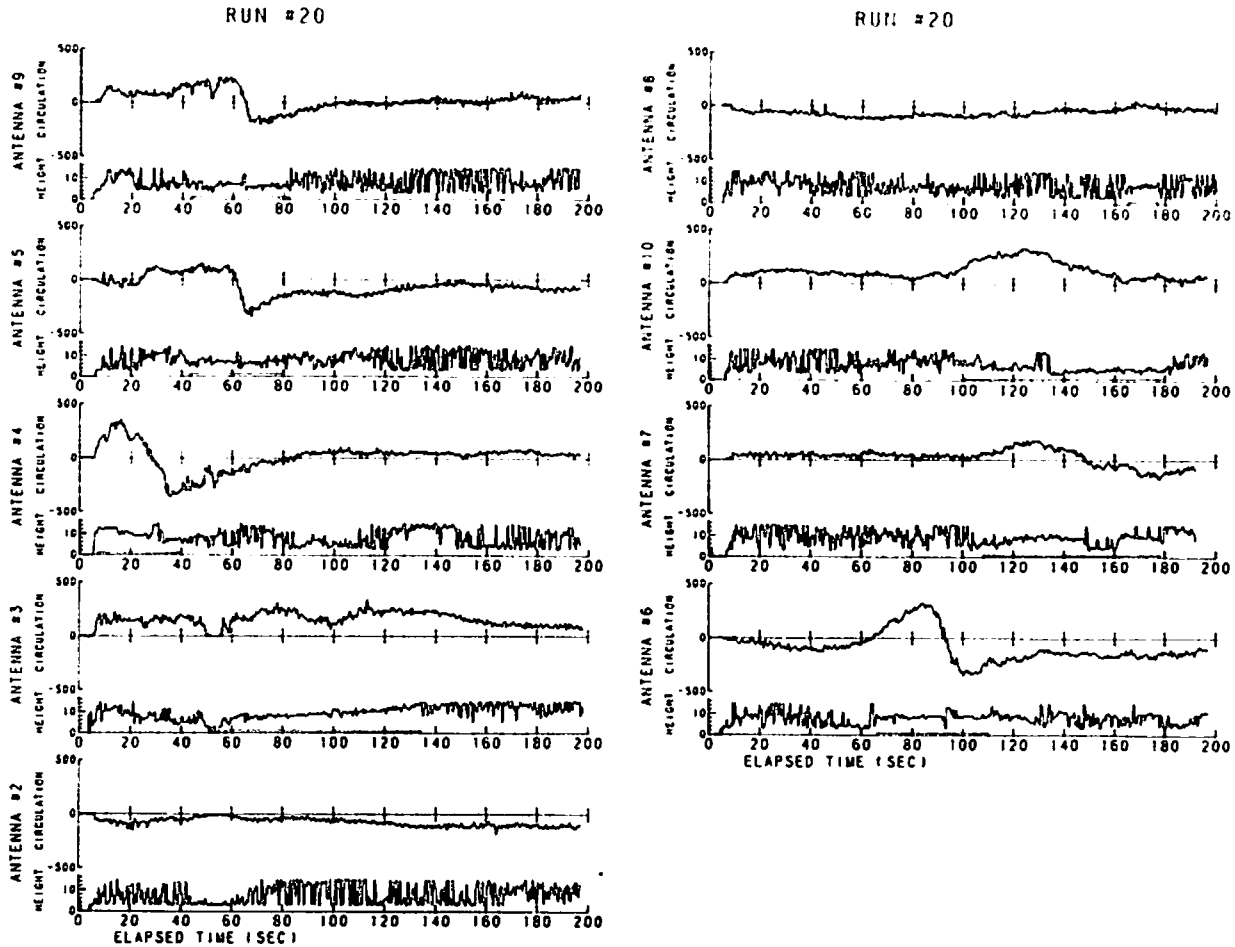

FIGURE 193. LINE-INTEGRAL AND HEIGHT DATA FOR RUN 20

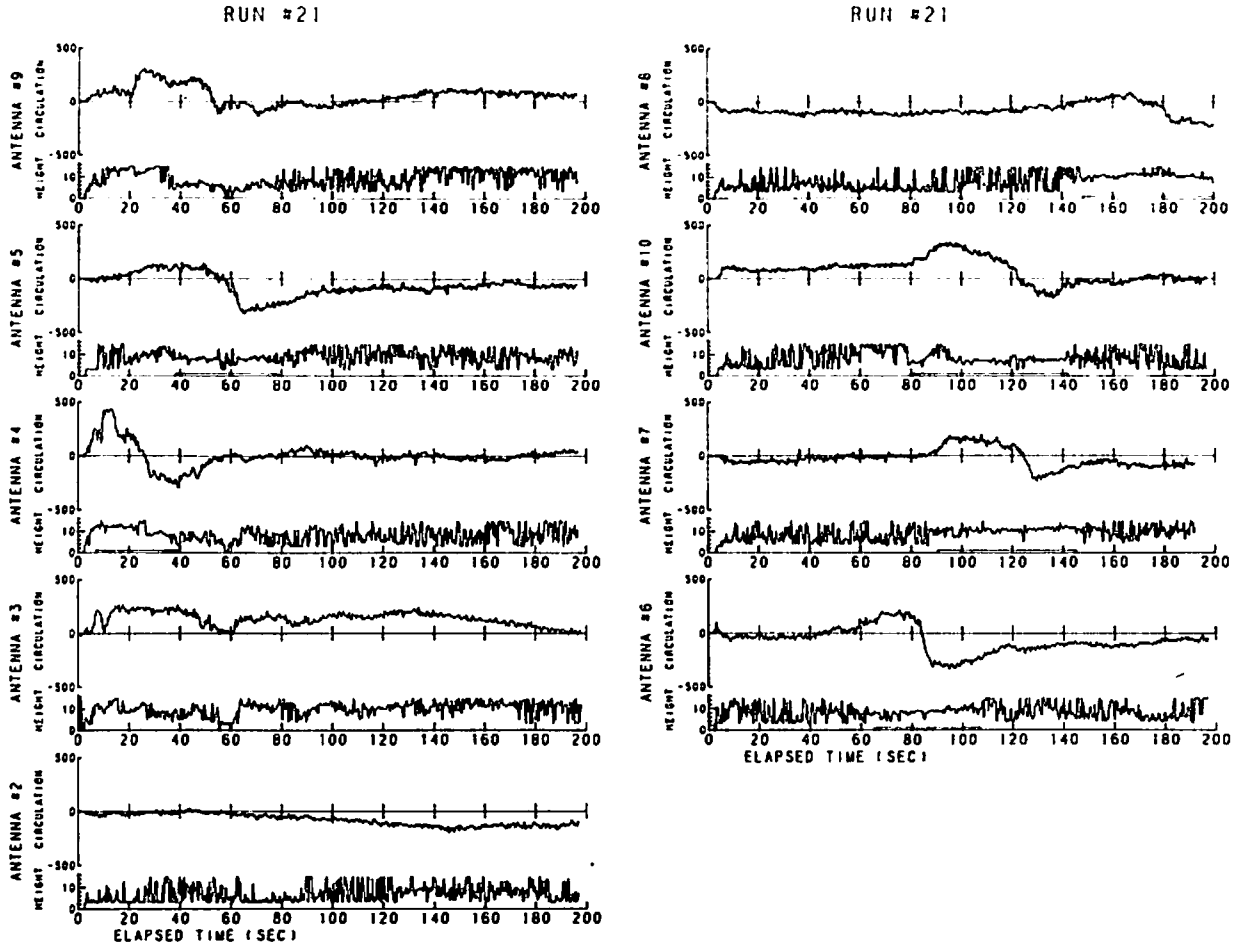

FIGURE 194. LINE-INTEGRAL AND HEIGHT DATA FOR RUN 21

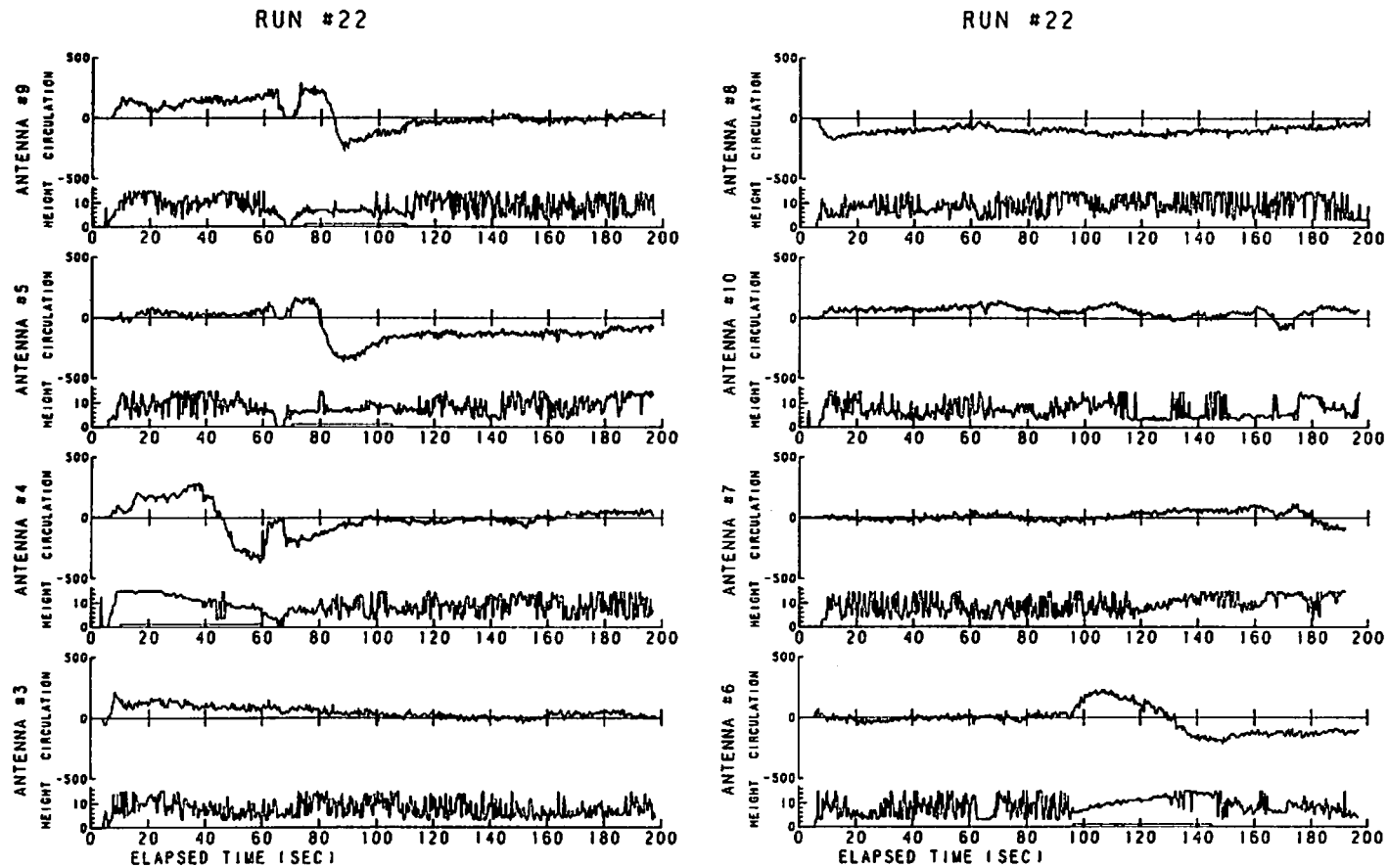

FIGURE 195. LINE-INTEGRAL AND HEIGHT DATA FOR RUN 22

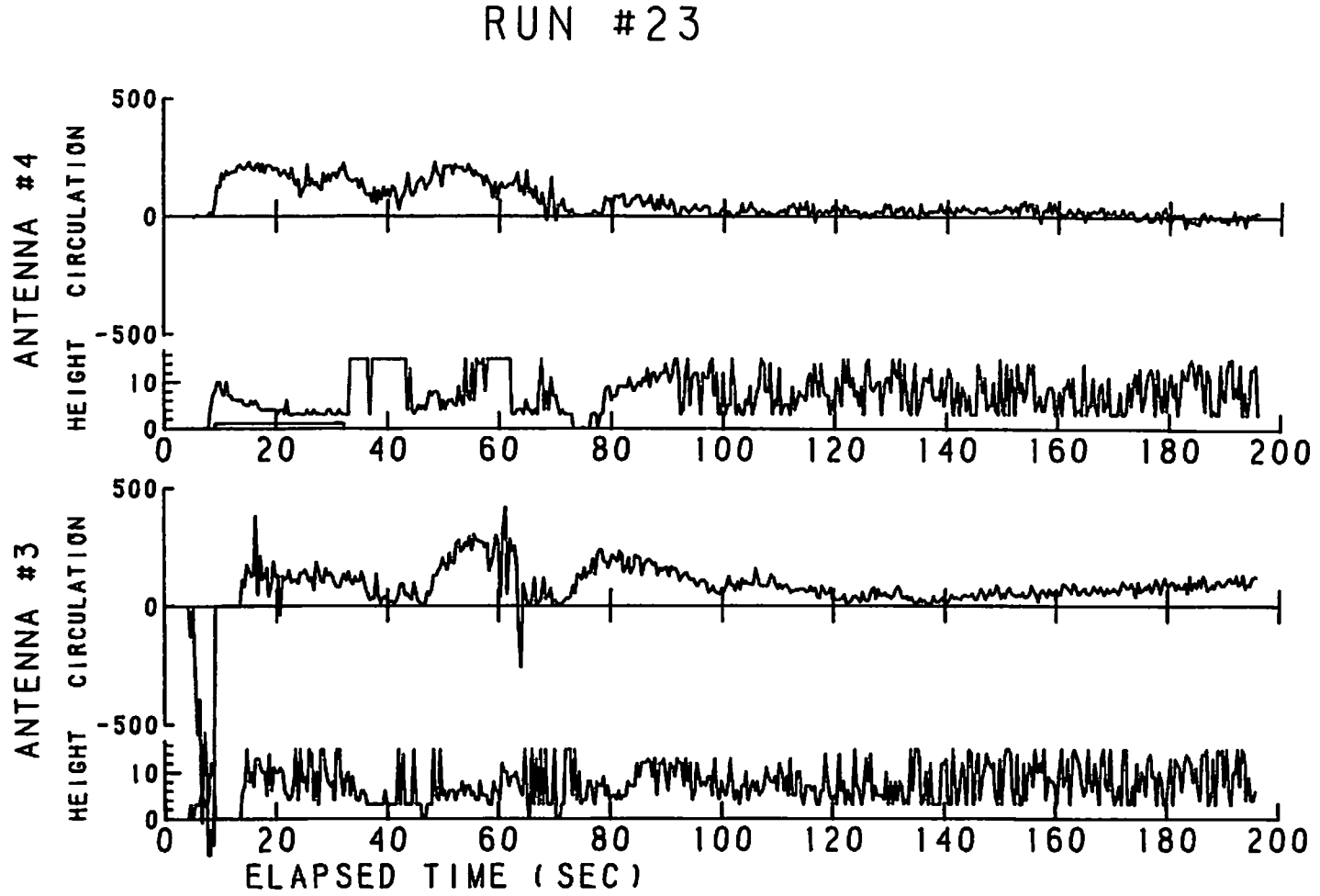

FIGURE 196. LINE-INTEGRAL AND HEIGHT DATA FOR RUN 23

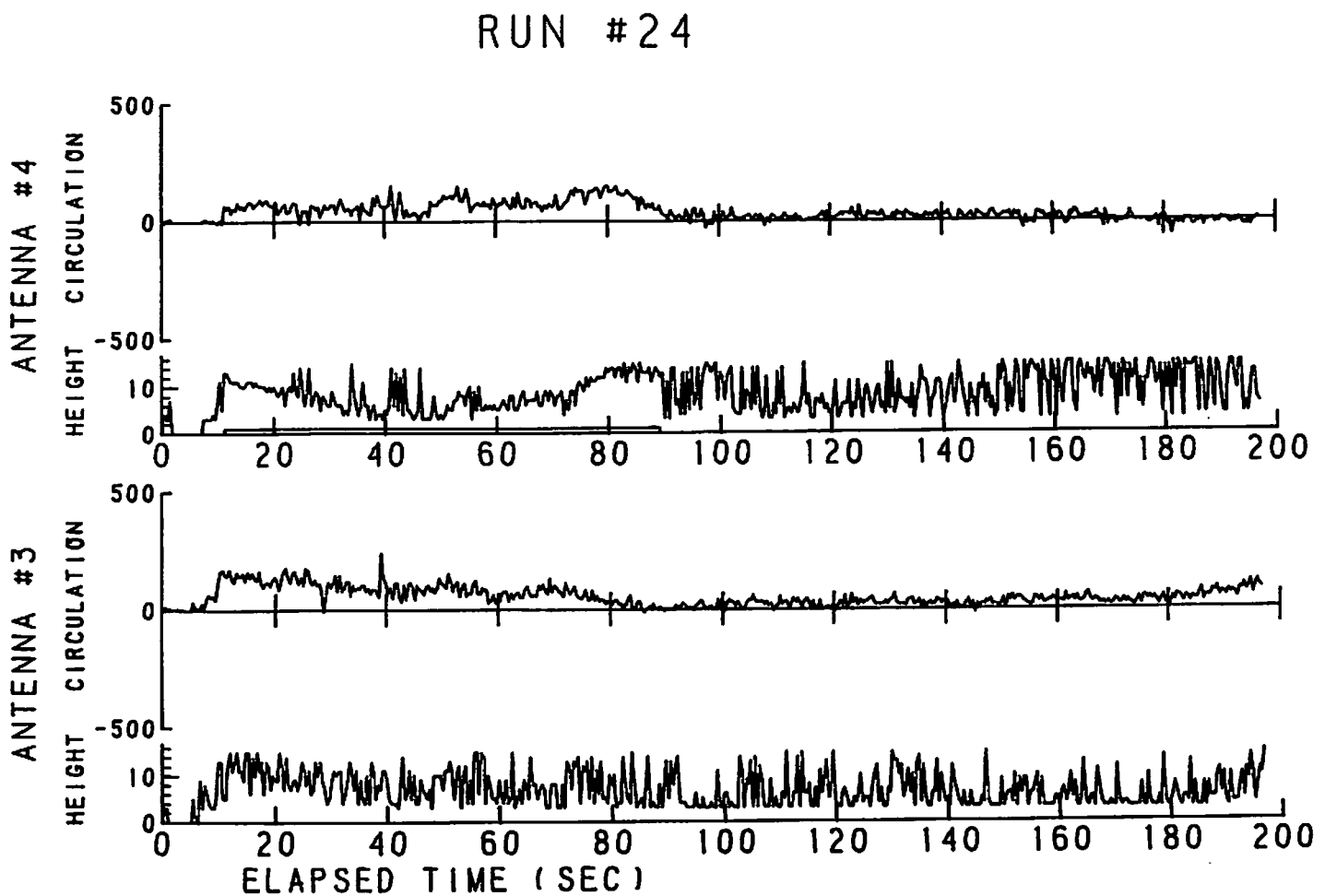

FIGURE 197. LINE-INTEGRAL AND HEIGHT DATA FOR RUN 24

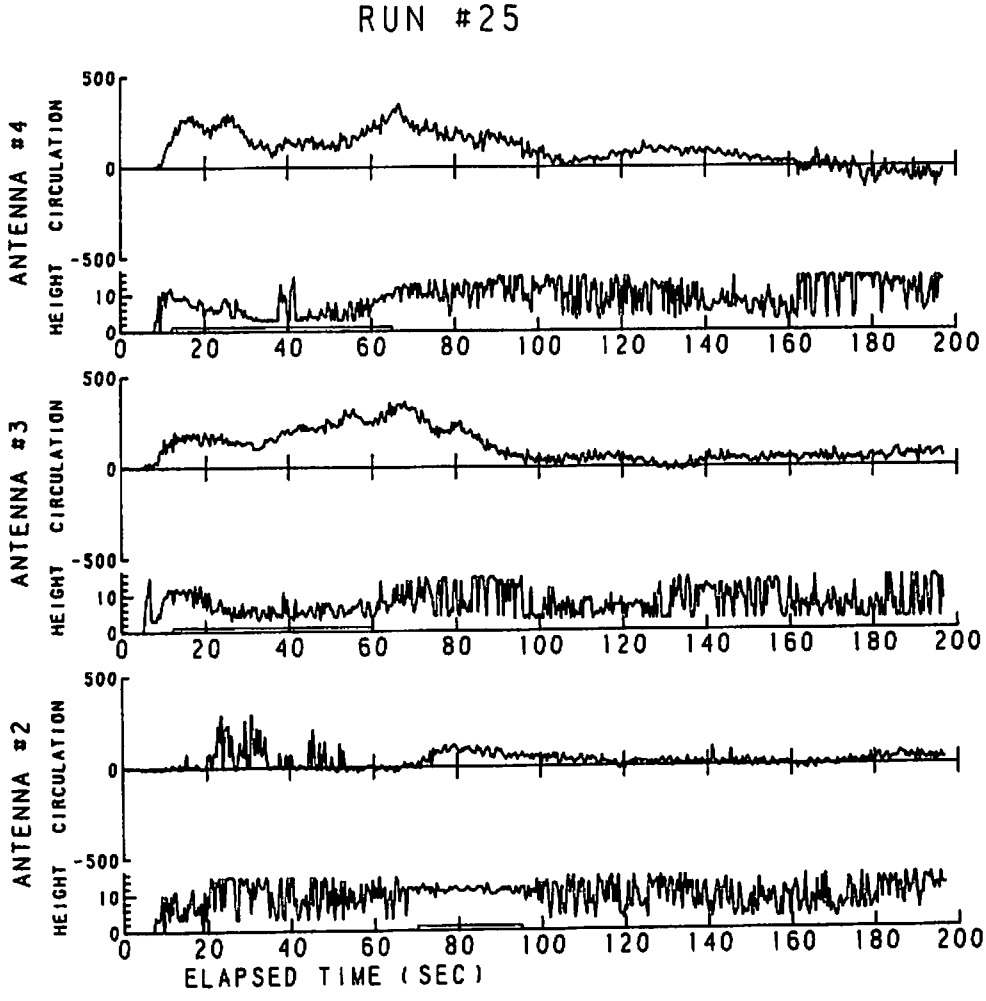

FIGURE 198. LINE-INTEGRAL AND HEIGHT DATA FOR RUN 25

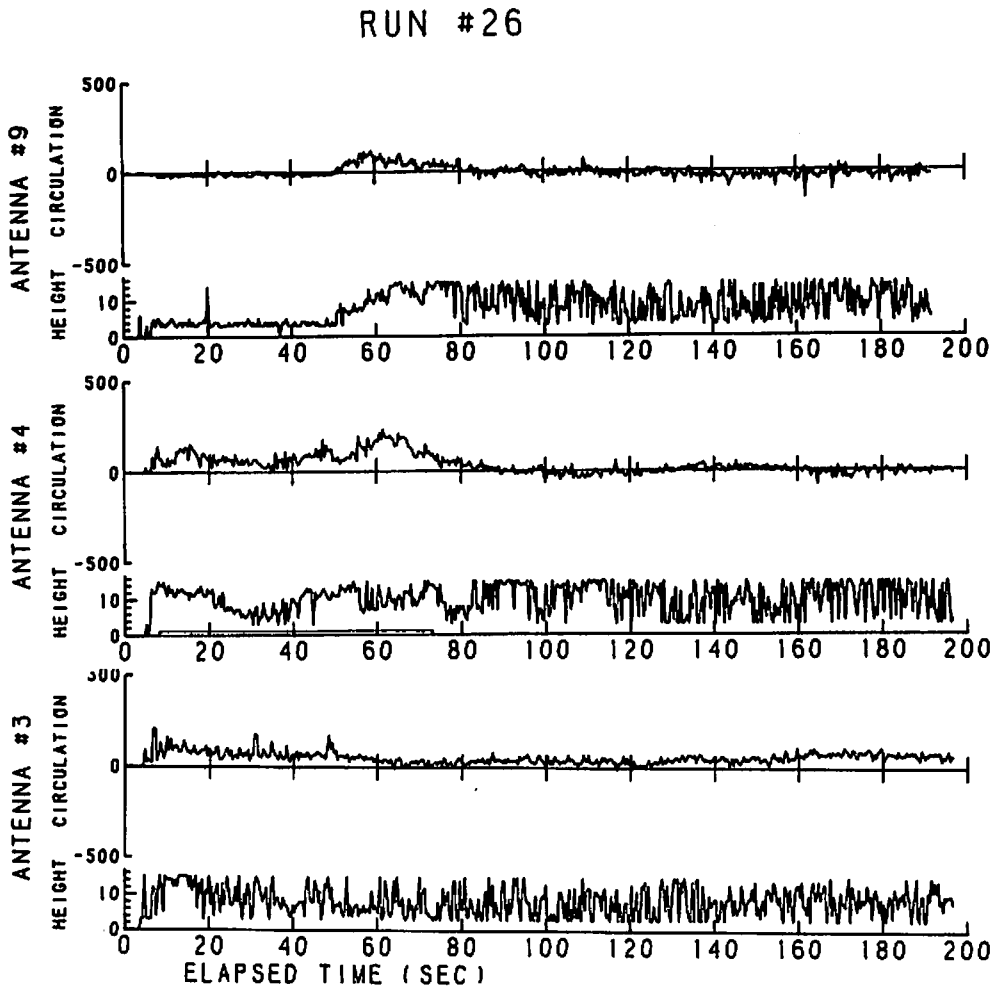

FIGURE 199. LINE-INTEGRAL AND HEIGHT DATA FOR RUN 26

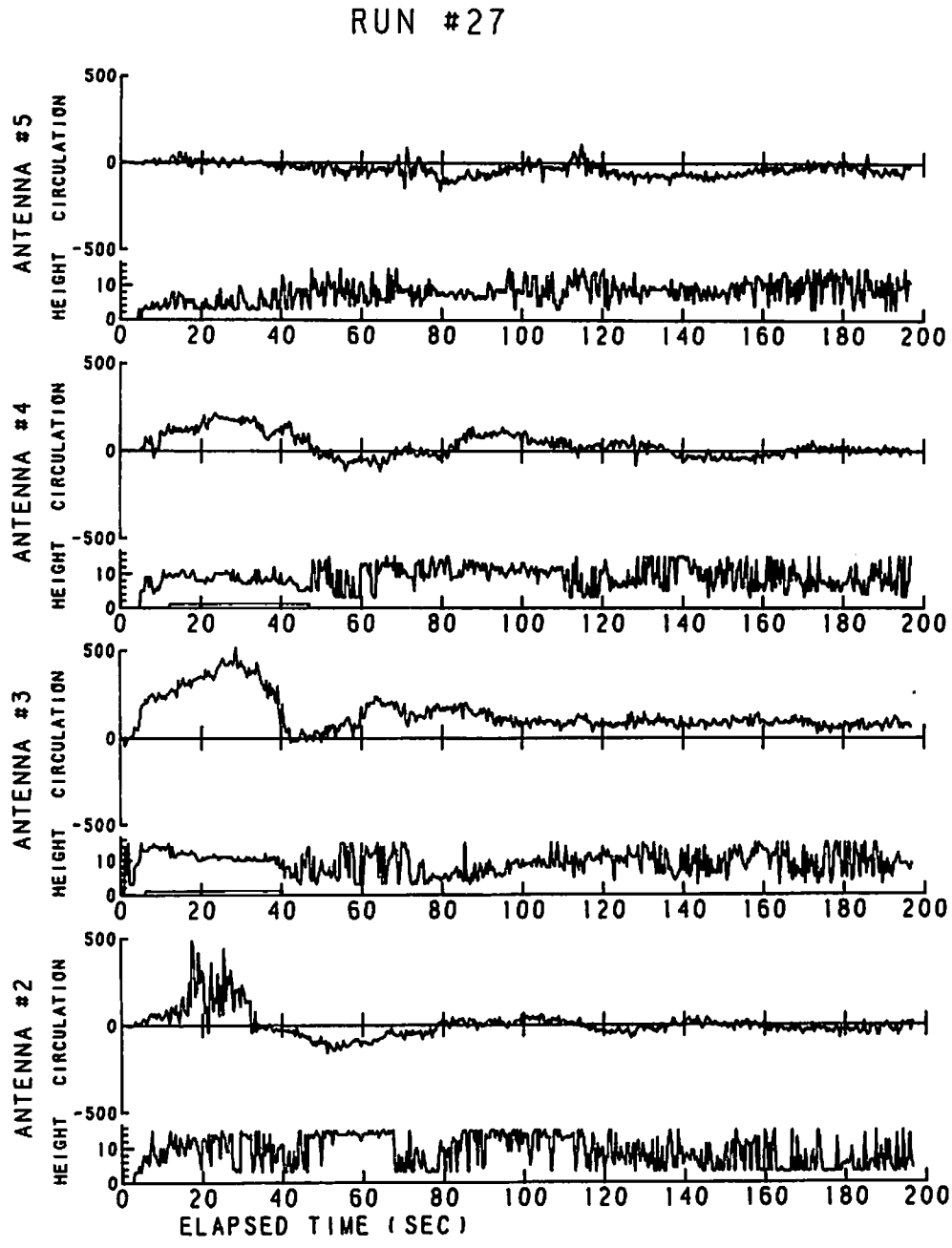

FIGURE 200. LINE-INTEGRAL AND HEIGHT DATA FOR RUN 27

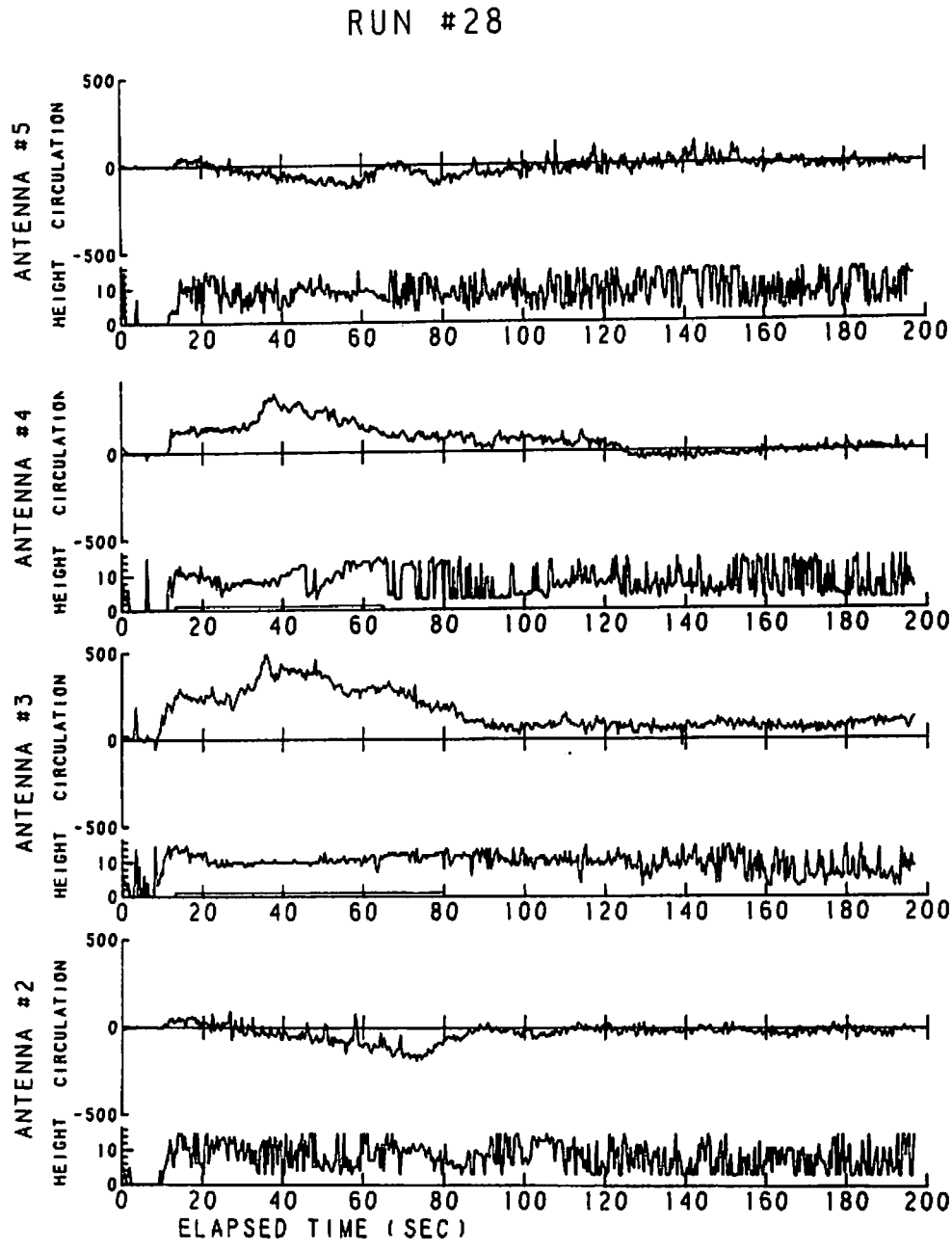

FIGURE 201. LINE-INTEGRAL AND HEIGHT DATA FOR RUN 28

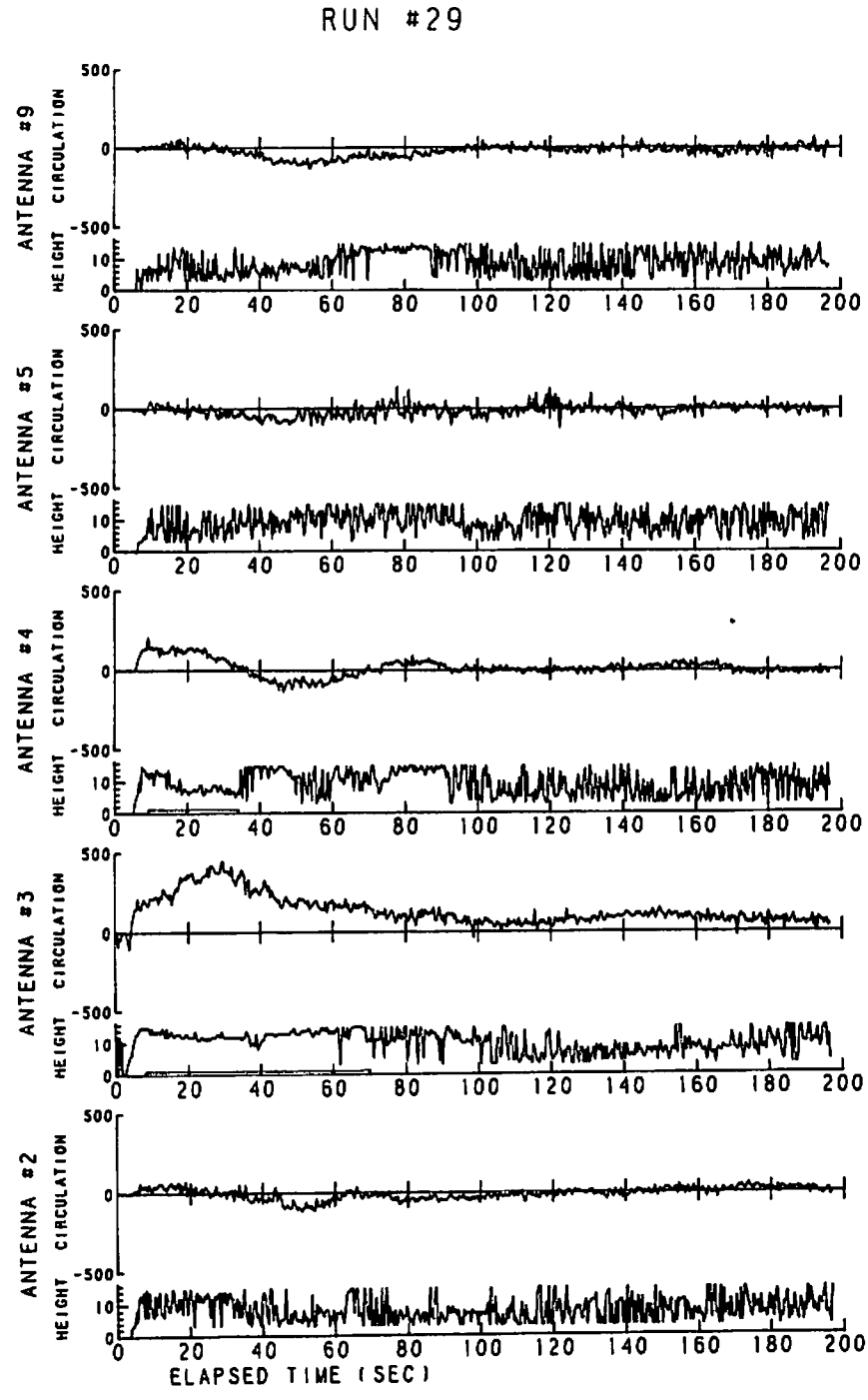

FIGURE 202. LINE-INTEGRAL AND HEIGHT DATA FOR RUN 29

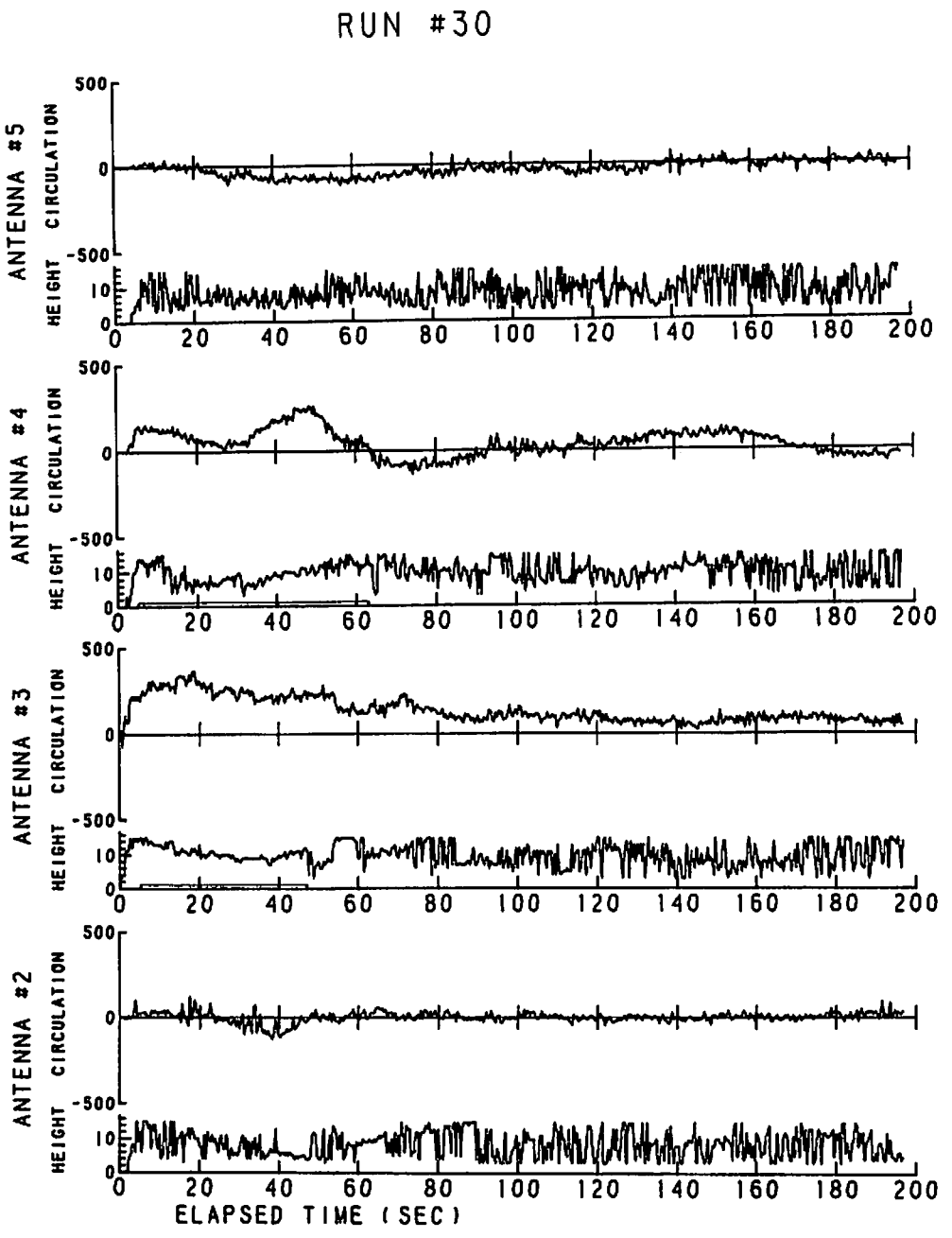

FIGURE 203. LINE-INTEGRAL AND HEIGHT DATA FOR RUN 30

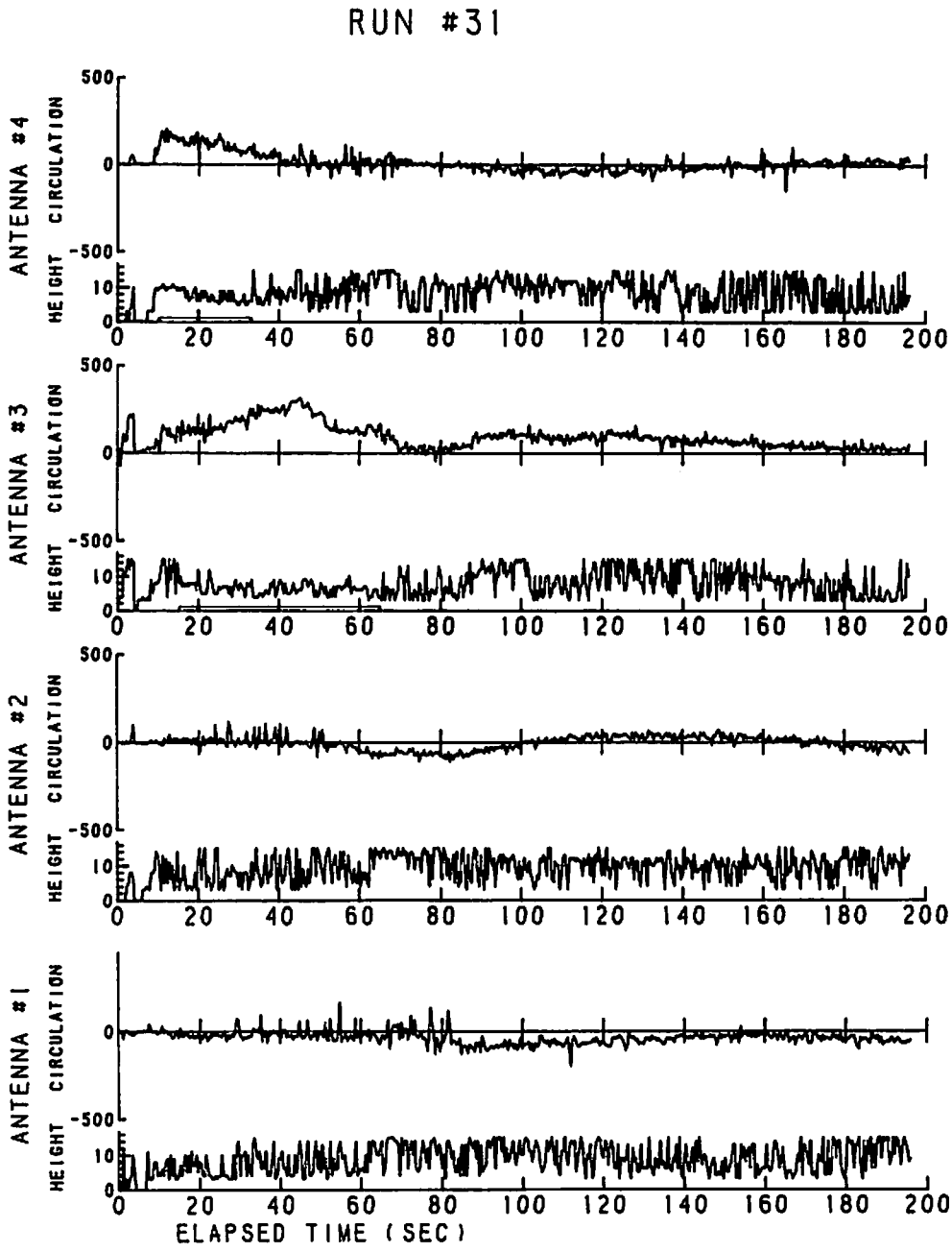

FIGURE 204. LINE-INTEGRAL AND HEIGHT DATA FOR RUN 31

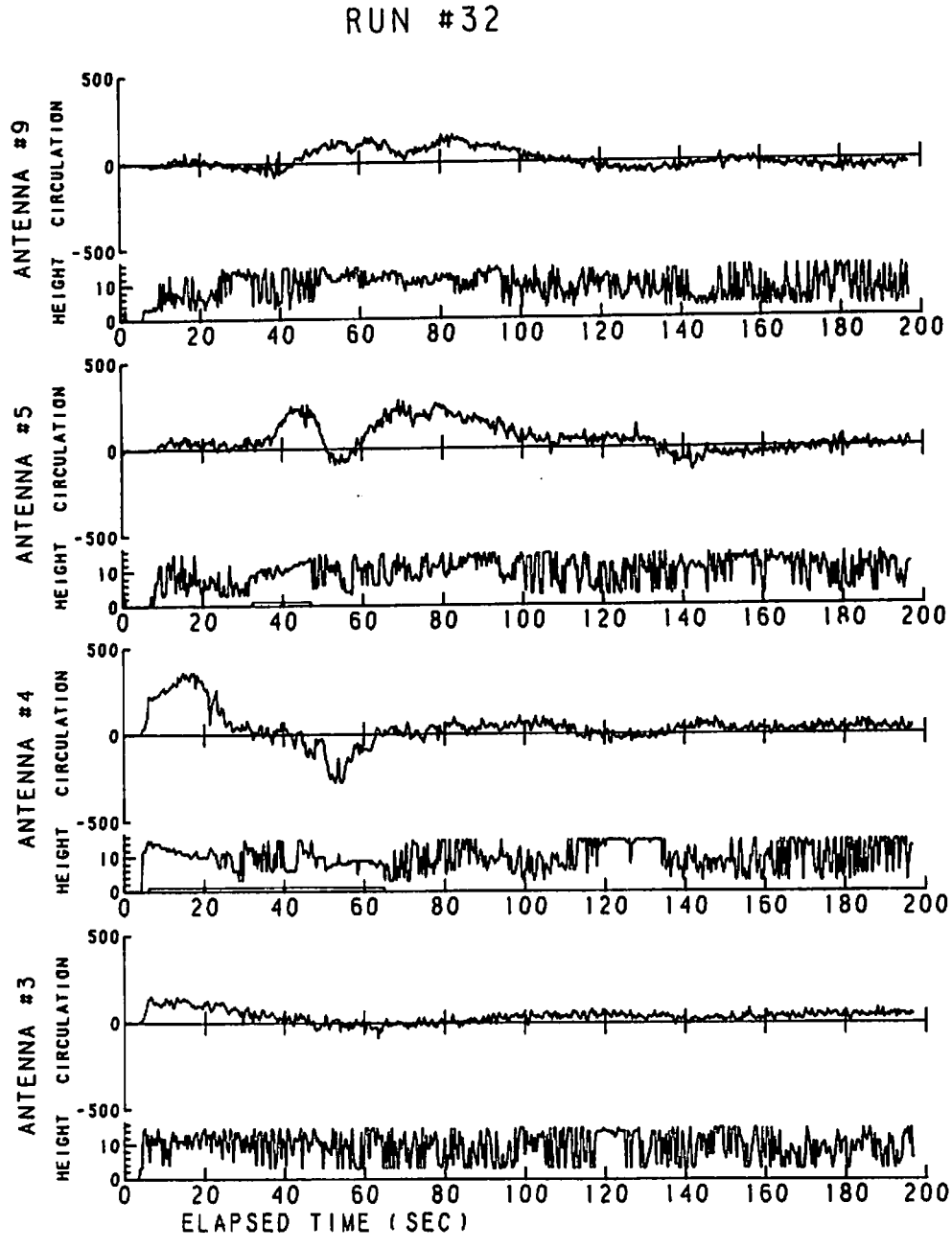

FIGURE 205. LINE-INTEGRAL AND HEIGHT DATA FOR RUN 32

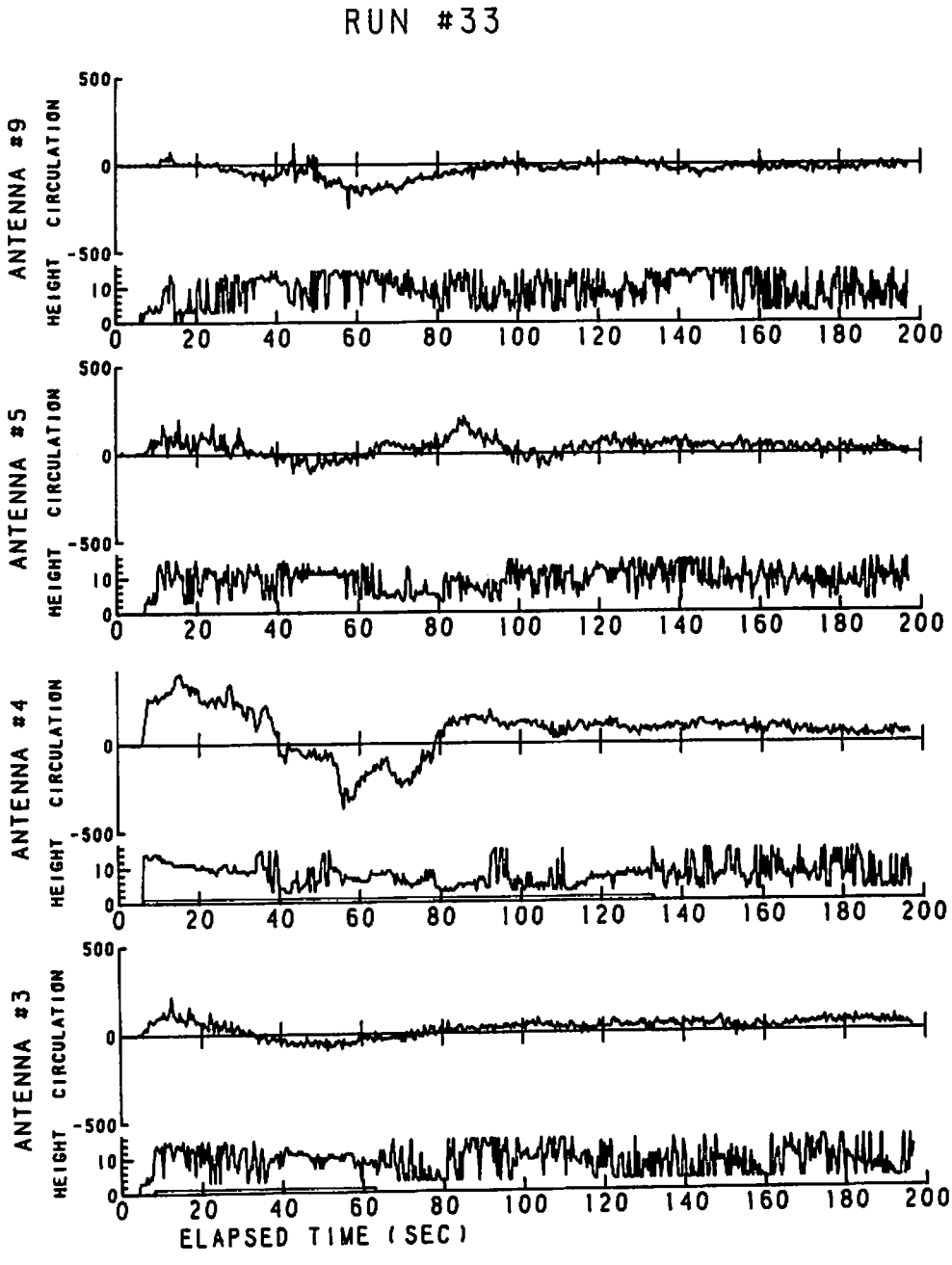

FIGURE 206. LINE-INTEGRAL AND HEIGHT DATA FOR RUN 33

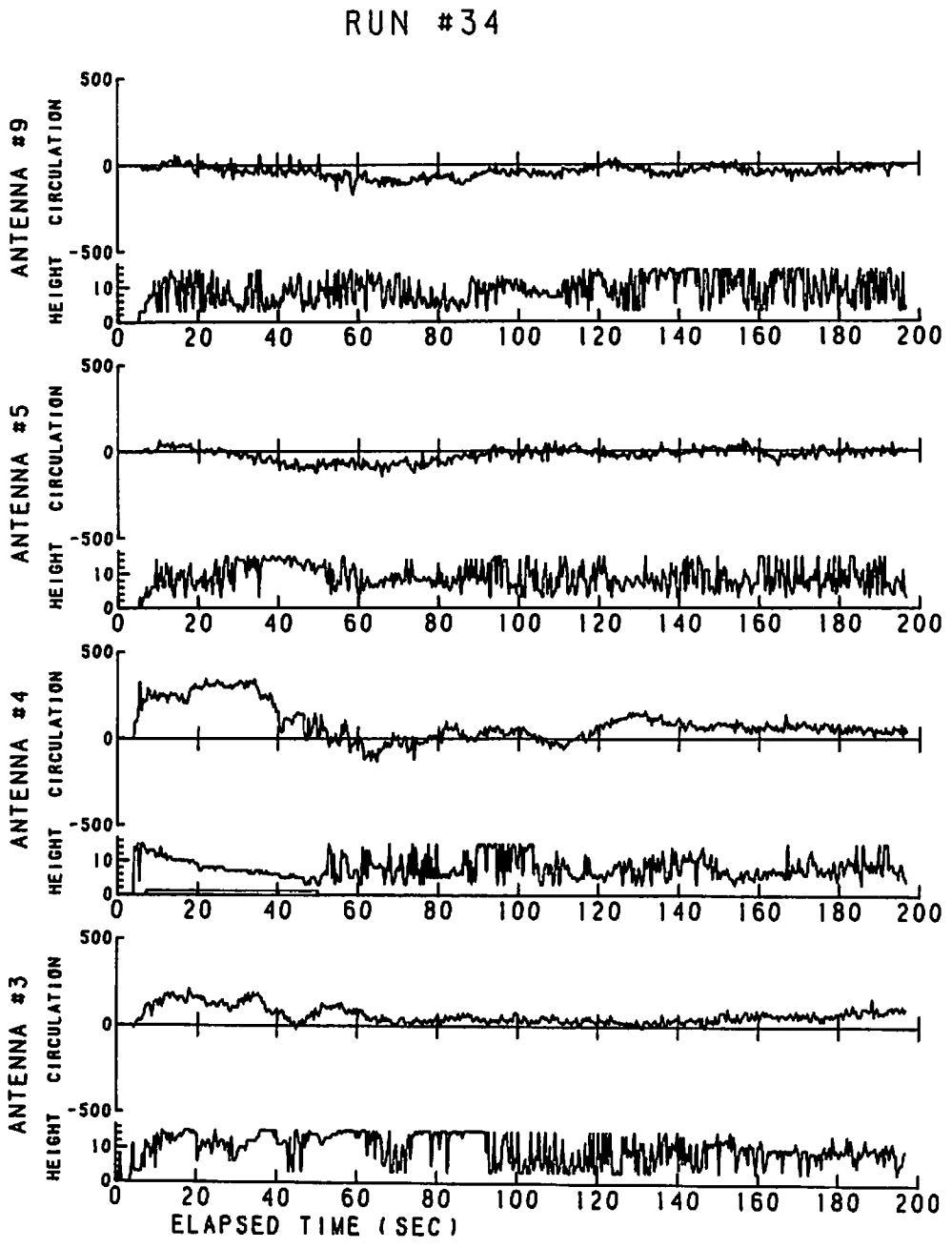

FIGURE 207. LINE-INTEGRAL AND HEIGHT DATA FOR RUN 34

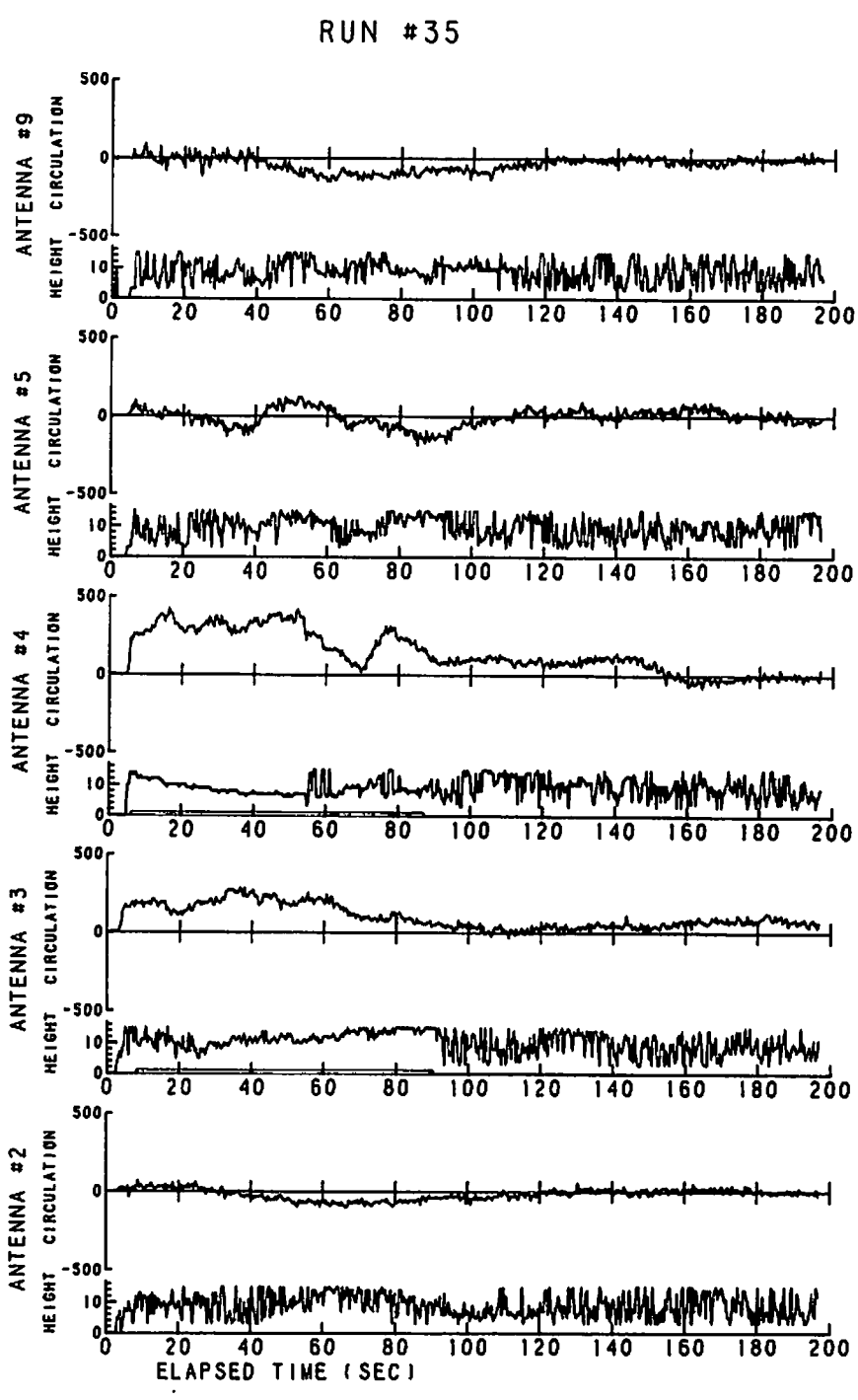

FIGURE 208. LINE-INTEGRAL AND HEIGHT DATA FOR RUN 35

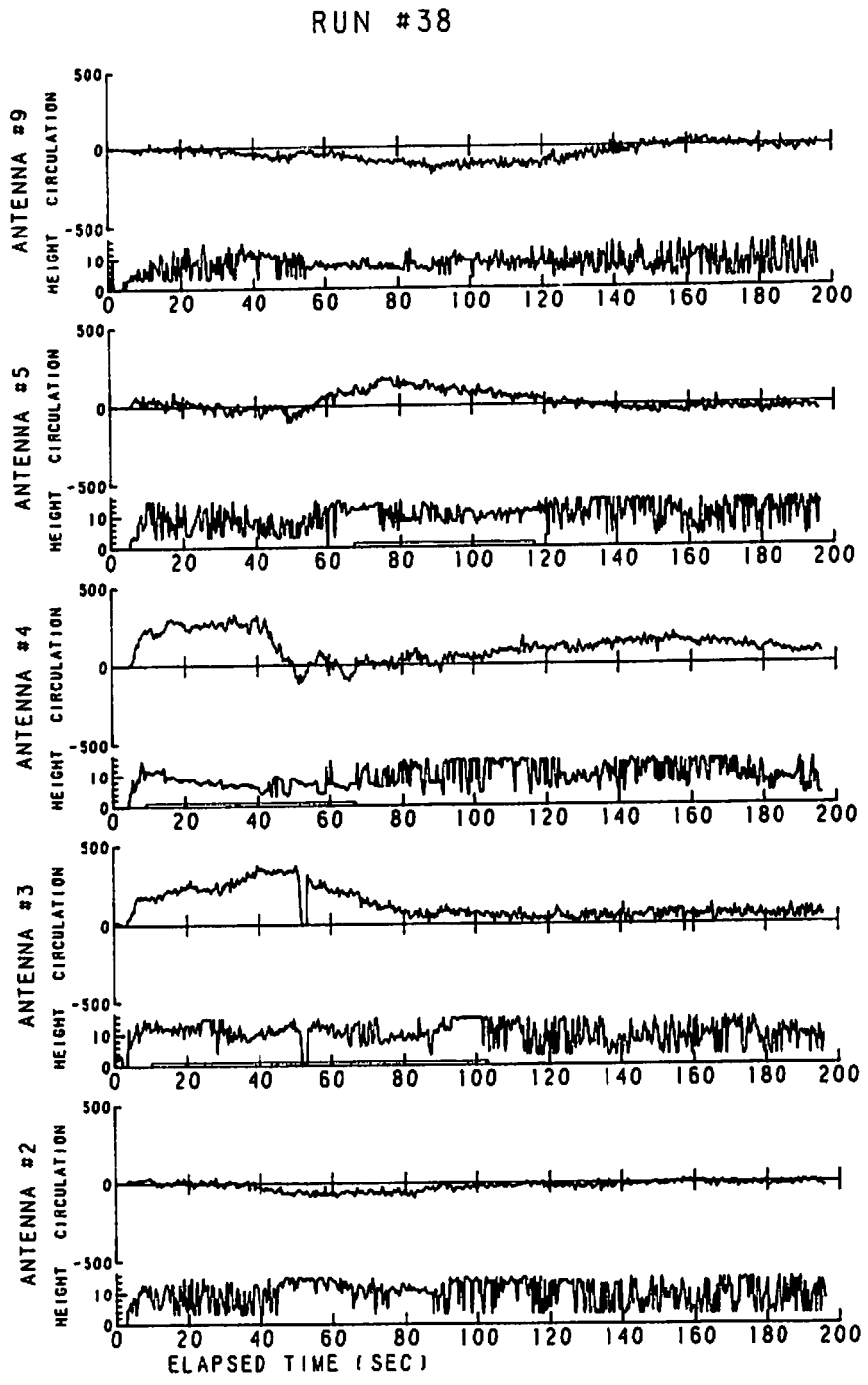

FIGURE 209. LINE-INTEGRAL AND HEIGHT DATA FOR RUN 38

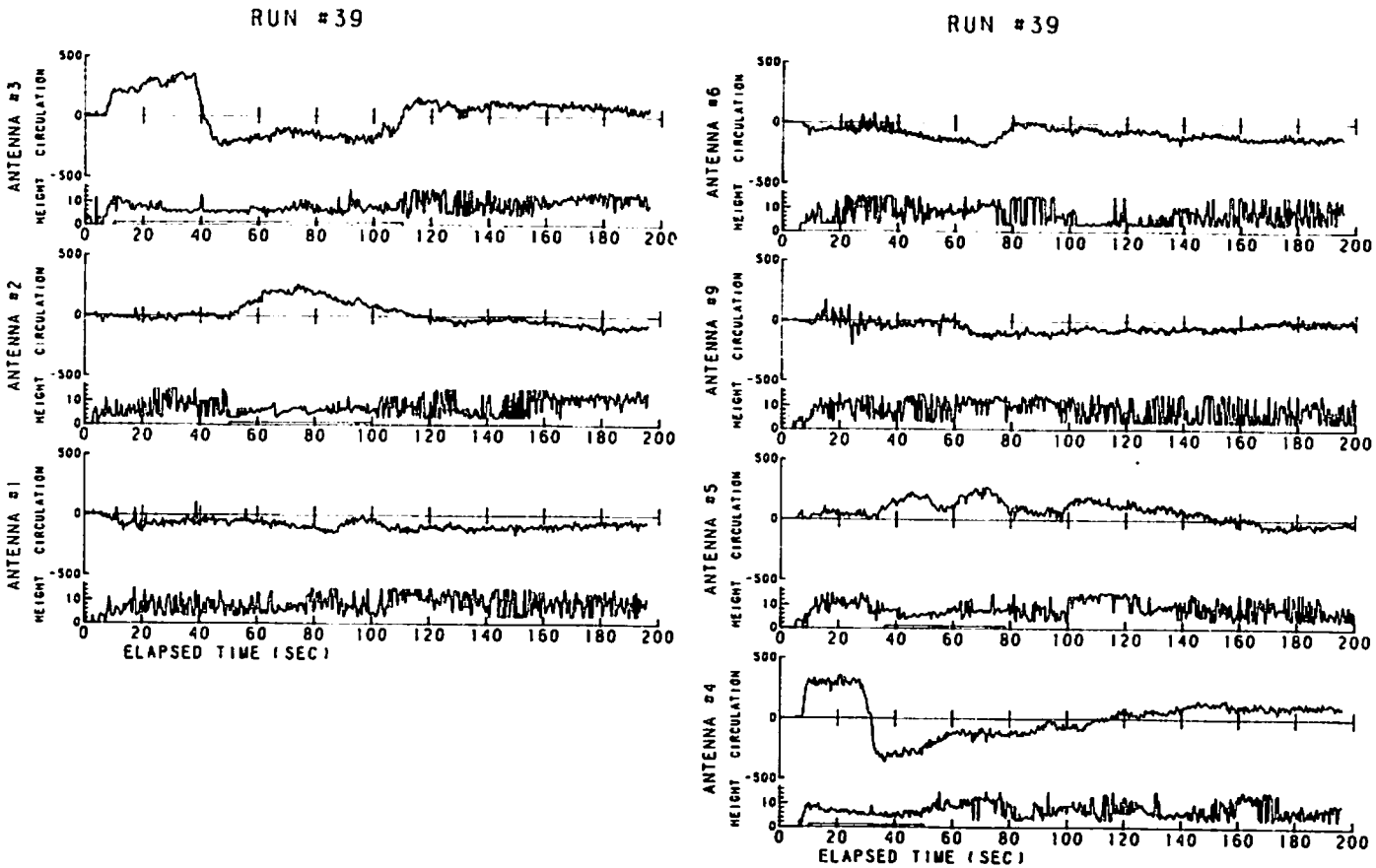

FIGURE 210. LINE-INTEGRAL AND HEIGHT DATA FOR RUN 39

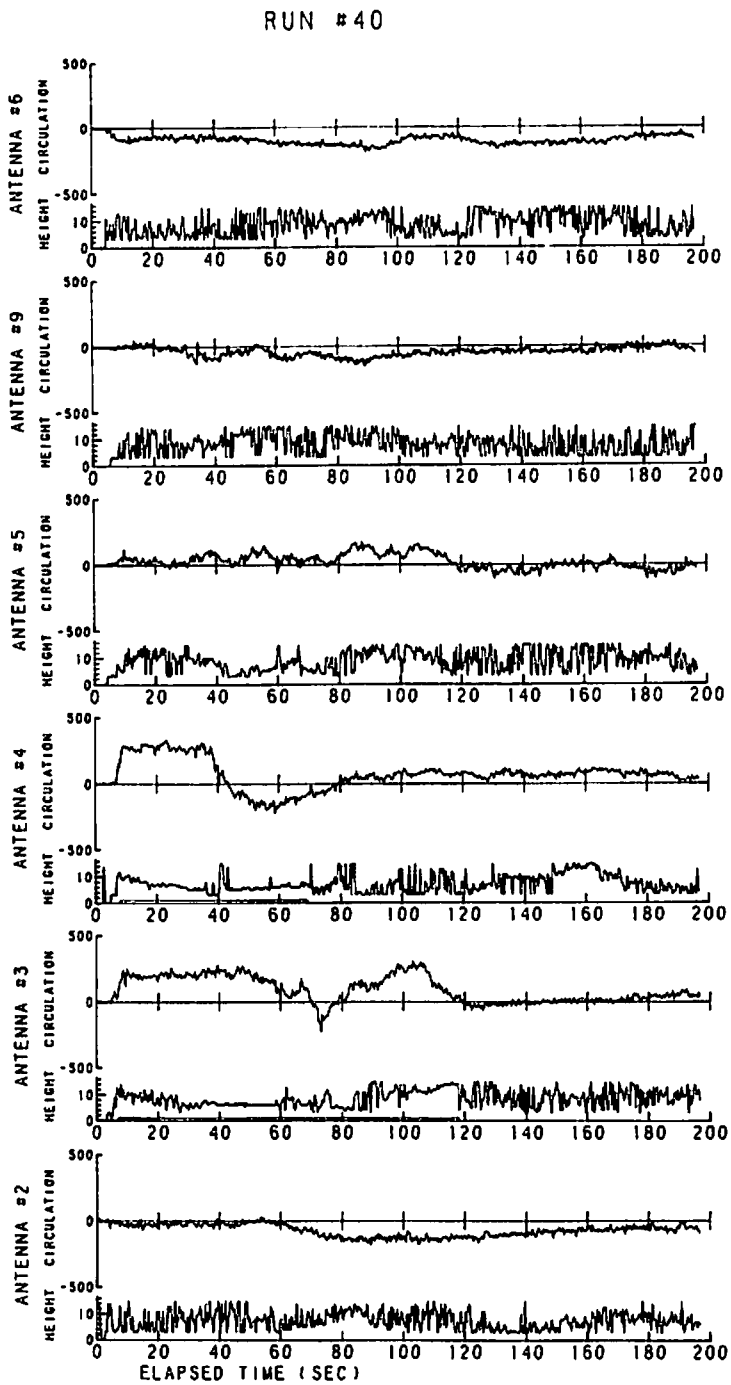

FIGURE 211. LINE-INTEGRAL AND HEIGHT DATA FOR RUN 40

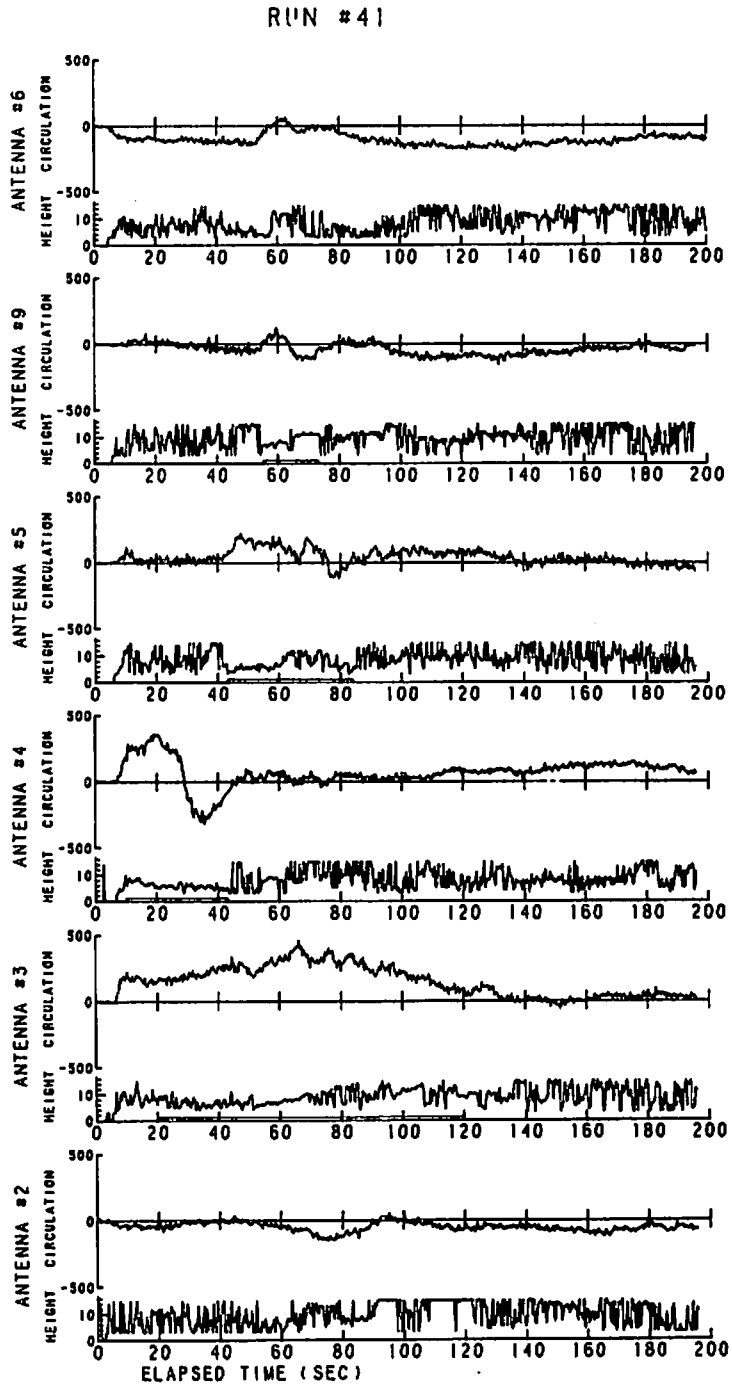

FIGURE 212. LINE-INTEGRAL AND HEIGHT DATA FOR RUN 41

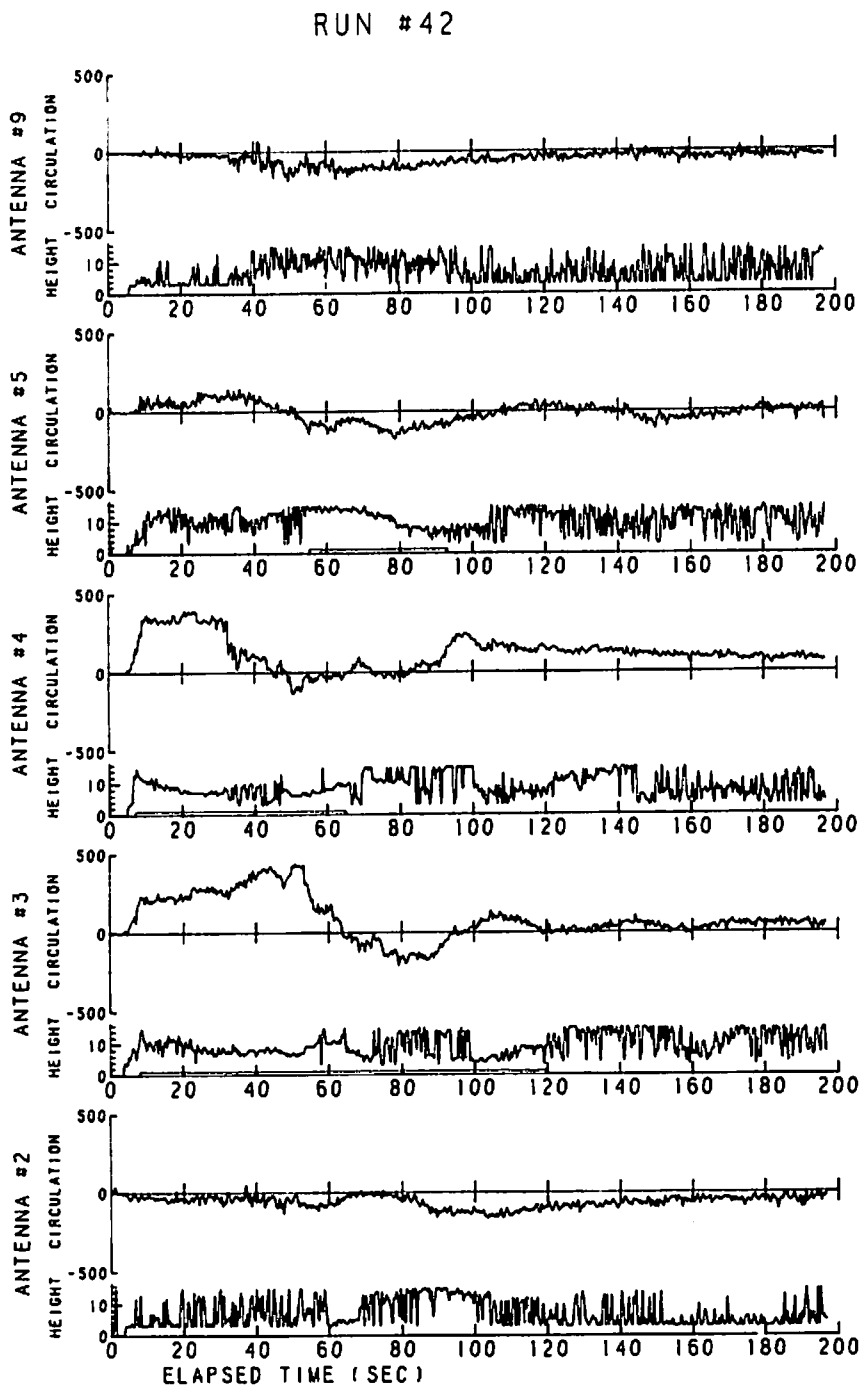

FIGURE 213. LINE-INTEGRAL AND HEIGHT DATA FOR RUN 42

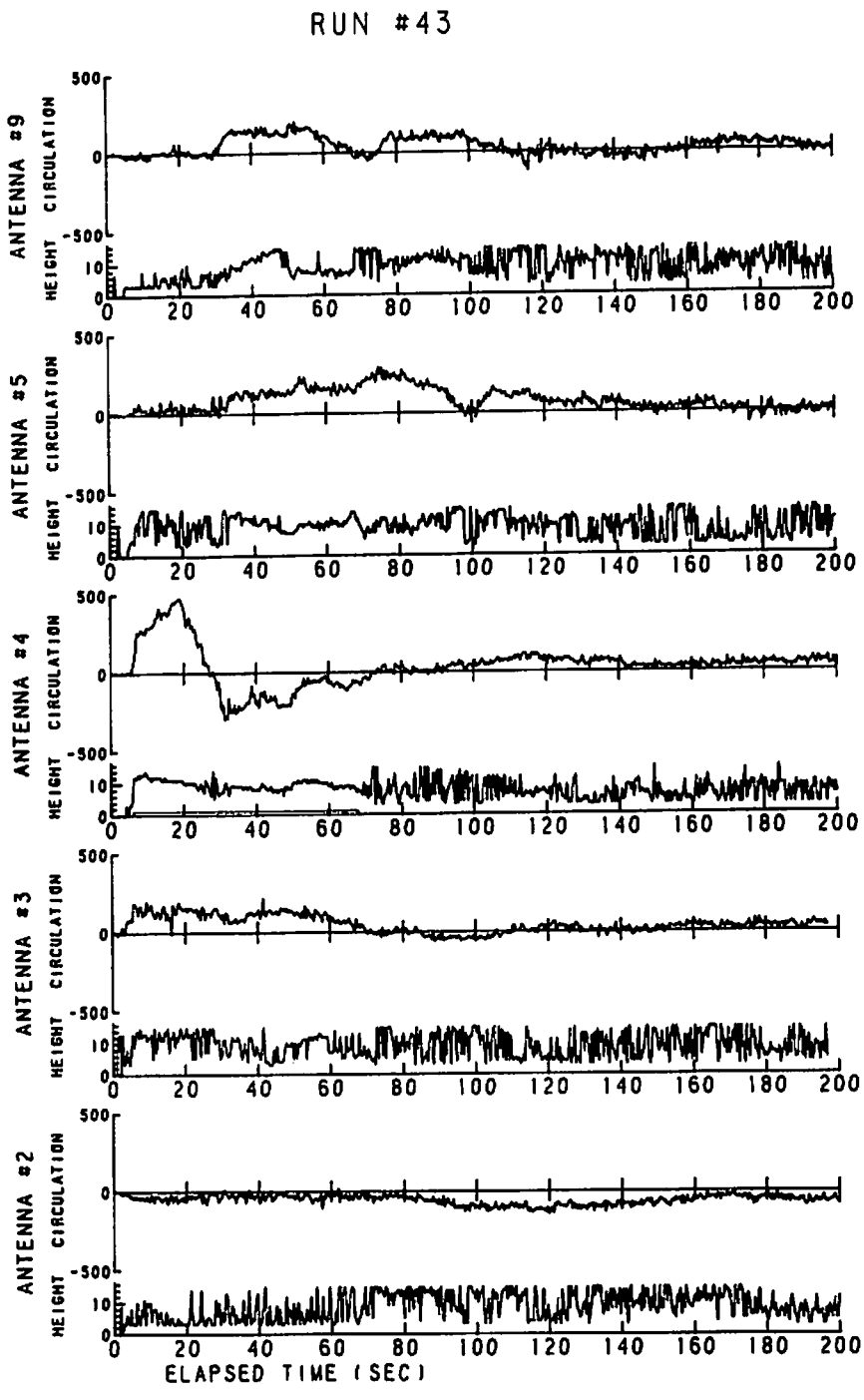

FIGURE 214. LINE-INTEGRAL AND HEIGHT DATA FOR RUN 43.

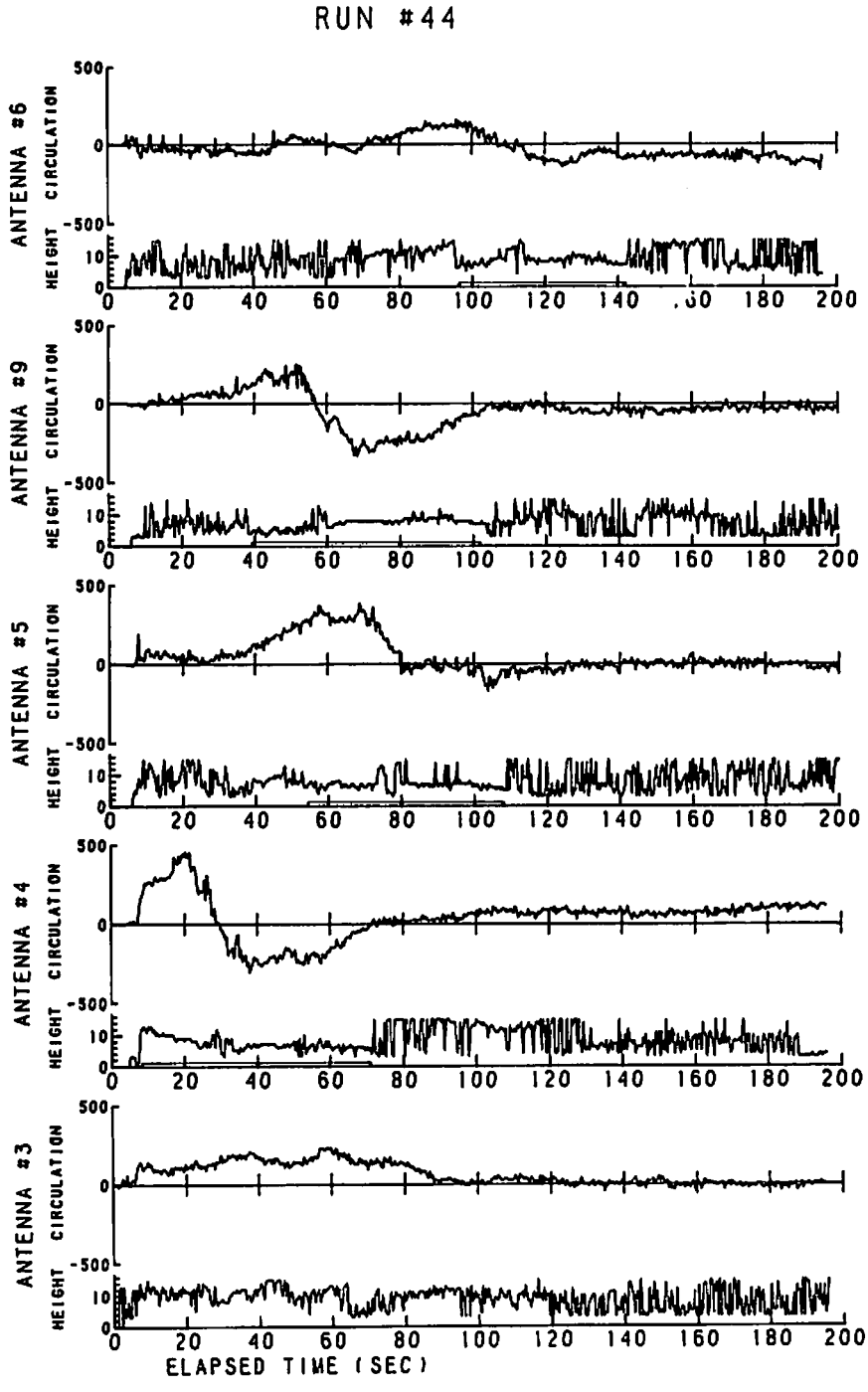

FIGURE 215. LINE-INTEGRAL AND HEIGHT DATA FOR RUN 44.

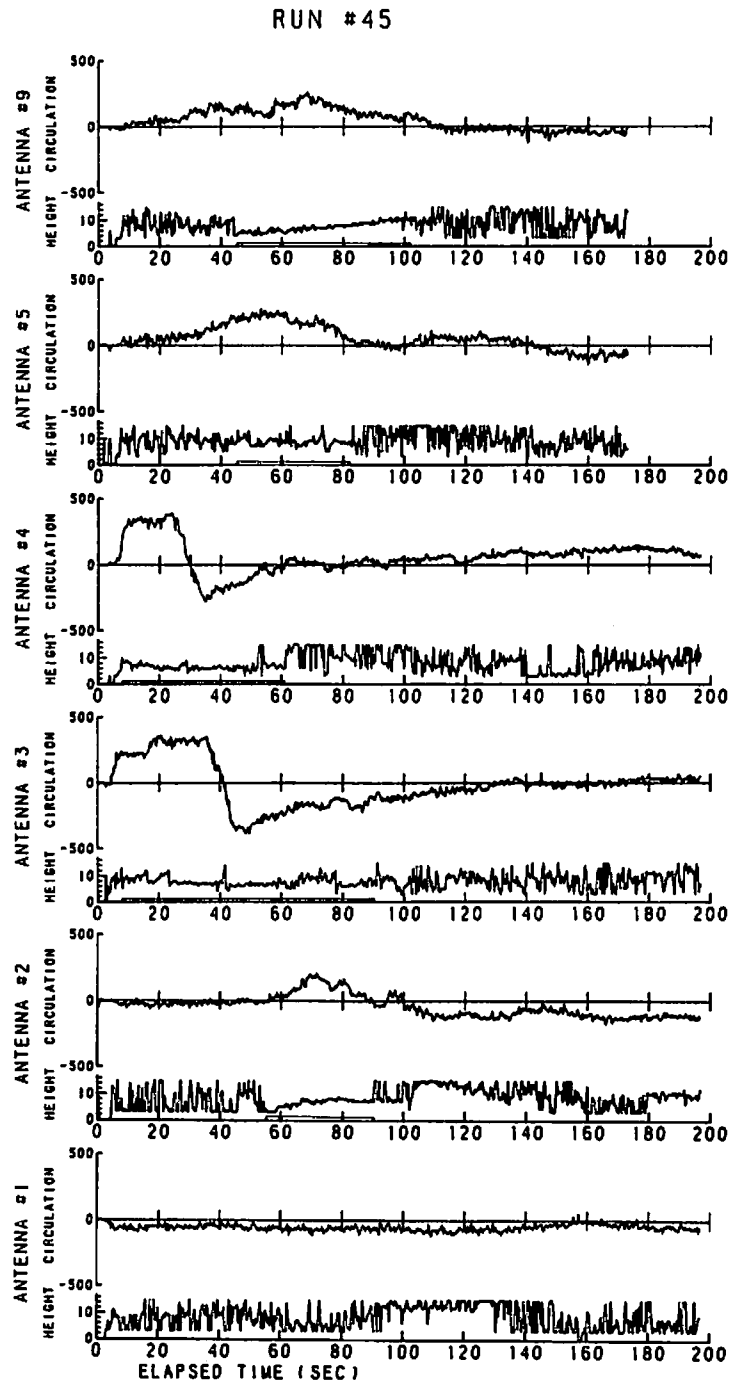

FIGURE 216. LINE-INTEGRAL AND HEIGHT DATA FOR RUN 45.

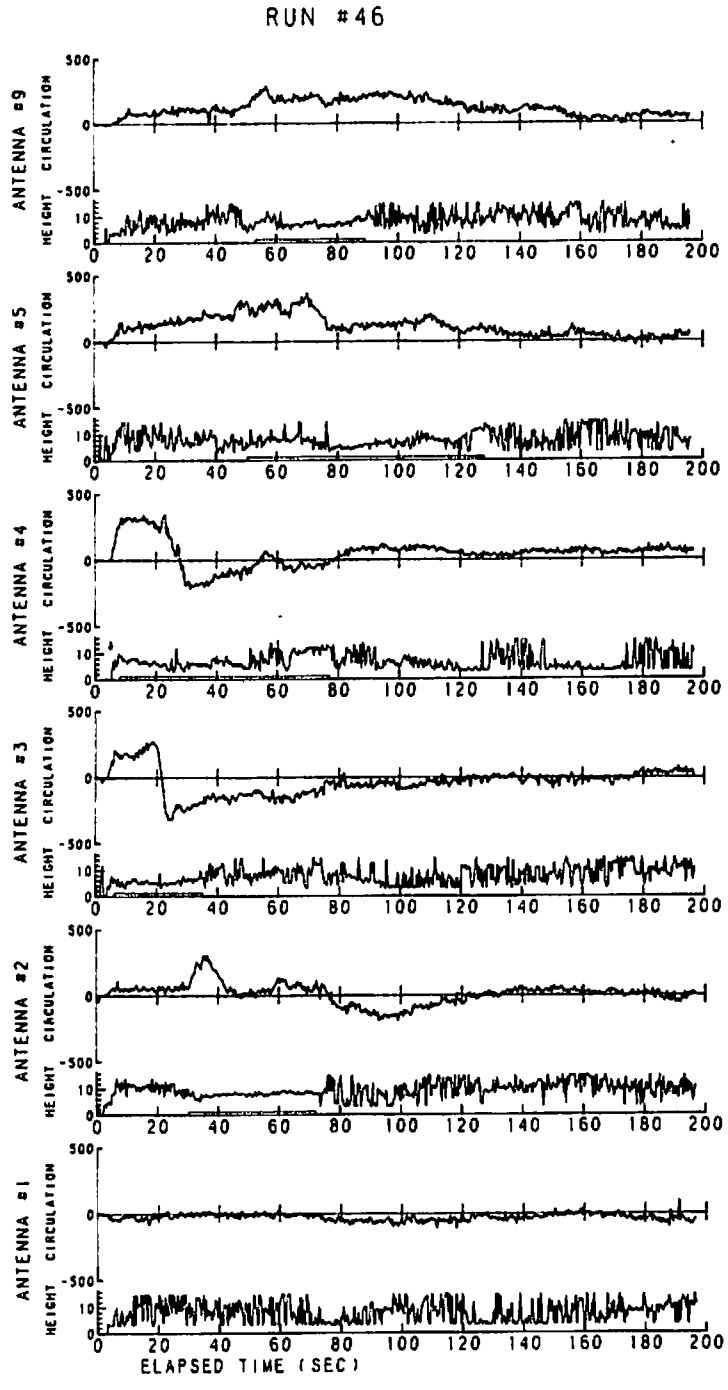

FIGURE 217. LINE-INTEGRAL AND HEIGHT DATA FOR RUN 46

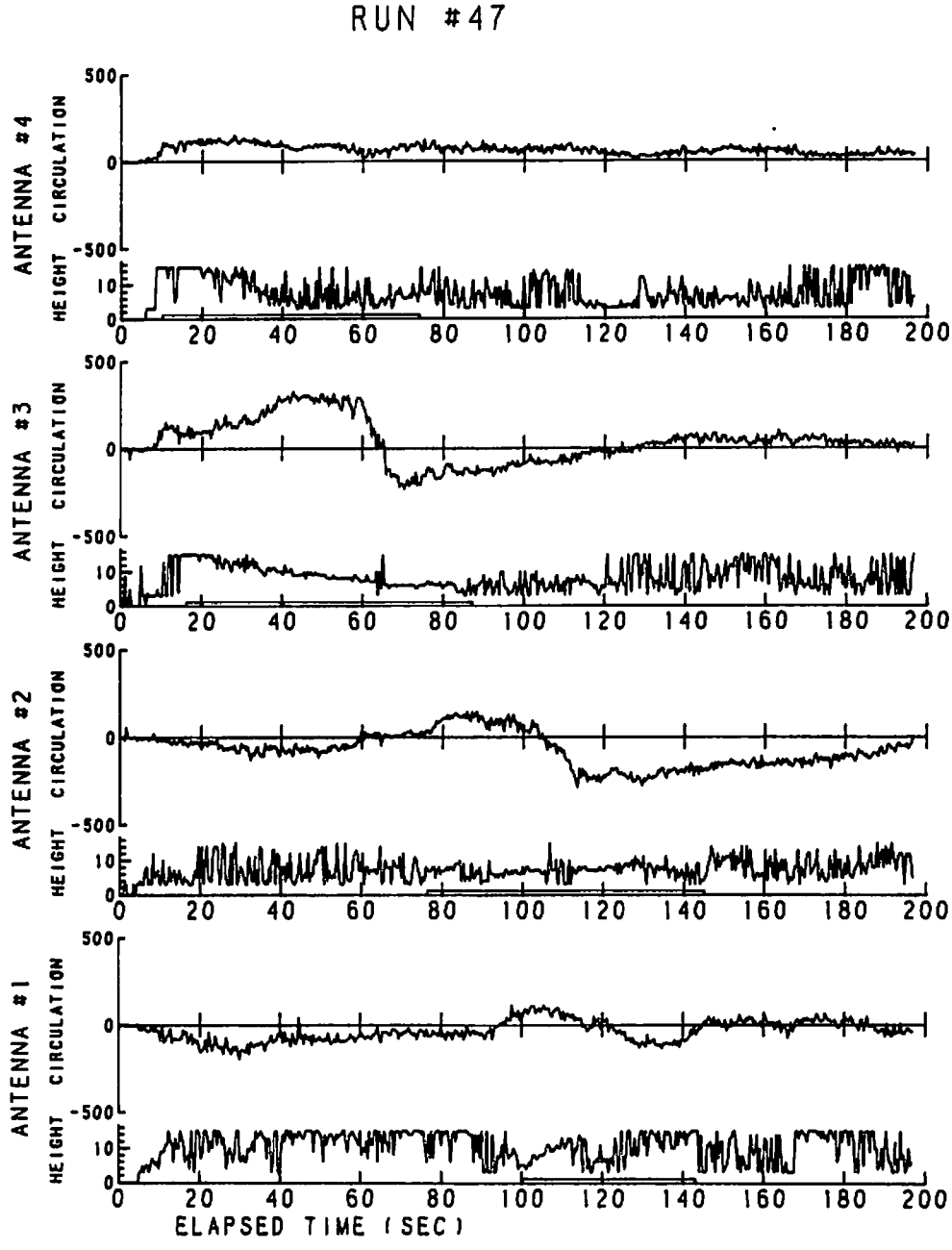

FIGURE 218. LINE-INTEGRAL AND HEIGHT DATA FOR RUN 47

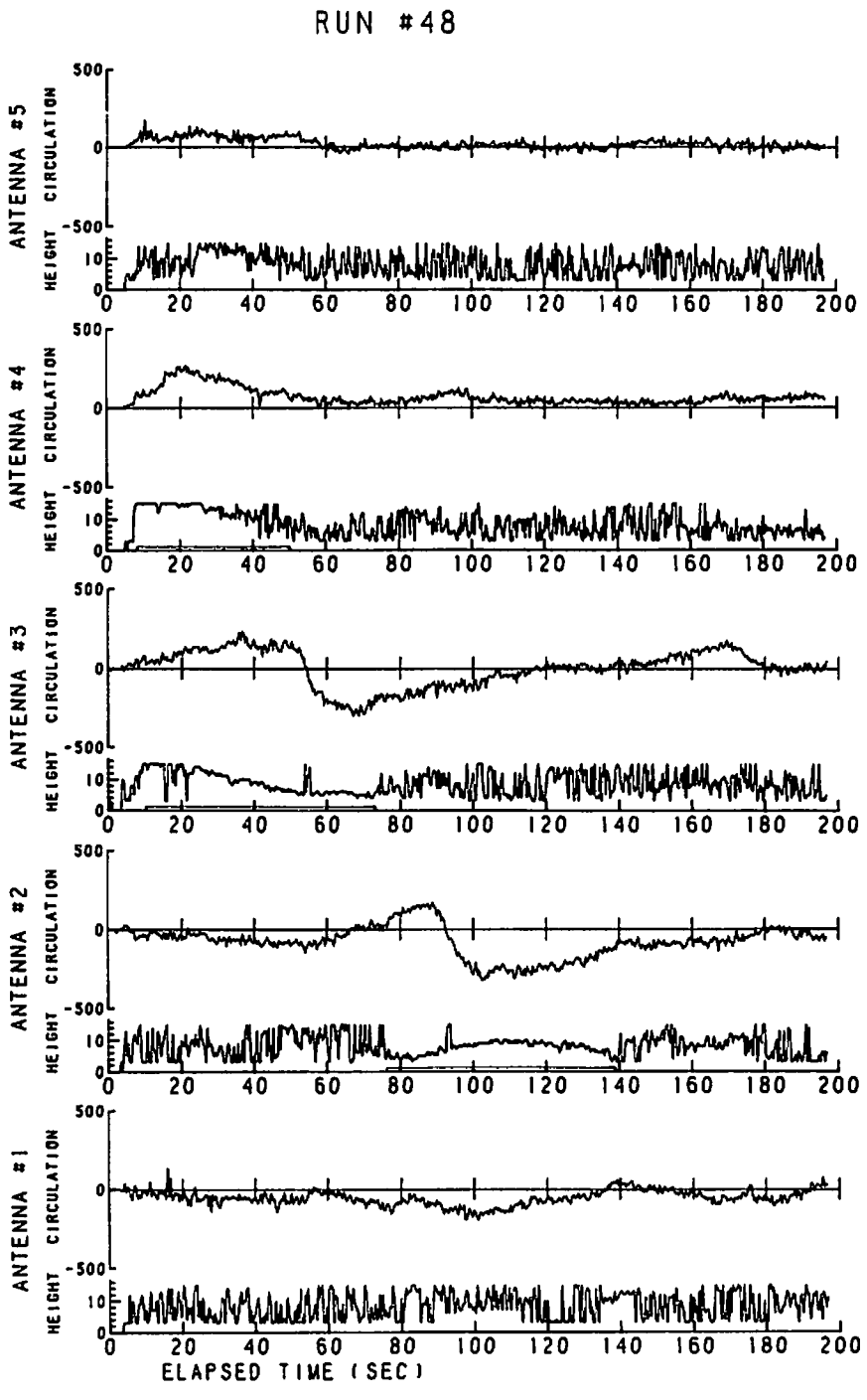

FIGURE 219. LINE-INTEGRAL AND HEIGHT DATA FOR RUN 48

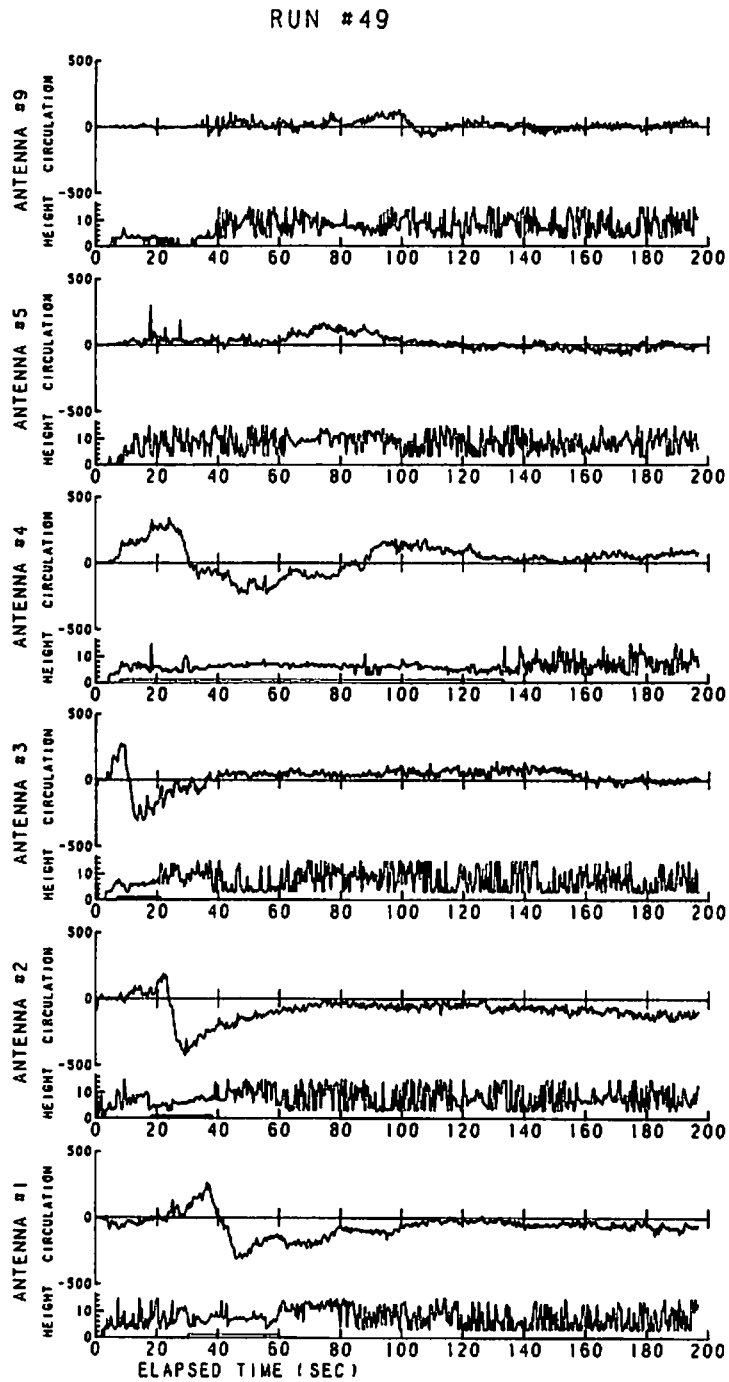

FIGURE 220. LINE-INTEGRAL AND HEIGHT DATA FOR RUN 49

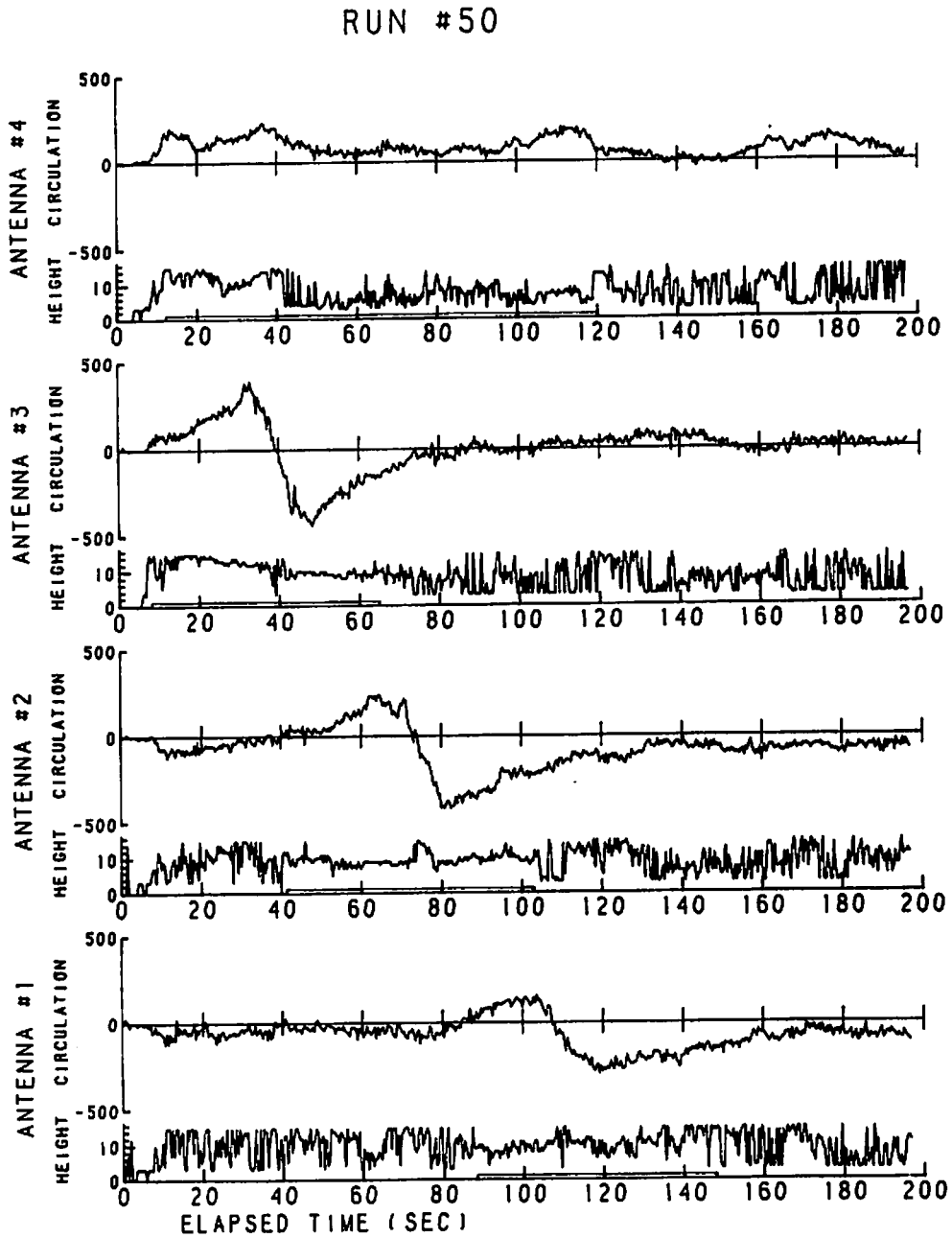

FIGURE 221. LINE-INTEGRAL AND HEIGHT DATA FOR RUN 50.

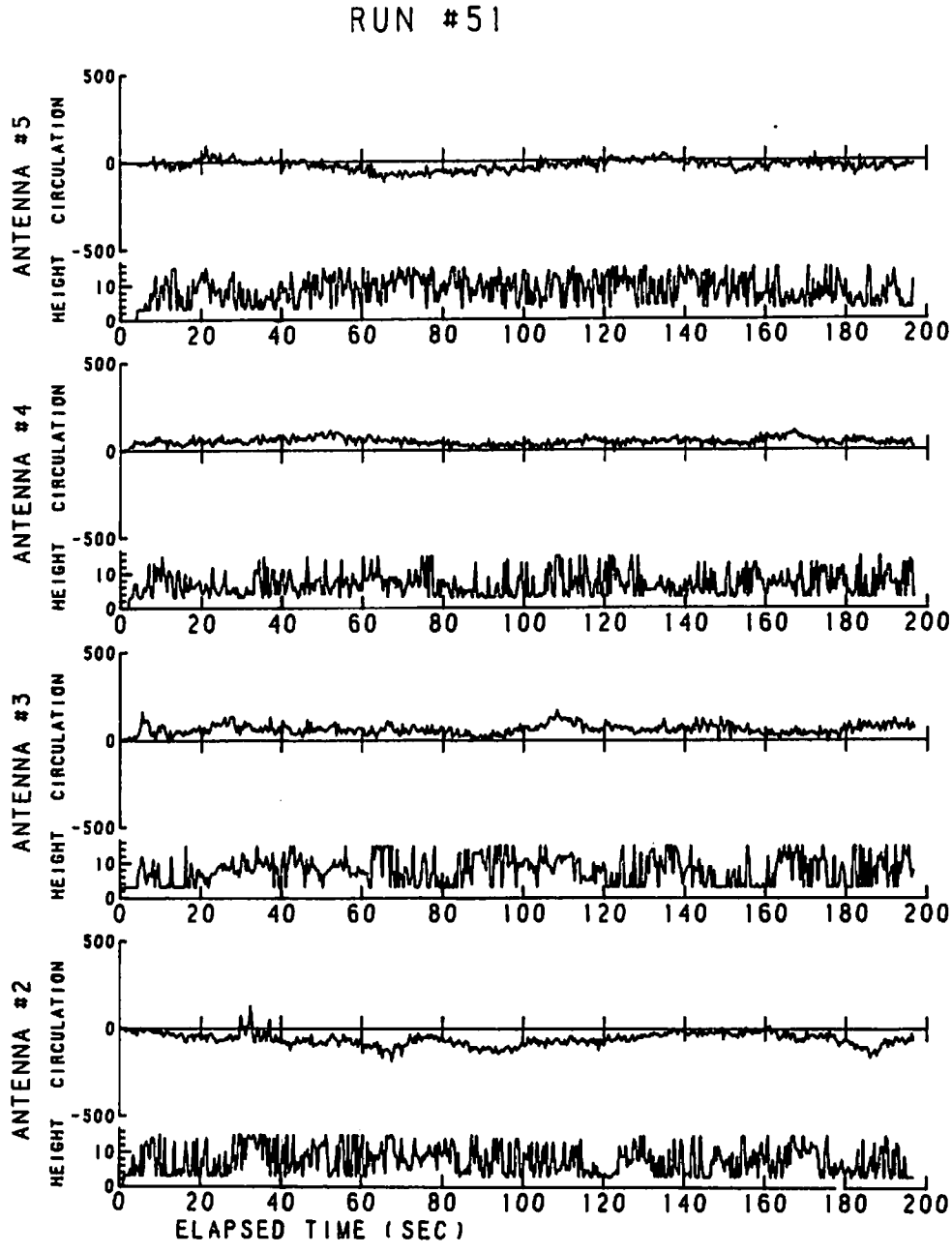

FIGURE 222. LINE-INTEGRAL AND HEIGHT DATA FOR RUN 51.

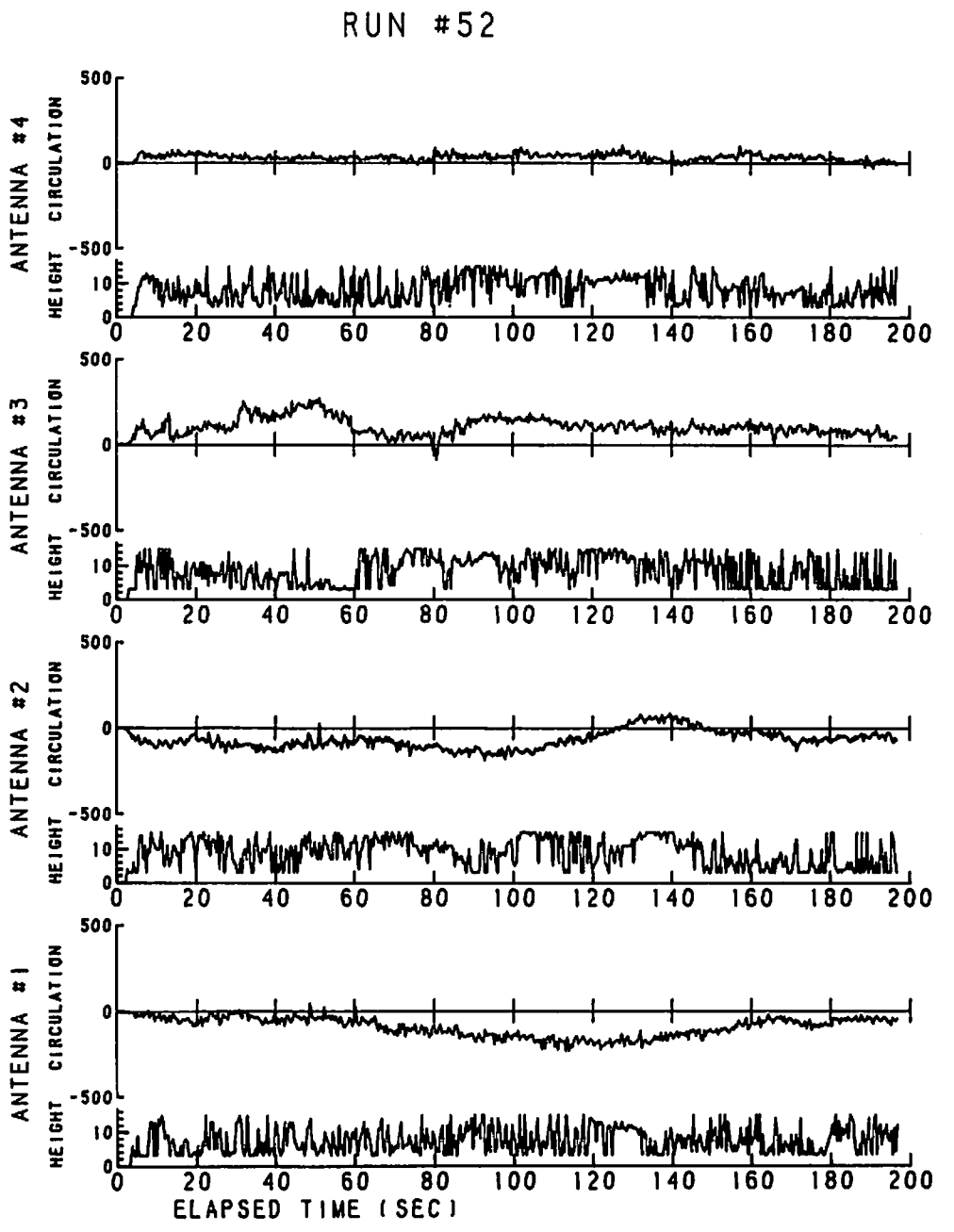

FIGURE 223. LINE-INTEGRAL AND HEIGHT DATA FOR RUN 52.

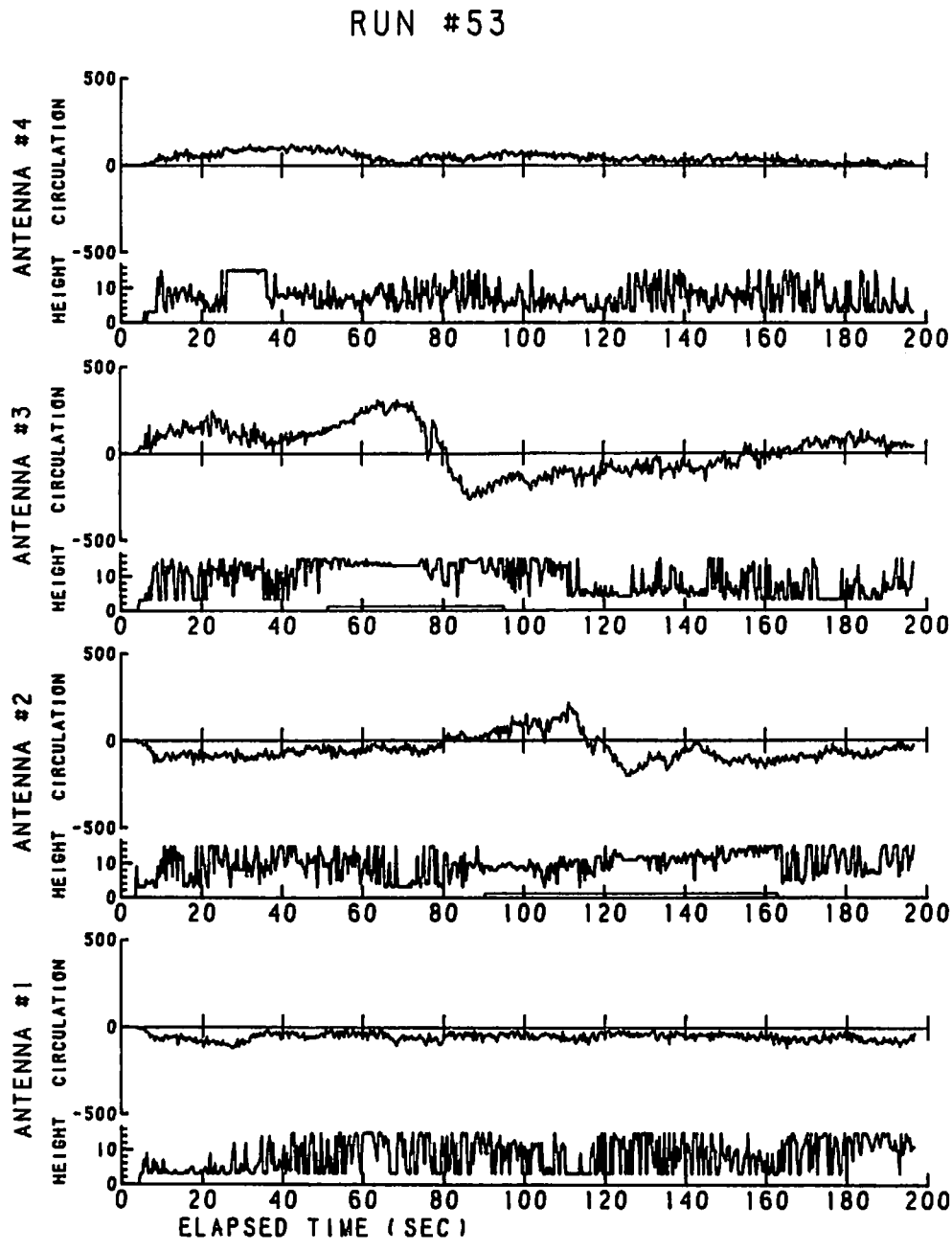

FIGURE 224. LINE-INTEGRAL AND HEIGHT DATA FOR RUN 53

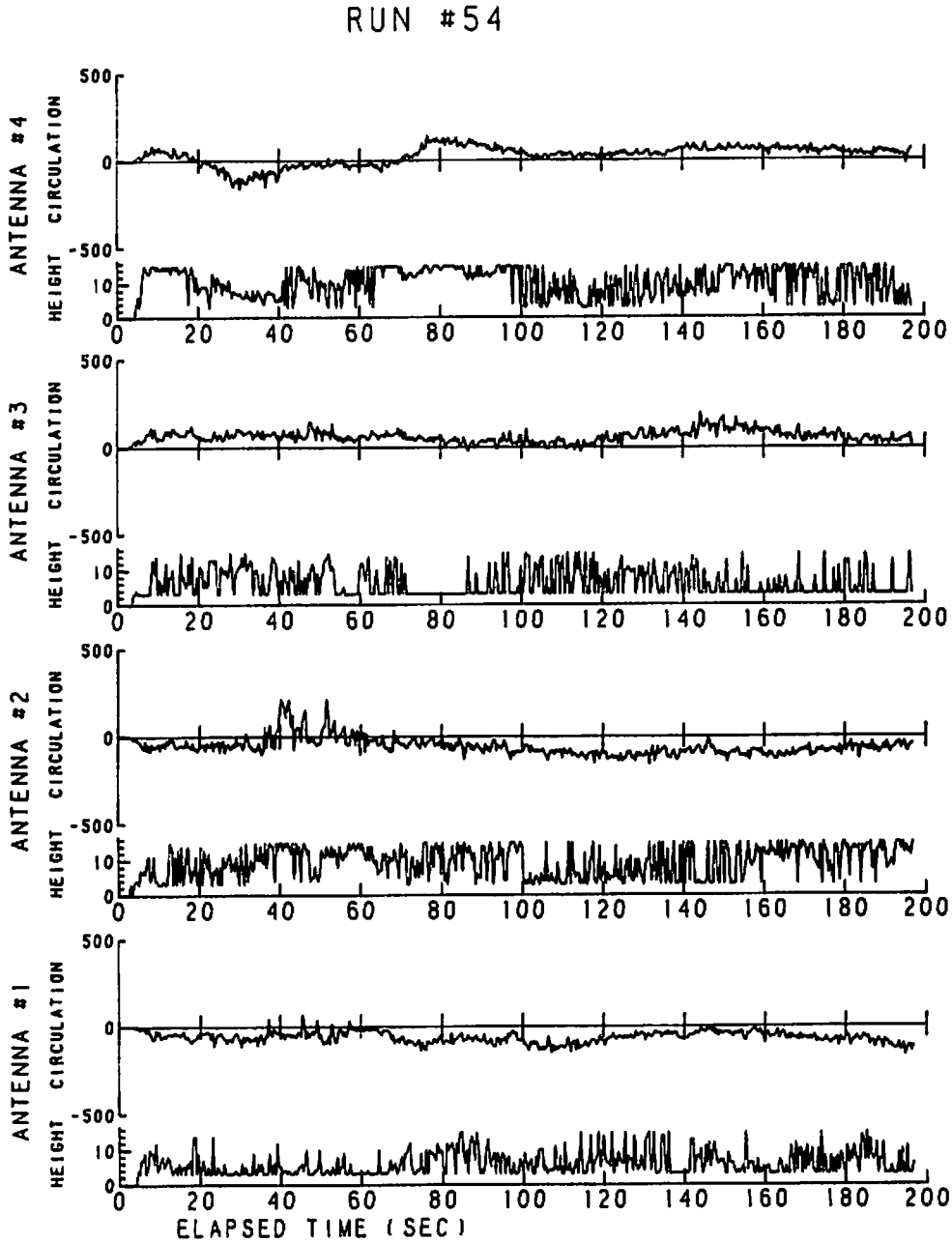

FIGURE 225. LINE-INTEGRAL AND HEIGHT DATA FOR RUN 54.

E.3 VORTEX-PROFILE PLOTS

The following plots show the vortex-velocity profiles for those vortices which passed over MAVSS antennas. A few such passages are omitted because of data-processing problems. One should note that these data are the only place in the report where the longitudinal variation in the vortices can be studied by comparing antennas with the same lateral distance offset (antennas 5 and 9, and antennas 7 and 10).

The data are plotted in two different formats which illustrate different features of the data. The first (as in Fig. 72) plots the vortex-velocity profiles and the rms frequency profiles for the five range gates around the vortex height. The solid lines are a least-squares fit to the velocity profile. The parameters of the fit are listed in the heading. The second format (as in Fig. 73) plots only the velocity profile for the range gate nearest the vortex core (i.e., with the largest correlation). This solid line is the least-square fit to this single range gate, and the parameters of the fit are listed on the plot. The lower plot shows the circulation corresponding to the velocity data; the positive and negative radius points are averaged. The pluses in the lower plot are the average circulation as a function of averaging radius.

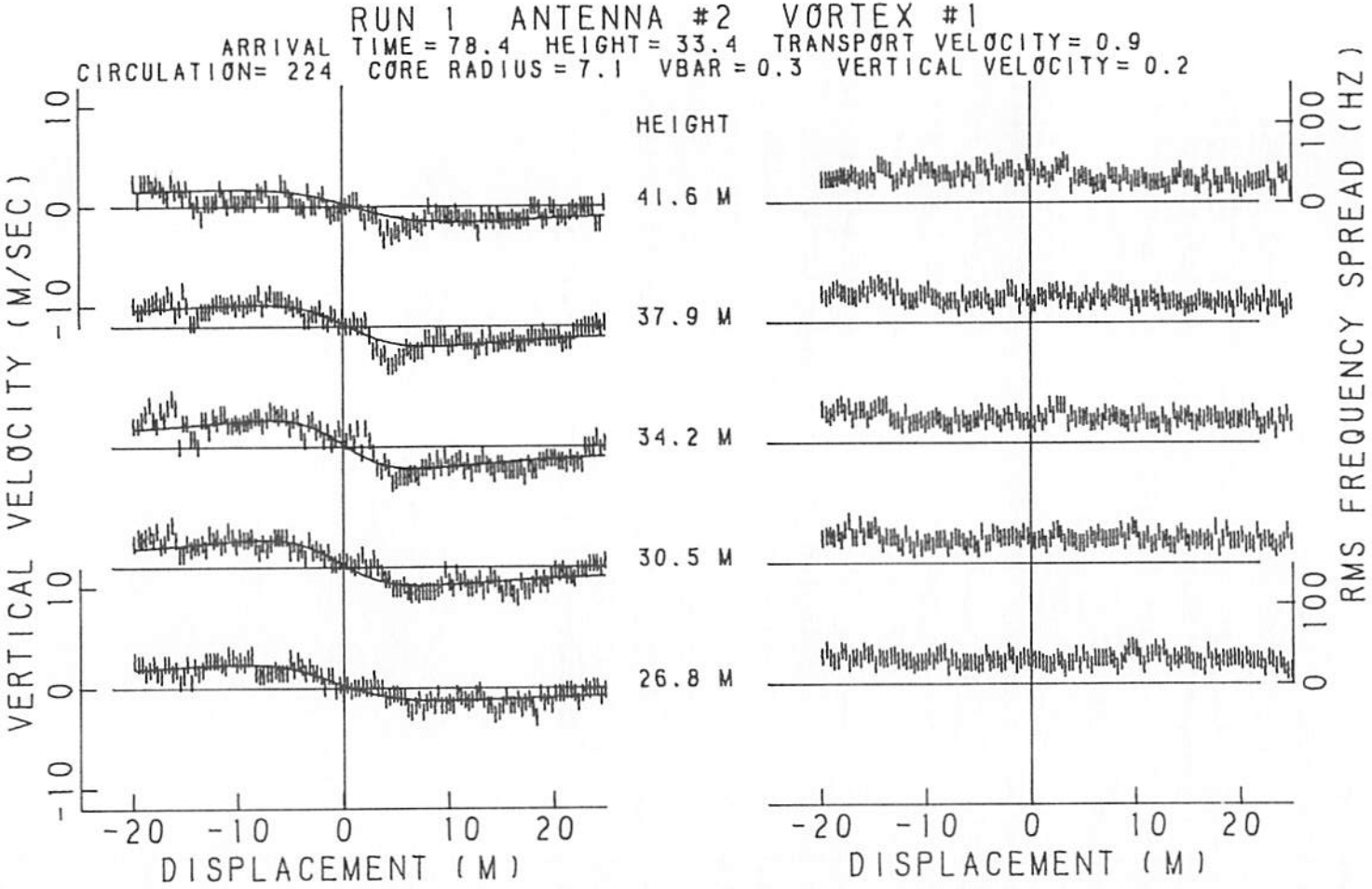

FIGURE 226. VELOCITY AND SPECTRAL WIDTH PROFILES FOR RUN 1, ANTENNA 2.

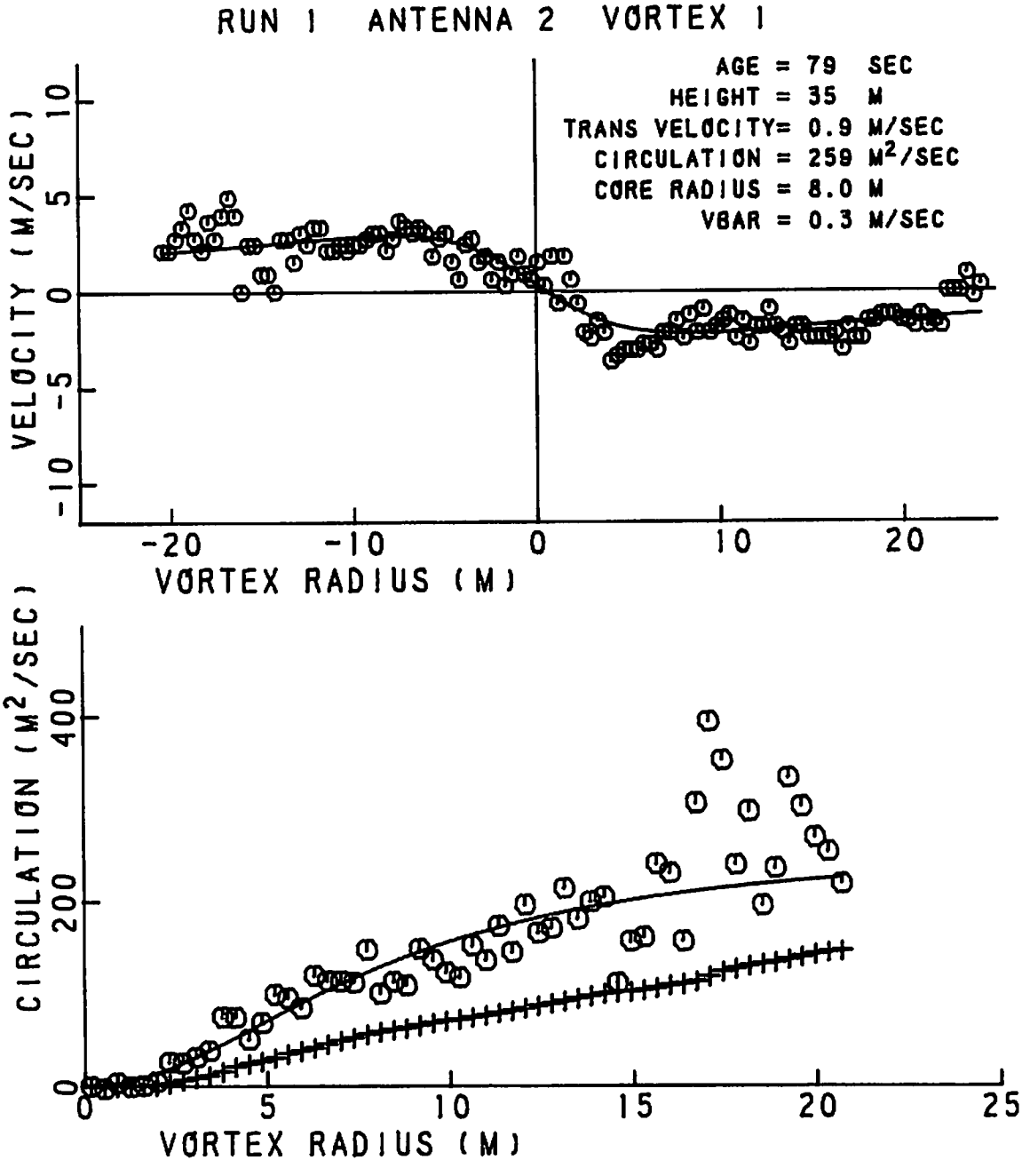

FIGURE 227. VELOCITY AND CIRCULATION PROFILES FOR RUN 1, ANTENNA 2.

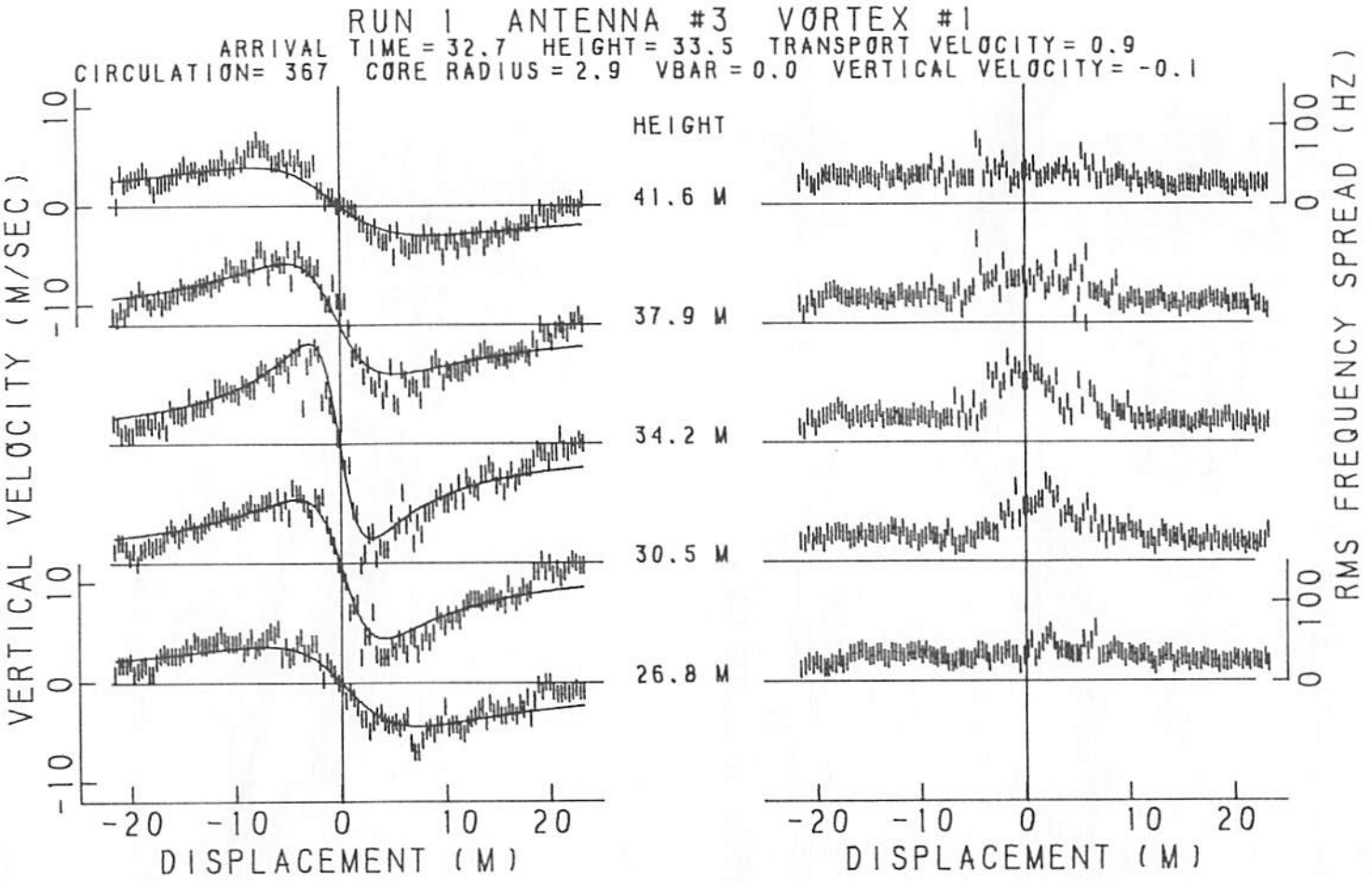

FIGURE 228. VELOCITY AND SPECTRAL WIDTH PROFILES FOR RUN 1, ANTENNA 3.

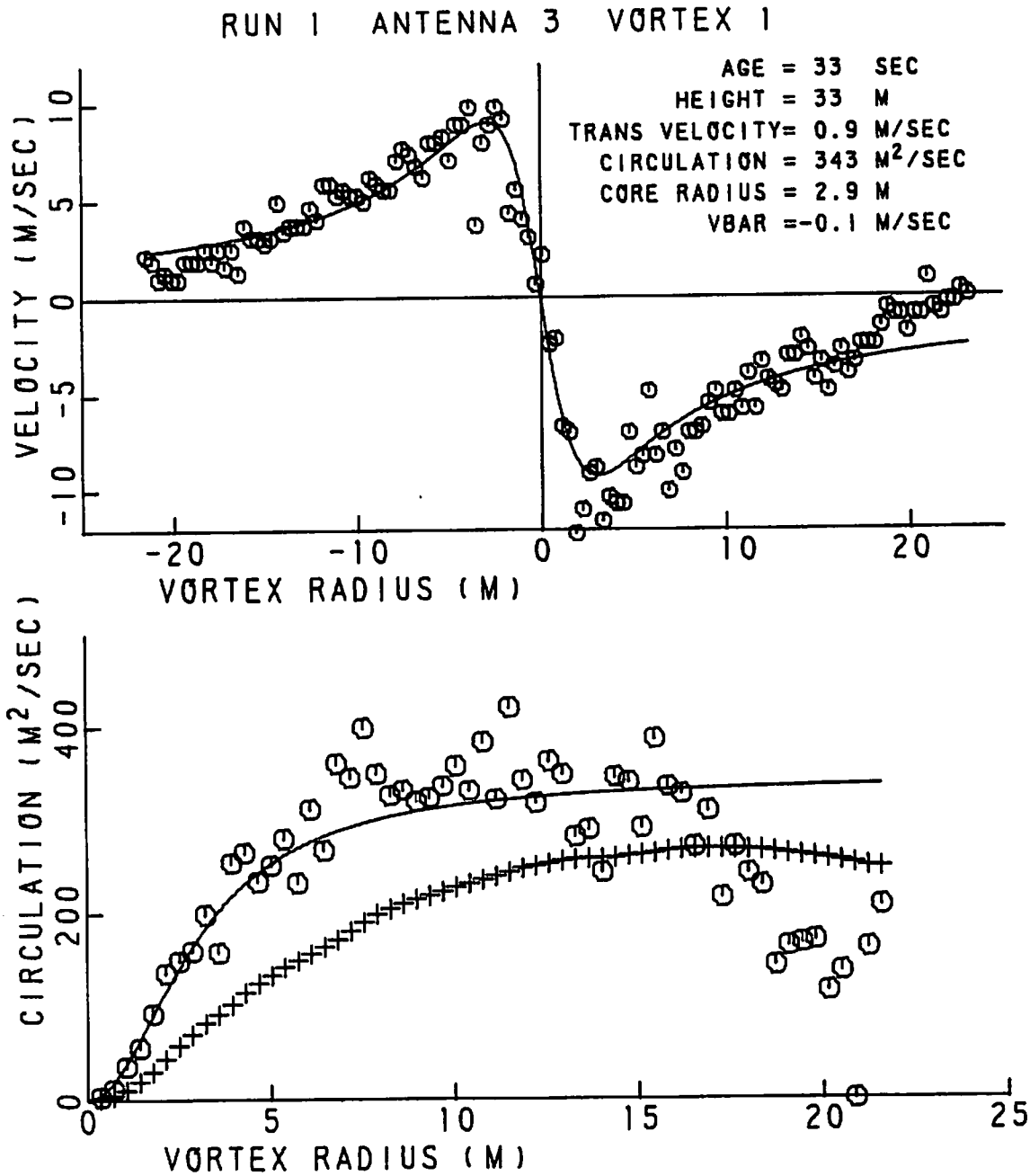

FIGURE 229. VELOCITY AND CIRCULATION PROFILES FOR RUN 1, ANTENNA 3.

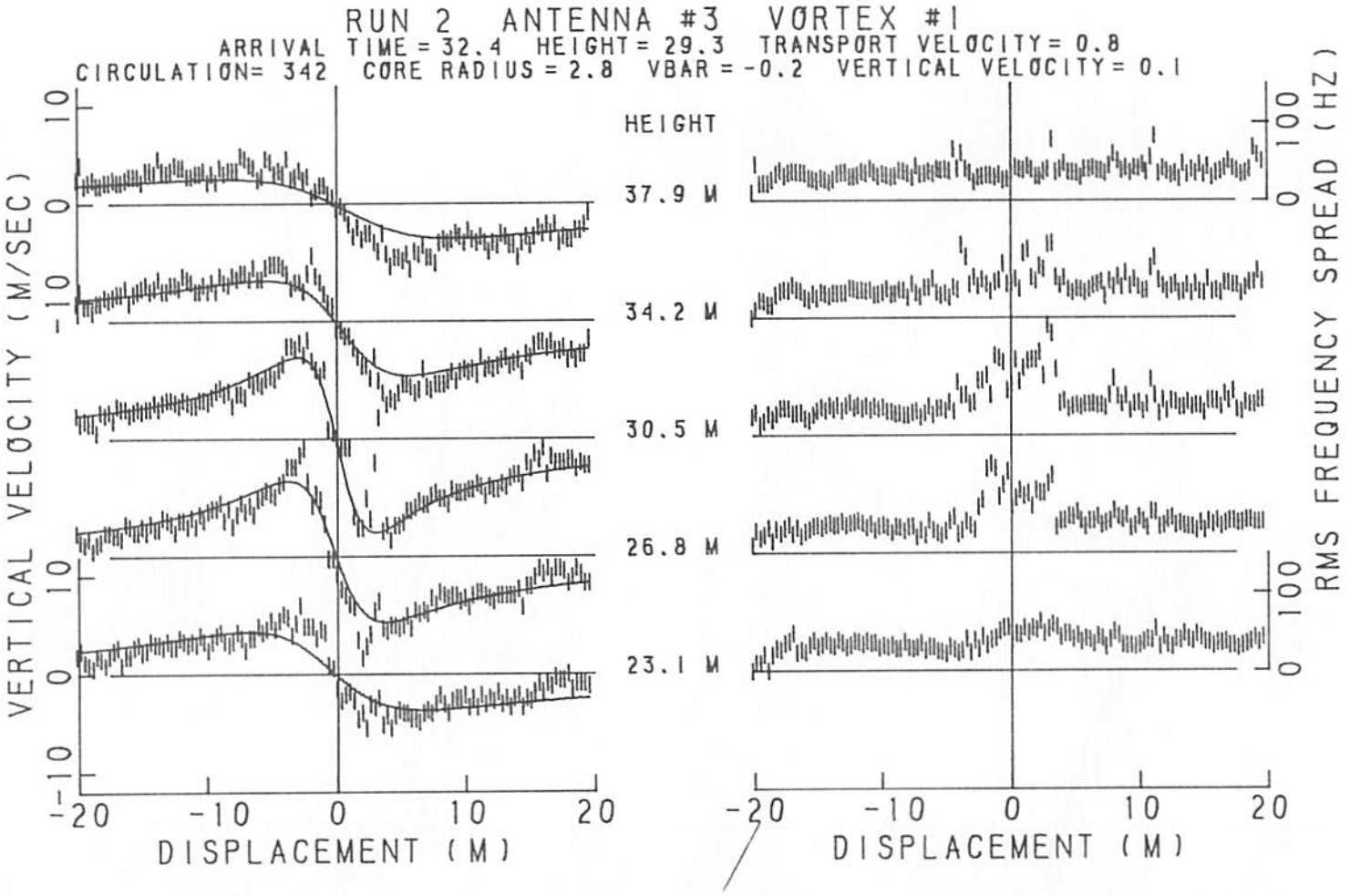

FIGURE 230. VELOCITY AND SPECTRAL WIDTH PROFILES FOR RUN 2, ANTENNA 3.

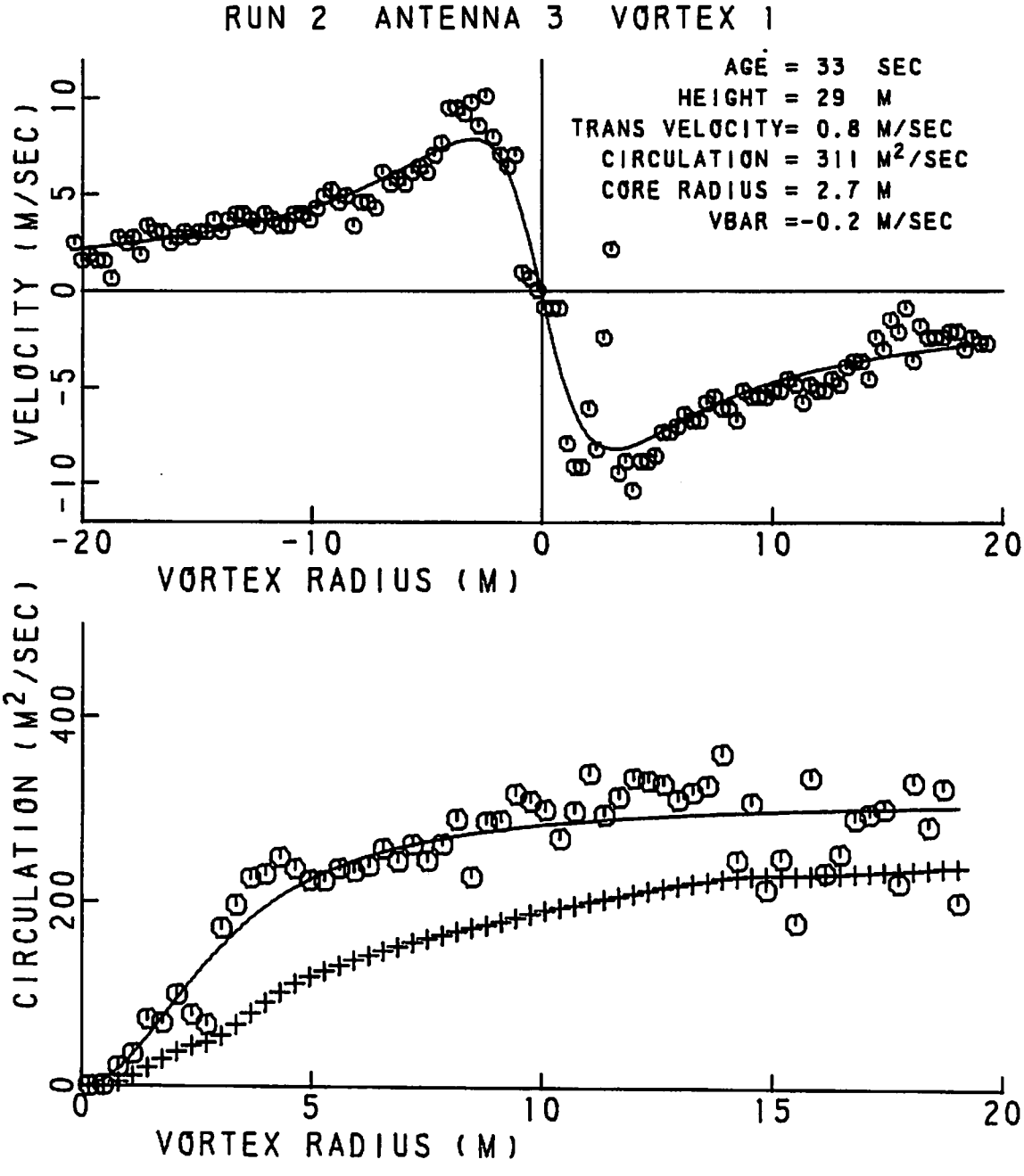

FIGURE 231. VELOCITY AND CIRCULATION PROFILES FOR RUN 2, ANTENNA 3.

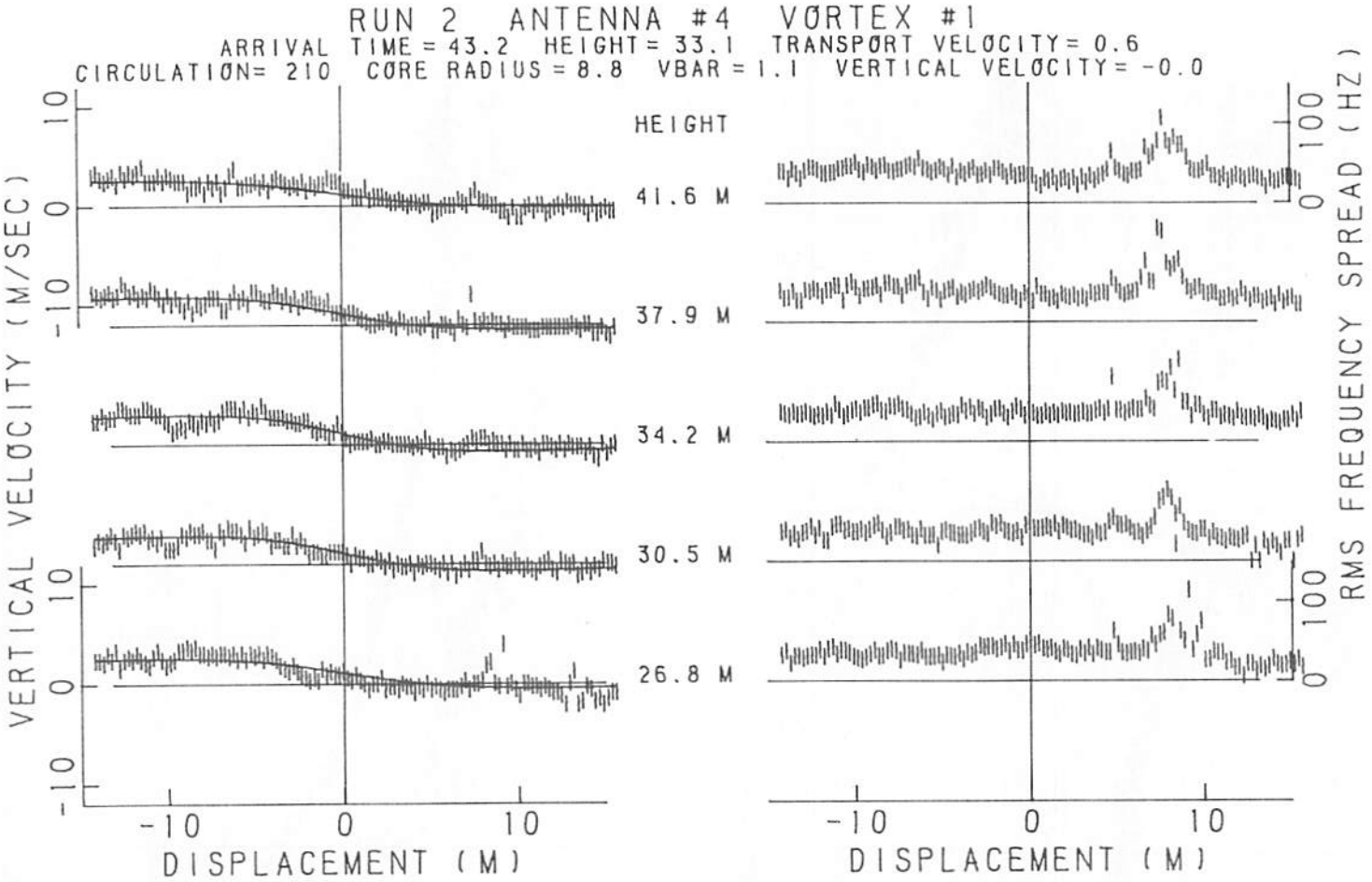

FIGURE 232. VELOCITY AND SPECTRAL WIDTH PROFILES FOR RUN 2, ANTENNA 4.

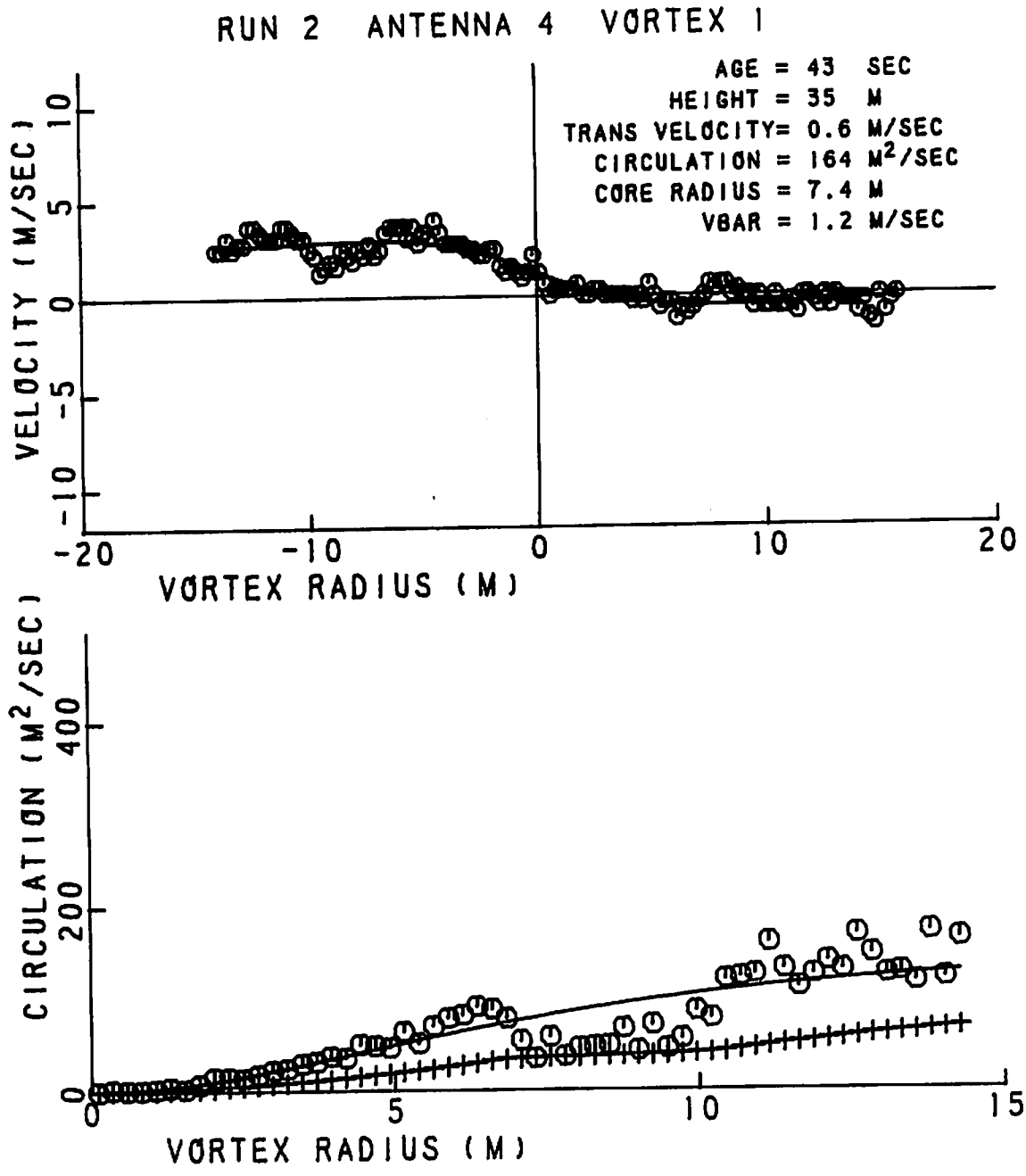

FIGURE 233. VELOCITY AND CIRCULATION PROFILES FOR RUN 2, ANTENNA 4

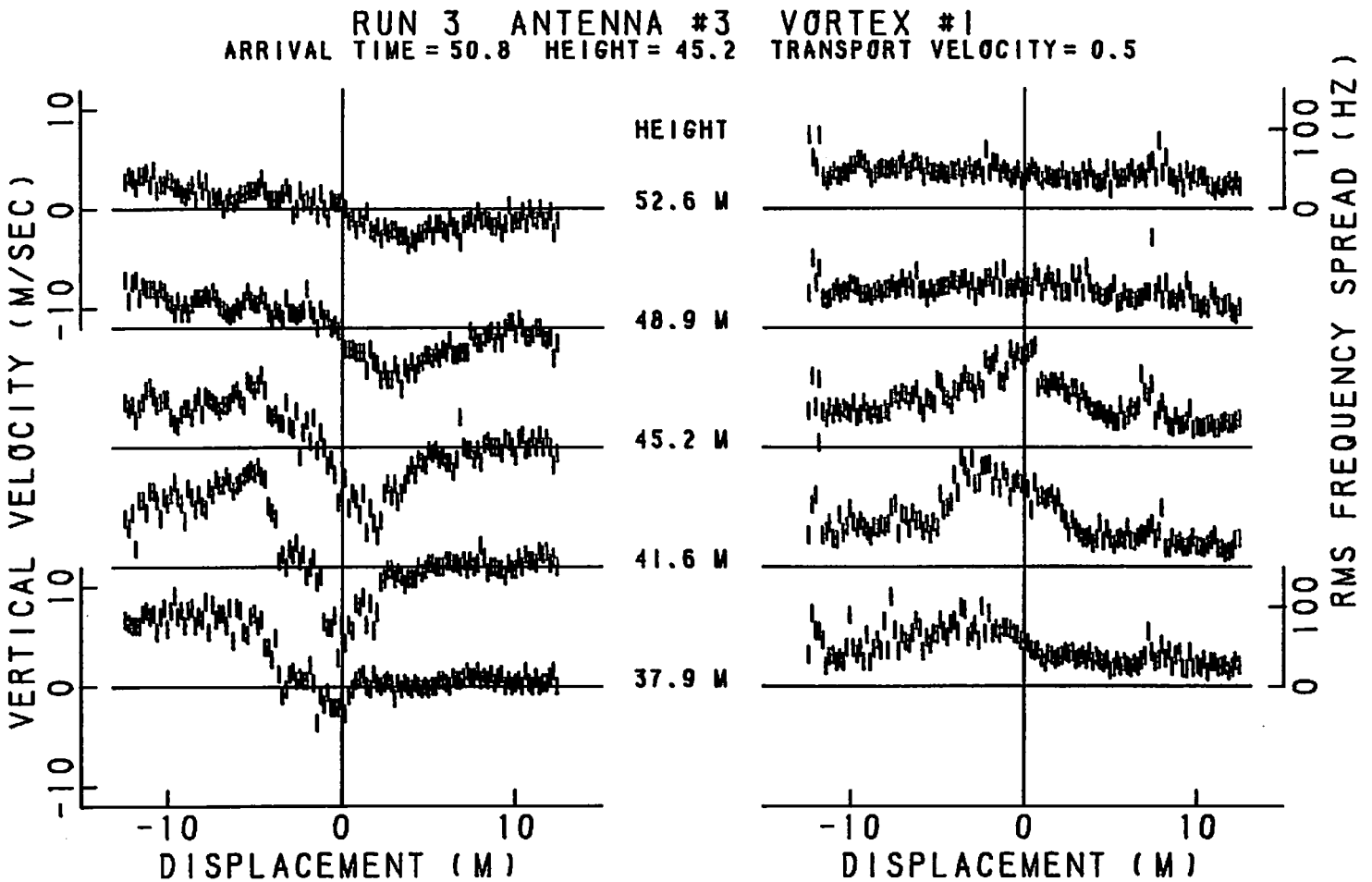

FIGURE 234. VELOCITY AND SPECTRAL WIDTH PROFILES FOR RUN 3, ANTENNA 3

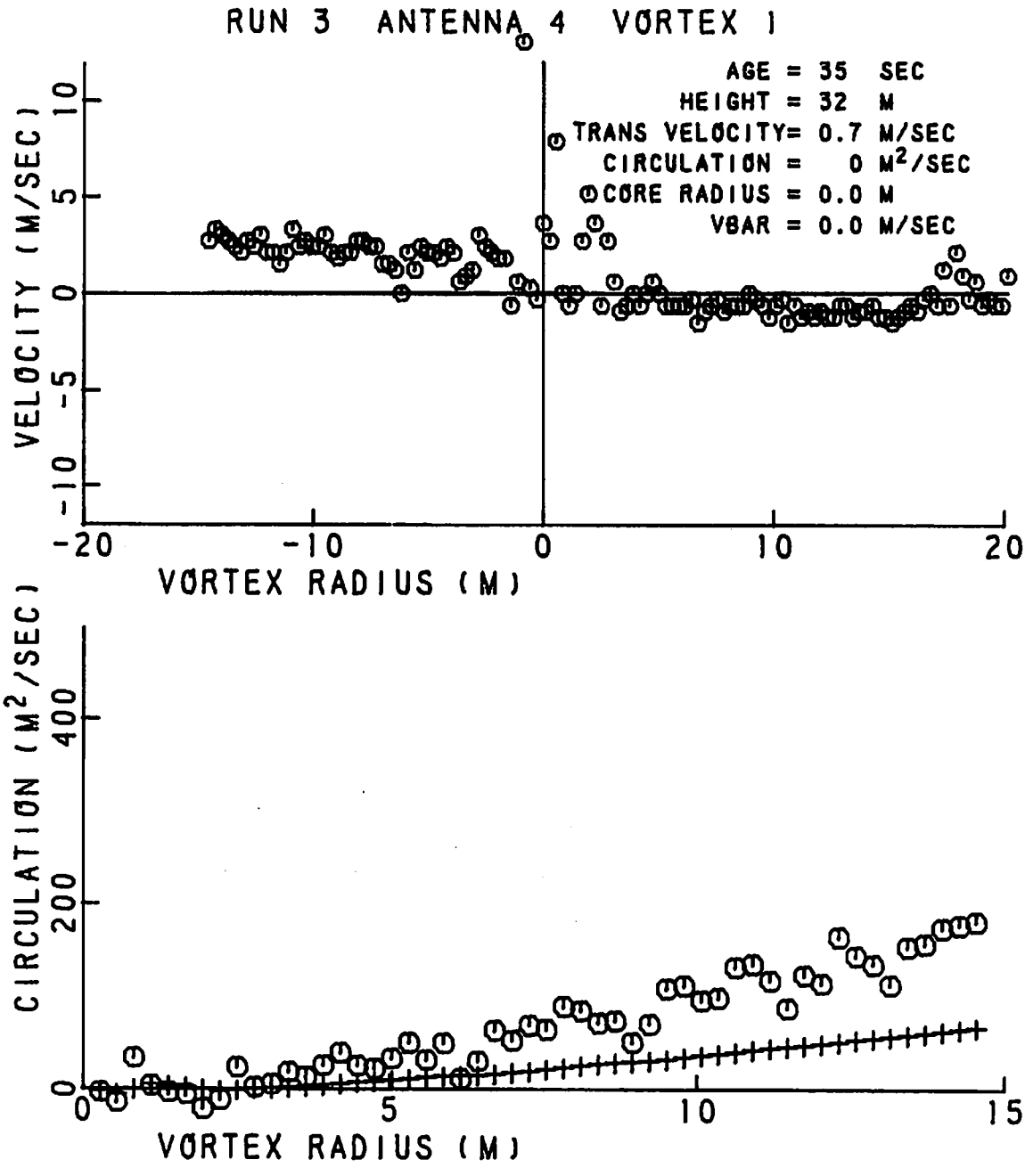

FIGURE 235. VELOCITY AND CIRCULATION PROFILES FOR RUN 3, ANTENNA 4.

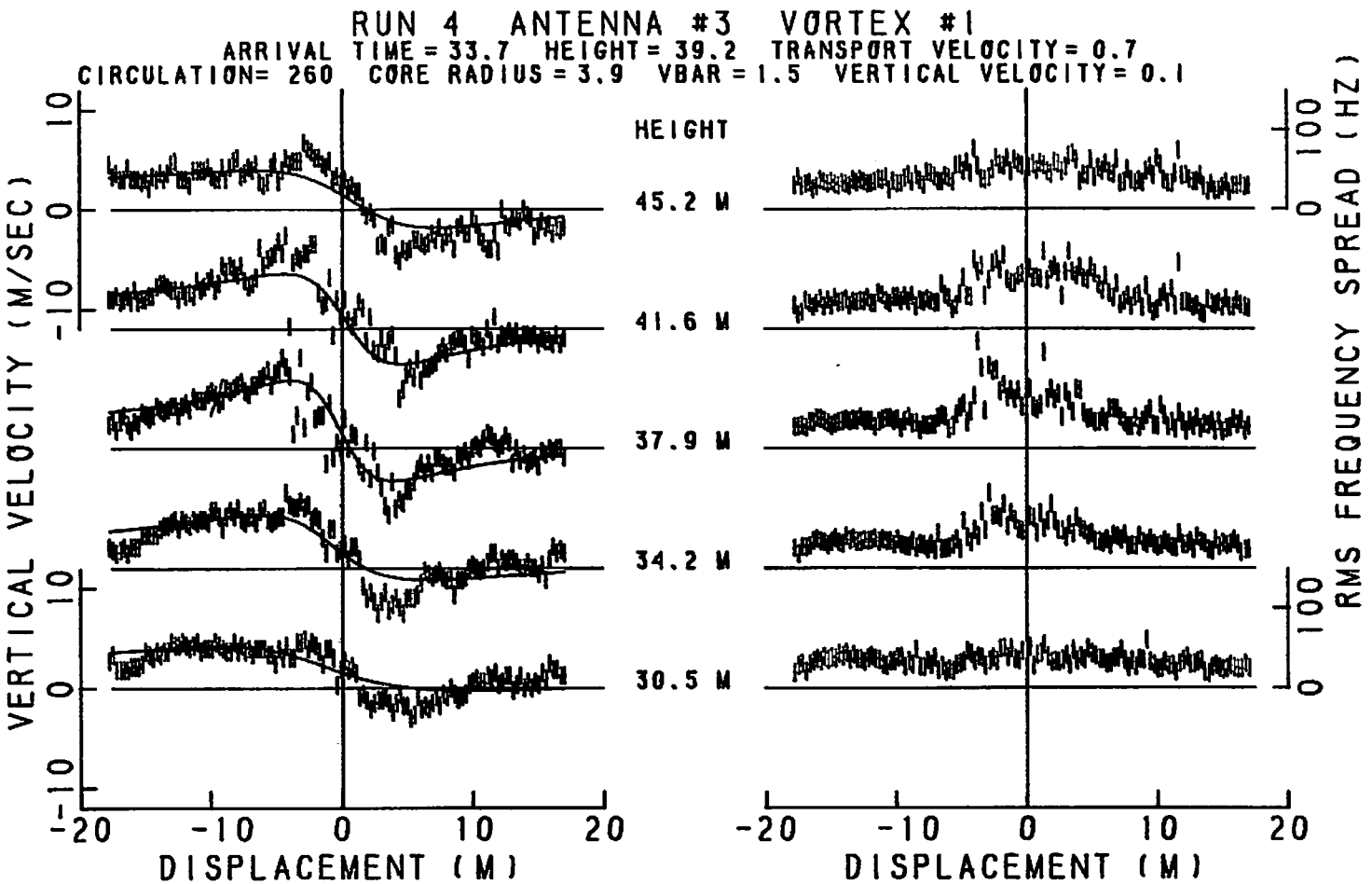

FIGURE 236. VELOCITY AND SPECTRAL WIDTH PROFILES FOR RUN 4, ANTENNA 3

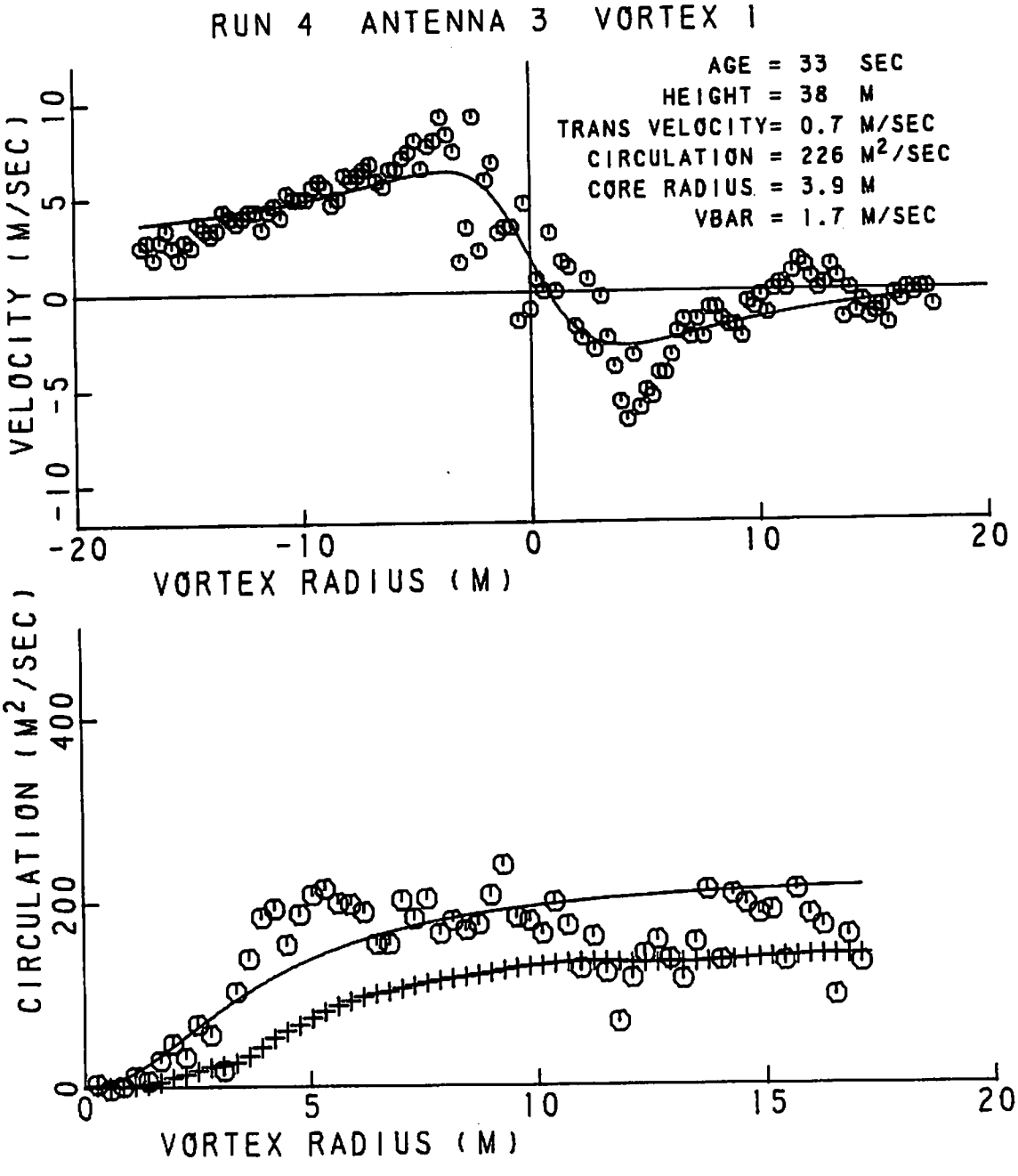

FIGURE 237. VELOCITY AND CIRCULATION PROFILES FOR RUN 4, ANTENNA 3

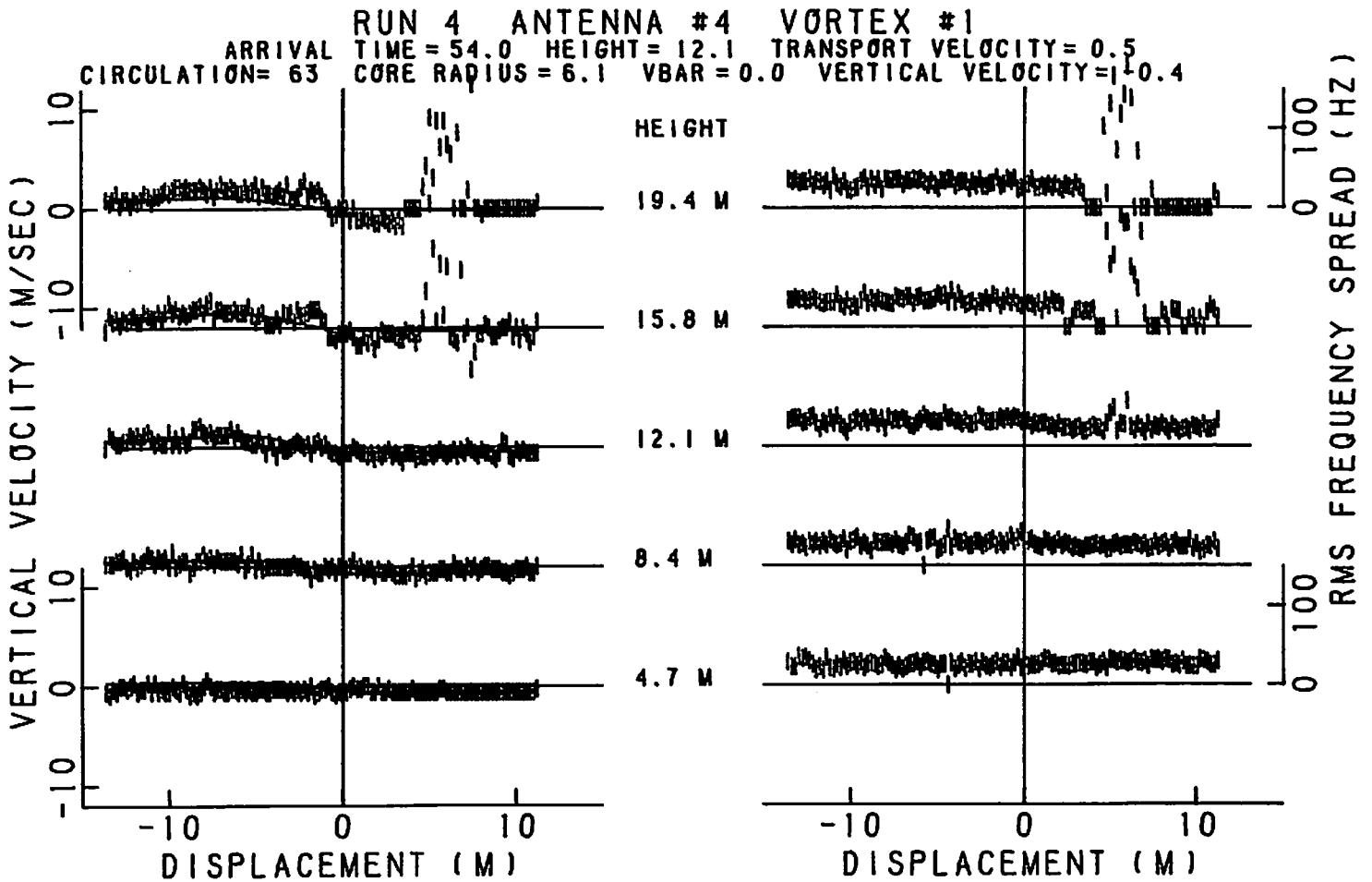

FIGURE 238. VELOCITY AND SPECTRAL WIDTH PROFILES FOR RUN 4, ANTENNA 4

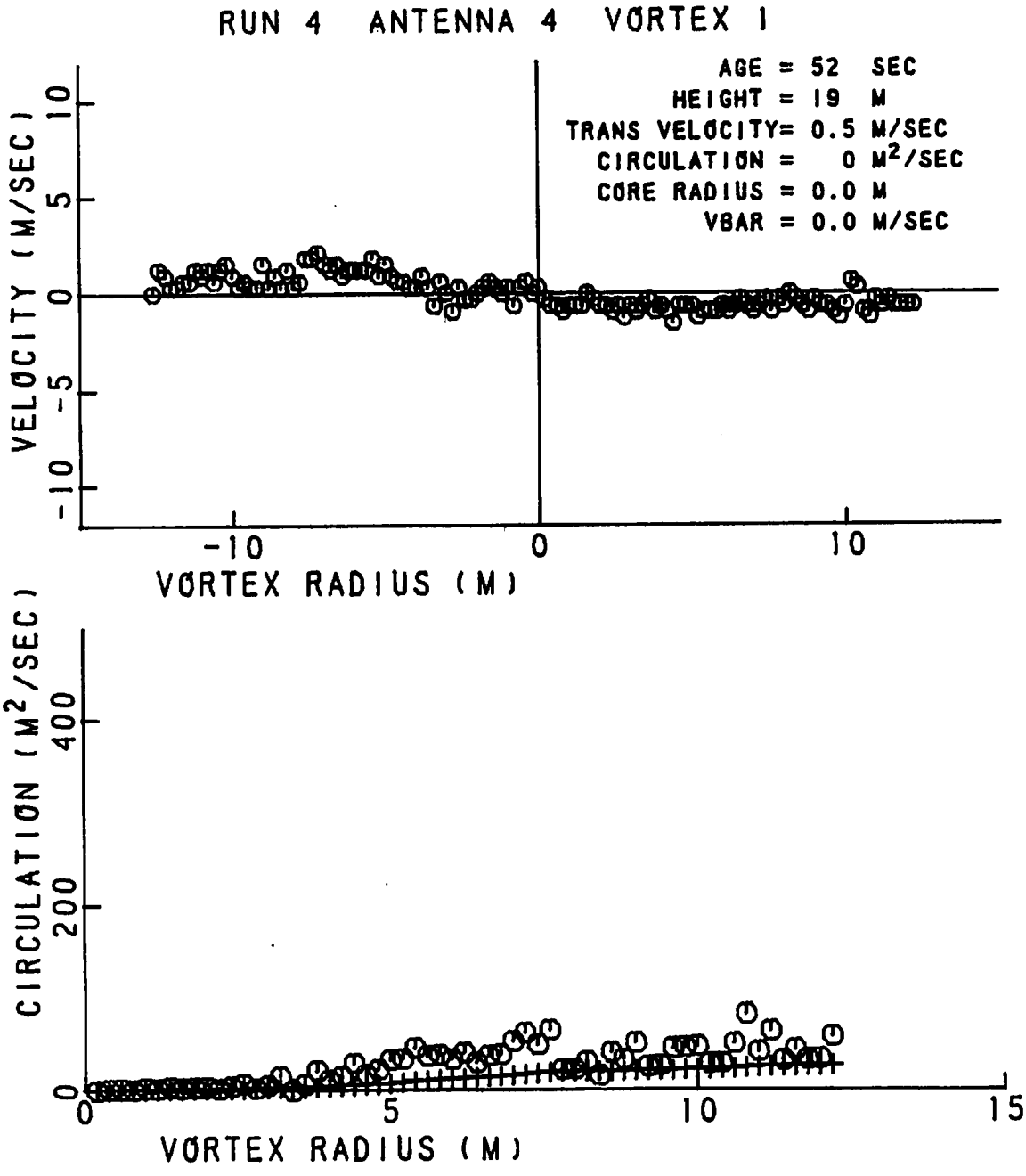

FIGURE 239. VELOCITY AND CIRCULATION PROFILES FOR RUN 4, ANTENNA 4

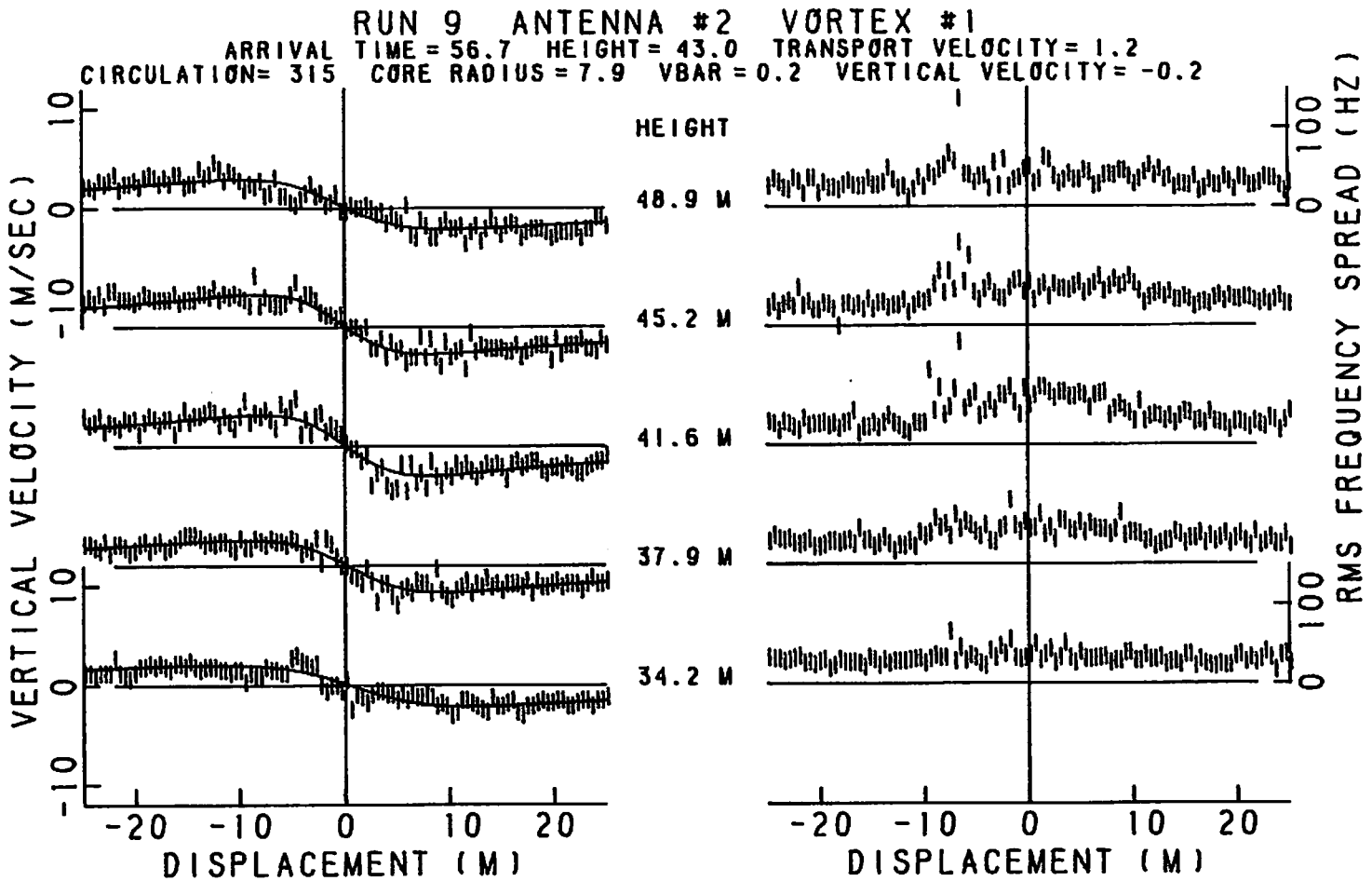

FIGURE 240. VELOCITY AND SPECTRAL WIDTH PROFILES FOR RUN 9, ANTENNA 2

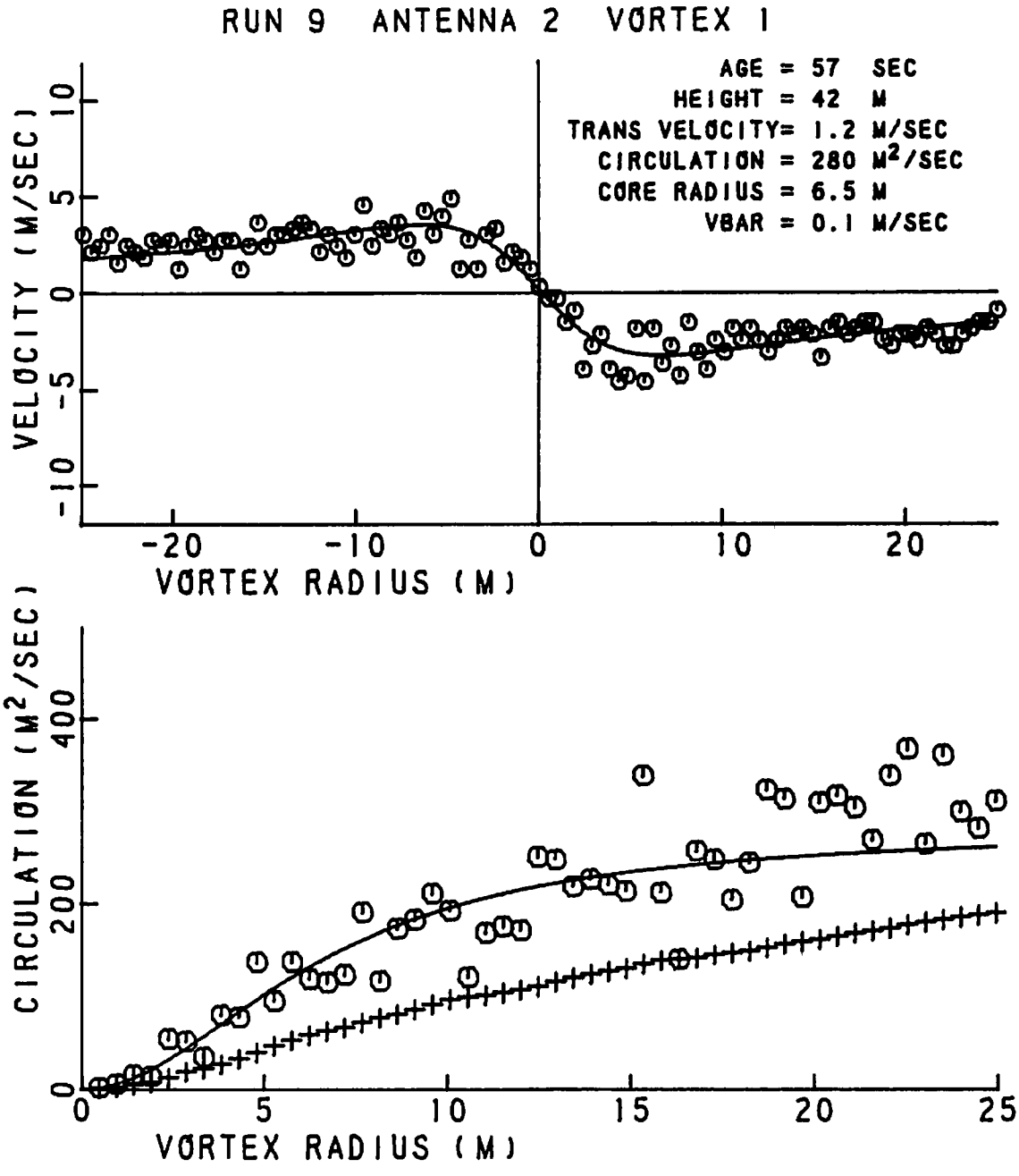

FIGURE 241. VELOCITY AND CIRCULATION PROFILES FOR RUN 9, ANTENNA 2

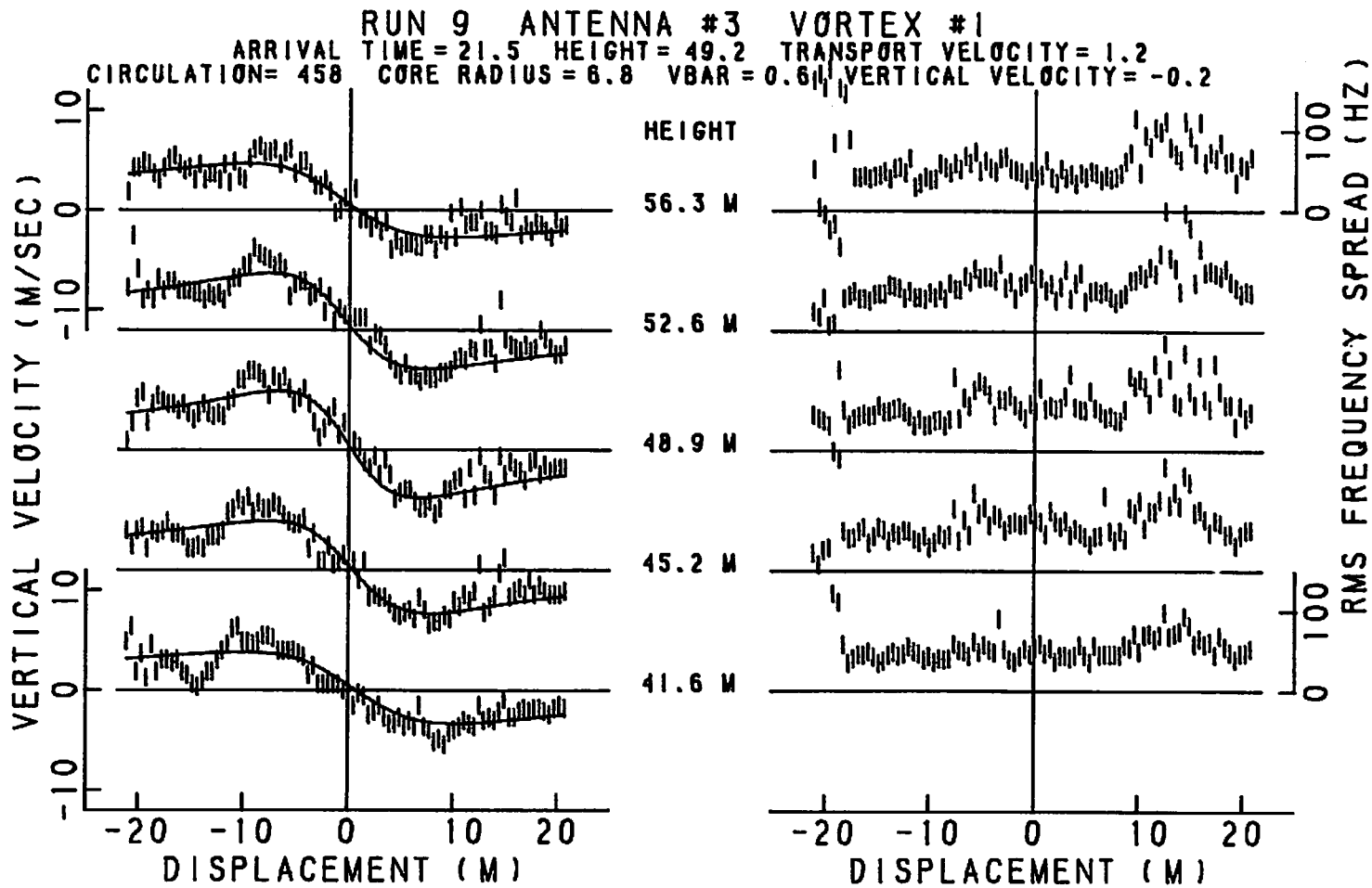

FIGURE 242. VELOCITY AND SPECTRAL WIDTH PROFILES FOR RUN 9, ANTENNA 3

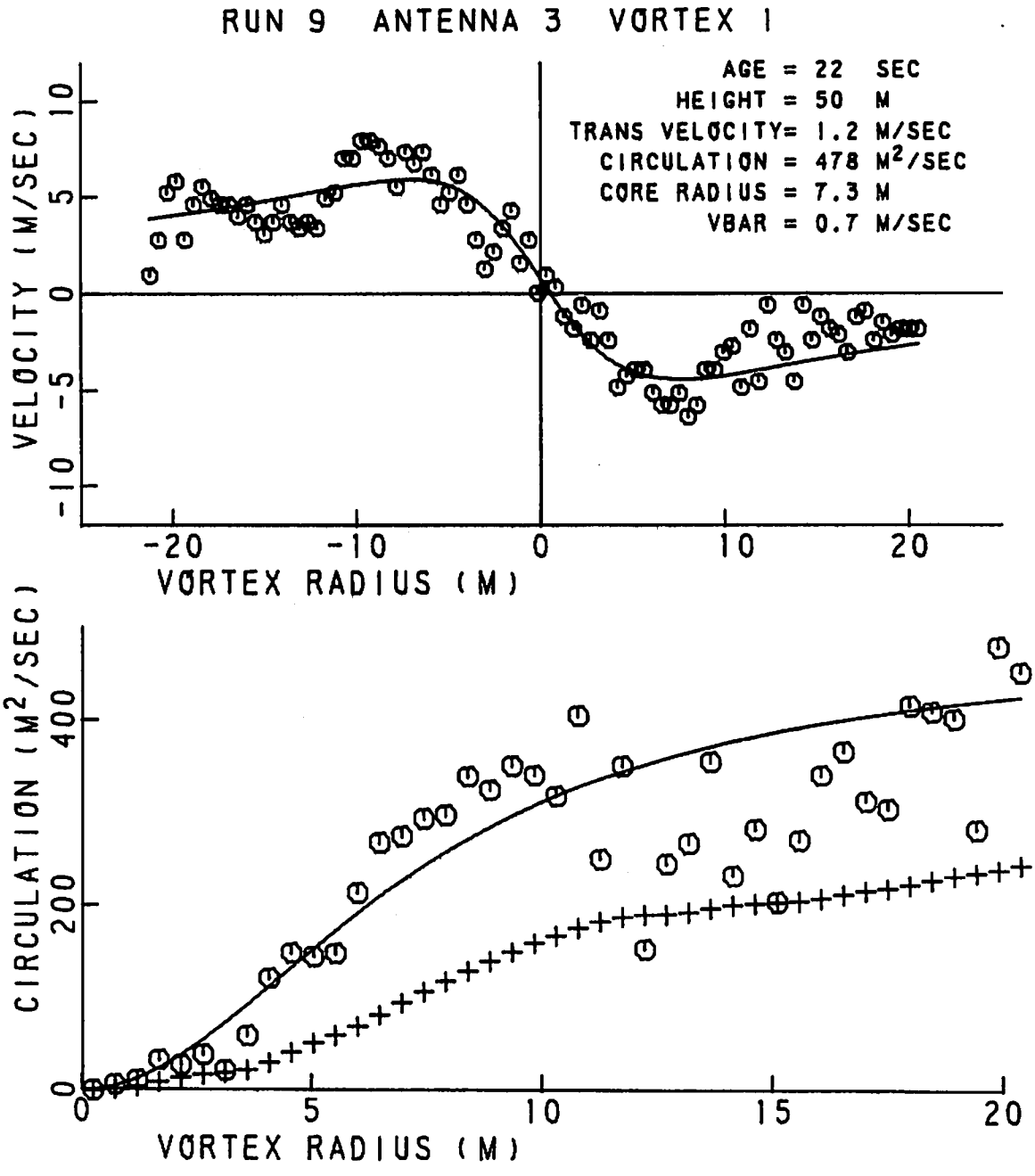

FIGURE 243. VELOCITY AND CIRCULATION PROFILES FOR RUN 9, ANTENNA 3

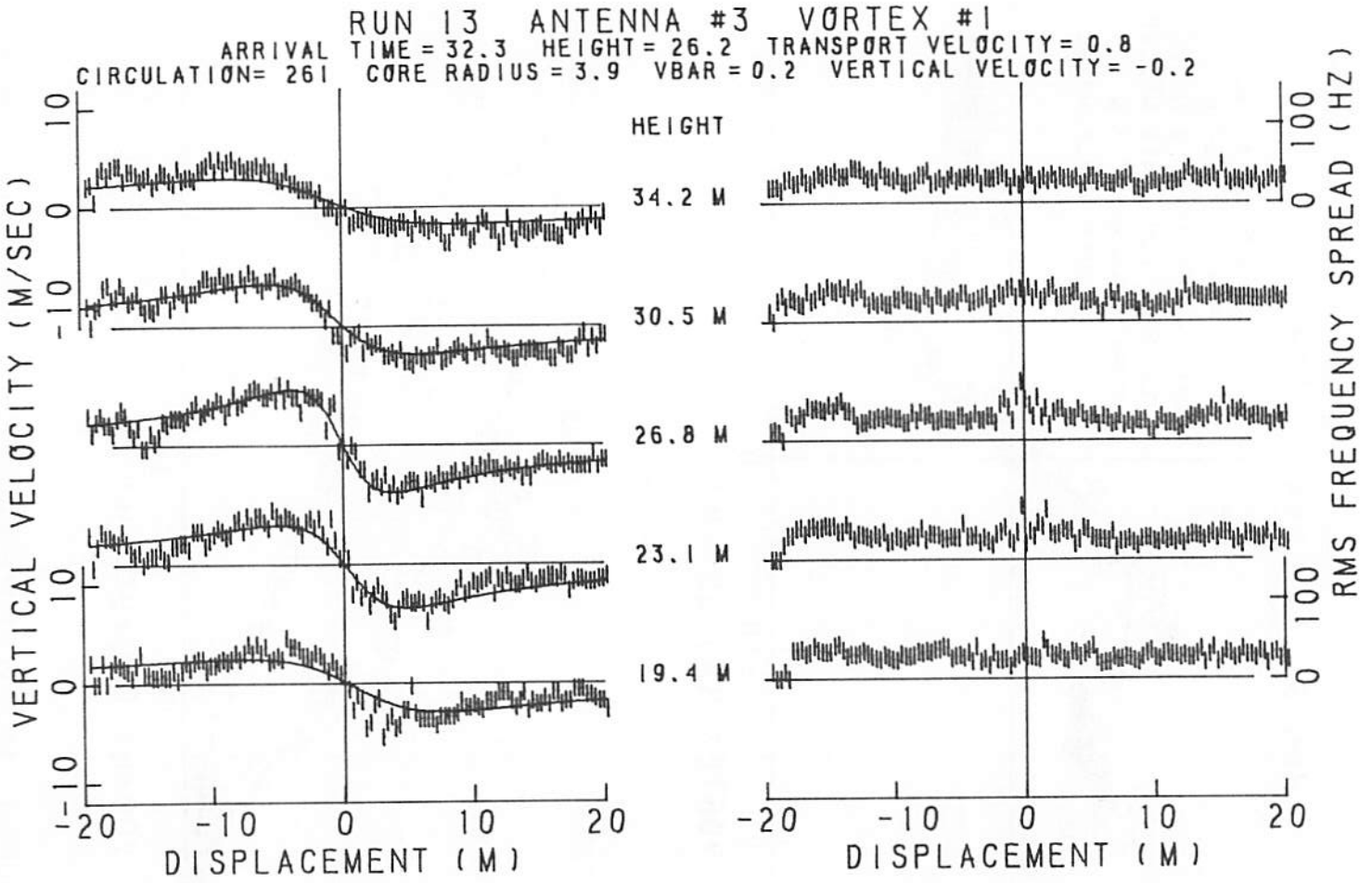

FIGURE 244. VELOCITY AND SPECTRAL WIDTH PROFILES FOR RUN 13, ANTENNA 3

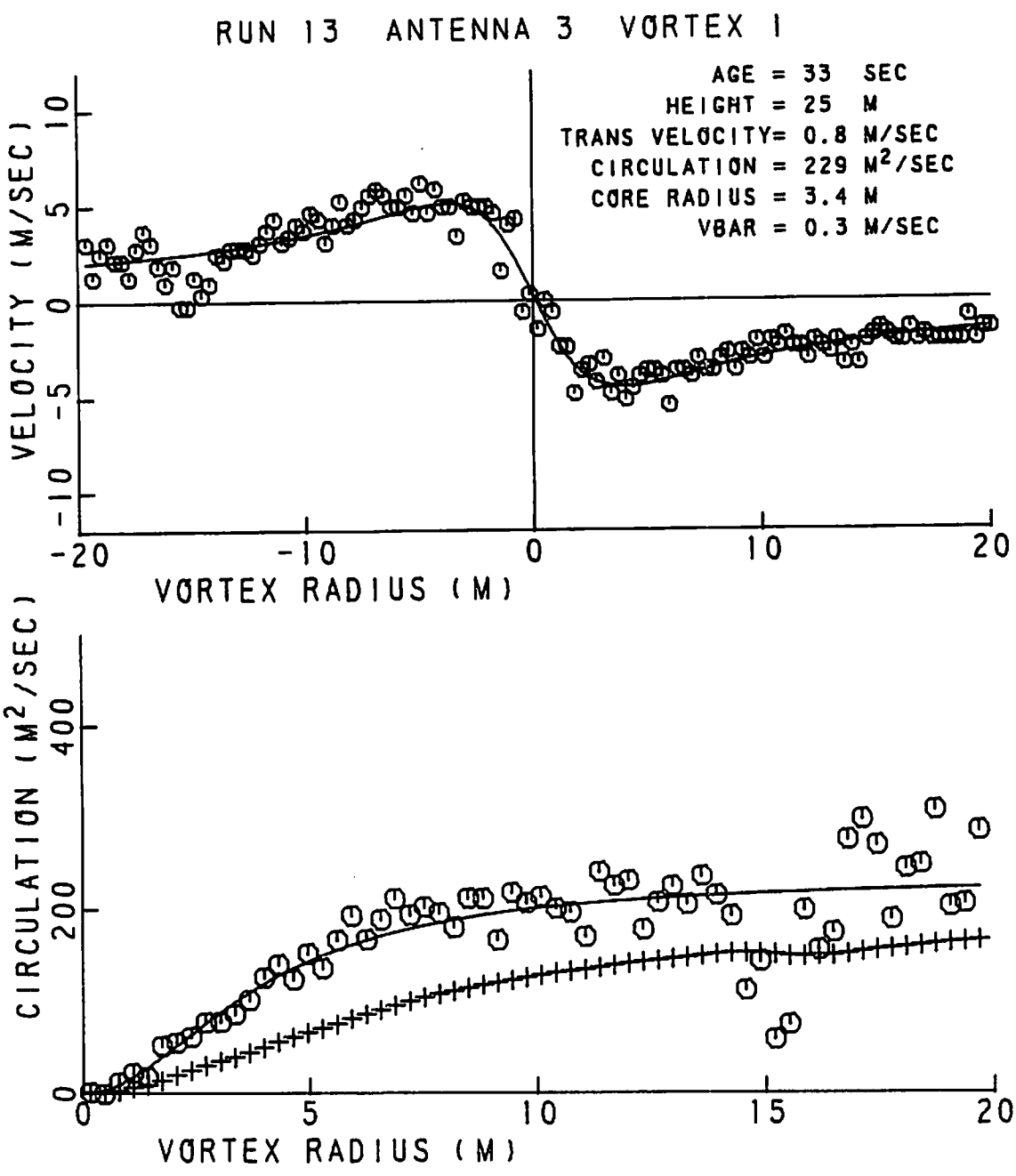

FIGURE 245. VELOCITY AND CIRCULATION PROFILES FOR RUN 13, ANTENNA 3

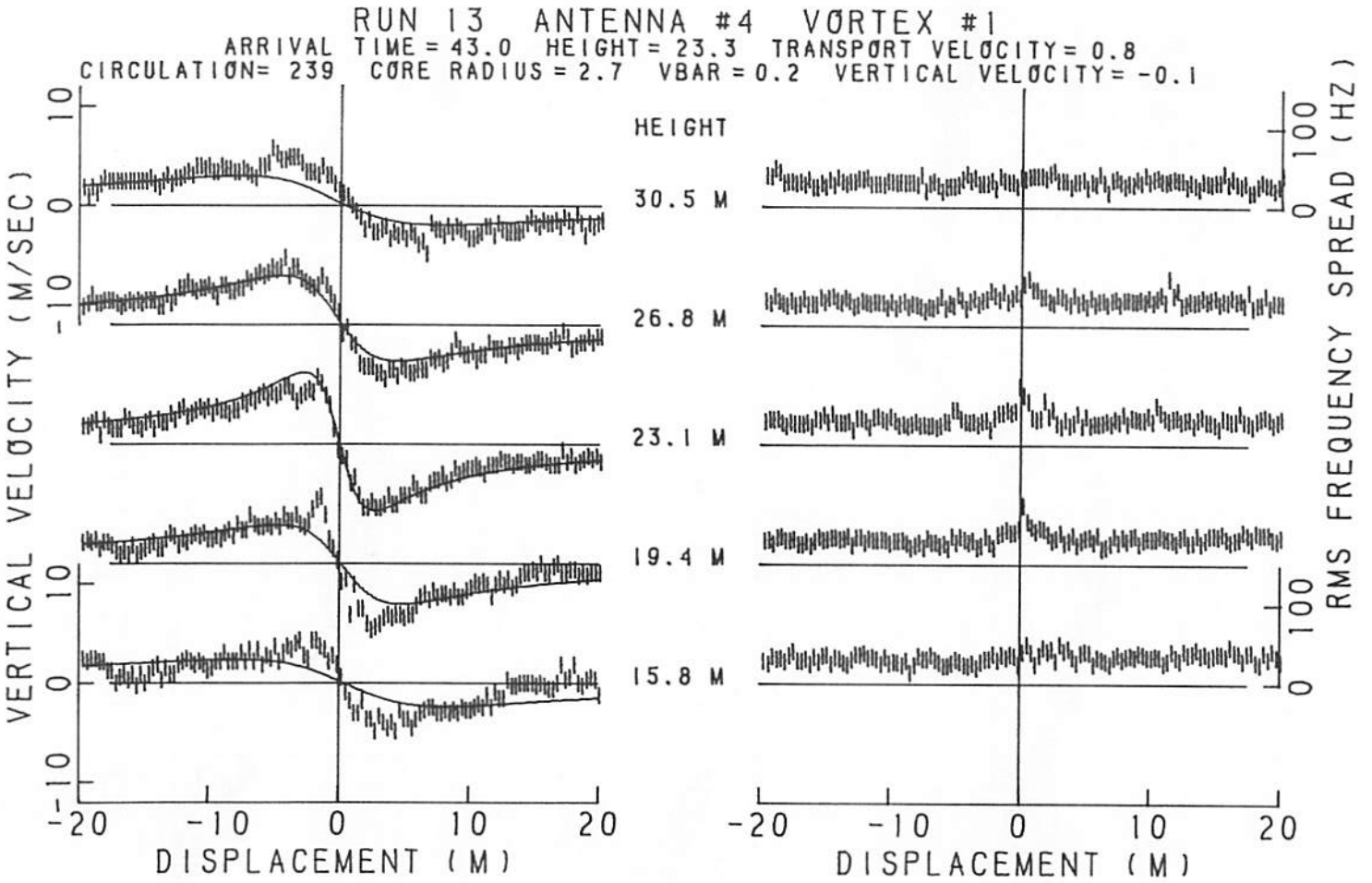

FIGURE 246. VELOCITY AND SPECTRAL WIDTH PROFILES FOR RUN 13, ANTENNA 4

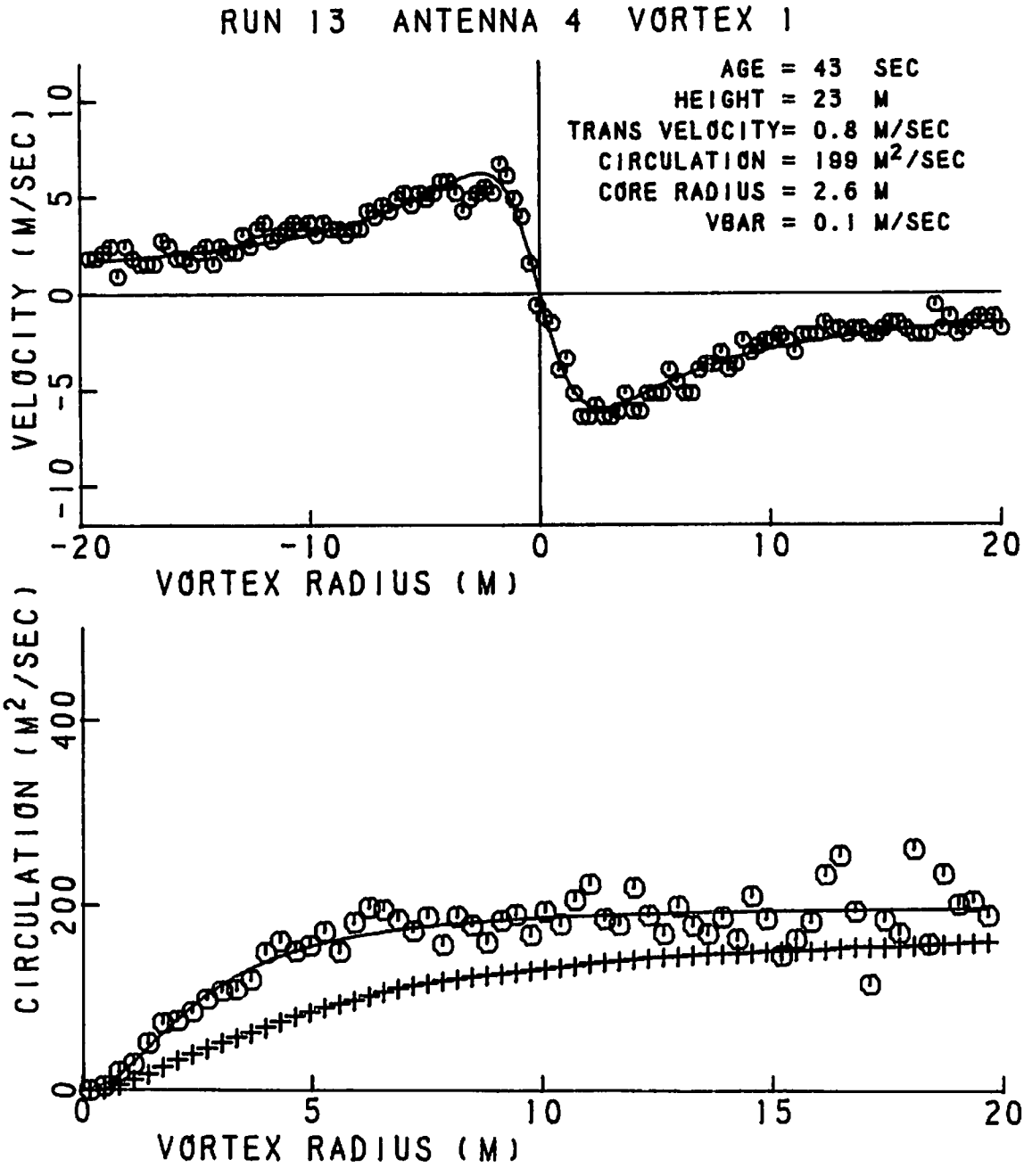

FIGURE 247. VELOCITY AND CIRCULATION PROFILES FOR RUN 13, ANTENNA 4

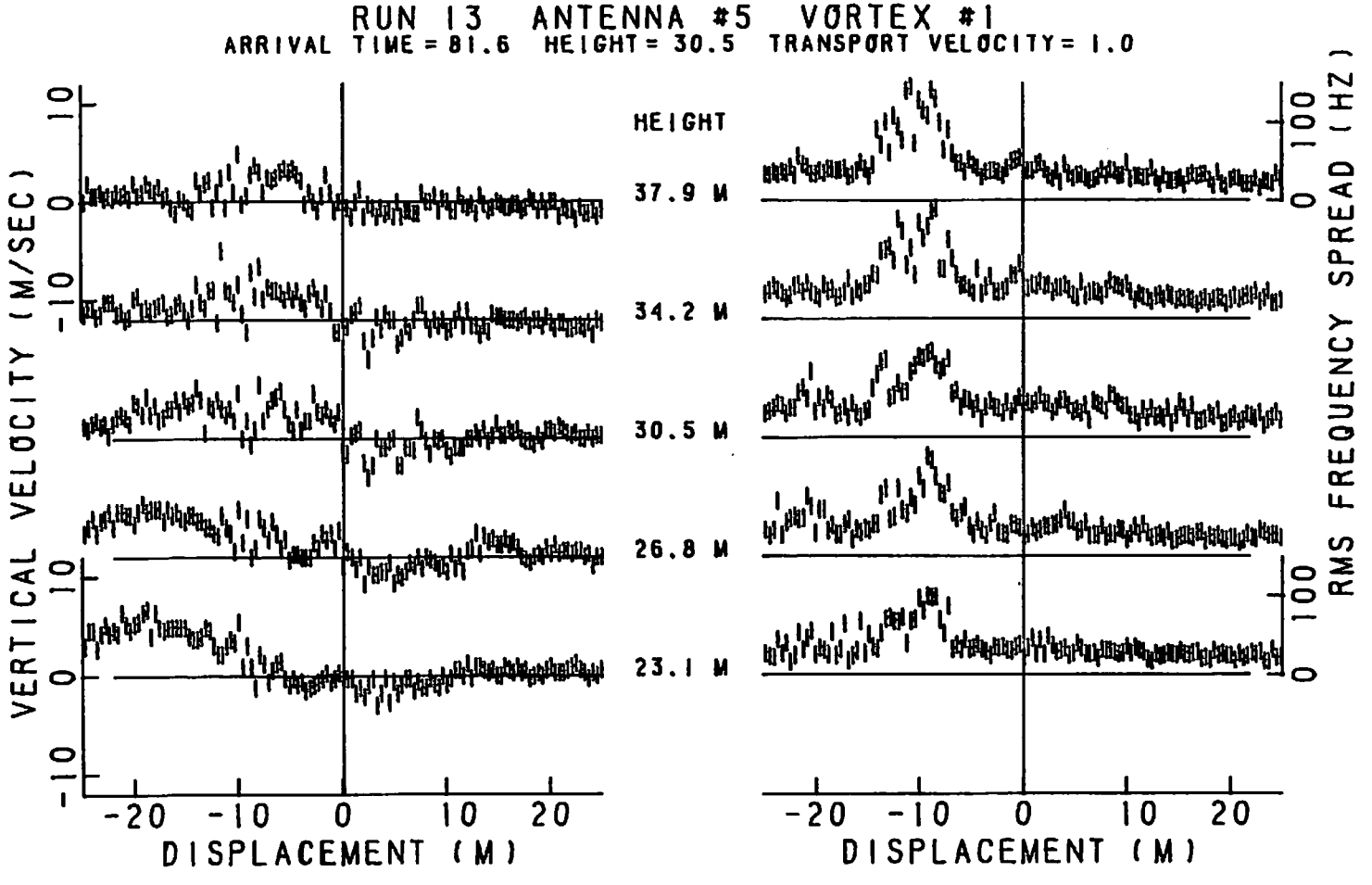

FIGURE 248. VELOCITY AND SPECTRAL WIDTH PROFILES FOR RUN 13, ANTENNA 5

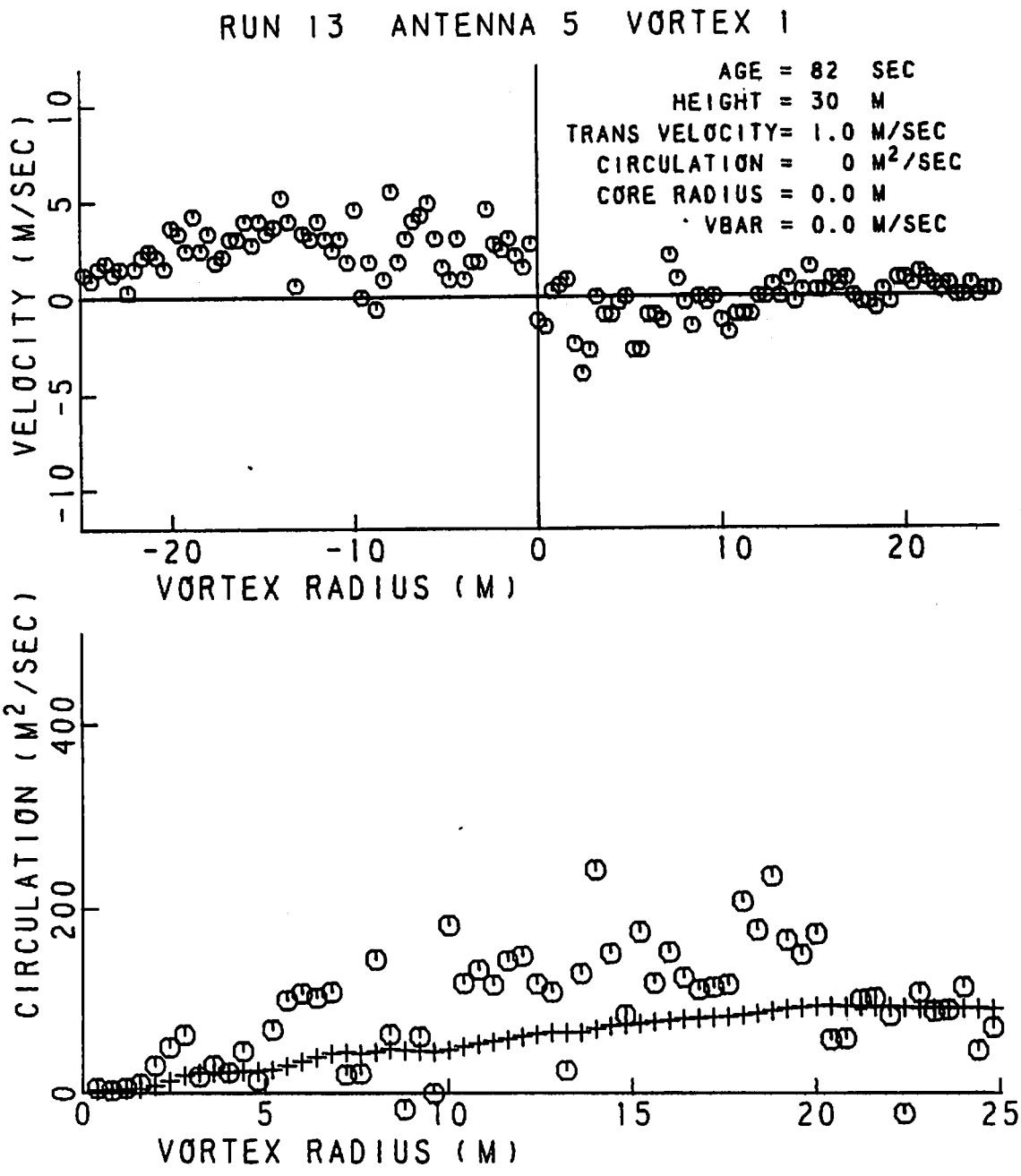

FIGURE 249. VELOCITY AND CIRCULATION PROFILES FOR RUN 13, ANTENNA 5

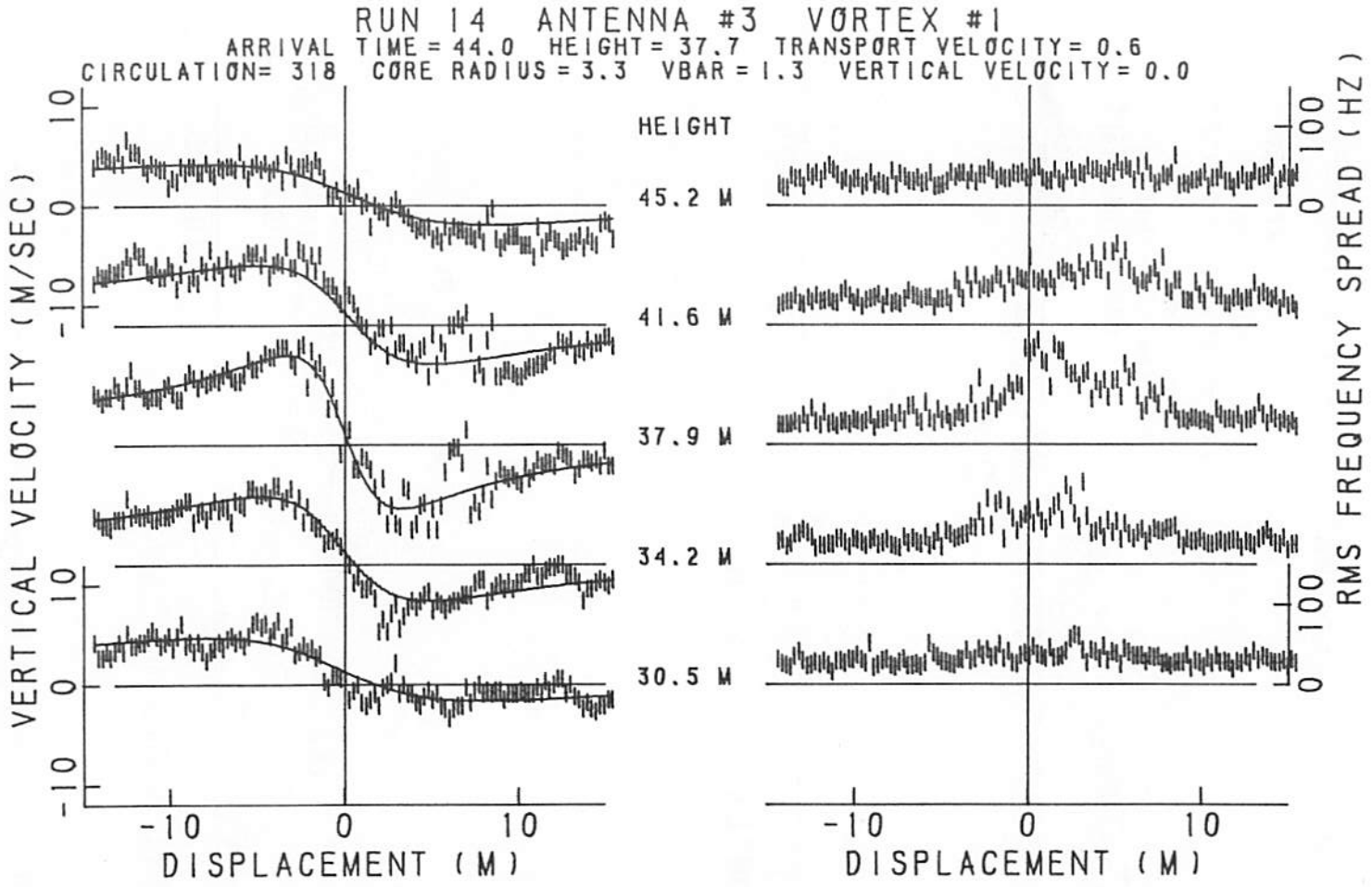

FIGURE 250. VELOCITY AND SPECTRAL WIDTH PROFILES FOR RUN 14, ANTENNA 3

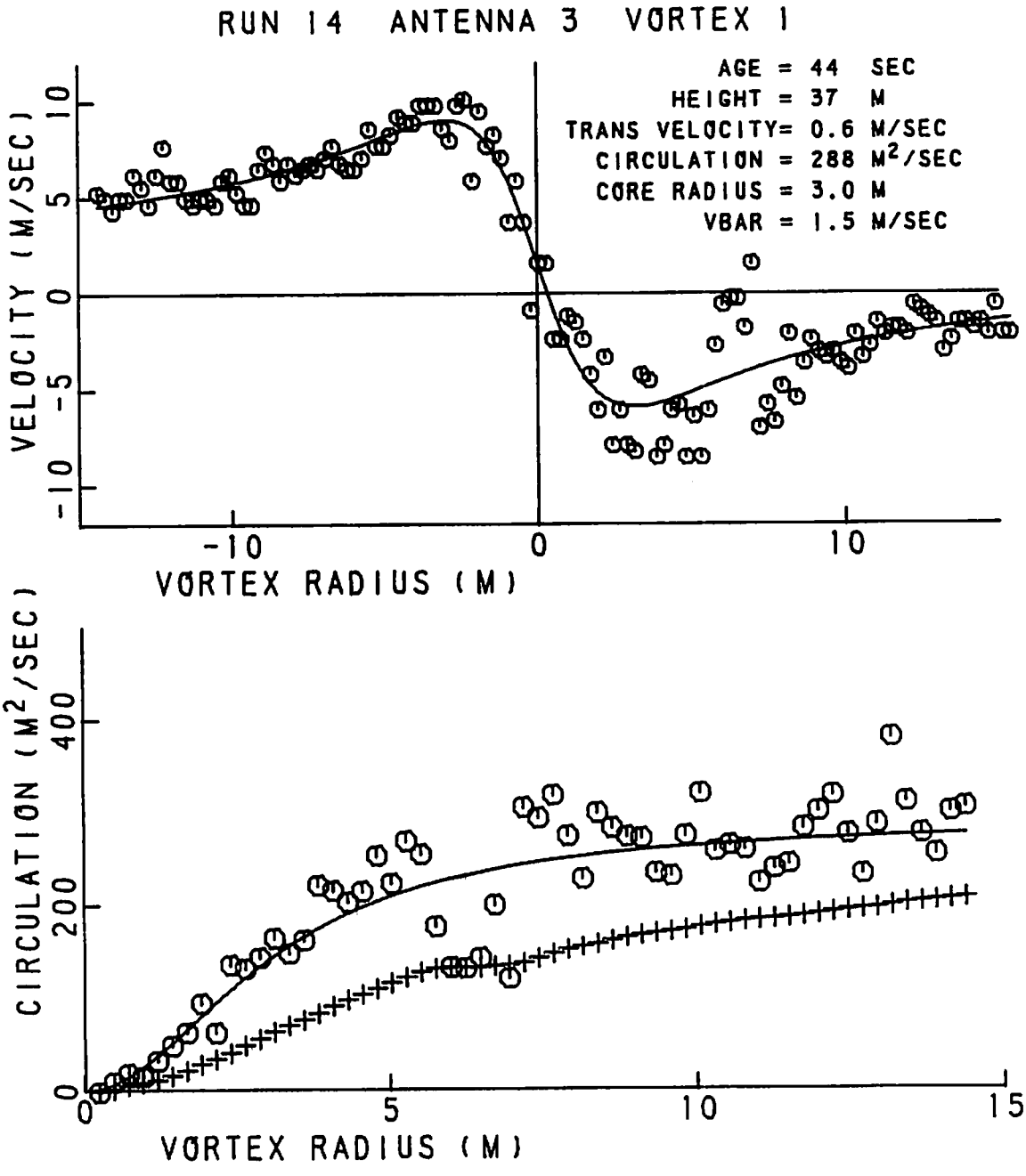

FIGURE 251. VELOCITY AND CIRCULATION PROFILES FOR RUN 14, ANTENNA 3

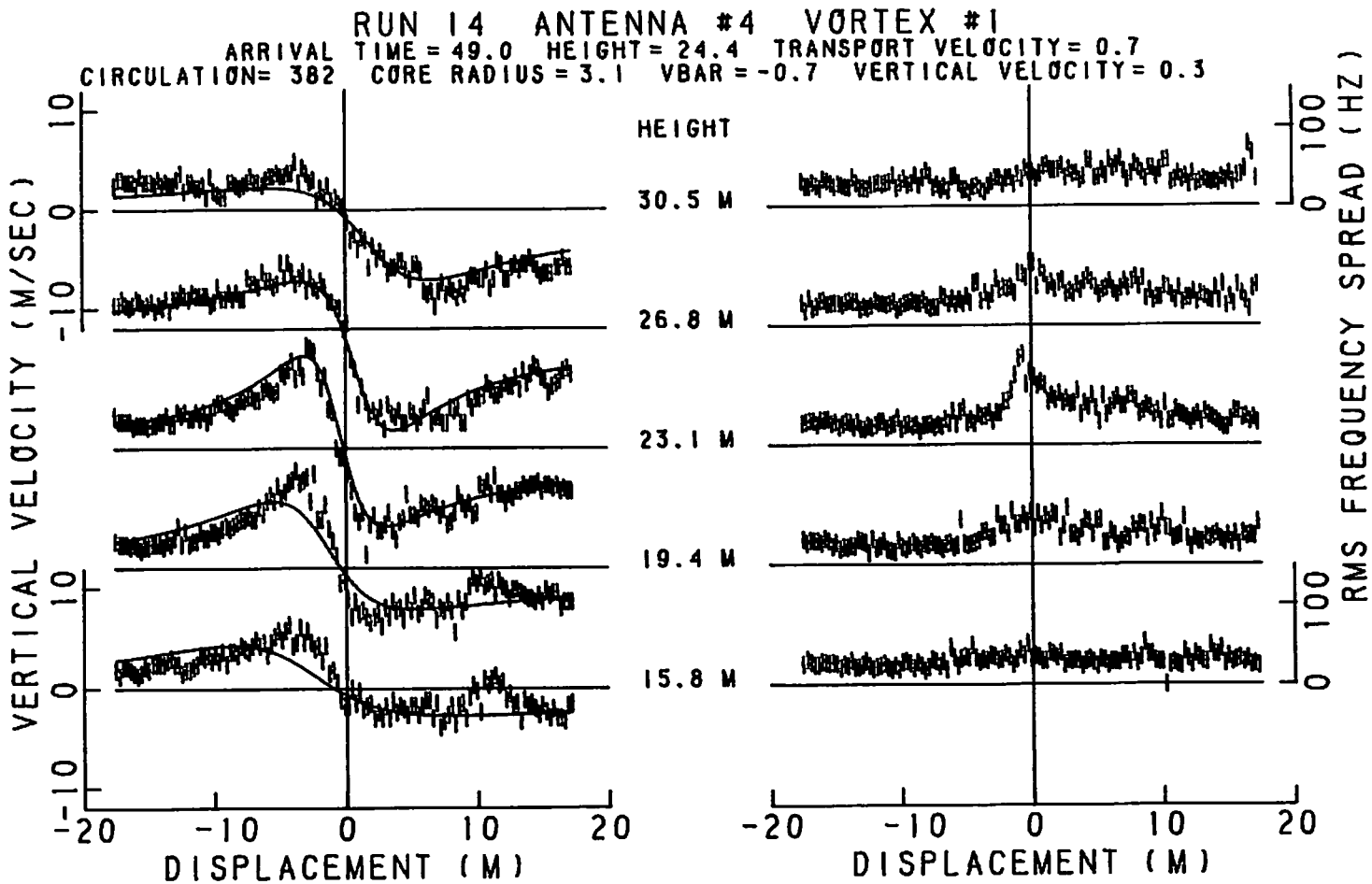

FIGURE 252. VELOCITY AND SPECTRAL WIDTH PROFILES FOR RUN 14, ANTENNA 4

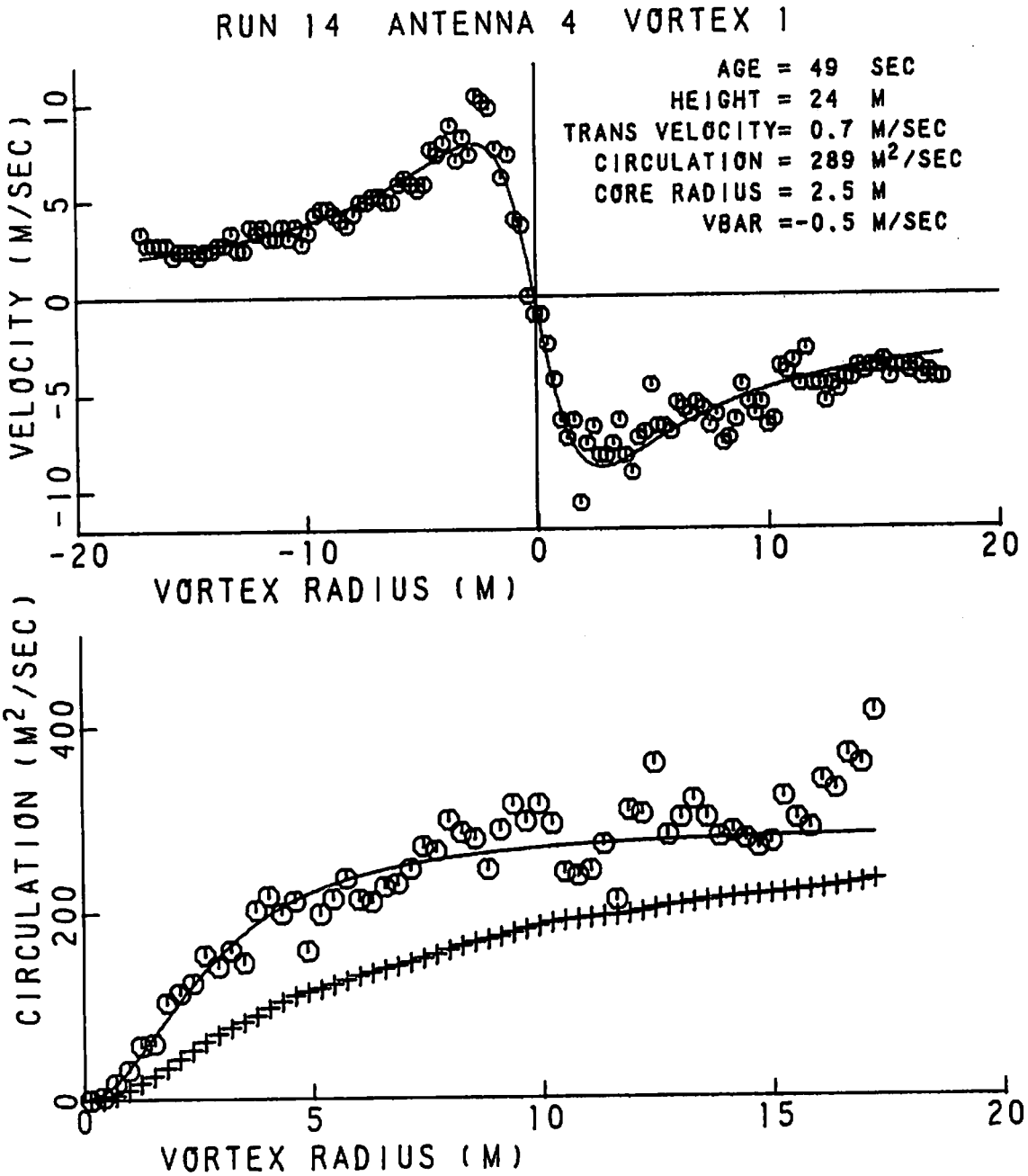

FIGURE 253. VELOCITY AND CIRCULATION PROFILES FOR RUN 14, ANTENNA 4

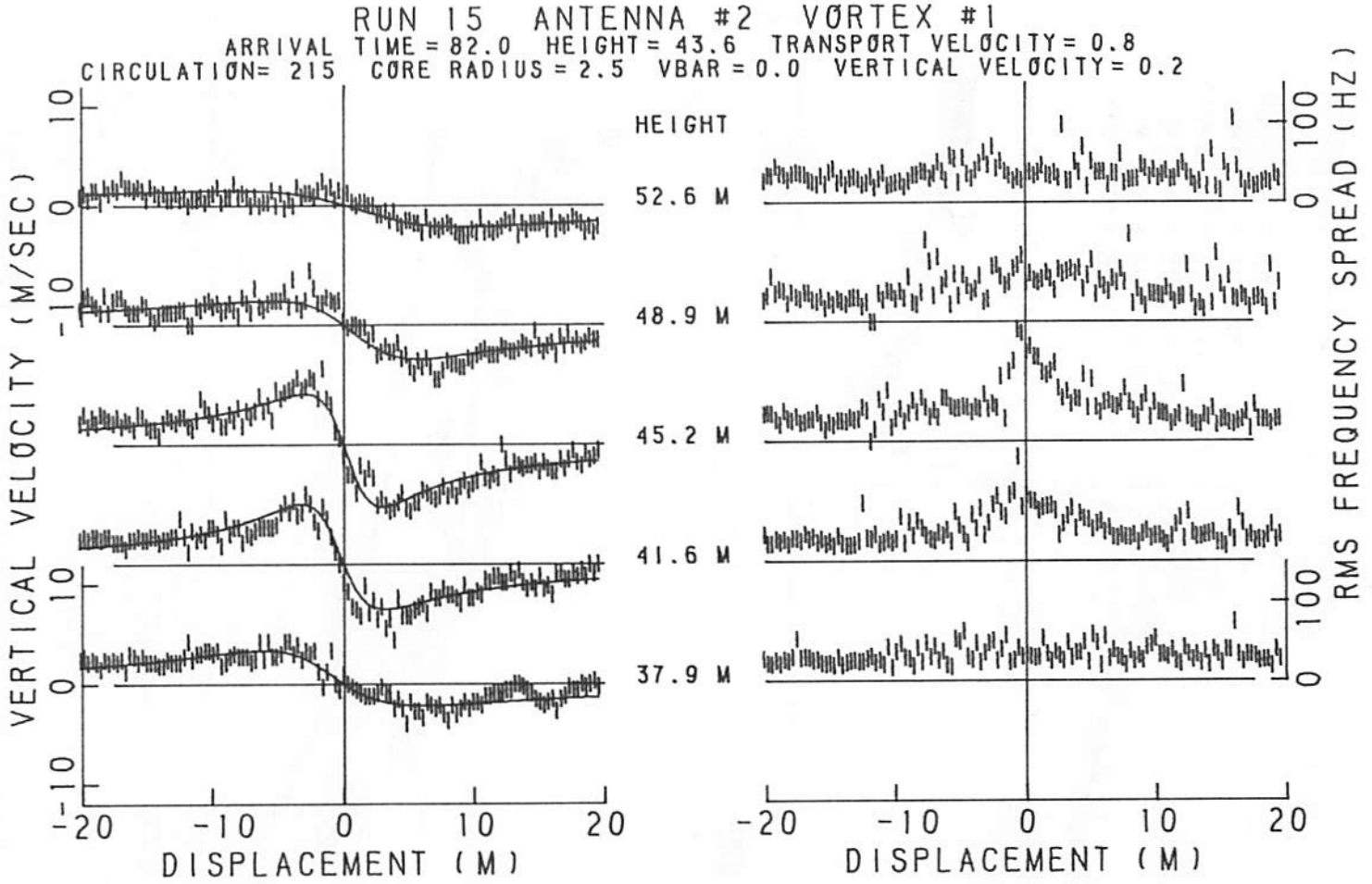

FIGURE 254. VELOCITY AND SPECTRAL WIDTH PROFILES FOR RUN 15, ANTENNA 2

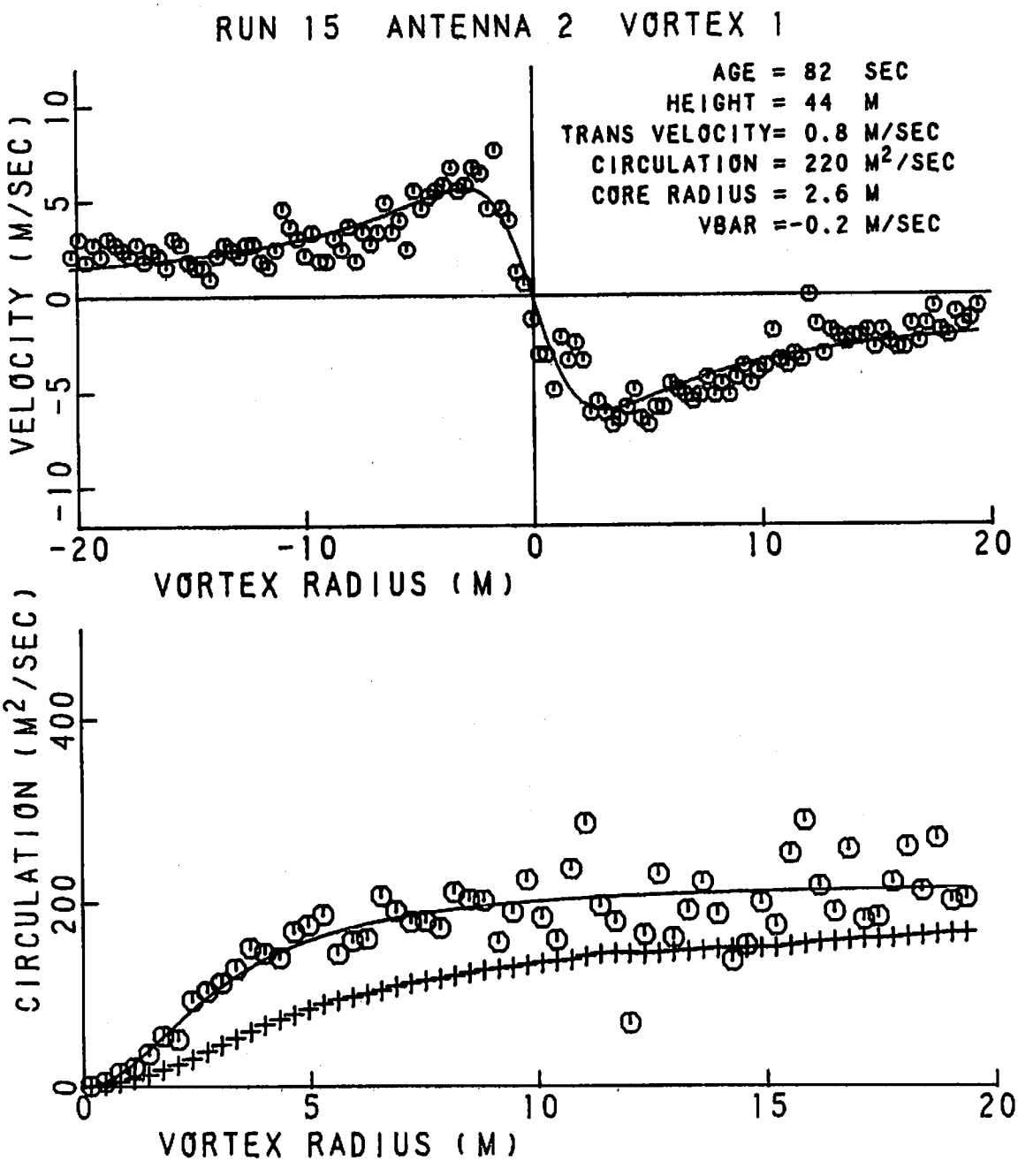

FIGURE 255. VELOCITY AND CIRCULATION PROFILES FOR RUN 15, ANTENNA 2

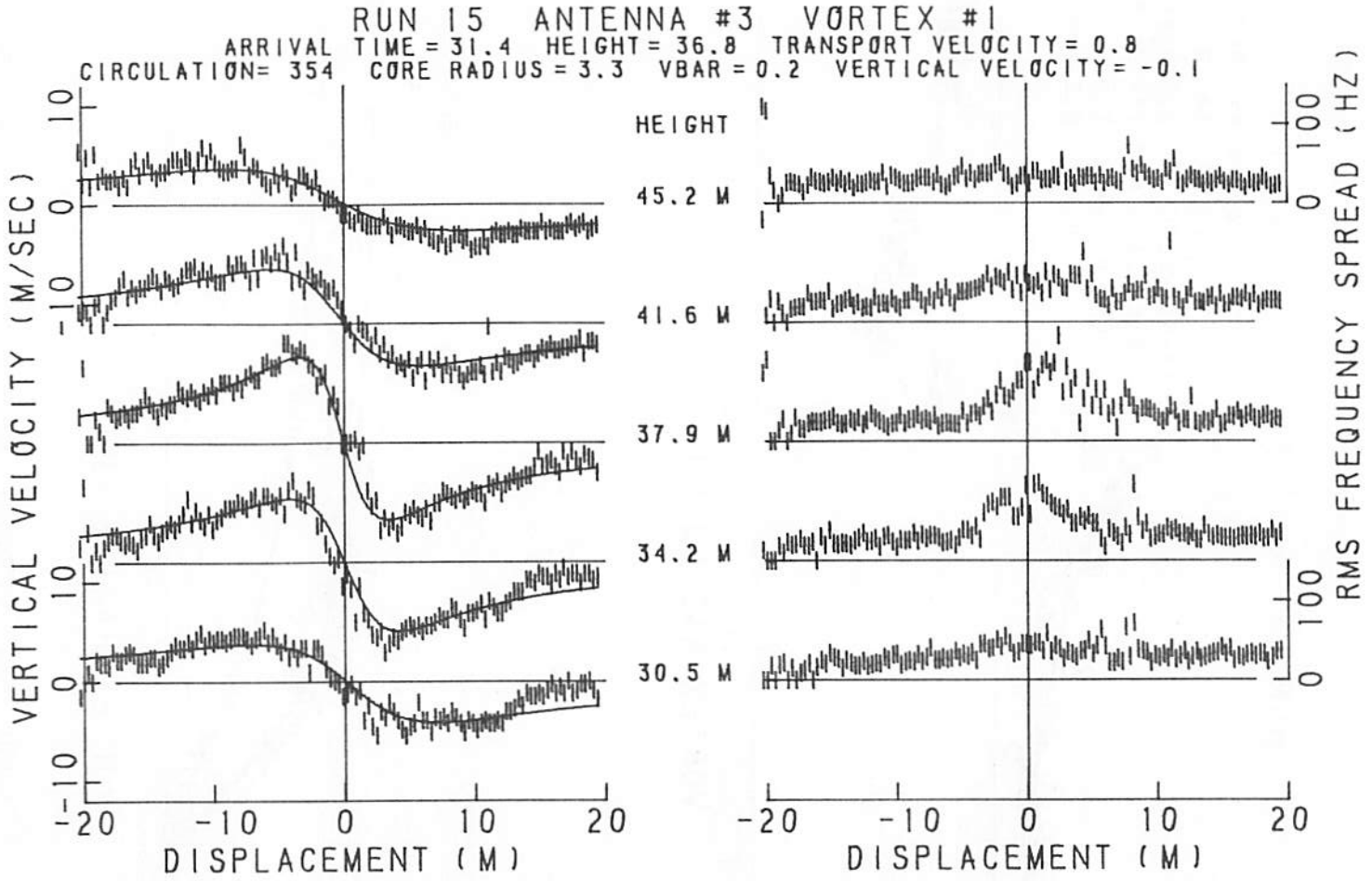

FIGURE 256. VELOCITY AND SPECTRAL WIDTH PROFILES FOR RUN 15, ANTENNA 3.

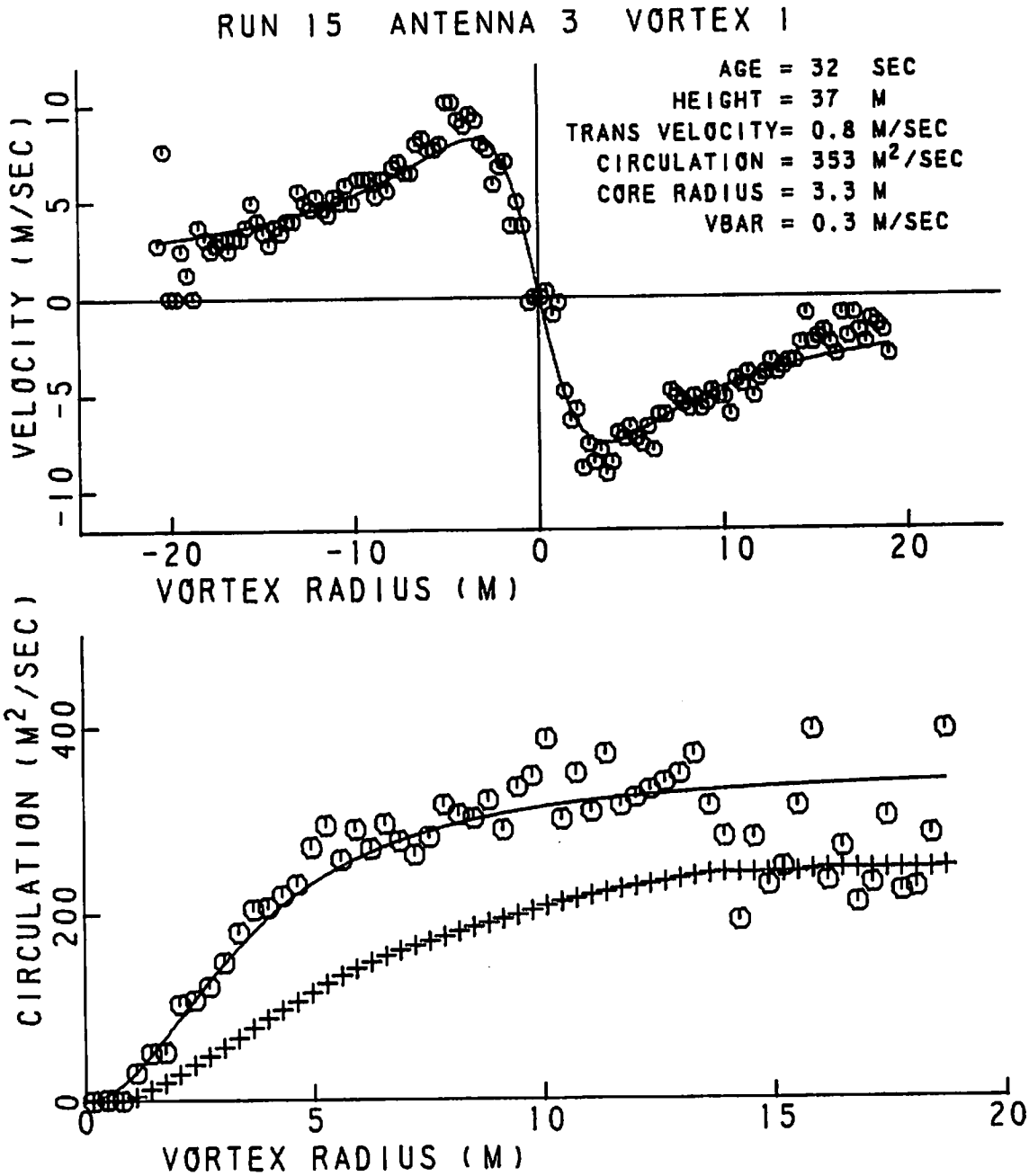

FIGURE 257. VELOCITY AND CIRCULATION PROFILES FOR RUN 15, ANTENNA 3

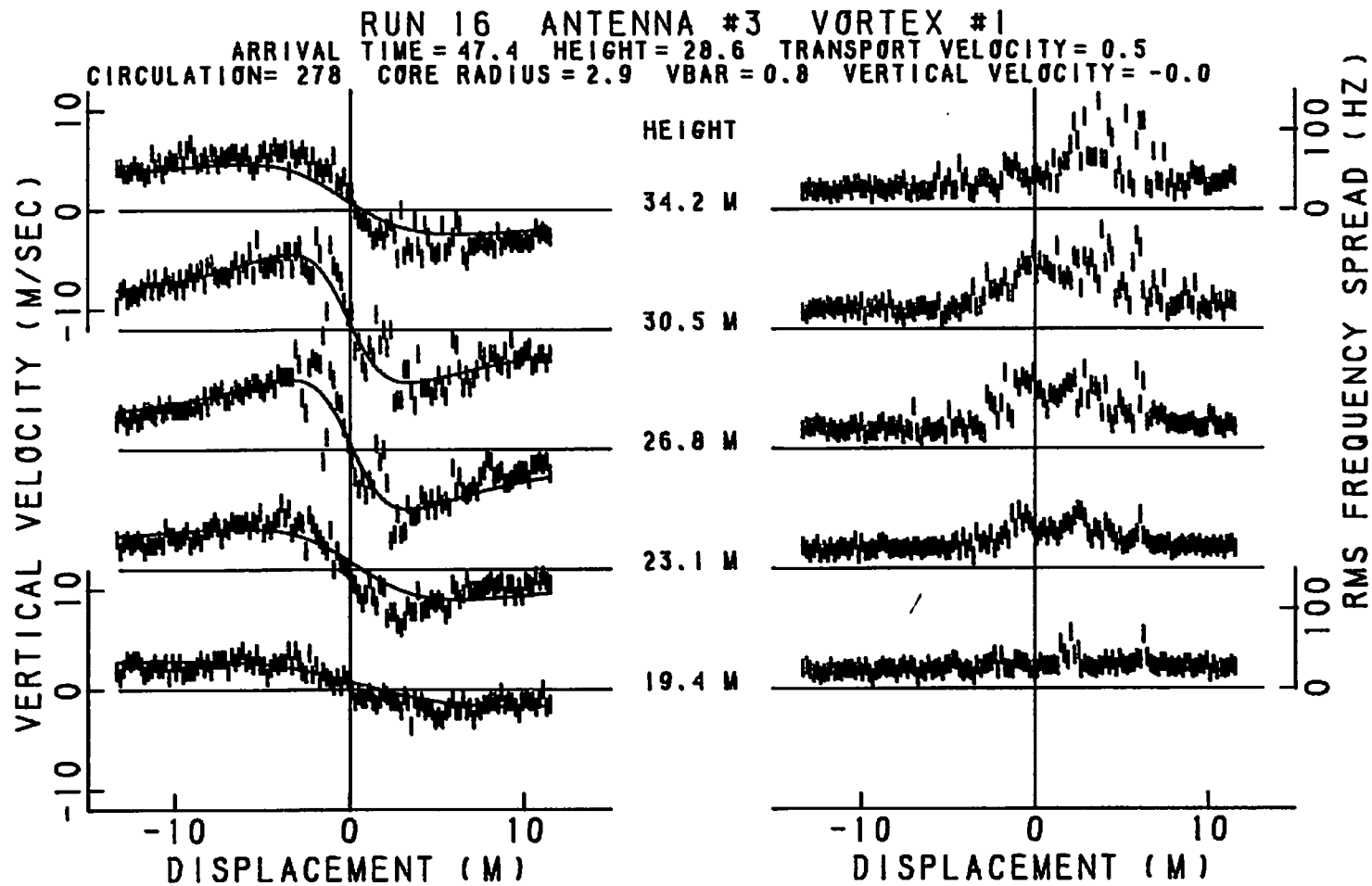

FIGURE 258. VELOCITY AND SPECTRAL WIDTH PROFILES FOR RUN 16, ANTENNA 3

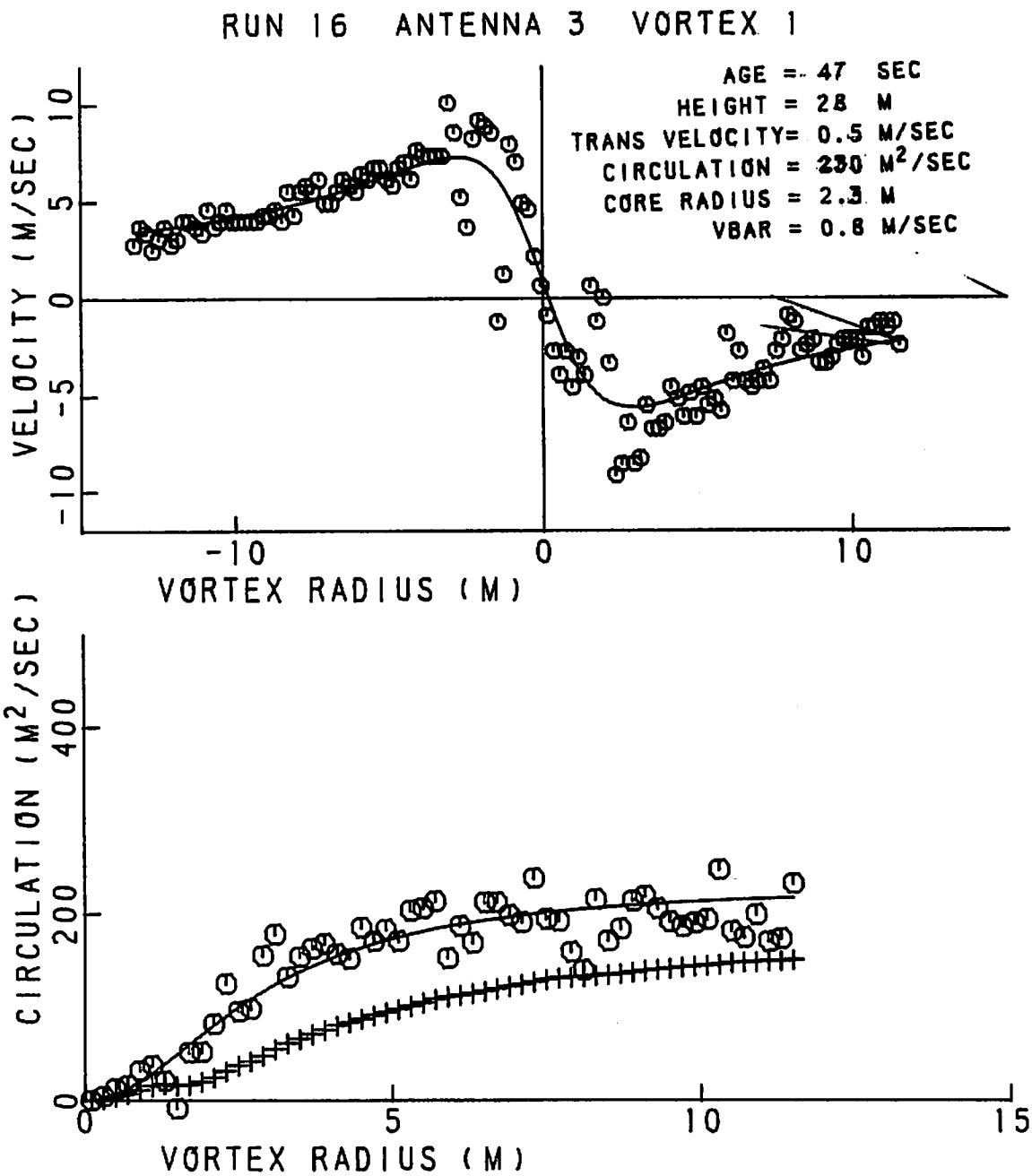

FIGURE 259. VELOCITY AND CIRCULATION PROFILES FOR RUN 16, ANTENNA 3

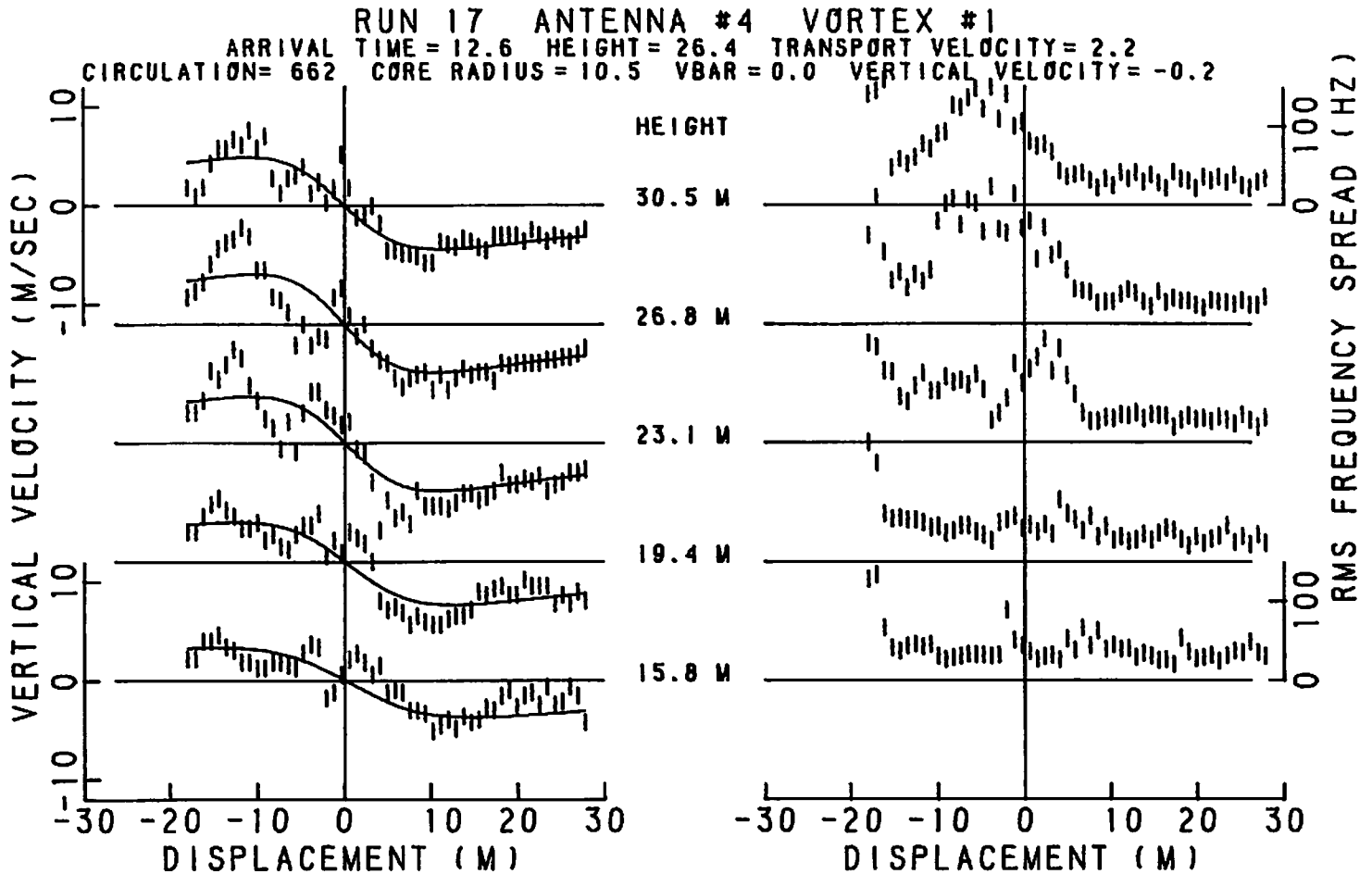

FIGURE 260. VELOCITY AND SPECTRAL WIDTH PROFILES FOR RUN 17, ANTENNA 4

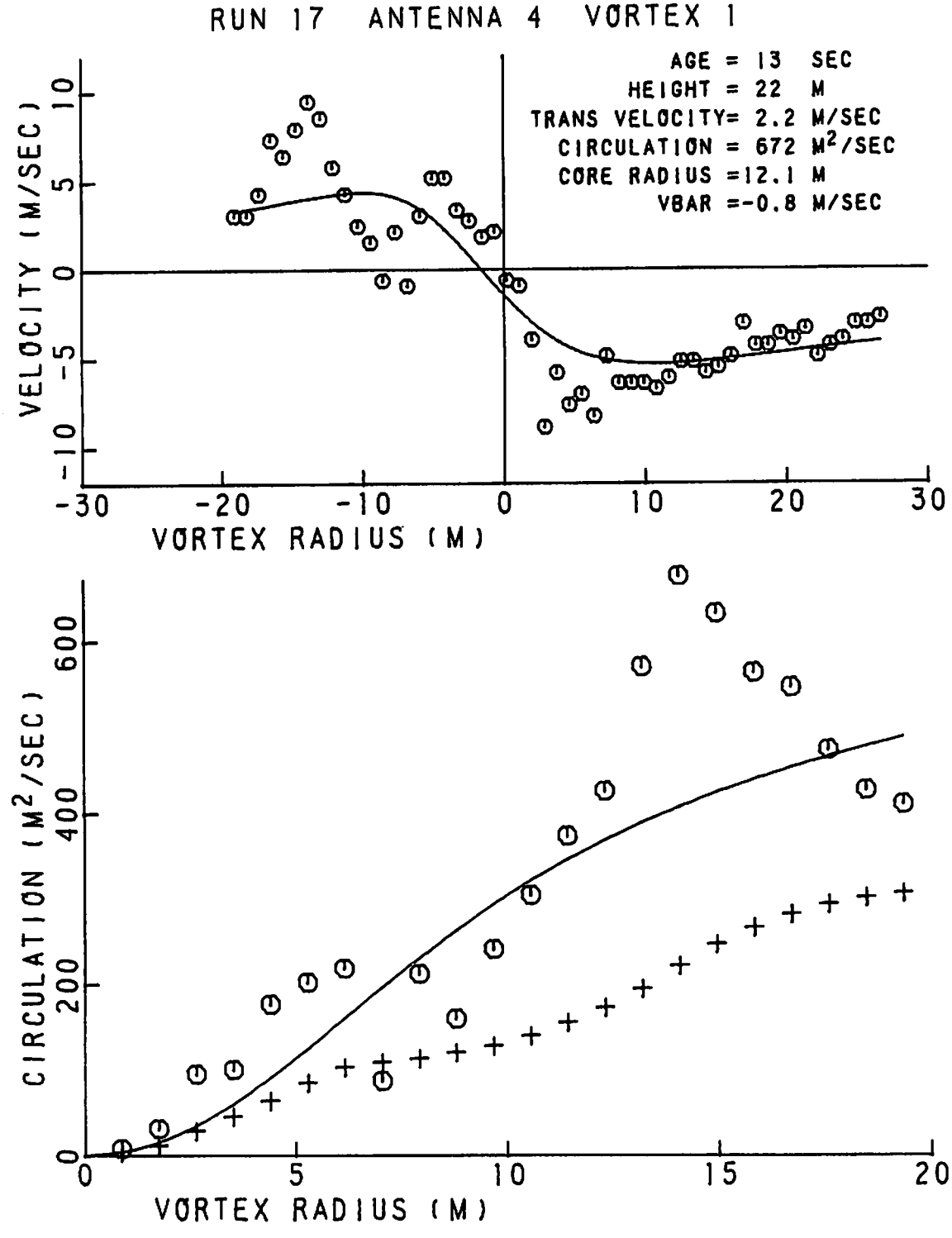

FIGURE 261. VELOCITY AND CIRCULATION PROFILES FOR RUN 17, ANTENNA 4

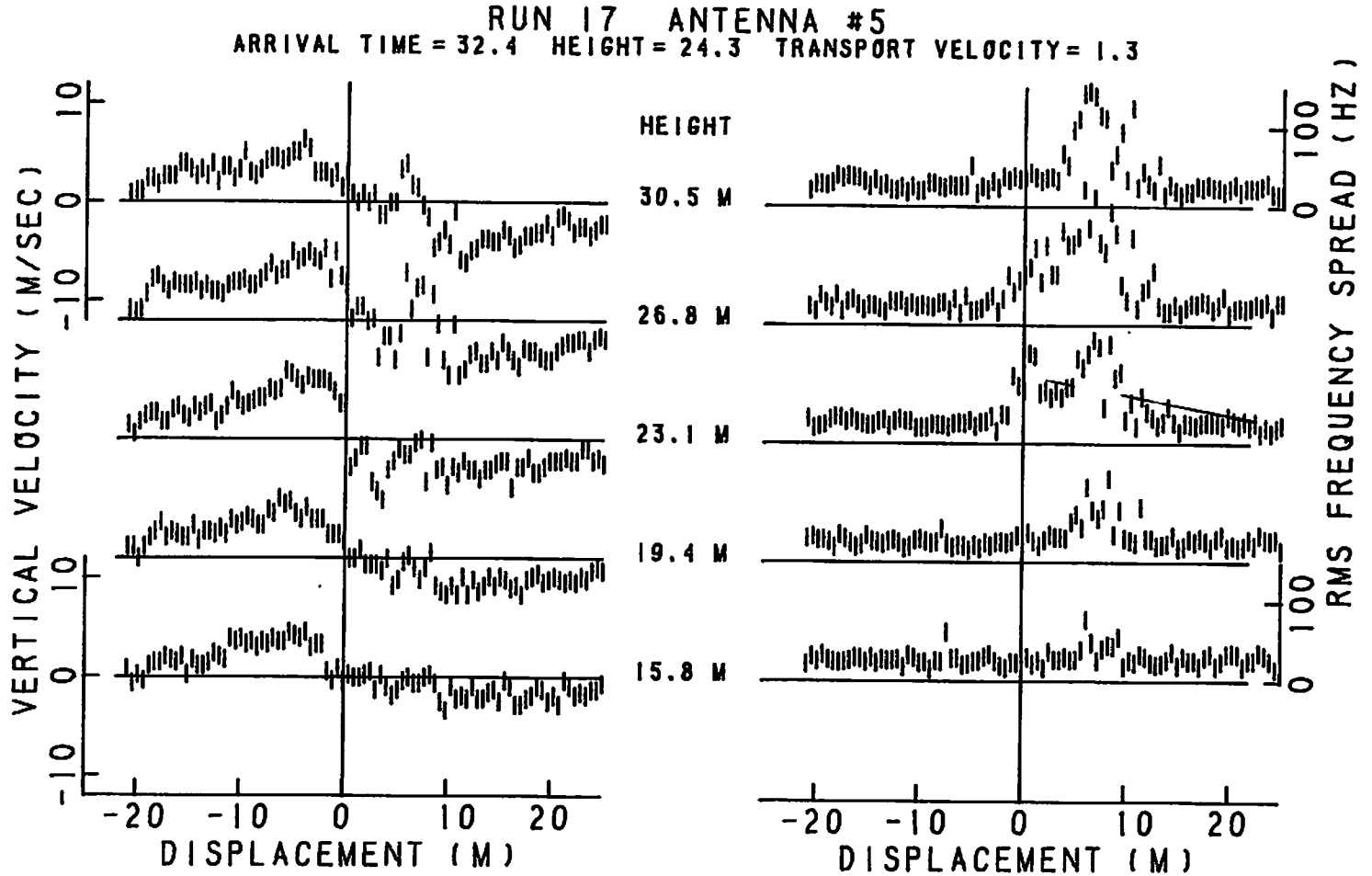

FIGURE 262. VELOCITY AND SPECTRAL WIDTH PROFILES FOR RUN 17, ANTENNA 5

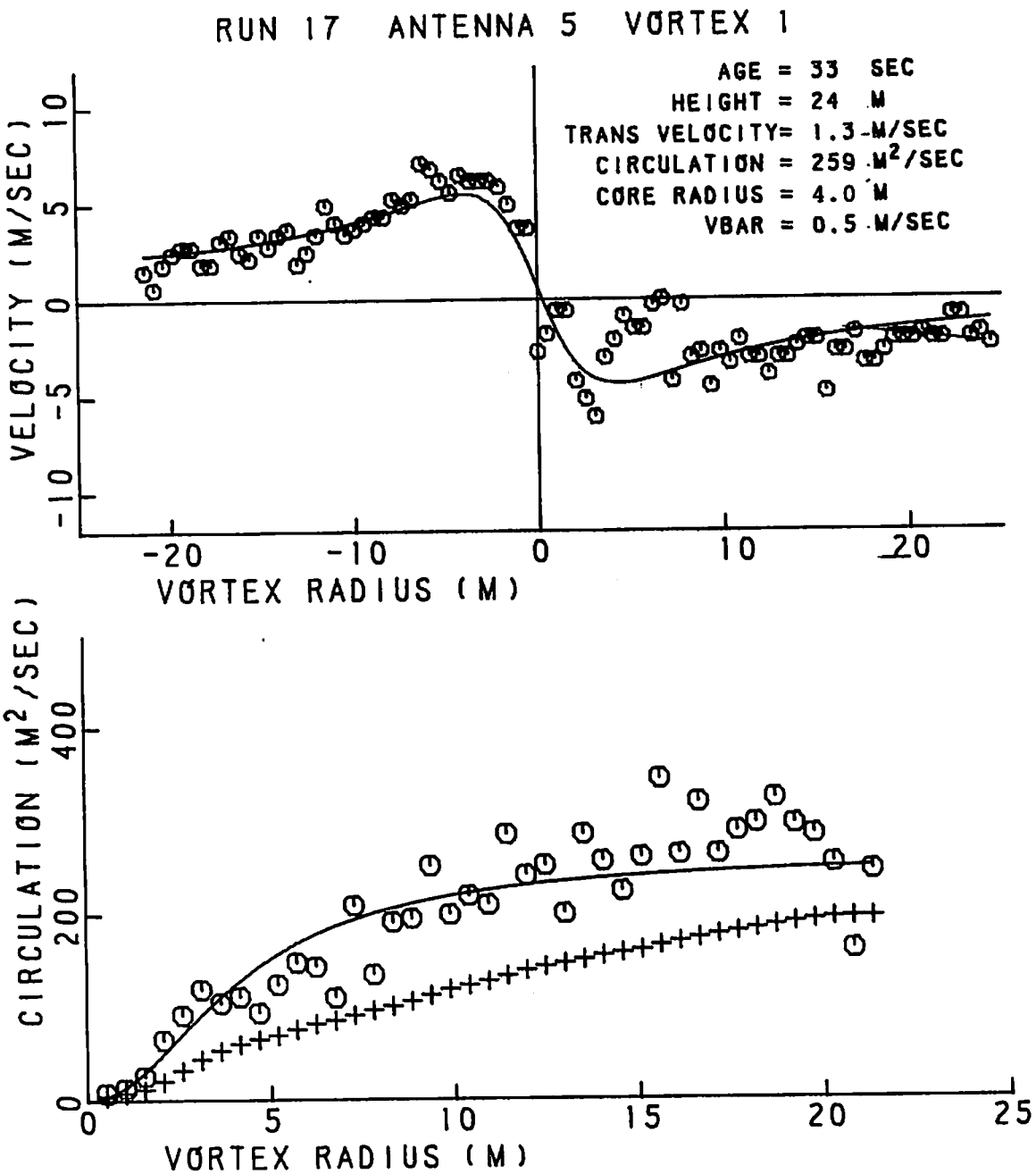

FIGURE 263. VELOCITY AND CIRCULATION PROFILES FOR RUN 17, ANTENNA 5

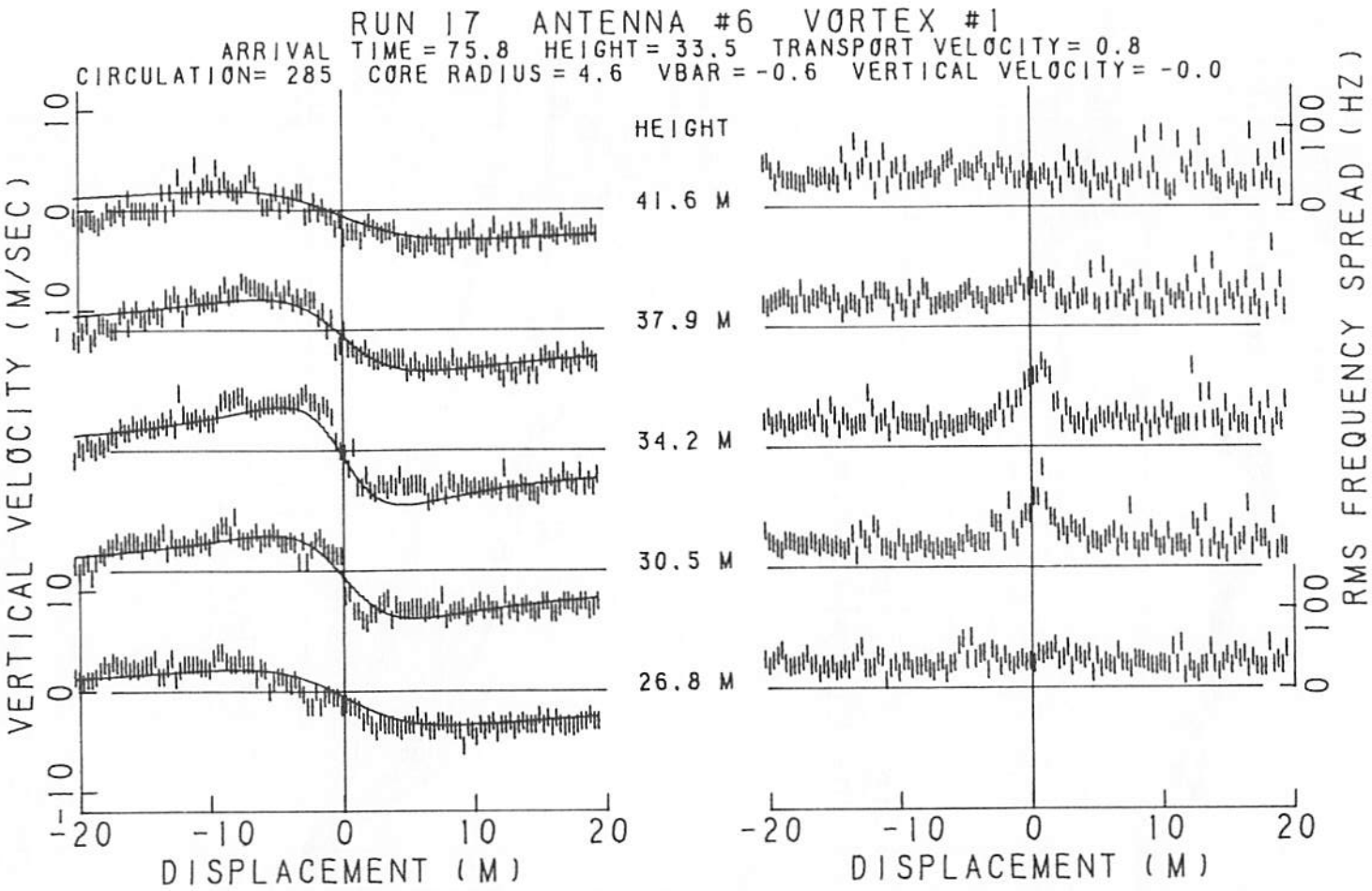

FIGURE 264. VELOCITY AND SPECTRAL WIDTH PROFILES FOR RUN 17, ANTENNA 6

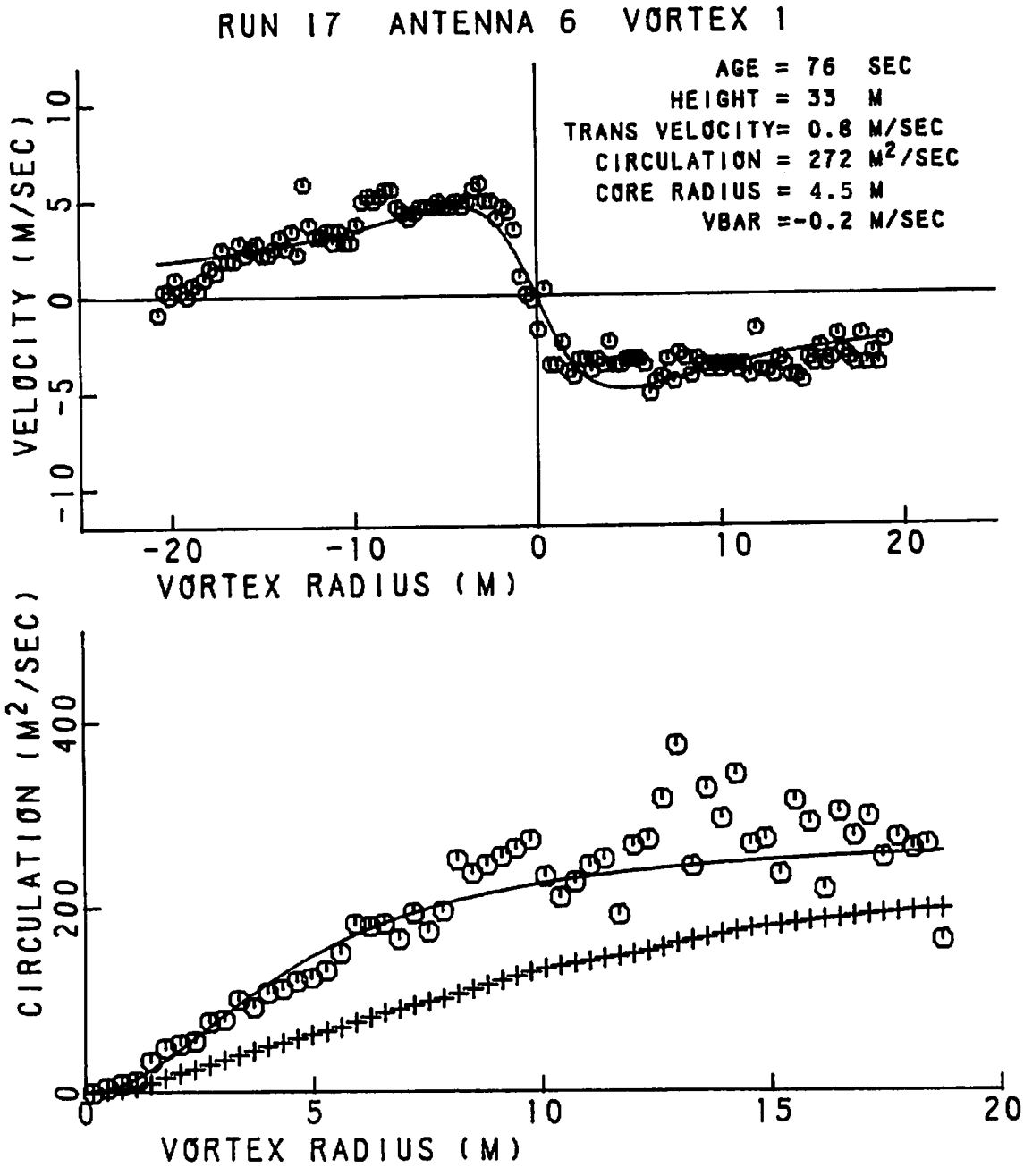

FIGURE 265. VELOCITY AND CIRCULATION PROFILES FOR RUN 17, ANTENNA 6

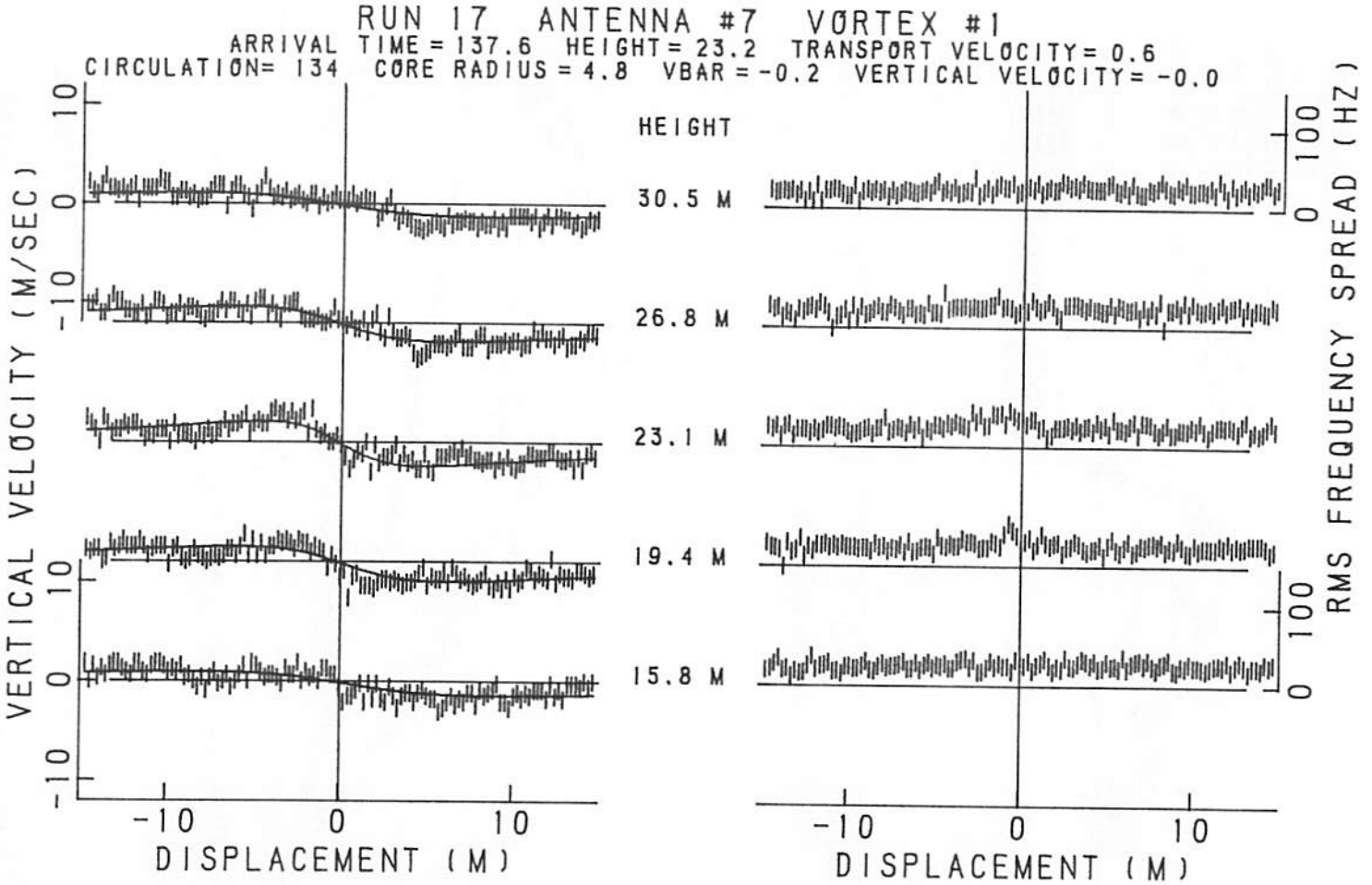

FIGURE 266. VELOCITY AND SPECTRAL WIDTH PROFILES FOR RUN 17, ANTENNA 7

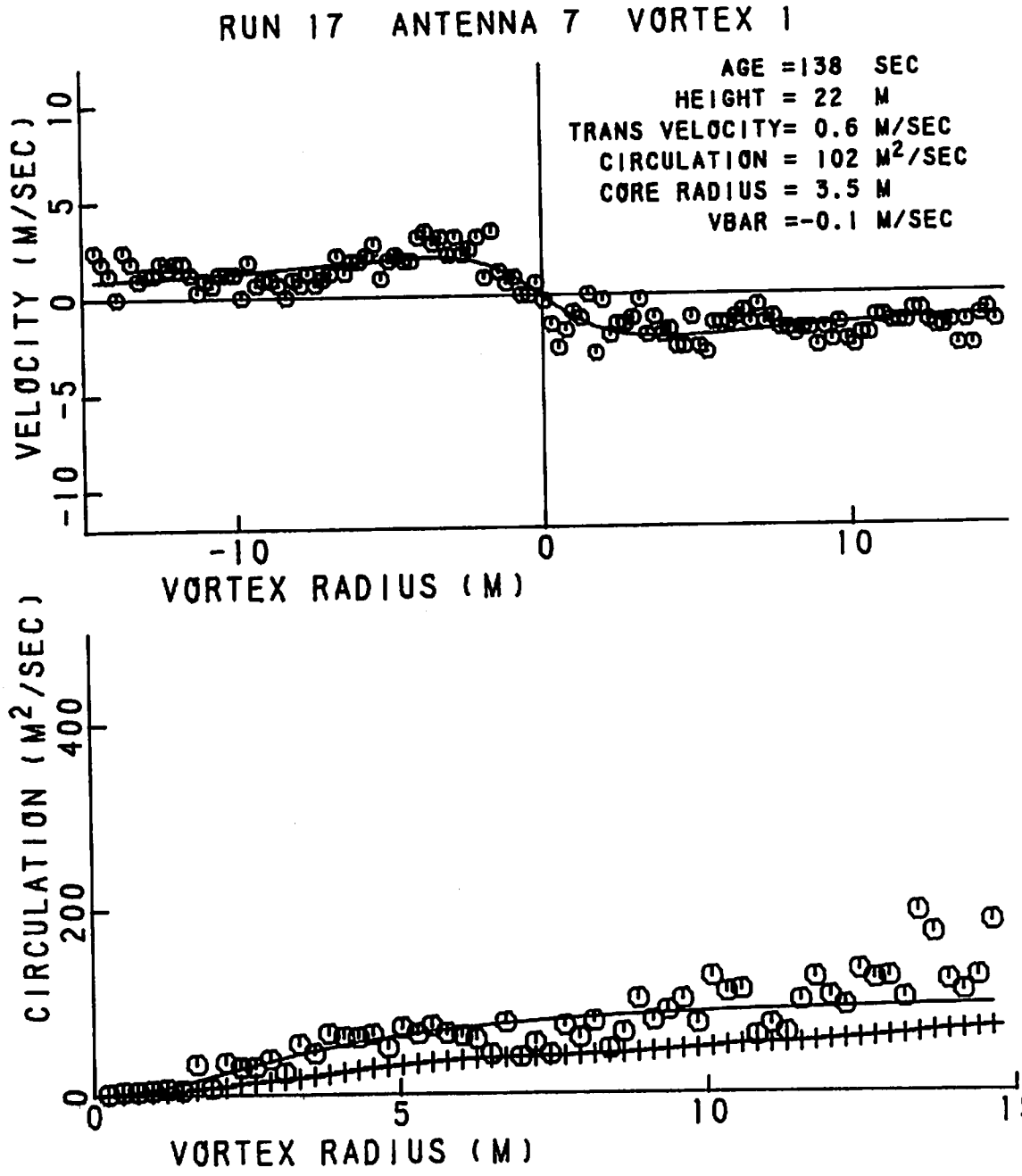

FIGURE 267. VELOCITY AND CIRCULATION PROFILES FOR RUN 17, ANTENNA 7

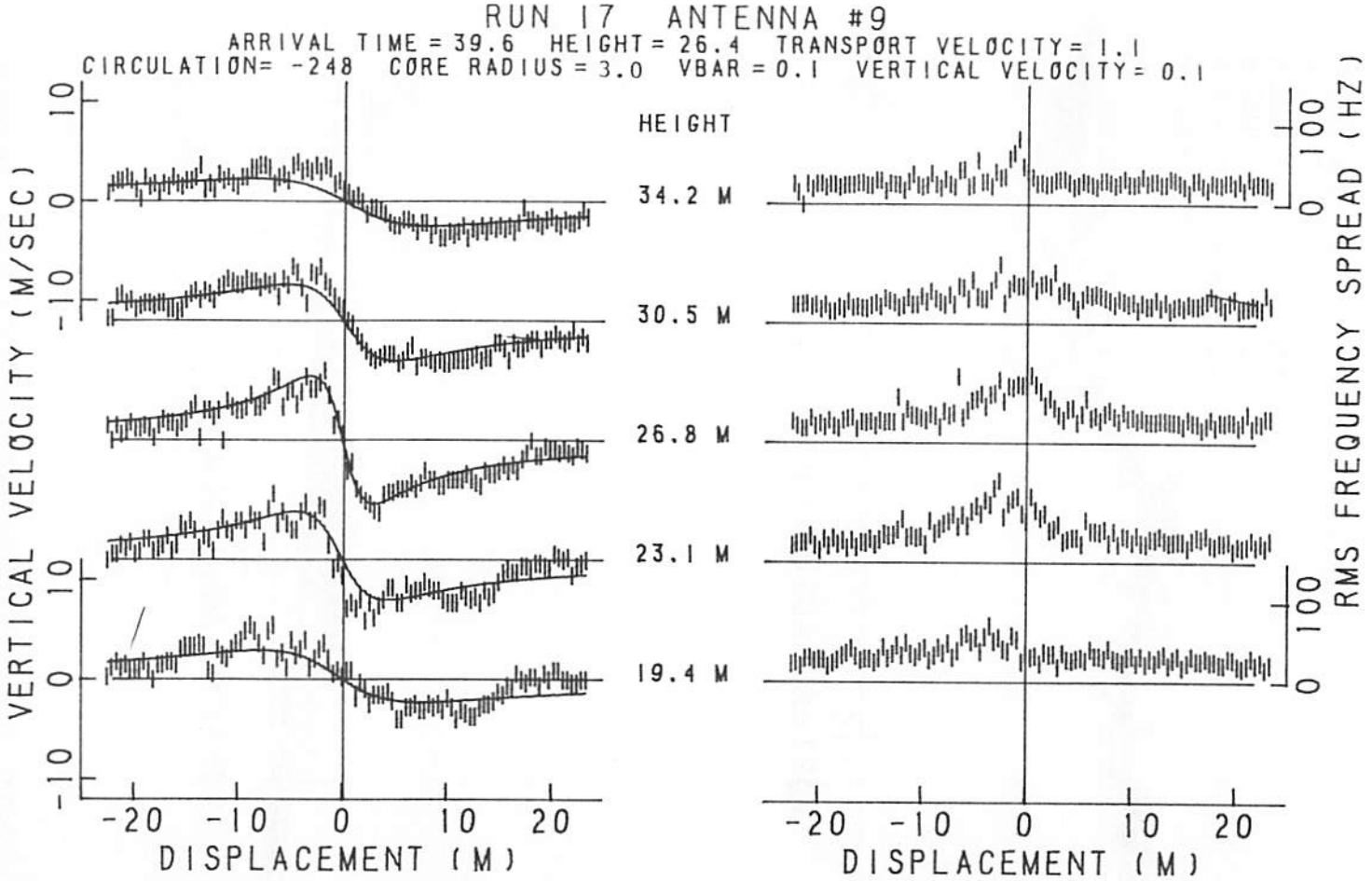

FIGURE 268. VELOCITY AND SPECTRAL WIDTH PROFILES FOR RUN 17, ANTENNA 9

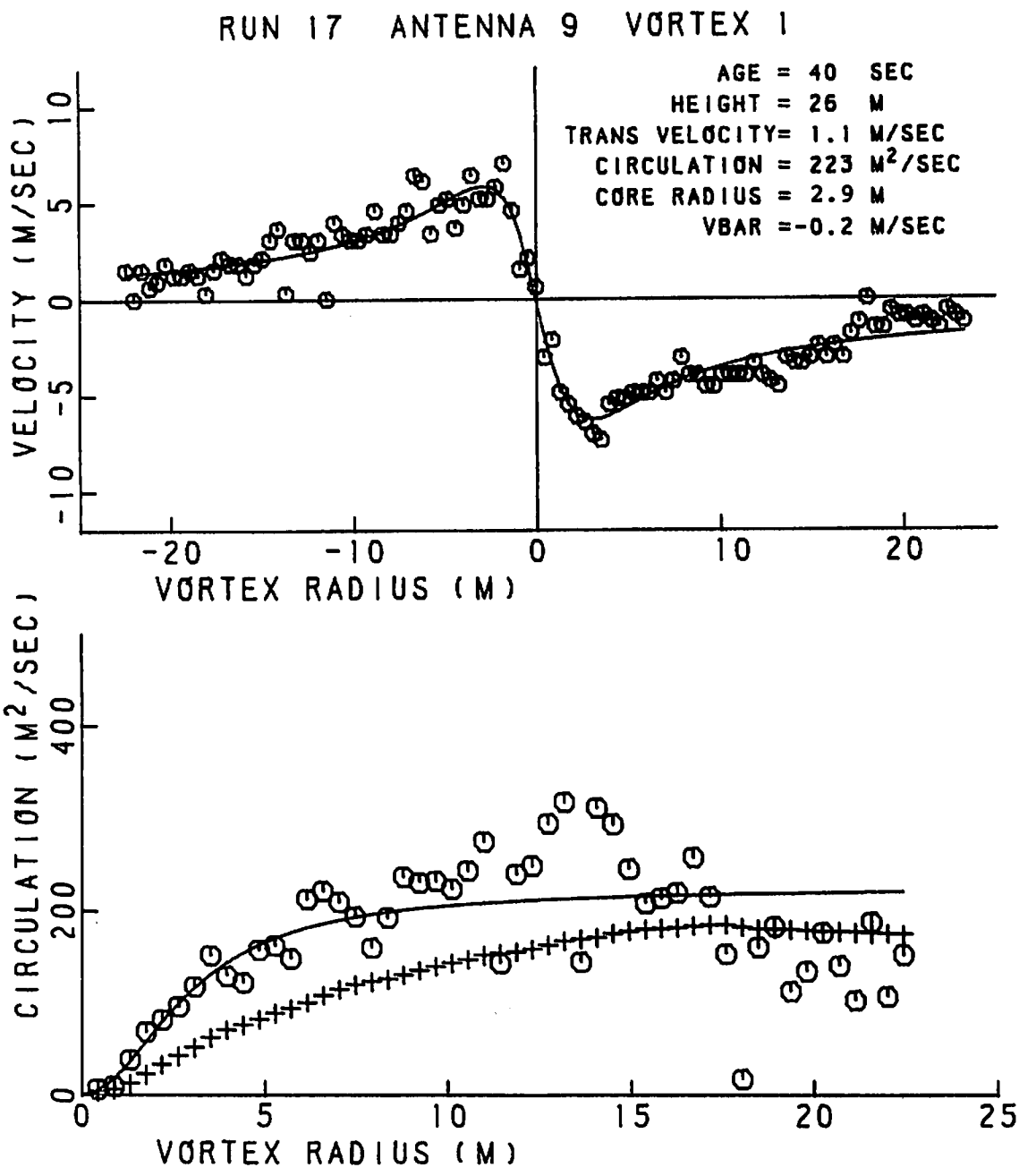

FIGURE 269. VELOCITY AND CIRCULATION PROFILES FOR RUN 17, ANTENNA 9

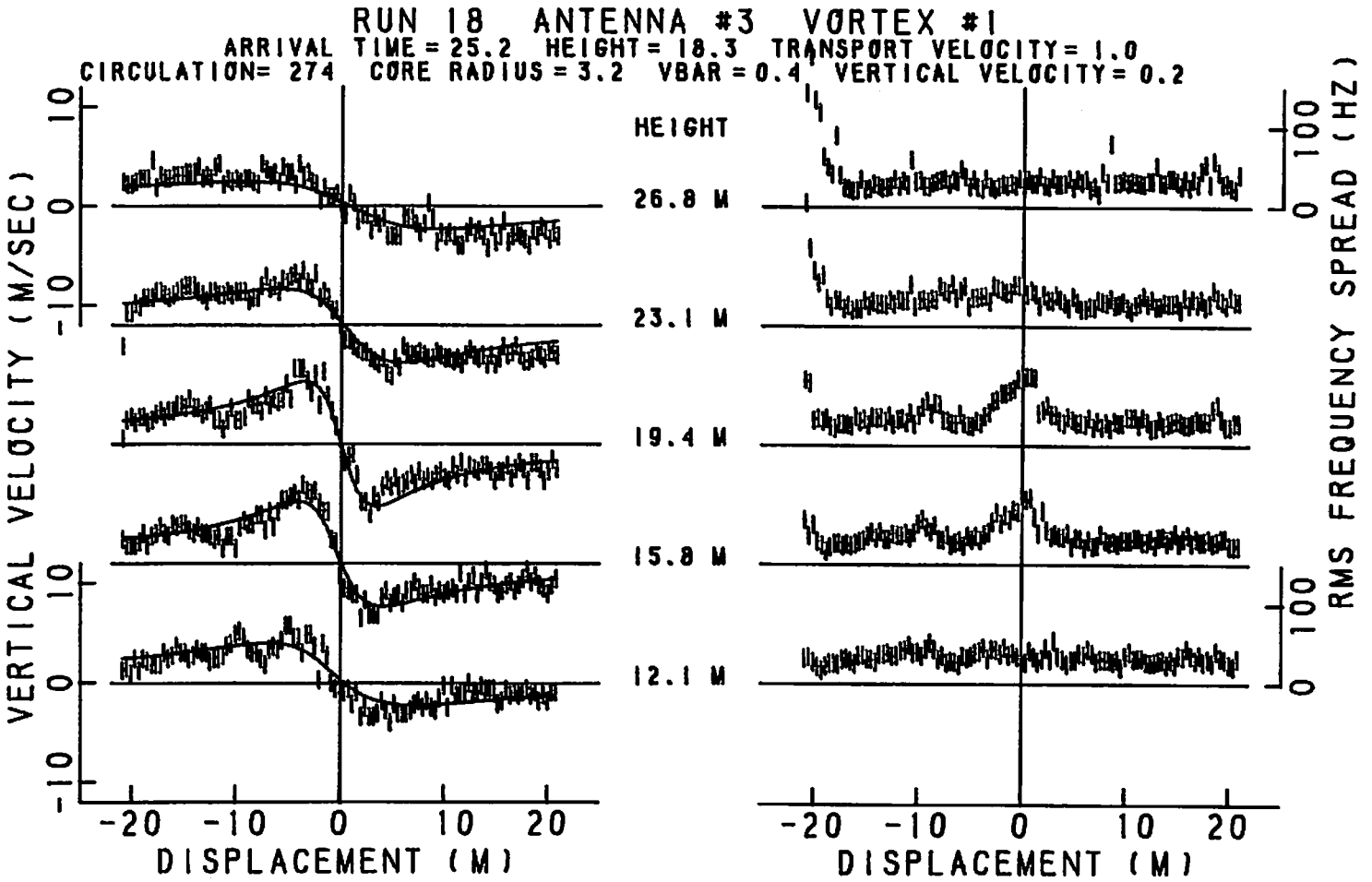

FIGURE 270. VELOCITY AND SPECTRAL WIDTH PROFILES FOR RUN 18, ANTENNA 3

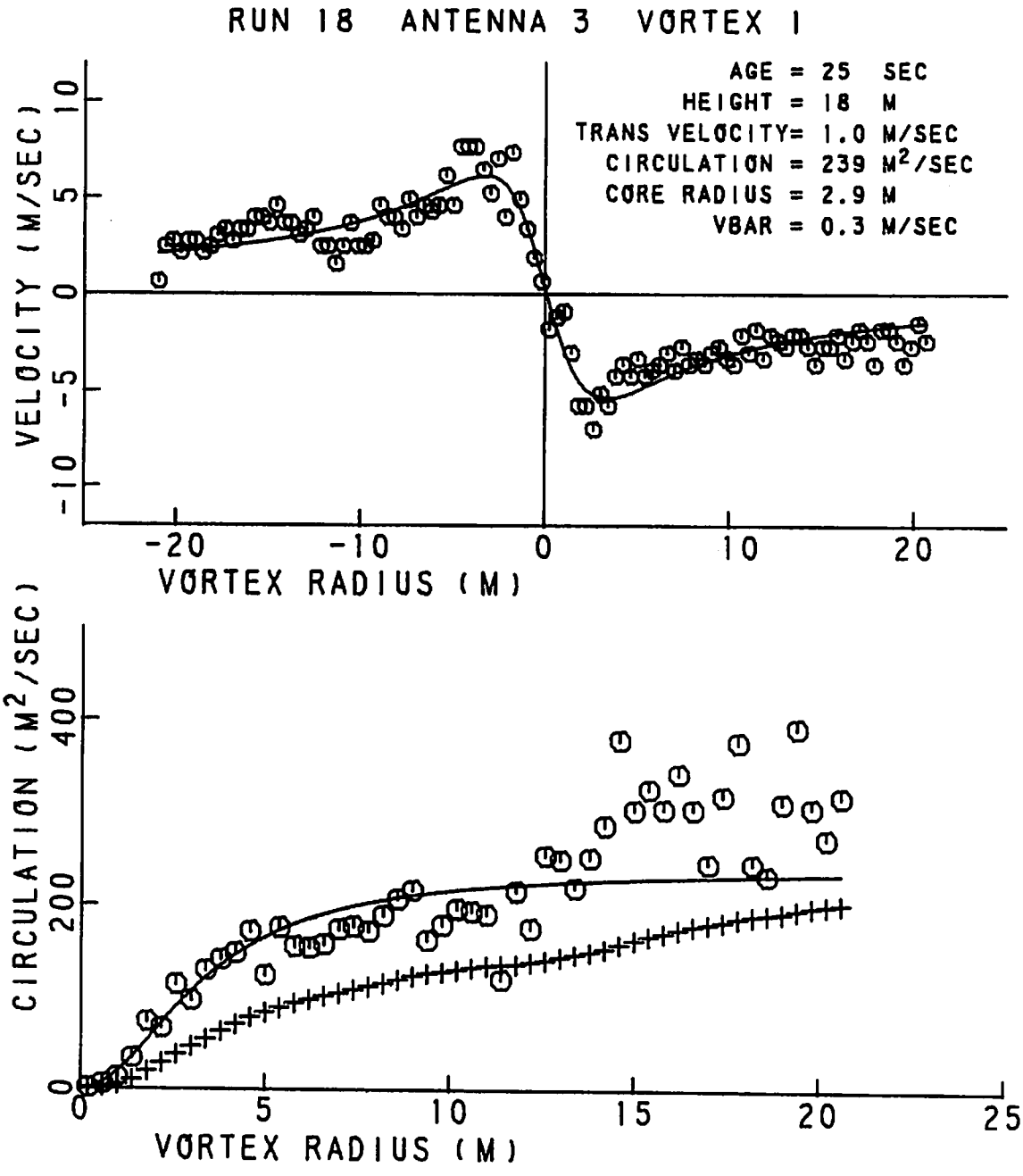

FIGURE 271. VELOCITY AND CIRCULATION PROFILES FOR RUN 18, ANTENNA 3

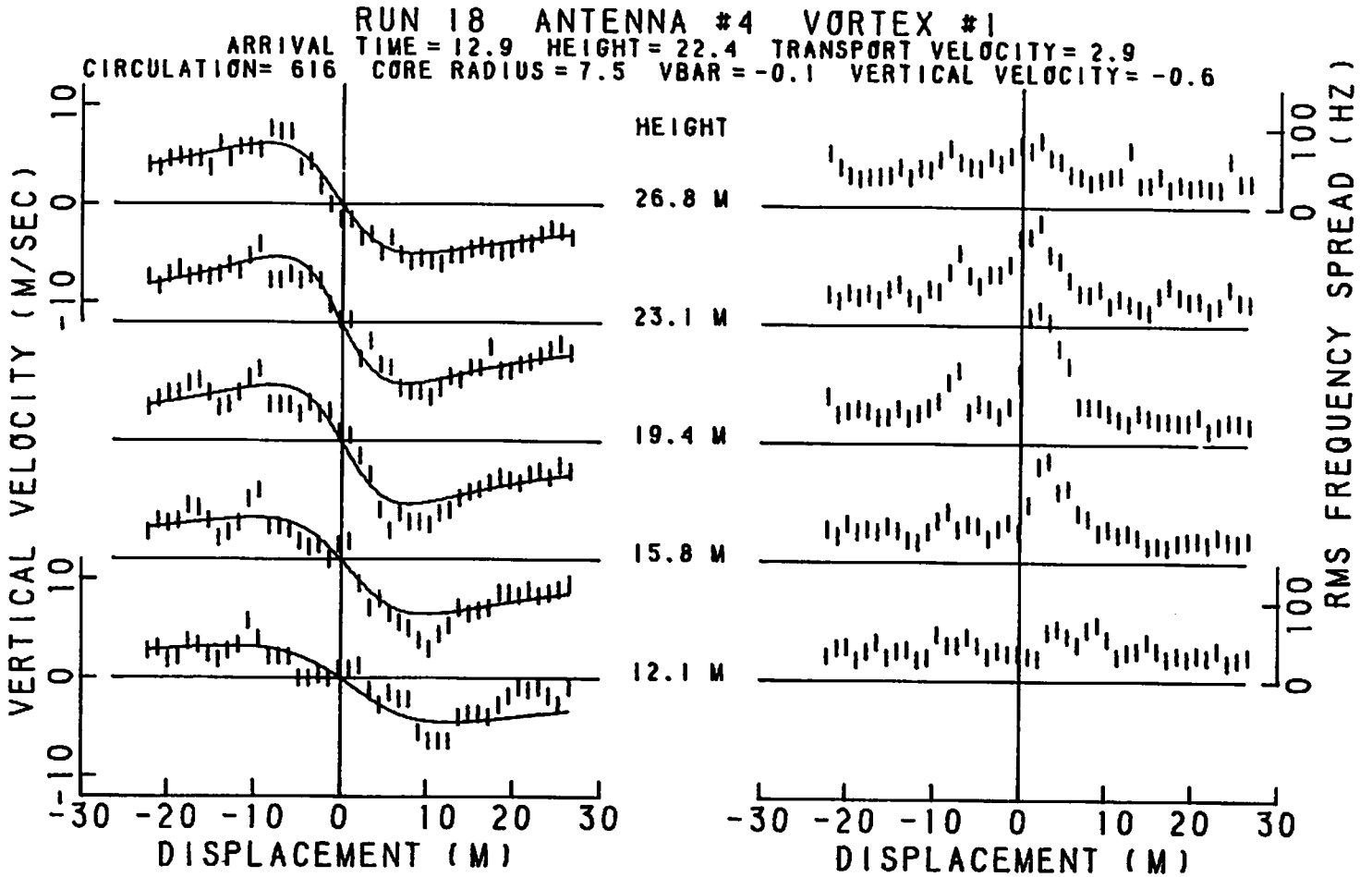

FIGURE 272. VELOCITY AND SPECTRAL WIDTH PROFILES FOR RUN 18, ANTENNA 4

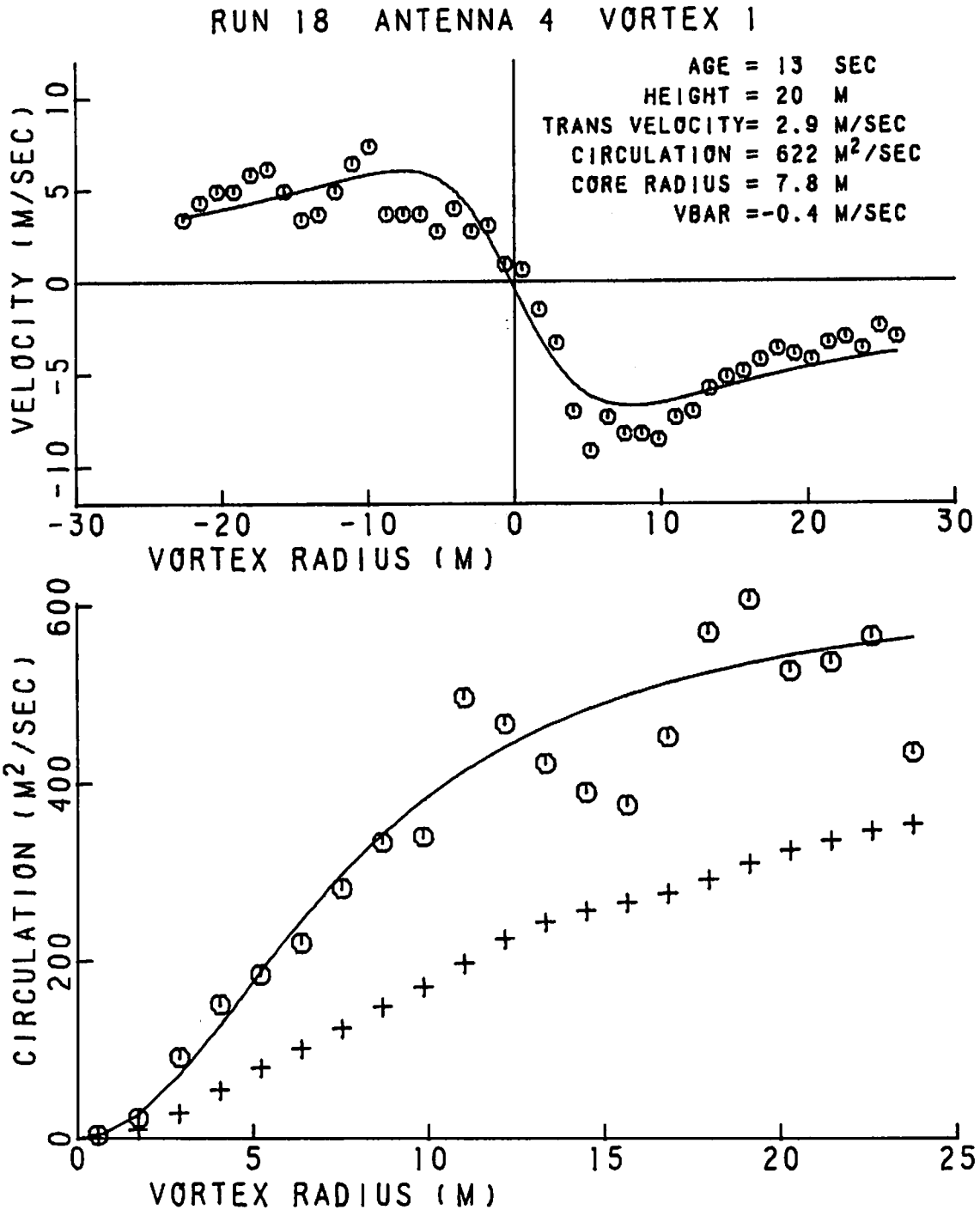

FIGURE 273. VELOCITY AND CIRCULATION PROFILES FOR FOR RUN 18, ANTENNA 4

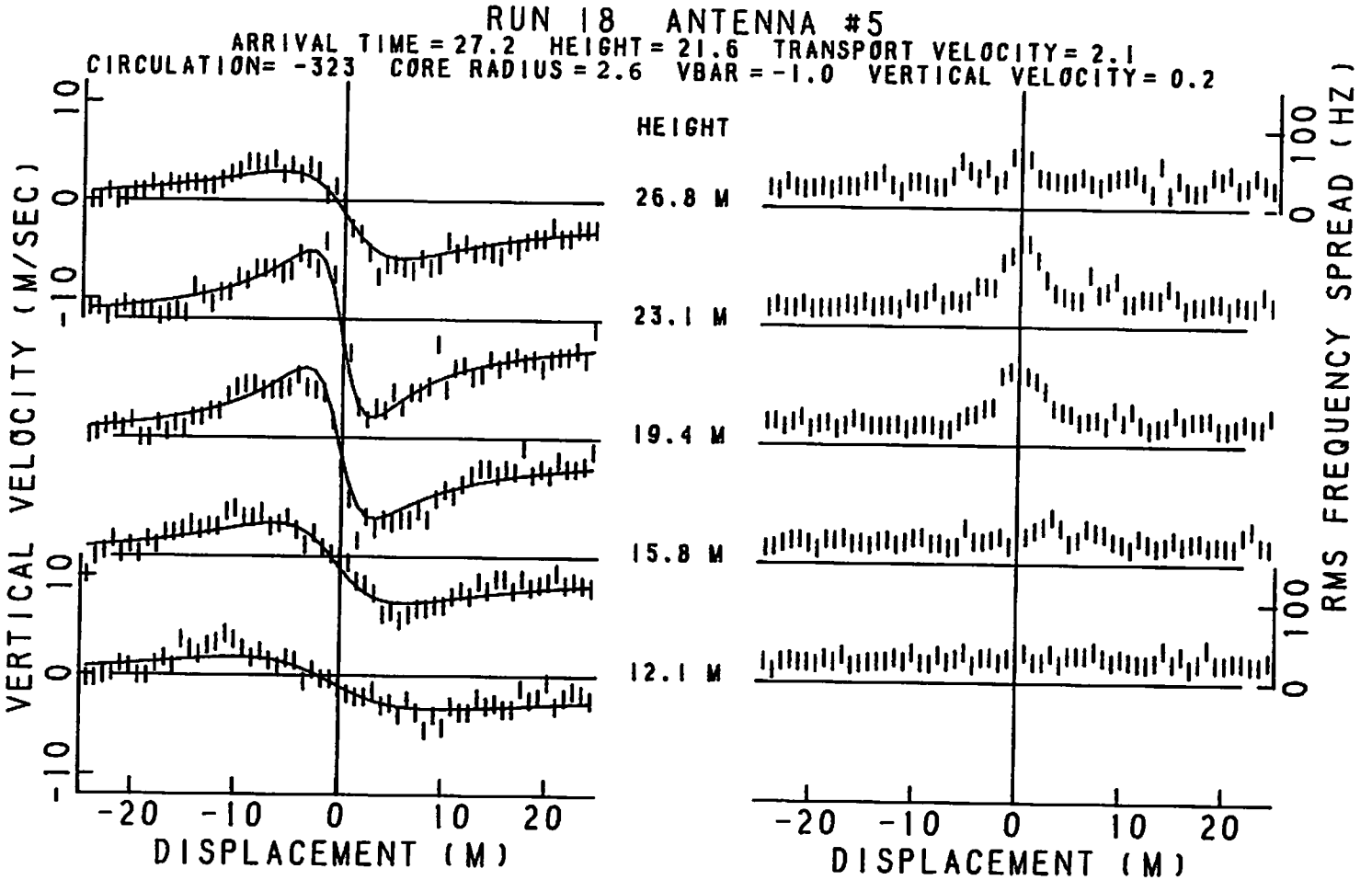

FIGURE 274. VELOCITY AND SPECTRAL WIDTH PROFILES FOR RUN 18, ANTENNA 5

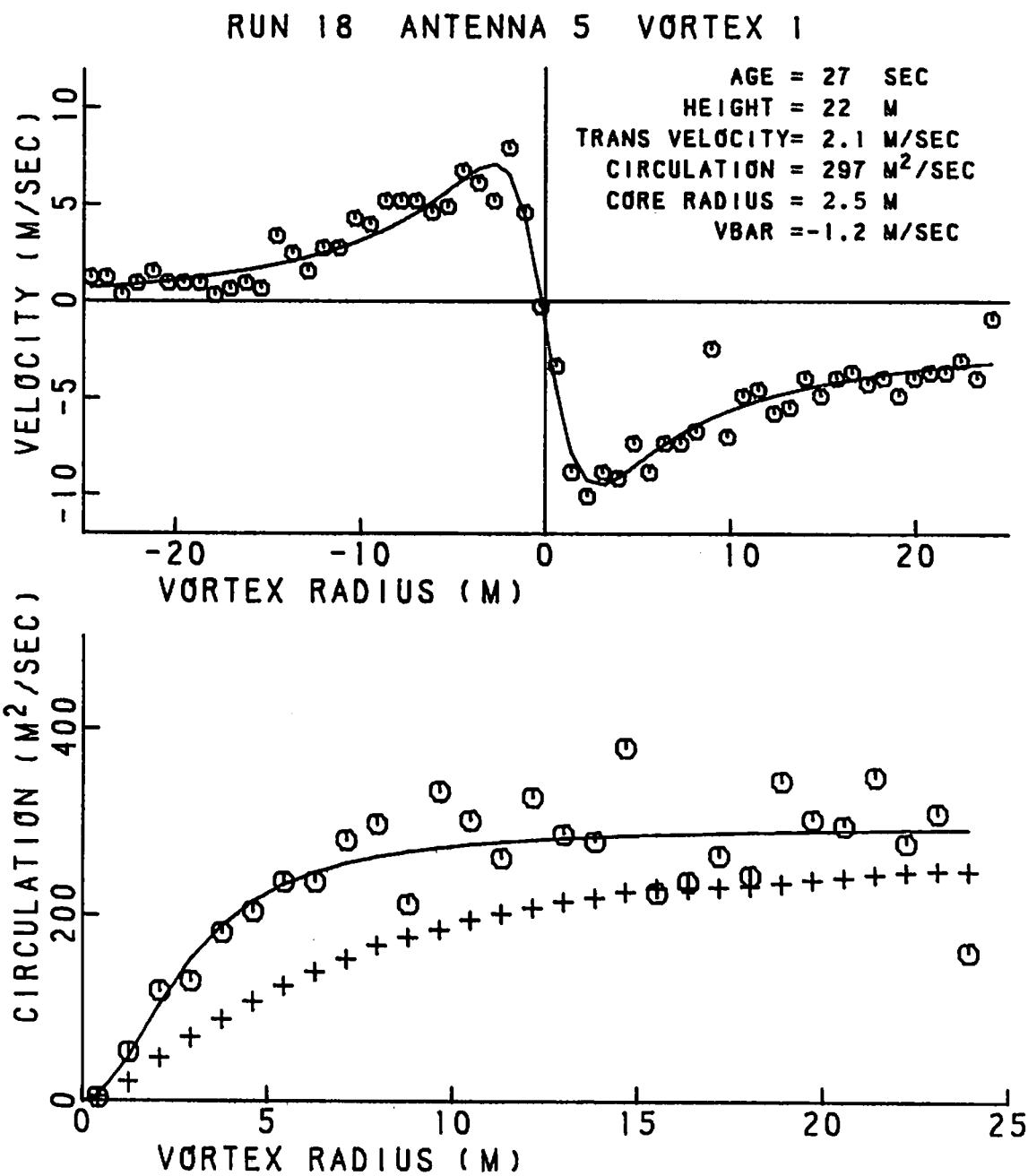

FIGURE 275. VELOCITY AND CIRCULATION PROFILES FOR RUN 18, ANTENNA 5

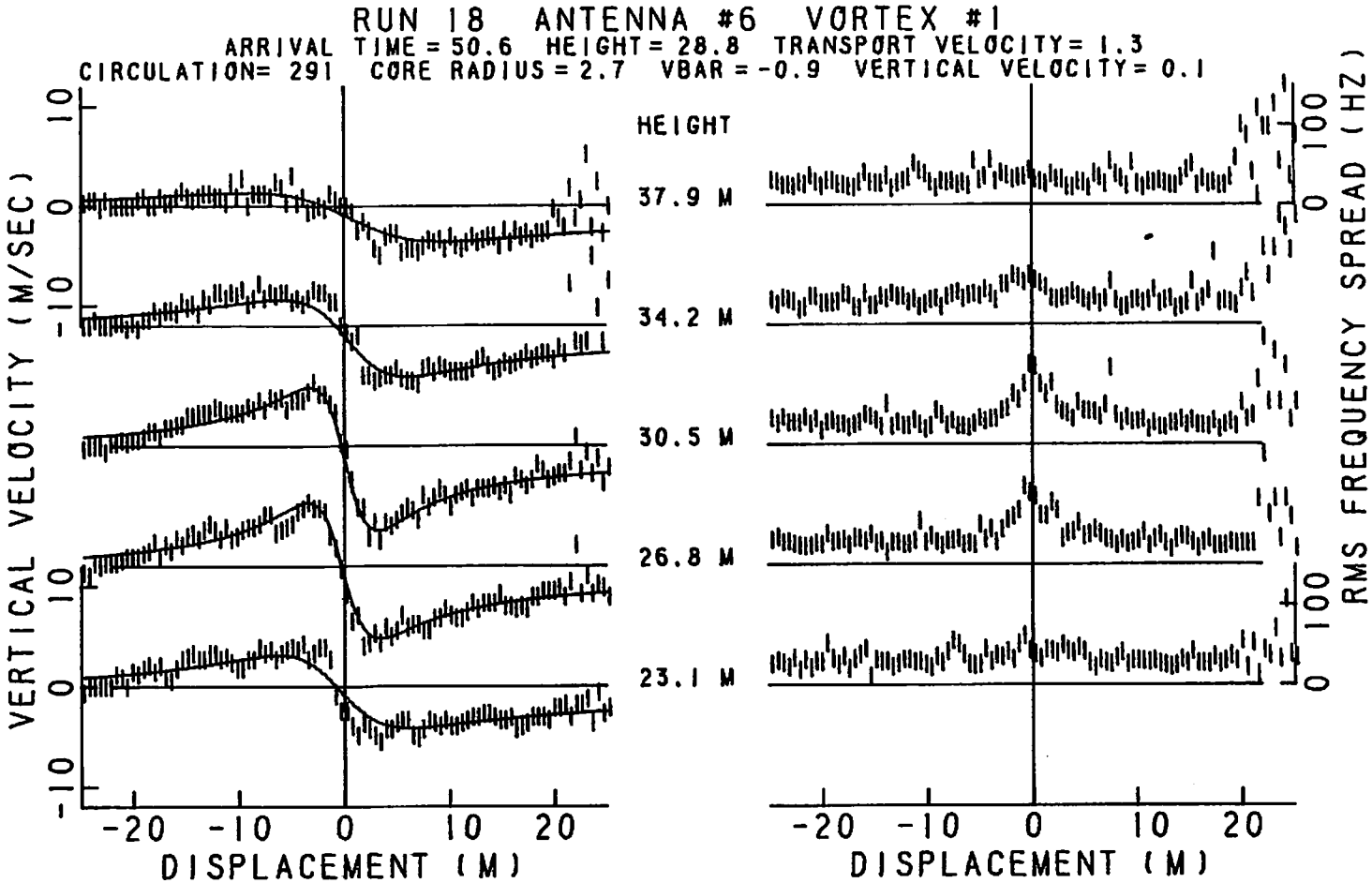

FIGURE 276. VELOCITY AND SPECTRAL WIDTH PROFILES FOR RUN 18, ANTENNA 6

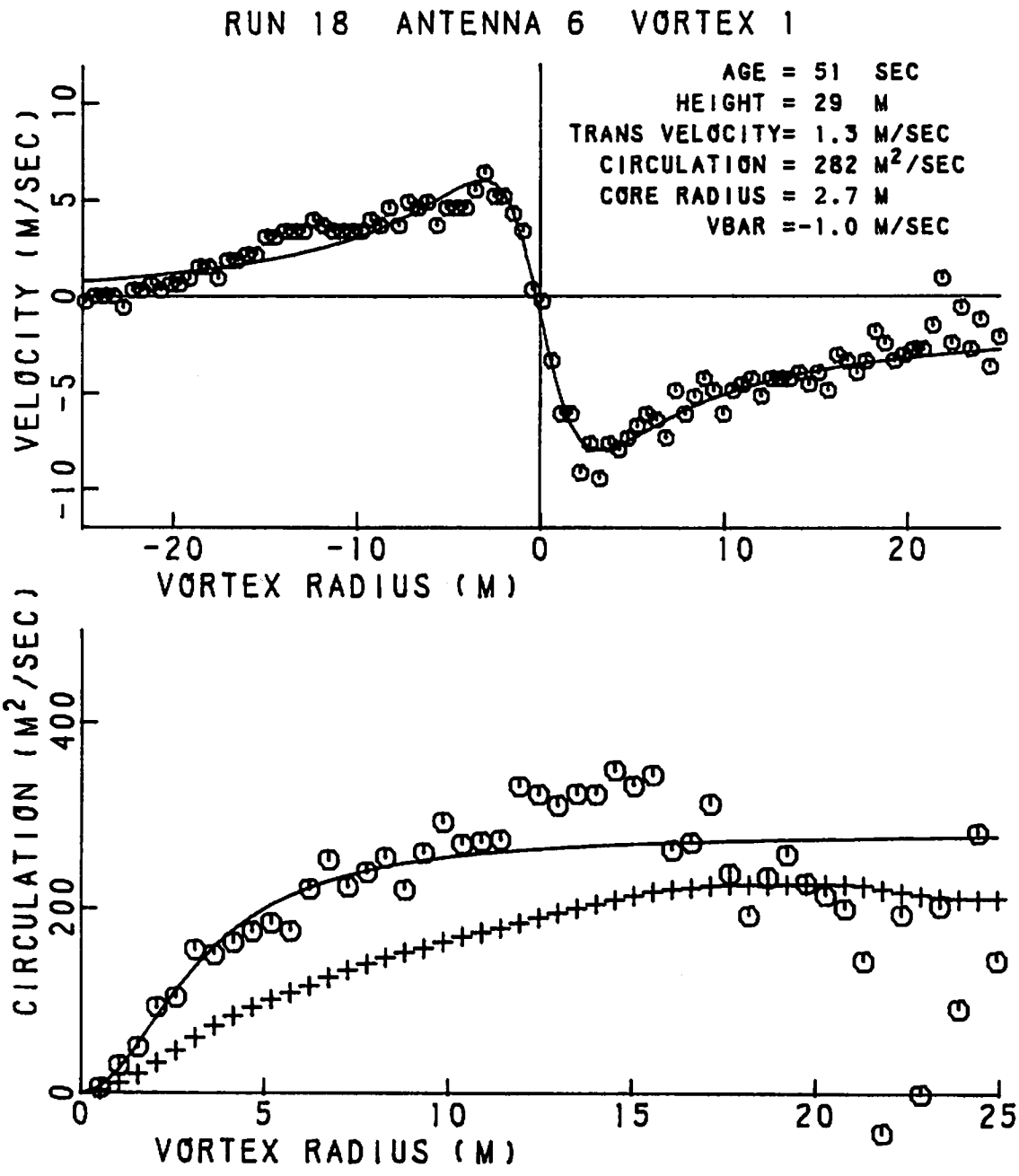

FIGURE 277. VELOCITY AND CIRCULATION PROFILES FOR RUN 18, ANTENNA 6

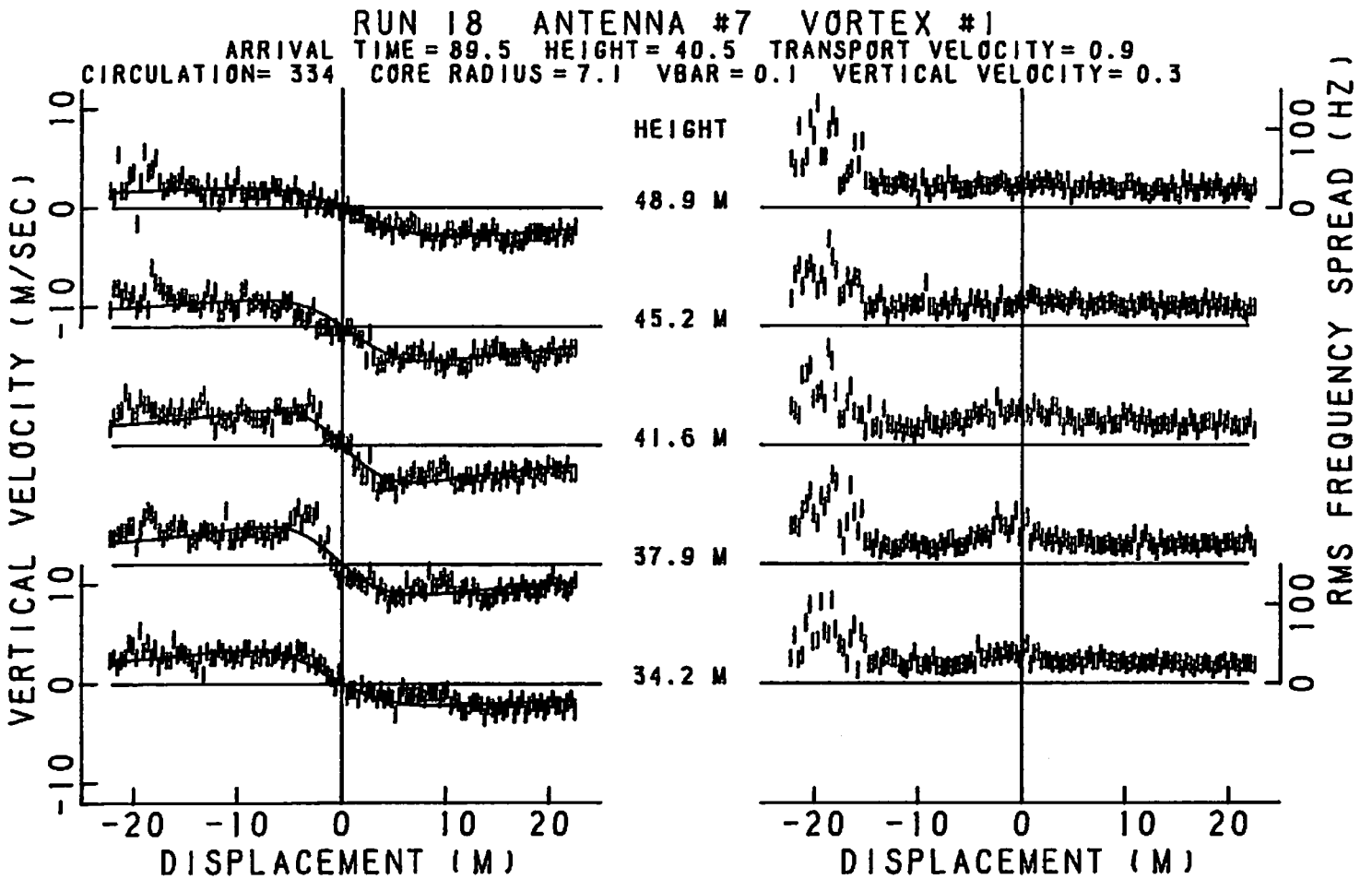

FIGURE 278. VELOCITY AND SPECTRAL WIDTH PROFILES FOR RUN 18, ANTENNA 7

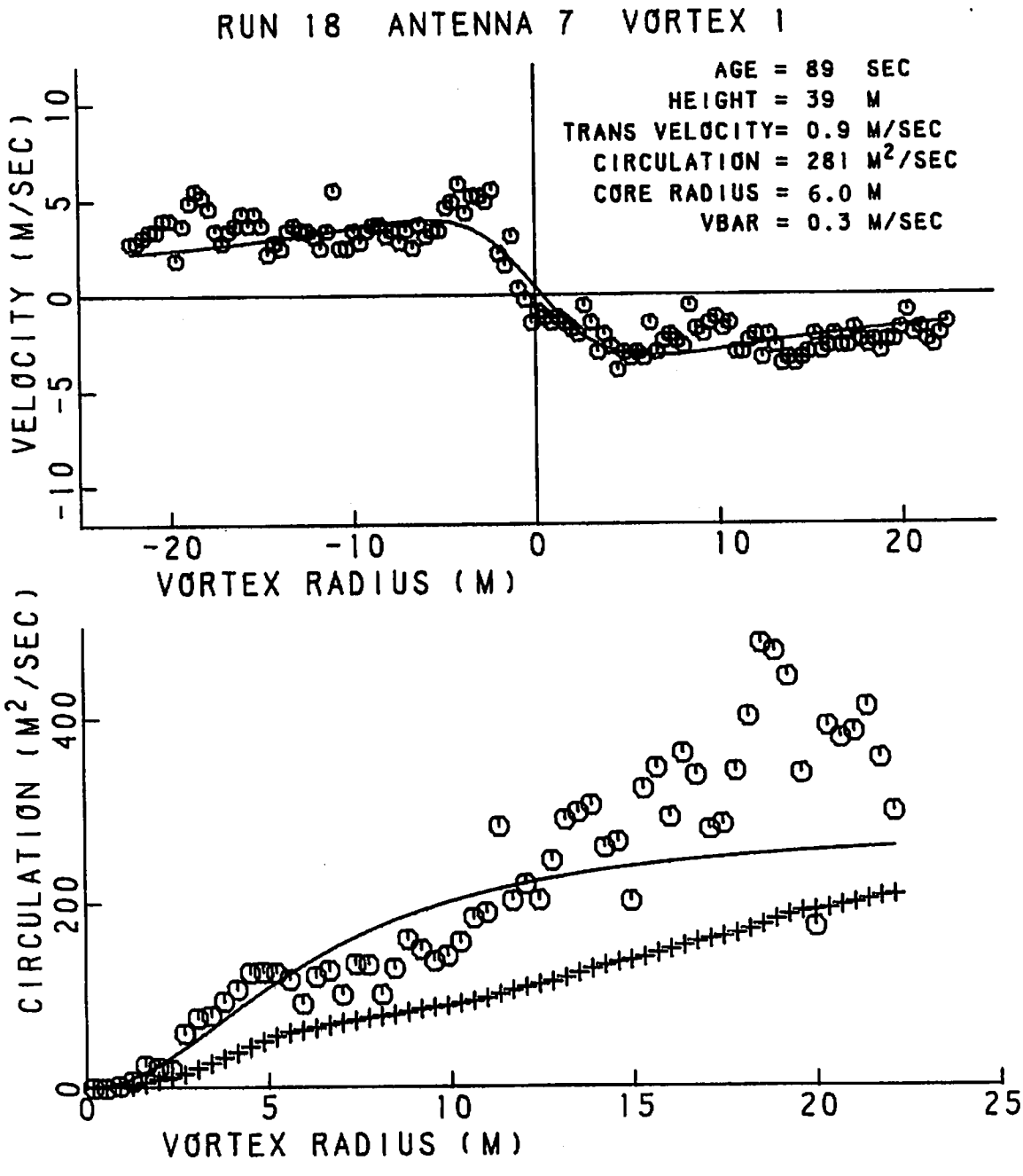

FIGURE 279. VELOCITY AND CIRCULATION PROFILES FOR RUN 18, ANTENNA 7

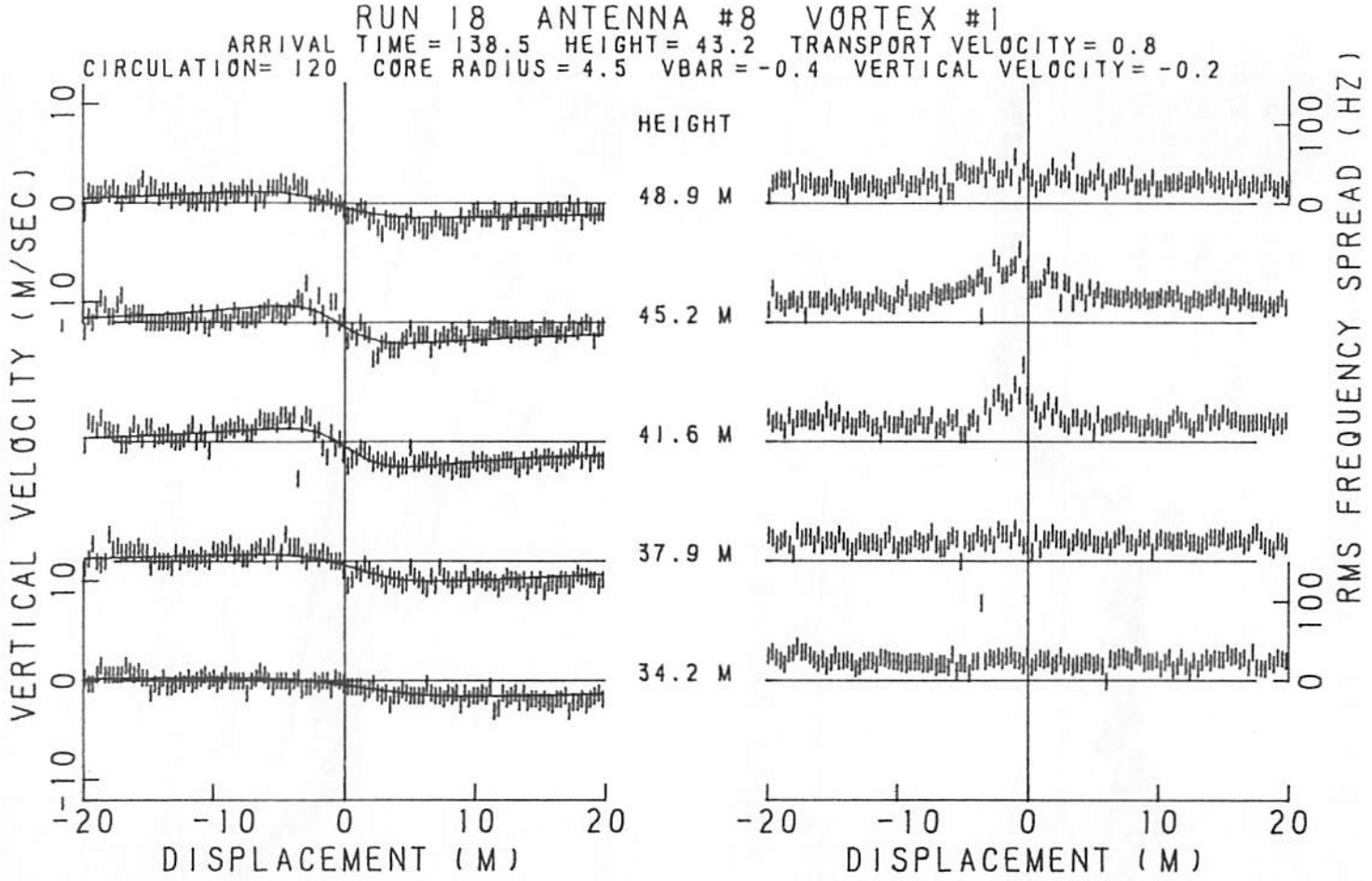

FIGURE 280. VELOCITY AND SPECTRAL WIDTH PROFILES FOR RUN 18, ANTENNA 8

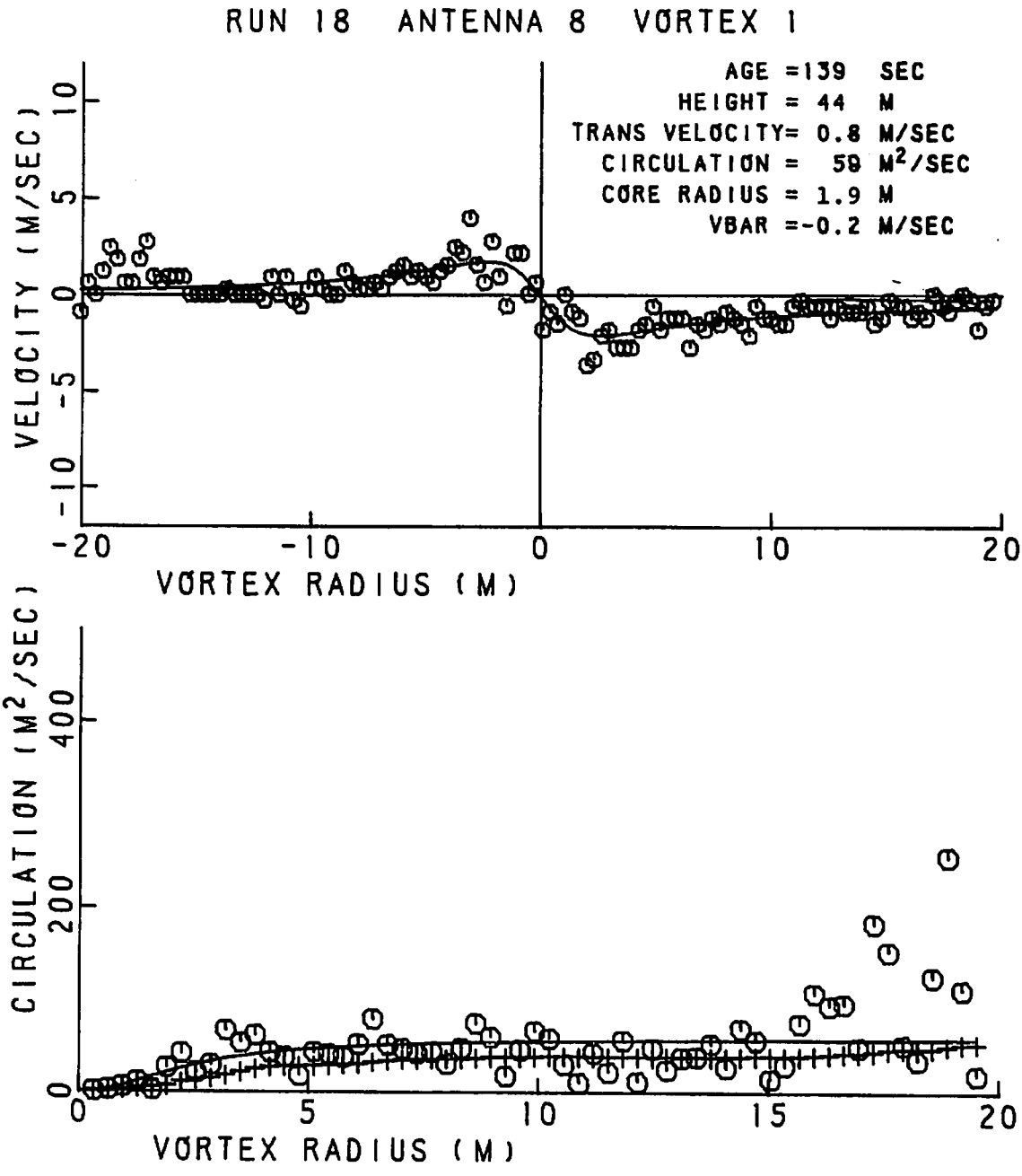

FIGURE 281. VELOCITY AND CIRCULATION PROFILES FOR RUN 18, ANTENNA 8

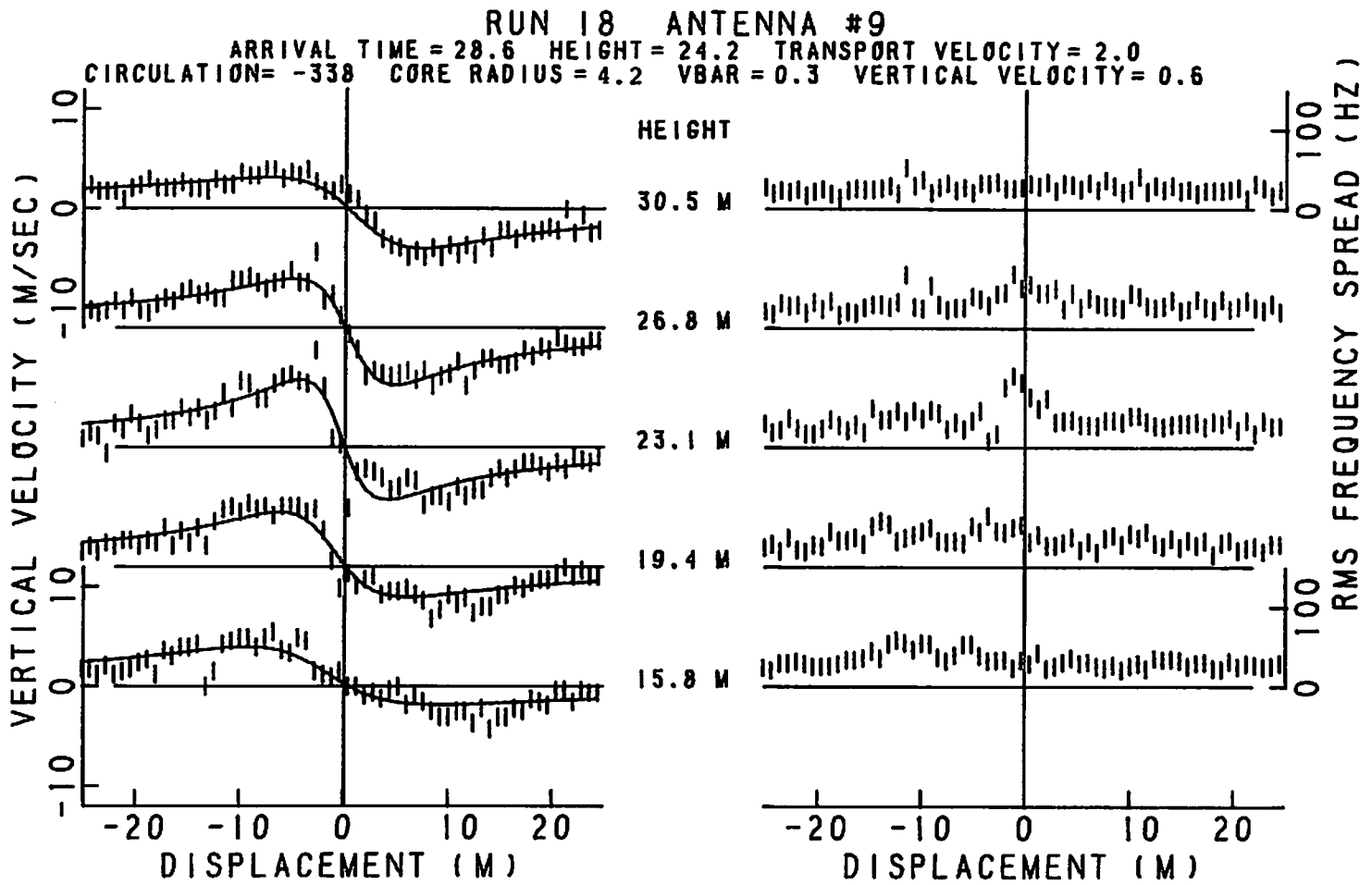

FIGURE 282. VELOCITY AND SPECTRAL WIDTH PROFILES FOR RUN 18, ANTENNA 9

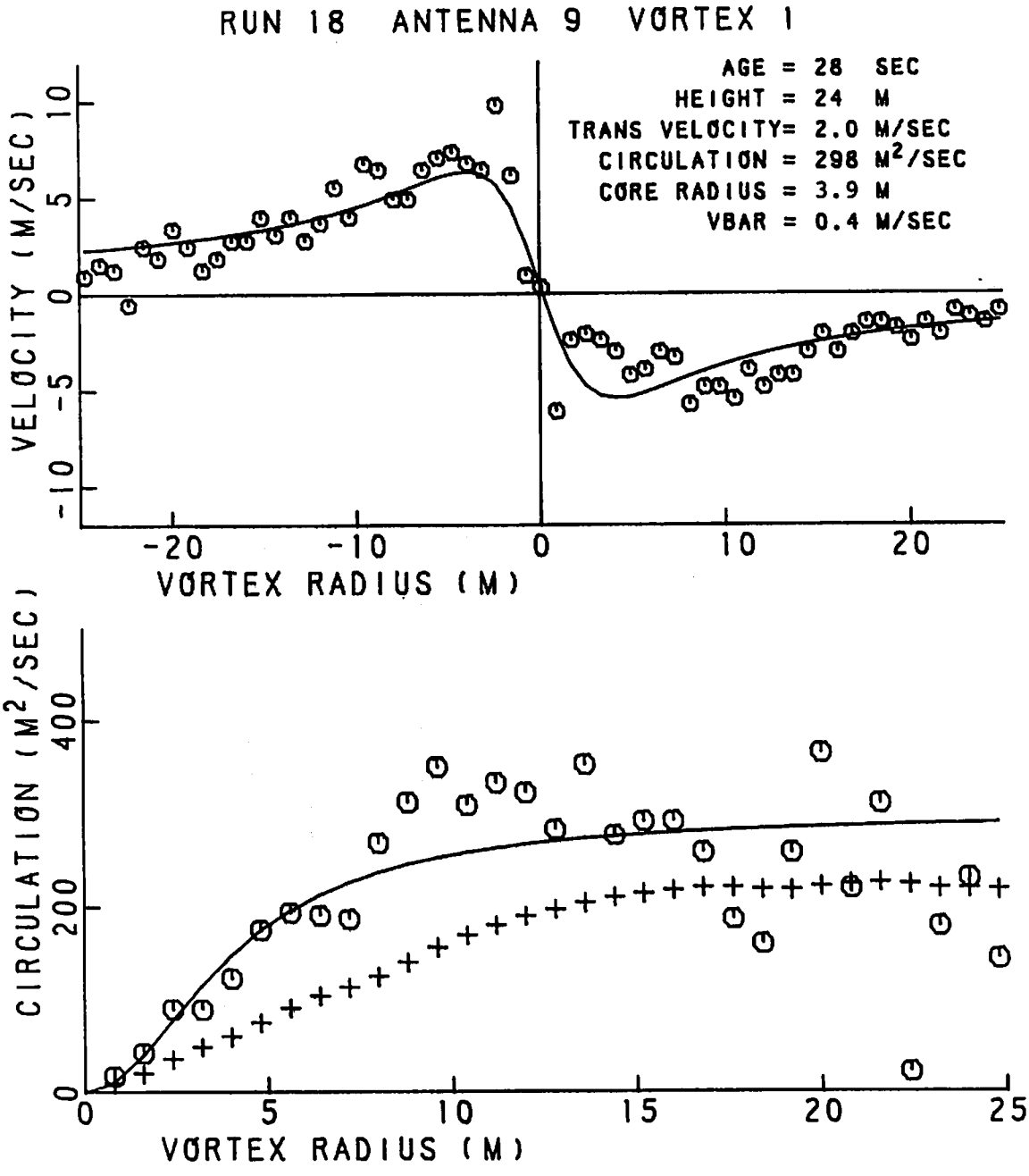

FIGURE 283. VELOCITY AND CIRCULATION PROFILES FOR RUN 18, ANTENNA 9

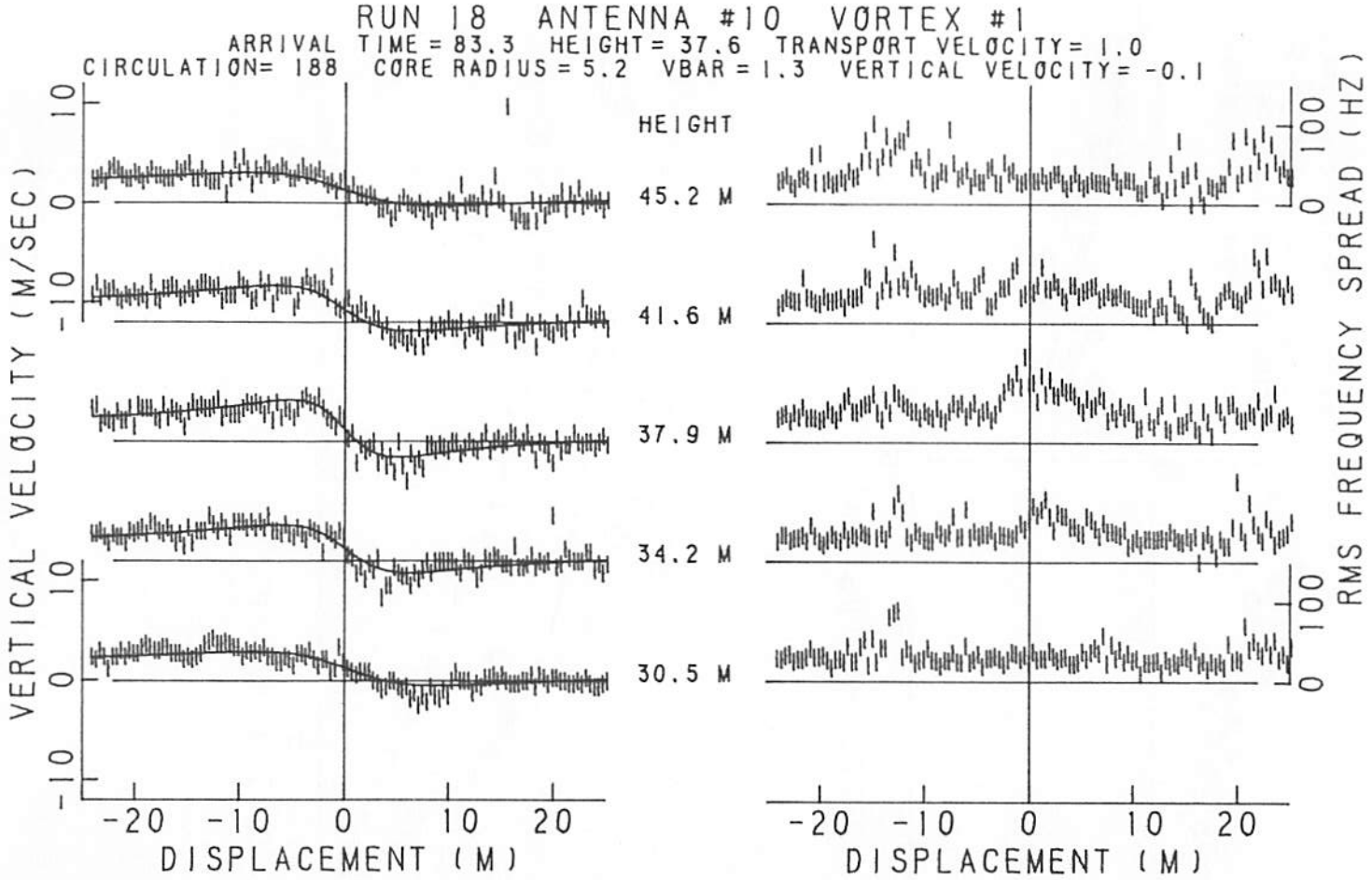

FIGURE 284. VELOCITY AND SPECTRAL WIDTH PROFILES FOR RUN 18, ANTENNA 10

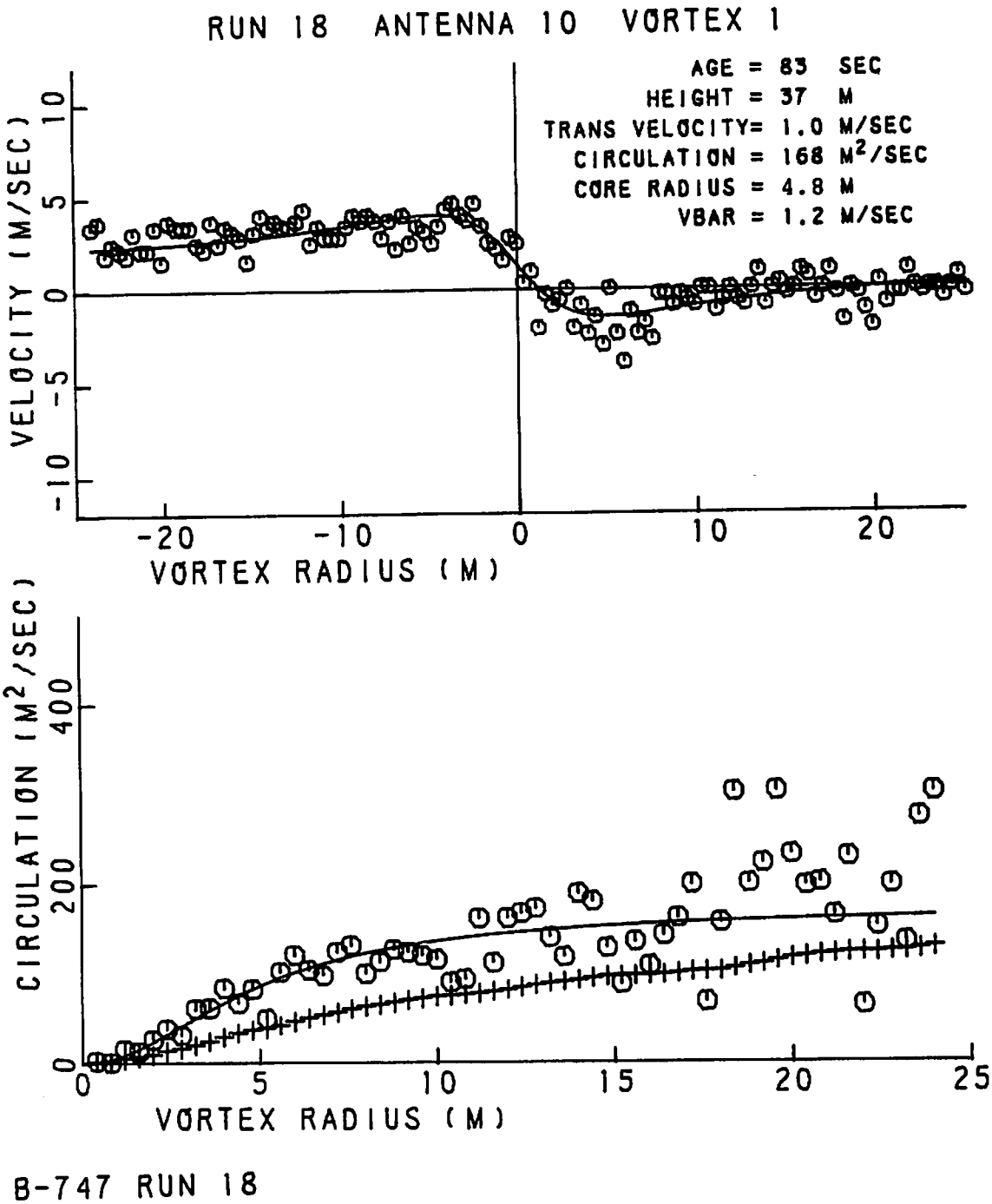

FIGURE 285. VELOCITY AND CIRCULATION PROFILES FOR RUN 18, ANTENNA 10

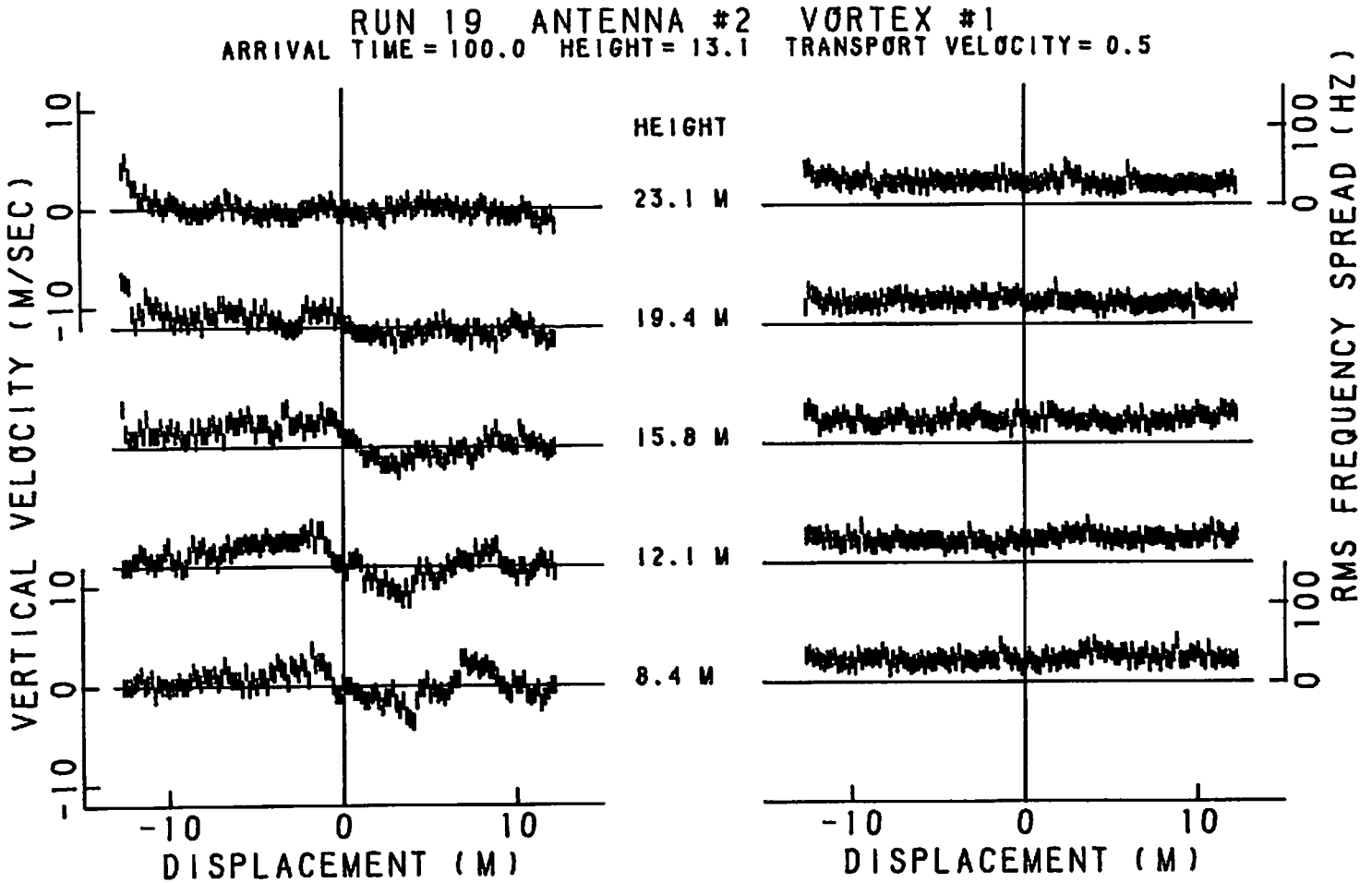

FIGURE 286. VELOCITY AND SPECTRAL WIDTH PROFILES FOR RUN 19, ANTENNA 2

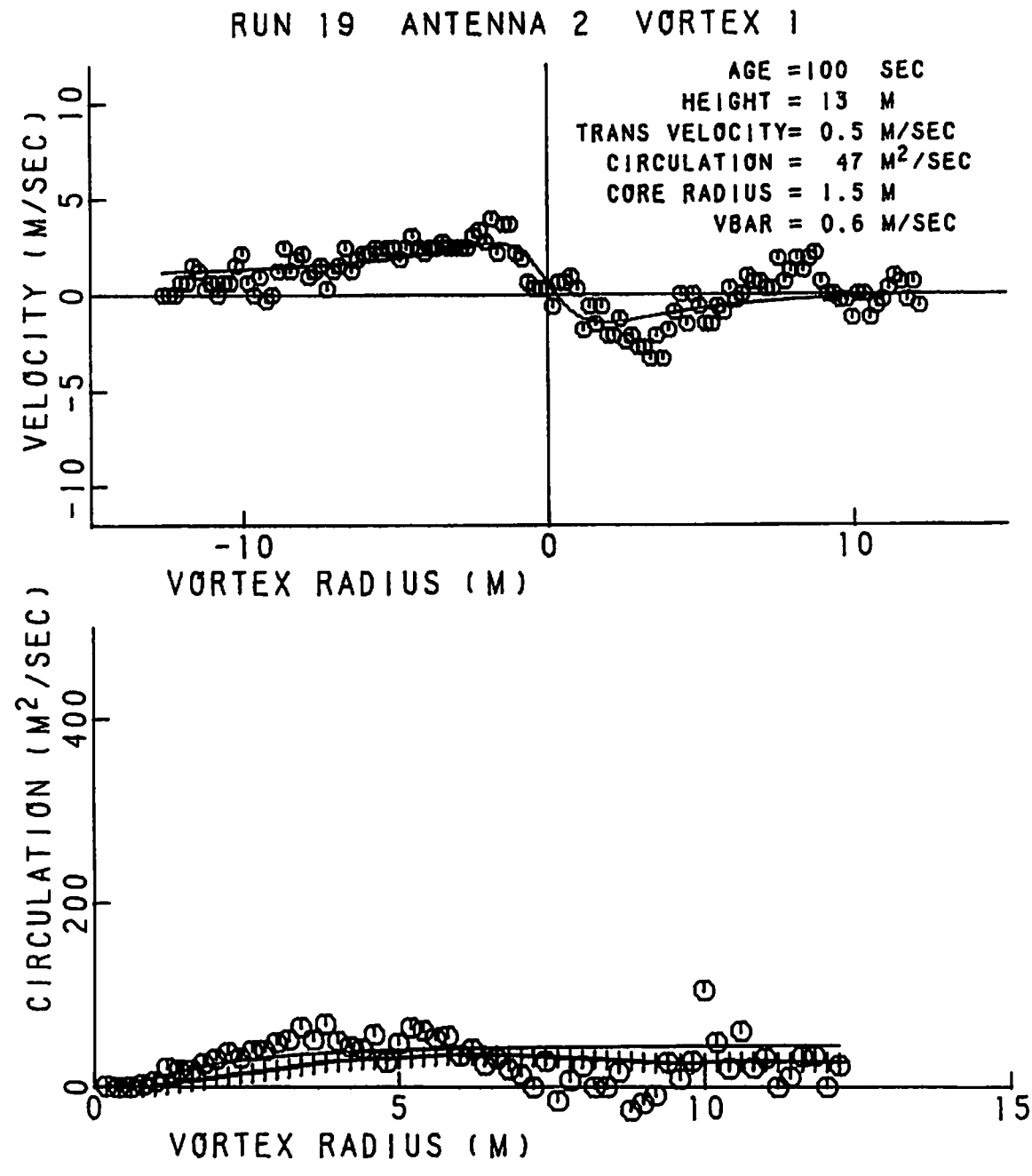

FIGURE 287. VELOCITY AND CIRCULATION PROFILES FOR RUN 19, ANTENNA 2

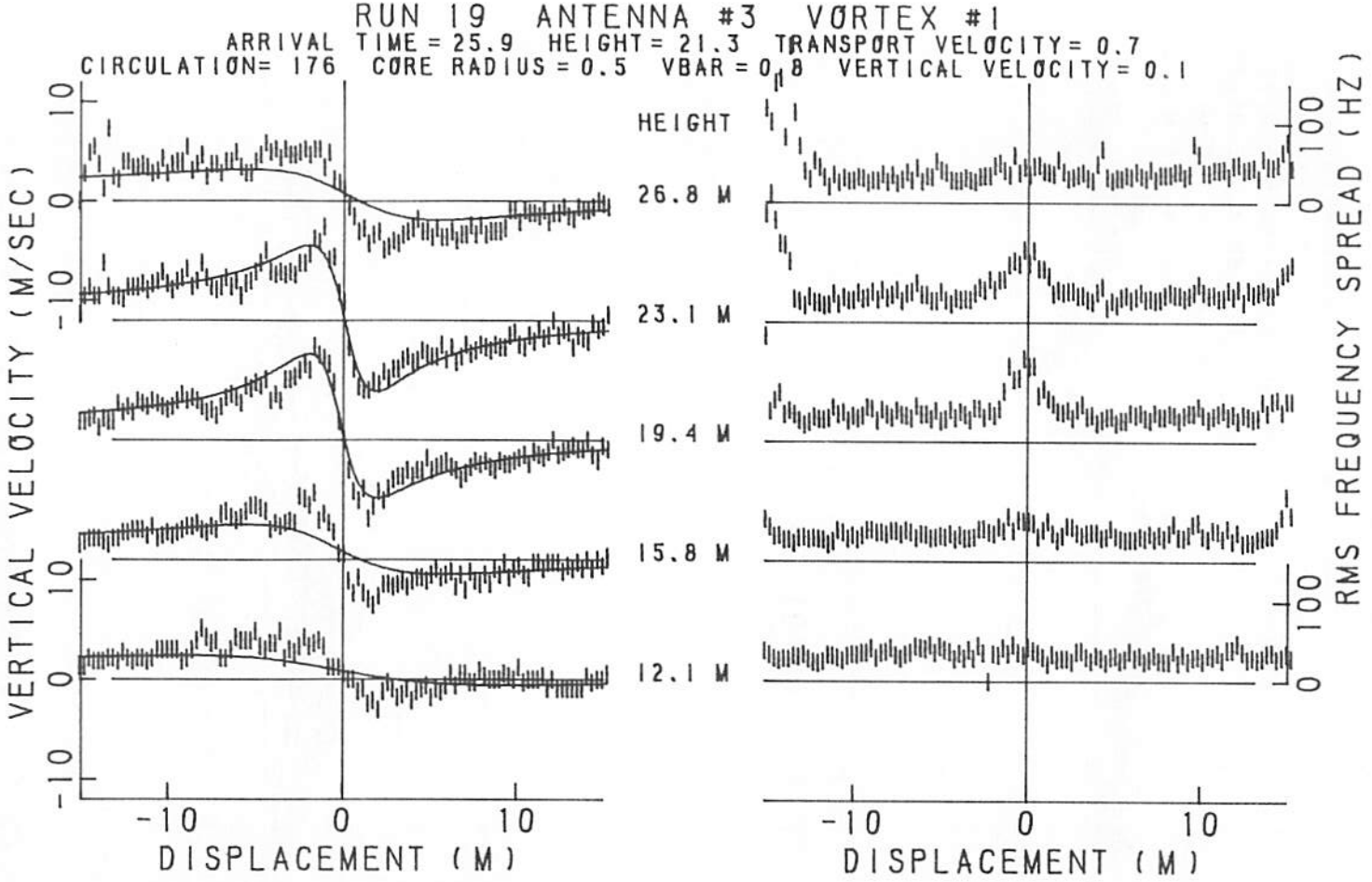

FIGURE 288. VELOCITY AND SPECTRAL WIDTH PROFILES FOR RUN 19, ANTENNA 3

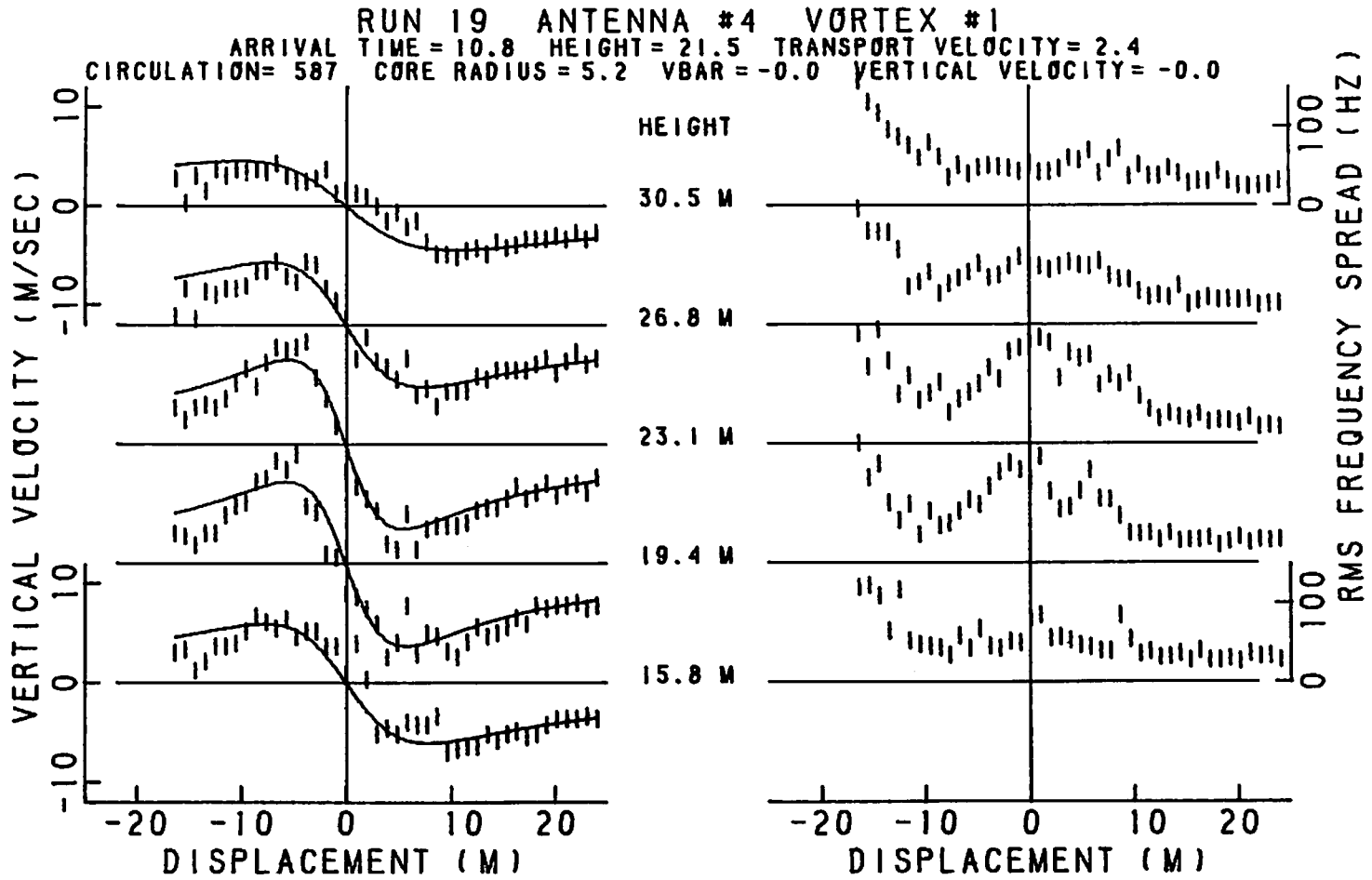

FIGURE 289. VELOCITY AND SPECTRAL WIDTH PROFILES FOR RUN 19, ANTENNA 4

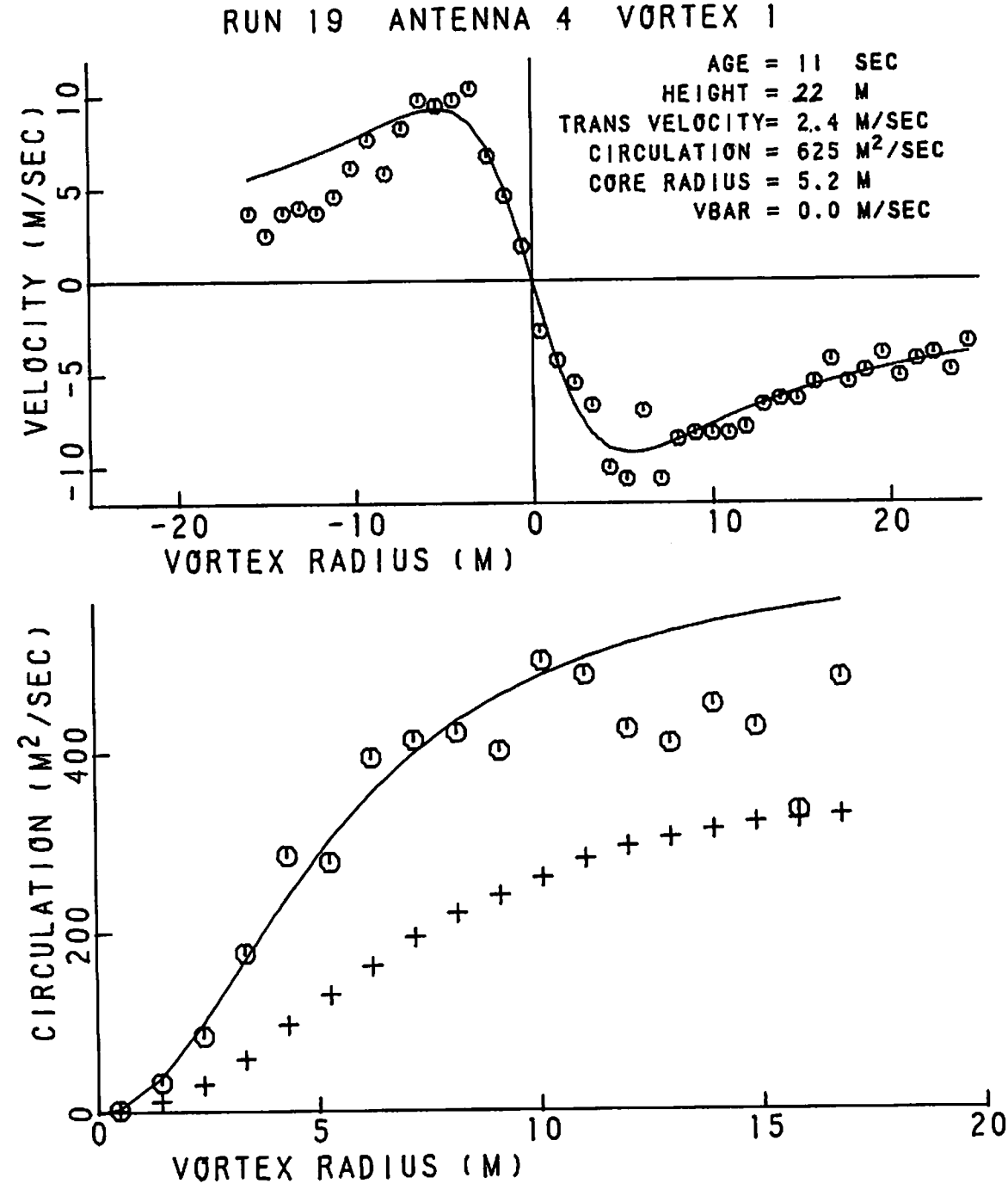

FIGURE 290. VELOCITY AND CIRCULATION PROFILES FOR RUN 19, ANTENNA 4

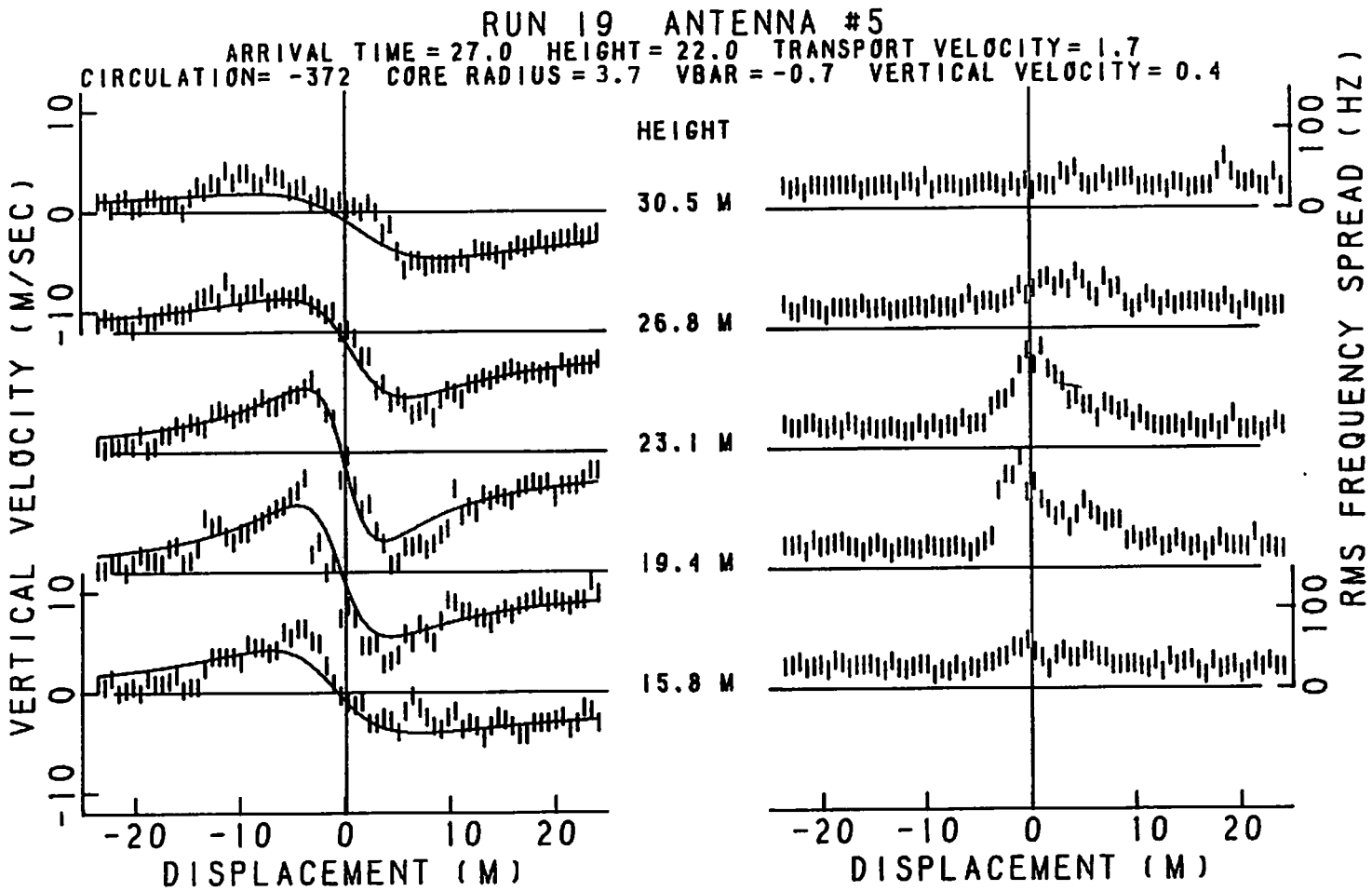

FIGURE 291. VELOCITY AND SPECTRAL WIDTH PROFILES FOR RUN 19, ANTENNA 5

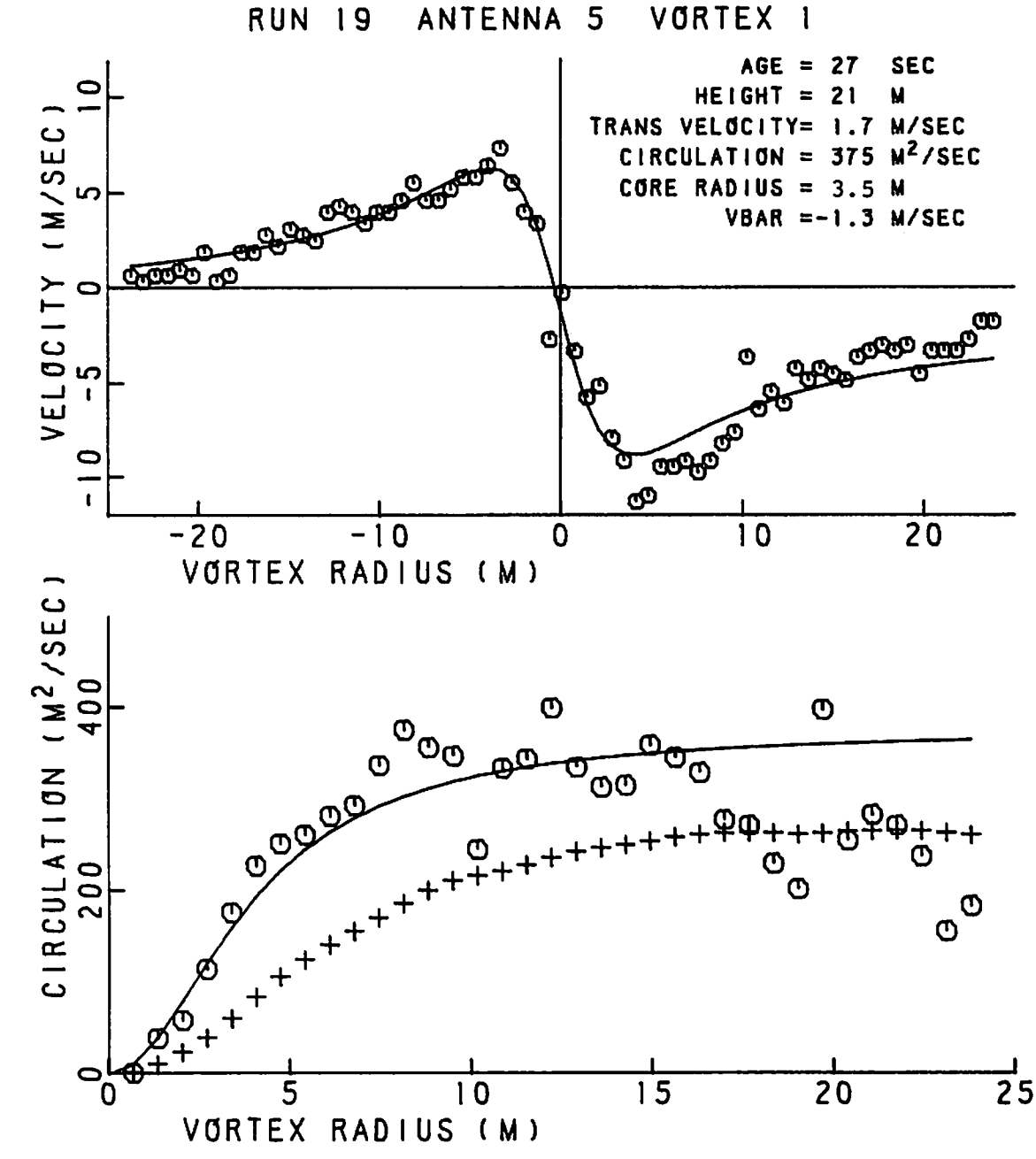

B-747 RUN 19

FIGURE 292. VELOCITY AND CIRCULATION PROFILES FOR RUN 19, ANTENNA 5

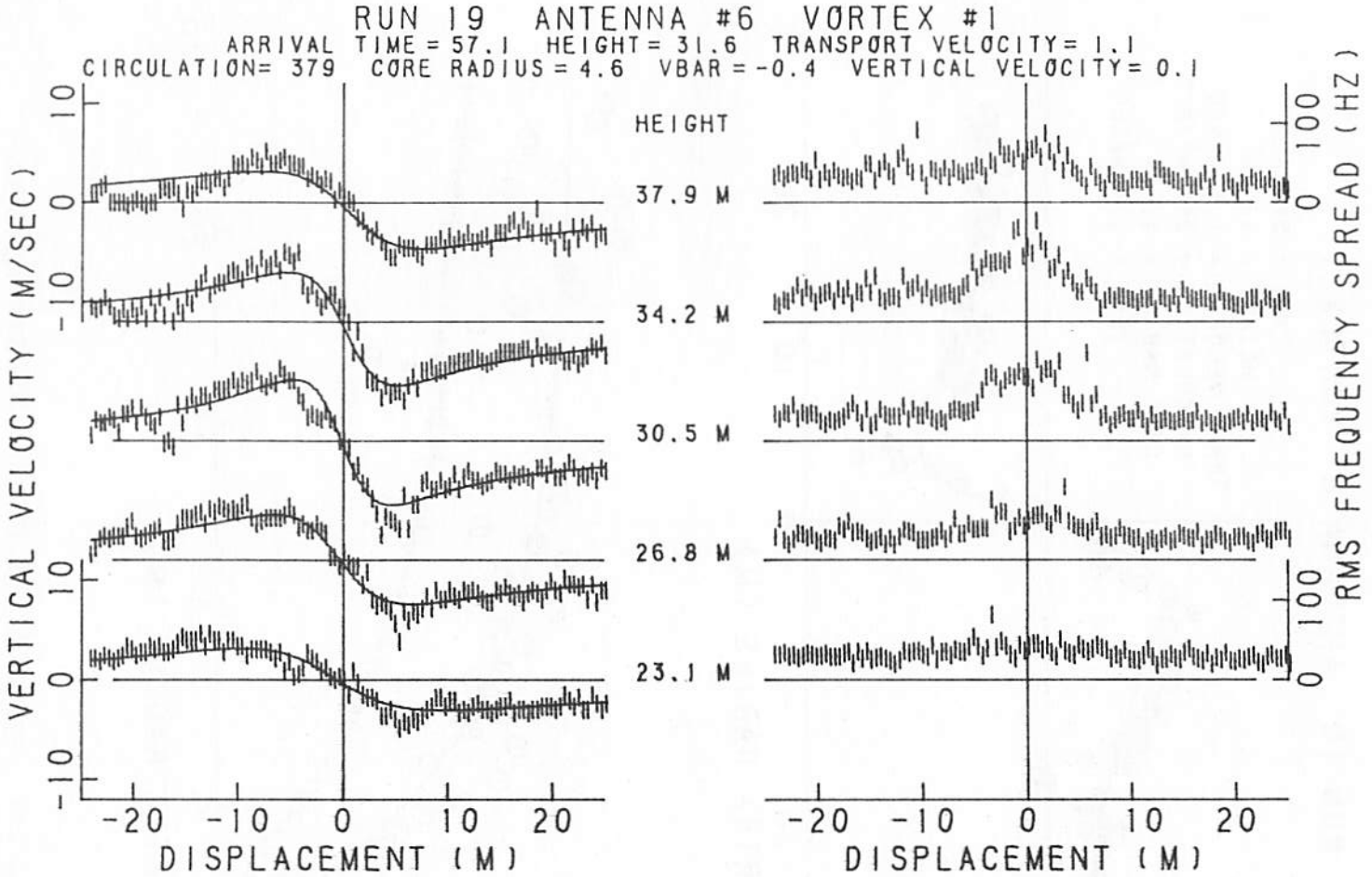

FIGURE 293. VELOCITY AND SPECTRAL WIDTH PROFILES FOR RUN 19, ANTENNA 6

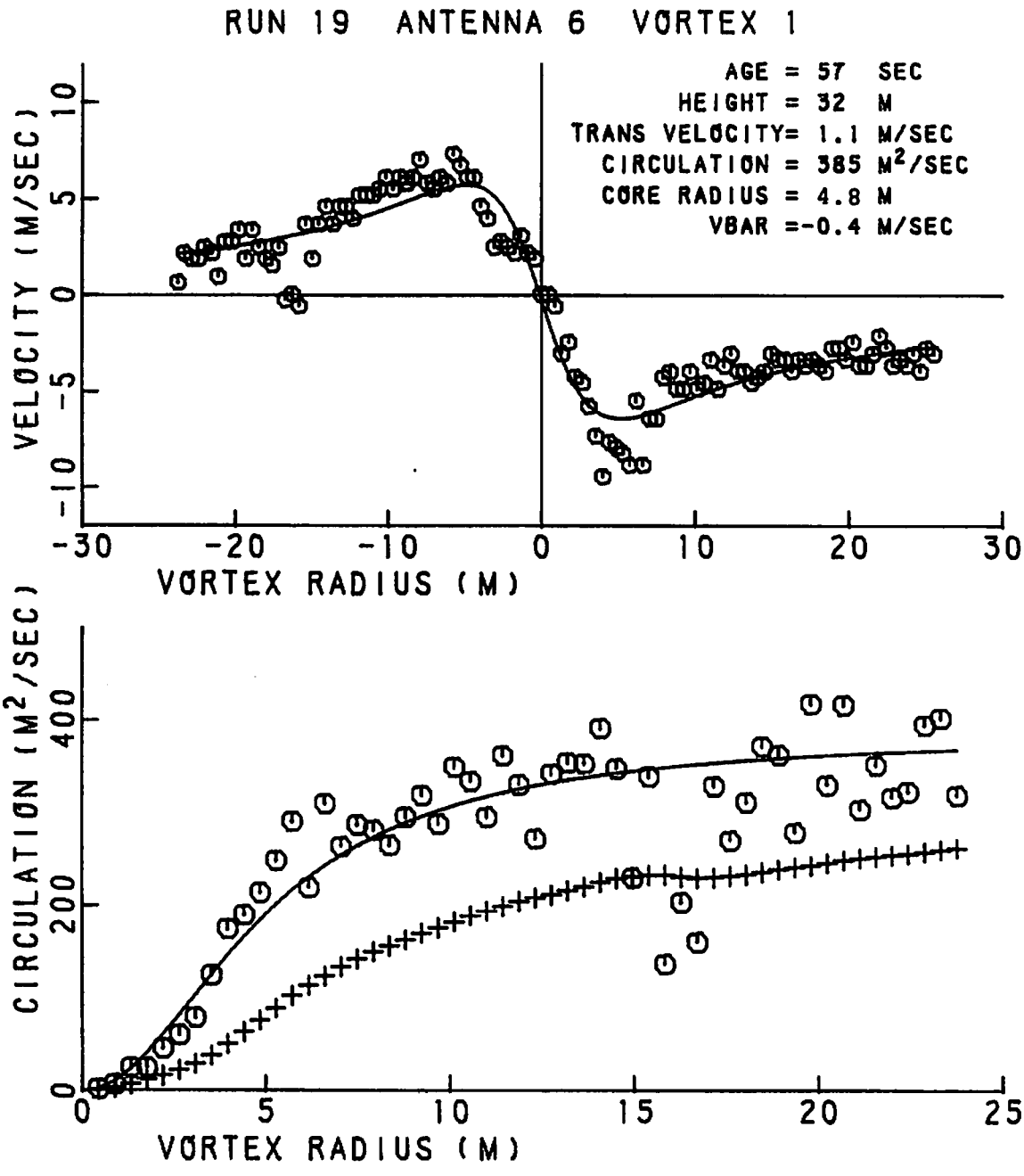

FIGURE 294. VELOCITY AND CIRCULATION PROFILES FOR RUN 19, ANTENNA 6

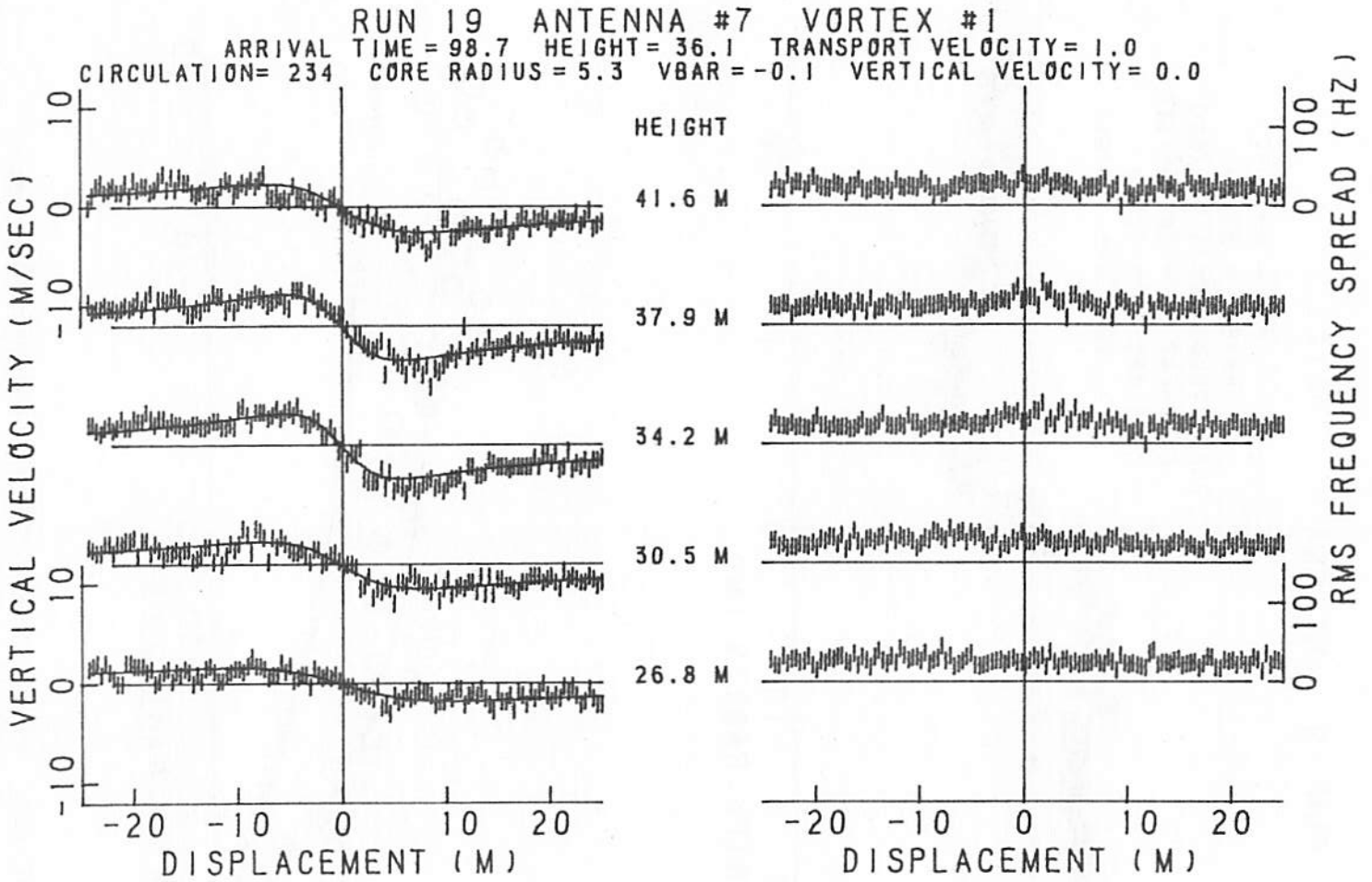

FIGURE 295. VELOCITY AND SPECTRAL WIDTH PROFILES FOR RUN 19, ANTENNA 7

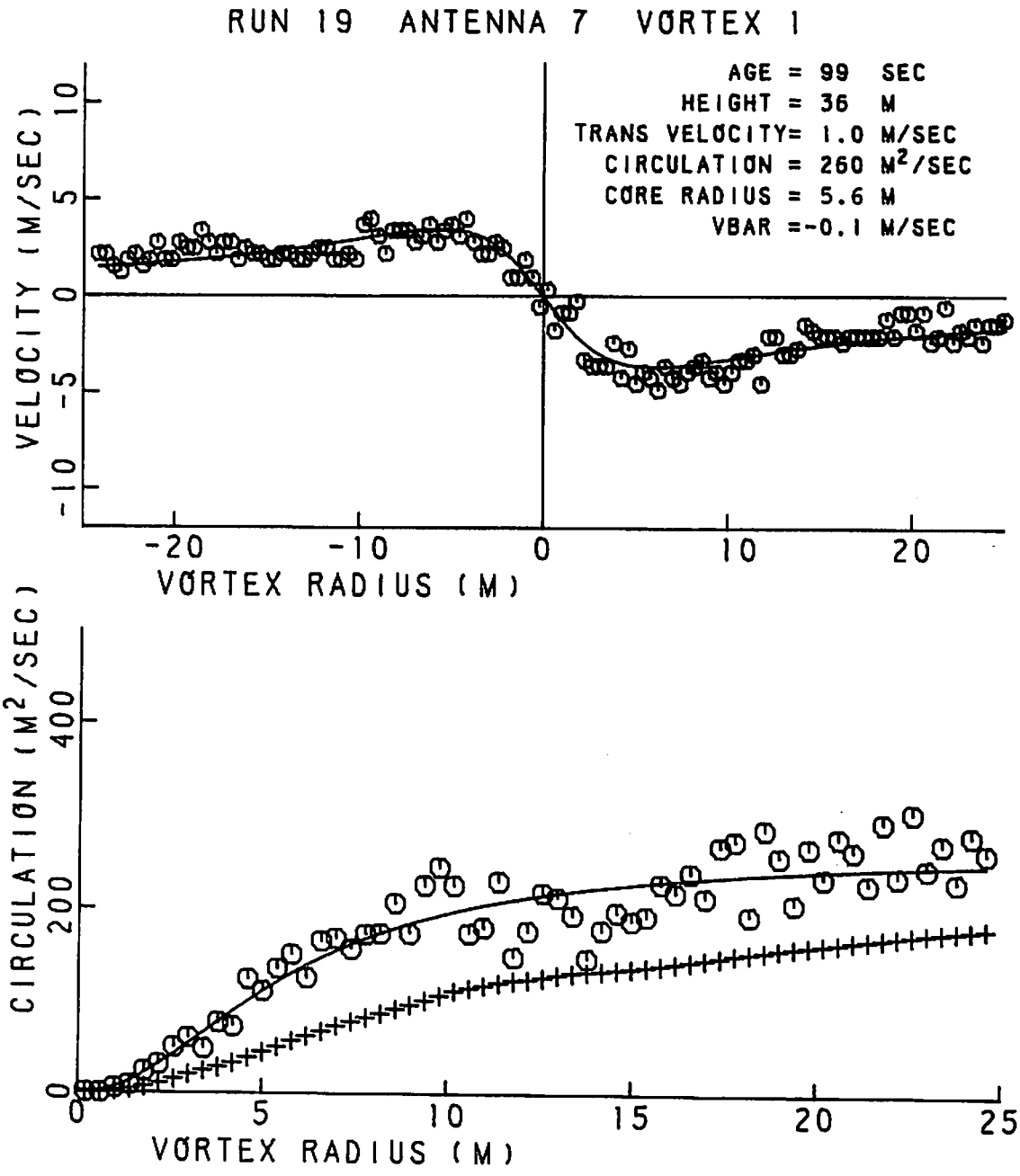

FIGURE 296. VELOCITY AND CIRCULATION PROFILES FOR RUN 19, ANTENNA 7

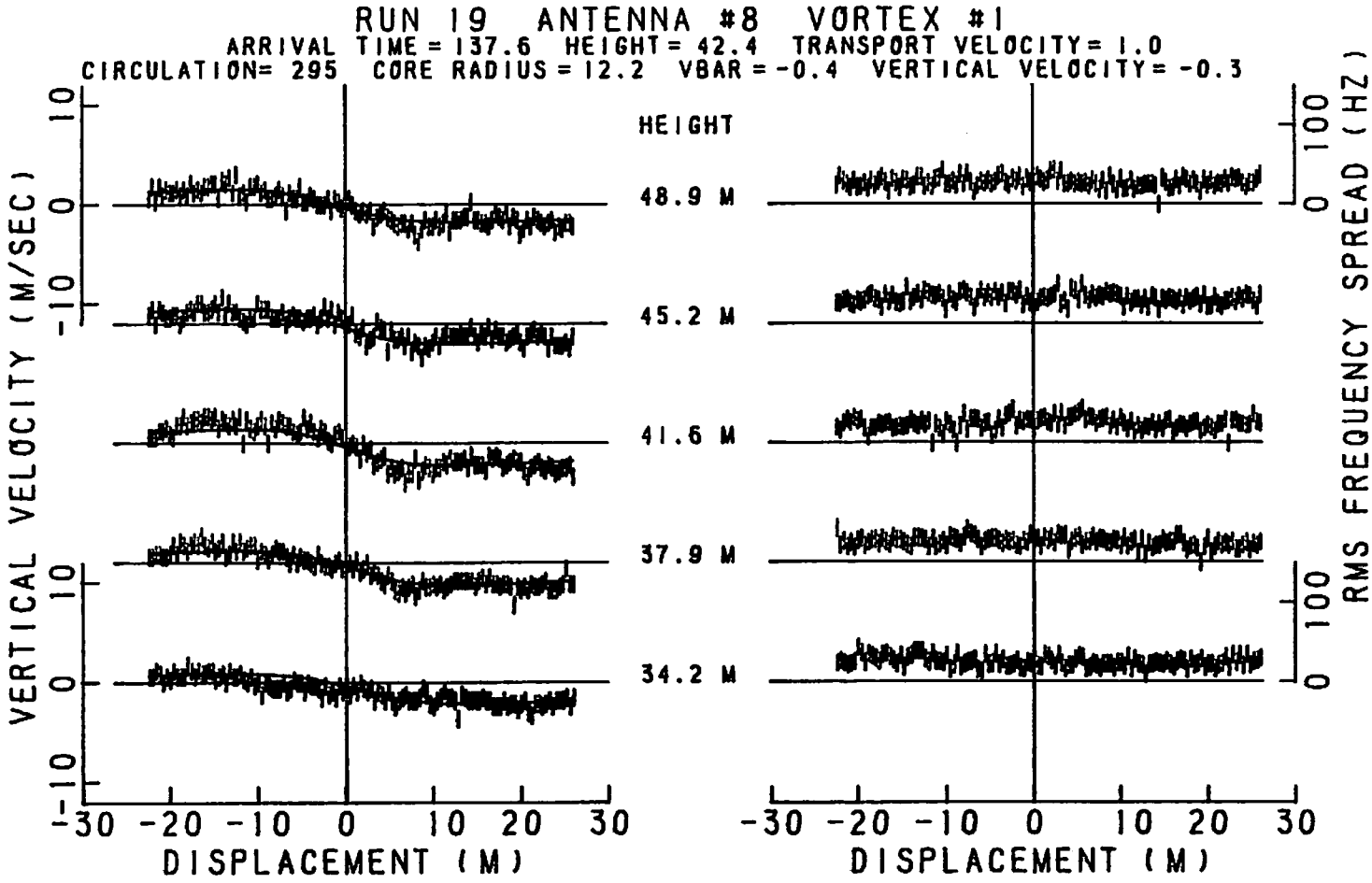

FIGURE 297. VELOCITY AND SPECTRAL WIDTH PROFILES FOR RUN 19, ANTENNA 8

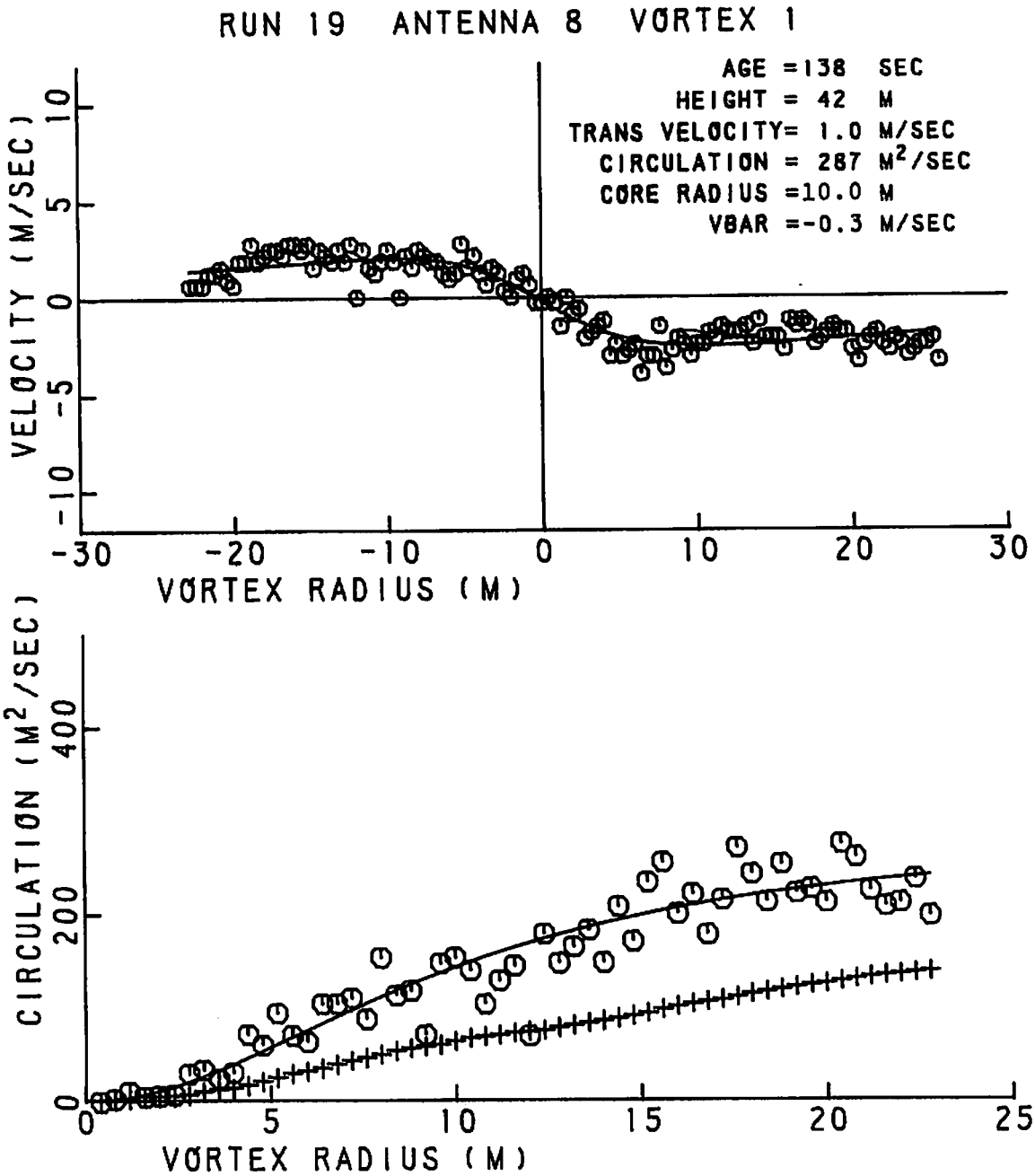

FIGURE 298. VELOCITY AND CIRCULATION PROFILES FOR RUN 19, ANTENNA 8

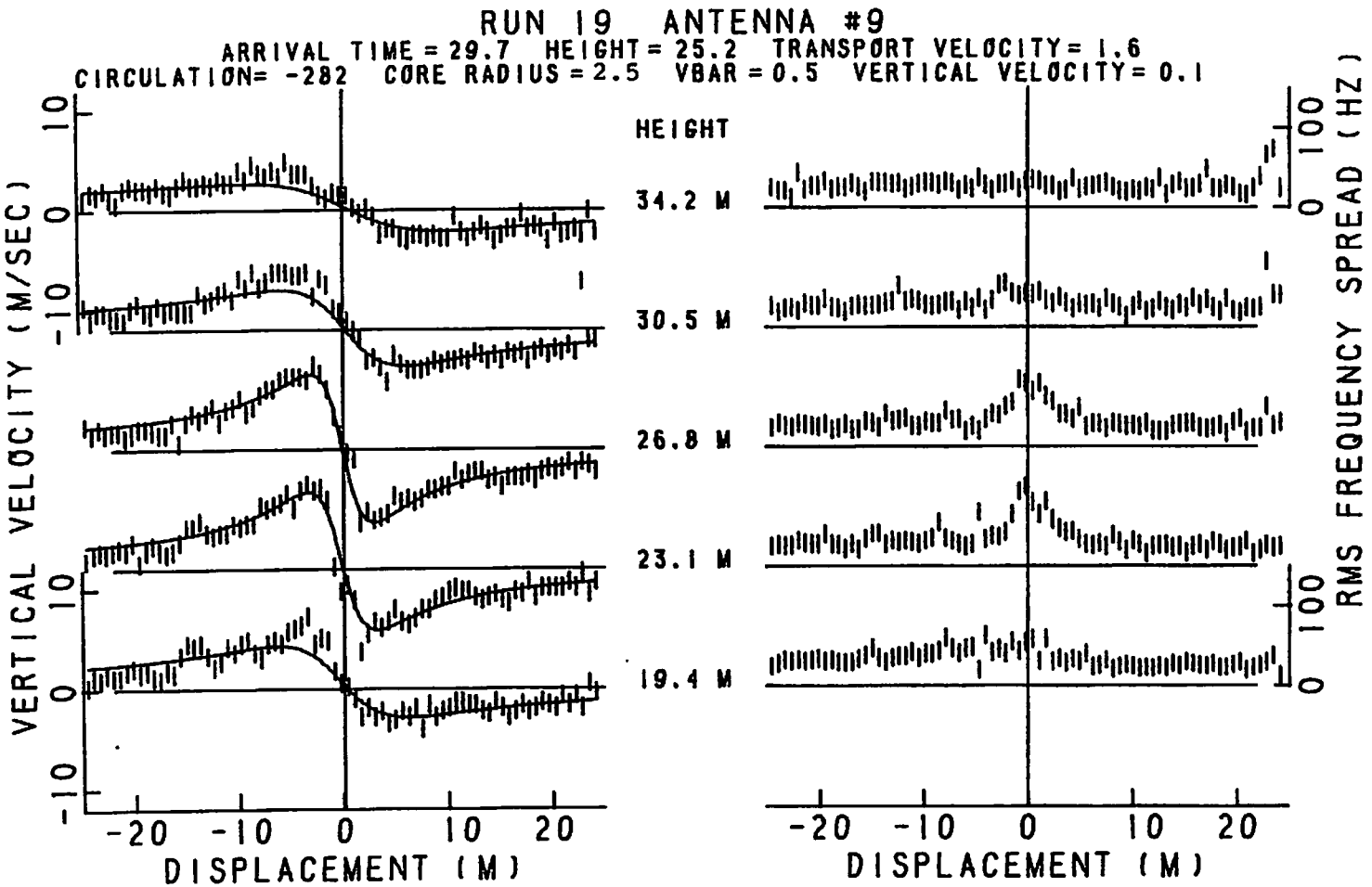

FIGURE 299. VELOCITY AND SPECTRAL WIDTH PROFILES FOR RUN 19, ANTENNA 9

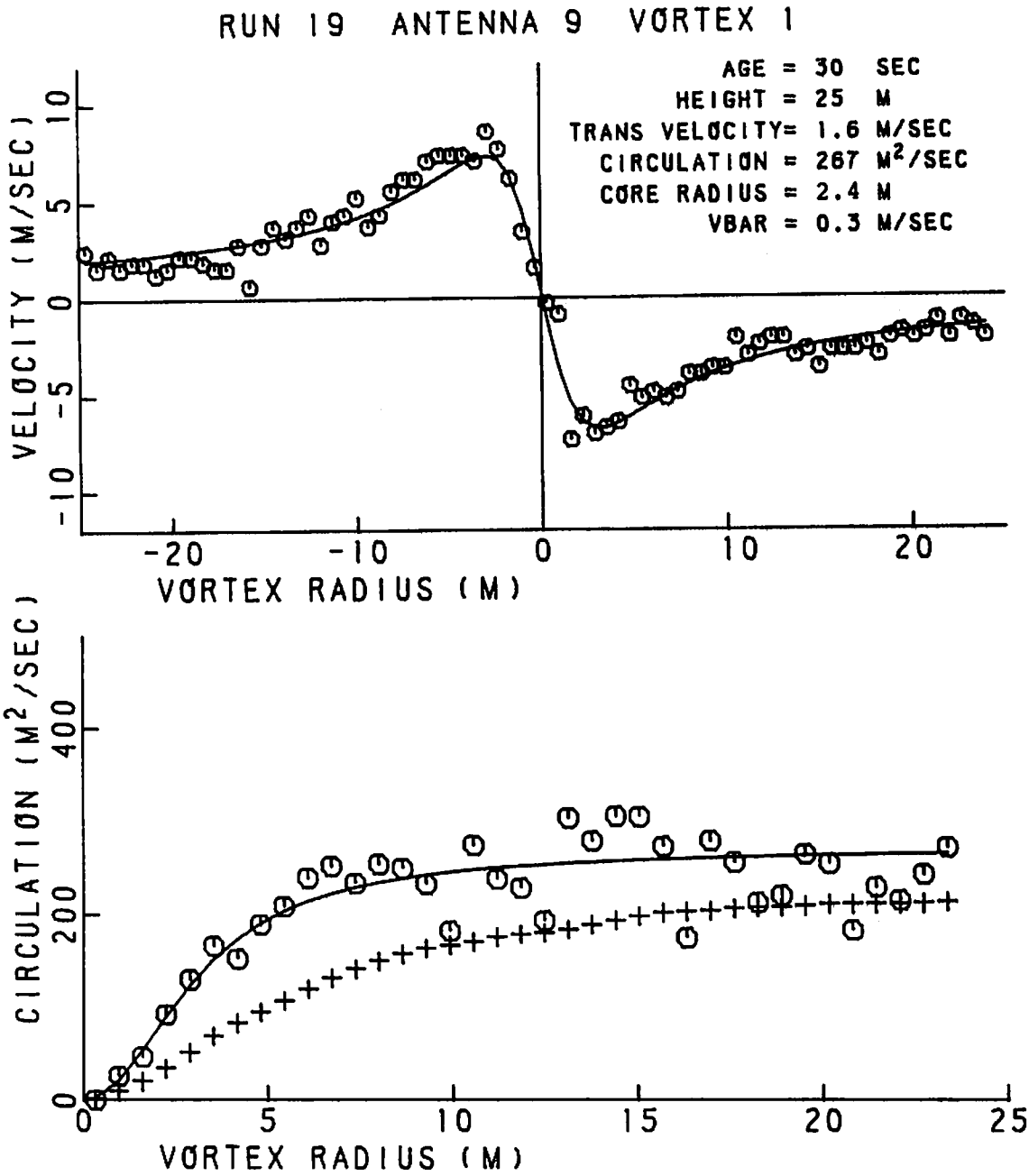

FIGURE 300. VELOCITY AND CIRCULATION PROFILES FOR RUN 19, ANTENNA 9

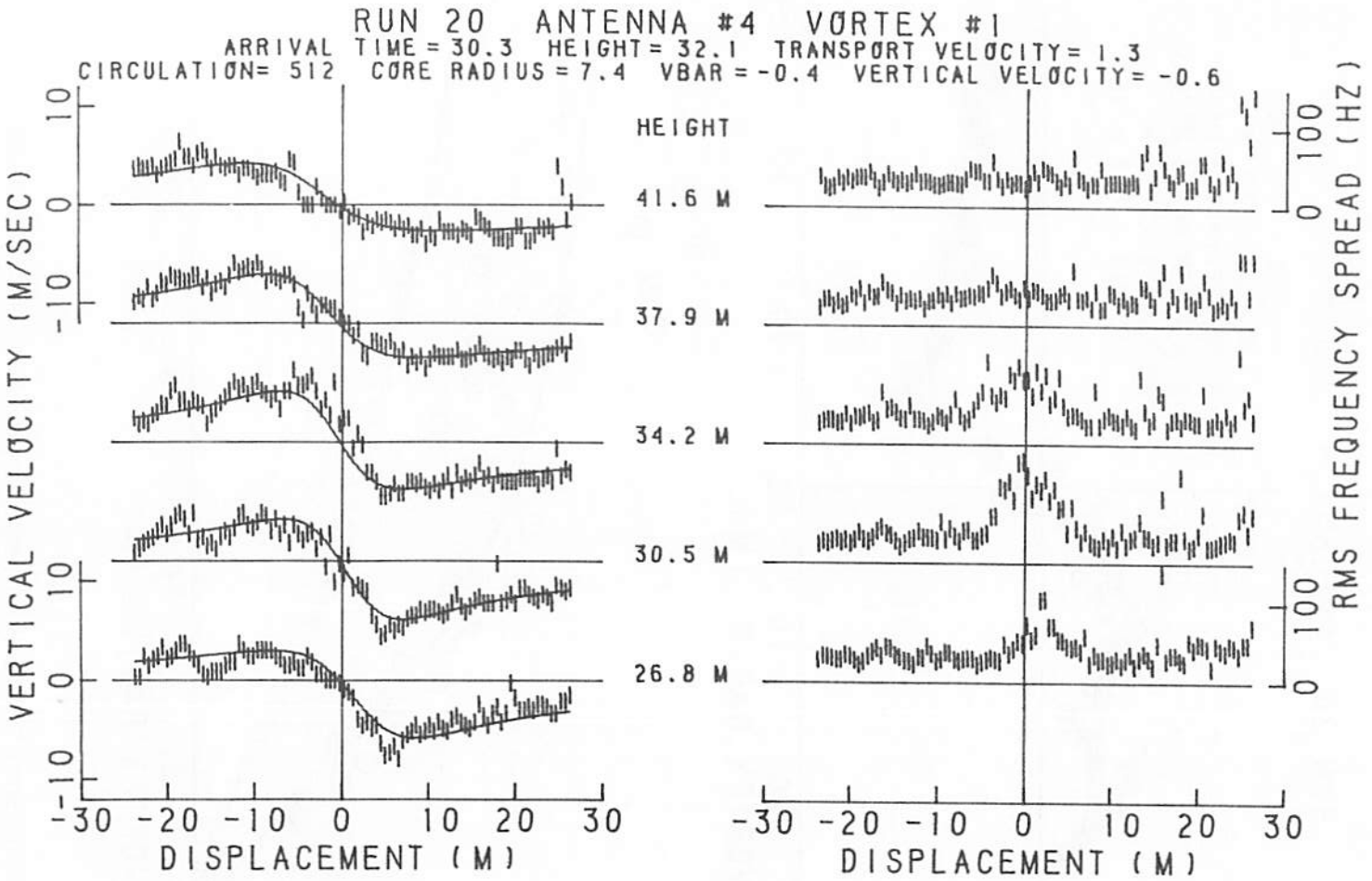

FIGURE 301. VELOCITY AND SPECTRAL WIDTH PROFILES FOR RUN 20, ANTENNA 4

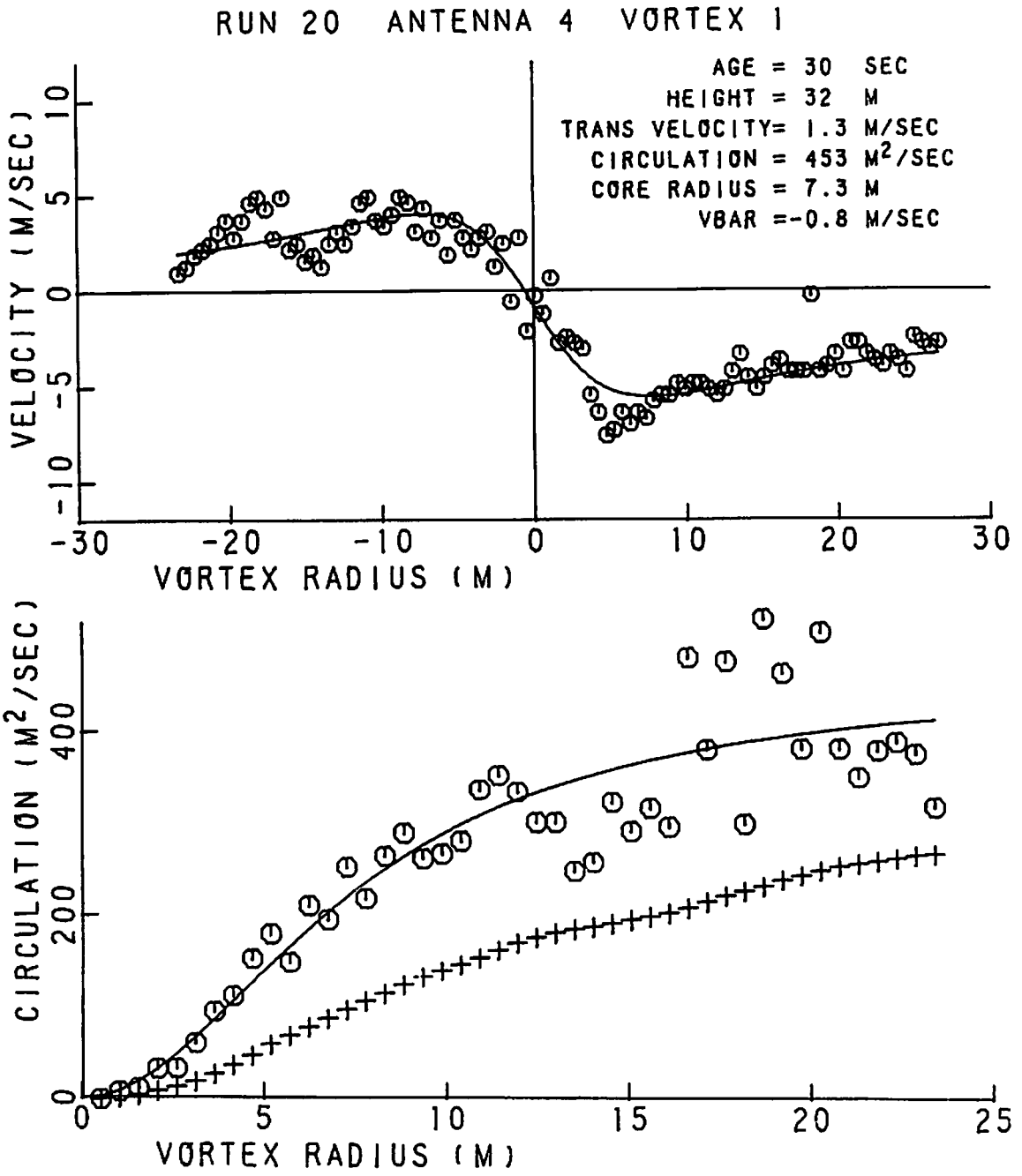

FIGURE 302. VELOCITY AND CIRCULATION PROFILES FOR RUN 20, ANTENNA 4

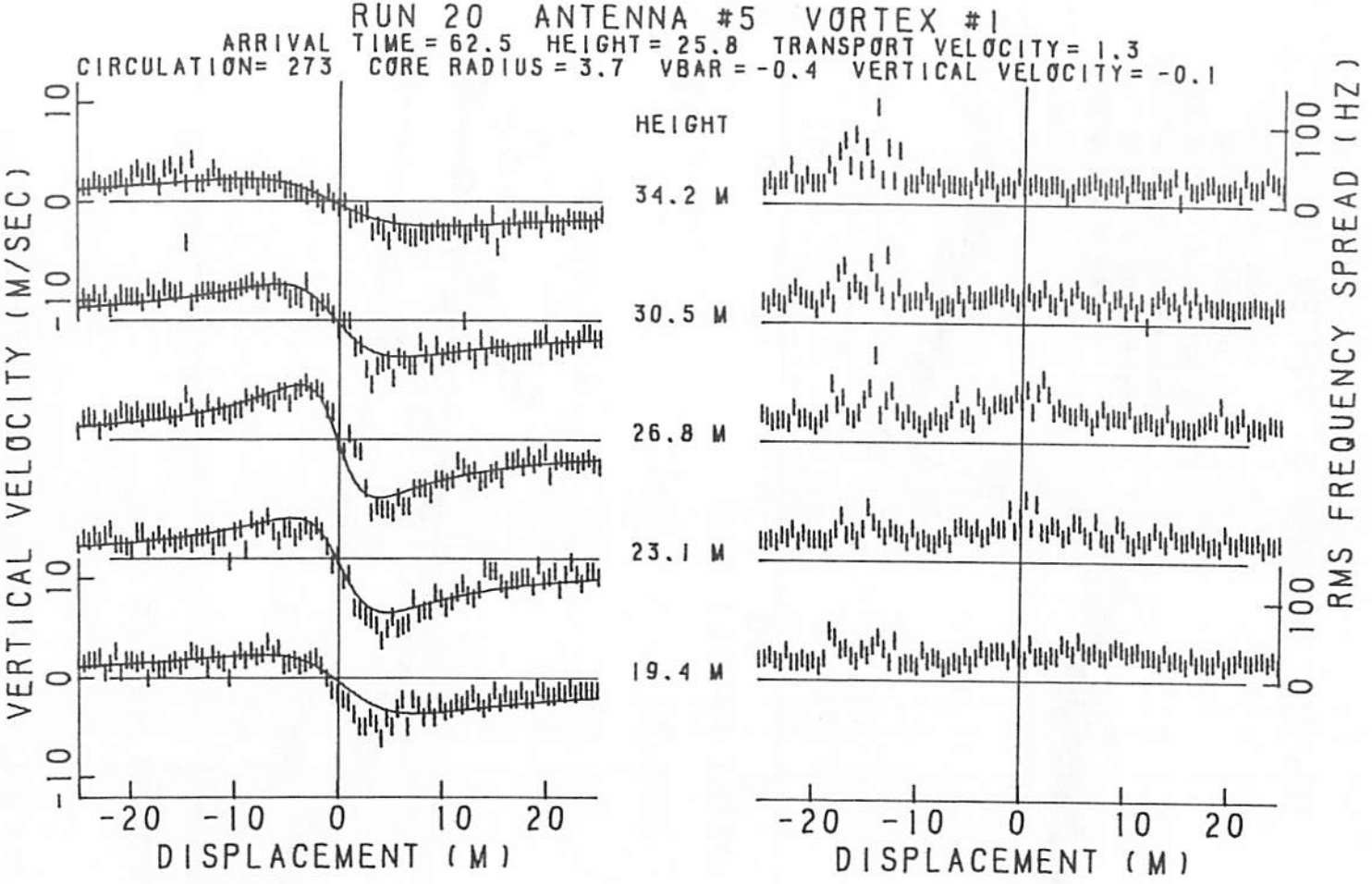

FIGURE 303. VELOCITY AND SPECTRAL WIDTH PROFILES FOR RUN 20, ANTENNA 5, VORTEX 1

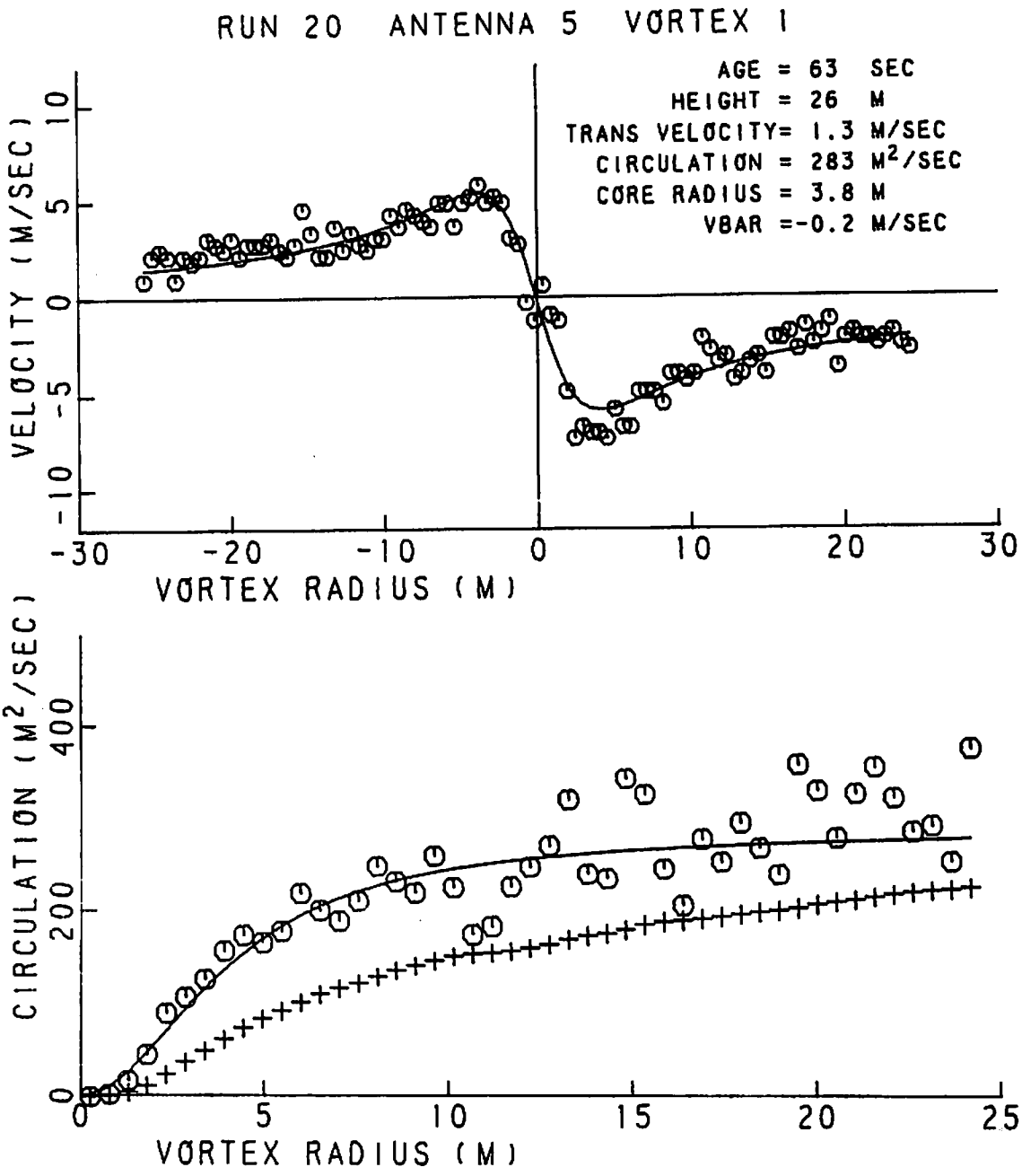

FIGURE 304. VELOCITY AND CIRCULATION PROFILES FOR RUN 20, ANTENNA 5, VORTEX 1

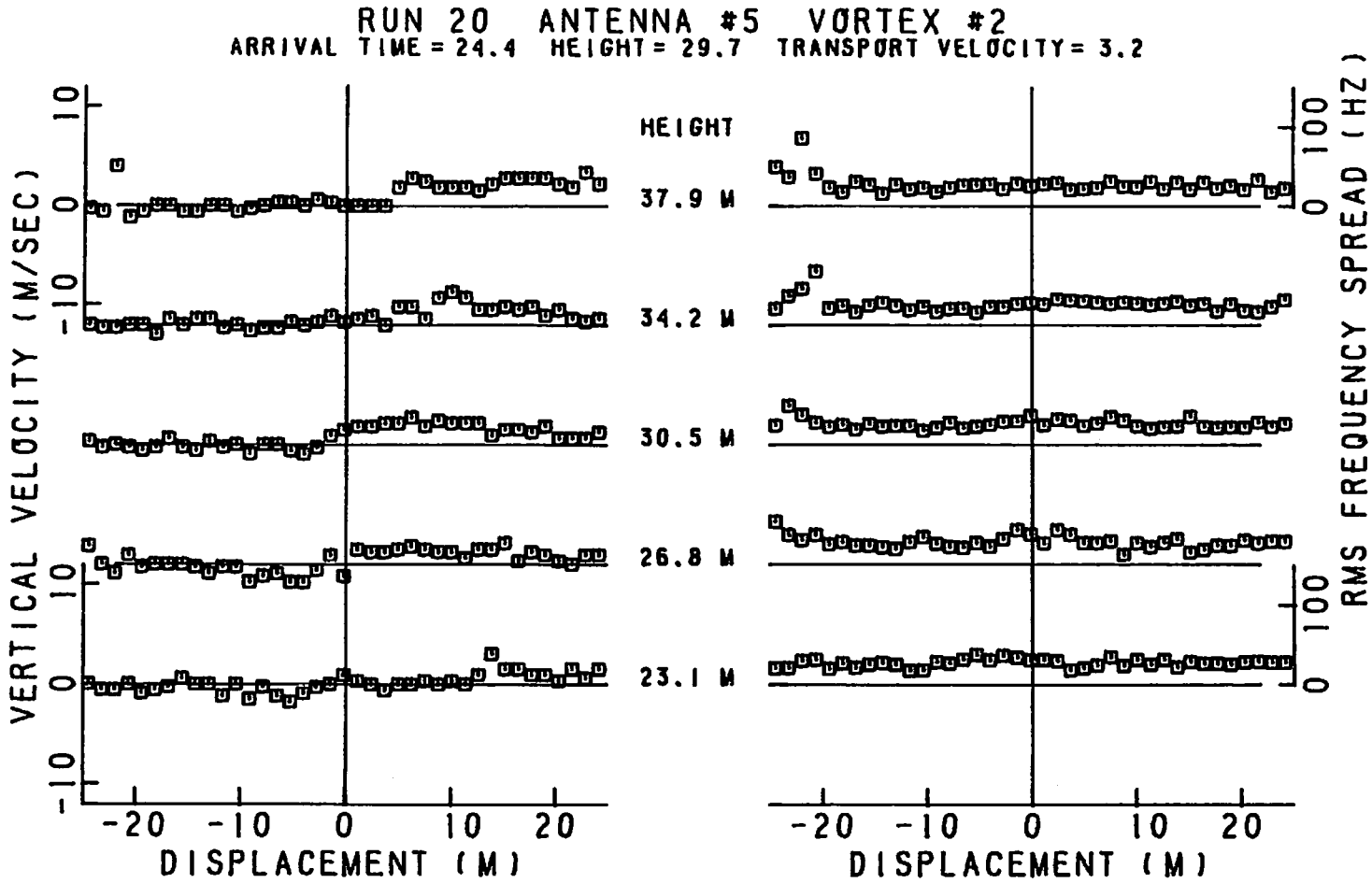

FIGURE 305. VELOCITY AND SPECTRAL WIDTH PROFILES FOR RUN 20, ANTENNA 5, VORTEX 2

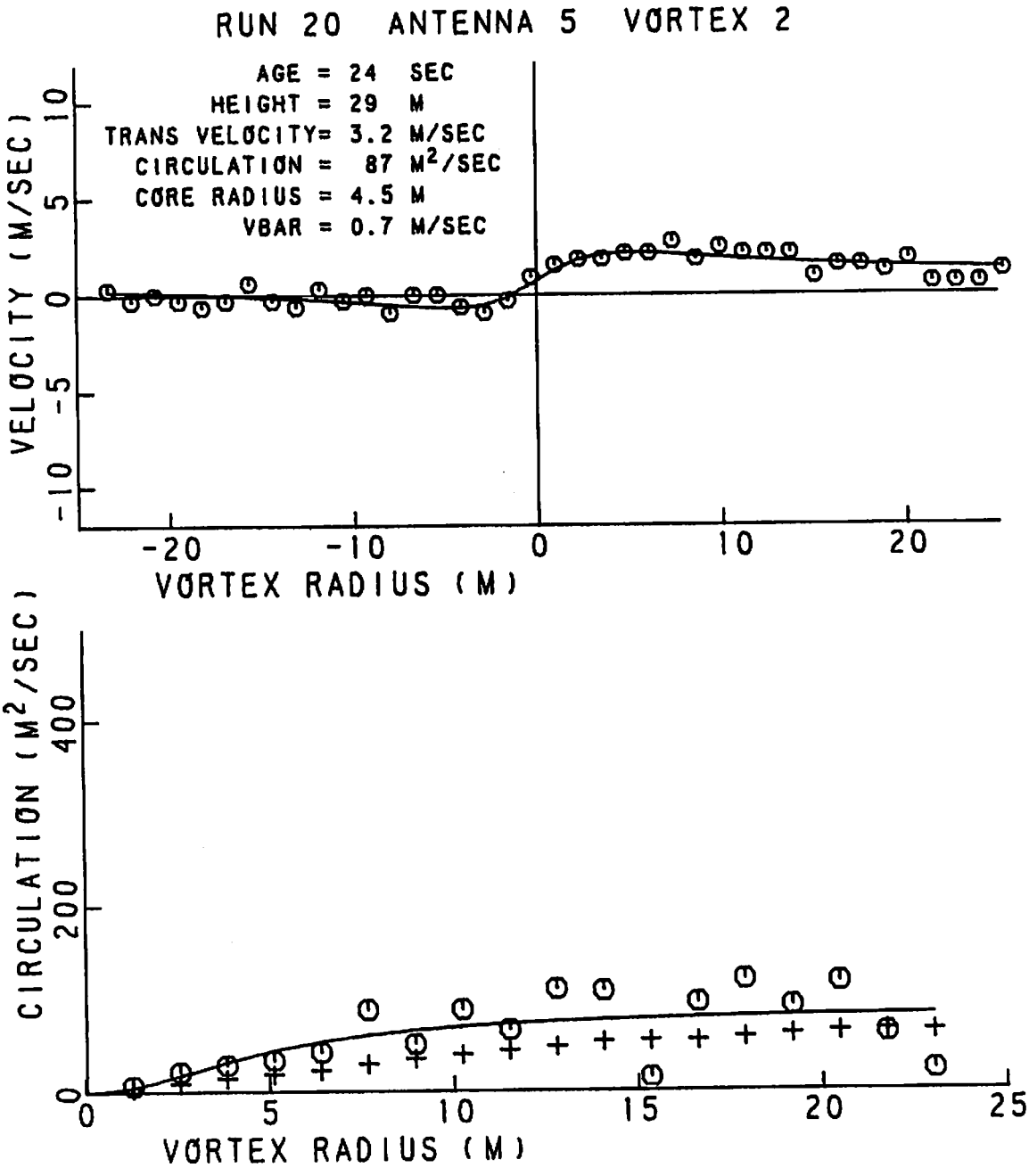

FIGURE 306. VELOCITY AND CIRCULATION PROFILES FOR RUN 20, ANTENNA 5, VORTEX 2

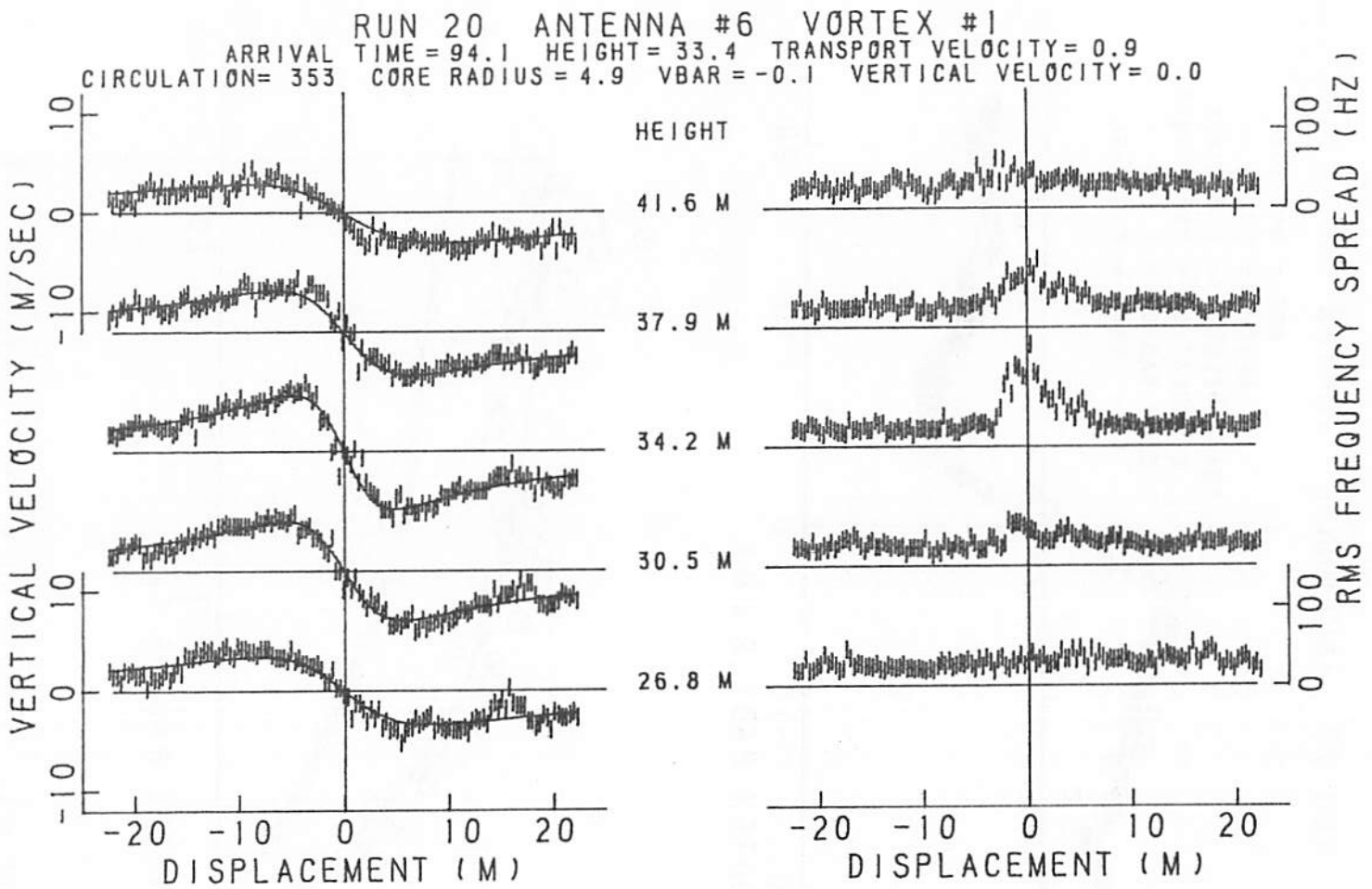

FIGURE 307. VELOCITY AND SPECTRAL WIDTH PROFILES FOR RUN 20, ANTENNA 6

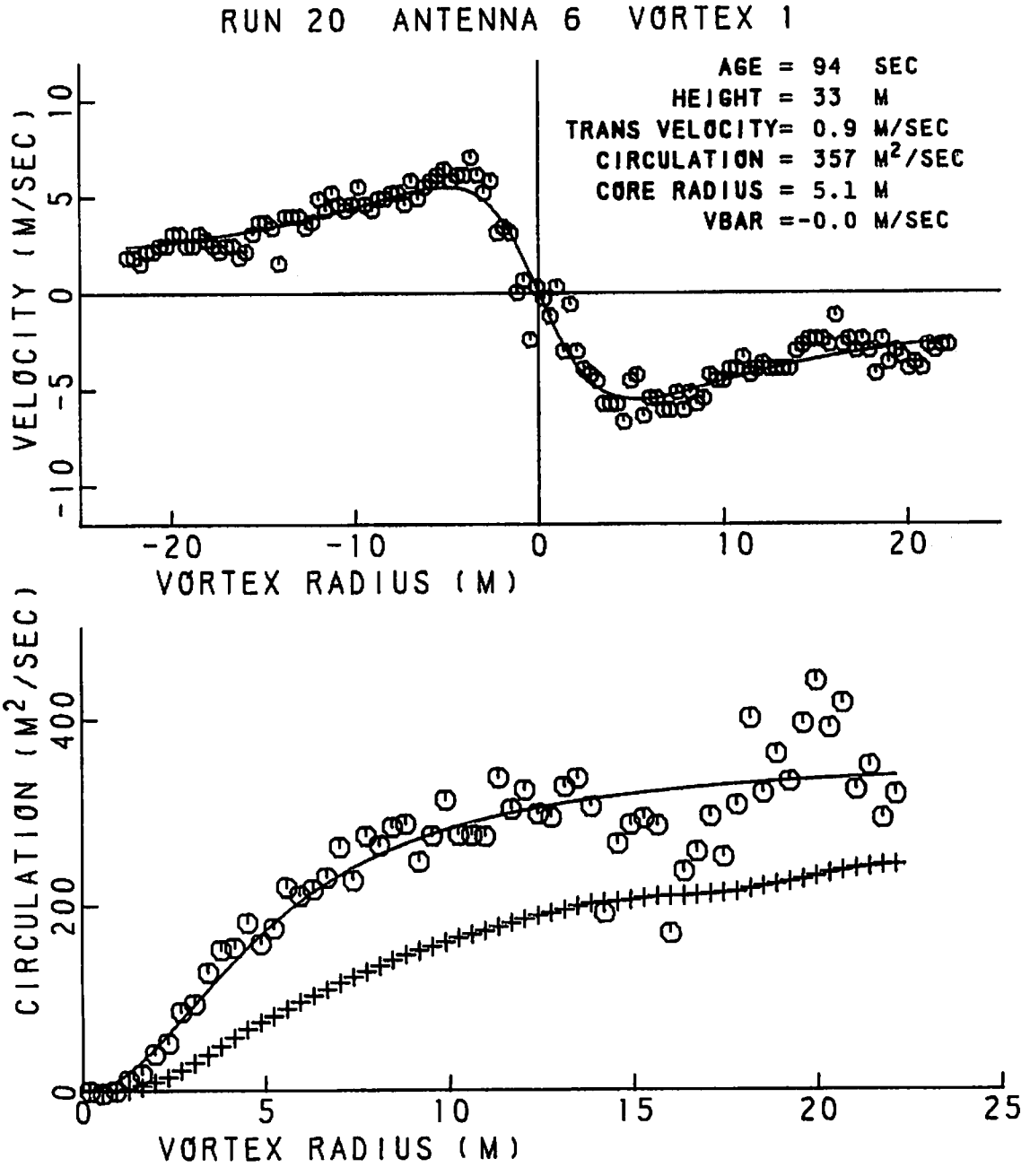

FIGURE 308. VELOCITY AND CIRCULATION PROFILES FOR RUN 20, ANTENNA 6

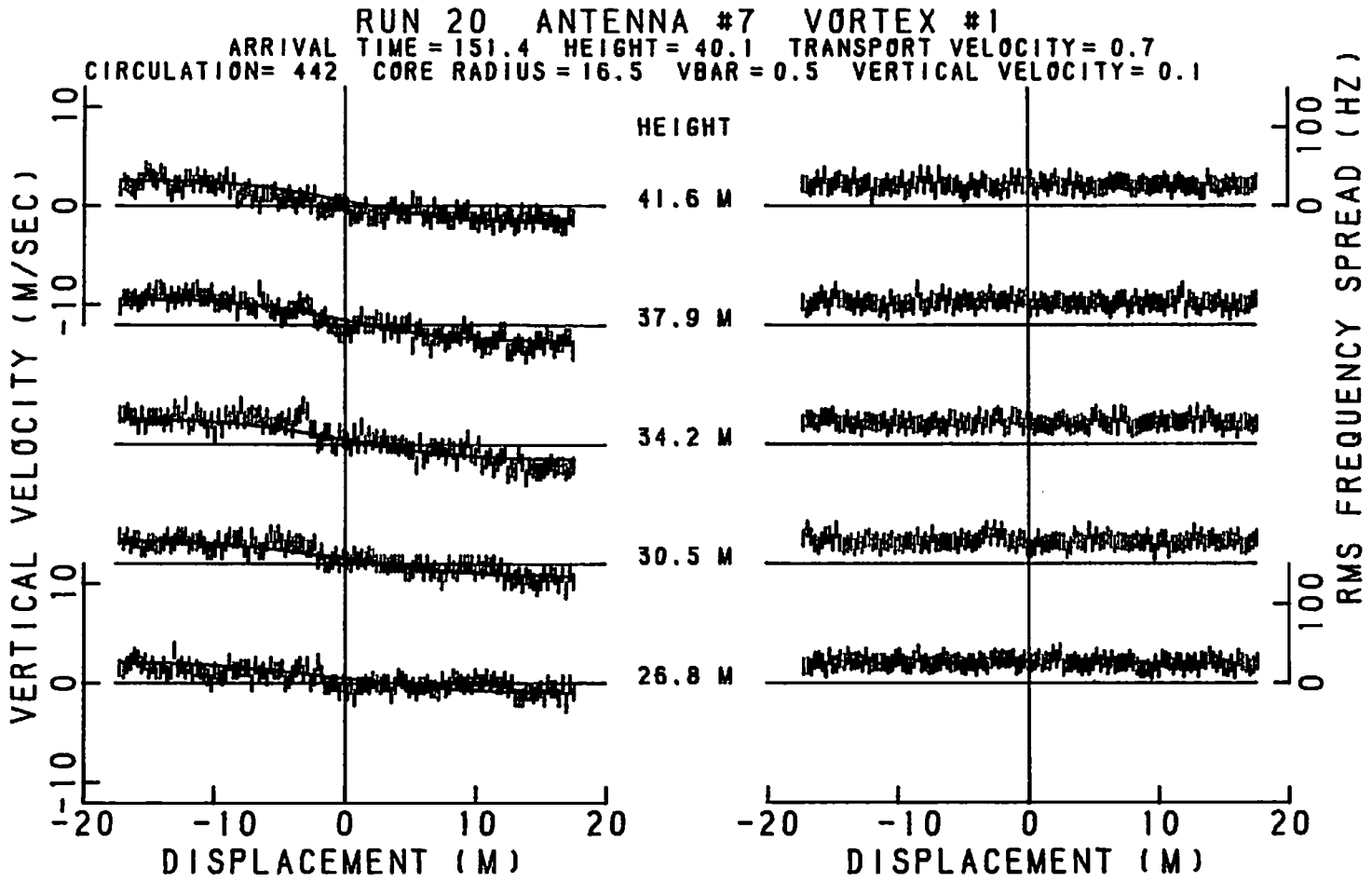

FIGURE 309. VELOCITY AND SPECTRAL WIDTH PROFILES FOR RUN 20, ANTENNA 7

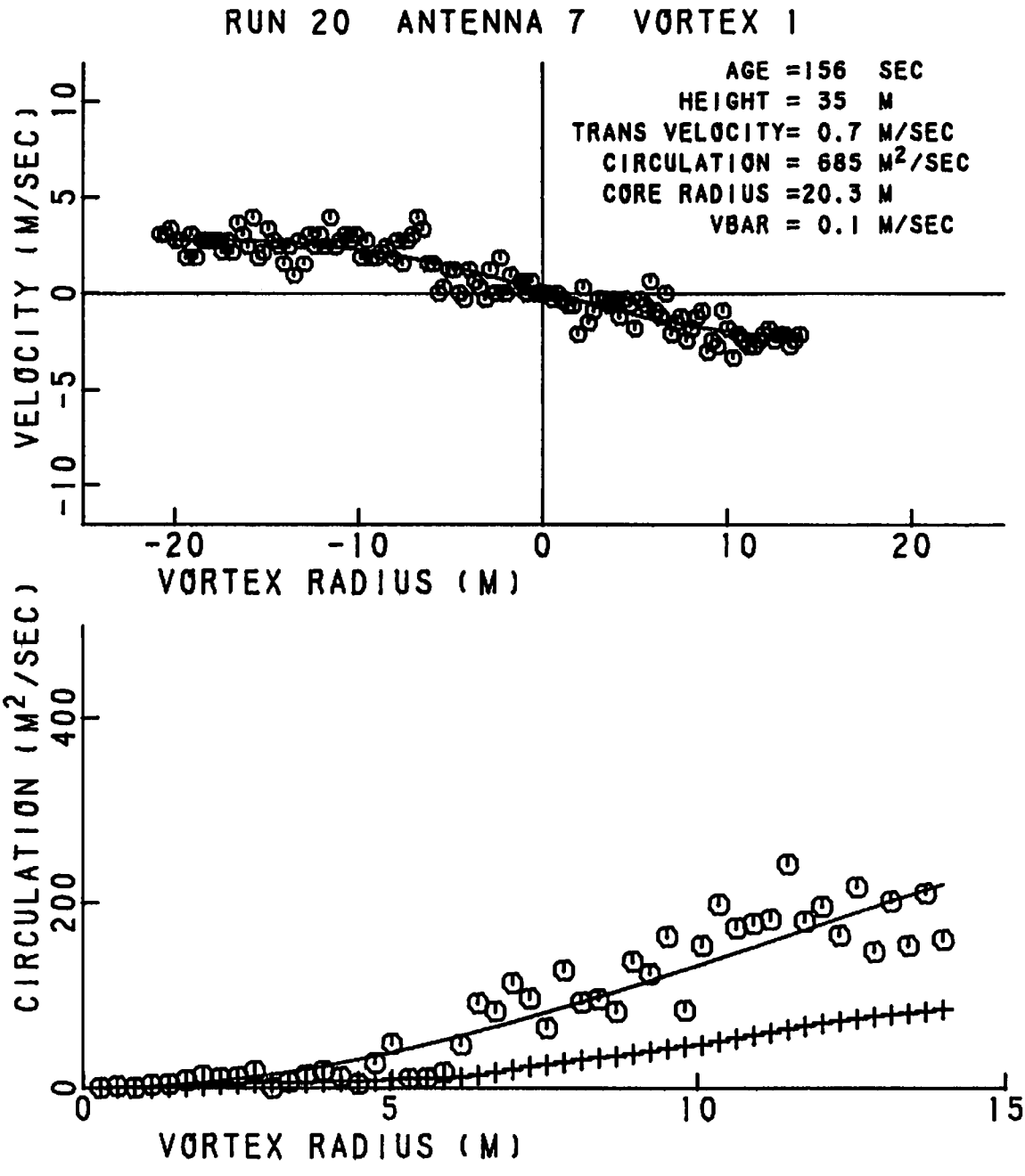

FIGURE 310. VELOCITY AND CIRCULATION PROFILES FOR RUN 20, ANTENNA 7

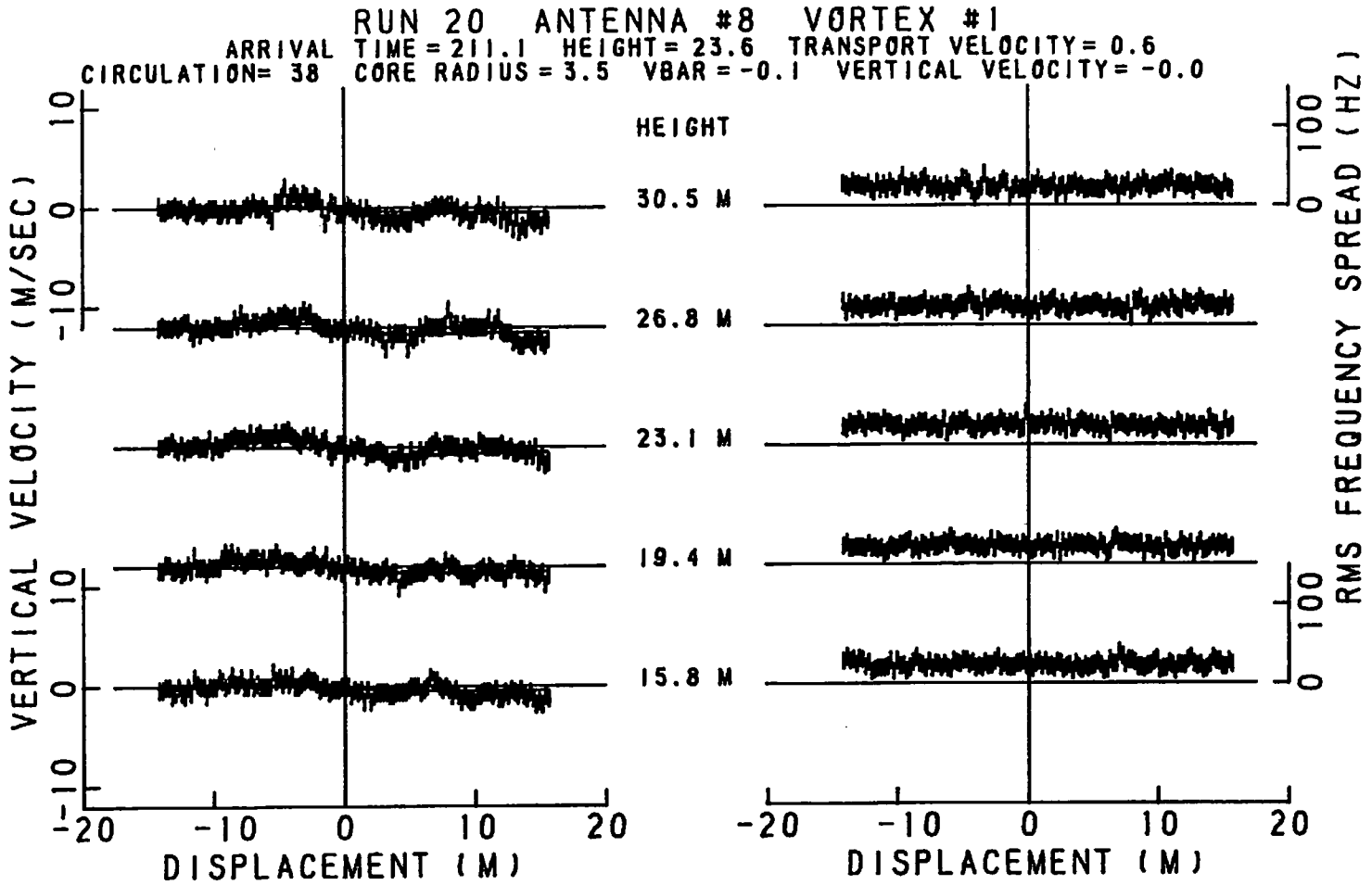

FIGURE 311. VELOCITY AND SPECTRAL WIDTH PROFILES FOR RUN 20, ANTENNA 8

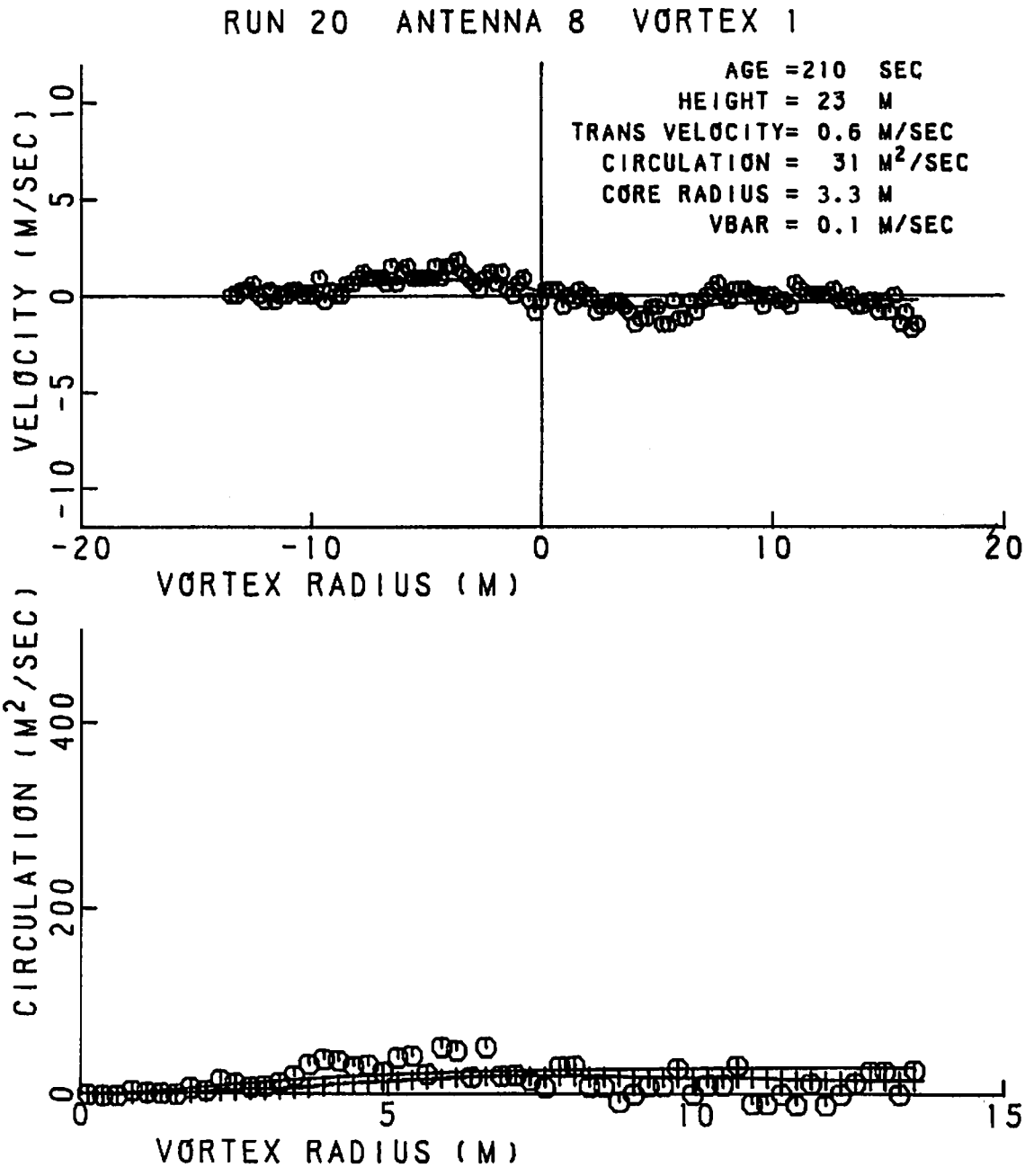

FIGURE 312. VELOCITY AND CIRCULATION PROFILES FOR RUN 20, ANTENNA 8

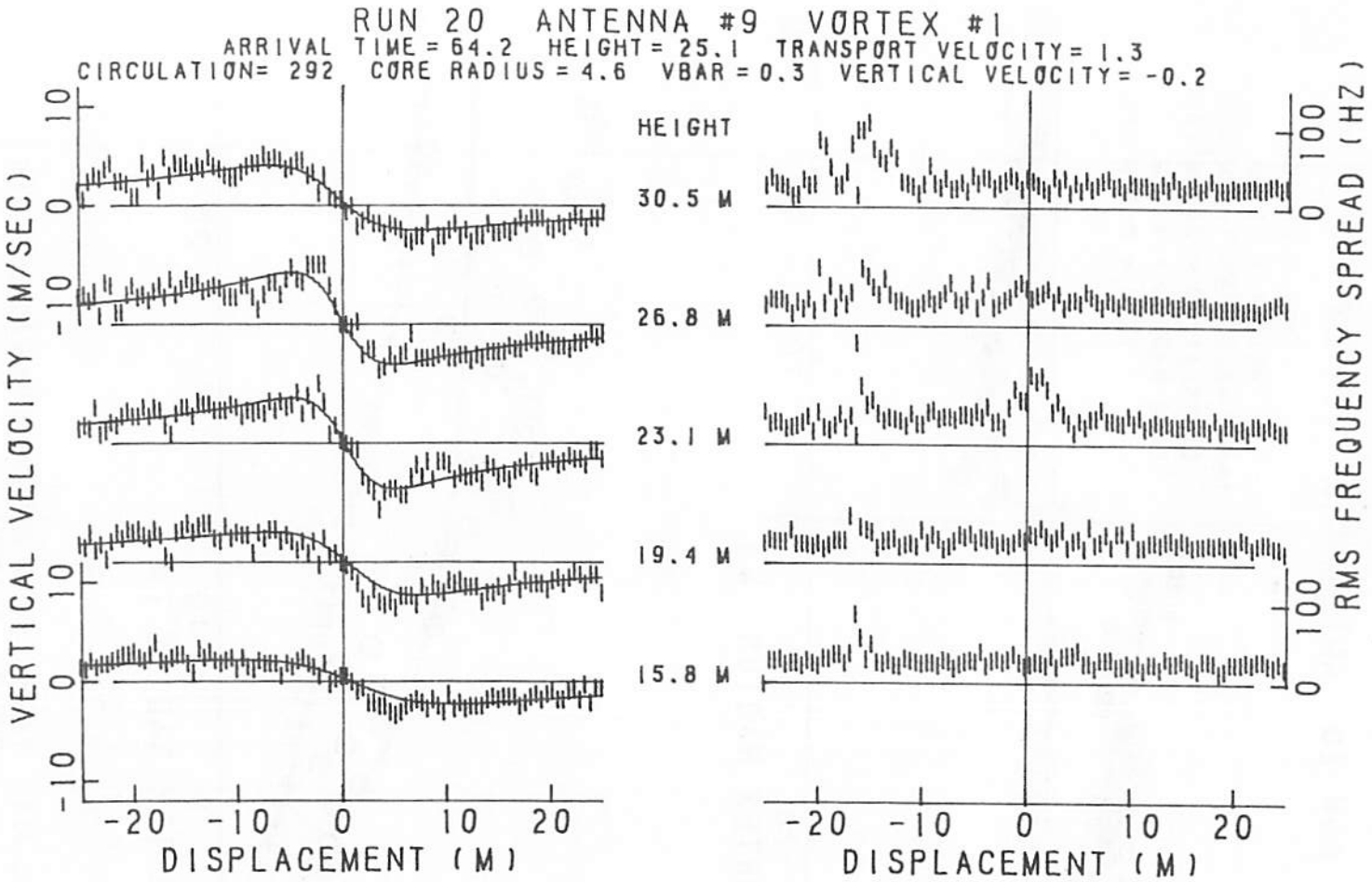

FIGURE 313. VELOCITY AND SPECTRAL WIDTH PROFILES FOR RUN 20, ANTENNA 9

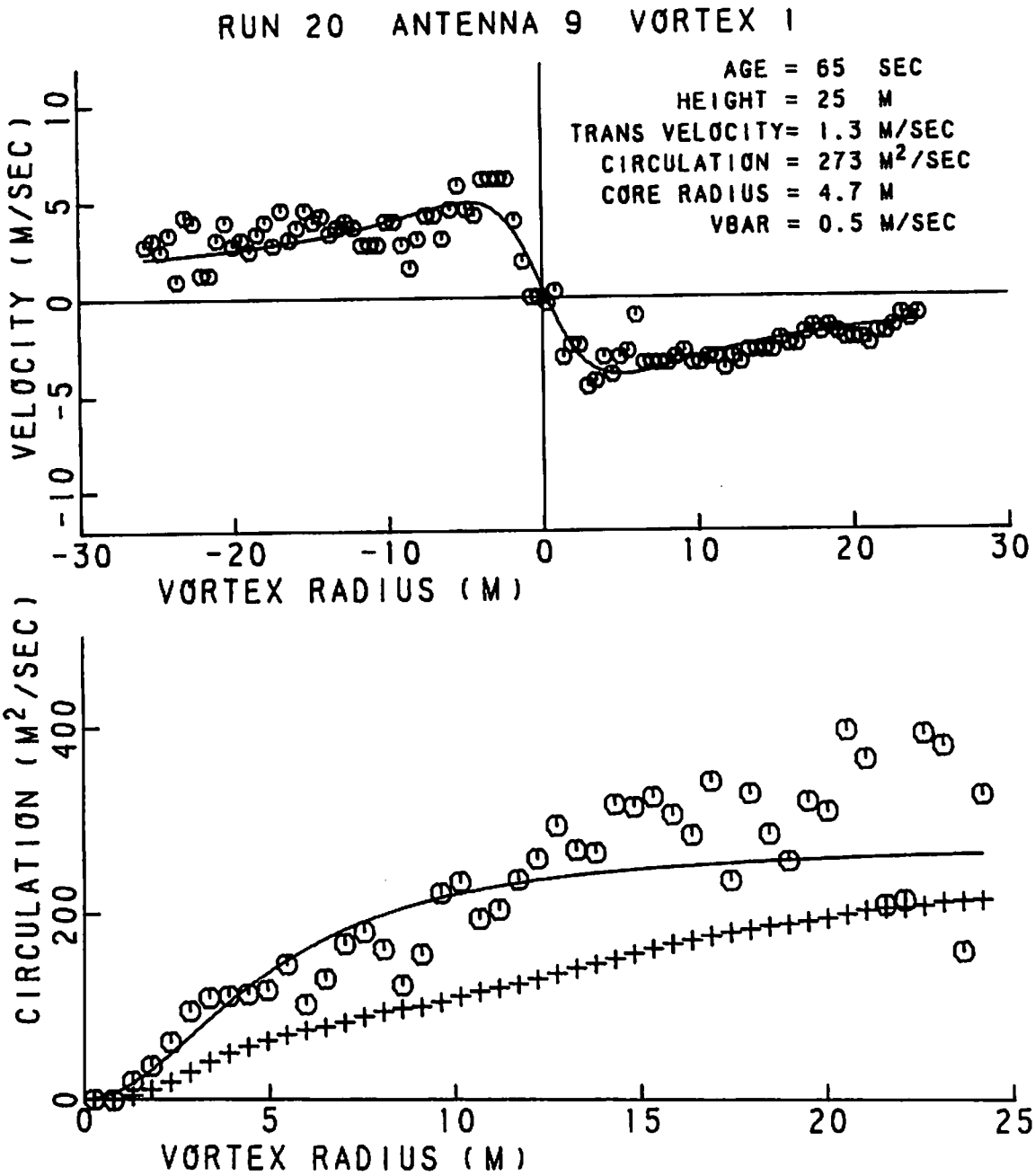

FIGURE 314. VELOCITY AND CIRCULATION PROFILES FOR RUN 20, ANTENNA 9

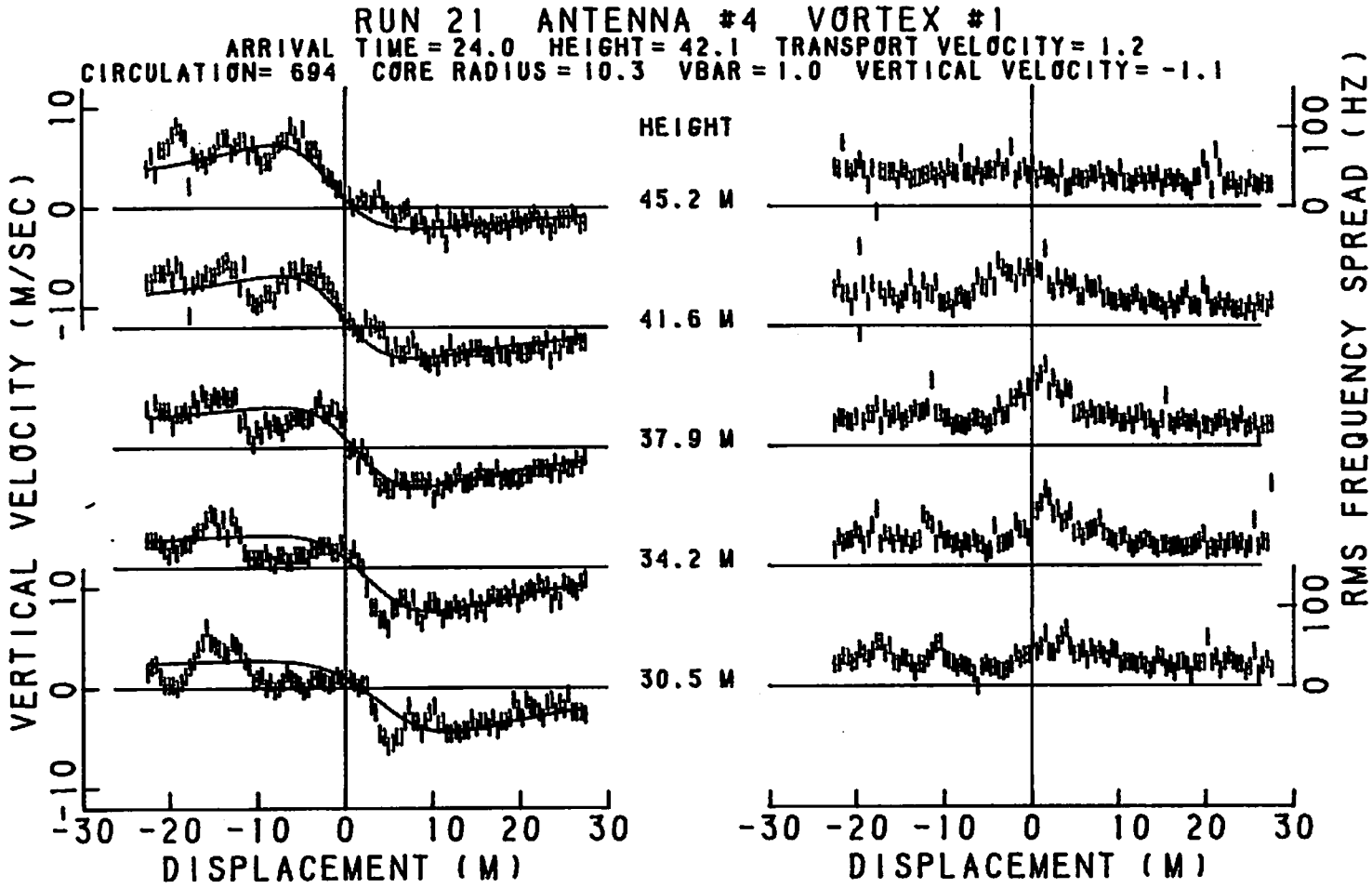

FIGURE 315. VELOCITY AND SPECTRAL WIDTH PROFILES FOR RUN 21, ANTENNA 4

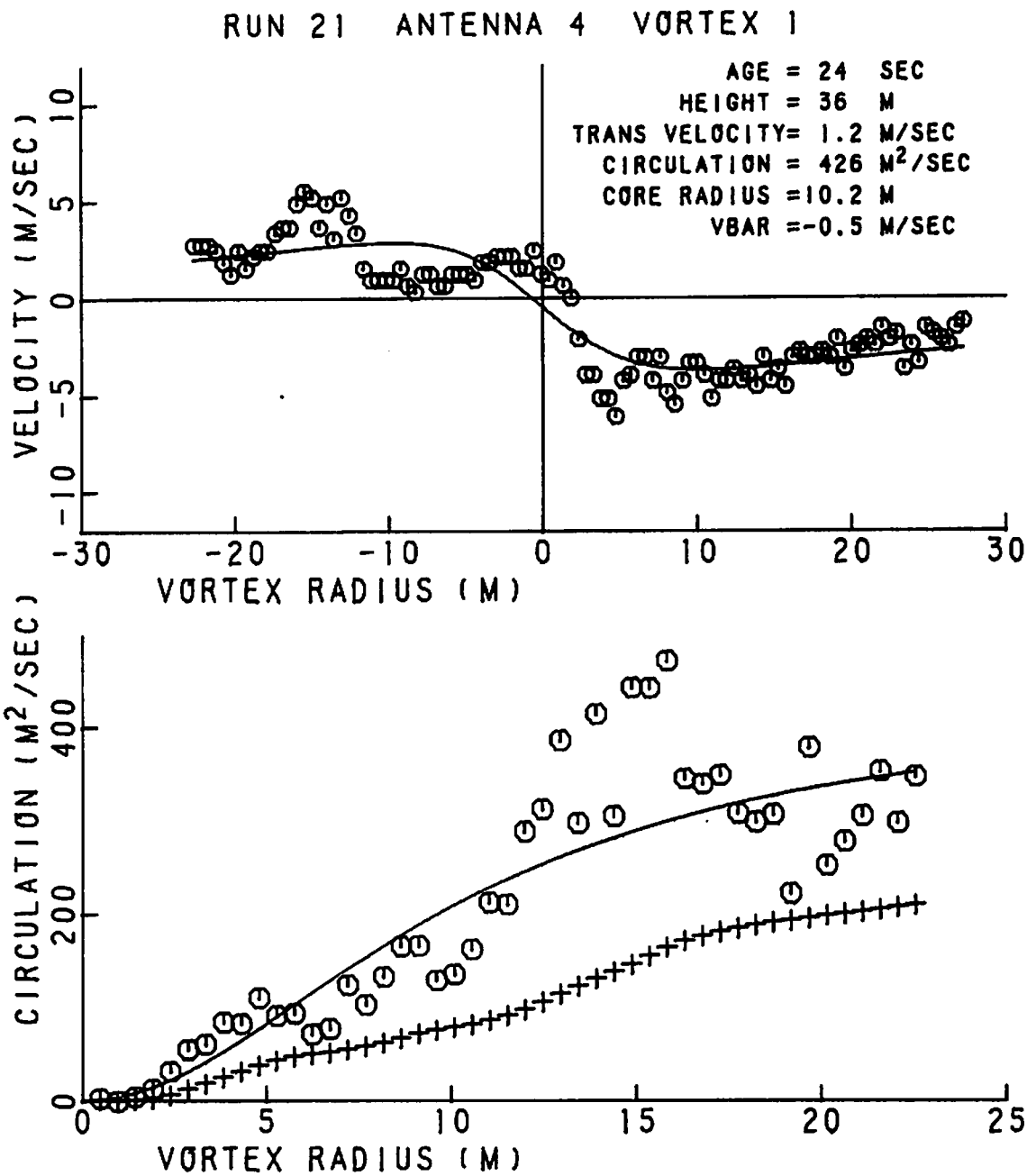

FIGURE 316. VELOCITY AND CIRCULATION PROFILES FOR RUN 21, ANTENNA 4

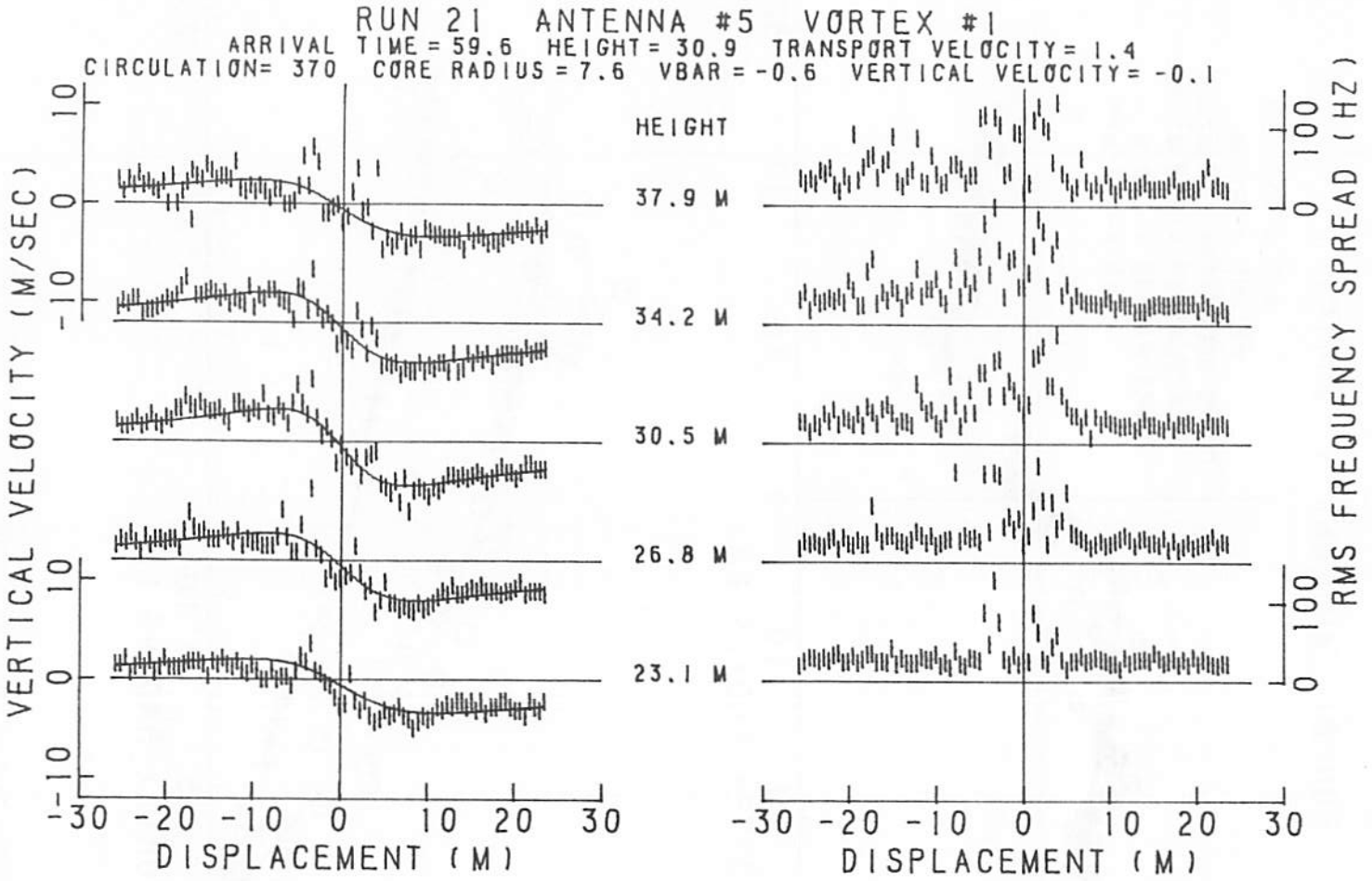

FIGURE 317. VELOCITY AND SPECTRAL WIDTH PROFILES FOR RUN 21, ANTENNA 5

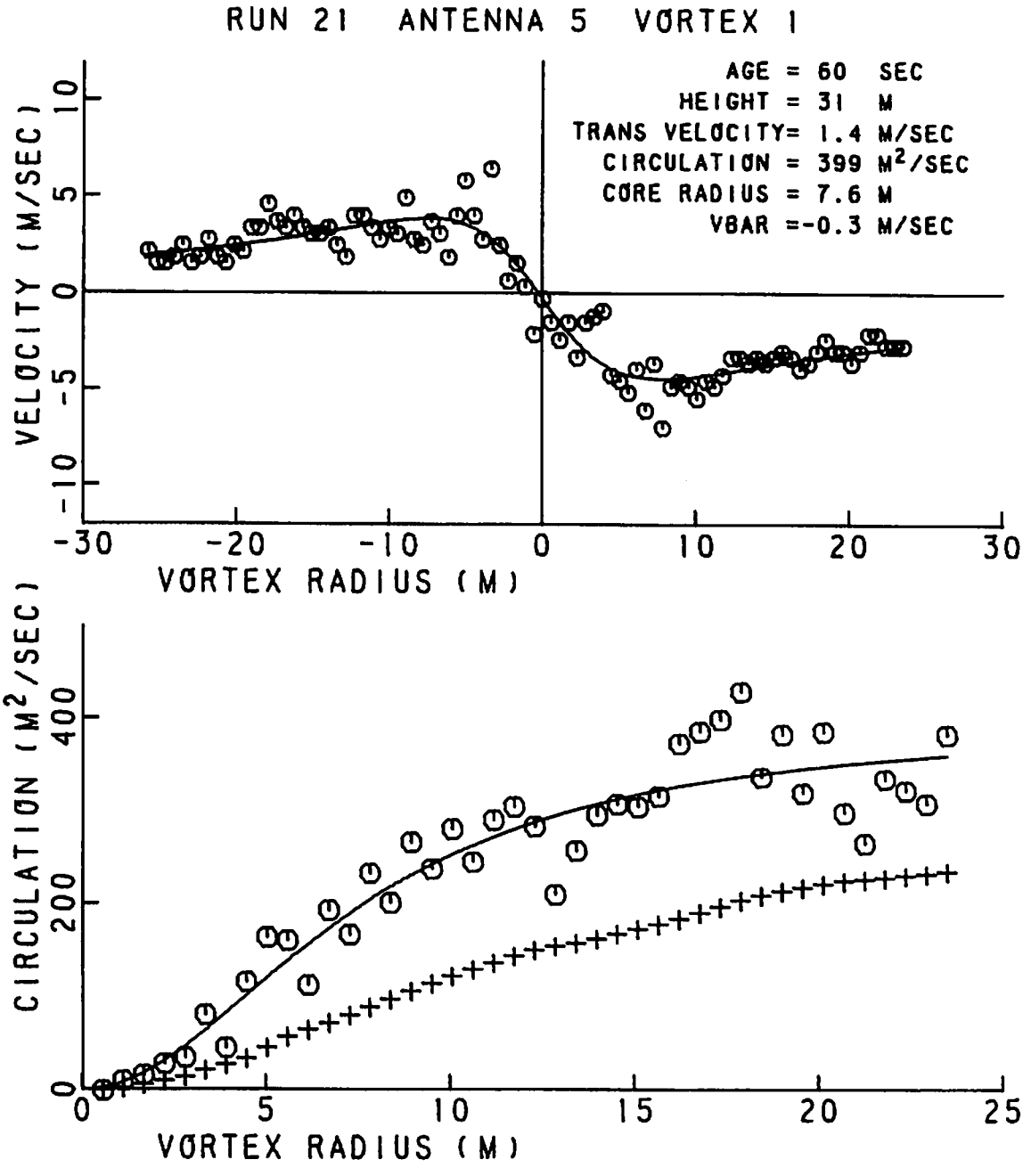

FIGURE 318. VELOCITY AND CIRCULATION PROFILES FOR RUN 21, ANTENNA 5

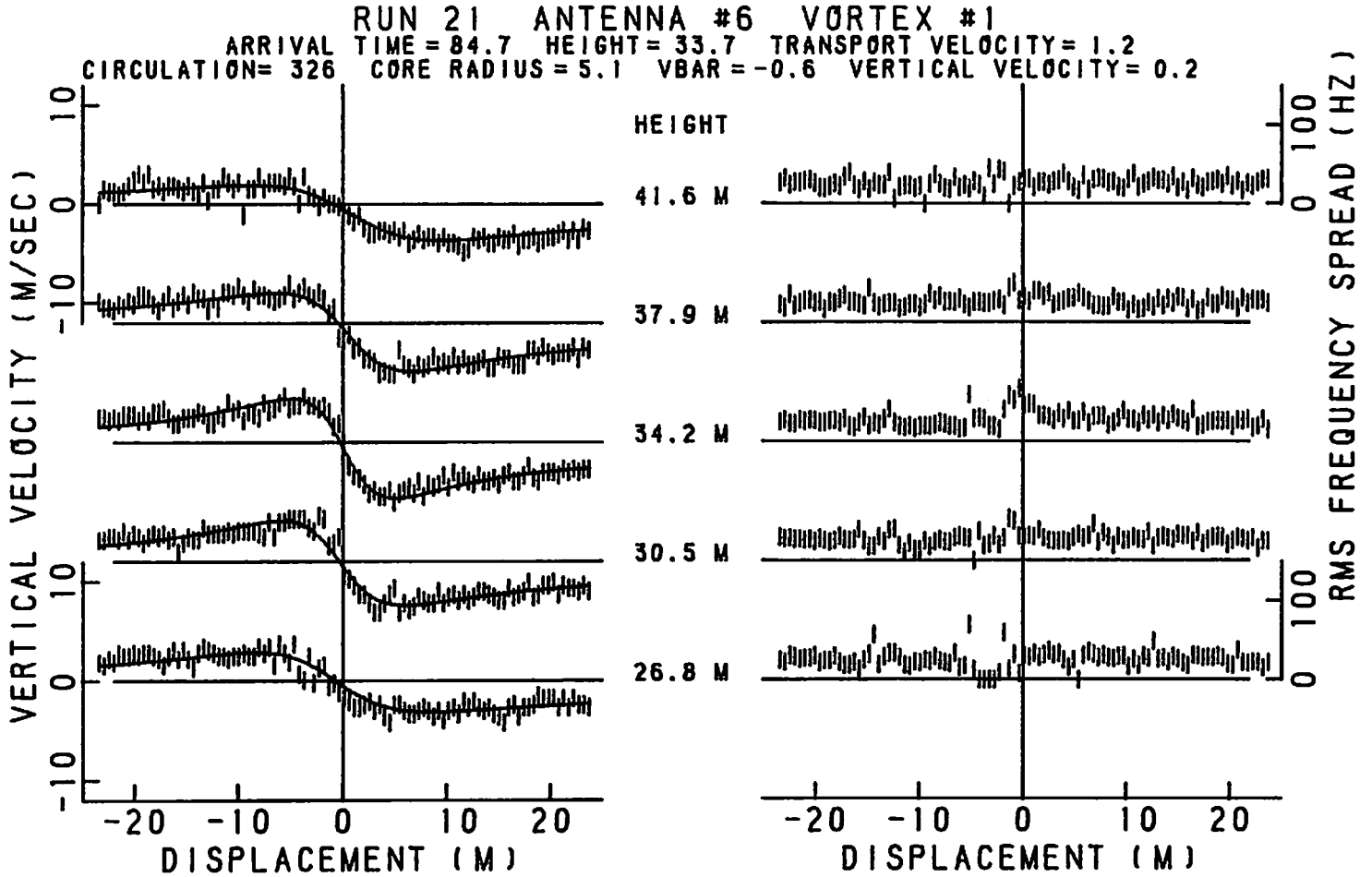

FIGURE 319. VELOCITY AND SPECTRAL WIDTH PROFILES FOR RUN 21, ANTENNA 6

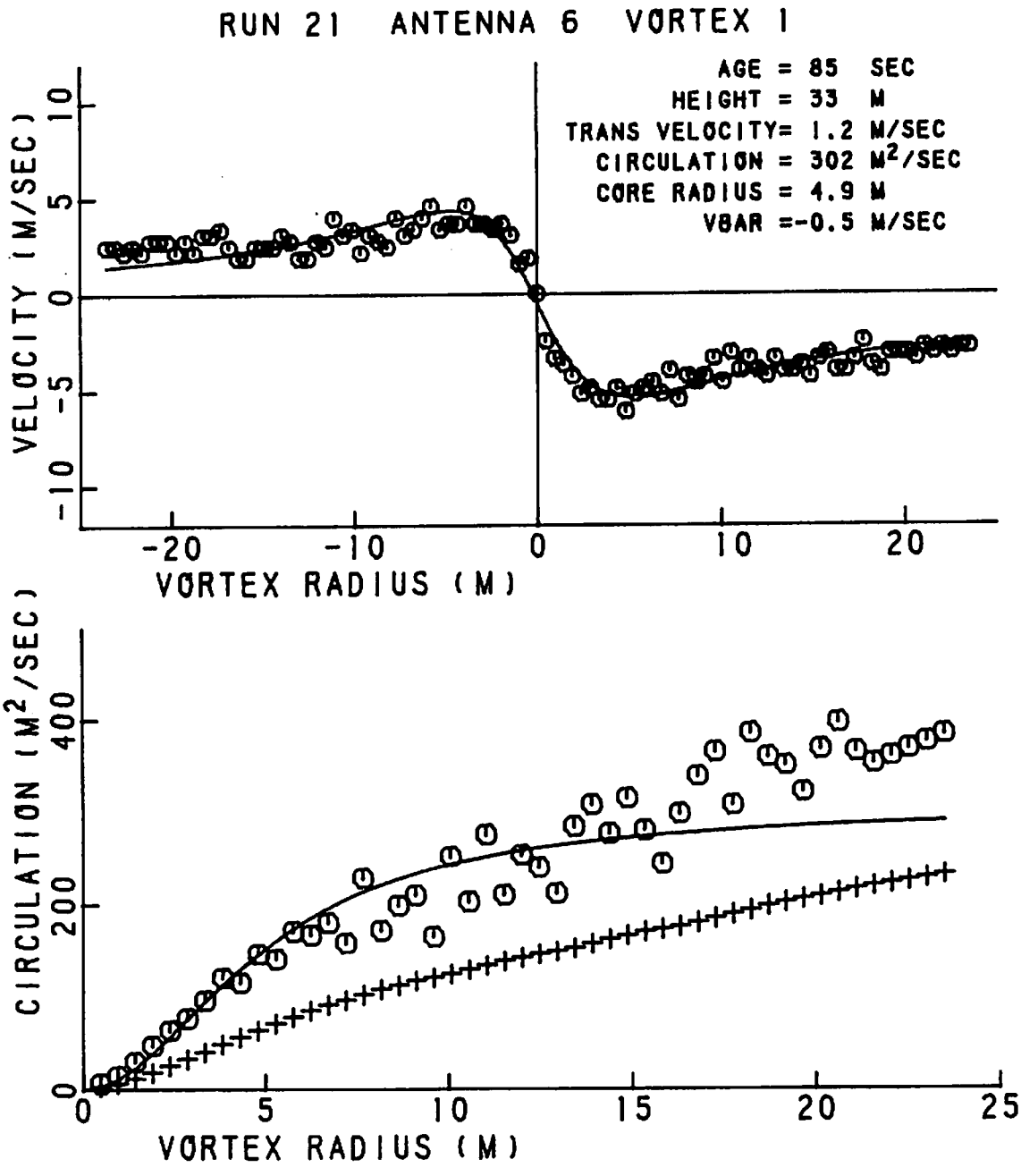

FIGURE 320. VELOCITY AND CIRCULATION PROFILES FOR RUN 21, ANTENNA 6

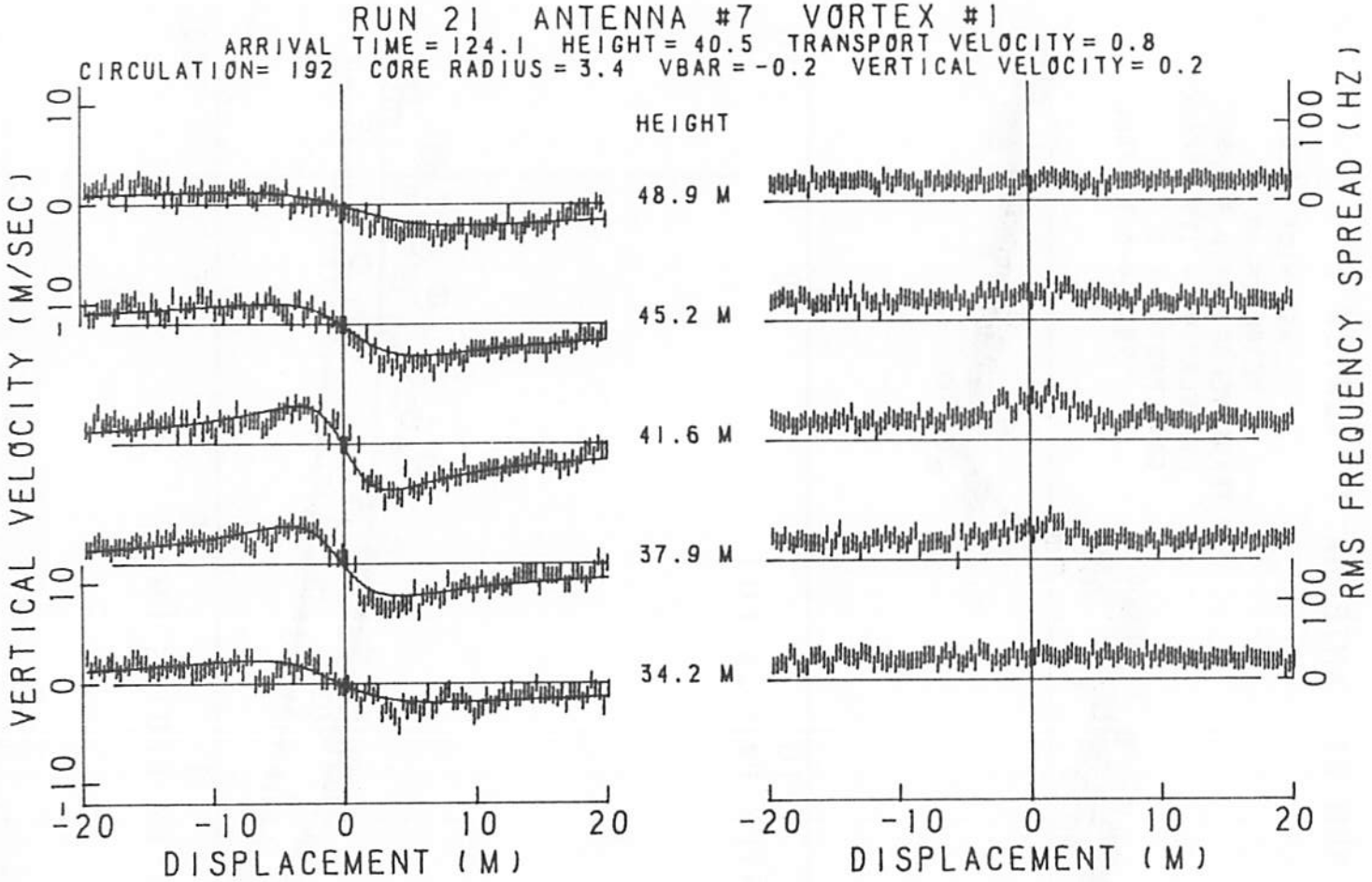

FIGURE 321. VELOCITY AND SPECTRAL WIDTH PROFILES FOR RUN 21, ANTENNA 7

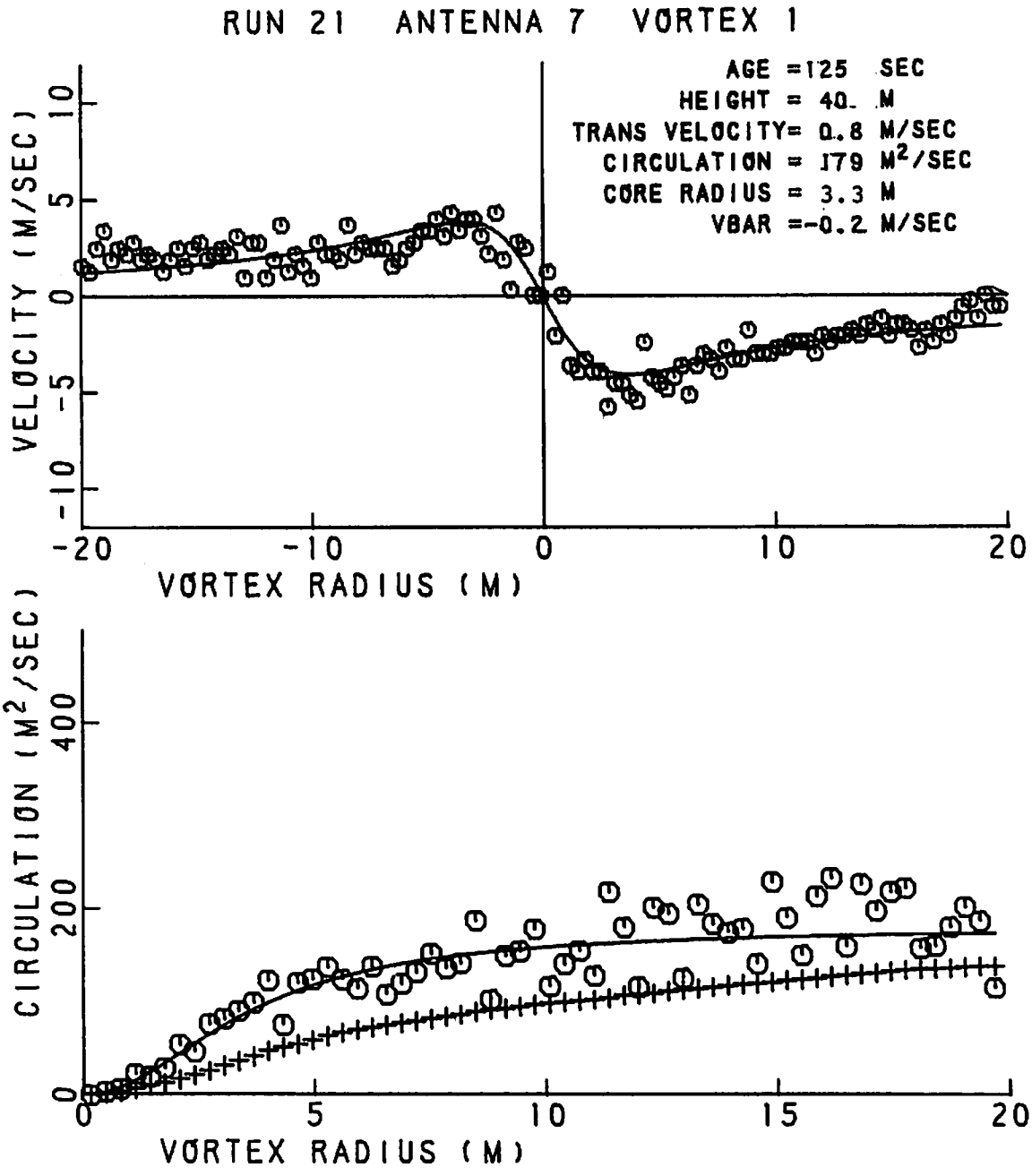

FIGURE 322. VELOCITY AND CIRCULATION PROFILES FOR RUN 21, ANTENNA 7

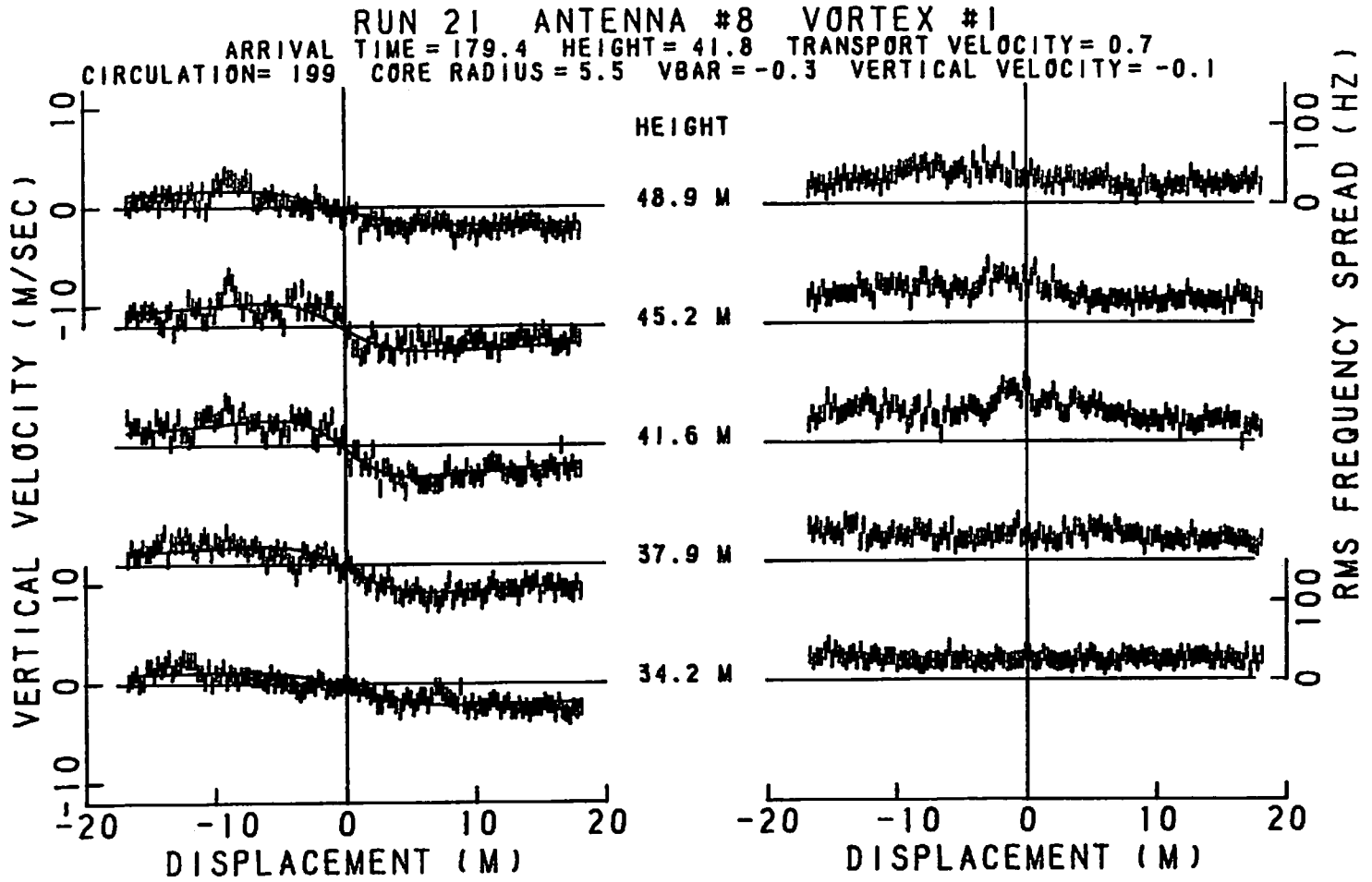

FIGURE 323. VELOCITY AND SPECTRAL WIDTH PROFILES FOR RUN 21, ANTENNA 8

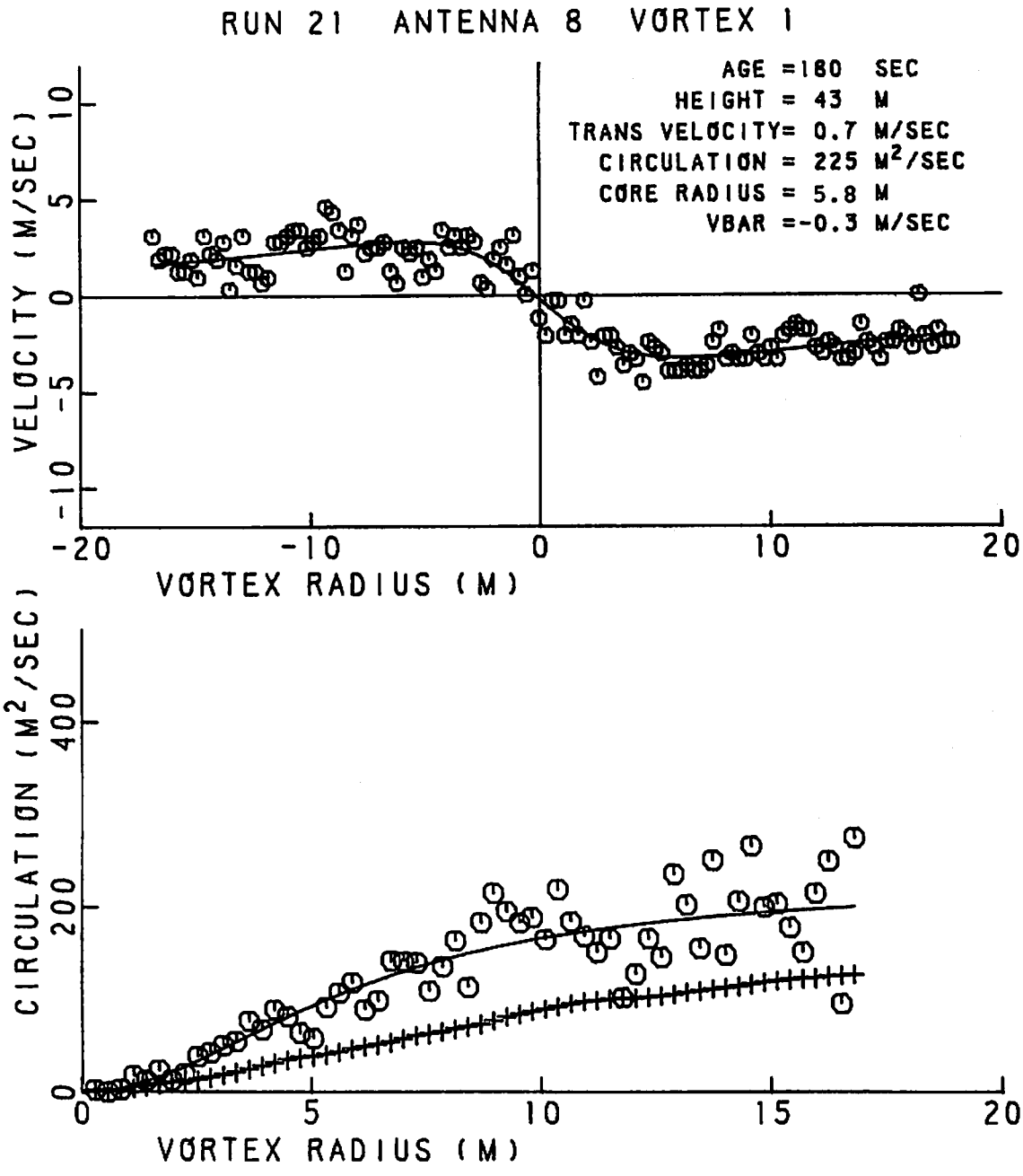

FIGURE 324. VELOCITY AND CIRCULATION PROFILES FOR RUN 21, ANTENNA 8

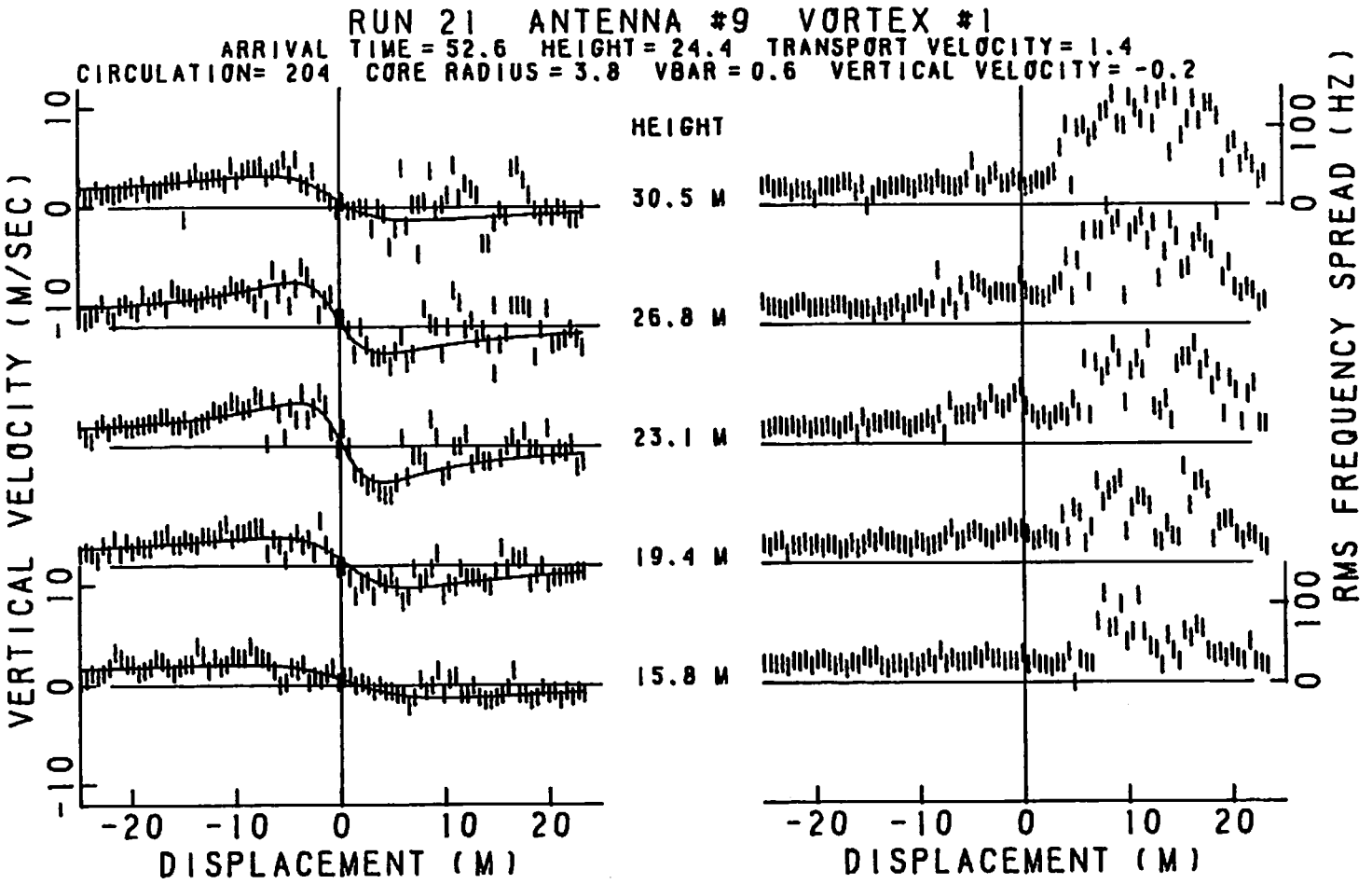

FIGURE 325. VELOCITY AND SPECTRAL WIDTH PROFILES FOR RUN 21, ANTENNA 9

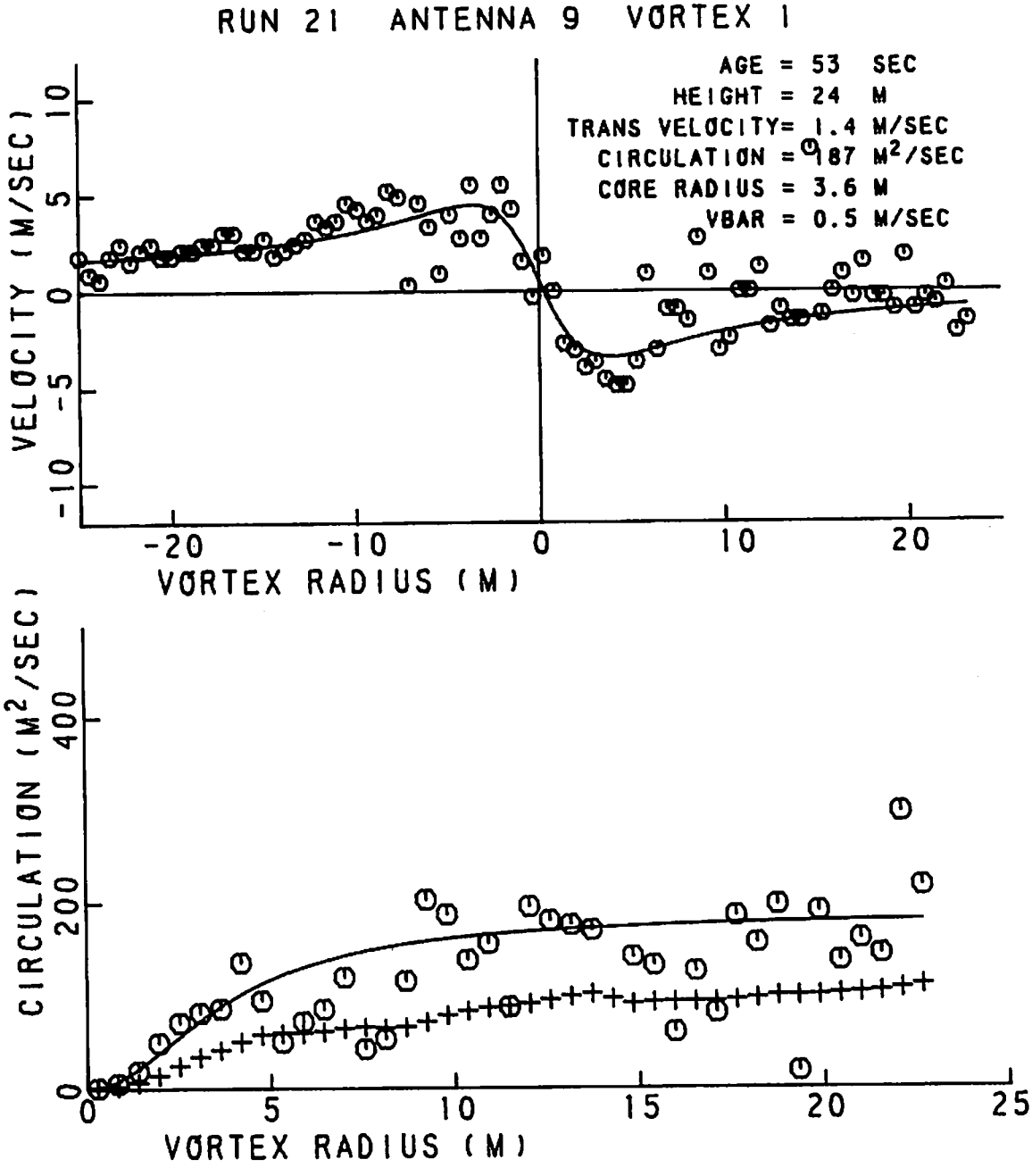

FIGURE 326. VELOCITY AND CIRCULATION PROFILES FOR RUN 21, ANTENNA 9

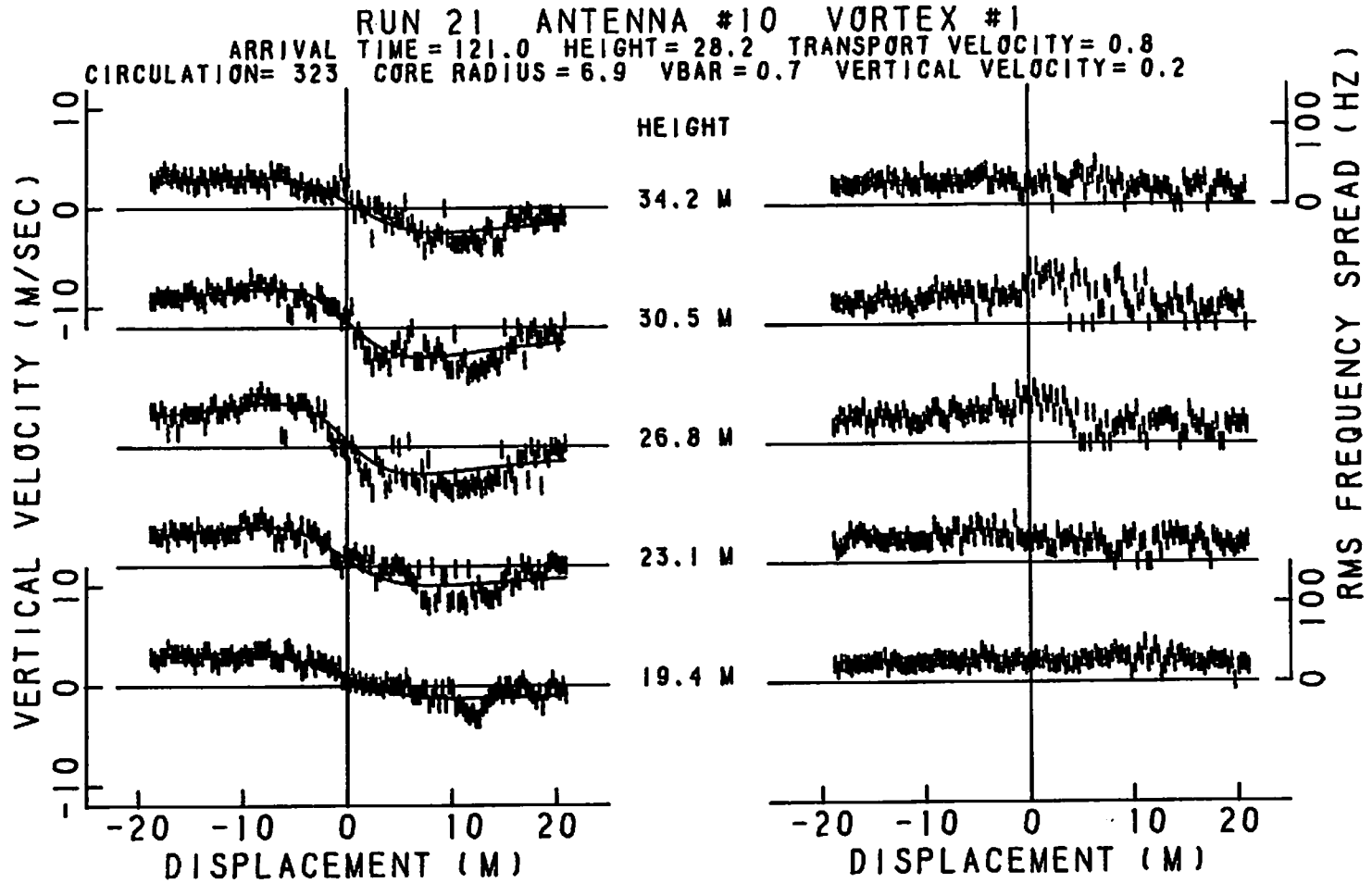

FIGURE 327. VELOCITY AND SPECTRAL WIDTH PROFILES FOR RUN 21, ANTENNA 10

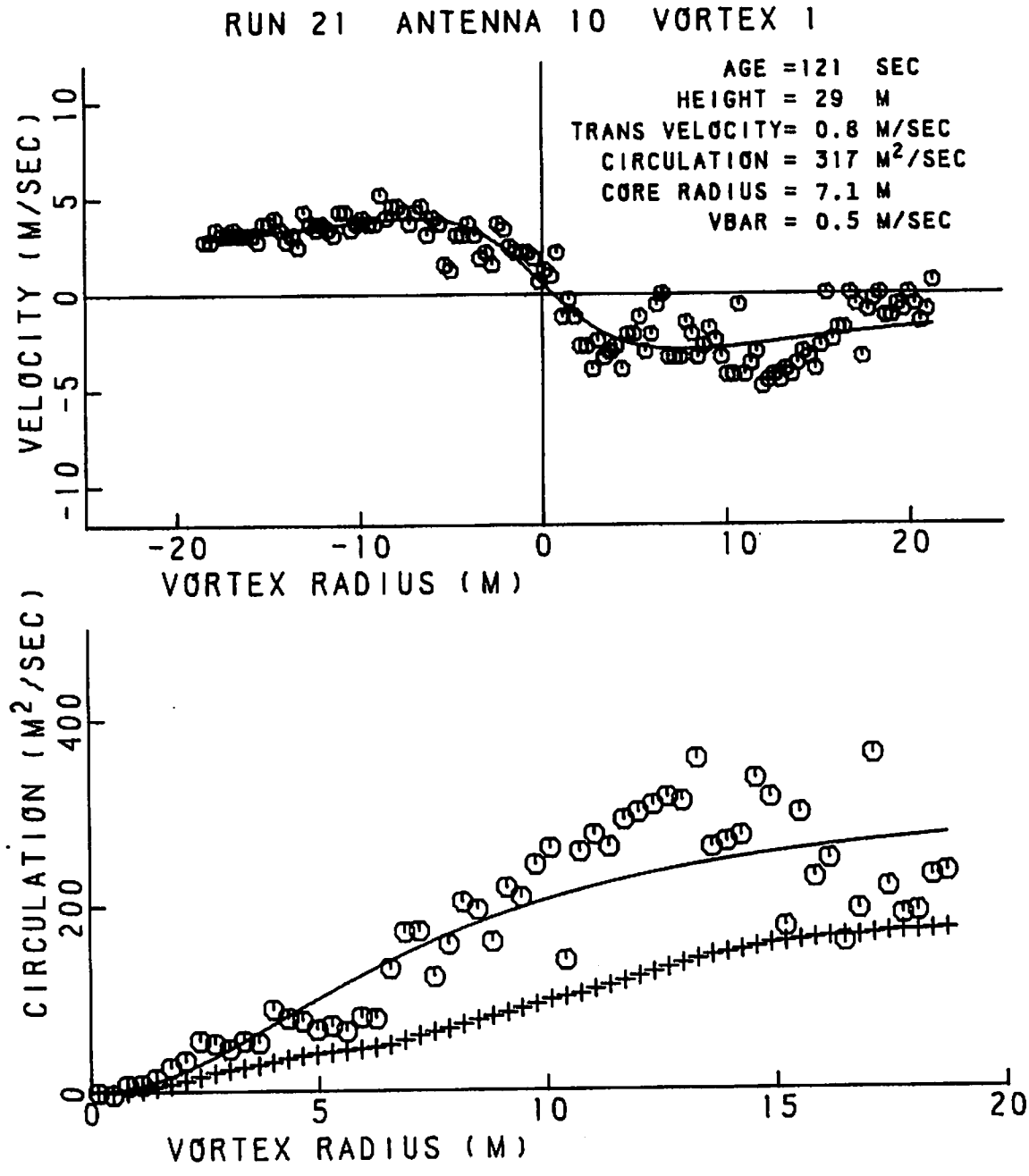

FIGURE 328. VELOCITY AND CIRCULATION PROFILES FOR RUN 21, ANTENNA 10

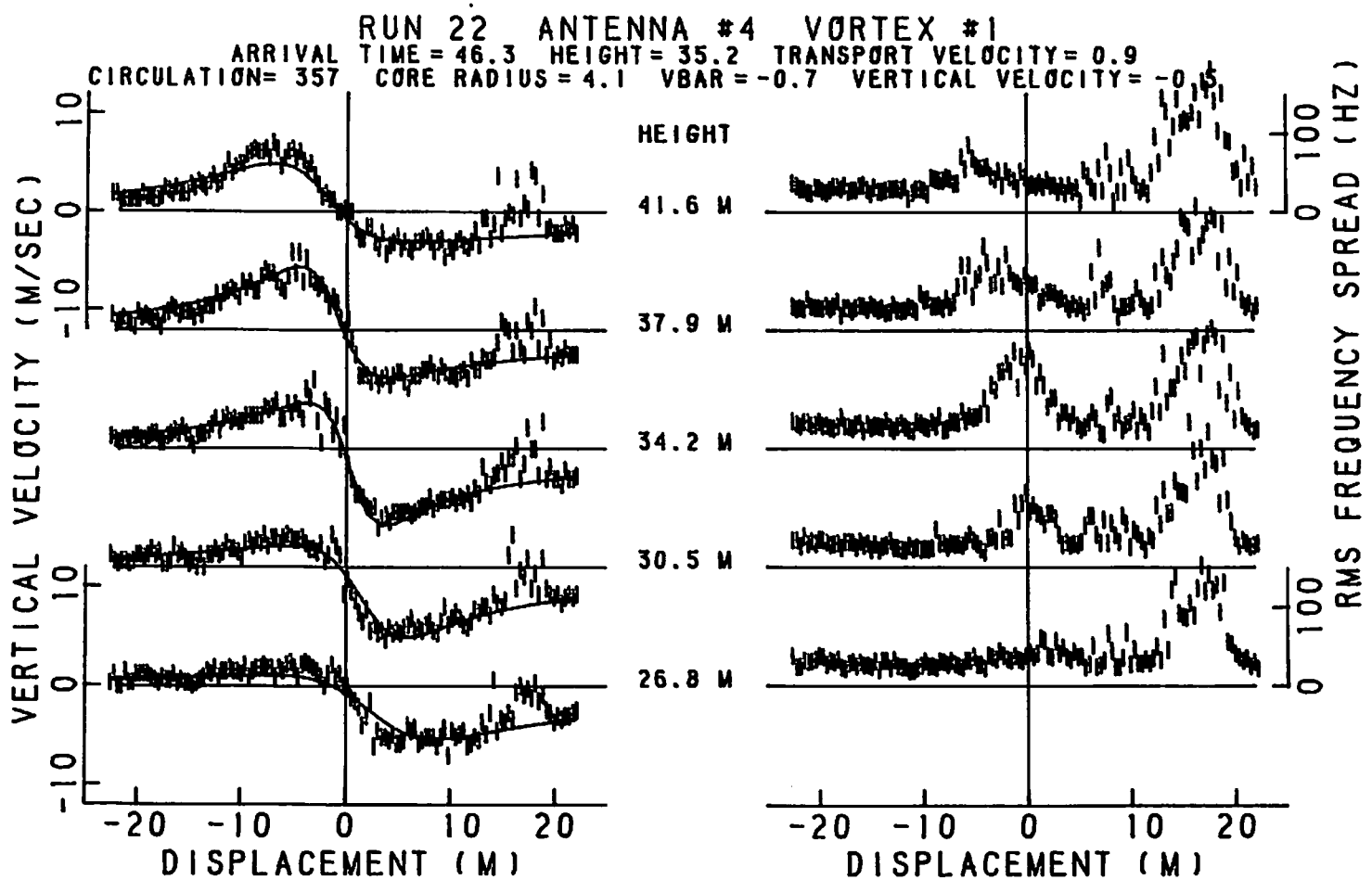

FIGURE 329. VELOCITY AND SPECTRAL WIDTH PROFILES FOR RUN 22, ANTENNA 4

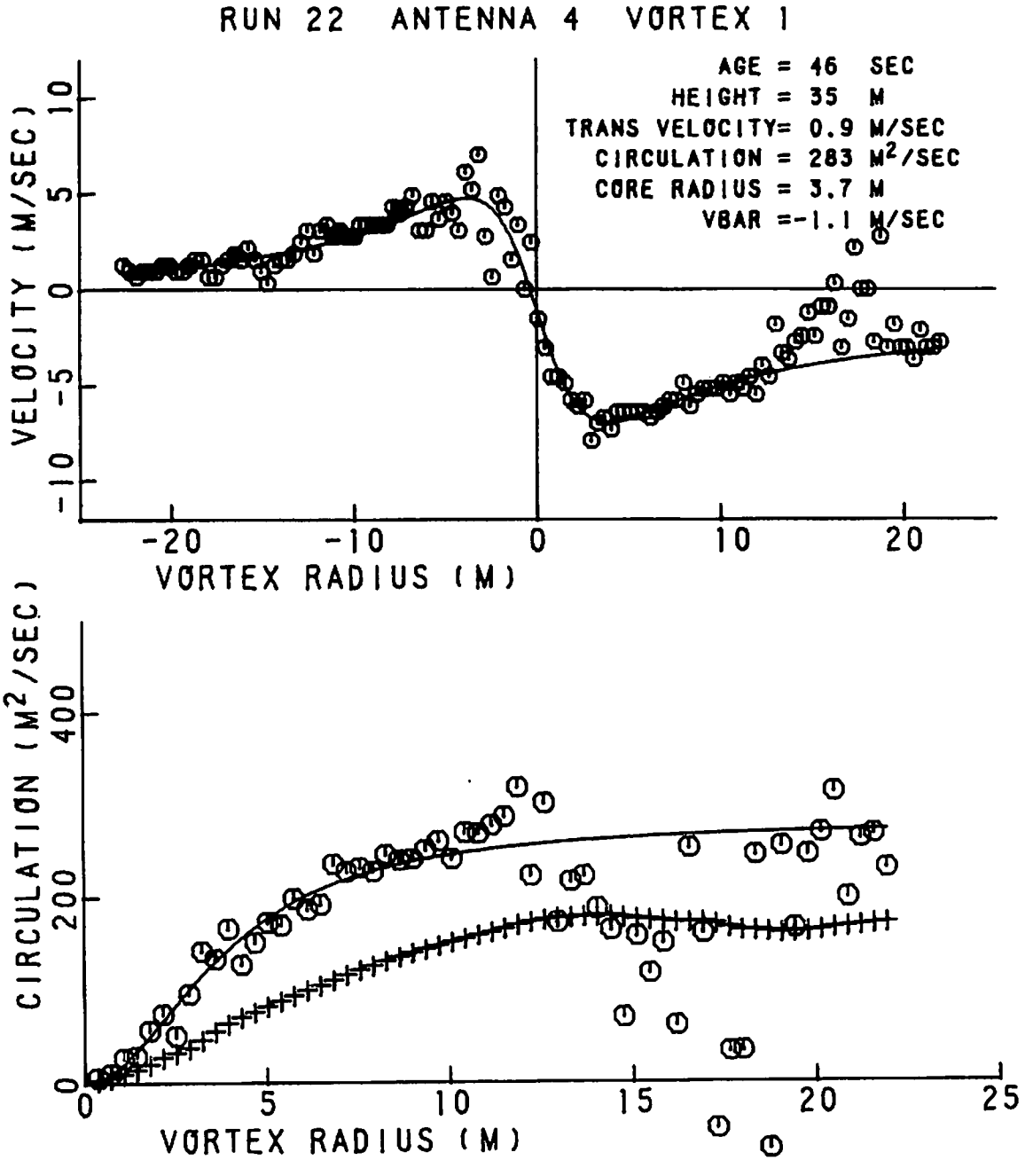

FIGURE 330. VELOCITY AND CIRCULATION PROFILES FOR RUN 22, ANTENNA 4

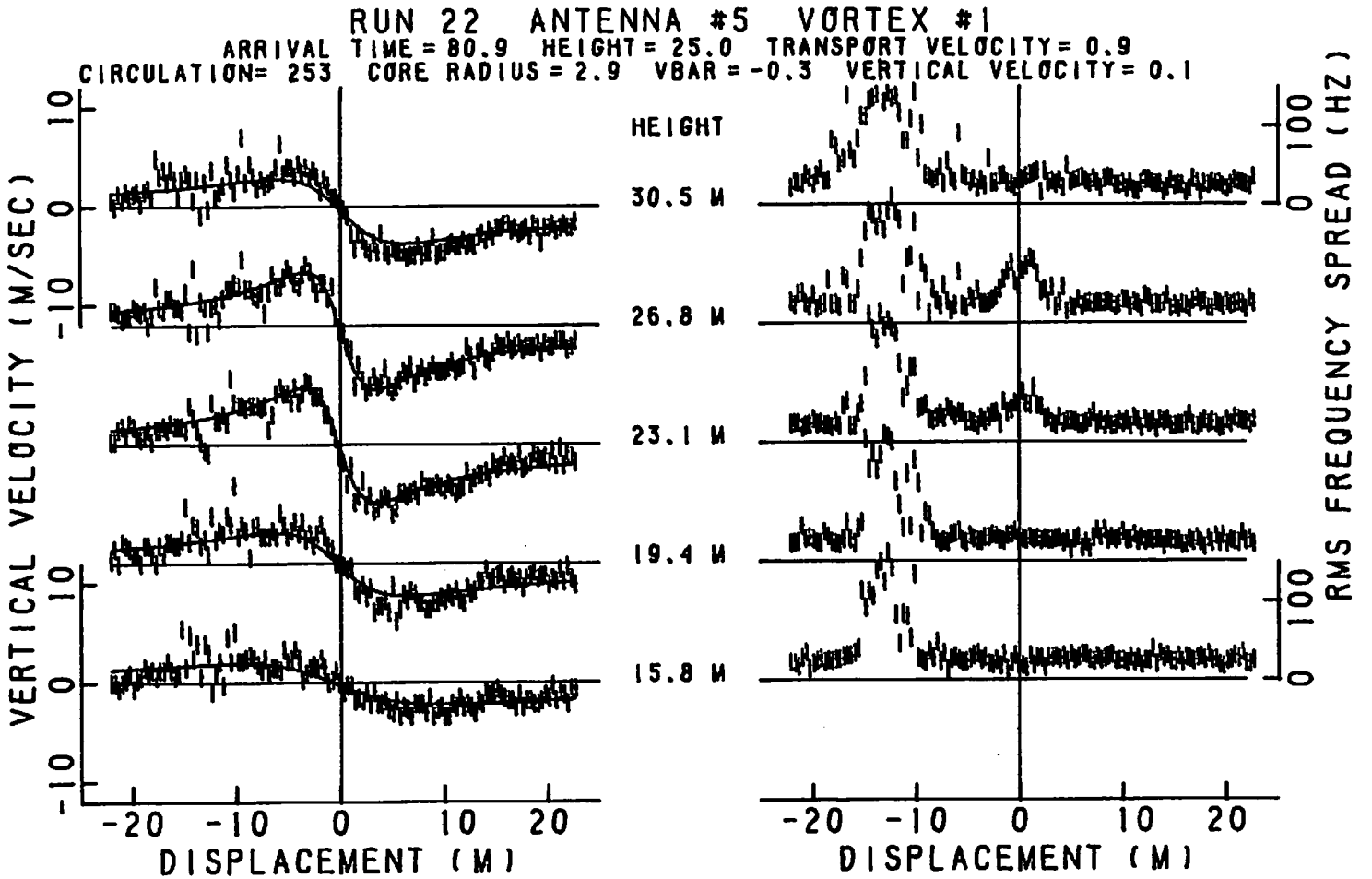

FIGURE 331. VELOCITY AND SPECTRAL WIDTH PROFILES FOR RUN 22, ANTENNA 5

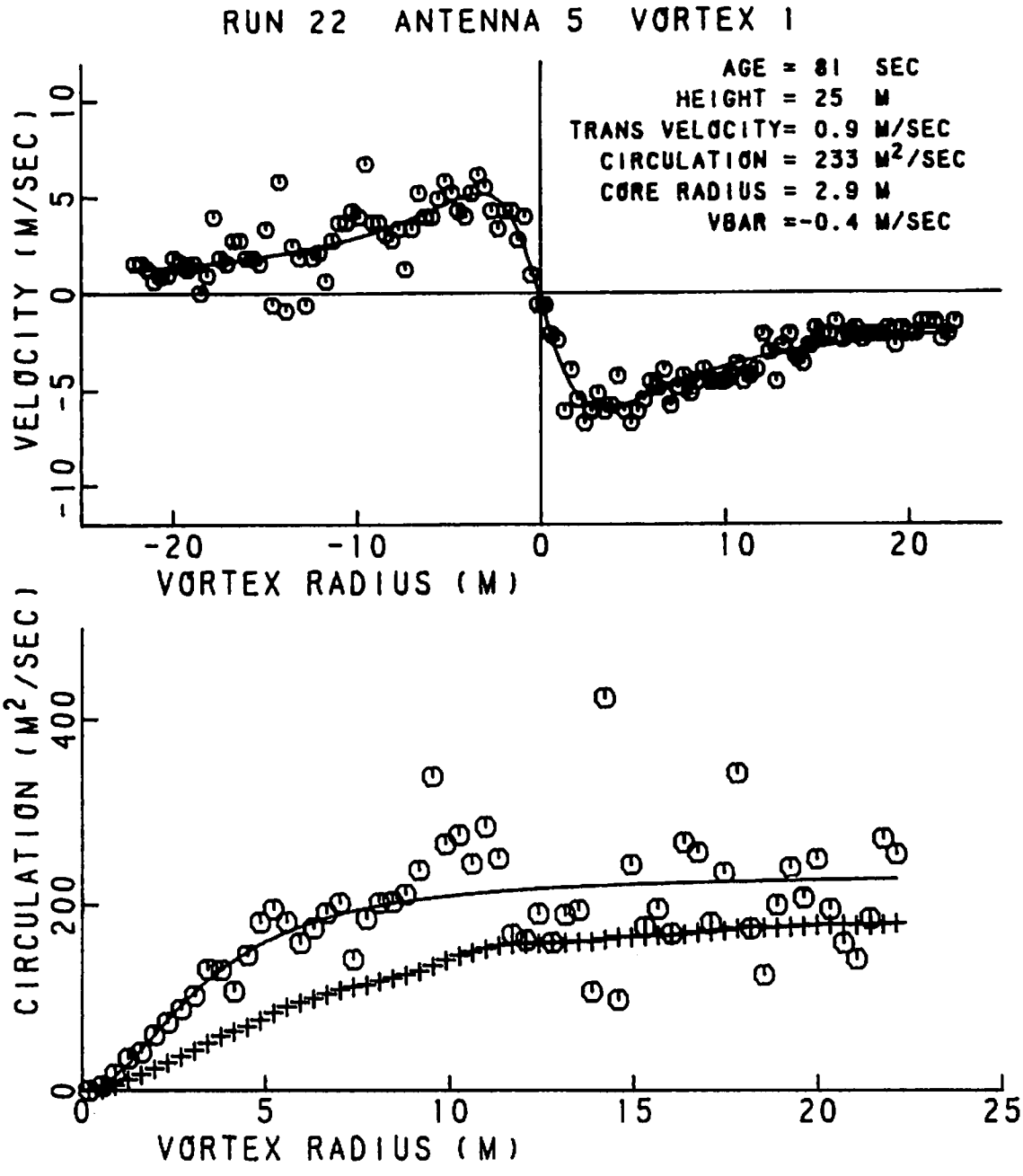

FIGURE 332. VELOCITY AND CIRCULATION PROFILES FOR RUN 22, ANTENNA 5

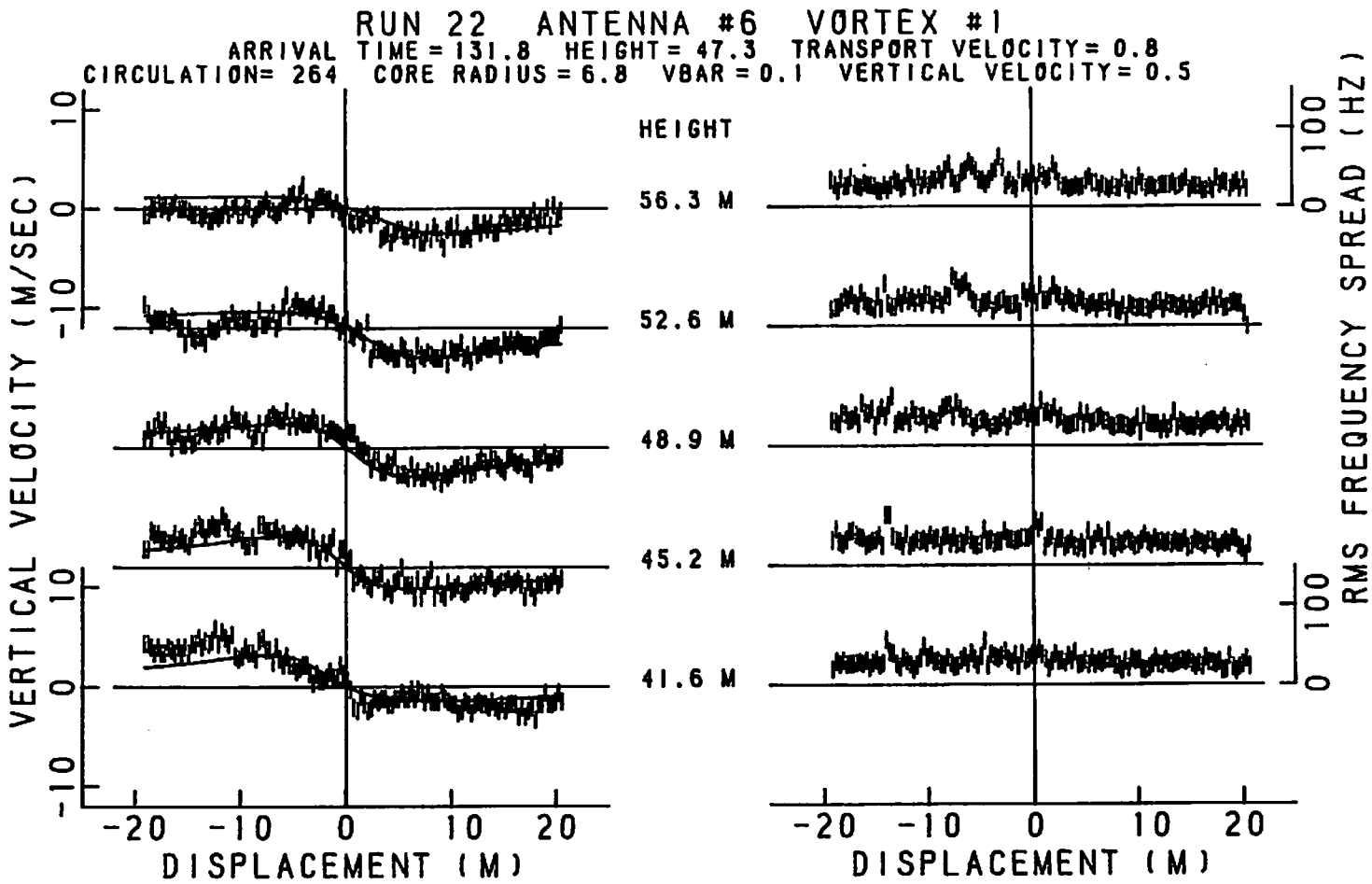

FIGURE 333. VELOCITY AND SPECTRAL WIDTH PROFILES FOR RUN 22, ANTENNA 6

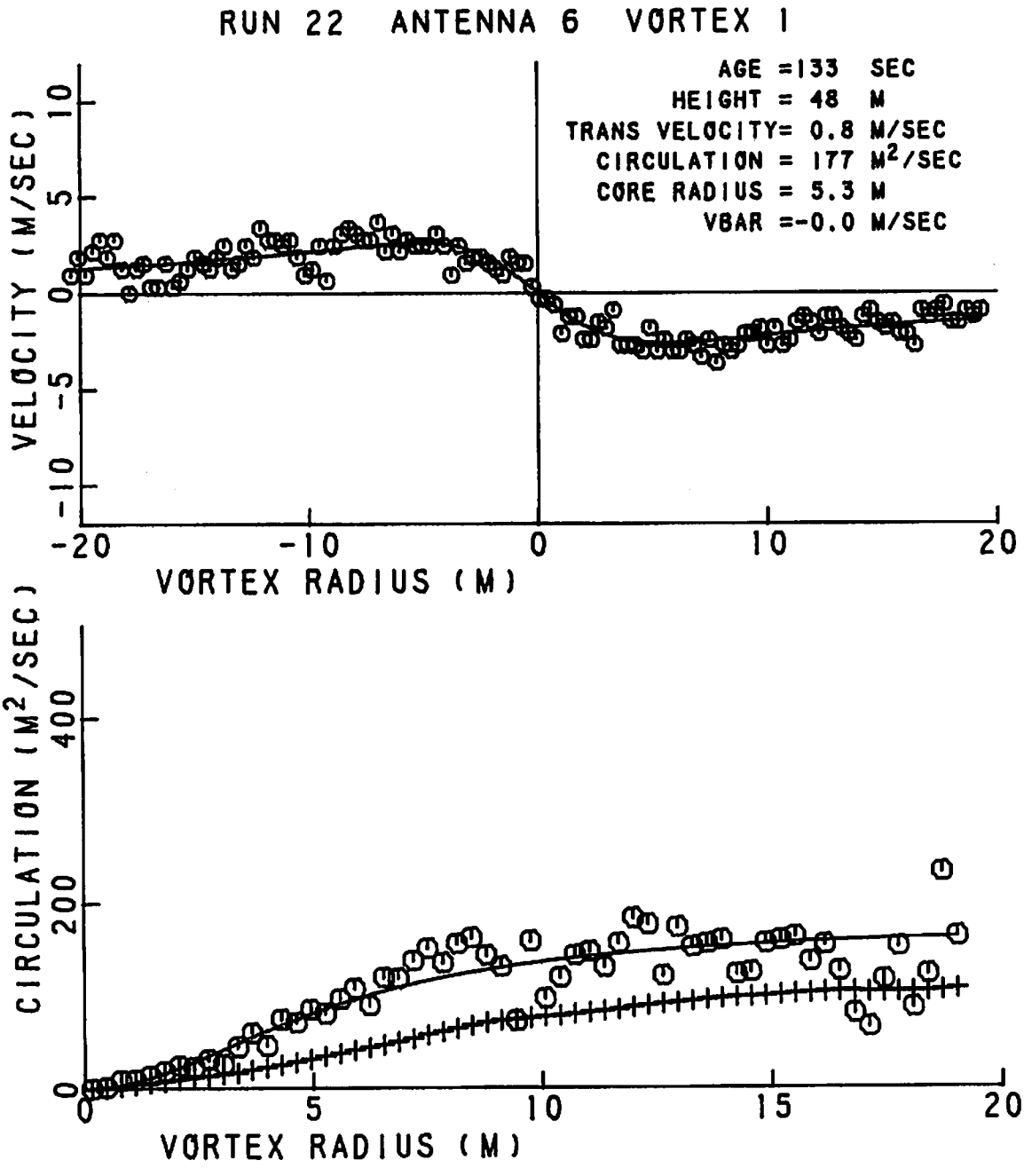

FIGURE 334. VELOCITY AND CIRCULATION PROFILES FOR RUN 22, ANTENNA 6

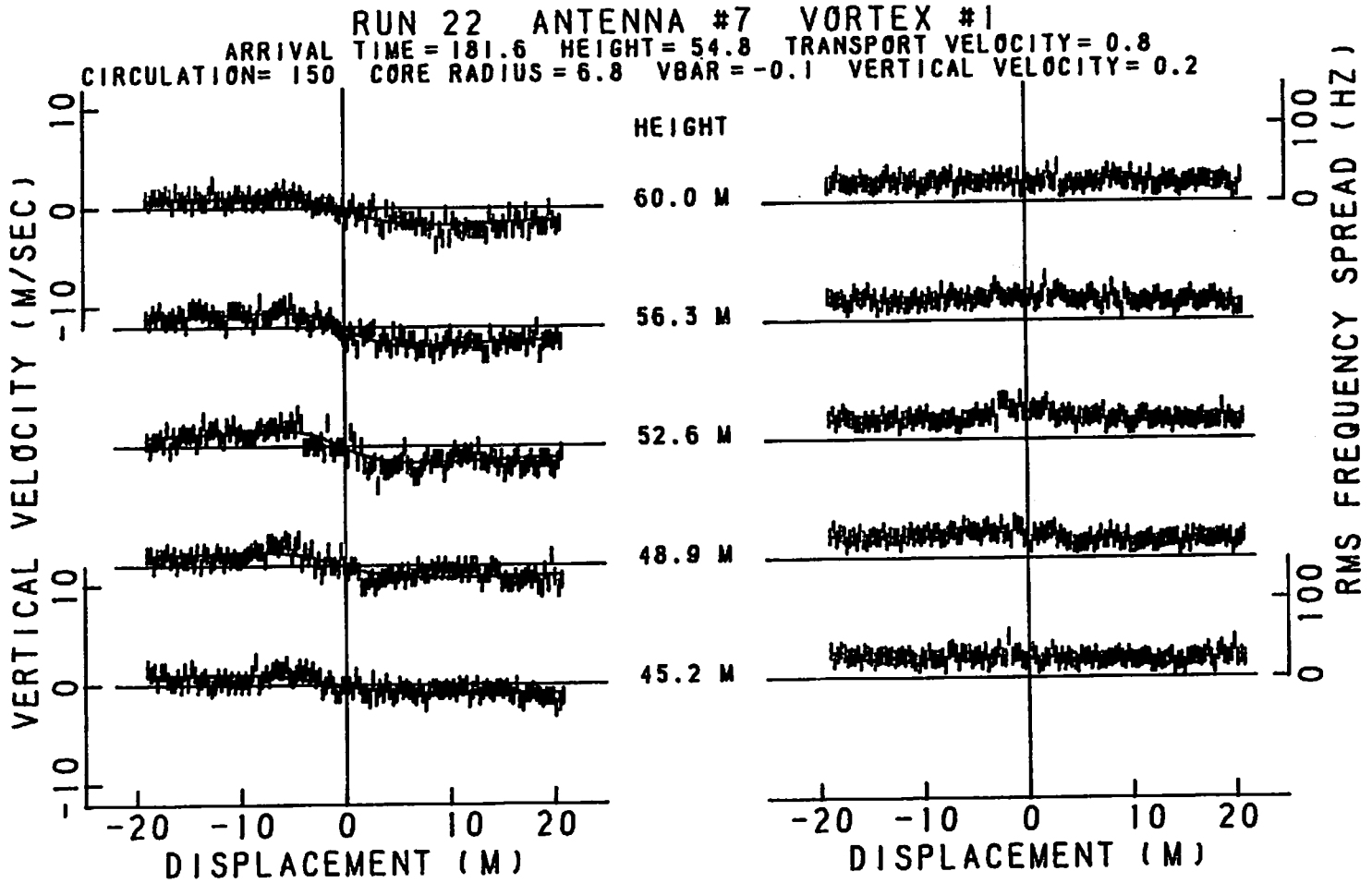

FIGURE 335. VELOCITY AND SPECTRAL WIDTH PROFILES FOR RUN 22, ANTENNA 7

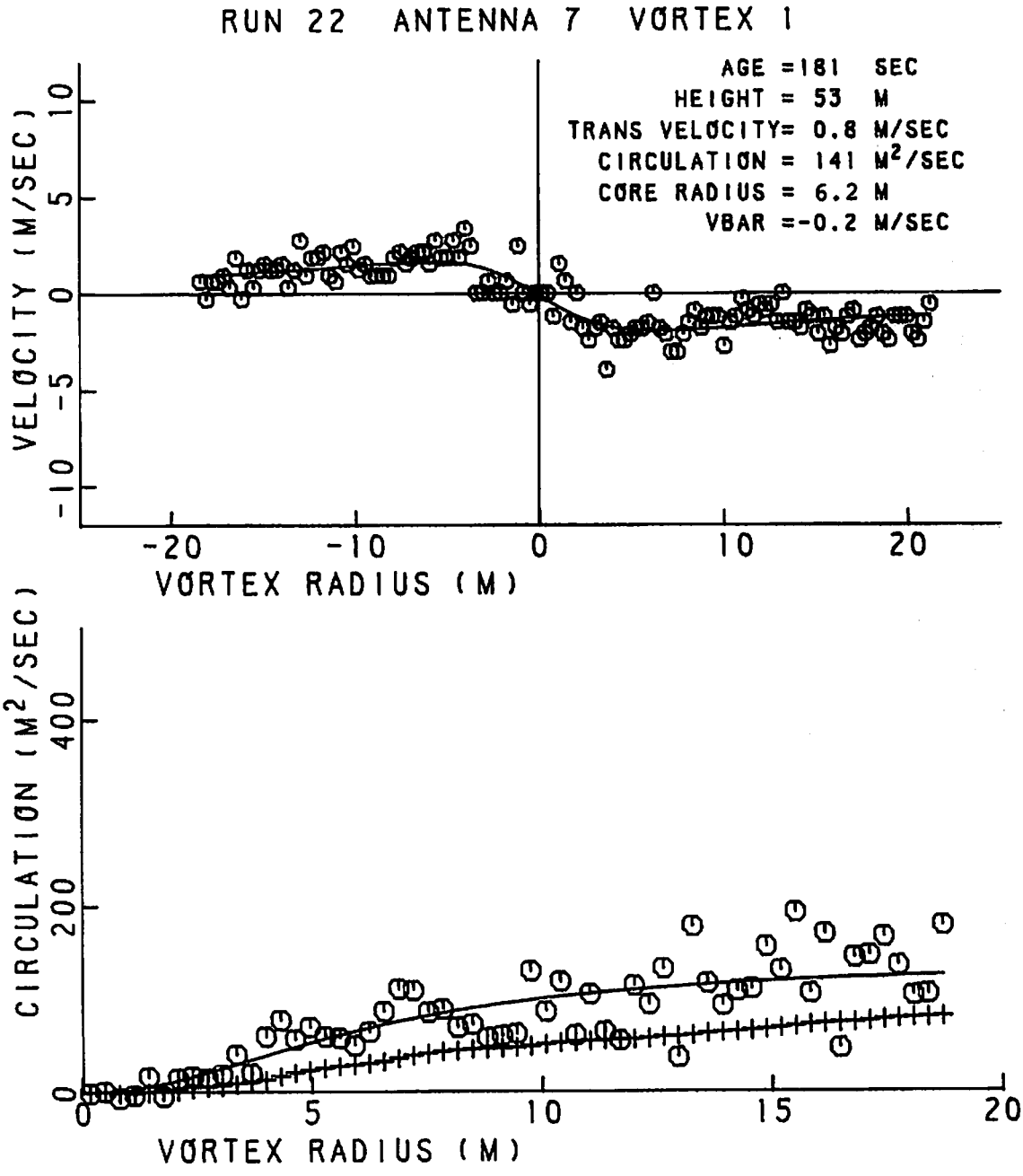

FIGURE 336. VELOCITY AND CIRCULATION PROFILES FOR RUN 22, ANTENNA 7

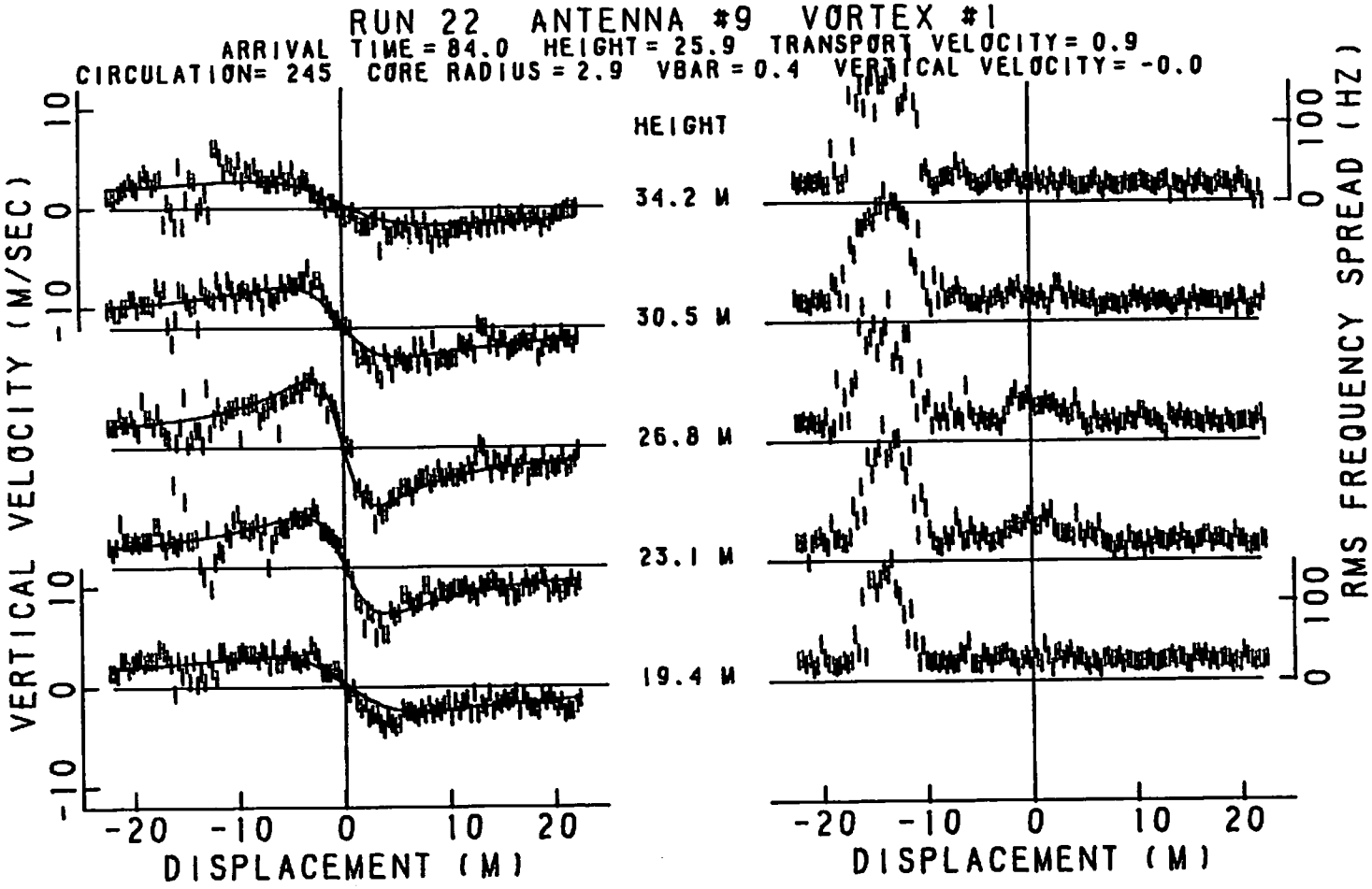

FIGURE 337. VELOCITY AND SPECTRAL WIDTH PROFILES FOR RUN 22, ANTENNA 9

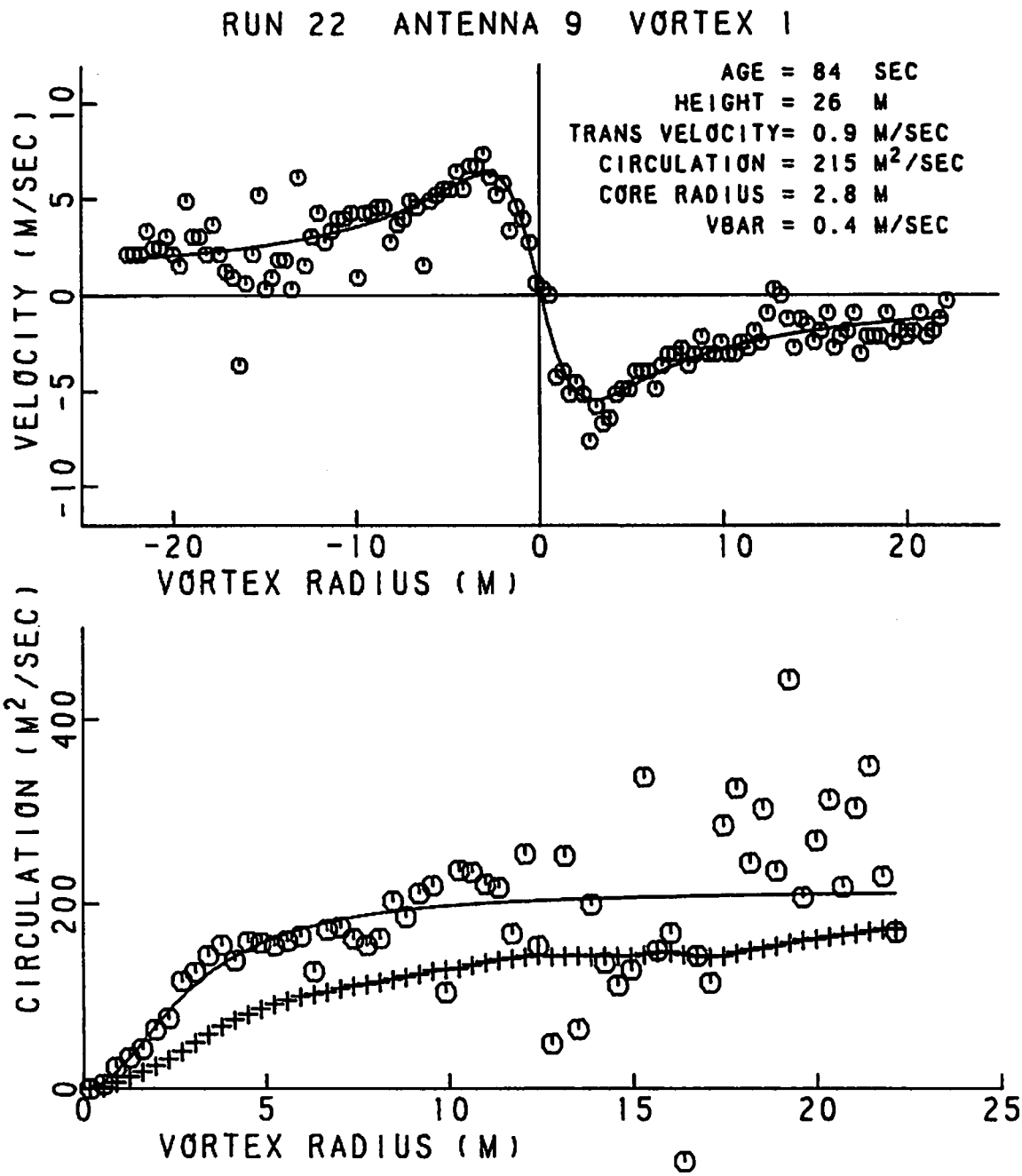

FIGURE 338. VELOCITY AND CIRCULATION PROFILES FOR RUN 22, ANTENNA 9

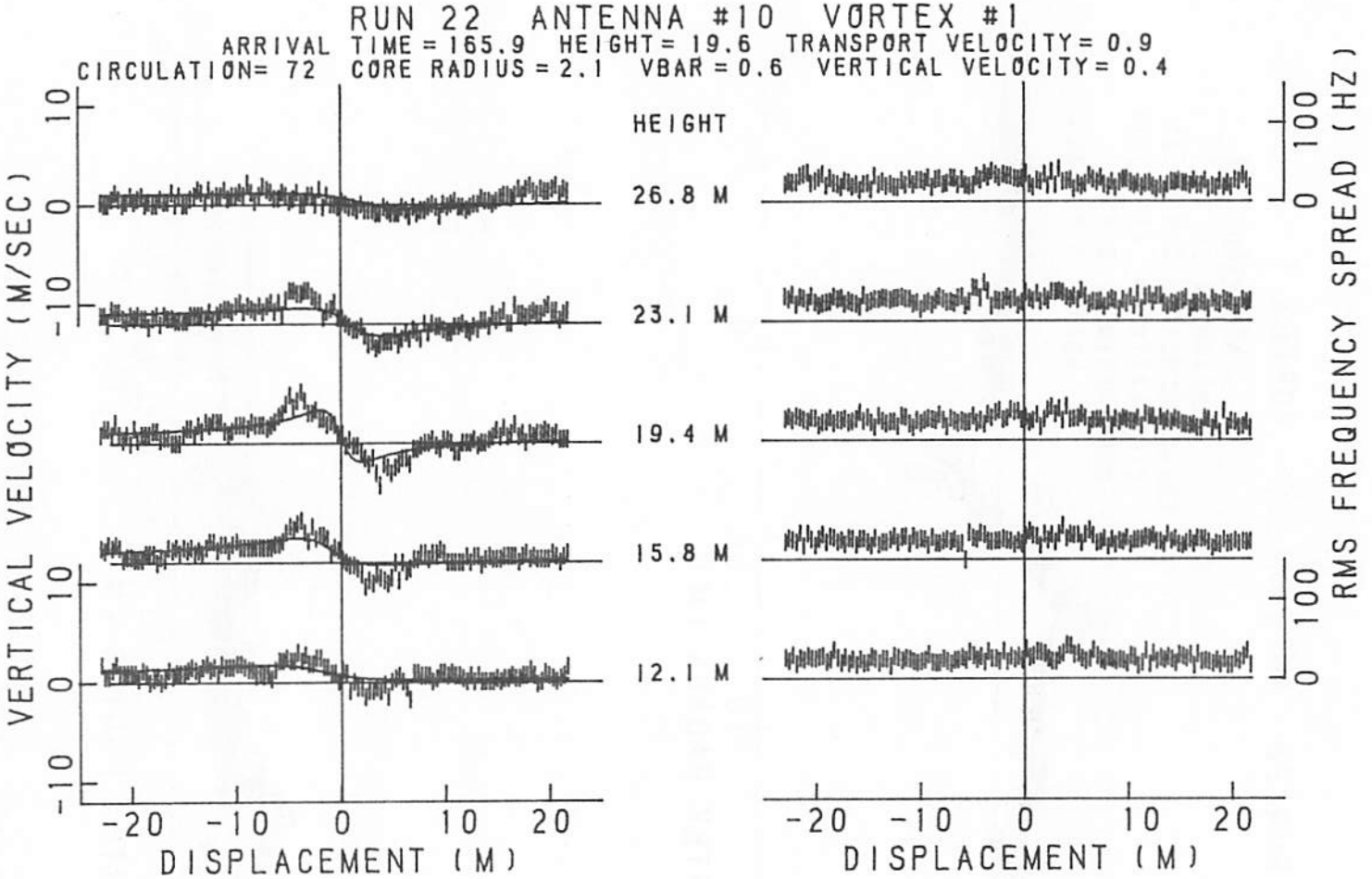

FIGURE 339. VELOCITY AND SPECTRAL WIDTH PROFILES FOR RUN 22, ANTENNA 10

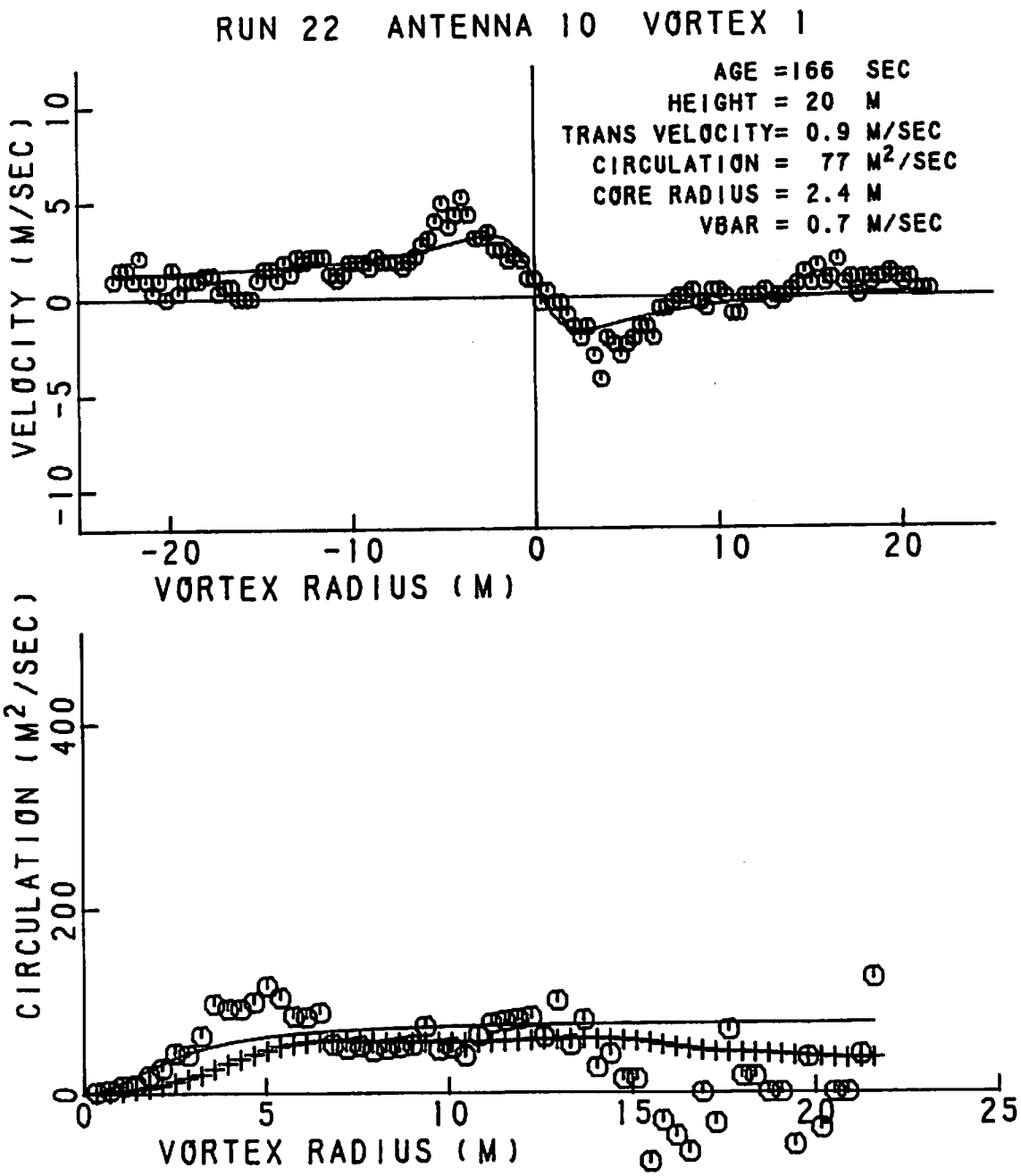

FIGURE 340. VELOCITY AND CIRCULATION PROFILES FOR RUN 22, ANTENNA 10

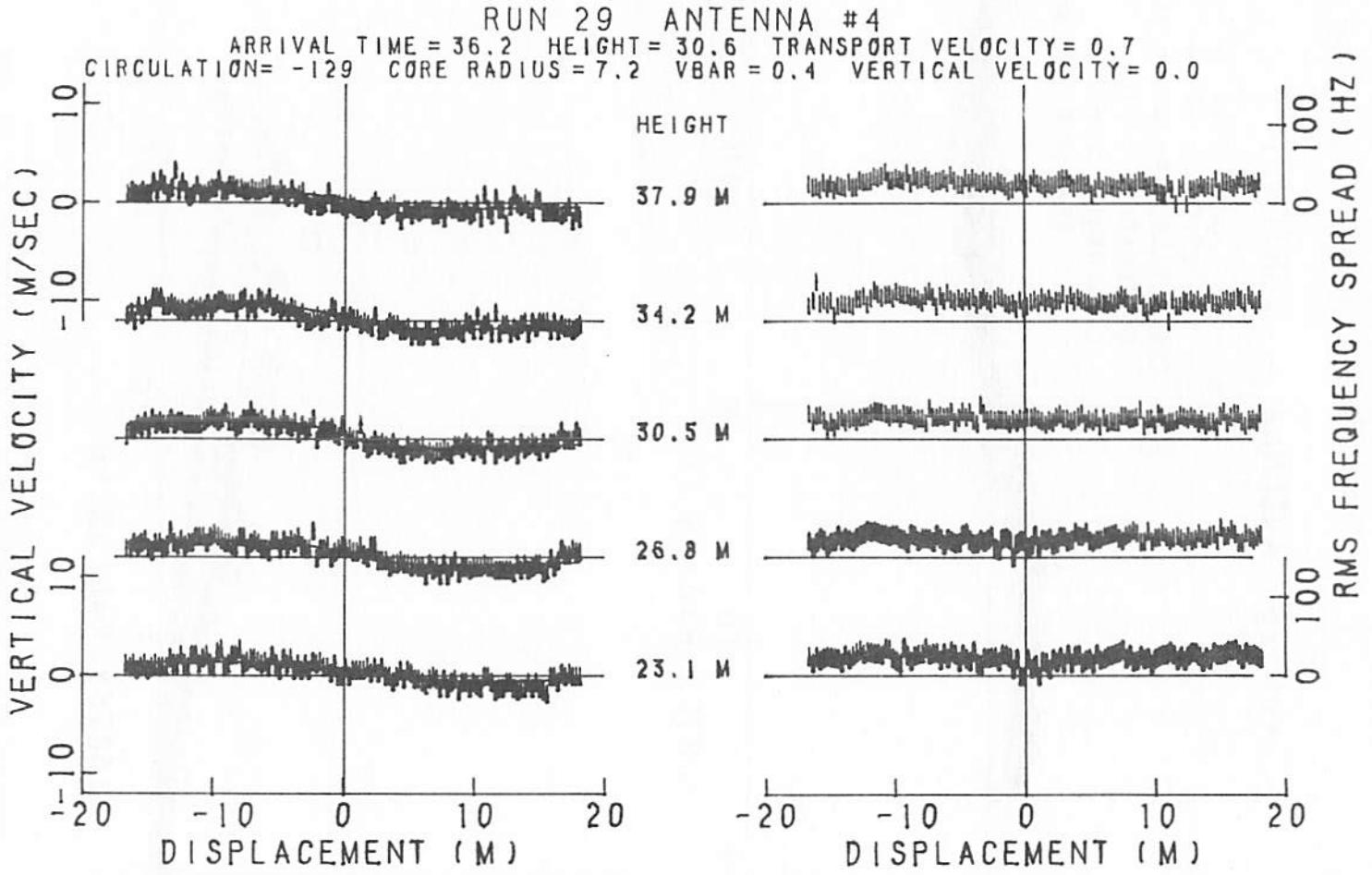

FIGURE 341. VELOCITY AND SPECTRAL WIDTH PROFILES FOR RUN 29, ANTENNA 4

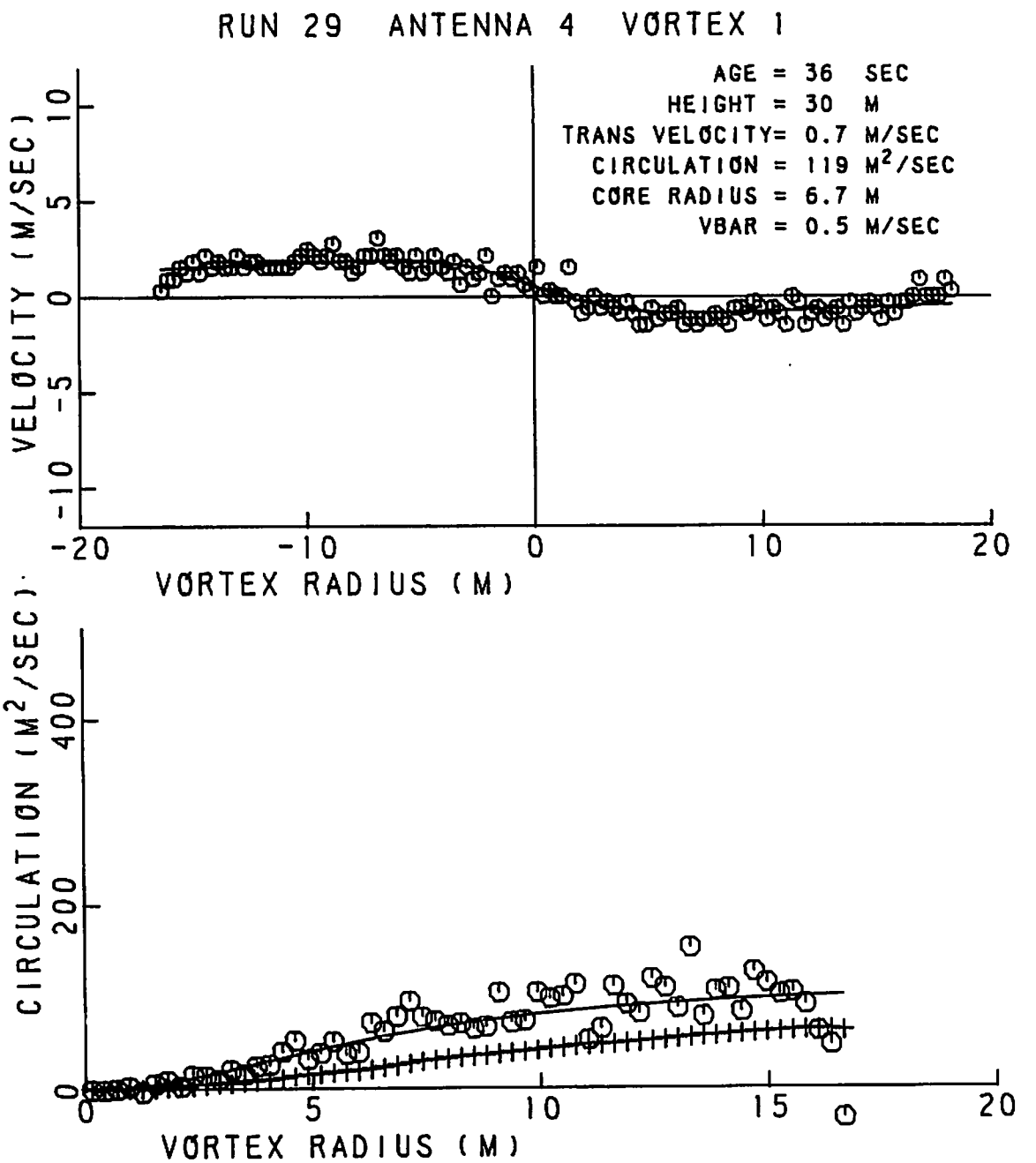

FIGURE 342. VELOCITY AND CIRCULATION PROFILES FOR RUN 29, ANTENNA 4

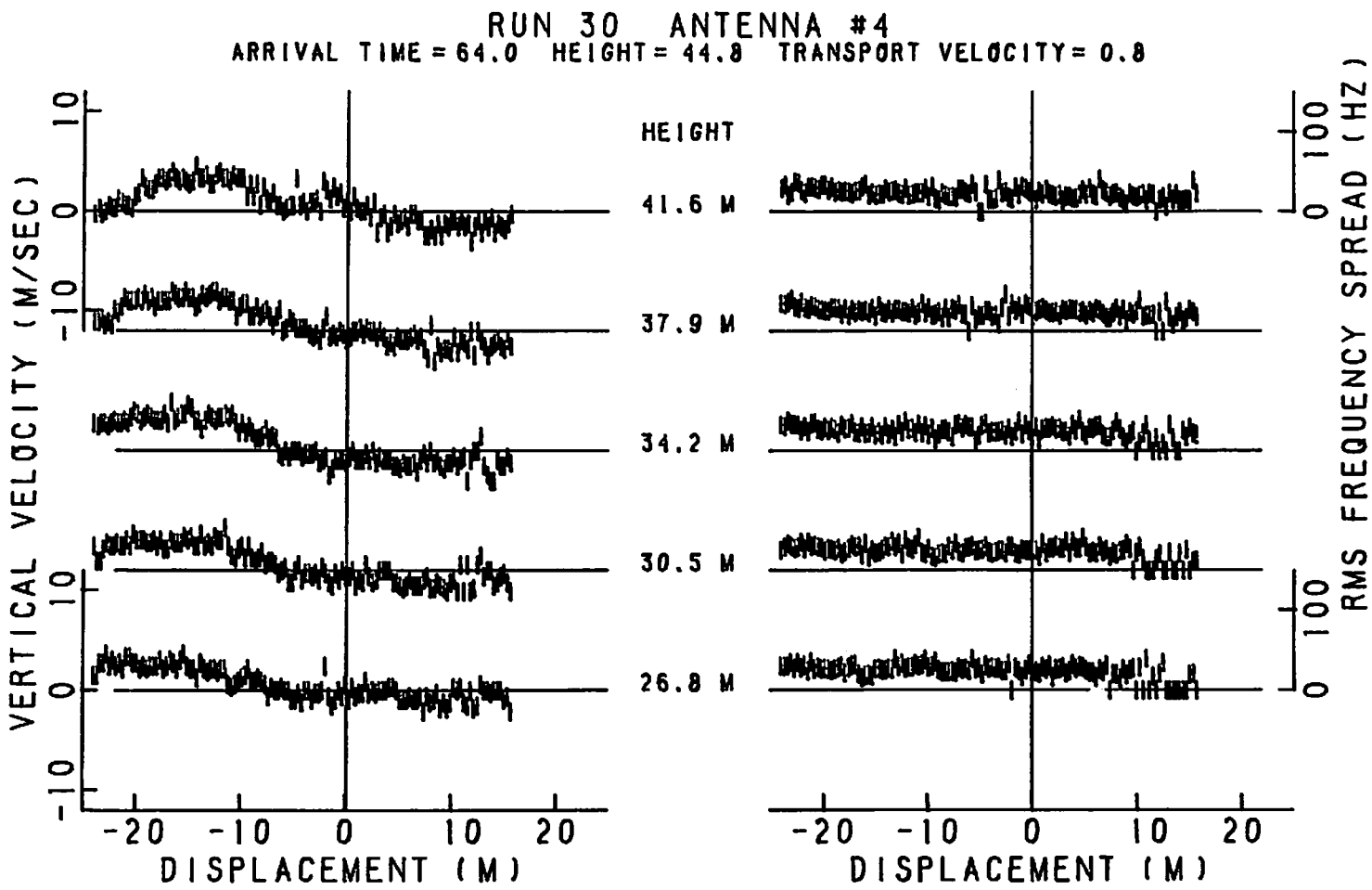

FIGURE 343. VELOCITY AND SPECTRAL WIDTH PROFILES FOR RUN 30, ANTENNA 4

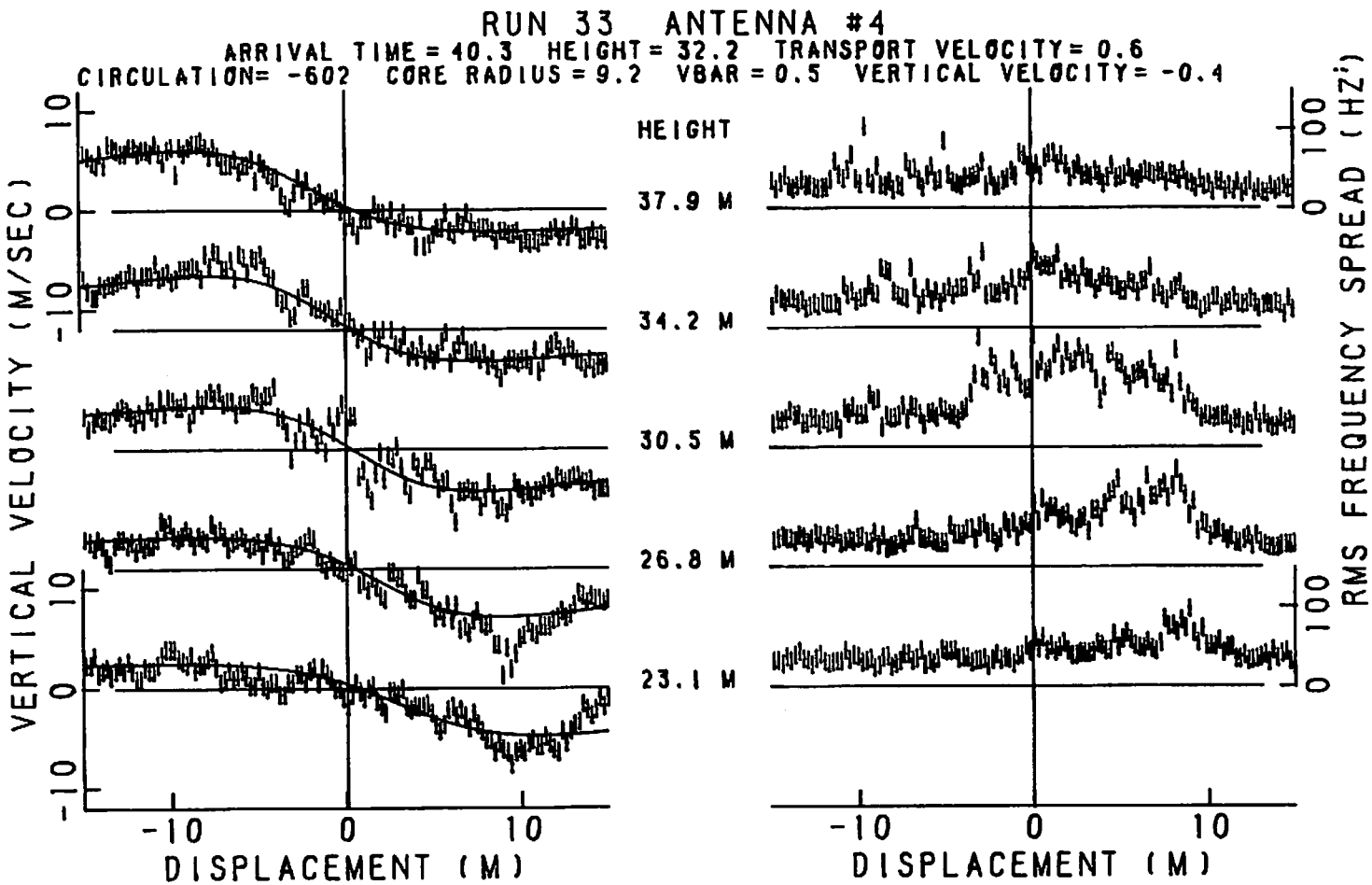

FIGURE 344. VELOCITY AND SPECTRAL WIDTH PROFILES FOR RUN 33, ANTENNA 4

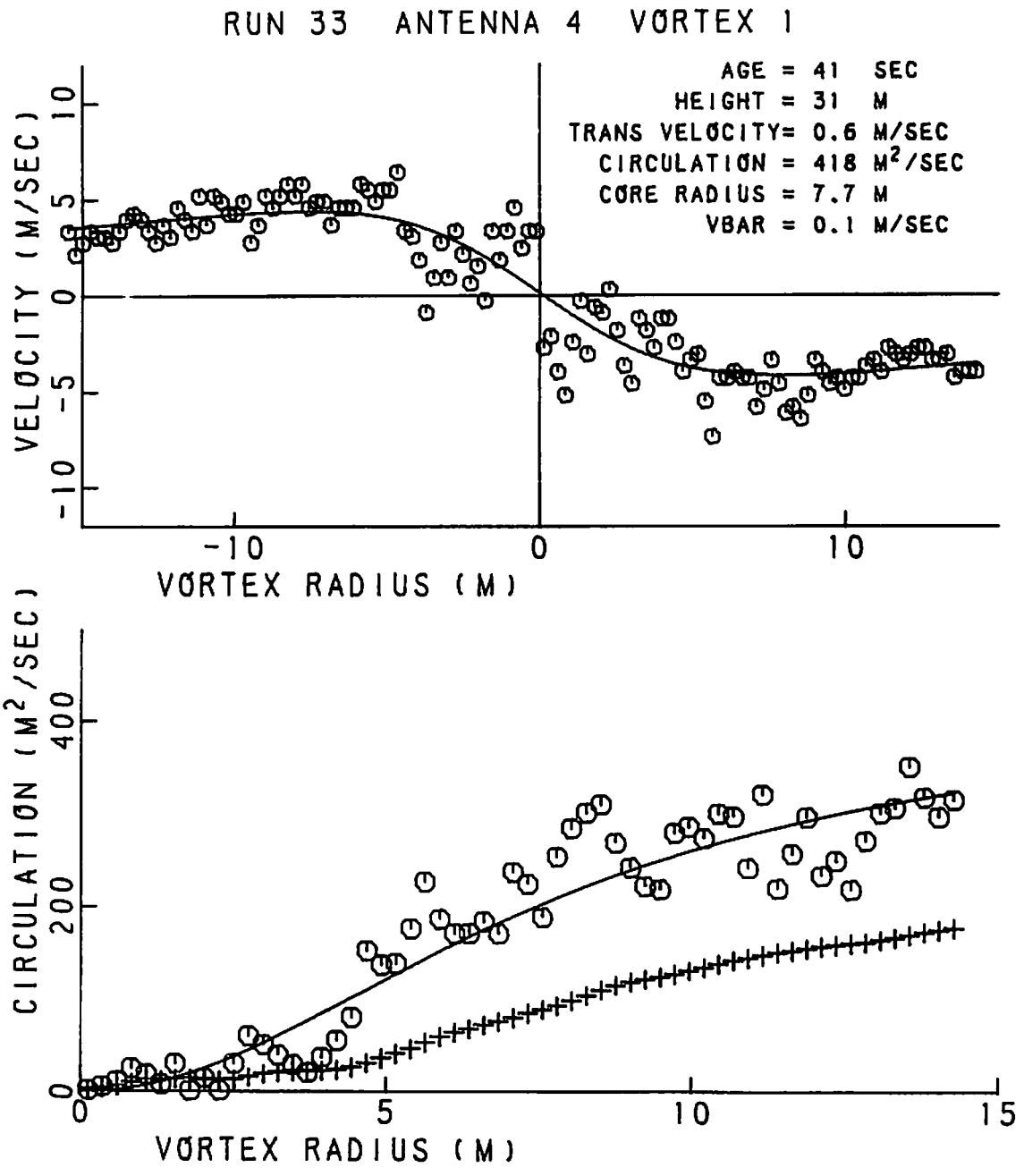

FIGURE 345. VELOCITY AND CIRCULATION PROFILES FOR RUN 33, ANTENNA 4

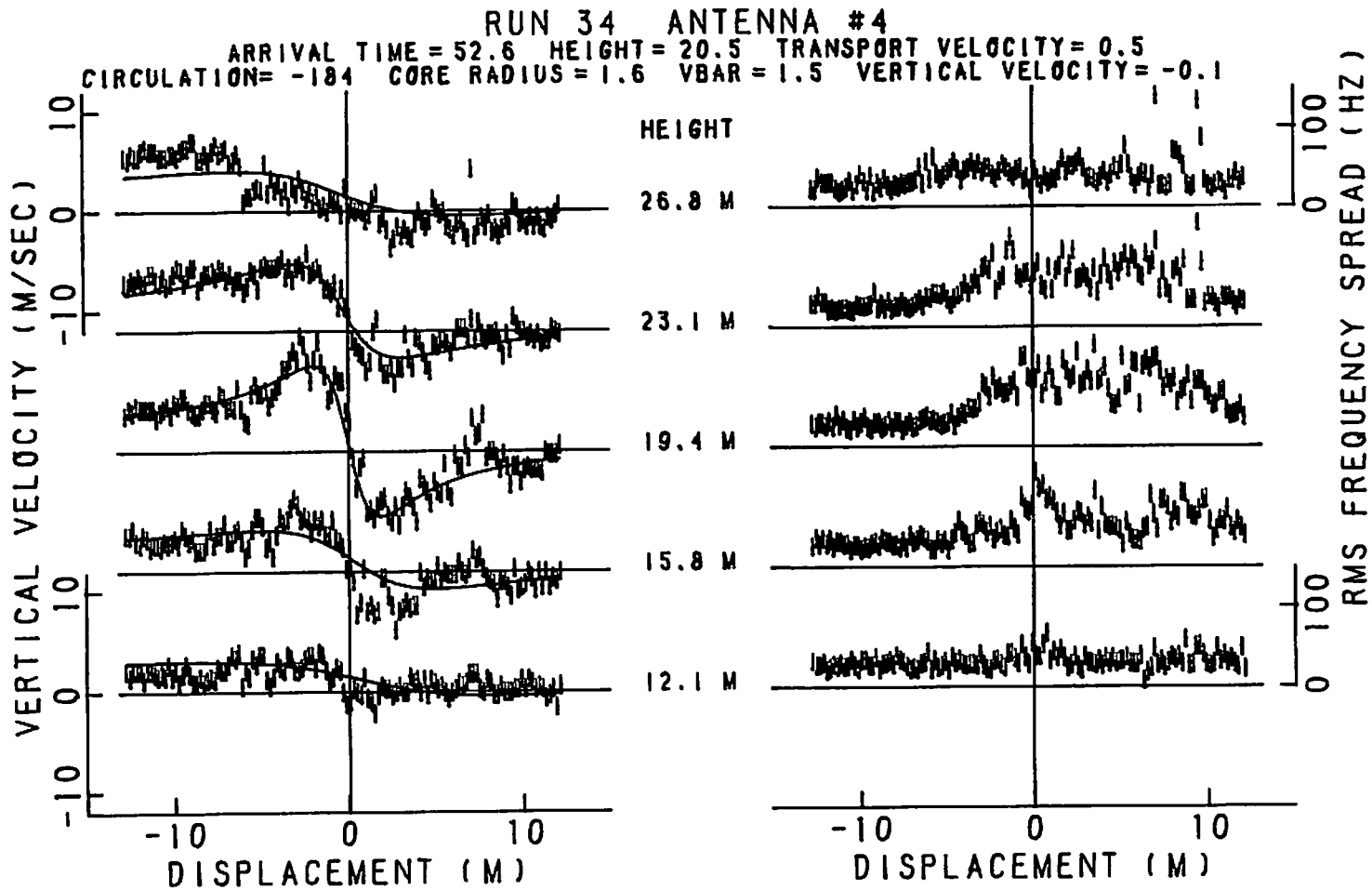

FIGURE 346. VELOCITY AND SPECTRAL WIDTH PROFILES FOR RUN 34, ANTENNA 4

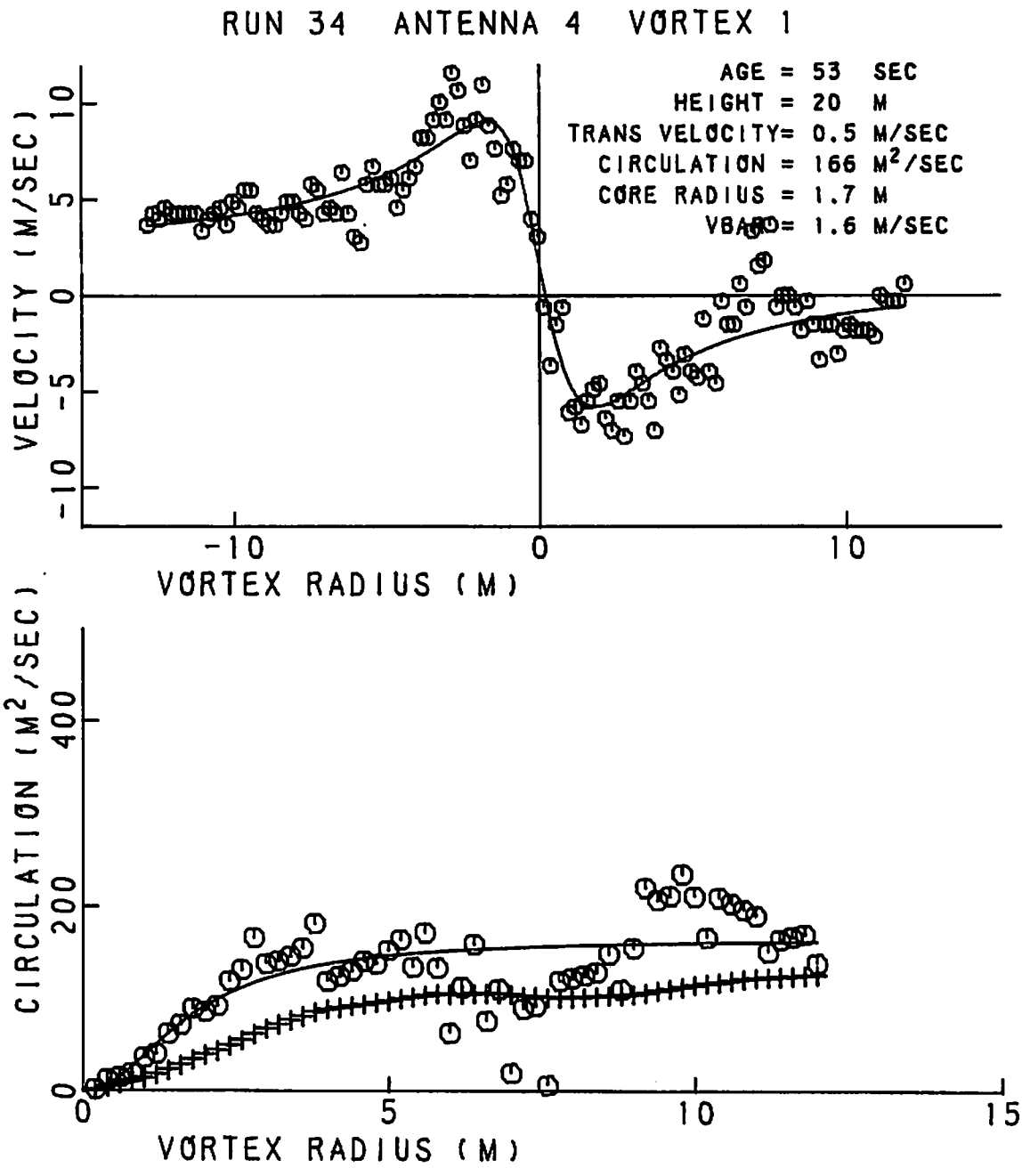

FIGURE 347. VELOCITY AND CIRCULATION PROFILES FOR RUN 34, ANTENNA 4

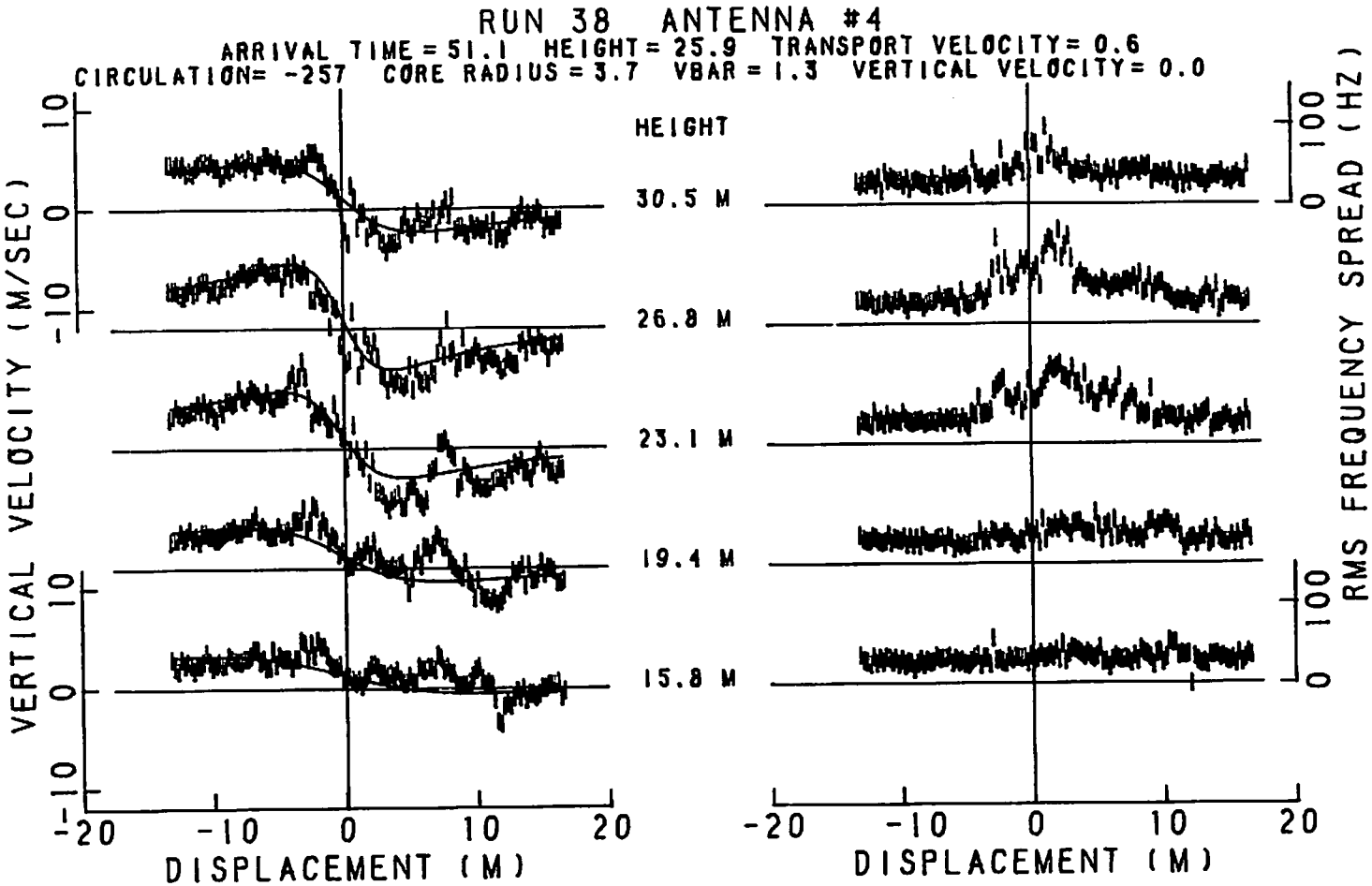

FIGURE 348. VELOCITY AND SPECTRAL WIDTH PROFILES FOR RUN 38, ANTENNA 4

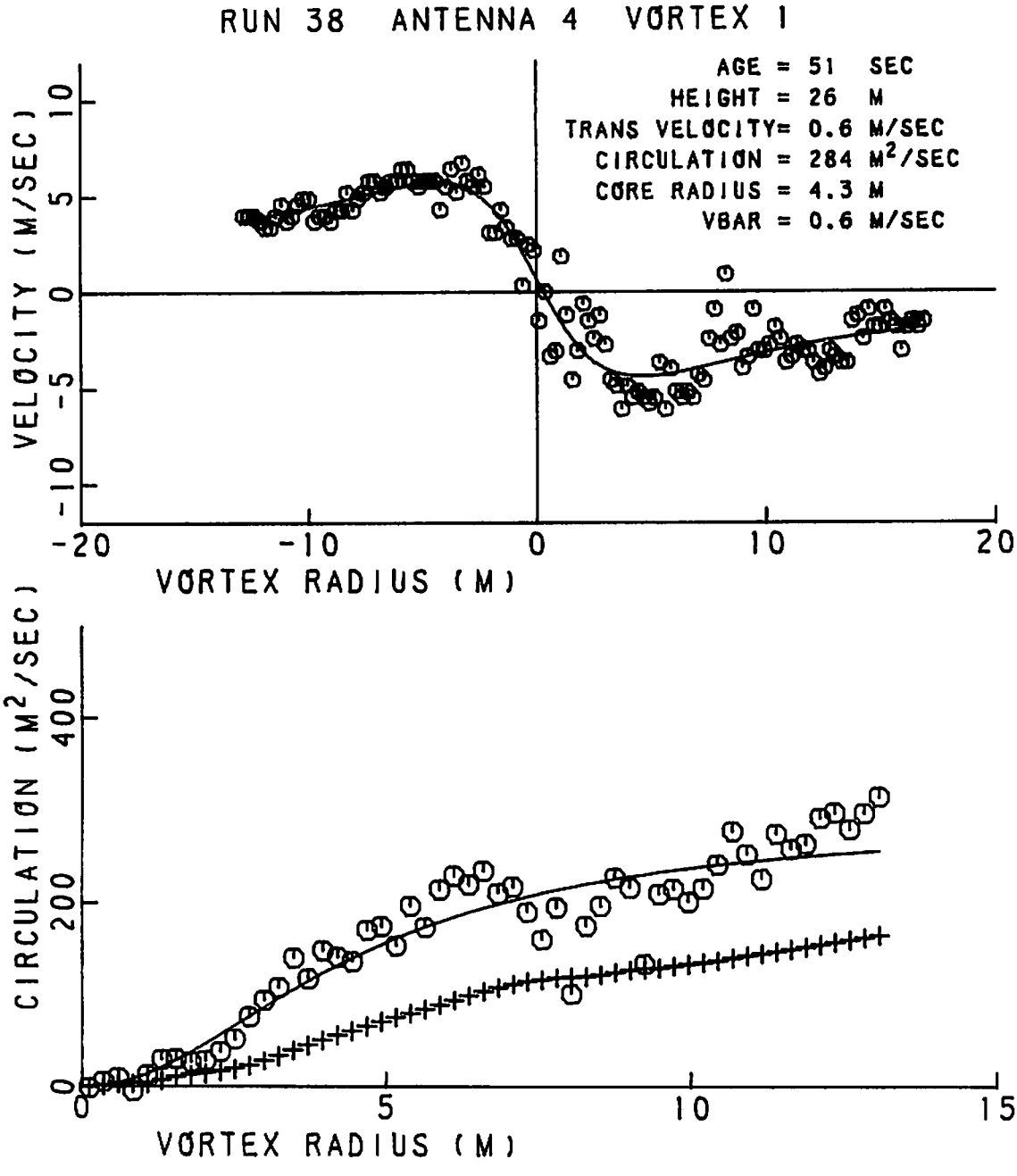

FIGURE 349. VELOCITY AND CIRCULATION PROFILES FOR RUN 38, ANTENNA 4

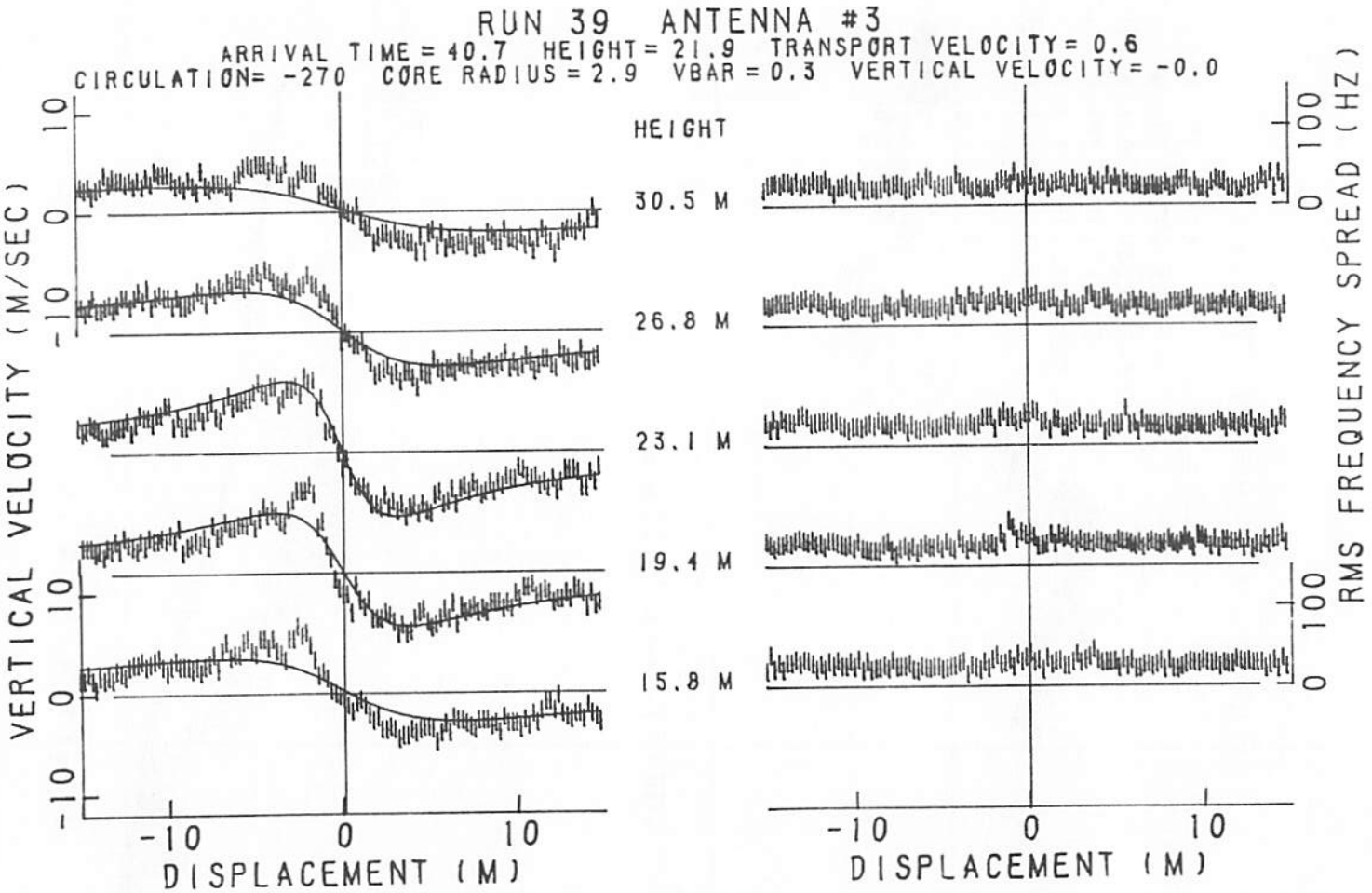

FIGURE 350. VELOCITY AND SPECTRAL WIDTH PROFILES FOR RUN 39, ANTENNA 3

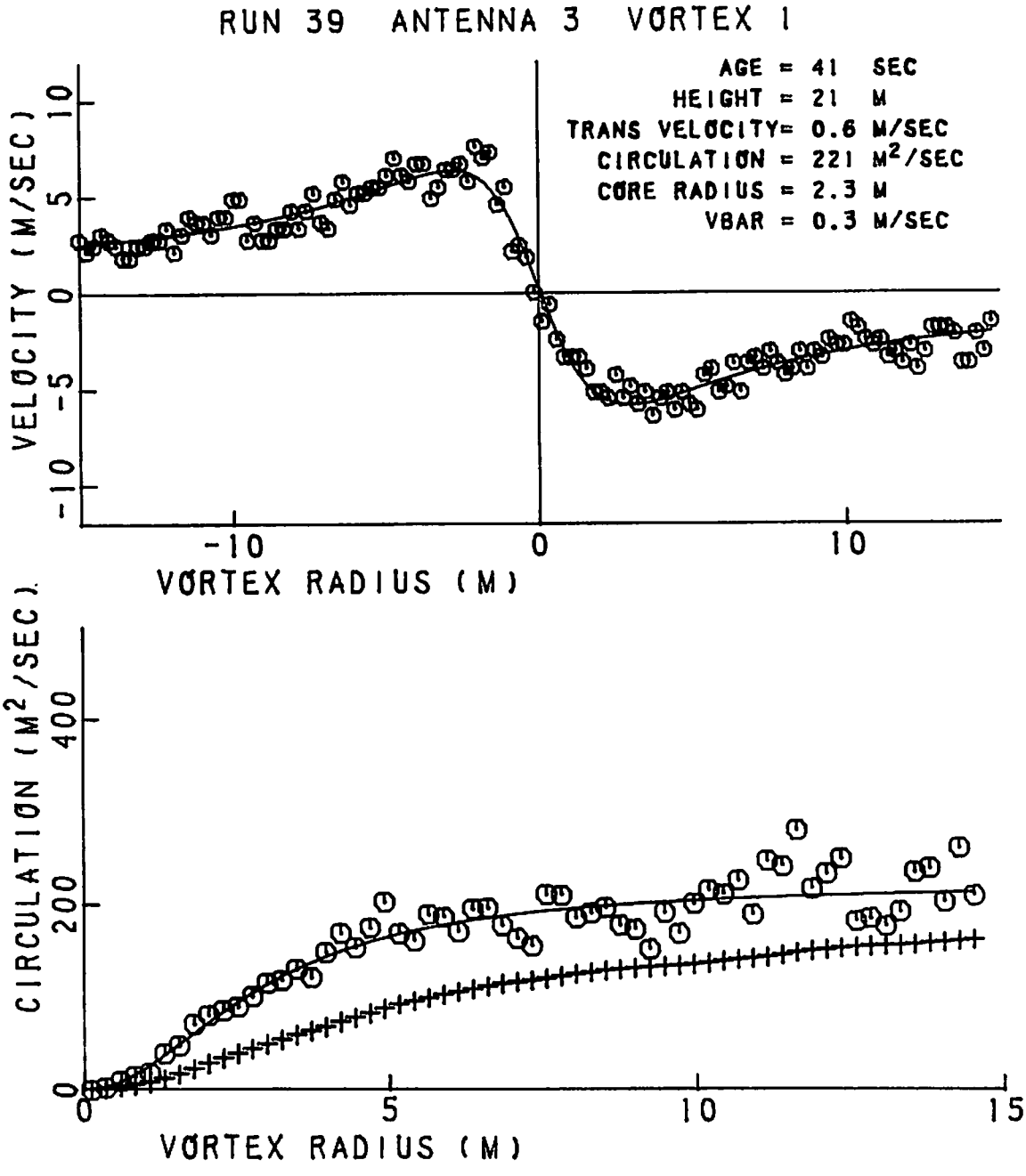

FIGURE 351. VELOCITY AND CIRCULATION PROFILES FOR RUN 39, ANTENNA 3

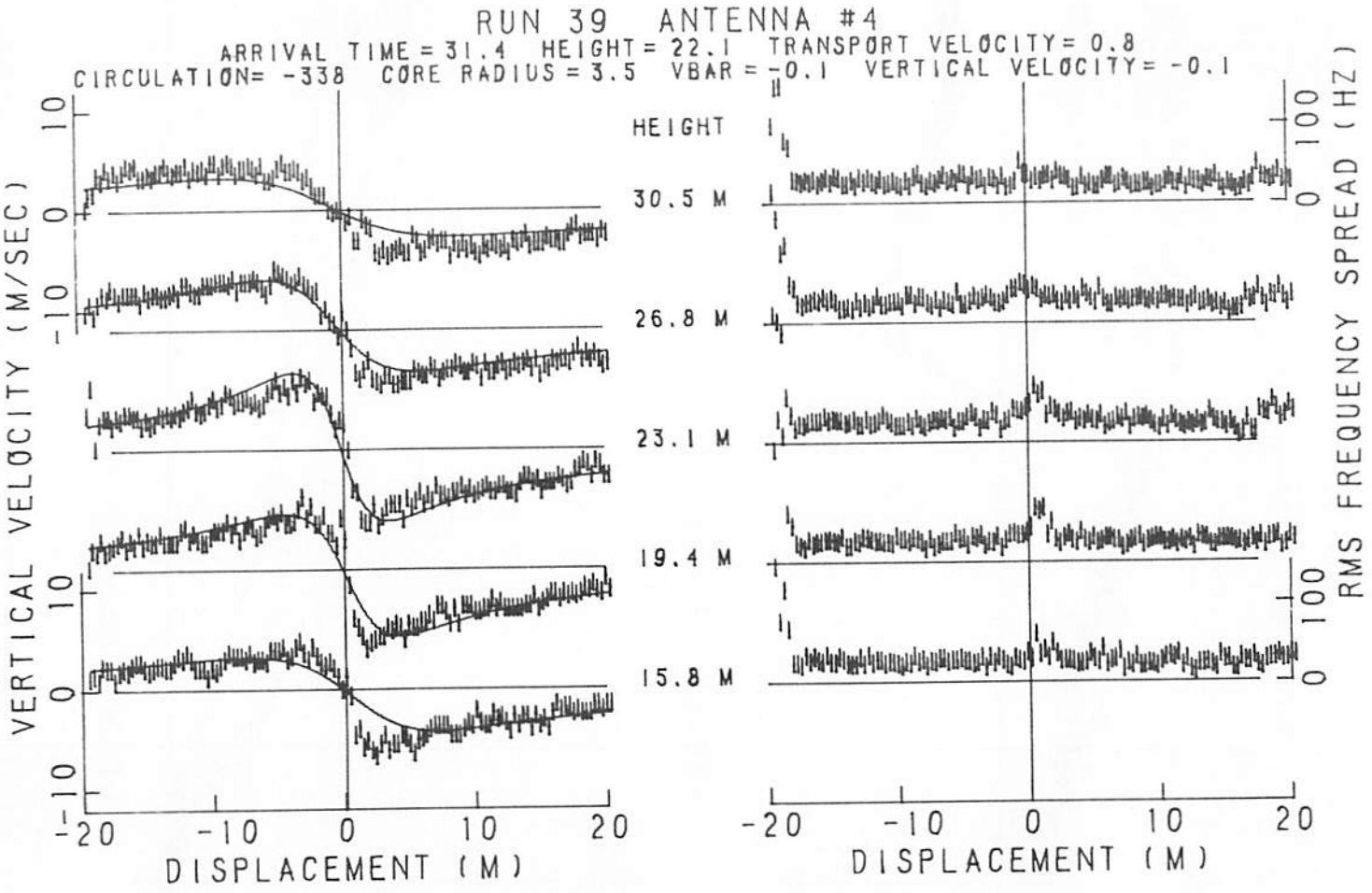

FIGURE 352. VELOCITY AND SPECTRAL WIDTH PROFILES FOR RUN 39, ANTENNA 4

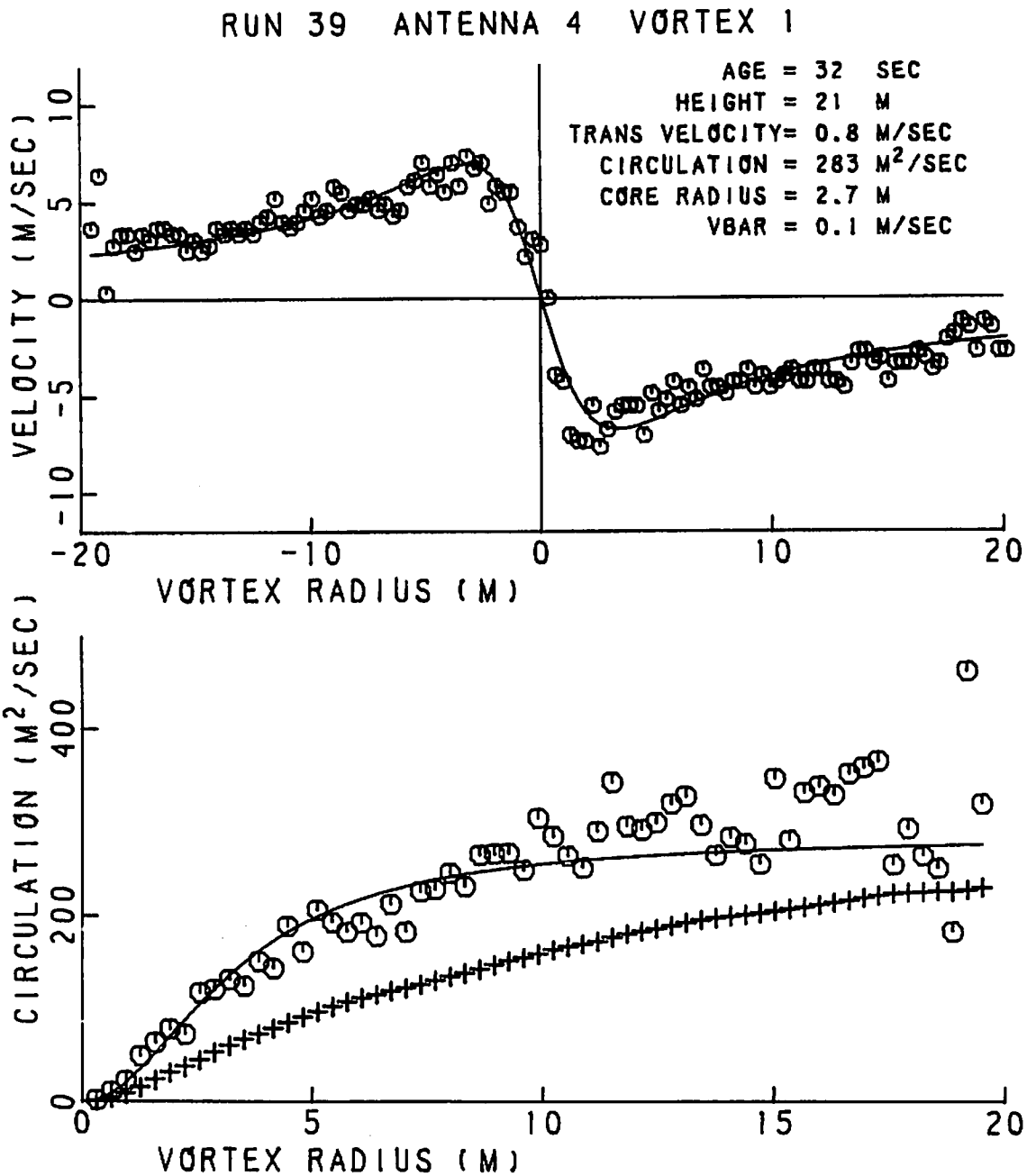

FIGURE 353. VELOCITY AND CIRCULATION PROFILES FOR RUN 39, ANTENNA 4

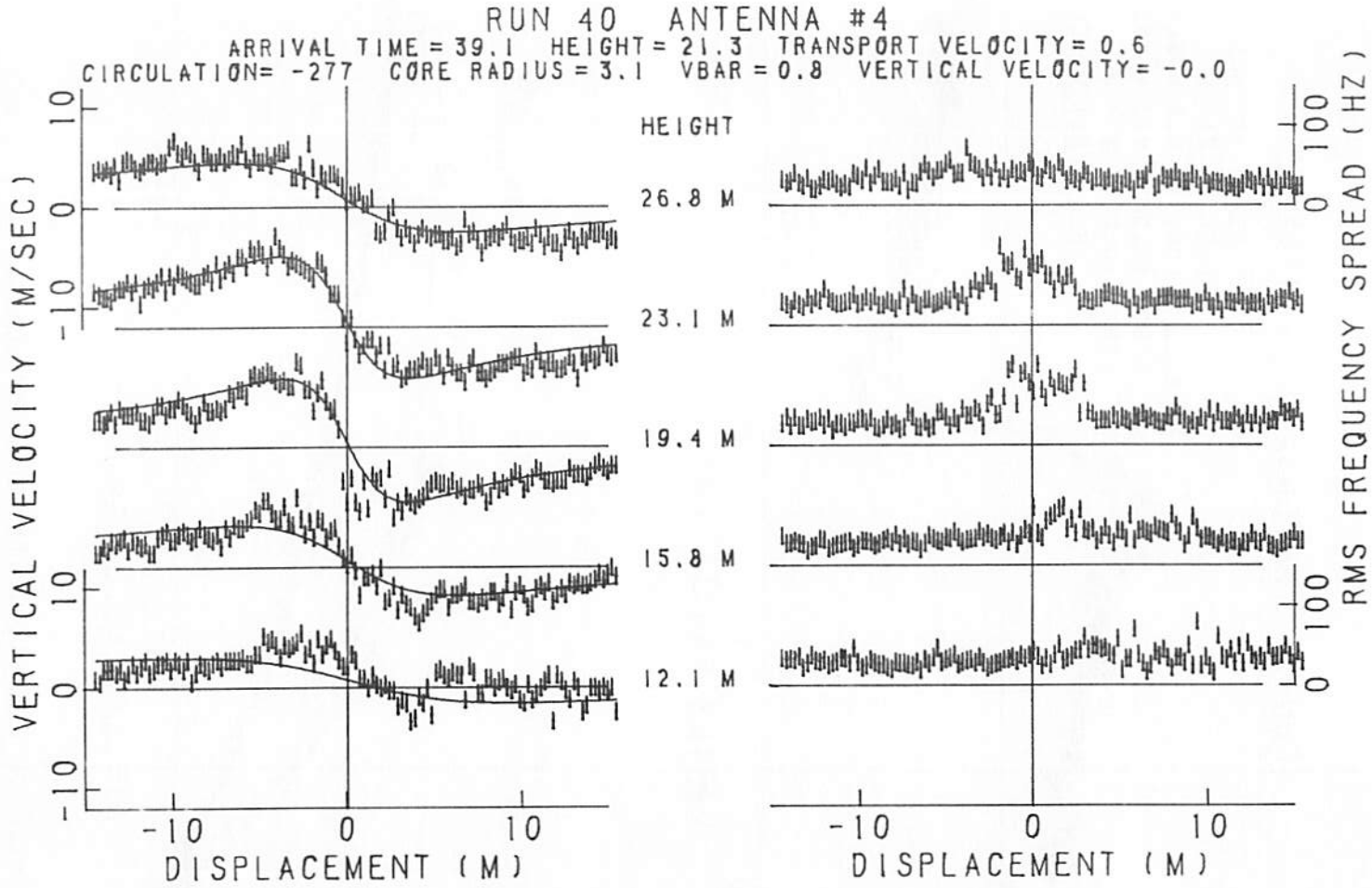

FIGURE 354. VELOCITY AND SPECTRAL WIDTH PROFILES FOR RUN 40, ANTENNA 4

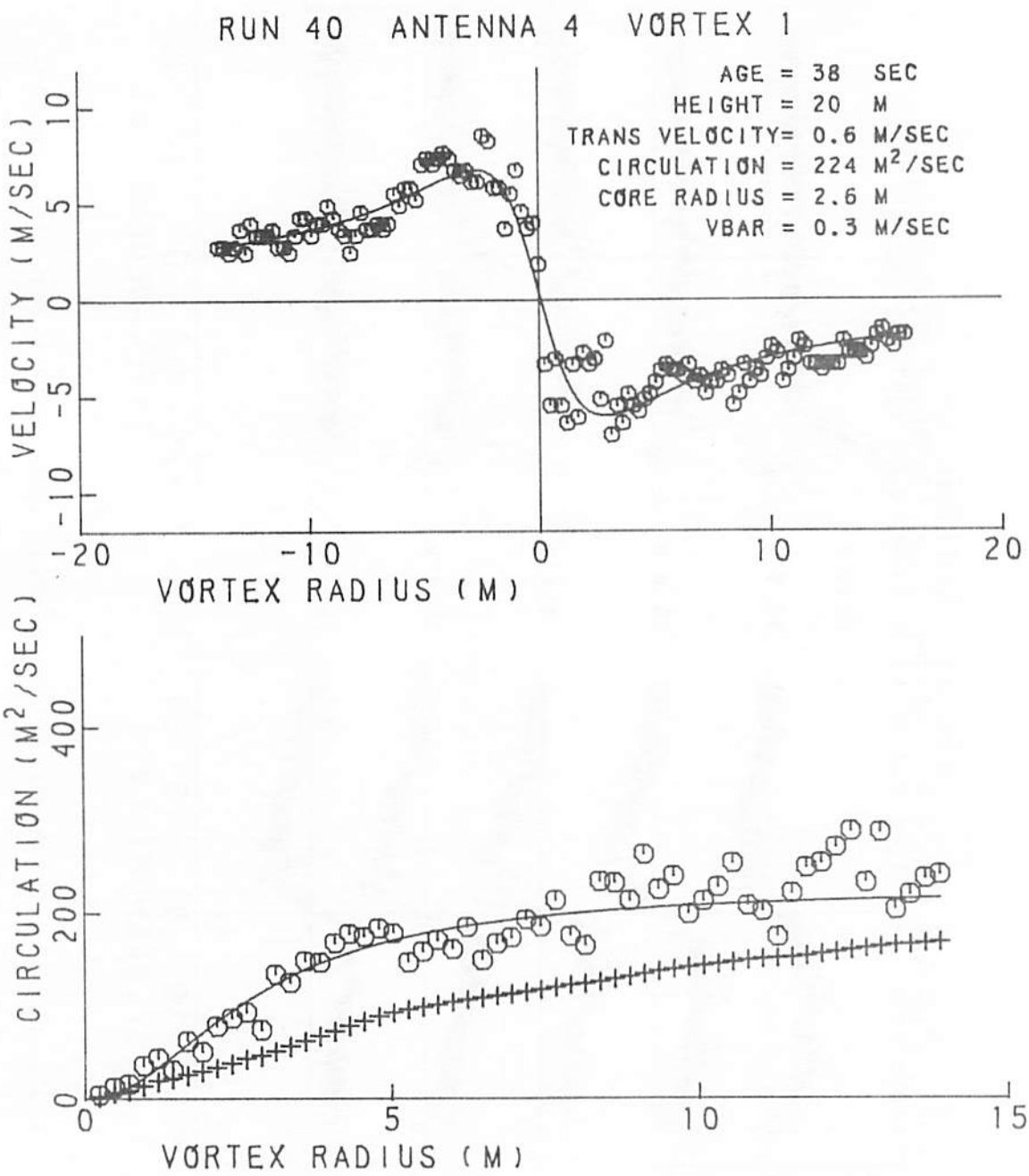

FIGURE 355. VELOCITY AND CIRCULATION PROFILES FOR RUN 40, ANTENNA 4

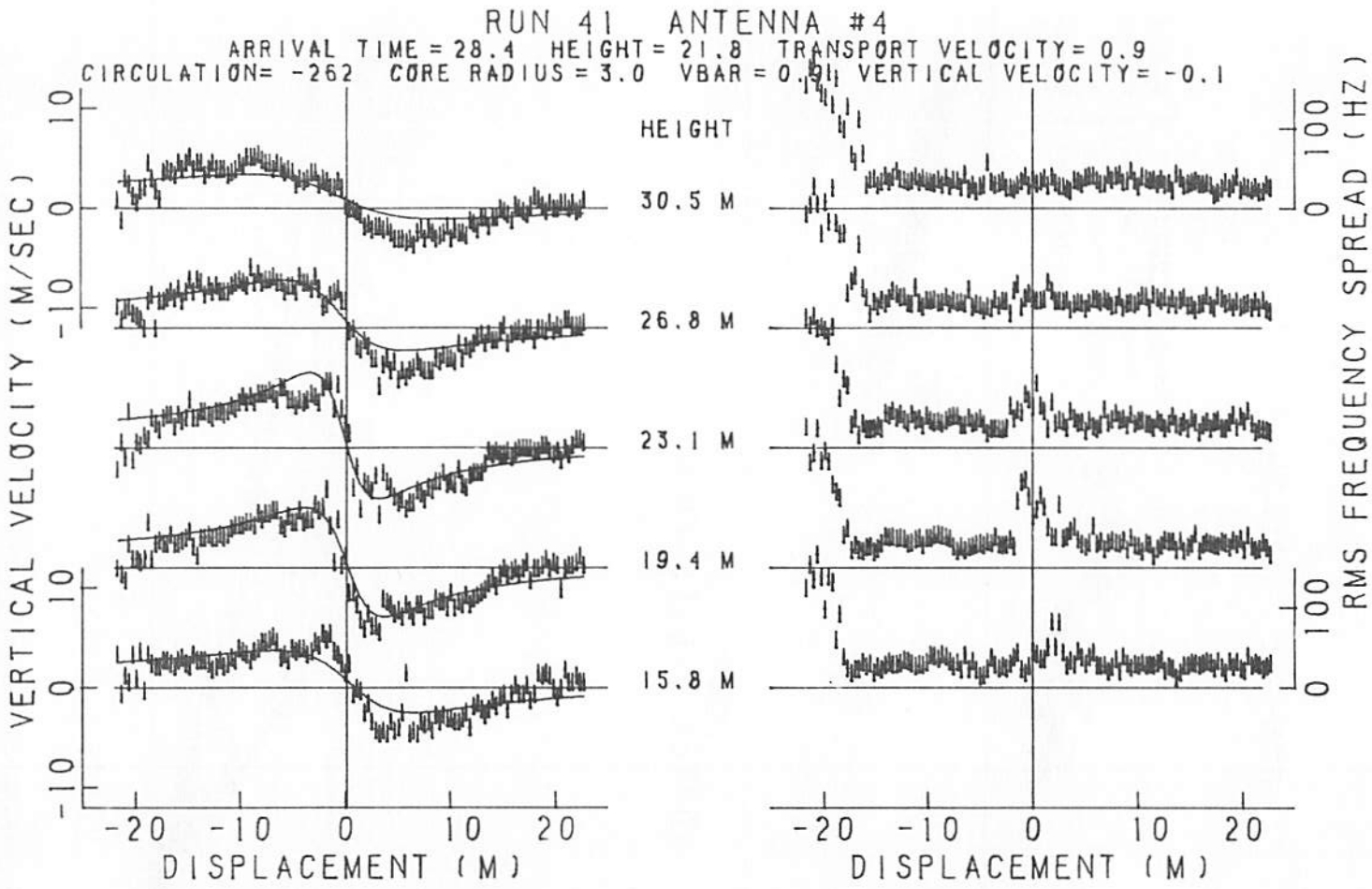

FIGURE 356. VELOCITY AND SPECTRAL WIDTH PROFILES FOR RUN 41, ANTENNA 4

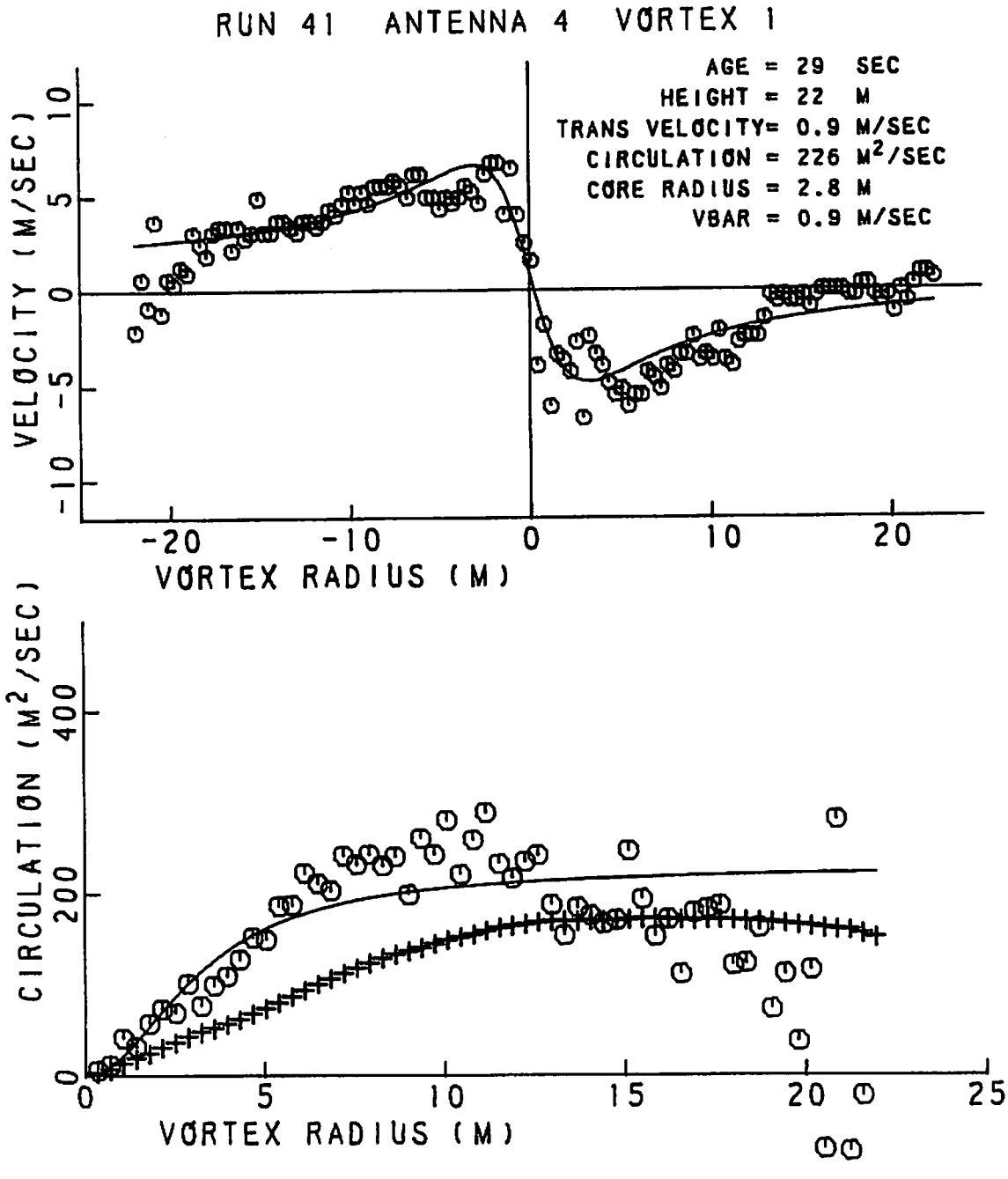

FIGURE 357. VELOCITY AND CIRCULATION PROFILES FOR RUN 41, ANTENNA 4

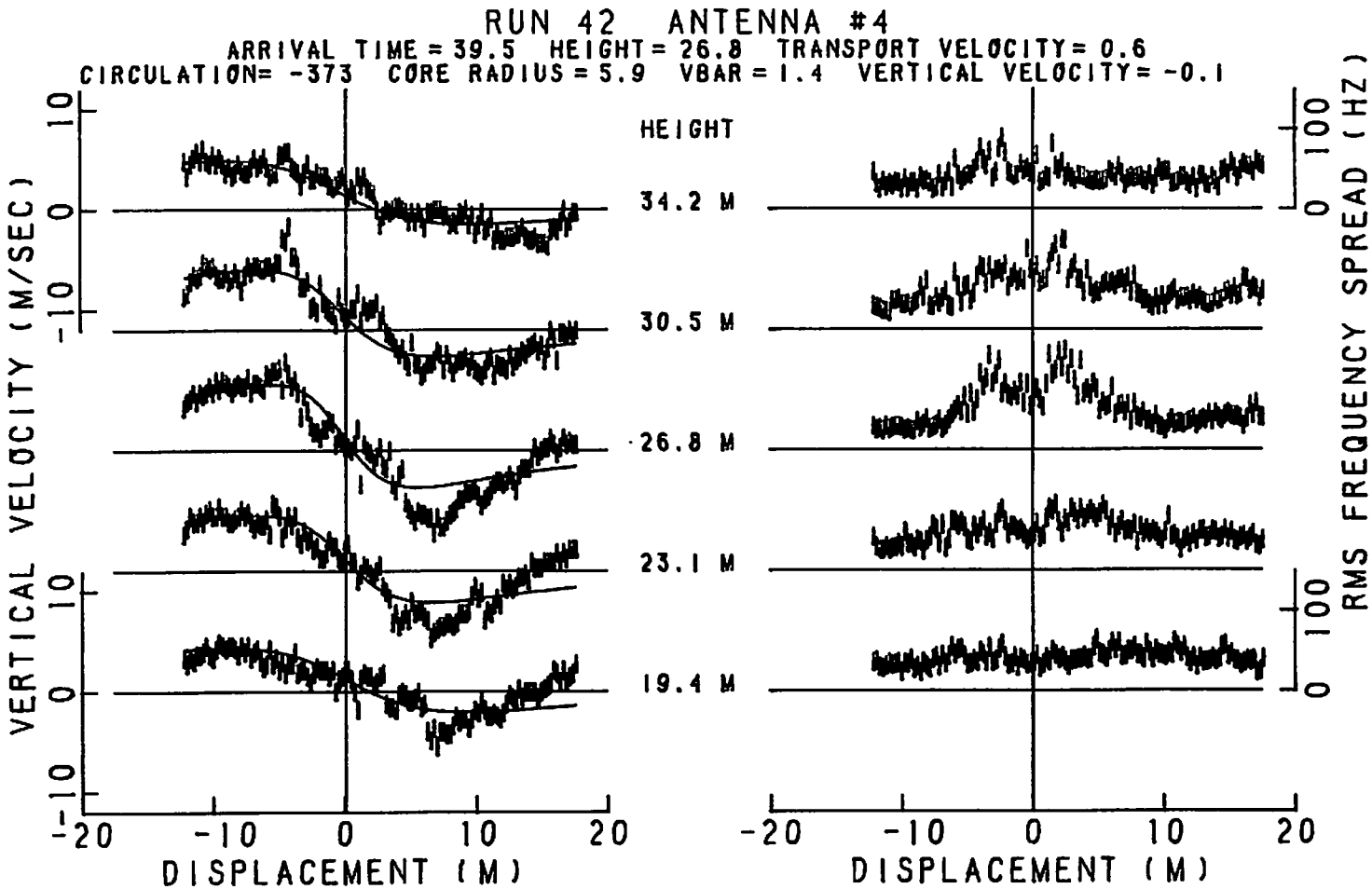

FIGURE 358. VELOCITY AND SPECTRAL WIDTH PROFILES FOR RUN 42, ANTENNA 4

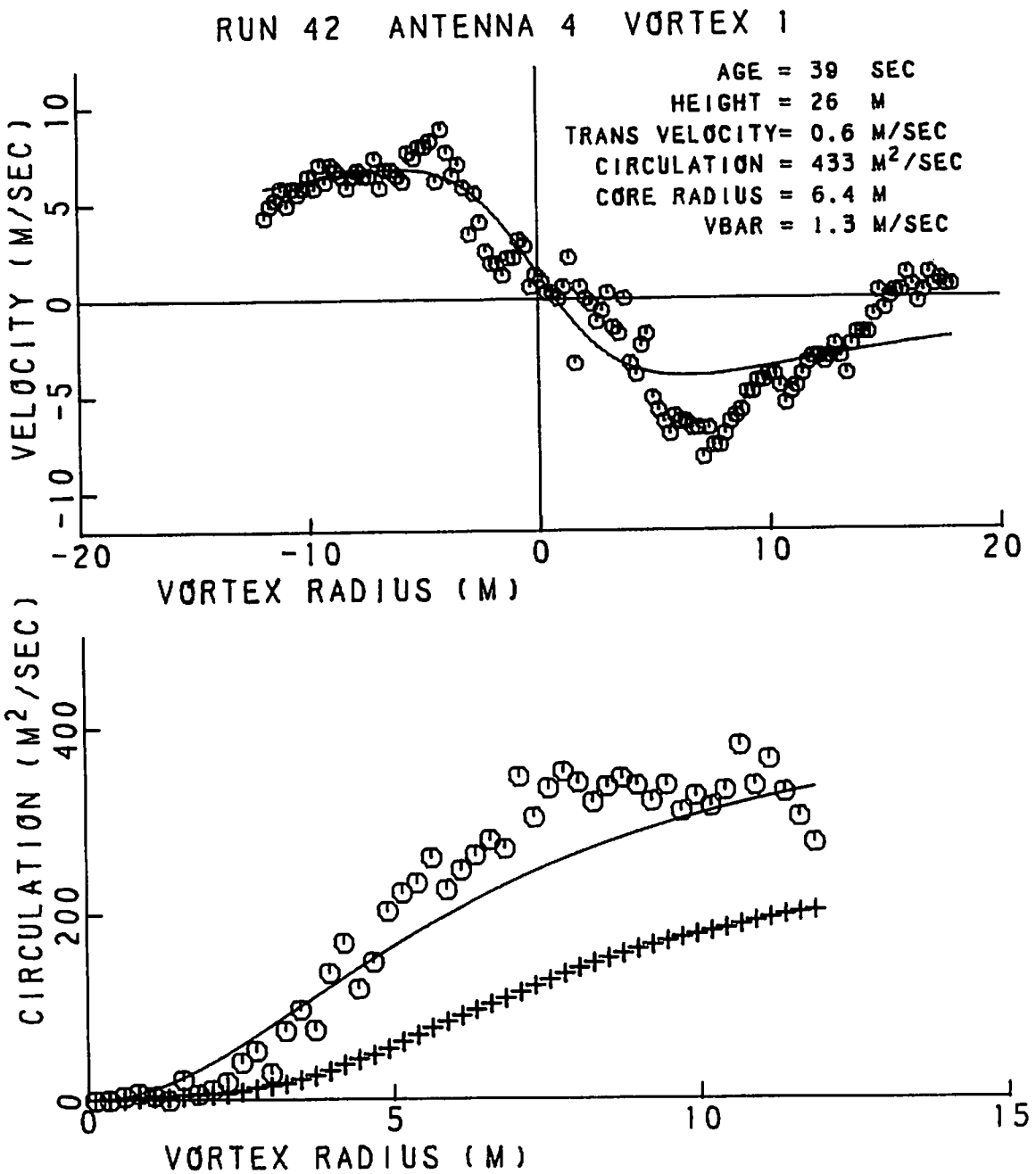

FIGURE 359. VELOCITY AND CIRCULATION PROFILES FOR RUN 42, ANTENNA 4

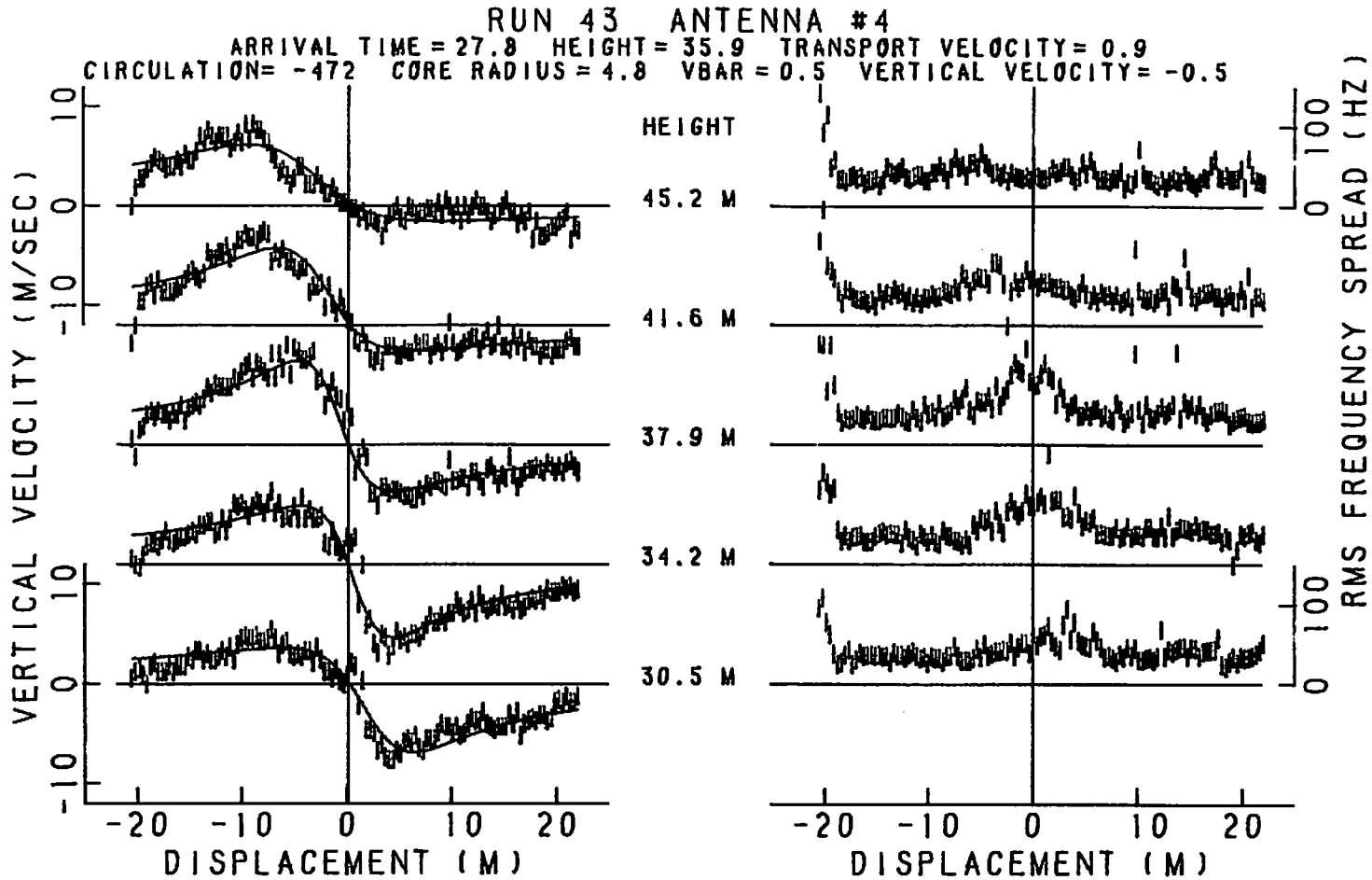

FIGURE 360. VELOCITY AND SPECTRAL WIDTH PROFILES FOR RUN 43, ANTENNA 4

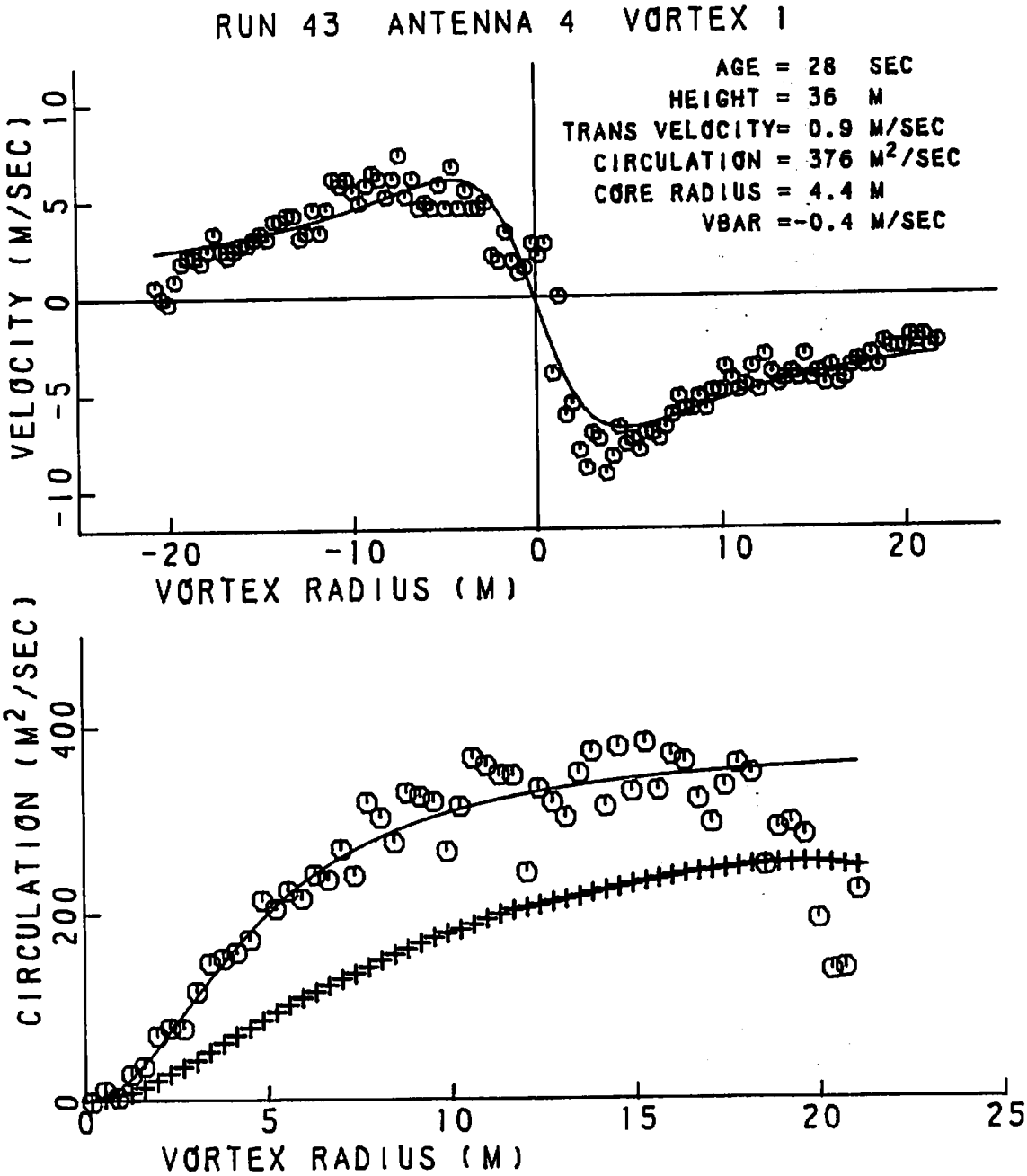

FIGURE 361. VELOCITY AND CIRCULATION PROFILES FOR RUN 43, ANTENNA 4

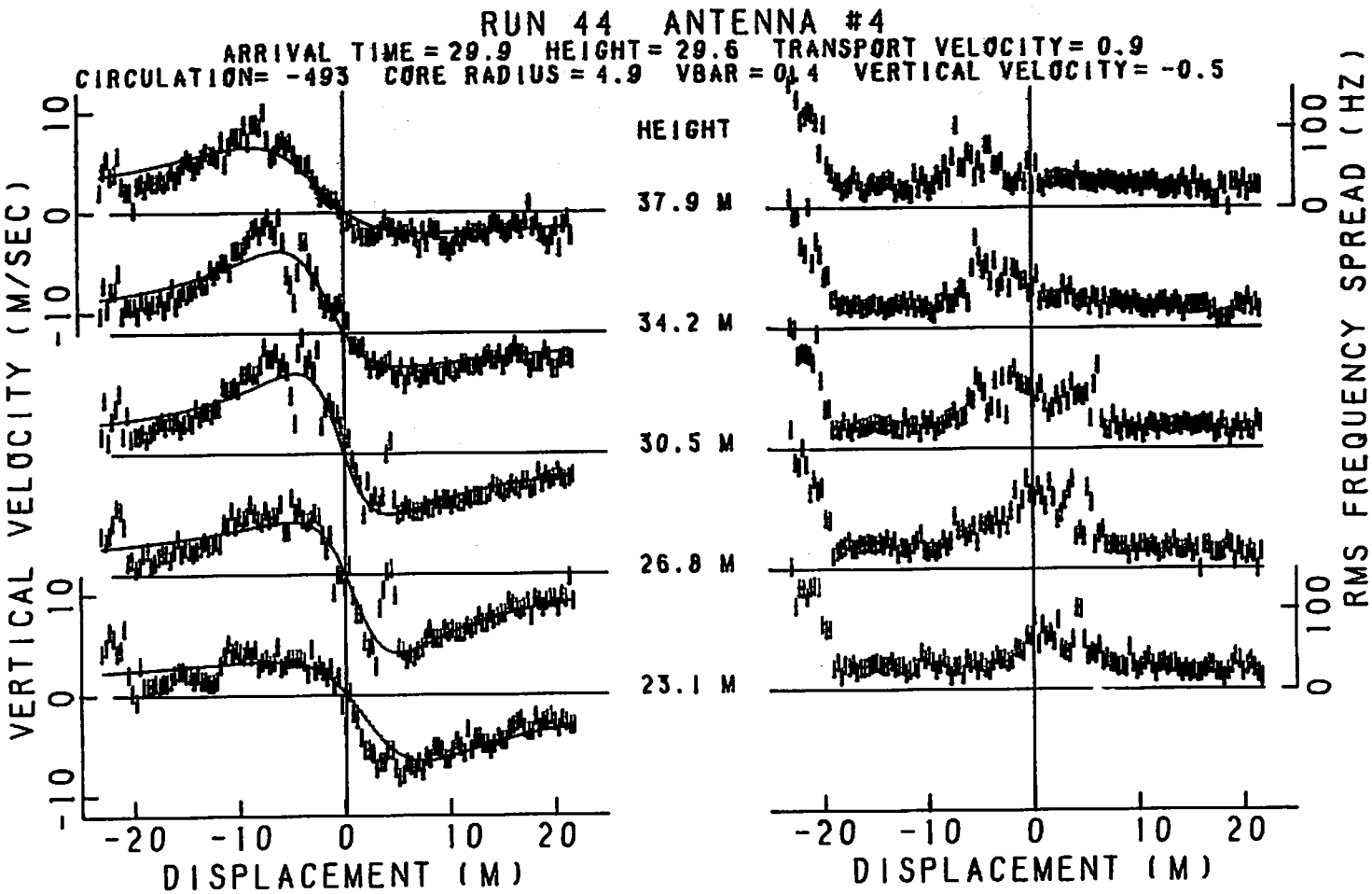

FIGURE 362. VELOCITY AND SPECTRAL WIDTH PROFILES FOR RUN 44, ANTENNA 4

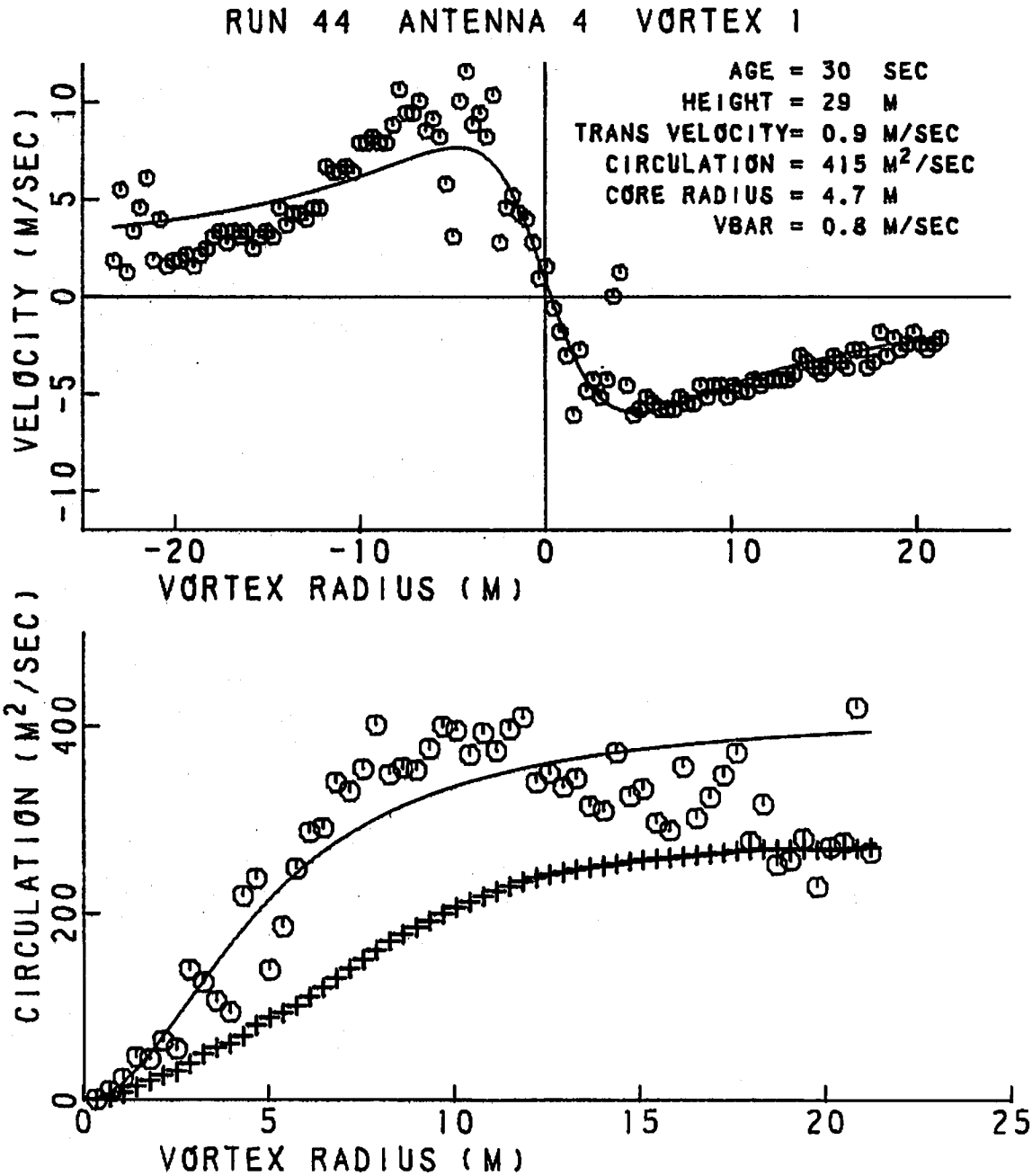

FIGURE 363. VELOCITY AND CIRCULATION PROFILES FOR RUN 44, ANTENNA 4

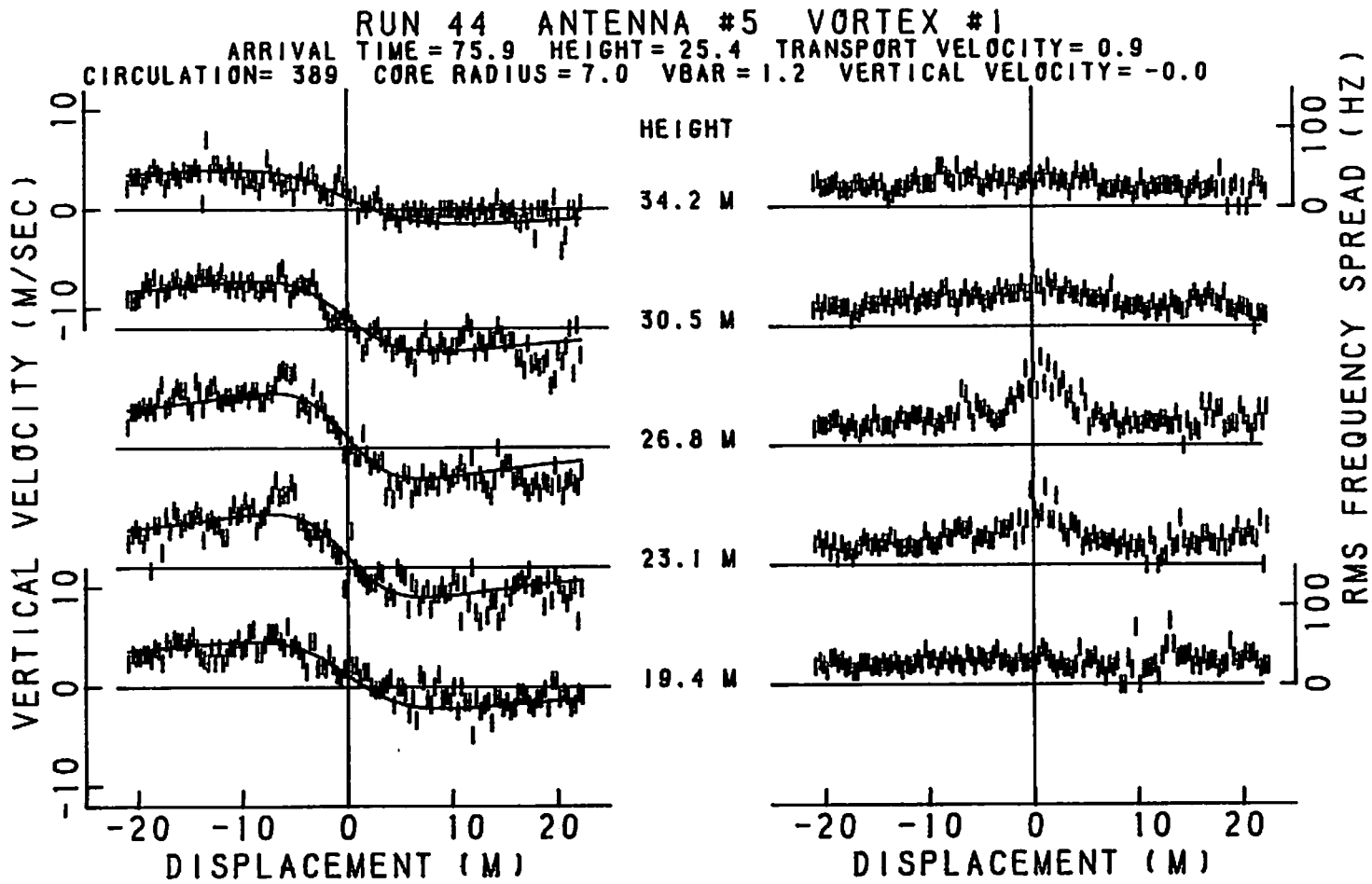

FIGURE 364. VELOCITY AND SPECTRAL WIDTH PROFILES FOR RUN 44, ANTENNA 5

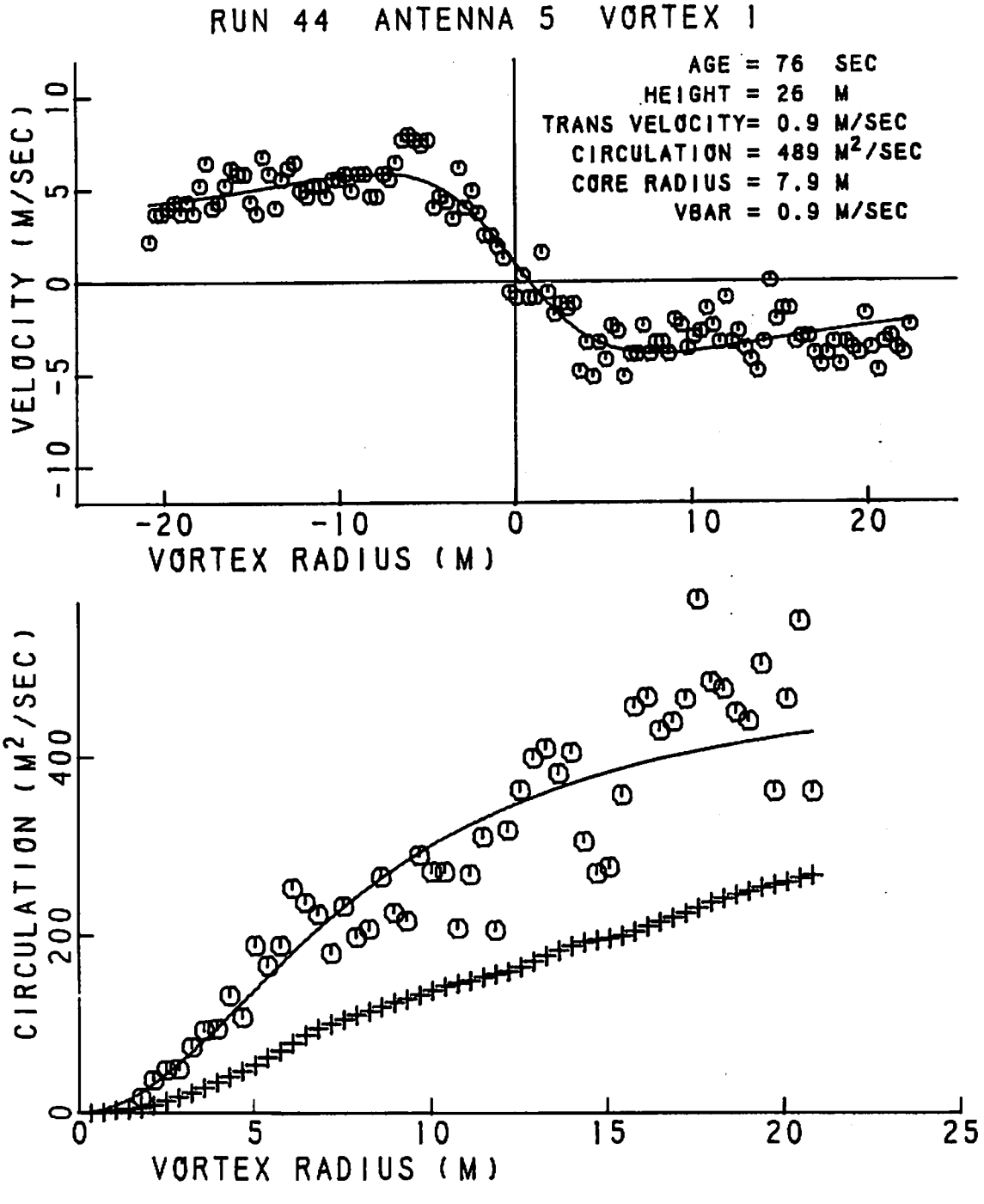

FIGURE 365. VELOCITY AND CIRCULATION PROFILES FOR RUN 44, ANTENNA 5

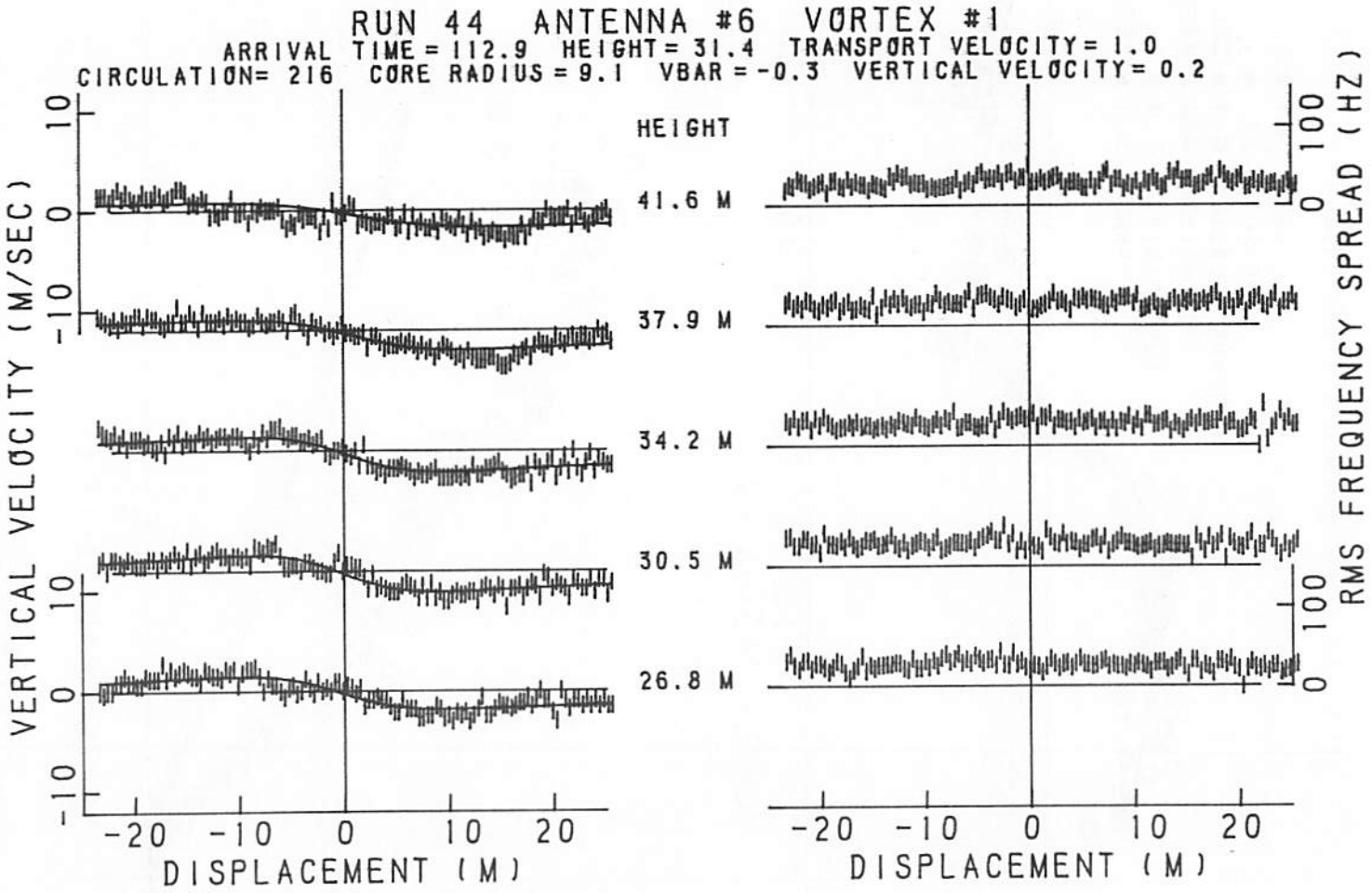

FIGURE 366. VELOCITY AND SPECTRAL WIDTH PROFILES FOR RUN 44, ANTENNA 6

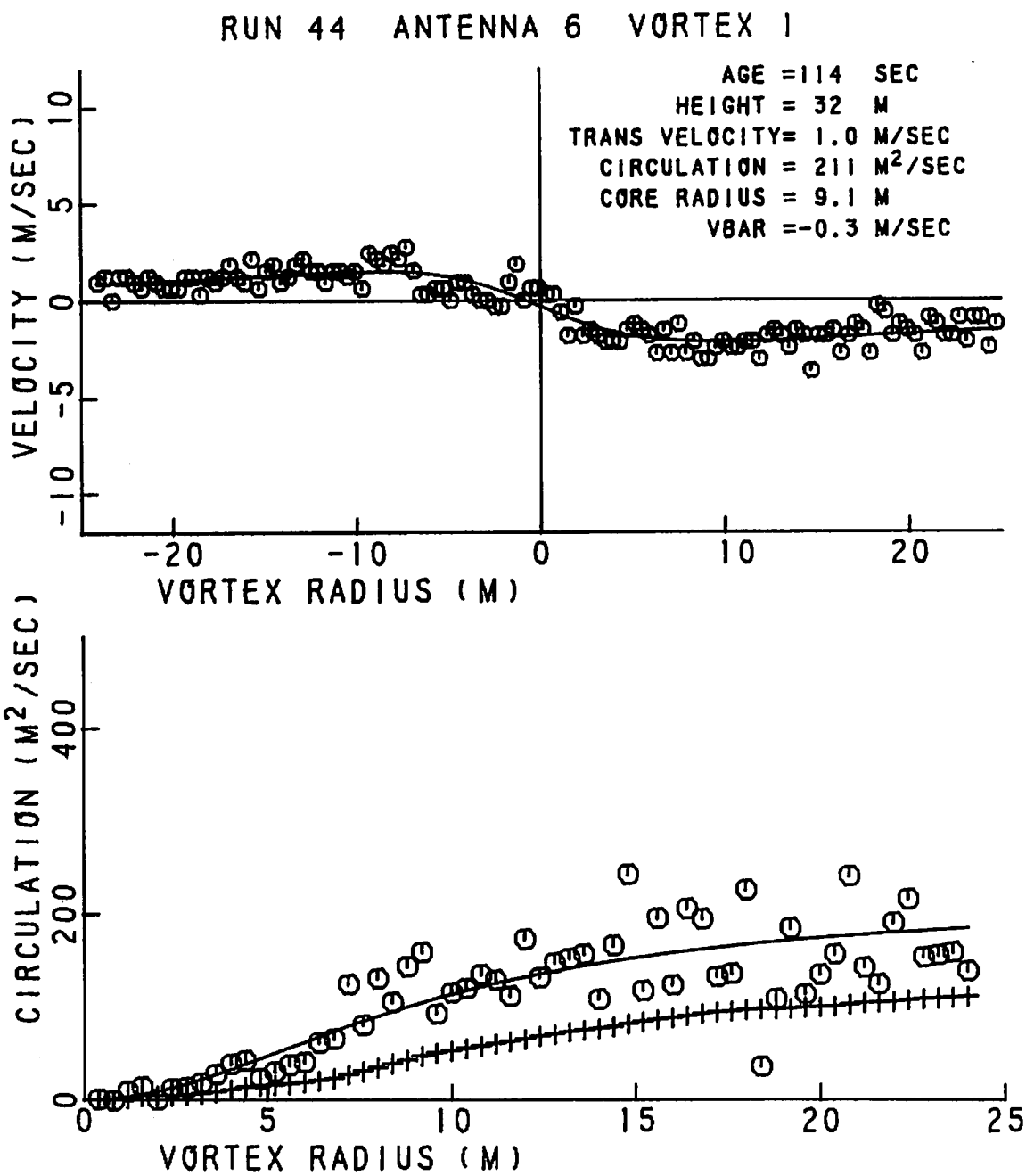

FIGURE 367. VELOCITY AND CIRCULATION PROFILES FOR RUN 44, ANTENNA 6

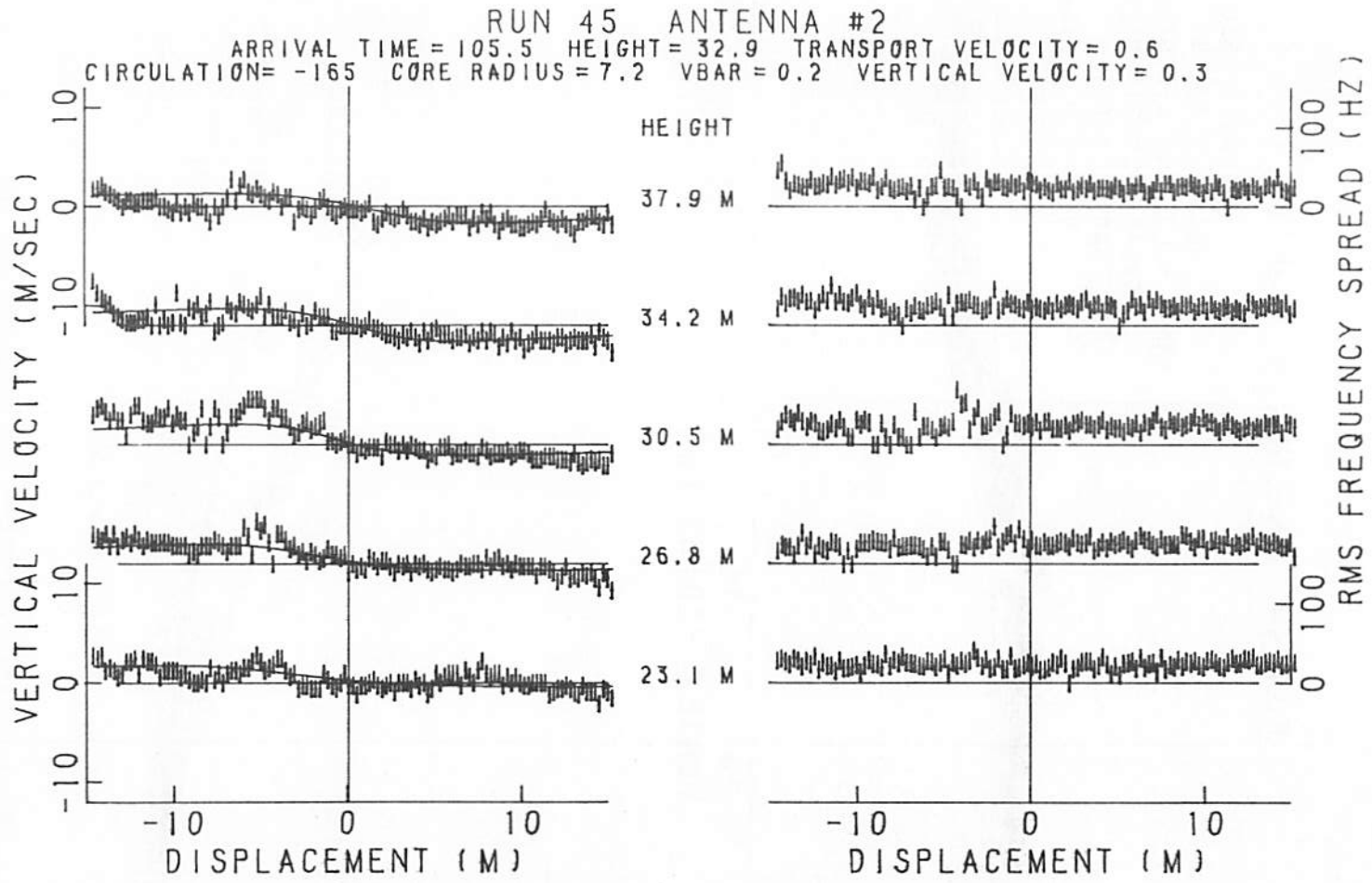

FIGURE 368. VELOCITY AND SPECTRAL WIDTH PROFILES FOR RUN 45, ANTENNA 2

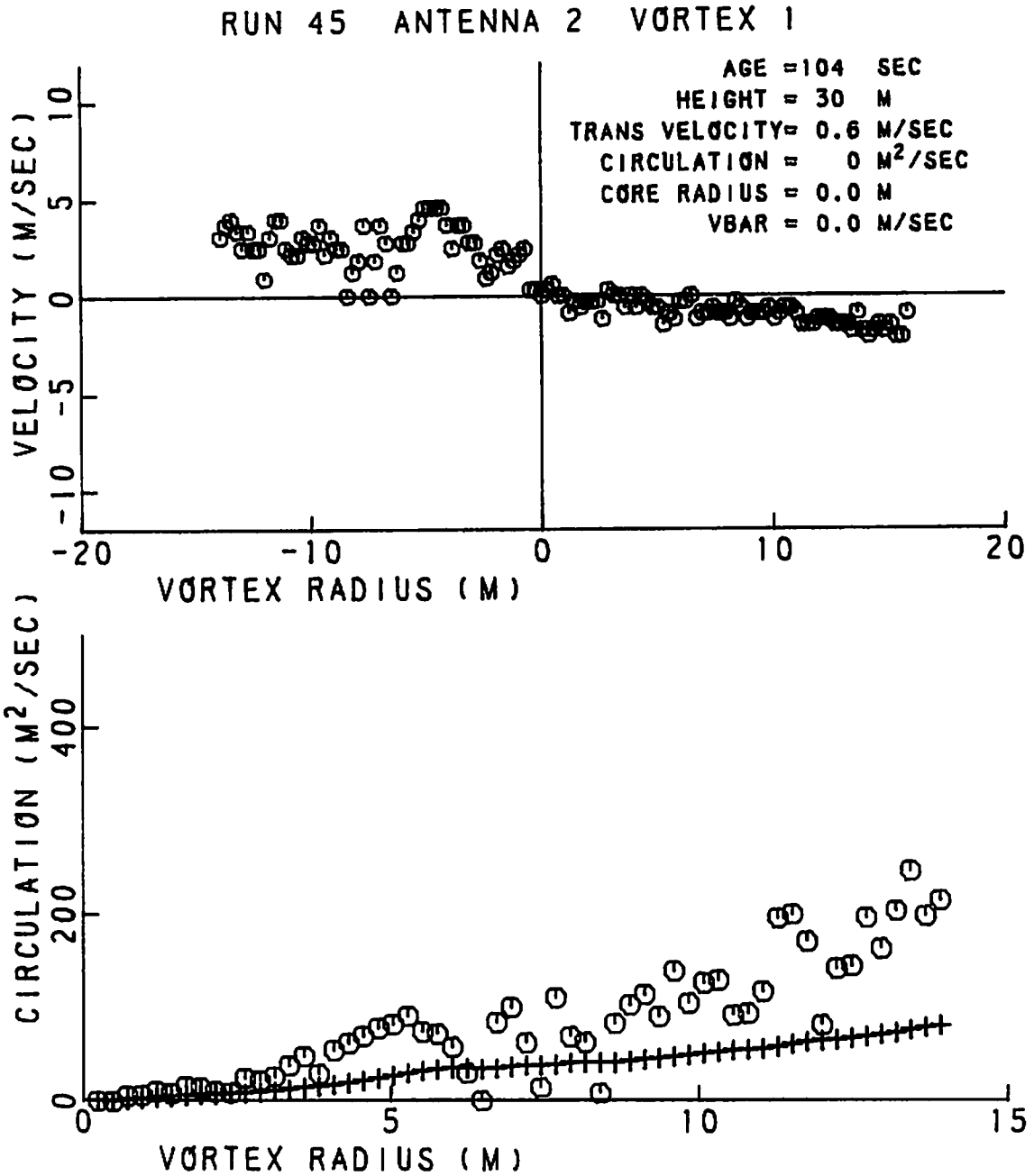

FIGURE 369. VELOCITY AND CIRCULATION PROFILES FOR FOR RUN 45, ANTENNA 2

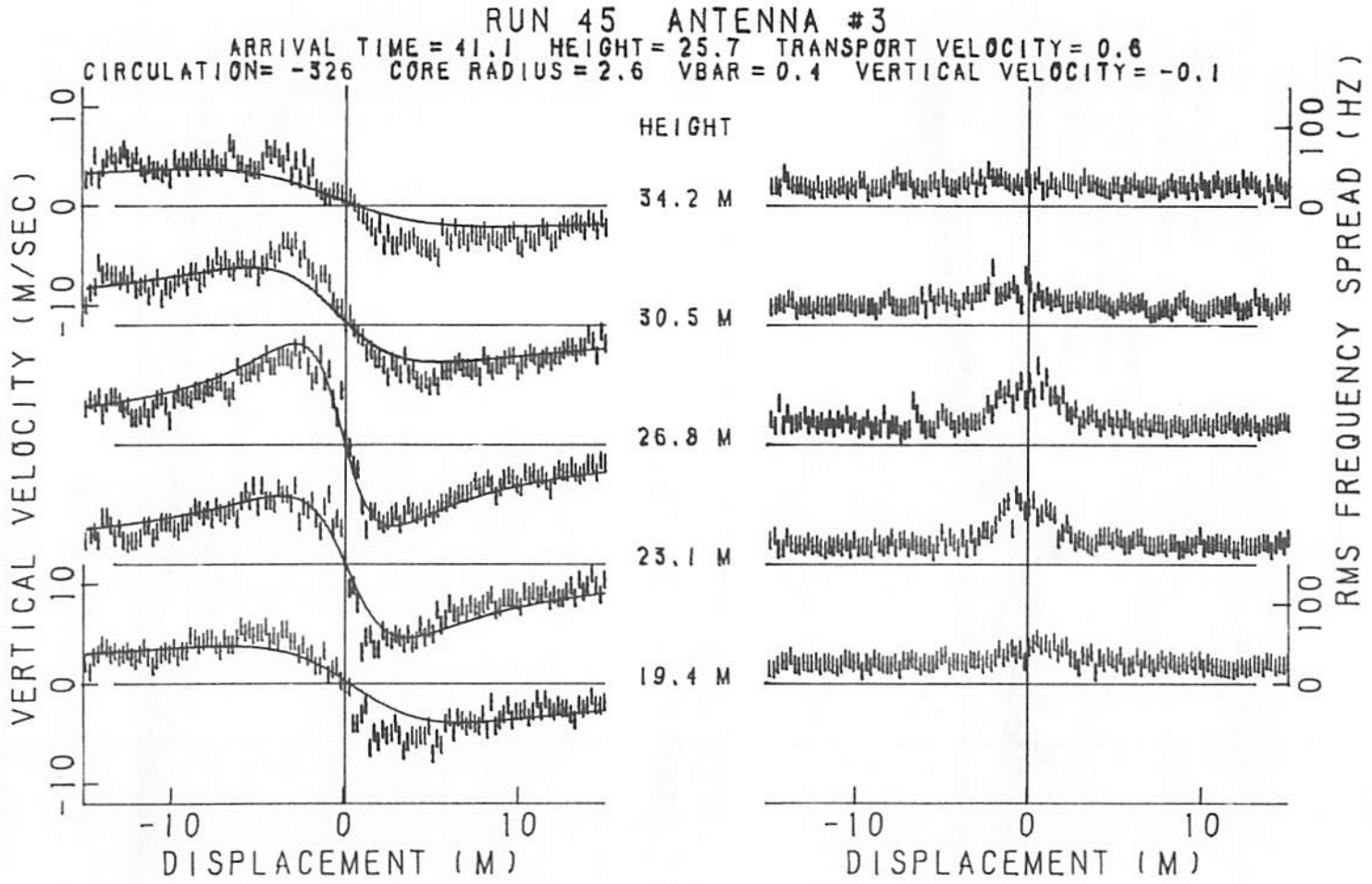

FIGURE 370. VELOCITY AND SPECTRAL WIDTH PROFILES FOR RUN 45, ANTENNA 3

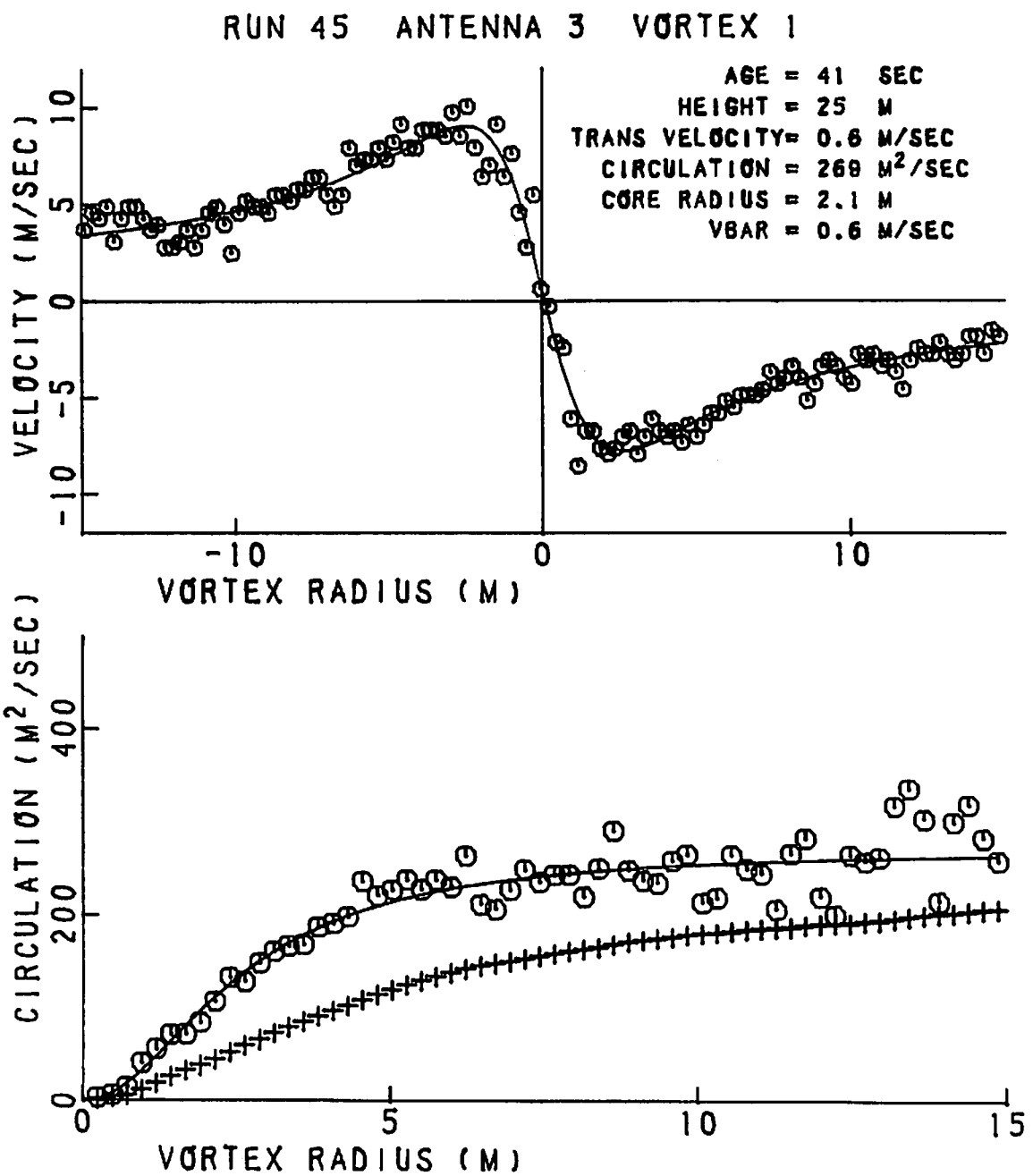

FIGURE 371. VELOCITY AND CIRCULATION PROFILES FOR RUN 45, ANTENNA 3

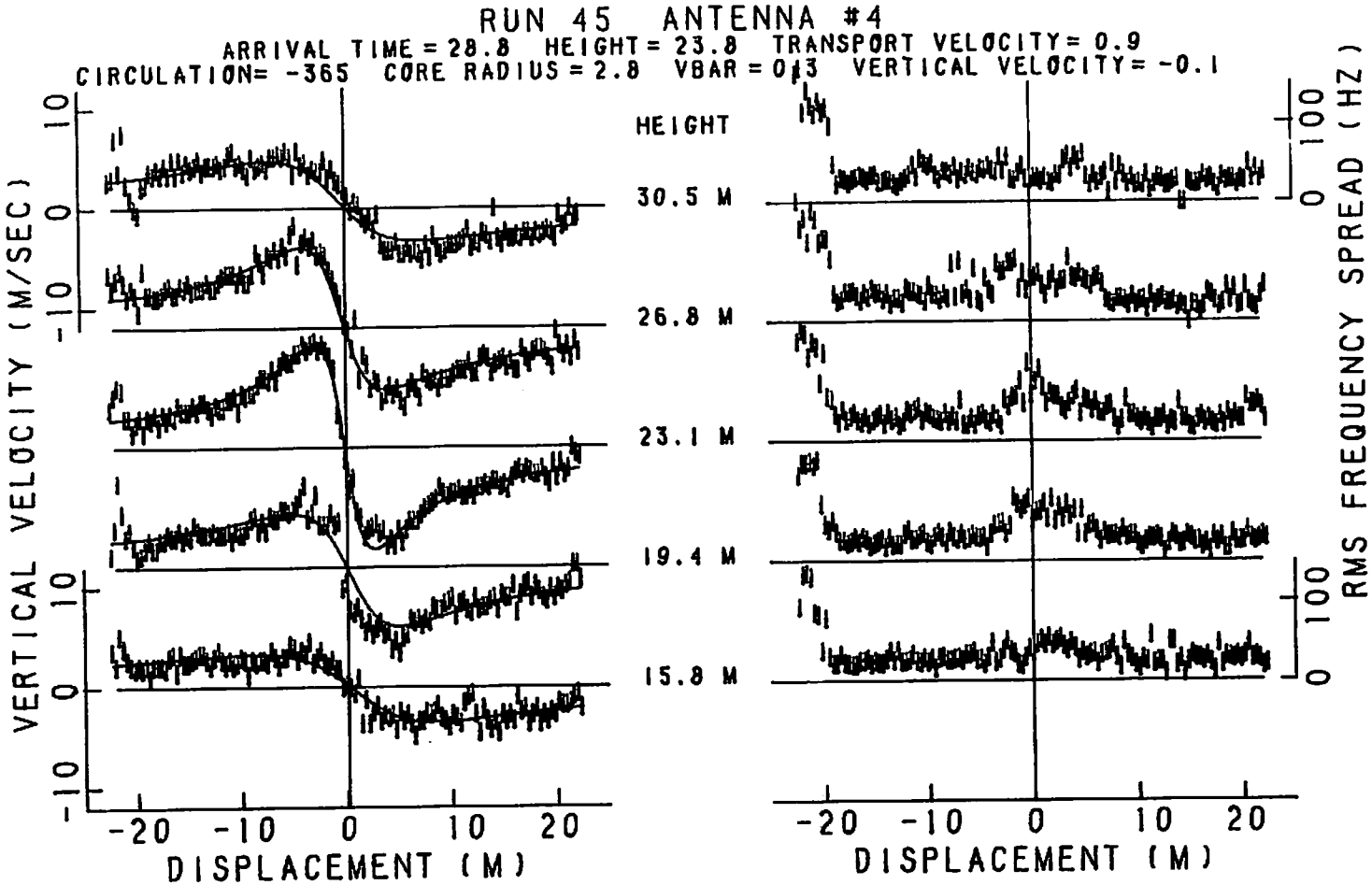

FIGURE 372. VELOCITY AND SPECTRAL WIDTH PROFILES FOR RUN 45, ANTENNA 4

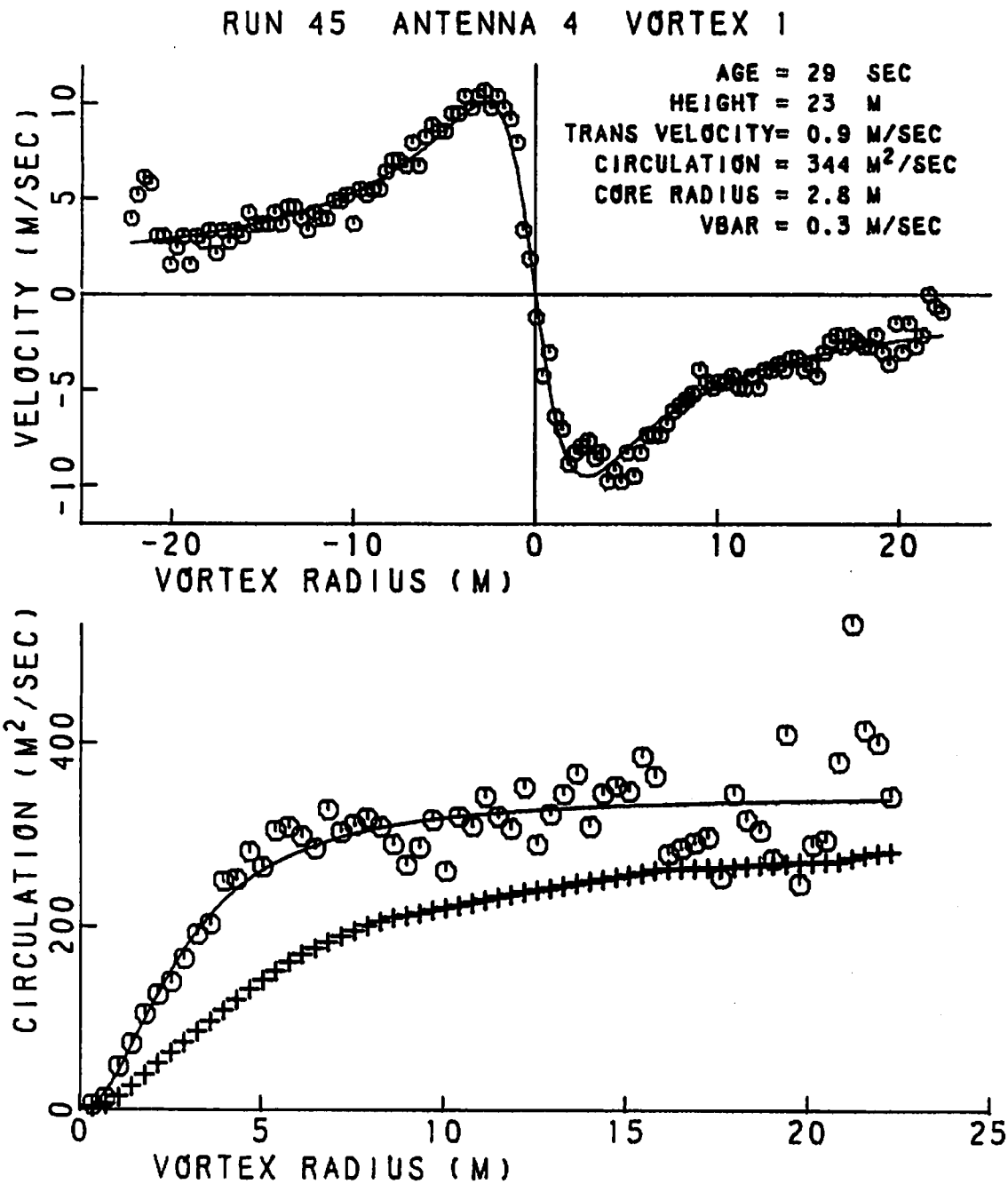

FIGURE 373. VELOCITY AND CIRCULATION PROFILES FOR RUN 45, ANTENNA 4

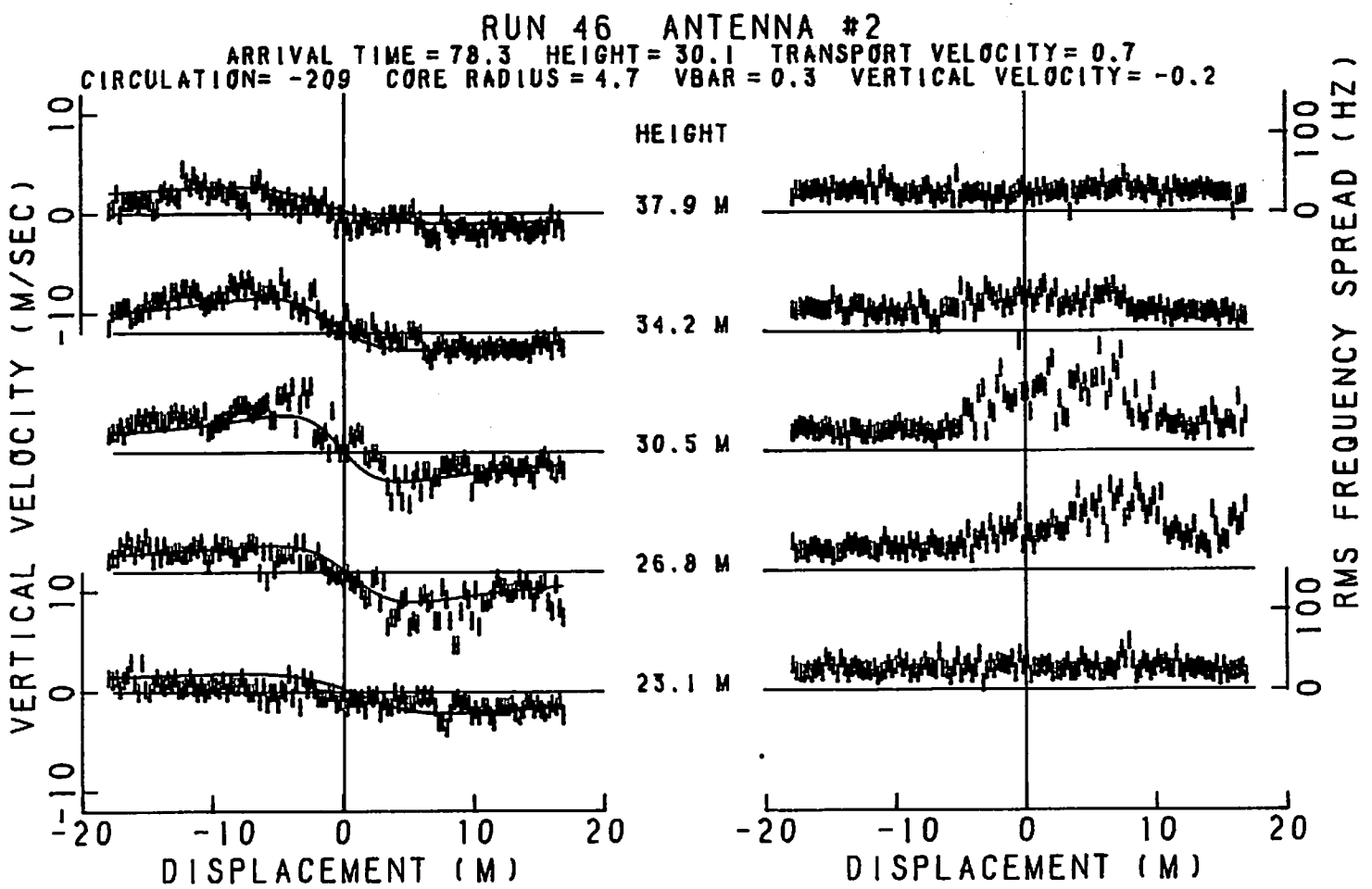

FIGURE 374. VELOCITY AND SPECTRAL WIDTH PROFILES FOR RUN 46, ANTENNA 2

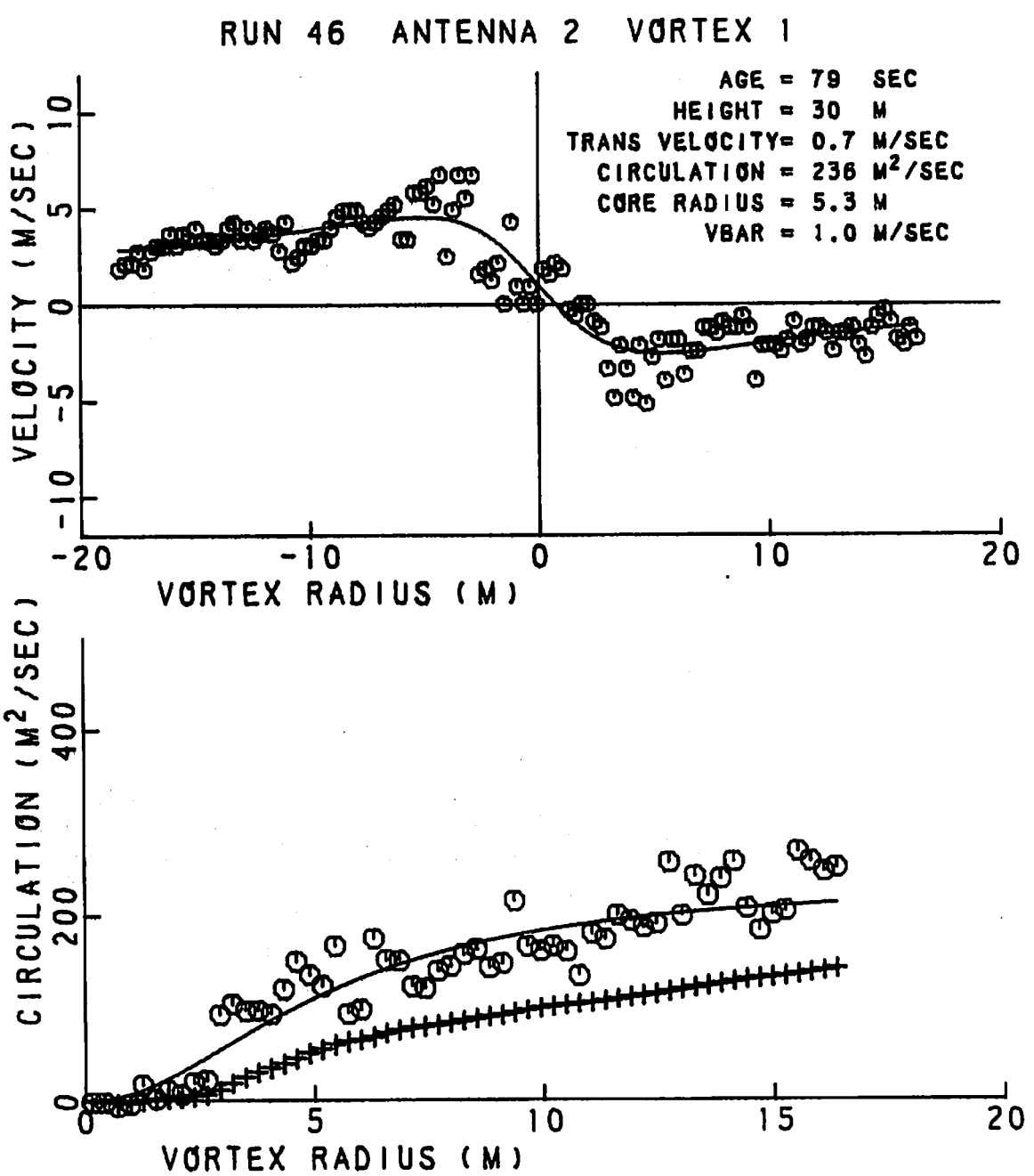

FIGURE 375. VELOCITY AND CIRCULATION PROFILES FOR RUN 46, ANTENNA 2

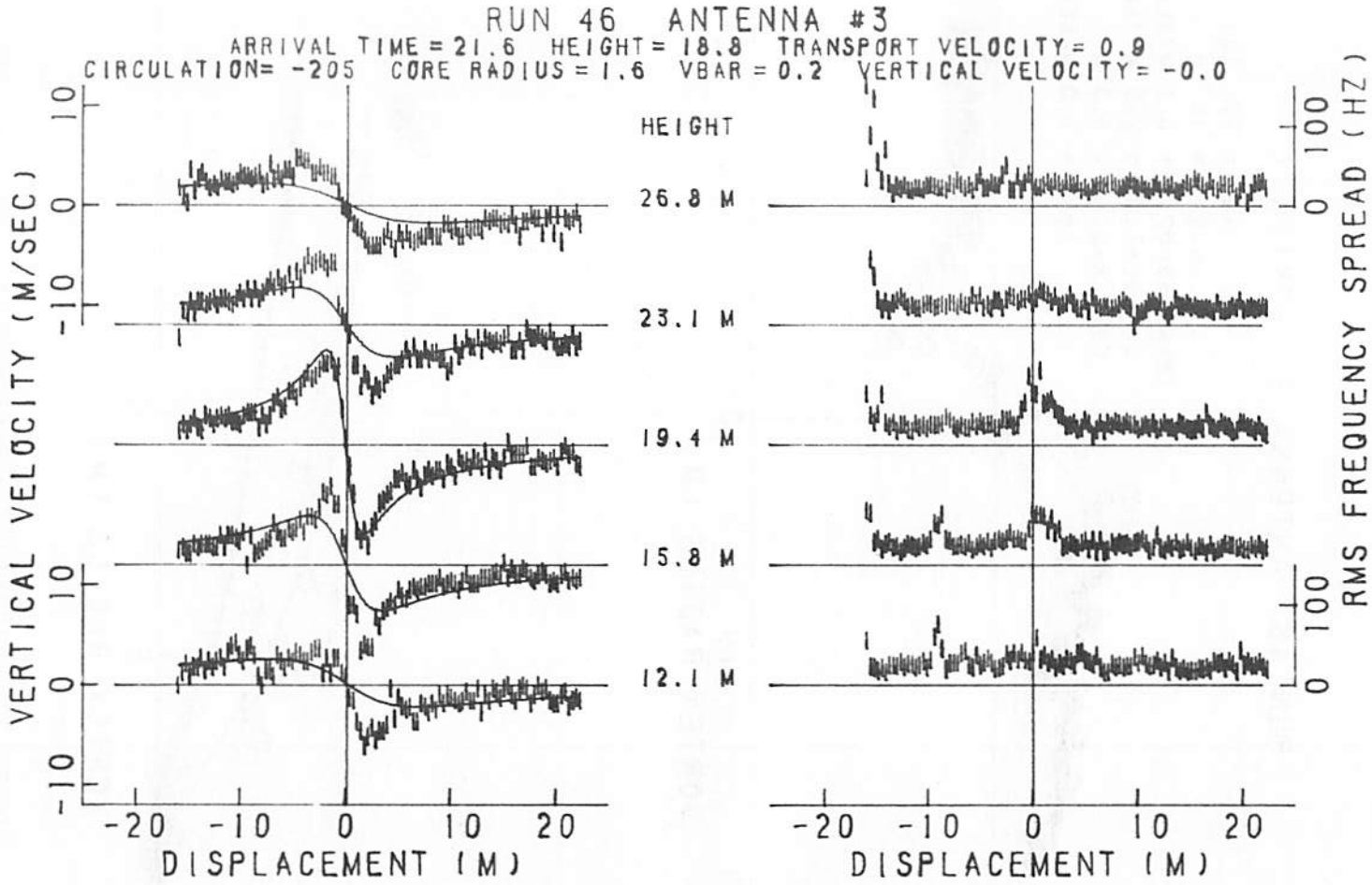

FIGURE 376. VELOCITY AND SPECTRAL WIDTH PROFILES FOR RUN 46, ANTENNA 3

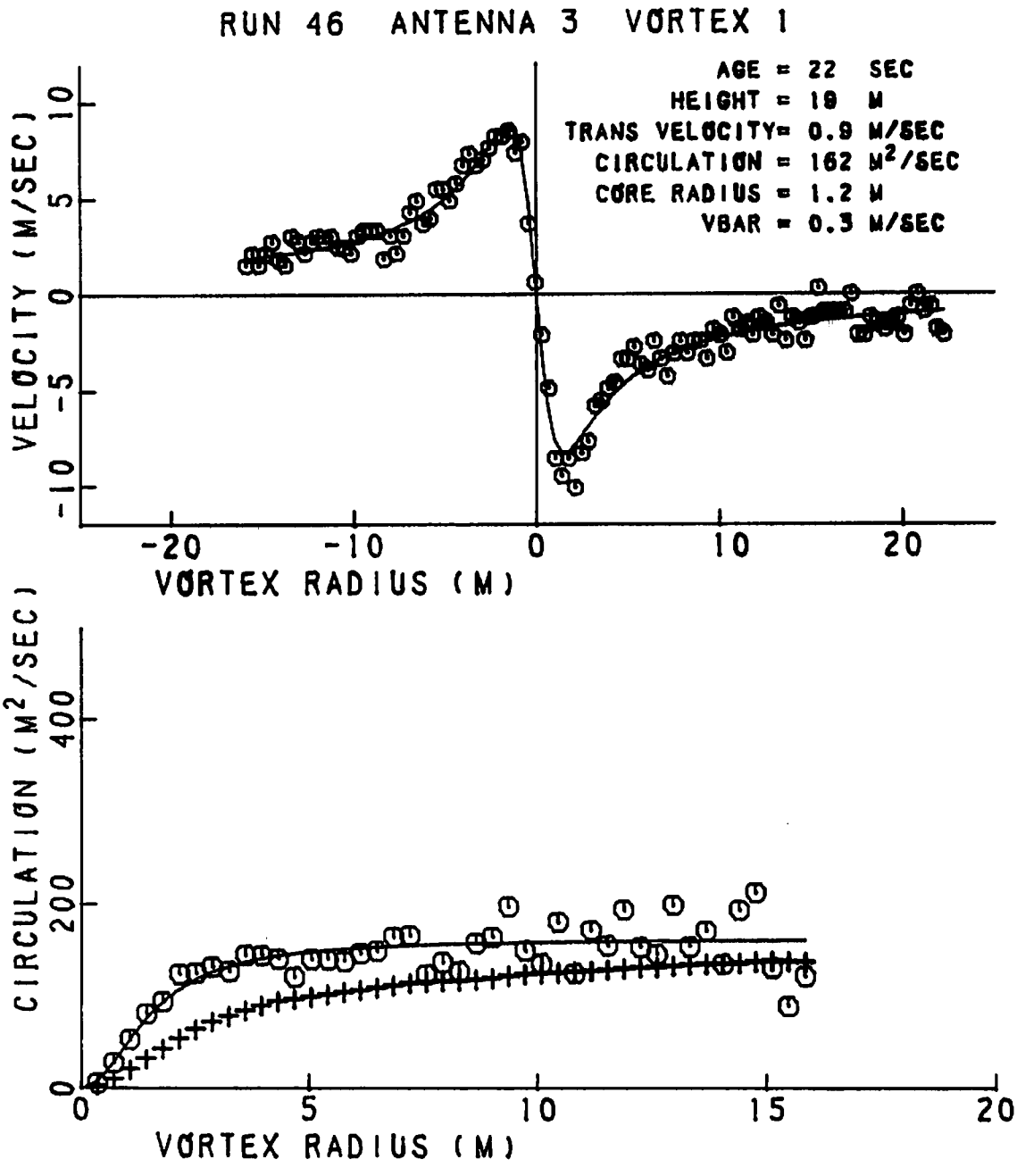

FIGURE 377. VELOCITY AND CIRCULATION PROFILES FOR RUN 46, ANTENNA 3

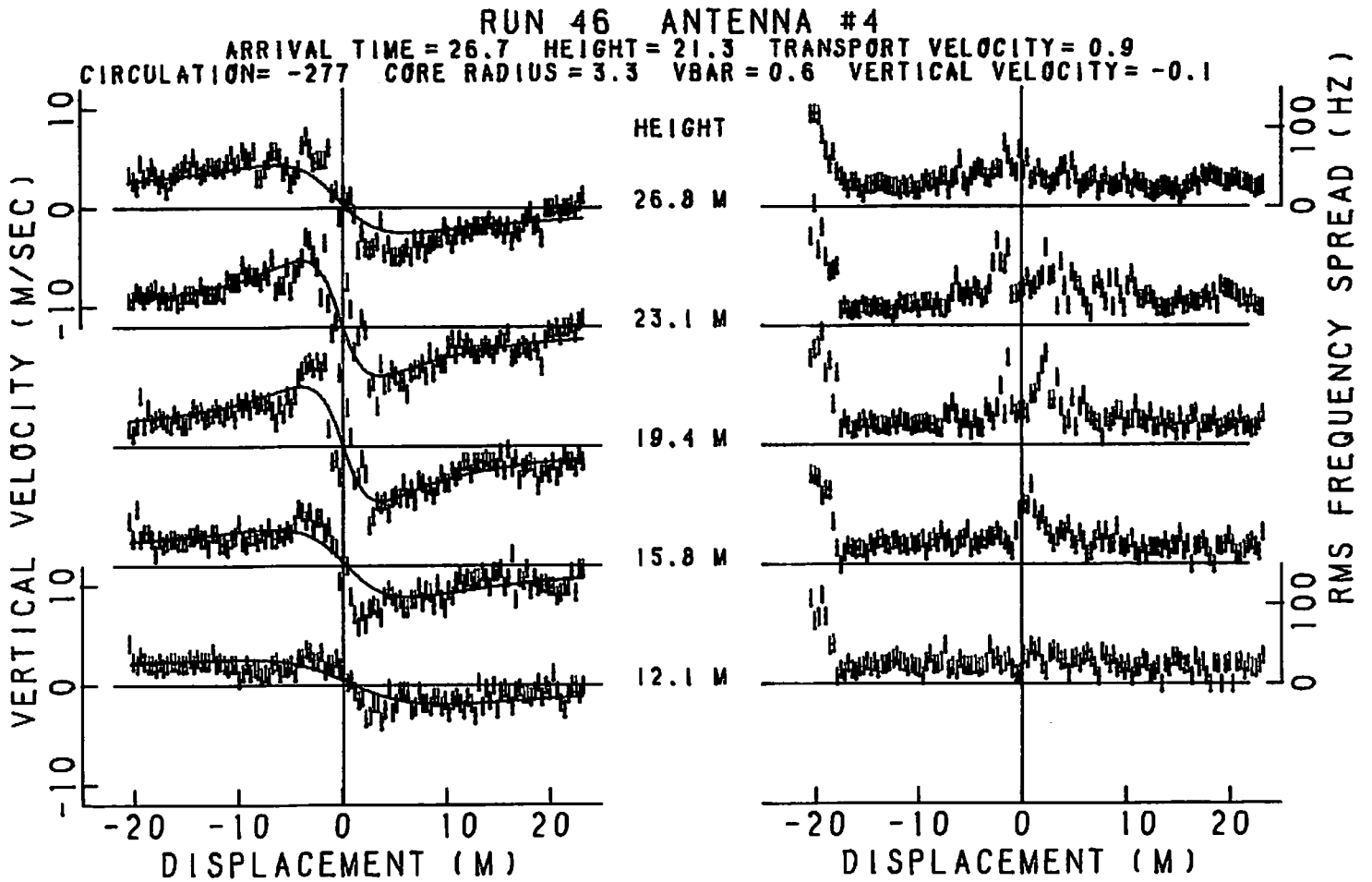

FIGURE 378. VELOCITY AND SPECTRAL WIDTH PROFILES FOR RUN 46, ANTENNA 4

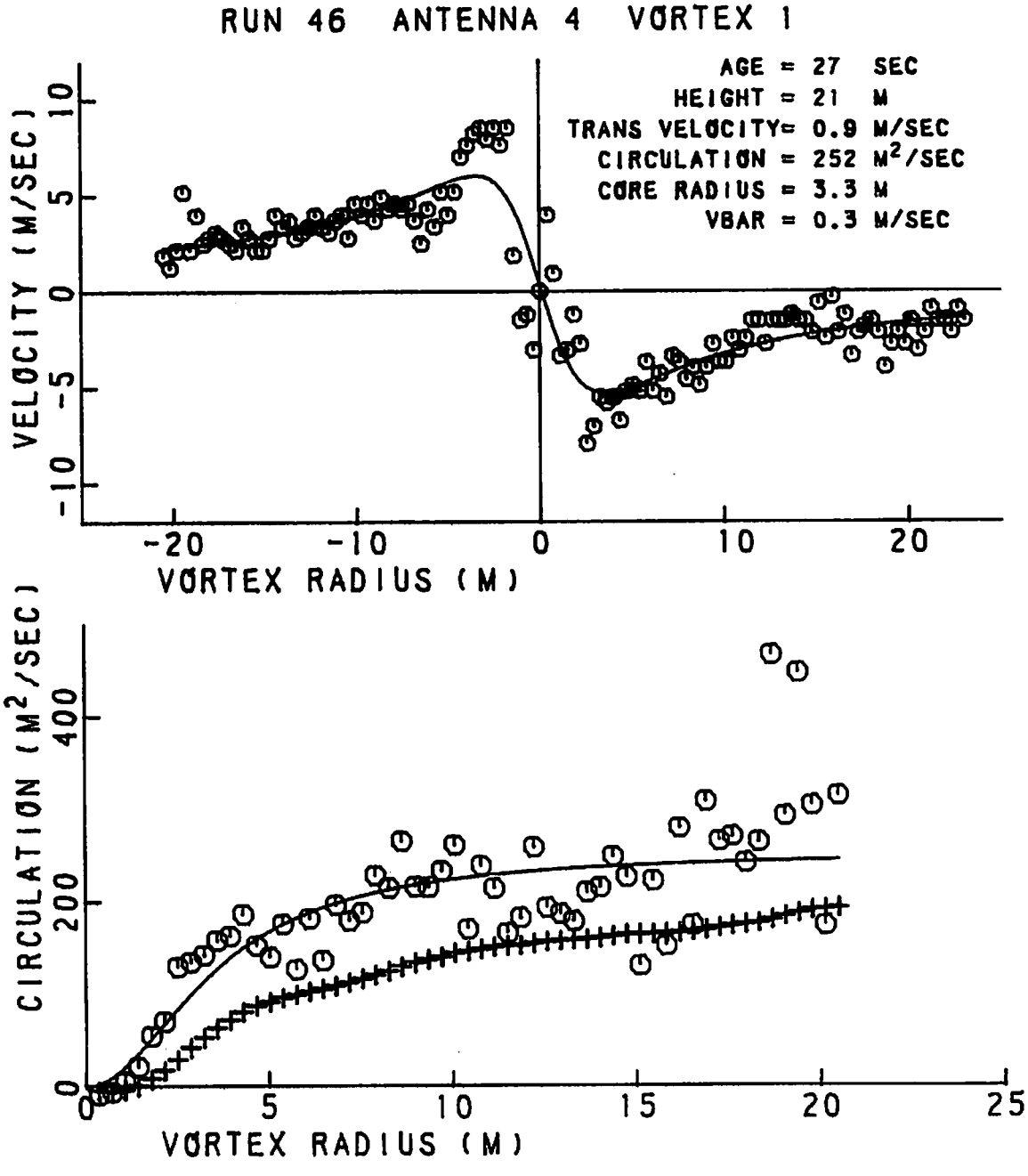

FIGURE 379. VELOCITY AND CIRCULATION PROFILES FOR RUN 46, ANTENNA 4

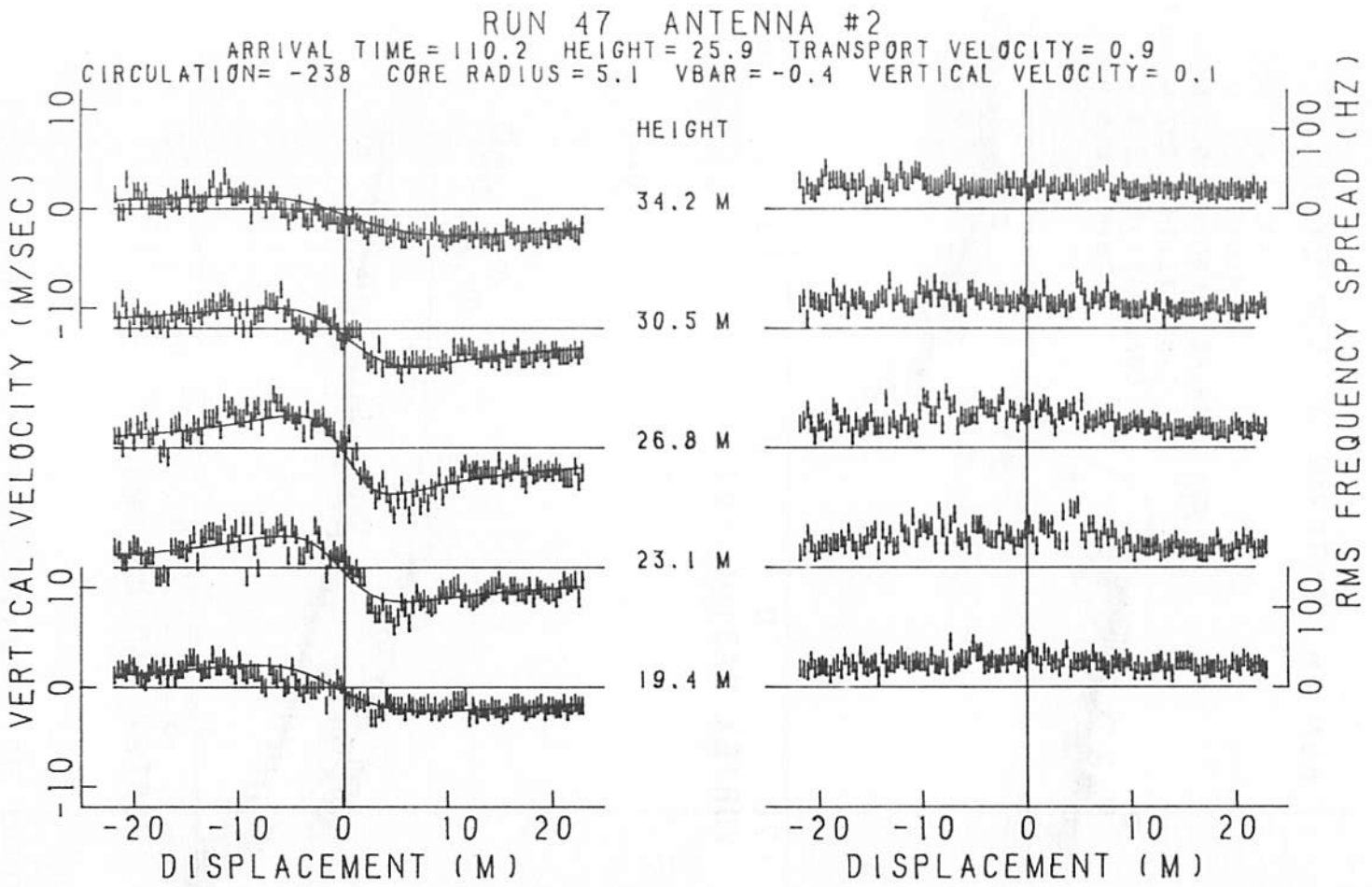

FIGURE 380. VELOCITY AND SPECTRAL WIDTH PROFILES FOR RUN 47, ANTENNA 2

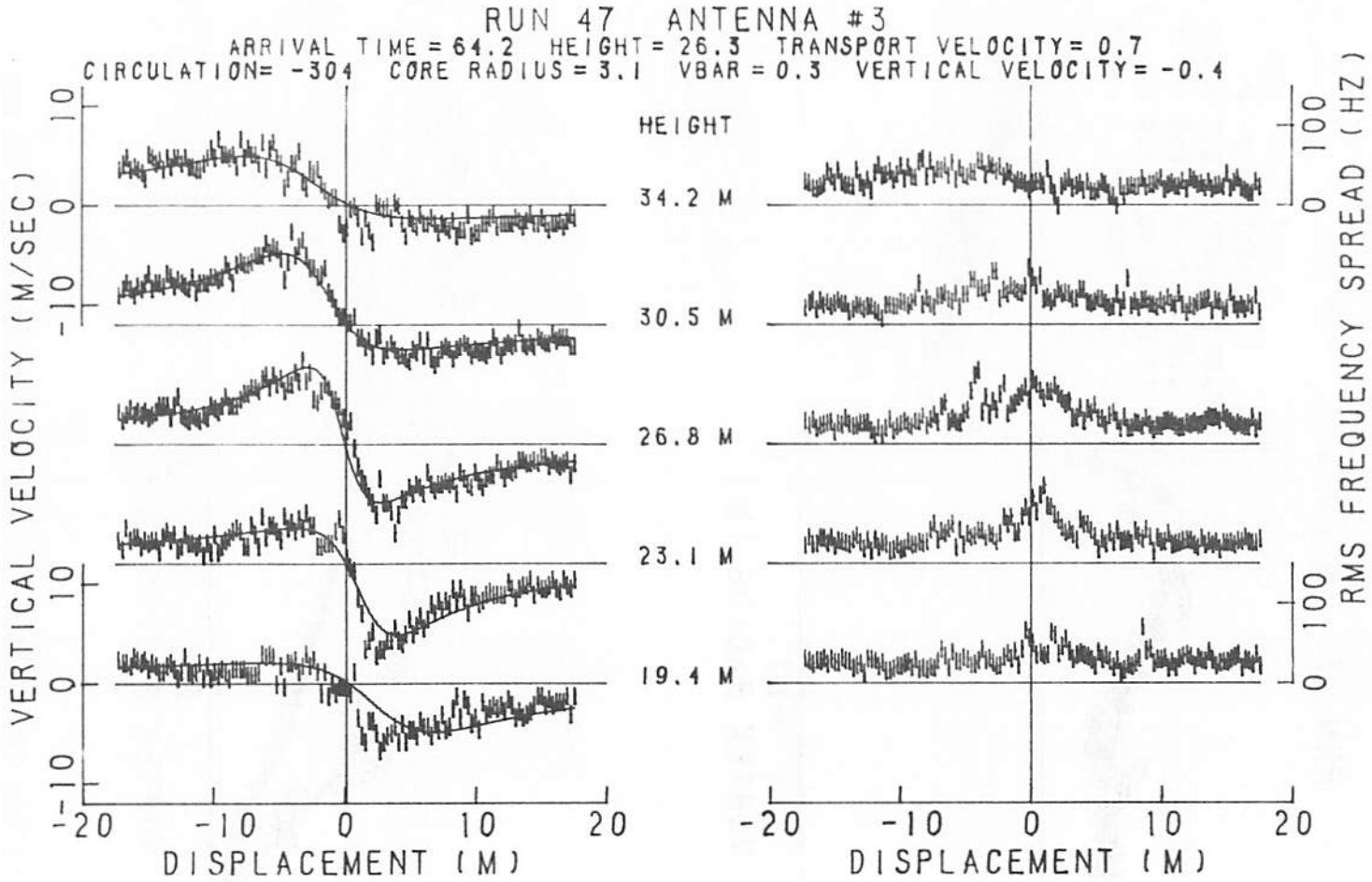

FIGURE 381. VELOCITY AND SPECTRAL WIDTH PROFILES FOR RUN 47, ANTENNA 3

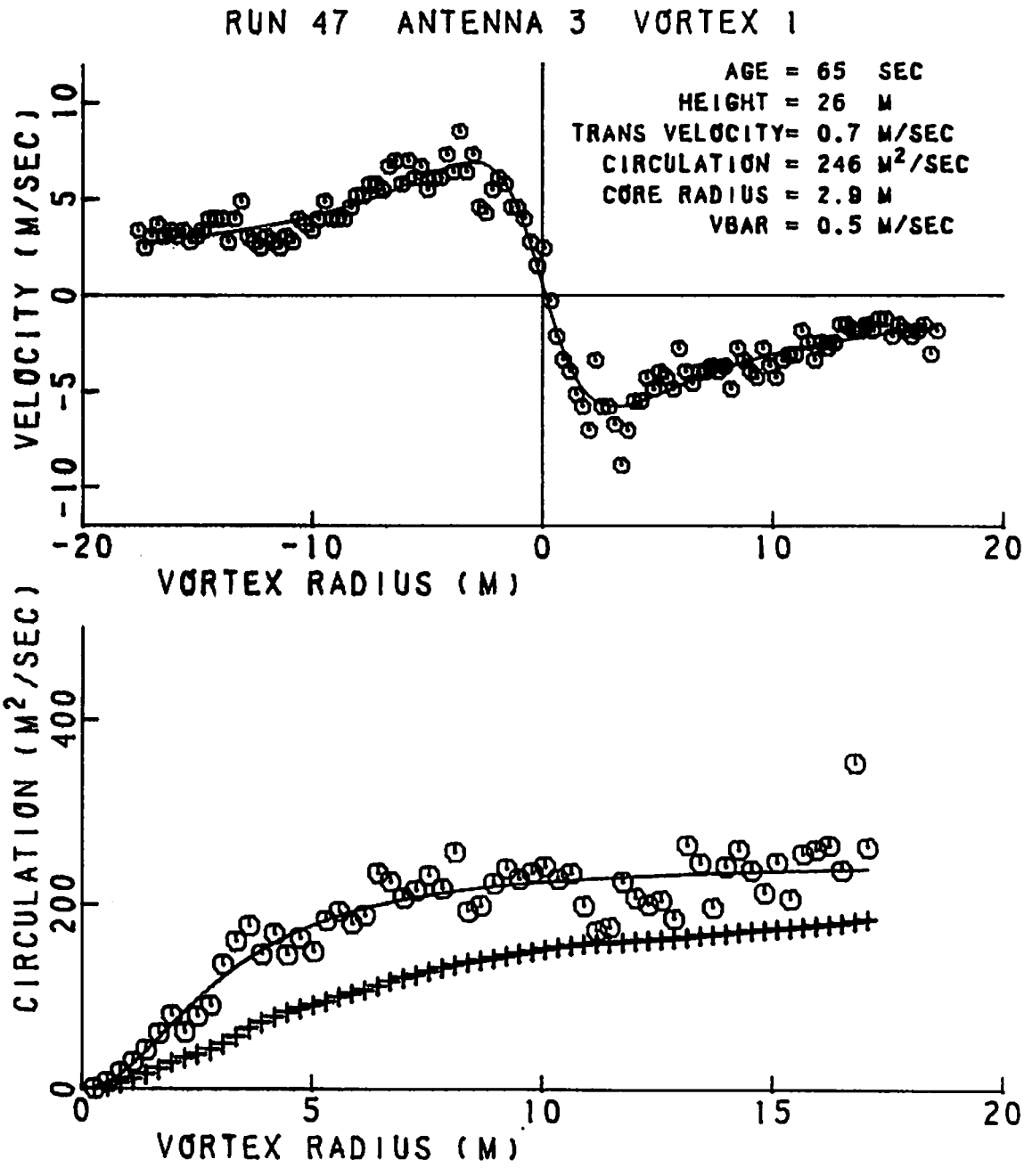

FIGURE 382. VELOCITY AND CIRCULATION PROFILES FOR RUN 47, ANTENNA 3

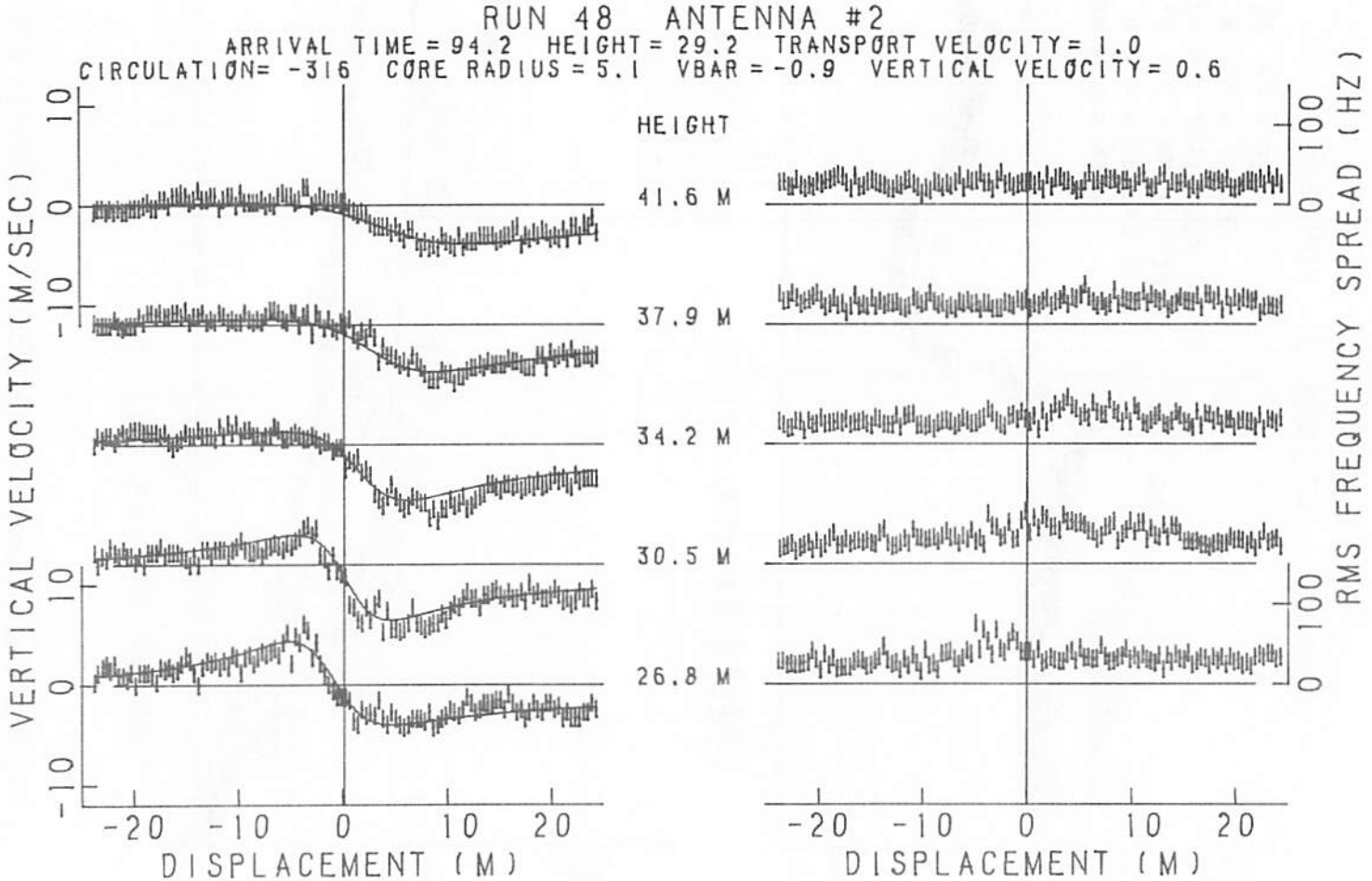

FIGURE 383. VELOCITY AND SPECTRAL WIDTH PROFILES FOR RUN 48, ANTENNA 2

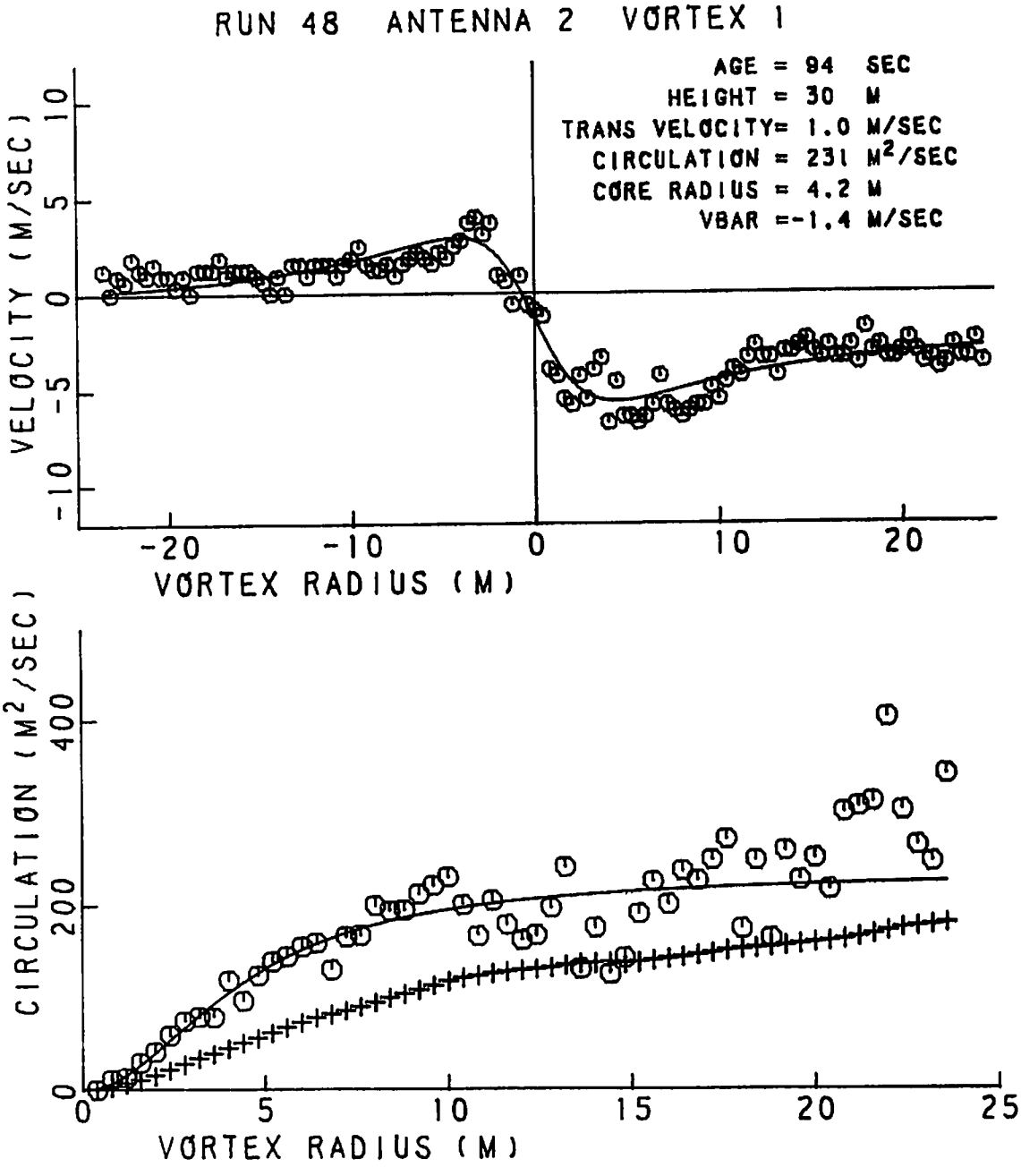

FIGURE 384. VELOCITY AND CIRCULATION PROFILES FOR RUN 48, ANTENNA 2

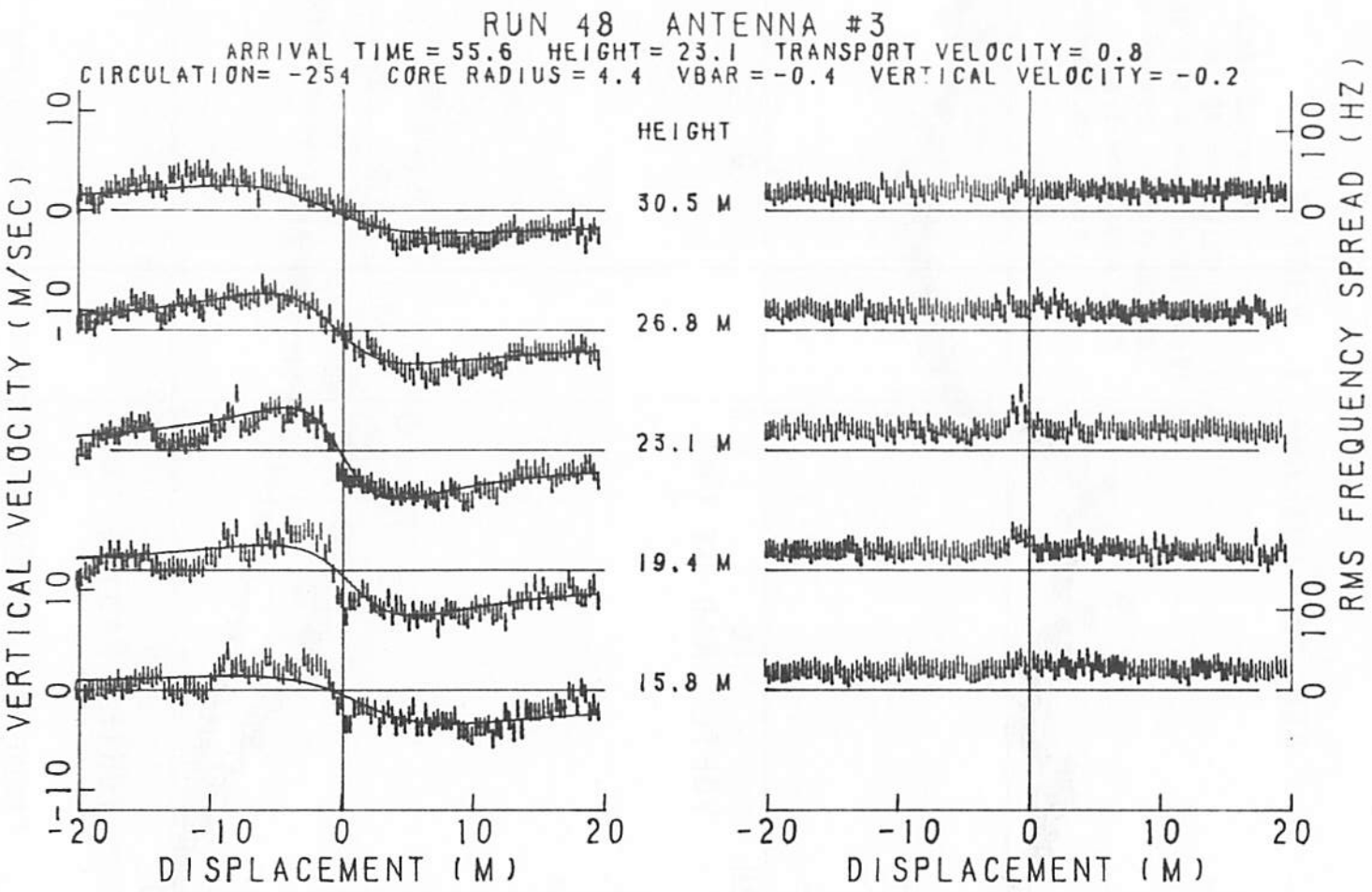

FIGURE 385. VELOCITY AND SPECTRAL WIDTH PROFILES FOR RUN 48, ANTENNA 3

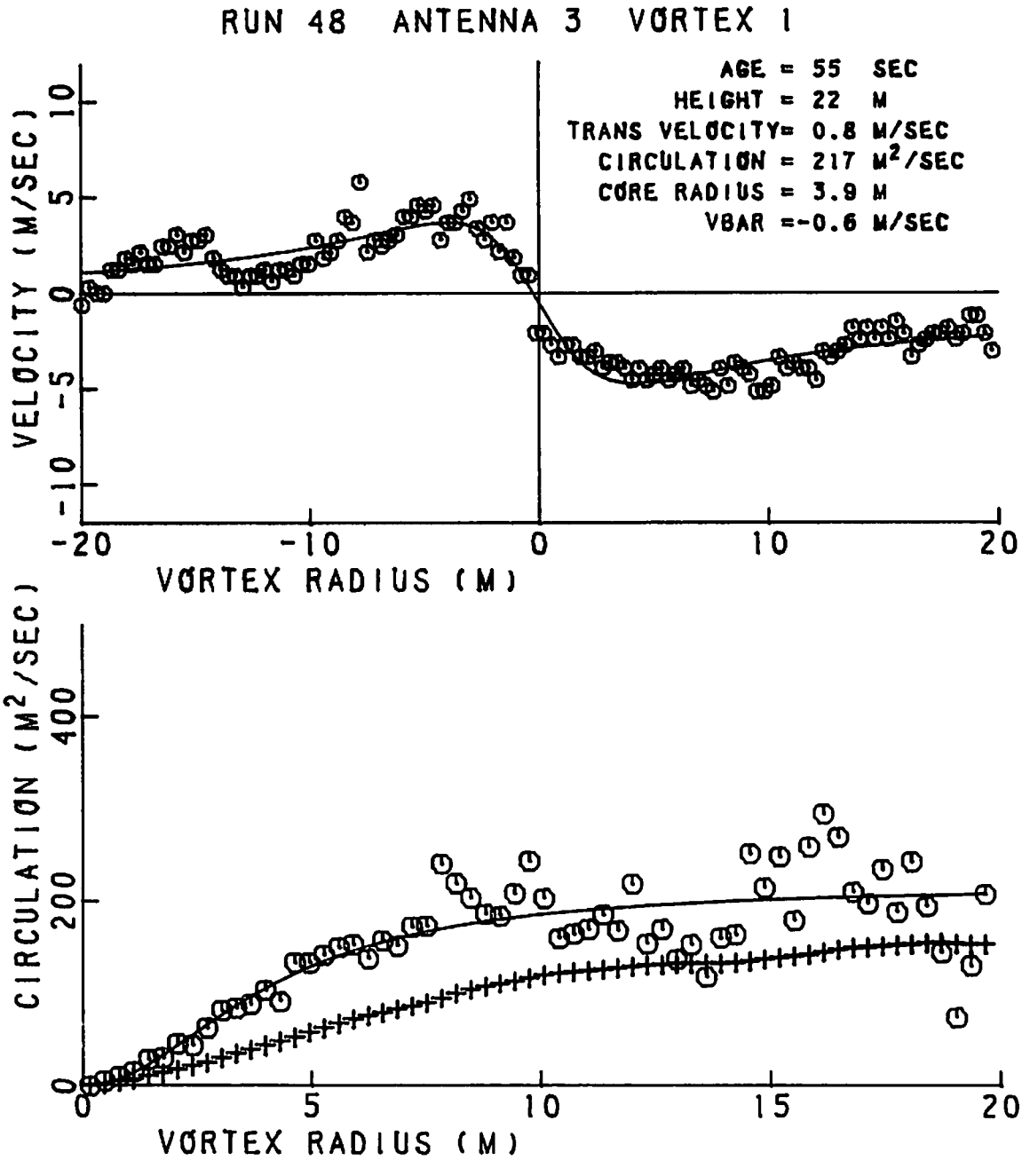

FIGURE 386. VELOCITY AND CIRCULATION PROFILES FOR RUN 48, ANTENNA 3

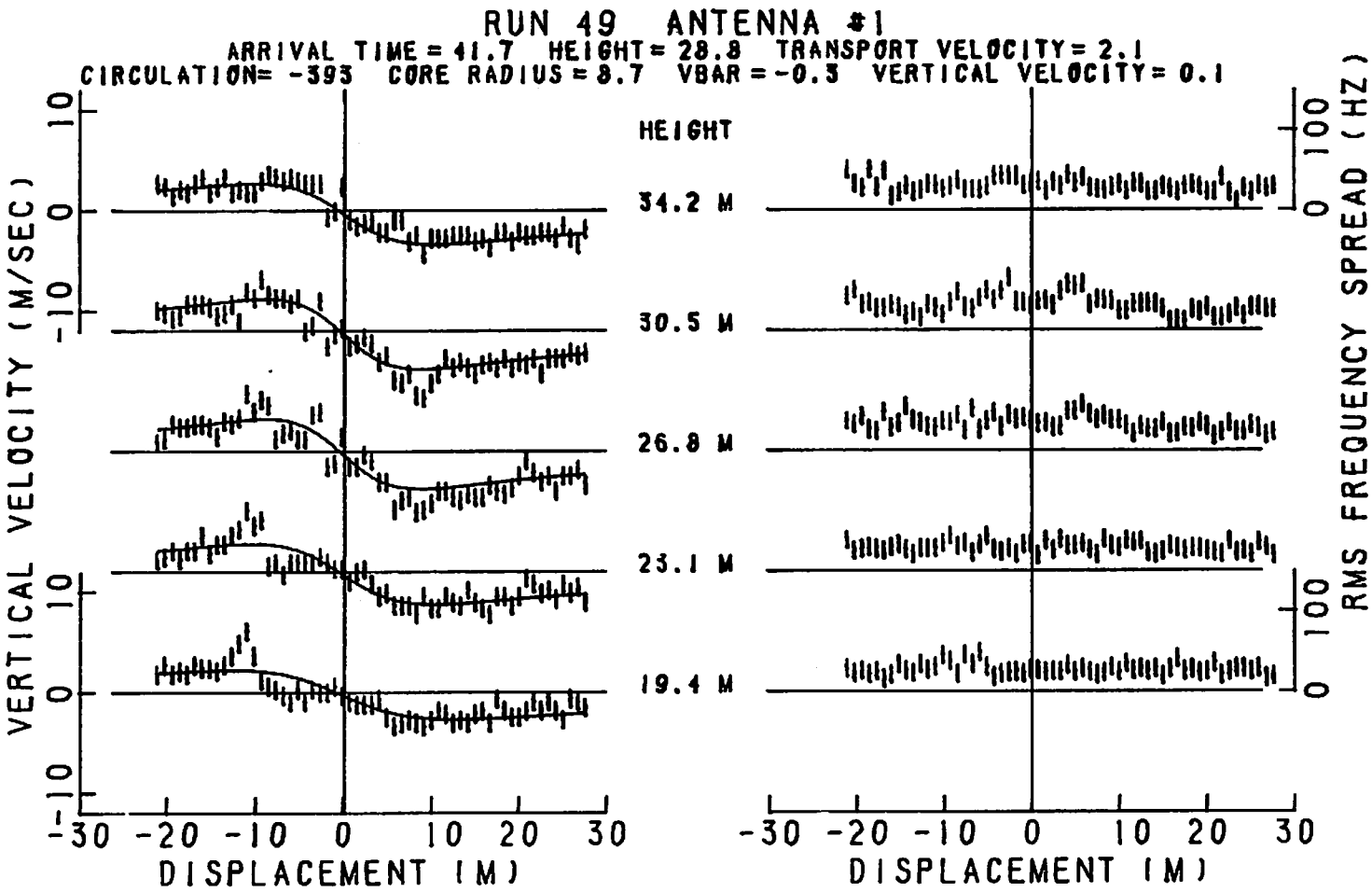

FIGURE 387. VELOCITY AND SPECTRAL WIDTH PROFILES FOR RUN 49, ANTENNA 1

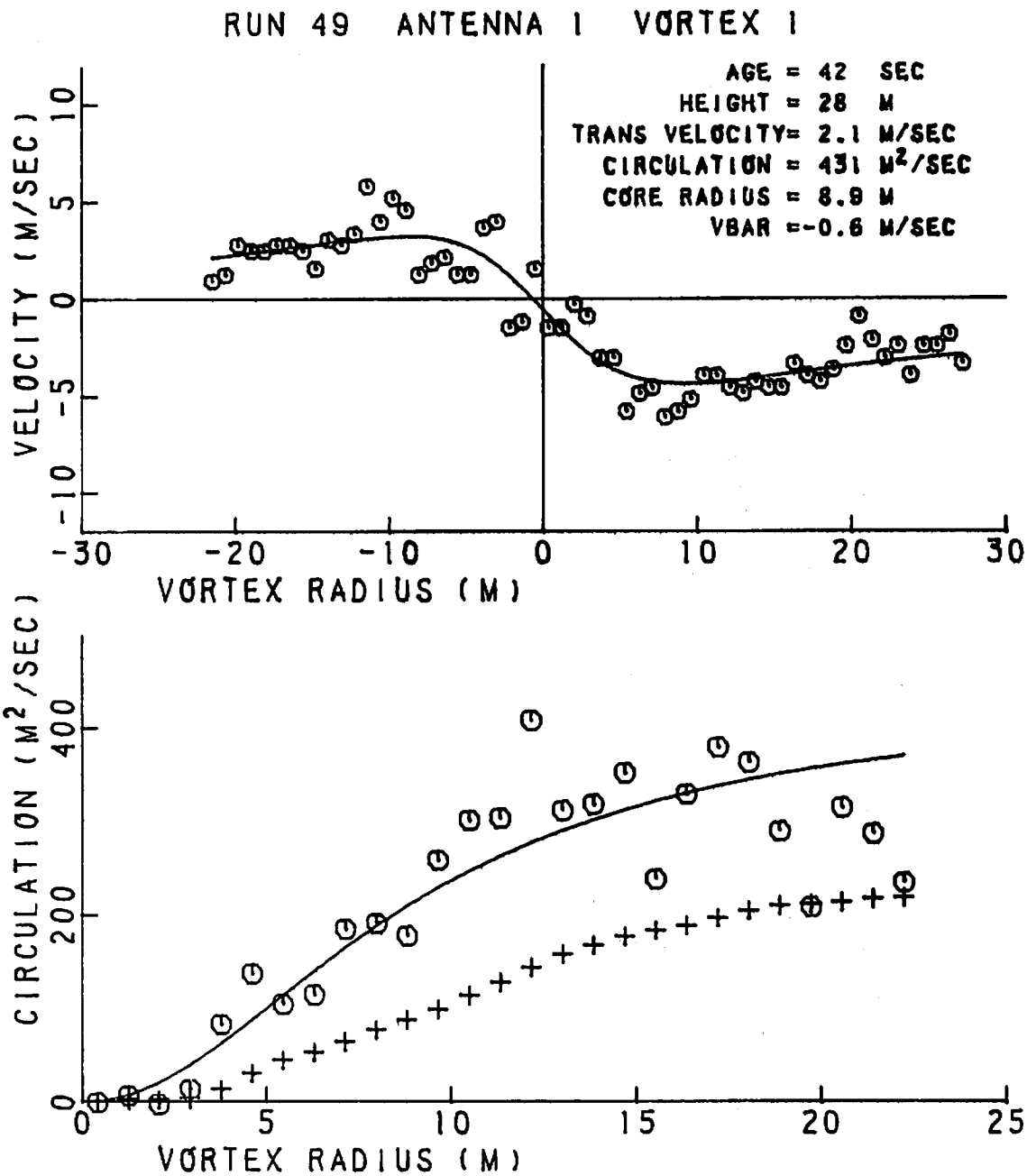

FIGURE 388. VELOCITY AND CIRCULATION PROFILES FOR RUN 49, ANTENNA 1

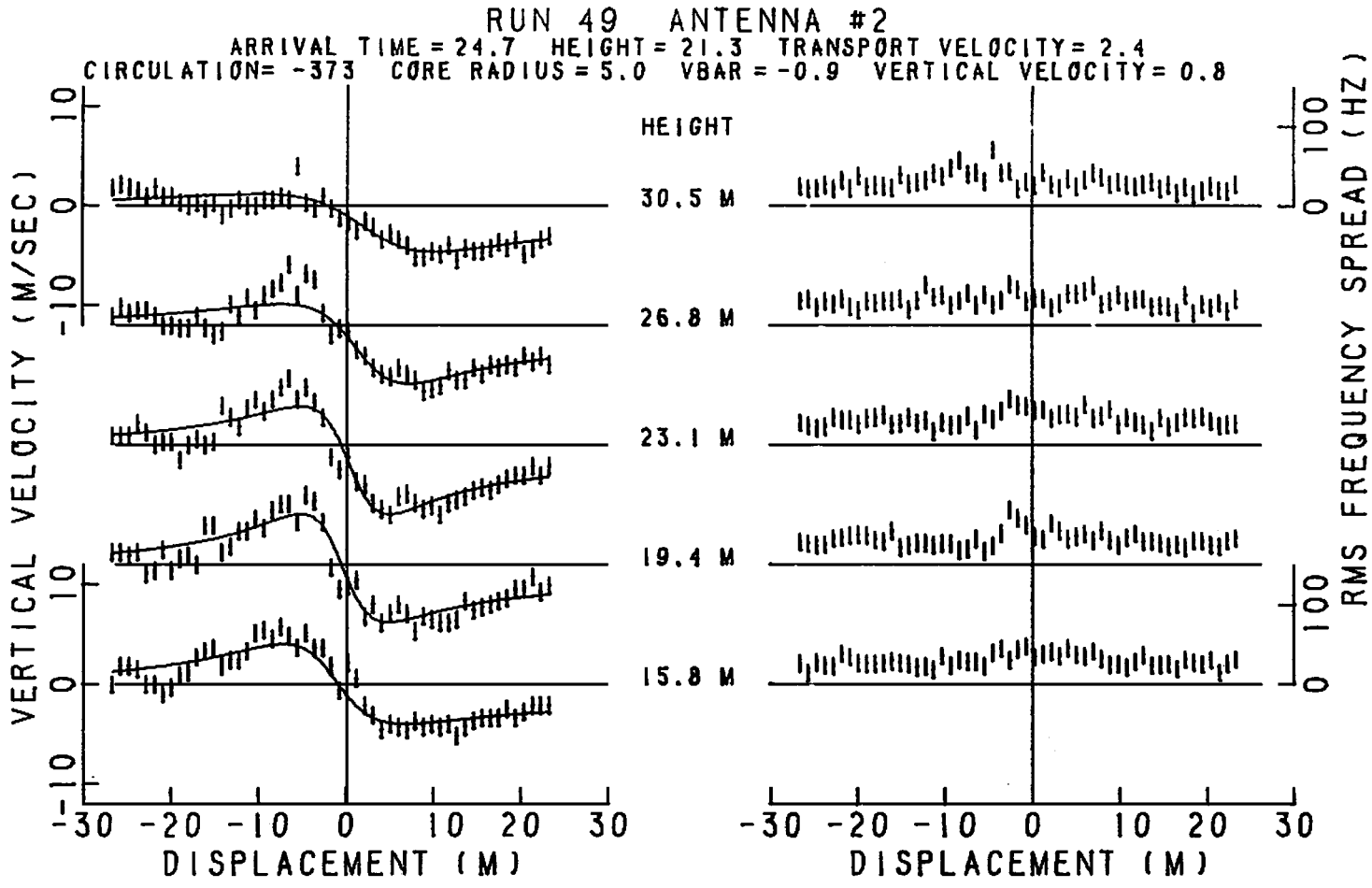

FIGURE 389. VELOCITY AND SPECTRAL WIDTH PROFILES FOR RUN 49, ANTENNA 2

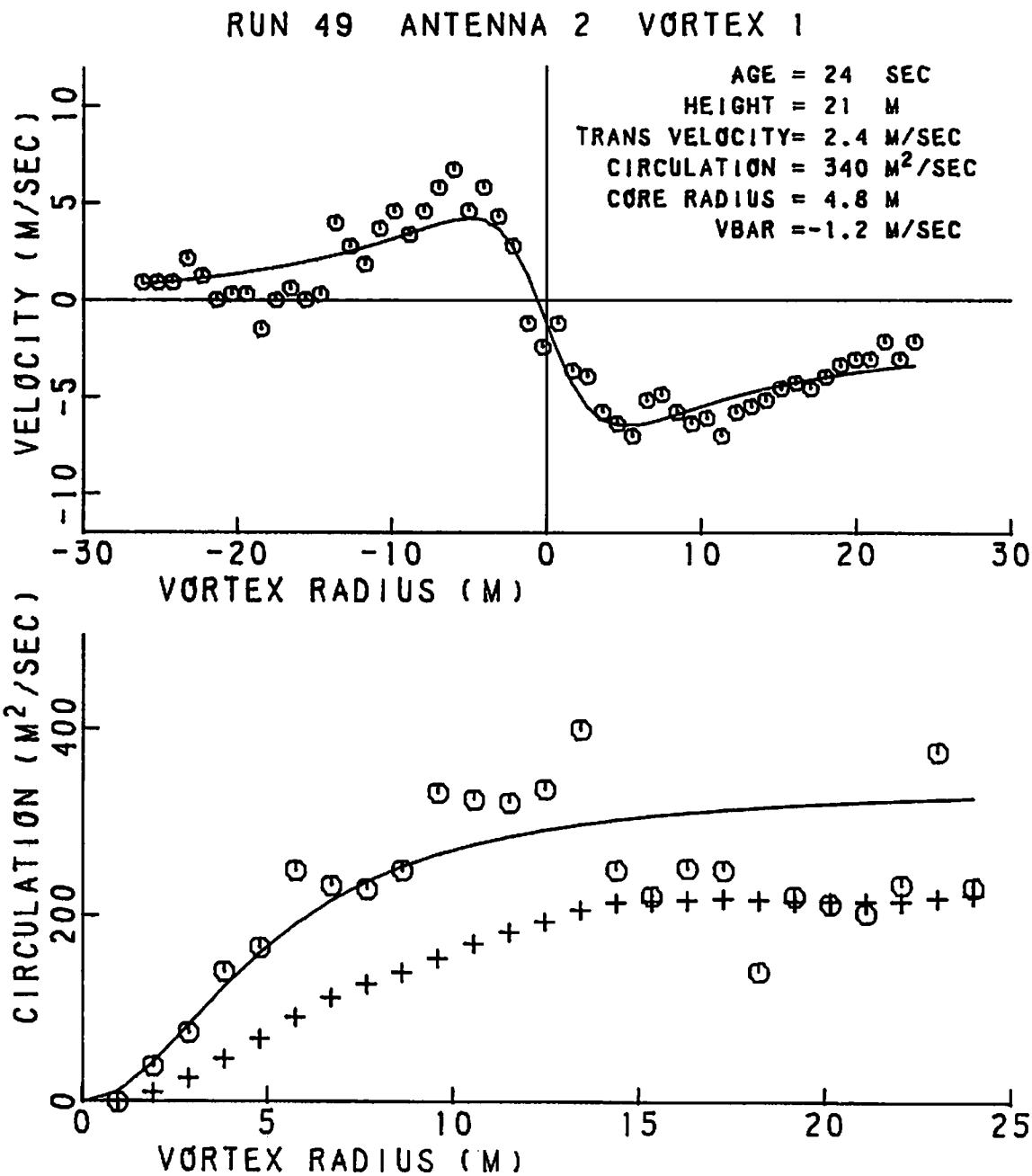

FIGURE 390. VELOCITY AND CIRCULATION PROFILES FOR RUN 49, ANTENNA 2

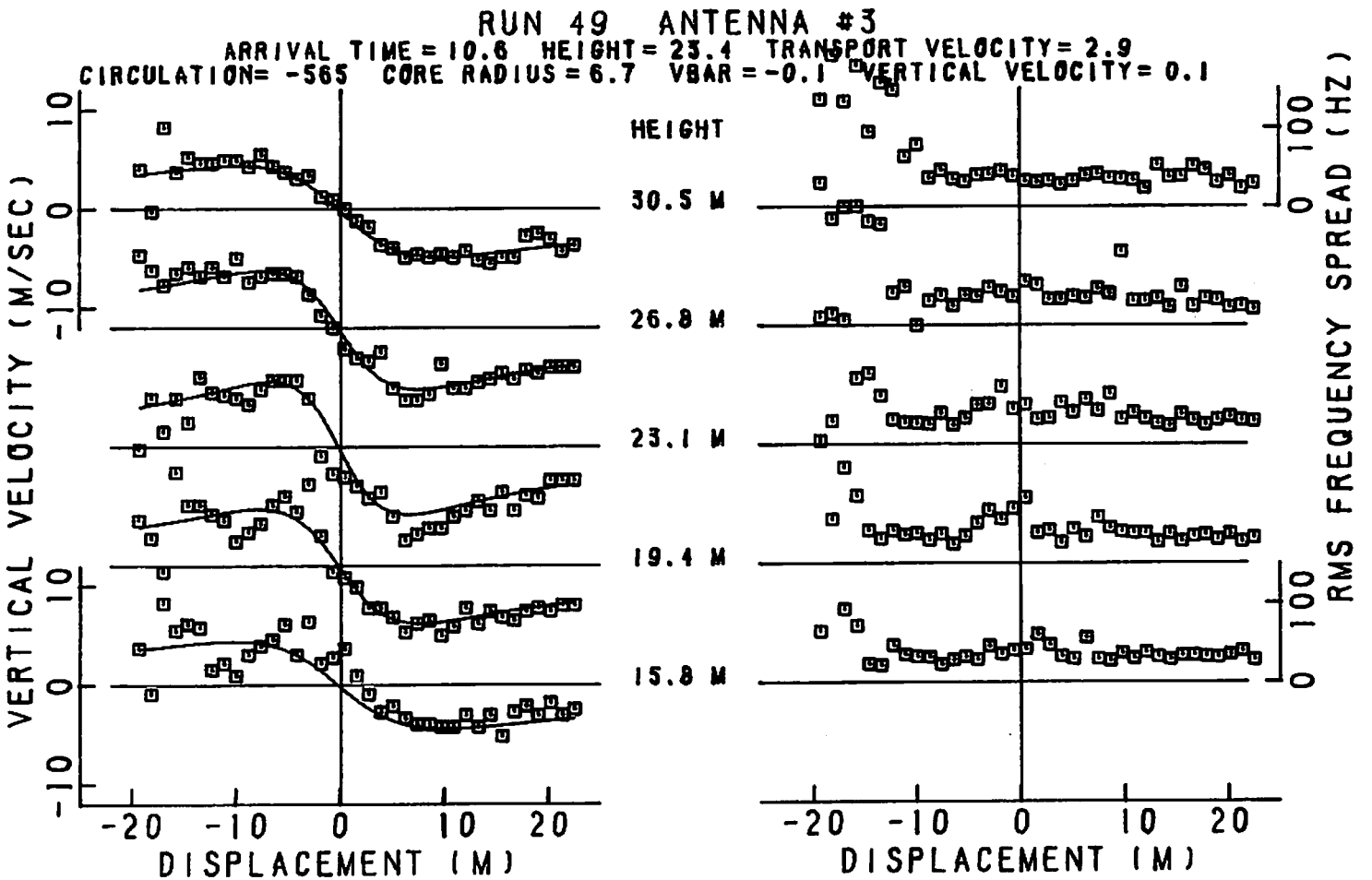

FIGURE 391. VELOCITY AND SPECTRAL WIDTH PROFILES FOR RUN 49, ANTENNA 3

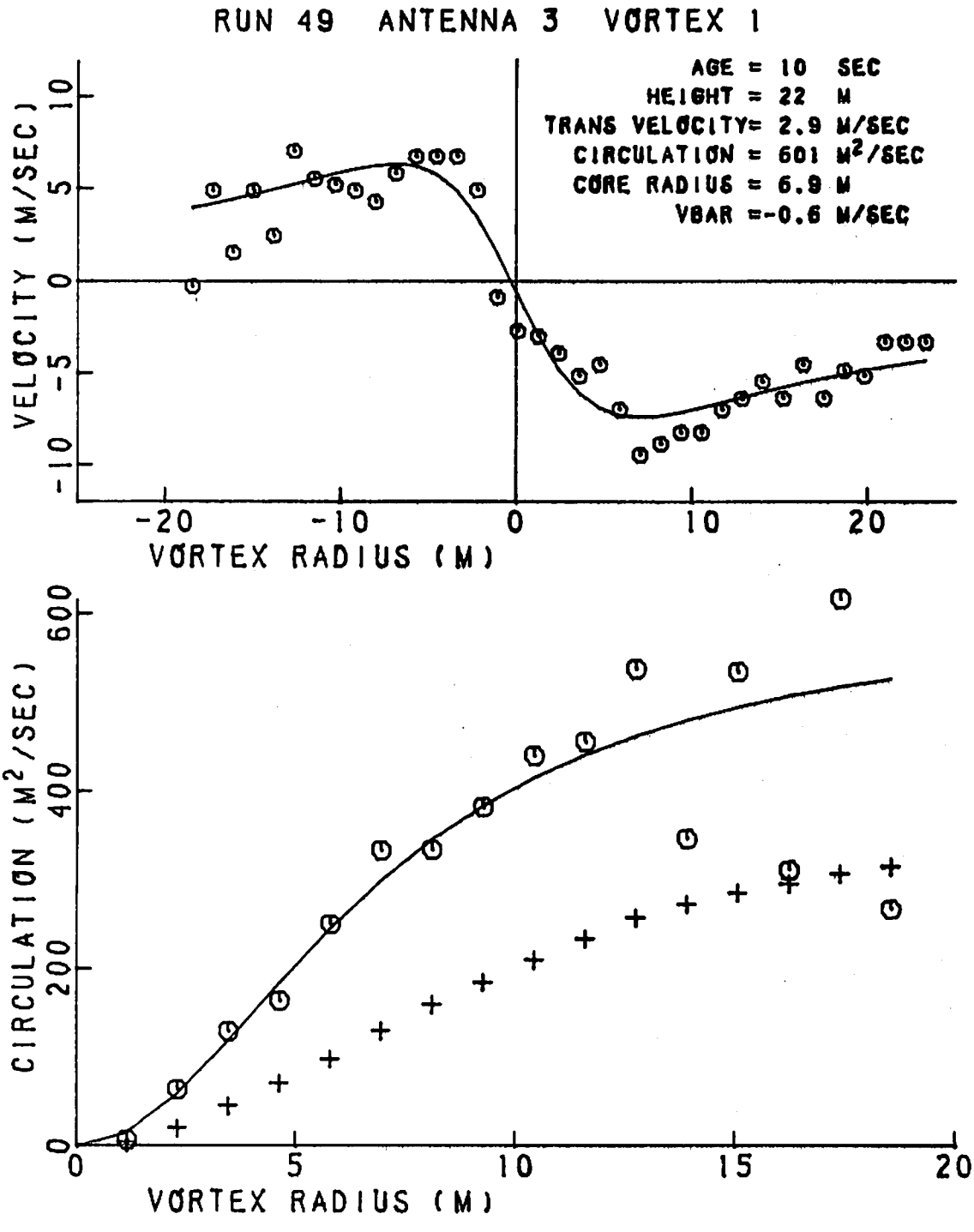

FIGURE 392. VELOCITY AND CIRCULATION PROFILES FOR RUN 49, ANTENNA 3

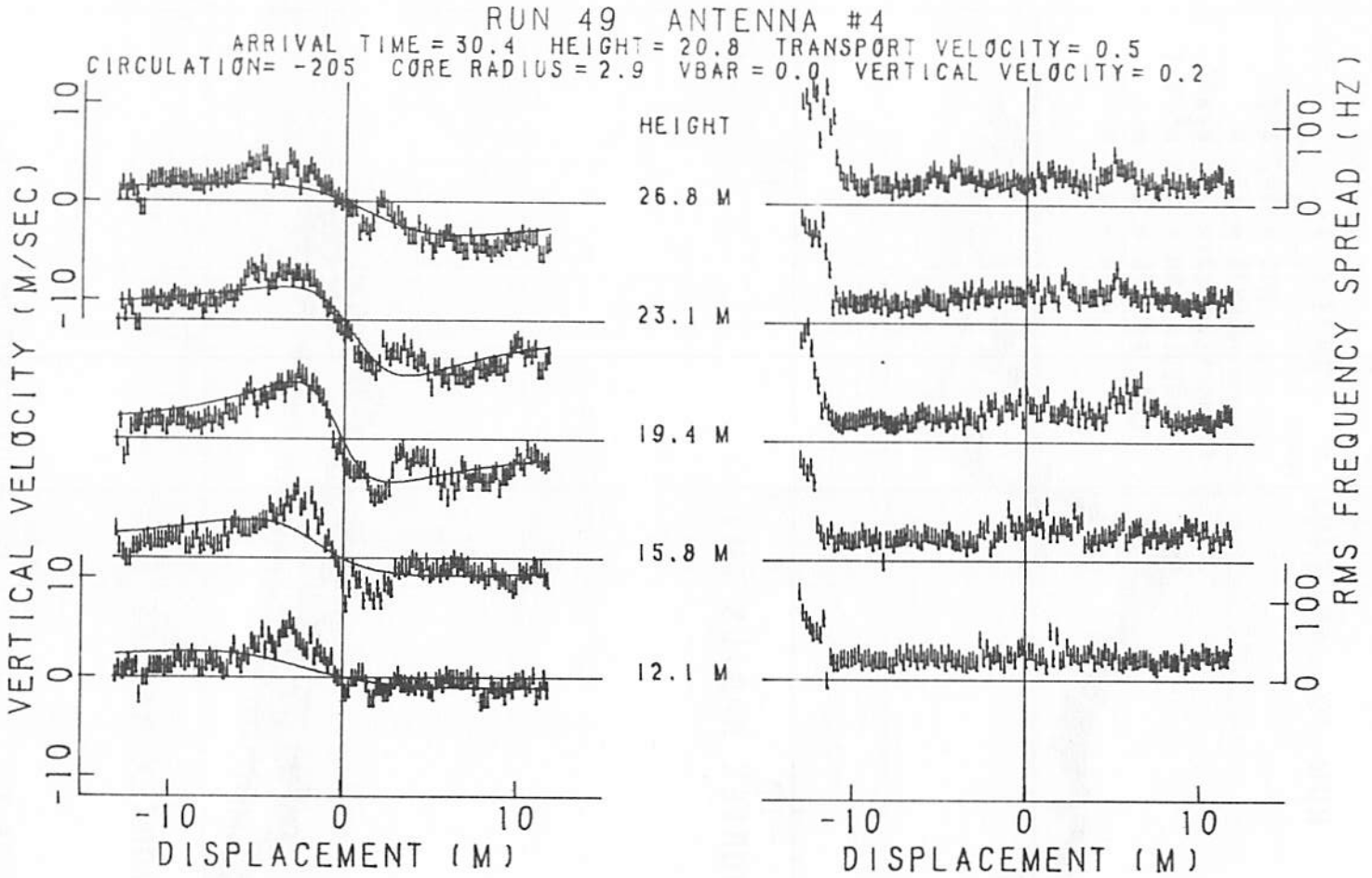

FIGURE 393. VELOCITY AND SPECTRAL WIDTH PROFILES FOR RUN 49, ANTENNA 4

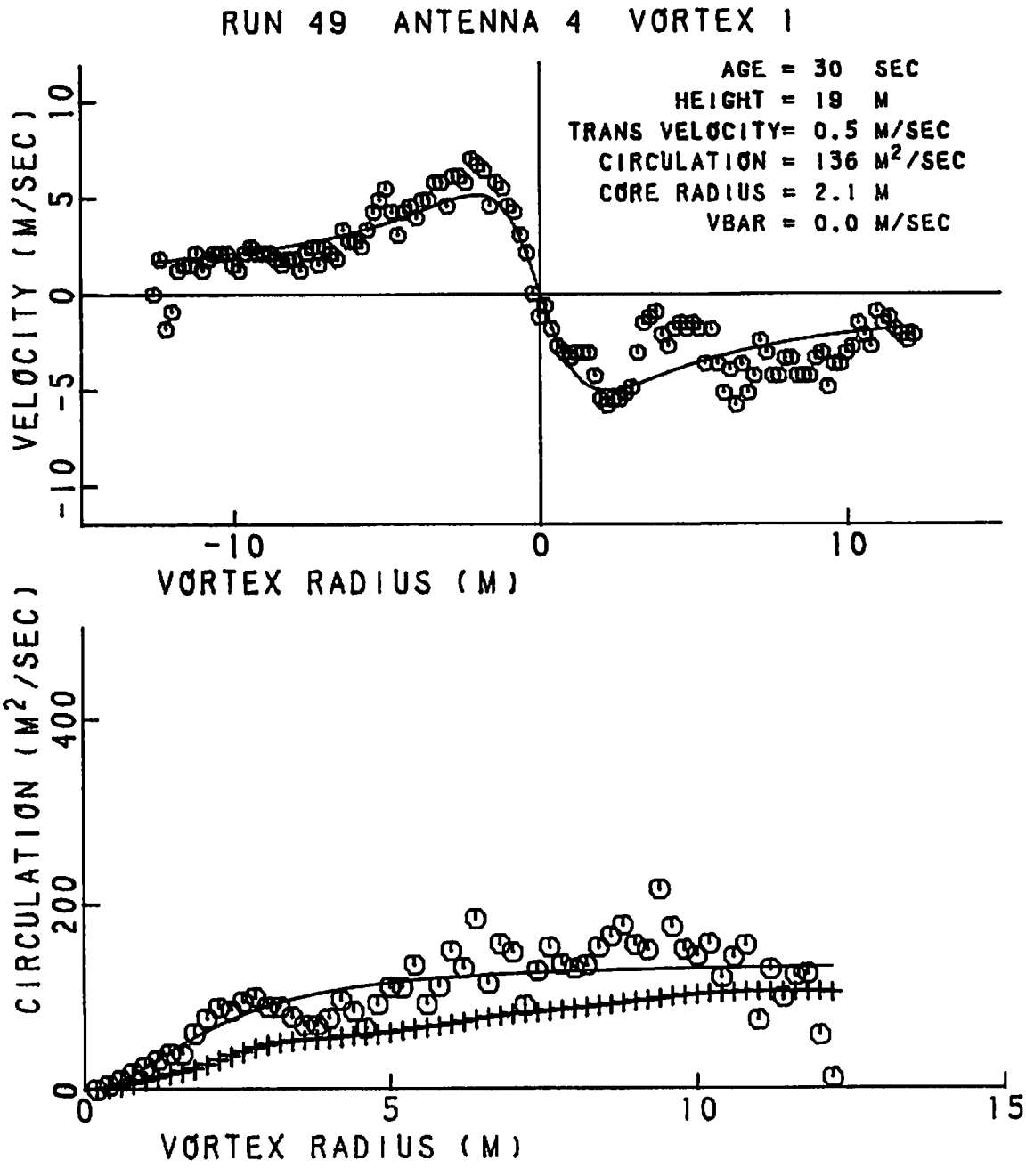

FIGURE 394. VELOCITY AND CIRCULATION PROFILES FOR RUN 49, ANTENNA 4

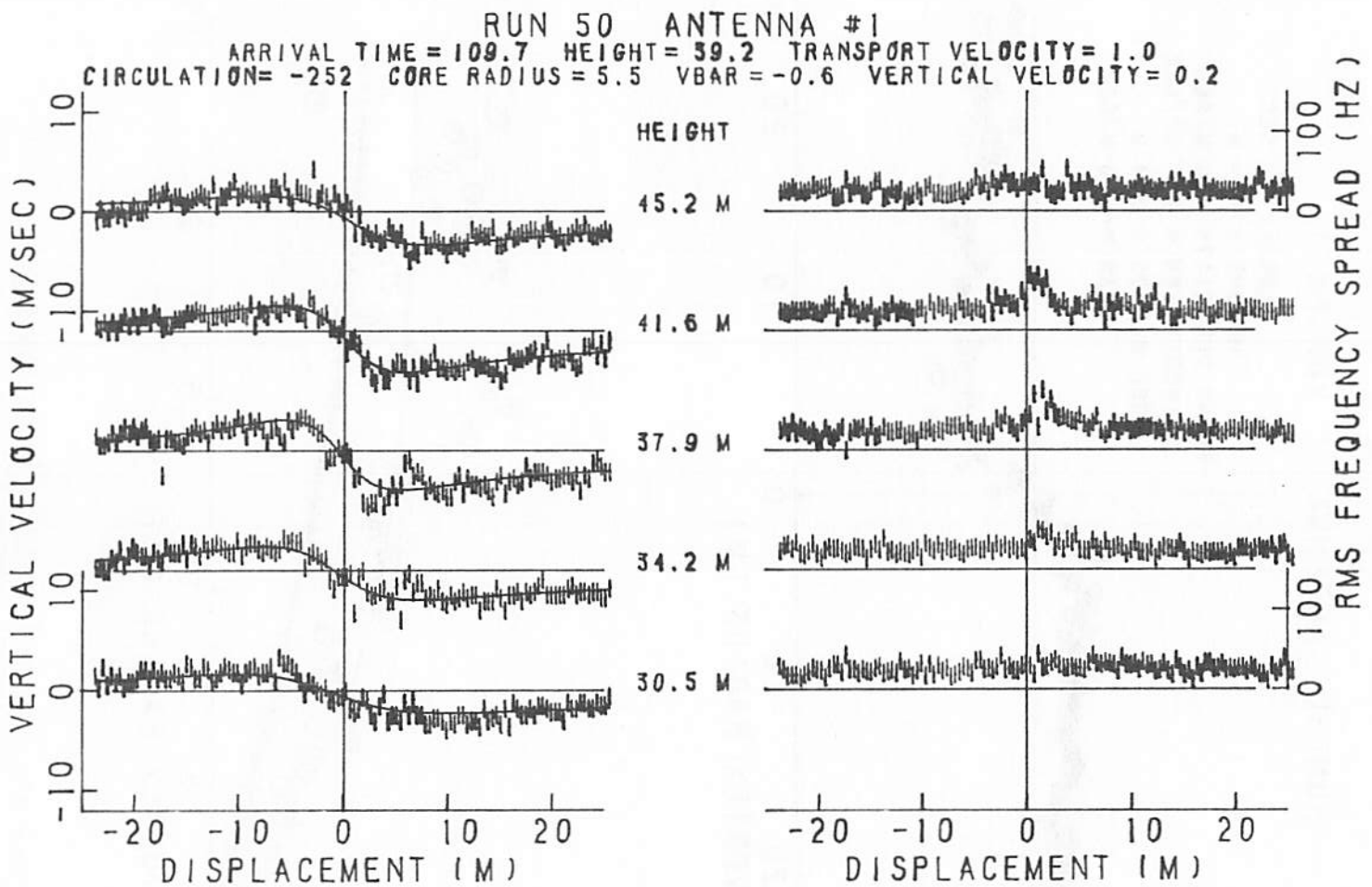

FIGURE 395. VELOCITY AND SPECTRAL WIDTH PROFILES FOR RUN 50, ANTENNA 1

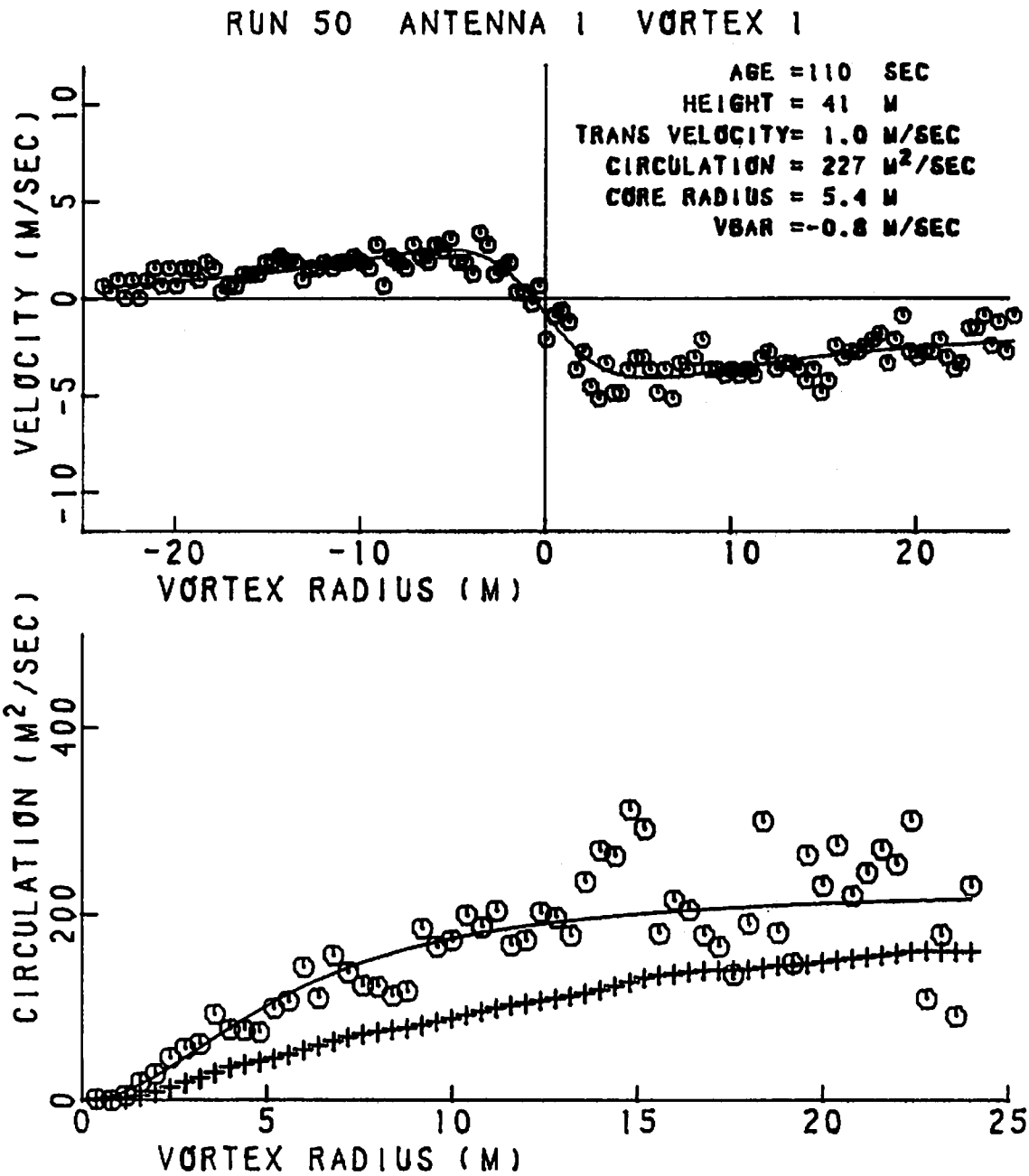

FIGURE 396. VELOCITY AND CIRCULATION PROFILES FOR RUN 50, ANTENNA 1

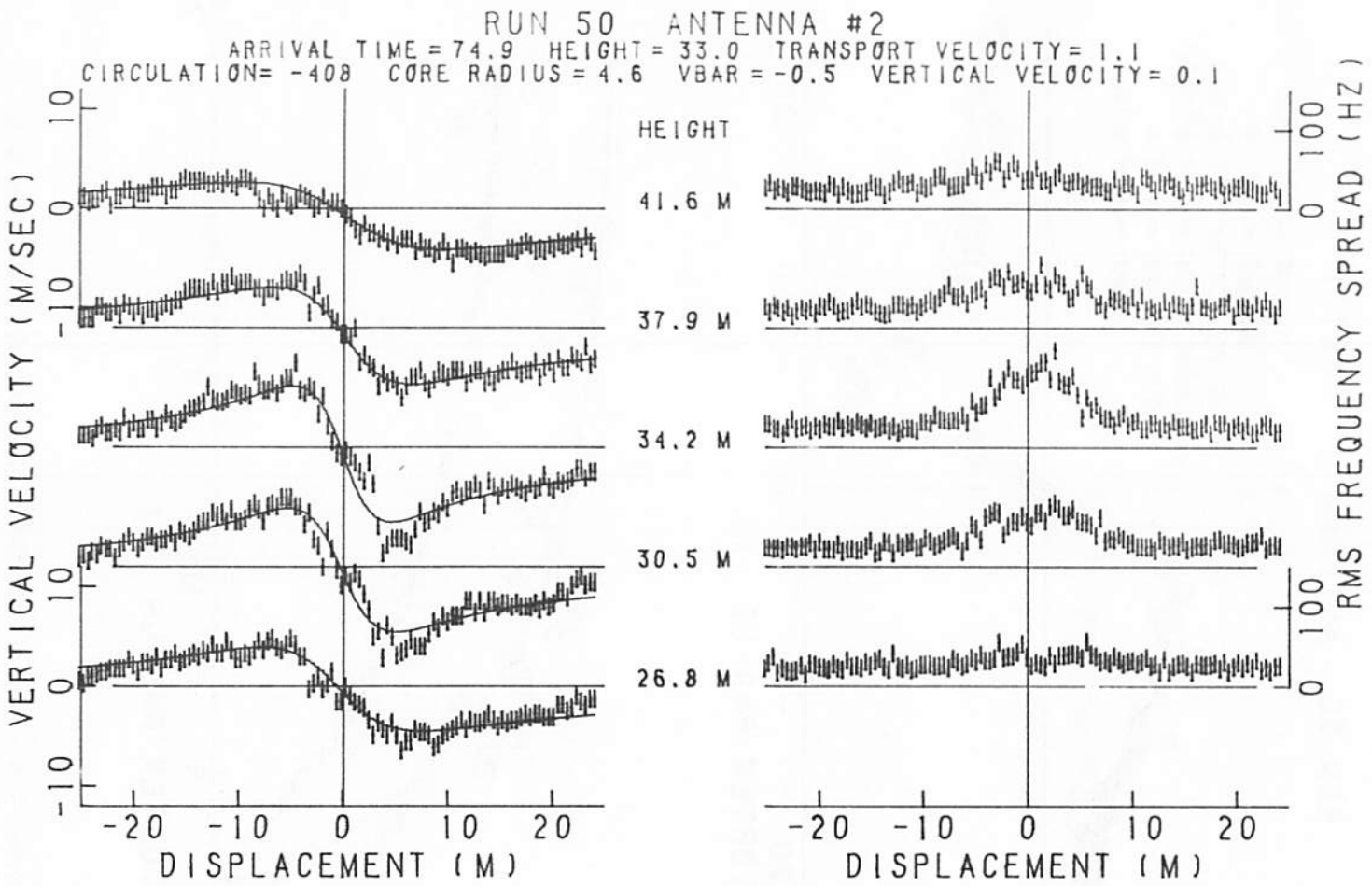

FIGURE 397. VELOCITY AND SPECTRAL WIDTH PROFILES FOR RUN 50, ANTENNA 2

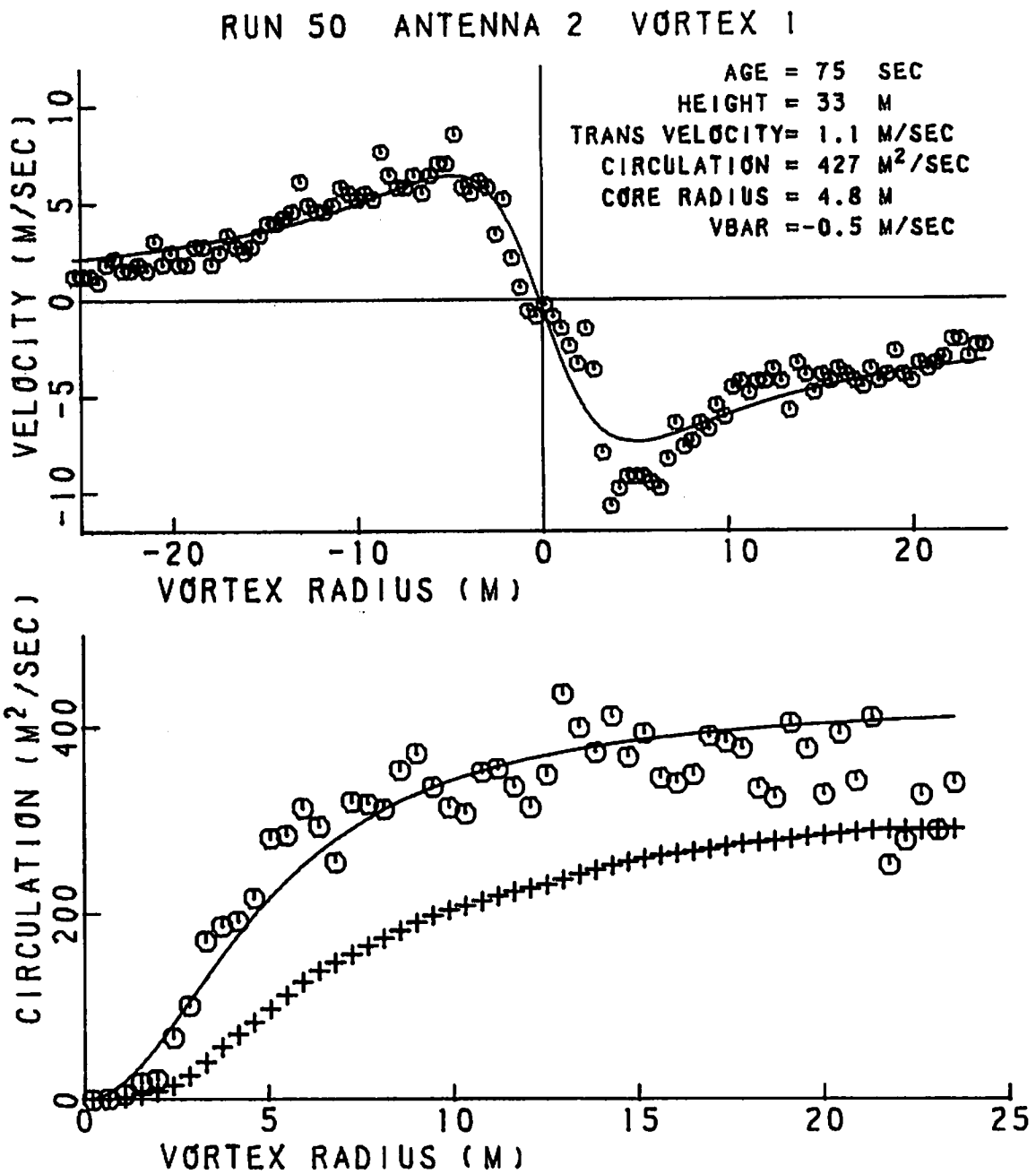

FIGURE 398. VELOCITY AND CIRCULATION PROFILES FOR RUN 50, ANTENNA 2

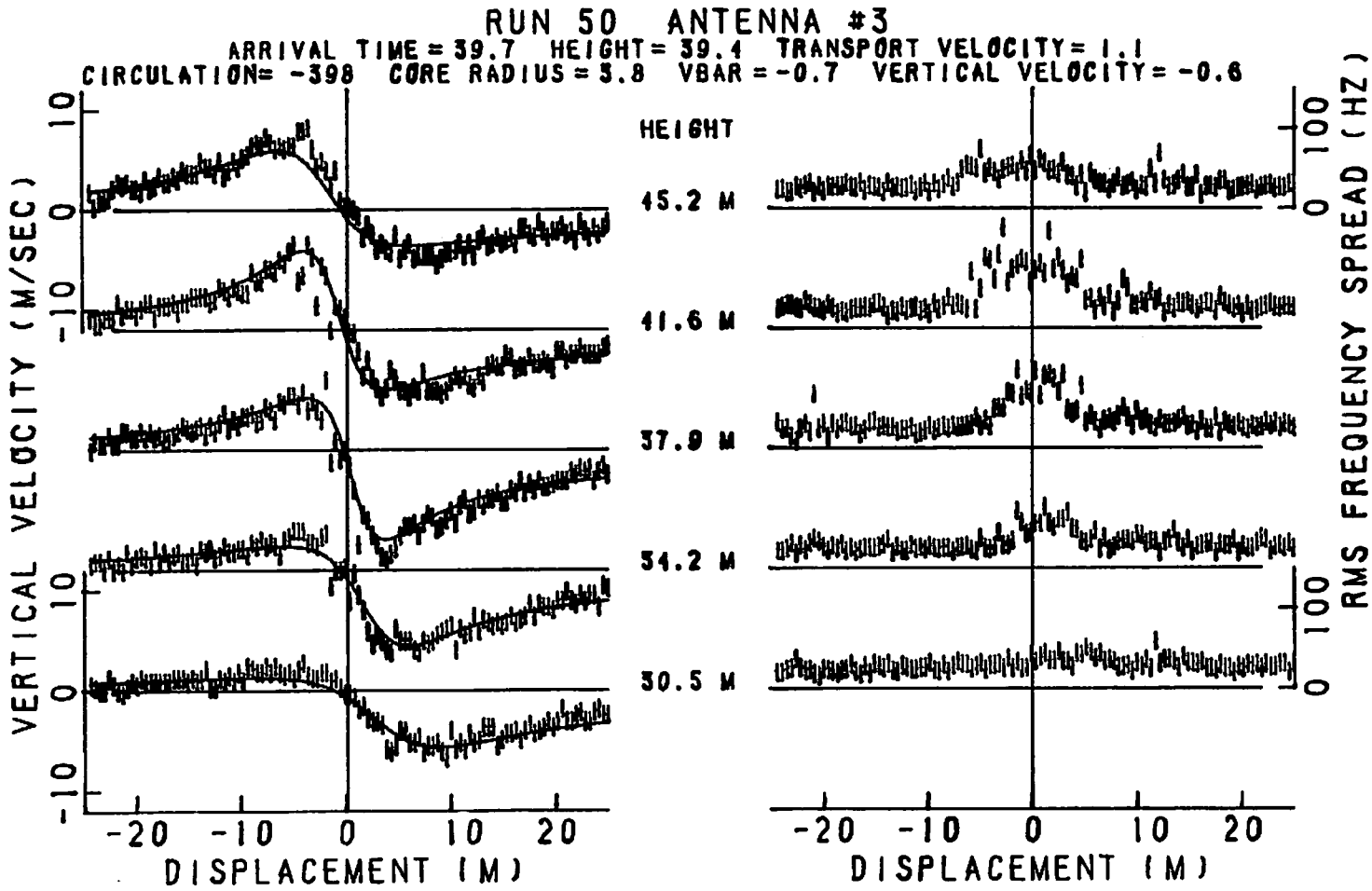

FIGURE 399. VELOCITY AND SPECTRAL WIDTH PROFILES FOR RUN 50, ANTENNA 3

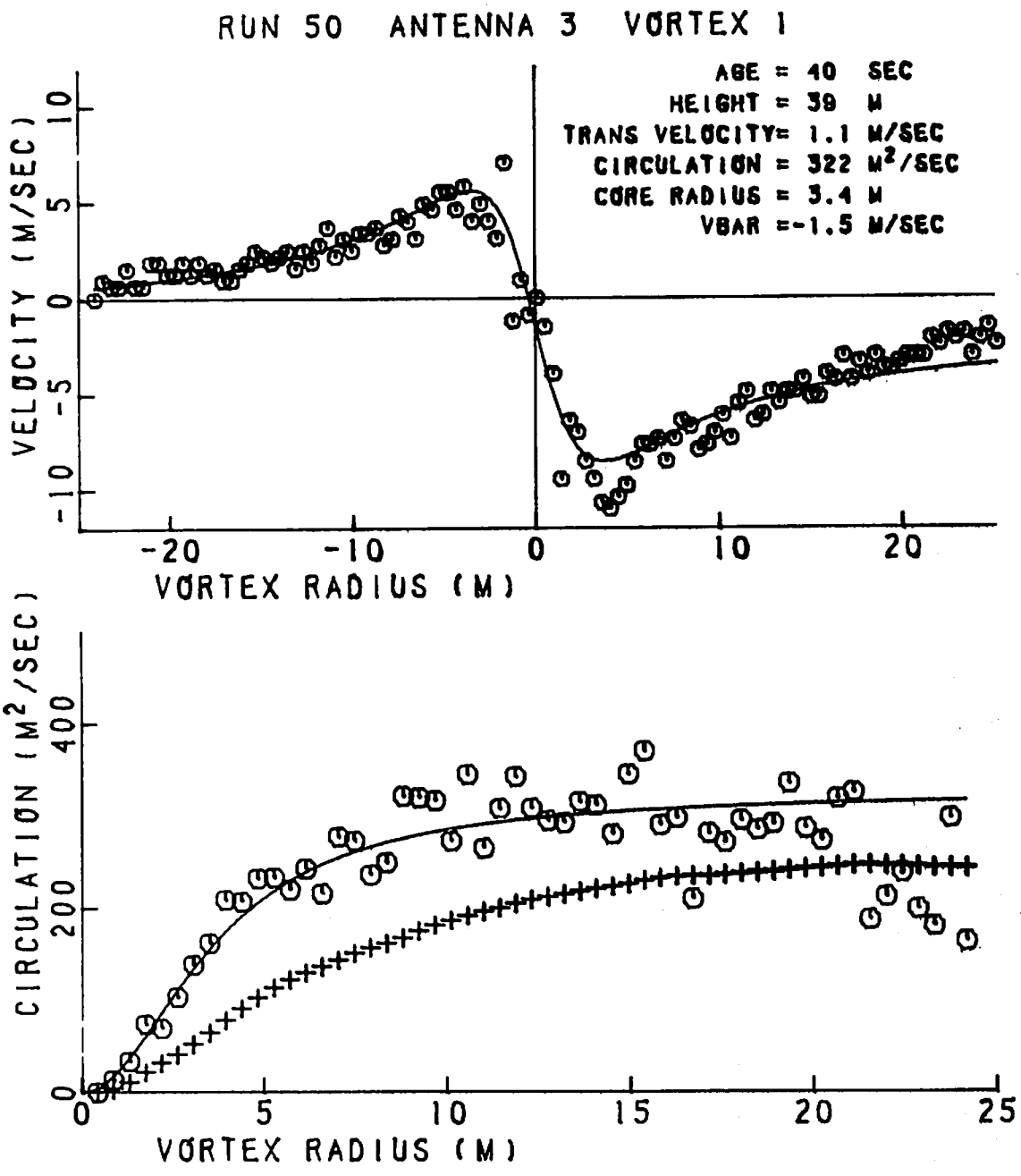

FIGURE 400. VELOCITY AND CIRCULATION PROFILES FOR RUN 50, ANTENNA 3

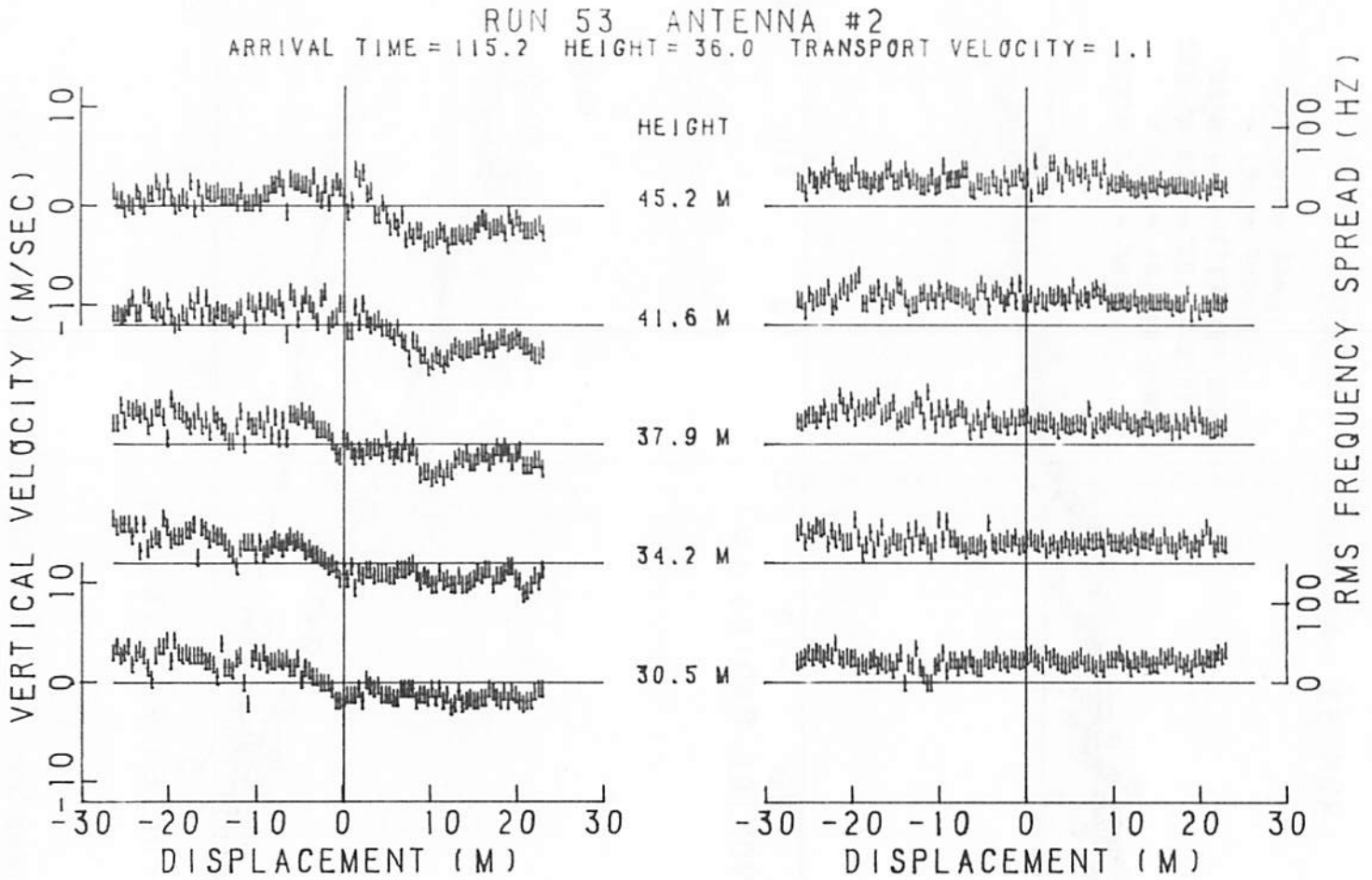

FIGURE 401. VELOCITY AND SPECTRAL WIDTH PROFILES FOR RUN 53, ANTENNA 2

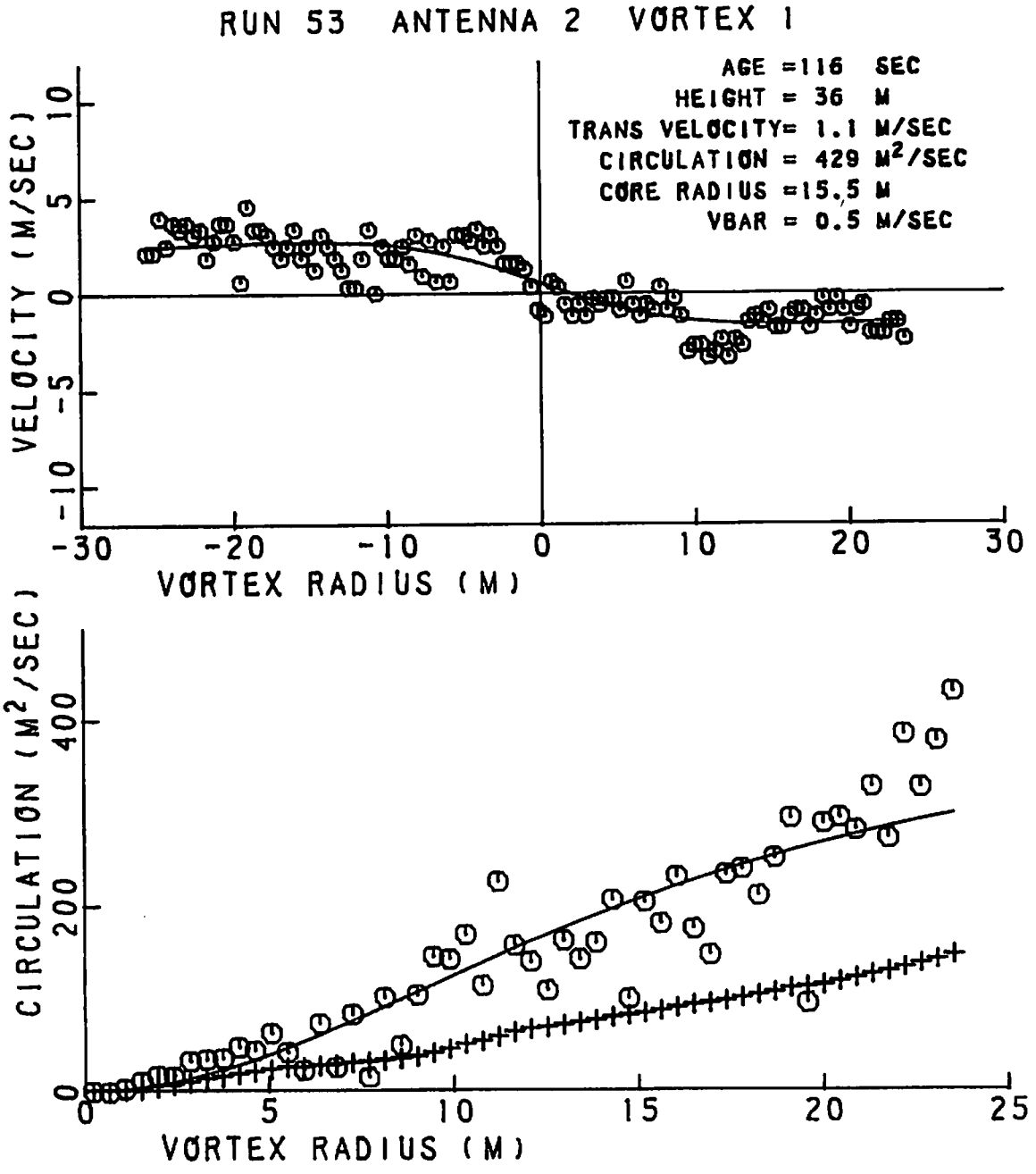

FIGURE 402. VELOCITY AND CIRCULATION PROFILES FOR RUN 53, ANTENNA 2

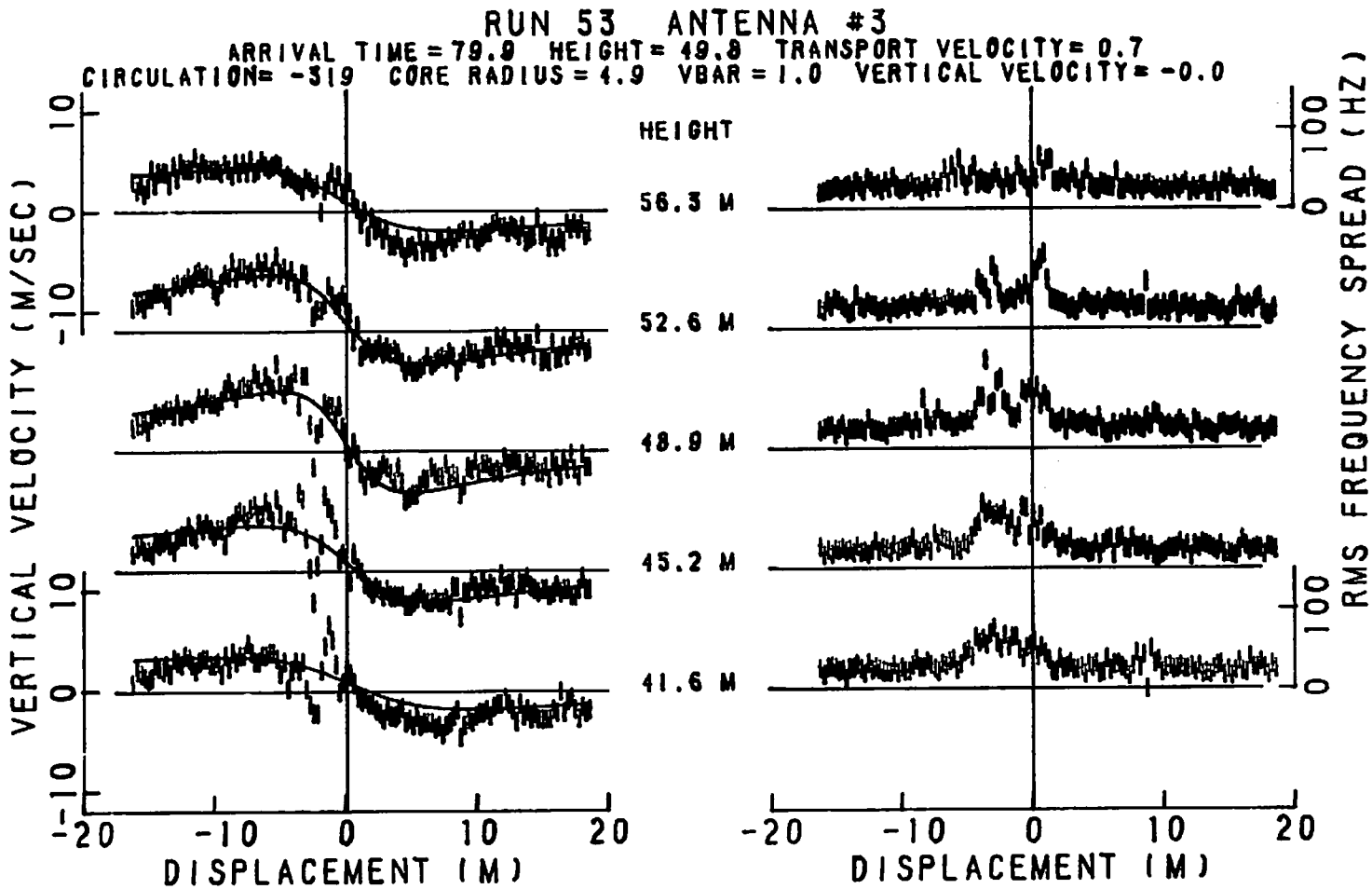

FIGURE 403. VELOCITY AND SPECTRAL WIDTH PROFILES FOR RUN 53, ANTENNA 3

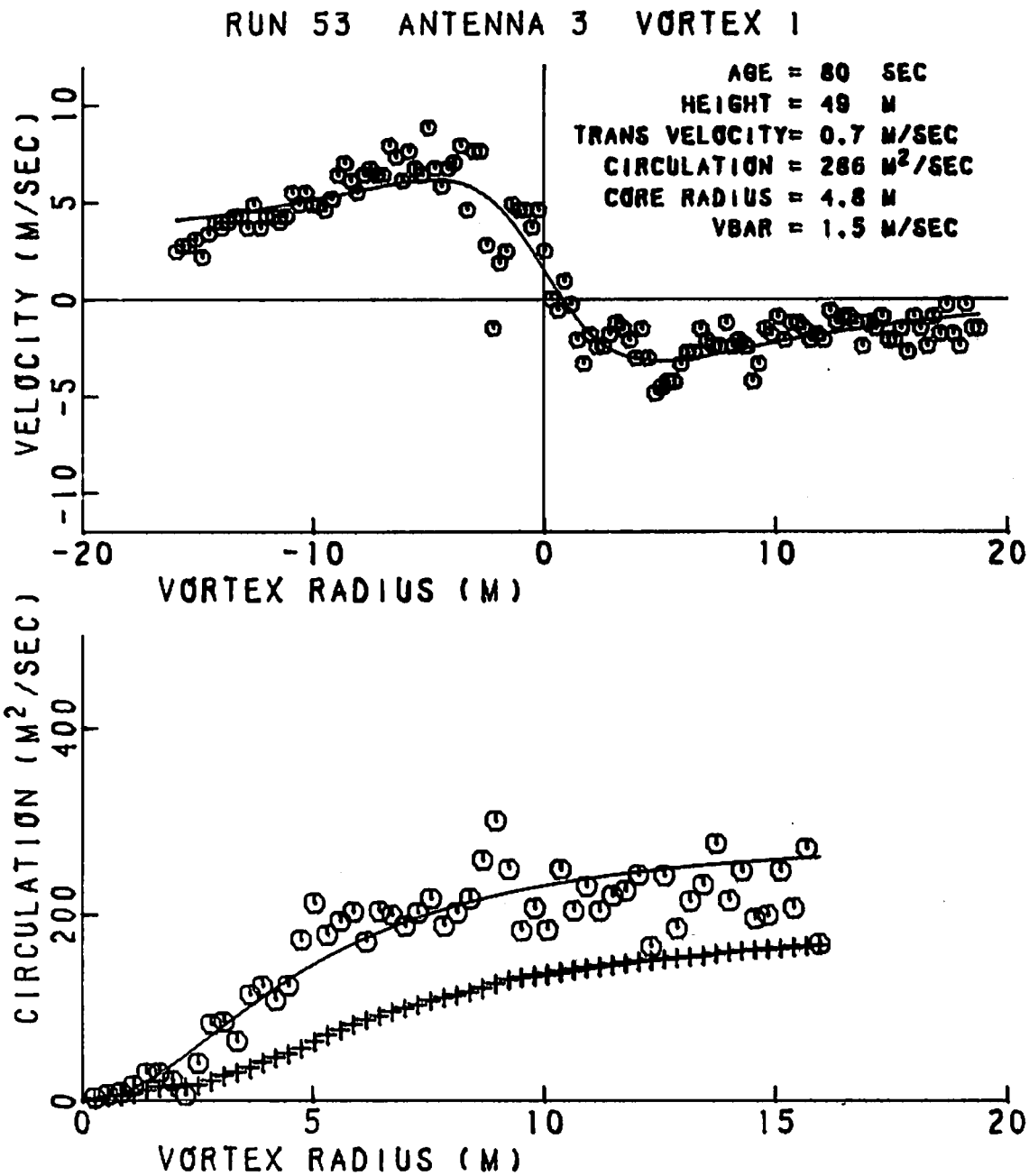

FIGURE 404. VELOCITY AND CIRCULATION PROFILES FOR RUN 53, ANTENNA 3

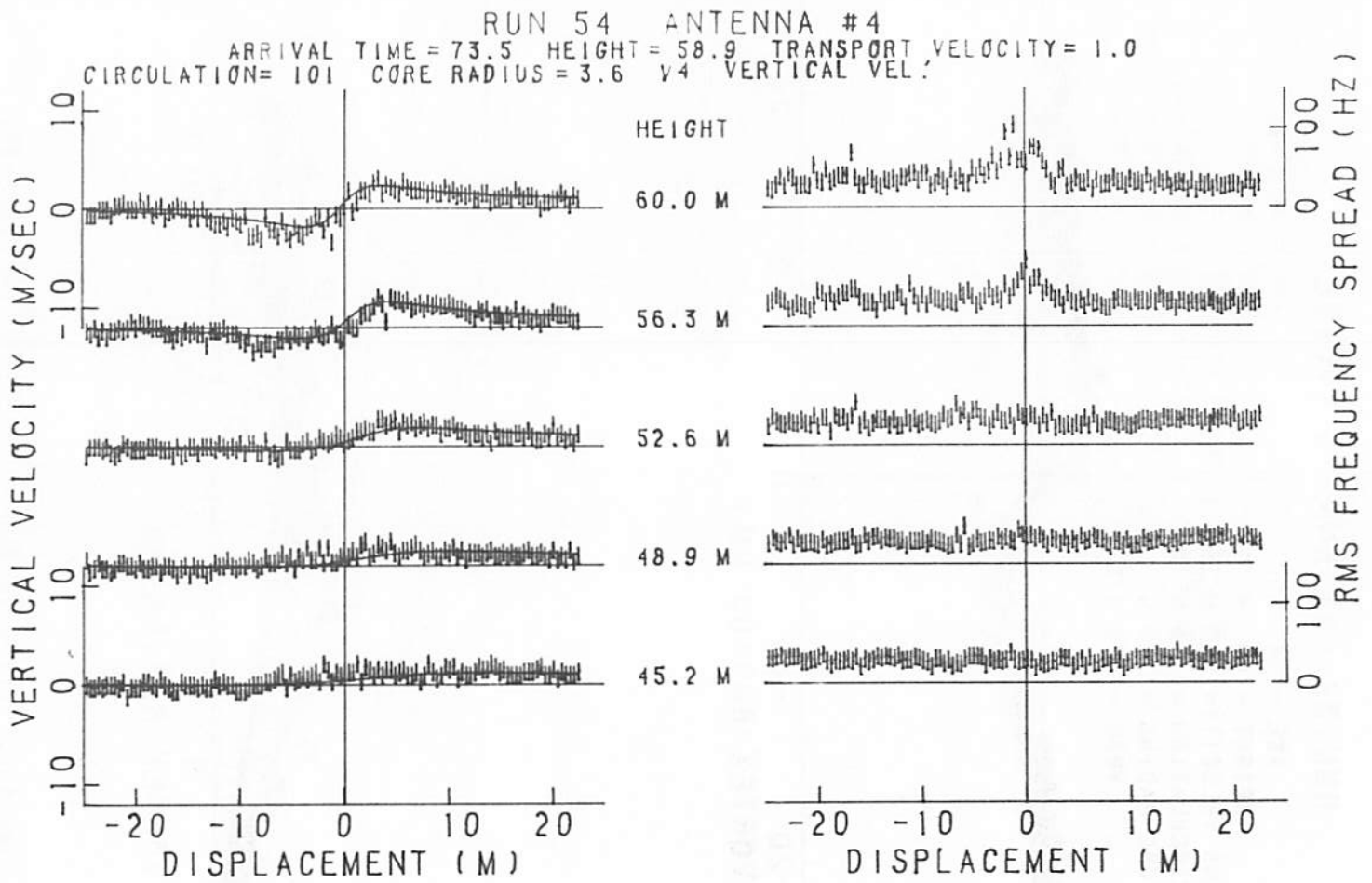

FIGURE 405. VELOCITY AND SPECTRAL WIDTH PROFILES FOR RUN 54, ANTENNA 4

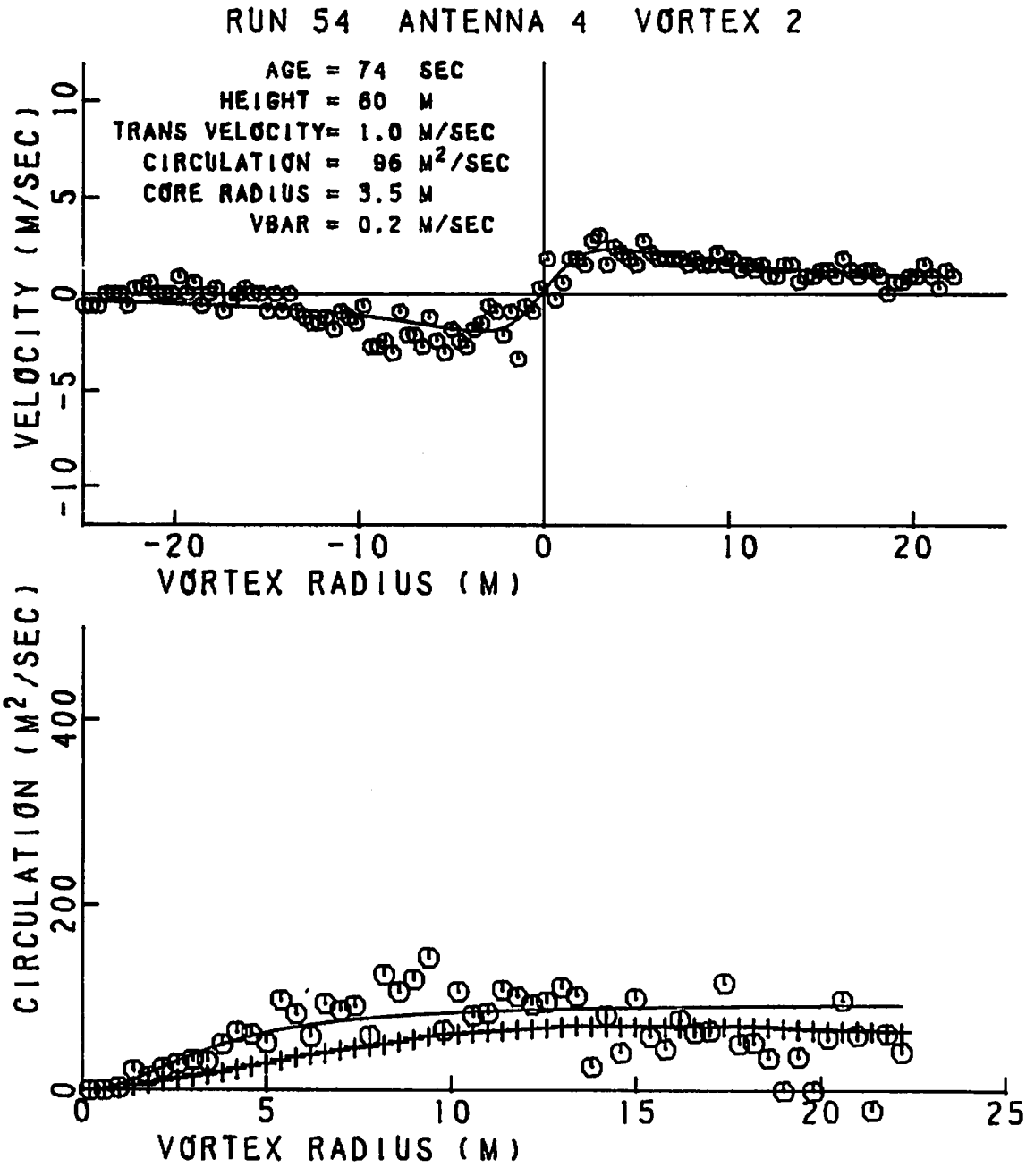

FIGURE 406. VELOCITY AND CIRCULATION PROFILES FOR RUN 54, ANTENNA 4

APPENDIX F
REFERENCES

1. Tombach, I.H., Bate, E.R., Jr., and MacCready, P.B., Jr., "Investigation of the Motion and Decay of the Vortex Wake of a Light Twin-Engine Aircraft," AV FR439, Oct. 1974, AeroVironment Inc., Pasadena, CA.

2. Barber, M.R., Kurkowski, R.L., Garodz, L.J., Robinson, G.H., Smith, H.J., Jacobsen, R.A., Stinnett, G.W., Jr., McMurtry, T.C., Tymczyszyn, J.J., Devereaux, R.L., and Bolster, A.J., "Flight Test Investigation of the Vortex Wake Characteristics Behind a Boeing 727 During Two-Segment and Normal ILS Approaches," FAA-NA-75-151, Jan. 1975, NASA Dryden Flight Research Center, Edwards, CA.

3. Tombach, I.H., Lissaman, P.B.S., Mullen, J.B., and Barker, S.J., "Aircraft Vortex Wake Decay Near the Ground," FAA-RD-77-46, May 1977, AeroVironment Inc., Pasadena, CA.

4. Brashears, M.R., Logan, N.A., and Hallock, J.N., "Effect of Wind Shear and Ground Plane on Aircraft Wake Vortices," J. Aircraft, Vol. 12, No. 10, Oct. 1975, p. 830-833.

5. Crow, S.C., "Stability Theory for a Pair of Trailing Vortices," A.I.A.A. J., Vol. 8, No. 12, Dec. 1970, p. 2172-2179.

6. Crow, S.C. and Bate, E.R., Jr., "Lifespan of Trailing Vortices in a Turbulent Atmosphere," J. Aircraft, Vol. 13, No. 7, July 1976, p. 476-482.

7. Tombach, I.H., Crow, S.C., and Bate, E.R., Jr., "Investigation of Vortex Wake Stability Near the Ground," AFOSR TR-75-1501, July 1975, AeroVironment Inc., Pasadena, CA.

8. Tombach, I.H., "Observations of Atmospheric Effects on Vortex Wake Behavior," J. Aircraft, Vol. 10, No. 11, Nov. 1973, p. 641-647.

9. Hallock, J.N., Winston, B.P., Burnham, D.C., Sullivan, T.E., McWilliams, I.G., and Wood, W.D., "Joint US/UK Vortex Tracking Program at Heathrow International Airport, Vol. II: Data Analysis," FAA-RD-76-58, II, Nov. 1977, DOT Transportation Systems Center, Cambridge, MA.

10. Hallock, J.N., Winston, B.P., Sullivan, T.E., and Burnham, D.C., "TSC Wake Vortex Data Base and Applications," In: Proceedings of the Aircraft Wake Vortices Conference, FAA-RD-77-68, June 1977, DOT Transportation Systems Center, Cambridge, MA.

11. Hallock, J.N., "Monitoring Wake Vortex Strength Decay Near the Ground," J. Aircraft, Vol. 13, No. 10, Oct. 1976, p. 830-832.

12. Krause, M.C., Morrison, L.K., Craven, C.E., Logan, N.A., and Lawrence, T.R., "Development of Theory and Experiments to Improve Understanding of Laser Doppler Systems," TR D306632, June 1973, Lockheed Missiles & Space Company, Huntsville, AL.

13. Brashears, M.R., Lawrence, T.R., and Zalay, A.D., "Mobile Laser Doppler System Check Out and Calibration," FAA-RD-77-48, Sep. 1976, Lockheed Missiles & Space Company, Huntsville, AL.

14. Sonnenschein, C.M. and Horrigan, F.A., "Signal to Noise Relationships for Coaxial Systems that Heterodyne Backscatter from the Atmosphere," Applied Optics, Vol. 10, No. 7, July 1971, p. 1600-1604.

15. Garodz, L.J., Lawrence, D.M., and Miller, N.J., "Measurement of the Trailing Vortex Systems of Large Transport Aircraft Using Tower Flyby and Flow Visualization," FAA-RD-75-127, Jan. 1976, National Aviation Facilities Experimental Center, Atlantic City, NJ.

16. Brashears, M.R. and Zalay, A.D., "Laser Doppler Velocimeter Measurements of B-747 Wake Vortex Characteristics," FAA-RD-77-85, Sep. 1977, Lockheed Missiles & Space Company, Huntsville, AL.

17. Bilbro, J.W., Jeffreys, H.B., Weaver, E.A., Huffaker, R.M., Craig, G.D., George, R.W., and Marrero, P.J., "Laser Doppler Velocimeter Wake Tests," FAA-RD-76-11, Mar. 1976, NASA Marshall Space Flight Center, Huntsville, AL.

18. Hoffman, E.R. and Joubert, P.M., "Turbulent Line Vortices," J. Fluid Mechanics, Vol. 16, Part 3, July 1963, p. 395-411.

19. Lamb, H., Hydrodynamics, 6th edition, Dover, NY, 1945, p. 222.

20. Burnham, D.C., Sullivan, T.E., and Wilk, L.S., "Measurement of Wake Vortex Strength by Means of Acoustic Back Scattering," J. Aircraft, Vol. 13, No. 11, Nov. 1976, p. 889-894.

21. Little, C.G., "Acoustic Methods for the Remote Probing of the Lower Atmosphere," Proc. IEEE, Vol. 57, No. 4, Apr. 1969, p. 571-578.

22. Tymczyszyn, J.J. and Barber, M.R., "Techniques for Early Demise of Vortices – A Pilot's View," In: Proceedings of Aircraft Wake Vortices Conference, FAA-RD-77-68, June 1977, DOT Transportation Systems Center, Cambridge MA.

23. Burnham, D.C., Kodis, R.D., and Sullivan, T.E., "Observations of Acoustic Ray Deflection by Aircraft Wake Vortices," J. Acoustical Soc., Vol. 52, No. 1, (Part 2), Mar. 1972, p. 431-433.

24. Rossow, V.J., "Alleviation of Lift-Generated Wakes by Vortex Interactions," In: Proceedings of the Aircraft Wake Vortices Conference, FAA-RD-77-68, June 1977, DOT Transportation Systems Center, Cambridge MA.

25. Church, E. and Quinn, A.O., Elements of Photogrammetry, Syracuse Univ. Press, Syracuse, NY, 1948, p. 7-27.

26. Merritt, E.L., Analytical Photogrammetry, Pitman, New York, NY, 1958, p. 80-134.

27. Baker, W.H., Elements of Photogrammetry, Ronald Press, New York, NY, 1960, p. 113-149.

220 copies

*U.S. GOVERNMENT PRINTING OFFICE: 1979 — 600-821/324

U.S. DEPARTMENT OF TRANSPORTATION
RESEARCH AND SPECIAL PROGRAMS ADMINISTRATION
TRANSPORTATION SYSTEMS CENTER
KENDALL SQUARE, CAMBRIDGE, MA. 02142

OFFICIAL BUSINESS
PENALTY FOR PRIVATE USE, $300

POSTAGE AND FEES PAID
U.S. DEPARTMENT OF TRANSPORTATION
613